AD-A009 659

AIRFRAME/PROPULSION INTERFERENCE

Advisory Group for Aerospace Research and
Development
Paris, France

March 1975

REPORT DOCUMENTATION PAGE

1. Recipient's Reference	2. Originator's Reference	3. Further Reference	4. Security Classification of Document
	AGARD-CP-150		UNCLASSIFIED

5. Originator	Advisory Group for Aerospace Research and Development North Atlantic Treaty Organization 7 rue Ancelle, 92200 Neuilly sur Seine, France

6. Title	Airframe/Propulsion Interference

7. Presented at	Rome, Italy

8. Author(s)	Various	9. Date	March 1975

10. Author's Address	Various	11. Pages	419

12. Distribution Statement	This document is distributed in accordance with AGARD policies and regulations, which are outlined on the Outside Back Covers of all AGARD publications.

13. Keywords/Descriptors		14. UDC
Air intakes　　　　　Afterbodies Jet engine inlets　　　Military aircraft Airframes　　　　　　Design Interactions　　　　　Proceedings		533.697.2

15. Abstract

Proceedings of the Fluid Dynamics Panel Symposium held in Rome, Italy, 3–6 September 1974. Twenty-seven papers and Round Table Discussion dealing with "Air Intakes and Airframe Inlet Interactions", "Nozzle/Aftbody Flow Fields and Airframe Interference", "Windtunnel Testing and Correlation with Flight Test" and "Integration Design and Accounting Procedures". Symposium objectives were updating of research information on airframe/propulsion interference effects, discussion in relation to the practical problems in design of combat and transport aircraft, and identification of gaps in present knowledge.
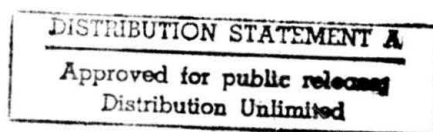
AGARD-CP-150

NORTH ATLANTIC TREATY ORGANIZATION

ADVISORY GROUP FOR AEROSPACE RESEARCH AND DEVELOPMENT

(ORGANISATION DU TRAITE DE L'ATLANTIQUE NORD)

AGARD Conference Proceedings No.150

AIRFRAME/PROPULSION INTERFERENCE
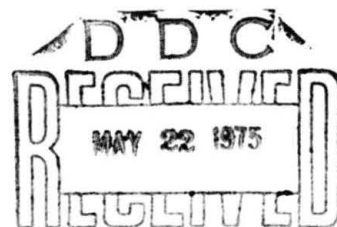
Papers and Discussion of the Fluid Dynamics Panel Symposium
held at Rome, Italy, 3–6 September 1974.

1. a

THE MISSION OF AGARD

The mission of AGARD is to bring together the leading personalities of the NATO nations in the fields of science and technology relating to aerospace for the following purposes:

— Exchanging of scientific and technical information;

— Continuously stimulating advances in the aerospace sciences relevant to strengthening the common defence posture;

— Improving the co-operation among member nations in aerospace research and development;

— Providing scientific and technical advice and assistance to the North Atlantic Military Committee in the field of aerospace research and development;

— Rendering scientific and technical assistance, as requested, to other NATO bodies and to member nations in connection with research and development problems in the aerospace field;

— Providing assistance to member nations for the purpose of increasing their scientific and technical potential;

— Recommending effective ways for the member nations to use their research and development capabilities for the common benefit of the NATO community.

The highest authority within AGARD is the National Delegates Board consisting of officially appointed senior representatives from each member nation. The mission of AGARD is carried out through the Panels which are composed of experts appointed by the National Delegates, the Consultant and Exchange Program and the Aerospace Applications Studies Program. The results of AGARD work are reported to the member nations and the NATO Authorities through the AGARD series of publications of which this is one.

Participation in AGARD activities is by invitation only and is normally limited to citizens of the NATO nations.

FOREWORD

This Symposium dealt with current work on the prediction and measurement in detail of the performance of subsonic, transonic and supersonic aircraft where integrated effects of aerodynamics and propulsion are involved. The objectives were an up-dating of research information on airframe/propulsion interference effects, discussion of these effects in relation to practical problems in the design of combat and transport aircraft, and identification of gaps in the present knowledge and understanding of the fluid flow phenomena of inlet, airframe, propulsion and nozzle combinations which should be taken into account in future research programmes.

The Symposium included a presentation of results by a joint PEP/FDP Working Group on Nozzle Testing Techniques in Transonic Flow, but these will be reported separately in an AGARDograph and are not included in these Proceedings. A Round Table Discussion, initiated by invited experts, concluded the Symposium and this is reported here.

The Symposium was held at the Palazzo Aeronautica, Rome, at the invitation of the Italian National Delegates to AGARD.

CONTENTS

PROBLEMES D'INTERACTIONS ENTRE LA PRISE D'AIR ET L'AVION

par Jacky LEYNAERT[*]

Office National d'Etudes et de Recherches Aérospatiales (ONERA)
92320 Châtillon (France)

Résumé

La définition des termes d'interaction entre la prise d'air et l'avion, et les voies théoriques et expérimentales suivies pour traiter le problème en subsonique et en supersonique sont rappelées.

Quelques exemples d'influence d'un écoulement non uniforme sur le fonctionnement d'une prise d'air supersonique, et d'adaptation de la prise d'air à ce champ, notamment en vol avec incidence ou dérapage, sont ensuite précisés.

INTAKE-AIRFRAME INTERACTION PROBLEMS

Abstract

The definition of the interaction terms between the air intake and the airframe, and the theoretical and experimental tools used to study the problem for subsonic or supersonic aircraft are presented.

Some examples of the influence of a non-uniform upstream flow on the internal flow characteristics of supersonic intakes are given, and some means of adjusting the inlet to a non-uniform flow, mainly for flight with incidence or yaw, are analysed.

Introduction

Les moteurs actuels des avions subsoniques nécessitent des fuseaux de grande dimension dont l'adaptation à la cellule constitue un problème majeur en aérodynamique. Si l'utilisation de moteurs double flux à taux de dilution appréciable était envisagée pour les avions supersoniques, en vue notamment de réduire le bruit, l'importance, déjà capitale pour ces avions, des études de prises d'air, d'arrière-corps, et d'intégration de l'ensemble de propulsion, en serait encore accentuée.

Une définition des termes d'interaction entre les éléments de cet ensemble et l'avion sera d'abord proposée.

Les calculs et méthodes d'essai concernant l'installation des fuseaux moteurs d'avion subsonique seront ensuite rappelés, et quelques remarques préciseront le problème des prises d'air à proximité du sol.

Les études de champ aérodynamique et d'interaction en supersonique seront enfin mentionnées, et des indications particulières seront données sur l'adaptation d'une prise d'air bidimensionnelle placée sous une voilure, en tenant compte notamment des effets du dérapage.

Bilan d'installation des moteurs

Pour établir le bilan de l'installation des moteurs à une altitude de vol et à un nombre de Mach donnés et préciser les termes d'interaction, il est nécessaire de tenir compte des effets de portance et de moment. On supposera pour cela qu'une configuration de l'avion non motorisé ou planeur a été définie, et que sa polaire équilibrée est donnée, le poids et le centre de gravité étant ceux de l'avion complet.

Soit P le point de cette polaire dont la portance Z équilibre le poids de l'avion complet. Au voisinage de P la polaire sera assimilée à sa tangente de pente $\Delta x/\Delta z = tg\,\mathcal{E}$ (fig. 1).

Soit P' le point de la même polaire qui correspond à l'incidence de vol en palier de l'avion complet. La différence de portance ΔZ du planeur de P' à P représente la portance de l'installation motrice.

La traînée en P', traînée du planeur à l'incidence de vol, est égale par définition à la poussée F de l'installation motrice. Sans portance ΔZ, l'incidence de vol de l'avion serait celle du point P ; le supplément de traînée correspondant, $\Delta X = \Delta Z\,tg\,\mathcal{E}$, que permet d'éviter la portance du fuseau, sera pris en compte en désignant par poussée corrigée Fc de l'installation motrice la somme Fc = F + $\Delta Z\,tg\,\mathcal{E}$. (Cette poussée corrigée est égale à la traînée du planeur en P, ce qui la définit directement).

---

[*] Chef de Division d'Aérodynamique Appliquée.

Si l'installation motrice est analysée en plusieurs éléments, tout élément i donnant une contribution ΔZ_i à la portance sera de même affecté d'une correction de poussée $\Delta Z_i tg\mathcal{E}$ comme indiqué sur la figure 2 ; la somme de ces deux éléments (positifs ou négatifs selon qu'il s'agit de termes de poussée ou de trainée) restituera ainsi Fc.

On notera que la portance et la trainée dues à l'équilibrage d'un moment éventuel doivent être comprises dans la définition de chaque terme élémentaire, comme elles le sont dans F.

Le moteur présente des caractéristiques nominales définies par le motoriste, pour des efficacités nominales de prises d'air et de tuyères données. Si ce moteur est supposé ajouté sans interaction au planeur précédent, on montre aisément que l'installation optimale, du point de vue propulsif, consiste à dévier le jet vers le bas d'un angle $\alpha j = \mathcal{E}$: soit $q_m V_j$ la poussée du jet supposé adapté à la pression p_∞ ; le jet étant dévié de αj, la portance $\Delta Z_j = q_m V_j \sin\alpha j$ permet une réduction de trainée $\Delta Z_j tg\mathcal{E}$, mais la perte de poussée vaut $q_m V_j (1 - \cos\alpha j)$; la différence, $q_m V_j (\sin\alpha j tg\mathcal{E} - 1 + \cos\alpha j)$, est bien maximale pour $\alpha j = \mathcal{E}^{(*)}$.

La poussée corrigée du jet, $q_m V_j (\cos\alpha j + \sin\alpha j tg\mathcal{E})$, est dans ce cas égale à $\dfrac{q_m V_j}{\cos\mathcal{E}}$, d'où la poussée nominale corrigée du moteur $F_{N_C} = \dfrac{q_m V_j}{\cos\mathcal{E}} - q_{m\infty} V_\infty$ (fig. 3).

La différence $F_{N_C} - F_C$ représente par définition la perte de poussée de l'installation, qui inclut les termes d'interaction. Pour faire apparaître ceux-ci, la perte de poussée sera analysée en pertes internes et trainées externes (fig. 4).

Les pertes internes comportent notamment :

- des termes de trainée : pièges à couche limite interne, dérivation du moteur, prises de débit auxiliaires, fuite par défaut d'étanchéité...

- des pertes de poussée, dues à une inclinaison non optimale du jet, et à des efficacités de tuyère et de prise d'air inférieures à leurs valeurs nominales

- la trainée d'équilibrage des forces internes

La trainée externe comprend de même (fig. 5) :

- la trainée d'un déviateur de couche-limite à l'amont de la prise d'air,

- la trainée de carène de la prise d'air

- la trainée additive (la prise d'air étant supposée capter son débit maximum)

- la trainée de refoulement d'un excédent de débit par la prise d'air, lorsqu'elle ne fonctionne pas à son débit maximum

- des trainées diverses : mâts, supports...

- la trainée d'arrière-corps (trainée de retreint, de passages auxiliaires, de culot)

- la trainée d'interaction.

La trainée d'interaction représente par conséquent la différence (positive ou négative) entre la poussée nominale corrigée du moteur et la poussée corrigée de l'installation motrice, déduction faite des pertes de poussée interne et des trainées propres des différents éléments de la motorisation, tous ces termes étant pris au sens corrigé défini plus haut.

La recherche d'un terme d'interaction optimisé est un élément important des études d'installation des moteurs sur les avions. Dans cette recherche, il faut évidemment considérer que les différents termes énumérés ne sont pas indépendants entre eux ; à partir d'une première étude de définition, il sera par exemple préférable pour des calculs d'optimisation de choisir comme polaire de référence celle d'un planeur équipé du fuseau choisi en première approximation, afin de mieux découpler les termes de trainée propre et de trainée d'interaction. De plus, d'autres éléments interviennent (poids, encombrement, ...) et tous sont à juger sur l'ensemble de la mission. La démarche proposée peut néanmoins servir de guide, et orienter les compromis nécessaires. Les aspects plus généraux du problème sont traités par exemple en références [2] et [3].

Installation des moteurs des avions subsoniques

Le choix de la configuration générale de l'installation : moteurs à l'arrière, sur l'aile, ..., repose sur diverses considérations dont certaines ne sont qu'indirectement liées à l'aérodynamique, comme par exemple le problème d'équilibrage compte tenu des déplacements du centre de gravité sur les avions à grand nombre de passagers, le flottement des structures, le bruit, le garde au sol, l'accessibilité des moteurs, etc... quelques unes de ces questions sont exposées par exemple en références [4] et [5].

Du point de vue aérodynamique, la règle élémentaire de la loi des aires sert encore souvent de base à la définition de l'installation des fuseaux-moteurs ([4 à 7]).

Dans le cas de fuseaux moteurs solidaires de la voilure, l'étude d'une répartition de portance elliptique, compte tenu des fuseaux, pour obtenir la trainée induite minimale, peut orienter la définition de l'ensemble aile + fuseau [8].

(*) On rectifiera, selon ce schéma, une erreur dans la définition de l'orientation optimale du jet et de Tn dans l'article "Engine installation aerodynamics" du document AGARD LS 67 "prediction methods for aircraft aerodynamic characteristics (1974)".

Les grandes lignes de l'installation des moteurs étant fixées, le calcul du champ d'interaction et de l'écoulement local autour d'une forme de fuseau moteur donnée permet de relever les zones de fortes survitesses ou de gradients de pression élevées, et, par des retouches successives, d'optimiser la configuration choisie [9], [10].

Les méthodes de calcul tridimensionnelles ne permettent encore pratiquement que de traiter l'écoulement incompressible, ou l'écoulement compressible par la transformation de Prandtl-Glauert ; on peut espérer que dans un proche avenir les travaux en cours permettront d'étendre ces calculs au transsonique.

La figure 6 de G.M. Bowes [11] montre une étude d'optimisation de la portance compte tenu des fuseaux selon J.L. Lundry [8], et reproduit un champ de vitesse tracé autour du mât support d'un ensemble aile-mât-nacelle optimisé. La portance latérale du mât, que traduit ce champ de vitesse, est une condition qui résulte du calcul d'optimisation de la traînée induite, par une distribution convenable de la portance en envergure.

L'étude expérimentale des interactions entre les fuseaux moteurs et l'avion est effectuée à l'aide de maquettes munies de fuseaux «motorisés». Les dispositifs actuels ne permettent généralement pas une représentation simultanée des débits captés et des jets. Une solution très approchée consiste à équiper le fuseau d'une soufflante miniaturisée entraînée par une turbine à air comprimé ; dans ce cas l'écart des coefficients de débit captés entre la maquette et le fuseau réel est peu élevé.

Le système de trompe représenté figure 7 permet également une simulation acceptable des jets ; pour minimiser l'influence d'une insuffisance du débit capté, on peut, dans ce cas, prévoir d'adapter la section d'entrée et la forme avant du fuseau au débit de la maquette, de façon à conserver autour du carénage un écoulement sans survitesse excessive.

Effet de sol

Un point particulier des études expérimentales d'interactions concernant les fuseaux subsoniques est celui de l'effet de sol.

Au point fixe, la couche limite au sol induite par l'aspiration de la prise d'air forme un tourbillon qui dégrade l'écoulement interne le long du profil inférieur (fig. 8).

Lorsque la couche limite au sol est amplifiée par un vent frontal ou transversal, le tourbillon prend d'abord une importance accrue, avant d'être «soufflé». La distorsion de l'écoulement interne passe ainsi par un maximum, et présente le profil de pression d'arrêt reproduit sur la figure.

Lorsqu'il s'agit du roulement au sol, sans vent, cette couche limite est inexistante, et le tourbillon ne peut se former. La simulation en soufflerie de l'effet de sol au décollage nécessite par conséquent la présence d'une paroi sans couche-limite. Ceci est confirmé par la visualisation de l'écoulement effectuée au tunnel hydrodynamique avec paroi fixe, et avec paroi mobile (méthode du «tapis roulant») (figure 8) : le tourbillon disparaît dans le second cas. Le même résultat pourrait sans doute être obtenu par un soufflage de la couche-limite de plancher, méthode plus simple à mettre en œuvre qu'une paroi mobile.

Au point fixe avec vent, un autre paramètre que la couche limite au sol à prendre en considération est le gradient horizontal de vent : ce gradient favorise et intensifie la formation du tourbillon, dans le sens préférentiel correspondant. La figure 9, selon D.E. Glenny [12], montre l'influence du «Nombre de Rossby», Ro, qui caractérise l'inverse du gradient de vent. L'intensité du tourbillon est ici repérée par la limite d'ingestion par l'entrée d'air de billes calibrées posées au sol. La courbe tracée montre que, pour un débit d'entrée donné, caractérisé par une vitesse V_1, le tourbillon n'est soufflé que pour une vitesse de vent V_c plus élevée lorsque le nombre de Rossby diminue, c'est-à-dire lorsque le gradient de vent augmente. Une limite inférieure d'ingestion est indiquée, à vitesse de vent quasi nulle ; elle montre que, dans ce cas, le tourbillon formé au sol en l'absence de vent est d'intensité suffisamment réduite pour qu'il n'y ait plus d'ingestion.

Des résultats théoriques et expérimentaux relatifs à la formation et à l'intensité du tourbillon sont également reportés référence [13].

Interactions prises d'air-avion en supersonique

Dans la définition des prises d'air en supersonique se pose en premier lieu, comme en subsonique, le choix de la configuration générale de l'avion et de l'installation des moteurs.

Sur les avions de grande dimension, il est généralement possible de placer les prises d'air à l'intrados des ailes, pour profiter de la compression pratiquement isentropique de l'écoulement par la voilure. Des fuseaux de section rectangulaire, profilés de telle sorte que leurs faces latérales épousent la forme des lignes de courant d'intrados, présentent l'intérêt de ne pas induire par ces flancs de traînée d'onde parasite. Les lignes générales des fuseaux «Concorde» répondent à cette conception (figure 10a). Lorsque les flancs s'écartent d'une telle orientation, un calcul des termes d'interaction entre le fuseau et la voilure peut être effectuée par une méthode d'écoulement supersonique linéarisée pour en optimiser les effets.

Des fuseaux de révolution placés vers la partie arrière, à l'intrados de la voilure, bénéficient d'une compensation entre la détente locale induite par la courbure de la voilure, et la compression de l'écoulement par le carénage avant du fuseau ; le champ résultant permet par ailleurs de réduire la traînée induite de l'aile par un effet de portance locale favorable [14]. Le bilan des termes d'interaction reporté figure 10b d'après A. Sigalla et T. Hallstaff [15] est dans ce cas nettement positif.

Sur les avions militaires, les prises d'air sont directement tributaires du champ du fuselage avant, qu'elles soient accolées au fuselage pour bénéficier d'une structure bien intégrée et d'une protection en dérapage par le champ local, ou séparées pour former deux fuseaux distincts, de traînées d'arrière corps plus favorables. Dans chaque cas, la définition du fuselage est alors essentielle par son

influence sur le fonctionnement des prises d'air aux différentes configurations de vol de l'avion [16, 17].

Calcul du champ du fuselage

Le calcul par la théorie des caractéristiques semi linéarisées autour d'un écoulement initial de révolution ne semble pas suffisant pour donner une description satisfaisante du champ du fuselage lorsque l'incidence dépasse quelques degrés si l'on en juge par les comparaisons reportées figure 11, selon P. Antonatos, L. Surber, D. Stava [17].

La méthode des caractéristiques en écoulement tridimensionnel est actuellement développée pour traiter ce problème en fluide parfait.

La méthode de Babenko,..., [18] permet de calculer par tranches successives l'écoulement derrière une nappe de choc unique ; un résultat de calcul obtenu par cette méthode à M = 6 sur un fuselage de type ogive-cylindre en incidence est reporté figure 12 à titre d'illustration. Le champ calculé sur la partie avant du fuselage est identique au champ réel, comme le montre la coïncidence du choc calculé avec le choc visualisé par la strioscopie. Des difficultés numériques apparaissent plus en aval, en raison des nombres de Mach très élevés calculés à la surface du cylindre dans ce cas particulier. L'expérience montre que ces zones localisées de très faibles pressions correspondent en réalité à l'établissement de tourbillons visqueux d'intrados.

Une méthode plus élaborée de calcul en fluide visqueux autour d'un corps élancé est illustrée figure 13, selon L. Walitt, J. Trulio, L. King [19]. Les auteurs notent que le calcul, effectué selon les équations de Navier-Stokes , pourrait être adapté au cas d'une viscosité turbulente ; la condition de paroi retenue est une vitesse tangente à la surface, et de composante nulle dans le plan de coupe normal à l'axe de l'avion. Cette hypothèse permet un calcul découplé, par tranches successives.

La méthode permet de faire apparaître les tourbillons que forme la couche limite d'un fuselage en incidence, l'effet visqueux transversal étant déterminant dans ce type d'écoulement. Appliquée au cas d'un fuselage avec cockpit (fig. 13) elle donne une bonne représentation de l'écoulement sur la partie avant du fuselage, mais l'interaction du choc de cockpit avec la couche limite, qui est un effet visqueux longitudinal, ne peut être prise en compte par le calcul, ce qui expliquerait l'écart avec l'expérience au voisinage et en aval de ce choc.

L'ensemble de ces résultats montre que si les méthodes de calcul actuelles permettent une prévision satisfaisante du champ supersonique du fuselage pour diverses configurations élancées, la mise au point de méthodes plus élaborées est nécessaire pour des configurations complexes peu profilées, du type fuselage avec cockpit, dont l'étude reste encore expérimentale.

Adaptation de la prise d'air au champ local

La configuration générale de la prise d'air et le champ local en amont de l'entrée étant donnés, l'étude peut se poursuivre par la recherche d'une adaptation de la prise d'air à ce champ local.

Un exemple de champ moyen d'écoulement devant une entrée d'air placée sous une voilure élancée, en incidence, est présenté figure 14. L'intrados se caractérise par une divergence des lignes de courant, et par une réduction des nombres de Mach locaux quand on s'écarte du fuselage vers le bord d'attaque de l'aile.

Une première adaptation consiste à rechercher l'orientation optimale d'une prise d'air donnée, dans ce champ. Dans le cas d'une prise d'air bidimensionnelle, les essais ont conduit à donner à l'entrée un dérapage un peu supérieur au dérapage moyen des lignes de courant. Ce dérapage accentué permet en effet de comprimer davantage l'écoulement au nombre de Mach le plus élevé qui attaque le flanc le plus proche du fuselage ; l'optimum, du point de vue efficacité et uniformité de l'écoulement interne, est atteint lorsque l'on obtient des nombres de Mach internes à peu près égaux sur chaque flanc. Dans ces conditions, l'entrée d'air offre pratiquement les mêmes performances qu'en écoulement uniforme. Sa sensibilité au dérapage est toutefois assez différente, et nettement dissymétrique. Les comparaisons avec les essais en écoulement uniforme montrent en effet que le comportement d'ensemble de la prise d'air en dérapage est dominé par l'écoulement local au droit du flanc dont la face externe est face au vent.

Ce comportement est résumé ci-après, selon une étude plus complète reportée en référence [20].

Adaptation de la prise d'air au dérapage

Les figures 15a et 15b représentent l'effet de contournement du flanc latéral observé en dérapage. Le bord d'attaque du flanc, situé derrière la nappe de choc engendrée par le dièdre amont de la prise d'air, est subsonique ; le contournement de ce bord d'attaque par l'écoulement transversal forme alors un tourbillon attaché, analogue au tourbillon d'intrados d'une aile delta à bords vifs attaquée en incidence. La nappe tourbillonnaire qui en résulte est évidemment néfaste à l'écoulement interne.

Comme indiqué sur la figure, une échancrure du flanc est un moyen simple d'adaptation au champ local ; une telle découpe provoque en effet une déviation locale des lignes de courant vers l'extérieur du flanc, dans un sens qui s'oppose au dérapage, ce qui permet d'éviter la formation du tourbillon.

Un second effet du dérapage résulte de l'inclinaison locale plus prononcée de la nappe de choc attachée au dièdre amont. Cet effet se comprend aisément quand le flanc a une forme d'étrave qui s'avance en amont de l'entrée (fig. 15c) : l'écoulement latéral incident est dévié suivant la face interne du flanc par une détente supersonique analogue à une détente de Prandtl-Meyer, et les nombres de Mach près du flanc sont plus élevés, d'où un choc attaché au dièdre amont plus incliné localement. Lorsque le flanc n'est pas débordant

(bord d'attaque subsonique rectiligne ou échancré), un effet moins élémentaire à concevoir mais de même sens général se produit également. Si cette détente provoquée par le dérapage a pour effet de faire pénétrer la nappe de choc à l'intérieur de la carène, selon la figure 15c, il en résulte une interaction forte avec la couche limite interne initiale d'où une dégradation de la pression d'arrêt locale et un épaississement de la couche limite susceptible de conduire à un décollement interne. Dans le cas d'une prise d'air du type représenté sur la figure, conçue de façon à permettre un diffuseur subsonique assez court, ce décollement apparaît le long de la carène au niveau de l'entrée du diffuseur. Une aspiration de la couche limite à ce niveau permet alors d'éviter le décollement, et contribue à améliorer de façon très sensible l'efficacité de la prise d'air et la distorsion de l'écoulement interne en dérapage.

Une autre solution consiste à découper localement le bord d'attaque de la carène, de telle sorte qu'il reste en retrait de la nappe de choc issue du dièdre amont, lorsque la prise d'air est en dérapage (fig. 16). Cette solution se révèle efficace, mais elle conduit à une traînée additive non négligeable, et à une légère perte d'efficacité, à dérapage nul. Elle est par contre très avantageuse lorsque le flanc latéral forme une étrave débordante, car elle permet de dévier hors de la prise d'air le sillage d'un bulbe de décollement de la couche limite du flanc, au point de convergence des chocs près du bord d'attaque de la carène.

Les résultats d'essai d'une telle prise d'air munie en outre d'une aspiration de la couche limite à l'entrée du diffuseur subsonique, sont présentés sur la figure 16, et comparés à une configuration «de référence», sans découpe ni aspiration. Le débit d'aspiration est de l'ordre de 0,5% du débit total ; le nombre de mach M = 2,05 est pratiquement le nombre de Mach d'adaptation de la prise d'air. On notera l'amélioration obtenue en efficacité et en distorsion ; (la limite de distorsion acceptable pour un moteur est de l'ordre de -DC60 $\simeq$ 0,30).

Ces remarques sur le fonctionnement en dérapage permettent de montrer que des modifications mineures de la configuration de la prise d'air donnent des différences notables de comportement dans un champ d'écoulement non uniforme, et qu'il est possible d'adapter la géométrie pour tenir compte de ce champ. Les solutions indiquées présentent l'avantage d'être simples, mais d'autres solutions telle qu'un dièdre amont et une rampe de compression supersonique de pentes variables en envergure ont également donné des résultats favorables.

Le problème est qu'on ne sait pas actuellement calculer les configurations d'écoulement du type indiqué figure 15c ; la prévision de détachement du choc d'entrée, par exemple, qui conditionne le dessin de la carène, n'est pas encore résolu en bidimensionnel, ni, à plus forte raison, en tridimensionnel.

Il faut donc recourir à une étude expérimentale qui n'est pas non plus exempte de difficultés lorsqu'il s'agit de définir des valeurs sures d'efficacité et de coefficients de distorsion ; vu l'importance des effets de couche-limite, les essais doivent être effectués à des nombres de Reynolds représentatifs, et avec des maquettes très précises assurant la conformité des profils de bord d'attaque, par exemple. L'étude paramétrique nécessaire peut demander de ce fait des moyens importants et de longues périodes d'essais, avec tests de fidélité et de précision.

Influence externe du fonctionnement de la prise d'air

L'adaptation de la prise d'air à son environnement n'est qu'un aspect des interactions prise d'air-avion. Un autre aspect est celui de l'influence du fonctionnement de la prise d'air sur l'avion en général.

Cette influence peut résulter de phénomènes de couplage en lacet par exemple entre les modes propres de la trajectoire de l'avion et la poussée des moteurs, elle même tributaire du système de réglage des prises d'air ; il s'agit alors davantage de problèmes d'intégration des différents systèmes de contrôle [21].

Un autre cas d'influence, qui est aussi généralement le plus sévère, est celui que représente le décrochage accidentel d'un compresseur ; ce décrochage provoque un refoulement de débit qui provoque vers l'amont une onde de choc intense («hammer shock»). Comme le phénomène est pratiquement instantané, le choc remonte largement en amont de l'entrée d'air, avant que les dispositifs de décharge usuels n'aient eu le temps d'intervenir. Le pompage du moteur qui suit ce décrochage est également de grande amplitude. Un dispositif pour étudier sur une maquette les effets de ce pompage est représenté figure 17, selon E. Carter [22], ainsi que des tracés de pressions mesurées.

Le dispositif comporte un papillon tournant qui ferme alternativement le col sonique de sortie du fuseau ; le papillon est monté sur un axe creux injectant par une fente un contre-débit, dans la phase de fermeture du col. Cet ensemble permet d'obtenir une même évolution des pressions internes qu'en cas de pompage d'un moteur, comme l'indiquent les tracés comparés reportés sur la figure. Sur ces tracés relatifs à deux prises d'air bidimensionnelles placées côte à côte et séparées par une étrave débordante, on remarquera que le pompage d'un moteur entraine à l'instant du second cycle le début du pompage du moteur voisin, alors que dans des cas moins sévères (pompage d'une prise d'air sans décrochage du moteur, par exemple) l'étrave permet d'éviter toute interaction.

Ces phénomènes soumettent l'avion à des efforts instationnaires importants ; lorsque le choc émerge de l'entrée et se propage contre le flanc du fuselage ou à l'intrados de la voilure, le décollement de la couche limite pariétale par ce choc conduit à des zones d'interaction de grandes surfaces qui peuvent induire des moments considérables [17, 23]. La figure 18 illustre le pompage à M=2 d'une prise d'air semi circulaire distante de la paroi d'une hauteur de couche limite. Les deux phases extrêmes d'un cycle de pompage sont présentées. Dans la phase de refoulement du débit vers l'amont, ce débit alimente principalement un décollement de la couche limite de paroi qui s'étend très en amont de l'entrée, comme le montre la visualisation. Les prises d'air bidimensionnelles dont les rampes de compression supersonique externe sont accolées à la voilure permettent de limiter ce type d'interaction, du fait que le choc émerge du côté de la carène, à l'opposé de la rampe, et par conséquent de la surface de l'aile.

Pour équilibrer les efforts subis par l'avion en cas de pompage, des dispositifs automatiques d'actions sur les gouvernes ou sur les moteurs symétriques sont maintenant presque systématiquement installés sur les avions volant à plus de Mach 2 [21] ; dans le cas des prises d'air du Concorde, la solution retenue est par exemple une action sur la gouverne de direction qui s'oppose au dérapage et au roulis en cas de panne d'un moteur [24].

Séparation de deux entrées

Un problème local d'interaction est celui déjà mentionné d'une prise d'air sur une prise d'air voisine. Dans le cas de deux fuseaux moteurs séparés, placés contre une voilure, une ailette verticale fixée sur l'aile entre les moteurs peut permettre d'éviter toute interaction si l'écartement des moteurs est insuffisant par lui-même. Cette ailette a pour effet notamment d'arrêter l'extension latérale du décollement de la couche limite de la voilure provoqué par l'émergence du choc d'une entrée en pompage [23].

Lorsqu'il s'agit de deux prises d'air bidimensionnelles accolées, une étrave de séparation convenablement dimensionnée peut assurer l'indépendance des deux prises d'air dans toutes les conditions, sauf éventuellement dans le cas d'un décrochage accidentel d'un moteur au régime maximum en supersonique élevé, comme mentionné précédemment.

A l'occasion d'une étude d'étraves de ce type, une remarque intéressante a pu être faite qui rejoint le problème d'influence d'un écoulement non uniforme sur la prise d'air et qui est la suivante :

Lorsque l'étrave débordante est une simple plaque plane, la couche limite qui se forme sur cette plaque et qui est fortement inter-actionnée par les ondes de choc et les gradients de pression élevés dans la région d'entrée de la prise d'air conduit à une perte sensible d'efficacité (fig. 19).

Lorsque la cloison forme un dièdre qui comprime latéralement l'écoulement d'entrée, cette compression supersonique supplémentaire favorise au contraire l'efficacité, et compense l'effet de la couche limite, donnant même parfois un résultat global plus favorable, comme l'indique la figure 19.

Par ailleurs, en utilisant cet effet de compression latéral, il s'est avéré possible de réduire légèrement la compression par la rampe, ainsi que la pente de la carène qui est associée à la déviation de l'écoulement par la rampe, et qui détermine la traînée ; ceci a été obtenu tout en conservant la même efficacité.

Cette orientation vers des formes plus tridimensionnelles permettant d'optimiser la prise d'air dans son bilan efficacité-traînée mériterait sans doute d'être approfondie, malgré le poids d'une étude qui ne peut être actuellement qu'en majeur partie expérimentale.

Conclusions

Quelques problèmes d'interactions prises d'air-avion et d'optimisation d'une prise d'air dans son environnement aérodynamique ont été présentés. L'accent a été mis sur l'étude locale des écoulements interne et externe à l'entrée de la prise d'air, ce qui n'exclut pas l'importance de nombreuses autres questions qui n'ont pu être abordées, comme par exemple l'incidence des distorsions internes discutée en référence [25].

Les exemples présentés font ressortir l'intérêt des méthodes théoriques actuellement développées pour calculer notamment l'écoulement potentiel du champ proche autour d'un avion transsonique, compte tenu des moteurs, ou encore l'écoulement autour d'un fuselage supersonique en incidence, compte tenu de la viscosité.

Ces exemples tendent toutefois en même temps à dégager des problèmes particuliers et des orientations nouvelles mettant en jeu des configurations tridimensionnelles complexes dont la solution théorique ne semble pas devoir être prochainement accessible, et qui nécessiteront par conséquent la poursuite de recherches expérimentales très élaborées.

Références

[1] Leynaert J. - Engine installation aerodynamics, dans AGARD Lecture Series LS 67 (1974) [3] (voir page 2).

[2] AGARD LS 56 - Aircraft performance - Prediction methods and optimization (1972).

[3] AGARD LS 67 - Prediction methods for aircraft aerodynamic characteristics (1974).

[4] Williams B. - Advanced technology transport configuration development - AIAA paper 72 756 (1972).

[5] Swann W., Sigalla A. - The problem of installing a modern high by-pass engine on a twin jet transport aircraft, dans Aerodynamic Drag AGARD Conf. Proc. n° 124 (1972).

[6] Aldridge S., Nye J. - Experimental results of high by-pass ratio turbo fan and wing aerodynamic interference, dans Aerodynamic Interference AGARD Conf. Proc. n° 71 (1970).

[7] Williams P., Stewart D. - The complex aerodynamic interference pattern due to rear fuselage mounted powerplants. AGARD CP n° 71 (1970).

[8] Landry J.L. - A numerical solution for the minimum induced drag, and the corresponding loading, of nonplanar wings. NASA CR 1218 (1968).

[9] Spangler S., Meundenhall, Dillenius M. - Theoretical investigations of ducted fan interference for transport-type aircraft. NASA SP 228 (1969).

[10] Hess J.L. and Faulkner S.M. - Determination of low speed interference effects by superposition. AGARD CP 71 (1971).

[11] Bowes G.M. - Aircraft lift and drag prediction measurement. AGARD LS 67 (1974).

[12] Glenny D.E. - Ingestion of débris into intake by vortex action. ARC CP n° 1114 (1970).

[13] Motycka D.L., Walter W.A. and Muller G.L. - An analytical and experimental study of inlet ground vortices. AIAA paper 73 1313 (1973).

[14] Kane E.J., Middleton W.D. - Considerations of aerodynamic interference in supersonic airplane design. AGARD CP 71 (1970).

[15] Sigalla A. and Hallstaff T.H. - Aerodynamic of powerplant installation on supersonic aircraft. Journal of Aircraft. July, August 1967.

[16] Ball W.H. and P.A. Ross - Experimental correlation of installation effets for inlet/airplane integrations. AIAA paper 71-759 (1971).

[17] Antonatos P.P., Surber L.E. and Stava D.J. - Inlet airframe interference and integrations, dans 'Airframe/Engine' Integration - AGARD LS 53 (1972).

[18] Babenko R.I., Voskressenky G.P., Lioubinov A.N. and Roussanov V.V. - Ecoulements à trois dimensions d'un gaz parfait autour d'un corps régulier. Edition Naouka, Moscou (1964).

[19] Walitt L., Trulio J.G., King L.S. - A numerical method for computing three dimensional viscous supersonic flow fields about slender bodies. NASA SP 228 (1969).

[20] Leynaert J., Brown T.W. and Collard D. - A study of the Concorde air-intake in yaw. 9th ICAS Congress, Haïfa (1974).

[21] Berry D.T. and Gilyard G.B. - Airframe/propulsion system interaction - an important factor in supersonic aircraft flight control. AIAA paper 73 831 (1973).

[22] Carter E.C. - Experimental determination of inlet characteristics and inlet and airframe interference. AGARD LS 53 (1972).

[23] Van Duine A., Rhoades W.W., Swan W.C. - Configuration aspects of propulsion installation on supersonic transports. AGARD CP 71 (1970).

[24] Leyman C.S., Morriss D.P. - Concorde powerplant development, dans Inlets and Nozzles for Aerospace Engines - AGARD CP 91 (1971).

[25] Carrière P. - Aperçu de quelques problèmes aérodynamiques actuels posés par les prises d'air supersoniques. 1er Congrès ISABE, Marseille, juin 1972. Edition provisoire : TP ONERA n° 1102.
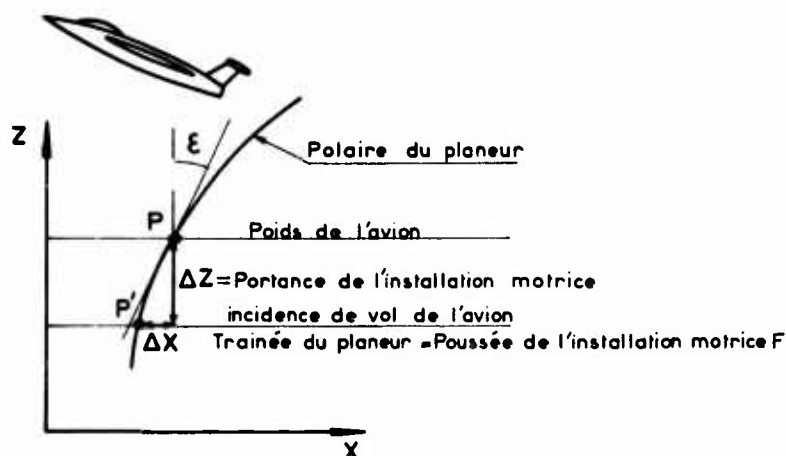
Fig. 1 - Installation motrice.

Poussée corrigée de l'installation motrice $F_c = F + \Delta X = F + \Delta Z \, tg \, \varepsilon$

Fig. 2 - Forces corrigées des éléments de l'installation motrice.

V_∞, P_∞

α_j

V_j P_∞

$$\left\{\begin{array}{c}\text{POUSSÉE NOMINALE CORRIGÉE}\\(\text{JET DÉFLÉCHI DE } \mathcal{E})\end{array}\right\} - \left\{\begin{array}{c}\text{POUSSÉE CORRIGÉE DE}\\ \text{L'INSTALLATION MOTRICE}\end{array}\right\}$$
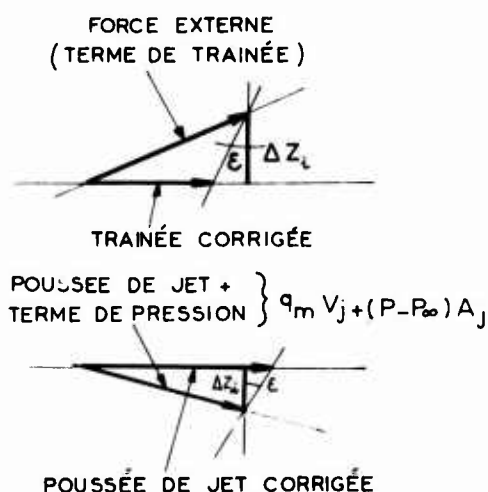
INSTALLATION OPTIMALE : $\alpha_j = \mathcal{E}$

Poussée nominale corrigée du jet :

$$q_m v_j (\cos\alpha_j + \sin\alpha_j \, tg\mathcal{E}) = \frac{q_m v_j}{\cos\mathcal{E}}$$

Poussée nominale corrigée du moteur :

$$F_{NC} = \frac{q_m v_j}{\cos\mathcal{E}} - q_{m\infty} V_\infty$$

Fig. 3 - Poussée nominale corrigée.

PERTE DE POUSSÉE DE L'INSTALLATION

PERTES INTERNES   **TRAINÉE EXTERNE**

- Trainées internes (pieges à couche limite, dérivation, fuite .....)
- Deflection non optimale du jet
- Efficacité de la tuyère
- Efficacité de la prise d'air
- Trainée d'équilibrage de la poussée

Fig. 4 - Bilan propulsif.

TRAINÉE EXTERNE

. Déviateur de couche limite

. Carène

. Trainée additive

. Trainée de refoulement du débit

. Mats , parasites

. Trainée d'arrière-corps

      Rétreints
      Passages auxiliaires
      Culots

TRAINÉE D'INTERACTION

      Nacelle de référence
      Prise d'air
      Arrière corps

Fig. 5 - Trainée externe et d'interaction.

ELLIPTIC , k = 1.0
OPTIMUM , k = 1.033
$C_{D_i} = \frac{C_L^2}{\pi A R k}$
REF : NASA CR - 1218

$\frac{C_\ell C}{C_L C_{Ref}}$

SEMISPAN
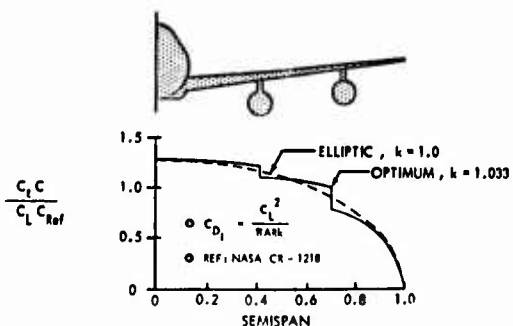
a) OPTIMISATION DE LA RÉPARTITION DE PORTANCE (JL. LUNDRY [8])

O PLAN VIEW

NACELLE

FLOW

O SIDE VIEW

WING
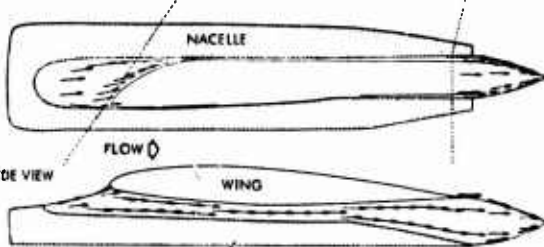
b) ÉTUDE LOCALE DE L'ÉCOULEMENT

Fig. 6 - Optimisation de l'ensemble aile-fuseaux (GM Bowes - [11]).

Section
AA

11 éjecteurs plats
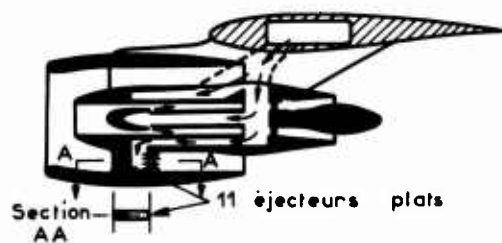
a) NACELLE ÉQUIPÉE D'UNE TROMPE
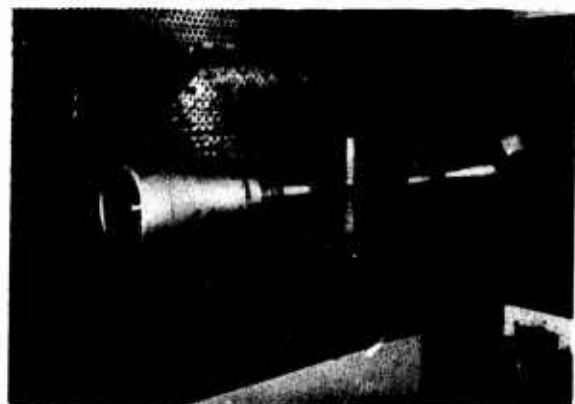
b) ESSAIS DE CALIBRATION (SOUFFLERIE ONERA S3 MODANE)

Fig. 7 - Maquette de nacelle pour étude des interactions.

POINT FIXE

Tourbillon peu intense

P_{iF}/P_{io}

0,8 0,9 1,0

ESSAI AVEC VENT ET COUCHE LIMITE DE SOL

Tourbillon

P_{iF}/P_{io}

0,8 0,9 1,0

ESSAI AVEC PLANCHER MOBILE
(ROULEMENT DE L'AVION)

Fig. 8 - Effet de sol.

VUE EN PLAN

Tourbillon

V1

V_c

L

Vent au sol

ÉLÉVATION

V1 D

H

$V_c/V1$

0,15

Pas d'ingestion

0,10

ingestion

$\begin{cases} \dfrac{H}{D} = 1,1 \\ V_c \text{ à } 55° \end{cases}$

0,05

0

0 10 20 30 Ro

NOMBRE DE ROSSBY $\quad Ro = \dfrac{V1}{\dfrac{dVc}{dL} \cdot D}$
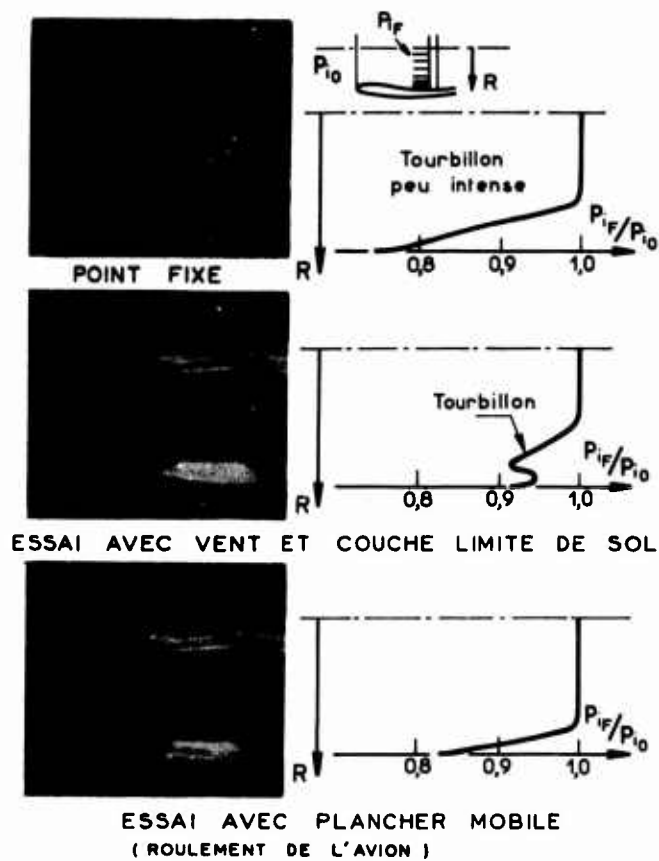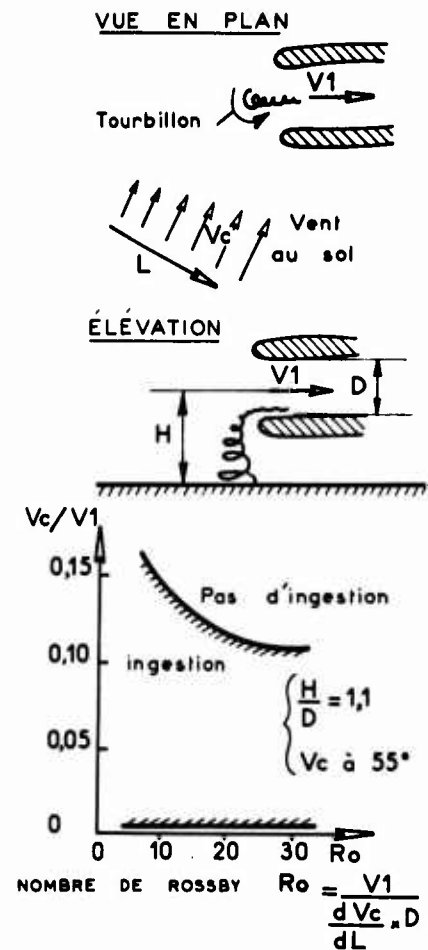
Fig. 9 - Effet de sol avec gradient de
vent horizontal
(D.E. Glenny - [11]).

a) NACELLES DE CONCORDE EN LIGNES DE COURANT

ΔCx

+0,01

Fuseau
sur aile

+0,005

Aile
sur fuseau

Nacelles de
révolution

-0,005

-0,01

Compression induite
d'intrados

Aile seule
(incidence réduite)

Total
net

Interaction
de
portance

Interaction
sans
portance

TRAINÉES D'INTÉRACTION

b) NACELLES DE RÉVOLUTION EN INTERACTION FAVORABLE
(A. SIGALLA and T.M. HALLSTAFF [13])
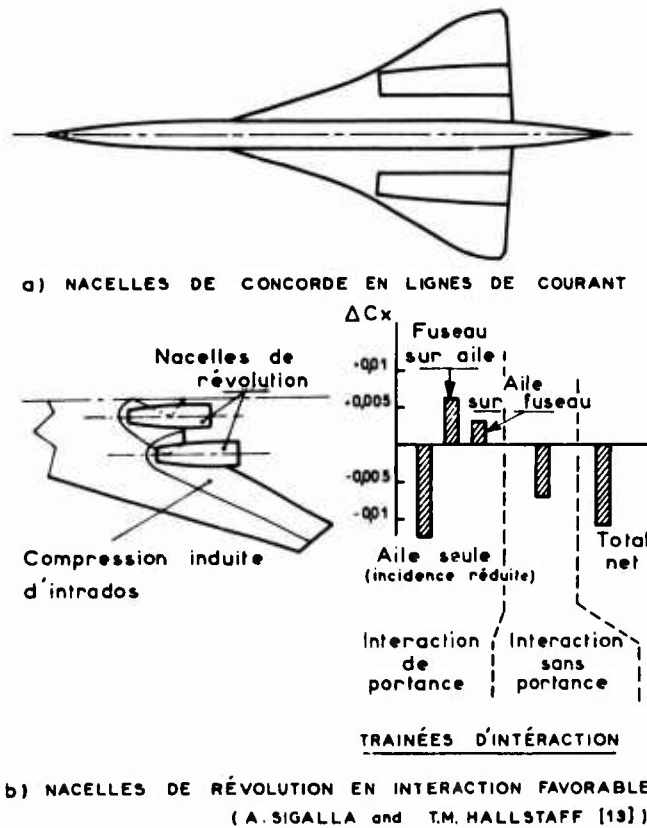
Fig. 10 - Installations de fuseaux sous l'aile en supersonique.

Coupe
fuselage

Plan de
sondage

FOREBODY A1

$M_o = 2,5$
$\alpha_o = 10°$
$\beta_o = 0°$

INCIDENCE, α_L SIDESLIP, β_L

10 12
14
18 16
-2 0 2

PREDICTIONS

INCIDENCE, α_L SIDESLIP, β_L

16
14
12
10
-2 0
1
2

TEST RESULTS

RÉSULTATS COMPARÉS AU CALCUL SEMI-LINÉARISÉ
(P. ANTONATOS , L.SURBER , D. STAVA [17])
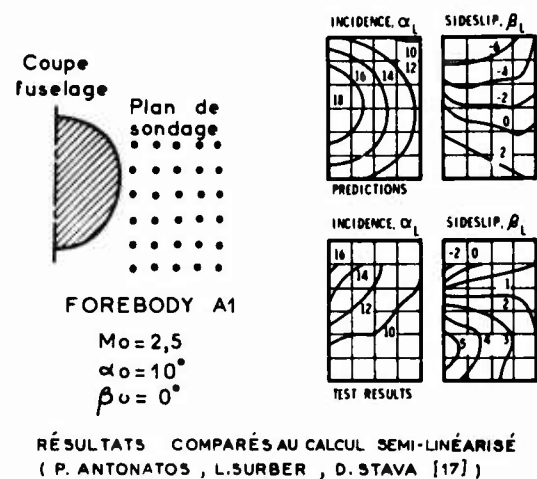
Fig. 11 - Champ de fuselage.

Points de calcul

STRIOSCOPIE
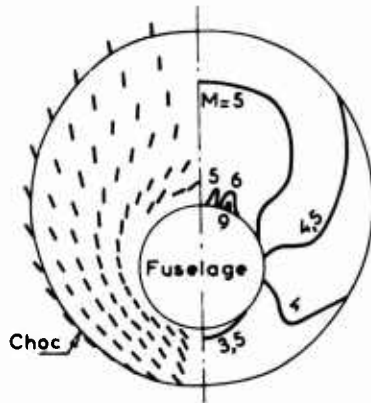
DIRECTIONS ET MACH LOCAUX
A 3,5 DIAMETRES DE LA POINTE M=6 α=15°

Fig. 12 - Calcul du champ de fuselage en incidence.
(ONERA - Méthode de Babenko).

ISOINCIDENCES   Mo = 2,5 αo = 15°

Fig. 13 - Calcul par une méthode approchée avec viscosité.
(L. Wallit, J.G. Trulio, L.S. King [19]).
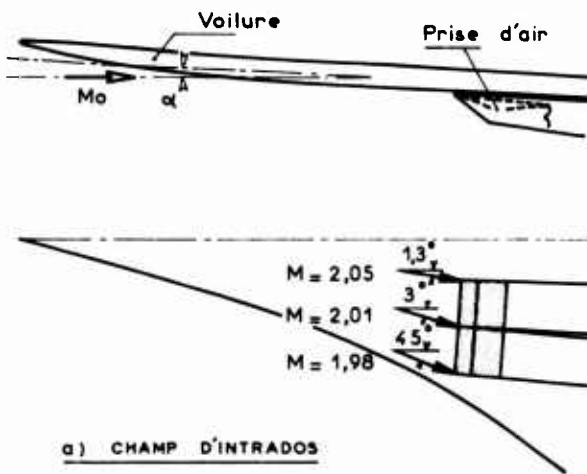
a) CHAMP D'INTRADOS
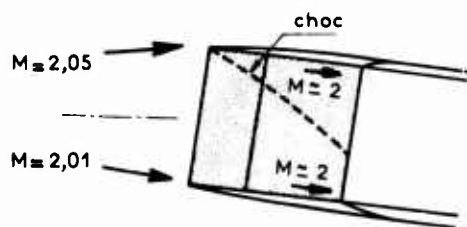
b) ORIENTATION OPTIMALE DE LA PRISE D'AIR

Fig. 14 - Adaptation au champ de la voilure.
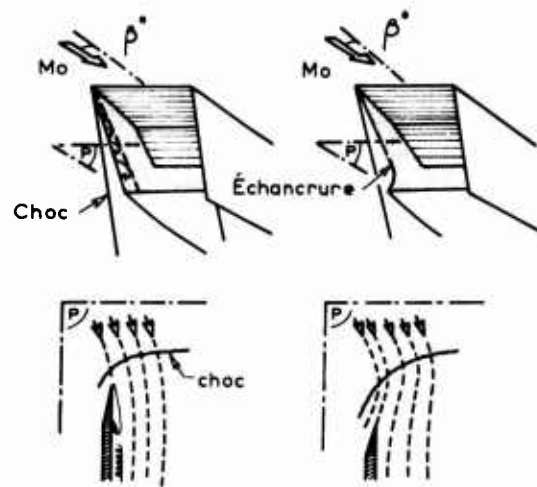
a) SANS ÉCHANCRURE   b) AVEC ÉCHANCRURE
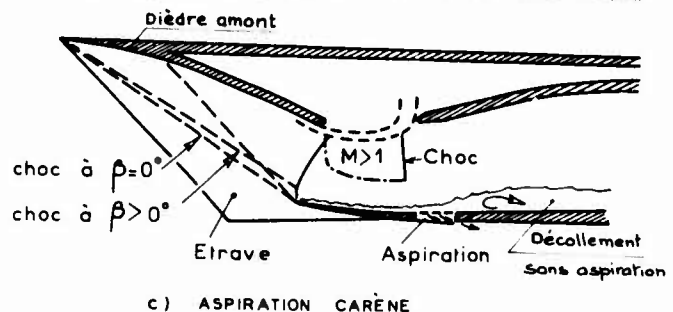
c) ASPIRATION CARÈNE

Fig. 15 - Modifications locales pour le dérapage.

Paroi interne
perforée

Découpe

Fente de sortie
de l'aspiration

a) VANNE ROTATIVE A CONTRE DÉBIT

Fig. 16 - Effets d'une aspiration et d'une découpe
Mo = 2,05.

Face moteur gauche
Paroi d'étrave droite
Rampe amont droite
Face moteur droite

MAQUETTE   AVION
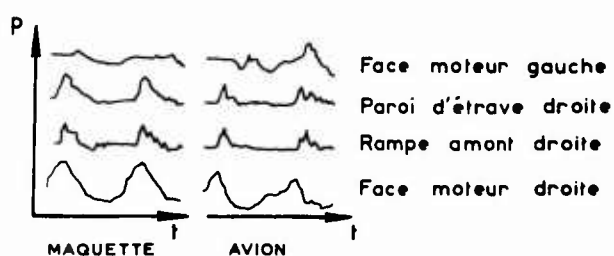
b) RELEVÉS DE PRESSIONS LOCALES

Fig. 17 - Pompage d'un moteur système de vannage et
comparaison de signaux (E.C. Carter - [19]).

PHASE D'INTERACTION MINIMALE

Dispositif de réglage de la couche limite incidente

PHASE D'INTERACTION MAXIMALE

Fig. 18 - Cycle de pompage d'une prise d'air semi-conique
près de la paroi. M = 2. Coefficient de débit moyen = 0,6.

Étrave
convergente

Efficacité

Étrave avec compression
Sans étrave
Étrave plane

Coefficient de débit
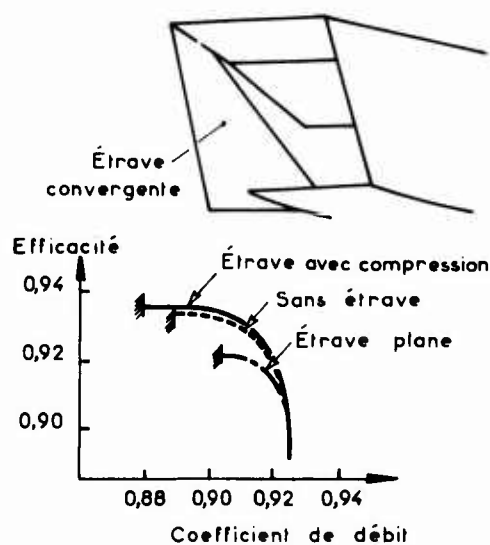
Fig. 19 - Prise d'air bidimensionnelle.
M = 2,08. Effet d'étrave.

A CRITERION FOR PREDICTION OF AIRFRAME INTEGRATION EFFECTS ON INLET STABILITY WITH APPLICATION TO ADVANCED FIGHTER AIRCRAFT

by

Gordon R. Hall*
Northrop Corporation, Aircraft Division
3901 W. Broadway
Hawthorne, California 90250, USA

SUMMARY

A simple criterion for the prediction of the effects of aircraft external flow field on installed inlet stability is presented. Wind tunnel data obtained from model tests of an advanced fighter aircraft are used to provide a base for discussion of installed inlet instability and to demonstrate the instability criterion. Specifically, two sources of supersonic inlet instability are identified, the instability mechanism is discussed and an instability criterion is defined, and application of the criterion is demonstrated. The sources of instability include ingestion of separated fuselage boundary layer at high aircraft attitude and ingestion of a vortex generated by a wing leading edge extension at negative attitude. A common stability criterion accounting for the effect of freestream Mach number, aircraft attitude, and inlet mass flow ratio is postulated and confirmed by available data. This same criterion is discussed in relation to observed cases of subsonic inlet instability and inlet instability resulting from slipstream ingestion. Application of the criterion to evaluate the effects of configuration changes on inlet stability boundaries is demonstrated.

1. INTRODUCTION

Past theories on the initiating mechanism of inlet buzz have focused upon isolated inlets operating in a uniform approaching flow field. These theories can generally be categorized as self-excited buzz wherein the disturbing force is an intrinsic property of the system oscillation and externally-excited buzz wherein the system oscillates in response to an external disturbing force. Duct resonance theories (e.g., Ref. 1-3) constitute the bulk of the self-excitation theories. Of the various externally-excited initiating mechanisms proposed, shock induced separation on the inlet compression surface (e.g., Ref. 4) and slipstream ingestion at the inlet cowl causing internal separation (e.g., Ref. 5) appear to be the most prominent origins of inlet buzz. However, neither of these mechanisms is either a necessary or a sufficient condition to precipitate inlet buzz. In both cases, the amount of throat blockage, or throttling effect, produced by the separated layers is an important factor in determining buzz initiation, the throat blockage effect generally leading to the positive slope criterion of pressure recovery with mass flow thought necessary for the self-regenerative oscillations of the buzz cycle.

In recent years, the requirement for high performance/highly maneuverable aircraft has typically led to close integration of the inlet into the airframe in order to minimize aircraft drag and attenuate flow angularity as seen by the inlet at high aircraft attitudes. As a result, the inlet typically ingests a flow field which has generally been processed by a fuselage forebody and wing. At high aircraft attitudes, the flow 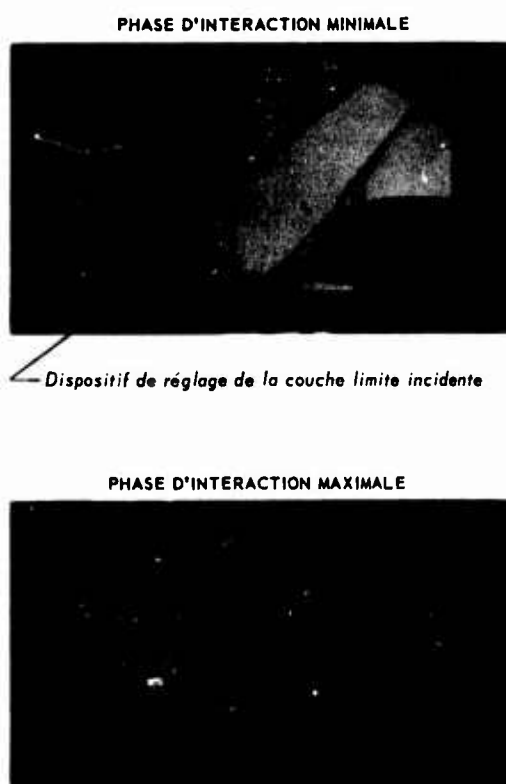field captured by the inlet may be non-uniform, either due to non-uniform compression of the inviscid stream and/or by thickening of upstream generated boundary layers which may not be fully contained by boundary layer diversion systems at extreme aircraft attitudes. Ingestion of regions of depressed oncoming flow by the inlet has recently been observed to cause inlet buzz. However, documentation and analysis of inlet buzz induced by non-uniform approaching flow fields do not appear to have been reported in the open literature.

Presented herein is a simple criterion relating inlet buzz to the characteristics of the flow field approaching the inlet. Predictions of incipient buzz based on the criterion are shown to be in good agreement with test data in accounting for the effects of inlet Mach number, aircraft attitude, and inlet mass flow ratio. Application of the criterion could be a valuable link in the configuration development process of future fighter aircraft by providing early identification of potential problems of inlet instability during preliminary flow field testing, thus allowing timely modifications in terms of inlet placement or aircraft configuration geometry upstream of the inlet.

2. MODEL TESTS

Much of the material presented is based on wind tunnel data from a 0.2 scale inlet/airframe model of an advanced fighter aircraft. This model was tested in the Arnold Engineering Development Center (AEDC) 16T Wind Tunnel over the Mach range $M_o = 0$ to 1.55 and in the AEDC 16S Wind Tunnel over the Mach range $M_o = 1.6$ to 2.2.

Figure 1 is a conceptual drawing of the 0.2 scale inlet/airframe model. The major elements of this model include a fuselage forebody and two side-mounted D-shape external compression inlets located in the flow field of the wing and forebody. Fuselage boundary layer diversion was achieved by both upward and downward deflection of the

---

*Manager, Internal Aerodynamics and Propulsion Research, Research and Technology Development Programs

approaching boundary layer. The upward diverted boundary layer was ducted through a slot in the wing leading edge extension (LEX). The inlets were fixed geometry with a single 7° compression ramp. Boundary layer control at supersonic Mach numbers was provided by compression ramp surface bleed upstream of, and through, the pressure rise corresponding to the inlet terminal shockwave.

The left inlet of the model was instrumented for steady state and dynamic performance at the compressor face. In addition, forward instrumentation was provided for upstream flow diagnostics. The forward instrumentation included inlet throat static pressure taps and boundary layer rakes and compression ramp static pressure taps. Inlet flow field was measured with total pressure rakes at the compression ramp leading edge of the right inlet.

In addition to data from the 0.2 scale inlet/airframe model, supporting data are provided from component tests of a 0.2 scale isolated inlet model and an .07 scale flow field model (without inlets) tested in Northrop's Supersonic 2 X 2 foot wind tunnel at M_0 = 2.0. These component models were similar in geometry to the corresponding components of the 0.2 scale inlet/airframe model.

3. STABLE OPERATION

Before proceeding with the discussion of inlet instability, it is instructive to comment briefly on the characteristics of the flow over the inlet when operating in the stable mode. With sufficient surface bleed, the compression ramp shock/boundary layer interaction was well controlled, resulting in inviscid shock system pressure recovery and low total pressure distortion at the inlet throat. Nominal surface bleed required to achieve this result was only about three percent of inlet airflow. This result is particularly significant considering the strength of the terminal shock (i.e., M≈2 normal shock) downstream of the relatively modest oblique leading edge shock produced by the fixed 7° compression ramp. Successful control of the strong terminal shock boundary layer interaction is attributed to the rather sophisticated design of the compression ramp boundary layer bleed system.

Without surface bleed, or with reduced surface bleed, massive shock induced separation prevailed above about M_0 = 1.5. Operation with this massive shock induced separation was found to be stable provided the inlet mass flow ratio was above a critical level (to be discussed later in more detail).

Figures 2 through 4 compare the characteristics of the flow over the compression ramp at M_0 = 2.0 with nominal and reduced surface bleed under conditions of stable operation. The data for these figures were taken from model tests of the 0.2 scale isolated inlet model tested at M_0 = 2.0 in the Northrop 2 X 2 foot wind tunnel. These data were selected because of the availability of Schlieren data, which were not obtained with the 0.2 scale inlet/airframe model. The pressure data, however, are representative of data obtained with the 0.2 scale inlet/airframe model operating at similar conditions.

Figure 2 clearly shows the stable separated region, and the separation shock associated with turning of the supersonic flow outside of the separated region, when the surface bleed is insufficient to prevent separation. With nominal surface bleed, no evidence of separation is apparent, although the Mach waves associated with the surface "roughness" presented by the bleed section are observed.

Figure 3 shows the corresponding static pressure distributions along the ramp centerline. For the separated flow case, the static pressure rise is smeared, increasing to a terminal level about twice that of the upstream level which, incidently, is in excellent agreement with the separation pressure rise correlations of Reference 6. For the attached flow case, the pressure rise corresponding to the normal shock is sharp, and the downstream pressure level is near the ideal value.

Figure 4 shows total pressure contours measured at the inlet throat. For the attached flow case, the total pressure is essentially uniform at about the ideal level. For the separated flow case, the total pressure is, of course, highly distorted. The high recovery in the central region reflects compression turning of the outer flow by the separated region (Figure 2) with an associated reduction in the strength of the terminal shock. Near the cowl, the flow is unaffected by the separation on the ramp, and the total pressure level in this region is similar to that for the attached case. Although the total pressure distortion at the inlet throat is extremely high, it is of interest to note that the average pressure recovery measured at the compressor face for the separated case is only about five percent lower than for the attached case. However, the measured turbulence levels were amplified several times. It is also of interest to note that high static pressure gradients exist across the inlet throat for the separated case in that the outboard region corresponds to the ideal static pressure behind the normal shock (P/P_{T0}≈0.6), while the compression ramp static pressures as seen in Figure 3 are at a level of P/P_{T0}≈.36.

4. STABILITY BOUNDARIES

During tests of the 0.2 scale inlet/airframe model in the AEDC 16S wind tunnel (M_0 = 1.6 to 2.2), certain phenomena causing inlet buzz* were identified. These phenomena, while changing in intensity and thus affecting the

---

*Inlet buzz was detected by monitoring the instantaneous space average compressor face total pressure on an oscilloscope. Buzz was typically characterized by a rather sudden onset of high amplitude discrete frequency pressure oscillations which occurred during a continuous change in inlet operating conditions. Superimposed on the discrete frequency pressure oscillations was a lower amplitude broadband turbulence.

incipient conditions of angle of attack (α), angle of sideslip (β), and inlet mass flow ratio under which inlet buzz occurred, did not change in their fundamental characteristics over the Mach range. As a result, the discussion which follows generally applies over the Mach range investigated, although selected Mach numbers are used to illustrate the various points of discussion.

Figures 5 and 6 show inlet stability boundaries measured at $M_0 = 2.0$. Inlet attitude capability (Figure 5) was found to be limited by two separately identifiable boundaries. These two boundaries were found to correspond to: (1) separation of the fuselage boundary layer ahead of the inlet at high angle of attack caused by impingement of the LEX shock on the boundary layer; and (2) a vortex generated by the LEX at negative lift conditions corresponding to negative angle of attack. Ingestion of viscous flow by the inlet was common to each of the destabilizing phenomena. Due to the magnitude of the viscous region ingested (and the location in the case of the wing glove vortex), variation in compression ramp boundary layer bleed was found to have negligible effect upon the stability boundaries.

The stability boundaries of Figure 5 correspond to maximum power airflow. Shown in Figure 6 is the effect of mass flow ratio (MFR) on inlet stability. In the primary α maneuvering range, the stability limit was found to be essentially constant, with good stability margin exhibited with respect to maximum power and idle airflow levels. Within this same range of α, the inlet capture streamtube was found to be virtually void of significant viscous flow.

The lower limit of stable MFR in the primary α maneuvering range was found to be governed by the forward extent of the compression surface bleed section; change in the forward extent of the bleed section was found to provide a lower stable MFR in a 1:1 relationship between the shift in forward extent of the bleed region and shift in the shock position with MFR. That is, inlet buzz was encountered under the condition of insufficient boundary layer bleed upstream of the terminal shock (thus fixing the forward most stable position of the terminal shock with respect to the leading edge of the bleed section), rather than by any inherent destabilization mechanism arising from the geometric relationship of shock position with respect to the inlet surfaces and inlet face. The critical amount of upstream bleed was found to be about one percent of the inlet flow, which corresponded to removal of somewhat less than the entire boundary layer.

It is of interest to note that, while insufficient compression surface bleed at low MFR led to inlet buzz, insufficient bleed at high MFR produced a stable shock induced separated region as discussed earlier (Figure 2). This difference is attributed to the increased throat blockage caused by the separated layer at lower MFR. That is, as the MFR is reduced, the separation origin moves upstream on the ramp and the separation thickness at the inlet throat increases, eventually reaching a critical value sufficient to initiate inlet buzz. This is illustrated schematically in Figure 7. Throat blockage greater than the critical value apparently corresponds to the positive slope criterion of pressure recovery with MFR thought necessary for the self-regenerative oscillations of the buzz cycle (e.g., Ref. 4). The difference in stability characteristics at high and low MFR is not due to slipstream ingestion at the outer cowl at low MFR (which is a well documented source of inlet buzz): based on Schlieren data from the 0.2 scale isolated inlet model tests, the slipstream generated by the intersection of the compression ramp leading edge shock with the terminal shock was not ingested by the inlet at any MFR.

At the α extremes of Figure 6, the viscous inlet flow field effects identified previously come into play. When these effects are prevalent, the stable angle of attack boundaries increase with increasing MFR. The reason for this is that the inlet throat static pressure decreases with increasing mass flow ratio, thus allowing the inlet to accept greater depressions in the external inlet flow field without destabilization. This statement will be elaborated upon in a later discussion of the destabilizing mechanism associated with depressions in the inlet flow field.

5. APPROACHING FLOW FIELD

Figure 8 shows the inlet total pressure field (corrected for shock loss) measured at the leading edge of the compression ramp for α/β conditions corresponding to the stable region and two buzz regions of Figure 5. Figure 8a shows a typical low attitude inlet flow field within the stable operating region of the inlet. The flow is well behaved and characterized by a fuselage boundary layer which is confined to the boundary layer diversion region between the fuselage and the compression ramp. The remainder of the flow field (i.e., inlet capture streamtube) is essentially uniform at freestream total pressure.

In contrast, Figures 8b and 8c show inlet flow field conditions corresponding to the two previously discussed regions of inlet buzz of Figure 5. These flow fields are characterized by relatively large regions of viscous flow (i.e., regions of high gradients in total pressure) which lie within the inlet capture streamtube. Although both of the flow fields of Figures 8b and 8c originate from different upstream phenomena, commonality exists in that both have a reduced total pressure region within the inlet capture streamtube and both resulted in inlet buzz. The association of reduced upstream total pressure with inlet instability is considered further in Figure 9.

6. INSTABILITY CRITERION

Figure 9 presents an inlet instability criterion that is related to the deficit in total pressure of the upstream flow field intercepted by the inlet. A typical static pressure distribution along the ramp of an external compression inlet is shown in Figure 9a. The function of the compression ramp is to reduce the velocity of the approaching supersonic flow to subsonic flow at the inlet cowl. This is accomplished through conversion of kinetic energy to pressure head, typically by the flow traversing through a series of oblique shock waves to reduce the supersonic

Mach number, and finally through a normal shockwave located a short distance upstream of the inlet cowl which reduces the flow velocity to a subsonic level. If one considers a streamtube of depressed upstream total pressure, it may be argued that if the total pressure of the depressed streamtube, less any shock losses encountered in the overall compression process, is not greater than the downstream static pressure as established by the bulk of the upstream flow at an undepressed level of upstream total pressure, then the depressed streamtube will be unable to negotiate the compression pressure rise without flow reversal and associated throat blockage and, hence, inlet instability may occur. The above criterion neglects the effect of viscosity which would have a favorable effect in accelerating the depressed streamtube along the length of the compression ramp through the action of fluid shear. This effect would be expected to prevail even very close to the wall, assuming compression ramp bleed removes the local boundary layer.

The importance of viscous effects on the proposed instability criterion of Figure 9 would be expected to be small within the external region of a typical supersonic inlet. That is, the work done on an element of fluid due to the rapid rise in static pressure along the ramp is typically large compared to the work done on an element of fluid due to fluid shear over that same distance. For example, using the geometry and flow conditions of the inlet described herein, and assuming the locally depressed flow field exhibits diffusion characteristics of an axisymmetric turbulent wake, it may be shown that the integral accelerating effect on the depressed streamtube due to fluid shear along the length of the compression ramp is less than ten percent of the integral decelerating effect due to pressure forces over the same length.* Furthermore, it is noted that this viscous effect could be accounted for if one were to define the inlet flow field reference plane at the inlet face rather than at the compression ramp leading edge. Typically, however, inlet flow field measurements have been, in the past, referenced to the compression ramp leading edge plane rather than to the inlet face plane, thus providing measurements of the flow field to be processed by the inlet.

Considering the foregoing, one would expect the proposed inviscid criterion to give reasonably good results in predicting inlet instability caused by total pressure depressions in the oncoming flow field. If so, early identification of potential problems of inlet instability could be obtained during preliminary flow field testing of a new aircraft configuration, and timely modifications in terms of inlet placement or configuration geometry upstream of the inlet could be made.

7. COMPARISON TO TEST DATA

Figure 10 shows comparison of measured stability boundaries and stability boundaries predicted by the upstream total/downstream static pressure criterion of Figure 9 at $M_0 = 1.6$ and $M_0 = 2.0$. The prediction method predicts the effect of model attitude on inlet stability quite well, both in the high angle of attack and negative angle of attack regions. It is recalled from Figure 8 that the high α condition corresponds to viscous flow over the compression ramp and negative α corresponds to a vortex entering the inlet from the upper outboard region. It is particularly significant that the single pressure criterion of Figure 9 works equally well in predicting the effect of these separate phenomena. As mentioned previously, neglect of viscous effects give a conservative estimation of the stability boundaries in neglecting the increase in total pressure of the depressed streamtubes in the streamwise direction. Another conservative factor is the requirement for a critical amount of throat blockage required to initiate inlet buzz. This factor is thought to be small, however, in that the area occupied by the depressed streamtube grows rapidly as the stagnation condition is approached.

Figure 11 shows additional comparisons of measured and predicted stability boundaries by bringing in the effect of MFR. That is, as the MFR is increased, the value of the downstream static pressure P_2 drops, which means that a lower level of incoming total pressure P_{T2} (and hence higher value of α) can be accepted by the inlet without instability. This is illustrated schematically in Figure 12, which also serves to illustrate the construction method of the predicted boundaries of Figure 11. As can be seen in Figure 11, the prediction method predicts the effect of MFR quite well, again both in the high α and negative α range. It is noted that, although measured values of P_2 were used for the foregoing comparisons, P_2 can be easily estimated within a few percent. Thus, the estimated stability boundaries would be virtually unchanged had only the external flow field been measured.

Figure 13 shows measured and predicted stability boundaries over the Mach range investigated in the AEDC 16S Wind Tunnel. The prediction method is seen to hold over the Mach range investigated, again both in the high α and negative α range.

In summary, the proposed inviscid criterion for prediction of inlet instability due to depressions in the oncoming flow field has been found to be in good agreement with measured supersonic inlet instability. This method has been demonstrated for two separate destabilizing phenomena and accounts for the effects of freestream Mach number, aircraft attitude, and inlet mass flow ratio. In neglecting viscous effects and the requirement for critical throat blockage, the method predicts stability boundaries which are slightly conservative.

---

*Similar estimates of the ratio of fluid shear to pressure effects within the subsonic diffuser provide the rationale for selection of the inlet throat as the reference downstream plane for the instability criterion as opposed to, say, the engine compressor face plane. That is, although the static pressure continues to rise along the length of the subsonic diffuser, it may be shown that the integral effect of fluid shear forces is of the same order as the integral effect of pressure forces within the diffuser; thus, deceleration of the depressed streamtube within the diffuser by pressure rise is roughly countered by acceleration due to fluid shear.

8. LOW MACH INSTABILITY

Thus far, discussions of inlet stability have focused upon tests of the 0.2 scale inlet/airframe model in the AEDC 16S Wind Tunnel over the Mach range 1.6 to 2.2. It is of interest to note that inlet instability was also encountered under some conditions at transonic, and even lower, Mach numbers during tests of the model in the AEDC 16T Wind Tunnel over the Mach range 0 to 1.4. Specifically, inlet "buzz" was encountered at a few extreme conditions of high model attitude in combination with low inlet MFR (i.e., MFR typically less than engine idle airflow) down to a Mach number as low as $M_0 = .55$.

Inlet buzz was detected by monitoring the instantaneous space average compressor face total pressure on an oscilloscope during a continuous decrease in inlet MFR. In addition, data were obtained simultaneously on magnetic tape. The onset of low Mach buzz was characterized by a relatively gradual build-up in amplitude with reduction in MFR, as opposed to the rather sudden onset of high amplitude buzz characteristic of supersonic operation. However, the wave form of the low Mach buzz was similar to that of the supersonic buzz in exhibiting high amplitude discrete frequency pressure oscillations of nearly constant amplitude, but without superposition of broadband turbulence typical of the supersonic buzz wave form.

A typical example of low Mach buzz is shown in Figure 14. Peak-to-peak pressure oscillations are about twenty percent of the freestream total pressure, with the positive peaks exceeding freestream total pressure. The frequency of the pressure oscillations is about 68 hz which is in excellent agreement with the theoretical open/closed* organ pipe frequency of the inlet duct calculated at 70 hz. Further, the pressure oscillations across the duct were found to be in phase as evidenced by comparing the instantaneous compressor face average total pressure to selected instantaneous measurements of individual compressor face pressures.

Although stability boundaries comparable to those defined supersonically were not measured at the lower Mach numbers, it is noted that the few isolated points detected were limited to low values of MFR ratio in combination with high model attitudes wherein fuselage boundary layer thickening was not contained between the inlet ramp and fuselage, but instead spilled over the inlet ramp as described previously at supersonic conditions. Due to the high angularity of the local flow at these conditions, the inlet flow field rakes were not considered accurate as evidenced by the less than 100 percent measured recovery in regions of the flow field known not to be influenced by upstream viscous effects (typically these regions were measured at about 95 percent recovery). However, in adjusting the measured levels of the inlet flow field to remove the effects of angularity, it appeared that, within the various tolerances involved, the instability criterion applied successfully to the supersonic tests was also applicable at the lower Mach numbers. That is, buzz occurred at lower Mach numbers when the inlet throat static pressure was increased (by reduction of MFR) to a level about equal to the minimum total pressure of the depressed region of flow field intercepted by the inlet. The observed gradual build-up in the subsonic buzz amplitude with decreasing MFR discussed earlier is attributed to the relatively low slope of inlet throat static pressure with MFR at low values of MFR where buzz was encountered.

Throat blockage, due to stagnation of the depressed external flow field, and associated positive slope of recovery with mass flow, is thought to play the same role in precipitating buzz at subsonic and supersonic freestream Mach numbers. The primary difference between the subsonic and supersonic Mach buzz is the coupling of the external shock system into the inlet system oscillation, which introduces broadband turbulence (generated by shock induced boundary layer separation) superimposed upon the duct resonance frequency.

9. SLIPSTREAM INGESTION

The foregoing discussions have linked the precipitation of inlet buzz to total pressure deficits in the approaching external flow field. For this class of disturbances, a simple flow field criterion which predicts supersonic inlet buzz has been described and confirmed by available wind tunnel data. The criterion accounts for the effects of freestream Mach number, aircraft attitude, and inlet mass flow ratio. The same criterion, although not comprehensibly demonstrated at subsonic Mach numbers, appears to be consistent with observed instances of inlet buzz encountered at subsonic Mach numbers. Due to the fundamental nature of the criterion, it is suggested that it may also govern the initiation of inlet buzz arising from sources other than non-uniform approaching external flow fields.

For example, consider the well documented evidence of inlet buzz caused by ingestion of a slipstream at the outer cowl of an inlet (Ref. 5 is a classical example). Slipstream ingestion typically occurs at reduced mass flow ratio and/or angle of attack when the compression surface oblique shock system intersects the terminal shock within the projected area of the inlet cowl. Although slipstream ingestion has been a common source of inlet buzz, it is neither a necessary nor sufficient condition to precipitate buzz. In pursuing this point, it is suggested that it is not the slipstream, per se, that is the cause of the inlet buzz, but rather the variation in total pressure of the flow downstream of the slipstream origin (triple shock point) combined with external subsonic diffusion between the triple point and the inlet face. This concept is discussed further in the paragraphs which follow.

Figure 15 shows a sequence of four Schlieren photographs, two of which clearly show slipstream ingestion without inlet instability. These data were obtained with the 0.2 scale isolated inlet model tested in the Northrop 2 X 2 foot wind tunnel at $M_0 = 2.0$. As noted in earlier discussion, the slipstream generated by the intersection of

---

*An open/closed duct was assumed for analysis since at the very low MFR's where buzz occurred, the downstream end of the duct is nearly closed.

the compression ramp leading edge shock with the terminal shock was not ingested by the inlet at any MFR with the inlet at the nominal angle of attack of zero degrees. Therefore, at zero degrees angle of attack, no information relating to the effect of slipstream ingestion on inlet stability was obtained. However, for selected tests, the inlet compression ramp was turned into the flow 5° (identified as θ = 5° in Figure 15). With this model orientation, the slipstream was ingested by the inlet at lower values of MFR as seen in Figure 15. At the highest MFR, the slipstream appears to be nearly at the inlet cowl and the inlet flow is stable. At the two intermediate MFR's, the slipstream is clearly ingested by the inlet, but the inlet flow remains stable. Only at the lowest MFR did the slipstream ingestion precipitate inlet buzz.

Figure 16 shows elements of the flow field in the vicinity of the triple shock point. Although the flow field at the triple point is very complicated due to shock curvature arising from the downstream influence of the subsonic flow, the flow a short distance above and below the triple point may be treated by plane wave shock relations. In applying plane wave shock relations, the total pressure loss above the triple point is greater than that below the triple point ($P_{TA} < P_{TB}$) due to the higher incoming Mach number above the triple point. Within a short distance downstream of the triple point, transverse static pressure balance is achieved and, due to the lower total pressure above the triple point, the velocity of the flow above the triple point is lower than that below the triple point. During the subsonic diffusion process between the triple point and the inlet throat, the static pressure rise reduces the velocity of the flow above the triple point more than it reduces the velocity of the flow below the triple point, thus compounding the initial upstream velocity differential. With sufficient total pressure differential and subsonic diffusion, stagnation of the flow above the triple point will occur, resulting in throat blockage and potential inlet instability.

Figure 17 shows internal total pressure profiles in the region of the outboard cowl (measured at the inlet throat) for each of the MFR conditions of Figure 15. For reference, the ideal total pressures* above and below the triple point immediately downstream of the terminal shock are indicated. At the highest MFR, the slipstream apparently has not entered the inlet as evidenced by the uniform recovery at a level about equal to the ideal level below the triple point. At the two intermediate MFR's, there is a region of reduced total pressure flow near the wall where the pressures closely coincide with the ideal total pressure above the triple point, while the total pressure of the flow farther from the wall corresponds closely to the ideal total pressure below the triple point. The two regions are joined by a shear layer which represents the slipstream after viscous diffusion between the triple point and the inlet throat. At the lowest MFR, the inlet is in buzz, and the total pressure profile reflects a time average of this buzz which extends beyond the end of the pressure rake.

It is noted that the wall static pressures have increased to a level nearly equal to the region of reduced total pressure at the two intermediate MFR's. This increase in static pressure reflects the increase in external subsonic diffusion with decreasing MFR. Although the wall static pressures are at about the same level as the region of reduced total pressure, the region is not considered to be one of boundary layer separation. Rather, this region reflects the reduced external total pressure and external subsonic diffusion which combine to stagnate the incoming flow. There is not significant internal static pressure gradient in this region to produce a boundary layer separation. On the other hand, the reduced external total pressure/subsonic diffusion is an expected result, with good quantitative agreement between the measured and predicted pressure recovery in this region.

The requirement for finite throat blockage produced by the stagnated flow prior to initiation of inlet buzz is evident in Figure 17. Specifically, at the MFR immediately prior to inlet buzz, the flow above the triple point has stagnated and probably reversed (indicated by total pressure levels less than wall static pressure), but the inlet flow remains stable. It is not until a critical blockage occurs that inlet buzz is encountered.

In summary, the same inlet instability criterion applied successfully in predicting inlet buzz caused by total pressure deficits in the approaching external flow field would appear to be an appropriate criterion for determination of the critical strength of an ingested slipstream required to precipitate inlet buzz, although additional comparisons to experimental data are desirable. At this point, it is of interest to note that the subject criterion appears to govern precipitation of inlet buzz caused by non-uniform flow fields from extremely different origins. Specifically, the slipstream generated non-uniform flow field originates from inviscid flow through shockwaves of different strengths, the low Mach externally generated non-uniform flow field originates from upstream subsonic viscous flows, and the supersonic externally generated non-uniform flow field originates predominately from upstream supersonic viscous flows.

10. APPLICATION OF THE CRITERION

Based upon the measurements of inlet stability from the first test of the 0.2 scale inlet/airframe model in AEDC 16S Wind Tunnel, various modifications to the configuration were investigated to extend the high angle of attack stability boundary at supersonic Mach numbers. No parallel attempt was made to extend the negative angle of attack boundary created by ingestion of the LEX vortex since the original boundary was not restrictive with respect to the desired α, β operating envelope. These modifications were evaluated, using an .07 scale flow field model tested at M_0 = 2.0 in Northrop's 2 X 2 foot Supersonic Wind Tunnel. This model was tested without an

---

*Ideal total pressures were calculated based on plane wave shock relations and accounting for downstream flow direction as indicated by the initial angle of the slipstream.

inlet,* and all evaluations were based upon inlet flow field measurements, forebody static pressure measurements, and oil flow visualization. A modified configuration which evolved from these tests was later confirmed in a second test of the 0.2 scale inlet/airframe model in the AEDC 16T Wind Tunnel, in which inlet stability boundaries were measured.

The effects of a sample modification to the configuration are shown in Figures 18 and 19. Figure 18 shows the effect of a modification to the slot in the LEX on inlet flow field. The effect of the slot modification was to reduce the static pressure rise caused by impingement of the LEX shockwave on the fuselage and provide a pressure relief region through the LEX for the forebody boundary layer to flow. As can be seen in Figure 18, the region of adverse viscous flow intercepted by the inlet is reduced considerably with the modified slot.

Figure 19 shows the measured extension of the high angle of attack stability boundary corresponding to the modified slot in the LEX. Since the modified configuration was tested only in the AEDC 16T Wind Tunnel, maximum test Mach number was slightly less than $M_O = 1.6$. Thus, the comparison of Figure 19 is made at $M_O = 1.6$, rather than at $M_O = 2.0$ where the .07 scale model flow field measurements were made. At $M_O = 1.6$, however, the desired increase in stability boundary was achieved, thus demonstrating the validity of the stability criterion as a useful tool for extending the stability boundary a specified amount. Further, due to the excellent agreement of the predicted and measured extension of the stability boundary at $M_O = 1.6$, it was concluded that previously planned confirmation tests with the modified configuration in the AEDC 16S Wind Tunnel at Mach numbers in excess of $M_O = 1.6$ were not required.

11. CONCLUSIONS

1. Supersonic inlet buzz was found to be caused by ingestion of upstream generated viscous flows. The destabilizing viscous flows included separated fuselage boundary layer at high aircraft attitude and a vortex generated by a wing leading edge extension at negative attitude. Increasing inlet mass flow ratio was found to extend the attitude for stable inlet operation.

2. In the range of aircraft attitude where the external flow field was free of viscous flow, good inlet stability margin with respect to maximum and idle power airflows was exhibited over the Mach range investigated. In this range of attitudes, the lower limit of stable mass flow ratio was found to be essentially constant, with the level governed by the forward extent of the compression surface bleed section.

3. Within the stable region of operation, the compression surface shock/boundary layer interaction was well controlled for normal shock Mach numbers as high as 2.0 using about three percent of inlet airflow. Without surface bleed, massive shock induced separation prevailed above freestream Mach numbers of about 1.5. However, inlet operation with the shock induced separation was stable provided the mass flow ratio was above a critical level.

4. A simple stability criterion which relates inlet buzz to characteristics of the flow field approaching the inlet was postulated. Predictions of inlet buzz based on the criterion were found to be in good agreement with available test data in accounting for the effects of freestream Mach number, aircraft attitude, and inlet mass flow ratio. The criterion states that if the total pressure of a streamtube intercepted by the inlet, less any shock losses encountered in the compression process, is not greater than the downstream static pressure, then flow reversal and associated inlet instability may occur.

5. Inlet buzz was encountered at a few extreme conditions of high model attitude in combination with low inlet mass flow ratio (less than engine idle airflow) at subsonic Mach numbers. The wave form of the subsonic buzz was similar to that of the supersonic buzz in exhibiting high amplitude discrete frequency pressure oscillations which corresponded to the duct resonance frequency. The same stability criterion applied successfully in predicting buzz at supersonic Mach numbers was found to be consistent with the observed instances of buzz at subsonic Mach numbers.

6. For selected tests, the effect of slipstream ingestion on inlet stability was studied. Although slipstream ingestion precipitated inlet buzz at some conditions, slipstream ingestion of itself was not a sufficient condition to precipitate buzz. The same stability criterion applied successfully in predicting buzz caused by total pressure depressions in the approaching external flow field, when applied locally to the region of flow between the slipstream origin and inlet face, would appear to be an appropriate criterion for determination of the critical strength of an ingested slipstream required to precipitate buzz.

7. Application of the stability criterion was demonstrated in the process of extending the inlet stability boundaries a specified amount based on flow field measurements. Future application of the criterion could be a valuable link in the configuration development process of fighter aircraft by providing early identification of potential problems of inlet instability during preliminary flow field testing, thus allowing timely modifications in terms of inlet placement or aircraft configuration geometry upstream of the inlet.

---

*Although this model had an inlet which could be installed, it was not designed for supersonic operation due to lack of compression ramp boundary layer control.

REFERENCES

1. Sterbentz, W. H. and Evvard, J. C., "Criterion for Prediction and Control of Ram-Jet Flow Pulsations," NACA TN 3506, August, 1955.

2. Sterbentz, W. H. and Davids, J., "Amplitude of Supersonic Diffuser Flow Pulsations," NACA TN 3572, October, 1955.

3. Mirels, H., "Acoustic Analysis of Ram-Jet Buzz," NACA TN 3574, November, 1955.

4. Dailey, C. L., "Supersonic Diffuser Instability," Journal of the Aeronautical Sciences, Vol. 22, No. 11, p. 733, November, 1955.

5. Ferri, A. and Nucci, L. M., "The Origin of Aerodynamic Instability of Supersonic Inlets at Subcritical Conditions," NACA RM L50K30, January, 1951.

6. Kuehn, D. M., "Experimental Investigation of the Pressure Rise Required for the Incipient Separation of Turbulent Boundary Layers in Two-Dimensional Supersonic Flow," NASA Memo 1-21-59A, February, 1959.

ACKNOWLEDGEMENT
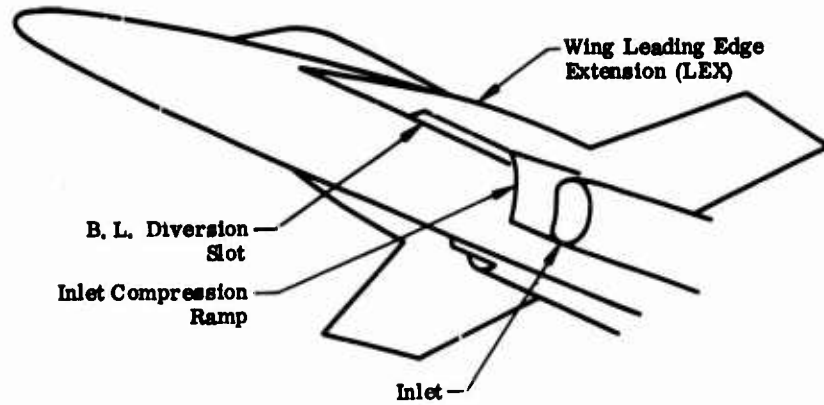
FIGURE 1. 0.2 SCALE INLET/AIRFRAME MODEL

$M_0 = 2.0$
$\alpha = 0$
Max. Power Airflow
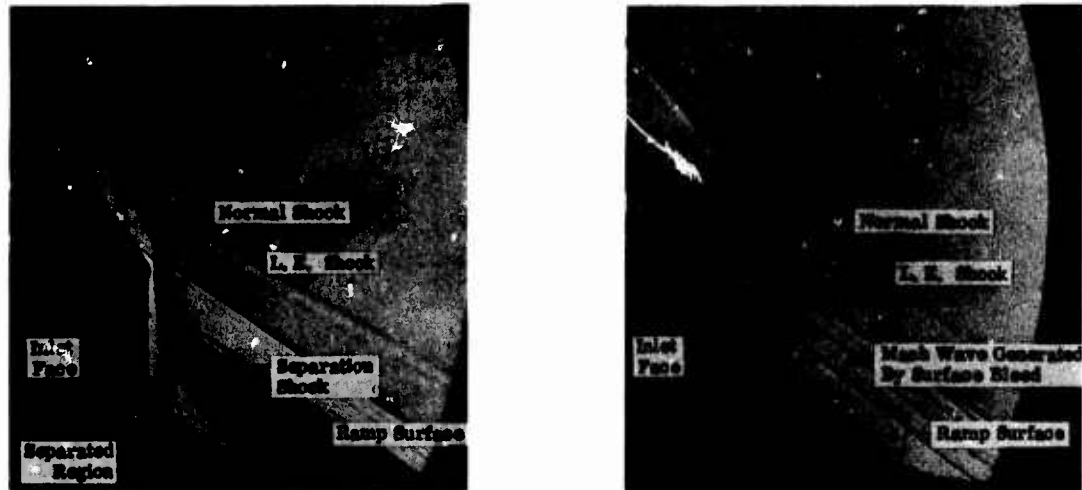
a) Reduced Bleed

b) Nominal Bleed

FIGURE 2. EFFECT OF BOUNDARY LAYER SUCTION ON STRONG SHOCK
BOUNDARY LAYER INTERACTION

$M_0 = 2.0$
$\alpha = 0$
Max. Power Airflow
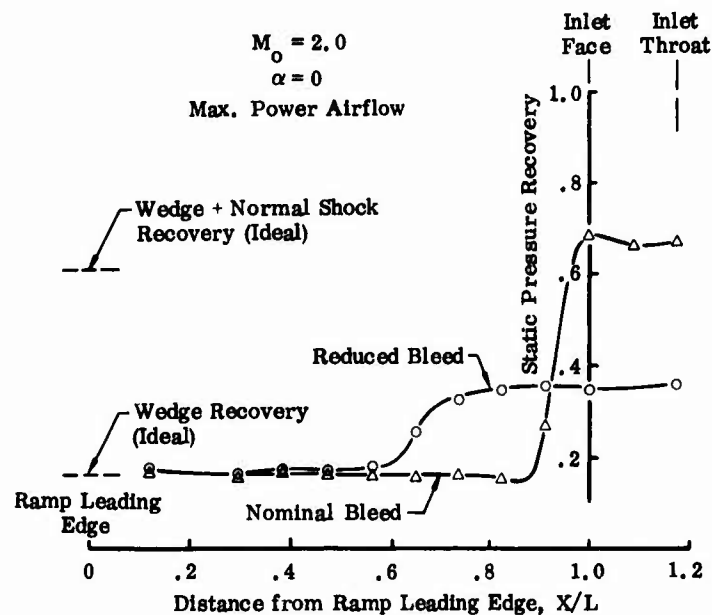
FIGURE 3. EFFECT OF BOUNDARY LAYER SUCTION ON RAMP
STATIC PRESSURE DISTRIBUTION

$M_O = 2.0$

$\alpha = 0$

Max. Power Airflow

Separated Region

$\frac{P_T}{P_{TO}} = 0.36$

0.40 0.60 0.80 0.90

a) Reduced Bleed

$\frac{P_T}{P_{TO}} = 0.70$

0.75 0.78

b) Nominal Bleed
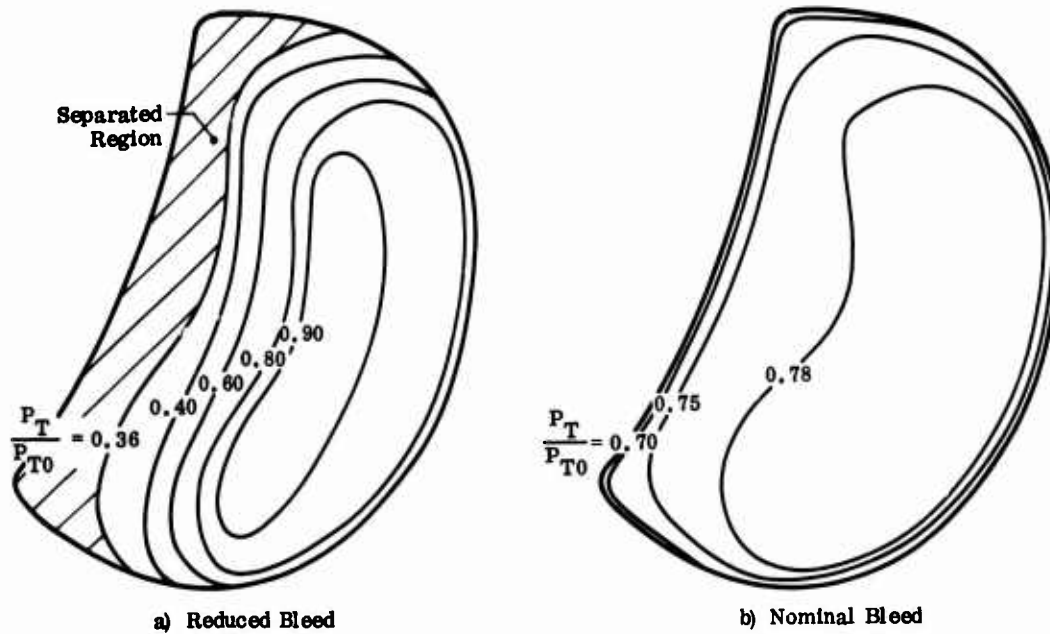
FIGURE 4. EFFECT OF BOUNDARY LAYER SUCTION ON INLET THROAT TOTAL PRESSURE PROFILES

$M_O = 2.0$

Max. Power Airflow

Buzz – Forebody B. L. Separation

Angle of Attack, α

Stable

Angle of Sideslip, β

(Windward) (Leeward)

Buzz – LEX Vortex
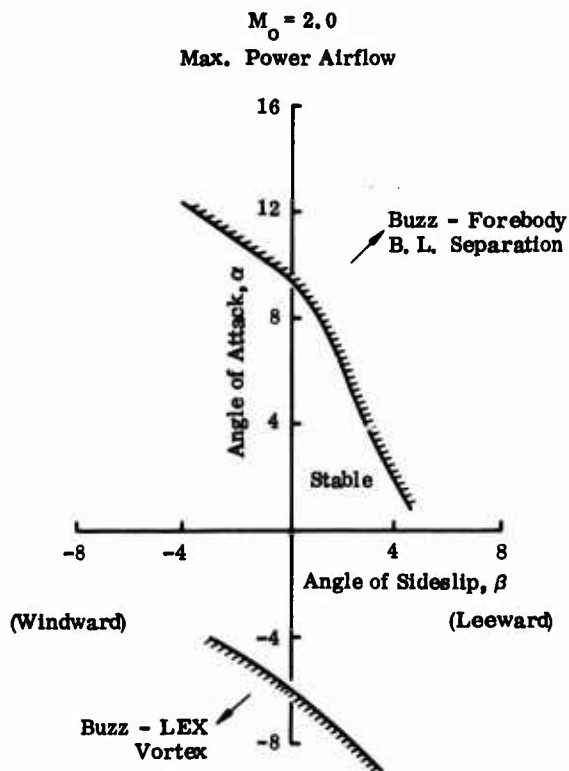
FIGURE 5. INLET STABILITY BOUNDARIES AT MAX POWER AIRFLOW

$M_O = 2.0$

$\beta = 0$

Buzz – Forebody B. L. Separation

Buzz – Insufficient Upstream B. L. Bleed

Angle of Attack, α

Idle Airflow

Max. Power Airflow

MFR

Buzz – LEX Vortex
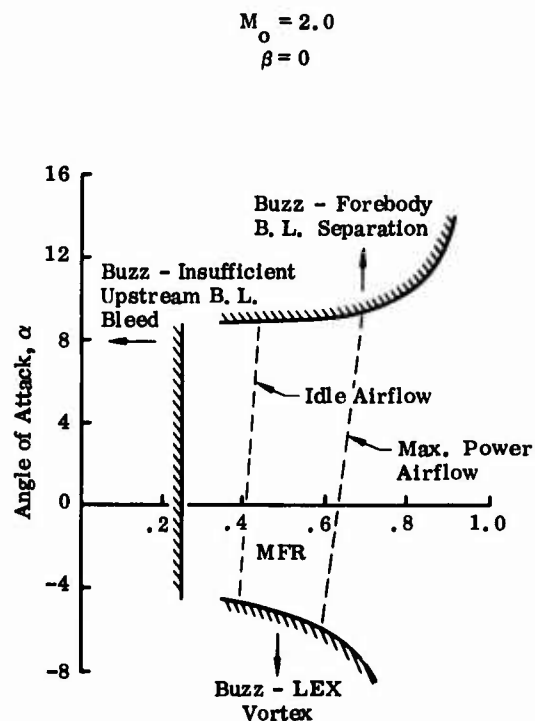
FIGURE 6. EFFECT OF MASS FLOW RATIO ON INLET STABILITY BOUNDARIES
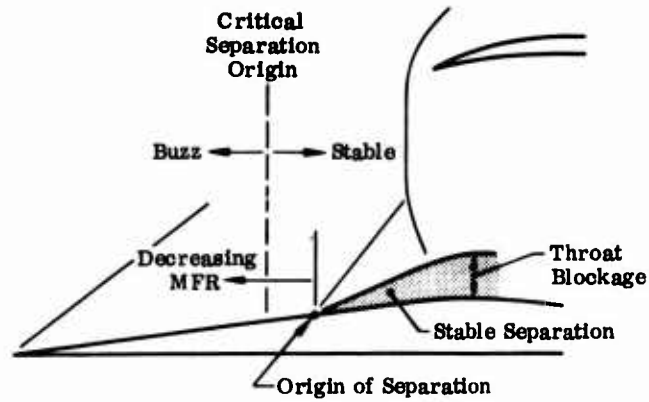
FIGURE 7. EFFECT OF MFR ON INLET STABILITY AT LOW
ANGLE OF ATTACK UNDER CONDITIONS OF
REDUCED SURFACE BLEED

$M_o = 2.0$

$\alpha = 3°, \beta = 0$

$\alpha = 9°, \beta = 4°$

$\alpha = -6°, \beta = 0$

a. Reference Condition (Stable)

b. Forebody Boundary Layer
Separation (Buzz)

c. LEX Vortex (Buzz)
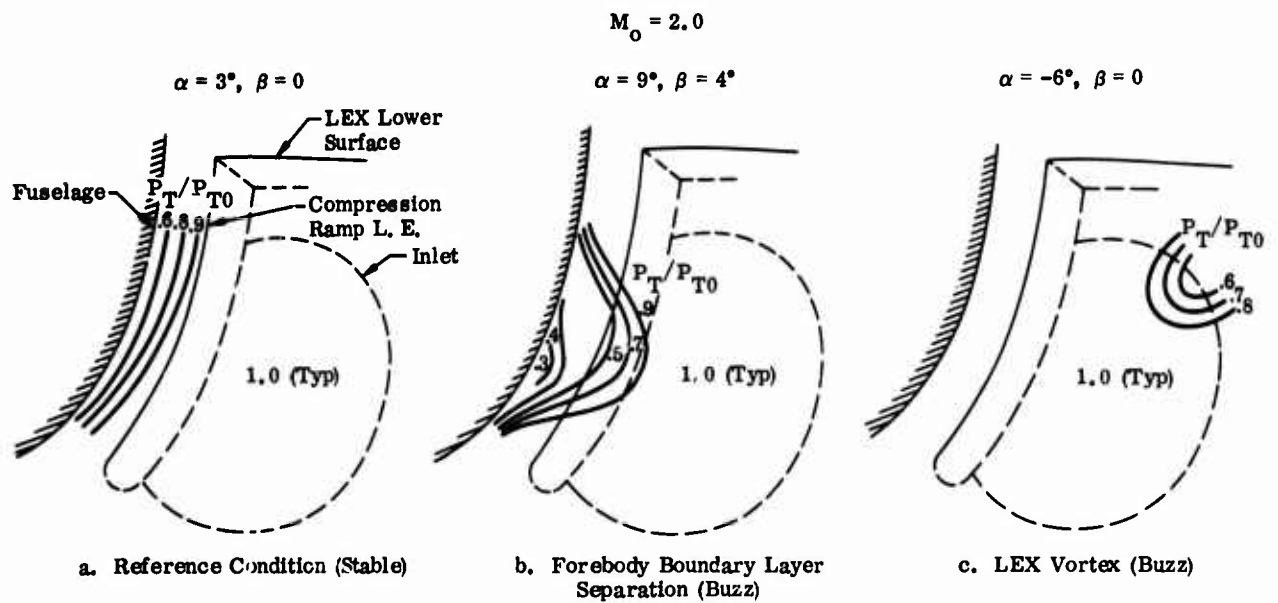
FIGURE 8. INLET FLOW FIELD TOTAL PRESSURE CONTOURS

a. Typical Compression Ramp Static
Pressure Distribution

b. Stable: $(P_{T1} - \Delta P_{T\ 1-2})_{aa} > P_2$

c. Unstable: $(P_{T1} - \Delta P_{T\ 1-2})_{aa} < P_2$
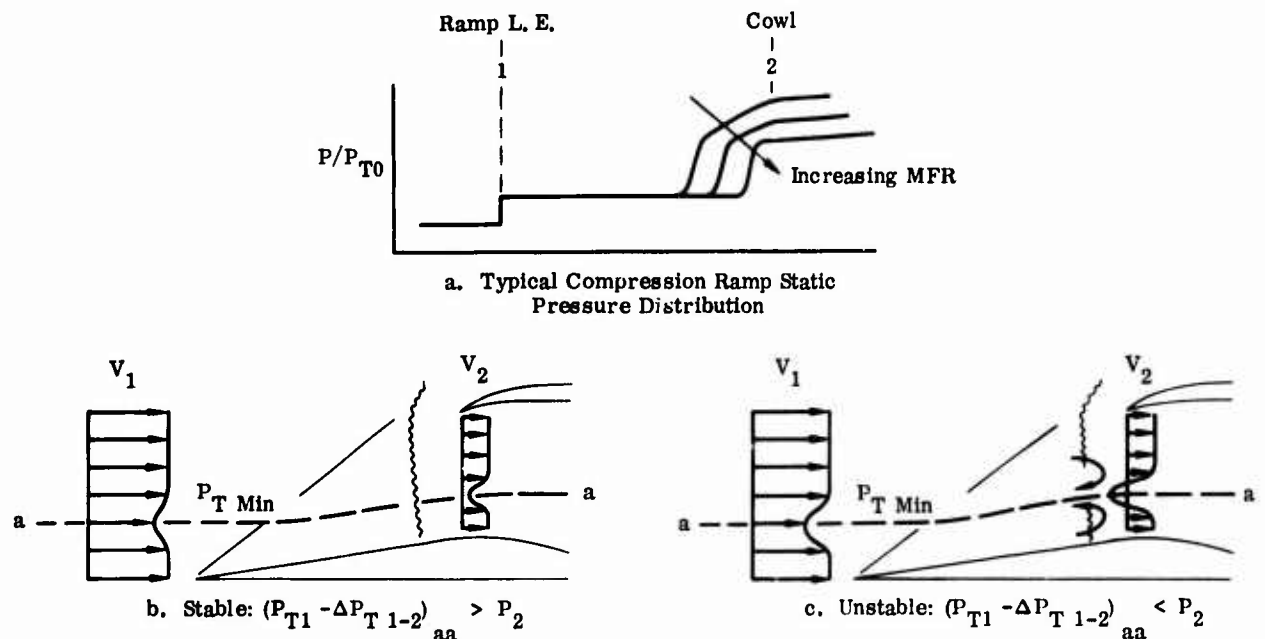
FIGURE 9. INLET INSTABILITY CRITERION

a. α/β Effect @ M_o = 1.6

b. α/β Effect @ M_o = 2.0

FIGURE 10. COMPARISON OF MEASURED AND ESTIMATED STABILITY BOUNDARIES

a. Effect of MFR @ M_o = 1.6

b. Effect of MFR @ M_o = 2.0
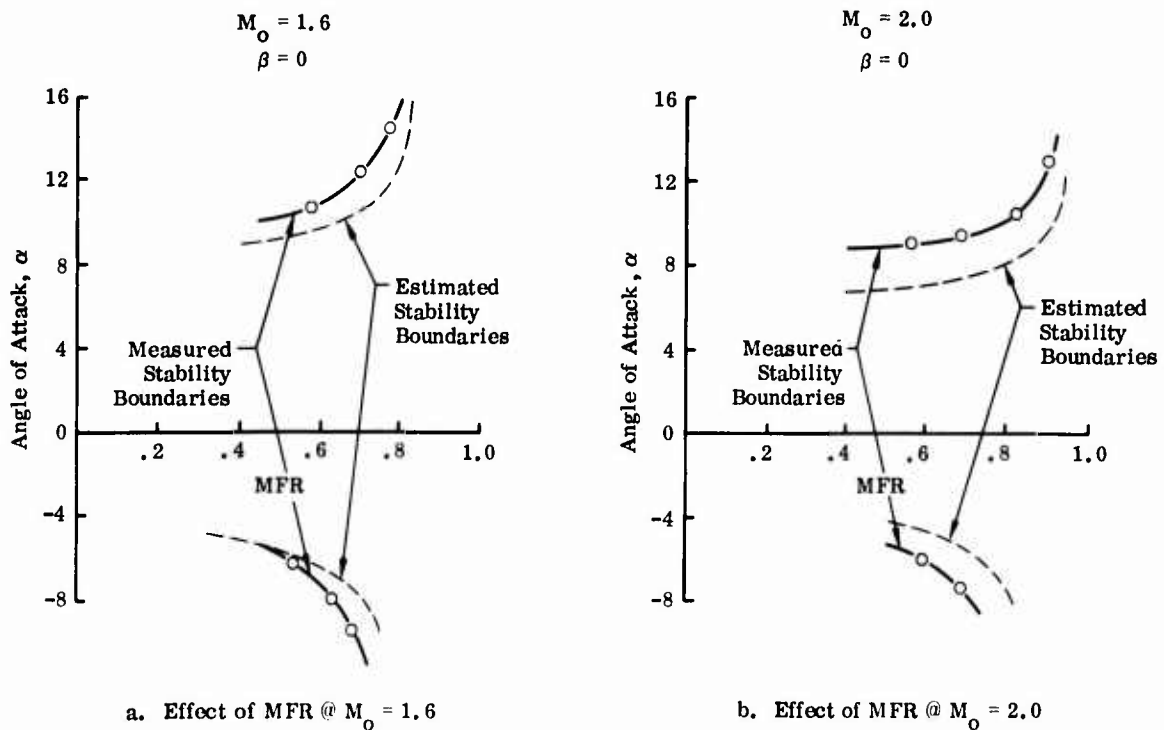
FIGURE 11. COMPARISON OF MEASURED AND ESTIMATED STABILITY BOUNDARIES

$$M_0 = 2.0$$
$$\beta = 0$$

a. $(P_{T2}/P_{T0})_{Min}$ vs α

b. P_2/P_{T0} vs MFR
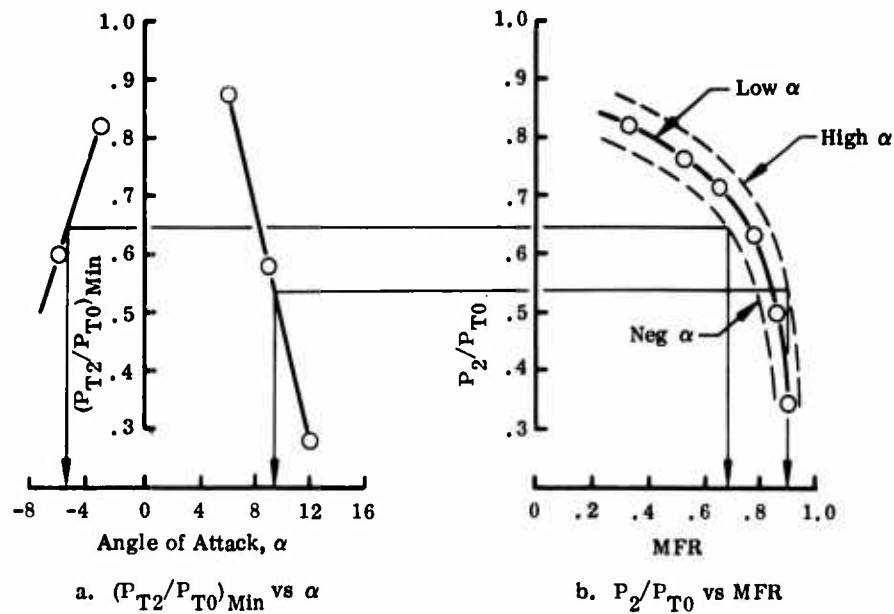
FIGURE 12. STABILITY BOUNDARY INPUTS

$\beta = 0$

Max. Power Airflow

- ● Measured Stability Boundary
- ○ Estimated Stability Boundary
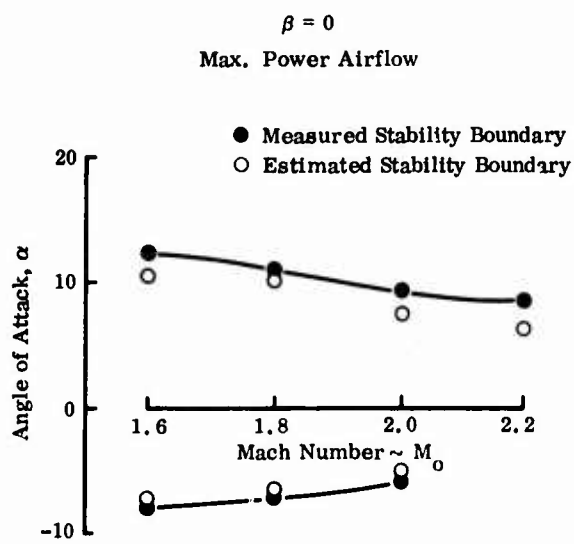
FIGURE 13. COMPARISON OF MEASURED AND
ESTIMATED STABILITY BOUNDARIES -
MACH NUMBER EFFECT

$$M_0 = 0.8$$
$$\alpha = 25°, \quad \beta = 10°$$
MFR ≈ 0.2 (Less than Idle Airflow)
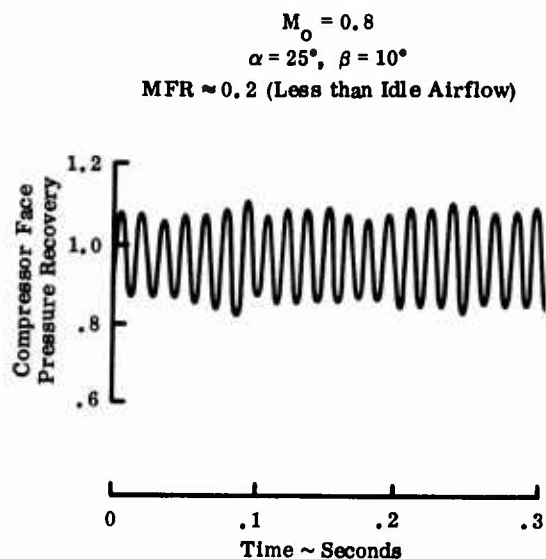
FIGURE 14. INLET "BUZZ" AT SUBSONIC
MACH NUMBER

$$M_O = 2.0$$
$$\theta = 5°$$

Note: Decreasing MFR from (a) to (d)

a) Stable   b) Stable   c) Stable   d) Buzz
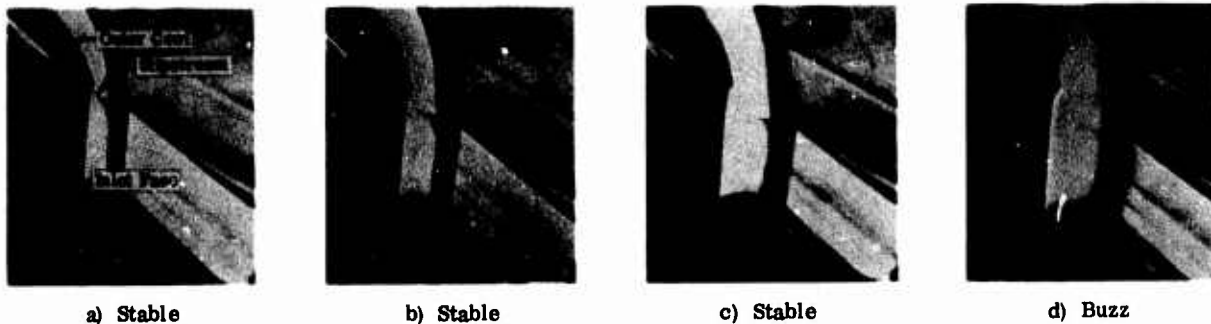
FIGURE 15. EFFECT OF SLIPSTREAM INGESTION ON INLET STABILITY
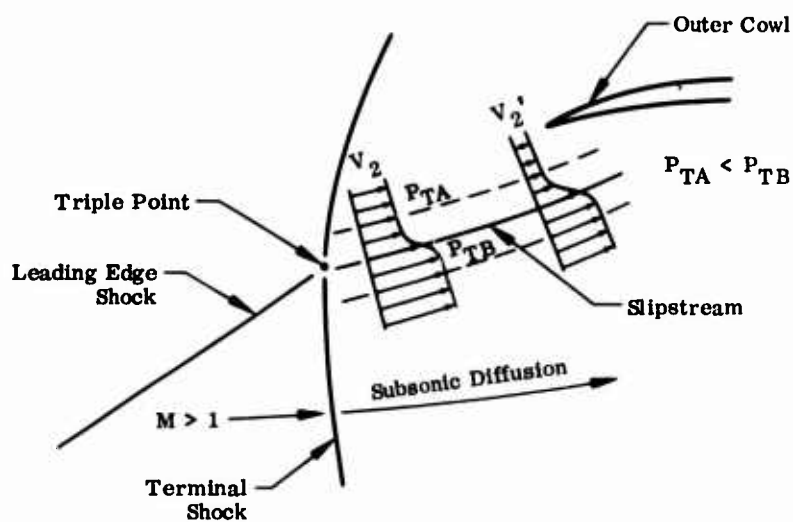
FIGURE 16. SUBSONIC FLOW FIELD BETWEEN TRIPLE
POINT AND INLET COWL
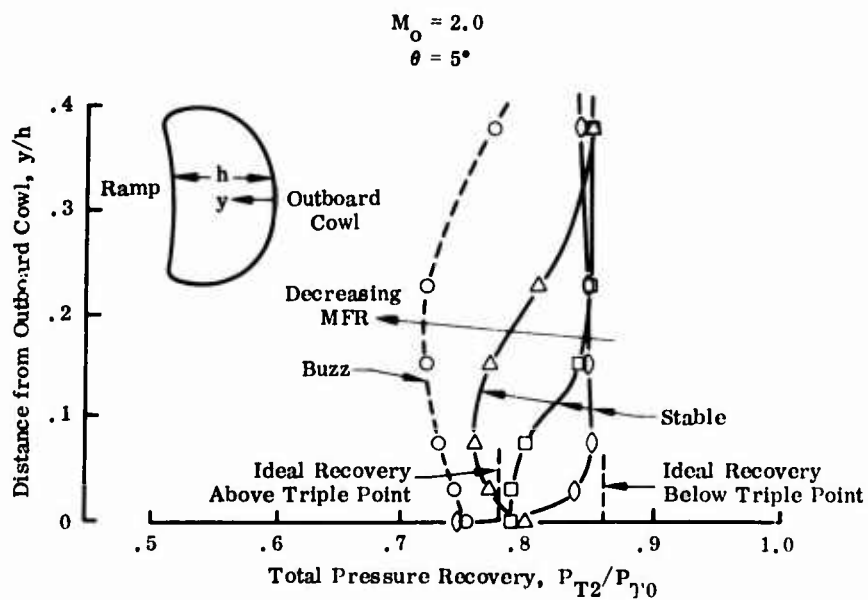
$$M_O = 2.0$$
$$\theta = 5°$$

FIGURE 17. EFFECT OF SLIPSTREAM INGESTION ON OUTBOARD
COWL TOTAL PRESSURE PROFILES

$$M_o = 2.0$$
$$\alpha = 9°, \beta = 4°$$

a. Original Slot   b. Modified Slot
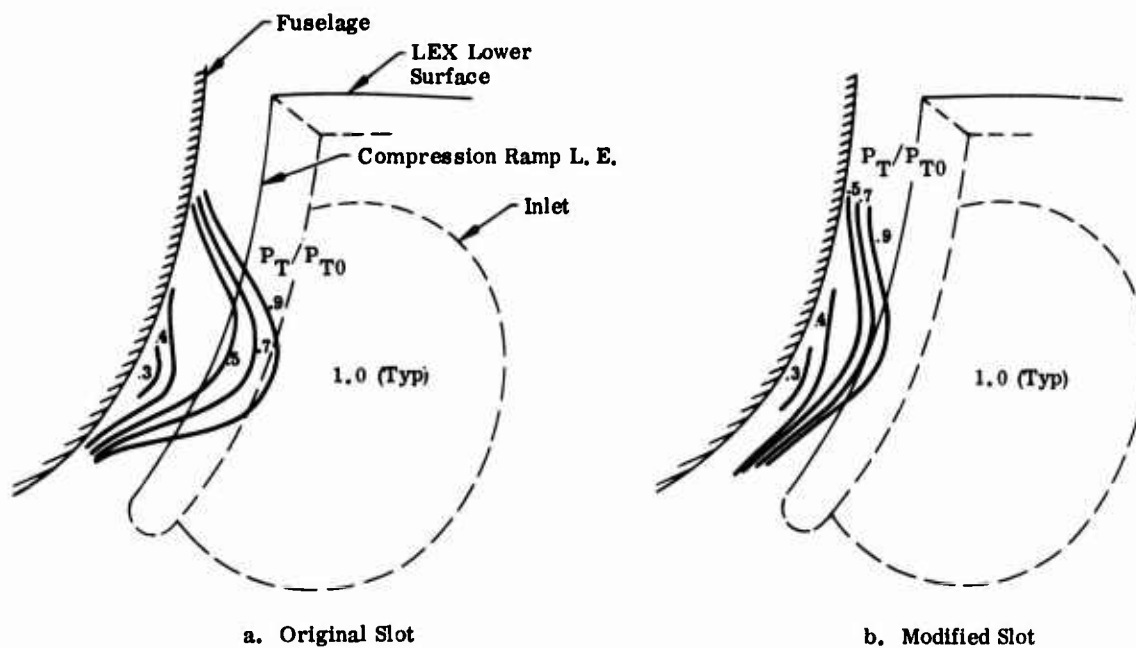
FIGURE 18. EFFECT OF LEX SLOT CONFIGURATION ON INLET
FLOW FIELD TOTAL PRESSURE AT HIGH α/β

$$M_o = 1.6$$
Max. Power Airflow
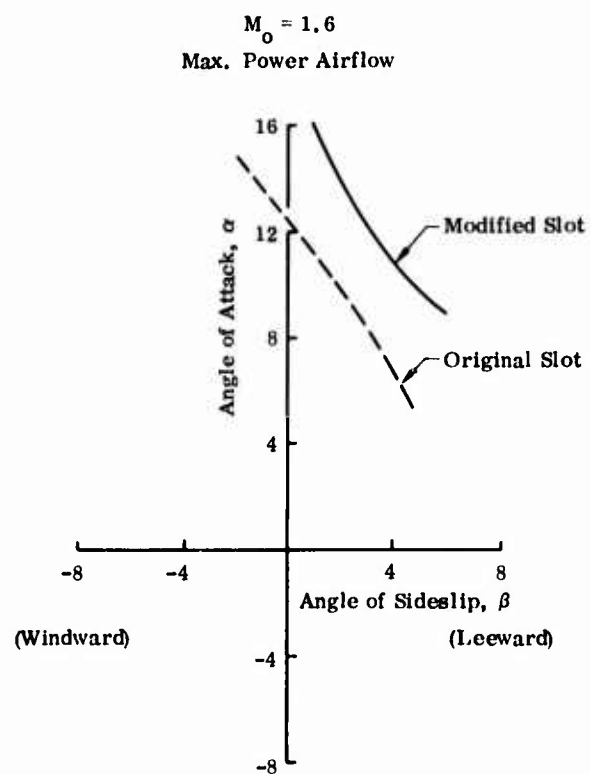
FIGURE 19. EFFECT OF LEX SLOT CONFIGURATION ON
MEASURED STABILITY BOUNDARIES

THE MEASUREMENT OF THE TRANSONIC SPILLAGE

DRAG OF A SUPERSONIC INTAKE

S.A.M.Thornley   and   E.C.Carter
Senior Project Supervisor   Deputy Chief Aerodynamicist

AIRCRAFT RESEARCH ASSOCIATION LTD.
Manton Lane
Bedford
MK41 7PF
England

SUMMARY

This paper describes the technique in current use at the Aircraft Research Association for the measurement of the transonic spillage drag of a two dimensional, ramp intake. The method requires the calibration of the intake duct system for both mass flow and exit momentum. The technique is equally applicable to supersonic testing. The achieved repeatability of the measurements allows intake configuration differentiation to $\pm$1% in aircraft drag for a typical supersonic fighter aircraft at high subsonic speed. Theoretically based calculations show satisfactory agreement with the measurements both for a range of intake mass flow and for intake ramp angle changes. The technique is economic and suitable for routine testing. General comment is made on the merits of three methods available for the measurement of spillage drag using the balance mounted, whole model technique, together with recommendations for further technique development.

NOTATION

|	
A_o	Freestream area of captured flow
$A1$	Intake reference area
A_t	Intake throat area
$A_o/A1$	Area ratio equal to the mass flow ratio
C_D	Drag coefficient on total intake reference area (2A1 for twin duct side intakes)
CDISMOM	Momentum discharge coefficient
CDISV	Venturi mass flow discharge coefficient
D	Drag
F_g	Gross thrust
F_n	Net thrust
H/P	Total pressure/static pressure
mV_o	Freestream momentum of the captured flow
$mV_e + A_e(P_e - P_o)$	Exit momentum + pressure term
$mV_t + A_t(P_t - P_o)$	Throat momentum + pressure term
(PU - PT)/PU	Venturi upstream - throat pressure/upstream pressure
X_{aft}	Axial force on the afterbody
X_{bal}	" " " " balance
X_{base}	" " " " base
X_{cowl}	" " " " cowl
X_{duct}	" " " " duct
X_{ext}	" " " " external surfaces except afterbody
X_{int}	" " as defined in figure 3
X_{pe}	" " on the pre-entry stream tube
X_r	" " " " ramp
θ	Throat flow inclination to freestream

1. INTRODUCTION

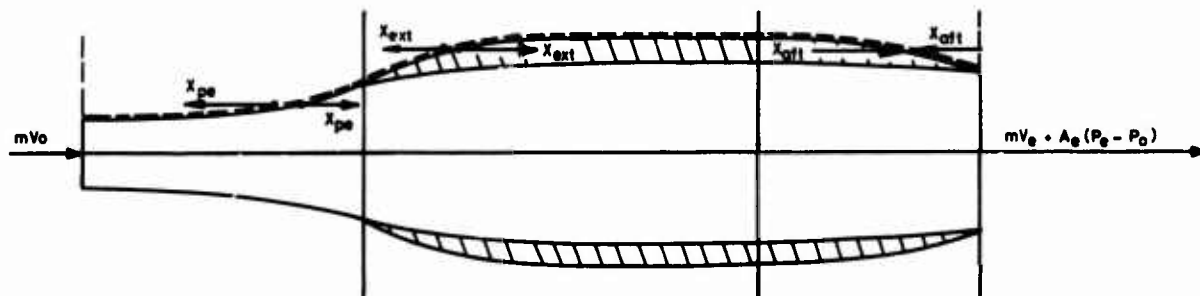Intakes designed for supersonic operation generally have sharp lips. When such an intake is operated at transonic speeds, the flow losses associated with the sharp lips can cause large drag penalties if the engine flows required at such speeds mean operation of the intake at flow ratios less than maximum. Such drag penalties are called spillage drag and some typical curves are shown in figure 1. For example the spillage drag slope of a sharp lipped, supersonic intake might typically be $\Delta C_D / \Delta(A_o/A_1) = -0.7$. This value is between 10 and ^{b}100 times greater than that of a good, axisymmetric, subsonic cowl, depending on the point of comparison. Thus the measurement of intake spillage drag is important for the estimation of aircraft performance for aircraft using sharp lipped intakes.

The steep drag slopes associated with sharp lipped intakes indicate very dirty external flows. The size of the values is typically of the same order as the drag of a flat plate normal to the airflow. Typical loss making features could be separations, vortices, or shocks. All these features should show in surface oil flow visualisation.

The importance of tests in a wind tunnel for intake spillage drag, or indeed for aircraft drag, can be further emphasised. The validity of current empirical correlations, employed by the performance groups of industry, is questionable when applied to the development of new configurations, by reason of the novel features of the configuration. The use of wind tunnel tests for such new configurations is less likely to miss the effects of the newness of the configuration on the aircraft drag. In such circumstances, the practical wind tunnel engineer would consider that a properly thought out series of models and tests, would estimate the projected aircraft drag to a considerably better confidence value than correlative data based on past configurations.

FIG.1 TYPICAL SUBSONIC SPILLAGE DRAG CURVES

This paper describes the principles and methods used at the Aircraft Research Association for the measurement of the spillage drag of a two-dimensional, ramp type intake. Particular attention is given to the calibration and validation of the results, together with recommendations for further technique development.

2. PRINCIPLES

NET FORCE FOR ACCELERATION / CLIMB $= mV_e + A_e(P_e - P_o) - mV_o - X_{ext} - X_{aft} - X_{pe}$

$= F_g - mV_o - (X_{ext} + X_{pe} + X_{aft})$

$= F_n - D$

$=$ THRUST - DRAG

FIG. 2. AIRCRAFT THRUST - DRAG

Figure 2 shows a simplified balance of the principal forces acting on an engine nacelle. Drag is measured on the aeroforce model for which the intake and exit flow conditions are measured. It is then adjusted to the correct intake flow using spillage drag test results and to the correct exit flow conditions using afterbody plus jet drag test results.

For a detailed balance of the forces involved, references 1 and 2 should be consulted. For the procedures and techniques suitable for the detailed balance, references 3 and 4 are available.
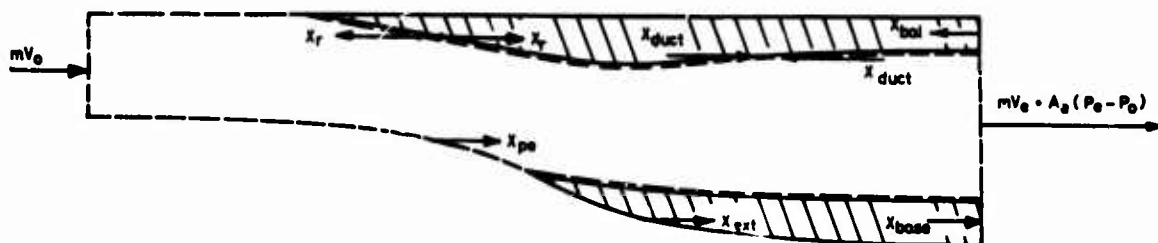
MODEL, $\quad X_{bal} = X_{ext} + X_{duct} + X_{base} + X_r$

STREAMTUBE, $\quad mV_e + A_e(P_e - P_o) = mV_o + X_{pe} - X_{duct} - X_r$

DEFINE, $\quad X_{int} = mV_o - (mV_e + A_e(P_e - P_o))$

THEN REQUIRED DRAG, $\quad X_{ext} + X_{pe} = X_{bal} - X_{duct} - X_{base} - X_r + (X_{duct} + X_r - X_{int})$

$$= X_{bal} - X_{base} - X_{int}$$

FIG. 3. BASIC EQUATIONS FOR SPILLAGE DRAG MODEL TESTING ON RAMP INTAKES

Figure 3 gives the equations applicable to the measurement of intake spillage drag. Here the equations are derived for the zero incidence case with a square ended exit flow in the freestream direction. More general equations are available in reference 4 and 5. Generally as the intake is throttled (for Ao < A_t) the increase of X_{pe} is wholly or partially offset by a reduction in X_{ext} due to thrust forces being developed on the cowl (subsonic flow). The change of (X_{ext} + X_{pe}) as the intake is throttled from some datum flow is called the spillage drag.

3. MODEL AND INSTRUMENTATION

The method uses the balance mounted, whole model approach with non-metric mass flow control. The technique and model layout is based on that described in reference 6. Figure 4 shows the model in schematic form.
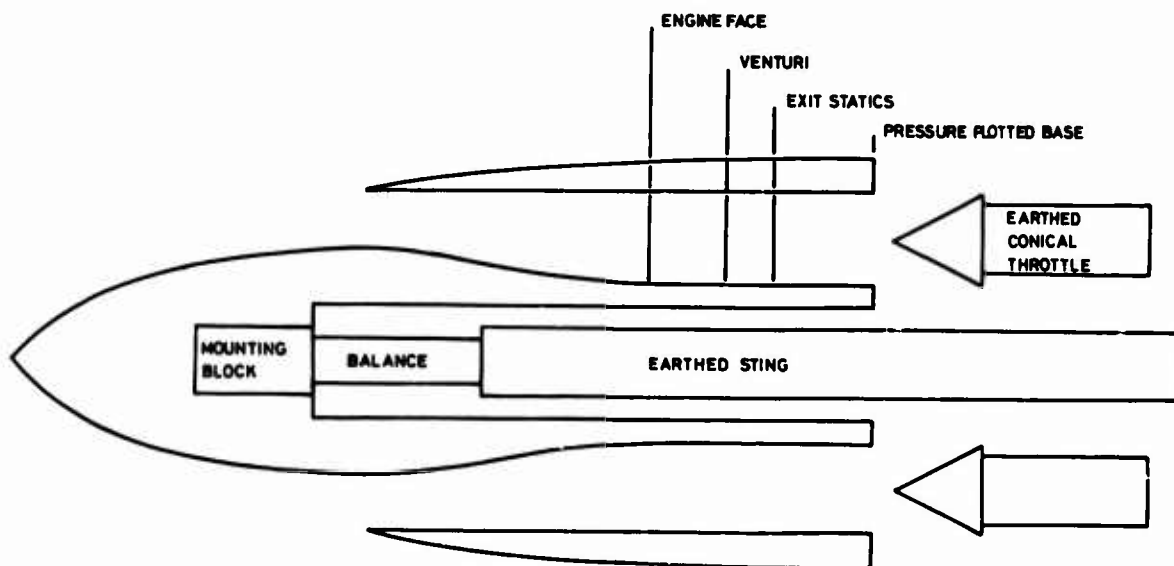
FIG. 4. MODEL INSTRUMENTATION

3-4

Twin side intakes and internal ducts are representative to the engine face. Aft of the engine face the duct was expanded slightly to suit a requirement for a subsonic test Mach number of 0.6 with full intake flow. Externally the fuselage was representative to about 3 intake heights downstream of the cowl lip plane and then blended into a constant section, parallel sided afterbody. The base was flat but carried thin flanges on the internal and external edges to promote clean flow separation. Stub wings were fitted as these might act as forward facing surfaces for the possible recovery of spill thrust rather than to give the correct upwash flowfield at the intake. The whole model was carried on a standard Aircraft Research Association 3" balance which was fitted into a massive, I section sting - see figure 5. The I section of the sting was convenient since considerable strength was required for the large normal force loads on the model yet the internal ducts of this particular model gave little space between the ducts at the engine face position. Thus the ducts fitted on either side of the I section. Aft of the engine face, where it was necessary to increase the duct diameter, the ducts were taken away from the model centreline using a short S bend.

The model carries comprehensive intake instrumentation. The starboard duct is used for intake performance and stability and the port duct for turbulence. Both ducts are of course instrumented for mass flow and exit momentum. It is important to measure engine face performance in the context of spillage drag since intake modifications that are aimed at reducing drag might affect engine face recovery or mass flow. Since ultimately thrust minus drag is of overall concern, both engine face performance and intake drag are necessary measurements.

FIG. 5. STING ASSEMBLY

Figure 6 is a view of the ducts and instrumentation. The starboard duct has a rotatable, two position, 12 arm pitot rake at the engine face plane for the measurement of pressure recovery and steady state distortion. Mass flow was measured in calibrated venturis. The exit statics for the measurement of exit momentum are downstream of the venturis in a constant diameter exit tube. Mass flow is controlled by an earthed, 60° conical plug throttle with linear position actuation and indication - see figure 7. The base is comprehensively pressure plotted to allow for the effects of changing base pressure as the throttles are driven. The model incorporates bleed ducts which carry venturis and exit statics for the measurement of bleed flow and momentum. The bleed flows are controlled by fixed area exit nozzles, the exit statics being at the nozzle throat.

FIG. 6. DUCTS AND INSTRUMENTATION

Extensive surface pressure plotting on the intake ramps and cowls was necessary for the diagnosis of the drag results.

Figure 6 shows the model instrumentation when the bottom 'tray' of the model fuselage is removed. Direct access is available to the scanivalves used for pressure measurements, to the wiring and plumbing for the scanivalves, and to the wiring for the turbulence transducers.
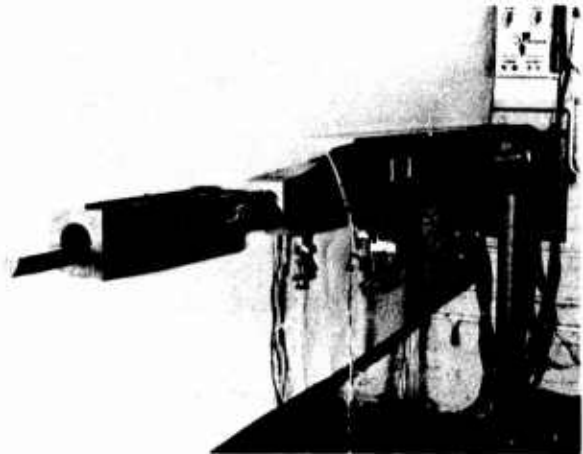

FIG. 7. BASE AND THROTTLE
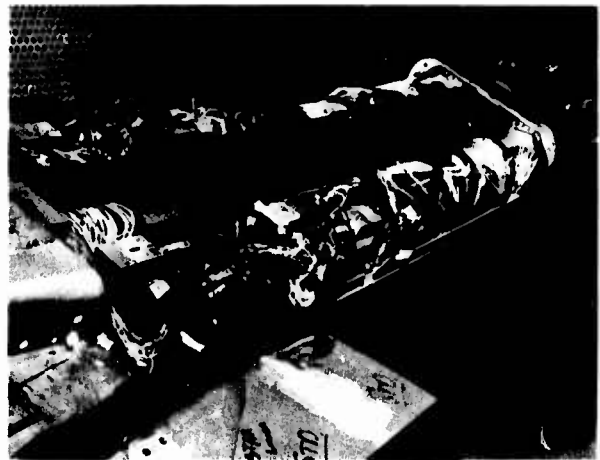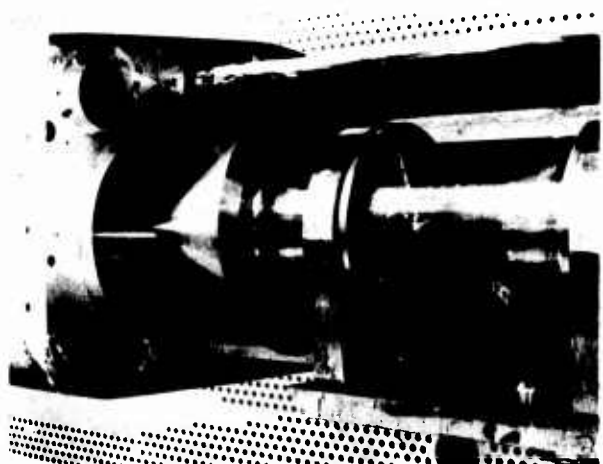
4. TUNNEL AND INSTRUMENTATION

The model has been tested transonically in the 8ft x 9ft tunnel at the Aircraft Research Association. Tests have been made in the Mach number range 0.5 to 1.3, Reynolds number 2.9 to 4.4 x 10^6 per foot, Reynolds number on capture height 0.9 to 1.3 x 10^6. Details of the tunnel are available in reference 7.

The instrumentation accuracy is

tunnel and other reference pressures	$\pm$ 0.03"Hg
scanivalve pressures as P/H	$\pm$ 0.003 at 30"Hg stagnation
incidence accuracy	~ 0.05°
balance calibration	$\pm$ ½% F.S.

balance temperature drift typically less than 1/3% F.S.

Accurate pressure and balance techniques must be available for this class of work since the final drag data is dependent on differencing large terms.

Special equipment was built to allow test point setting and monitoring. An on-line X-Y plotter was used to show pressure recovery versus mass flow. Analog circuits from transducers recording six engine face pitot pressures gave pressure recovery, and further analog circuits from transducers recording venturi upstream pressure and differential pressure gave mass flow. A dynamic transducer was displayed on an oscilloscope to show duct flow stability.

5. DATA REDUCTION

The procedure is shown in block diagram form in figure 8. All terms are in practice brought to non-dimensional form as soon as possible and calculations are carried out in non-dimensional form. The force terms are non-dimensionalised by dividing by the dynamic pressure times the total intake capture area (2A1 for twin duct side intakes).

Tabulated output, computer plotting and data on magnetic tape are routinely produced.

Small practical difficulties arose with the use of venturis. The venturi differential pressure is only single signed regardless of flow direction. The bleed system at low freestream Mach numbers sometimes flows in reverse. A pitot in the bleed duct venturi is now used to check flow direction. It is also possible at the higher freestream Mach numbers to choke the main duct venturis. Limits have been built into the procedure to eliminate such data.
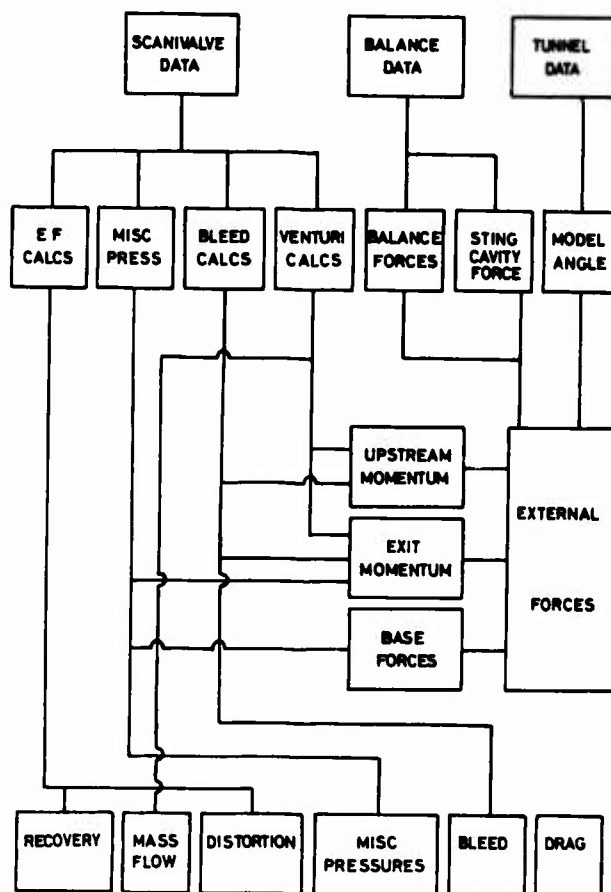
FIG. 8. DATA REDUCTION

6. CALIBRATION

6.1. Mass flow calibration

Accuracy of mass flow measurement is important for all intake test work. For spillage drag tests on intakes, the effect of mass flow errors on the use of the data, depends both on the type of error and the shape of the spillage drag curve. For example, for linear drag curves with only zero shift type errors of mass flow, the slope of the curve is important and this would be determined satisfactorily. However other types of error are common and the shape of the drag curves can be far from linear. Thus for intake drag work accuracy of mass flow is important. If aircraft drag is to be estimated, then accurate mass flow measurements must be made also for the aeroforce model, in order to match the test data from both the aeroforce and the intake drag model at some datum mass flow.

Since the model was designed to use flow through ducts in the transonic speed range, the available pressure differential to drive the duct flow led to the choice of a venturi for mass flow measurement rather than the sonic exit method. The use of a 'good' venturi according to standard venturi practice would have yielded an unworkable model length. From the available model length, to suit the working section of the tunnel and the model and support system, it was necessary to use a venturi of length about equal to one duct diameter. Thus the best approach was to ensure the venturi size suits model length limitations and to calibrate for accuracy.

The shape of the venturi is shown in figure 9. The throat area was sized for the requirement of full intake flow when the intake throat is a maximum, whilst maintaining an adequate contraction to give a pressure differential suitable to the instrumentation accuracy and the required mass flow accuracy. Thus the maximum throat Mach number was as high as 0.75. In retrospect the venturi and duct design could probably be improved, particularly by increasing the area upstream of the contraction. The design of venturis to suit the model limitations with large duct flows is an area of design largely outside existing venturi practice.
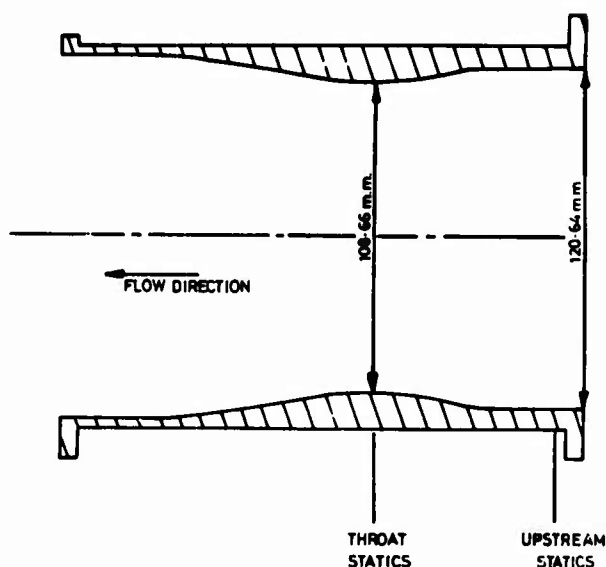
FIG. 9. VENTURI GEOMETRY
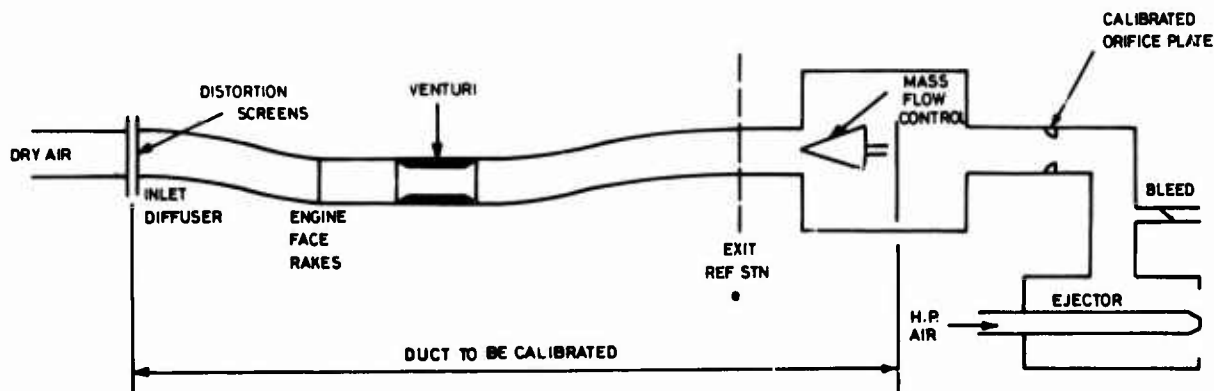
FIG. 10. MASS FLOW CALIBRATION

Calibration was carried out at the National Gas Turbine Establishment, Pyestock, England, where a proven flow rig was available. Upstream of the engine face, the duct was represented to the end of the intake ramps. Gauzes were used to introduce distortion, though in practice the calibration distortions were not wholly representative of the later tunnel test distortions where large radial distortions were found at the engine face. Since the engine face pitot rake supports cause flow losses, some smoothing and mixing of the flow occurs downstream of the support struts. Within the range of calibration distortions appropriate to the transonic operation of the model, the venturi was found to be insensitive to the engine face distortion, see figure 11.

The ducts were effectively recalibrated 2½ years later when the exit flow profile was measured to give a momentum discharge coefficient - see section 6.2. In these later tests some larger distortions appropriate to supersonic operation were used. These tests indicated that at the lower mass flows and higher distortions occurring during supersonic intake operation, the venturi did not give mass flow reliably. Consequently for supersonic testing the mass flow is now derived from a sonic exit area technique using a measurement of the throttle plug position. At transonic distortion levels, the discharge coefficient repeatability between the two calibrations was ½%.
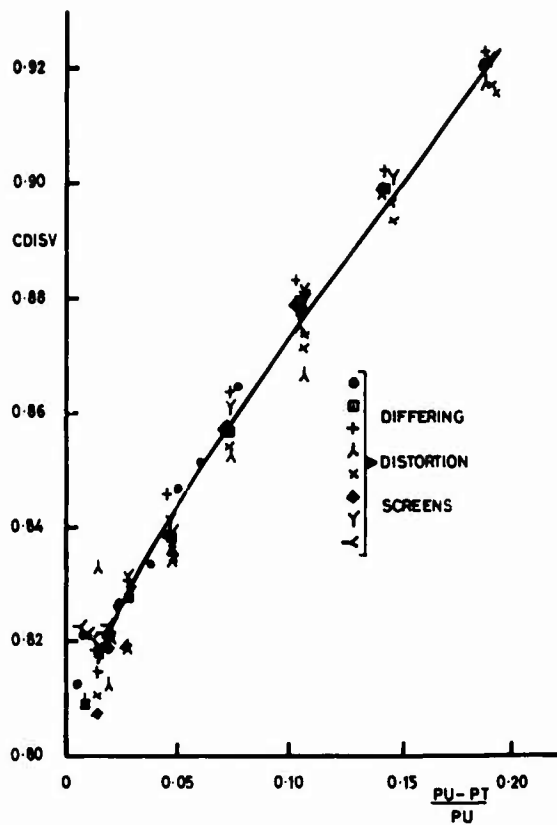
FIG. 11. CDISV ~ $\frac{PU-PT}{PU}$

6.2. Momentum discharge coefficient calibration

The exit momentum plus pressure term is $mV_e + A_e(P_e - P_o)$. The static pressure term is measured at the exit wall statics and assumed uniform across the duct. The velocity term is derived from the measured exit statics and the venturi mass flow, using one-dimensional duct flow equations.

To allow for distortion at the exit station, a 'momentum discharge coefficient' needs to be applied to the exit momentum plus pressure term to compensate for the difference between the actual profile and the assumed profile. This momentum discharge coefficient is greater than 1.0. For example, if there is a hole in the flow then the measured mass flow must cross the rest of the exit station area with a greater velocity than if the flow had been one-dimensional. Thus the velocity is greater than one-dimensional flow and the velocity momentum term is larger.

The effect of the flow profile on the exit momentum was studied during the model design stage by calculations based on various assumed profiles. Profiles of pitot pressure relative to duct static pressure were integrated to find integrated mass flow and momentum. The integrated mass flow and the duct static pressures were then combined to yield a momentum from 1D flow equations to simulate the combination of venturi mass flow and exit static pressures. The integrated momentum was then compared with the one-dimensional momentum. The results of these calculations are shown in figure 12. The calculations were also made for a range of exit Mach numbers and these emphasised the need to keep the exit Mach number low so that the exit momentum was dominated by the pressure term. However it must be remembered that the exit momentum term is a large one that is subsequently differenced from the upstream momentum so that momentum discharge coefficients need to be known correspondingly more accurately.
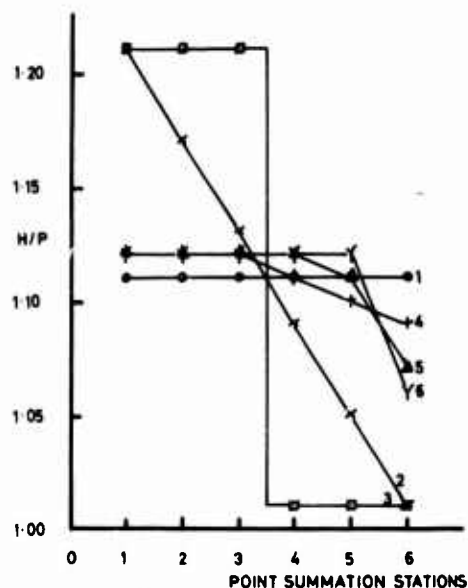
CASE	SYMBOL	PROFILE TYPE	MOMENTUM DISCHARGE COEFFICIENT
1	●	UNIFORM	1·000
2	×	LINEAR	1·134
3	▫	STEP	1·367
4	+	UNIFORM CENTRE + BOUNDARY LAYER	1·002
5	▲	"	1·007
6	Y	"	1·011

FIG. 12. EFFECT OF PITOT PRESSURE PROFILE ON THE EXIT MOMENTUM DISCHARGE COEFFICIENT

The model was initially tested using a momentum discharge coefficient of 1.0 as a consequence of the calculations made. Subsequent to testing, the engine face profile was used in the above calculation procedure. The worst error, if the engine face pitot profile distortion applied at the exit was about 2% of the drag level. Since the venturi calibration suggested that the mass flow measurement is insensitive to engine face distortion, then the effects of the engine face distortion on momentum are also likely to be small or independent of engine face distortion. Comparative testing of differing intake configurations is then practical.

The initial tests also showed that the use of bleed did not affect the drag data significantly. This was encouraging since the change of bleed from off to on gave differing engine face distortions and so the effect of the engine face distortion on the exit momentum was small. At a later stage of the model testing, results of a similar model at the Royal Aircraft Establishment, Bedford became available. Differences between these two sets of results led to a need to check the validity of the assumptions of the exit pitot pressure profile for the model. Two possible sources of distortion were identified aft of the engine face. Firstly, the S bend between the engine face and the venturi could produce distortion. The bend was needed to shift the duct centreline away from the sting to allow for duct expansion. The bend is fairly short since model length was a limitation. Secondly the mass flow venturi could produce distortion since the throat Mach numbers are high and again the venturi is short because of model length limitations.

The exit duct was fitted with the pitot and static rake shown in figure 13. The rake carried 12 arms of pitot tubes. For each arm, 6 pitot tubes were placed at radii corresponding to equal area weighting and the seventh tube was close to the duct wall to measure the effect of the boundary layer. A central pitot was also fitted. 6 stream statics were mounted on the rake and the wall statics were increased from 4 to 12. The rake was arranged so as not to interfere with the exit throttle and tests were carried c t in the same calibration rig at the National Gas Turbine Establishment as was used for the original mass flow calibration.

FIG. 13. EXIT PITOT AND STATIC RAKE
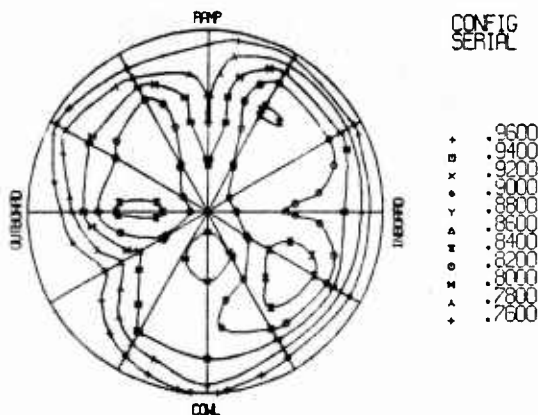
FIG. 14. EXIT PITOT PRESSURE CONTOUR

Figure 14 shows a typical pitot pressure contour at the exit station at full flow. The pitot pressures and the static pressures were integrated to give both mass flow and momentum. The integration for mass flow was typically within $\pm 1\%$ of the rig mass flow which indicates that the measurements are an accurate description of the flow. The integration for the exit momentum was compared with the standard model method outlined above and an effective exit momentum discharge coefficient was calculated. Results are shown
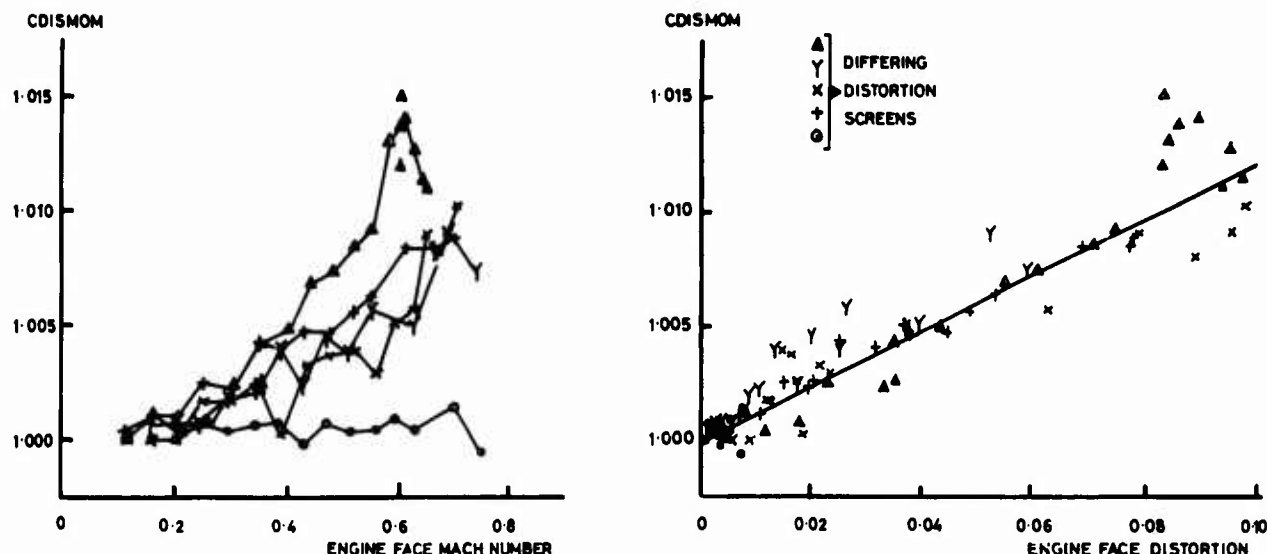
FIG. 15. EXIT MOMENTUM DISCHARGE COEFFICIENT

in figure 15, the differing symbols representing differing distortion screens. Tests were done for a range of engine face distortions and the momentum discharge coefficient was correlated against an engine face distortion parameter. The correlation has now been applied to the data reduction programme for the wind tunnel testing.

The exit station Mach number is very significant in the degree by which the flow profile at the exit station changes the drag data. Changes to the model at the intake end resulted in larger mass flows than during the initial model testing so that the exit flow profile was more significant. Again, in retrospect, the venturi and exit duct design could probably be improved. It is suggested that for this sort of test a duct Mach number not greater than 0.3 at the venturi upstream station and at the exit station is desirable. Also for testing at the higher freestream Mach numbers it would be practicable to incorporate flow smoothing screens in the ducts.

7. REPEATABILITY

An analytical approach to data accuracy was not attempted. Instead, following tunnel testing, real data was modified to simulate a variety of possible errors. This approach allows errors typical of the instrumentation system to be introduced. The computation of the modified data uses the established data reduction programme and comparison of the results with the results from the unmodified data indicates the most significant terms. Drag levels can be affected by errors in tunnel stagnation pressure measurement and errors in the base pressure due to zero shift type errors in the scanivalve pressure system. Drag slopes can be affected by errors in the tunnel reference pressures and by zero shift plus sensitivity errors peculiar to the scanivalve calibrating system. Errors in the venturi discharge coefficient have a comparatively small effect on drag level but some effect on slope. Accurate pitch setting is required for consistent drag levels. Accurate axial and normal forces are required from the balance as both contribute to drag when resolving the forces from balance axes to wind axes.

Datum cases are run for each phase of testing in the tunnel. The repeatability within a test phase typically will allow configuration differentiation of the order of 1% of aircraft drag at high subsonic speeds. The repeatability between phases is 3 times worse than typical instrumentation accuracy should give and the causes of the non-repeatability have not been found.

The effect of bleed is to alter the engine face distortion. Additionally the total intake capture flow is split into two streams so that the force and exit momentum balance is changed. The bleed venturis were not calibrated, a discharge coefficient being estimated from standard practice. Generally drag data bleed on to bleed off compares to about 0.02. This agreement is considered satisfactory and confirms that for transonic engine face distortion levels, the effects of the distortion on the exit momentum and hence overall drag levels, is small.

8. COMPARISON WITH THEORY
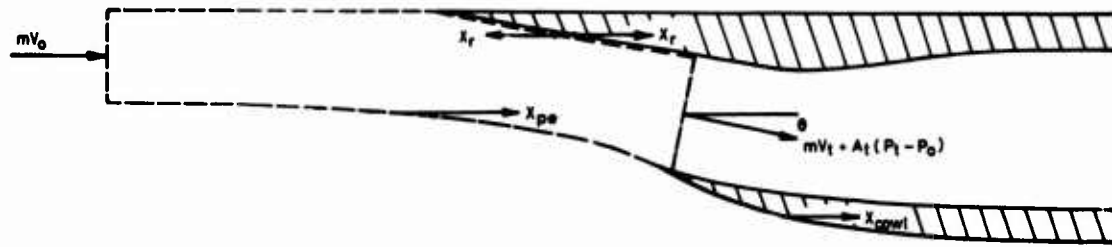
STREAMTUBE $mV_0 \cdot X_{pe} = X_r \cdot (mV_t \cdot A_t(P_t - P_0)) \cos \theta$

PRE ENTRY DRAG $X_{pe} = X_r \cdot (mV_t \cdot A_t(P_t - P_0)) \cos \theta - mV_0$

SPILLAGE DRAG $\Delta(X_{pe} \cdot X_{ext}) = \Delta(X_{pe} \cdot X_{cowl})$

FIG. 16. PRE ENTRY DRAG AND SPILLAGE DRAG CALCULATION

Theoretically based calculations have been made according to the methods of reference 8. Figure 16 shows the calculation procedure. The throat momentum is calculated by assuming isentropic flow between the freestream and the throat and that one dimensional flow theory is adequate. The ramp and cowl forces are found by the integration of measured pressures. The calculations have been made for each test data point using achieved test mass flows and pressure measurements. Figures 17 and 18 show the development of the pre-entry drag and the spillage drag respectively. (Common practice is followed in naming the pre-entry, ramp and cowl forces, as drag, though strictly they are only axial forces on restricted areas of the flow model).
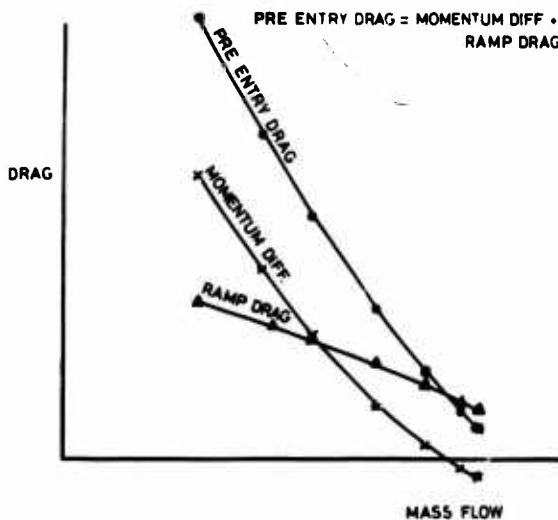
FIG. 17. PRE ENTRY DRAG
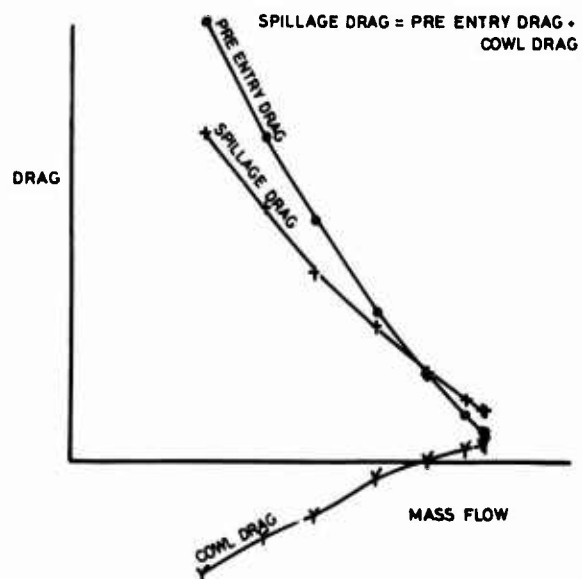
FIG. 18. SPILLAGE DRAG

The results of the calculations have been compared with the drag changes measured on the model. Figure 19 shows two such comparisons, for varying mass flow and for varying ramp angle. The data is for a freestream Mach No. of 0.9 and small positive incidence. The agreement is generally less satisfactory at other Mach No's and incidences. It is surprising that the agreement is as good as it is in view of differences between the simple one dimensional flow model, figure 16, and the complex 3 dimensional flow patterns around such an intake when installed on the side of a fuselage, and in view of the limited pressure plotting data.

These calculations demonstrate the importance of pressure plotting on the ramp and cowl surfaces. The build-up of the spillage drag shown in figures 17 and 18 is not possible without such pressure plotting. However the data does not allow a breakdown of where the flow losses which represent the spillage drag occur. Surface flow visualisation or pitot and static rakes in the external flow may prove helpful for such a breakdown.

9. TECHNIQUE COMMENT

Figure 20 shows 3 possible model systems for the measurement of spillage drag using the general approach of a balance mounted, whole model rather than a balance mounted intake. Figures 21a,b,c show typical breakdowns of the loads for the 3 systems. The base and internal forces would be derived from pressure measurements in all 3 systems.

Figure 21a shows the load breakdown for the interchangeable nozzle technique. The loads have been estimated from the data of figure 21b so that the comparison between the techniques is clear. For this technique the internal force term is small and the balance records a force near to the required drag. This technique therefore gives good answers if good balance technique is available. However the method is not compatible with production testing since mass flow is not a mechanized variable (it is comparable to doing aeroforce model testing with fixed crank pieces between model and support instead of a pitching mechanism). For intake work, mass flow is the main variable and must be mechanized. For the taking of performance or turbulence data, fixed interchangeable nozzles would not allow flexibility. A mechanized variable area exit nozzle for drag testing is yet to be designed. No insurmountable difficulties should prevent a 2 dimensional approach but full base pressure plotting over the variable base area needs to be available.

FIG. 19. COMPARISON OF EXPERIMENTAL AND CALCULATED VALUES
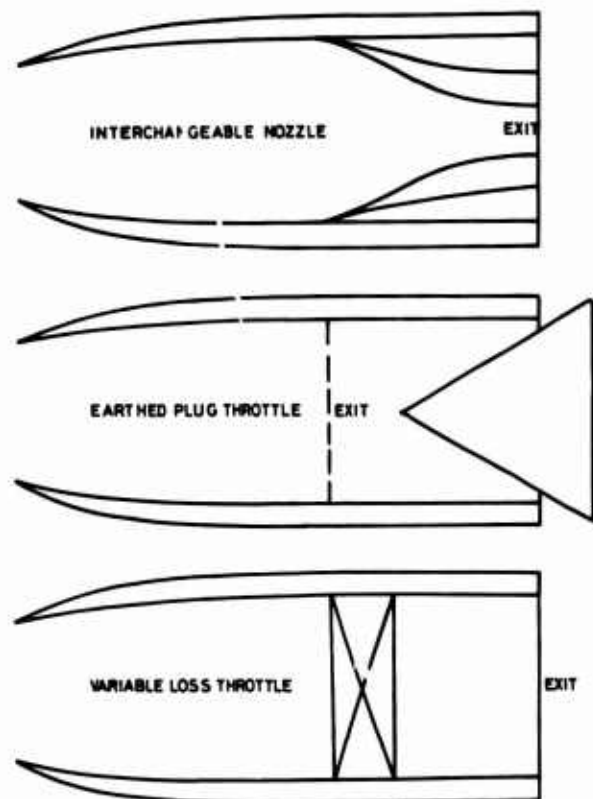
FIG. 20. MODEL SYSTEMS FOR SPILLAGE DRAG.

Figure 21b shows the load breakdown for the earthed plug throttle technique as is used for the testing described in this paper. The balance axial force and the internal force changes are large compared with the resultant external drag, and so errors can easily arise when the terms are differenced to give external drag. Moreover, the rate of change of the balance and internal terms with mass flow is very rapid at the maximum mass flow end of the curves, so that it is very easy to get considerable data scatter in this region. However provided good balance technique and pressure measuring technique are available, satisfactory data is obtained.

Figure 21c shows the load breakdown which might occur using an alternative, untried approach. To vary mass flow the duct is fitted with a variable loss, internal throttle. The loads have been estimated from the data of figure 21b, but may be dependent on the detail sizing of the exit duct and the base areas. The rate of change of balance force and internal force with mass flow is now small compared to figure 21b, so that the possible errors of slope due to differencing are minimised. The rate of change of balance force in the range of likely mass flow is similar to the rate of change of external drag and no very large rates of change occur near maximum mass flow. A variable loss throttle might be readily mechanized.

Note generally, that good balance accuracy is required. However, standard 6 component balances used for aeroforce work can be used since model size, either with stub wings or without stub wings, can generally be larger than the aeroforce model. The data accuracy in coefficient form is then at least as good as the aeroforce model data.

a) INTERCHANGEABLE NOZZLE TECHNIQUE   b) EARTHED PLUG THROTTLE TECHNIQUE   c) VARIABLE LOSS THROTTLE TECHNIQUE
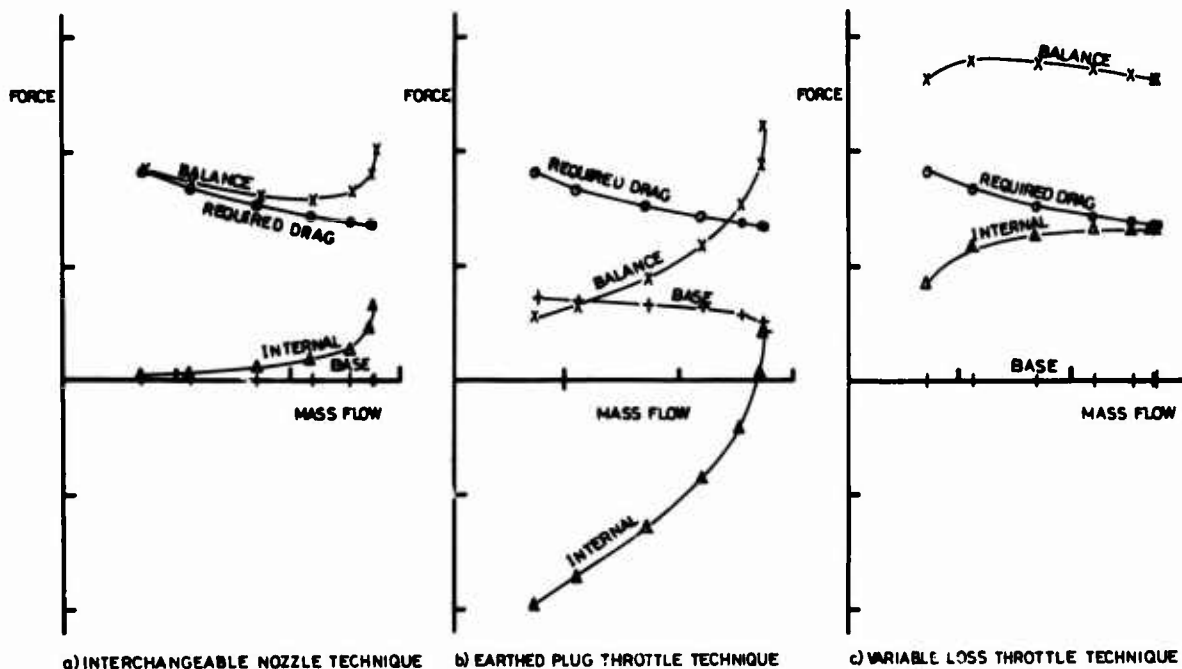
FIG. 21 BREAKDOWN OF COMPONENTS FOR 3 MODEL SYSTEMS

The measurement of the transonic spillage drag of supersonic intakes involves combining balance forces with momentum forces derived from pressure measurements. The techniques and achieved accuracies are not well established. It is important therefore, that effort be made available for technique development. Testing of standard intakes, developing either full pre-entry force or of known good shape, would be useful for checking model techniques at subsonic speeds. It is also considered that the systems outlined in figures 21a,c would be worth a trial, that is, a mechanized "interchangeable" nozzle and a mechanized variable loss throttle.

10.   CONCLUSIONS

1.   A technique is described which differentiates intake configuration drag and spillage drag to ⁻1% of the drag coefficient of a typical supersonic fighter aircraft at high subsonic speed.

2.   The data agrees with theoretically based calculations.

3.   The technique is economic and suitable for routine testing.

4.   Further technique development is desirable and proposals are made.

REFERENCES

1.	W.A.Mair et al	Definitions of the thrust of a jet engine and of the internal drag of a ducted body. Journal R.Ae.Soc. Vol.59, No.536, Aug.1955, pp 517 - 526.
2.	W.A.Mair et al	Definitions to be used in the description and analysis of drag. Journal R.Ae.Soc. Vol.62, Nov.1958, pp 796 - 801.
3.	A.E.Fuhs	'ngine integration and thrust/drag definition. AGARD-LS-53, May 1972, paper 7.
4.	E.C.Carter	Experimental determination of inlet characteristics and inlet and airframe interference. AGARD-LS-53, May 1972, paper 3.
5.	J.W.Britton, M.D.Dobson	A note on the internal drag, lift and pitching moment of a ducted body. RAE TM Aero 1292. 1971.
6.	M.D.Dobson, E.L.Goldsmith	The external drag at subsonic and supersonic speeds of fuselage-side intakes for strike-fighter aircraft. ICAS 70/49. 1970.
7.	A.B.Haines, J.C.M.Jones	The centre-line Mach number distributions and auxiliary suction requirement for the A.R.A. 9ft x 8ft Transonic Wind Tunnel. A.R.A.Report No.2. April 1958.
8.	M.C.Neale	The drag of variable ramp intakes at high subsonic Mach Number. N.G.T.E. Note 653. 1967.

AN EXPERIMENTAL INVESTIGATION OF THE COMPONENT DRAG COMPOSITION OF
A TWO-DIMENSIONAL INLET AT TRANSONIC AND SUPERSONIC SPEEDS

Clifton J. Callahan[†]
Grumman Aerospace Corporation
Bethpage, New York 11714, USA

SUMMARY

An experimental study was performed to establish the separate drag force contributions of the principal components of a rectangular, two-dimensional, external compression type, supersonic air induction inlet system. Concurrently, inlet system performance was measured in terms of engine face total pressure recovery and spacial flow distortion, and the possibility for tradeoff between inlet system drag and performance was explored.

A scale model of the forebody, including air inlet and duct systems, of an advanced, twin engine, strike aircraft was employed for the study. The wind tunnel model arrangement utilized a dual-balance technique to measure forebody and the inlet forces separately. The effects on the air induction system and vehicle forebody due to inlet component changes and varying propulsion air flow requirement have thus been identified.

The major inlet variables in the investigation included cowling lip and sidewall geometries, boundary layer bleed and air bypass exhaust configuration, and compression surface deflection schedule. The wind tunnel testing was conducted in closed circuit, continuous flow test facilities over a full range of supersonic and transonic speeds and representative ranges of vehicle angles of attack and sideslip.

Three significant aspects of the program are addressed in this paper: inlet and vehicle configuration integration, wind tunnel model arrangement for force data measurement, and measured drag and performance results. Although only incomplete experimental data may be shown at this time, the total matrix of acquired data to be published shortly is described. These data can be broadly divided according to cowling, side wall, and bleed/bypass effects, in order to display major trends in drag and performance for the investigated transonic and supersonic speed regimes. It is expected that these data will provide an array of design information previously unavailable to the induction system engineer.

NOTATION

A_c	Inlet cross sectional area
A_o	Cross sectional area of captured stream tube
C_D	Drag coefficient
FRL	Fuselage reference line
h	Altitude
IRL	Inlet reference line
M	Mach number
M_o	Free-stream mach number
P_{t_o}	Free-stream stagnation pressure
P_{t_2}	Compressor entrance stagnation pressure
T_r	Sea level reference temperature
T_{t_2}	Compressor entrance stagnation temperature
W	Airflow
α	Angle of attack
β	Side slip angle
δ	Pressure ratio, P_{t_2}/P_r
ϵ	Compression surface deflection angle
η_r	Stagnation pressure recovery, P_{t_2}/P_{t_o}
θ	Temperature ratio, T_{t_2}/T_r

[†] Advanced Development Project Engineer, Supersonic Inlet Technology

1. INTRODUCTION

In meeting the challenges of the 1980's, advanced high-speed aircraft will demand the fullest utilization of airframe/propulsion technology. To accomplish this goal, it will be essential to have the broadest possible understanding of the coupling between major subsystem and overall flight vehicle performance. In this regard, the supersonic air induction system has recently attracted considerable attention. The interest has focused on developing a fuller understanding of inlet component drag composition and the coupling between component drag variations and the installed performance of this major subsystem.

Under sponsorship of the United States Air Force a significant program† was begun in early 1972 to experimentally evaluate the individual contributions made by supersonic inlet components to overall inlet system drag. A concomitant goal of this program has been the exploration of a possible tradeoff between inlet system drag and performance, as it affects aircraft mission effectiveness. To date, the program has focused on the conventional all-external compression-type inlet system, operating in both the transonic and the supersonic flight regimes.

To assure a realistic framework for the overall study, a representative advanced strike aircraft configuration was established to meet the requirements of a representative strike mission scenario. The defined mission and its range serves as the reference for the induction system/mission effectiveness sensitivity analysis, while the aircraft configuration itself provided the basic geometry for wind tunnel model design.

This paper begins with a brief outline of the reference mission and aircraft configuration, followed by a detailed review of the theoretical and practical considerations of the inlet design. Then, the wind tunnel model assembly is described with particular attention given to the measurement techniques employed for pressure, mass flow and, most importantly, inlet force. Wind tunnel testing conditions are discussed next, including the test sections, operating conditions and model attitudes. Finally, the testing which has been completed is summarized, and some preliminary experimental results are presented. Typical measured performance results are shown, and inlet cowling region force data are employed to illustrate possible tradeoff alternatives for the induction system. An outline of the full data assembly which will be made available shortly, completes the discussion.

2. BASELINE MISSION SCENARIO

The baseline mission scenario comprises the following segments (see Fig. 1):

- Takeoff and climb to best cruise altitude

- Cruise out at subsonic speed to the forward edge of the battle area

- Penetration at sea level altitude and transonic speed

- "Pop-up" in target area, followed by combat engagement

- Climb and acceleration to supersonic speed and return dash

- Lapse to subsonic cruise, followed by loiter and landing.
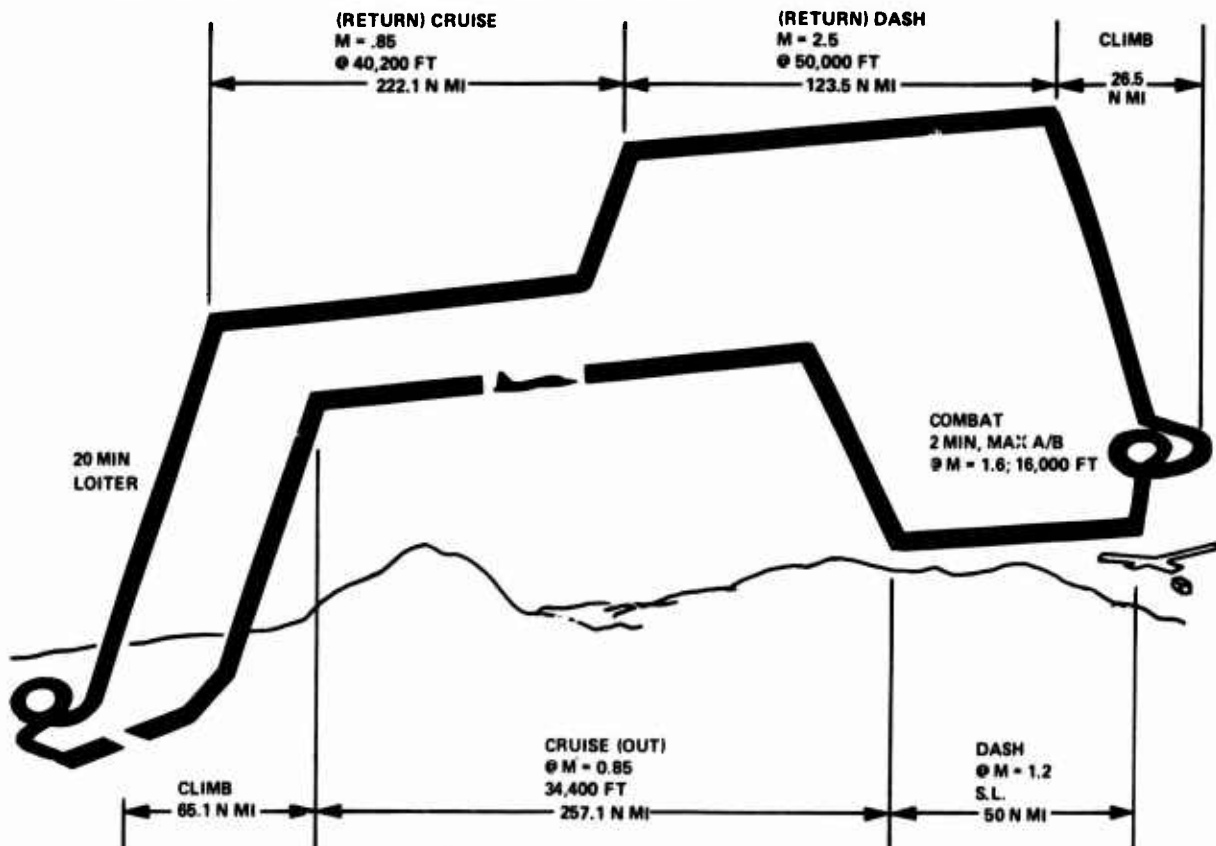
Fig. 1 Baseline Mission Scenario

As will be discussed subsequently, each of the mission speed regimes represents a wind tunnel test condition for the experimental program. Sustained flight at each of the prime Mach numbers was important to the selection of the mission scenario in order to give meaning to the subsequent inlet/mission sensitivity analyses. The baseline radius of action (approximately 380 nautical miles) was dictated by model/wind tunnel constraints which restricted the basic aircraft size. The distances for each segment of the mission are the result of detailed flight performance computation for the baseline aircraft.

3. BASELINE AIRCRAFT DESIGN

3.1. Basic Configuration

As illustrated in Fig. 2, the baseline aircraft configuration is a twin-jet tactical vehicle utilizing rectangular, two-dimensional air induction systems located close to the vehicle fuselage. The inlets are positioned near the mid waterline plane, falling below and blending into the wing upper surface, with horizontally oriented compression surfaces.
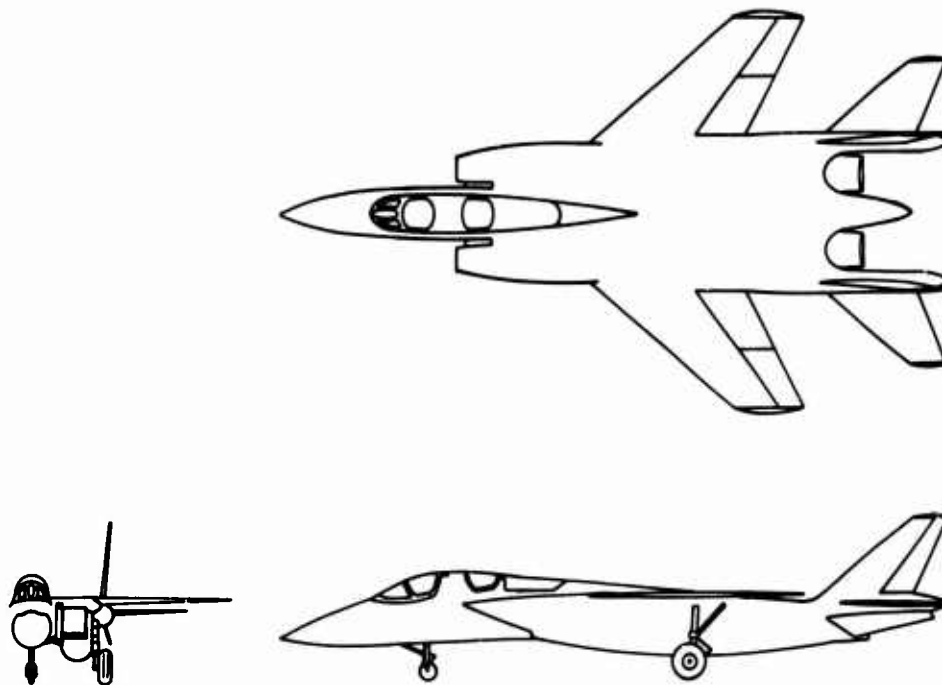
Fig. 2 Baseline Aircraft

The aircraft has a gross take off weight of 75,000 pounds, which includes a maximum fuel capacity of 29,700 pounds. The aircraft was sized to meet all requirements of the baseline mission, including specific excess power requirements, utilizing a 125 psf wing loading and a thrust loading equal to .65.

Aircraft propulsion is provided by two augmented advanced turbofan engines sized for $F^* = 24,400$ pounds sea level static thrust. For the sustained speed regimes of the baseline mission, each engine has the corrected airflow requirements shown in Table 1. This schedule is used subsequently to define engine/inlet match point performance levels from the experimental results.

Table 1 Corrected Airflow Requirements For Each Engine

Mach No.	Altitude, ft	Air Flow (W $\sqrt{\theta}/\delta$) lb/sec
2.5	50,000	110
1.6	16,000	147
1.2	Sea Level	156
0	Sea Level	156

3.2 Inlet/Air Frame Integration

A number of studies (e.g., Ref 1-3) have been conducted to investigate the effect of forward fuselage geometry and protuberances on the quality of the local flow field approaching the supersonic air induction system entrance plane. The effects on both inlet system performance and on compressor face flow distortion have been extensively explored. As a result of these studies, inlet/fuselage design criteria have been established, especially for the tactical fighter class of aircraft, to assist in avoiding serious inlet system performance penalties.

During aircraft configuration evolution for this program, low fuselage flow field interaction on the inlet systems was emphasized. Thus, the forebody shape and the position of the inlets were modified according to the results of detailed flow field analyses. For this purpose, the inlet leading edge station flow fields produced by candidate

fuselage forebody/canopy configurations were examined in detail using an inviscid, three-dimensional flow field computational technique developed for supersonic flow by Moretti (Ref 4). The numerical procedure employs a forward marching, finite difference scheme of second-order accuracy to integrate the governing Euler equations in each region of continuous flow; and across discontinuities, which include both leading and imbedded shock waves, the Rankine-Hugoniot relations are fully satisfied. By using conformal mapping of body cross-sectional shapes from the physical plane in to transformed computational planes, the method permits accurate flow field prediction for even very complex geometries.

To achieve a satisfactory flow field environment at the inlet system entrance, it was necessary to modify the forward fuselage shape and to relocate the inlet capture zone relative to the fuselage. (See Fig. 3.) Fig. 3a shows reduction in both local flow angle of attack and sidewash angle accomplished by simple fuselage geometry changes. These included increasing nose droop angle from 6° to 9° and increasing fuselage nose semi-vertex angle from 18.5° to 20.5°. Fig. 3b illustrates the effect of inlet capture zone relocation. The inlet is lowered relative to the canopy/fuselage shoulder line and the shoulder has been "softened". In addition, fuselage bottom corners were softened moderately to reduce inlet flow field degradation with increasing vehicle angle of attack. The induction system relocation yielded a further reduction in local flow sidewash and downwash due to the airframe canopy. The remaining downwash naturally had to be considered in the design of the forward compression surface of the inlet.

4. MISSION SENSITIVITY ANALYSIS

The mission sensitivity analysis was conducted in order to be able to assess the impact of changes in inlet pressure recovery and inlet drag on mission effectiveness in terms of incremental range changes. The analysis involved the baseline aircraft design (Fig. 2) equipped with moveable surface, two-dimensional, all-external compression type inlet systems. The inlets were sized to provide full-scale capture areas of 1020 square inches each.

Grumman's digital computer codes were used to provide installed propulsion system performance and overall aircraft flight performance. To facilitate the analysis, a basic aircraft polar and baseline inlet performance parameters were derived analytically. The basic un-installed powerplant data were obtained from data packages for advance engines, supplied by Pratt and Whitney Aircraft. In addition to accounting for induction system effects, the basic propulsion data were corrected to account realistically for engine air bleed, power extraction, and exhaust nozzle performance and drag.

The methodology for the sensitivity analysis began with the establishment of detailed baseline mission performance as reflected in the mission profile (Fig. 1). Next, inlet performance and inlet drag levels were perturbed separately, over suitable intervals about their baseline levels, for each independent segment of the mission profile. For each parameter variation, mission total range was re-evaluated holding the penetration leg distance and combat time at their baseline values. The remaining mission leg distances and the overall mission range thus resulted as "fallout" from the computations.

The computed sensitivity of mission range to induction system pressure recovery performance and drag level is shown in Fig. 4 and 5, respectively. The inlet parameter perturbations are taken as variations about the corresponding baseline values. As shown, the impact of both inlet parameters is greatest during the seal level penetration dash at transonic speed. This is not a surprising result. For the combat segment, range decreases with increasing inlet pressure recovery performance, due to the increase in fuel flow at fixed (maximum reheat) engine power setting; but the inlet drag variation has no effect on range because this is a fixed power setting condition rather than a matched thrust/drag flight condition.

5. INLET DESIGN

The baseline inlet for the investigation, is a rectangular, two-dimensional all-external compression design with three external compression surfaces, (Fig. 6). The initial compression surface is fixed and the inlet cowling is fixed, yielding a conventional constant capture area induction system design. The second and the third external compression surfaces together with the subsonic diffuser ramp may be rotated independently about their respective hinge axes. Inboard and outboard side walls are provided to control lateral flow spillage from the inlet. Finally, the design embodies a bleed/bypass slot located just downstream from the cowl closure station, for the purpose of boundary layer and excess flow management. The throat slot flow is connected via a plenum region to a fully articulated convergent exit door located at the aircraft wing top surface.

Typical design methodology for the conventional inlet involves the basic selection of compression surface lengths and surface deflection schedules which provide optimum performance with no shock wave or vortex sheet ingestion. Consideration is also given to achieving favorable viscous flow and interaction behavior. Because of the exploratory nature of the present induction system investigation, however, the inlet was also designed for operation with compression surface deflection schedules that would have functional dependence on aircraft angle of attack as well as on flight Mach number. In this paper the schedules are denoted as variable schedule $\left[F(\alpha; M_0)\right]$ and fixed schedule $\left[g(M_0)\right]$.

Although ramp deflection schedule selection for the supersonic inlet is certainly straight forward, it is perhaps worth while to point out the simple graphical approach used here. The Mach 2.5 flight condition is used to illustrate the approach. A carpet plot for inlet supersonic pressure recovery is constructed using the angular deflections of the second and third compression surfaces as arguments. (See Fig. 7.) Superimposed on the plot is the locus of total supersonic turning above which shock wave detachment should be anticipated. The basic plot is nothing more than the well known Oswatitsch result; however, it is apparent that alternate schedule choices and tradeoff possibilities can be readily seen.

Following the approach illustrated in Fig. 7, optimum compression surface deflection schedules were selected over an angle-of-attack range from -3° to +10°. In this manner, the variable compression ramp schedule was established at each flight Mach number of interest. At the same time, the deflection schedules corresponding to zero angle of attack at each Mach number established the so called fixed compression surface schedules. Next, a Grumman digital computer code (Ref 5) was used to select compression surface lengths for minimum additive drag while rigorously avoiding either vortex or shock wave ingestion over the prescribed angle of attack range. range.

$M_0 = 2.50$
$\alpha_0 = 0°$

LOCAL FLOW ANGLE OF ATTACK

LOCAL FLOW SIDEWASH ANGLE

FOREBODY SHAPE MODIFICATION

(a)

SOFTENED CANOPY BLEND

INLET SYSTEM RELOCATED

(b)

SOFTENED BOTTOM CORNER
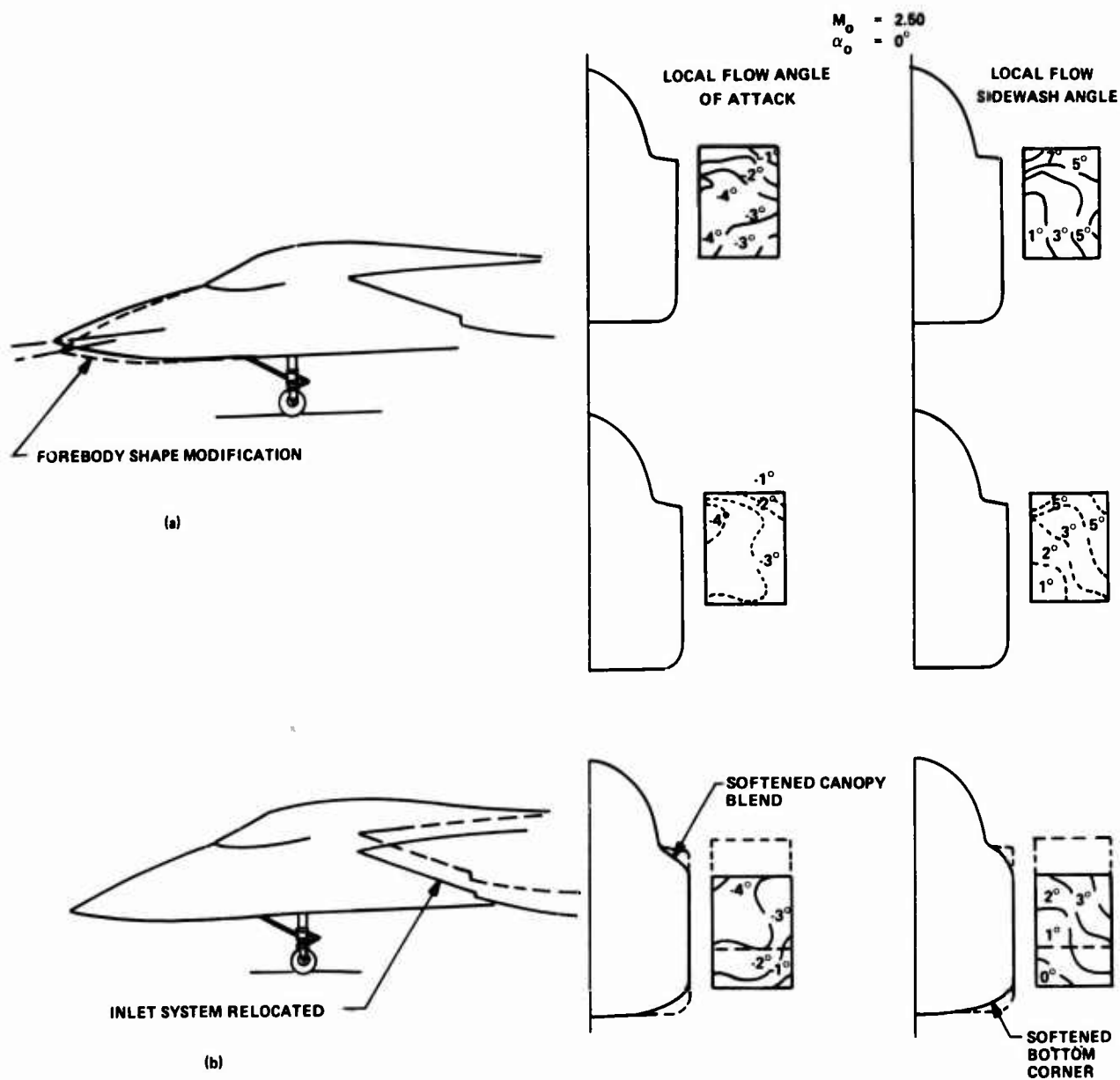
Fig. 3 Induction System/Airframe Integration

Figure 8 shows the theoretical shock wave structure at the Mach 2.5 design point and the extremes of operating angle of attack. As may be seen, significant shock-wave-generated flow spillage is predicted for the inlet at zero degrees angle of attack. The high spillage results directly from the compromise made necessary in inlet cowl leading edge positioning in order to accommodate the variable compression schedule requirement. This was not considered to be a serious performance constraint, however, since increases in inlet capture ratio (A_0/A_c) would be attainable at only small expense in pressure recovery performance. (See Fig. 9.)

6.   WIND TUNNEL MODEL DESIGN

The general arrangement of the wind tunnel model is shown in Fig. 10. The actual model assembly is a 1/6.43 scale representation of the forebody and canopy of the baseline aircraft together with complete twin supersonic air induction systems. (See Fig. 11 and 12.) The overall model assembly is supported by means of a central sting, and the inlets are connected to separate exhaust ducts which house the plug valve assemblies used for inlet mass flow regulation.

4-6

Fig. 4 Effect of Inlet Pressure Recovery on Mission Range

Fig. 5 Effect of Inlet Dragon Mission Range

Fig. 6 Induction System Design

Fig. 7 Theoretical Performance of a Four-Shock Two-Dimension Inlet

(a) FIXED COMPRESSION SCHEDULE (b) VARIABLE COMPRESSION SCHEDULE

Fig. 8 Theoretical Shockwave Patterns at Mach 2.5

Fig. 9 Inlet Operating Envelope at Mach 2.5

The major objective of the experimental program is to measure inlet system forces and the accompanying interference forces on the airframe. For this purpose, a dual balance technique (see Fig. 10) has been employed so that forebody forces and inlet system forces may be measured independently. The force measurement units are designated as the main balance and the inlet balance system, respectively. The balance installations have been designed so that the overall inlet/forebody model is metric as a whole, while the left hand inlet and duct assembly alone is independently metric.

The main balance is a six-component internal strain gage force balance which attaches directly to the model support sting. The model inlet/forebody assembly, in turn, is mounted directly to the main balance. The inlet balance system, on the other hand, consists of a pair of three-component internal strain gage force balances which support the left hand inlet and duct assembly at its juncture with the wing glove root of the vehicle. As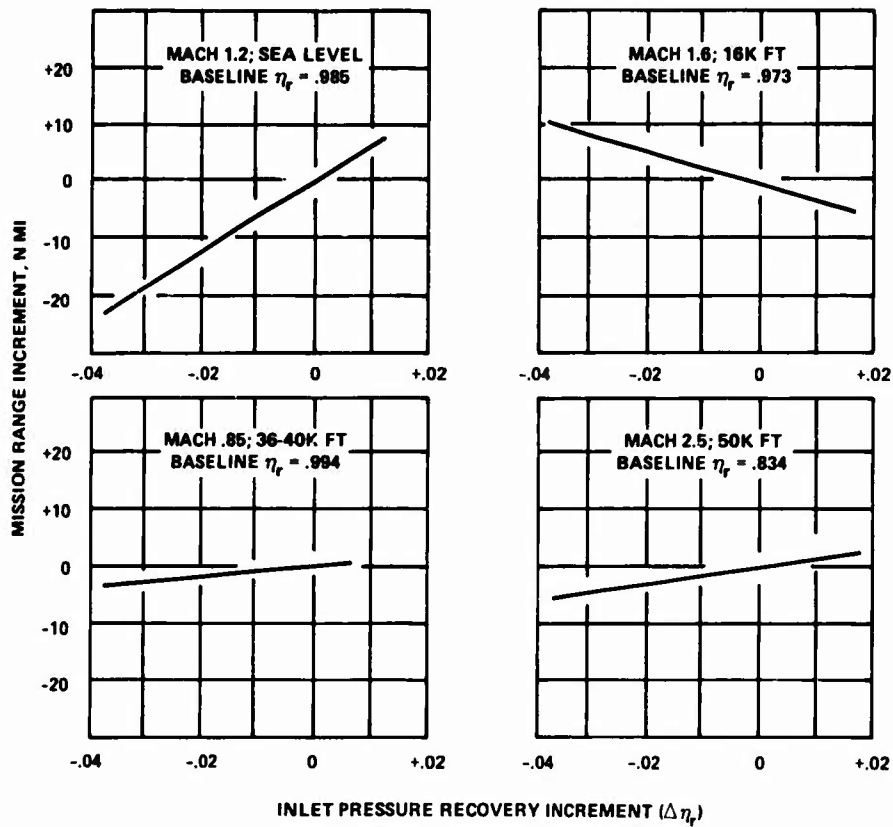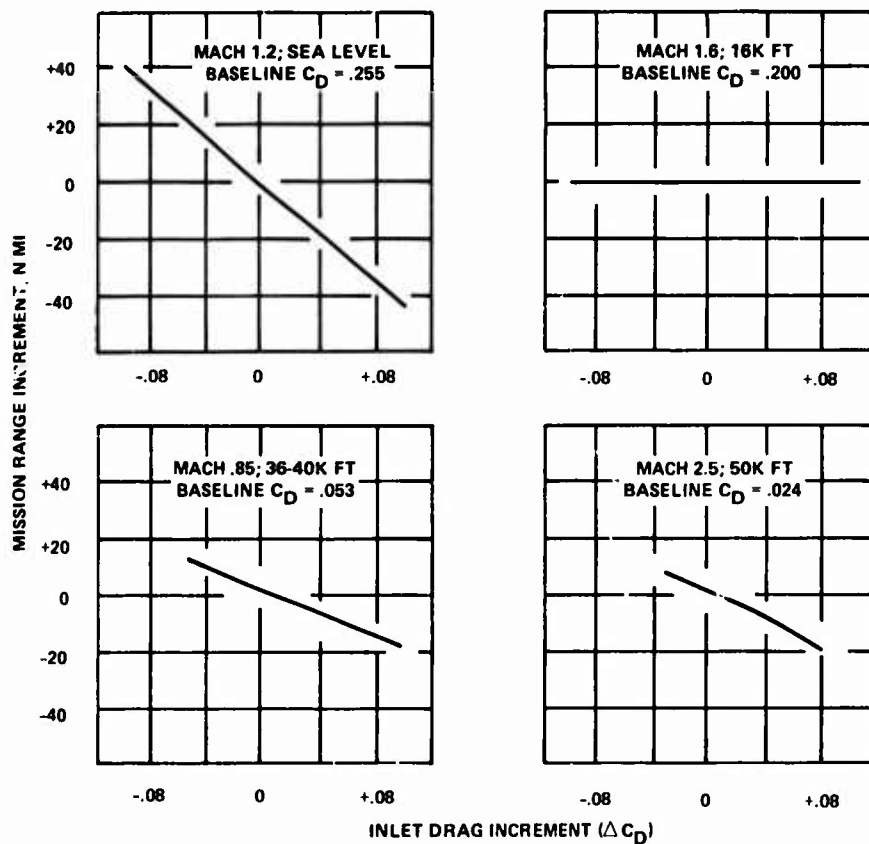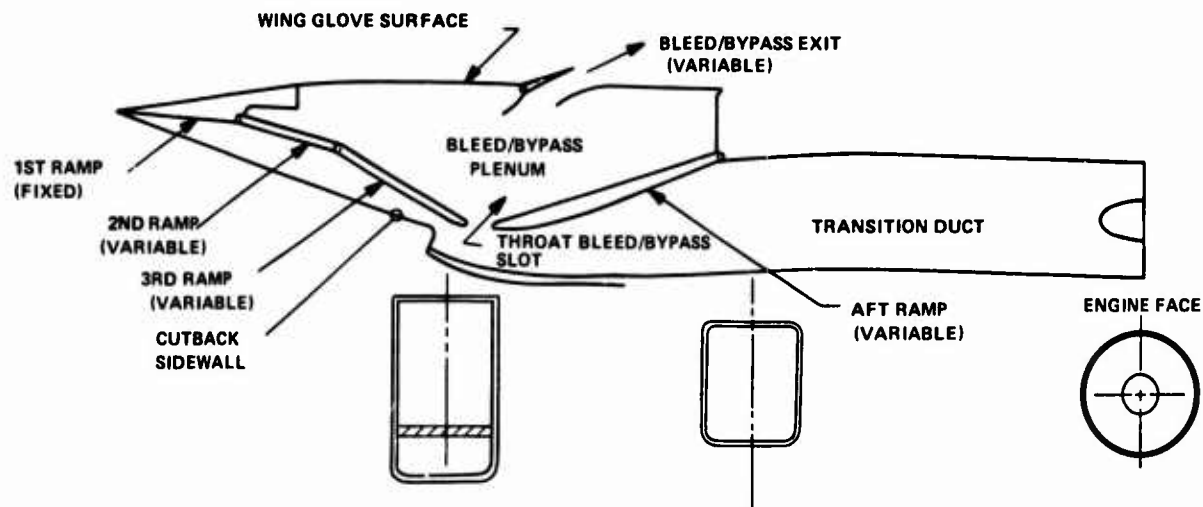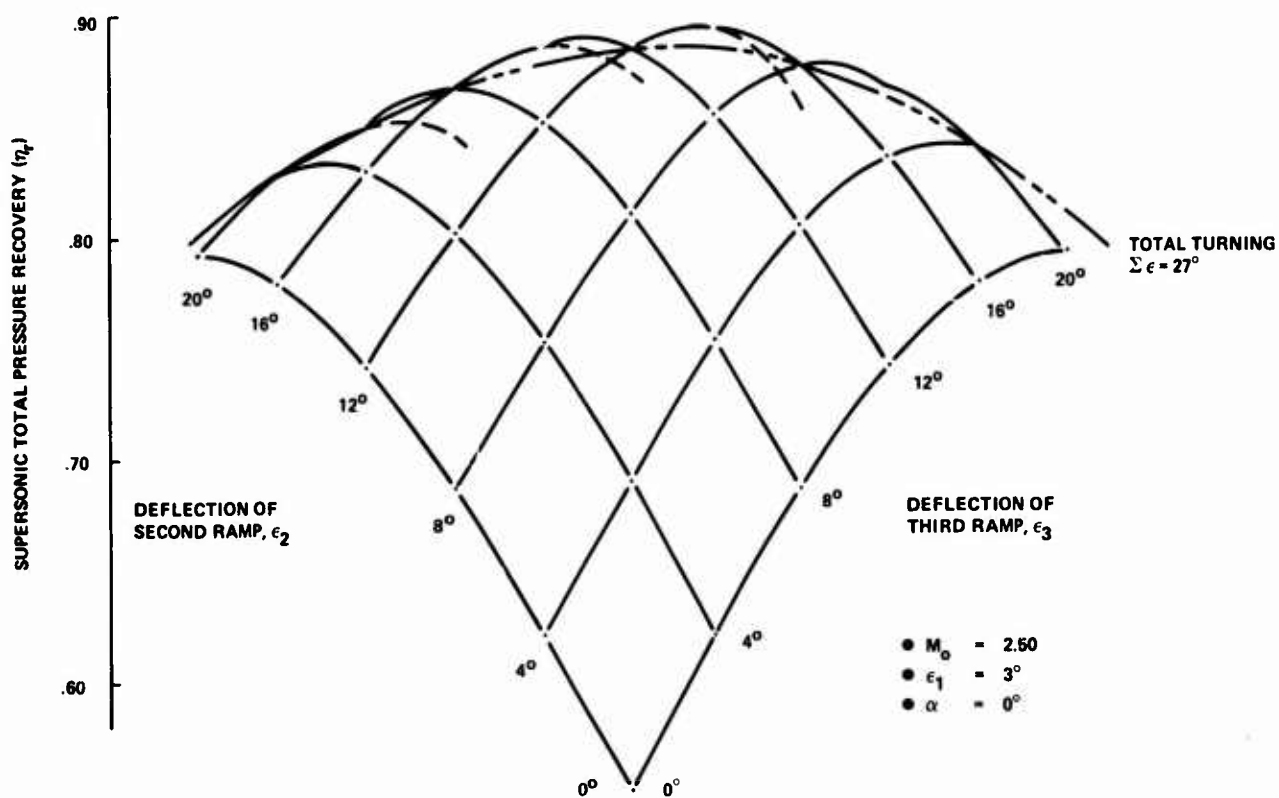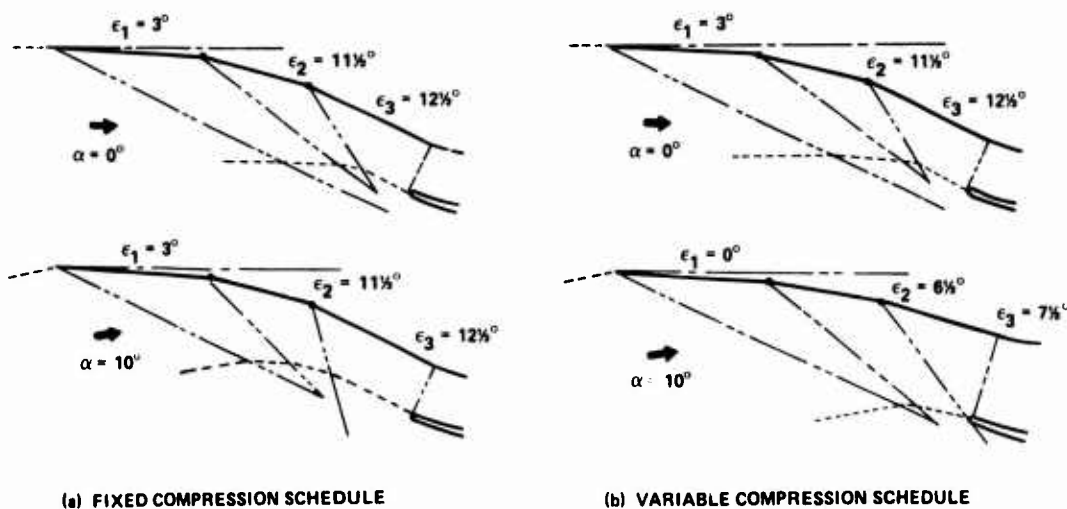 shown in Fig. 13, the inlet force balances are positioned at the inboard and outboard external walls of the inlet duct, with the metric/non-metric interface between the inlet and the forebody assembly maintained by a labyrinth seal arrangement.

The induction system internal ducting on each side of the model duplicates the complete subsonic diffuser passage up to the engine compressor entrance station. This ducting is integral to the metric sections of the model. Downstream of the compressor entrance station, non-metric ducting extends through plug-type, choked-flow throttle valves which provide each inlet with airflow regulation and flow-rate measurement. Coupling between the metric and non-metric ducts is accomplished with a zero leakage, flexible bellows assembly. (See Fig. 10 and 14.)

In addition to the direct force measurement systems, the wind tunnel model is provided with extensive pressure instrumentation for the acquisition of overall induction system pressure recovery and detailed model surface pressure data. Compressor face station stagnation pressure recovery is measured using a 48-probe steady-state pressure rake, and approximately 300 static pressure orifices are distributed over inlet surfaces areas of interest. The inlet bleed/bypass plenum and exit slot are also instrumented to enable the computation of air flow.

In addition to remote control of angle of attack and sideslip attitude, model components which can be remotely controlled during testing include the inlet compression surfaces, the subsonic diffuser ramp, and the bleed/bypass flow exit door. Inlet airflow is regulated by remote operation of the main duct throttle plugs.

7. INLET SYSTEM ALTERNATE COMPONENTS

To evaluate inlet system component drag and the possibility for drag/performance tradeoff, a number of alternate inlet components were selected. These are four cowl lip geometries (see Fig. 15) and four inlet sidewall geometries (Fig. 16). The fundamental criteria in the design was to have each alternate component exhibit a change in only one significant geometric parameter.

All inlet Cowlings were designed with a 3:1 elliptical leading edge.

● Cowling C-1 was selected as the baseline geometry. The major axis of the elliptical lip parallels the number three compression surface of the inlet at its Mach 2.5 theoretical design point.

● Cowling C-2 displays a thickened lip which is formed by a factor of two increase in the semi-minor axis of the outer elliptical contour. The internal contour of the baseline lip has been preserved identically.

● Cowling C-3 was derived from the basic lip configuration by a reduction in the slope of the internal contour at the point of tangency with the initial ellipse. The basic external shape of the cowling is not changed.

● Cowling C-4 was designed with the major axis of the leading edge parallel to the inlet reference line.

Inlet alternate side plates, S-1 through S-4, have been classified as blunt or sharp, with either of two angles of cut-back for lateral flow relief.

All cowls and side plates were extensively instrumented in order to obtain detailed surface static pressure distributions and to permit computation of component force coefficients through integration.

8. MODEL TESTING

The inlet/forebody wind tunnel model was designed with specific provision for adaptation to test facilities at the United States NASA/Ames Research Center. The facilities used in the investigation have been the 9 by 7-foot supersonic and 11 by 11-foot transonic test sections of the NASA Unitary Plan Wind Tunnel. These are high Reynolds number, continuous-flow, closed-circuit wind tunnels.

6-COMPONENT INLET-FOREBODY
ASSEMBLY BALANCE

PRESSURE ASSEMBLY
RIGHT SIDE

METRIC ASSEMBLY,
LEFT SIDE
(3-COMPONENT INLET BALANCE)

Fig. 10 Inlet/Forebody Model Assembly

Fig. 11 1/6.43 Scale Model in 9 ft X 7 ft Supersonic Test Section

Supersonic testing was conducted at Mach 2.5 and 1.6, and transonic testing was conducted at Mach 1.2 and .85. In general, all testing was conducted in the Reynolds number range 2.0×10^6/foot to 2.5×10^6/foot. The model test attitudes included the angle of attack range 0° to +10° and the side slip angle range 0° to ±4°. For all testing, the inlet system airflow was regulated from supercritical through subcritical, up to onset of buzz instability.

Two periods of wind tunnel testing have been completed. The first of these involved 125 hours of testing during the middle of 1973, while the second period consisting of approximately 90 hours of testing has just been completed in July 1974.

In the first period of testing, an unfortunate condition of physical grounding between metric and non-metric sections of the wind tunnel model resulted in the unacceptability of most force balance measurements. All model pressure data, however, including the detailed inlet surface pressure measurements, are quite useful to the assessment of inlet performance and component force terms. Some inlet force balance difficulties were also experienced during the second period of testing; however a serious loss of force data is not expected.

Because final processing of the wind tunnel data acquired in the second test period is not completed, it will be necessary to rely on the first period pressure results exclusively in the data discussion which follows.

9. EXPERIMENTAL DATA

This last part of the paper presents typical experimental results which illustrate the broad nature of the investigation. The baseline induction system which is employed in the inlet component drag study is found to afford levels of internal performance which are consistent with modern induction systems of this type. Moreover, the quality of the compressor entrance air flow delivered by the induction system is found to be excellent. Although based only on pressure measurements from the first period testing, certain possibilities for tradeoff between inlet component drag and performance can be identified.

Fig. 12 1/6.43 Scale Wind Tunnel Model In 11 ft Transonic Test Section
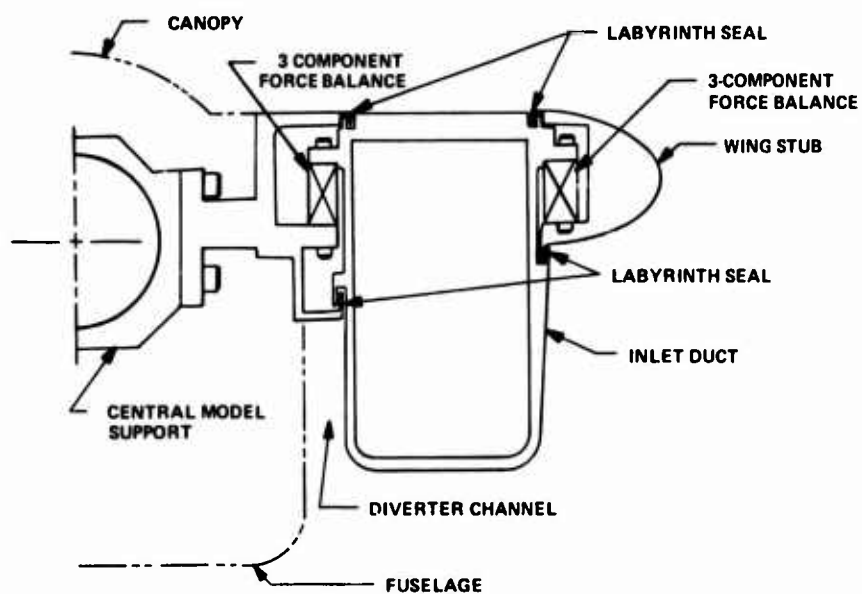
Fig. 13 Metric Inlet Installation
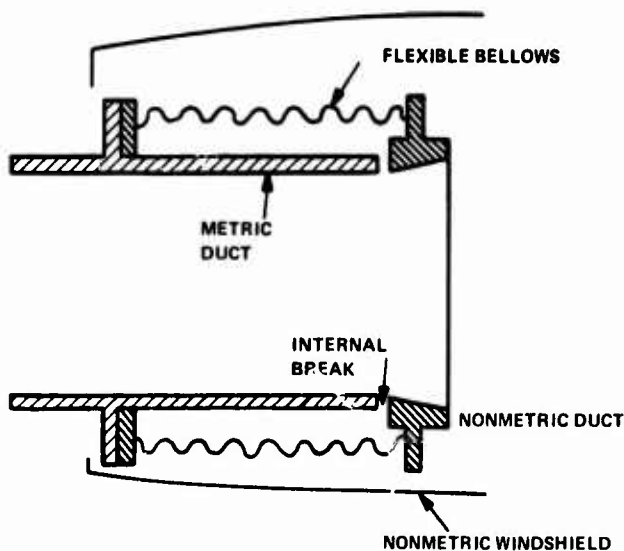
Fig. 14 Main Duct Bellows System

Fig. 17 shows engine matched condition pressure recovery performance for the baseline air induction system over the flight Mach number range investigated. The quality of airflow supplied by the baseline induction system is illustrated in Fig. 18. Here measured compressor entrance steady-state pressure profiles corresponding to 0° and +10° angles of attack are shown for the Mach 2.5 flight condition.

By combination of the four inlet cowling shapes and the four side plate geometries, sixteen substantially different supersonic inlet configurations may be assembled. Not all of these possible inlet arrangements could be tested, because of practical limits on wind tunnel test time. For the configurations tested, however, assessment extended to investigation of the effects of compression surface scheduling and to inlet maneuvering performance. Fig. 19 illustrates the effect of two slightly different compression schedules on inlet cruise performance at Mach 2.5. Fig. 20, presents Mach 2.5 maneuvering performance for a second alternate inlet configuration.

Our particular interest is in the effect of the various inlet components on induction system and interference drag. These effects must be viewed simultaneously with the component effects on induction system performance.

Examples of the effects of inlet cowling and sideplate choice are shown in Figs. 21 through 23. In Figure 21, induction system pressure recovery performance and the cowling external pressure drag term are shown for various cowl choices and the same sideplate configuration at Mach 2.50 cruise operation. The results clearly illustrate for this inlet that improved performance is accompanied by increas s in cowl pressure drag. An opposite trend is found when the effects of inlet sideplate geometry are considered.

Fig. 22 presents inlet performance and cowl pressure drag term data for the same cowl, but different sideplate geometries. The sideplate giving lower inlet performance also results in the production of a slightly lower cowl pressure drag term. Naturally, no general conclusion is possible without considering the total inlet drag effect, as well as the interference effect, but these trends do begin to suggest a possibility for tradeoff between performance and drag.
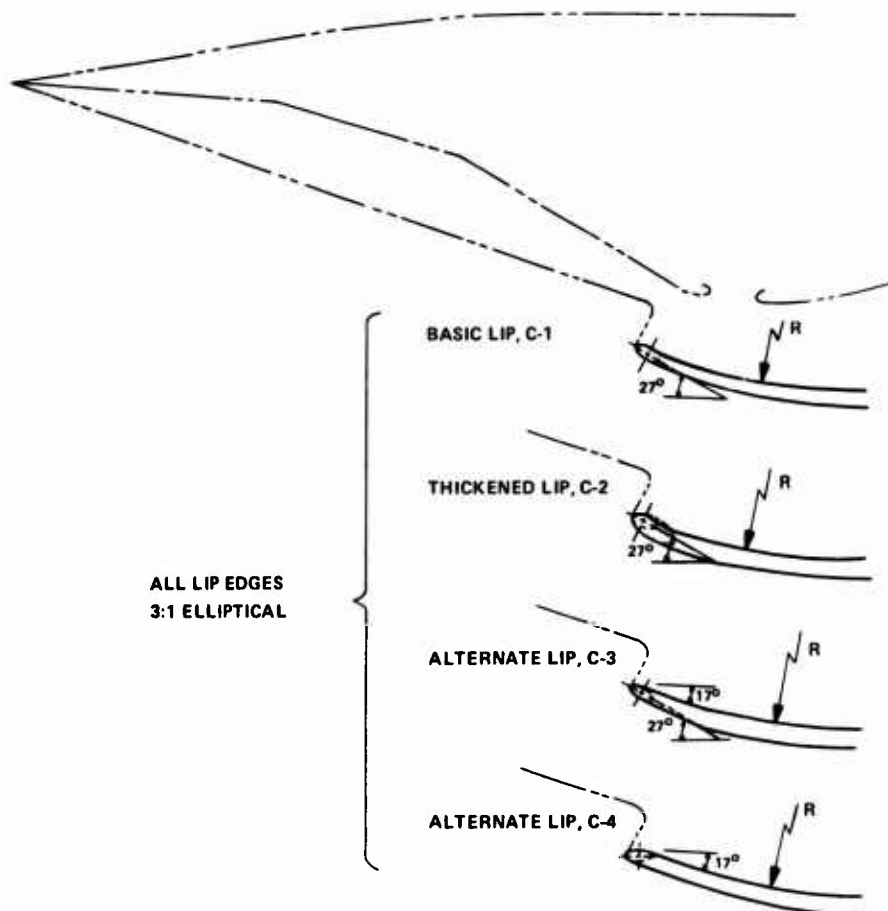
Fig. 15 Cowling Lip Shapes

SIDEWALL	φ
S-1, S-4	20°
S-2, S-3	18°

INNER SURFACE

S-2 / S-3

S-1 / S-4

R

SHARP
S-1
S-2

BLUNT
(3:1 ELLIPSE)
S-3
S-4

10°
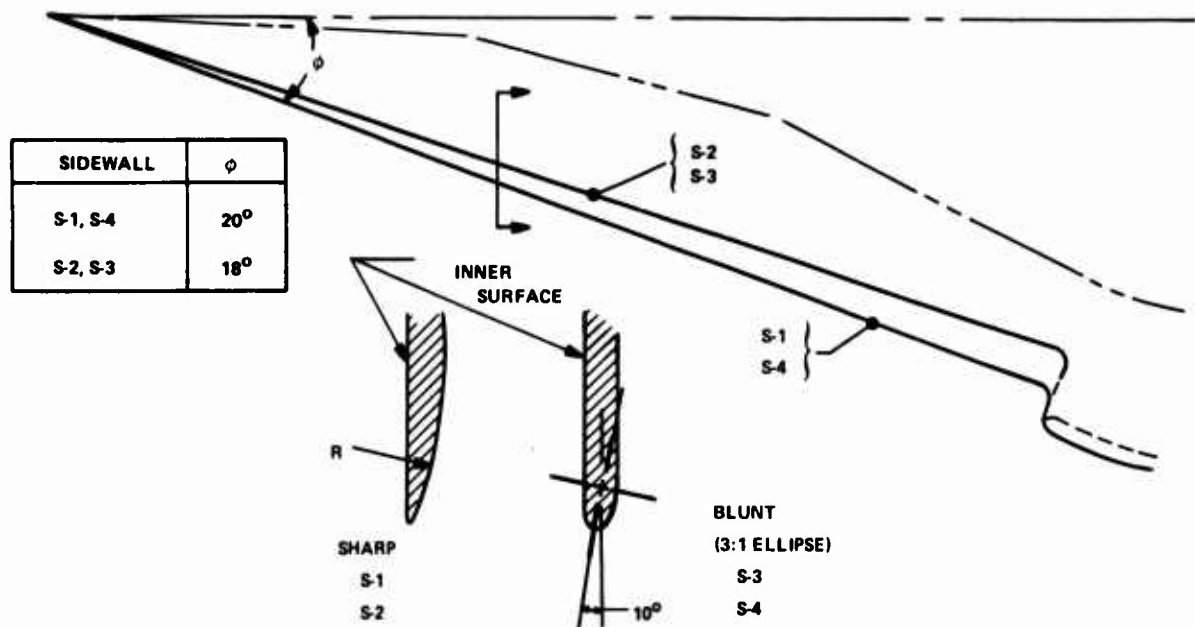
Fig. 16 Inlet Sidewalls
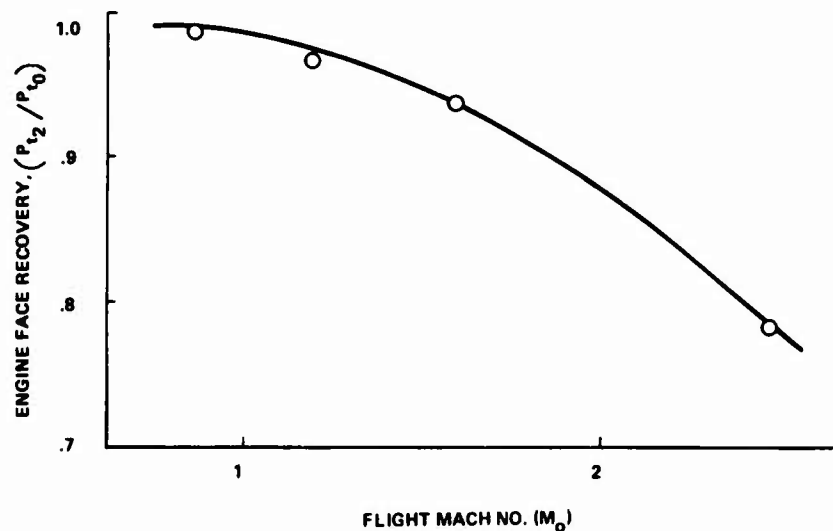
Fig. 17 Inlet Performance at Inlet Match Point

(Y-axis: ENGINE FACE RECOVERY, (P_{t_2}/P_{t_0}); X-axis: FLIGHT MACH NO. (M_0))

The importance of changes in inlet pressure recovery and drag to mission effectiveness during Mach 1.2 penetration flight was discussed early in the paper. An example of the effect of cowling geometry on induction system performance and cowl pressure drag measurements at transonic speed is shown in Fig. 23 to complete the discussion.

An overview of the total experimental program has been assembled in Table 2. The Summary shows the complete inlet configuration and wind tunnel test condition matrix for which data have already been acquired. For the inlet configurations and the test conditions shown, bleed/bypass exit variation and compression schedule variation effects were explored as secondary variables, with angle of attack and yaw angle range extending between 0° and 10° and 0° and ±4°, respectively. These data will furnish the final parametric analyses for the overall study program. We expect that these data will be published in an appropriate report in the near future.

10. CONCLUSION

At this time, two extensive periods of wind tunnel testing have been completed, employing a representative all-external compression type air induction system. The pressure data from first period testing together with the pressure and force data from second period testing are expected to provide new insights into the drag characteristics of the principal components of advance air induction systems.

$$\left(\frac{P_t - P_{t_{AVG}}}{P_{t_{AVG}}}\right) \text{, PERCENT}$$

$\alpha_o = 0°$ $\alpha_o = 10°$
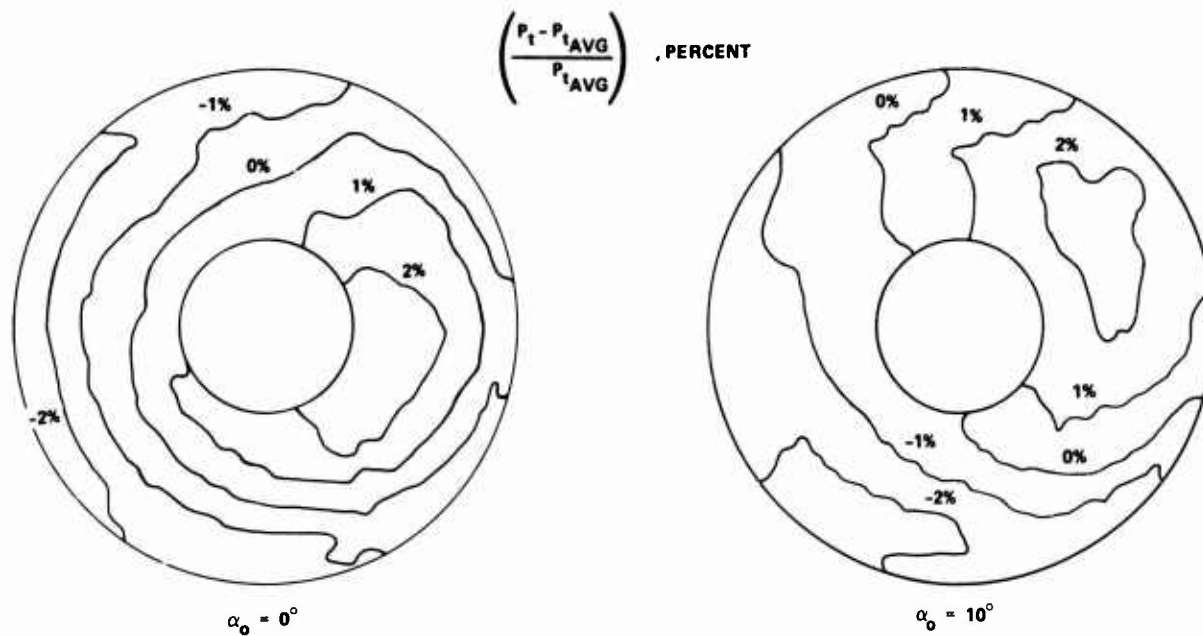
Fig. 18 Engine Face Pressure Distribution

Table 2   Inlet Test Summary
(Configuration and Mach Number)

COWLING GEOMETRY	SIDEWALL GEOMETRY			
	S_1	S_2	S_3	S_4
C_1	2.50*	2.50	2.50	2.50
	1.60	1.60	1.60	1.60
	1.20			
	.85			
C_2	2.50			
	1.60			
	1.20			
	.85			
C_3	2.50			
	1.60			
C_4	2.50	2.50		
	1.60			
	1.20			
	.85			
* Includes Survey of Reynolds Number Effect.				
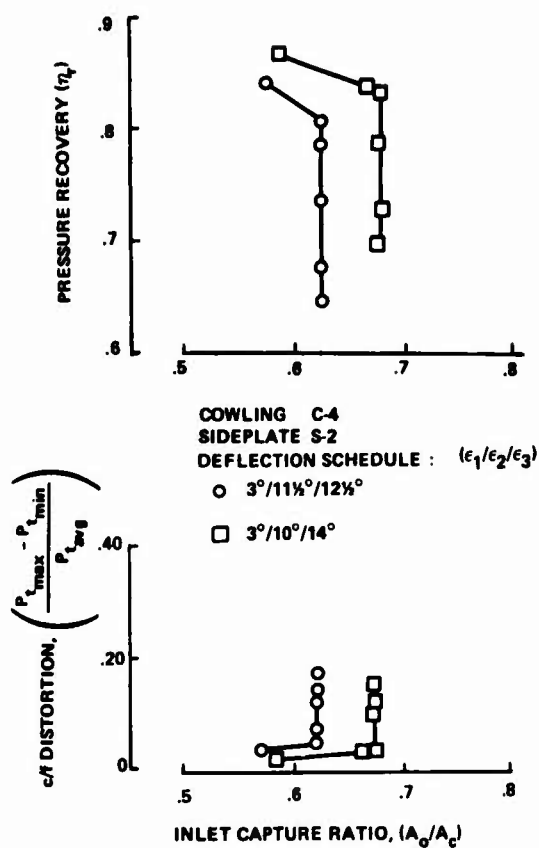
Fig. 19 Effect of Compression Surface Deflection Schedule at Mach 2.5
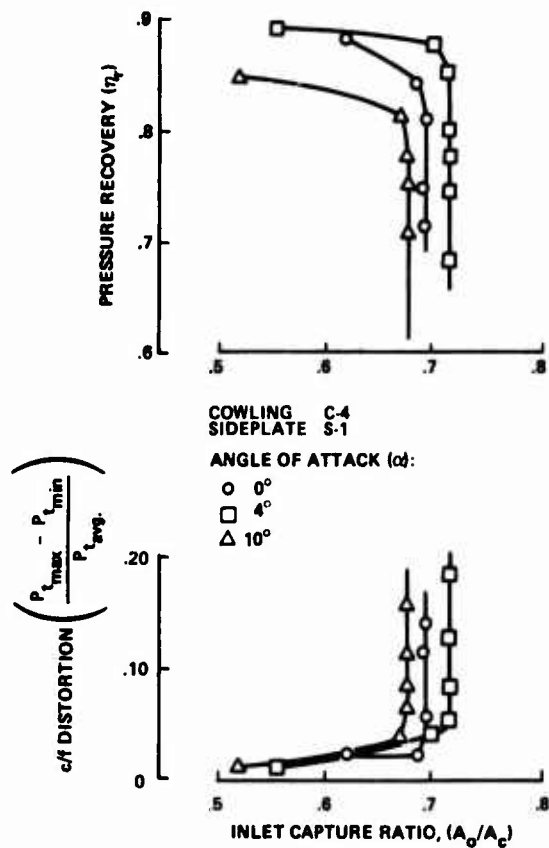
Fig. 20 Angle of Attack Effect at Mach 2.5
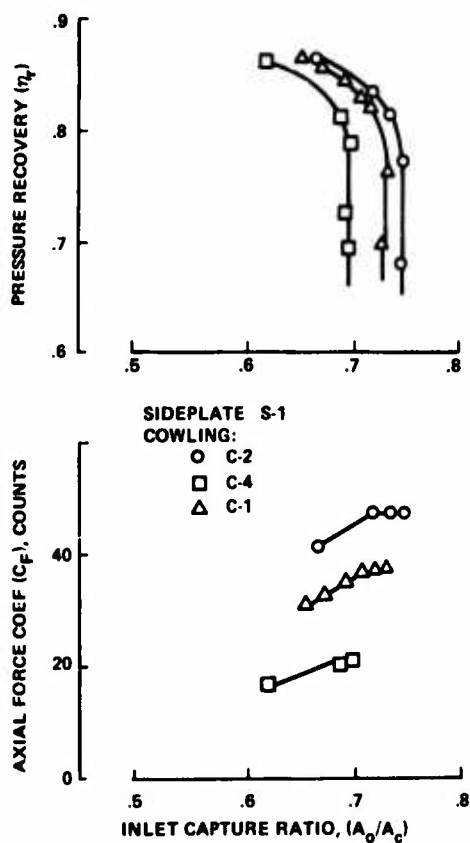
Fig. 21 Effect of Cowling Shape at Mach 2.5
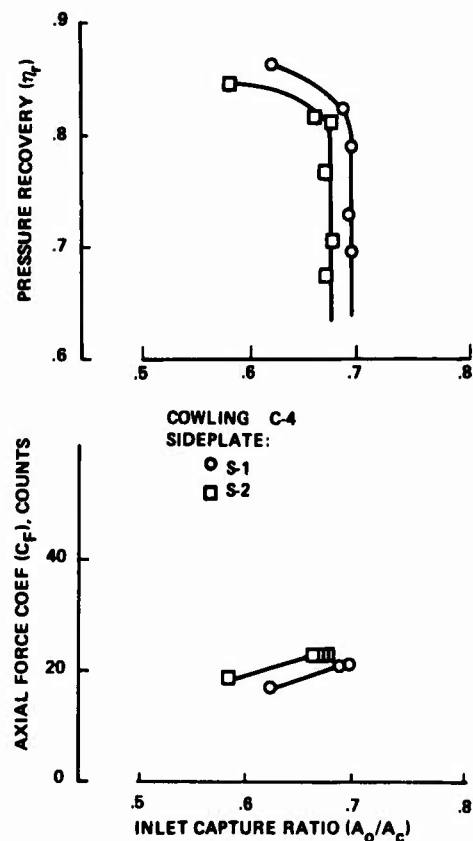
Fig. 22 Effect of Sideplate Grometry at Mach 2.5
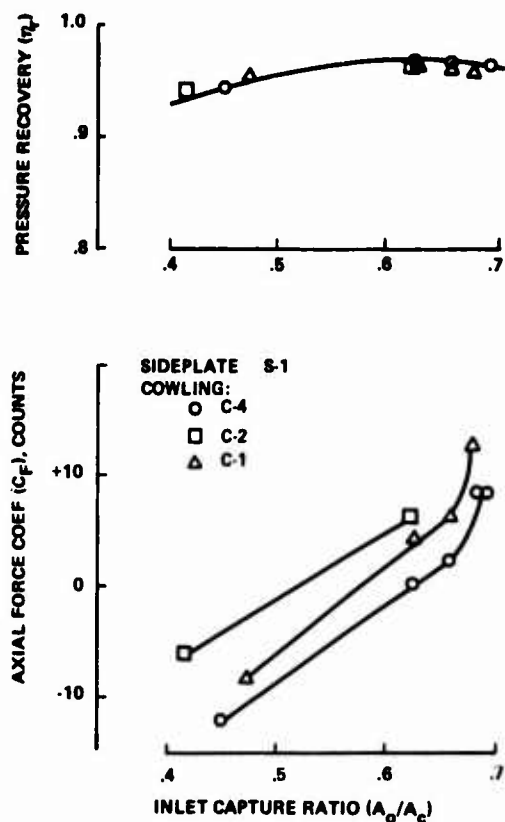
Fig. 23 Effect of Cowling Shape at Mach 2.5

A similar program of experimental work has been considered for the purpose of investigating mixed compression type air induction systems, which employ combined external and internal flow field compression. Together with the current results, this would give the possibility for a very broad comparison between the two different basic types of advance induction system. The basic wind tunnel model and the techniques already developed would be easily adopted to such an effort.

11. REFERENCES

1. Cawthon, J. A., Truax, P.P., et al., Supersonic Inlet Design and Airframe-Inlet Integration Program (Project Tailor-Mate), Vol I, II, and III, Air Force Flight Dynamics Laboratory Report AFFDL-TR-71-124, May 1973.

2. Cawthon, J. A., Truax, P. P., and Savage, T. M., Advanced Inlet Study (Tailor-Mate II), Air Force Flight Dynamics Laboratory Report AFFDL-TR-73-72, June 1973.

3. Prokop, C., Investigation of the Effects of Airframe Design on Inlet Flow Fields, Air Force Flight Dynamics Laboratory Report AFFDC-TR-72-11, 1972.

4. Marconi, F. and Salas, M., Computation of Three-Dimensional Flows About Aircraft Configurations, Computers and Fluid, Vol 1, pp 185-195, Pergamon Press, 1973.

5. Callahan, C. J., A Computerized Design Analysis for Rectangular Supersonic Inlets, Grumman Aerospace Corporation, Advanced Development Report ADR 01-03-72.5, December 1972.

JET INTERFERENCE OF A PODDED ENGINE INSTALLATION
AT CRUISE CONDITIONS

by
B. Munniksma and F. Jaarsma
National Aerospace Laboratory N.L.R.
The Netherlands

SUMMARY

In this paper the results of an experimental wind tunnel test program on the wing-pylon-bypass engine combination of the Airbus A 300 B airplane are presented. In this test program only aerodynamic interference due to the engine jet was considered.

For determining the interference drag due to the engine jet as well as to have the possibility to extrapolate the test results from model reference conditions to full scale a test scheme was developed. To prove the validity of the assumptions of this scheme several intermediate steps were made.

As the engine jet-airframe interference is mutual, also effects of the external flow on the internal engine nozzle flow causing engine shifting has to be considered.

In order to estimate the magnitude of this influence of the external flow field a two-dimensional model of the fan nozzle has been tested using an optical technique. From these tests the specific features of the fan nozzle flow field ranging from subcritical via supercritical to choked conditions are described.

SOMMAIRE

Dans ce rapport les résultats d'un essai avec une maquette de l'avion Airbus A 300 B sont presentés. Dans cet essai on n'a considéré que l'interférence due au jet du moteur.

Un schéma d'essai a été ébauché pour déterminer la trainée d'interférence due au jet du moteur, ainsi que pour extrapoler les résultats aux conditions de vol.

Quelques essais intermédiaires ont eu lieu pour éprouver la validité des suppositions de ce schéma.

Afin d'estimer la grandeur de l'influence de l'écoulement externe sur l'écoulement à l'intérieur du tuyère une maquette bi-dimensionelle du tuyère du fan a été essayée dont l'ecoulement a été visualisé à l'aide d'un interféromètre.

En utilisant les résultats de cet essai l'écoulement du jet du fan a été décrit, allant de subcritique via supercritique jusqu'aux conditions de blocage.

INTRODUCTION

During the development of modern jet aircraft somewhere in the wind tunnel program a series of tests are planned with the purpose of studying the engine installation effect on the aircraft aerodynamic characteristics. As described in references 1 and 2 these tests can sometimes be separated in a study of inlet effects only and of afterbody and jet effects only. In other cases the best solution in the wind tunnel seems to be to study simultaneously the inlet and exhaust effects. In all these wind tunnel programs the increments due to the engine installation effects have to be determined with respect to a reference wind tunnel model, generally with through flow nacelles.

In specially designed propulsive wind tunnel models some kind of engine simulation has to be taken into account. For inlet tests only the exit area can simply be increased in order to accomodate the required inlet airflow. For studying exhaust effects some device has to be installed that simulates at least the engine jet flow.

To evaluate the drag increments due to engine installation effects a wind tunnel test scheme has to be developed with which all contributions to the airframe-engine interference can be determined. This scheme has to be compatible with the definition of the reference model and with the thrust definition of the engine manufacturer. In the present paper such a scheme is described concerning the new European Airliner Airbus A 300 B, which came recently into service (Fig. 1). This wide body aircraft is propelled by two G-E CF6-50 fan engines located underneath the wings such that the jet exit flow is passing closely to the wing lower surface. Preliminary studies (Ref. 3) concerning such an engine installation showed that the fan jet mainly influences the pressure distribution of the wing lower surface. Conversely the flow field of the wing might disturb the flow field of the fan jet which flows over the core engine cowl. Hence lift and drag changes as related to the reference model might be expected.

Since the Airbus A 300 B is a high economy jet airliner increments in drag and thrust at cruise conditions are the most important terms to be determined in a wind tunnel program. This paper describes such a program in which attention is given to the jet effects on drag increase and thrust losses.

SCHEME TO DETERMINE DRAG AND THRUST INCREMENTS

To determine the total external drag of a full scale airplane at cruise conditions the first items which have to be known are the external drag of a complete wind tunnel model with free flow nacelles and the engine thrust definition. In the present case of the G-E CF6-50 engine the gross thrust is defined as:

$$F_g = F_{g28} + F_{g8} \tag{1}$$

where F_g is the measured thrust on the test bed increased by the absolute value of the computed scrubbing drag (friction drag) along the core engine, along the wetted area of the pylon and along the core engine plug. So F_{g28} is the momentum flux leaving the fan nozzle plus the pressure forces along the core engine cowl and the wetted pylon area with respect to static pressure at cruise altitude:

$$F_{g28} = \int_{A_{exit\,fan}} (\rho_{28} V_{28}^2 + P_{28} - P_\infty)\, dA + \int_{\substack{core\ engine\ cowl \\ wetted\ pylon\ area}} (P - P_r)\, dA \tag{2a}$$

similarily

$$F_{g8} = \int\limits_{A_{\text{exit core engine}}} (\rho_8 V^2_8 + P_8 - P_\infty)\, dA + \int\limits_{\text{plug}} (P - P_\infty)\, dA \tag{2b}$$

The gross thrust coefficients are defined as:

$$C_{F_{28}} = \frac{F_{g28}}{F_{g\ id.28}} \quad \text{and} \quad C_{F_8} = \frac{F_{g8}}{F_{g\ id.8}} \tag{3}$$

where $F_{g\ id.}$ is defined as the ideal thrust value based on nozzle mass flow and average jet total pressure. The net thrust is defined as:

$$F_N = C_{F_{28}} \cdot F_{g\ id.28} + C_{F_8} \cdot F_{g\ id.8} - D_{\text{scrubbing}} - D_{\text{ram}} \tag{4}$$

The scrubbing drag $(D_{\text{scrubbing}})$ based on computation is given by the engine manufacturer. It is assumed that its value is not affected by external flow.
If the reference drag of the aircraft is defined as:

$$D_{\text{ref.}} = D_{\substack{\text{balance} \\ \text{ref.model}}} - D_{\substack{\text{friction model} \\ \text{external}}} - D_{\substack{\text{internal free} \\ \text{flow nacelles}}} - D_{\text{support}} \tag{5}$$

then the following equilibrium equation can be written for the full scale aircraft in flight, expressed in coefficients:

$$C_{D_{\text{ref.}}} + \Delta C_{D_{\text{spill}}} + \Delta C_{D_{P_{\text{jet}}}} + C_{D_{\substack{\text{fr.ext.} \\ \text{aircraft}}}} + C_{D_{\text{parasite}}} + \Delta C_{D_{\text{induced}}} + \Delta C_{D_{\text{trim}}} - (C_{T_{\text{net}}} + \Delta C_{T_{\text{net}}} - \Delta C_{T_{\text{jet 0}}}) = 0 \ . \tag{6}$$

The various terms refer to the following:

$C_{D_{\text{ref.}}}$ is obvious from the previous definition.

$\Delta C_{D_{\text{spill}}}$ is the difference in inlet drag due to a different mass flow ratio (or ratio of the free captured stream tube area to the intake highlight area) at the reference model and during flight. The spillage drag is equal to the additive drag (pressure forces acting on the inlet stream tube until the stagnation line) minus the inlet lip suction forces. Ideally this term is zero, but as at high Mach numbers the spillage is positive there is a spillage drag due to viscous effects and shock formation at the outer side of the inlet lip. The magnitude of this spillage drag depends on the mass flow ratio. Since the reference model usually spills more than the free flight nacelle, the term $\Delta C_{D_{\text{spill}}}$ will generally be negative. Determination of this term was outside the scope of the present investigation.

$\Delta C_{D_{P_{\text{jet}}}}$ is the difference in pressure drag due to jet flow with respect to the free flow nacelle.

$C_{D_{\substack{\text{fr.ext.} \\ \text{aircraft}}}}$ is the external friction drag of the full scale aircraft, excluding the scrubbing drag due to the engine flow.

$C_{D_{\text{parasite}}}$ is the drag due to external elements such as antennes not represented on the wind tunnel model.

$\Delta C_{D_{\text{induced}}}$ is the induced drag as a consequence of lift changes due to the engine flow : $\frac{dC_D}{dC_L} \Delta C_L$.

$\Delta C_{D_{\text{trim}}}$ is the increase in drag for obtaining aircraft equilibrium.

$C_{T_{\text{net}}}$ is the net thrust coefficient defined as $C_{T_{\text{net}}} = \dfrac{F_{\text{net}}}{1/2\ \rho V^2_\infty \cdot A_{\text{ref}}}$

$\Delta C_{T_{\text{net}}}$ is the change in net thrust due to external flow. In many circumstances, even at supercritical nozzle flow as will be seen later, the external flow will influence the nozzle flow field resulting in shifts in the thrust coefficients and discharge coefficients. The latter will then influence the ram drag term.

$\Delta C_{T_{\text{jet 0}}}$ is the pressure thrust on the core engine cowl etc. at static conditions and equivalent to the last term in equation 2. Since this external thrust on core engine cowl was not specified by the engine manufacturer, it was necessary to determine this term in the wind tunnel program.

The purpose of the present investigation was to determine $\Delta C_{D_{P_{\text{jet}}}}$ and $\Delta C_{T_{\text{jet 0}}}$ and to gather knowledge of the nozzle flow field in order to determine possible changes of $\Delta C_{T_{\text{net}}}$. Since these terms are so-called

pressure drag terms it was decided to establish their value by integration of the measured pressure distribution, rather then by overall force balance measurements. To evaluate the increments from overall force balance measurements a very high force balance accuracy would have been required in addition to very precise measurements of flow and jet total pressure. Nevertheless it was decided to incorporate force balance measurements and flow measurements, in order to check the functioning of the engine simulator.

The next item to be established was the extent of engine flow simulation and the related steps in the wind tunnel program. Since emphasis was placed on the exhaust flow field only two fundamentaly different techniques can be applied namely:

- jet flow with partial inlet flow simulation

- jet flow achieved by external sources only (a faired inlet)

The first technique requires a device to increase the inlet air flow total pressure such as a miniature turbo driven fan or an ejector.
The latter system has been chosen for this test under consideration because:

- the system is more simple
- provide better exhaust nozzle flow field simulation   } as compared to miniature driven fans.
- is better controlable
- is cheaper

With this technique it has to be shown that completely fairing the inlet has only minor effects on the flow field around the wing, pylon and near the nozzles. Evidence that fairing is allowed can be concluded from tests as described in reference 4 and also from preliminary tests at NLR of which the results are briefly discussed in reference 2. This choice then leads automatically to the next five steps in the wind tunnel program.

Step 1 : Test of a model with a free flow nacelle to determine the reference conditions (model geometrically identic to full scale).

Step 2 : Test of the model with a faired engine inlet. Cold air must be supplied to the fan and core engine exhaust in order to simulate the nozzle flow of the free flow nacelle. This model will give the new reference condition for the powered version and the certainty that fairing the inlet with respect to the free flow nacelle is allowed.

Step 3 : Test of the model with full blowing engine without wind, giving the reference state of the static engine. From this test the pressure forces on the external engine surfaces at Mach $M_\infty = 0$ can be obtained which are comparable with the real engine. This step gives the term $\Delta C_{T_{jet\ 0}}$.

Step 4 : Test of the model at Mach $M_\infty = 0.8$ with full blowing jet, simulating the real engine conditions according to the expected power settings of the flight envelope and some off-design points, yielding $\Delta C_{D_{P_{jet}}}$.

Step 5 : Examination of the fan nozzle flow field in order to establish possible changes in C_T due to external flow.

A schematic layout of the test program is given in figure 2.

FACILITIES, MODELS AND INSTRUMENTATION

The model tests concerning the first four steps were conducted in the NLR transonic wind tunnel (HST) at a Mach number $M_\infty = 0.8$. (Ref. 5). The tunnel was operated during the tests at a total pressure of 1 atm. to allow the injected model engine mass flow to be easily vented in order to maintain a constant total pressure. This pressure level was also required to safely duct the required air mass flow to the engine nacelle in view of the limited space in the pylon. To easily duct the mass flow to the model a semi-span model configuration was used (Fig. 3).

For the powered models (step 3 and 4) compressed air was used to simulate the fan jet flow and the hot decomposition products of 75 % hydrogen peroxide for simulation of the core engine flow. These hot decomposition products very closely simulate the core engine jet properties as is described in references 1 and 2. This was not the only reason for utilizing hydrogen peroxide. Since the engine flow consists of two flow streams, it was desirable to supply two independently controllable flows to the model also. Since the space in the pylon is very limited, supply of a high density propellant like hydrogen peroxide through this critical area simplifies the test set-up.

The airflow to the model, supplied from a 600 m³, 40 atm. pressure vessel, was controlled by a "throttle valve" and metered by a sharp edge orifice device. The supplied air was heated by a heat exchanger to a suitable temperature close to the total air temperature in the wind tunnel. The liquid hydrogen peroxide was supplied and controlled by applying a high pressure drive gas above the liquid surface in a pressure vessel. The hydrogen peroxide flow was metered by a turbine flow meter.
For both flow metering systems the accuracy of mass flow was expected to be within ± 0.5 %.
The fuselage and the wing of the semi-span model were attached to an external five component strain gage balance situated on the outside of the side wall of the test section. Air and hydrogen peroxide were supplied to the model passing this balance. Interactions due to supply line stiffness, internal pressure and momentum exchange were small and calibrated.

The semi-span model had a scale of 1 to 19 giving a Reynoldsnumber based on mean aerodynamic chord of $Re = 4.7 \times 10^6$. For boundary layer control transition strips approximately 3 mm wide and consisting of number 150 carborumdum grain set in a plastic adhesive were situated on the upper and lower surfaces at about 5 % chord length.

The semi circular fuselage contained the pressure sensing equipment consisting of fourteen 48 port scannivalves. The horizontal tailplane was omitted.

During the investigation three model engine configurations were required, namely:

model engine conf. 1 : a free flow nacelle, without the core engine plug.

model engine conf. 2 : a model engine with faired inlet, simulating exit conditions equal to the free flow nacelle.

model engine conf. 3 : a model engine with faired inlet, which simulated the scaled real engine exhaust conditions.

For all three configurations the internal jet pipe contouring, from maximum jet pipe area to exit plane, was scaled according to real engine co-ordinates.

In order to minimize model manufacturing induced inaccuracies, the external engine and pylon shell surfaces along which pressure distributions have to be measured were the same for all three configurations. Model configuration changes were accomplished by replacing inserts (see fig. 4).

As tests were concentrated on airframe-engine interference pressure taps were only located in regions of interest (fig. 5). The wing chordwise pressure distributions were measured at three spanwise stations on the upper side of the wing and at six stations on the lower side close to the pylon-wing junction. On the pylon the chordwise pressure distribution was measured at six stations on both sides of the pylon. On the fan cowl and engine cowl 10 rows of respectively 6 and 12 pressure taps in flow direction were circumferentially distributed.

During the tests of configurations 2 and 3 the engine conditions were set according to internally measured reference pressures in the jet pipes which were first calibrated with total pressure rakes in the exit planes (fig. 6). The fan total pressure rake contained 60 pressure tubes distributed over 10 rows. For the powered engine version (with conical plug) the core engine rake contained 24 pressure tubes and for the natural flow models (without plug) 25 pressure tubes distributed over 6 rows.

Distribution of the pressure tubes of the rakes in radial direction was dictated by area weight considerations. Furthermore the model engine has been fitted with static pressure taps inside the jet pipes close to the nozzle exit planes (20 for the fan and 6 for the core engine) and with thermocouples for measuring jet total temperatures.

From the calibration of the jet total pressure it could be concluded that model engine settings according to the calibrated reference pressures were reliable. The probability of measuring the true mean total pressure was 99 % within the accuracy limits of $\pm$ 0.2 % $\frac{P_{tj}}{P_\infty}$.

To obtain detailed information on the fan nozzle flow field in order to determine whether a term $\Delta C_{T_{net}}$ exists, a planar version of the fan nozzle was manufactured and tested in a Ludwieg tube type of facility (Fig. 7). The dimensions of the nozzle were: slit height 12.4 mm and width 63 mm. The observations of the flow field were accomplished using a Mach-Zehnder interferometer set at infinity. Using the Ludwieg type of approach ensured completely turbulence-free flow, hence yielding optimal fringe shapes. The observed fringes are isotachs except for locations close to the walls. The Ludwieg tube provides easy operation procedures and yields very reproducible results during a running time of 30 millisec.

RESULTS

Inlet fairing

Configuration 2 should yield new reference conditions for configuration 3 with full blowing. Hence the pressure distributions of configuration 2 have to be close to those of configuration 1 with the free flow nacelle. In particular to ascertain that no mutual interference exists between the inlet flow field and the exhausts field, there should be a section on the fan cowl where the static pressures are independent of the conditions at the inlet and at the fan nozzle.

Two inlet fairing lengths have been tested. Figure 8 gives a comparison of typical pressure distributions on the fan cowl, core engine cowl, pylon and wing. It is seen that fairing the inlet has practically no influence on the pressure distribution on all parts except for the most forward part of the fan cowl. This strongly supports the already existing evidence that fairing the inlet is allowed for such airplane configurations. The most slender inlet fairing yielded the best simulated pressure distribution on the fan cowl. Hence, this fairing was selected for use in configuration 3 for full blowing. Simulating natural flow blowing nozzles, shifts of the fan and core engine nozzle discharge coefficients at increasing angle of incidence had to be taken into account. Since the overall shift was larger than the relative shift, an average was set for the simulated mass fluxes to the fan and core engine nozzles. The total mass flow for simulated natural blowing was corrected according to figure 9.

From these test series it could be concluded that model configuration 2 is a reliable new reference model for determining $\Delta C_{D_{pjet}}$.

Determination of $\Delta C_{D_{pjet}}$

Figure 10 gives several plots of the effect of full jet blowing on the pressure distributions on several parts of the model. Also a comparison is given with the free flow conditions. Again it can be seen that in the proximity of the jets the jet effects are an order of magnitude larger than the inlet fairing effects. It is observed that jet effects are strongest on the lower inboard side of the wing and at pylon stations downstream of the fan exit plane. A remarkable increase of the peak suction is observed on the lower side of the wing at a station $X/C = 0.2$, at an angle of incidence $\alpha = 0$ degrees. This peak suction diminishes if the angle of incidence is increased (Fig. 11). Also this suction peak decreases in outboard as well as in inboard spanwise direction. The suction peak on the wing corresponds to another suction peak on the inboard side of the engine cowl at the same model station and on the inboard side of the pylon at local chord length $X/C = 0.6$. Both suction peaks on engine and pylon decrease slightly at positive angles of incidence.

The static pressures on the fan cowl aft end increase slightly due to jet effects. This means that jet pluming dominates jet suction due to jet mixing.

It must be emphasized that powered conditions corresponding to the flight envelope are simulated, which means that the nozzle pressure ratios are taken as a function of angle of incidence.

Of course the jet effects are largest on the core engine cowl where the wavy structure of the fan jet flow is clearly visible.

Integration of these pressure-forces towards a drag term yields the results as depicted in figure 12. The drag rise on the core engine and pylon is for about 50 % compensated by thrust terms on fan cowl and wing.

Determination of $\Delta C_{T_{jet\,0}}$.

The pressure distributions on the core engine at static (no wind) conditions are shown in figure 13 and compared at the same conditions with external flow. As might be expected due to external flow the wavy pattern alters appreciably and the average pressure level becomes lower. Also the wing flow field has a marked effect on the fan jet structure. Integration of the pressure distribution on the core engine yields a thrust term of 1 to 2 drag counts, the pylon a thrust term of 0.6 drag counts, and the fan cowl a drag term of 0.1 drag counts, the latter due to jet suction.

Determination of $\Delta C_{D_{induced}}$.

Caused by a shift in pressure distribution on the wing lower surface due to jet effects, the total lift coefficient decreases somewhat with respect to the free flow nacelle. Utilizing the force balance results for the lift component the change in lift can be easily determined. Knowing the derivative $\dfrac{dC_D}{dC_L}$ of the complete reference model, $\Delta C_{D_{induced}}$ is about 1 drag count. Although this term is small compared to other jet interference terms, it cannot be neglected.

Determination of $\Delta C_{T_{net}}$

As already mentioned, in order to decide on a possible existance of $\Delta C_{T_{net}}$, the best way is to determine the nozzle flow field.
Since the core engine nozzle is slightly of the convergent-divergent type, no influence due to external flow might be expected for this nozzle. Besides the core engine nozzle flow field is shielded by the fan jet. The fan nozzle is of the convergent type, and might be considered as planar. Taking into account only the nozzle internal convergence half angle and not considering the nozzle internal shape, a choking pressure ratio P_{T_j}/P_∞ of 2.46 might be expected, based on arguments as described in references 6 and 7 for example.
This pressure ratio is just within the range of interest for the present engine flying at Mach number $M_\infty = 0.8$. Due to inner wall curvature the choking pressure ratio will be reduced, to what extent is unknown however.
Figure 14 shows interferograms of the fan nozzle flow field at six pressure ratios ranging from sub-critical to above choked conditions. Since the interferometer is set at infinity the fringes correspond to isotachs.
Figure 15 is a typical example of the computed flow field as derived from the interferogram, including some typical characteristics. From this picture it could be concluded that due to inner wall-curvature the choking pressure ratio is reduced to 2.16. This value agrees very well with the location of the sonic lines as derived from other interferograms as is shown in figure 16.
With external flow the maximum pressure coefficient on the fan cowl near the fan nozzle lip is $C_p = 0.15$. This means that the fan nozzle choking pressure ratio with external flow is about 2.31 which is well below the nozzle pressure ratio as applied in the wind tunnel program. However, at constant power setting the fan nozzle will be non-choked at a flight Mach number below $M_\infty = 0.76$. In that case an effect will be observed of the external flow on the net thrust of the engine. For the case studied in this investigation $\Delta C_{T_{net}} = 0$.

Total jet interference drag.

Adding all interference terms due to engine installation effects according to equation 6 (see fig.17) it can be concluded that for the flight envelope points considered the total jet interference is 6 to 8 drag counts. The major interference occurs on the core engine cowl.

CONCLUDING REMARKS

The presented wind tunnel test program for determining engine induced drag rises, starting from reference wind tunnel models and engine thrust definition has been successful. It is shown that fairing the inlet is allowed giving new reference conditions. Most jet interference drag occurs on the core engine cowl and pylon. The fan cowl and the wing give some induced thrust terms. The induced drag due to lift losses is small but not negligible. The external flow will not influence the nozzle thrust and discharge coefficients at cruise conditions, though at only slightly lower flying speeds the net thrust will be affected by the external flow. The observed total jet interference amounts to about 2.5 % of the total airplane drag and therefore has to be considered in the thrust-drag-accounting scheme of the airplane.

REFERENCES

1. A. Ferri, F. Jaarsma and R. Monti "Engine-Airplane Interference and Wall Corrections in Transonic Wind Tunnel Tests".
   AGARD AR-36-71, 1971.

2. F. Jaarsma, "Experimental Determination of Nozzle Characteristics and Nozzle Airframe Interference".
   AGARD-LS-53, 1972.

3. D.J. Raney, A.J. Kurn and J.A. Bagley, "Wind Tunnel Investigation of Jet interference for Under-wing Installation of High Bypass Ratio Engines".
RAE TR 68049, 1968.

4. G. Pauly, "Interim Note on Tests with a Wing-Mounted Fan Nacelle with the Fan Jet Simulated by Cold Air Blowing and Alternatively by a Fan Generator Shroud".
A.R.A. C.P. No. 1111, 1970.

5. Users Guide, Part 1, Publication of N.L.R.

6. R.E. Norwood, "Two-dimensional transonic Gas jets".
Proceedings 4th U.S. National Congress of Applied Mechanics, Berkely, 1962.

7. J.L. Solignac et J. Délerny, "Contribution à l'étude Aérodynamique des Systèmes Propulsifs à Double Flux".
ONERA T.P. 1050 (1972).

ACKNOWLEDGEMENTS

Figure 1   Picture of the engine installation of Airbus A 300 B
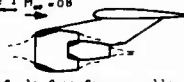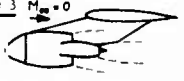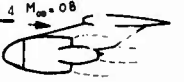
Model conf. and test conditions	Measurements	Objectives
Testserie 1 $M_\infty = .08$ Model conf. 1: free flow nacelle, α range: $-.50 \div 1.25$ degrees	Exit total pressures. Surface and internal static pressures.	Internal drag. Reference state 1.
Testserie 2 $M_\infty = .08$ Model conf. 2: faired inlet, simulating exit conditions of free flow nacelles $P_{t_J}/P_{t_\infty} = 1$ α range: $-.50 \div 1.25$ degrees	Exit total pressures against internal jet pipe pressure. Surface and internal static pressures.	Calibration of model engine for natural flow simulation. Inlet fairing allowed? Choice of best type of inlet fairing. Reference state 2.
Testserie 3 $M_\infty = 0$ Model conf. 3: faired inlet, simulating jet conditions of real jet $P_{t_J}/P_\infty = 2.4$	Exit total pressures against internal jet pipe pressure. Surface and internal static pressures.	Calibration of model engine. Reference state static engine conditions.
Testserie 4 $M_\infty = .08$ Model conf. 3: faired inlet, simulating jet conditions of real engine. α range: $-.50 \div 1.25$ degrees.	Surface and internal static pressures.	Interference pressure drag due to engine jets.
Testserie 5 2-D model of the fan nozzle. $P_{t_J}/P_\infty = 1.5 \div 3.0$, $M_\infty = 0$	Flowfield by interferometry.	Establish choked pressure ratio and sonic line shapes

Figure 2   Layout of the testprogram
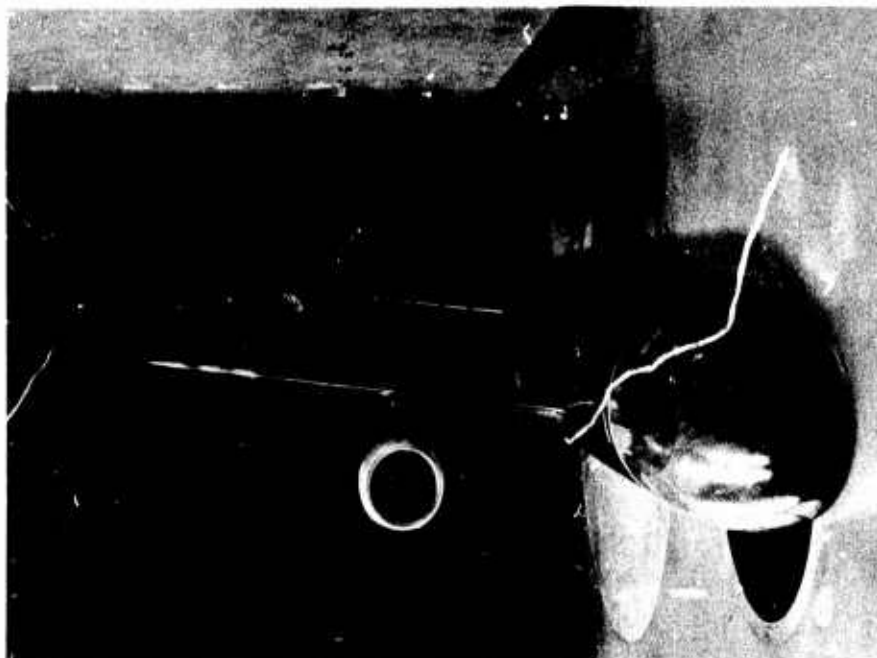
Figure 3 Semi span model configuration in the wind tunnel
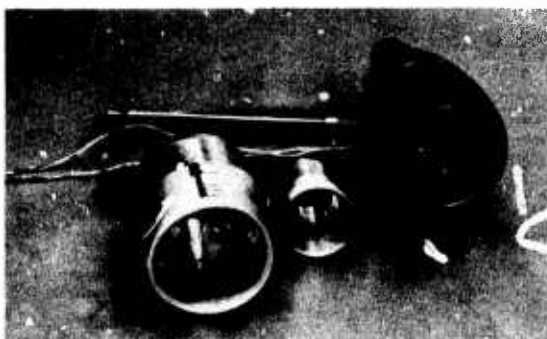
Figure 4a Inserts for natural flow
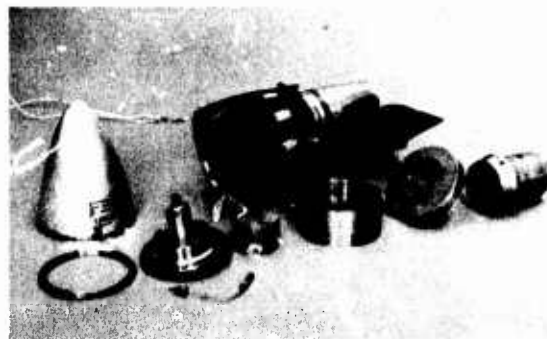
Figure 4b Fairing and inserts for natural flow

Figure 4c Fairing and inserts for simulation
of powered fan jet
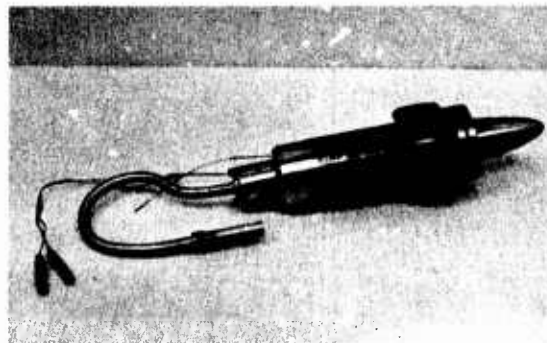
Figure 4d Hydrogen peroxide decomposer for
simulation of core engine jet

Figure 4 Three model engine configurations with inserts

Side view engine installation

Rear view engine

Inboard side

Outboard side

Inboard

Wing lowerside

Outboard
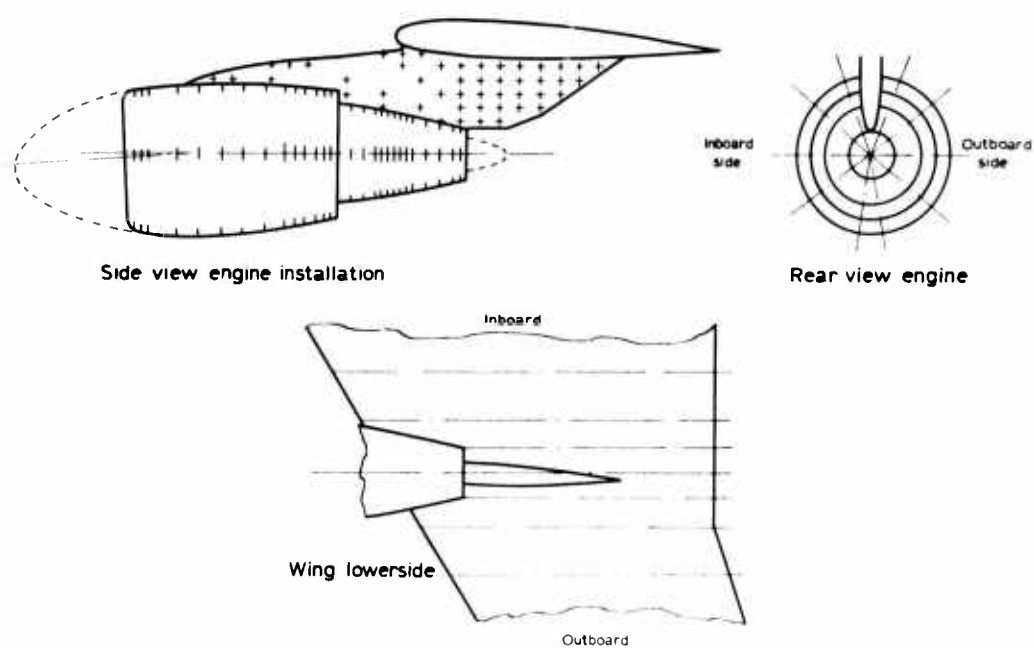
Figure 5 Pressure tap locations
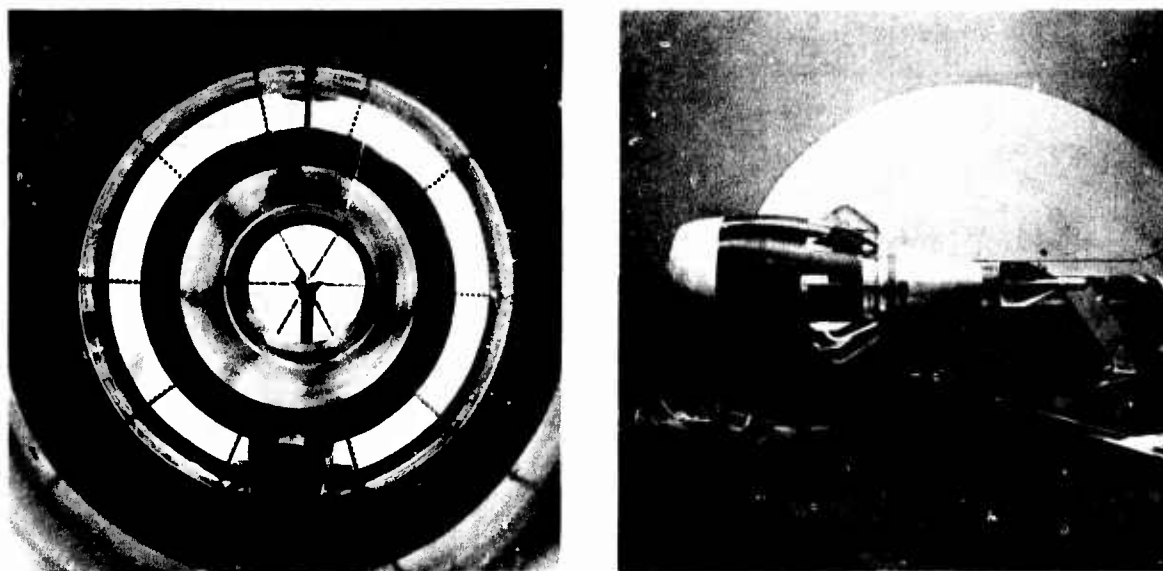
Figure 6 Total pressure rakes in exit planes
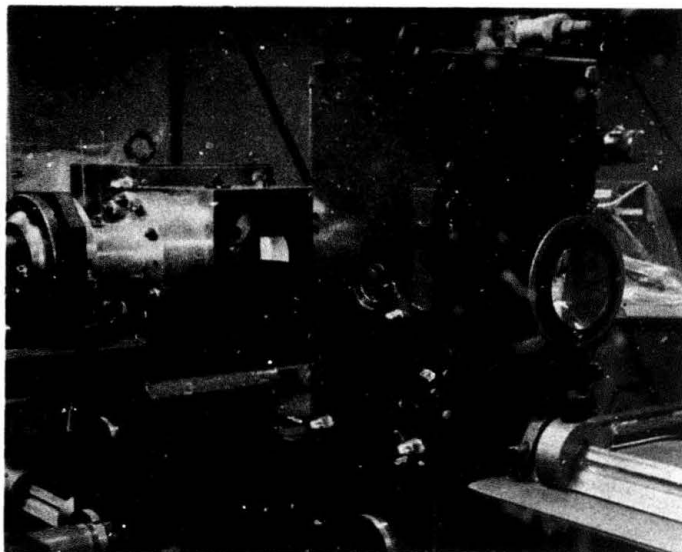
Figure 7   Test section of Ludwiegtube for fan nozzle flow field observation.
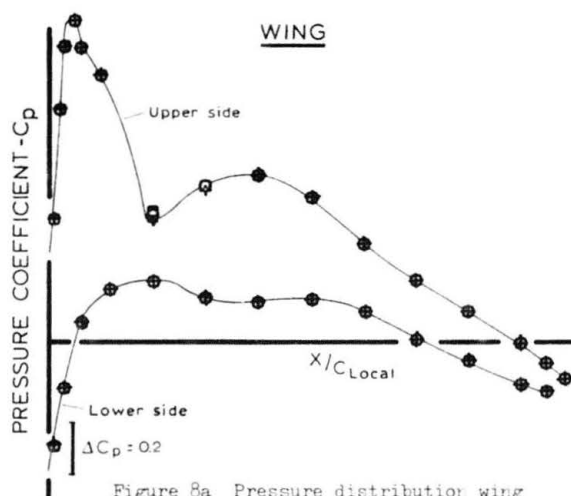
Figure 8a   Pressure distribution wing
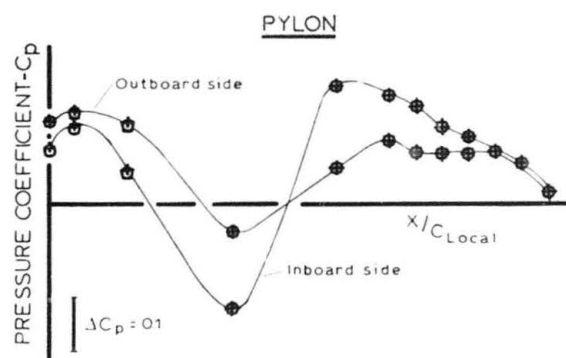
Figure 8b   Pressure distribution pylon
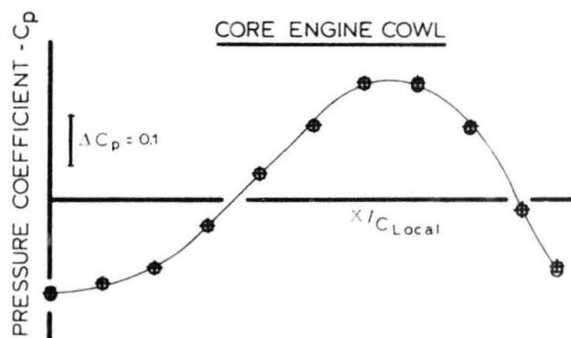
Figure 8c   Pressure distribution core engine cowl
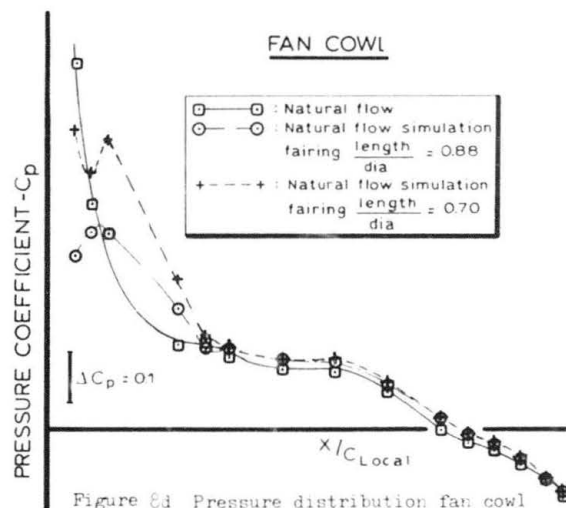
Figure 8d   Pressure distribution fan cowl

Figure 8   Comparison of natural flow nacelle with natural flow simulation.
Two inlet fairing lengths. $M_\infty = 0.8$, $\alpha = 0.5$ degrees.
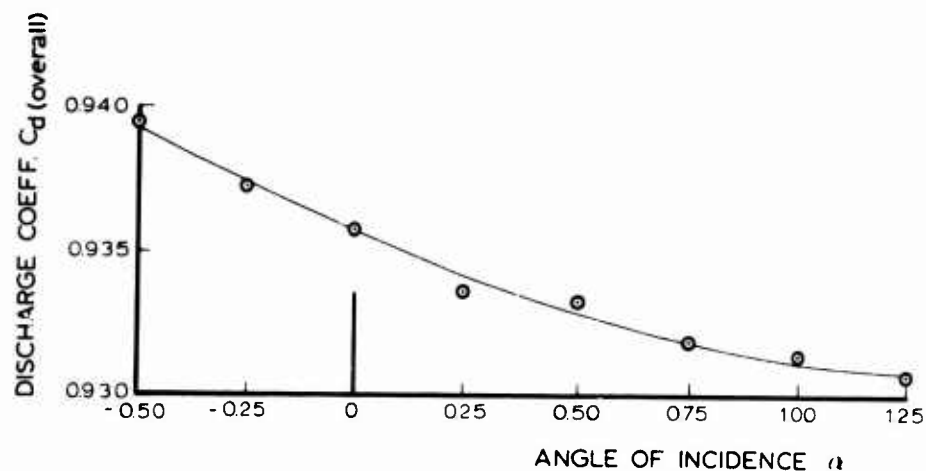
Figure 9 Overall discharge coefficient for both nozzles at natural flow
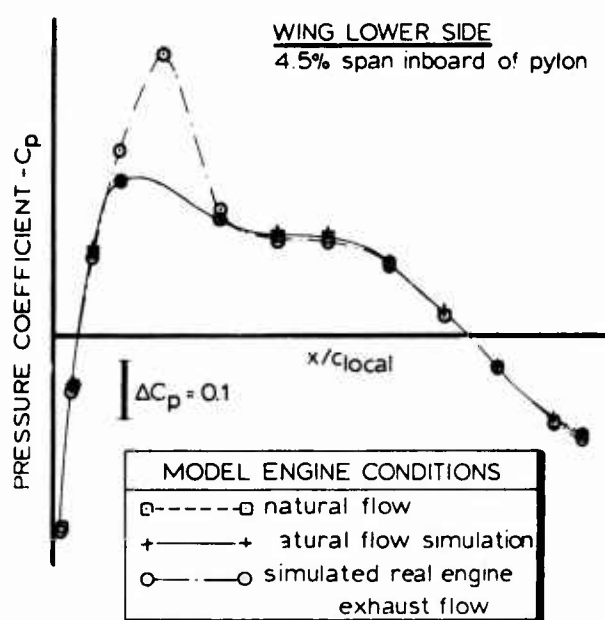
Figure 10a Pressure distribution wing lower side
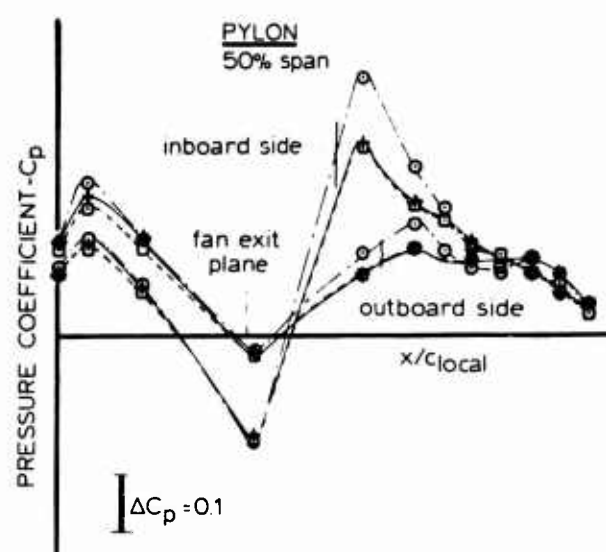
Figure 10b Pressure distribution pylon
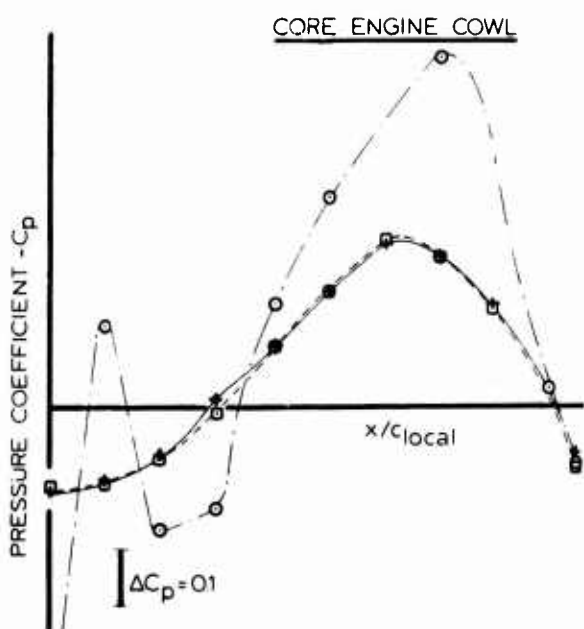
Figure 10c Pressure distribution core engine cowl
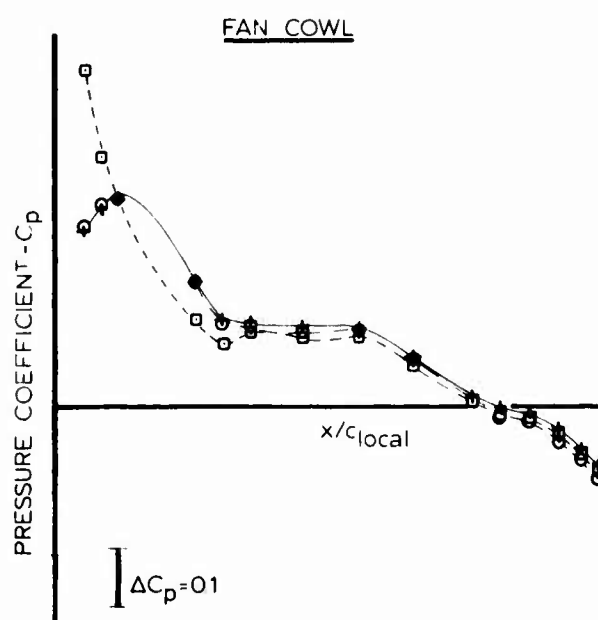
Figure 10d Pressure distribution fan cowl

Figure 10 Comparison of pressure distribution for free flow blowing, simulated free flow blowing and full engine blowing

WING LOWER SIDE
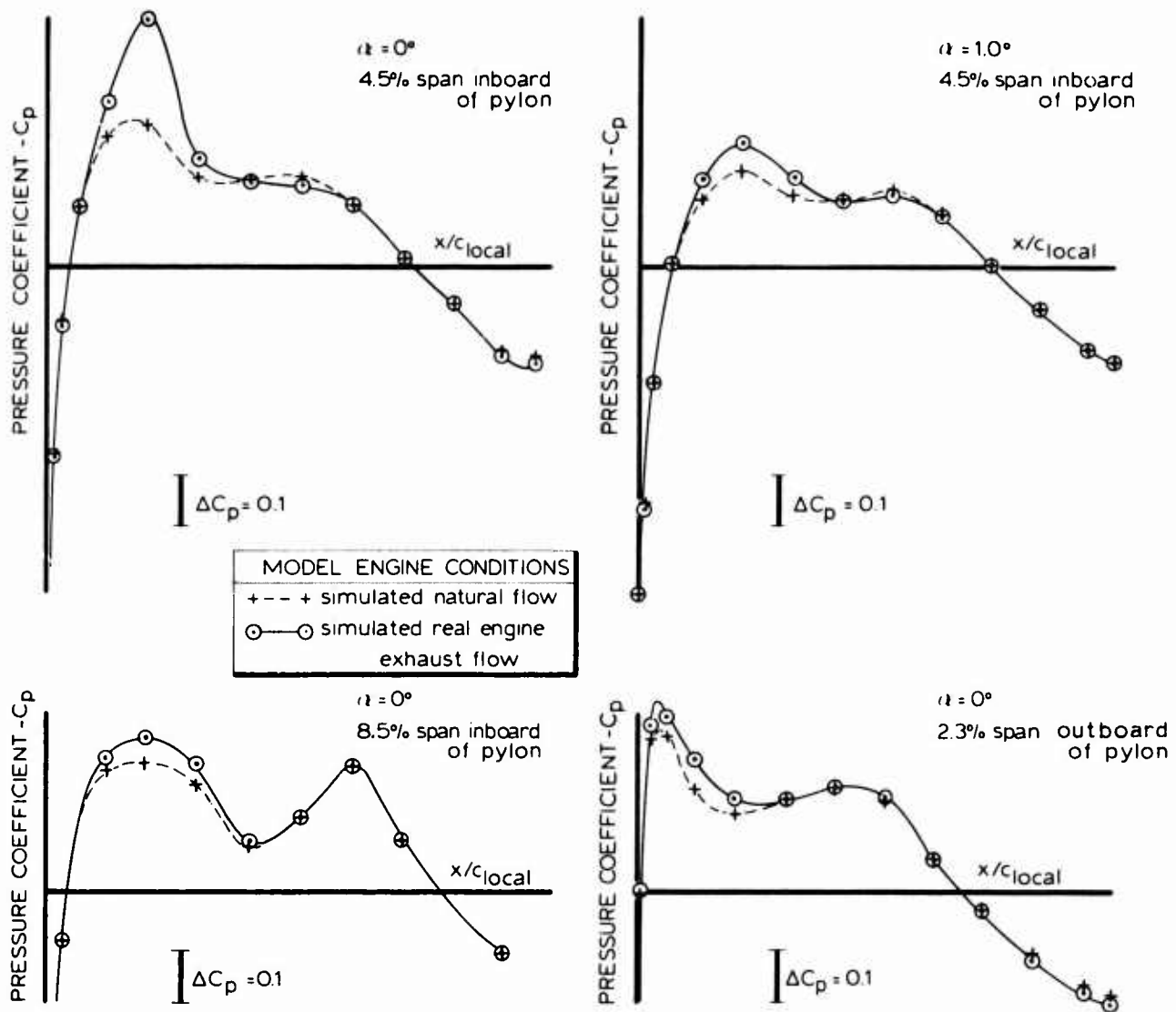
Figure 11   Pressure distribution on the wing lower surface versus α and spanwise position.
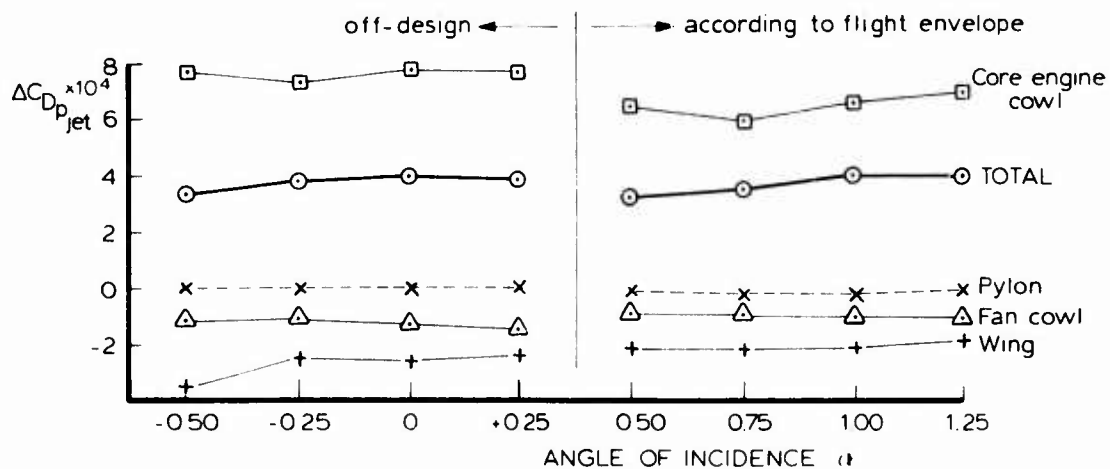
Figure 12 $\Delta C_{D_{p_{jet}}}$ versus α for wing, pylon, fan cowl and core engine cowl
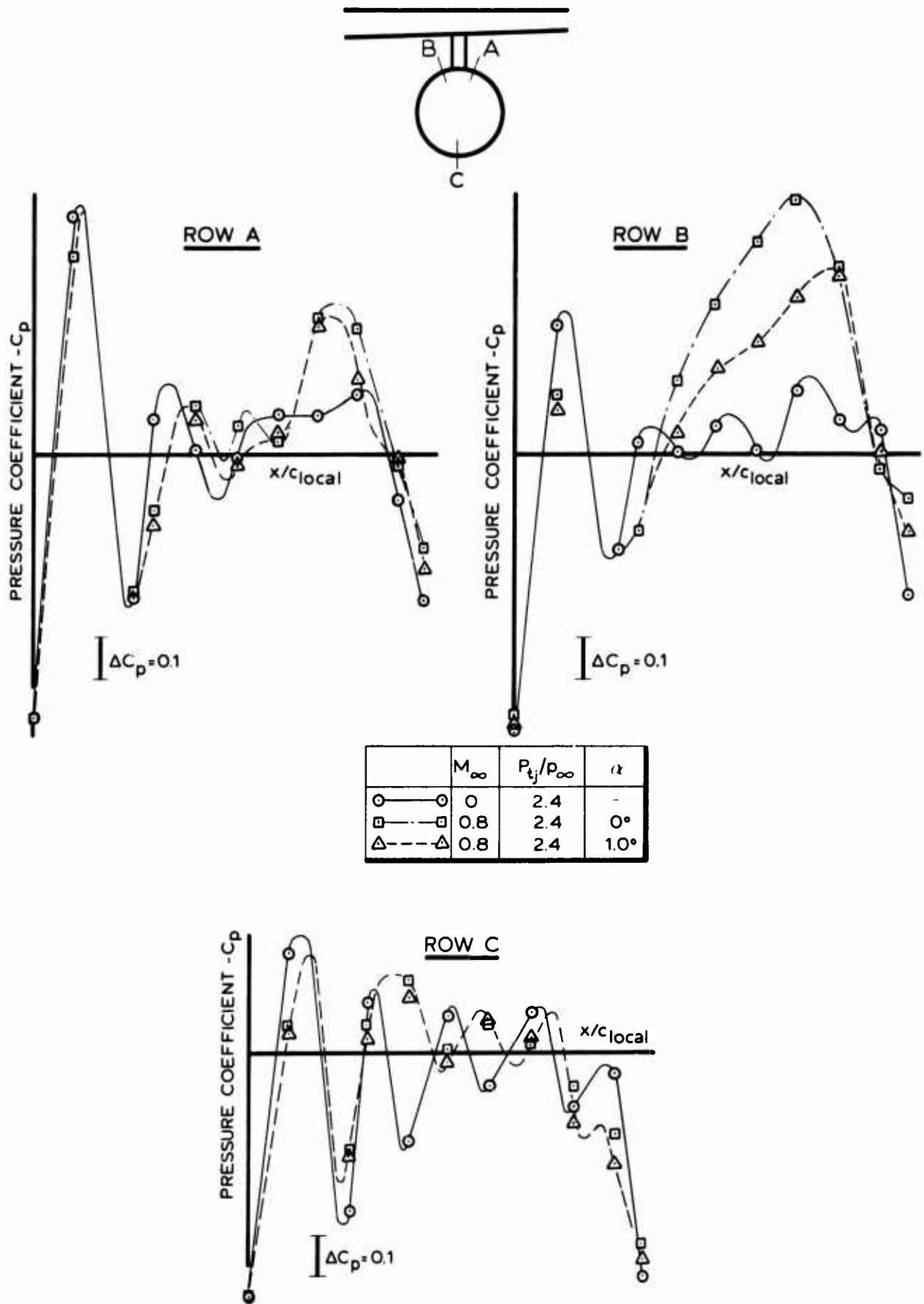
Figure 13 Comparison of core engine pressure distribution for full engine blowing with and without external wind
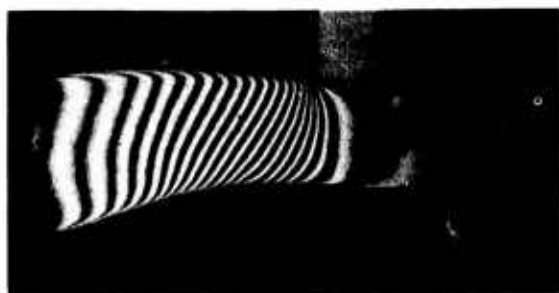
$P_{t_j}/P_\infty = 1.77$
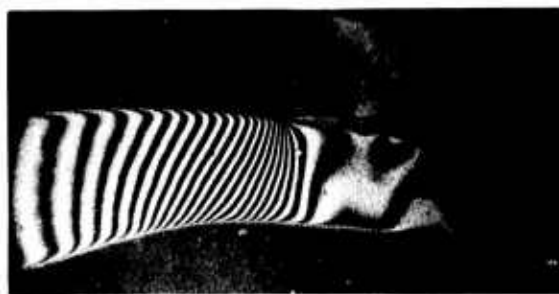
$P_{t_j}/P_\infty = 1.87$
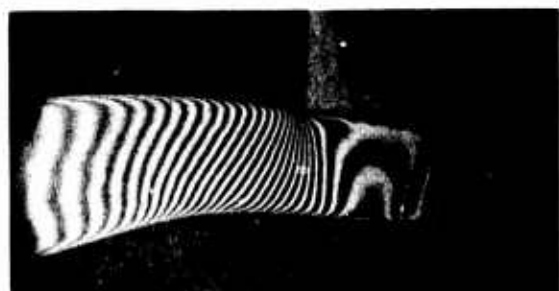
$P_{t_j}/P_\infty = 1.95$
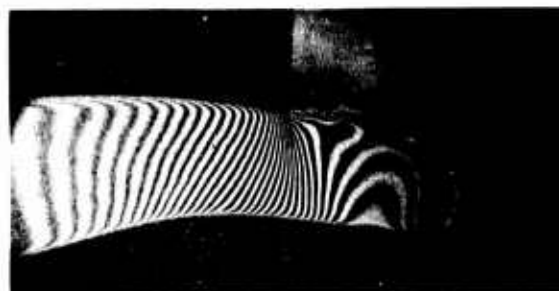
$P_{t_j}/P_\infty = 2.07$
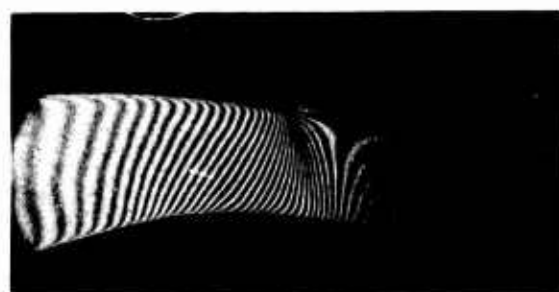
$P_{t_j}/P_\infty = 2.17$
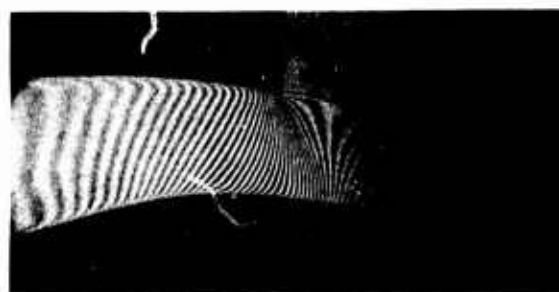
$P_{t_j}/P_\infty = 2.37$

Figure 1. Interferogram of fan nozzle flow field. Interferometer set at infinity. Fringes correspond to isotachs. Illumination 2μsec. $\Delta \rho_{fringe}$ 0.00709 kgsec^2/ m^4
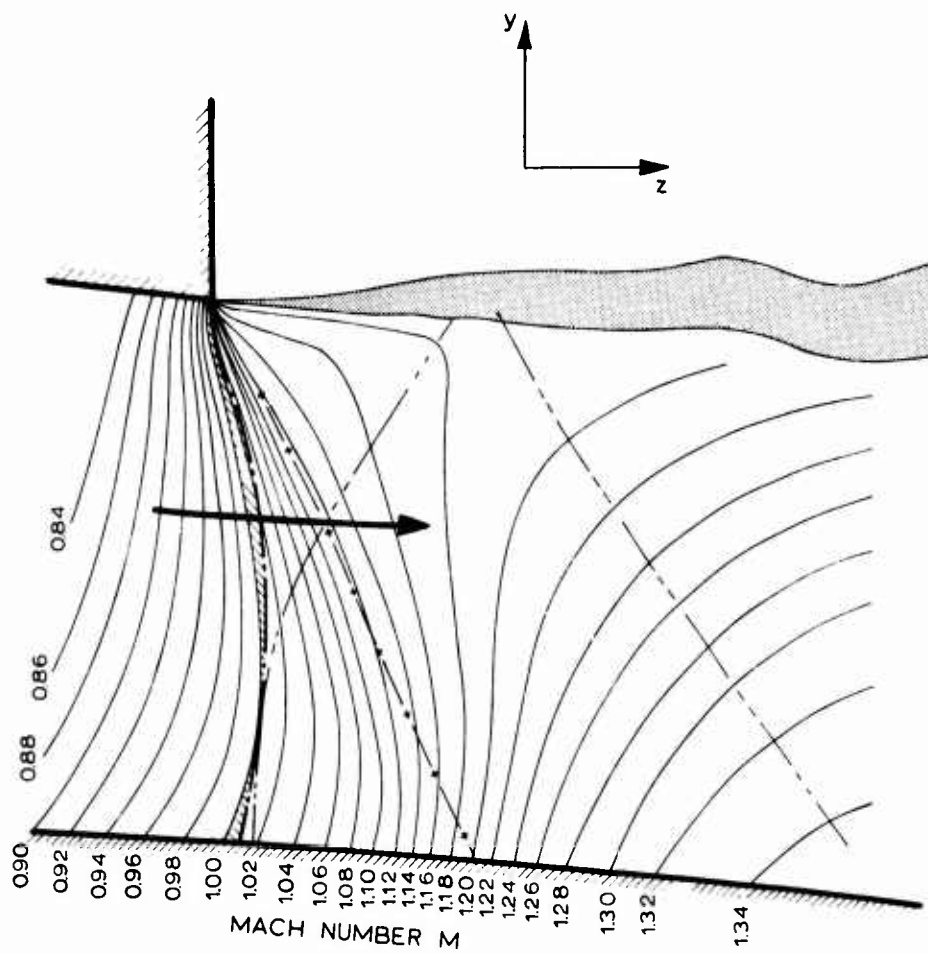
Figure 15 Fan nozzle flow field from interferogram, no external flow, $P_{t_j}/P_\infty = 2.38$
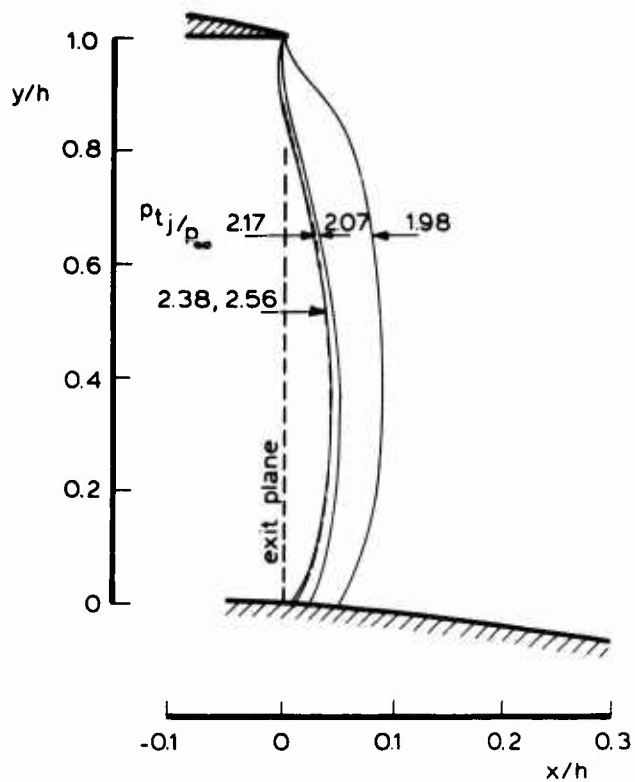
Figure 16 Location of the sonic line in the fan nozzle as a function of the total pressure ratio
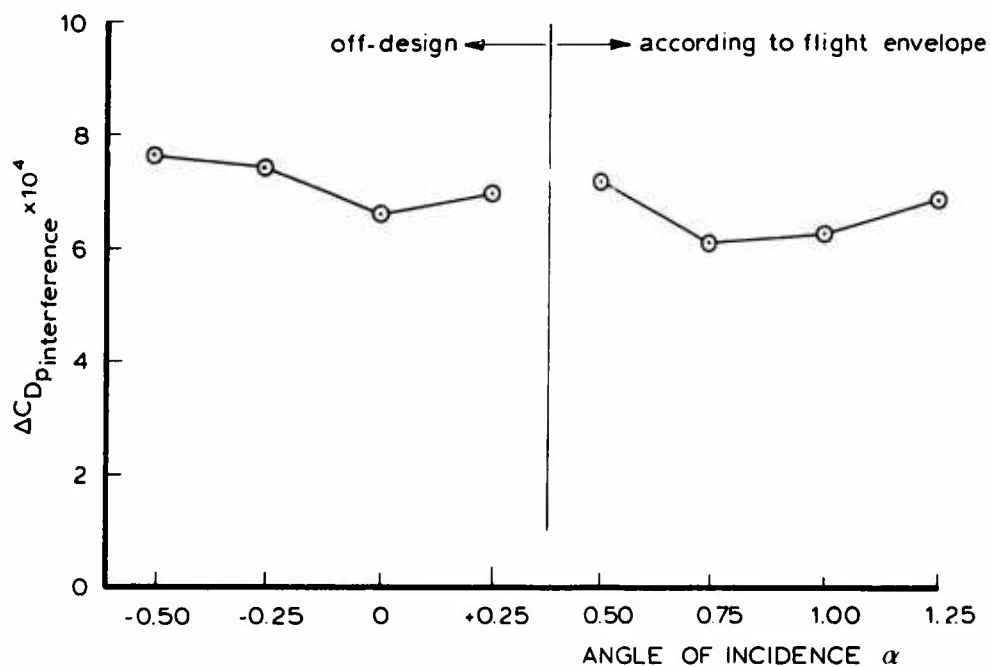
Figure 17 Total interference drag versus angle of incidence α

EFFET DES CONDITIONS EXTERIEURES SUR LE FONCTIONNEMENT D'UNE TUYÈRE
SUPERSONIQUE DOUBLE-FLUX

par Guy de Richemont
Avions Marcel Dassault - Bréguet Aviation 91120 St Cloud

et J. Délery
Office National d'Etudes et de Recherches Aérospatiales (ONERA) 92320 Châtillon

RESUME

La conception d'avions militaires aptes à remplir des missions variées nécessite une étude très attentive du dispositif propulseur compte tenu des conditions de compatibilité avec l'écoulement extérieur. Une des solutions à ce problème d'adaptation se concrétise par un dispositif bi-flux constitué de deux tuyères à section variable. La présente communication s'intéresse plus spécialement aux régimes de fonctionnement où le jet primaire recolle sur la tuyère secondaire. On analyse en détail, sur des configurations typiques, l'évolution des phénomènes en fonction de la pression extérieure et de la distance séparant le plan de sortie de l'injecteur primaire de l'extrémité de la tuyère. L'étude a mis en évidence l'effet des conditions extérieures sur le fonctionnement de la tuyère et permis de préciser les circonstances dans lesquelles se produit le désamorçage. On expose ensuite certaines méthodes de calcul qui permettent de prédire avec une précision convenable les performances de la tuyère.

EFFECT OF EXTERNAL CONDITIONS ON THE FUNCTIONING OF A
DUAL FLOW SUPERSONIC NOZZLE

Summary

The design of versatile military aircraft implies a very careful study of the propulsion system, taking into account interferences with the external flow. A possible solution to this difficult problem of adaptation is that of a dual flow system consisting of two nozzles with variable sections. The present paper is more particularly concerned with flow regimes where the primary jet impiges on the secondary nozzle. It analyses the evolution of the phenomena when the external pressure and the distance between primary injector exhaust plane and the nozzle exit are varied. This experimental study has shown the influence of the external conditions upon the functioning of the nozzle. In a second part theoretical methods are given which allow a reasonable prediction of nozzle performance under such conditions.

NOTATIONS.-

Symboles -

A_c : aire du col primaire.

B : lèvre de sortie de la tuyère secondaire.

C_f : coefficient de frottement pariétal.

C_q :   "   d'injection généralisé.

C_T :   "   de poussée.

D_e : diamètre de la section de sortie de la tuyère secondaire.

D_c : diamètre du col primaire.

F_j : poussée brute conventionnelle.

F_{is} :   "   "   en écoulement isentropique.

F : facteur géométrique $F = (\int_0^L y\, dS)/(L\, Y_R)$

H_i : paramètre de forme (incompressible).

K_p : coefficient de pression.

K_1 : premier point critique.

K_2 : deuxième   "   .

L : longueur de la frontière du jet non visqueux isobare.

M : nombre de Mach.

p : pression.

q : pression dynamique $\left(q = \frac{1}{2} \rho V^2 \right)$

q_j : débit primaire.

q_s :   "   secondaire.

R : point de recollement.

S : abscisse.

T : température absolue.

T_c : traînée de culot.

V : vitesse.

x : abscisse.

X : distance inter-tuyères.

α : angle de convergence de l'injecteur primaire.

β : angle de convergence de la tuyère secondaire.

γ : rapport des chaleurs spécifiques.

δ : épaisseur physique de la couche dissipative.

δ^* : " de déplacement " "

θ : " de quantité de mouvement.

ρ : masse spécifique.

σ : paramètre de mélange turbulent.

τ : tension de frottement.

$\psi, \bar{\psi}$: angles de recollement.

Indices -

i : désigne les conditions génératrices.

j : " " relatives au jet primaire.

a : désigne les conditions ambiantes extérieures.

1 : " " relatives à la zone isobare (cavité).

R : désigne les conditions au recollement.

$*$: " " au désamorçage.

$-$: " " pour le recollement non perturbé.

1 - INTRODUCTION.-

La conception d'avions militaires aptes à remplir des missions variées nécessite une étude particulièrement attentive du dispositif propulseur. D'une part la post-combustion indispensable en supersonique impose une section de sortie largement variable, d'autre part le domaine de vol est très étendu en nombre de Mach et altitude. Ces conditions rendent difficile l'adaptation de l'arrière-corps à tous les régimes de vol. Ainsi pour situer l'intérêt de ces études, citons l'exemple d'essais en vol qui ont montré des diminutions de traînée voisines de 10% en subsonique par suppression de décollements. Même en l'absence de tels phénomènes les gains potentiels sont importants. De plus sur le plan des qualités de vol, les décollements, du fait de leur instabilité, provoquent parfois des mouvements latéraux incontrôlables. La disparition de ces phénomènes peut être considérée comme un sous-produit de la recherche d'un bon écoulement.

Une des solutions à ce problème d'adaptation se concrétise par un ensemble de deux tuyères à section variable, appelé dans la suite éjecteur (figure 1):

- une tuyère primaire dont le rôle est de réguler la section critique du jet chaud en fonction des conditions moteur,

- une tuyère secondaire assurant deux rôles principaux : tout d'abord guidage et mélange du flux froid de ventilation et du jet chaud, ensuite adaptation des formes intérieures et extérieures de l'arrière-corps aux conditions de vol.

TUYERE DOUBLE FLUX
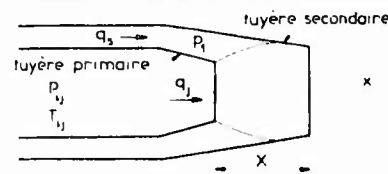
a. Schéma de la tuyère
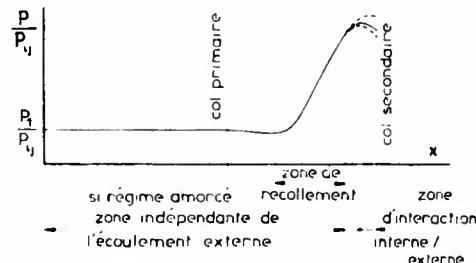
b. Loi de pression interne sur la tuyère secondaire
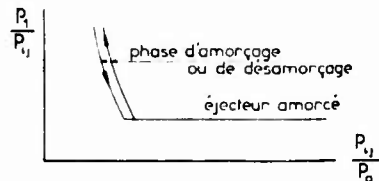
c. Amorçage de la tuyère

FIG. 1

Se limitant aux cas où le débit secondaire est faible, deux types de fonctionnement peuvent se présenter :

1 - le jet primaire ne frappe pas la tuyère secondaire. Alors, la zone inter-tuyères est sensiblement isobare,

2 - le jet primaire recolle sur la tuyère secondaire. Ce phénomène s'accompagne d'une recompression avec choc, parfois suivie d'une détente sur la face interne de cette tuyère.

Nous ne nous intéresserons ici qu'au deuxième cas. L'expérience montre alors (figure 1C) que si l'on augmente suffisamment le taux de détente (rapport de la pression génératrice p_{ij} du jet primaire à la pression ambiante externe p_a) la loi de pressions internes réduite p/p_{ij} (x) devient en grande partie indépendante de p_a, à l'exception d'une petite zone située en aval du recollement où se manifeste l'interaction entre les écoulements interne et externe (figure 1b); en particulier la pression de cavité p_1 devient proportionnelle à la pression génératrice p_{ij} .

Ce régime est appelé ici "fonctionnement en éjecteur amorcé". Il fait l'objet des méthodes de calcul exposées dans la suite.

Même en se limitant à ce régime on doit encore distinguer deux modes de fonctionnement liés à la distance X séparant les plans de sortie des deux tuyères. Partant d'une longueur X importante et se plaçant, pour simplifier, dans le cas où la tuyère

secondaire est cylindrique l'expérience montre qu'un raccourcissement est d'abord sans effet sur le niveau des pressions internes (en particulier la pression de cavité p_1 est invariable), puis se traduit ensuite par une baisse générale des pressions. On passe alors du régime "éjecteur long", où le recollement est régulier, au régime "éjecteur court" où le recollement est perturbé par l'extrémité de la tuyère.

La présente communication comprend d'abord une partie essentiellement expérimentale où l'on s'est efforcé de préciser le fonctionnement de la tuyère dans le régime "éjecteur court" en portant plus spécialement son attention sur l'influence des conditions externes. Pour des raisons de simplification technologique d'une part et afin d'analyser plus commodément les phénomènes d'autre part, l'effet de l'écoulement extérieur réel est simulé par une pression ambiante p_a constante mais dont le niveau peut être ajusté.

Dans une deuxième partie sont présentées des méthodes de calcul qui permettent de prédire, avec une précision convenable, les performances de la tuyère en régime amorcé, c'est-à-dire lorsque les pressions internes ne dépendent pas de façon sensible des conditions extérieures.

2 - ANALYSE EXPÉRIMENTALE DU FONCTIONNEMENT D'UN ÉJECTEUR SUPERSONIQUE COURT.-

2.1 - Montage expérimental et technique de mesure.

Le montage expérimental utilisé pour cette étude est représenté schématiquement figure 2. Il simule une tuyère à deux flux dont le jet débouche dans une atmosphère au repos.

La tuyère primaire est constituée d'un injecteur tronconique de 30 mm de diamètre au col. L'angle de convergence α est variable; les essais ont été effectués pour $\alpha = 10$ et 20°. Le flux primaire est un jet d'air dont la pression génératrice p_{ij} peut être ajustée jusqu'à une valeur maximale de 5,5 bars. Le minimum de p_{ij} voisin de 2,5 bars, est imposé par la condition d'obtenir un jet dont la couche de mélange est turbulente depuis l'origine. La température génératrice T_{ij} était proche de 260 K. L'alimentation de la tuyère se fait par un tube amont de 680 mm de long et de 80 mm de diamètre contenant plusieurs filtres anti-turbulent. Ce tube

fait office de chambre de tranquillisation après les trois étages de détente qui ont fait passer la pression de 250 bars à la valeur p_{ij} voulue.

La tuyère secondaire, jouant le rôle de paroi de reprise pour le jet, est un élément interchangeable. Trois types de reprise ont été essayés (voir figure 3) : d'abord un manchon cylindrique de 50 mm de diamètre. Bien que peu réaliste, une telle forme permet, en raison de sa simplicité, une interprétation plus commode des phénomènes, ainsi que nous le verrons plus loin. Les deux autres tuyères sont de forme tronconique présentant des angles de convergence β égaux à 7 et 15° respectivement. Leur diamètre de sortie D_e est égal à 40 mm. Chaque reprise est équipée de prises de pression statique disposées au voisinage d'une même génératrice avec un pas de 1 mm.

La tuyère secondaire débouche dans une chambre cylindrique de 100 mm de diamètre faisant office de caisson à pression constante. En aval, cette chambre est reliée à un dispositif d'aspiration dont la régulation permet d'ajuster p_a. Ainsi, agissant simultanément sur p_a et sur p_{ij} on est en mesure de réaliser des rapports p_a/p_{ij} assez largement variables.

La tuyère secondaire et le caisson qui lui est solidaire, sont montés sur un chariot (voir figure 2) qui peut être animé d'un mouvement de translation par rapport à la tuyère primaire. Un tel dispositif permet de faire varier continuement la distance X séparant le plan de sortie de l'injecteur de celui de la reprise.

Les éléments supportant les tuyères primaire et secondaire constituent un ensemble cylindre-piston délimitant une cavité étanche dans laquelle peut être pratiquée une injection d'air simulant un éventuel deuxième flux. Cette possibilité n'a pas été utilisée pour les présents essais qui ne concernent que le cas où le débit secondaire est nul ($q_s = 0$).

DEFINITION DES TUYERES

a _ Tuyères primaires

b _ Tuyères secondaires

FIG. 3

SCHEMA DU DISPOSITIF EXPERIMENTAL
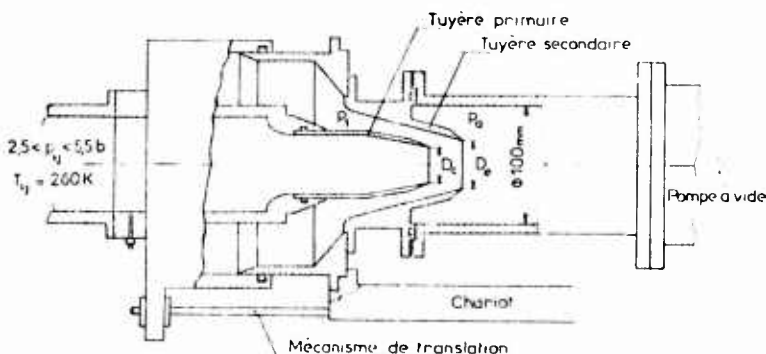
FIG. 2
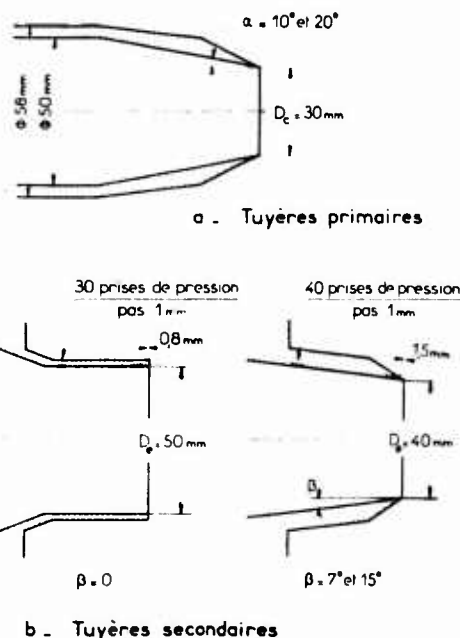
La procédure expérimentale adoptée a été
la suivante : pour chaque couple tuyère
primaire - reprise secondaire* et en se
plaçant à des rapports p_a/p_{ij} différents,
on a fait varier la distance X , depuis
une profondeur suffisante pour que le jet
primaire recolle sans être influencé par
les circonstances aval, jusqu'à la valeur
limite où, compte tenu de la pression p_a ,
le jet ne peut plus recoller sur la reprise.
Pour chaque distance X considérée, la
répartition de pression sur la reprise a
été relevée et les pressions p_1 , p_a et
p_{ij} ont été mesurées.

2.2 - Résultats expérimentaux.

Une vue d'ensemble des phénomènes est
donnée sur les figures 4, 5 et 6 qui
montrent les distributions pariétales de
pression pour trois des configurations
étudiées dans des cas où, le rapport p_a/p_{ij}
étant maintenu fixe, on fait largement
varier la distance X . Sur la figure 7
sont tracées les évolutions correspondantes
de la pression de cavité p_1 qui est une
grandeur caractéristique du processus de
recollement.

Dans l'exemple relatif à la reprise
cylindrique ($\beta = 0$), la pression ambiante
p_a est largement supérieure aux pressions
régnant dans la tuyère lorsque le recolle-
ment est régulier, c'est-à-dire non
perturbé (p_a/p_{ij} = 0,245 pour un niveau
maximal de pression interne de 0,198). On
constate que la pression de cavité p_1 est
indépendante à la fois de X et de p_a
tant que X est supérieur à 26 mm. En deçà
de cette valeur, p_1/p_{ij} croît légèrement
mettant ainsi en évidence une influence de
la pression aval sur le recollement. Si X
est inférieur à 24,5 mm, le jet primaire ne
peut plus recoller sur la reprise. La
pression dans la tuyère s'établit alors à
un niveau sensiblement constant et voisin
de p_a .

Pour la reprise tronconique d'angle de
convergence $\beta = 7°$, les répartitions
pariétales ainsi que l'évolution de p_1/p_{ij}
mettent en évidence des phénomènes particu-
lièrement intéressants. Dans l'exemple
choisi, p_a/p_{ij}, égal à 0,216, est nettement
inférieur au niveau maximal de pression
atteint dans la tuyère. Considérant la
courbe p_1/p_{ij} fonction de X , on peut
y distinguer trois régions.

Pour X compris entre 24 et 34 mm
(domaine 1) le recollement n'est pas
influencé par les circonstances aval : il
ne dépend que des conditions amont et
locales résultant de la détente du jet
ainsi que de la pente de la paroi. De ce
fait, la croissance de p_1/p_{ij} lorsque X
diminue est due ici aux changements géomé-
triques provenant du déplacement injecteur
primaire reprise. Quand X devient
inférieur à 24 mm,(domaine 2) l'effet de
la détente se produisant à la lèvre B de
la tuyère se fait sentir. En conséquence,
on observe une diminution de la pression
de cavité jusqu'au moment où X étant
inférieur à 12,5 mm, le jet ne recolle plus
sur la reprise.

---

* en fait, la majorité des essais ont été
effectués avec l'injecteur d'angle α = 10°,
ce paramètre n'ayant qu'une faible influence
sur les phénomènes étudiés.

Pour X supérieur à 34 mm (domaine 3) se
produisent des phénomènes également très
instructifs bien que ne faisant pas inter-
venir directement la pression extérieure p_a.
Quand X est égal à 35 mm, la détente qui
se produisait jusque là en aval de la zone
du recollement est déplacée et précédée
par une seconde compression très rapide.
Un tel changement est dû à l'existence
d'un point triple I lié à la présence d'un
disque de Mach dans le jet supersonique.
En effet, pour $X > 35$ mm, le choc oblique
montant c_2 issu de I se réfléchit sur la
frontière du jet à l'extérieur de la tuyère.

REPARTITION DE PRESSION
SUR LA TUYERE SECONDAIRE

$\frac{P_a}{P_{ij}} = 0,245$ $\alpha = 10°$ $\beta = 0$

FIG. 4

REPARTITION DE PRESSION
SUR LA TUYERE SECONDAIRE

$\frac{P_a}{P_{ij}} = 0,216$ $\alpha = 10°$ $\beta = 7°$

FIG. 5

REPARTITION DE PRESSION
SUR LA TUYERE SECONDAIRE

$$\frac{P_a}{P_{ij}} = 0.213 \qquad \alpha = 10° \qquad \beta = 15°$$

FIG. 6

EVOLUTION DE LA PRESSION DE CAVITE
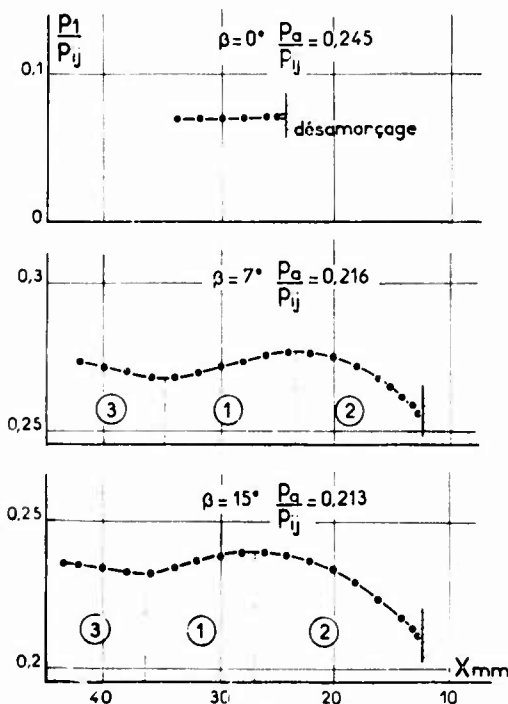
FIG. 7

Lorsque X est voisin de 35 mm, C_2 percute la paroi de reprise. La réflexion de C_2 s'accompagne alors de la formation d'un choc descendant C_3 et se traduit par une montée rapide de la pression pariétale. Tant que X est inférieur à 36 mm, le recollement du jet ne semble pas influencé par cette compression, mais dès que X est plus grand que 36 mm une interaction se fait sentir. Elle entraîne une augmentation de la pression de cavité P_1.

Des phénomènes analogues sont observés dans le cas de la reprise d'angle $\beta = 15°$. On notera cependant que l'interaction en compression n'apparaît pas sur les courbes

de la figure 6 de façon aussi manifeste que dans l'exemple précédent.

Afin de mieux comprendre le processus d'interaction et de préciser les circonstances proches du désamorçage du jet, des expériences systématiques ont été effectuées en faisant varier la pression ambiante P_a. Les figures 8, 9 et 10, relatives respectivement à $\beta = 0$, 7 et 15° montrent quelques unes des répartitions pariétales $P/P_{ij} = f(S)$ relevées pour des X décroissants et pour quatre valeurs du rapport P_a/P_{ij}. Toutes les courbes ont une allure commune; pour les valeurs les plus basses de P_a/P_{ij}, le désamorçage - c'est-à-dire la valeur limite de X en dessous de laquelle le jet ne peut plus recoller sur la reprise - est précédé d'une décroissance très nette de la pression de cavité. En revanche, pour les P_a/P_{ij} élevés, réalisés seulement lorsque $\beta = 0$, on n'observe qu'une faible augmentation de P_1 qui se produit peu de temps avant le désamorçage. Les figures 11 et 12 montrent la variation de P_1/P_{ij} en fonction de la distance réduite X/D_c pour les trois tuyères étudiées. Ainsi qu'il a déjà été dit, quand β est différent de 0 (figure 12), P_1/P_{ij} varie avec X/D_c même en l'absence d'influence aval. Il est loisible d'estimer une courbe $\bar{P_1}/P_i = f(X/D_c)$ qui correspondrait à un recollement "libre" se produisant sur une paroi tronconique assez longue pour que les conditions extérieures ne se fassent pas sentir. L'interaction se traduit alors par des évolutions de P_1 qui s'écartent de cette courbe "de base".

La figure 13 donne les distances réduites de désamorçage X^*/D_c en fonction de P_a/P_{ij}. Rappelons que, par commodité, le désamorçage est ici défini comme le moment où le jet ne peut plus recoller sur la paroi de reprise. Cette définition

DISTRIBUTIONS PARIETALES
DE PRESSION PERTURBEES

$$\alpha = 10° \qquad \beta = 0°$$
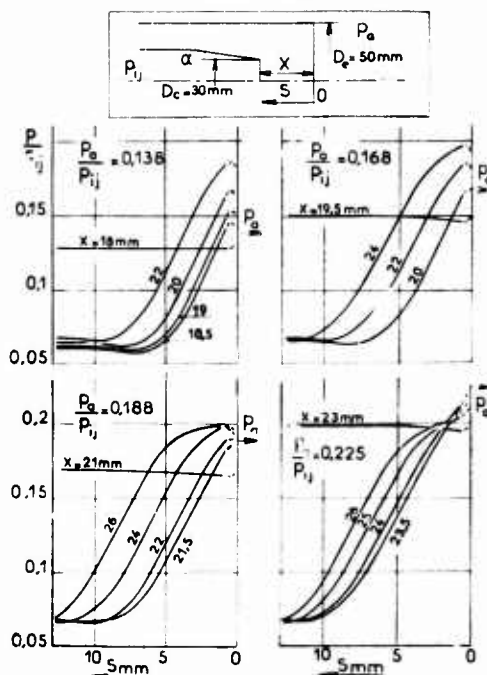
FIG. 8

DISTRIBUTIONS PARIETALES
DE PRESSION PERTURBEES

$\alpha = 10°$ $\beta = 7°$
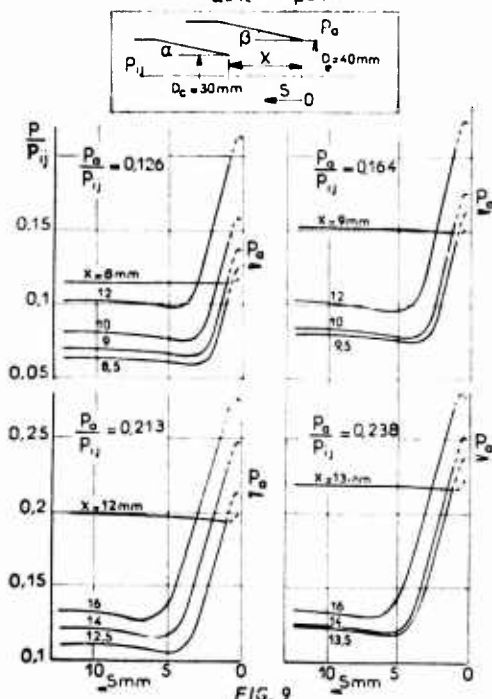
$D_c = 30\,mm$ $D_a = 40\,mm$ S = 0

$\frac{P}{P_{ij}}$

$\frac{P_a}{P_{ij}} = 0,126$

$\frac{P_a}{P_{ij}} = 0,164$

0,15
0,1
0,05

X = 8 mm
12
10
9
8,5

X = 9 mm
12
10
9,5

$\frac{P_a}{P_{ij}} = 0,213$

$\frac{P_a}{P_{ij}} = 0,238$

0,25
0,2
0,15
0,1

X = 12 mm
16
14
12,5

X = 13,4 mm
16
13,5

10 S mm 5 0

FIG. 9

DISTRIBUTIONS PARIETALES
DE PRESSION PERTURBEES

$\alpha = 10°$ $\beta = 15°$

$D_c = 30\,mm$ $D_a = 40\,mm$ S = 0

$\frac{P}{P_{ij}}$

$\frac{P_a}{P_{ij}} = 0,127$

$\frac{P_a}{P_{ij}} = 0,155$

0,15
0,1

X = 7,5 mm
12
10
9
8

X = 8,5 mm
14
12
10
9

$\frac{P_a}{P_{ij}} = 0,205$

$\frac{P_a}{P_{ij}} = 0,226$

0,25
0,2
0,15

X = 11,5 mm
16
14

X = 12,5 mm
16
14
13

10 S mm 5 0

FIG. 10

EFFET DE PERTURBATION
SUR LA PRESSION DE CAVITE

$\alpha = 10°$

$\frac{P_1}{P_{ij}}$

$\frac{P_a}{P_{ij}}$

$\beta = 15°$
- 0,128
- 0,153
- 0,204
- 0,213

$\overline{P_1}$

$\overline{P_1}$

$\beta = 7°$
- 0,135
- 0,194
- 0,216
- 0,237
- 0,238

0,20
0,15
0,10
0,05

0,5 1 $\frac{X}{D_c}$

FIG. 12
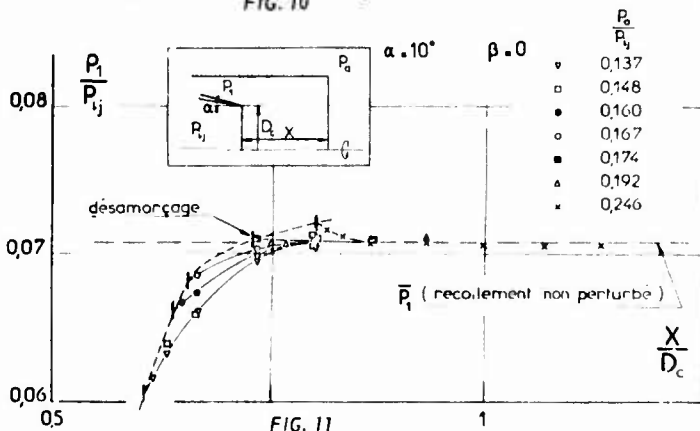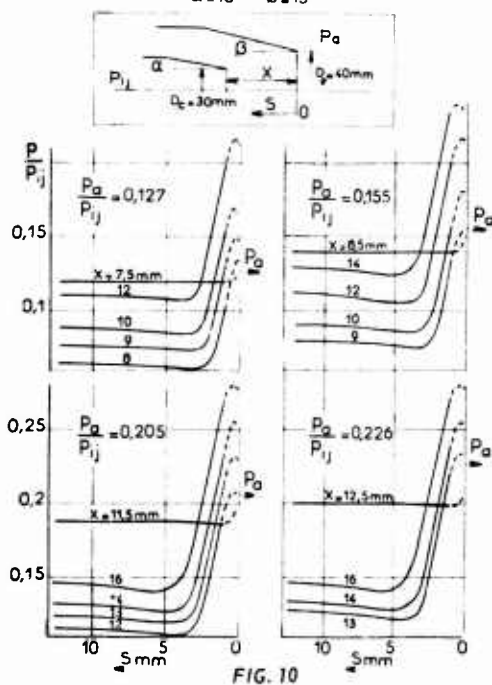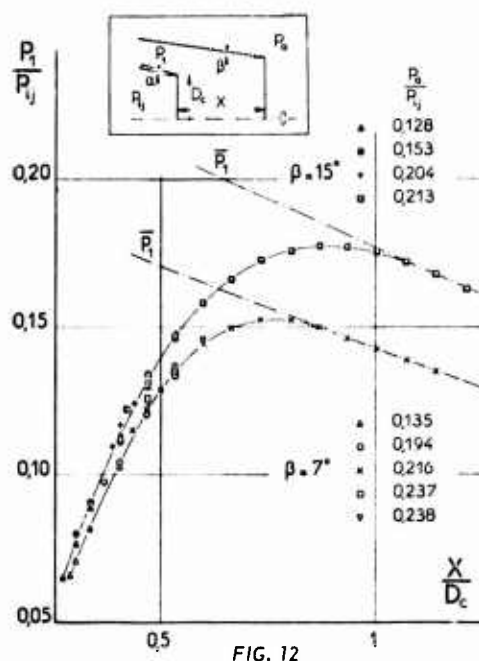
DISTANCES REDUITES DE DESAMORÇAGE
(X* limite pour le recollement du jet primaire)

$\frac{P_a}{P_{ij}}$

0,2
0,1

$\beta = 0$

$\frac{X^*}{D_c}$

0,6 0,7 0,8 0,9

0,2
0,1

$\beta = 7°$

0,2
0,1

$\beta = 15°$

$\frac{X^*}{D_c}$

0,2 0,3 0,4 0,5

FIG. 13

$\alpha = 10°$ $\beta = 0$

$\frac{P_1}{P_{ij}}$

$\frac{P_a}{P_{ij}}$
- 0,137
- 0,148
- 0,160
- 0,167
- 0,174
- 0,192
- 0,246

0,08
0,07
0,06

désamorçage

$\overline{P_1}$ (recollement non perturbé)

$\frac{X}{D_c}$

0,5 **FIG. 11** 1
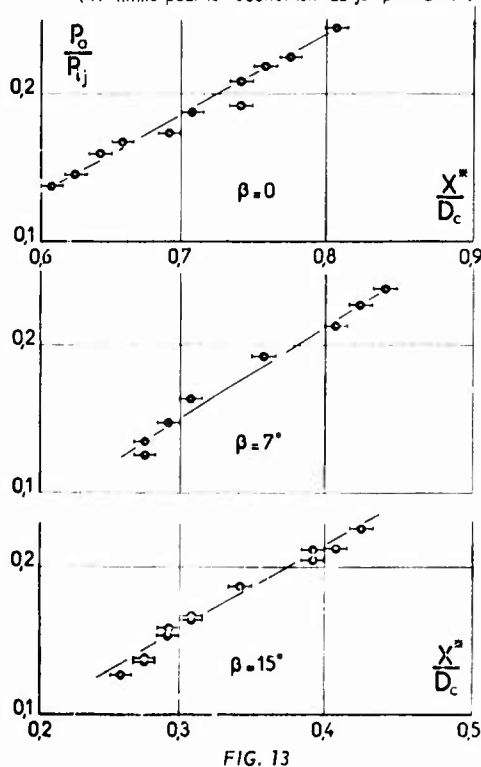
EFFET DE PERTURBATION SUR LA
PRESSION DE CAVITE

particulièr. à cet aspect des phénomènes ne doit pa. tre confondue avec celle qui correspond au cas des éjecteurs fortement raccourcis, où la tuyère est dite amorcée lorsque p_1 est indépendante de p_a pour des valeurs p_a/p_{ij} très faibles.

Les points portés figure 13 présentent une dispersion et une incertitude attribuables à la difficulté de déterminer avec précision et bonne reproductibilité un phénomène entaché d'hystérésis.

2.3 - Interprétation des résultats.-

Les phénomènes observés au cours de cette étude s'interprètent en grande partie, à partir de la notion de points critiques dont l'existence a été démontrée par des expériences antérieures effectuées à l'O.N.E.R.A. [1-2]. Soit $\bar{p}(x)$ la répartition pariétale de pression pour un recollement turbulent non perturbé, supposé plan afin de simplifier. Le recollement est perturbé en imposant au point Q, d'abscisse x_Q variable une pression p_a réglable. On constate alors l'existence de deux points particuliers K_1 et K_2 pour la position de Q (voir figure 14).

POINTS CRITIQUES K1 ET K2
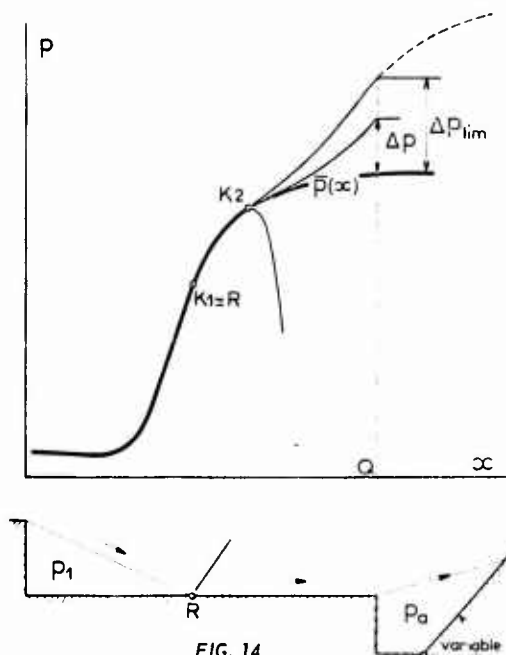
FIG. 14

a - Si Q est entre K_1 et K_2, la pression suit la courbe $\bar{p}(x)$ pour $x < x_Q$ pourvu que p_a soit ajustée à la valeur $\bar{p}(x_Q)$. Sinon la perturbation s'étend à toute la zone décollée.

b - Si Q est en aval de K_2, la distribution de pression est indépendante de p_a, à condition toutefois que p_a soit inférieure à un niveau maximal $p_{a\,lim} = \bar{p}(x) + \Delta p$; l'écart Δp tendant vers zéro quand Q s'approche de K_2. Ce résultat s'explique par le fait qu'une perturbation de pression positive se propage vers l'amont, selon un processus d'interaction visqueuse forte, sur une distance ℓ d'autant plus longue que Δp est plus grand. Tant que l'origine de l'interaction est en aval de K_2, le recollement est inchangé jusqu'en K_2. En revanche,

si cette origine remonte en amont de K_2, l'ensemble du phénomène est influencé en vertu de a). Dans le cas où Δp est négatif, les perturbations admissibles peuvent être beaucoup plus intenses. En effet, les détentes ont, surtout en turbulent, des longueurs d'interaction très courtes.

D'après ces considérations, le point K_2 jouit des propriétés du point critique prévu par les méthodes intégrales du type Crocco-Lees [3 - 4], alors que K_1 semble se confondre avec le point de recollement R.

Les présentes expériences confirment le fait que le recollement et en particulier la pression de cavité p_1, ne sont pas affectés par les conditions extérieures, à condition que la distance inter-tuyères X soit suffisante. Plus précisément, il est possible de déterminer une longueur limite X permettant de situer K_2 qu'il est plus significatif de repérer par rapport au point de recollement R. L'échelle du montage étant trop réduite pour que R puisse être localisé avec précision par visualisation au moyen d'un film pariétal, le point de recollement est ici placé à l'endroit où la pression locale égale la pression d'arrêt $p_{i\ell}$ sur la ligne limite du mélange turbulent isobare à p_1.

Cette approximation suppose que le recollement est un processus assez rapide pour que les effets visqueux soient négligeables entre la fin du mélange et R. La pression $p_{i\ell}$ a été calculée à partir de la théorie simplifiée de Korst [5] en tenant compte d'un effet de couche limite initiale, qui bien que très faible dans le cas présent, ne peut cependant être entièrement négligée. Le point K_2 est déterminé en notant la position à partir de laquelle p_1 s'écarte de l'évolution $\bar{p}_1(X)$ qui serait la sienne en l'absence de perturbation.

Lorsque p_a est inférieure aux pressions locales, on peut admettre que K_2 est confondu avec la lèvre B de la tuyère secondaire par suite de la très faible distance de remontée des détentes. Quand le recollement est perturbé en compression, K_2 est localisé à l'origine de la courbe d'interaction pour laquelle on note une déviation sensible de p_1.

Les distances RK_2 ainsi définies ont été d'abord normalisées par la longueur L de la frontière du jet supersonique non visqueux supposé isobare jusqu'à son impact avec la reprise (voir figure 15 a). En fait, l'épaisseur Δ_R de la portion subsonique de la couche dissipative au niveau du point de recollement semble être une échelle plus caractéristique du phénomène [6]. Δ_R s'écrit sous la forme :

$$\Delta_R = \frac{\Delta}{\delta}(M_R, H_{i_R})\,\delta_R$$

où δ_R est l'épaisseur totale de la zone dissipative en R et Δ/δ une fonction du nombre de Mach au recollement M_R et d'un paramètre de forme H_{i_R} caractérisant le profil de vitesse au recollement que nous supposerons invariant. Il est vraisemblable d'admettre que δ_R est proportionnelle à l'épaisseur de la zone de mélange isobare, ainsi :

$$\delta_R \propto \frac{L}{\sigma}$$

où σ est un paramètre de mélange fonction du nombre de Mach M_1 et de la géométrie. En écoulement de révolution :

$$\sigma = \frac{\sigma_{\bar{p}}}{F}$$

où F est un facteur géométrique d'expression :

$$F = \frac{\int_0^L Y \, dS}{L Y_R}$$

Y désignant la distance à l'axe et l'intégrale $\int_0^L Y \, dS$ étant calculée le long de la ligne de jet isobare.

Ainsi :

$$\Delta_R \, \infty \, \Delta_R^* = \left(\frac{\Delta}{\delta}\right)_R \frac{L F}{\sigma_{\bar{p}}} \, .$$

On constate, figure 15 b, que $\overline{RK_2}/\Delta_R^*$ demeure sensiblement constant et voisin de 10 pour des configurations variées (écoulements plan et de révolution) et des nombres de Mach M_1 différents.

POSITION DU POINT CRITIQUE K₂
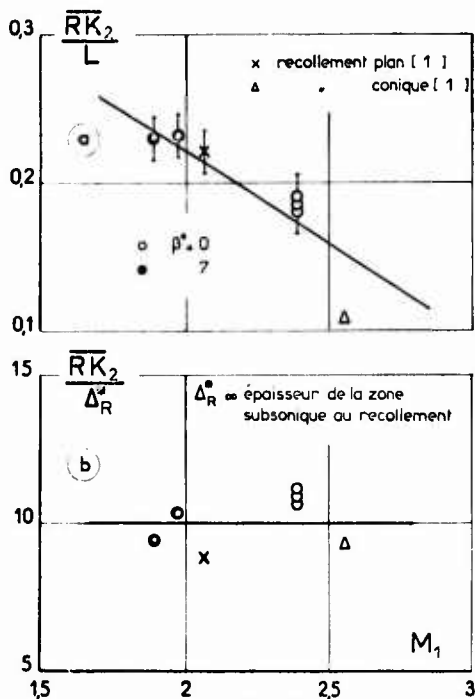
FIG. 15

Etudions à présent l'effet de la perturbation créé par $\bar{p}_a$ sur la pression de cavité $\bar{p}_1$. L'examen des figures 11 et 12 met en évidence les faits suivants :

- quand la pression $\bar{p}_a$ est inférieure aux valeurs locales de la répartition de base $\bar{p}(x)$ dans le voisinage du recollement, $\bar{p}_1$ devient inférieure au niveau non perturbé $\bar{p}_1$. Si l'interaction en détente est très forte, $\bar{p}_1$ devient indépendante de $\bar{p}_a$ (ce phénomène est surtout apparent figure 12). Tout se passe alors comme si $\bar{p}_1$ n'était fonction que de la distance X , le recollement se modifiant de façon telle que R soit à une distance bien déterminée du bord de fuite B. Un tel régime où $\bar{p}_a$ est sans effet sur $\bar{p}_1$ et donc sur l'écoulement dans la tuyère est appelé, par convention, fonctionnement en éjecteur court amorcé et se prête au calcul selon une méthode

exposée § 3. Par commodité, le point R dont la localisation n'est possible que si on connait la répartition de pression au recollement est alors remplacé par le point d'impact de la ligne isobare qui elle peut être déterminée en fonction de $\bar{p}_1$ seule (voir la corrélation donnée figure 19).

- pour les détentes moins intenses ainsi que pour les compressions on note une dépendance de $\bar{p}_1$ à la fois à l'égard de X et de $\bar{p}_a$ (voir figure 11). Dans de tels cas il n'existe pas encore de méthodes de calcul permettant de prédire ce double effet.

Précisons maintenant les circonstances dans lesquelles survient ce que nous appelons ici le désamorçage, c'est-à-dire l'instant où le jet ne peut plus recoller sur la tuyère secondaire. La figure 16a donne les valeurs $\bar{p}_1^*$ de la pression de cavité $\bar{p}_1$ immédiatement avant le désamorçage sous forme de l'écart relatif $(\bar{p}_1^* - \bar{p}_1)/\bar{p}_1$ fonction de $(\bar{p}_a - \bar{p}_R)/\bar{p}_R$ où $\bar{p}_R$ est la pression au point de recollement pour la configuration non perturbée (nous avons adopté ici $\bar{p}_R$ car c'est une grandeur $\bar{p}_R = \bar{p}_{il}$ directement accessible à partir de $\bar{p}_1$, quantité également calculable).

CONDITIONS AU DESAMORÇAGE
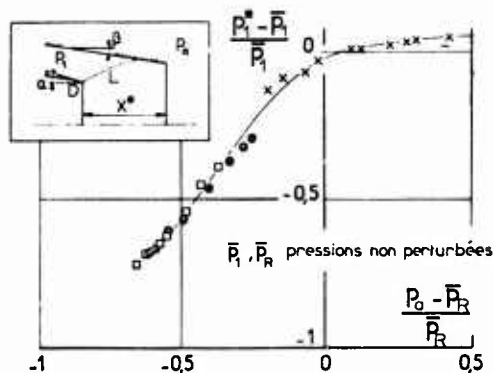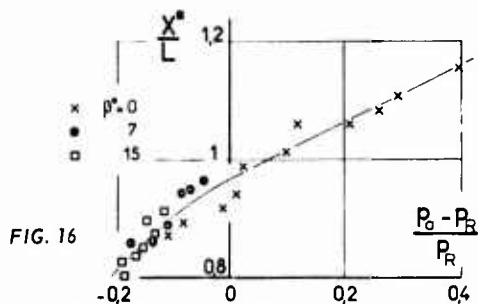
FIG. 16

On notera :

- lorsque $\bar{p}_a$ est inférieure à $\bar{p}_R$, le désamorçage peut être précédé par une très forte interaction en détente de $\bar{p}_1$,

- pour les valeurs de $\bar{p}_a$ supérieure à $\bar{p}_R$, le désamorçage se produit brutalement sans que $\bar{p}_1$ soit auparavant interactionné en compression de façon sensible.

Figure 16b sont portées les profondeurs X^* (normalisées par la longueur L) pour lesquelles le désamorçage se produit. Ce renseignement peut être directement utilisé dans la pratique.

Enfin, la figure 17 montre l'évolution de la distance réduite $\overline{RB}/L$ séparant le point de recollement du bord de fuite en fonction du rapport p_a/p_R . Quand p_a/p_R est inférieur à l'unité (interaction en détente), la longueur $\overline{RB}$ devient très courte; en revanche, pour les compressions $(p_a/p_R > 1)$, le désamorçage survient lorsque la perturbation est appliquée à une distance en aval de R d'autant plus grande que $\frac{p_a}{p_R}$ s'éloigne de 1.

DISTANCE D'INTERACTION AU DESAMORCAGE
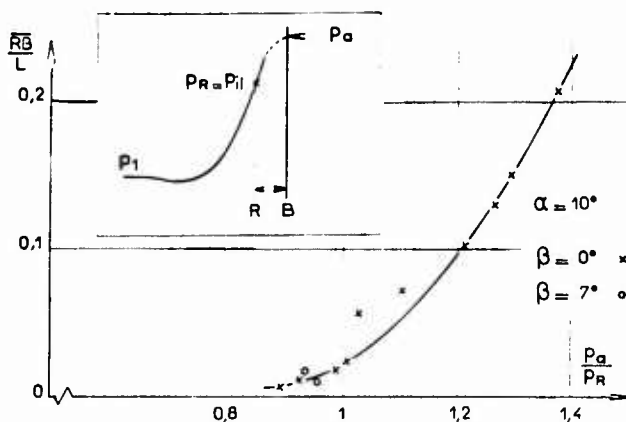
FIG. 17

3 - METHODES PRATIQUES DE CALCUL.-

Le but recherché est la détermination de la répartition de pression et de frottement sur la tuyère secondaire afin d'en déduire la poussée de l'éjecteur. Il s'agit de calculer :

- la pression de cavité p_1 en fonction de la géométrie de la tuyère et du débit secondaire q_s , compte tenu des caractéristiques du jet primaire (débit q_j , conditions génératrices p_{ij} , T_{ij} , richesse du mélange carburé si le jet est chaud),

- la recompression accompagnant le recollement puis la détente éventuelle en aval de ce dernier,

- le frottement sur la reprise,

- l'interaction en compression traduisant une remontée possible de la pression ambiante p_a dans la couche limite recollée.

3.1 - Cas de l'éjecteur long.-

L'interprétation des expériences du paragraphe précédent conduit à définir ce fonctionnement par la condition que les perturbations résultant des conditions extérieures ne remontent pas en amont du point critique K_2 .

Dans ce type de régime, la méthode la plus satisfaisante pour évaluer la pression de cavité p_1 est basée sur le concept de loi angulaire de recollement [7 - 8]. Les bases de ce calcul sont exposées de façon détaillée en Annexe. Une fois p_1 connue, la répartition de pression sur la tuyère secondaire est déterminée en combinant les effets visqueux et non visqueux (voir figure 18).

CALCUL DE LA REPARTITION DE PRESSION INTERNE SUR LA TUYERE SECONDAIRE
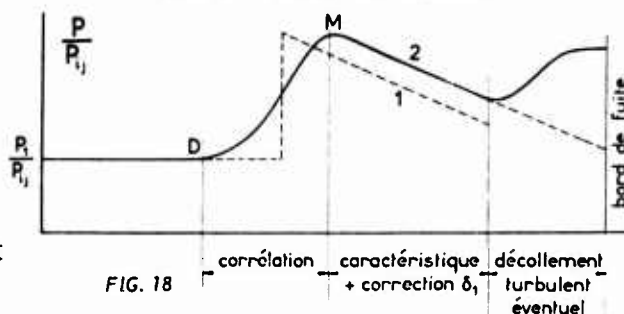
FIG. 18

- la recompression DM est mise en place à l'aide de corrélations expérimentales [9] qui permettent, en particulier, de situer les points D et M et d'évaluer le coefficient de pression
$$K_{p_M} = (p_M - p_1)/q_1$$
- la détente subséquente est calculée par la méthode des caractéristiques (courbe 1). Si une correction consistant à déplacer la paroi d'une distance égale à l'épaisseur de déplacement δ^* après recollement est effectuée, on obtient la courbe 2 qui est ensuite raccordée à la recompression.

L'expérience montre qu'une diminution du taux de détente p_{ij}/p_a peut entraîner une remontée de pression près du bord de fuite et même un décollement qui, s'il atteint le point critique K_2 , provoque le désamorçage de la tuyère.

Le décollement peut être prévu à partir de lois de similitude [10] qui permettent d'établir un critère de décollement naissant et de calculer la compression liée au décollement.

Le calcul du frottement sur la tuyère secondaire est basé sur la relation de Ludwieg et Tillman qui donne le coefficient de frottement incompressible C_{f_i} en fonction du paramètre de forme H_i et du nombre de Reynolds calculé avec l'épaisseur de quantité de mouvement θ . Le C_f compressible est ensuite déduit de la formule :
$$C_f = C_{f_i} (1 + 0,144 \, M_e^2)^{-0,578} .$$

Il s'agit donc de déterminer les évolutions de H_i et de θ , d'abord pour la fraction du mélange située au dessus de la ligne limite puis pour la couche limite en aval du recollement. Pour cela on procède de la façon suivante :

- les effets de la détente sur la couche limite initiale et de la compression sur le mélange (lors du recollement) sont calculés par la méthode de Reshotko et Tucker [11] ,

- entre les deux, la structure de la couche de mélange isobare est définie par la méthode de Kubota et Dewey [12] ,

- dans la recompression en aval du recollement H_i est évalué selon une technique proposée par Mc. Donald [13] ,

- plus en aval enfin, θ est calculé à partir de l'équation intégrale de Von Kàrmàn où H_i est supposé constant.

Pour la tuyère primaire seule, la poussée brute conventionnelle à la pression p_a est (si l'écoulement au col est supposé uniforme et la couche limite négligée) :

$$F_j = q_j \, V_j + (p_j - p_a) \, A_c \ .$$

La poussée globale conventionnelle F_{ej} au point fixe s'obtient en retranchant à la poussée interne de la tuyère primaire la traînée de culot définie par :

$$T_c = \int_1^3 (p_a - p) \, dA + \int_2^3 \tau \, dS - q_s \, V_s$$

où A = section droite,

S = surface mouillée de la reprise,

τ = tension de frottement (en fait intégrée seulement en aval du recollement).

En raison des faibles débits secondaires et des grandes sections de passage $(V_s \simeq 0)$, $q_s \, V_s$ est négligé.

Afin de se comparer aux résultats existants (notamment ceux publiés par le NACA), nous calculons à partir de F_{ej} et F_j le coefficient :

$$C_T = \frac{\text{poussée globale de l'éjecteur}}{\text{poussée de la tuyère primaire seule}} = 1 - \frac{T_c}{F_j}$$

3.2 - Cas de l'éjecteur court.-

Ainsi que l'a montré l'étude expérimentale qui précède lorsque la tuyère secondaire est raccourcie, le recollement du jet primaire est influencé par les conditions extérieures. Cet effet se fait sentir, rappelons le quand l'origine de la perturbation atteint un point critique K_2 lié au recollement non perturbé, qui se produirait sur une paroi prolongée indéfiniment.

Dans ces circonstances, la pression de cavité p_1 est, en règle générale à la fois fonction de l'intensité de la perturbation (mesurée par p_1/p_R , par exemple) et de son point d'application relativement au recollement, c'est-à-dire de X .

Toutefois, on a observé que pour une perturbation en détente suffisamment forte $(p_a \ll p_R)$, p_1 devenait pratiquement indépendante de p_a , la distance X étant le seul paramètre d'influence. On a alors défini un régime d'éjecteur court amorcé en ce sens que l'écoulement dans la tuyère ne dépendait plus des conditions aval. La méthode de calcul qui va maintenant être exposée ne s'applique qu'à ce type de fonctionnement. Le processus adopté, largement empirique, est le suivant :

a - on détermine d'abord le point de fonctionnement A de l'éjecteur long de la famille considérée dans le cas où la couche limite initiale et le débit secondaire sont nuls. Pour faire ce calcul il est donc supposé que la tuyère secondaire se prolonge indéfiniment.

b - le point de recollement R étant, pour des raisons de commodité, confondu avec le point d'impact de la ligne de jet isobare, le point critique K_2 est mis en place. Pour cela on utilise plutôt la corrélation donnée figure 19 qui permet de déterminer la configuration limite pour laquelle K_2 est au bord de fuite B . Si, dans le cas traité, le point de coordonnées M_1 et $\overline{RB}\,F/L$ est au dessus de la courbe "éjecteur limite", on a affaire à un éjecteur "long", sinon l'éjecteur est "court". L'application de la loi angulaire de recollement doit alors être modifiée comme suit.

c - l'exploitation de diverses expériences a montré que l'angle de référence $\overline{\psi}$ augmente beaucoup plus vite avec M_1 dans le cas d'un recollement singulier tel que celui qui se produit pour un éjecteur court (voir figure 20). En outre, il a été constaté que l'écart $\Delta\overline{\psi}$ dû au raccourcissement de la paroi est très sensiblement égal à l'angle $\Delta\varphi$ (voir figure 21) que font les directions $\overline{OK_2}$ et $\overline{OB}$, K_2 étant le point critique pour le recollement non perturbé qui se produirait sur une paroi suffisamment longue. Ainsi qu'on le constate figures 22 et 23, cette loi empirique permet de retrouver, avec une bonne approximation les résultats relatifs à des éjecteurs courts non ventilés $(q_s = 0)$.

EVOLUTION DE LA DISTANCE CRITIQUE REDUITE AVEC LE MACH

EJECTEURS SANS VENTILATION, LIMITES OU COURTS

FIG. 19
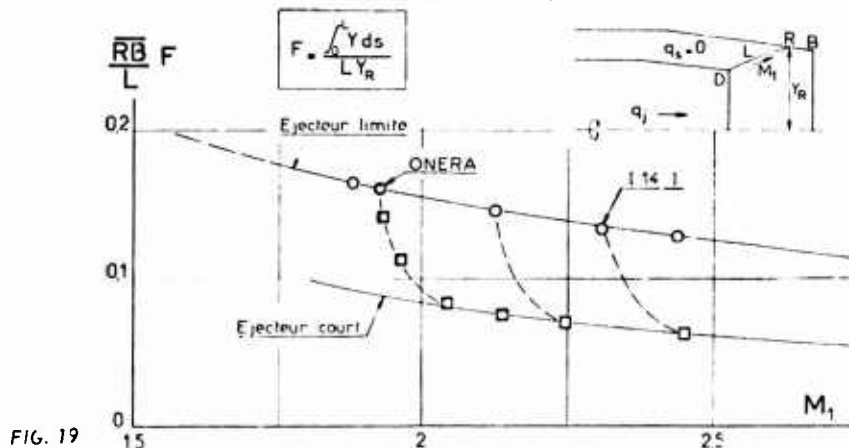
ANGLE DE RECOLLEMENT POUR DES EJECTEURS CYLINDRIQUES LONGS OU COURTS

FIG. 20
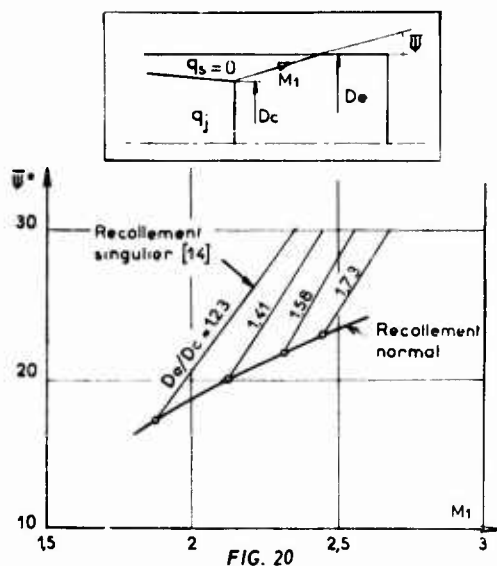
CORRECTION DU CRITERE ANGULAIRE POUR UN EJECTEUR COURT

FIG. 21
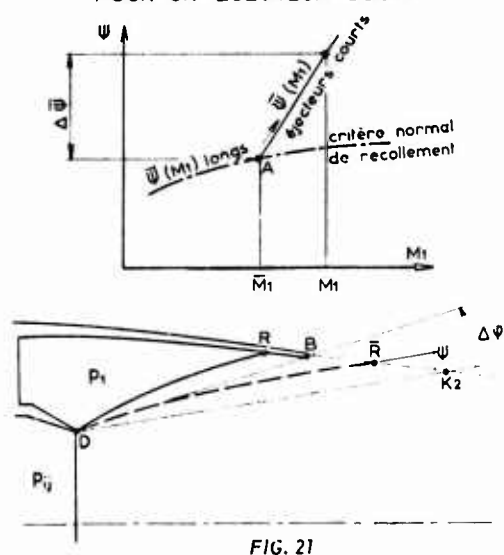
VALIDITE DU CRITERE ANGULAIRE DE RECOLLEMENT SINGULIER POUR EJECTEURS COURTS
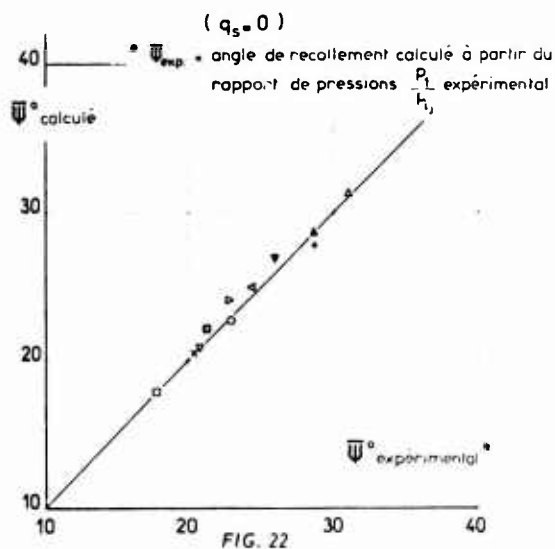
($q_s = 0$)

$\overline{\psi}°_{exp}$ = angle de recollement calculé à partir du rapport de pressions $\frac{P_1}{P_{ij}}$ expérimental

FIG. 22

PRESSION DE CAVITE EN FONCTION DE LA DISTANCE ENTRE COLS

FIG. 23a

PRESSION DE CAVITE EN FONCTION DE LA DISTANCE ENTRE COLS

FIG. 23b
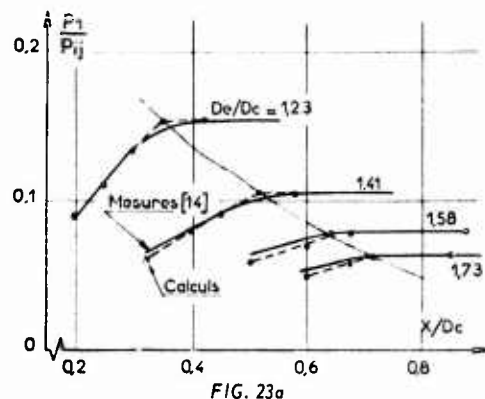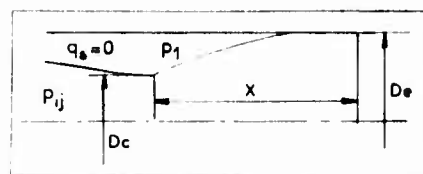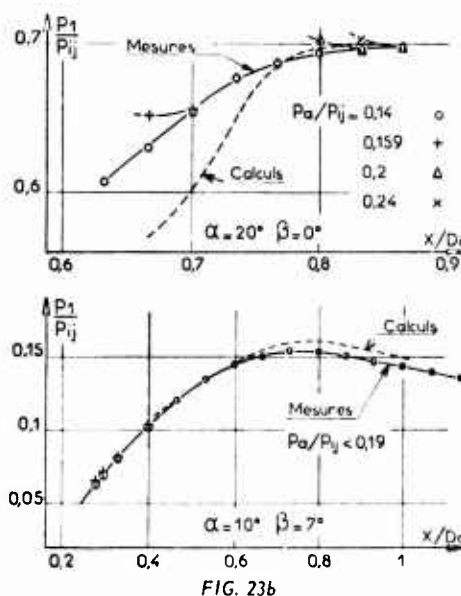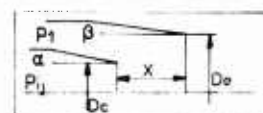
d — si le débit secondaire q_s n'est pas nul. un écart $\Delta \psi (q_s)$ est d'abord calculé en procédant comme indiqué en a – b – c $\Delta \psi (q_s = 0)$, ayant été préalablement déterminé , on applique la correction finale :

$$\Delta \psi = \Delta \psi (q_s) - \Delta \psi (q_s = 0) .$$

Les calculs sont comparés à l'expérience figures 24 et 25. La figure 24 montre des évolutions de la pression de cavité p_1 en fonction du taux d'injection secondaire q_s / q_j .

PRESSION DE CAVITE D'EJECTEURS AMORCES
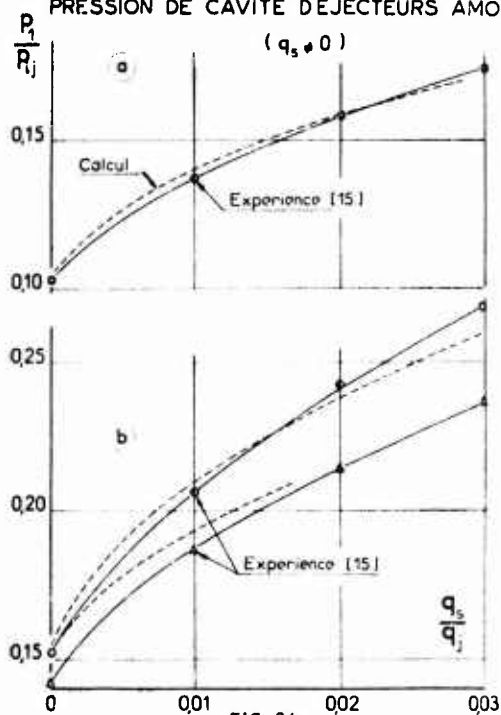
$(q_s \neq 0)$

FIG. 24a

PRESSION DE CAVITE D'EJECTEURS AMORCES

$(q_s \neq 0)$

FIG. 24b

PRESSION DE CAVITE D'EJECTEURS AMORCES

$(q_s \neq 0)$

à $\frac{P_1}{P_{ij}} > 0.25$ le recollement est transsonique

FIG. 24c
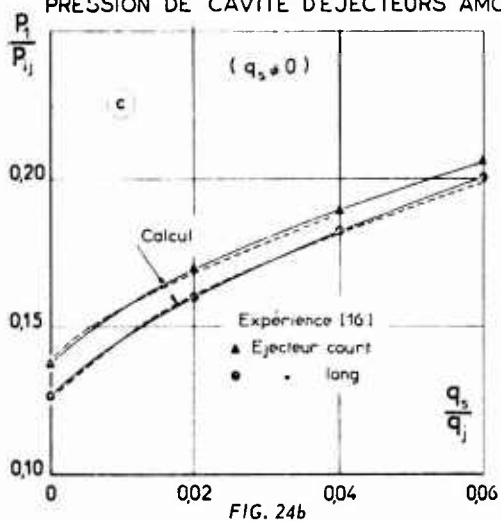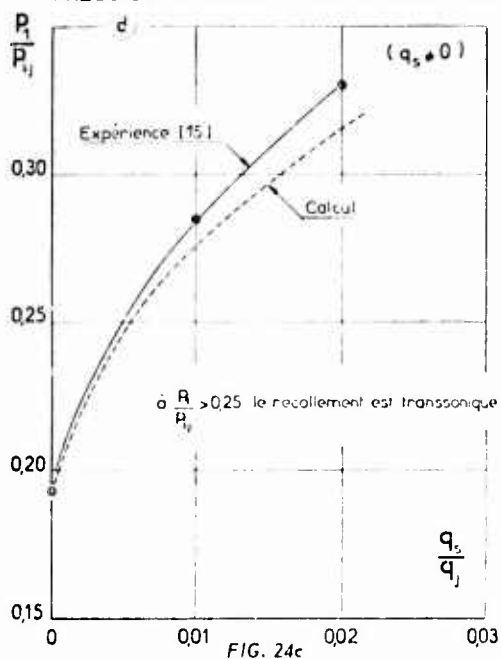
On constate que la concordance des résultats est dans l'ensemble satisfaisante. Des écarts importants n'existent que pour l'exemple d où le recollement devient transsonique. Ils s'expliquent par le fait que la loi de recollement utilisée n'est valable que si l'écoulement demeure entièrement supersonique. Les prédictions du coefficient de poussée C_T sont également très bonnes. Il est à noter que les mesures, tirées d'essais assez anciens ne sont pas très précises. Les calculs ont montré que le frottement sur la tuyère secondaire est pratiquement négligeable (inférieur à 0,3%) de la poussée primaire même pour les éjecteurs longs.

COEFFICIENT DE POUSSEE
EN FONCTION DE LA VENTILATION

FIG. 25a

COEFFICIENT DE POUSSEE
EN FONCTION DE LA VENTILATION

FIG. 25b
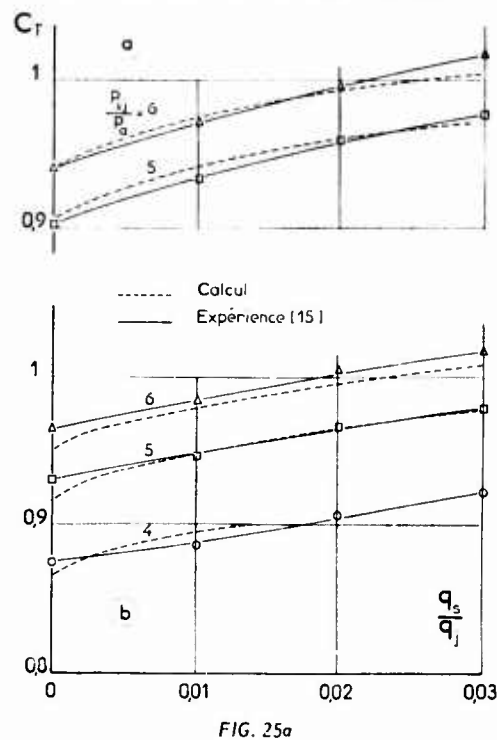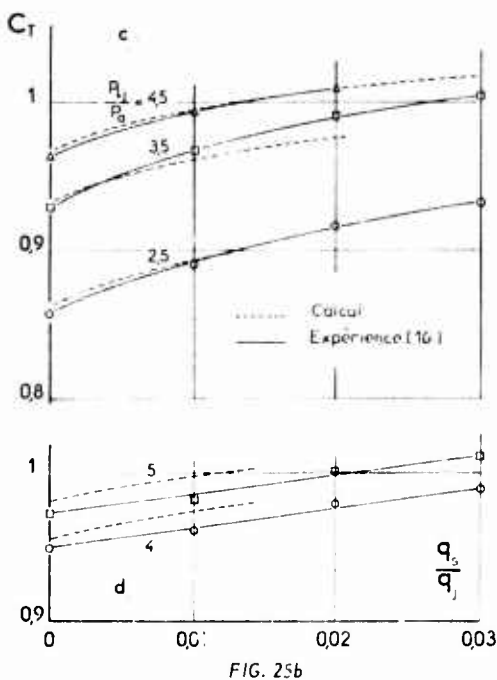
4 - CONCLUSION.-

La première partie, de nature expérimentale, a permis de préciser l'effet d'une pression extérieure p_a variable lorsqu'on diminue la distance X séparant le plan de sortie de l'injecteur primaire de l'extrémité B de la tuyère. Elle a mis en évidence les faits suivants :

- si la perturbation créée par p_a est en aval d'un point critique K_2 , le recollement du jet primaire, (en particulier la pression de cavité p_1), n'est pas influencé par p_a . Une corrélation est proposée qui permet de situer K_2 par rapport au point de recollement R .

- si la perturbation remonte en amont de K_2, le recollement se trouve modifié et en règle générale p_1 est à la fois fonction de X et de p_a . Toutefois si p_a est très inférieure à la pression en R , p_1 devient indépendante de p_a et donc ne dépend plus, en première approximation, que de la distance X . On peut ainsi définir un régime de fonctionnement en éjecteur court amorcé.

- enfin, il existe une distance X minimale, d'autant plus courte que p_a est plus faible, en deçà de laquelle le jet primaire ne peut plus recoller sur la paroi de reprise secondaire.

Dans la seconde partie, sont proposées des méthodes de calcul qui permettent de prédire les performances de la tuyère en régime amorcé (éjecteur long ou court).

Les résultats obtenus se comparent favorablement à l'expérience.

Les essais et les calculs montrent qu'un éjecteur à paroi secondaire convergente peut faire gagner de la poussée, à condition de limiter suffisamment l'expansion du jet primaire pour que la pression de cavité soit supérieure à la pression ambiante au taux de détente imposé.

Comme d'autre part, l'amorçage entraîne une perte de poussée plus faible sur un éjecteur court que sur un éjecteur long, on conçoit l'intérêt de ce type de tuyères, puisqu'il semble que l'on puisse en tirer une bonne efficacité de propulsion au prix d'une mécanique assez simple et d'un poids raisonnable.

ANNEXE

METHODE DE CALCUL DE LA PRESSION DE CAVITE.-
(cas de l'éjecteur long).

La détermination de la pression de cavité p_1 utilise une loi angulaire de recollement appliquée d'abord au cas plan.

Les expériences systématiques faites à l'ONERA ont fourni les renseignements empiriques permettant d'étendre cette méthode aux configurations axisymétriques.

Sous sa forme linéarisée, la loi de recollement s'écrit :

$$(A-1) \quad \psi = \overline{\psi}(M_1, \gamma) + \frac{\partial \psi}{\partial C_q}(M_1, \gamma) \, C_q$$

où :

- ψ est l'angle d'impact sur la paroi de la frontière du jet non visqueux isobare à la pression p_1 (voir figure 26),

- $\overline{\psi}$ est l'angle de recollement dans les conditions de référence, c'est-à-dire en l'absence de couche limite initiale et d'injection de masse dans la cavité ($q_s = 0$),

- C_q est un coefficient de débit généralisé qui regroupe les effets d'injection, de quantité de mouvement et de couche limite initiale. Il s'écrit :

$$(A-2) \quad C_q = \frac{q_s \left(1 - \frac{V_s}{u_1}\right)}{\rho_1 u_1 L} + \frac{\theta}{L + x_0}$$

où x_0 est un décalage d'origine qui permet de tenir compte de l'influence de la couche limite sur le mélange turbulent isobare.

CRITERE ANGULAIRE DE RECOLLEMENT EN ECOULEMENT TURBULENT DE REVOLUTION

FIG. 26
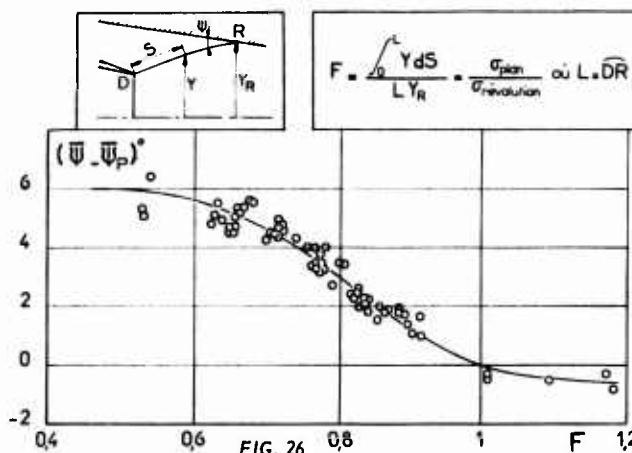
En écoulement de révolution, l'angle de recollement de référence se met sous la forme :

$$\overline{\psi} = \overline{\psi}_P (M_1, \gamma) + \Delta \overline{\psi} (F)$$

où $\overline{\psi}_P$ est l'angle de recollement en écoulement plan et $\Delta \overline{\psi}$ l'écart dû à l'effet de révolution qui est exprimé par le facteur géométrique F :

$$F = \frac{\int_0^L Y \, dS}{L \, Y_R}$$

F n'est autre que le rapport des coefficients de mélange σ en écoulements plan et axisymétrique.

Quant à la dérivée $\partial \psi / \partial C_q$, l'expérience a montré que la loi $\partial \psi / \partial C_q (M_1)$ tirée du critère de Korst [17] était satisfaisante.

Le calcul de la pression de cavité p_1 pour un débit secondaire q_s donné se fait par une méthode inverse en tâtonnant sur p_1/p_{ij} . Pour chaque rapport p_1/p_{ij} la ligne de jet isobare est déterminée par la méthode des caractéristiques à partir de données initiales fournies par le calcul ou l'expérience pour une série de convergents tronconiques [9] . Connaissant ψ, F et M_1, la loi fondamentale (A-1) donne C_q puis (A-2) le débit injecté q_s .

Le calcul est arrêté quand le recollement disparaît, c'est-à-dire lorsque C_q devient supérieur à la valeur pour laquelle la ligne limite est rejetée à l'infini.

REFERENCES

1   Sirieix M, Mirande J. et Délery J.

     "Expériences fondamentales sur le recollement
     turbulent d'un jet supersonique"
     Agard CP N° 4 (1966).

2   Carrière P.

     "Aperçu de quelques résultats nouveaux
     obtenus à l'ONERA sur les phénomènes de
     décollement et de recollement"
     Gamm – Tagung Ljubljana 1972 – Zamm 53 –
     T3 – T14 (1973).

3   Crocco L. et Lees L.

     "A mixing theory for the interaction between
     dissipative flows and nearly isentropic
     streams", JAS, Vol. 19 N° 10 (1952).

4   Lees L. et Reeves B.L.
     "Supersonic separated and reattaching laminar
     flows-1-general theory and application to
     adiabatic boundary layer – shock wave
     interactions". AIAA Journal, Vol. 2 N° 11
     (1964).

5   Korst H.H., Page R.H. et Childs M.E.

     "Compressible two-dimensional jet mixing at
     constant pressure". University of Illinois,
     ME-TN-392-1 (1954).

6   Suggestion de J. Mirande.

7   Carrière P. et Sirieix M.

     "Facteurs d'influence du recollement d'un
     écoulement supersonique". 10ème Congrès
     International de Mécanique Appliquée,
     Stresa, Italie (1960).

8   Carrière P.

     "Recherches récentes effectuées à l'ONERA
     sur les problèmes de recollement"
     7ème Symposium de Mécanique des Fluides,
     Jurata, Pologne (1965).

9   Solignac J.L. et Délery J.

     "Contribution à l'étude aérodynamique des
     systèmes propulsifs à double flux".
     Israel Journal of Technology, Vol. 10,
     N° 1 – 2, p. 97 – 111 (1972).

10   Carrière P., Sirieix M. et Solignac J.L.

     "Propriétés de similitude des phénomènes de
     décollement laminaire ou turbulent en
     écoulement supersonique non uniforme"
     12ème Congrès International de Mécanique
     Appliquée, Université de Stanford (1968).

11   Reshotko E. et Tucker M.

     "Effect of a discontinuity on turbulent
     boundary layer thickness parameters with
     application to shock induced separation".
     NACA TN 3454 (1955).

12   Kubota T. et Dewey C.F. Jr.

     "Momentum integral methods for the laminar
     free shear layer". AIAA Journal, Vol. 2,
     N° 4 (1964).

13   Mc Donald H.

     "Turbulent shear-layer reattachment with
     special emphasis on the base pressure
     problem" B.A.C. (1963).

14   Glotov G.F. et Moroz E.K.

     "Etude expérimentale du recollement d'un
     écoulement supersonique turbulent" (1969).

15   Greathouse et Hollister

     "Air flow and thrust characteristics of
     several cylindrical cooling air ejectors
     with a primary to secondary temperature
     ratio of 1.0 ". NACA RM E52L24 (1953).

16   Greathouse et Hollister

     "Preliminary air flow and thrust calibra-
     tions of several conical cooling air
     ejectors with a primary to secondary
     temperature ratio of 1.0". NACA RM E52E21
     et E52F26 (1952).

17   Korst H.H., Page R.H. et Childs M.E.

     "A theory for base pressure in transsonic
     and supersonic flow". University of
     Illinois, ME TN 392-2 (1955).

SUBSONIC BASE AND BOATTAIL DRAG: AN ANALYTICAL APPROACH

J. K. Quermann
Vought Systems Division
LTV Aerospace Corporation
Dallas, Texas 75222

SUMMARY

Methods of subsonic potential flow have been applied to the calculation of base and boattail drag. For configurations with a base the Korst method has been extended to subsonic flow by incorporating a standard family of free streamline shapes and a semi empirical scheme for selecting the total pressure on the dividing streamline. The potential flow around the shape defined by the body, free streamline, and jet establishes the base and boattail pressures. Significant parts of the drag associated with the base actually appear on the boattail. In the absence of a base the effect of the jet shape is felt by the boattail. With an underexpanded supersonic jet a portion of the thrust which would otherwise be lost in external expansion is recovered on the boattail. The fraction recovered drops rapidly with increasing jet pressure ratio.

Results are compared with flight and wind tunnel tests on the Vought A-7 Airplane.

NOTATION

A_n C_p at point n when C_{L_t} and C_{p_b} are zero, see equation 8

B_n $\dfrac{\partial C_{p_n}}{\partial C_{p_b}}$ see equation 8

C_n $\dfrac{\partial C_{p_n}}{\partial C_{L_t}}$ see equation 8

C_D drag coefficient $\dfrac{D}{1/2\rho V^2 S}$

C_{L_t} tail lift coefficient

C_p pressure coefficient $\dfrac{P - P_\infty}{1/2\rho V^2}$

C_{p_B} base pressure coefficient

D drag

L fuselage length

M Mach number

N parameter relating the total pressure on the dividing streamline to base pressure and a static pressure, see equations 4 and 5

N' parameter relating the total pressure on the dividing streamline, the base pressure and the total pressure of the least energetic of the two flows, see equation 6

P_∞ free stream static pressure

P_B base static pressure

P_{div} total pressure on dividing streamline

P_o total pressure

P_{shock} static pressure downstream of closure shock

R gas constant

r radius of the body

V velocity of free stream

X distance along free streamline starting from the separation point; also axial distance from the nose.

Y distance normal to the free streamline

γ ratio of specific heats

ρ density slugs/cu. ft.

σ a factor which defines the rate at which a mixing layer grows, see equation 2

ω angle between intersecting flows at closure, degrees

1. INTRODUCTION

The interaction between the external flow around an airplane and a propulsive jet represents a potentially large contribution to thrust minus drag. While it is possible to design away some of the problems for specific flight conditions (by using a shallow boattail and a fully expanded converging-diverging nozzle, for example) conflicting requirements make it difficult to do so over the entire range of flight conditions. In particular, the nozzle exit diameter is usually relatively small at subsonic speeds. This plus other limitations often leads to a steep boattail angle with a large aft facing area or to blunt base. The drag at subsonic speeds remains important because of the time spent in cruise and loiter.

At Vought Systems Division of LTV Aerospace, a three pronged attack is being made on the problem. Included are analytical studies, flight test and wind tunnel tests with hot and cold jets. Because of the difficulties involved in measuring the interaction in both flight test and in the wind tunnel we are seeking an analytical approach which will predict the effect of the major design parameters.

The well known methods of subsonic potential flow theory are applied to the interaction problem for axisymmetric flow. Two basic configurations are considered: (1) Configuration with no base and no separation. Here the effect of increasing jet pressure ratio is to increase the boattail pressures, thus recovering some thrust which would otherwise be lost in external expansion. At the same time, adverse pressure gradients are made worse, leading to possible separation. (2) Configurations with a finite base. Here the problem is to determine the base pressure and the associated boattail pressures. The results are compared with flight test and wind tunnel tests of the A-7 airplane.

2. APPROACH

The general approach is to consider the potential flow around a shape which is made up of the fuselage proper, a free streamline bounding the separated flow at the base (if any) and the interface between the jet and the external flow. The jet plays a role in establishing the shape of the boundary, but once the boundary is established it is the external flow which fixes the details of the pressure distribution.

The specific approach is to use procedures which have been well established in other applications and to add the necessary modifications and additional assumptions necessary to fit the present problem. Approximations are used where appropriate to speed the process or where a more exact method is not yet available. Figure 1 summarizes the source of the methods used for the configuration with a base.

```
┌─────────────────┐      ┌─────────────────┐      ┌─────────────────┐
│     KORST       │      │    SUBSONIC     │      │      NEW        │
│ SUPERSONIC BASE │      │   POTENTIAL     │      │   CONCEPTS      │
│    PRESSURE     │      │     FLOW        │      │                 │
└─────────────────┘      └─────────────────┘      └─────────────────┘

● BASIC APPROACH         ● EXTERNAL PRESSURE       ● SHAPE OF FREE
● JET SHAPE                DISTRIBUTION              STREAMLINE
● MIXING VELOCITY                                  ● CLOSURE CONDITION
  PROFILES

                         ┌─────────────────┐
                         │  SUBSONIC BASE  │
                         │  AND BOATTAIL   │
                         │    PRESSURE     │
                         └─────────────────┘
```
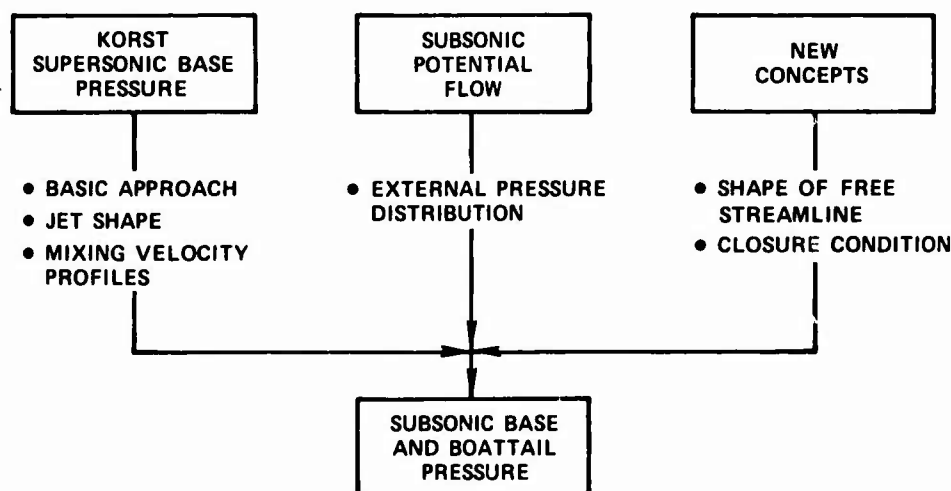
Figure 1. Summary of the Approach

From our version of Korst method for supersonic flow comes: the basic approach of obtaining equilibrium in the mass and energy flowing into and out of the separated region; the shape of the jet plume as a function of jet pressure ratio, ratio of specific heats, γ, and gas constant, R; the shape of the velocity profile in the mixing layers along the boundaries of the separated region and the rate at which these layers grow with distance. From a potential flow program of the type developed by Smith and Hess comes the external pressure distribution. To weld these components into a method for computing the base pressure we add a family of curves which represent the shape of the free streamline as a function of the base pressure and a closure condition which leads to the selection of the total pressure on the dividing streamline as a function of the geometry and state of the two fluids where they come together. For the present, a largely empirical relation is used.

To study the effect of the external expansion of the jet when there is no base we develop an effective jet shape which will have essentially the same effect on the boattail as a more precise jet which contains a series of oscillations.

The various components are discussed in the following paragraphs.

3. THE POTENTIAL FLOW SOLUTION

The potential flow is calculated by a program similar to that described by Smith and Pierce in reference 1. The principal difference is in the method of describing the surface and the distribution of source and sink strength on the surface. Reference 1 divides the body into a series of frustums of a cone each with a constant source strength over the entire surface. Boundary conditions are met at the center of each frustum. In the present solution the surface and the source strength distribution are considered continuous except where there are kinks in the slope of the body. Suck a kink will occur at the base where the boattail intersects a cylindrical sting or a propulsive jet. At the kinks the source strength is discontinuous. The boundary conditions are met at a discrete number of points, 101 in this study. Drag is computed using the equation:

$$C_D = \int_{r_b}^{r_{max}} C_p \; d(\frac{r}{r_{max}})^2 \qquad (1)$$

Because the calculation of drag by integrating the pressure distribution results in a small difference between large numbers, the method has been carefully checked for accuracy. In potential flow it can be shown that the drag of a body with a constant diameter sting is always zero. Such a body is ideal for checking the method since it retains the troublesome kink. Based on the frontal area, the RMS value of C_D for eight configurations was .0009. The largest absolute value was -.002. There is some systematic error which suggests that a significant part of this small error is associated with the pressures near the kink. These results are accurate enough for this study.

3.1 Compressibility Correction

The potential flow solution applies to incompressible flow. A modification of the Goethert compressibility correction is used to extend the results to other Mach numbers. In general compressibility corrections are considered applicable as long as the local Mach numbers remain subsonic. However, because of the stringent requirements for drag calculations the applicability has been checked.

Following the derivation of the Goethert correction in reference 2, the procedure may be summarized as follows:

1) Compute the incompressible flow on a body which has been stretched by the factor $\frac{1}{\sqrt{1-M^2}}$

2) Convert the local velocity ratio $\frac{V}{V_\infty}$ to components along and normal to the freestream direction.

3) Multiply the normal component by $\frac{1}{\sqrt{1-M^2}} = \sqrt{F}$

4) Multiply the difference between the parallel component and freestream velocity by $\frac{1}{1-M^2} = F$

5) Combine the parallel and normal components to find the resultant velocity ratio for compressible flow.

6) Use the Bernoulli equation to obtain the pressure coefficient.

Numerically, this procedure fails in step 4 when V/V_∞ is small. This is not unexpected, since the Goethert correction is derived for slender bodies. To improve the correction for small V/V_∞ and to prevent failure during a computer run an arbitrary modification has been added to the Goethert correction. To make the stagnation pressure correct for all Mach numbers the multiplying factor in steps 4 and 5 should be 1.0. The Goethert correction is considered correct when the local velocity is equal to the freestream velocity. To provide a continuous variation between these points, a straight line variation of the multiplying factor F used in steps 4 and 5 is assumed, see Figure 2.

When the modified correction is applied to a fuselage with a cylindrical sting the drag will not remain zero. Most of the deviation is caused by the pressures near the stagnation point at the nose. The variation of pressure with Mach number on the boattail is relatively well behaved. Figure 3 shows the compressibility correction for a typical case. The details will vary slightly with the configuration. Each curve represents the variation at a fixed location. Note that as one approaches the base (the more positive pressures) the variation approaches that expected for two-dimensional flow where:

$$C_p = C_{p_{M=0}} \frac{1}{\sqrt{1-M^2}}$$

The fact that the annular flow acts nearly two dimensionally is seen again in the steep adverse pressure gradients near the base, figure 17, and should be kept in mind when appraising steep boattail angles.
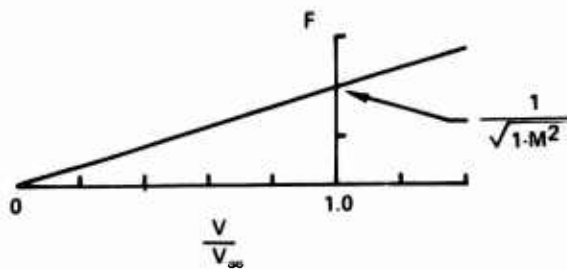
Figure 2. Modification of the Compressibility Correction

Figure 3. Variation of Pressure with Mach Number

4. THE KORST METHOD

The Korst method for calculating the base pressure at supersonic speeds has been used for some time, see references 3 and 4. In particular, reference 4 documents a program similar to the version used at Vought. The chief difference is in the description of the shape of the free streamline defining the jet and external flows. Addy uses the method of characteristics. To save time we use a curve fit based on the data of reference 5 for the jet and reference 6 for the external flow.

Figure 4. Korst Model

The major features of the Korst model may be summarized as follows: See figure 4.

(1) The shape of the free streamlines shown in figure 4a are determined by assuming that they have a constant pressure equal to an assumed base pressure. In supersonic flow, the method of characteristics or an appropriate approximation is normally used. This defines the length of the free streamline and their intersection angle at the closure of the separated region.

(2) The shear between the outer flows and the relatively quiet air in the cavity leads to the development of a mixing layer where the velocity varies from zero to the velocity of the outer stream. Although methods have been developed for accounting for an initial boundary layer these do not seem to improve the accuracy unless the free streamlines are very long compared to the boundary layer thickness. We will assume no initial boundary layer. The velocity profiles are then similar with a shape:

$$\frac{V}{V_\infty} = \frac{1}{2} \left(1 + \text{ERF} \frac{\sigma y}{x}\right) \tag{2}$$

where

$$\sigma = 12 + 2.758M \tag{3}$$

represents the rate at which the mixing layer grows.

(3) The mixing velocity profile is superimposed on the inviscid free boundaries as shown in figure 4b. The locus of points with two particular values of velocity ratio have special significance. One, shown dashed in the figure, represents the separating streamline; along it there is no net exchange of mass between the outer flow and the cavity. The other is the dividing streamline. This separates the flow which proceeds on downstream from that which turns upstream and is trapped in the separated region. The total pressure is the same for both flows, but the position relative to the separating streamline is different if the outer velocities are different. Thus, as shown in figure 4b one of the flows supplies a net mass and the other removes a net amount of mass per unit of time.

(4) The total pressure on the dividing streamline is related to the static pressure downstream of the closure. In early studies it was assumed that the dividing streamline total pressure is

equal to the static pressure downstream of the shocks which occur at the closure in supersonic flow. When viscous effects are included the static pressure rises gradually and the total pressure on the dividing streamline is different. But the relation between the pressures can be expressed in terms of a single constant N.

$$N = \frac{P_{div} - P_B}{P_{shock} - P_B} \tag{4}$$

(5) The solution for base pressure is found by making successive estimates of base pressure until there is no net flow into or out of the separated region. Note that it is a simple matter to include an additional source of gas (bleed) into the balance.

(6) While it is not shown in the figure there is a corresponding profile for total temperature. A similar balance for energy into the separated region yields the base temperature and allows appropriate changes in density which may affect the mass balance. With both mass and temperature balance the effect of the hot jet is taken into account. The effect of the ratio of specific boats, γ, is considered in establishing the shape of the boundaries. The gas constant, R, is considered in evaluating the density.

5. EXTENSION TO SUBSONIC FLOW

Subsonic external flow differs from supersonic flow in two important respects with regard to application of the Korst base pressure method. First, it is no longer possible to find the shape of the free streamline by starting at the corner and proceeding downstream finding the shape as you go. To find a constant pressure surface one would have to use an iteration approach where the flow over the entire fuselage-free streamline-jet boundary would have to be considered for each iteration. Second, there is no longer a sharp pressure rise through a closure shock. At the present state of the art an empirical relation is required to replace equation 4.

5.1 Shape of the External Free Streamline

Rather than using a lengthy iteration to find a constant pressure surface it is more expedient to select a family of shapes which will approximate constant pressure surfaces. At Vought we have been using this approach to speed up supersonic calculations. Experiments show that the pressure is not really constant, thus by selecting shapes which more nearly match measured pressures it is possible to have a practical method for computation and to improve the accuracy at the same time.

(a) Dividing Streamline Contour

(b) Static Pressure Variation Along Dividing Streamline
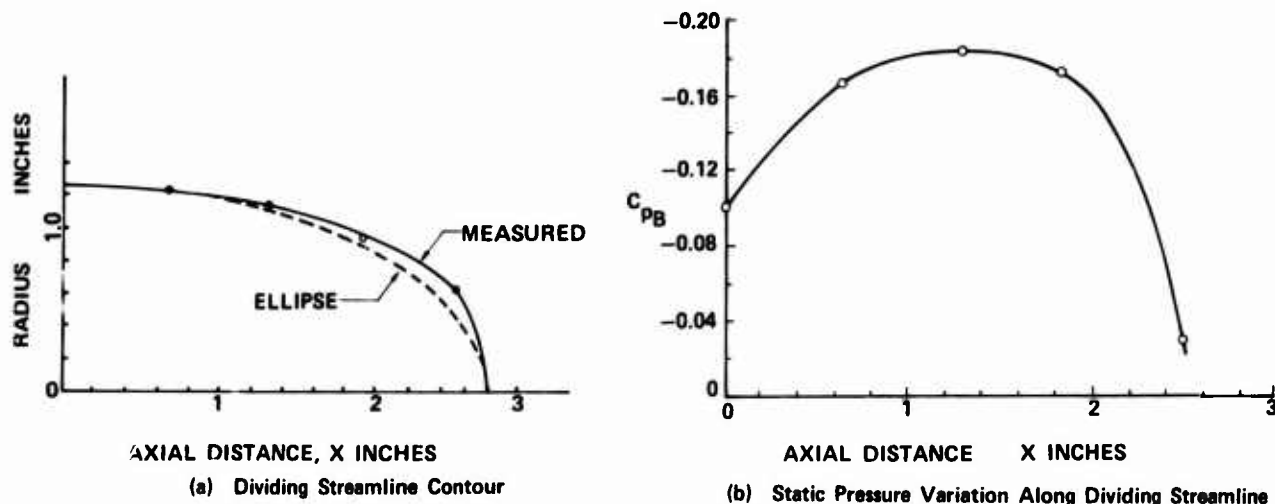
Figure 5. Measured Conditions Along Free Streamline Behind Cut Off Cylinder

Figure 5 shows experimental results taken from reference 7. Note that the shape is slightly fuller than an ellipse. Such a shape can be fitted with a "super ellipse" with the form:

$$\left|\frac{x}{a}\right|^n + \left|\frac{y}{b}\right|^n = 1 \tag{5}$$

where variations in the exponent control the fullness of the figure. $n = 2$ corresponds to an ellipse, $n > 2$ makes the shape fuller with the shape approaching a rectangle as $n \to \infty$. With $n < 2$ the shape becomes more pointed, at $n = 1$ the shape is a diamond and for $n < 1$ the curve becomes concave rather than convex.

Figure 6 shows the calculated pressure distribution over a cylinder plus an $n = 2$ and an $n = 2.2$ super ellipses.

It appears that a super ellipse with $n = 2.1$ will provide a good approximation to the shape of the pressure distribution of figure 5 and is consistent with the shape.

(a) Shape of Simulated Dividing Streamline.
(Infinite Cylinder Upstream)

(b) Static Pressure on Streamline
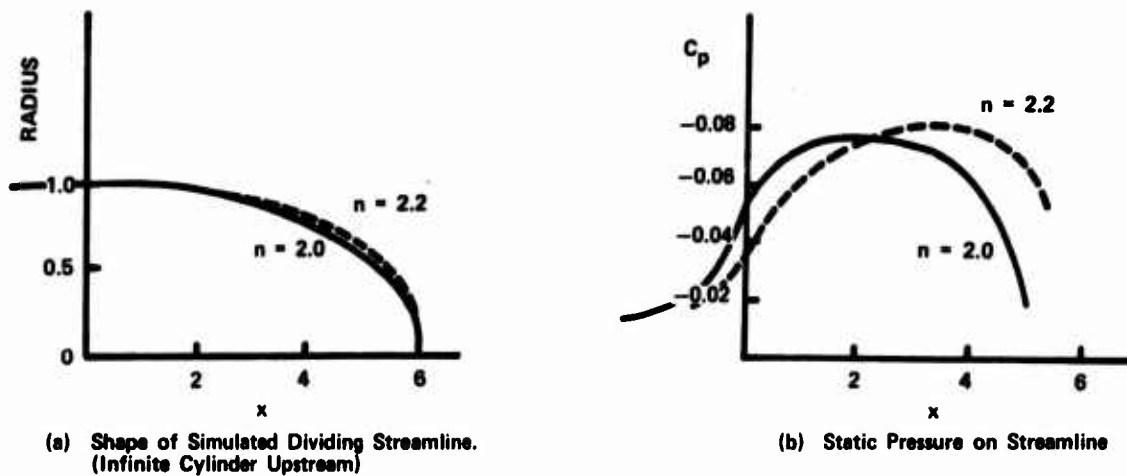
Figure 6. Calculated Pressures for Fineness Ratio 6 Shapes

With this background we assume that the external free streamline surfaces are represented by a portion of a super ellipse which is tangent to the boattail. Figure 7 shows a typical set. Since the pressure is not constant, an average over the first 1/3 of the length is used to define a base pressure.
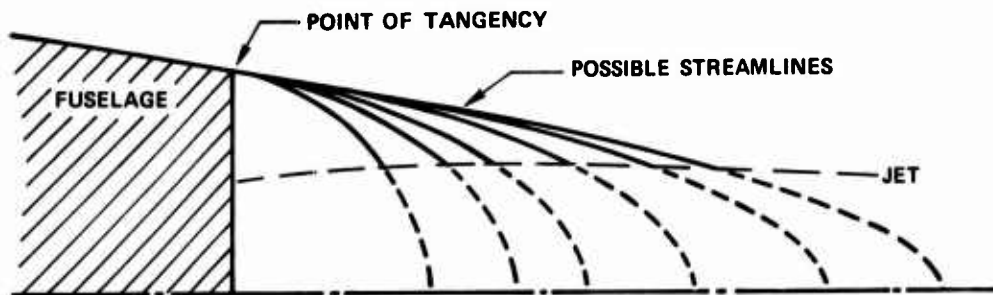
Figure 7. Family of External Free Streamlines

5.2 Subsonic Closure Condition

The condition which determines the total pressure on the dividing streamline contains the real key to success. An empirical relation is formulated, consistent with the physics of the flow, and calibrated using experimental data.

Equation 4 shows the definition of the closure parameter, N, for supersonic flow. The values of N are normally less than 1. In references 8 and 9, Nash used the same formulation for subsonic flow except the pressure behind the shock is replaced with the free stream static pressure.

$$N = \frac{P_{div} - P_B}{P_\infty - P_B} \tag{6}$$

(a) Parameter N'
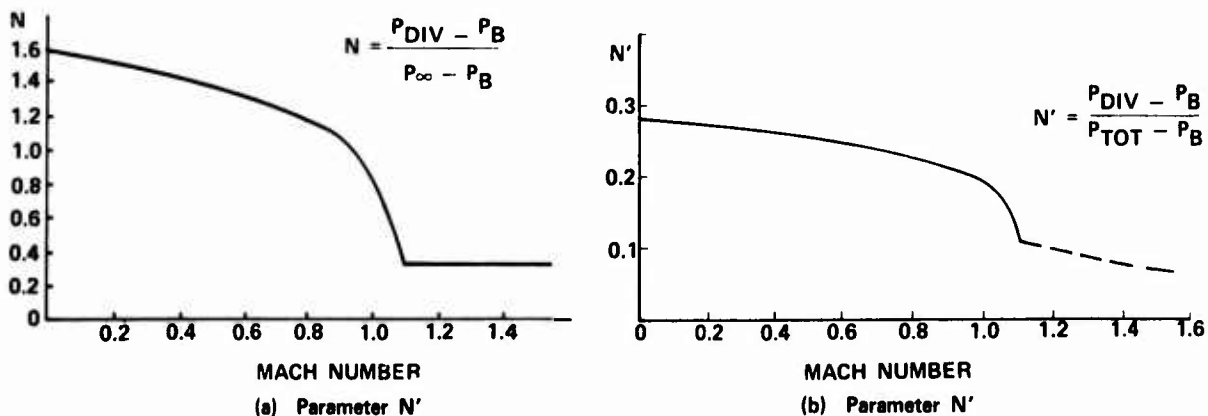
(b) Parameter N'

Figure 8. Subsonic Closure Parameters.
Aft Facing Step, Ref. 8, 9

Figure 8a shows the parameter for flow past a two dimensional aft facing step, reference 8 and 9. Note that the values of N may be greater than 1.

This formulation does not seem appropriate. It is not tied to the local pressure near the closure as in the supersonic case, and there is no safeguard to prevent impossible values of the total pressure on the dividing streamline if the result is applied to other configurations.

In the present analysis total pressure has been selected as the reference pressure. Thus:

$$N' = \frac{P_{div} - P_B}{P_{tot} - P_B} \tag{7}$$

where P_{tot} is the total pressure of the least energetic fluid; usually the external flow. With this formulation, the pressure on the dividing streamline is always within bounds as long as N' is less than one. Figure 8b shows the data of figure 8a converted to N'. An additional advantage is a smaller variation with Mach number.

Flight test data for the A-7 airplane has been used to calibrate the closure condition for the two-fluid problem. The process consisted of adjusting the value of N' until the calculated base pressure matched the measured value. The resulting values of N' are probably functions of a number of variables. The intersection angle between the two flows must be one of the principal variables. While it will not establish a region of constant pressure like that behind the shock in the supersonic flow it will have an effect on the external and the average local pressure in subsonic flow. Figure 9 shows a plot of N' as a function of the interaction angle. The curve follows the expected pattern with N' increasing with ω. The agreement is improved by making the slope a function of the jet pressure ratio.
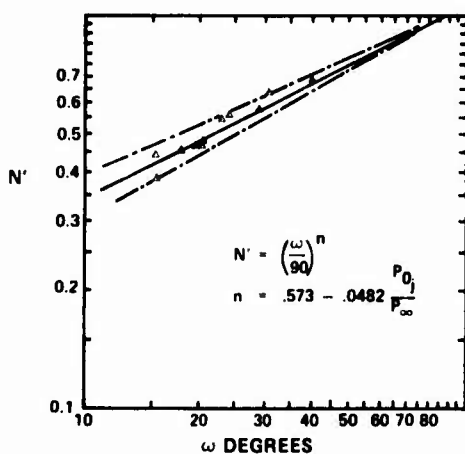
Figure 9. N' Determined from A-7E Data
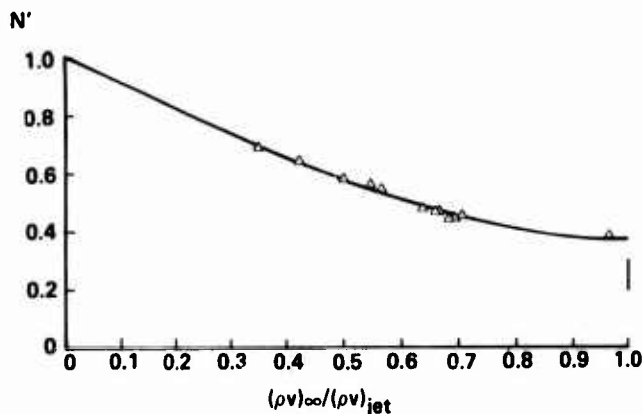
Figure 10. Variation of N' with Momentum Ratio

Another parameter which may be important is the ratio of the momentum, ρV, of the external and jet flows. The fluid with the large momentum is expected to dominate. The nature of N' is such that its maximum value is one. At the other extreme the ρV ratio is one. Figure 10 shows the A-7 data. The data for an aft facing step from figure 8 is shown as a band at ρV ratio of one since the wall acts like a mirror. While the data fits a single curve in figure 10 this formulation has not led to satisfactory convergence in the computer program.

It seems that both of the parameters discussed above are important. However, the two curves are not independent. The large values of ω occur at small values of $(\rho V)/(\rho V)_j$. In order to separate the effect and to improve the estimate of N' it will be necessary to have additional data for many different configurations. For the remainder of the paper the relation shown in Figure 9 will be adopted.

5.3 The Jet Shape

The shape of a supersonic jet between the exit and the interaction with the external flow is based on a curve fit of the data of reference 5. This includes the effect of the ratio of specific heats, the nozzle exit Mach number, and the nozzle exit angle. For subsonic jets a contraction is considered if the nozzle is convergent, otherwise the diameter is considered constant.

Downstream of the interaction with the external flow, the jet - external interface is considered to be cylindrical. This assumption is compatible with the A-7 problem where the base is large compared to the jet and the jet pressure ratios are relatively small. In a typical case the interaction takes place at or downstream of the maximum expansion of the underexpanded jet. Deviations from a cylinder downstream are small. The principal effects of the jet expansion appear in the increased diameter at the intersection and in the determination of N' which depends on the angle of the intersection.

In a general case, particularly those with a smaller base and larger pressure ratio, a better definition of the jet external flow interface is required. As a first approximation a method such as that described in the next paragraph for the no base case is suggested.

In approximating the shape of the jet-external-flow interface in the no base configuration the goal is to obtain an accurate estimate of the force on the boattail. Two general concepts are employed. (1) In potential flow a non lifting body with an open end has zero drag if the cross section remains constant

Figure 11. Approximation of Supersonic Plume

as it goes to infinity. Thus a body with a cylindrical sting will have zero drag. If the sting has a bump with a net positive drag then to maintain zero overall drag the body will experience a net negative drag. On the other hand a bump on the sting with no net drag will induce no net force on the body. (2) In linearized theory a supersonic jet in a subsonic flow produces an undamped series of bumps or oscillations, see reference 10. If the oscillations are stationary and undamped, then they must experience zero force. As a result they individually must induce no force on the boattail. For practical purposes the long string of oscillations can be replaced by a cylinder which also has zero drag. Figure 11 shows the resulting approximation. The cylindrical diameter is that of the jet expanded to ambient pressure. The fairing from the exit to this diameter is tangent to the cylinder at the length of one full oscillation; it falls inside the true boundary.

6.0 RESULTS

The methods described above have been applied to the A-7 airplane configuration, figure 12. The A-7 airplane is powered by a single Allison TF-41 fan jet engine which exhausts through a slightly convergent tail pipe into a rather large elliptical base. The base has the wide dimension from side to side. The nozzle exit is in the lower part of the base in the plane of the base. Extensive flight and wind tunnel test measurements of the base pressure and a number of pressures on the boattail are available, see reference 11. The calculations have been made for a body of revolution with the same variation of cross sectional area as the fuselage. The jet is assumed to act along the centerline.
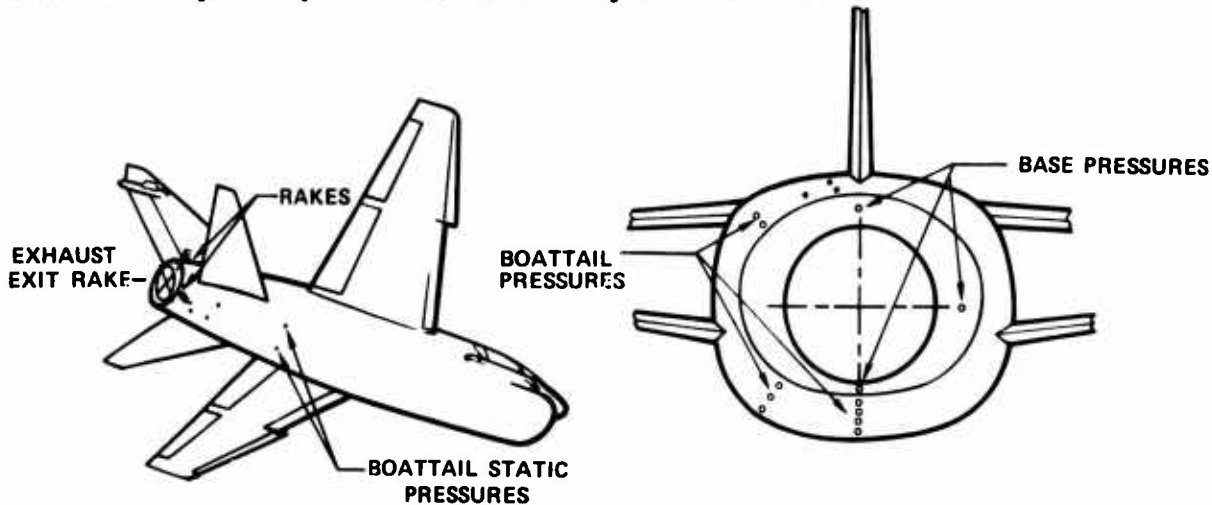
Figure 12. Configuration for Flight Test

Figure 13 shows a comparison between the calculated and flight test measurements. Figure 13a shows the variation of base pressure in level flight at two altitudes. This presentation has the advantage of showing the relative effect of the base pressure on the drag of the airplane in normal operation. But altitude and Mach number are not primary variables. The apparent altitude effect is due to a change in thrust caused by induced drag. Figure 13b shows the variation of base pressure with the jet pressure ratio while the airplane Mach number and altitude are held constant (the airplane climbs or descends).
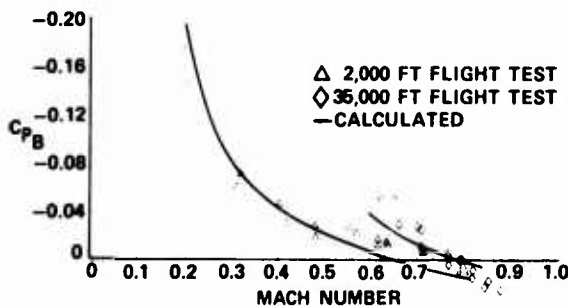
(a) Variation in Level Flight
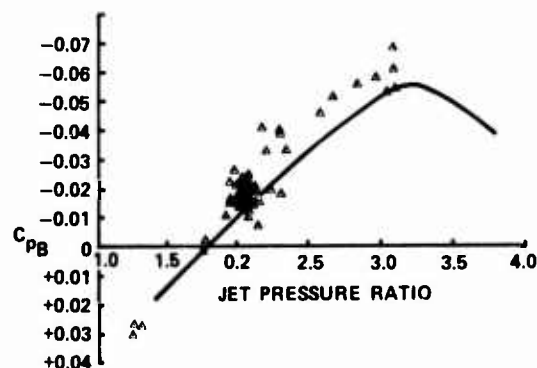
(b) Variation with Jet Pressure Ratio

Figure 13. Base Pressure

The agreement between the calculation and flight test is satisfactory over the range of test variables. This cannot really be considered a check of the method because, as discussed above the equation defining N' was derived from the same data (although not the same points). What it shows is that a simple empirical relation for N' will produce most of the features shown by the experiments. It gives confidence that the method will predict the effect of design variables not covered by the test. In addition to the effects of changes in geometry this includes the effect of the addition of bleed air and the differences to be expected between hot and cold jets in wind tunnel testing.

Figure 13b also shows the predicted variation of base pressure at jet pressures higher than those tested. Note that the base pressure reaches a minimum and then becomes more positive. This occurs as the plume expands enough to affect the interaction angle between the flows.
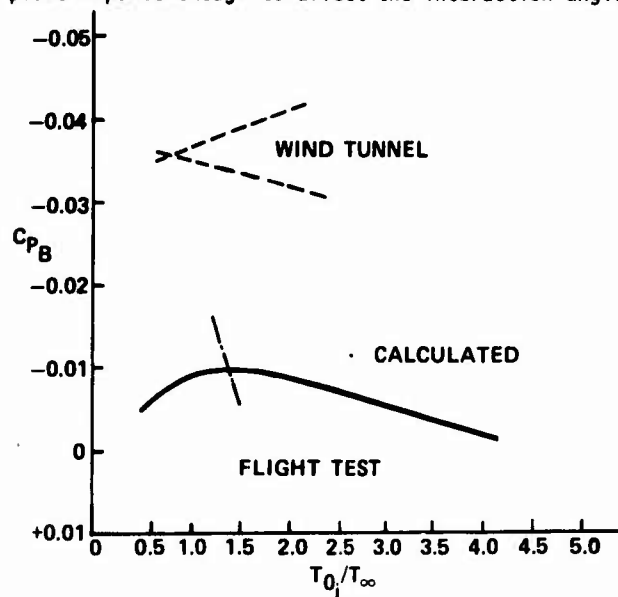
Figure 14. Effect of Jet Temperature
M = 0.6, Jet Pressure Ratio = 2.0

Figure 14 shows the effect of jet temperatures on base pressure at a fixed external Mach number and jet pressure ratio. The peak on the calculated curve is unexpected. It is apparently due to the fact that temperature affects both velocity and density. At the higher temperatures the reduction of density in mixing layers is the dominating feature. Note that the flat part of the curve occurs in the temperature range which includes fan engines and cold jet wind tunnel models. If these results are verified, cold testing should give good results for fan engines. Conflicting trends are available from the A-7 wind tunnel tests. The variation falls between the two boundaries shown (the level of the pressure is considered too negative). Flight tests do not provide a significant range of temperatures at a constant pressure ratio. The available evidence suggests that temperature at a rate several times larger than the calculated rate.

The calculated variation is due to temperature alone. The variation from wind tunnel and flight test may include some influence of other variables such as γ and changes in airplane attitude. Further work is required to resolve the differences.

Figure 15 shows predictions, based on calculations, of the effect of bleed air, figure 15a, and the axial location of the nozzle exit, figure 15b. Based on these results one can reduce the base drag by extending the nozzle exit and by adding bleed gas.

(a) Base Bleed

(b) Nozzle Extension
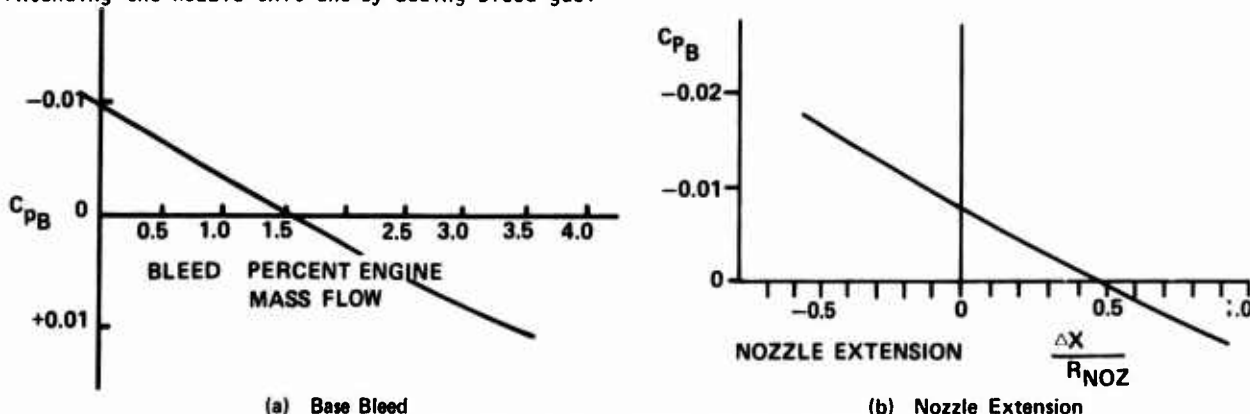
Figure 15. Predicted Effect of Design Variables
M = 0.6, Jet Pressure Ratio = 2.0

The pressures on the boattail of the airplane in flight are affected by the tail surfaces as well as by the fuselage shape and the engine operation. To separate these effects a least squares fit has been made using the following equation:

$$C_{p_n} = A_n + B_n C_{p_B} + C_n C_{L_t} \tag{8}$$

In wind tunnel tests the nominal tail angle is zero, but there were no measurements of downwash or tail lift to verify C_{L_t}. There are also pressure increments of unmeasured magnitude due to the support system and wall effects.

Figure 16 shows the boattail pressure distribution for configurations with a base. Figure 16a shows the axial distribution of boattail pressure coefficients for low to moderate jet pressure ratios when $C_{L_t} = 0$, $C_{p_B} = 0$. When the jet pressure ratio exceeds 3, roughly, the effect of the plume expansion will be felt on the boattail and there will be a series of curves, one for each jet pressure ratio. Pressures shown for flight test and wind tunnel test are the A_n coefficients of equation 8 averaged for several taps around the circumference. Note that the boundary layer is neglected in the calculation. If the displacement thickness were included the pressures would be slightly more negative. Differences between the calculated and flight test pressures are consistent with the expected influence of the tails. The reason for

the deviation of the wind tunnel measurements is not known. It may be due, in part, to support and wall interference.

(a) Boattail Pressures at $C_{p_B} = 0$

(b) Effect of Jet
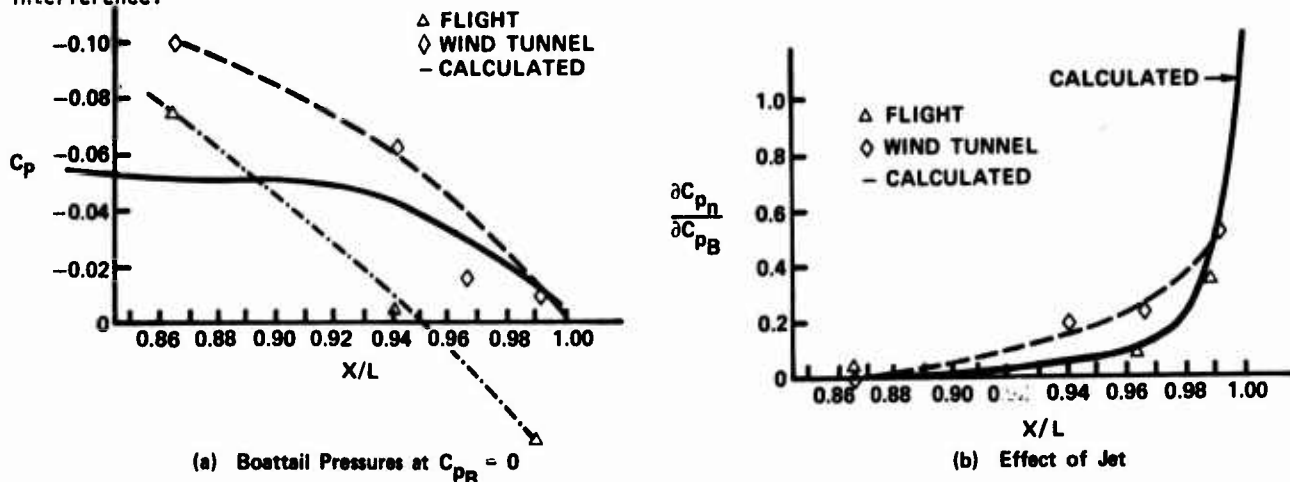
Figure 16. Boattail Pressure Distribution on Configuration with a Base
M = 0.6 Jet Pressure Ratio < 3.

Figure 16b presents the interaction between the jet and external flow as it affects the boattail pressures. $\partial C_{p_n}/\partial C_{p_b}$ is the B_n coefficient of equation 8. Note that the boattail pressure variation follows that of the base. An increase in jet pressure causes a more negative base pressure, hence an increase in base drag. The corresponding more negative pressures on the boattail produce an increase in boattail drag. Based on the calculated pressures $\Delta C_{D_{BT}} = 0.37 \Delta C_{D_B}$. There are not enough pressure taps to make a similar integration based on flight test data alone, but the agreement with the calculated $\partial C_p/\partial C_{p_b}$ suggests that $\Delta C_{D_{BT}}$ is about the same. Corresponding data from the wind tunnel tests are less accurate because of large scatter in individual points, but the same trends are apparent.

Figure 17 shows the boattail pressure distribution when there is no base. Figure 17a shows the pressures for a jet pressure ratio of approximately 1.9. The calculations are based on a cylindrical jet with no boundary layer. The rapid increase in pressure near the base is typical of a two dimensional flow approaching a kink. Rapid thickening of the boundary layer tends to eliminate this in practice. Wind tunnel data have been analyzed using a least squares fit of the type shown in equation 8 where C_{p_B} is replaced with the jet expansion $\frac{\Delta r}{r}$ and there is no tail effect.

(a) Cylindrical Jet

(b) Effect of Jet
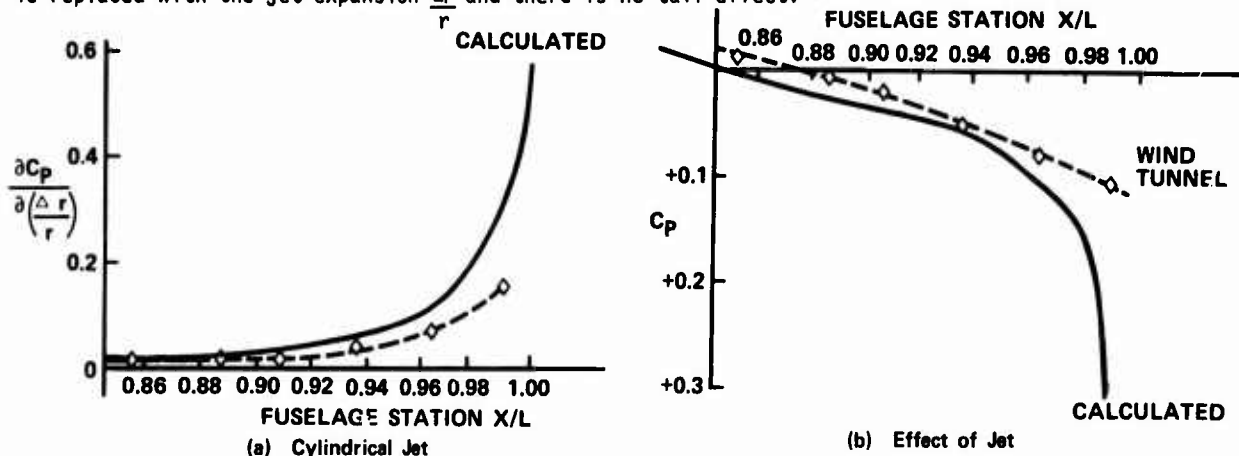
Figure 17. Boattail Pressure Distribution, No Base
M = 0.8

The rate of change of boattail pressure with jet expansion is considered linear for moderate pressure ratios. Data from wind tunnel tests show the same general shape as the calculated results, but the magnitudes are lower. This is probably due to the boundary layer, or more precisely, the differences in the growth rate of the boundary layer produced by the increased jet pressure. Note that the boattail pressures become more positive with increased jet pressure. This is opposite in sign from the results shown in figure 16 for the configuration with a base as long as the base pressure becomes more negative with increasing jet pressure. As shown in figure 13 continuing increases in jet pressure ratio will eventually produce a more positive base pressure and more positive boattail pressures for the finite base configuration. Experimental results for configurations without a base often show a reduction in boattail pressure (drag increase) for small increases in jet pressure while larger jet pressures show the expected pressure increases. This has been attributed to entrainment of the external fluid by the jet. In view of the present analysis it seems likely that the effect may be associated with a local separation. Such a separation will act much like a blunt base. The increase in boattail pressure may be integrated to determine an increment of thrust on the boattail. In effect, the boattail is acting much like a diverging nozzle. A measure of the efficiency of such a nozzle, based on calculated results, is shown in figure 18. Coupling ratio is the ratio of the increment in thrust on the boattail to the increment in thrust which could be recovered with an ideal convergent-divergent nozzle. Note that the coupling ratio is high for jets which are only slightly underexpanded, but it drops rapidly for larger pressure ratios.
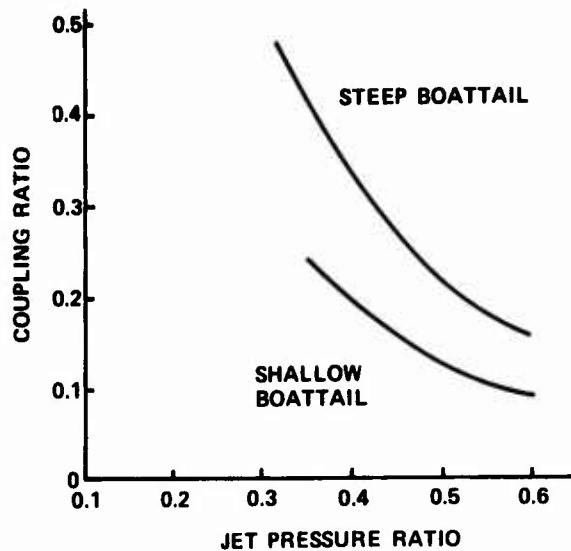
Figure 18. Calculated Coupling Ratio, M = 0.6

7. CONCLUDING REMARKS

This study is a first order attempt to consider the primary effects involved in the interaction of a subsonic external flow with a propulsive jet using potential flow theory. It is shown that the interaction may be studied in terms of the effect of the jet on the effective boundary for the external inviscid flow. With this approach the jet plays an important role in establishing the shape of the free streamline in the configuration with a base and of the interface between the two flows. But once the shape is established, potential flow of the external fluid will establish the distribution of pressures felt by the remainder of the airplane. The external flow provides a mechanism for transferring some of the drag due to a base onto the boattail and for recovering some of the thrust which would otherwise be lost in external expansion. The amount of thrust which can be recovered is limited.

The method is general enough to include the effects of most variables. This includes the geometry, the properties of each of two fluids and of a bleed gas dumped into the base region. Much remains to be done. The principle areas needing improvement include: a more general approximation for the closure condition and a method for including the boundary layer and mixing layer along the interface between the two fluids.

REFERENCES

1. Smith, A. M. O. and Pierce, Jesse: Exact Solution of the Neumann Problem. Calculation of non-circulatory plane and axially symmetric flows about or within arbitrary boundaries. Douglas Aircraft Co., Report ES 26988, 1958. Also: Hess, J. L. and Smith, A. M. O.: Calculation of Potential Flow about Arbitrary Bodies. Progress in Aeronautical Sciences, Volume 8, edited by D. Kucheman, p. 1.

2. Mathews, Clarence N.: A Comparison of the Experimental Subsonic Pressure Distribution about Several Bodies of Revolution with Pressure Distribution Computed by Means of the Linearized Theory. NACA Technical Note 2519, February 1952.

3. Korst, H. H.: A Theory for Base Pressure in Transonic and Supersonic Flow. Journal of Applied Mechanics, Volume 23, pp. 593-600, 1956.

4. Addy, A. L.: Analysis of the Axisymmetric Base Pressure and Base Temperature Problem with Supersonic Interacting Freestream - Nozzle Flows Based on the Flow Model of Korst, et. al. Part 1: A Computer Program and Representative Results for Cylindrical Afterbodies. U.S. Army Missile Command Report RD-TR-69-12, July 1969.

5. Love, E. S., Grigsby, C. E., Lee, L. P., and Woodling, M. J.: Experimental and Theoretical Studies of Axisymmetric Free Jets. NASA TR-R6, 1959.

6. Sims, J. L.: Results of the Computation of Supersonic Flow Fields Aft of Circular Cylindrical Bodies of Revolution by the Method of Characteristics. Army Ballistic Missile Agency Report DA-R-49, 1958.

7. McErlean, D. P. and Przirembel, C. E. G.: The Turbulent Near Wake of an Axisymmetric Body at Subsonic Speeds, AIAA Paper 70-797, July 1970

8. Nash, J. F.: An Analysis of Two-Dimensional Turbulent Base Flow, Including the Effect of the Approaching Boundary Layer, British R&M 3344, 1963.

9. Nash, J. F.: An Analysis of the Subsonic Flow Past Symmetrical Blunt-Trailing-Edge Airfoil Sections at Zero Incidence in the Absence of a Vortex Street, British R&M 3436, 1966.

10. Pai, Sheh I.: Fluid Dynamics of Jets. D. Van Nostrand Co., pp 55. Also: Supersonic Flow of a Two-Dimensional Jet in Uniform Stream. Institute of Aero Science, Volume 19, No. 1, January 1952.

11. Walker, S. C.: Isolating Nozzle-Afterbody Interaction Parameters and Size Effects - A New Approach AGARD Conference Proceedings on Airframe/Propulsion Interference, paper 18.

COUPLAGE ENTRE L'ECOULEMENT AUTOUR D'UN ARRIERE-CORPS ET LE JET
PROPULSIF EN THEORIE DE FLUIDE PARFAIT

par Roland Maria Sube, Jean-Jacques Chattot et Georges Gillon

Office National d'Etudes et de Recherches Aérospatiales (ONERA)
92320 Châtillon

RESUME

Les effets de couplage entre les écoulements externe et interne sont examinés dans le cadre de la théorie des fluides parfaits. Ces phénomènes concernent essentiellement les écoulements autour des arrière-corps.

La première partie de cet exposé se rapporte à l'étude de l'interaction de deux écoulements subcritiques coaxiaux. Le calcul de chaque écoule ment interne et externe est effectué au moyen d'une méthode aux éléments finis.
La forme du jet est déterminée par approximations successives en utilisant une méthode pseudo-hodographique.

La deuxième partie de cet exposé concerne l'interaction d'un jet supersonique avec un écoulement externe subsonique ou transsonique. Le jet interne supersonique est calculé en utilisant la méthode des caractéristiques. Les conditions de couplage entre l'écoulement interne et l'écoulement externe sont remplies, en utilisant une procédure iterative semblable a celle proposée par Young, mais étendue ici aux écoulements externes compressibles sub et trans-soniques.

La troisième partie de l'exposé donne une comparaison avec des résultats expérimentaux.

COUPLING BETWEEN THE FLOW AROUND AFTERBODIES AND PROPULSIVE JETS IN THE INVISCID FLOW THEORY

SUMMARY

The interference effects between external and internal flows are examined in the framework of the inviscid flow theory. These phenomena are connected mainly with flows around afterbodies.

The first part of the paper is devoted to the study of subcritical axisymmetrical interacting flows.
The computation of both internal and external flows is carried out using a finite element method. The results make it possible to determine the shape of the jet using a pseudo-hodographic method, with an iterative procedure.

The second part concerns the interference effects of a supersonic internal flow with subsonic or transonic external flows. The supersonic internal jet is computed using the method of characteristics. The coupling conditions between the internal and the external flows are taken into account, using an iterative procedure in a way similar to that proposed by Young, but extended here to compressible external flows.

A comparison with existing experimental results is presented.

LISTE DES SYMBOLES

Indices

i caractérise des conditions d'arrêt,

j se rapporte à des grandeurs définies dans l'écoulement interne,

e se rapporte à des grandeurs définies dans l'écoulement externe,

$*$ caractérise des grandeurs dimensionnelles,

$réf$ caractérise les grandeurs de référence,

1 caractérise les conditions amont,

2 caractérise les conditions aval.

Grandeurs géométriques

$\vec{Ox}, \vec{Or}$ axes de référence,

L^* longueur de référence,

M_L point courant sur la surface libre,

$R, R_A, R_B ...$ rayons pris dans le domaine géométrique,

y distance normale à la paroi ou à la ligne de glissement.

Grandeurs physiques

M nombre de Mach,

M_∞ ou M_{e1} nombre de Mach amont dans l'écoulement externe,

$M_{réf}$ ou M_{j1} nombre de Mach de référence (= nombre de Mach amont dans l'écoulement interne),

P pression statique,

P_∞ ou P_{e1} pression statique amont dans l'écoulement externe,

ς masse volumique,

T température absolue,

s^* entropie spécifique,

h_i^* enthalpie d'arrêt,

C_P chaleur spécifique à pression constante,

C_v chaleur spécifique à volume constant,

γ C_P / C_v

V module de la vitesse,

u, v — composantes axiale et radiale de la vitesse,

ψ — fonction de courant,

K_p — $(p^* - p_{ei}^*)/(\frac{1}{2}\, \rho_{ei}^* V_{ei}^{*2})$

δ — épaisseur de la couche limite,

u_e — vitesse à la frontière δ de la couche limite,

δ_1 — $\displaystyle\int_0^\delta \left(1 - \frac{\rho u}{\rho_e u_e}\right) dy$

δ_2 — $\displaystyle\int_0^\delta \frac{\rho u}{\rho_e u_e}\left(1 - \frac{u}{u_e}\right) dy$

H — δ_1 / δ_2

H_{inc} — $\displaystyle\left[\int_0^\delta \left(1 - \frac{u}{u_e}\right) dy\right] \Big/ \left[\int_0^\delta \frac{u}{u_e}\left(1 - \frac{u}{u_e}\right) dy\right]$

$\mathcal{D}$ — domaine physique,

Symboles Mathématiques

$O\alpha\beta$ — repère du plan transformé quasi-conforme,

ε — pas du maillage dans le plan transformé,

χ_i, η_j — fonctions-test,

P_j — désignation d'un pavé,

γ_j — centre du pavé P_j,

k — nombre de pavés,

$O\lambda\mu$ — repère du plan transformé conforme.

1 - INTRODUCTION

La connaissance des effets d'interaction entre les écoulements externe et interne est fondamentale pour l'étude de l'aérodynamique des arrière-corps afin d'obtenir notamment une évaluation précise de leur trainée. L'évolution du jet, à la sortie d'une tuyère peut intervenir, en effet, de façon assez sensible sur la répartition des pressions en amont du bord de fuite de l'arrière-corps spécialement dans le cas où l'écoulement interne est sous détendu. Le but de ce travail est donc de définir des moyens de calcul permettant d'aborder l'étude de ces phénomènes d'interaction, en se plaçant tout d'abord dans le cadre d'une théorie de fluide parfait, de manière à pouvoir disposer d'un outil permettant de traiter le problème de couplage dans son ensemble et de délimiter ensuite par référence à l'expérience, l'importance des effets liés à la viscosité. Pour cela on examinera successivement trois problèmes différant par la nature des équations qui régissent les écoulements en présence :

Le jet subsonique débouchant dans un écoulement externe subsonique,
Le jet supersonique débouchant dans un écoulement externe subsonique et le jet supersonique débouchant dans un écoulement externe transsonique.

La première partie de cet exposé se rapporte donc à l'étude, dans le cadre de la théorie des fluides parfaits, de l'interaction de deux écoulements subcritiques coaxiaux. La méthode de calcul utilisée exposée de façon détaillée est une extension aux écoulements de fluides compressibles, de méthodes itératives mises au point au L.I.M.S.I ** [4] à [8] pour étudier les jets axisymétriques rotationnels de fluide incompressible.

La deuxième partie de l'exposé est consacrée à l'étude du couplage qui s'établit entre un jet supersonique et un écoulement extérieur subsonique ou transsonique. La procédure de calcul est, ici encore, itérative et semblable à celle proposée par Young [9]. le jet supersonique étant calculé par la méthode des caractéristiques, l'écoulement extérieur lorsqu'il est supercritique par la méthode des petites perturbations transsoniques appliquée aux corps élancés.

La troisième partie, enfin, est consacrée aux applications.
Les résultats théoriques obtenus pour chacun des cas de calcul présentés sont confrontés avec des mesures expérimentales existantes.

2 - JET SUBSONIQUE EN PRESENCE D'UN ECOULEMENT EXTERNE SUBSONIQUE.

2.1 Equation du mouvement

L'équation* du tourbillon des écoulements stationnaires compressibles axisymétriques s'écrit :

$$(1)\quad \frac{\partial}{\partial x^*}\left(\frac{1}{r^*\rho^*}\frac{\partial\psi^*}{\partial x^*}\right) + \frac{\partial}{\partial r^*}\left(\frac{1}{r^*\rho^*}\frac{\partial\psi^*}{\partial r^*}\right) = S^*$$

où ψ^* est la fonction de courant de l'écoulement ; celle-ci est liée aux composantes méridiennes u^* et v^* de la vitesse (fig.1) par les relations :

$$(2)\quad \rho^* r^* u^* = \frac{\partial\psi^*}{\partial r^*}\ , \quad \rho^* r^* v^* = -\frac{\partial\psi^*}{\partial x^*}$$

$\overrightarrow{Ox}$ et $\overrightarrow{Or}$ sont les axes d'un repère cartésien situé dans un plan méridien fixé, $\overrightarrow{Ox}$ étant également axe de symétrie de l'écoulement. ρ^* est la masse volumique du fluide.

Pour des écoulements méridiens, l'expression générale de S^* est :

$$(3)\quad S^* = \rho^* r^* \left(-T^*\frac{ds^*}{d\psi^*} + \frac{dh_i^*}{d\psi^*}\right)$$

où T^* est la température, s^* l'entropie spécifique et h_i^* l'enthalpie totale.
Dans ce qui suit, on étudiera des écoulements de gaz calorifiquement parfaits où l'enthalpie d'arrêt et l'entropie spécifique sont uniformes dans chacun des écoulements ; le second membre S^* de (1) est alors identiquement nul. L'équation (1) reste inchangée par rapport aux nouvelles variables sans dimension suivantes :

$$(4)\quad \psi = \frac{\psi^*}{\rho_{ref}^* V_{ref}^* L^{*2}}\ , \quad \rho = \frac{\rho^*}{\rho_{ref}^*}\ , \quad x = \frac{x^*}{L^*}\ , \quad r = \frac{r^*}{L^*}$$

** Laboratoire d'Informatique pour la mécanique et les Sciences de l'Ingénieur, CNRS.

* Les astérisques indiquent que les variables auxquels ils se rapportent sont dimensionnées.

où L^*, ϱ^* ref, V^* ref sont des grandeurs de référence précisées plus loin.
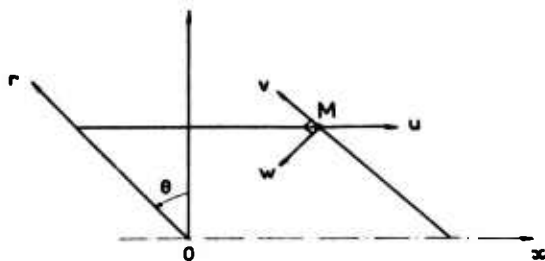
Fig.1 DEFINITION DU SYSTEME DE COORDONNEES CYLINDRIQUES

La relation entre ψ et ϱ s'écrit sous forme implicite :

$$(5) \quad \varrho = \left\{ 1 + \frac{\gamma-1}{2} M_{ref}^2 \left[1 - \frac{1}{r^2} \cdot \frac{1}{V_{ref}^{*2}} \cdot \frac{1}{\varrho^2} \left[\left(\frac{\partial \psi}{\partial x} \right)^2 + \left(\frac{\partial \psi}{\partial r} \right)^2 \right] \right] \right\}^{\frac{1}{\gamma-1}}$$

où M réf est le nombre de Mach de référence.

2.2 Conditions aux limites

On considère (fig.2) deux écoulements coaxiaux, compressibles subcritiques, l'un extérieur à un arrière-corps de trace méridienne EFG, l'autre intérieur.
Les deux écoulements sont séparés en aval de l'arrière-corps par une ligne de glissement de trace F H. L'enthalpie d'arrêt et l'entropie spécifique sont supposées uniformes dans chacun des écoulements.
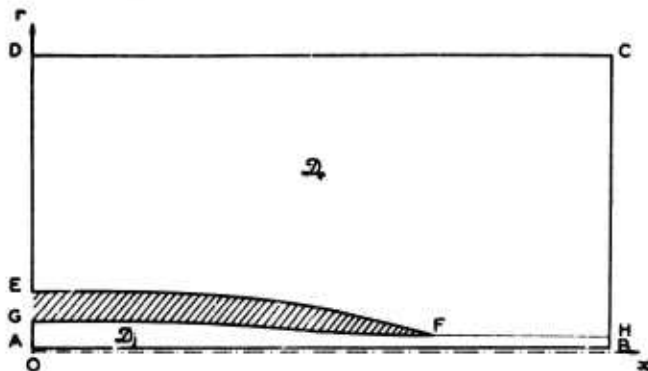
Fig.2 MERIDIENNE DU DOMAINE PHYSIQUE

Pour les besoins du calcul, le domaine physique est limité en amont et en aval par des plans de traces méridiennes OD et BC respectivement, ainsi que par deux cylindres droits coaxiaux, de rayons R_A^* et R_D^*, de traces AB et DC. Dans un plan méridien (fig.2), ce domaine peut être subdivisé en deux : $\mathcal{D}_e$ de contour EFHCDE et $\mathcal{D}_j$ de contour ABHFGA.+

Dans ce qui suit, les indices j et e désignent les grandeurs relatives aux écoulements interne et externe respectivement ; les indices 1 et 2 indiquent que les variables ainsi indicées concernent des points situés dans les plans OD et BC ; l'indice i caractérise les conditions d'arrêt.

+ la limitation du Domaine $\mathcal{D}_j$ par la ligne AB voisine de l'axe est introduite pour éviter les difficultés numériques qui interviennent dans le calcul de (4) lorsque r^* tend vers O.

Les données du problème sont, outre la géométrie de l'arrière-corps, les températures d'arrêt T_{ij} et T_{ie}, les nombres de Mach amont M_{j1} et M_{e1}, les chaleurs spécifiques C_{vj}, C_{ve}, C_{pj} et C_{pe} et leurs rapports γ_j et γ_e.

Les conditions aux limites sont celles usuelles aux problèmes à frontières connues, mais la présence d'une frontière libre implique que l'on ait, en plus des conditions de débit et de glissement, une condition d'équilibre sur FH et une condition de Kutta-Joukowski au bord de fuite F de l'arrière-corps. Cette dernière a pour conséquence qu'il n'est pas possible de se fixer d'emblée toutes les conditions aux limites, l'une de celles-ci devant dépendre de la forme définitive du jet.

On pose :

$$(6) \quad \varrho_{ref}^* = \varrho_{j1}^* \;,\; V_{ref}^* = V_{j1}^* \;,\; M_{ref} = M_{j1} \;,\; L^* = \overline{OG} = R_e^*$$

Les conditions aux limites s'écrivent, pour une forme donnée du jet et en supposant que les deux écoulements sont uniformes à l'amont :

$$(7) \quad \frac{\partial \psi}{\partial n} = 0 \quad \text{sur AG, ED, BH, et HC}$$
$$\text{(}\vec{n} \text{ étant le vecteur normal au contour)}$$

$$(8) \quad \psi = \frac{R_A^{*2}}{2} \quad \text{sur AB}$$

$$(9) \quad \psi = \frac{1}{2} \quad \text{sur GFH et EFH}$$

$$(10) \quad \psi = \frac{1}{2} + \frac{V_{e1}^*}{V_{j1}^*} \cdot \frac{\varrho_{e1}^*}{\varrho_{j1}^*} \cdot \frac{R_D^{*2} - R_E^{*2}}{2} \quad \text{sur DC}$$

Calcul de ψ sur la frontière extérieure.

La condition (10) dépend des données géométriques R_D^* et R_E^*, mais également des rapports V_{e1}^*/V_{j1}^* et $\varrho_{e1}^*/\varrho_{j1}^*$

Le premier : V_{e1}^*/V_{j1}^* est défini par les données du problème :

$$(11) \quad \frac{V_{e1}^*}{V_{j1}^*} = \frac{M_{e1}}{M_{j1}} \cdot \left(\frac{C_{pe} T_{ie}}{C_{pj} T_{ij}} \right)^{\frac{1}{2}} \cdot \left(\frac{A}{B} \right)^{\frac{1}{2}}$$

$$\text{avec } A = 1 + \frac{\gamma_j - 1}{2} M_{j1}^2 \quad \text{et} \quad B = 1 + \frac{\gamma_e - 1}{2} M_{e1}^2$$

Par contre $\varrho_{e1}^*/\varrho_{j1}^*$ ne peut être fixé qu'une fois que la forme de la ligne de glissement est connue. Dans ce cas et moyennant l'hypothèse d'une pression transversalement uniforme en 2, les nombres de Mach M_{j2} et M_{e2} sont donnés par les relations implicites :

$$(12) \quad \Sigma_j (M_{j2}) = \Sigma_j (M_{j1}) \cdot \frac{R_H^2 - R_B^2}{R_B^2 - R_A^2}$$

$$(13) \quad \Sigma_e (M_{e2}) = \Sigma_e (M_{e1}) \cdot \frac{R_C^2 - R_H^2}{R_D^2 - R_E^2}$$

dans lesquelles $\Sigma (M)$ est la fonction du nombre de Mach, définissant l'évolution des lois de section d'un écoulement monodimensionnel isentropique.

Connaissant M_{j1} et M_{e1} on en déduit tout d'abord le rapport des pressions génératrices des deux écoulements:

$$(14) \quad \frac{p_{ie}}{p_{ij}} = \frac{\varpi_j (M_{j1})}{\varpi_e (M_{e1})}$$

$\varpi (M)$ étant la fonction $\frac{p}{p_i} (M)$,
et par voie de conséquence:

$$(15) \quad \frac{\varrho_{e1}}{\varrho_{j1}} = \frac{\left(1+\frac{\gamma_e-1}{2} M_{e1}^2\right)^{-\frac{1}{\gamma_e-1}}}{\left(1+\frac{\gamma_j-1}{2} M_{j1}^2\right)^{-\frac{1}{\gamma_j-1}}} \cdot \frac{p_{ie}}{p_{ij}} \cdot \frac{T_{ij}}{T_{ie}} \cdot \frac{C_{pj}-C_{vj}}{C_{pe}-C_{ve}}$$

Condition d'équilibre de la surface de glissement :

Les conditions (7)-(10) ont été écrites en supposant connue la forme de la surface libre. Celle-ci est en fait une des inconnues du problème qui est déterminée en écrivant sur FH la condition supplémentaire de continuité des pressions :

$$p_{jM}^* = p_{eM}^* \quad \text{pour tout point M situé sur FH.}$$

Cette condition s'écrit encore :

$$(16) \quad p_{ij}^* \left[\frac{1+(A-1)\left(1-\frac{V_{jM}^{*1}}{V_{j1}^{*1}}\right)}{A}\right]^{\frac{\gamma_j}{\gamma_j-1}} = p_{ie}^* \left[\frac{1+(B-1)\left(1-\frac{V_{eM}^{*1}}{V_{e1}^{*1}}\right)}{B}\right]^{\frac{\gamma_e}{\gamma_e-1}}$$

2.3 Procédure générale de résolution

Celle-ci est nécessairement itérative et se développe de la manière suivante :
on se donne au départ une forme arbitraire de la frontière FH. Ce choix constitue la première approximation. A ce moment, ainsi qu'à chacune des itérations suivantes, le problème se ramène à la résolution de l'équation (1) à l'intérieur des deux domaines indépendants $\mathcal{D}_e$ et $\mathcal{D}_j$ à frontières connues avec les conditions (7), (9) et (10) dans ($\mathcal{D}_e$) et (7), (8) et (9) dans ($\mathcal{D}_j$).

Le couplage existant entre les deux écoulements ne sera pris en compte par le calcul que lors du passage d'une approximation de la frontière libre à la suivante.

Pour effectuer chaque résolution, on construit une solution numérique approchée de l'équation (1) par une méthode de Galerkin dans ($\mathcal{D}_j$) puis dans ($\mathcal{D}_e$).

Celle-ci utilise une famille de fonctions-test nécessitant pour leur définition une partition du domaine physique par des pavés. Ces pavés recouvrent exactement chacun des domaines considérés et sont constitués à partir d'un maillage curviligne. Dans les problèmes étudiés précédemment [4, 5, 6, 7, 8] une méthode de calcul automatique de maillages curvilignes construits à l'aide de fonctions harmoniques était utilisée. Les applications présentées au paragraphe 4 ayant toutes un domaine de définition à contour presque rectangulaire, un maillage dont la construction par ordinateur se révèle simple et rapide a été utilisé (fig.3) ; ce maillage est réalisé à l'aide d'une première famille de courbes ($\alpha = C^{te}$) qui sont des droites verticales convenablement espacées pour les besoins du problème ; chacun des segments verticaux ainsi construit est ensuite divisé selon une loi simple (n segments, égaux dans ($\mathcal{D}_j$), ou suivant une loi de progression arithmétique dans ($\mathcal{D}_e$)) ; en joignant les noeuds ainsi obtenus on construit une deuxième famille de courbes ($\beta = C^{te}$).

Les courbes $\alpha = C^{te}$, $\beta = C^{te}$ recouvrent les domaines de définition ($\mathcal{D}_j$) et ($\mathcal{D}_e$) par un maillage régulier, de pas ε dans le plan transformé (α , β).

Ce maillage permet de construire des pavés hexagonaux P_j (fig. 4 a et 4 b) définis par les courbes :

$$(17) \begin{cases} \alpha (x,r) = \alpha_j - \varepsilon ; & \alpha (x,r) = \alpha_j + \varepsilon \\ \beta (x,r) = \beta_j - \varepsilon ; & \beta (x,r) = \beta_j + \varepsilon \\ \alpha (x,r) - \beta (x,r) = \alpha_j - \beta_j - \varepsilon \\ \alpha (x,r) + \beta (x,r) = \alpha_j + \beta_j + \varepsilon \end{cases}$$

où α_j et β_j , sont les coordonnées du centre N_j du pavé P_j.

La procédure de résolution du problème comprend deux boucles d'approximations successives, imbriquées l'une dans l'autre : l'une dite "interne" correspond au calcul de la masse volumique ϱ qui figure comme coefficient dans l'équation (1), l'autre dite externe correspond à la recherche de la surface libre ; cette démarche met en oeuvre une procédure numérique qui va être examinée maintenant de façon détaillée.
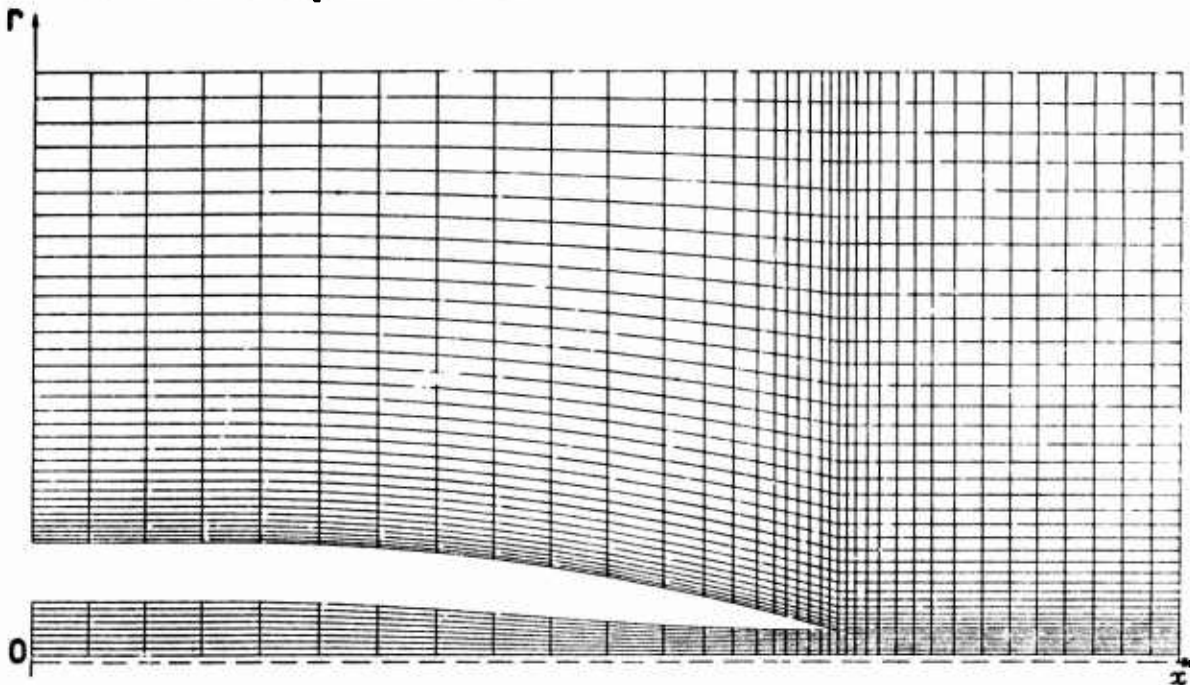

Fig.3 REPRESENTATION DU DOMAINE PHYSIQUE PAR UN MAILLAGE CURVILIGNE

2.4 Résolution numérique

On montre [1] que la formulation forte du problème
(équation (1) + conditions (7)-(10) est équivalente à la
formulation faible suivante :

Etant donnée l'intégrale :

$$(18) \quad \iint_{\mathcal{D}} \frac{1}{\zeta^2}\left(\frac{\partial \psi}{\partial x}\cdot\frac{\partial \varphi}{\partial x} + \frac{\partial \psi}{\partial z}\cdot\frac{\partial \varphi}{\partial z}\right) dx\,dz = 0$$

où ($\mathcal{D}$) représente soit ($\mathcal{D}_j$) soit ($\mathcal{D}_e$) et les
conditions (7) à (10), la formulation faible du problème
revient à chercher une fonction ψ remplissant
les conditions (7) à (10) et vérifiant (18) pour toute
fonction φ qui satisfait la condition :

$$(19) \quad \varphi = 0 \quad \text{sur} \quad AB, GFH, EFH \text{ et } DC$$

Les fonctions φ et ψ sont toutes deux de carré
sommable et admettent des dérivées premières, au sens
des distributions, de carré sommable (propriété 1)

Soit η_j une famille totale de fonctions test vérifi-
ant la condition (19) et la propriété 1. On définit
les fonctions ψ^k et φ^k à l'aide des relations
suivantes :

$$(20) \quad \psi^k = \sum_{j=1}^{k} \eta_j(x,z)\,\psi_j^k$$

$$(21) \quad \varphi^k = \sum_{j=1}^{k} \eta_j(x,z)\,\varphi_j^k$$

dans lesquelles k est le nombre de pavés, et φ_j^k
et ψ_j^k les valeurs des fonctions φ^k et ψ^k au
centre η_j du pavé hexagonal de rang j .

On choisit les fonctions test de la manière
suivante :

$\eta_i(x_i, z_i)=1$, x_i et z_i étant les coordonnées du
centre η_i du pavé hexagonal P_i ;

$\eta_i(x,z) = 0$ si x et z sont les coordonnées d'un
point situé à l'extérieur ou sur le contour du pavé
P_i ;

$\eta_i(x,z)$ est linéaire par morceaux par rapport aux
variables α et β si le point de coordonnées
(x,z) est intérieur à P_i ;

$\sum_{i=1}^{k}\eta_i(x,z)=1$ pour tout point de coordonnées (x,z)
appartenant à ($\mathcal{D}$).

Pour le calcul des valeurs de η_i, $\frac{\partial \eta_i}{\partial \alpha}$ et $\frac{\partial \eta_i}{\partial \beta}$
on divise chaque pavé P_i en six triangles (fig.4).
Le tableau de la fig.5 donne les valeurs cherchées à
l'intérieur de ces six triangles.

Fig.4b REPRESENTATION D'UN PAVE

DANS LE PLAN TRANSFORME

En remplaçant les fonctions φ et ψ dans
(18) par les expressions de φ^k et ψ^k respec-
tivement, on obtient :

$$(22) \quad \sum_{i=1}^{k}\sum_{j=1}^{k}\left[\iint_{\mathcal{D}}\frac{1}{\zeta^2}\left(\frac{\partial \eta_i}{\partial x}\cdot\frac{\partial \eta_j}{\partial x} + \frac{\partial \eta_i}{\partial z}\cdot\frac{\partial \eta_j}{\partial z}\right)\varphi_j^k\psi_i^k\,dx\,dz\right]=0$$

qui doit être vérifiée quelle que soit la fonction
φ^k , ce qui implique :

$$(23) \quad \sum_{i=1}^{k}\left[\iint_{\mathcal{D}}\frac{1}{\zeta^2}\left(\frac{\partial \eta_i}{\partial x}\cdot\frac{\partial \eta_j}{\partial x} + \frac{\partial \eta_i}{\partial z}\cdot\frac{\partial \eta_j}{\partial z}\right)\psi_i^k\,dx\,dz\right]=0 ,$$
$$\text{pour } j=1,2,\ldots,k$$

En posant :

$$(24) \quad a_{ij} = \iint_{\mathcal{D}}\frac{1}{\zeta^2}\left(\frac{\partial \eta_i}{\partial x}\cdot\frac{\partial \eta_j}{\partial x} + \frac{\partial \eta_i}{\partial z}\cdot\frac{\partial \eta_j}{\partial z}\right)dx\,dz ,$$

(23) s'écrit alors :

$$(25) \quad \sum_{i=1}^{k} a_{ij}\,\psi_i^k = 0 \quad , \text{pour } j = 1, 2, \ldots, k$$

On démontre [2] et [3] que la solution ψ^k du
système linéaire (25) converge vers la solution ψ
de (1) lorsque $k \to \infty$. Les coefficients
d'influence a_{ij} peuvent être exprimés dans le
plan (α , β) :

$$(26) \quad a_{ij}=\iint_{\widetilde{\mathcal{D}}}\frac{1}{\zeta^2}\left\{P\frac{\partial \eta_i}{\partial \alpha}\frac{\partial \eta_j}{\partial \alpha} - Q\left(\frac{\partial \eta_i}{\partial \alpha}\frac{\partial \eta_j}{\partial \beta}+\frac{\partial \eta_i}{\partial \beta}\frac{\partial \eta_j}{\partial \alpha}\right)+R\frac{\partial \eta_i}{\partial \beta}\frac{\partial \eta_j}{\partial \beta}\right\}d\alpha\,d\beta$$

où ($\widetilde{\mathcal{D}}$) est l'homologue de ($\mathcal{D}$) dans le plan
(α , β).
avec

$$P = \frac{1}{J}\left[\left(\frac{\partial x}{\partial \beta}\right)^2+\left(\frac{\partial z}{\partial \beta}\right)^2\right]$$

$$Q = \frac{1}{J}\left[\frac{\partial x}{\partial \alpha}\cdot\frac{\partial x}{\partial \beta} + \frac{\partial z}{\partial \alpha}\cdot\frac{\partial z}{\partial \beta}\right]$$

$$R = \frac{1}{J}\left[\left(\frac{\partial x}{\partial \alpha}\right)^2+\left(\frac{\partial z}{\partial \alpha}\right)^2\right]$$

	T_1	T_2	T_3	T_4	T_5	T_6
η_i	$1-\left(\frac{\alpha+\beta-m\varepsilon-n\varepsilon}{\varepsilon}\right)$	$1-\left(\frac{\beta-n\varepsilon}{\varepsilon}\right)$	$1+\left(\frac{\alpha-m\varepsilon}{\varepsilon}\right)$	$1+\left(\frac{\alpha+\beta-m\varepsilon-n\varepsilon}{\varepsilon}\right)$	$1+\left(\frac{\beta-n\varepsilon}{\varepsilon}\right)$	$1-\left(\frac{\alpha-m\varepsilon}{\varepsilon}\right)$
$\frac{\partial \eta_i}{\partial \alpha}$	$-\frac{1}{\varepsilon}$	0	$\frac{1}{\varepsilon}$	$\frac{1}{\varepsilon}$	0	$-\frac{1}{\varepsilon}$
$\frac{\partial \eta_i}{\partial \beta}$	$-\frac{1}{\varepsilon}$	$-\frac{1}{\varepsilon}$	0	$\frac{1}{\varepsilon}$	$\frac{1}{\varepsilon}$	0

Fig.4a REPRESENTATION D'UN PAVE

DANS LE PLAN PHYSIQUE

Fig.5 EXPRESSION DES FONCTIONS TEST

ET DE LEURS DERIVEES SUR UN PAVE

où J est le jacobien de la transformation $(\alpha, \beta) \Rightarrow (x, \imath)$

$$J = \frac{\partial x}{\partial \alpha} \frac{\partial \imath}{\partial \beta} - \frac{\partial x}{\partial \beta} \frac{\partial \imath}{\partial \alpha}$$

A partir de la relation (26) et du tableau de la figure 5 , le calcul des coefficients a_{ij} peut être effectué après avoir remarqué que les expressions qui les définissent ne sont pas nulles si et seulement si les pavés P_i et P_j ne sont pas disjoints. Il en est ainsi lorsque $\uparrow_j$ est l'un des six points voisins de $\uparrow_i$ ou $\uparrow_i$ lui-même.
Il en résulte plusieurs cas de calcul correspondant aux diverses positions relatives de P_i et P_j . On trouvera en [4] le détail de ces calculs.
Examinons maintenant la procédure suivie pour tenir compte des variations de ρ qui figure explicitement dans l'expression des coefficients a_{ij} comme le montre (26) et qui d'autre part est lié à la fonction de courant par la relation implicite (5) . Le calcul de ρ est effectué d'une manière itérative selon le schéma suivant :

supposons que ce calcul en soit rendu à la $n^{ème}$ approximation sur la frontière libre et à la $m^{ème}$ sur ρ , et que les solutions ψ_m^n et ρ_m^n aient été calculées ; on obtient d'abord ρ_{m+1}^n par la relation :

$$(27) \quad \rho_{m+1}^n = \left\{ 1 + \frac{\gamma-1}{2} M_{ij}^2 \left[1 - \frac{1}{(\rho_m^n)^2} \cdot \frac{G^2}{V_{ij}^{*2}} \right] \right\}^{\frac{1}{\gamma-1}}$$

avec

$$(28) \quad G^2 = \frac{1}{\imath^2} \left[\left(\frac{\partial \psi_m^n}{\partial x} \right)^2 + \left(\frac{\partial \psi_m^n}{\partial \imath} \right)^2 \right]$$

γ et ρ désignant respectivement le rapport des chaleurs spécifiques et la masse volumique de l'écoulement intérieur ou de l'écoulement extérieur.

Dans chaque triangle élémentaire on considère que G garde une valeur constante de même que ρ .
ψ_{m+1}^n est obtenu ensuite en résolvant le système linéaire (25) .
Les itérations sur ρ et ψ sont poursuivies jusqu'à convergence.

Remarque : En ce qui concerne la résolution de (25) il convient de souligner que la matrice des coefficients a_{ij} est définie positive, heptadiagonale à diagonale principale prépondérante ce qui permet d'appliquer les méthodes itératives classiques (S.O.R. par exemple) à la résolution de ce système linéaire.

2.5 Méthode de recherche de la frontière de glissement FH.

Cette méthode est une extension de la procédure utilisée pour l'étude des jets incompressibles [7 - 8]. Examinons tout d'abord les conditions qui doivent être satisfaites la long de FH.

En tout point M de cette frontière l'équilibre des pressions définie par la relation (16) doit être réalisé. Cette relation est équivalente à :

$$(29) \quad \left(\frac{V_j}{V_e} \right)_M = K = \left\{ - \left[\left(\frac{P_{ei}^2}{P_i^2} \right)^{\frac{\gamma_i-1}{\gamma_i}} \frac{A}{B} \left[1 + \frac{\gamma_i-1}{2} M_{ei}^2 \left(1 - \frac{V_{ei}^{*2}}{V_e^{*2}} \right) \right] - 1 \right] \frac{2}{(\gamma_i-1)M_j^2} + 1 \right\}^{\frac{1}{2}}$$

Considérons maintenant la fonction analytique $F = \lambda + i\mu$ qui effectue la représentation conforme de $(\mathcal{D}_j)$ sur un rectangle $(\mathcal{D}_j)$, de manière que sur les frontières du jet la condition $\mu = C^{te}$ soit assurée, alors que dans les sections d'entrée et de sortie on ait $\lambda = C^{te}$.

Soient $\mathcal{M}$ et θ le module et l'argument de $\frac{dF}{d\mathfrak{z}}$ $(\mathfrak{z} = x + i\imath)$. L'expression de la vitesse en tout point M de FH peut s'écrire :

$$(30) \quad V_{jM} = \frac{\mathcal{M}_M}{(\rho \imath)_M} \frac{d\psi}{d\mu}$$

Compte tenu de la condition d'équilibre (29) le module $\mathcal{M}_M$ doit satisfaire la relation :

$$(31) \quad \mathcal{M}_M = \frac{K (V_e)_M (\rho_j \imath)_M}{\frac{d\psi}{d\mu}}$$

Cette relation associe à la distribution des vitesses de l'écoulement extérieur le long de FH, un facteur $\mathcal{M}_M$ lié à la forme de la ligne de jet

et permet par conséquent, de dégager un schéma itératif dans la recherche de la position d'équilibre de FH qui est le suivant :

$$(32) \quad \left(\mathcal{M}_M \right)^{n+1} = \left[\frac{K (V_e)_M (\rho_j \imath)_M}{\frac{d\psi}{d\mu}} \right]^n$$

dans cette expression n est le numéro d'itération sur la forme du jet.

Ce schéma conduit à la séquence d'opérations ci-après :
Connaissant à l'itération n une forme approchée de FH, on calcule alors l'écoulement à l'intérieur des domaines $\mathcal{D}_j$ et $\mathcal{D}_e$; on en déduit la distribution des vitesses $(V_e)_M$ sur FH pour le domaine extérieur et d'une façon générale toutes les grandeurs intervenant au second membre de l'expression (31) .
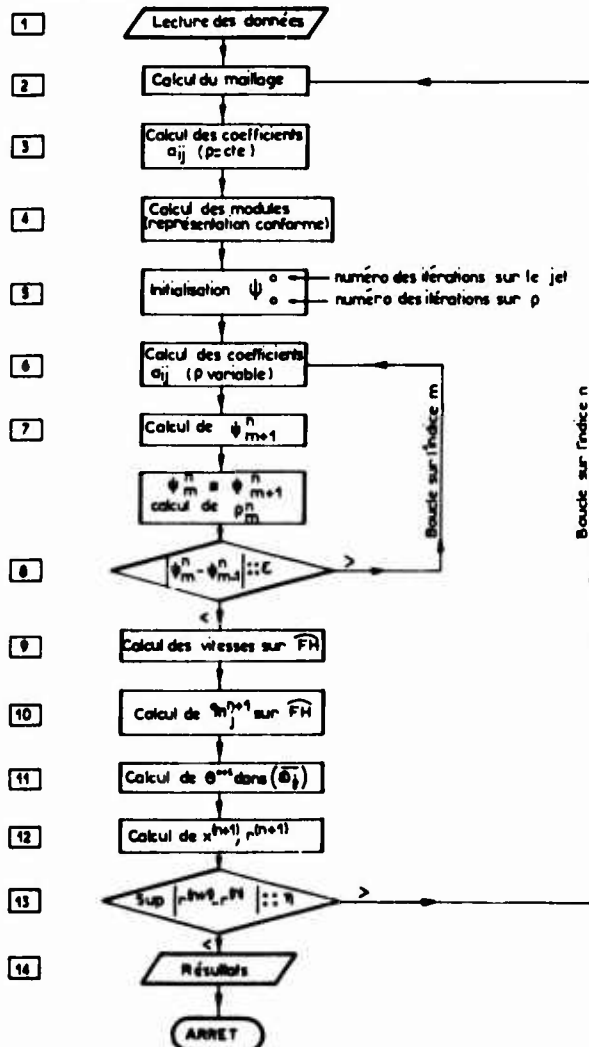

Fig 6 . Organigramme des opérations numériques

La relation (32) fournit alors la valeur de $(M_2)^{n+1}$
Il reste à déterminer tout d'abord l'argument
$(\theta_M)^{n+1}$ de la représentation conforme
(θ et $\text{Log}\,M$ sont des fonctions conjuguées) et
ensuite par retour au plan physique la forme
approchée du jet pour l'itération $n+1$.

On arrête le calcul, lorsque la condition suivante
est remplie :

$$\text{Max}_{(FM)}\ |\,z_M^{n+1} - z_M^n\,| < \eta$$

η étant de l'ordre de 0,001.

En général une dizaine d'itérations sont nécessaires
à partir de conditions initiales qui sont par
exemple un jet cylindrique droit.

L'enchainement des opérations numériques conduisant
à la résolution complète du problème se trouve
schématisé sur l'organigramme de la fig.6

3 - JET SUPERSONIQUE EN PRESENCE D'UN ECOULEMENT EXTERIEUR SUBSONIQUE OU TRANSSONIQUE

3.1 Jusqu'à présent, seules les situations
où l'écoulement interne engendre à la sortie de
l'arrière-corps un jet subsonique ont été examinées.
Dans les applications, le cas le plus fréquent
est toutefois celui où ce jet est supersonique et
provoque, spécialement lorsque l'écoulement interne
en sortie de tuyère est sous détendu, les effets
d'interaction avec l'écoulement externe les plus
marqués.

Le couplage qui s'établit alors en aval de
l'arrière-corps, a été examiné en s'inspirant
largement des travaux effectués par Young [9].

3.2 Procédure utilisée :

La solution assurant les conditions d'équilibre du
jet en présence de l'écoulement extérieur
(rappelées § 2) est obtenue selon le processus
itératif suivant :

On détermine tout d'abord le contour extérieur du
jet supersonique isobare issu de la tuyère interne
et détendu à la pression p_{ei} de l'écoulement
externe uniforme en amont de l'arrière-corps.

Ensuite, on calcule l'écoulement autour de l'obstacle
formé par l'arrière-corps, prolongé par le jet
considéré comme un corps solide. Ce calcul fournit
une répartition des pressions non uniforme le long
de ce contour qui est utilisée, au cours d'une
seconde itération, comme conditions aux limites
pour le calcul d'un jet non isobare, et le processus
est répété jusqu'à convergence du procédé. Cela
signifie ici, que la loi $z(x)$ définissant la
méridienne du jet ne change plus de façon significa-
tive à partir de l'itération n, l'écart

$$\text{Max}_{FM}\ |\,z^{n+1} - z^n\,|$$

étant inférieur à une valeur

η fixée à l'avance et qui est de l'ordre de 0,001.
Cette convergence est généralement obtenue au bout
de 5 à 6 itérations

3.3 Calcul du jet supersonique

La méthode utilisée pour définir la ligne de courant
frontière du jet supersonique est décrite de façon
détaillée Ref.[10].

L'écoulement interne étant supposé connu en particu-
lier, sur une caractéristique issue du Bord de
fuite de l'arrière-corps, les étapes du calcul de
l'écoulement supersonique aval à partir de ces do-
maines initiales sont les suivantes :

a) calcul de la détente centrée qui se produit
au Bord de fuite, lorsque l'écoulement interne est
sous détendu (le seul cas considéré ici) ;

b) calcul de l'écoulement en aval de cette détente
pour des conditions de pression imposées à la
frontière du jet par une loi connue $p(x)$, la
formation d'ondes de choc par focalisation
de caractéristiques d'une même famille issues de la
frontière du jet étant notamment traitée de façon
rigoureuse.

Toutefois, ce calcul est effectué sur une étendue
limitée, de manière à ne pas accroitre exagérément
le temps de passage sur ordinateur. En fait,
considérant que l'évolution au cours des itérations
successives de la structure du jet en aval du 1er
minimum de section qui apparait en x_m au delà
du Bord de fuite est sans effet sur la distribution
des pressions au contour de l'arrière-corps, pour
des raisons de simplicité, le jet a été arbitraire-
ment représenté pour $x \geqslant x_m$ par un cylindre.

Parmi les difficultés rencontrées au cours d'un tel
calcul, signalons celle qui se manifeste lors de la
détermination de la frontière du jet au voisinage
immédiat du Bord de fuite de l'arrière-corps.
Lorsque l'on néglige les effets de la viscosité, le
bord de fuite est un point d'arrêt pour l'écoulement
externe, lorsque $p_{ij}/p_{ia} \geqslant 1$, pour l'écoulement
interne lorsque $p_{ij}/p_{ia} \leqslant 1$ (condition de

Joukowski), au voisinage duquel la vitesse évolue
de façon extrêmement rapide.

En réalité, les effets de la viscosité, au niveau de
la confluence (qu'il y ait ou non décollement
de l'écoulement externe) entrainent une réduction
sensible de la pression en ce point, pression qui est
en fait significativement plus faible que p_{ia}.

Compte tenu de cette circonstance, la détente ini-
tiale du jet a été systématiquement calculée, pour
une pression de l'écoulement externe égale non pas
à p_{ia} mais à la valeur obtenue par
extrapolation linéaire de la pression calculée au
premier point du maillage, situé en aval du Bord de
fuite.

3.4. Calcul de l'écoulement externe

3.4.1 Méthodes et conditions de calcul :

Dans le cas où cet écoulement est partout subcritique
la méthode développée § 2 s'applique à toute
forme d'arrière-corps et permet en particulier
de s'affranchir des hypothèses restrictives de corps
élancés.

Par contre cette méthode n'est pas applicable au cas
où l'écoulement externe est transsonique, cas qui
couvre un domaine d'application extrêmement important
spécialement dans le cadre des études d'interaction
écoulements interne-externe relatives aux arrière-
corps.

C'est pourquoi, la mise en oeuvre d'une méthode des
petites perturbations transsoniques a été effectuée,
afin de disposer d'un moyen permettant une étude
préliminaire de ces phénomènes.

3.4.2 Calcul de l'écoulement externe par la métho-
de des petites perturbations transsoniques.

L'hypothèse de petites perturbations pour l'écou-
lement extérieur, soit

$$\left|\frac{V^x - V_{ei}^x}{V_{ei}^x}\right| \ll 1$$

conduit à des équations simplifiées décrivant le mouvement axisymétrique d'un fluide parfait compressible. L'écart par rapport à l'écoulement uniforme dépend, en ordre de grandeur, d'un paramètre τ caractéristique de la pente de la paroi ou de la ligne de glissement (supposée ici connue, et donc traitée comme une paroi). De plus dans le cas des écoulements transsoniques, le passage à la limite $\tau \mapsto 0$ conduit à une équation de type mixte si on fait tendre le nombre de Mach à l'infini vers l'unité, tout en maintenant le rapport $(1-M_{\infty}^2)/\tau^2$ d'ordre $O(1)$ (Ashley, Holt; and Landahl, Marten [11]).

En première approximation on trouve qu'il existe un potentiel de perturbation satisfaisant à l'équation mixte et non-linéaire :

$$\left[K_e - (\gamma_e+1)\frac{\partial \varphi}{\partial x}\right]\frac{\partial^2 \varphi}{\partial x^2} + \frac{1}{\tau}\frac{\partial}{\partial \tau}\left(\tau \frac{\partial \varphi}{\partial \tau}\right) = 0$$

et assujetti à la condition de glissement sur l'obstacle:

$$\lim_{\tau \mapsto 0} \tau \frac{\partial \varphi}{\partial \tau} = R \frac{dR}{dx}$$

et à l'infini au comportement asymptotique :

$$\lim_{x^2+\tau^2 \mapsto \infty} \varphi = 0$$

γ est le rapport des chaleurs spécifiques.
K est le paramètre de similitude transsonique, dont l'expression la plus courante est :

$$K = \frac{1 - M_{\infty}^2}{(M_{\infty}\tau)^2}$$

Les variables réduites sont définies par les relations suivantes :

$$\Phi = u_{e1}(x + \tau^2 \varphi) \quad ; \quad \tilde{\tau} = \tau \tau$$

Le rayon du corps ou la distance radiale de la ligne de glissement sont donnés par :

$$\tau_e = \tau R(x)$$

L'équation est résolue par une méthode de différences finies utilisant un schéma mixte tenant compte du type local de l'équation, ainsi :

lorsque $K - (\gamma+1)\frac{\partial \varphi}{\partial x} \geqslant 0$, l'écoulement est sub-

sonique et l'équation est de type elliptique ; on utilise des expressions centrées pour $\frac{\partial}{\partial x}$ et $\frac{\partial}{\partial \tau}$;

lorsque $K - (\gamma+1)\frac{\partial \varphi}{\partial x} < 0$, l'écoulement est su-

personique et l'équation est de type hyperbolique ; on utilise des expressions décentrées avancées pour $\frac{\partial}{\partial x}$.

Cette méthode conduit, pour les valeurs du potentiel sur une colonne $x = $ constante, à un système d'équations dont la matrice des coefficients est tridiagonale à diagonale dominante. La résolution est très rapide si on utilise un algorithme d'élimination directe. On peut introduire un facteur de relaxation ω voisin de 1,8 en subsonique et 0,9 en supersonique. Le plan est balayé itérativement jusqu'à convergence, celle-ci étant atteinte en pratique au bout de quelques centaines de cycles (400) pour un maillage non uniforme de 80 x 30 noeuds.

Comme dans l'article de Krupp et Murman [12] la condition de glissement est appliquée sur un petit cylindre proche de l'axe de symétrie. Lorsque la convergence est obtenue, le potentiel est interpolé linéairement aux mailles du réseau afin d'obtenir sa valeur $\varphi_e(x)$ sur le corps ou sur la ligne de glissement. Le coefficient de pression est alors calculé par la formule :

$$K_p = -\tau^2 \left[2 \frac{d\varphi_e}{dx} - \left(\frac{dR}{dx}\right)^2\right]$$

qui tient compte de la contribution dûe à la composante verticale de la vitesse, non négligeable en théorie des corps élancés.

Le contour extérieur du jet qui prolonge l'arrière corps et définit avec celui-ci la forme de l'obstacle auquel est appliqué la méthode de relaxation décrite, est évidemment donné par la méthode des caractéristiques lorsqu'il s'agit d'un jet nettement supersonique. Dans le cas où le taux de détente est faible $(P_{ij}/P_{\infty} \sim 2)$, ce qui correspond au cas d'un jet sonique ou faiblement supersonique, pour lequel les variations de section sont très petites, l'approximation d'un jet à section constante a été retenue.

4 - APPLICATIONS - COMPARAISON AVEC L'EXPERIENCE

4.1 - Configurations étudiées

Les formes géométriques externes des arrière-corps retenus sont représentées figure 7 où l'on trouvera également le tableau de cotes des méridiennes.

Cotes des arrière-corps I

$x=$	0	0,088	0,179	0,270	0,361	0,452	0,544	0,635
$\frac{x}{L}$	0,726	0,790	0,836	0,872	0,918	0,945	0,973	1
$\frac{r}{D}$	0,5	0,498	0,489	0,475	0,454	0,427	0,394	0,353
	0,306	0,269	0,241	0,217	0,185	0,165	0,145	0,124

II

$x=$	0	0,131	0,255	0,379	0,503	0,627	0,714	0,777
$\frac{x}{L}$	0,826	0,863	0,888	0,913	0,938	0,963	0,981	1
$\frac{r}{D}$	0,5	0,497	0,485	0,463	0,434	0,401	0,372	0,345
	0,319	0,297	0,281	0,265	0,248	0,230	0,218	0,208

L=longueur de l'AR-corps (partie évolutive)
D=diamètre maximal
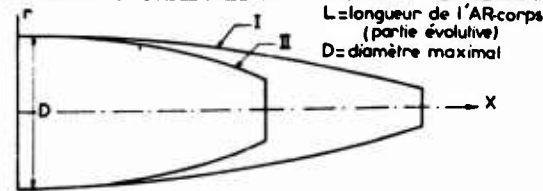
Fig.7 FORMES GEOMETRIQUES DES ARRIERE-CORPS ETUDIES

La configuration I est extraite d'une étude expérimentale présentée réf. [13]. Elle se caractérise par un élancement assez important et un rapport de troncature $(\tau_{min}/\tau_{maître\ couple} \simeq 0,25)$ assez faible.

De cette même référence ont été tirés les résultats d'essais effectués dans le tunnel transsonique de 8 pieds de Langley Field.

La configuration II, est l'une des configurations test, dite tuyère 10°, retenues par le groupe de travail Agard chargé sous la Direction du Pr Ferri de discuter les méthodes d'essais d'arrière-corps et de tuyères.

Les points expérimentaux correspondants proviennent des résultats d'essais effectués par l'A.E.D.C.

Les différents calculs entrepris, sont résumés dans le tableau ci-après où sont notamment définis les 2 paramètres qui caractérisent les conditions de calcul sur une configuration donnée :

- le nombre de Mach M_{∞} supposé uniforme en amont du maître couple.

- le taux de détente P_{ij}/P_{∞} de l'écoulement interne.

Dans tous les cas, les deux écoulements confluents possèdent des températures d'arrêt voisines de l'ambiante et une valeur de γ égale à 1,4 (air froid).

On notera que les calculs effectués par la méthode d'éléments finis (§ 2) ont été volontairement limités à une valeur maximale du nombre de Mach M_{∞} de 0,8 de manière à maintenir à un faible niveau les effets dûs à la limitation transversale du domaine physique de calcul.

Arrière-corps	M_∞	$\dfrac{P_{ij}}{P_\infty}$	Méthode de calcul
I	0,8	1,6 2 5	E. F. P. P. E.F. P.P.
	0,9	2 5	P. P. P. P.
II	0,8	2 7	P. P. E.F. P.P.
	0,95	2 7	P. P. P. P.

Nota: P.P. Méthode des petites perturbations transsoniques (§ 3)

E.F. Méthode d'éléments finis (§ 2)

4.2 - Présentation des résultats

4.2.1 Ecoulement externe subcritique

Les résultats sont présentés sous forme de courbes $K_p(\bar{X})$ et comparés à l'expérience fig. 8 et 9.

En ce qui concerne la configuration I, les méthodes de calcul utilisées conduisent à des résultats très voisins, assez bien recoupés par l'expérience sauf au voisinage du Bord de fuite, où des effets d'interaction visqueuse assez marqués apparaissent, les recompressions obtenues en l'absence de visco - sité étant sensiblement plus élevées que dans le cas réel pour les raisons indiquées en 3.3.

Fig. 8a ARRIERE-CORPS n° I
COMPARAISON CALCUL EXPERIENCE

Calcul ------ petites perturbations transsoniques
——— éléments finis

Fig. 8b ARRIERE-CORPS n° I
COMPARAISON CALCUL EXPERIENCE

Calcul ------ petites perturbations transsoniques
——— éléments finis

Fig. 8c ARRIERE-CORPS n° I
COMPARAISON CALCUL-EXPERIENCE

Calcul ------ petites perturbations transsoniques

Fig. 8d ARRIERE-CORPS n° I
COMPARAISON CALCUL-EXPERIENCE

Calcul ------ petites perturbations transsoniques
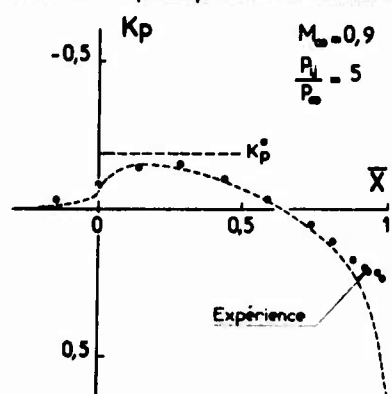
L'influence du taux de détente du jet et par suite de sa forme extérieure est très faible dans les calculs de fluide parfait.

L'expérience montre que cette influence se trouve en fait limitée au domaine s'étendant immédiate- ment en amont du Bord de fuite sur environ 15% de la longueur totale de l'arrière-corps où les écarts existant entre calcul et expérience sont importants.

En ce qui concerne la configuration II dont l'élancement est plus modéré, on notera pour $M_\infty = 0,8$ et $1 < \dfrac{P_{ij}}{P_\infty} \leq 2$ (fig.9a) qu'un désaccord

assez sensible entre théorie de fluide parfait et expérience apparait à partir du maximum de vitesse, désaccord qui s'accuse au fur et à mesure que l'on se rapproche du Bord de fuite.

Fig. 9a ARRIERE-CORPS n° II
COMPARAISON CALCUL EXPERIENCE

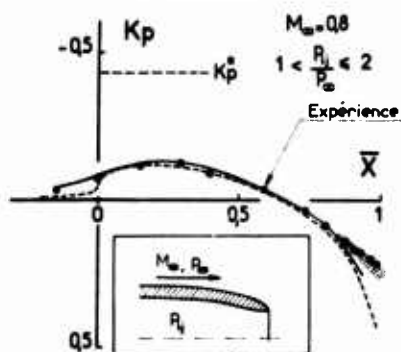Calcul ------ petites perturbations transsoniques

Fig 9b. ARRIERE-CORPS n° II
COMPARAISON CALCUL EXPERIENCE

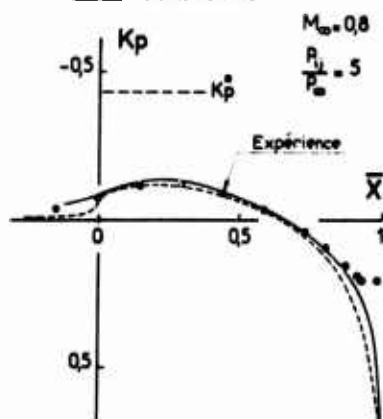Calcul ...... petites perturbations transsoniques
———— éléments finis

Fig. 9c ARRIERE-CORPS n° II
COMPARAISON CALCUL-EXPERIENCE

Calcul ------ petites perturbations transsoniques

Fig.9d ARRIERE-CORPS n° II
COMPARAISON CALCUL-EXPERIENCE
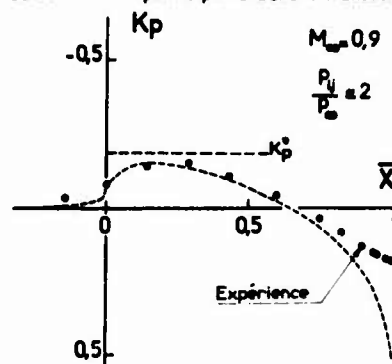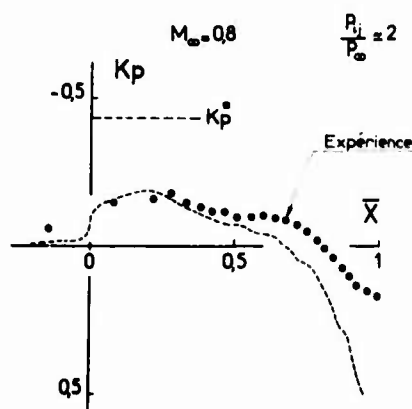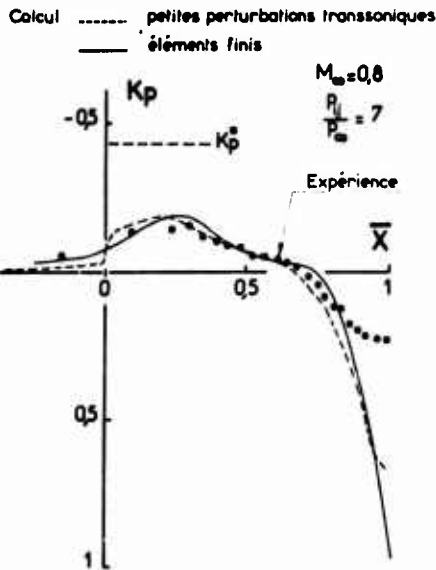
Calcul ------ petites perturbations transsoniques
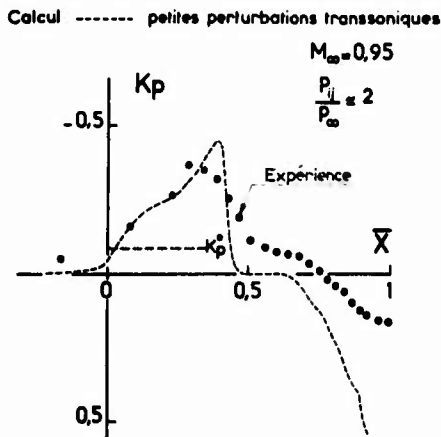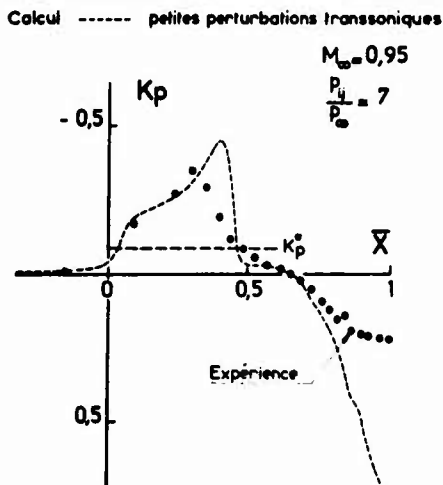
Si les résultats expérimentaux sont mieux recoupés en moyenne, pour la valeur $P_{ij}/P_{\infty} = 7$ du taux de détente (fig.9 b), cet accord est assez fortuit et provient essentiellement de la variation dans le sens d'une recompression accrue qu'a subi la distribution expérimentale $K_p(\bar{X})$ sous l'effet de l'interaction, alors que le calcul de fluide parfait n'est que très peu modifié lorsque P_{ij}/P_{∞} varie.

4.2.2 Écoulement externe supercritique

Pour des taux de détente assez faibles ($P_{ij}/P_{\infty} \sim 2$, fig. 9 c) , l'évolution des pressions pariétales dans la zone supersonique de l'écoulement peut être considérée comme correctement prévue par la théorie des petites perturbations transsoniques, de même que la position moyenne de l'onde de choc. Par contre des écarts sensibles avec l'expérience apparaissent en aval où la pression théorique correspondant à une configuration de choc droit est très supérieure à la pression expérimentale résultant du processus d'interaction couche limite onde de choc qui conduit à une solution du type choc oblique.

De même que dans le cas subcritique et contrairement à ce que l'on pouvait attendre, le calcul non visqueux ne met en évidence aucune influence sensible du taux de détente P_{ij}/P_{∞} (lorsque celui-ci passe de 2 à 7 environ) aussi bien sur la position de l'onde de choc que sur la forme de la recompression en aval, alors que l'expérience fait apparaitre un effet sensible en particulier sur la position de l'onde de choc.

4.2.3 Tentative de prise en compte de certains effets dûs à la viscosité.

La première constatation qui se dégage de cette confrontation il est vrai limitée, est que la nature visqueuse de l'écoulement joue un rôle essentiel dans les phénomènes d'interaction écoulement interne-externe.

Deux catégories de problème sont clairement mises en évidence:

a) d'une part, lorsque l'écoulement est supercritique, le phénomène d'interaction couche limite-onde de choc conduit à des recompressions en aval du choc très différentes de celles que prévoit la solution de fluide parfait ;

b) d'autre part, l'évolution de la couche limite au voisinage du point de confluence résulte d'un processus de forte interaction visqueuse qui modifie sensiblement la distribution des pressions calculées en l'absence de viscosité.

Nous n'examinerons pas ici le traitement des phénomènes d'interaction couche limite-onde de choc. Nous nous contenterons d'aborder la partie b) dans le cas où l'écoulement externe est subcritique.

La première démarche consiste à tenir compte des effets de déplacement des couches dissipatives, la loi d'évolution $\delta_1(x)$ étant obtenue par un calcul classique de couche limite. Cette expérience numérique a été entreprise dans le cadre de la méthode d'éléments finis exposée § 2.

La ligne de glissement qui sépare les écoulements interne et externe est alors remplacée par une bande étroite correspondant à l'effet de déplacement des lignes de courant frontière de ces écoulements, les conditions d'équilibre local (égalité des pressions) étant assurées en des points homologues, définis en première approximation par l'intersection de ces lignes de courant avec une normale à l'axe de symétrie.

Le calcul de l'épaisseur de déplacement $\delta_1(x)$ (fig. 10 a) a été effectué, en utilisant la méthode intégrale développée par Green et Alii [14] qui permet d'obtenir δ_1 à la paroi de l'arrière-corps et le long de la frontière du jet.

L'application de cette technique de calcul à la configuration II, pour un nombre de Mach $M_{\infty} = 0,8$

et un taux de détente $P_{ij}/P_{\infty} = 7$ est présentée fig.11, le nombre de Reynolds R_D étant égal à 10^6 et l'épaisseur initiale $\left(\delta_1/D\right)_{X=0}$ de l'ordre de 2%.

On observe comme prévu, une légère diminution des vitesses sur l'obstacle, mais pas d'amélioration significative de la forme de recompression au voisinage du Bord de fuite. Le calcul classique de couche limite conduit donc à une estimation incorrecte de la variation de δ_1 dans cette région . Pour s'en convaincre, il suffit de se reporter à la fig. 10 b qui montre à grande échelle la situation dans le plan physique de la frontière des écoulements interne et externe décalée de l'épaisseur δ_1 (x) calculée(courbe a). Cette courbe présente un point anguleux très prononcé et impose donc un point d'arrêt dans le calcul de fluide parfait associé.
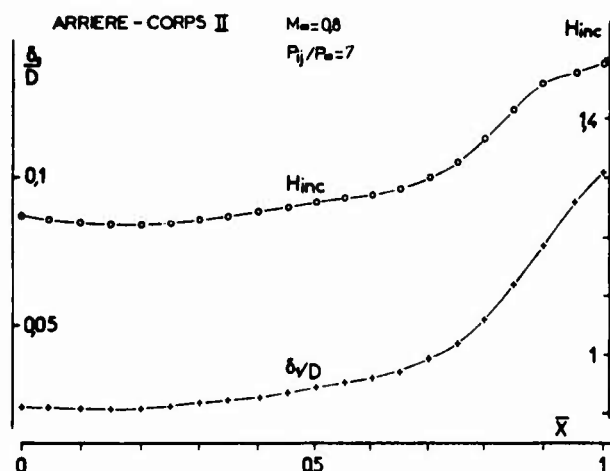
Fig 10a. EVOLUTION DES COUCHES LIMITES CALCULEES
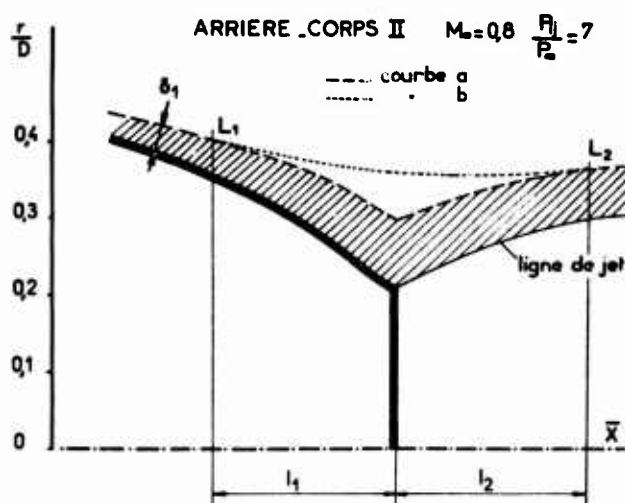
Fig 10 b : Représentation de l'effet de déplacement $\delta_1(\bar{X})$ dans le plan physique

Le traitement rigoureux de l'écoulement visqueux au voisinage du point de confluence est actuellement un problème ouvert que l'on ne peut traiter d'une manière exacte dans le cadre des équations classiques de la couche limite. A titre de palliatif, Taguirov (communication privée) a proposé une méthode empirique permettant de représenter l'effet de déplacement au voisinage du point de confluence d'une manière approchée inspirée par l'expérience.

Le domaine concerné peut être subdivisé en deux régions d'étendue respective ℓ_1 et ℓ_2 (figure 10 b) situées de part et d'autre du Bord de fuite.

L'origine L_1 de la première coïncide sensiblement avec l'apparition d'une forte croissance de la pente $d\delta_1/dx$ (fig. 10 a), éventuellement provoquée par le décollement de la couche limite. Elle peut être définie de façon plus précise en se fixant une valeur convenablement choisie du paramètre

$$\xi = \frac{\delta_1}{\gamma M^2} \frac{d \log P}{dx} \qquad (\xi = 0,014)$$

La seconde région ℓ_2 , est celle où se produit la confluence des couches dissipatives des écoulements interne et externe ; elle inclut, lorsqu'il existe un décollement amont, la zone de recollement de la couche limite de l'écoulement externe sur le jet. Les deux principaux paramètres qui régissent le phénomène de confluence sont donc ξ et ℓ_2/ℓ_1.

Taguirov propose de retenir la valeur $\ell_2/\ell_1 = 1$ et de représenter l'évolution $\delta_1(x)$ entre L_1 et L_2 par un polynôme de lissage assurant la continuité des pentes en L_1 et L_2 (courbe b fig. 10 b).

Les calculs effectués en utilisant cette règle sont représentés fig. 11.

Fig. 11 ARRIERE-CORPS n°II
COMPARAISON CALCUL EXPERIENCE

$$M_\infty = 0,8 \qquad \frac{P_j}{P_\infty} = 7$$

Calcul éléments finis fluide parfait
- .... sans effet de déplacement ($\delta_1(x)$)
- ———— avec effet de déplacement
- — — — lissage au bord de fuite
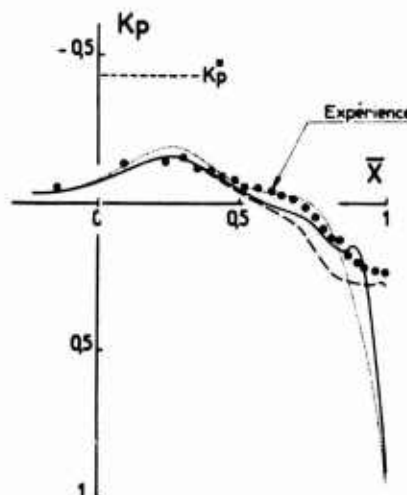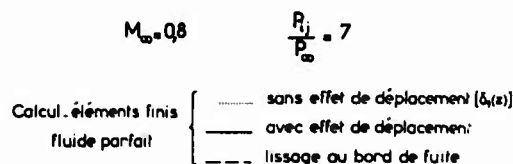
La courbe $K_p(\bar{X})$ correspondante, bien qu'elle ne coïncide pas avec les points expérimentaux présente toutefois une image assez réaliste de l'évolution réelle.

La mise en oeuvre pratique d'une telle méthode, nécessiterait bien entendu un nombre d'expériences numériques beaucoup plus important, assorti d'une analyse expérimentale détaillée permettant notamment de fixer avec plus de précision les valeurs des paramètres ξ et ℓ_2/ℓ_1.

5 - CONCLUSION -

Les résultats présentés ne constituent qu'une étape d'un programme plus général d'étude des phénomènes d'interaction écoulements interne - externe.

Les méthodes de calcul décrites permettent de traiter les problèmes de confluence dans le cadre d'une théorie de fluide parfait, pour des écoulements externes irrotationnels subsoniques ou transsoniques.

Dans le cas où l'écoulement externe est subsonique, la technique d'éléments finis proposée permet de

prendre en compte des formes géométriques d'arrière corps qui peuvent être complexes.

La procédure itérative utilisée, a conduit, dans le cadre des applications envisagées, à la convergence de la solution au bout d'un nombre d'itérations limité.

La comparaison des résultats obtenus avec l'expérience a mis en évidence la nature essentiellement visqueuse des phénomènes d'interaction écoulements interne - externe.
La prise en compte des effets de déplacement de la couche limite par des moyens traditionnels, ne conduit pas à des résultats satisfaisants, le problème essentiel demeurant la prévision de ces effets au voisinage du Bord de fuite aussi bien en amont qu'à l'aval. Faute d'une théorie parfaitement établie, permettant de décrire les phénomènes dissipatifs au niveau de la confluence, la méthode semi-empirique de lissage proposée par Taguirov semble devoir apporter une solution provisoire, à condition toutefois d'améliorer à partir de données expérimentales les divers critères qu'elle met en jeu.

Sur le plan des objectifs de recherche prévus à court et moyen terme nous signalerons :

- l'extension de la méthode d'éléments finis au cas où les écoulements confluents sont rotationnels, de manière à décrire de façon plus réaliste et plus précise ce phénomène et à introduire par la suite des techniques de calcul du type double couche pour représenter les effets dissipatifs ;

- l'amélioration de la prévision des effets d'interaction couche limite - onde de chocs ;

- à plus long terme le calcul complet du phénomène de couplage écoulement dissipatif écoulement de fluide parfait.

REFERENCES

1. Lions L., Magenes E., "Problèmes aux limites non homogènes et applications", Dunod, Paris, 1968.

2. Mikhlin S.G., "Variational Method in Mathematical Physics," Pergamon Press, Elmsford, N.Y., 1964.

3. Temam R., "Analyse Numérique," Collection Sup. Armand Colin, 1970.

4. Bellevaux Cl., "Oscillation propre d'un Bassin Tournant. Courant Induit par le Vent sur un Bassin", N° AO 4407, Thèse de doctorat d'Etat, Université de Paris, France, 1970.

5. Bellevaux Cl and Maille M. "Oscillations libres d'un Bassin en Rotation," Communication au 3ème Congrès International sur les Méthodes Numériques en Mécanique des Fluides. Paris, July 1972. A paraitre aux éd. Springer, Berlin.

6. Bellevaux Cl. and Maria-Sube R., "Détermination de lignes de Jets dans des Ecoulements Rotationnels Axisymétriques, 2ème partie : Résolution Numérique. J. Mécanique 11 (1972).

7. Maria-Sube R., "Résolution de problèmes de jets rotationnels de révolution," n° AO 8103, Thèse de Doctorat d'état, Université de Paris VI, France, 1972.

8. Maria-Sube R., "Numerical Solution to Free Surface Axisymmetric Rotational Flows," J. Computational Phys. 16, No 2 (1974) 127 - 149.

9. Young C., "A Theoretical Investigation of Supersonic Jets in Subsonic Flow Fields," RAE Technical Report 72 181 - ARC 34 318, Sept. (1972).

10. Diringer P., "Détermination par la méthode des caractéristiques d'écoulements supersoniques associés à une loi de pression donnée," La Recherche Aérospatiale n° 130 - 1969.

11. Holt A. and Marten L., "Aerodynamics of wings and Bodies," Addison - Wesley Publishing Co, Reading Mars 1965.

12. Krupp J.A. and Murman E.M., "Computation of Transonic Flows past lifting airfoils and slender Bodies," AIAA Journal, vol 10, n° 7 (1972).

13. Henry Jr B.Z. and Cahn M.S., "Pressure distributions over a series of related afterbody shapes as affected by propulsive jet at transonic speeds," NACA RM 456 K 05, 1957.

14. Green J.E., Weeks D.J., Brooman J.W.F., "Prediction of turbulent boundary layers and wakes in compressible flow by a lag-entrainment method. RAE - TR 72 231 (1973).

"LOW SPEED INJECTION EFFECTS ON THE AERODYNAMIC PERFORMANCE AT TRANSONIC SPEED"*
by
Renzo Piva**

Aerospace Laboratory, New York University
and
Aerodynamic Institute, University of Rome

SUMMARY

The problem concerning the possible reduction of the transonic drag for a high speed airplane has been studied to enhance the aerodynamic performance when, at low altitudes, the drag must be minimized.

Attention has been focused on decreasing the drag forces on the aft portion of the vehicle.

An experimental investigation has been conducted to determine the effect, on afterbody drag, of the injection of a small amount of air spilled from the propulsive system, having low stagnation pressure, in the rear of the model. The purpose of this injection is to avoid overexpansion of the flow and to increase the average pressure on the aft section.

The alteration of the external transonic flow field in the region of the shock-boundary layer interaction is the basic concept.

The main problem to be investigated is where the injection is most effective and the amount of air required to avoid downstream reattachment. The present work describes some results of such an investigation.

The required amount of air was relatively low, because of the high sensitivity of the interaction region to any small change in the flow regime.

LIST OF SYMBOLS

C_p = pressure coefficient

C_D = drag coefficient

$\dot{m}_j$ = injection mass flow

$\dot{m}\,eq$ = equivalent mass flow through the body frontal area

M = Mach number

M_∞ = freestream Mach number

s = longitudinal coordinate along the body

A = body frontal area

$A_{(x)}$ = body trasversal area

x = longitudinal coordinate along the test section

ξ = nondimensional axial location of maximum diameter

Subscripts

T = Total

A = Afterbody

F = Forebody

1. INTRODUCTION

The problem concerning the possible reduction of the drag for a high speed airplane flying at low altitudes in transonic flow regime has been studied.

At transonic speeds and high Reynolds numbers pressure drag predominantes and is usually concentrated in the afterbody region, due to the local formation of shocks; then to reduce the total drag, attention must be focused on decreasing the drag forces on the aft portion of the vehicle. An experimental investigation has been conducted to determine the effect, on afterbody drag, of the injection of a small amount of air, spilled from the propulsive system, having low stagnation pressure, in the rear of the model. The purpose of this injection is to avoid overexpasion of the flow and to increase the aver-

age pressure on the aft section.

It is possible thus to enhance the aerodynamic performance, with a negligible loss in the propulsion stream, when, at low altitudes, the drag must be minimized.

The basic concept is to alter the external transonic flow field in the region of the shock-boundary layer interaction.

In the region of the afterbody the flow becomes locally supersonic and therefore overexpands. It must then become subsonic by passing through a shock wave and thus, drag is generated. The extent of the overexpansion and of the subsequent shock is reduced if the pressure rise across the shock separates the boundary layer and produces upstream effects.

To reduce transonic drag, it appears then promising to induce a boundary layer separation, by injecting a small amount of low velocity air near the wall, which causes the boundary layer profile to be similar to a profile near the separation region.

The main problem to be investigated is where the injection is most effective and the amount of air required to avoid downstream reattachment. The present work describes some results of such an investigation. For the present preliminary studies, an axisymmetric model was used, as representative of an airplane configuration following the equivalent area rule concept that has been shown to be valid in transonic flow for determining the drag of a complete configuration. Following this equivalence the drag reduction on an axisymmetric configuration can be related to that on a three-dimensional body.

2. DESCRIPTION OF THE EXPERIMENTAL EQUIPMENT

A transonic blowdown type wind tunnel facility at New York University Aerospace Laboratory was used in the present investigation.

The slotted area was 12% of the total wall area and the slots discharged into a surrounding constant pressure chamber. With this percentage it was possible to obtain a uniform Mach number over approximately one test section diameter |Ref. 1|.

Since the present investigation was concerned with the base flow region, in order to avoid large wall effect, the model was mounted on a central body concentric with the test section.

The additional advantage of the present arrangement is the possibility of simulating a wide range of Reynolds numbers by varying the pressure and by artificially thickening the boundary layer. In this manner a portion of the complete flow fiel around a given body can be accurately simulated without having to test the entire shape, and it is possible to obtain the necessary scaling to achieve complete similarity to the real flight conditions.

In fact, the boundary layer shock interaction phenomenon is very sensitive to the boundary layer thickness, velocity profile, and transition point location, relative to the interaction region, besides the unit Reynolds number |Ref. 2| and the potential flow (i.e., the shock strength). This is more pronounced when a large merged separated region prevails after the shock. However, the scaling effects and similarity with the real flight conditions are not crucial here since only a comparative investigation of the flow field with and without injection was the primary purpose of the investigation.

Two models with different geometry were tested to provide two different types of base flow separation.

Model I with a small streamwise cervature and model II with a large streamwise curvature.

The two models give a different basic flow field when injection is not present. In the first one the separated flow after the shock reattaches downstream, in the second the flow after the main shock is completely separated.

The pressure was measured along the bodies at the locations of the pressure taps. The pressure distribution on the slotted sleeve and on the tunnel walls was also measured. The infinity conditions were determined with pitot probes before and after the test section.

The base injection was effected by 12 longitudinal slots .032 inches wide along the models at their base. Different injection lengths and positions were obtained by closing part of the slots. The pressure in the model chamber can be controlled to have different subsonic injection velocities.

3. DESCRIPTION OF THE EXPERIMENTS AND RESULTS

The flow field on the afterbody portion of a vehicle flying at transonic speed is mainly controlled by the shock boundary layer interaction phenomenon. The main transonic shock induces a boundary layer separation and the consequent flow field structure is strongly dependent on the slope of the afterbody and on the main stream conditions. A local low speed injection may greatly modify the flow field, acting as a change in the previous two parameters. The basic no-injection flow field is analogous to the two-dimensional case |Refs. 2, 3, 4|. Schlieren photographs and explanatory sketches for the two experimental models are shown in Figs. 1 and 2. The low speed separated region spreades the shock in many compression waves near the wall giving rise to a lambda shock followed by a small supersonic region ("supersonic tongue").

The shock induced separation forms a local bubble, and the reattachment point
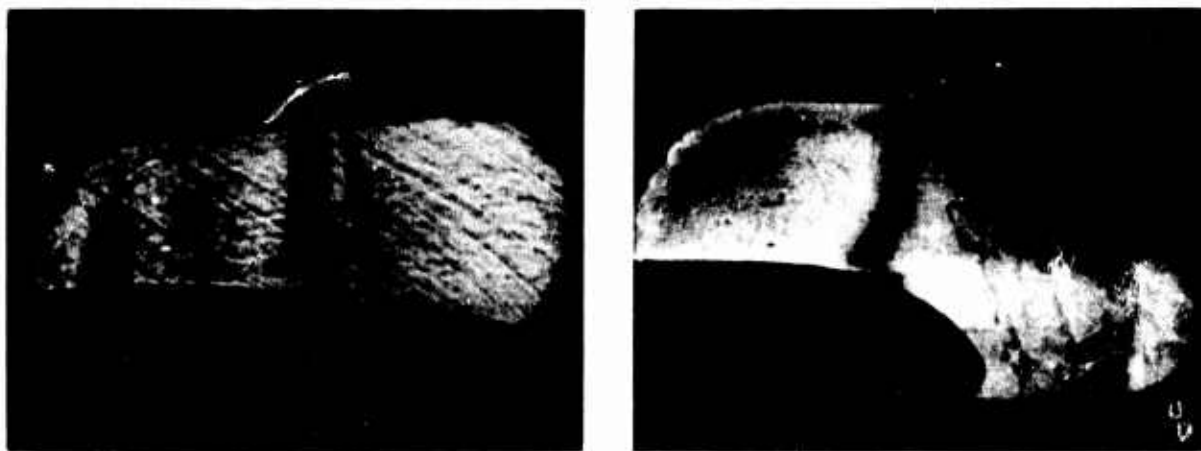
a)   b)

Fig. 1 Schlieren photographs for models I and II
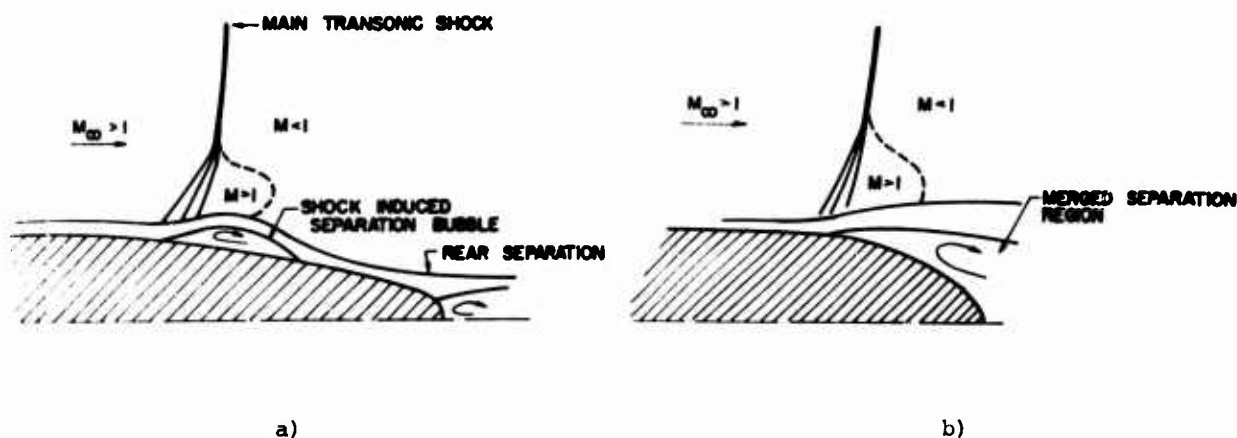
a)   b)

Fig. 2 Flow Field Sketches for Model I and II

moves downstream as the strength of the shock increases. A second rear separation may occur, because of the adverse pressure gradient, in the subsonic flow approaching the end point of the body (Fig. 1a). This rear separation strongly depends on the local pressure gradient and on the history of the boundary layer (i.e., transition, boundary layer thickness and profile). For large curvature bodies or large boundary layer thicknesses, the two separated regions may interact and merge producing an amplification of the effects of the disturbance at the foot of the shock (Fig. 2b). The pressure distributions (Fig. 3) confirm qualitatively the illustrated flow field models and show in particular, in the subsonic region before the end point, a recovery of pressure for Model I and a large separated region, beginning from the shock, for Model II.

Low speed normal injection of mass flow through the slots of the models (in the boundary layer shock interaction region) results in a modification of the boundary layer conditions and the model contour, and as a consequence in a change of the flow field configuration. More specifically the injected mass flow has three effects:

a) The injected mass acts as an obstruction that induces the separation of the boundary layer and consequently induces a shock modifying the transonic basic shock system.

b) The changed boundary layer conditions and in particular, velocity profile and thickness modify the separated regions behind the shock.

c) The equivalent body shape which is a function of the mass injected, changes the main transonic shock position in order to recover to the same end pressure.

Different combinations of the three effects a, b, and c, give rise to different flow fields, that can be represented by two flow field schemes. They are illustrated by Schlieren photographs for the two experimental models (Figs. 4 and 5) and explanatory sketches (Fig. 6).

The boundary layer separates because of the normal injection and induces a shock. Depending on the initial station of the injection the shock moves upstream reducing the supersonic region and so increasing the average pressure on the basic part of the body
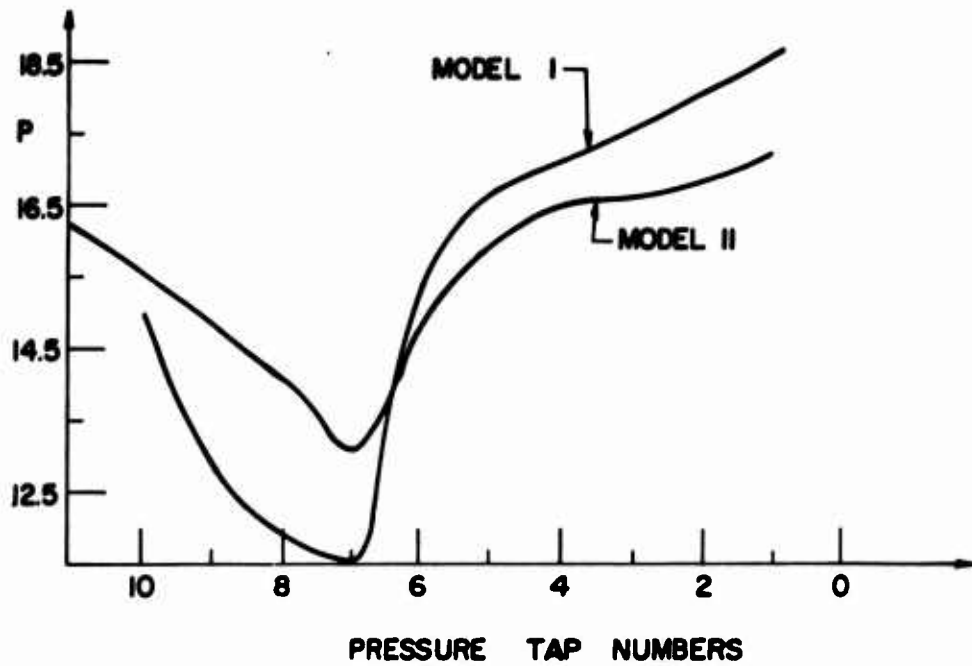
Fig. 3 Typical Pressure Distribution without Injection for Model I and II
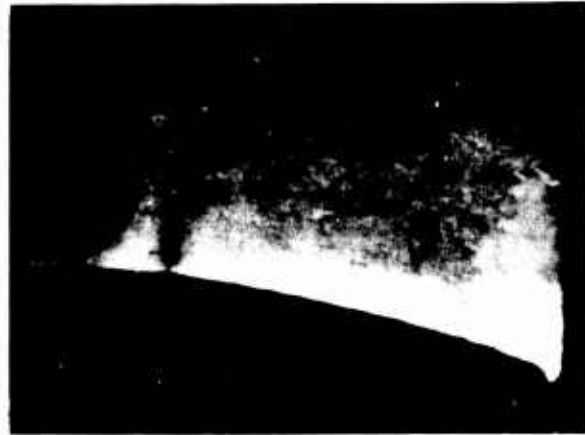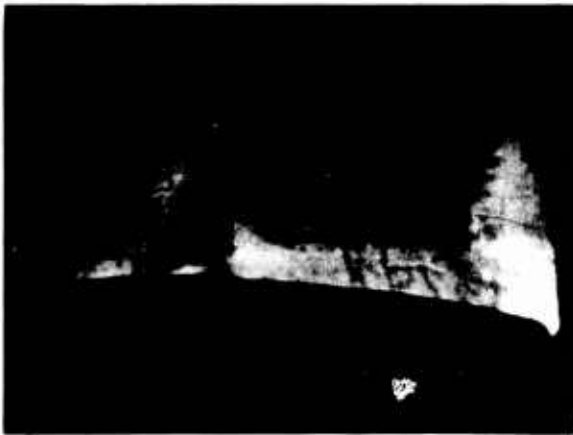
Fig. 4 Schlieren photographs for model I with injection
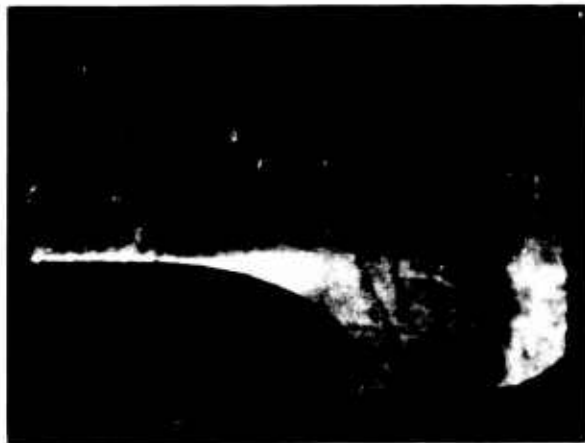
Fig. 5 Schlieren photographs for model II with injection
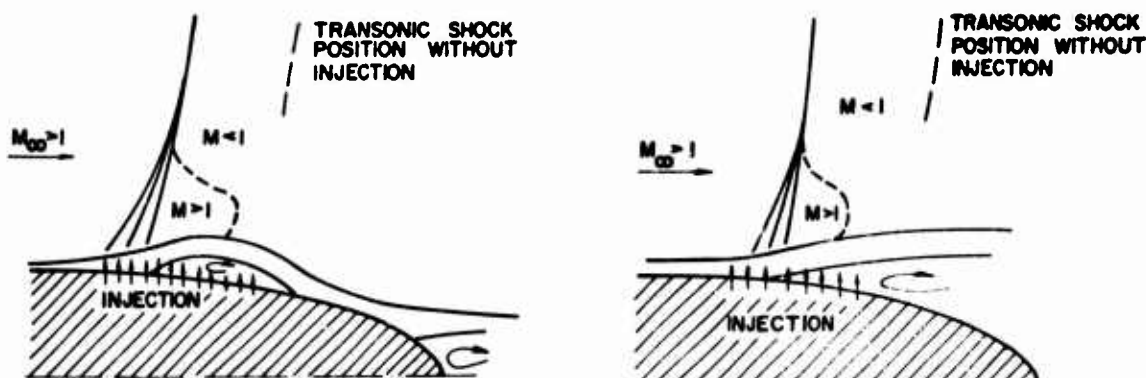
Fig. 6 Flow Field Sketches for Model I and II with Injection

(Fig. 6a). The shock is the main normal transonic shock if the position is consistent with the end pressure to be reached. The main shock can move upstream with respect to the no injection position if the flow is separated behind the shock so that the pressure recovery is reduced. This configuration has been obtained for Model II (large streamwise curvature) or for Model I when the injected mass flow is large.

If the injection is initiated too far upstream or the mass flow is not sufficiently large such that the flow is not completely separated, the shock induced by the injection must be an oblique shock, because a normal shock would not be able to match the end pressure. After the obblique shock, the flow being still supersonic, reattaches producing an expansion followed by the main transonic shock (Fig. 6b). The position of the shock is, also in this case, determined by the end pressure recovery that is fixed by the separation and the mass flow injected. Different types of separated regions may exist after the main shock depending on the boundary layer conditions and the strength of the shock. Also in this case, the presence of the oblique shock reduces the Mach number from the initial injection station on and therefore the average pressure on the afterbody increases.

The recovery of pressure on the afterbody with injection is now generally lower because the mass injected and the separated region (s), amplified or generated by the injection, prevent the flow from decelerating in this region. The pressure increase due to the reduction of the supersonic region length is generally larger than the loss of recovery on the end of the body. A lower drag is therefore obtained. Typical pressure distributions are shown in Fig. 7 e 8 for the two cases compared with the corresponding
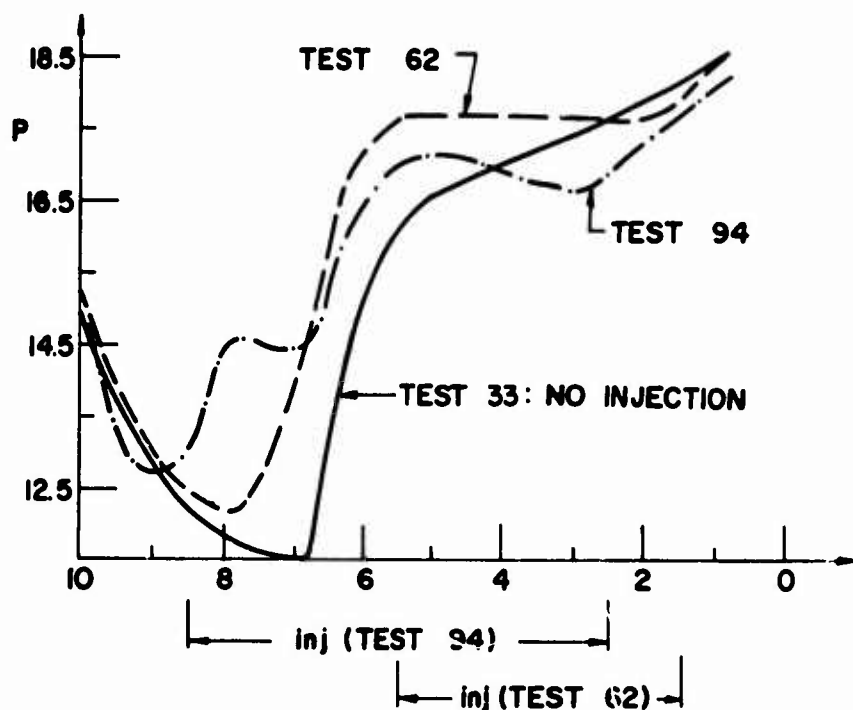
Fig. 7 Typical Pressure Distribution for Model I with Injection
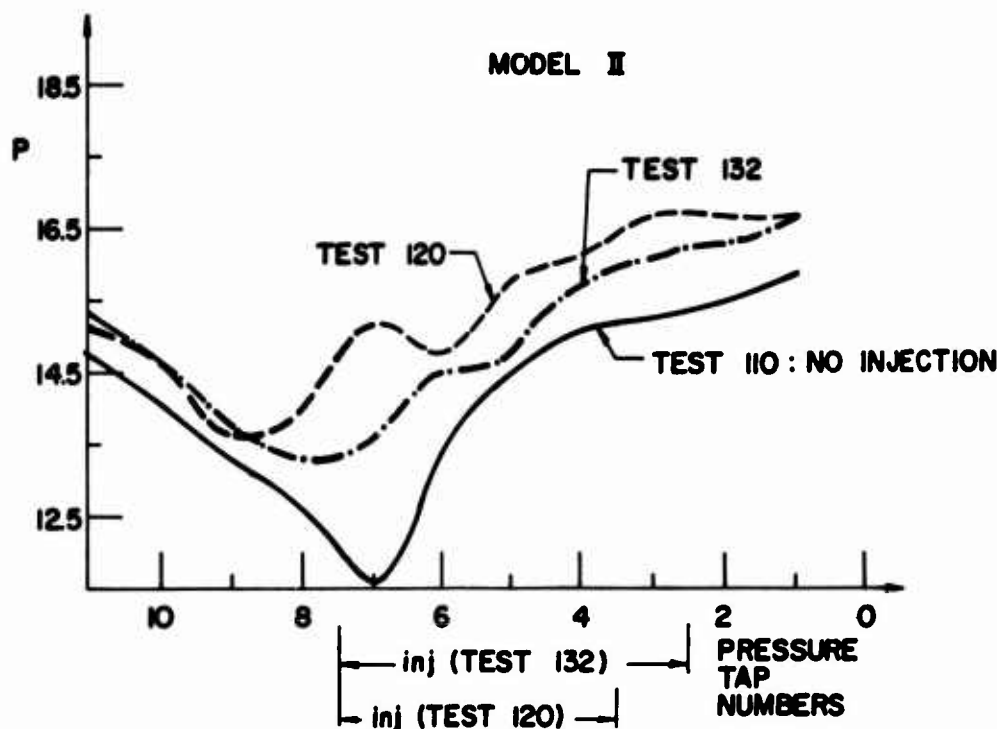
Fig. 8 Typical Pressure Distribution for Model II with Injection

no injection case, the complete series of results for various injection conditions and for the two experimental models are reported in |Ref. 1|

The pressure coefficient distributions on the two experimental models were measured for different values of the following parameters:

a) Extension and location of the injection region

b) Mass flow injected and consequently velocity of injection

c) M_∞ and upstream conditions

The values of these parameters are shown in the diagrams corresponding to each experimental case.

The pressure distribution on the model is particularly sensitive to the injection location. A comparison of the pressure distribution results with different injection extension and location but at the same M_∞ and injection flow rate is presented in Fig. 9. A comparison of the pressure distribution results with different injection rates but fixed injection rates but fired injection location and M_∞ is shown in Fig. 10.

A few results for different M_∞ while maintaining the same injection flow rate and injection position are shown in Fig. 11. An increase in the free stream Mach number moves the main shock downstream and the flow field is qualitatively the same.

The nominal test conditions for the present experiment were a stagnation pressure of 30 psia and ambient air temperature (520°R). This resulted in a local Reynolds number of the order of 10^6/ft.

4. DISCUSSION OF THE RESULTS

The pressure distributions obtained from the experiments show in general that with an appropriate injection, the supersonic region is reduced. Consequently, the pressure is locally higher, but also the recovery on the end of the body is lower because of the larger separated region and the injected mass flow. The two effects counteract each other, hence the total force on the afterbody must be calculated to give a representative parameter of the effectiveness of the injection in the various cases. The afterbody drag coefficient

$$C_{DA} = \int_o^{x_F} \frac{C_p(x)A'(x)dx}{A}$$

has been calculated in finite elements from the pressure distribution measured.

The percent form drag reduction due to the afterbody injection on a typical flight vehicle at transonic speed was determined by calculating the vehicles total drag,
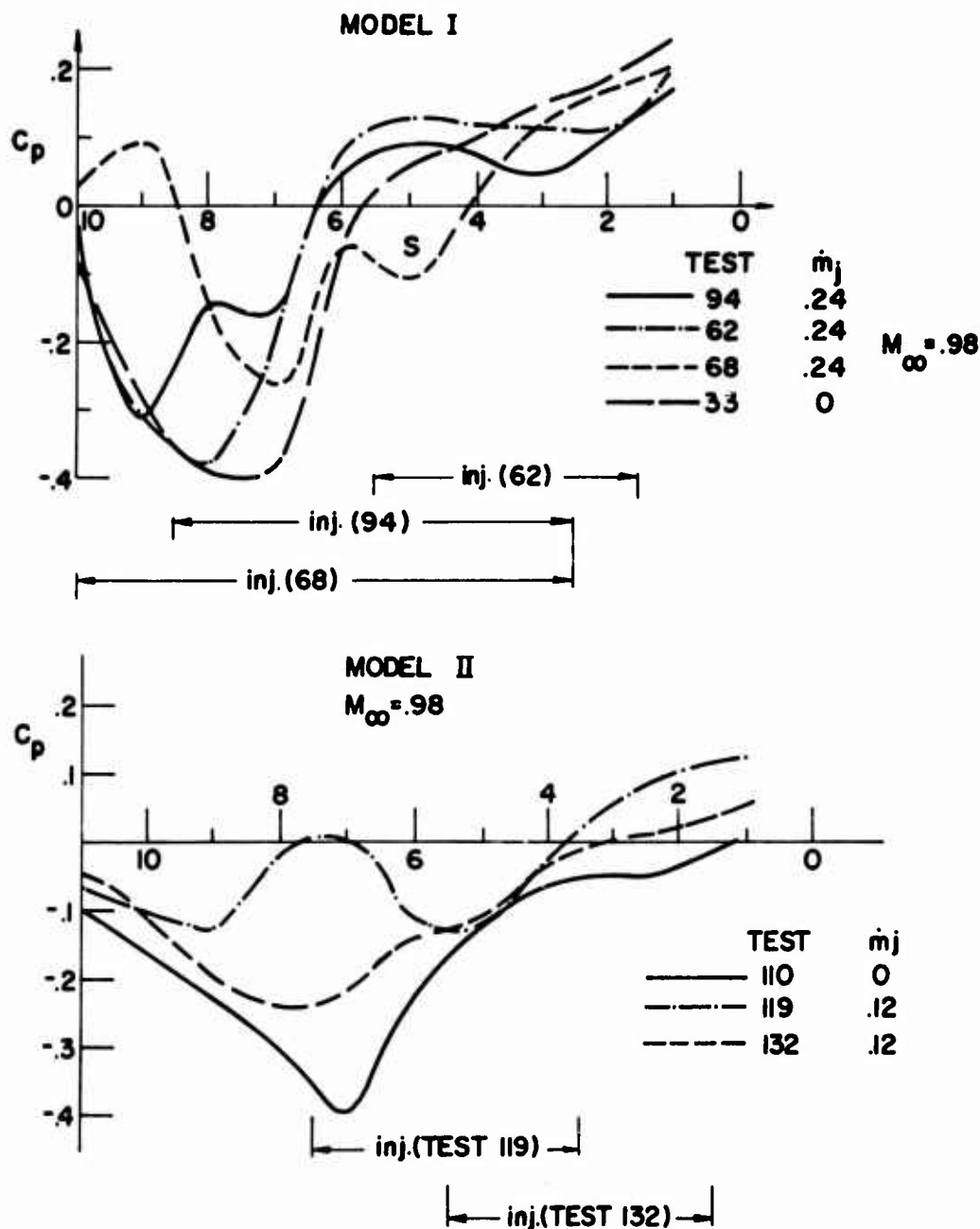
Fig. 9 Pressure Coefficient Distributions for Different Extensions and Locations of the injection Region

i.e., forebody and afterbody, with and without injection.

The forebody form drag coefficients were taken from |Ref. 5|, while the afterbody drag was determined for the present two configurations without injection. The difference in drag coefficient with afterbody injection for some of the more interesting conditions and some results are presented in Fig. 12. For the small curvature afterbody a negative form drag can be obtained, while for the large curvature afterbody the net form drag is nearly zero, i.e., the forebody drag is canceled by the afterbody force. Also the skin friction drag is consistentally reduced with injection due to the separation flow being in the upstream direction. No estimate of this effect was made here.

From a technical point of view it is interesting to express the injected mass flow as a function of the equivalent mass flow (at free stream conditions) through the frontal area of the model.

The correlation presented in Fig. 13 shows that the percentages necessary to obtain sensible changes in the flow field and large reductions of the drag, are very low and suitable for practical applications. The drag penalty due to the injection momentum loss is that due to the injection momentum component normal to the axis which is lost while the axial component is retained. This drag penalty is proportional to $(1 - \cos \delta_j)\dot{m}_j V_j$ and is very small compared to the net form drag.

5. CONCLUSIONS

The problem concerning the reduction of drag for an airplane at transonic speed,
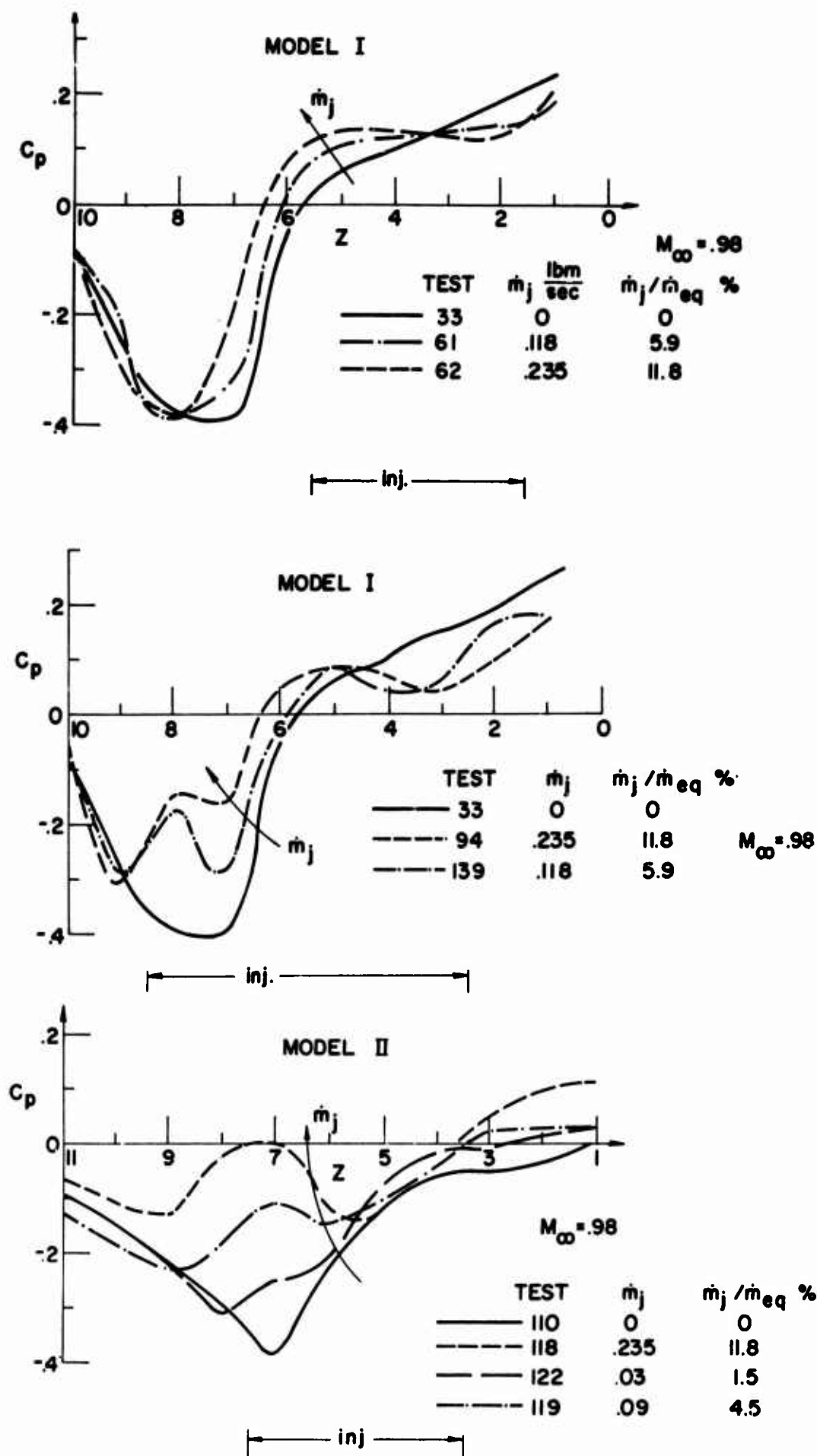
Fig. 10 Pressure Coefficient Distributions for Different Injection Mass Flows
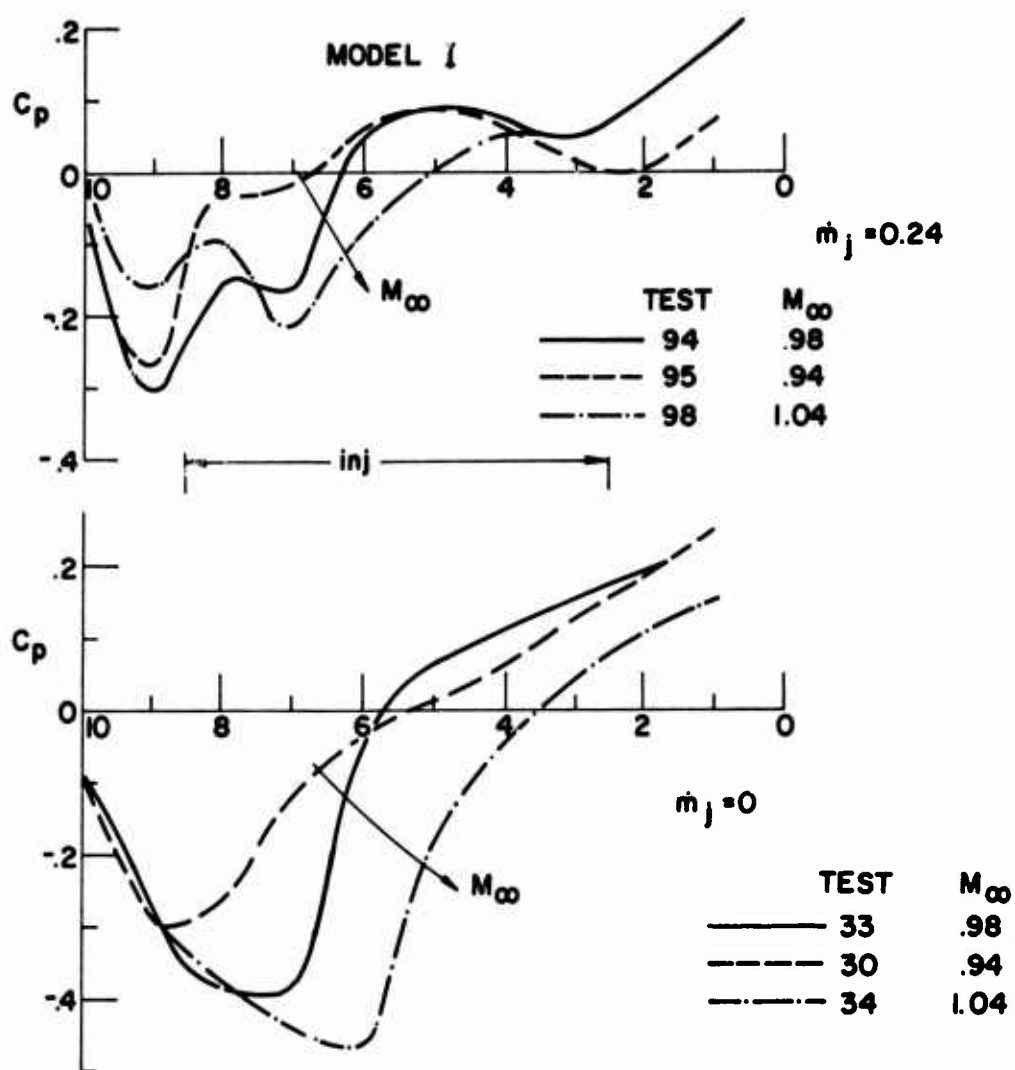
Fig. 11 Pressure Coefficient Distribution for Different Values of M_∞
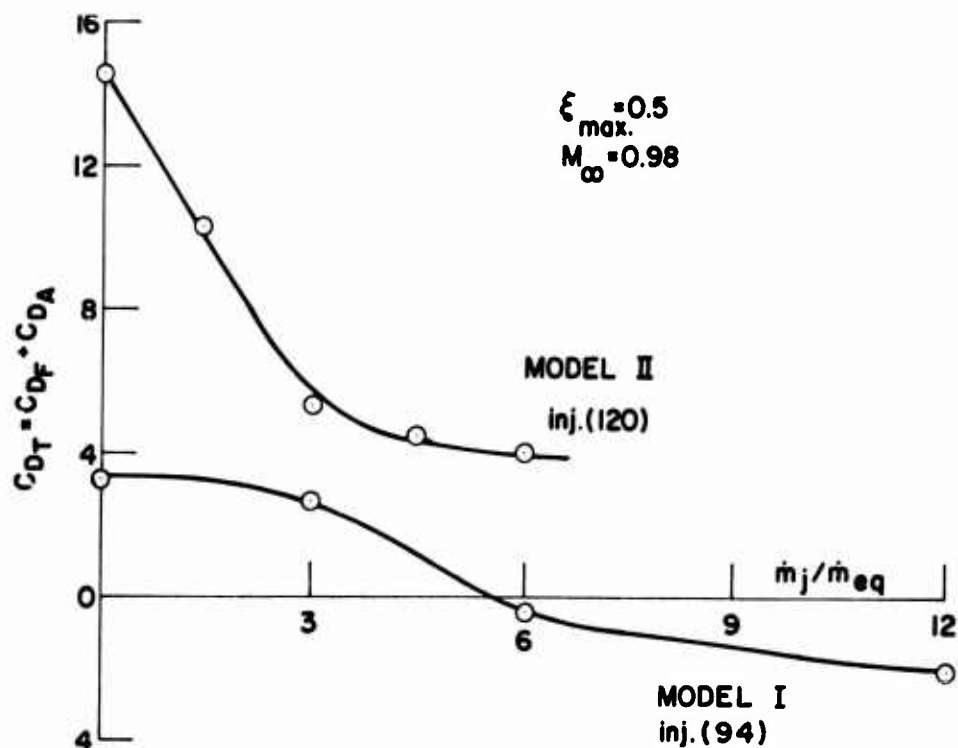
Fig. 12 Total drag coefficient variation with injection mass flow
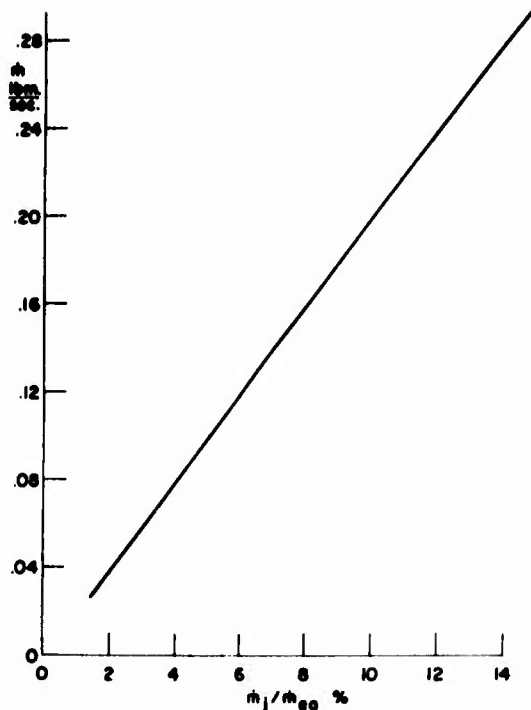
Fig. 13 Injected mass flow vs. Equivalent Mass
Flow Through the body frontal area

has been investigated.

An experimental investigation was con
ducted on an axisymmetric model to determi-
ne the effect on afterbody drag of the
injection of a small amount of air from the
propulsive system in the rear of the model.

The external transonic flow field in
the shock-boundary layer interaction region,
was altered, increasing the average pressu-
re on the aft section. The amount of air, to
be injected, in order to obtain a sensible
reduction in the total drag, was relatively
low (of the order of 5% of the equivalent
mass flow through the frontal area of the
body) since the interaction was found to be
highly sensitive to any small change in the
flow regime.

These percentages, which result in a
negligible decrease in the propulsive stream,
are very effective to reduce the total drag
and to enhance thus the overall aerodynamic
performance.

REFERENCES

1. PIVA, R., DE JESUS, C., "The effect of injection on base drag at transonic speed"
             NYU-AA-72-19

2. PEARCEY, H.H., HAINES, A.B., and OSBORNE, J., "The Interaction Between Local Ef-
             fects at the Shock and Rear Separation," Transonic Aerodynamics, AGARD
             Conference Proceedings No. 35, September 1968.

3. SEDDON, J., "The Flow Produced by Interaction of a Turbulent Boundary Layer with a
             Normal Shock Wave of Strength Sufficient to Cause Separation", Arc.
             R & M, No 3502, March 1960.

4. LITTLE, B.H., "Effects of Initial Turbulent Boundary Layer on Shock-Induced Separa-
             tion in Transonic Flow", von Karman Inst. for Fluid Dynamics Number
             TN-39, Brussels, Belgium, October 1967.

5. McDAVITT, J.B., TAYLOR, R.A., "Pressure Distributions at Transonic Speeds for Slender
             Bodies Having Various Axial Locations of Maximum Diameter", NACATN-4280

ACKNOWLEDGEMENT

ETUDE DE L'INTERFERENCE DE L'ECOULEMENT EXTERNE

ET DES CONDITIONS D'INSTALLATION SUR LES PERFORMANCES

DES INVERSEURS DE POUSSEE

par J.M.HARDY et J.P.CARRE - S.N.E.C.M.A.

Centre d'Essais de Melun-Villaroche

La mise au point des inverseurs de poussée est généralement faite dans des bancs d'essais de moteurs en l'absence d'écoulement externe. L'inverseur de jet déviant un débit élevé modifie considérablement le champ aérodynamique autour de l'avion. Inversement, la vitesse de vol et les conditions d'installations réagissent sur le fonctionnement des inverseurs. Cette interaction dépend de l'organisation de l'inverseur. A l'aide d'essais de maquettes effectués sur deux types d'inverseurs au cours de l'étude de l'arrière-corps de CONCORDE nous étudierons les mécanismes d'interaction. Nous analyserons le comportement de deux systèmes d'inversion. A l'aide des essais effectués au point fixe, puis en soufflerie avec écoulement externe à l'O.N.E.R.A., on mettra en évidence des écarts de comportement des inverseurs, et on présentera une étude des mécanismes d'interaction mettant en évidence un paramètre de corrélation permettant d'extrapoler les résultats de l'inverseur obtenus au point fixe dans les divers cas de fonctionnement. Une étude du bilan de l'effort de décélération sera présentée, on montrera la répercussion du Mach de vol sur les pressions de culot des inverseurs qui se traduit par une augmentation non négligeable de la force de décélération.

On étudiera la répercussion du taux de réingestion (augmentation de la température d'entrée-moteur due au retour des gaz éjectés par l'inverseur) sur la force réelle de freinage de l'avion. Dans ce bilan, nous montrerons la part importante résultant de la traînée de captation, croissant avec le Mach, et nous montrerons que le choix de la configuration d'inversion optimale, compte-tenu de ces éléments, peut être différent de la configuration optimale au point fixe.

A la vue des divers éléments énumérés ci-dessus, on développera des considérations générales sur la conception des inverseurs.

RESEARCH ABOUT EFFECTS OF EXTERNAL FLOW AND

AIRCRAFT INSTALLATION CONDITIONS ON

THRUST REVERSERS PERFORMANCES

by J.M.HARDY and J.P.CARRE from S.N.E.C.M.A.

Development of Thrust Reversers is generally carried out in engine test cells without external flow. As Thrust Reversers deviate a significant amount of flow this modifies considerably the aerodynamic field surrouding an aircraft. Inversely, flight speed as well as aircraft installation conditions react on the operating characteristics of Thrust Reversers. This interaction is contingent on the Thrust Reversers design arrangement. We will analyze interaction mechanisms using test data collected with two types of Thrust Reversers during an investigation carried out on the CONCORDE afterbody. We will show the differences in behaviour existing between the reversers, as revealed by tests carried out with no external flow, and with external flow in the O.N.E.R.A. wind tunnel installation. Then an investigation on interaction mechanisms will be presented, bringing out a correlation parameter which makes it possible to extrapolate Thrust Reverser results obtained in static conditions for various running configurations. A balance of deceleration forces will be analysed, and we will show the effects of flight Mach number on the Reversers base pressure values.

Consequences of the reingestion rate (increase of engine intake temperature due to recirculation of hot gases from the reverser) on the aircraft effective braking forces will be investigated. We will under-line, in this force balance, how significant is the contribution of capture drag, which increases will the Mach number, and we will show that the choice of the optimum reverse thrust configuration, when taking these factors into consideration, may be differing from the optimum configuration in run-up conditions.

Taking into account the various data mentioned above, we will then develop general considerations on Thrust Reverser design.

<u>ETUDE DE L'INTERFERENCE DE L'ECOULEMENT EXTERNE</u>
<u>ET DES CONDITIONS D'INSTALLATION SUR LES PERFORMANCES</u>
<u>DES INVERSEURS DE POUSSEE</u>
par J.M.HARDY et J.P.CARRE - S.N.E.C.M.A.

Congrès AGARD - ROME 1974

NOTATIONS

P_j Pression totale jet primaire

T_j Température jet primaire

W_j Débit jet primaire

A_j Section géométrique de la tuyère primaire

V_j Vitesse du jet primaire

P_s Pression interne de l'arrière-corps dans le canal secondaire

P_c Pression derrière les obstacles d'inversion de poussée

X_G Poussée brute jet direct

X_R Poussée brute en inversion de poussée

X_{NR} Poussée nette en inversion de poussée

$K_T = X_G / P_j A_j \bullet$

$C_T = K_T / K_T \bullet$ Nota : $\bullet$ caractérise les valeurs isentropiques mono-dimensionnelles

M_o Mach de vol

V_o Vitesse de vol

P_o Pression statique de l'écoulement externe

T_1 Température d'entrée du moteur

LISTE DES REFERENCES

Réf.0 : Monsieur CARRIERE - Recherche Aérospatiale n° 1974- 2

Réf.1 : H.Y.CHANG et J.P.WAIDELICH - "A mathematical model for the behaviour of thrust reversers"
(A.I.A.A. Paper n° 69 - 3

Réf.2 : Monsieur KADOSH - Thèse de doctorat - Université de PARIS - 1959

Réf.3 : "Etude des écoulements dans les éjecteurs transsoniques"
2ème Symposium on Air Breathing Engines (I.C.A.S.) - SHEFFIELD 1974 - J.M.HARDY - L.DUTOUQUET

Réf.4 : "Calcul des performances d'une tuyère propulsive convergente"
9ème Congrès I.C.A.S. - HAIFA - 1974 - J.L.SOLIGNAC - M.FENAIN - L.DUTOUQUET

Réf.5 : S.I.A. Mars 1972 - Revue ingénieur automobile 6/7 - 1972
Monsieur JUMELLE - S.N.E.C.M.A.

1. INTRODUCTION

Les études d'optimisation des inverseurs de poussée sont généralement faites au point fixe sur une base expérimentale. L'évolution des conditions d'utilisation des inverseurs (inversion de poussée en vol) conduit aujourd'hui à remettre en cause cette façon de faire. Une remarque de Monsieur CARRIERE (ONERA) montre que le mécanisme de freinage dû aux inverseurs est fondamentalement différent au point fixe et en vol. Des essais récents sur avion ont montré que les conditions d'installation influaient de façon importante aussi bien sur les phénomènes de réingestion que de fonctionnement de l'inverseur lui-même.

Si on ajoute à ces remarques le fait que le choix du système d'inversion optimum en vol est condition-né par le cycle du moteur auquel il est destiné, on est convaincu que l'optimisation d'un inverseur n'est pas aisée.

Nous retiendrons que cette optimisation ne peut être valablement faite qu'à partir d'essais de maquet-tes effectués en soufflerie sur des configurations suffisamment représentatives des conditions d'ins-tallation, ceci associé à des méthodes de calcul permettant d'une part l'analyse des essais, d'autre part l'étude des performances du système propulsif en inversion de poussée.

2. SCHEMATISATION DE L'ECOULEMENT EN INVERSION - METHODE DE CALCUL

2.1. Cas du fonctionnement au point fixe

Dans ce cas le Mach externe est nul et l'écoulement peut être schématisé comme présenté planche 1 (fig.1). L'application du théorème des quantités de mouvement donne comme expression de la contre-poussée : $X_R = W_j V_j \cos \theta$.

On voit dans ce cas que l'effet de contre-poussée est dû au fait qu'une certaine quantité de débit est déviée par un obstacle et renvoyée vers l'amont à la vitesse V_j.

2.2. Cas du fonctionnement en vol

Dans ce cas le Mach externe n'est pas nul. L'effort propulsif en décélérateur du système de pro-pulsion correspond à la somme de deux termes : une traînée d'entrée égale à $W_j V_o$ et une poussée de sortie égale à $W_j V_j$, ces deux termes étant évalués respectivement à l'infini amont et l'infini aval. En jet direct l'expression de l'effort propulsif sera : $X_N = W_j V_j - W_1 V_o$.

En inversion de poussée l'écoulement peut être représenté par la schématisation présentée planche 1 (fig.2 et 3). La présence d'un écoulement externe modifie la direction du vecteur vitesse V_j qui, initialement dirigé vers l'amont, est ramené vers l'aval, à l'infini, sa direction est parallèle à la direction de la vitesse externe.

En écoulement potentiel (fig.2) ce changement de direction s'effectue sans perte. Dans le plan infini aval les vecteurs vitesse V_j en inversion de poussée et en jet direct sont donc identiques en direction et en intensité (réf. 0), le jet contourne sans décollement l'obstacle d'inversion de poussée (traînée nulle).

L'expression de la poussée obtenue en inversion est donc identique à celle obtenue en jet direct. On voit donc qu'en écoulement potentiel il n'y a pas d'effort de freinage possible par inverseur de poussée dès que le Mach externe est différent de 0. D'autre part, le corps formé par la carène et les lignes de courant amont et aval n'ayant pas de traînée en écoulement potentiel subsonique, il faut imputer à des phénomènes d'interaction visqueuse les effets de freinage observés en vol, avec inverseur de poussée.

On se convaincra de l'intensité de ces effets d'interaction visqueuse si l'on remarque que la pression sur l'axe, en aval de l'obstacle, perpendiculaire à l'écoulement interne, devrait être égale à la pression d'arrêt de cet écoulement, alors qu'elle est, en réalité, inférieure à la pression statique ambiante.

Le schéma avec viscosité présenté sur la planche 1 (fig.3) montre que, dans la réalité, le jet décolle de l'obstacle et que la contre-poussée est due, d'une part à la traînée de l'obstacle de façon analogue au point fixe, d'autre part à la traînée due à la dépression existant dans le culot.

2.3. Remarque

Les mécanismes de destruction de la poussée et de l'obtention de l'effort de décélération sont donc fondamentalement différents au point fixe et avec écoulement externe. La conception des inverseurs doit tenir compte de ce fait. La recherche du taux maximum de contre-poussée au point fixe ne se justifie que dans la mesure où l'on admet que les interactions visqueuses seront d'au-tant plus importantes que l'intensité du vecteur vitesse et la déviation qu'il doit subir entre son origine et l'infini aval seront élevées.

Pour l'étude d'un inverseur, on devra s'efforcer de s'intéresser au maximum au champ aérodynami-que externe, faire en sorte que la section d'arrière-corps en aval du système d'inversion soit maximum et qu'il règne à son culot la pression la plus faible possible.

La constatation de ce phénomène montre également que, lors d'essais en soufflerie, la maquette doit être aussi petite que possible ou la soufflerie de dimension importante afin que les condi-tions de parois ne modifient pas sensiblement le développement du mélange du jet avec l'écoule-ment externe.

2.4. Méthode de calcul

Avant de pouvoir estimer par le calcul les phénomènes d'interaction visqueuse, il faut déjà posséder des méthodes de calcul décrivant correctement l'écoulement potentiel. Des méthodes de dimensionnement des inverseurs ont été proposées par CHANG (réf.1) en écoulement bidimensionnel incompressible et par KADOSH (réf.2) en écoulement bidimensionnel avec correction de compressibilité.

Actuellement la S.N.E.C.M.A. développe une méthode exacte en écoulement bidimensionnel compressible basée sur une méthode hodographique dérivée des travaux DUTOUQUET-FENAIN (réf.3 et 4). Cette méthode donne une description détaillée du jet en inversion. Elle permettra en particulier l'étude des grilles d'inverseur. A titre d'illustration, nous présentons planches 2 et 3 les premiers résultats de calculs. Sur la planche 2 figure une étude d'écoulement dévié par un obstacle normal à la direction du jet. Sur la demi-figure du bas sont représentées les iso Mach, sur la demi-figure du haut les lignes de courant.

Sur la planche 3 nous présentons l'effet de la longueur réduite d'un obstacle d'angle donné sur les performances d'un inverseur.

Le couplage d'une telle méthode avec une méthode traitant le mélange de l'écoulement interne avec l'écoulement externe devrait permettre l'étude des phénomènes d'interaction.

3. ETUDE EXPERIMENTALE DE L'INTERACTION DE L'ECOULEMENT EXTERNE SUR LES PERFORMANCES DES INVERSEURS

Nous étudierons les résultats d'essais relatifs à deux types d'inverseurs pour lesquels les interactions de l'écoulement externe se manifestent de façon différente.

3.1. Inverseur type 1

La planche 4 présente un schéma relatif à ce type d'inverseur. Le taux de détente de fonctionnement normal est supercritique compte-tenu des conditions géométriques, l'écoulement au col de la tuyère primaire est subsonique et il y a blocage de l'écoulement au niveau des grilles de l'inverseur.

L'interaction des écoulements interne et externe est donc limitée en ce qui concerne le fonctionnement proprement dit de l'inverseur. Par contre, les effets d'interaction au culot des obstacles peuvent être mis en évidence.

Sur la planche 5 nous présentons les caractéristiques de fonctionnement d'un tel inverseur obtenues au point fixe.

Figure 1 : Evolution du coefficient de poussée en fonction du taux de détente.

Figure 2 : Evolution de la pression interne en fonction du taux de détente.

Figure 3 : Evolution de la section efficace de la tuyère primaire en fonction du taux de détente.

La figure 3 montre que la section efficace de la tuyère primaire en inversion de poussée est inférieure à la section efficace en jet direct, ce qui traduit le déplacement du col sonique à l'aval. Sur cette planche, les deux courbes obtenues en inversion de poussée sont relatives à deux positions des portes tertiaires.

La planche 6 présente l'évolution des performances de l'inverseur de poussée en fonction du nombre de Mach de l'écoulement externe pour un taux de détente donné.

Figure 1 : Coefficient de poussée fonction du nombre de Mach

Figure 2 : Pression interne fonction du Mach

Figure 3 : Pression de culot (face aval des obstacles) fonction du Mach

Figure 4 : Section efficace de la tuyère primaire fonction du Mach

L'examen de la figure 2 montre que la pression interne est peu influencée par le Mach de vol, c'est-à-dire que le fonctionnement interne de l'inverseur peut être considéré comme figé.

L'évolution légère de la section critique du tube de courant visible figure 4 peut être alors imputée à un effet de striction dû à l'écoulement externe au niveau des grilles de l'inverseur.

La figure 3 montre que la pression s'exerçant sur la face aval des obstacles est fortement influencée par le nombre de Mach. La chute de cette pression est responsable de l'évolution du taux de contre-poussée visible sur la figure 1, courbe "a". A partir de ces valeurs de pression et de la connaissance de la section intéressée, on peut calculer l'effort et corriger le coefficient de poussée pour le ramener à une pression de culot égale à p_0. Le résultat de ce calcul est visible figure 1, courbe "b". On voit alors que, correction faite, le coefficient de contre-poussée est pratiquement indépendant du nombre de Mach. L'accroissement du taux de contre-poussée en fonction du Mach de vol est très important : environ 40 % entre $M_0 = 0$ et $M_0 = 0,7$. Il est lié à l'établissement d'un faible niveau de pression sur les surfaces importantes. Il y a donc lieu de soigner particulièrement l'organisation de l'inverseur pour pouvoir bénéficier au maximum de cet effet.

3.2. Inverseur type 2

La planche 7 présente le schéma de l'inverseur considéré. Dans ce type d'inverseur la section sonique de l'écoulement reste localisée au col de la tuyère primaire. Pour un taux de détente

suffisamment élevé, l'écoulement dans l'ensemble d'éjection, d'abord supersonique, subit une recompression par choc pour devenir subsonique avant d'être dévié par les obstacles, la position de ce choc dépendant de la géométrie des coquilles d'inversion. La planche 8 présente les caractéristiques d'un tel inverseur au point fixe.

Figure 1 : évolution du coefficient de poussée en fonction du taux de détente

Figure 2 : évolution de la pression interne en fonction du taux de détente

Figure 3 : évolution de la section efficace de la tuyère primaire en fonction du taux de détente.

On peut remarquer sur cette dernière figure que, contrairement à l'inverseur type 1, le braquage des coquilles d'inversion de poussée ne modifie pas la valeur de la section efficace de la tuyère primaire. Le col reste donc localisé dans le plan d'éjection primaire. L'écoulement dans le système d'éjection étant subsonique en aval du choc, on imagine aisément que l'écoulement externe aura un effet non négligeable sur l'écoulement interne. D'autre part, comme dans le cas précédent, l'interaction des deux écoulements sera responsable de l'établissement d'un niveau de pression assez faible dans le culot formé par les obstacles d'inversion de poussée.

Sur la planche 9 nous donnons l'évolution des caractéristiques de fonctionnement de l'inverseur en fonction du Mach de vol pour deux définitions du taux de détente : P_j/p_o, rapport de la pression génératrice du jet primaire à la pression statique de l'écoulement externe et P_j/P_s, rapport de la pression génératrice du jet primaire à la pression statique interne du système d'inversion.

La figure 1 est relative au coefficient de poussée :

Courbe "a" : $P_j/p_o = C^{te}$

Courbe "b" : $P_j/P_s = C^{te}$

La figure 2 représente l'évolution des pressions internes :

Courbe "a" : $P_j/p_o = C^{te}$

Courbe "b" : $P_j/P_s = C^{te}$

La figure 3 est relative à la section critique de l'écoulement primaire.

Sur cette dernière figure on voit qu'à P_j/P_s donné (courbe "b") le Mach de vol est sans effet sur la section, ce qui n'est pas le cas à P_j/p_o donné (courbe "a").

D'autre part, on peut voir sur les figures 1 et 2 qu'à P_j/p_o donné les points correspondant aux essais au point fixe ne sont pas situés sur les courbes représentant les évolutions en fonction du Mach de vol, l'écart de poussée visible correspondant à l'établissement d'un niveau de pression interne différent dû à l'effet de l'écoulement externe. Si maintenant nous examinons figure 1 la courbe "b" correspondant à l'évolution du coefficient de poussée à P_j/P_s donné, nous voyons que cette anomalie a disparu.

L'étude de la figure 2 montre que le Mach de vol est responsable d'une variation importante du niveau de pression interne, cela aussi bien à P_j/P_s donné qu'à P_j/p_o donné. L'ensemble de ces constatations met bien en évidence l'interaction des écoulements interne et externe sur le fonctionnement proprement dit de l'inverseur.

D'autre part, dans ce cas comme dans le cas précédent, le niveau de pression du culot des obstacles diminue sensiblement quand le Mach de vol croît, entraînant ainsi une augmentation de la contre-poussée. On peut voir, figure 1 "courbe c", qu'après correction de la traînée de culot, le coefficient de poussée à $P_j/P_s = C^{te}$ est sensiblement indépendant du Mach de vol.

Sur la planche 10, nous avons tracé pour les deux types d'inverseurs l'évolution de la traînée de culot en fonction du Mach de vol. On peut voir que cet effet est loin d'être négligeable; il représente un pourcentage de l'ordre de 40 % de la contre-poussée observée à $M_o = 0,90$.

Sur la planche 11, et toujours pour l'inverseur type 2, nous avons tracé l'évolution de la contre-poussée en fonction du taux de détente paramétrée en Mach de vol. On peut voir, figure 1, que la contre-poussée maximum associée à une modification de la fonction aérodynamique interne de l'inverseur est atteinte à un taux de détente P_j/p_o d'autant plus élevé que le Mach est important. L'examen de la figure 2 où les mêmes courbes ont été tracées, cette fois par rapport au taux de détente interne P_j/P_s, montre que la valeur maximale de la contre-poussée est bien atteinte pour une valeur donnée de ce taux de détente. Si nous avions effectué la correction due à la traînée de culot, nous aurions trouvé une courbe unique.

3.3. <u>Remarque</u>

Nous venons d'examiner deux types d'inverseurs où les interactions des écoulements interne et externe se manifestent de deux façons différentes.

<u>Inverseur type 1</u>

Interaction sur le fonctionnement interne, interaction importante au culot.

<u>Inverseur type 2</u>

Interaction importante aussi bien sur l'écoulement interne qu'au culot des obstacles.

On voit dans les deux cas qu'après identification de ces interactions le choix de paramètres convenables permet de chiffrer ces interactions, d'établir un bilan et une schématisation des phénomènes. On remarque aussi que le comportement des deux inverseurs est différent; en effet, dans le cas de l'inverseur type 2, l'augmentation de cont. poussée avec le Mach de vol due à la traînée de culot est réduite par la réduction du taux de dét. e interne, ce qui n'est pas le cas dans l'inverseur type 1.

Dans l'état actuel de nos connaissances, seuls des essais peuvent nous donner les éléments nécessaires à la prise en compte de ces interactions dans le calcul de l'effort de freinage dû aux systèmes d'inversion de poussée.

4. ETUDE DE L'INTERFERENCE DU JET DEVIE SUR L'EFFORT DE FREINAGE (REINGESTION)

Lorsque la vitesse de roulage de l'avion diminue, on observe d'une façon générale une augmentation de la température d'entrée du réacteur due à l'absorption par le moteur de gaz chauds provenant de l'écoulement dévié. La vitesse à laquelle apparaît ce phénomène dépend des conditions d'avionnage et de l'organisation de l'inverseur. La répercussion de cette élévation de température sur l'effort de décélération dépend de la régulation du moteur. Pour illustrer l'importance de ce phénomène, nous présentons, à titre indicatif, planche 12, l'évolution des performances d'un inverseur à M_o = 0,30 en fonction de l'élévation moyenne de la température entrée-moteur pour deux hypothèses de fonctionnement. Dans cette étude nous avons considéré que la géométrie du système d'éjection était figée (section primaire constante).

Sur la figure 1 est tracé le rapport des poussées brutes.

Sur la figure 2 est donné le rapport des traînées de captation.

Sur la figure 3 nous présentons le rapport des poussées nettes en inversion, c'est-à-dire des efforts de décélération.

Sur ces figures, les courbes "a" correspondent à la performance d'un inverseur non influencé par TI et les courbes "b" aux performances d'un réacteur en inversion à régime constant. La zone hachurée représente la perte d'effort de freinage due au phénomène de réingestion. On peut voir en particulier que, pour une élévation de température de 50°, l'effort de freinage sera réduit de 1/3.

Lors de l'étude des inverseurs on doit chercher à réduire cet effet. L'utilisation d'inverseurs à grilles permettant d'obtenir une direction dans deux plans de nappes de gaz inversés permet, lors des essais sur avion du dispositif d'inversion de poussée, de diriger ces nappes de façon à minimiser l'effet de réingestion et d'abaisser la vitesse à partir de laquelle apparaissent les phénomènes. Les phénomènes de réingestion sont régis à la fois par l'écoulement dévié et l'écoulement autour de l'avion en présence du sol. Les conditions d'installation jouent donc un grand rôle et si ce phénomène peut être dégrossi en soufflerie à l'aide d'une maquette représentant l'avion complet, la géométrie de l'inverseur ne peut être finalisée que sur l'avion. On peut remarquer en particulier que des inverseurs donnant des taux d'inversion de poussée plus modestes, mais évitant les phénomènes de réingestion, sont susceptibles de donner sur avion un effort de freinage supérieur à des inverseurs plus performants mais mal étudiés du point de vue réingestion.

L'introduction dans la régulation du moteur de la température d'entrée TI est également susceptible de réduire le déficit de poussée.

5. OPTIMISATION DE LA CONFIGURATION D'INVERSION EN FONCTION DES CONDITIONS DE VOL

De plus en plus les inverseurs sont utilisés en vol pour décélérer les avions et obtenir des vitesses de descente élevées. L'étude présentée ici a été faite pour trois valeurs du Mach de vol :

M_o = 0   correspondant au point fixe

M_o = 0.3   correspondant sensiblement a l'atterrissage

M_o = 0,9   correspondant à une utilisation en vol comme aérofrein.

Les essais en soufflerie nous ont donné pour chacun des Mach de vol considérés les coefficients de poussée de l'inverseur compte-tenu des problèmes d'interaction, ceci pour diverses valeurs de la section de la tuyère primaire.

On doit toutefois remarquer que, lors de ces essais, seule était représentée sur la maquette la nacelle moteur.

Sur la planche 13 nous avons fait figurer les valeurs de la poussée brute en inversion de poussée pour trois valeurs de A_j rapportées à la valeur de cette poussée obtenue pour la section minimale de la tuyère primaire. On peut voir que l'influence de A_j est d'autant plus faible que le Mach est élevé, ceci s'expliquant par le fait que le terme traînée de culot devient de plus en plus important dans le bilan.

Si l'on considère l'effort de freinage en vol, il est la somme de la traînée de captation et de la contre-poussée brute :

$$\frac{X_{NR}}{P_o} = \frac{X_R}{P_o} + \frac{W_{capt} V_o}{P_o}$$

On note que, à P_j/p_o donné, X_R/p_o décroît quand A_j croît. Le terme W_{capt}/p_o par contre croît avec A_j.

Le second terme de la poussée X_{NR} prenant d'autant plus d'importance que le Mach de vol est élevé alors que l'influence de A_j sur X_R s'amenuise, il en résulte que la configuration de vol jouera un rôle important dans l'optimisation de l'inverseur. D'autre part, pour un A_j et un taux de détente donnés, si :

$$\frac{W_j \sqrt{T_J}}{P_o}$$

est fixe, il n'en est pas de même de : $\quad \dfrac{W_{capt} \sqrt{T_o}}{P_o} = \dfrac{W_j \sqrt{T_j}}{P_o} \quad \dfrac{\sqrt{T_o}}{\sqrt{T_j}}$

qui dépend de la valeur de T_j/T_o, donc du cycle du moteur. Ceci met en évidence que l'étude de la configuration optimum d'un inverseur en vol dépend du réacteur auquel est destiné cet inverseur. La planche 14 illustre les remarques présentées ci-dessus. Le calcul a été effectué à partir des éléments de la planche 13 pour un réacteur mono flux à haut taux de compression. Il pourrait être modifié pour des réacteurs double flux à fort taux de dilution.

Cette planche montre que si la configuration d'inversion de poussée optimale au point fixe correspond à la section minimale, à $M_o = 0,9$, l'effort de freinage est pratiquement indépendant de la section de la tuyère primaire.

Le retassement important des courbes visible à $M_o = 0,3$ suggère que, pour certains moteurs, l'optimisation de la configuration d'inversion de poussée, dans les conditions d'atterrissage, pourrait être différente de celle au point fixe.

6. CONCLUSIONS

L'étude présentée ici pour deux types particuliers d'inverseurs, ne trouve sa généralisation que sur la philosophie de conception et d'expérimentation des inverseurs. Le fait que l'effort de freinage dû à ces dispositifs est imputable à deux mécanismes différents, au point fixe et en vol, que les interactions des écoulements interne et externe dépendent de l'organisation même des systèmes et que les conditions d'installation réagissent aussi bien sur les phénomènes de réingestion que sur les phénomènes d'interaction visqueuse conduit à penser que, seuls, des essais avec écoulement externe sur des maquettes les plus représentatives possibles, pourront permettre d'approcher la solution optimale qui, en tout état de cause, ne sera finalisée qu'après essais sur avion.

Toutefois, les considérations présentées ici permettent, lors de l'étude des dispositifs, de les organiser en vue de bénéficier au maximum des phénomènes d'interaction.

SCHEMATISATION des ECOULEMENTS .

POINT FIXE M₀=0   1

$$XR = D_g \, V_g \, \cos \theta$$
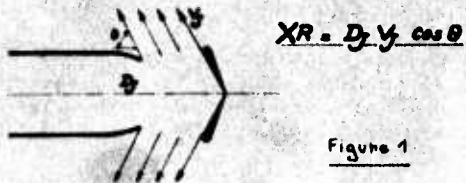
Figure 1

AVEC ECOULEMENT EXTERNE M₀≠0

Ecoulement potentiel
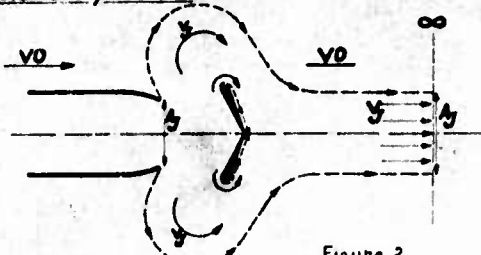
Figure 2

Ecoulement réel
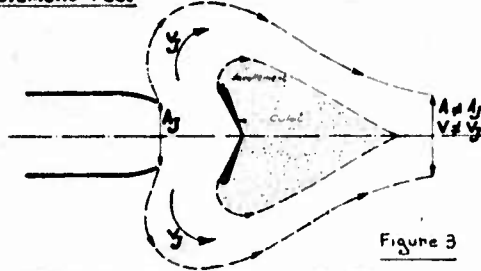
Figure 3

Etude théorique de l'écoulement   2
dans un inverseur

M₀ = 0

ligne isobare
ligne de courant

iso Mach
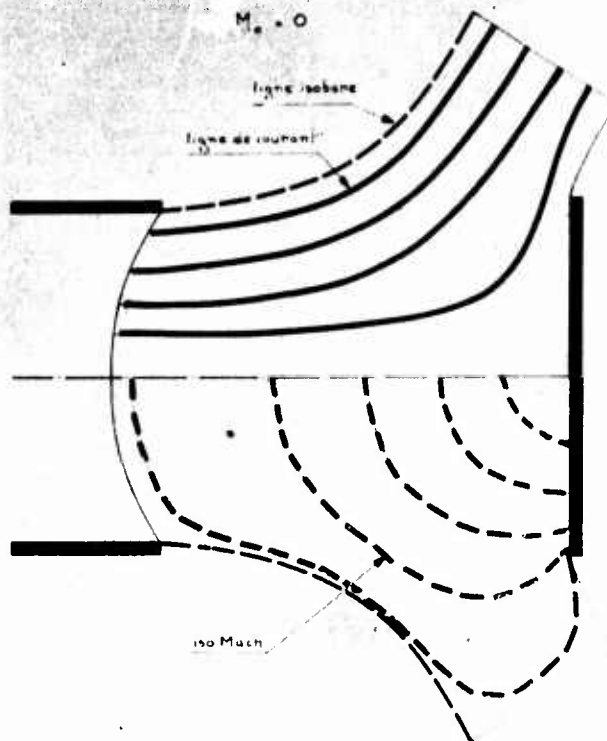
Etude théorique de l'effet de la longueur de l'obstacle d'inversion sur la performance

3

POUSSÉE ⟶   POUSSÉE HAUTE NULLE   ⟵ CONTRE POUSSÉE   Cos θ
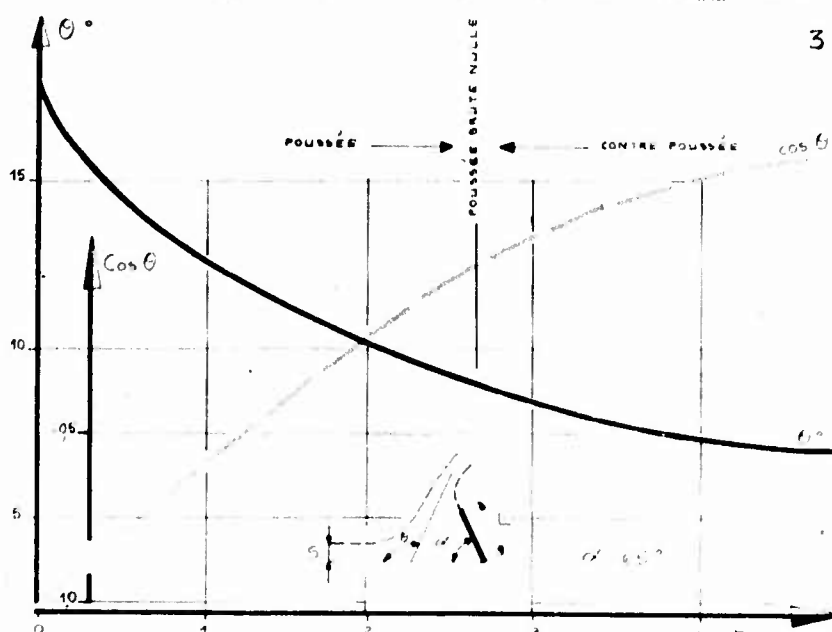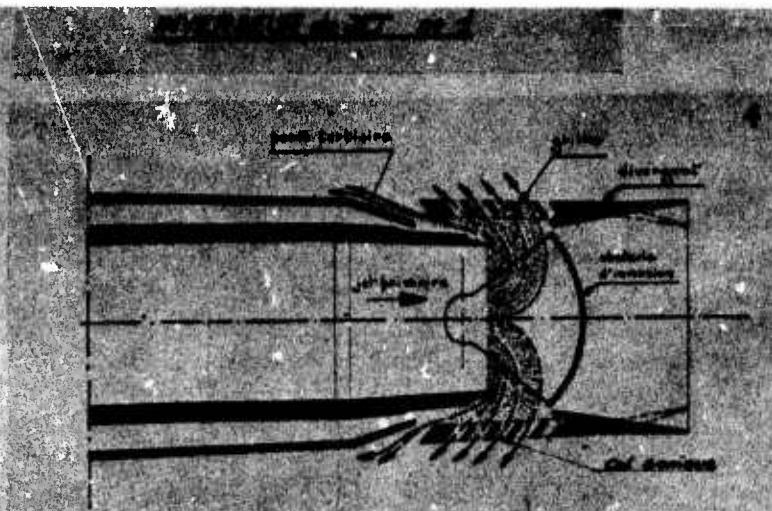
Performance inverseur type 1 au point fixe 5

C_T

portes ouvertes

$-0,4$

$-0,5$

portes fermées

Figure 1

P_3/p_0

portes fermées

2

portes ouvertes

1

Figure 2

A_J^* (cm²)

7000

jet direct

6000

portes ouvertes

jet inverse

5000

portes fermées

4000

Figure 3

1   2   3   4 P_3/p_0

Effet du Mach de vol 6

Performance inverseur type 1

C_T

portes ouvertes   b'

$-0,4$

$-0,5$

portes fermées   'a'

$-0,6$

Figure 1

P_3/p_0 (pression interne)

portes fermées

1,5

portes ouvertes

1,0

Figure 2

P_c/p_0 (pression de culot)

1,0

portes fermées

portes ouvertes

0,9

Figure 3

A_J^* (cm²)

portes ouvertes

5000

portes fermées

4000

Figure 4

0   0,1 0,2 0,3 0,4 0,5 0,6 0,7 M_0

INVERSEUR de JET n° 2

7

jet primaire
obstacle d'inverseur
choc

Performance inverseur type 2 au point fixe 8

C_T
-0,8
-0,4
Figure 1

P_3/P_0
1,0
0,9
Figure 2

$A_J^*(cm^2)$
jet inverse
4000
jet direct
3000
Figure 3
1   2   3 P_{J_i}/P_0
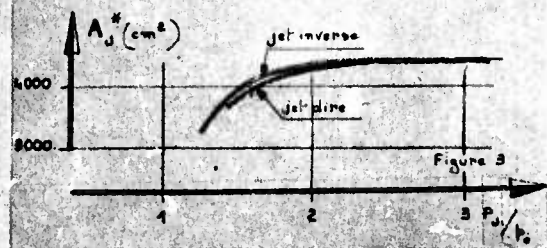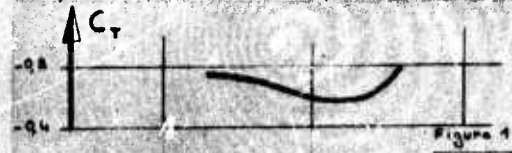
Effet du Mach de vol [Performance inverseur type 2] 9

K_T (Poussée.)
point fixe
-0,3
-0,4
Figure 1

P_3/P_0 (Pression interne)
1,2
1,1
1,0
0,3
Figure 2

$A_J^*(cm^2)$
5000
4000
Figure 3
0   0,1 0,2 0,3 0,4 0,5 0,6 0,7 0,8 M_0
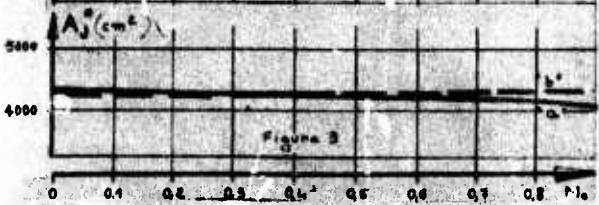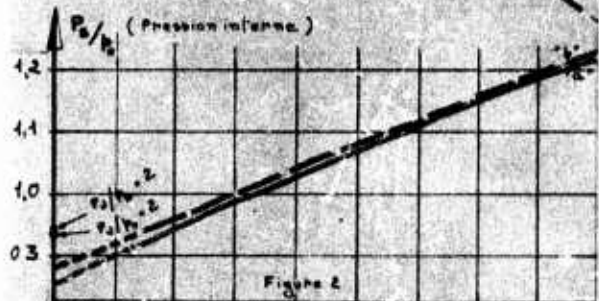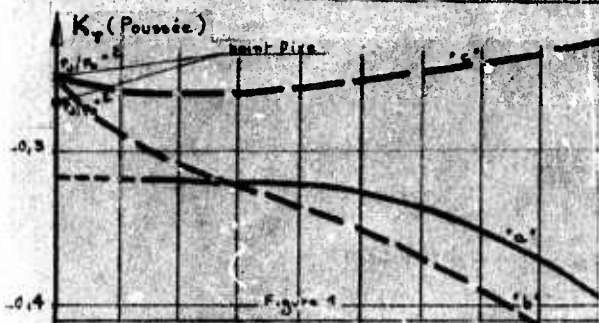
Evolution de la traînée de culot d'obstacle 10
avec le Mach de vol

ΔK_T
0   inverseur type 1 P_3/P_0 = 2
-0,1 inverseur type 2 P_3/P_0 = 2
portes ouvertes
-0,2 portes fermées
0,1 0,2 0,3 0,4 0,5 0,6 0,7 M_0
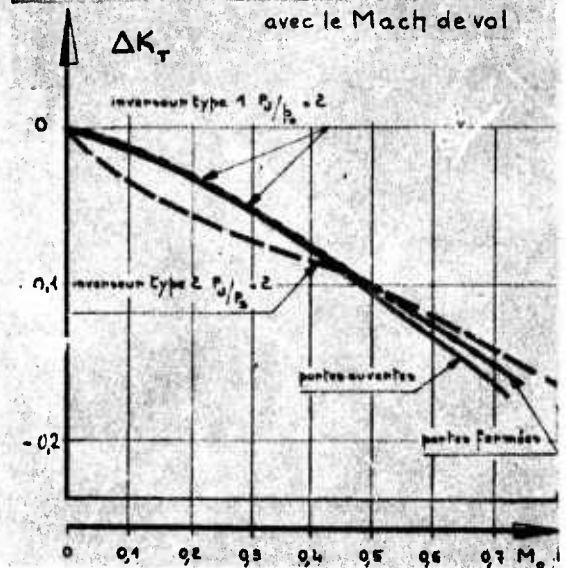
Effet du Mach de vol sur le fonctionnement interne de l'inverseur type 2

Figure 1

Figure 2

valeur à $M_o = 0,9$ après correction de la trainée de culot
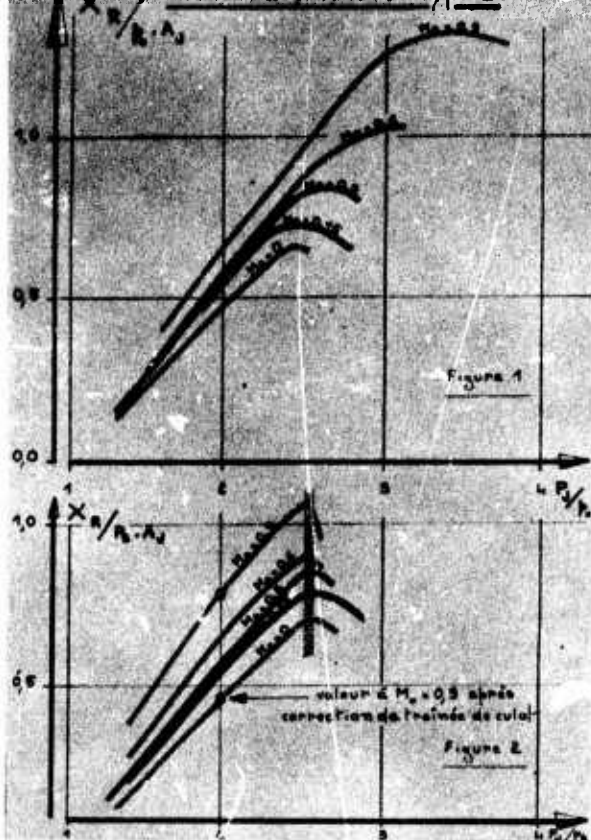
Effet du ΔT de réingestion sur les performances d'un inverseur $M_o = 0,3$

$\dfrac{X_{R\Delta T}}{X_{R\Delta T.O}}$ (Poussée brute)

Figure 1

$\dfrac{X_{\infty\Delta T}}{X_{\infty\Delta T.O}}$ (Trainée de captation)

Figure 2

$\dfrac{X_{NR\Delta T}}{X_{NR\Delta T.O}}$ (Effort de freinage)

Figure 3
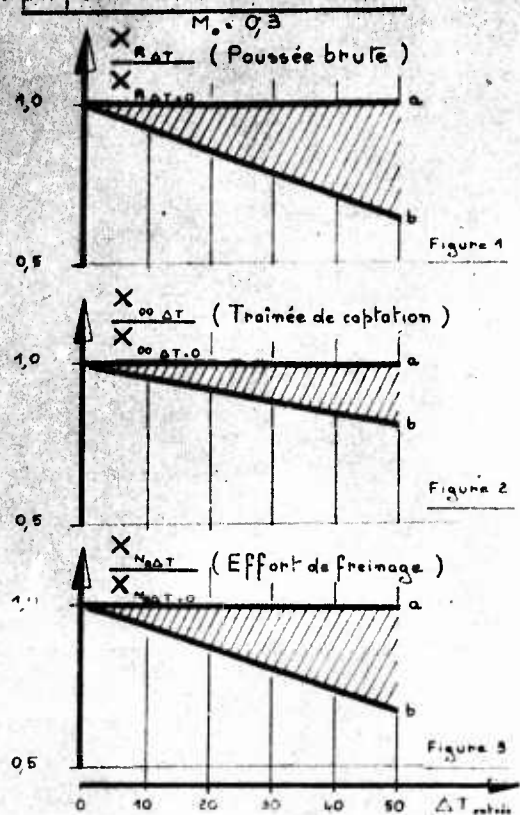
Effet de la section de sortie du jet primaire sur les performances d'un inverseur (contre-poussée brute)

$\dfrac{X_{RA_J}}{X_{RA_{J min}}}$

$M_o = 0$ $M_o = 0,3$ $M_o = 0,9$

$A_J / A_{J min} = 1$ $A_J / A_{J min} = 1$ $A_J / A_{J min} = 1$

1,03   1,03   1,03

1,18   1,18   1,18

1,23   1,23   1,23
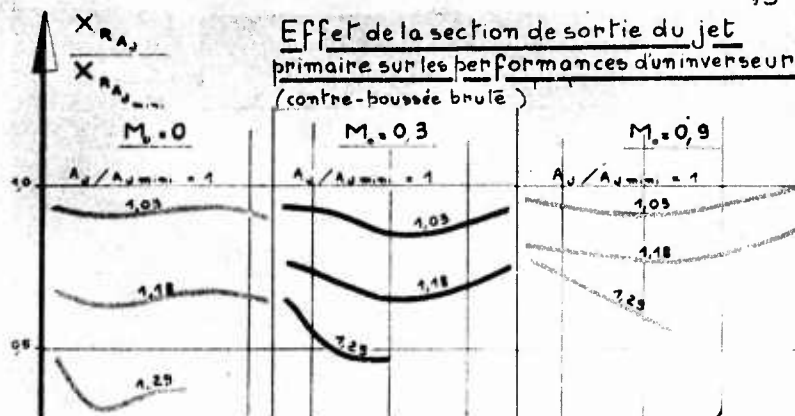
Effet de la section de sortie du jet primaire sur les performances d'un inverseur (effort de freinage)

$\dfrac{X_{NRA_J}}{X_{NRA_{J min}}}$

$M_o = 0$ $M_o = 0,3$ $M_o = 0,9$

$A_J / A_{J min} = 1$ $A_J / A_{J min} = 1$ $A_J / A_{J min} = 1$

1,03   1,03   1,03

1,18   1,18   1,18

1,23   1,23
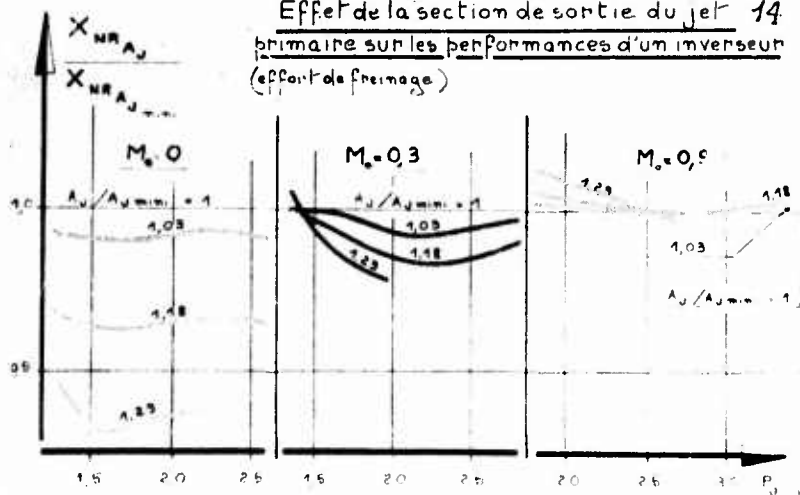
REVERSE THRUST EXPERIENCE ON THE CONCORDE

A.C. Willmer, Group Leader, Powerplant Aerodynamics
and
R.L. Scotland, Group Leader, Stability and Control

British Aircraft Corporation Limited
Commercial Aircraft Division
Filton

SUMMARY

Reverse thrust is used as a means of deceleration on many aircraft. Practical limitations to its use are set by the following airframe/propulsion interference effects :-

- hot gas ingestion

- aircraft handling

The reverse thrust force may also differ from that measured on a test bed due to interference.

Model tests to determine these interference effects for the Concorde aircraft have been carried out. This paper describes the several test techniques used and compares the model results with those inferred from tests on the prototype and production aircraft.

NOTATION

C_D Drag Coefficient

C_L Lift Coefficient

C_m Pitching Moment Coefficient

d Effective diameter of reverser exit on the nacelle underside

h Height of lower reverser exit above ground

$N2_{STD}$ Reduced H.P. spool speed $\dfrac{N2}{N2D}\sqrt{\dfrac{288.1}{T_1}}$

P_J Jet pipe total pressure

P_J' Effective total pressure at reverser exit

P_o Atmospheric static pressure

q_J Reverser dynamic head $= P_J' - P_o$

q_o Freestream dynamic head $= \frac{1}{2}\rho v^2$

S Wing area

T_1 Freestream total temperature

V Freestream Velocity

V_R Relative Velocity $= \sqrt{\dfrac{q_o}{q_J}}$

W Aircraft Weight

x Distance along the nacelle axis measured forward from the reverser

x_A Value of x at the auxiliary inlet

X_R Net reverse thrust

α Aircraft incidence

γ Longitudinal acceleration

θ Vertical jet deflection measured downwards from the nacelle axis

μ Coefficient of rolling friction

ρ Air density

ϕ Horizontal jet deflection measured from the nacelle axis.
Positive direction is away from the fuselage

$\Delta P = P_J - P_J'$

$\Delta X_R = X_{R_{aircraft}} - X_{R_{model}}$

1. INTRODUCTION

Thrust reversers are used on a large number of aircraft to provide a means of rapid deceleration. In practice the use of reversers is limited by powerplant/airframe interactions which are apparent as

- re-ingestion of exhaust gas at certain conditions

- modification of reverse thrust forces measured on an engine test bed

- modification of aircraft handling

Attempts have been made to simulate these interference effects for Concorde on a variety of models.

2. REVERSER CONFIGURATION

Two types of reverse thrust configuration have been tested on Concorde.

The prototype aircraft were fitted with Type 10 nozzles (fig. 1) which have reverse thrust buckets just downstream of the primary nozzles. These deflect the exhaust flow through cascades which control the efflux direction.

The normal configuration was designed to give vertical deflection $\theta = 47°$ and a lateral deflection $\phi = +10°$ (outboard) and -10° (inboard). Two other configurations were tested for special purposes. In these the vertical deflection was essentially unchanged but the lateral deflection on the nacelle lower surfaces was made +20° (outboard and inboard) for configuration 2 and +10° (outboard), +20° (inboard) for configuration 3.

Production aircraft are fitted with Type 28 nozzles (fig. 2). This design has one set of moveable parts which combine the functions of the reverser buckets and secondary nozzle petals. The bucket deflection is 0 for supersonic cruise, 20° for subsonic conditions and 73° for reverse thrust. This angle is measured from the outside surface of the bucket to the nacelle datum and the angle of the inner surface in the reverse position is 65°.
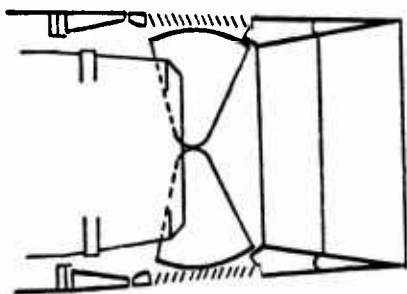
Supersonic Cruise
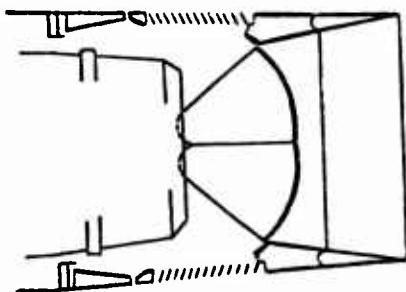
Reverse Thrust

Fig. 1. Type 10 nozzle sketch

Supersonic Cruise   Reverse Thrust
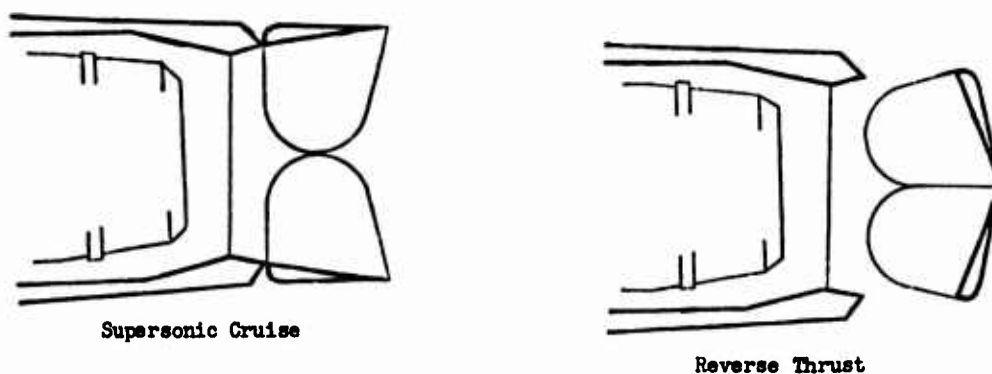
Fig. 2. Type 28 nozzle sketch

3.   REVERSE THRUST RE-INGESTION

Model tests have been done using

-    a half aircraft model with cold flow tested in the Filton No. 4 tunnel

-    a half aircraft model with hot flow tested in the Rolls Royce re-ingestion tunnel
(RJ3) at Patchway

-    a full aircraft model with hot flow suspended from the NGTE 136 research vehicle
and tested on the runway at Farnborough.

3.1   Cold flow half model

Fig. 3 shows the general arrangement of model G.16. This is a 1/18th scale half model of the production Concorde with T.28 nozzles. It is mounted on a short ground board to reduce the effects of ground board boundary layer. The calculated δ/h at the intake plane is 0.212.

Air is supplied independently to the two nozzles represented from a high pressure air supply. These nozzles have correct scale representations of the primary nozzles and the bucket internal surfaces.

High pressure air is supplied to jet pumps which induce an appropriate flow through the model intakes. The intakes include representation of the auxiliary inlets on the nacelle lower surface.
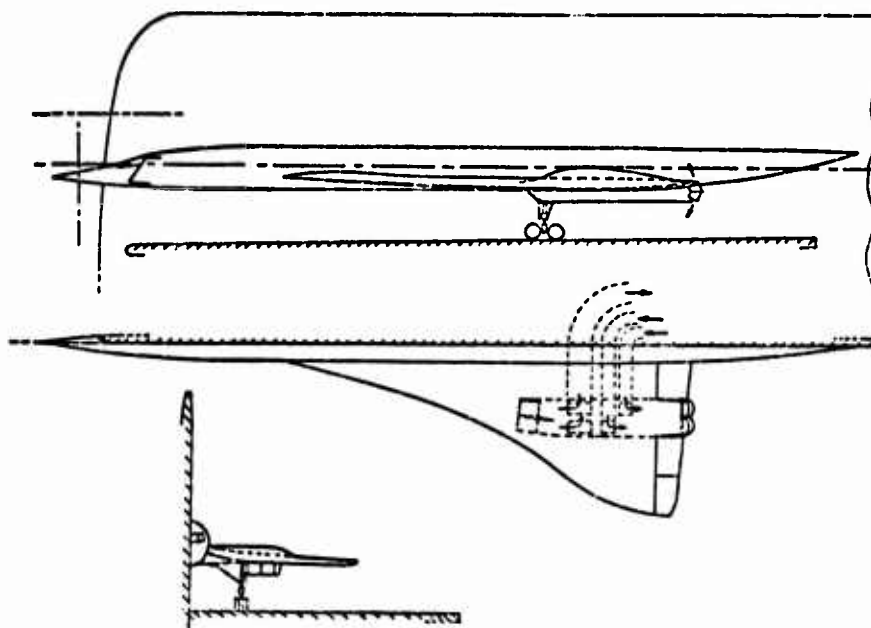
Fig. 3. General arrangement of model G.16

The upper wing surface is distorted to allow the airlines to be carried between the nacelle and fuselage.

The forward extent of the jet efflux was determined by observing the mist produced by spraying a small amount of water into the jet pipes through atomising nozzles. Illumination came from a vertical slit of light projected from well upstream of the model. This slit could be set to illuminate the centre line of either intake. Typical pictures are shown in fig. 4. The entry of exhaust air into the intake was also determined by wetness indicators inside the intake.

For a typical test run, the required intake flows and jet pressure ratios were set up with the tunnel air speed at its maximum value (142 Kt). The tunnel speed was then reduced in stages.

Fig. 4. Mist flow patterns from model G.16

$$\frac{P_J}{P_o} = 2.1$$
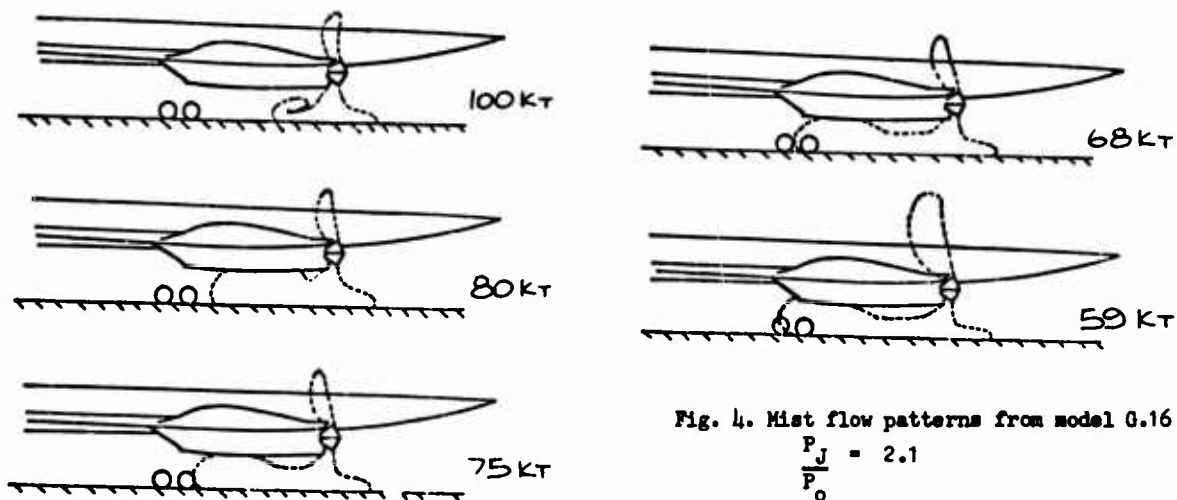
V = 80 Knots
(135 ft/sec)

V = 68 Knots
(114 ft/sec)

Fig. 5. Ground flow patterns from model G.16. $\frac{P_J}{P_o} = 2.1$

V = 59 Knots
(100 ft/sec)

Additional information on the flow patterns was obtained by oil flow tests on the ground plate, using dry jet air. A typical example is shown in fig. 5.

Re-ingestion speeds agree well whether defined by the wetness indicators or by the mist and oil flow pictures showing the efflux reaching the rear lip of the auxiliary inlet (fig. 6).

3.2 Hot flow half model

This model is at 1/15 scale. It was mounted using the floor of the open circuit tunnel to represent the ground. The boundary layer immersion is not very different to G.16, the calculated δ/h being 0.230.

The intake and airframe representation is similar to that described above for G.16. The nozzles, however were represented by two cascades exhausting from a plenum chamber at the rear of the nacelle (fig. 7). This arrangement allowed a range of vertical and lateral deflection angles to be tested. Exhaust flow from the top of the nacelle was not represented.

⊙ Mist pattern
+ Ground pattern
△ Wetness sensor
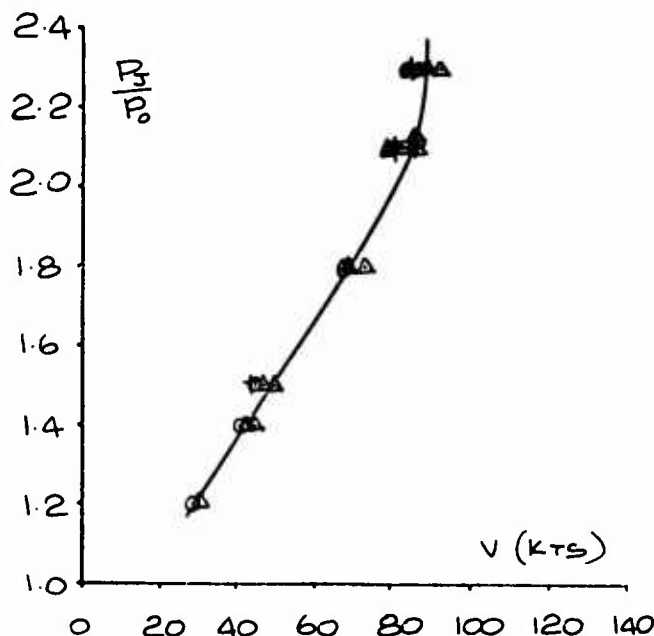
Fig. 6. Model G.16 re-ingestion boundary. Auxiliary inlet open

Fig. 7. Exhaust plenum chamber on Rolls Royce hot model

High pressure air at $400^{\circ}C$ was supplied to the plenum chamber from a single Olympus combustion can. A rapid acting valve enabled the hot air to be exhausted to atmosphere when not required for the model, thus avoiding heat soak on the model.

Intake air temperature was observed by a rake of eight rapid response thermocouples in each intake at the engine face position.

The jet total pressure was defined by 4 static pressures in the plenum chamber. A baffle plate destroyed the entry velocity (fig. 7) and close agreement between the static pressures was obtained.

The intake temperatures and tunnel speed were recorded on ultra violet film, and at a fixed intake and nozzle flow condition the tunnel speed was reduced from its maximum (58 kt) until re-ingestion occurred. This point was defined by a rise of temperature for one or more thermocouples.

Results for different cascade designs are shown in fig. 8. This shows the data in the relative velocity form used in ref. 1, where $V_R = \sqrt{q_0/q_J}$ and $q_J = P_J' - P_o$. The value of h/d is in fact constant for all these tests at 2.87 and χ/h for the auxiliary inlet position is 3.80. The scatter from up to 8 nozzle pressure ratios at each geometry is indicated by the vertical lines.

The effect of lateral deflection is seen to be almost linear for 73° and 65° vertical deflection. However, with the jets swept further forward to $\Theta = 45°$ the effect of lateral deflection is much more dramatic. This presumably occurs because the jet stagnation point on the ground moves closer to the position of the wing leading edge for a given $\emptyset$ at low values of Θ and the jet "escapes" from under the wing more readily.
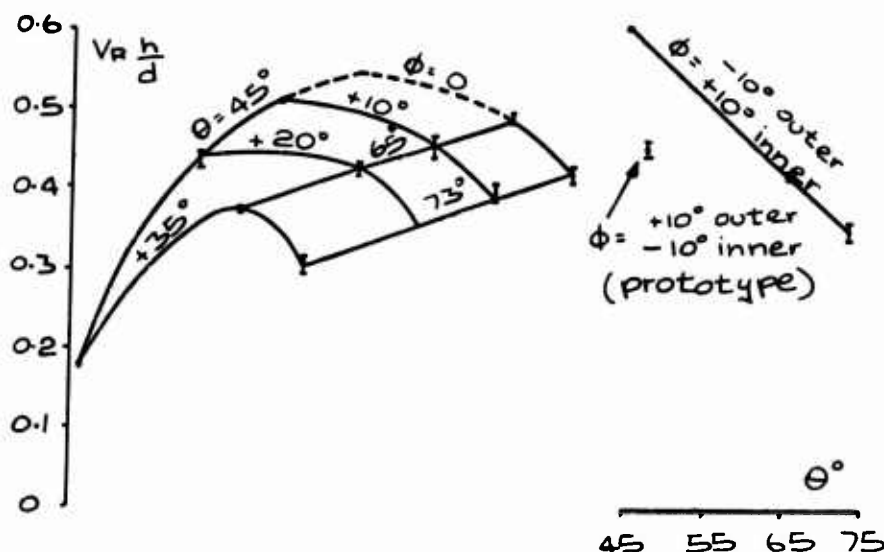
Fig. 8. Re-ingestion boundaries from the Rolls Royce hot model. Auxiliary inlets open

3.3 NGTE Vehicle mounted model

This is a 1/15 scale complete aircraft model which is suspended from an A frame outrigger mounted from the NGTE 136 high speed research vehicle (fig. 9). The model is supported at scale height above the ground, but the undercarriage is not represented for mechanical reasons.

Fig. 9. NGTE research vehicle

The vehicle, diesel powered at low speeds, is propelled for high speed testing by an Avon Mk. 204 jet engine, which also provides compressor bleed air to the model. This air is used both to induce the intake flow and also as the exhaust gas. For this use it is further heated to 530°C by combustion in a Dart combustion chamber mounted in the model fuselage and is exhausted through scale representations of the T.28 nozzle on the port side of the model. The starboard nacelle has no exhaust flow.

Re-ingestion is detected by thermocouples in the port intakes, the temperatures together with vehicle speed and jet pressure and temperature being recorded on a UV recorder.

The model combustion chamber is lit whilst the vehicle is stationary and the Avon engine speed is set to give the required model pressure ratio and left at that setting. Then the vehicle propulsion nozzles are set to the "full ahead" position and the vehicle accelerated to a speed about 15 kt above the expected re-ingestion speed. The propulsion nozzles are then moved to the reverse configuration producing a deceleration of about 2 to 3 kt/sec. until re-ingestion is obtained.

Maximum speeds used were about 90 kt which was set by the length of the Farnborough runway and brakes-only stopping distance. Heat generation at the outboard supporting wheel also gave rise to concern, but in principal higher speeds are achievable.

The advantages of this type of test are that

- there are no tunnel interference effects

- no tunnel limitations on gas temperature

- no ground boundary layer

- accurate mechanical ground speed measurement

Disadvantages are

- reliance on weather conditions

- difficulty in controlling model height above the ground during tests. Repeat runs are necessary to reduce this effect.

Tests have been carried out with varying model height as well as for a range of jet pressure ratios. The results are included in fig. 11.

3.4 Comparison of model tests for T.28 Nozzle

When comparing results from models with scale nozzle representation (G.16 and NGTE model) with results from a plenum chamber model (hot half model) care must be taken over the interpretation of the measured jet pressures. Considerable turning losses occur between the jet pipe and the point at which the flow leaves the reverser, and these are not represented on a plenum chamber model.

It has been possible to determine these turning losses for the T.28 by two means. Firstly force tests were available on a scale isolated nozzle with cold flow. The efflux flow angles were also determined on this model using oil flow visualisation on plates mounted well clear of the model. By comparing the measured force with the flow direction and jet pipe pressure it is possible to estimate the turning loss (fig. 10).

Secondly it can be postulated that the re-ingestion results from a model such as G.16 should collapse to a unique value of V_R where q_J is defined on an effective exit pressure. By trial and error a set of losses was produced which allowed the mean line of fig. 6 to be represented in this way. These are also shown in fig. 10 and are in very good agreement with those derived from the force measurements.

Fig. 10. Reverser pressure losses on Type 28 nozzle

Using these turning losses for the G.16 and NGTE results, the position of the efflux front is given in fig. 11.

This figure includes G.16 mist photograph results for tests with equal pressure ratios for inner and outer nozzles and also results for non-equal pressures. For these cases a mean value of q_J was used. The diameter of d_J was calculated from the sum of both nozzle exit areas.
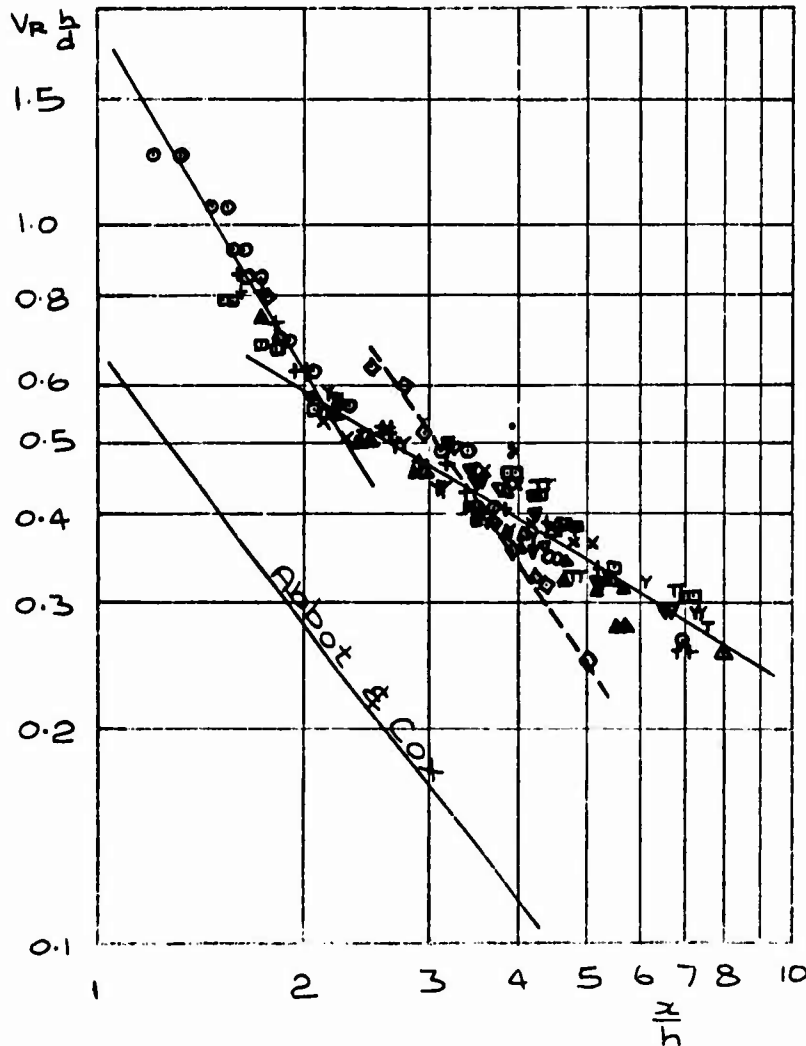
Fig. 11. Reverse efflux front position for type 28 nozzle

The two hot models give results at re-ingestion only (jet efflux at the auxiliary inlet station). The NGTE results however include variation of the model height h.

The collapse of the data is surprisingly good. Disrupting influences might be expected due to the variation of efflux angle with pressure ratio referred to previously and also due to changes in effective exit area with pressure ratio. G.16 tests also showed that the flow is unsteady.

For a given value of x/h the appropriate $V_R h/d$ is distinctly higher than that predicted for the nominal configuration ($\phi = 0, \theta = 25°$) from the data of ref. 2 for jets without airframe interference. The logrithmic plot also illustrates the abrupt change in power law at $V_R h/d \simeq 0.57$ which seems to apply to all tests except that with blowing on one nozzle only. The areas of efflux on the ground for various $V_R h/d$ are approximately shown on fig. 12, derived from the G.16 oil flow photographs. These do not show anything significant occurring at the critical $V_R h/d$. The effect cannot be the onset of interference between the two sides of the aircraft since the NGTE model, which has no exhaust on one side, shows the same trend as the half models.

A possible explanation is that as the efflux front advances, the induced upwash ahead of it causes a vortex to spring from the wing leading edge. This vortex induces a forward velocity component beneath the wing thus reducing the local value of q_0.

The three models show some differences in mean level. The highest value of V_R h/d is returned by the Rolls Royce half hot model and the lowest by the NGTE vehicle rig. This difference is in the expected direction since the NGTE model has no spurious boundary layer effects and only has exhaust flow on one side of the model. The difference between the Rolls Royce model and G.16 is much larger than would be estimated by comparing simple calculations of mean "free stream" momentum between the ground and the wing for the two models.

3.5 Prototype Aircraft Results

Fig. 13 shows the re-ingestion data gathered from prototype aircraft in the datum configuration ($\emptyset = 47°$, $\theta = \pm10°$) presented in terms of jet pipe pressure ratio and forward speed.

As speed is reduced at a given pressure ratio, slight rough running (oscillations noted on the trace of engine HP compressor delivery pressure P_3) is first encountered. Some 15 kt below this a rise in temperature can be measured at the compressor face. This seems to be related to the incidence of compressor surge.

Fig. 12. Model G.16 ground flow patterns

It was stated previously that the flow situation during reverse is unsteady. This unsteadiness propagated forward of the reverse efflux is the probable explanation of the rough running seen before hot gas enters the intake.

The only model tests which can be compared with the prototype aircraft are those on the Rolls Royce half model. These have to be slightly adjusted for the difference in nozzle - intake length between prototype and production aircraft and this was done using the power law derived from fig. 11. No reliable turning loss information is available for the T.10 nozzle and so that for T.28 (fig. 10) has been used to give the model line shown on fig. 13. This is about 10 kt worse than the aircraft speed for temperature rise over most of the pressure ratio range.

Fig. 13. Prototype re-ingestion measurements. Datum configuration

The second configuration tested on the prototype 001 had lateral deflection of +20° on both inboard and outboard nozzles. This re-design entailed a 4.4% reduction in exit area for the lower cascades. The model data from fig. 8 interpreted at the reduced exit area would indicate a 3-6 kt improvement from the datum configuration but the aircraft shows an improvement of 10-16 kt (fig. 14).

Some of the taxi tests used to evaluate this configuration (tests were done in both directions along the runway) had a 12 kt crosswind component. This seems to increase the rough running speed band but not to alter the ingestion speed.

Fig. 14. Prototype re-ingestion measurements.
Configuration 2.
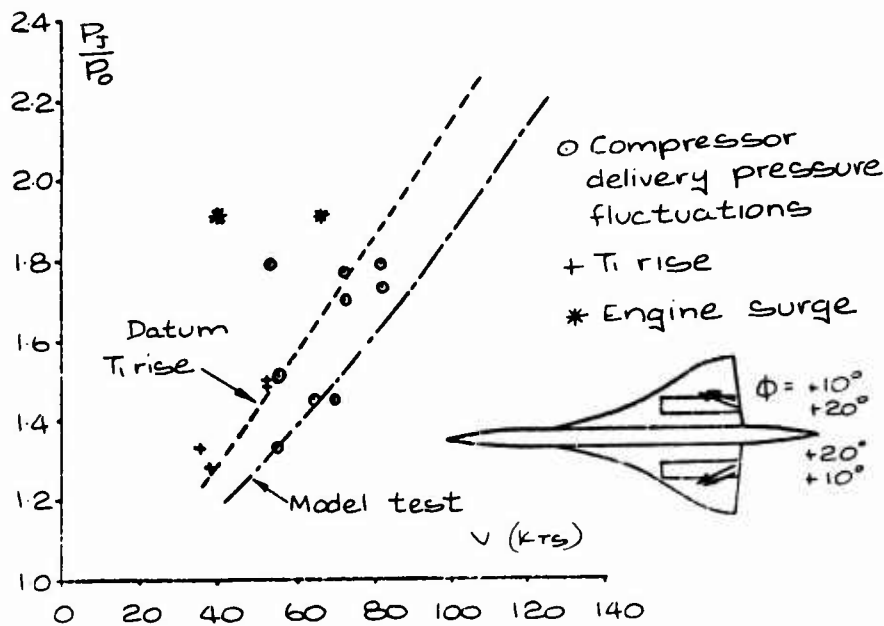
Fig. 15. Prototype re-ingestion measurements
Configuration 3

The third config-
uration tested on the
prototype 001 had
lateral deflections of
+10° outboard and +20°
inboard with an area
increase of 2.8% relative
to the datum. This
configuration was not
tested on the model, but
if it is considered to
be equivalent to a +15°
+15° configuration the
model indicates a 4-9
kt deterioration relative
to the datum. The
aircraft results show no
change from the datum
(fig. 15).

3.6 **Production Aircraft
Results**

Fig. 16 shows re-
ingestion measurements
together with estimates
derived from the three
models.

Only rough running
and surge points are
shown here. Temperature
measurements have been
made for about half the
cases shown, and these
indicated that the
temperature rise is co-
incident with the onset
of roughness. This is
different to the proto-
type situation and is
not fully explained by
the faster response of
the temperature probes
used on the production
aircraft.

All three models
predict re-ingestion at
lower speeds than those
observed on the aircraft.
This again is contrary
to prototype experience.

It is worth noting
that on many occasions
aircraft have operated
to the left of the surge
band of fig. 16 without
experiencing surge. The
surges experienced have
been mild, they have not
always been noticed by
the crews, and have never
led to engine flame-out.

4. REVERSE THRUST FORCES

4.1 Model Tests

The tests used by SNECMA to synthesise a reverse thrust performance brochure consisted of
models at 1/20 scale of a single nozzle. This was sting mounted and included no wing representation.
Tests covered a range of speeds to cover the in-flight reverse cases as well as ground-borne cases.

At zero forward speed, data from full scale engine test bed trials was used.

Fig. 16. Production re-ingestion measurements

4.2 Ground Borne Reverse Thrust

Tests have been carried out on the pre-production aircraft 02 in which the deceleration of the aircraft was measured under the influence of reverse thrust, but with no wheel braking applied. These tests covered a range of aircraft speeds and power settings and were conducted both as accelerate-stop tests and in the course of normal landings. Deceleration was measured at the aircraft inertial platform. These tests were analysed by Aerospatiale to obtain the reverse thrust force per engine. The assumptions made in this analysis are :-

- Aerodynamic lift and drag are unmodified by reverse thrust. The values used are given by tunnel tests with a ground board with corrections to full scale Reynolds number

- The coefficient of rolling friction is constant with speed. The value used was obtained from taxi tests with engines at forward idle. By comparing accelerations with four engines operating with those obtained with two engines operating and two engines cut, the weight and speed being the same for both tests, the thrust of an engine at forward idle may be deduced. This value may then be used, with the aerodynamic data described above and the measured accelerations, to calculate a value for the coefficient of rolling friction. This calculation gave μ = 0.016 at a speed of 35 kt.

The influence coefficients shown in table 1 indicate that the errors introduced into the determination of reverse thrust by these assumptions is not as serious at might be imagined. The main sources of error probably lie in the measurement of weight and acceleration.

TABLE 1

Effect of errors on reverse thrust determination
$$V = 90 \text{ kt}$$

N_2 Std. %	74	80	85
$\frac{\partial X_R}{\partial C_D} \cdot \frac{C_D}{X_R}$	-0.28	-0.17	-0.14
$\frac{\partial X_R}{\partial \mu} \cdot \frac{\mu}{X_R}$	-0.55	-0.34	-0.23
$\frac{\partial X_R}{\partial \delta} \cdot \frac{\delta}{X_R}$	-2.27	-1.88	-1.61
$\frac{\partial X_R}{\partial W} \cdot \frac{W}{X_R}$	-2.84	-2.22	-1.83
$\frac{\partial X_R}{\partial V} \cdot \frac{V}{X_R}$	-0.72	-0.52	-0.44

The data obtained from these tests are presented in fig. 17. A strong interference effect is seen which drops the thrust by 30% relative to prediction over the range of V_R h/d tested.

Little is known of the flow conditions which give rise to this thrust loss at low V_R h/d. It was noted during G.16 tests that the efflux leaving the reverser was swept further aft when the ground board was present than in free air conditions. The angle θ was measured at zero forward speed and $P_J/P_0 = 2.1$ using an oil flow visualisation technique and was found to be 32° in free air and 14° with the ground board. This would represent a thrust loss of 27% assuming constant turning losses in the reverser. A lift force of 12% of free air X_R is also implied if the upper efflux is assumed to be unaltered. This lift force represents the effect on the aircraft of the pressure field generated beneath it by the reverse efflux and the loss in thrust represents the efflux momentum which generates this pressure field.

Taxi 5 6 7 16 Flight 83 84 86 87 90 98 99 100

Symbol L ⌐ ⌐ ⌐ ⊙ + △ × □ T ▽ Y
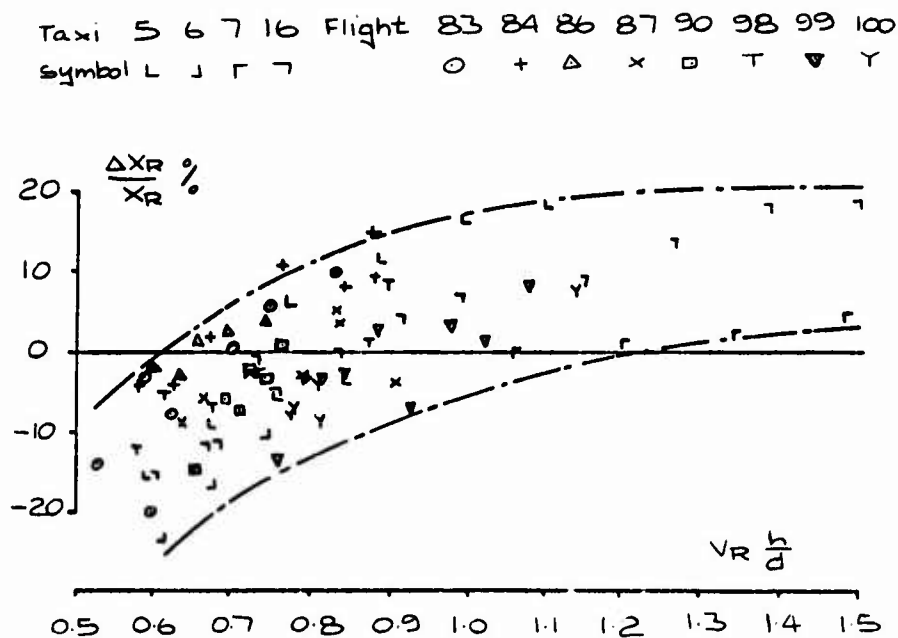
Fig. 17. Measured ground-borne reverse thrust on aircraft 02
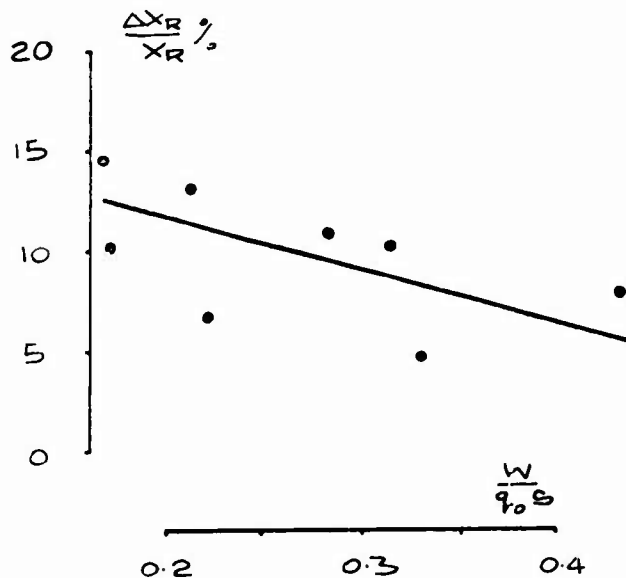
Fig. 18. Measured airborne reverse thrust

4.3 Airborne Reverse Thrust

Airborne reverse thrust performance has been tested on pre-production aircraft 02. In these tests reverse thrust at idle setting was used on two engines, the other two being at forward idle. This configuration resulted in descent rates of up to 6,000 ft/min at constant calibrated air speed. The tests covered a speed range of 250 - 350 kt CAS at altitudes between 9,000 ft and 32,000 ft.

Reverse thrust force was deduced from the measured flight path assuming that the lift and drag characteristics were unaffected by reverse thrust. Lift and drag data had previously been established by flight tests on this aircraft.

Fig. 18 shows the results obtained. At low values of C_L the force is about 12% greater than predicted from isolated model tests. This agrees with the ground borne tests at high V_R h/d which are for an incidence of 2°. As C_L increases there is a 7% loss of thrust over the range considered.

5. EFFECTS ON HANDLING OF IN-FLIGHT REVERSE

5.1 Prototype Model Tests

Wind tunnel tests were made on a 1/18th scale model with simulation of the reverser nozzle efflux by blowing through tubes introduced through the rear of the nacelles but not connected to the model (Fig. 19). The reversers, as Type 10, were represented by a plenum and cascade. The nacelles being blocked, there was no representation of the appropriate flow at the intake, but these effects were available from complimentary tests.

In this fashion six component measurements were made of the interference effects of the use of thrust reverse at various mass flow conditions, for various combinations of engines in forward or reverse configuration.

It is seen (Fig. 20) that there is a progressive loss of lift with increasing dynamic head of the reverse efflux, proportionately stronger at lower pressure, and slightly more significant at higher incidence. The effects are somewhat smaller with the outer engines reversed as compared with inners reversed.

The effect on pitching moment (Fig. 21) is seen to be very marked in the

Fig. 19. Prototype model testing

pitch-up sense, particularly at high C_L, and these effects too are proportionately stronger at low reverse efflux pressure. Again the effects for the outer engines in reverse are somewhat smaller than those for the inners in reverse.

These results, indicated that reverse should be restricted to speeds above 220 knots ($C_L \doteq 0.4$), and idling engines only ($q_J/q_o \doteq 1.5$).
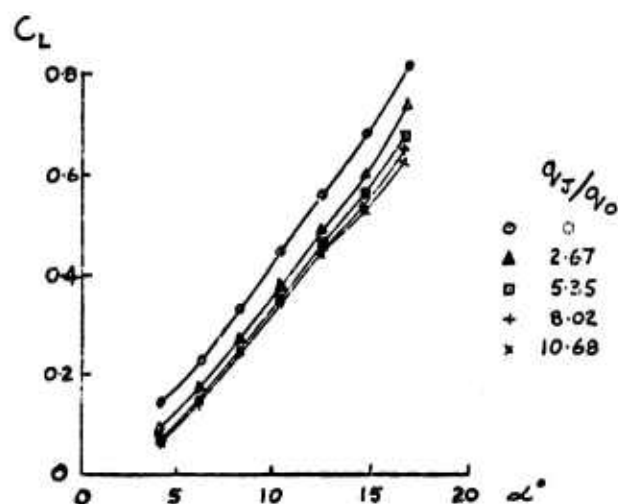
Fig. 20. Prototype model tests. Effect of inner engines in reverse on lift coefficient
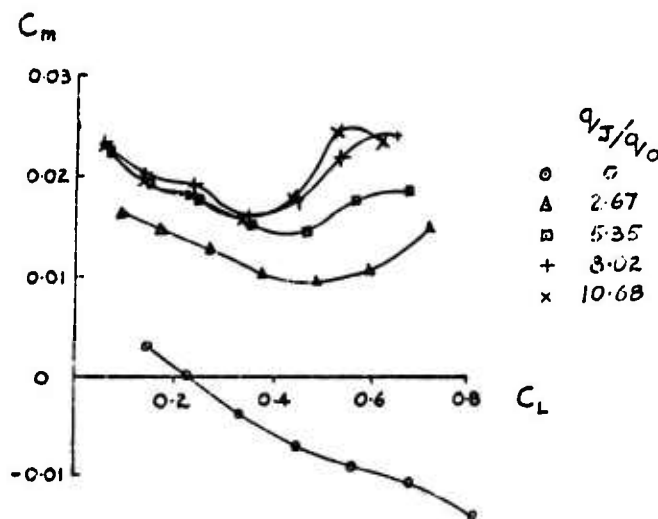
Fig. 21. Prototype model tests. Effect of inner engines in reverse on pitching moment

5.2 Production Model Tests

With the introduction of the Type 28 nozzles with the reverse efflux further aft on the wing, it was hoped that the interference effects on pitching moment would be significantly reduced.

Wind tunnel tests were again made on a 1/18th scale model, but by using a hollow strut, with an air bearing device at the model mounting, the constraints of the air delivery tubes used in prototype tests were avoided. Air was carried through the model to inducers in the nacelles (Fig. 22) which with suitable baffling allowed a simulation of the intake and exhaust flow conditions. Pressure surveys of the efflux in wind-off conditions showed that the efflux shape and the turning angle of the reversers were being adequately represented.

The results are presented with the actual reverse thrust contribution subtracted such that only the interference effects are shown, as for the prototype results.
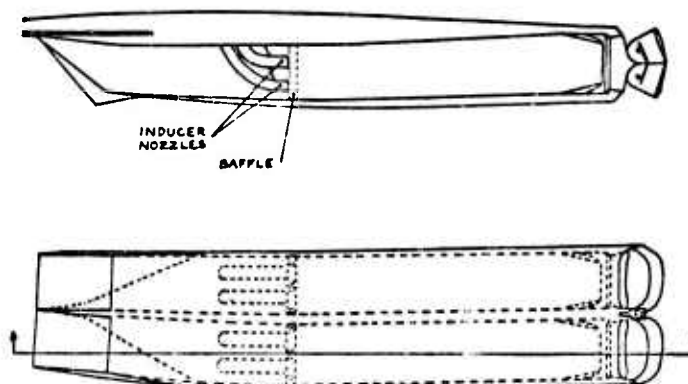
Fig. 22. Production model nacelle

The effects on lift (Fig. 23) are very small, and the effects on pitching moment (Fig. 24) are considerably reduced compared to those of the prototype. Results with the outers in reverse are similar to those presented for the inners. There is no sign of any pitch-up effects at high C_L; only an increment in pitching moment, largely invariant with C_L, but proportional to the dynamic head of the reverse efflux. It must be noted however that the maximum dynamic head tested was less than half that tested on the prototype.
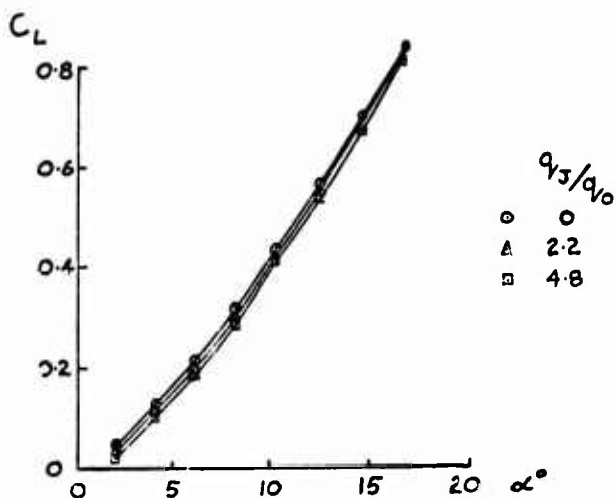
Fig. 23. Production model tests. Effect
of inner engines in reverse on lift coefficient
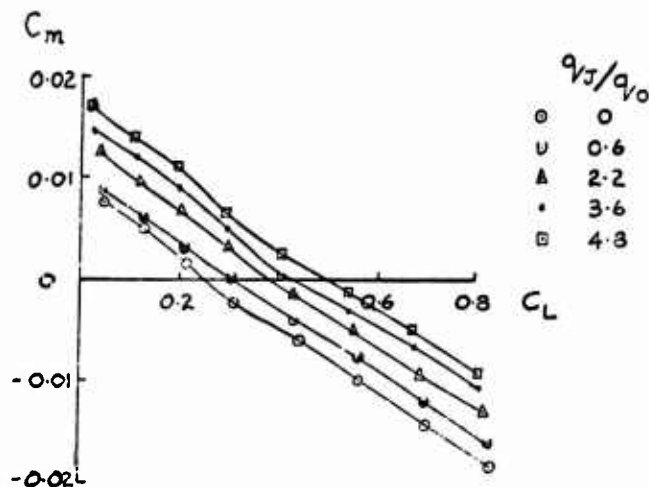
Fig. 24. Production model tests. Effect of
inner engines in reverse on pitching moment

5.3 Comparison with Flight Results

The change of trim due to selection of reverse thrust on the aircraft has been compared with
estimates made using the tunnel results. The estimates include the actual thrust contributions
as well as the interference effects, and also take account of the reduced control effectiveness due
to reverse (this can be as much as 15% for the reverse efflux pressures used in flight). The trim
changes are the difference between the forward idle thrust condition prior to selection and the
steady state following the pushover to the new descent flight path angle after selection of reverse.

It is seen (Fig. 25) that the prototype flight measured changes in trim are much smaller
than the estimates; negligible change at lower speeds and perhaps 50% of estimated at higher speeds.

Comparison of flight results from pre-series aircraft 02 (substantially the production
configuration) with estimates using production model results shows a more reasonable agreement
(Fig. 26).

Some of the discrepancy of the prototype results may be explained by aeroelasticity, since
there is a significant loading change on the aft part of the wing which will induce a twist at the
tip giving a nose down pitching moment, such an effect will be considerably less on the production
type aircraft.
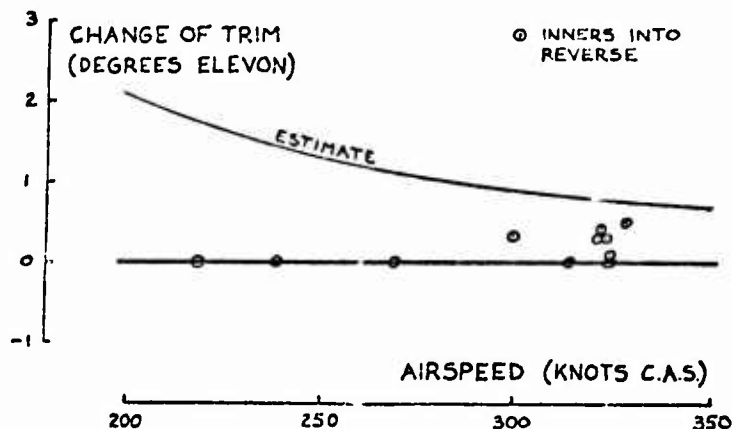
Fig. 25. Prototype flight test results
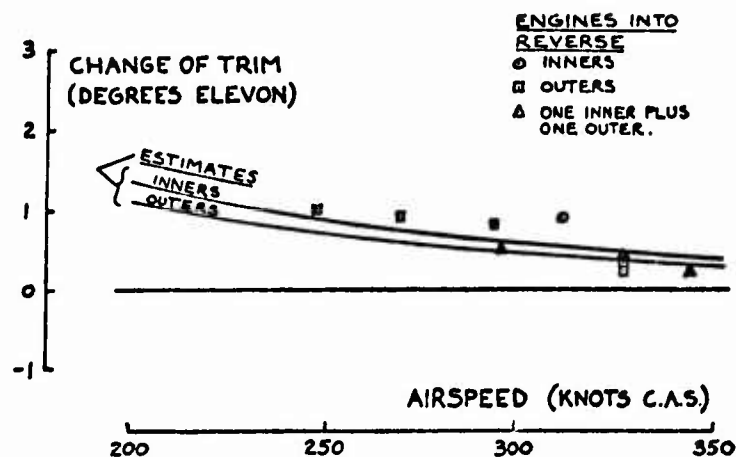
Fig. 26. Production aircraft flight test results

CONCLUSIONS

Re-ingestion flows can be simulated with hot or cold flows. The results may be scaled provided reverser turning losses are allowed for.

Application of model re-ingestion tests at full scale may be difficult since induced flow effects ⋅ ὁ the intake can be important.

Interference effects can reduce the ground borne reverse thrust force by 30%.

Stability effects of airborne reverse thrust can be represented in model tests, but application at full scale requires knowledge of the control power and aeroelastic effects of reverse application.

References

1.   R.A. Tyler and R.G. Williamson : Wind tunnel testing of V/STOL engine models - some observed flow interaction and tunnel effects.   AGARD-CPP-91-71

2.   W.A. Abbot : Studies of flow fields created by vertical and inclined jets when stationary or moving over a horizontal surface.   ARC. CP. 911

REYNOLDS NUMBER EFFECTS ON FORE- AND AFTBODY PRESSURE DRAG

Felix Aulehla and Geert Besigk

Messerschmitt-Bölkow-Blohm GmbH
Unternehmensbereich Flugzeuge
D 8 München 80
Postfach 801160
Germany

SUMMARY

Recent aftbody drag results obtained from different transonic wind tunnel measurements showed such large increases in aftbody pressure drag with increasing Reynolds number that extrapolation to full scale became questionable. The present paper tries to clarify this unexpected Reynolds number effect and also contributes to an improved testing technique.

An analysis of a wind tunnel investigation at Mach number 0,8 on a series of axisymmetric bodies showed as main result that varying Reynolds number produces opposite changes in pressure drag on fore - and aftbody, respectively. It is explained that this result could very well be caused by wind tunnel interference. As a consequence, to determine aftbody drag correctly it will be required either to test in interference free wind tunnels or to take into account the compensating effects on the forebody.

Furthermore, it is pointed out that modifications in aftbody geometry affect forebody drag. Results from the commonly used aftbody test rigs with forebodies fixed to the ground therefore need appropriate corrections.

Finally, the sensitivity of drag components with respect to the location of split lines is discussed. It is shown that subdividing the boattail is not advisable from an accuracy point of view.

LIST OF SYMBOLS

A	Cross-section of body	M_o	Free stream Mach number
A_{max}	Maximum cross-section of body	P_o	Free stream static pressure
C_D	Drag coefficient, referred to maximum body cross-section area, $D/q_o A_{max}$	P_{T_j}	Jet total pressure
		q_o	Free stream dynamic pressure, $0,5\rho_o V_o^2$
C_{D_F}	Friction drag coefficient		
		R	Radius of body
C_{D_P}	Pressure drag coefficient	Re	Reynolds No., based on length of body; Re_1 = lowest, Re_3 = highest value tested
C'_{D_P}	$(2\pi/A_{max}) \int_{R=0}^{R} C_P R dR$	S	Wetted surface
C_{D_T}	Total drag coefficient, $C_{D_P} + C_{D_F}$	V_o	Free stream velocity
$C_{D_{T\,0\%}}$	C_{D_T} of profile with zero thickness		
C_P	Pressure coefficient, $(P - P_o)/q_o$		
$\overline{C}_P$	Mean value of C_P over $0 < x/L < 1,0$	SUBSCRIPTS AND ABBREVIATIONS	
ΔC_P	Difference in C_P relative to intermediate Reynolds number Re_2, $C_{P\,Re} - C_{P\,Re_2}$	AB	Aftbody
		FB	Forebody
		W/T	Wind tunnel
$\overline{\Delta C_P}$	Mean value of ΔC_P over $0 < x/L < 1,0$		
D	Drag		
ΔD	Drag difference		
F	Measured gross thrust		
L	Ideal length of body (beyond sting intersection, to $R = 0$)		

1. INTRODUCTION

The correlation of wind tunnel results obtained from small scale models with full scale flight measurements is an old problem in drag determination since the real flight Reynolds numbers can be very seldom achieved. In the past, therefore, one attempted to build models as big as possible and also to cover large Reynolds number ranges. This led to the construction of huge wind tunnels and, for the high densities and Reynolds numbers respectively, to enormous installed power levels. In order to raise the accuracy of measurement, one also tried to weigh only a minimum of wetted surfaces when making force measurements, i.e. it was attempted not to weigh the complete model but only a part of it. When measuring aftbody drag, therefore, the forebody and also the wing and tailplanes were fixed to the ground.

The Reynolds number investigations which were conducted in these facilities (wind tunnel plus test rig) did not always lead to the hoped for clarification of the Reynolds number influence. On the contrary, some of these measurements produced such unexpected results that fundamental doubts arouse about their validity. This paper attempts to clarify some of these dubious Reynolds number effects and also to illustrate basic interrelations, thereby contributing to a better drag synthesis as well as to an improved testing technique.

2. UNEXPECTED REYNOLDS NUMBER INFLUENCE
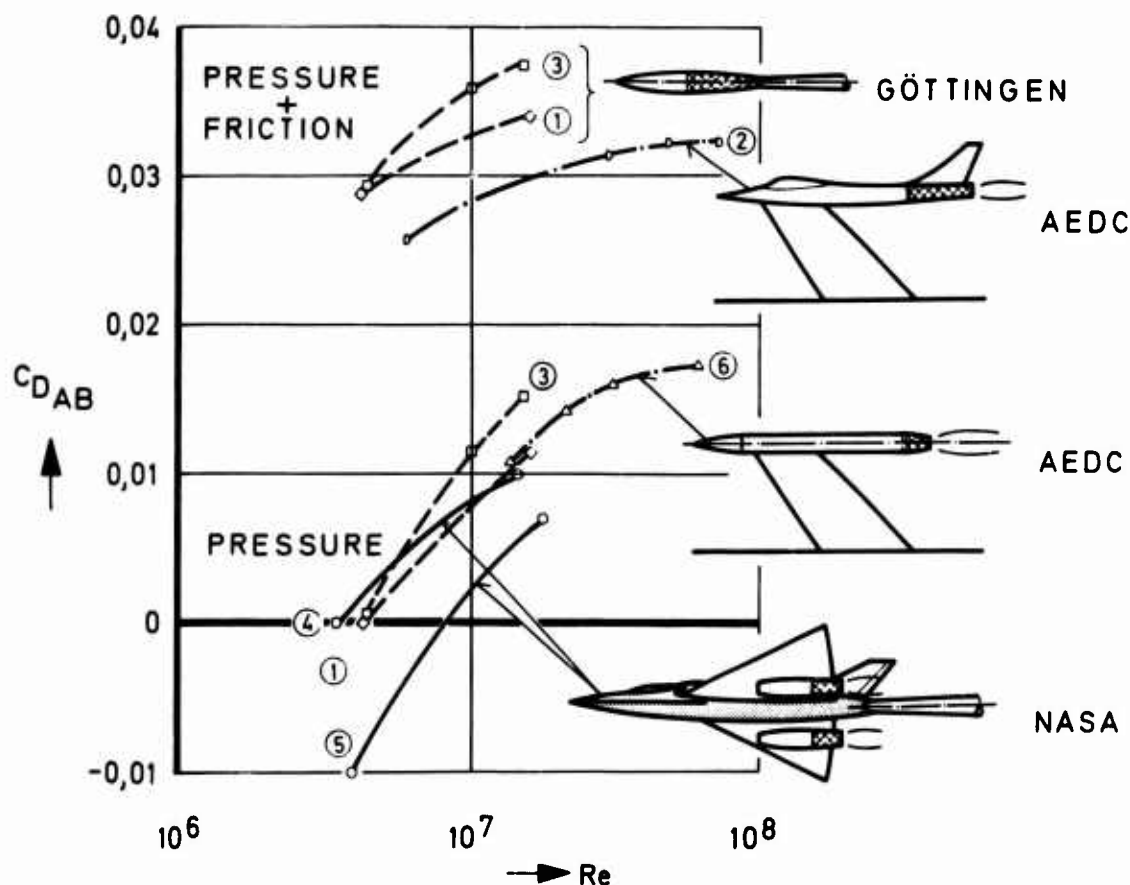
Fig. 1   Reynolds number effect on aftbody drag

Aftbody drag levels recently measured with different models in different tunnels showed an increase in aftbody pressure drag with increasing Reynolds number (fig. 1). Adding friction reduces this increase but does not eliminate it. However, a decreasing tendency had been expected similar to the fully turbulent flat plate or similar to profile drags for slender airfoils (compare e.g. profile drag values computed by Squire and Young, ref. 1). The rapid rise of aftbody drag with Reynolds number makes it questionable whether these data can be extrapolated to full scale. Even when, as widely practised, one uses only differences in drag from wind tunnel measurements, the problem regarding the drag difference between aftbody No. 1 and No. 3 remains essentially the same, because curves 1 and 3 are not parallel to each other.

Curve No.	M_o	$\dfrac{P_{Tj}}{P_o}$		Ref
1	} 0,8	-	AB1 } axisym. body	2
3			AB3	3
2	0,9	3	twin jet fighter	4
4	0,6	?	J-85 nacelle on	5
5	0,9		F-106	
6	0,6	3	axisym. body	6

Fig. 2 Model Configurations

Curves 1 and 3 in fig. 1 stem from wind tunnel measurements conducted by MBB in the 1m x 1m transonic tunnel of DFVLR Göttingen without jet and with different boattail angles (ref. 2 and 3).

Curve 2 was obtained with a strut mounted twin jet fighter model tested by the Air Force Flight Dynamics Laboratory in the 16 ft. transonic tunnel of the Arnold Engineering Development Center (ref. 4).

Curve 6 also results from an AFFDL test in the same AEDC transonic wind tunnel. Here, a single jet model with a cylindrical midbody was used.

Curves 4 and 5 have been obtained with two wind tunnel models of the F-106 with underwing installed J-85 nacelles in the 8 ft. x 6 ft. supersonic wind tunnel of NASA Lewis (ref. 5). It will be explained later that negative aftbody drags may very well be found, depending e.g. on the start of the pressure integration (curve 5).

The variation of Reynolds number was achieved in these investigations by altering the density, except with the NASA tests in which two models of different sizes were used: the smaller model had a scale of 0,05, the larger model, which was a half model, a scale of 0,22. The method of drag determination was not identical: in the Göttingen tests, the total drag (pressure + friction) of the complete, i.e. undivided fuselage was weighed by an internal strain gauge balance. The longitudinal pressure distribution was also measured in one row on the upper side of the body. Several pressure tappings at corresponding locations on the lower side were used as an additional check of the incidence being zero. In the AEDC tests, curve 2, only the twin jet aftbody was attached to the balance, leaving forebody and tailplanes fixed to the ground, whereas curve 6 was obtained from a mere pressure plotting.

3. TAKING INTO ACCOUNT THE FOREBODY

These unexpected test results led to the question of whether taking into consideration the complete body (fore- plus aftbody) might not bring back the familiar drag picture, i.e. whether or not the Reynolds number could have opposite effects on fore- and aftbody. To illustrate the basic interrelations between pressure drag of the fore- and aftbody, the simple case of inviscid flow past an ellipsoid of revolution is considered. Fig. 3 shows that with increasing relative thickness, the separating forces in the maximum cross section can attain large values. These separating forces result from pressure integration on fore- and aftbody respectively (half body, not closed). In the assessment of aftbody drag, however, mostly test rigs are used which weigh only the aftbody leaving the forebody fixed to the ground (fig.23, ref. 7).

It will now be shown that this testing technique may only be used if appropriate corrections are applied. Furthermore, to explain the phenomenon of the Reynolds number effects and to investigate the feasibility of weighing only body sections instead of the complete model, an analysis of wind tunnel measurements conducted in 1971/72 is presented in the following paragraphs.

Fig. 3 Separating forces on ellipsoid of revolution in incompressible inviscid flow

4. GÖTTINGEN MEASUREMENTS

FOREBODY

$$y_v = a_v x^3 + b_v x^2 + c_v x$$

$$a_v = y_{max}/x_1^3$$
$$b_v = -3y_{max}/x_1^2$$
$$c_v = 3y_{max}/x_1$$

L = theoretical length of
bodies = 800 mm

AFTBODY

$$y_h = a_h x^3 + b_h x^2 + c_h x + d$$

$$a_h = y_{max}/(x_2 - x_3)^3$$
$$b_h = -3x_2 y_{max}/(x_2 - x_3)^3$$
$$c_h = 3x_2^2 y_{max}/(x_2 - x_3)^3$$
$$d = (x_3 y_{max}/(x_2 - x_3)^3) \cdot (3x_2 x_3 - x_3^2 - 3x_2^2)$$

AFTBODY	x_2-values
1	0,5 L
2	0,625L
3	0,6875L
4	0,75L
5	0,8125L

AFTBODY No. : 5 3 1

Ø30

Ø120

L = 800 mm

4.1. Windtunnel and Models

The tests were conducted in the 1m x 1m transonic wind tunnel of DFVLR Göttingen. The rectangular test section has four perforated walls, two of which can be rotated from +1° to -2°. The perforation consists of inclined holes yielding an open-area ratio of 6 %. Pressurizing or evacuating the tunnel allowed a variation of the Reynolds number by the factor 4 (ref. 11). The models were bodies of revolution with a common forebody and five interchangeable aftbodies, referred to in fig. 1. The body contours are defined above.

The model with aftbody No. 1 had no cylindrical midbody; thus fore- and aftbody had the same contours. The cross-section distributions and the wetted surfaces are shown in fig. 4.

WETTED SURFACE

CYLINDER

CROSS-SECTION

STING

x/L
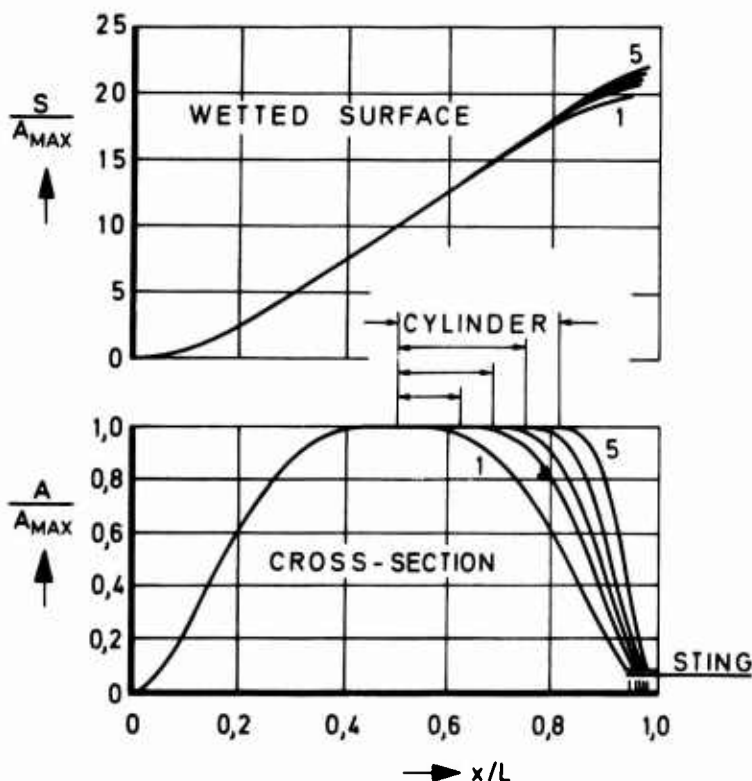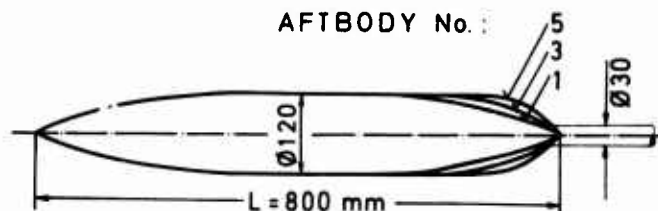
Fig. 4   Model geometry
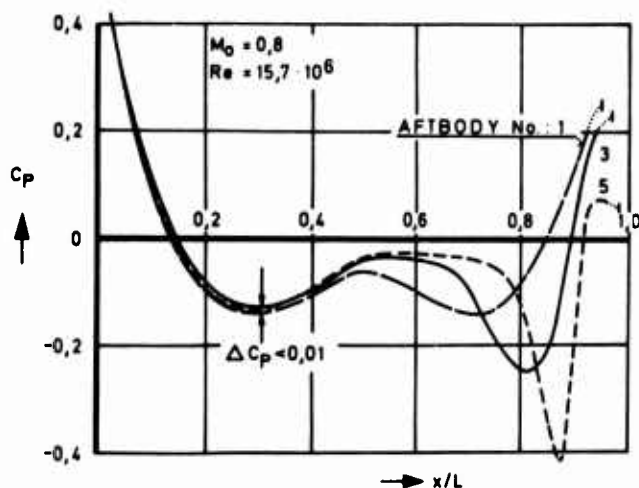
Fig. 5 Effect of aftbody geometry on forebody pressure distribution

4.2. Results

4.2.1. Effect of Aftbody Geometry

The variation of aftbody shape naturally leads to the largest changes in pressure distribution on the rear body; on the forebody there are at the same time only minor changes in pressure distribution. In wind tunnel measurements with forebodies fixed to the ground the surface pressures near the split station forebody/aftbody are therefore in practice often taken as a criterion for a possible upstream influence: if the change of these pressures is sufficiently small, e. g. smaller than 1 %, then no noteworthy changes in forebody drag are expected. In the measurements discussed in this paper a slender boat-tail (No. 1) was replaced by a steeper one (No. 3). Due to this alteration the surface pressure coefficients at the split station changed only by $\Delta C_P = 0,02$; on the greater part of the forebody ($x/L < 0,45$) these changes were even below $\Delta C_P = 0,01$ (fig. 5). The forebody pressure drag, however, increased at the same time from 0,0099 to 0,0147, i. e. by 48 % (fig. 6). This amounts to no less than 6,8 % of the total drag (pressure + friction) of the complete body. (The C_{D_P}-curves in fig. 6 respresent the surface pressure coefficients integrated from the nose of the body to an arbitrary station x/L). For the testing technique in wind tunnels and for flight measurements it follows therefrom that optimizing the aftbody drag by measuring the aftbody alone does not yield valid results, except if appropriate computed corrections are applied to the forebody drag. That is, by omitting such corrections one may succeed in merely transferring the drag problem to the forward end (compare ref. 7, p. 4 - 3) and in an incorrect overall aircraft drag synthesis.

An example of such a computed correction is shown in the upper half of fig. 6. The MBB Subsonic Panel Method (ref. 8)was used for this end neglecting viscosity effects. The agreement between measured and computed drag changes is only qualitatively good. At present it cannot be stated whether the experimental or the theoretical method is more reliable since both are not yet sufficiently exact and since even bigger discrepancies are encountered occasionally. With some optimism and without considering possible systematic errors the mean error in the measured pressure drag is estimated to be of the order of $\pm$ 0,001, which is relatively large. To quantitatively confirm this upstream influence the measurements described above were repeated with the forebody attached to the balance and the aftbody fixed to the ground. These results will be reported in detail in a later paper.

While there are noticeable changes in pressure drag on the forebody, the corresponding changes on the aftbody are below measuring accuracy and this in spite of the fact that it is on the aftbody where the largest changes in pressure distribution take place. That is,in fig. 6 the pressure drags for aftbodies No. 1 and 3 equal 0, 0003 and 0, 0008 resp. This result again emphasizes the necessity of taking into account the forebody.

Fig. 6 Effect of aftbody geometry on pressure drag

4.2.2. Location of Split Lines

Fig. 7 shows a typical aftbody test rig on which the twin jet aftbody is subdivided into the portion of the airframe manufacturer as well as into the portion of the engine manufacturer (protruding nozzle). Such a subdivision occasionally is made following the example of splitting the contractual responsibilities in the development of an aircraft project. The nozzle is then weighed either against the jet pipe or against the boattail. That such a subdividing is not advisable from an accuracy point of view is shown in fig. 8. Here, the total drag integrated from the fuselage nose up to an arbitrary station x/L is plotted against axial distance. The balance for the boattail measures the positive drag B (region of low pressure) while the balance for the nozzle boattail weighs an almost equally large drag N, however, of negative sign (high pressure region). That is, by introducing an additional split line one has burdened oneself with the problem of the difference of two almost equally large values. If B and N can each be measured with an accuracy of, say, 1 %, then the maximum relative error for the total aftbody drag in fig. 8 will amount to 9 %.

If during a wind tunnel measurement Reynolds number, i.e. total pressure is varied, subdividing the model causes additional difficulties because the drag values of the model portions nozzle, boattail, midbody and forebody vary differently with Reynolds number, thus further complicating the synthesis of the aircraft drag (fig. 9). This unorthodox Reynolds number influence on single model components is dealt with in more detail in the following.

4.2.3. Reynolds Number Effects

In fig. 10 the pressure distribution of body No. 3 is plotted. Increasing the Reynolds number lowered the pressures on both, the forebody and the aftbody.
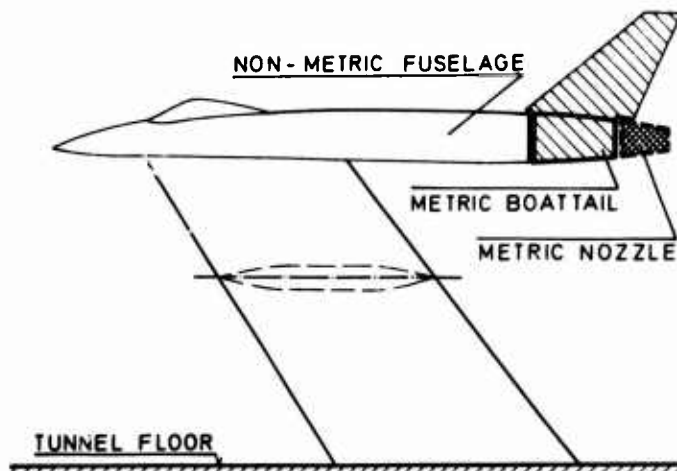
Fig. 7 Typical aftbody test rig with subdivided boattail
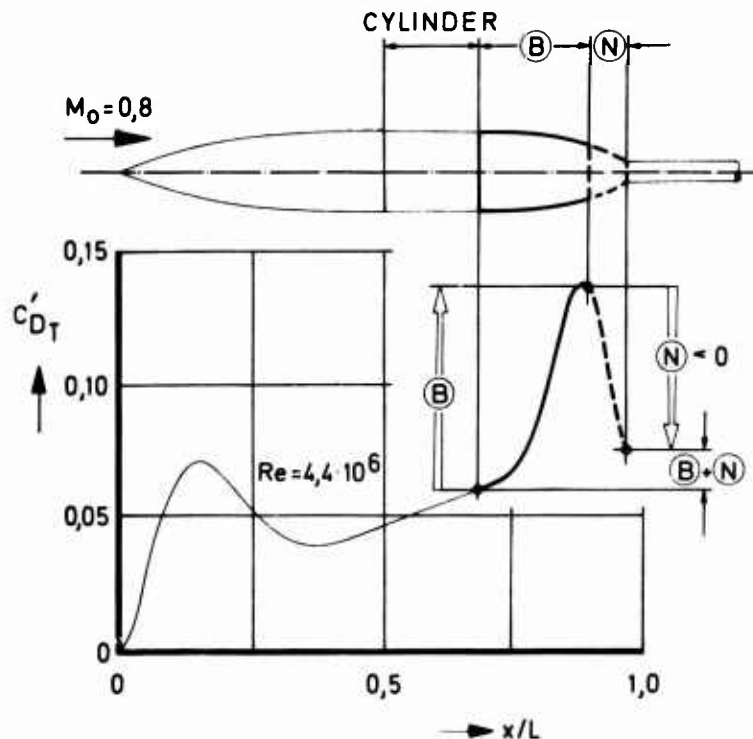
Fig. 8 Drag of boattail subdivisions
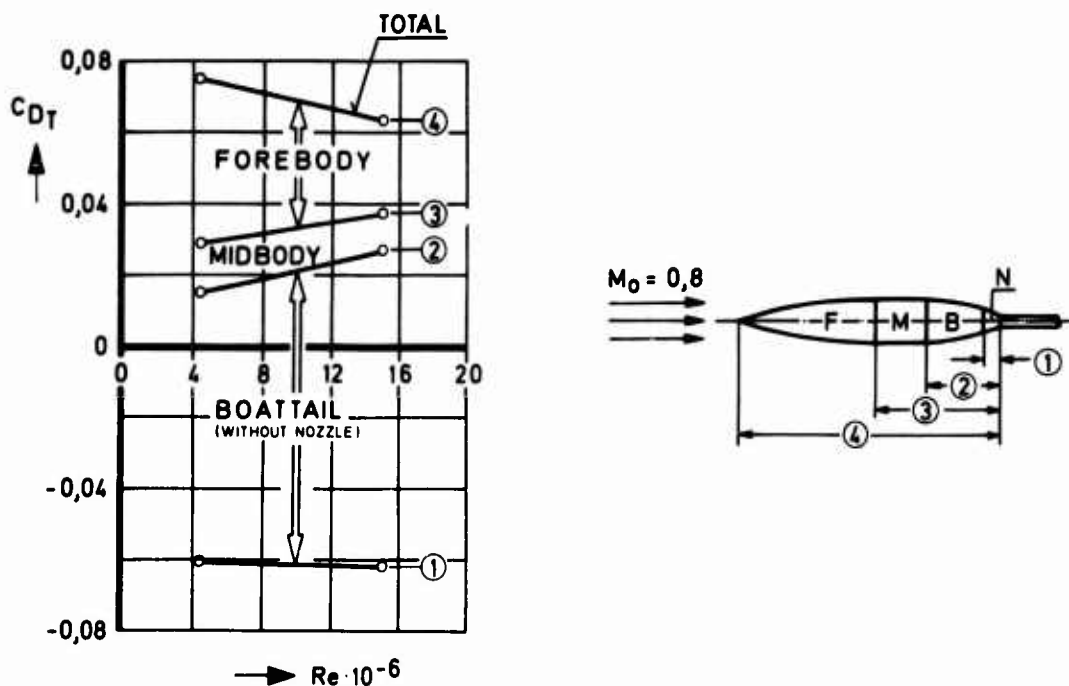
Fig. 9   Reynolds number effect on body subdivisions
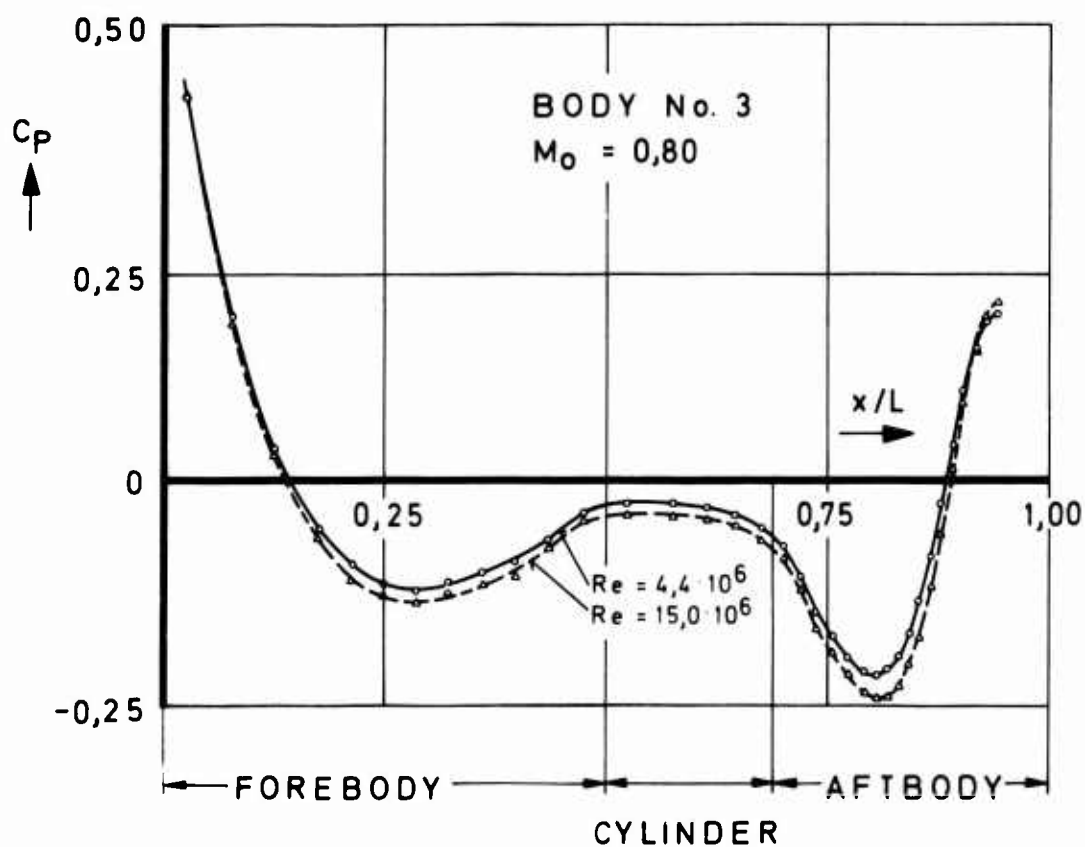
Fig. 10   Reynolds number effect on pressure distribution
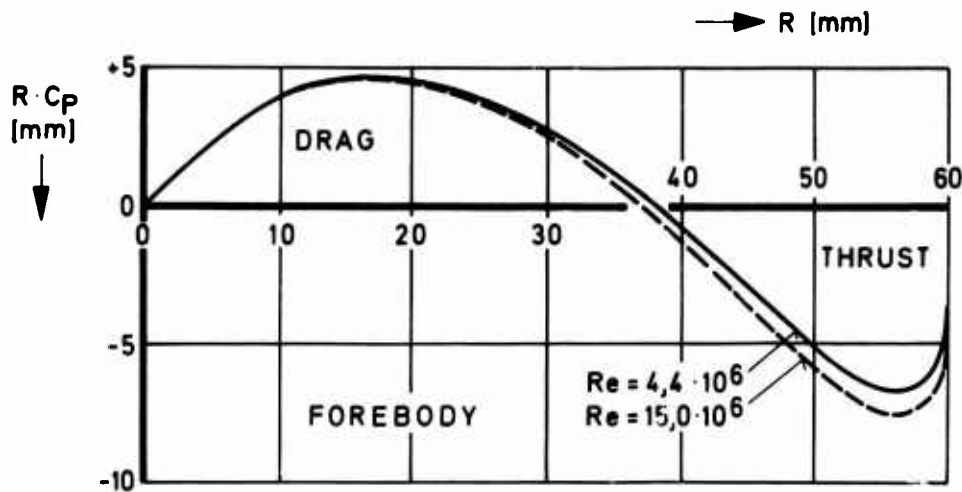
Fig. 11   Axial forces on forebody
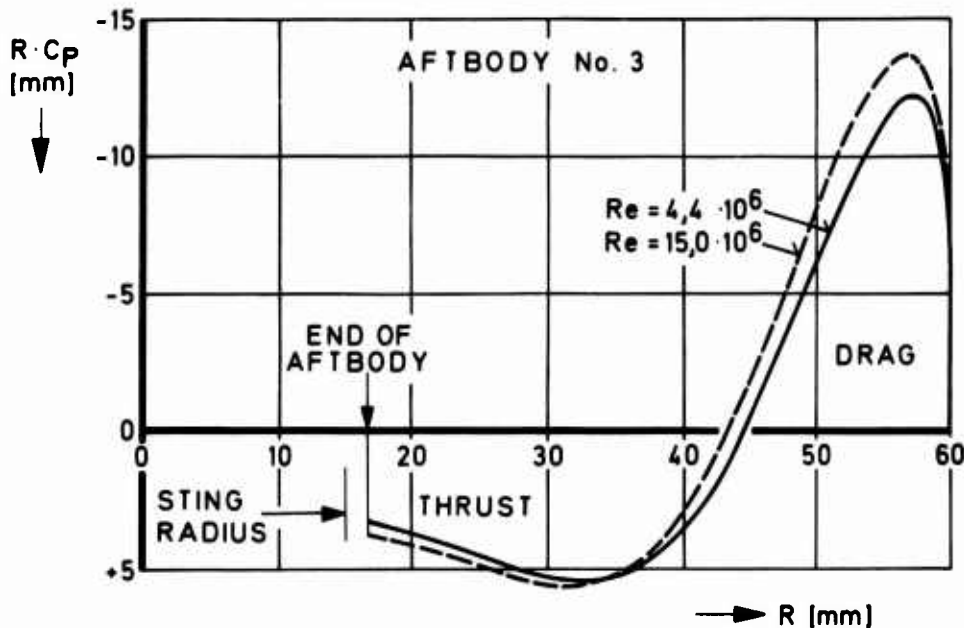
Fig. 12   Axial forces on aftbody

Boundary layer transition was triggered by a carborundum roughness strip which extended from x/L = 0,05 to 0,0575. The grain size was 0,15 mm. The areas under the curves in fig. 11 and 12 represent the corresponding drag and thrust respectively. It is evident that on the forebody as well as on the aftbody thrust and drag are about equal in magnitude whereby they compensate each other almost completely. From this it follows that in drag determination the pressure distribution has to be obtained - no matter whether by theoretical or experimental means - with very high accuracy. This is also why the methods for computing pressure distributions have so far not been satisfactory for an accurate assessment of pressure drag. Fig. 11 can also be used to illustrate the sensitivity of pressure drag towards changes in pressure distribution in general, i.e. independent of Reynolds number effects: if the solid line is lowered merely to the dotted line, which corresponds to an overall reduction $\Delta C_P = 0,012$, the forebody pressure drag is reduced by no less than 83 % as will be shown in fig. 13. In other words, to quote the forebody pressure drag with an accuracy of ± 7 % the mean error in the C_P-distribution has to be smaller than ± 0,001.

Integrating the $R \cdot C_P$-curves in fig. 11 and 12 from the nose of the body (R = 0) up to an arbitrary limit of integration R yields the running sum of the pressure drag coefficient C'_{D_P} in fig. 13. This coefficient enables one to read off the pressure drag not only of the complete body but of body portions as well, which is done by taking the difference of the C'_{D_P} at the beginning and the end of the portion.
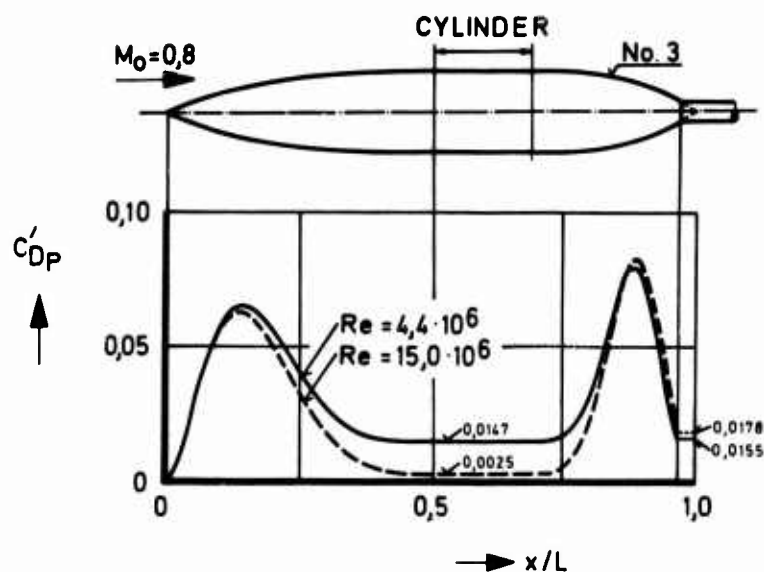
Fig. 13 Reynolds number effect on pressure drag

Increasing the Reynolds number as in the example of fig. 13 results in a reduction of the forebody pressure drag coefficient from 0,0147 to 0,0025, i.e. by 83 %. This corresponds to about 16 % of the total drag of the complete body. On the aftbody this Reynolds number influence is reversed: at the lower Reynolds number the pressure drag is about equal to zero. At the larger Re-number, however, the afterbody pressure drag coefficient is read off as 0,0178 - 0,0025 = 0,0153. Thus, increasing the Reynolds number causes here a rise in aftbody drag by a factor of 19, which is still 20 % of the total drag of the complete body. Adding friction to the pressure drags of fig. 13 gives fig. 14. The friction drag of the complete body was obtained from the difference between the drag from the balance (fig. 15) minus the integrated pressure distribution. The distribution of that friction drag over the body length was theoretically determined (ref. 9).
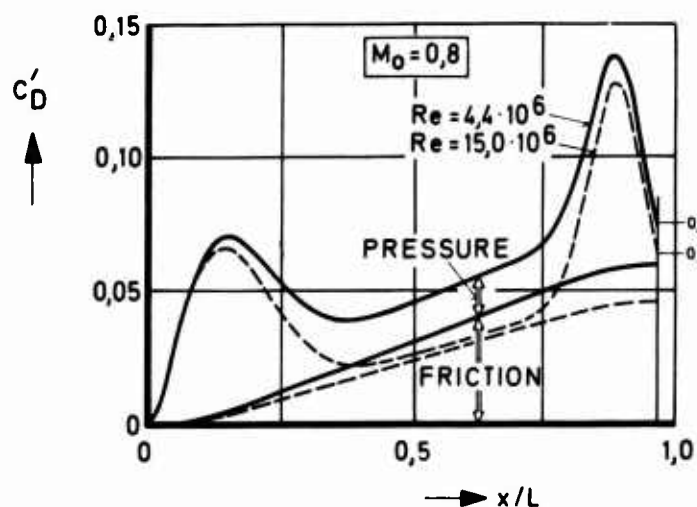
The individual drag components for the forebody (x/L = 0, 5) and for the complete body (x/L ≈ 1, 0) can be taken from fig. 14. These drag components are plotted in fig. 16 for the three measured Reynolds numbers: the pressure drags of both aftbody and forebody change considerably with Reynolds number while the sum of these two components remains almost constant. The friction drag of the fully turbulent flat plate is also shown for comparison; this friction is above the "measured" friction by 11 % at the low Reynolds number and 18, 5 % at the high Reynolds number.

Fig. 14 Reynolds number effect on pressure and friction drag
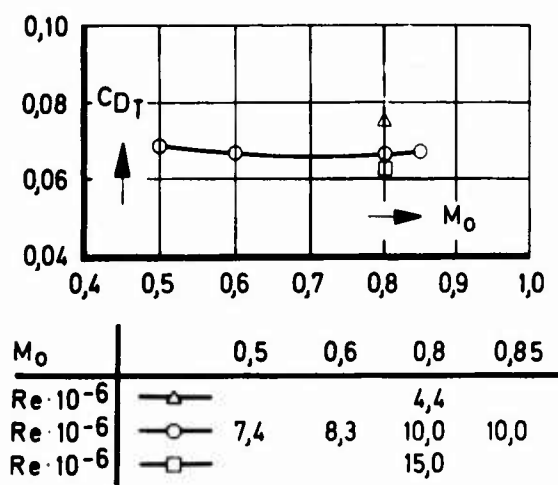
Fig. 15 Drag of complete body No. 3, force measurement
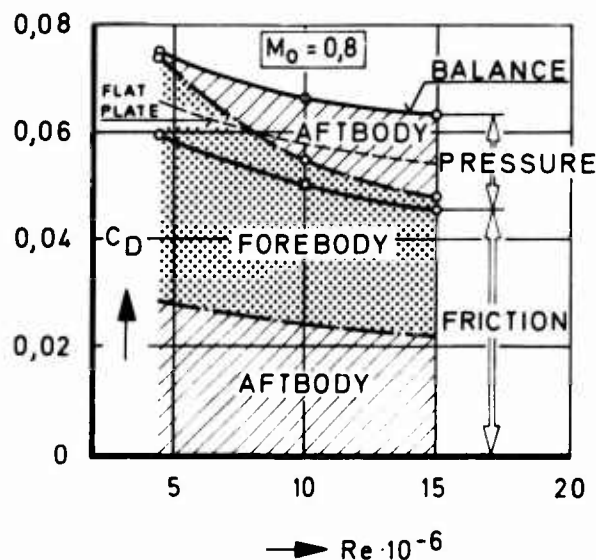
Fig. 16 Reynolds number effect on pressure and friction drag of fore- and aftbody No. 3
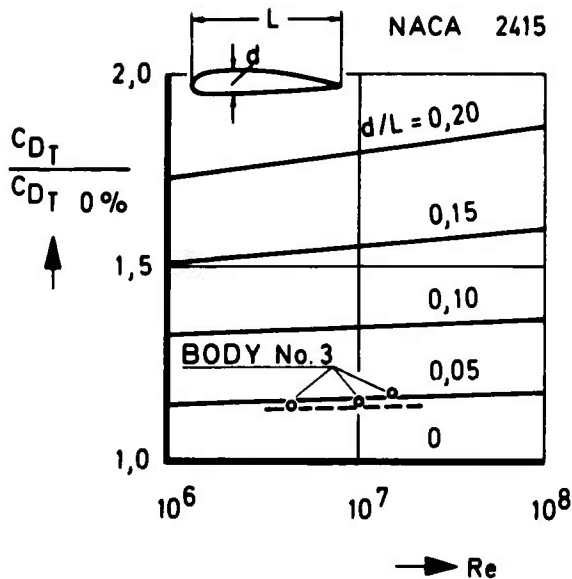
Fig. 17   Increase of relative profile drag with Reynolds number

As a further comparison the profile drags computed in ref. 1 for the incompressible, fully turbulent case were considered and were divided in each case by the drag of the profile of zero thickness (flat plate), fig. 17. It is seen that the profile drag of slender profiles lies above the value of the flat plate by an almost constant factor in the Reynolds number range under consideration. In this context is should be remembered that the flat plate skin friction is reduced to 50 % when the Reynolds number is raised from 10^6 to 10^8. The total drag of the complete body No. 3 measured at $M_o = 0, 8$ was also divided by the friction drag of the fully turbulent flat plate and plotted in the same diagram. To allow for the difference between two-dimensional and three-dimensional bodies the ordinates of the curve for $d/L= 0, 15$ were reduced to 25 % in a first approximation (compare ref. 10) and plotted as dashed line in the same figure. There is good agreement between this dashed line and the weighed drag of body No. 3 having also a relative thickness of 15 %. If only the pressure drag instead of the total drag is referred to the flat plate friction, then a quite similar trend with Reynolds number is found. The pressure drag of the complete body, therefore, seems to be correct. However, whether the aft- and forebody pressure drags are correct remainst still unclear. This question will be critically reviewed in the next chapter.
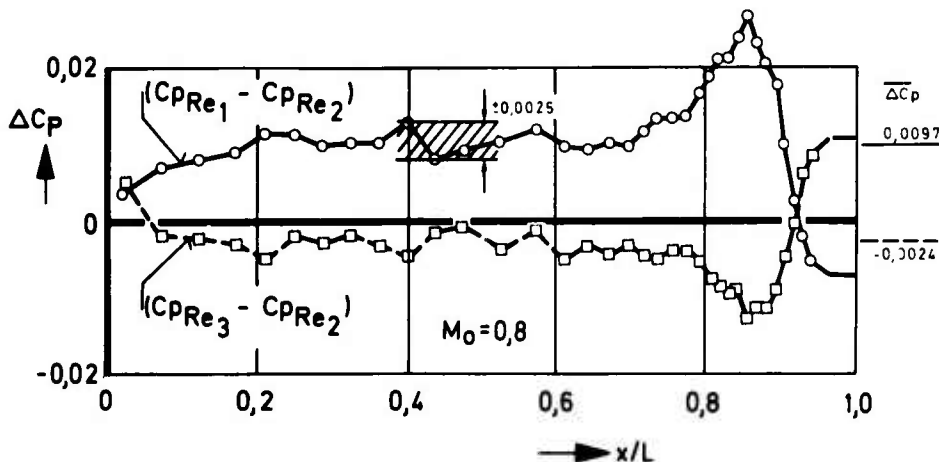
$Re_1 = 4,4 \cdot 10^6$
$Re_2 = 10,0 \cdot 10^6$
$Re_3 = 15,0 \cdot 10^6$

Fig. 18   Change in body pressure distribution due to change in Reynolds number

5. WIND TUNNEL INTERFERENCE

The test results reported in this paper do not include any flight data, but stem exclusively from transonic wind tunnels with ventilated test sections. It was suspected, therefore, that the Reynolds number effects shown in the preceeding chapters might have been caused by wind tunnel wall interference. To investigate this possibility, let us first consider the pressure changes on the model, fig. 18. Changing the Reynolds number caused here an almost constant shift in the pressure distribution over the greater part of the body: increasing the Reynolds number lowered the pressures; reducing the Reynolds number increased them. The scatter of the differences in the individual pressure coefficients ΔC_P lies well within a band of $\pm 0, 0025$ (maximum error). The probable value of the integrated pressure differencies i. e. of the differential pressure drag coefficient ΔC_{D_P} can therefore be quoted with an accuracy of better than $\pm 0, 001$ (mean error). This value was mentioned in chapter 4. 2. 1. The good accuracy in ΔC_P is also reflected in fig. 10 where the original curves i. e. the C_P-distributions are plotted.

Fig. 19 shows the pressure distribution on the upper wall of the test section. There is no pronounced overall pressure gradient along the test section. The mean value at this Reynolds number is slightly positive (+0, 0023). The ragged shape of the curve is probably due to surface imperfections at the pressure tappings, which were not installed with the same great care as on the model, and, above all, due to the presence of the wall perforation itself with its non-uniform crossflow characteristics. Still, the general scatter here is rather large. Even when only the pressure differences resulting from a change in Reynolds number are plotted the raggedness is not reduced, as shown on fig. 20. If, however, the mean values of these differences in C_P are plotted against Reynolds number there is a surprising agreement between the pressure changes on the model and those on the wall (fig. 21). Therefrom it is concluded that the free stream static pressure, which in fact is determined from a measurement in the
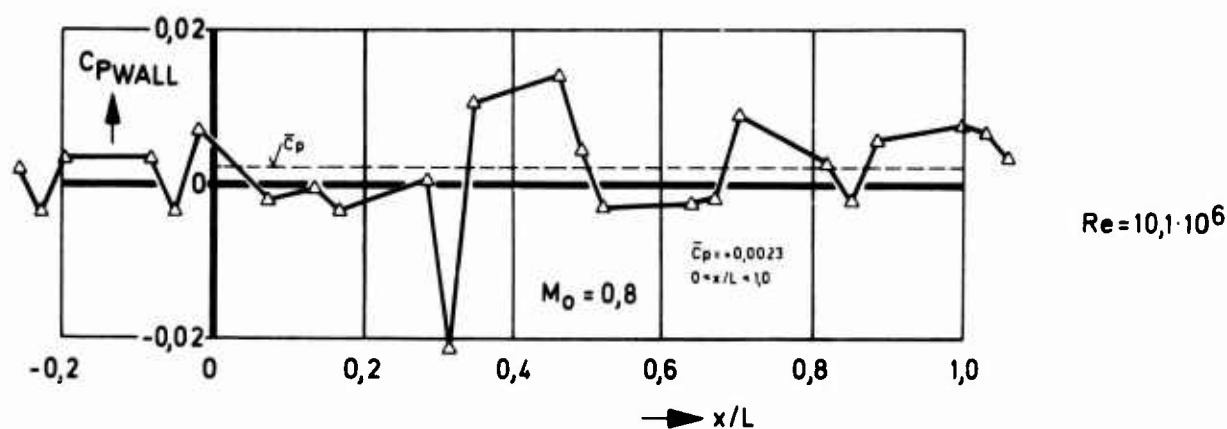
Fig. 19 Wind tunnel wall pressure distribution with body No. 3 installed
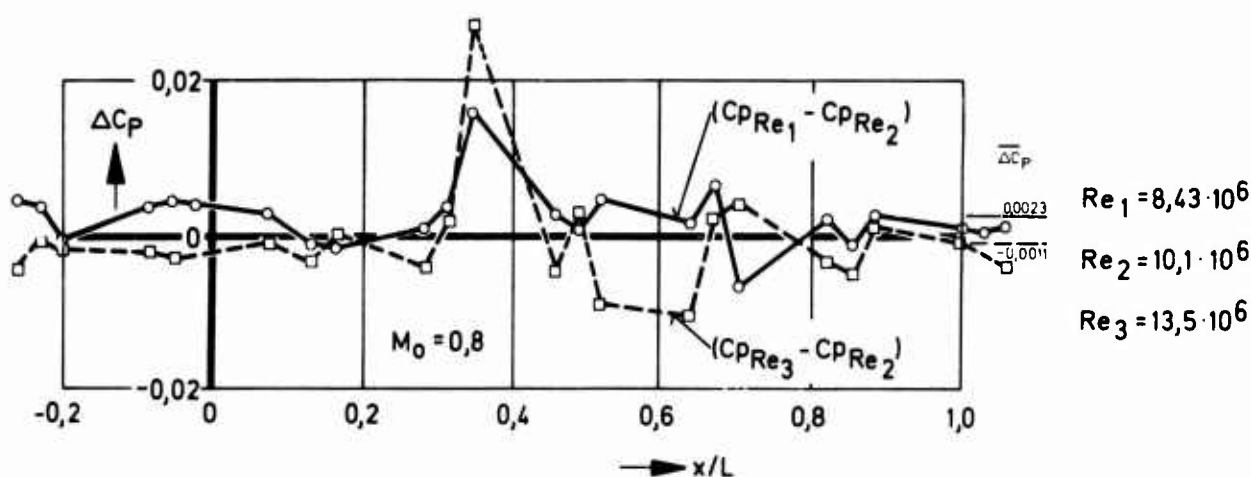
Fig. 20 Change in wind tunnel wall pressure distribution due to change in Reynolds number

Fig. 21 Comparison of averaged changes in pressure coefficients on model and tunnel wall
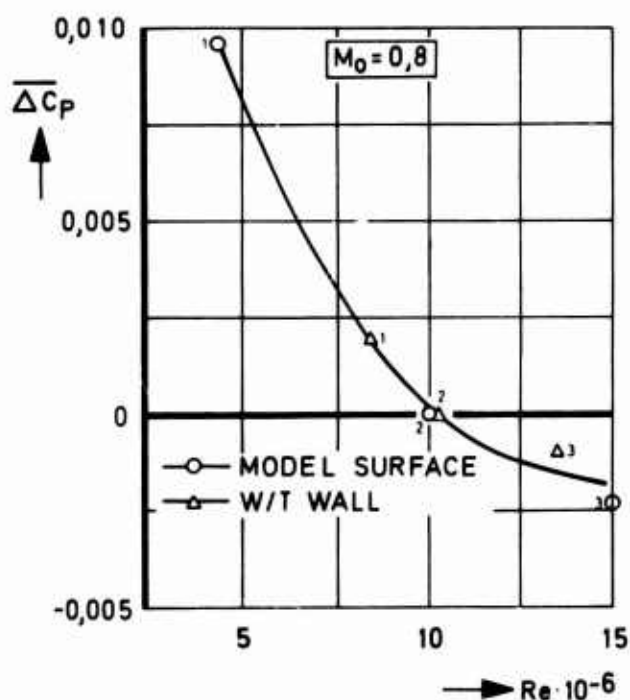
surrounding plenum chamber, was affected by a systematic error. Since increasing Reynolds number, i.e. raising the tunnel total pressure resulted in a drop in the averaged ΔC_P it is further concluded that the free stream static pressure determined from a measurement of the plenum chamber pressure was slightly too high relative to the effective static pressure in the test section. At this point it should be mentioned that the wall pressures were obtained from a single run at $M_O = 0,8$ over a relatively small Reynolds number range (with body No. 3 installed in the tunnel). Follow-on tests are therefore planned for the near future.

Fig. 22   Changes in drag due to deviations from nominal static pressure

Fig. 22 tries to illustrate the sensitivity of half and complete bodies respectively towards two types of deviations from the nominal tunnel static pressure: in the left half of the figure a constant pressure shift was assumed, whereas the right half shows a pressure gradient (fig. 22a and b). With these assumed deviations the aft- and forebody pressure drag changes for model No. 3 were computed (fig. 22c). The pressure gradient, in the right half of this figure, affects both forebody and aftbody in the same sense resulting in an even steeper increase in pressure drag for the complete body amounting to $\Delta C_{D_P}/\Delta C_P = 1,35$. The constant pressure shift on the other hand, changes forebody and aftbody pressure drag almost by the same amount, however, in an opposite sense whereby the sum of these two drag changes cancel each other virtually completely (small sting diameter). So far only drag changes have been discussed. If, however, a value for the pressure drag of the complete body is assumed, say 0, 016 (dashed line) then a deviation ΔC_P greater than 0, 016 will cause a change in pressure drag of the half body, i. e. of the fore- and aftbod respectively, which is greater than the pressure drag of the complete body itself. In other words, ... aftbody drag testing where the forebody is not taken into account, the measured aftbody (pressure) drag will attain arbitrarily great values, depending on the free stream underpressure (deviation from nominal). If the forebody is also on the balance then this high sensitivity towards free stream static pressure deviations disappears. In fig. 22d the measured pressure drags of fore- and aftbody are plotted, this time, however, not against Reynolds number, but against the mean values of the differential pressure coefficients shown in fig. 21. The three points dividing the fore- and aftbody pressure drag lie on a straight line.

Comparing measured with computed values it would appear that at least as far as the pressure drags of the half bodies are concerned, the changes in these pressure drags were not so much caused by true Reynolds number effects but primarily by deviations in the free stream static pressure. As far as the complete body is concerned, the slight increase in pressure drag with Reynolds number shown in fig. 22d is probably a correct result, which agrees with the expected trend (compare fig. 21).

Looking at fig. 22d, no matter for what Reynolds number and $\overline{\Delta C_P}$ respectively, it is not clear what exact proportion of the pressure drag of the complete body can be assigned to the fore- and aftbody drag components. The $\overline{\Delta C_P} = 0$ position was purely arbitrarily chosen as the reference value for fig. 21. If interference free conditions had been achieved at $(\overline{C_P})$ wall $= 0$, then virtually all of the pressure drag is on the aftbody leaving only 12 % for the forebody. If, in addition, one tried to correct the measured "Reynolds" number trend for halfbodies, one could think of applying the pressure changes on the wall (fig. 21) to the model. In doing so, a forebody pressure drag is obtained which is almost independent of Reynolds number. However, to justify such a correction further work is required in this respect.

6. CONCLUDING REMARKS

In this paper a Reynolds number investigation conducted with small scale axisymmetric bodies in a transonic wind tunnel was analyzed with the aim of explaining some of the unexpected Reynolds number effects measured recently by MBB and others. It is expected that most of the conclusion drawn in this paper will also apply to those wind tunnels which produced similar Reynolds number results. To confirm this supposition similar measurements on wind tunnel wall C_P-distribution and other data on crossflow characteristics of ventilated test sections for all such tests are required. Those statements which do not apply to Reynolds number effects but to aftbody testing in general like location of split lines, and interrelation of forebody/aftbody flow fields should hold. The main results and conclusions are summarized below.

6.1. Split Line Location

It has been shown that aftbody drag is sensitive to the location of the dividing line aftbody/forebody; also, subdividing the boattail by introducing an additional split line near the nozzle is not advisable from an accuracy point of view in force measurements.

6.2. Forebody Flow Field

It is clear that there is a definite interrelation between the flow fields on the aftbody and that of the forebody. Correct aftbody testing, particularly aftbody testing pertaining to given aircraft configurations, therefore, needs duplicating the forebody and, at least to some extent, also the flow field of the wing. If on a test rig the forebody is not on the balance, the drag changes on the forebody must be accounted for by measured or computed corrections. The latter, however, have so far not been sufficiently accurate.

6.3. Sensitivity

Halfbodies, i. e. aftbodies or forebodies are much more sensitive to small deviations in free stream static pressure from the nominal value than complete bodies. This applies to both, pressure integration and force measurement (correction of internal pressure). As the pressure drag coefficient of a halfbody is directly proportional to the mean pressure coefficient on the body surface, the mean error in the integrated pressure coefficients should not be greater than $\pm$ 0, 001 if the pressure drag of the complete body is to be determined with an accuracy of $\pm$ 7 to 10% (slender body, no separation).
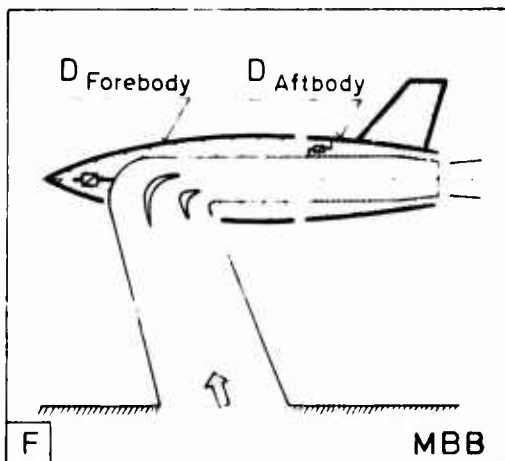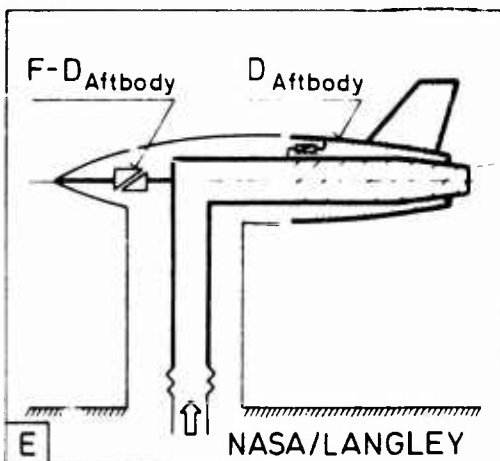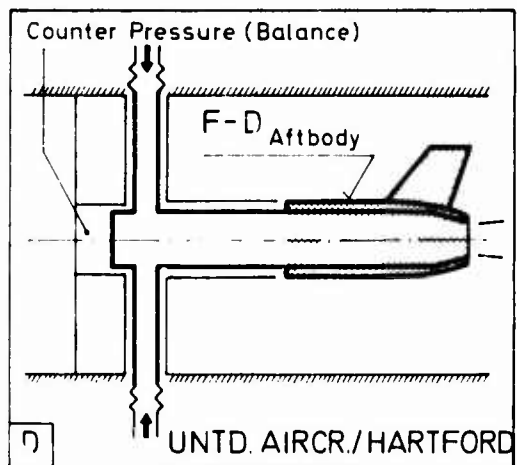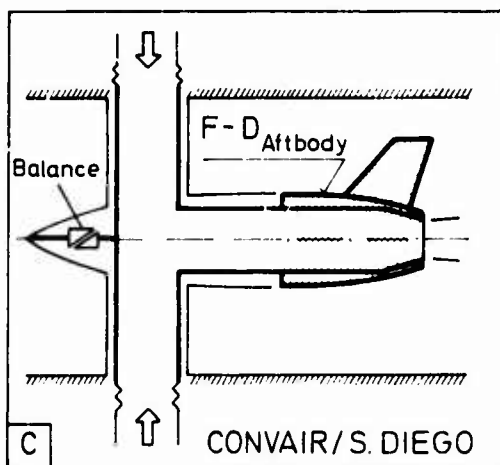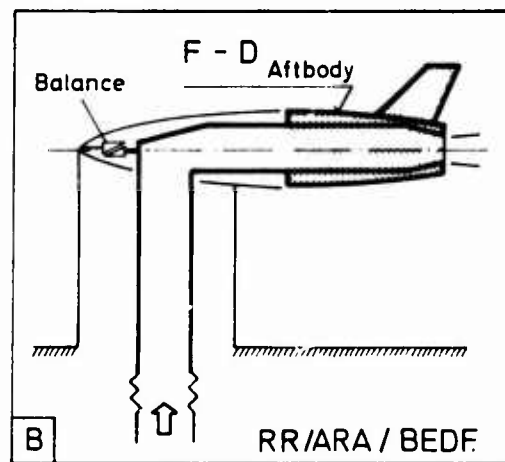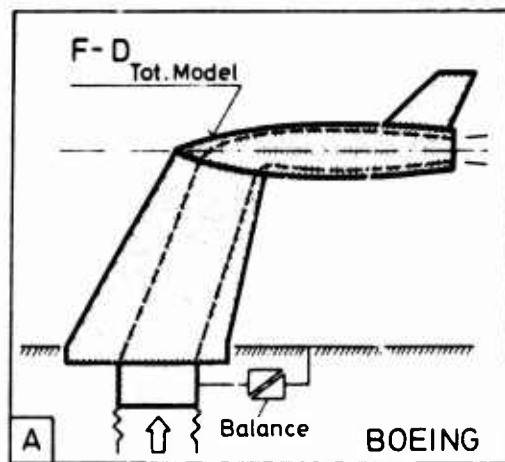
Fig. 23   Aftbody drag test rigs

6.4. Wind Tunnel Interference

As long as appropriate corrections for the wind tunnel interference effects in variable Reynolds number testing are not available, one should measure the drag of complete bodies rather than the drag of aftbodies in order to make use of the compensating effects on the forebody. In this context it is recommended to apply the measuring technique described in ref. 7 as "Single Jet Reference Model".

6.5. Correlation with Other Results

An almost identical rise in aftbody drag with Reynolds number has been found in the AEDC and NASA tests shown in the first figure. As a first step towards clarification one could therefore assume that the causes were the same. With the NASA tests, Reynolds number was not varied by changing the density but by varying the model size resulting in different blockages. The results discussed in this paper showed how sensitive aftbody pressure drag is towards altered crossflow conditions at the wind tunnel wall. Therefore, the same aftbody shape tested as halfbody either in different wind tunnels or in the same tunnel with a different blockage will give very different aftbody drag values.

7. REFERENCES

1	H. B. Squire, A. D. Young	The calculation of the profile drag of aerofoils ARC RM 1838 (1938), also in ref. 12, chapter XXV
2	G. Besigk	Halbempirische Theorie zur Bestimmung des Heckwiderstandes MBB-Report UFE 628/1-70, March 1971
3	G. Besigk	Influence of Reynolds Number on Drag Evaluation MBB. Report UFE 1078, 1974
4	P. P. Antonatos, L. E. Surber, J. A. Laughrey, D. J. Stava	Assessment of the Influence of Inlet and Aftbody/Nozzle Performance on Total Aircraft Drag AGARD-CP-124 (15), 1973
5	R. Chamberlin, B. J. Blaha	Flight and Wind Tunnel Investigation of the Effects of Reynolds Number on Installed Boattail Drag at Subsonic Speeds AIAA Paper No. 73-139. 1973
6	G. K. Richey	Preliminary Data of the AGARD Ad Hoc Study "Improved Nozzle Testing Techniques in Transonic Flow" AFFDL, March 1974
7	F. Aulehla, K. Lotter	Nozzle/Airframe Interference and Integration AGARD-LS-53, 4 (pages 4-1 to 4-25), 1972
8	N. Bretthauer, W. Kraus	Das MBB-Unterschall-Panel-Verfahren. Teil 1: Das Verdrängungs-problem ohne Auftrieb in kompressibler Strömung MBB-Report UFE 632-70, 1970
9	J. G. Rotta	Fortran IV-Rechenprogramm für Grenzschichten bei kompressiblen ebenen und achsensymmetrischen Strömungen AVA-Bericht No. 68R 03 (1968)
10	N. Scholz	Über eine rationelle Berechnung des Strömungswiderstandes schlanker Körper mit beliebig rauher Oberfläche Jb. Schiffbautechn. Ges. 45, 244-259 (1951) also in ref. 12, chapt. XXV
11	H. Ludwieg, Dr. W. Lorenz-Meyer W. Schneider	Der transsonische Windkanal der aerodynamischen Versuchsanstalt Göttingen Jahrbuch 1966 der WGLR
12	H. Schlichting	Grenzschicht-Theorie Verlag G. Braun, Karlsruhe (1964)

THE SUBSONIC BASE DRAG OF CYLINDRICAL TWIN-JET AND SINGLE-JET AFTERBODIES

J. Reid
A.R.G. Mundell
J.F.W. Crane

Aerodynamics Department,
Royal Aircraft Establishment,
Farnborough, Hampshire,
England

SUMMARY

This paper is mainly concerned with the effect of forebody and support interference on the base drag of cylindrical twin-jet afterbodies in wind tunnel tests at subsonic speeds. Two almost identical after-bodies have been tested, one in a strong interference field and the other nearly free from interference. The results illustrate the importance of the effect and also serve to test two methods of correction. Supplementary tests show that the base drag of a cylindrical twin-jet afterbody tends to be slightly greater than that of the equivalent axisymmetric configuration. Finally a method of correlation is described whereby the base drag of both twin-jet and single-jet models may be expressed in linear form.

NOTATION

a_J	total nozzle throat area
a_∞	cross-sectional area of cylindrical afterbody
a_J/a_∞	jet area ratio
δ	boundary layer thickness in base plane
M_∞	free stream Mach number
$_tp_J$	jet stagnation pressure
P_∞	free stream static pressure
$_tp_J/P_\infty$	jet pressure ratio
r	radius of equivalent axisymmetric cylinder

Pressure, drag and thrust coefficients (defined in sections 4 and 5)

C_p''	interference pressure coefficient
$(C_p)_B$	base pressure coefficient
$(C_p)_B^*$	corrected base pressure coefficient
$(C_D)_B$	base drag coefficient
$(C_D)_B^*$	corrected base drag coefficient
$\Delta(C_D)_B$	incremental base drag coefficient
C_T	nozzle thrust coefficient
ΔC_T	incremental nozzle thrust coefficient

1 INTRODUCTION

The concern of this paper is the estimation of aircraft afterbody drag from wind tunnel tests on a model. In such tests it is often the practice to close the normal air intake with a streamlined bullet and supply the jet with high pressure air introduced through the model support system. The bulkiness of the combined model support and air supply tends to distort the overall shape of the model and alter the inter-ference field which partly determines the afterbody drag. On this account the measured drag of the model differs from that of the full scale aircraft, and, indeed, results from the same afterbody tested on different rigs frequently disagree. One way of resolving this situation is to correct the results with reference to a standard forebody, an appropriate choice being an infinitely long cylindrical forebody for which the interference field vanishes everywhere. We therefore seek a method of correction which cancels the effect of the interference field.

A simple approach to this problem[1] is to measure the interference field by a separate test in which the normal afterbody is replaced by a long cylindrical reference afterbody. The measured pressure coefficient at any point on the jet model is then corrected by subtracting the measured pressure coefficient at the corresponding point on the reference model. This procedure, discussed in more detail later, is clearly an approximation which assumes that the pressure fields due to the forebody and afterbody separately may be combined by simple addition. The prime object of the present work is to provide a direct experimental check on this assumption.

At the same time, engine installations with twin convergent nozzles housed in an asymmetric afterbody are much favoured in present strike fighter designs, and it is of interest to investigate the drag of one such configuration and to compare it with the equivalent axisymmetric case. Much experimental work could be saved were it possible to establish a correspondence between the two.

With these points in mind, the drag of three related jet models has been measured at subsonic speeds[2,3]. In the first of these, model A, the afterbody is cylindrical but non-circular in section and two convergent nozzles discharge from the bluff base. This model is subject to severe interference caused by the forebody and support system. In model B the afterbody is essentially a scaled-down replica of model A, but it is supported by a long cylindrical upstream sting, so that the interference field is very weak. Model C is the axisymmetric equivalent of model B, and it, also, is virtually free from interference, being supported in similar fashion. These three cylindrical configurations were chosen, not as practical designs, but for their suitability as research models.

2   APPARATUS

The arrangement of model A is shown in Fig.1. At the heart of this design lies the cylindrical but non-circular centrebody, which is formed integral with an unswept wing. Upstream an elliptical nose fairs into this centrebody, while a cylindrical afterbody with bluff base and twin nozzles extends downstream. Each of the two propelling nozzles is of the twin stream type with a central primary nozzle and annular secondary nozzle. The primary nozzle is convergent with a circular arc contraction and parallel throat while the secondary nozzle, also convergent, is conical. The stagnation pressure in each primary jet pipe is measured by an axial pitot point connected to a calibrated Bourdon gauge, and since the two readings were practically identical, the jet stagnation pressure $(_tp_J)$ is taken as their arithmetic mean. Throughout the experiment the secondary supply pipes were blanked so that there is no secondary flow, the primary nozzles being surrounded by sealed annular cavities. No balance is installed in this model, the base drag being determined by numerical integration of the base pressure distribution, measured by five scanivalves housed in the nose. As an insurance against systematic error each of these was invariably checked by a separate pressure point independently connected to a mercury gauge. Transition strips made of small glass balls are fixed to the wing and nose.

Fig.2 shows the cylindrical afterbody, formed in cross-section by two semicircles joined by their common tangents. The ratio of total nozzle throat area to maximum cross-sectional area (a_J/a_∞) is 0.144, while the jet spacing is 1.75 times the primary nozzle throat diameter. For reasons of symmetry only half the base is instrumented, the pressure points in the solid surface being disposed as shown, while the pressure in the sealed annular cavities is measured internally.

Model A was tested in the RAE transonic tunnel at Farnborough, a continuous tunnel with variable density operating on a closed circuit. The working section is rectangular (2.4 m × 1.8 m) with bevelled corners and all four walls are slotted to give an open area ratio of 11 per cent, the model blockage ratio being 2 per cent. Fig.3 shows the method of installation. Attached to each wing tip is a hollow side member which projects through the tunnel floor. These encase pipes supplying the jet air, which passes thence through holes in the wing into a central plenum chamber. At the rear the side members are attached to a horizontal beam lying well above the jet efflux, which is bolted to the standard tunnel sting. Additional rigidity is secured by clamping the legs of the side members to the main tunnel structure beneath the floor. Incidence may be changed by unclamping the legs and rotating the sting in a vertical plane.

The afterbody of model B, shown in Fig.4, is virtually a replica of model A on a reduced scale (×0.35). A minor difference exists in that the sealed cavity surrounding each nozzle in the latter is replaced by solid base in the former, but this can have little effect on the base drag. The essential difference between the two models lies in the forebody geometry and method of installation. Model B was installed, as shown by Fig.5, in the RAE jet interference tunnel. This is a free jet tunnel with a subsonic, axisymmetric liner 0.25 m in diameter. The afterbody is supported in the free jet by a cylindrical sting, identical in cross-section, which extends upstream through the throat of the liner into the approach chamber, where it is rigidly secured to the tunnel walls. Air for the model jets is ducted through this sting, the whole installation being made as short as practicable in order to limit the thickness of the boundary layer on the afterbody. By adopting this method of support interference effects were practically eliminated in the tests on model B.

In model C (Fig.6) the afterbody is cylindrical but circular in cross-section and a single convergent nozzle discharges coaxially from the bluff base. The jet area ratio (a_J/a_∞) is again equal to 0.144, so that this model is the axisymmetric equivalent of model B. It, also, was installed on an upstream sting in the jet interference tunnel and tested in a virtually uniform field.

It may be noted that the blockage ratio of models B and C is 4 per cent. This exceeds the corresponding value for model A (2 per cent) and is, in fact, greater than is normally acceptable in tests at high subsonic speeds. Preliminary tests were therefore made, without jet flow, on two circular bluff based cylinders of blockage ratio 4 per cent and 1 per cent respectively. No difference in base pressure could be detected at Mach numbers between 0.5 and 0.9 and it was inferred that, mounted on an upstream sting in a free jet, tunnel constraints do not significantly affect the base pressure of models B and C over this range of Mach number.

3   THE EXPERIMENT

All tests on model A were made at zero incidence and without secondary flow at a free stream unit Reynolds number of 8.2×10^6 m^{-1}. The free stream stagnation temperature lay between 30°C and 50°C, while the jet stagnation temperature was approximately 30°C. In the runs with primary jet flow the jet pressure ratio ($_t p_J/p_\infty$) ranged from 2 to 5 at $M_\infty = 0.6$ and 0.7, and from 2 to 6 at $M_\infty = 0.8$ and 0.9. Additional tests were also made at all four Mach numbers without primary jet flow, the supply pipes being blanked at entry to the model.

Normally, the runs with jet flow were made at constant Mach number and the jet pressure ratio was increased in integral steps. At each operating point the relevant tunnel and jet pressures were read visually, the output from the scanivalves measuring the base pressure being recorded automatically on punched paper tape. A problem arose with this latter measurement since, early in the experiment, a significant fluctuation in base pressure was observed. Consequently, since the scanivalve readings are virtually instantaneous, repeated scans at the same operating conditions yielded pressure coefficients which occasionally differed appreciably. Attempts were made to achieve a time-averaged value by including a simple integrating network in the output circuit, and also by restricting the pressure lines. These measures met with little success and the solution eventually adopted was to scan the valves three times at each operating point and average the data numerically. The averaged results agree well with independent measurements using mercury gauges.

Models B and C were tested at free stream Mach numbers ranging from 0.5 to 0.9 with a constant free stream stagnation pressure of 40 kN/m^2, the stagnation temperature of both free stream and jets being approximately 30°C. Corresponding to these conditions the unit Reynolds number increased from 4.0×10^6 m^{-1} at $M_\infty = 0.5$ to 5.7×10^6 m^{-1} at $M_\infty = 0.9$. At each Mach number a range of jet pressure ratio was covered, including a point without jet flow. The test procedure was similar to that described above except that in this instance time-averaged values of the base pressure were recorded on mercury gauges so that difficulties due to unsteadiness did not arise.

Although no boundary layer measurements were made on models A, B and C, previous tests with similar models indicate a well developed turbulent profile in the base plane, and approximate calculations using flat plate methods predict a thickness at the base of 15.8 mm for model A and 5.7 mm for models B and C. In the table below these results are compared in terms of δ/r, where δ is the boundary layer thickness in the base plane and r is the radius of the equivalent axisymmetric cylinder.

Estimated boundary layer thickness

Model	δ (mm)	r (mm)	δ/r
A	15.8	71.0	0.22
B	5.7	24.9	0.23
C	5.7	25.4	0.22

It will be seen that δ/r is practically the same in each case, and although these are only approximate calculated values, it seems that differences in boundary layer thickness can have little effect on the relative base drag of the three models.

4   INTERFERENCE CORRECTIONS

To each jet model there corresponds a reference model in which the afterbody is replaced by a long cylinder, without jets, and identical in cross-section. The length of this cylinder is sufficient to ensure that the pressure field in the region of interest is not affected by the base flow. Hence the surface pressure distribution, determined by a separate test, gives an accurate measure of the interference field. The base drag of the jet model is then corrected for interference in the following manner.

Let the base of the jet model lie in a given plane (X) in the working section, and let $(C_p)_B$ denote the pressure coefficient at a given point on the base. Further, let C_p'' denote the mean pressure coefficient around the reference model in plane (X). Then the corrected local pressure coefficient on the base of the jet model is defined by

$$(C_p)_B^* = (C_p)_B - C_p'' \quad . \tag{1}$$

We note that the interference pressure coefficient (C_p'') is a function of M_∞ only and is applied to all points on the base of the jet model.

A similar correction is applied to the base drag coefficient on the jet model. Thus, the uncorrected base drag coefficient is defined by

$$(C_D)_B = -\frac{1}{a_\infty} \iint (C_p)_B \, da \tag{2}$$

and the corrected base drag coefficient by

$$(C_D)_B^* = -\frac{1}{a_\infty} \iint (C_p)_B^* \, da \tag{3}$$

where da is an element of base area and the surface integral is taken over the solid base (and the sealed annular cavities in the case of model A), but excludes the nozzles, with or without jet flow.

Combining Eqs.(1), (2) and (3) gives

$$(C_D)_B^* = (C_D)_B + \left(1 - \frac{a_J}{a_\infty}\right) C_p''$$ (4)

where $a_J/a_\infty = 0.144$ for all three models.

The principle of this method of correction is shown schematically in Fig.7. Here the pressure field created by the top model is assumed to be equal, at any point, to the sum of the fields produced by the middle and lower models. It follows, with the definitions given above, that $(C_p)_B^*$ is the base pressure coefficient on the lower (datum) model, and hence is determined solely by the operating conditions and base geometry.

The interference pressure coefficients (C_p'') measured on the three reference models are compared in Fig.8. Considering first the case of model A we see that C_p'' is relatively small up to $M_\infty = 0.7$, but increases rapidly with further increase in Mach number. This characteristic is caused by a region of supersonic flow followed by a shock wave and boundary layer separation which forms on the wing at high subsonic Mach numbers. In oil flow photographs a shock first appears on the wing at $M_\infty = 0.83$ and this moves downstream, increases in strength and spreads across the centrebody at higher Mach numbers, giving rise to large positive pressure coefficients on the afterbody. Further downstream these should decay fairly rapidly to zero but this process is probably delayed by the side supports, which tend to channel the flow. Clearly, at high subsonic speeds the base lies in a strong interference field, so that this model provides a stringent test of the correction method.

In contrast, the corresponding curves for models B and C (Fig.8) show that C_p'' is very small over the whole range of Mach number. This comparative freedom from interference results from the use of an upstream sting to support the models and is difficult to achieve by other means. Its importance lies in the fact that models B and C thus serve as absolute standards of comparison.

5   RESULTS

The base drag of models A and B is compared in Fig.9 in terms of $(C_D)_B$, the uncorrected drag coefficient. The essential point here is that the geometry of afterbody and base is virtually the same for both models, the observed difference in drag being due to the change in forebody shape, which alters the interference field. Clearly this effect is most important and if results from different rigs are to be compared it is essential to allow for changes in the interference field by correcting the drag measurements with reference to a standard forebody. This may conveniently be taken as an infinite cylinder, for which the interference field vanishes.

A simple method of correction has been described above, and we may now test this experimentally by comparing the corrected base drag of model A with the corrected base drag of model B. If the method is valid the two sets of results should be identical. The comparison is made in Fig.10, which shows that the results are by no means identical, although the difference between them is less than the difference between the uncorrected results shown in Fig.9. It seems, therefore, that this method partly cancels the effect of the interference field but does not do so entirely, and although probably adequate when the required correction is small, it leads to unacceptable errors when interference is strong.

Fortunately a better method is available, based on the use of $\Delta(C_D)_B$, the increment in $(C_D)_B$ relative to the jet-off value at the same Mach number. The results for both models, plotted in these terms, are shown in Fig.11 and it is immediately apparent that the two sets of values agree quite closely. With one exception, the difference between corresponding points does not, in fact, exceed 0.02 over the whole field of measurement. On this evidence it seems that $\Delta(C_D)_B$ is practically independent of forebody interference, whereas $(C_D)_B$ and $(C_D)_B^*$ are not. To convert $\Delta(C_D)_B$ to $(C_D)_B$ we have, of course, still to determine the jet-off base drag, but this is a simpler problem experimentally, which can be solved by conventional methods.

Fig.12 shows the drag results for models B and C. Both models are practically free from forebody interference, so that this is a straightforward comparison between an asymmetric twin-jet model (B) and the axisymmetric equivalent model (C). Inspection shows that, without jet flow, the base drag is independent of Mach number and almost the same in each case. With jet flow the drag of model B is greater than that of model C, but the difference only becomes appreciable at the higher values of jet pressure ratio. Both sets of curves exhibit the rapid increase in base drag with increase in jet pressure ratio characteristic of cylindrical afterbodies.

The drag results may be expressed more concisely by plotting $\sqrt{1 - M_\infty^2}\ \Delta(C_D)_B$ against ΔC_T, where $\Delta(C_D)_B$ is the increment in $(C_D)_B$ relative to the jet-off value at the same Mach number. ΔC_T is the increment in C_T relative to the jet-off value at the same Mach number. C_T is the theoretical nozzle thrust coefficient defined by

$$C_T = \frac{2}{\gamma M_\infty^2} \frac{1}{p_\infty a_\infty} \iint \left[\rho u^2 + (p - p_\infty)\right] da$$

where the surface integral is taken over the nozzle exit area, with or without jet flow, and is evaluated assuming one-dimensional isentropic flow within the nozzle.

This form of correlation is applied to all three models in Fig.13. It will be seen (left hand graph) that the points for both models A and B are grouped quite closely about a single straight line, the correspondence being surprisingly good over so wide a range. Further (right hand graph), the same linear dependence also holds for model C, but in this case the gradient of the line is smaller. In general terms, the results for each model approximate to a straight line through the origin, whose gradient depends on the geometry of the afterbody, but not on the geometry of the forebody. This implies that $\Delta(C_D)_B$ is approximately determined over the whole of the operating range by two experimental points, one with jet flow and one without, at any convenient Mach number.

Although C_T has been used to correlate results before[4], the present method, which was discovered empirically, is apparently new. As yet it lacks a physical basis and its useful range may be limited.

6   CONCLUSIONS

It has been shown (Fig.9) that forebody interference can seriously affect the base drag coefficient $(C_D)_B$ and it is therefore desirable, when comparing the drag of different models, first to eliminate the effect of the interference field. A method commonly used for this purpose is to subtract from the base pressure coefficient on the jet model the pressure coefficient at the corresponding axial station on a long cylinder replacing the jet model. The corrected base drag coefficient $(C_D)_B^*$ is then assumed to be independent of forebody interference, but it has been further shown (Fig.10) that this assumption is in error. On the other hand, the incremental base drag coefficient $\Delta(C_D)_B$ relative to the jet-off condition is scarcely affected by the interference field (Fig.11) and, moreover, shows a simple linear correlation against jet thrust coefficient which depends only on the base geometry (Fig.13). We conclude, therefore, that $\Delta(C_D)_B$ is practically independent of forebody interference, whereas $(C_D)_B$ and $(C_D)_B^*$ are not.

A final word of caution may be appropriate here in that general results are rarely found in this field and the conclusions reached above may not always be applicable. Further, we have only considered the effect of the forebody on the base drag of a cylindrical afterbody. In practical aircraft designs a boat-tailed afterbody and base are normally combined with the forebody and it is the total drag of this combination which is important. With configurations of this type a complex situation arises in which it is necessary to consider not only the effect of the forebody on afterbody drag, but also the converse. This problem is receiving attention.

REFERENCES

1   O.M. Pozniak, A.B. Haines: Afterbody drag measurement at transonic speeds on a series of twin and single jet afterbodies terminating at the jet exit. ARC Current Paper No.1266 (1973)

2   J. Reid, A.R.G. Mundell, J.F.W. Crane: The subsonic base drag of an asymmetric cylinder with twin convergent nozzles and an axisymmetric cylinder with a single convergent nozzle. Part 1.
RAE Technical Report, Unpublished (1974)

3   J. Reid: The subsonic base drag of an asymmetric cylinder with twin convergent nozzles and an axisymmetric cylinder with a single convergent nozzle. Part 2. RAE Technical Report, Unpublished (1974)

4   C.E. Brazzel, J.H. Henderson: An empirical technique for estimating power-on base drag of bodies of revolution with a single jet exhaust. AGARD Conference Proceedings No.10 (1966)
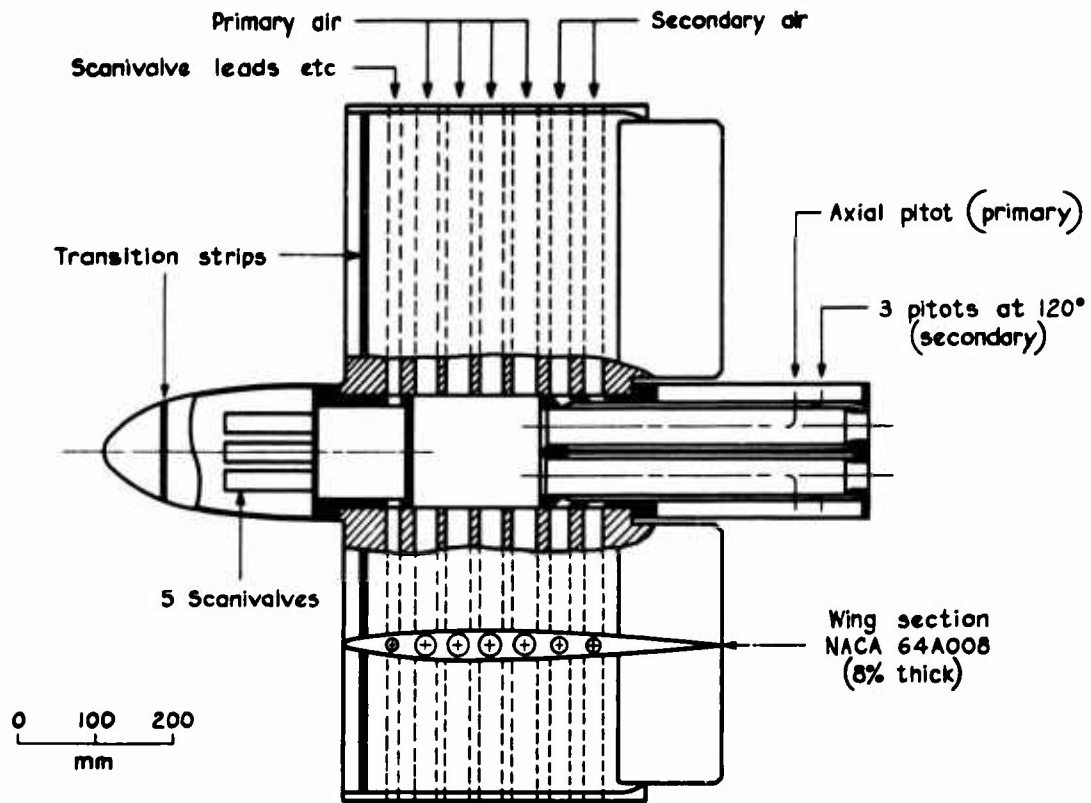
Fig. 1 Model A. General view
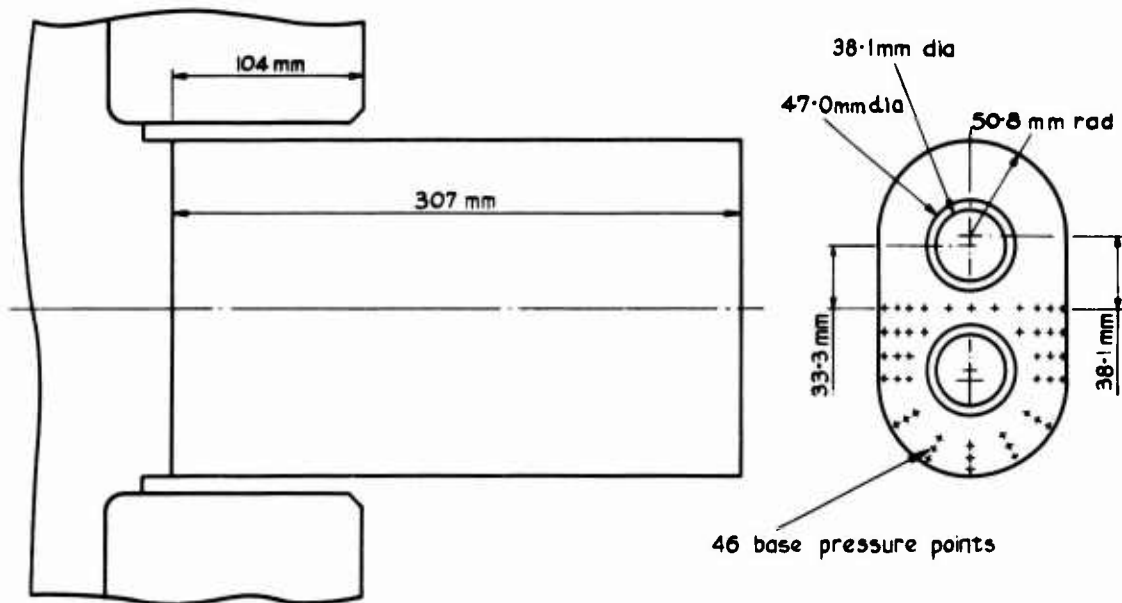
Fig. 2 Model A. Afterbody
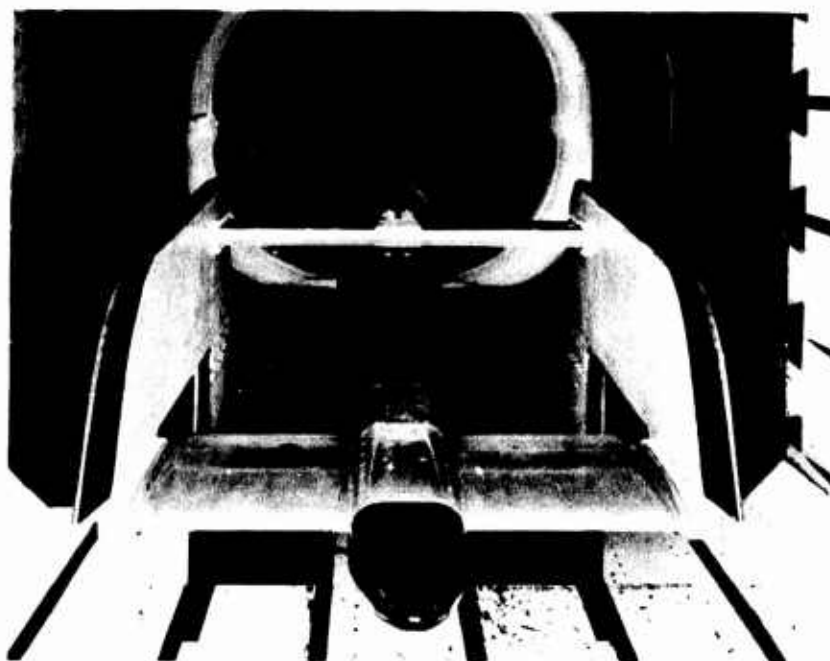
Fig.3   Model A in transonic tunnel
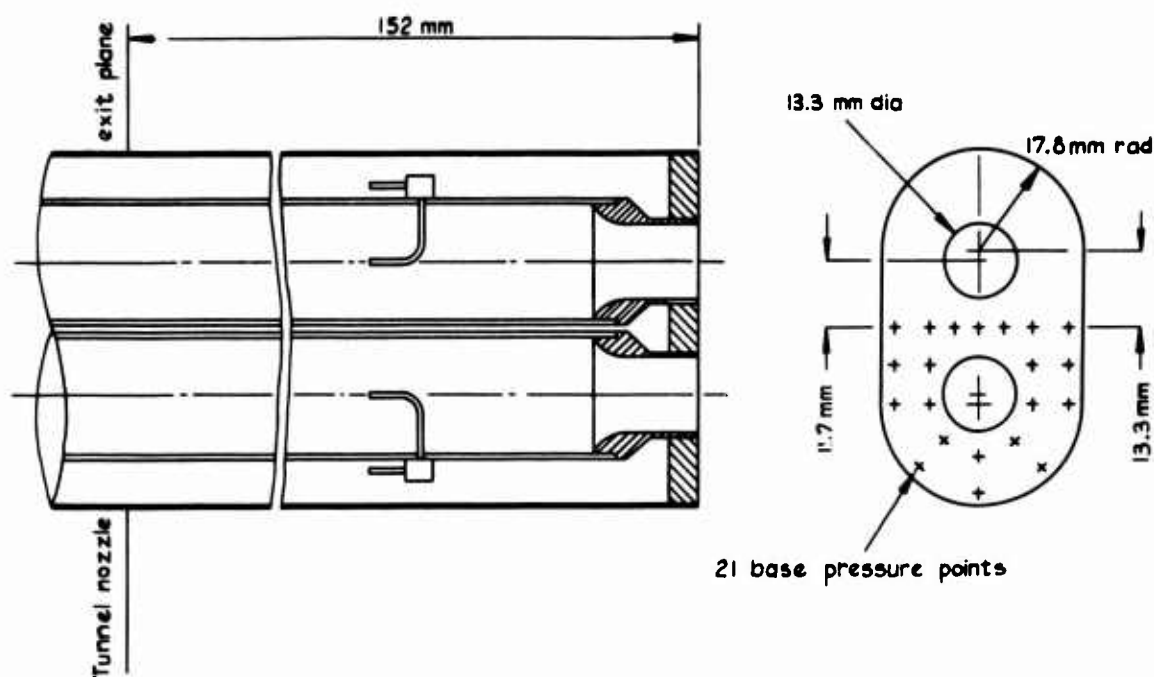
Fig.4 Model B
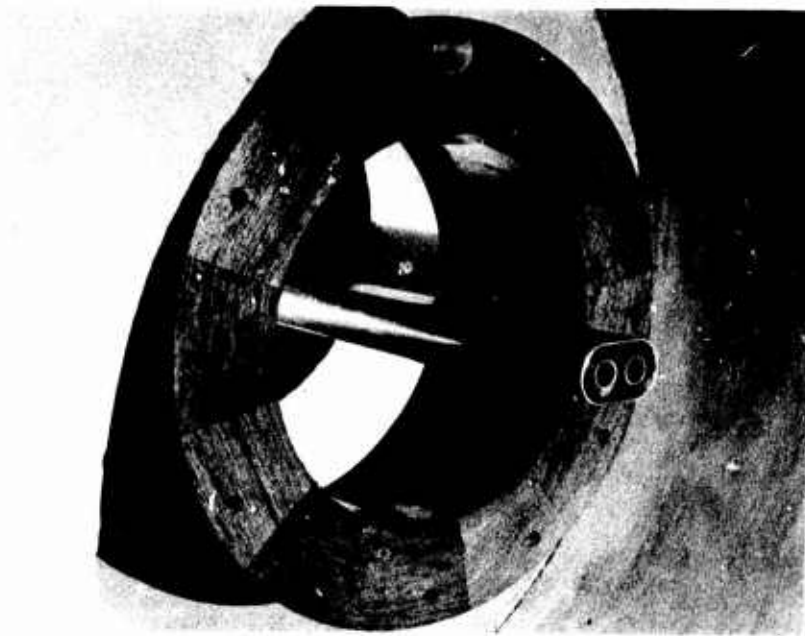
Fig.5   Model B in jet interference tunnel
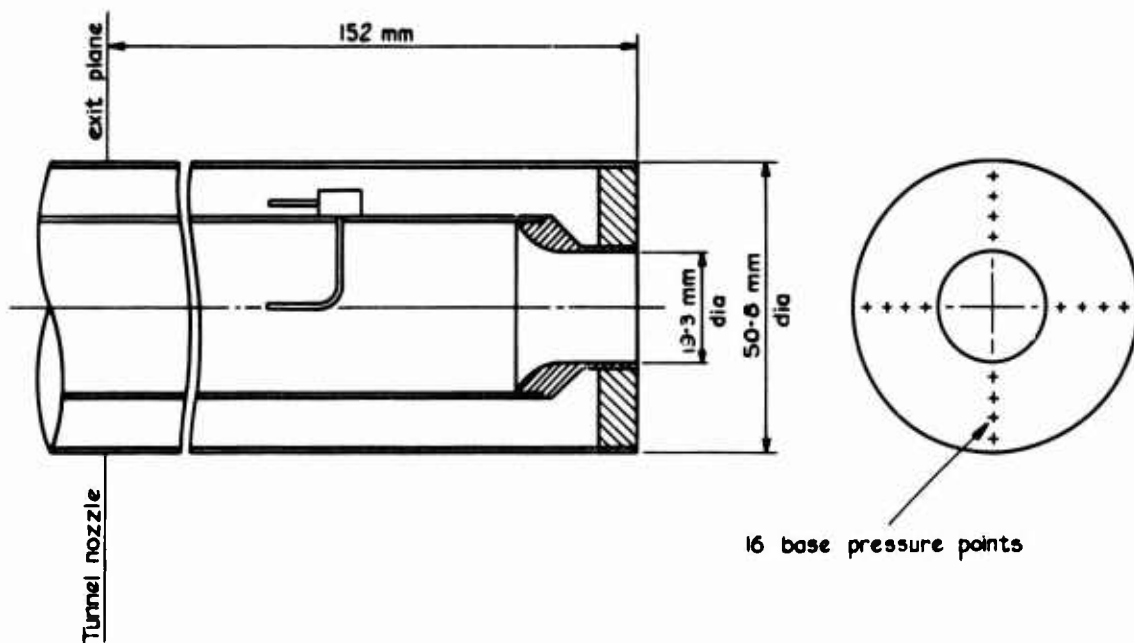
Fig. 6   Model C
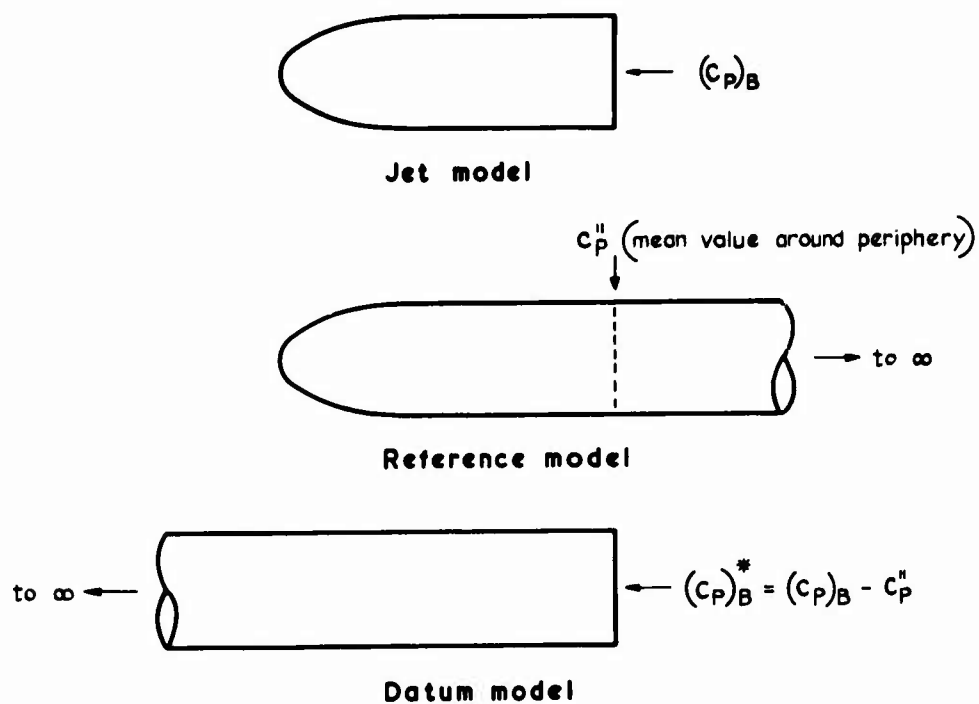
Fig. 7 Principle of correction method
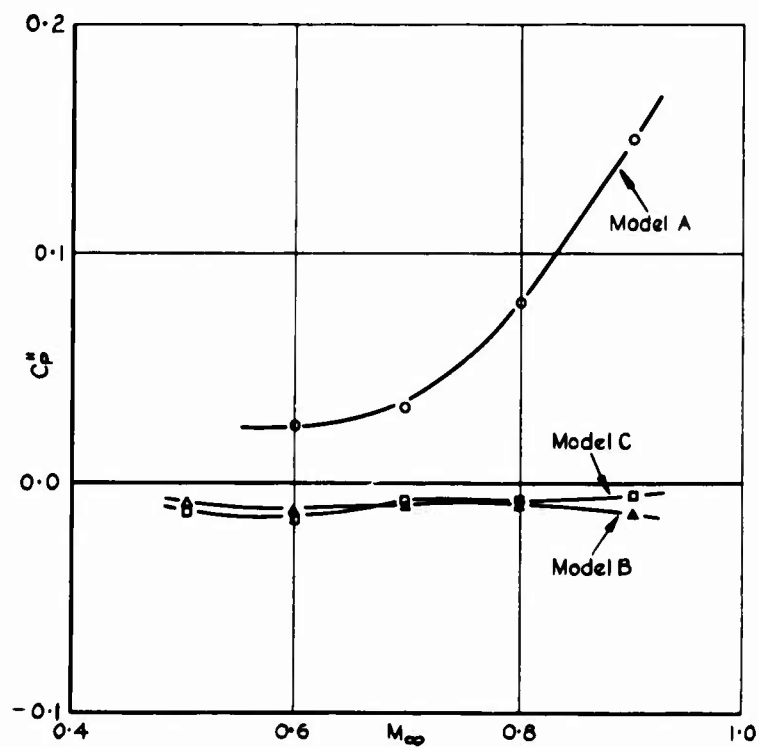
Fig. 8 Interference pressure coefficients
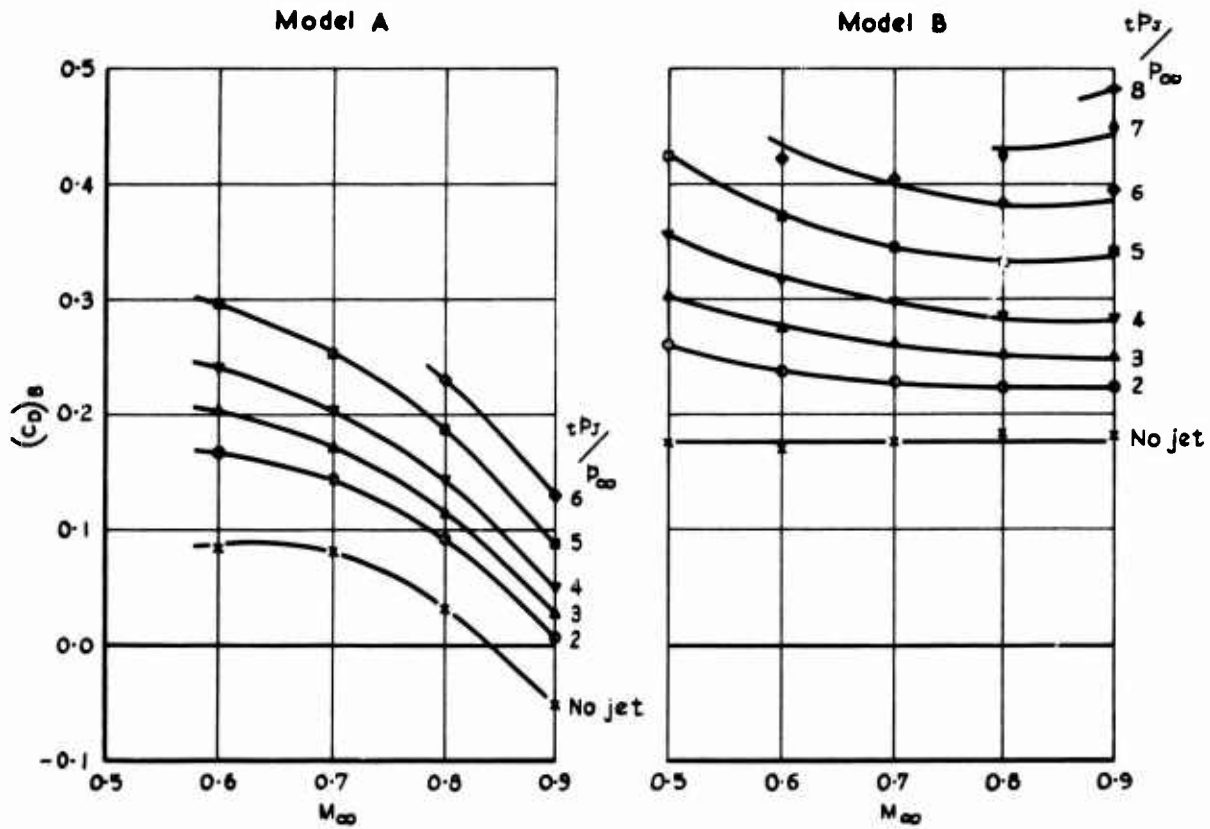
Fig. 9 Uncorrected base drag. Models A & B
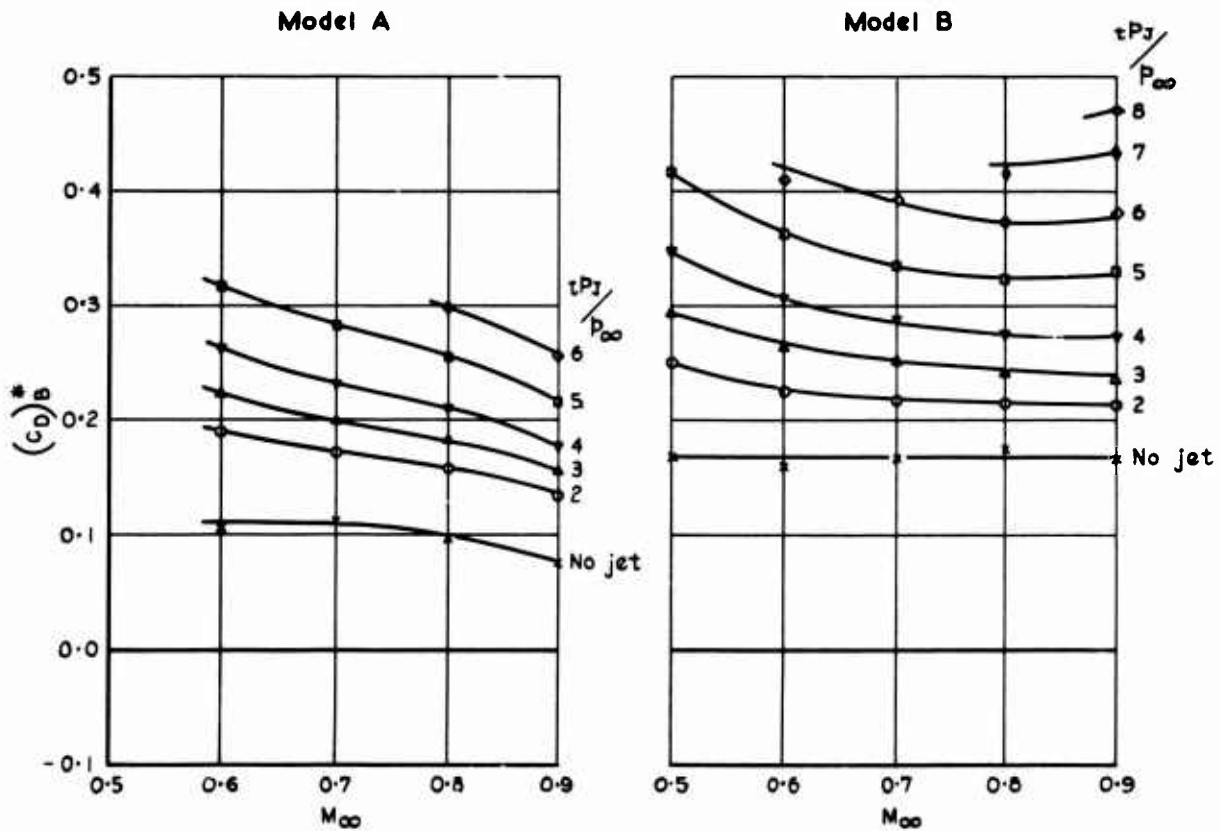
Fig. 10 Corrected base drag. Models A & B
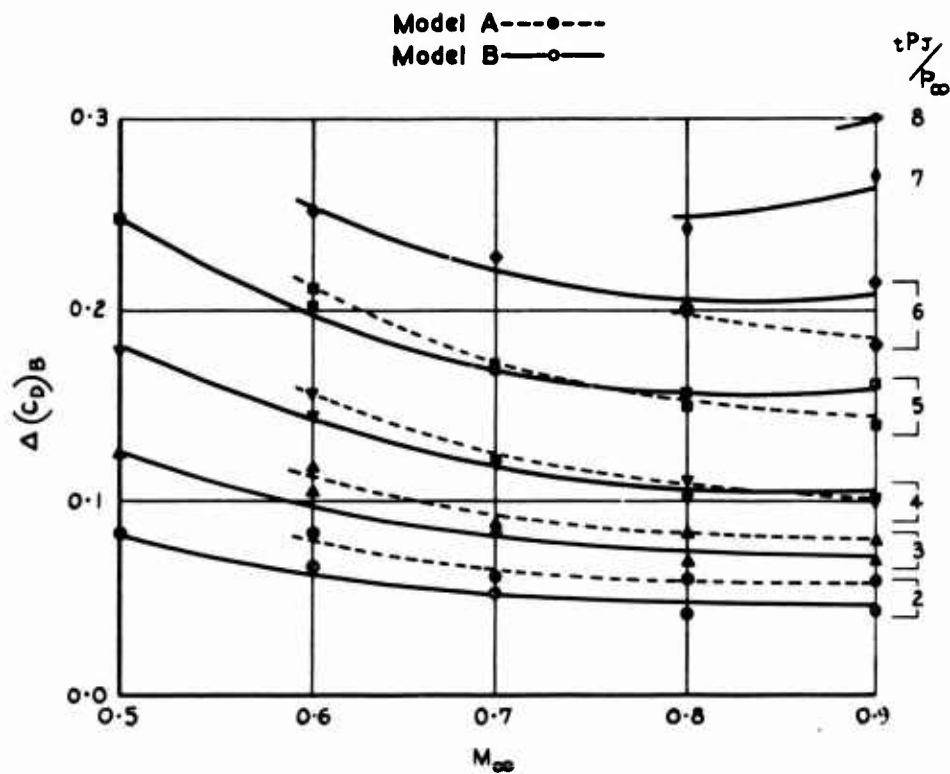
Fig. 11 Incremental base drag. Models A & B
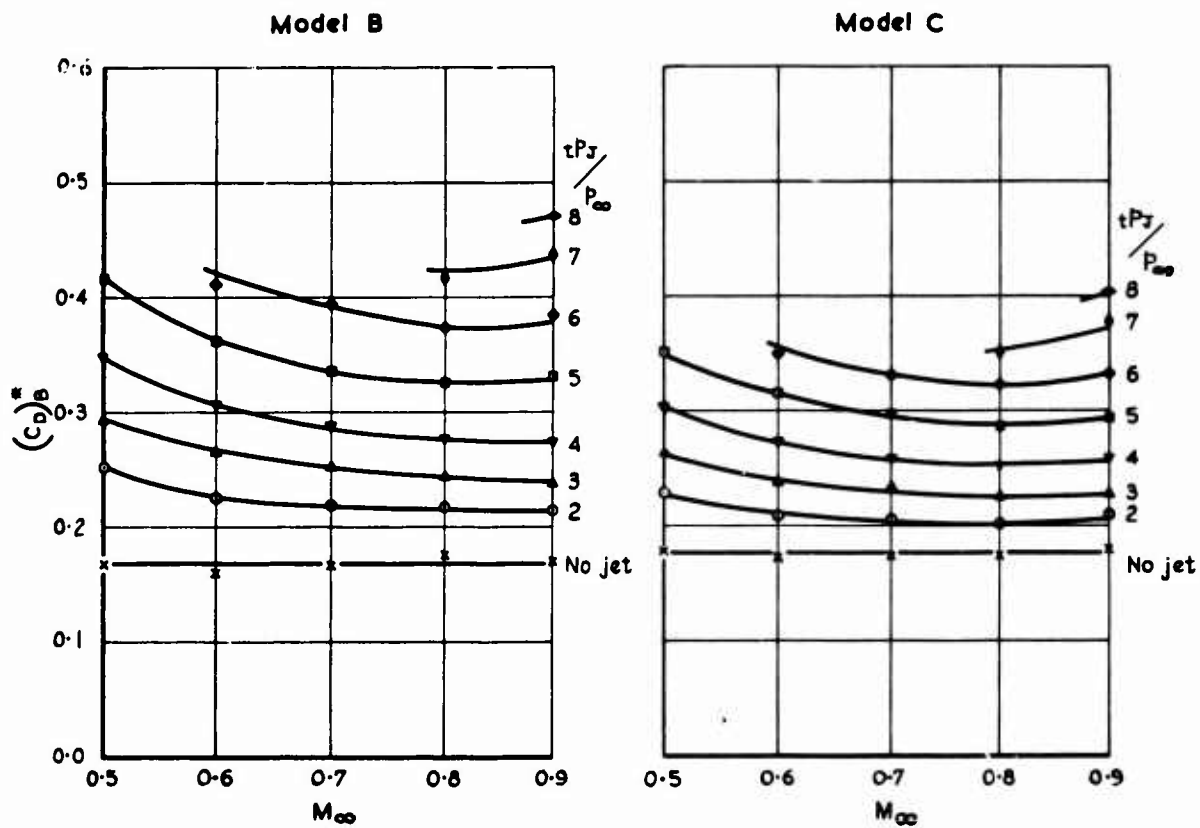
Fig. 12 Corrected base drag. Models B & C
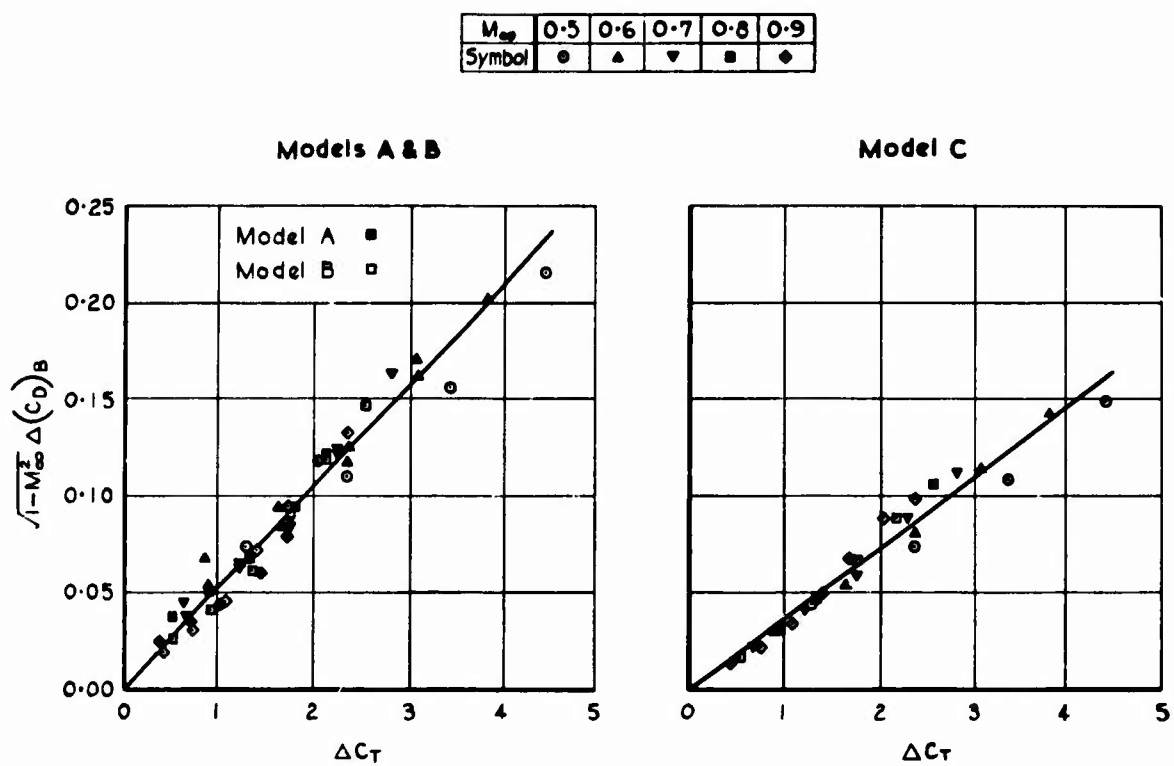
Fig. 13 Correlated base drag. Models A, B & C

WRITTEN CONTRIBUTIONS ON PAPER 13

Mr O.M.Pozniak, ARA Bedford, UK: The importance of accounting for support and forebody interference on after-body drag is apparent from a number of contributions to this Symposium and hence an investigation into the validity of these corrections is very welcome. The method in which the interference flow field is obtained from cylindrical afterbody pressure measurements (Reference 1, Paper 13) has several advantages:–

(a) it is based on a relatively simple test which can be performed with most existing rigs and offers a possibility of standardising results;

(b) in inviscid potential flow it should account for the mutual buoyancy between forebody/support and afterbody and permit the correct optimisation of overall aircraft drag from measurements of afterbody drag alone;

(c) corrects for possible errors in tunnel static pressure that were argued to be the cause of unexpected Reynolds number effects on afterbody drag. (F.Aulehla, Paper 12).

The tests by Reid show that this form of correction is, regrettably, not adequate for completely separated flow and very large support interferences. The question arises whether these conditions are so stringent that they are too unrepresentative and may lead us to disregard a method of correction which for more realistic configurations with principally attached flow would be expected to be applicable, and could lead to results from different rigs being more generally applicable. It should also be noted that frequently, free-flow "aero-force" model is used as a datum and then only differences in interference relative to the configuration are significant. Turning to the possible alternatives in the paper, there are often practical difficulties in obtaining good quality jet-off results on jet exhaust rigs and there is the extra expense of separate tests to obtain the jet-off datum in interference free conditions, – some comments on the best way of achieving this would be welcome.

With these thoughts in mind it is most heartening to hear towards the end of the paper that these problems are receiving attention; these investigations deserve full support and hopefully will not be too long delayed.

Comment by Mr J.Reid: The simple linear method of correction referred to by Mr Pozniak has, indeed, the important advantages which he mentions, and I am far from suggesting that it should be entirely discarded. Rather, the purpose of my paper was to show that it is not a general method and that it breaks down in some circumstances; notably on a cylindrical afterbody with separated base flow and strong support interference. Under less stringent conditions, for example when a fully boat-tailed model is tested in a weak interference field, the method may well be adequate, although direct experimental proof of this is lacking. Moreover, it is as well to remember that on most strike-fighter aircraft the flow is not entirely attached and the afterbody may lie in a relatively strong interference field.

As regards the alternative method of correction based on incremental drag coefficients it is not necessary to use a jet rig, with its bulky support system, to measure the jet-off datum drag. For this purpose I had in mind a test on a separate model installed on a slender support system of conventional design, and relatively free from interference.

May I thank Mr Pozniak for his encouraging remarks on the course of our future research programme, which is being actively pursued.

ON SOME PROBLEMS ENCOUNTERED IN A THEORETICAL STUDY OF THE EXTERNAL FLOW OVER A NOZZLE CONFIGURATION IN TRANSONIC FLIGHT*

By

T. H. Moulden and J. M. Wu

The University of Tennessee Space Institute
Tullahoma, Tennessee 37388 USA

and

D. J. Spring

U. S. Army Missile Command
Redstone Arsenal, Alabama 35809 USA

September 1974

SUMMARY

The paper draws attention to the lack of information, both experimental and theoretical, concerning the transonic flow over an engine configuration operating at various thrust levels. Due to this situation, the physical behavior of the flow is not completely understood. It is shown, from the data that is available that the flow is of great complexity. In particular, when the free stream Mach number is just supersonic, it is found that the confluence between the jet and the external flow is still more nearly subsonic in nature. This observation implies that the usual theories for supersonic base flow are not applicable to this situation. Calculations from such a theory are presented and discussed in the light of experimental evidence. It is recommended that considerable effort be spent in developing theoretical tools based upon solutions to more exact equations and that more fundamental experiments should be performed.

NOTATION			SUFFICES		
M	Mach number		∞	Free stream condition
p	Pressure		c	Chamber or total pressure
r, z	Cylindrical coordinates		J	Jet exit condition
x	Location along body		a	Approach value
L	Body length		b	Base
θ	Boattail or flare angle		p	Plateau value
R_e	Reynolds number		s	Separation condition
C_p	Pressure coefficient		L	Body length
h	Step height			

1. INTRODUCTION

Consider the exhaust jet of a propulsion system issuing from a circular nozzle exit plane in the direction of a near sonic free stream. The physical situation and basic symbolism are presented diagramatically on Figure (1).

The discussion is thus relevent to both an installed engine configuration and to a rocket mounted centrally in a body of revolution. While each configuration does maintain its own particular problems, there are sufficient areas of common concern to make a dual treatment meaningful.
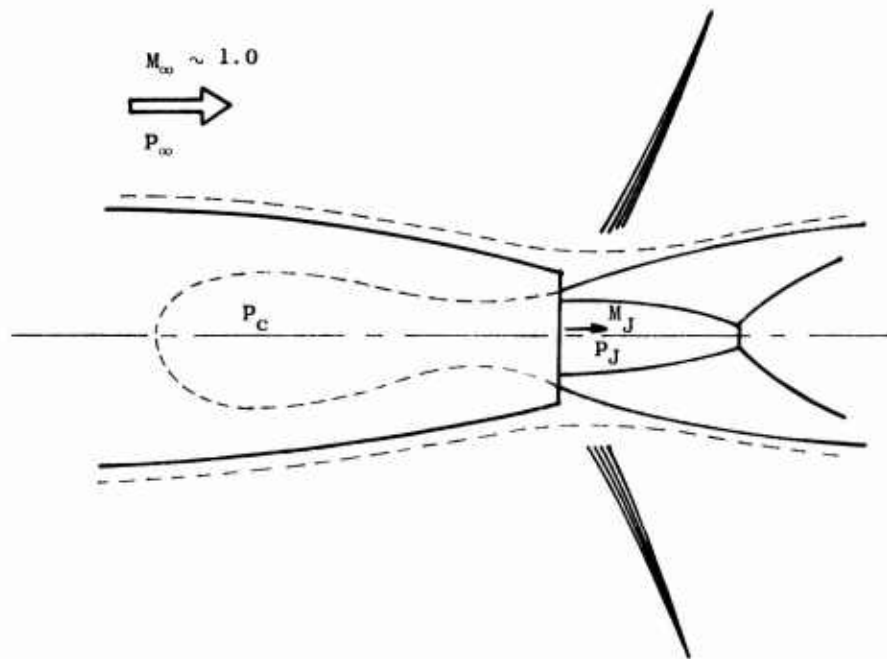
Figure 1. Diagram of the basic configuration.

Throughout the discussion, the main interest will be associated with the external flow while the efflux from the propulsive system is only acknowledged insofar as it supports a shear layer for confluence with the external flow. The external environment sensed by the jet will naturally influence the jet shape implying that the jet itself cannot be considered in isolation from the external stream. The internal structure of the jet will not, however, feature in the current work; except in cases where such is significant to the discussion in hand. For the rocket exhaust, the jet boundary can be adequately determined from the method of characteristics if the thrust coefficient is not too small. It will be assumed that such a calculation has been performed.

In principle, the problem is well defined. Given a specific configuration characterized by body shape and jet exit conditions along with a suitably specified free stream, what is the flow field? In particular, how does the jet exhaust influence the flow over the body ahead of the nozzle exit plane? If separation is engendered by the exhaust how detremental is this to the overall vehicle performance? Of interest here would be the drag penalty for a jet aircraft application or the loss of stability and controllability for a missile.

The objective of this work is to outline some of the difficulties and areas where knowledge is lacking in the prediction of such flow fields. Of particular interest to the discussion is the type of flows that pertain within a range of free stream Mach numbers close to unity. However, since the equivalent supersonic flow is better understood, such will be taken as a reference for comparison.

2. THEORETICAL OUTLINE

Until the recent advances in computer technology and numerical analysis, it was

taken, except in some very trivial situations, that the Navier-Stokes equations were too formidable to succumb to exact analysis techniques. Hence there has been vast expendature of effort on the development of approximation methods, and for a whole body of relevant problems, such techniques are highly appropriate. Indeed, the rapid advances in aerodynamic sophistication over the years is immediately attributable to this generation of approximate theories. Most spectacular among these lies the successes of boundary layer theory.

While the usefullness of boundary layer theory is not called in question in a general sense, there are many practical problems that cannot be handled by such techniques. Pre-eminent among these problems is that of flow separation. A particularly difficult sub-class of separated flow are those associated with conditions where both subsonic and supersonic local Mach numbers occur in juxtaposition.

With thinking very much influenced by boundary layer theory concepts, the classical procedures for treating separated supersonic flows (Refs. 1, 2, 3) have reduced the flow field to two regions. These are an outer region of inviscid (usually potential) motion and an inner viscous flow. In supersonic flow, the small perturbation potential flow solution is particularly simple so that a matching with the inner solution is readily established. The principle differences between the two major approaches lies in the treatment of the inner region. The integral approach (Ref. 2) solves the boundary layer integral equations with suitable assumed families of velocity profiles and other empirical information as required. This work is extendable to transonic flow (Ref. 4) when the overall flow features are predictable. The most significant feature of the work described in Ref. (4) for two-dimensional flows is the realization that the modification to the flow field that is brought about by the strong interaction can be very large. The same large differences are present in flows over bodies of revolution, as evidenced by the data shown in Figure 2. This particular flow will feature again in later discussions.
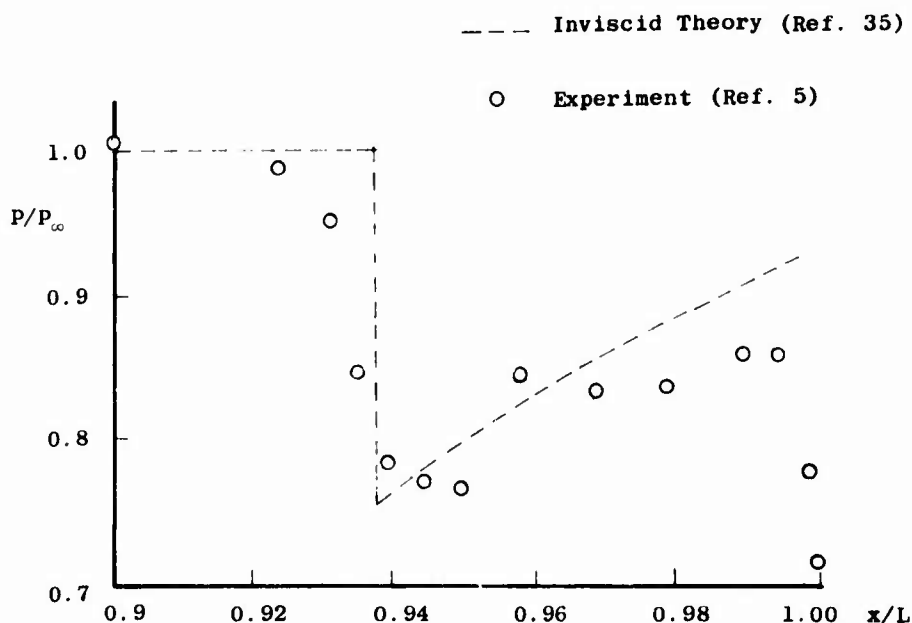
Figure 2. Experimental data (from Ref. 5) for flow over a 6.4° boattail $M_\infty = 1.1$

In the component approach, the inner viscous region is separated into various parts, each of which is determined to the best available approximation. Thus, there will be an approaching boundary layer which has developed from the front of the body, a separation region, a free shear layer and finally a reattachment zone. Each of these two principle methods will be commented upon further in what follows.

In broad outline, the major attraction of the integral method is its ready matching with the external flow without the embarrassment of a separation point singularity. The component approach, however, attempts to provide greater detail in the viscous flow but is less easily matched with an external flow--particularly when the latter is subsonic in nature.

The problem for a separated flow is somewhat more complex than its counterpart for a flow without separation. In the latter case it is possible to achieve adequate results by simply adding in a displacement effect (Refs. 6, 7, 8). For purely subsonic flows (Ref. 6) very good agreement between theory and experiment has been achieved. Similarly in transonic flow (Refs. 7, 8) the results are encouraging. However, for a body of revolution (Ref. 7) the viscous effect was found to be very small. Only for a lifting body where the boundary layer development becomes more significant is the correction large.

3. SOME REMARKS ON THE COMPONENT APPROACH

The basis of this approach to separated flow problems is well known (Refs. 1, 3) and need not be elaborated upon. Herein, it is intended to discuss some of the difficulties that arise when the method is applied to a transonic ($M \gtrsim 1.0$) flow. Parallel with the discussion will be an indication of the nature of the flow as determined from the available experimental evidence.

Consider the flow situation depicted on Figure (3).
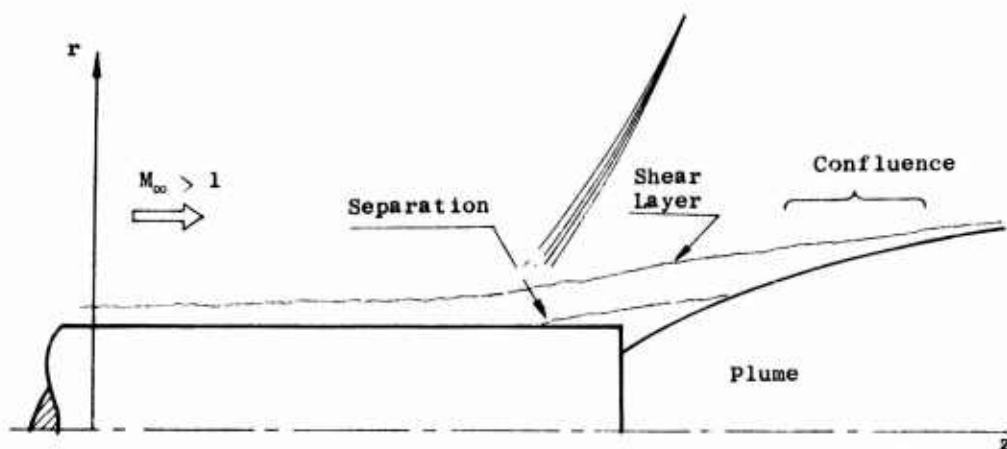
Figure 3. Transonic separated flow geometry.
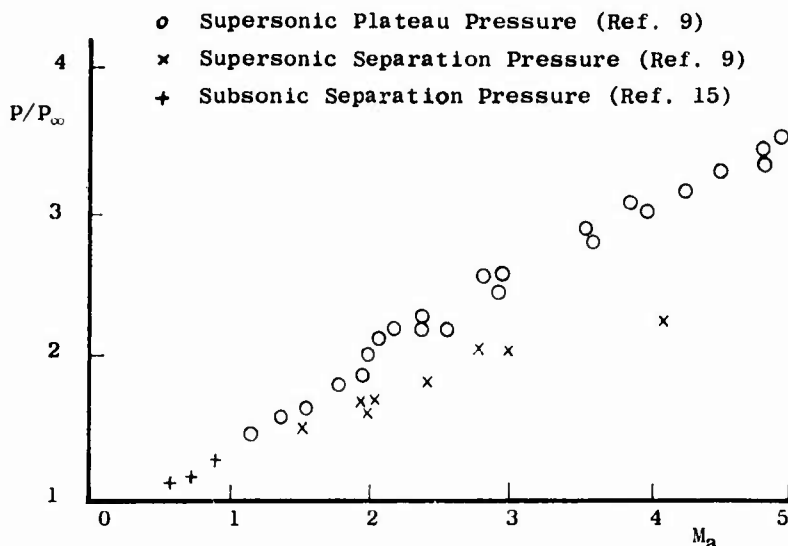
Figure 4. Data for separaration and plateau pressure

When the flow is quite supersonic ($M_\infty \sim O(2)$) the initial conditions at the start of the turbulent separation are subject to (albeit approximate) analysis (Refs. 9 to 12) so that relations are available for the pressure rise and flow deflection angle as functions of the approach Mach number. Such criteria are presented in Fig. (4).

This figure—which shows both the separation and plateau pressures—indicates the situation throughout the Mach

number range. In the range $1 \lesssim M_\infty < 1.5$ considerable difficulties arise. Firstly, (Ref. 13) there is very little data available, and what data does exist shows fair scatter. In addition, for Mach numbers below about M = 1.2, a normal shock is not of sufficient strength to create a separation of the turbulent boundary layer (Ref. 14). In this case, the nicety of the supersonic separation is lost and the phenomenon is essentially a subsonic one (even though the free stream may be just supersonic). Also included on Figure (4) is some experimental data (from Ref. 15) for the separation pressure in subsonic flow. It should be noted that the form of the pressure rise in subsonic flow is such that the plateau pressure has no meaning. Thus on Figure (5) is plotted the pressure rise through separation for both subsonic and supersonic flow over a forward facing step--Refs. (15, 16). The significant contraction of the length scale as the approach Mach number becomes supersonic should be noted. In subsonic flow the separation occurs very near the peak pressure. Then as the Mach number increases to supersonic values, the peak pressure remains as the plateau pressure, but the separation point moves ahead (relative to the pressure distribution) and approaches the inflexion point in the pressure curve.
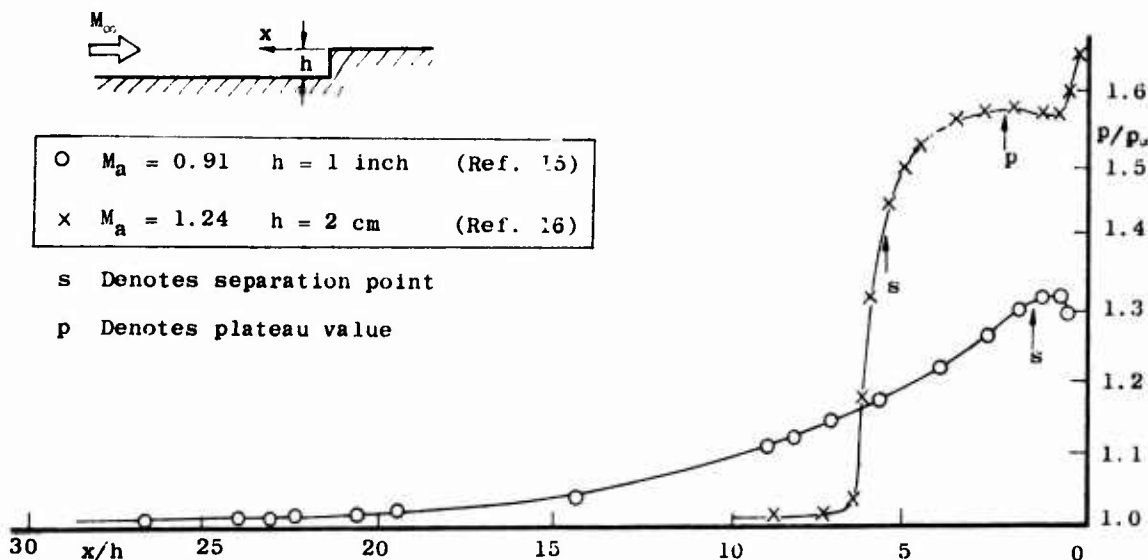
Figure 5. Pressure distributions ahead of a forward facing step

Associated with the inability of a shock wave to separate the boundary layer at low supersonic Mach number is the observation that the entire interaction length becomes considerably greater since the flow is then unable to make a rapid turn through a shockwave. The pressure rise becomes more or less isentropic in nature.

The implications of this change in form of the pressure field associated with the external flow are significant as far as the boundary layer development and calculation are concerned. Thus, in the supersonic flow case, the boundary-layer develops under a pressure field related to the body shape and then suffers a rapid rotation and leaves the body surface. In transonic flow this situation does not pertain and the boundary layer develops under a slowly rising pressure and ultimately suffers a separation. As far as prediction is concerned, empirical relations are available for estimating the change in integral properties of the turbulent boundary layer undergoing a rapid separation (Refs. 10, 14). But the turbulent boundary layer development through separation under a gradual pressure increase is a subject for much comment. This will not be attempted herein.

Differences in the free shear layer development are also evident. For the case of significant turning in a supersonic flow, this layer may fairly well be represented by the constant pressure mixing model. For transonic flow, this is in no way adequate due to the increased length scales and prevailing pressure gradients. A more satisfactory treatment would solve the boundary layer equations with a suitable empirical description of the turbulent mixing.

The experiments currently under way (Ref. 15) will be of great assistance in providing a better understanding of these problems associated with transonic separation, but there is also room for considerable more work.

As an example of the differences between a supersonic and a higher transonic flow, the flow over a conical afterbody may be considered. In supersonic flow, the situation is shown diagramatically in Figure (6)--after Ref. (13).

Such a flow can be treated by the component approach and reasonable results obtained (Ref. 17). However, when the free-stream Mach number is only a little greater than sonic the flow is far more complex and not readily discussed by existing theories.

Figure (7) shows the measured pressures on the surface of such a body (with a 6.3° conical boattail) at a free stream Mach number of 1.1. Schlieren photographs of such flows, Figure (8), clearly indicate where the shock waves are generated. For a subsonic free stream, the shock occurrs just downstream of the boattail corner, while in the low supersonic flow case, the shock is present in the interaction region. This situation should be compared to that pertaining in two dimensional configurations as discussed in Ref. (18).
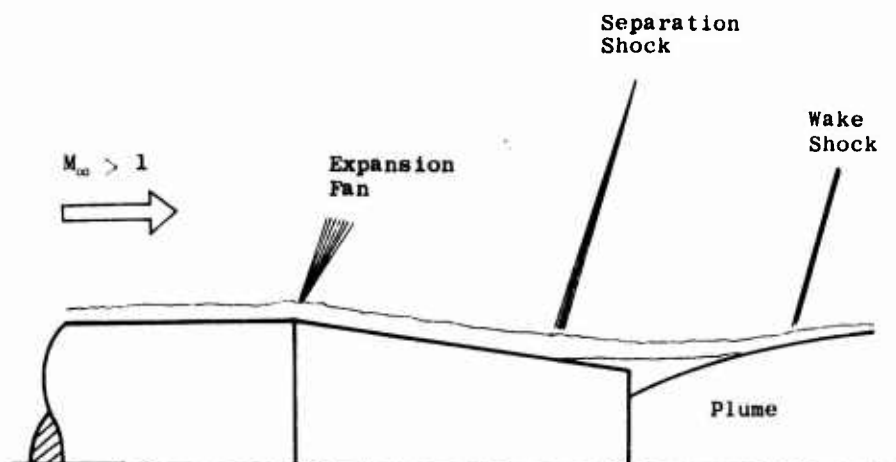
Figure 6.   Supersonic flow over a boattail body.

The implications of these observations follow directly as far as calculative techniques are concerned. The flow ahead of the interaction on the boattail are in no way reminiscent of a supersonic flow. This can be further demonstrated as follows. Figure (9) shows the experimental data of Ref. (5) plotted as base pressure against boattail angle, with nozzle thrust (i.e. chamber pressure) as a parameter.

Here, as the thrust is increased, the base pressure tends to a limiting value (particularly at large boattail angles) which is far below the Plateau pressure associated with separation at the quoted free stream Mach number*. Reference to Figure (4) shows that the limit base pressure shown in Figure (9) is far lower than any expected plateau pressure in a supersonic separation; but could be assigned an equivalent subsonic condition. It can be anticipated, therefore, that any theory based upon the empirical data

Figure 7.   Flow over a 9.5° boattail for $M_\infty = 1.1$

*Ref. (20) indicates that, for parallel sided afterbodies, this plateau pressure presented in Figure (4) is a good indication of the limit base pressure for large nozzle thrust.
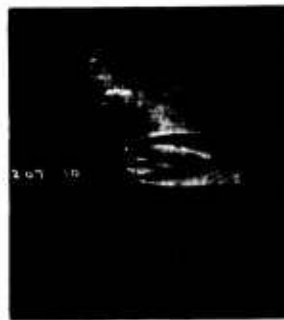
a) $M_\infty = 1.1$ $P_C/P_\infty = 49.9$ b) $M_\infty = 0.9$ $P_C/P_\infty = 61.6$

Figure 8.   Schlieren Photographs For Body With 9.5 Degree Boattail

relating to flow separation discussed above, will not be too rewarding when applied to such a configuration. Figure (10) shows this expectation to be confirmed. In the intermediate thrust coefficient range, the agreement between theory and experiment is adequate for engineering applications. However, under the higher thrust conditions, the theory greatly overestimates the base pressure. This is because the plateau pressure data of Figure (4) is used in the theory while the data of Figure (9) shows this to be inapplicable to boattail configurations. For the parallel sided afterbody, the theory gives better agreement--Figure (11)--at higher thrust coefficient. A Schlieren photograph of this flow is shown in Figure (12).

The whole flow development needs greater consideration. In the present work we restrict the discussion of the flow development to only those areas that are pertinent to the theme in progress. Greater details will appear in Ref. 21. A sequence of Schlieren photographs are shown in Figure (13). These are for the flow at $M_\infty = 1.1$ over a body with a 9.5 degree boattail. The jet pressure ratios are as indicated. At the intermediate thrust levels--Figure (13 c, d)--where the theory and experiment is giving the best agreement, it is seen that the flow field is most nearly like the theoretical model. In this situation there is a shock in the wake region close to the confluence of the separated shear layer and the plume boundary.

Further increases of jet pressure ratio cause this wake shock to progress forward and become associated with the separation on the boattail surface. The confluence region is then more reminiscent of a subsonic flow. At this point the classical supersonic base flow theory has no validity, even though the free stream conditions are supersonic. Changes in both free stream Mach number and body geometry just change the jet thrust level at which the theory loses applicability.

Figure 9.   Base pressure changes with boattail angle.
          $M_\infty = 1.1$ From Ref. (5)
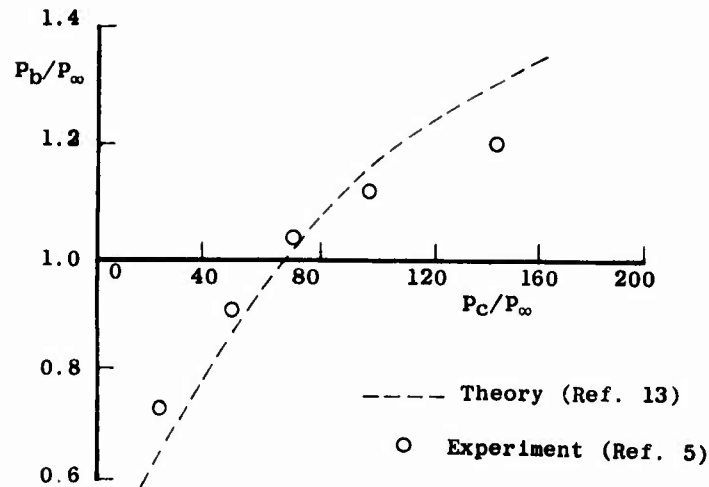
Figure 10. Theoretical solution for base pressure on body with 6.4° boattail. $M_\infty = 1.1$.
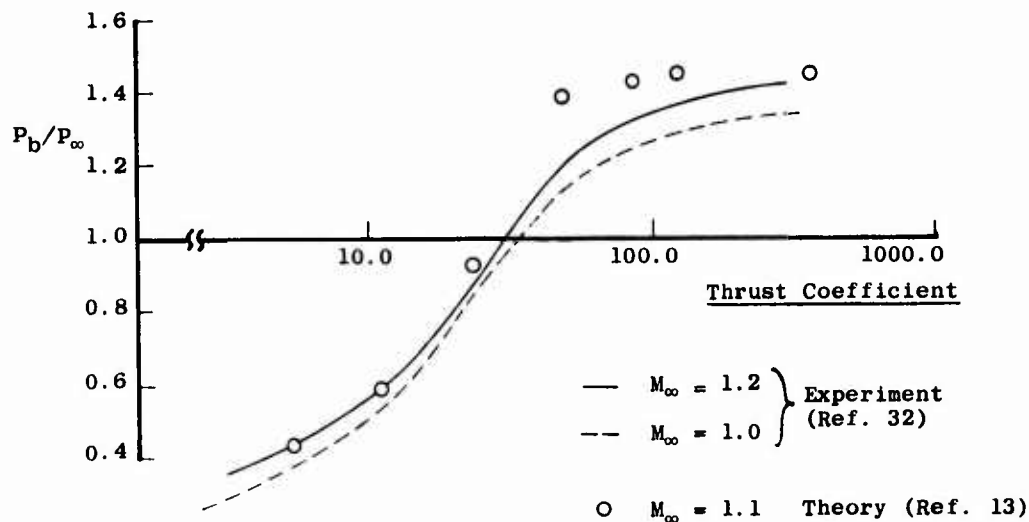
Figure 11. Base pressure prediction for parallel sided afterbody.

4. ON INTEGRAL METHODS

By virtue of a formal integration of the boundary layer momentum and moment of momentum equations across the boundary layer, a set of equations for the integral thickness can be established. By selection of a profile family and a compressibility transformation, these integral quantities may be related so that equations for just the displacement thickness and form factor result.

For a laminar flow this procedure is somewhat defensible provided the error associated with replacing the boundary layer velocity profile by an N-parameter curve fit is acknowledged. However, if the profile family utilized is sufficiently powerful for the application in hand, then its precise form is of little consequence. The success of the method in supersonic flow (Ref. 22) suggests that these approximations are entirely adequate.
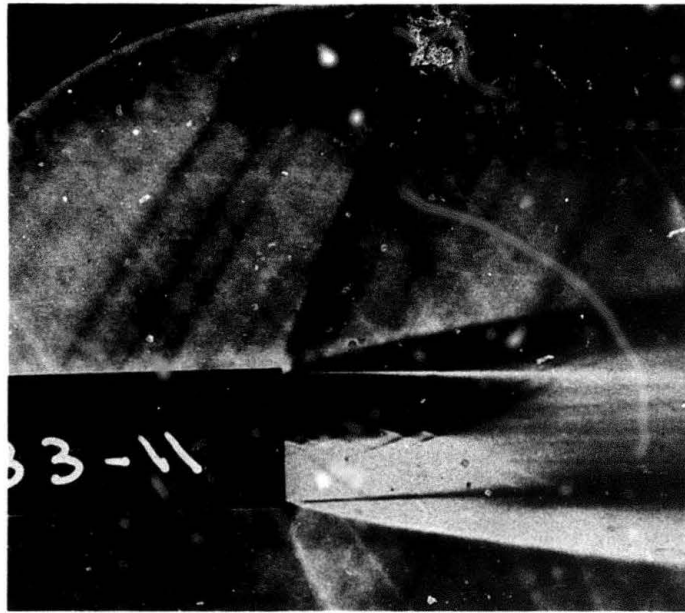
Figure 12.   Schlieren Photograph For Flow At M_∞ = 1.2 Past Parallel Sided Body.--From Ref. (32).   Thrust Coefficient = 35.56
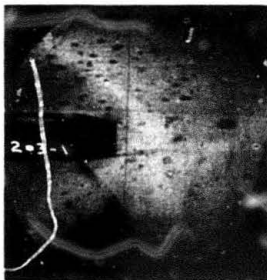
a)   No jet
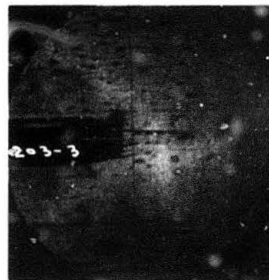
b) P_C/P_∞ = 7.22
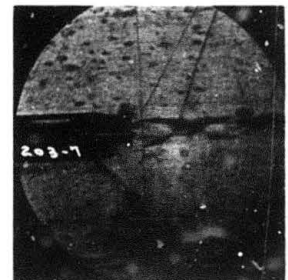
c) P_C/P_∞ = 26.01

d) P_C/P_∞ = 39.50
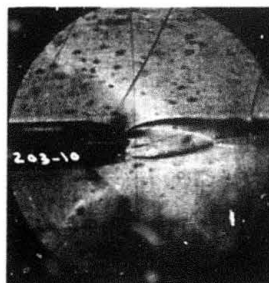
e) P_C/P_∞ = 73.27
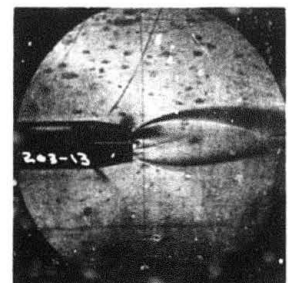
f) P_C/P_x = 144.19

Figure 13.   Schlieren Photographs For Body With 9.5 Degree Boattail at M_∞ = 1.1

In practical cases where the boundary layer flow is turbulent over a large portion of the body surface, the situation is somewhat different. As noted above, the method relies heavily upon a family of velocity profiles expressing the form of the boundary layer in constant property flow. Hence both a family of velocity profiles and a transformation theory are required. In a turbulent flow the velocity profile is very much dictated by the turbulent momentum transfer processes which, at best, are not well understood. Hence, it is unlikely that an adequate representation of the compressible turbulent boundary layer can be achieved in this manner. Due also to the complexity of the turbulence kinetic energy equation (Ref. 24) it appears that the relation between a shear stress profile and the velocity field would not be easy to establish. However, for engineering calculations, sufficient accuracy may be attainable. For example, the separated flow profile family of Alber (Refs. 25, 26) show some promise in such applications.

That the difference between a laminar and turbulent boundary layer is important and must be included in the calculation procedure is shown in Ref. (4) where it is indicated that the flow field over the airfoil can be greatly changed just on replacing the laminar wake by a turbulent one. The importance of transition position in experimental work is, of course, too well known to require elaboration.

In applications of the integral approach where the external flow is transonic and determined from a numerical solution of the transonic flow small disturbance equation (Ref. 4 say) there is a greater likelihood that the complexities of the confluence region will be better represented than they are in a component approach. Thus, while one may argue that the viscous contribution has not been handled to the greatest satisfaction it is true that the external flow will be a good representation. In particular, the change from supersonic to subsonic type confluence can be handled with this mode of external flow representation. It can be expected, therefore, that more satisfactory results would be obtainable from this approach.

This remark does not imply that great efforts should be expended on such work. Rather, it is felt and discussed at length in Section 5, that efforts should be placed in the determination of solutions to the exact equations.

The application of integral methods to axisymmetric flows does not seem to have received too much attention and a direct comparison between it and the component approach is not possible for an engine configuration at this time.

5. FURTHER DISCUSSION

Much of the above discussion has been devoted to highlighting some of the deficiencies that appear in existing calculation techniques for separated flows. Most of the comments made referred most acutely to transonic flows where the pertaining physical phenomena are less well known. At this point, it seems appropriate to indicate some areas where it is felt additional effort would be most beneficial to the stated aim of calculating transonic flow fields with separation induced by a nozzle exhaust.

Most urgent among the many requirements is more experimental data. Such data should be collected over a very wide Reynolds number range so that many of the existing anomalies between free-flight and wind tunnel testing (Ref. 27) can be clarified. To be of most moment, experiments should be detailed and fundamental in nature. In particular boundary layer velocity profiles and turbulence data are of great importance. Specific simple geometries (Ref. 15) rather than more ad hoc experiments (Refs. 26, 28) are essential as the starting point for such experimental work.

From the theoretical aspect, it is desirable that efforts be expended towards the development of solutions to exact equations. With the existing expertise in numerical methods it would appear that such is a rewarding enterprise. Indeed for potential flow, methods are well developed for the solution of transonic problems. Exact solutions (Ref. 33) are available as well as many solutions to the small disturbance equation (Ref. 34 for example).

The major effort should be centered around establishing solutions for the viscous-dominated portion of the flow. Where the flow is laminar, the exact Navier-Stokes equations can be solved--or at least a well posed boundary value problem can be written down. For the practical case of interest when the boundary layer and wake are turbulent in nature, the situation is still bleak. Thus, the remarks made above concerning lack of information on the structure of the turbulent boundary layer--particularly near separation--still pertain. However, the situation is now more acute. A full treatment of the exact equations would only be justified if the turbulence model were sufficiently well developed to allow specification of this turbulence structure to the same level of accuracy as the equations to be solved.

In other words, while for laminar flow there is merit in attempting solutions of the Navier-Stokes equations, the currently available models for turbulence are sufficiently poor to make a solution of the corresponding equations of little meaning. This remark does not imply that techniques for solving Navier-Stokes type boundary value problems should not be attempted. On the contrary, every effort in this direction

should be made. Then when further developments in the understanding of turbulence are available, the situation will be well in hand.

All the above remarks have been addressed to the problem of an isolated single body of revolution. Such a configuration will not be of interest in any engineering problem. Rather, for a rocket, fins will be attached and most probably the vehicle would be spin stabalized. In an aircraft configuration, an engine pod would be strut mounted in an interference field from both wing and fuselage. It need hardly be said that if so many unresolved questions surround the calculation of the body of revolution flow, then the highly three-dimensional practical flows is even further removed.

6. RECOMMENDATIONS AND FINAL REMARKS

The above comments have stressed the need for both additional experimental work and for the development of improved calculative techniques. The experiments should be of a detailed and fundamental nature, while the theoretical work should take best advantage of modern computing facilities and of the knowledge obtained from the experiments.

REFERENCES

1. Korst, H. H., "A Theory For Base Pressure in Transonic and Supersonic Flow", J. Appl. Mech. Vol. 23, p. 593, 1956.

2. Crocco, L. and Lees, L., "A Mixing Theory for the Interaction Between Dissipative Flows and Nearly Isentropic Streams", J. Aero Sci., Vol. 19, p. 647, 1952.

3. Chapman, D. R., "An Analysis of Base Pressure at Supersonic Velocities and Comparison with Experiment", NACA TN 2137, 1950.

4. Klineberg, J. M. and Steger, J. L., "Calculation of Separated Flows at Subsonic and Transonic Speeds", Proceedings Third International Conference on Numerical Methods in Fluid Dynamics, 1972.

5. Rubin, D. V., "A Transonic Investigation of Jet Plume Effects On Base and Afterbody Pressures of Boattail and Flare Bodies of Revolution", U. S. Army Missile Command RD-TR-70-10, 1970.

6. Lock, R. C., Powell, B. J., Sells, C. C., and Wilby, P. G., "The Prediction of Aerofoil Pressure Distributions for Subcritical Viscous Flow", AGARD CP 35, 1968.

7. Moulden, T. H., Spring, D. J., Saisi, R. D., Aoyama, K. and Wu, J. M., "Bodies of Revolution at Transonic Speeds: Estimation of the Reynolds Number Effects", AGARD CP 83, 1971.

8. Enseki, F. K., "A Calculation Method for the Turbulent Transonic Viscous-Inviscid Interaction on Airfoils", AIAA Paper 72-5, 1972.

9. Zukoski, E. E., "Turbulent Boundary-Layer Separation in Front of a Forward Facing Step", AIAA Journal, Vol. 5, p. 1746, 1967.

10. Mager, A., "On the Model of the Free Shock Separated Turbulent Boundary Layer", J. Aero. Sci. Vol. 23, p. 181, 1956.

11. McDonald, H., "A Study of the Turbulent Separated Flow Region Occurring at a Compression Corner in Supersonic Flow", JFM, Vol. 22, p. 481, 1965.

12. Nash, J. F., "An Analysis of the Two-Dimensional Turbulent Base Flow Including The Effect of the Approaching Boundary-Layer", ARC R&M 3344, 1963.

13. Wu, J. M., Moulden, T. H., Venghaus, H. H., Spring, D. J., and Henderson, J. H., "Plume Induced Separation From a Single Nozzle Exhaust at Transonic Flight Speed", Proceedings 7th JANNAF Plume Technology Meeting, 1973.

14. Lunsdaine, E. and Fathy, A., "Effect of Normal Shock on Turbulent Boundary-Layer Parameters", J. Basic Eng., p. 567, 1971.

15. Wu, J. M., Moulden, T. H., Elfstrom, G. H., Reddy, K. C., Chen, C. H., Nygaard, R, Shen, L., Venghaus, H. H., and Anjaneyulu, K., "Fundamental Studies of Subsonic and Transonic Flow Separation--Summary Report", AEDC Technical Report in printing, 1974.

16. Wilson, R., and Maurer, F., "An Experimental Investigation of Turbulent Separated Boundary Layers at Low Supersonic Mach Numbers", DRL FB 70-30, 1970.

17.   Addy, A. L., "Experimental-Theoretical Correlation of Supersonic Jet-on Base Pressure for Cylindrical After-Bodies", AIAA J. of Aircraft, Vol. 7, p. 474, 1970.

18.   Howell, R. H., and Korst, H. H., "Drag Associated with Separated Flow Over Two-Dimensional V-Shaped Notches Under Transonic and Supersonic Conditions", NASA CR 1132, 1968.

19.   Wu, J. M. et al Experimental Data to Appear.

20.   Deep, R. A., Henderson, J. H., and Brazzel, C. E., "Thrust Effects on Missile Aerodynamics", U. S. Army Missile Command Rept. RD-TR-71-9, 1971.

21.   Moulden, T. H., Wu, J. M., and Spring D. J., "Towards a Model for Plume Induced Separation in Transonic Flow", To appear.

22.   Klineberg, J. M., Kubo.a, T., and Lees, L., "Theory of Exhaust Plume and Boundary Layer Interactions at Supersonic Speeds", AIAA J. Vol. 10, p. 581, 1972.

23.   Lewis, J. E., Kubota, T. and Webb, W. H., "Transformation Theory for the Adiabatic Compressible Turbulent Boundary Layer with Pressure Gradient", AIAA J. Vol. 8, p. 1644, 1970.

24.   Nash, J. F., and Patel, V. C., "Three-Dimensional Turbulent Boundary-Layers", Scientific and Technical Books, Inc., 1972.

25.   Alber, I. E., "Similar Solutions for a Family of Separated Turbulent Boundary Layers", AIAA Paper 71-203, 1971.

26.   Alber, I. E., Bacon, J. W., Masson, B. S., and Collins, D. J., "An Experimental Investigation of Turbulent Transonic Viscous-Inviscid Interactions", AIAA J. Vol. 11, p. 620, 1973.

27.   Heiser, W., Private Communication, Advanced Propulsion Lab, Wright-Patterson Air Force Base, Ohio.

28.   Stanewsky, E., and Little, B. H., "Studies of Separation and Reattachment in Transonic Flow", AIAA Paper 70-541, 1970.

29.   Chapman, D. R., Kuehn, D. M., and Larson, H. K., "Investigations of Separated Flows in Supersonic and Subsonic Streams with Emphasis on the Effects of Transition", NACA Rept. 1356, 1958.

30.   Seddon, J., "The Flow Produced by Interaction of a Turbulent Boundary-Layer with a Normal Shock of Sufficient Strength to Cause Separation", ARC R&M 3502, 1960.

31.   Bogdonoff, S. M., and Keppler, C. E., "Separation of a Supersonic Turbulent Boundary Layer", J. Aero Sci., Vol. 22, p. 414, 1955.

32.   Henderson, J. H., "Results of Transonic Wind Tunnel Investigations to Determine the Effects of Nozzle Geometry and Jet Plume on the Aerodynamics of a Body of Revolution", U. S. Army Missile Command RD-72-77, 1972.

33.   Colehour, J. L., "Transonic Flow Analysis Using a Streamline Coordinate Transformation Procedure", AIAA Paper 73-657, 1973.

34.   Murman, E. M., and Cole, J. D., "Calculation of Plane Steady Transonic Flows", AIAA J. Vol. 9, p. 114, 1971.

35.   Wu, J. M., and Aoyama, K., "Pressure Distributions for Axisymmetric Bodies with Discontinuous Curvature in Transonic Flow", U. S. Army Missile Command, RD-TR-70-25, 1970; see also AIAA Paper 72-137, 1972.

TWIN JET EXHAUST SYSTEM TEST TECHNIQUES

BY

RONALD J. GLIDEWELL*

ARTHUR E. FANNING, LT.*

AIR FORCE AERO PROPULSION LABORATORY
WRIGHT-PATTERSON AIR FORCE BASE, OHIO
USA

SUMMARY

The problem of integrating airframe and propulsion system requires that the various wind tunnel models, used in accomplishing the task, simulate as accurately as possible the internal and external flowfields that will be experienced on the airplane itself. This is particularly true for those models which are tested to define inlet and exhaust system interactions with the airplane flowfield. Exact simulation is, however, prohibited by the limitations of wind tunnel test techniques. For the Jet Effects Model, such limitations include the interference effects associated with the model support system, exhaust plume simulation and the use of inlet fairings in substitution for flowing inlets. This paper uses information from a variety of sources to assess the impact of these model limitations on the accuracy of afterbody performance measured on twin jet models.

NOTATION

C_D Afterbody drag coefficient, $D/q_\infty S$
C_L Afterbody lift coefficient, $L/q_\infty S$
C_m Afterbody pitching-mount coefficient, $P\text{-}M/q_\infty S\bar{c}$
$\bar{c}$ Reference wing chord length
$\dot{m}/\dot{m}_0$ Inlet mass flow ratio
M, M_∞ Free-stream Mach number
NPR   Nozzle pressure ratio, P_{Tj}/P_∞
P_{Tj} Nozzle total pressure
P_∞ Free-stream static pressure
q_∞ Free-stream dynamic pressure
S Reference wing area
α Model angle of attack
δ_H Horizontal tail incident angle

1. INTRODUCTION

The integration of airframe and propulsion system is a complex process that involves a number of wind tunnel tests for its accomplishment. Two of these tests are directed specifically at defining the interactions of the inlet and the exhaust system with the external flowfield that occur with changes in throttle position. These interactions are many-faceted and can have a variety of effects, either positive or negative, on total airplane performance. It is therefore essential that these models duplicate as closely as possible the flowfield of the airplane in order to ensure the proper assessment of throttle sensitive performance.

This paper is concerned with the test directed at the definition of interactions between the exhaust system and the external flowfield, commonly known as the "jet effects" test, for twin engine exhaust system installations. Duplication of the airplane flowfield on the Jet Effects Model is complicated for a variety of reasons, the most obvious being a problem which is inherent in any wind tunnel test, the effects of the model support system.

The presence of the support system not only influences the model flowfield but also contributes largely to the total blockage of the test article in the wind tunnel. Historically, Jet Effects Models are mounted on a strut support system. This type of support contributes very heavily to wind tunnel blockage and has strong interference effects on the model flowfield, particularly in the important transonic regime of Mach numbers. Consequently, it is desirable that alternative means of model support be explored which have the potential for reduced interference and blockage effects. Two types of support system are investigated in this paper, namely a wing-tip support system and a dual-sting support system.

Another problem associated with jet effects testing is the effect of simulating the flowing exhaust plume with either a solid body or an annular jet. The use of a dual-sting support system requires such simulation of the exhaust flow and it is often desirable to use solid plume simulation from the standpoint of reduced model complexity. This paper then assesses the accuracy of exhaust plume simulation in duplicating the interaction of the exhaust stream with the external flowfield.

A third problem encountered in jet effects tests has to do with the proper simulation of the inlet flow effects in the model flowfield. It is virtually without exception that inlets on a Jet Effects Model are "faired over". It has been assumed that this has had negligible effects on the model relative to flowing inlets. There is little data to support this assumption and its likely to be erroneous for one principal reason. The inlet streamtube of a flowing inlet is effectively "spilled" into the model flowfield which is likely to cause a severe alteration of the aerodynamic characteristics of the afterbody. This paper attempts to determine this effect with the rather limited amount of data available for the comparison of flow-through and faired-over inlets. It also investigates the sensitivity of the Jet Effects Model flowfield to inlet fairing design.

*Aerospace Engineer

2. MODEL SUPPORT SYSTEMS

Historically, Jet Effects Models have been supported by a strut extending from the tunnel floor to the model forebody. A typical strut support arrangement is illustrated in Figure 2-1. Properly designed, this type of model support can have minimal interference effects at subsonic and supersonic wind tunnel Mach numbers. However, it has been observed to have strong interference effects at transonic Mach numbers as seen in Figure 2-2 where levels approach $\triangle C_D = .0020$ or as much as nearly forty per cent of measured drag on the afterbody at subsonic Mach numbers. A second drawback of the strut support system is its contribution to wind tunnel blockage of the test article which, as with the arrangement shown in Figure 2-1, can exceed that of the model itself.

Variations have been made in strut support arrangements in an attempt to reduce both interference and blockage effects. The arrangement shown in Figure 2-3 has the strut support attached to an extension from the model nose. This can reduce flowfield interference and overall blockage of the model as can readily be seen. However, the extended "nose" aggravates an already complicated problem in wind tunnel testing, the problem of boundary layer growth on the model. Another variation in the basic strut support is a forward-swept strut, either overhead or underside, as shown in Figure 2-4. This arrangement can also place a great deal of the support system blockage ahead of the model, but as can be seen in Figure 2-5, does nothing to improve interference with the model flowfield, especially at high transonic Mach numbers when interference amounts to more than $\triangle C_D = .0030$, better than thirty percent of measured afterbody drag.

An alternative to the strut support is offered with the wing tip support system. An example of this type of support is shown in Figure 2-6. While this arrangement can necessitate distortion of the wing planform for passage of instrumentation and high pressure air, it has features which make it attractive for jet effects testing. First, the large part of support system blockage is placed downstream of the model. For the arrangement in Figure 2-6, the wing tip support contributes less than twenty-five per cent to wind tunnel blockage. Second, the wing-tip support does not directly disturb the model afterbody flowfield as does the strut support. Shock reflections on the afterbody from the support booms are not evident from the comparison in Figure 2-7 of the afterbody drag with two different nose shapes for the support booms, one a conical shape and the other an outward facing ramp. Interference effects of the wing-tip support system are shown in Figure 2-8 for a number of model configurations. At supersonic Mach numbers they are as high as $\triangle C_D = .0015$. In the important transonic regime, however, interference levels remain below $\triangle C_D = .0010$. For all mach numbers, interference effects remain within eleven percent of measured afterbody drag for all configurations that were tested.

A second alternative to the strut support system is a dual sting support system, an example of which is shown in Figure 2-9. This technique places all support system blockage downstream of the test article and has no direct interference with the model flowfield. This type of support can, however, have limited dynamic capability which in turn restricts the model angle-of-attack that can be safely achieved at higher tunnel Reynold's numbers. The dual-sting support also pre-supposes that the exhaust plume can be accurately simulated with either a solid body or an annular flow about the sting bodies. This aspect of the interference effects of the dual-sting support is covered in the following section. There is also an interference effect on the afterbody flowfield associated with the position of the main sting structure relative to the nozzle exit.

The effect of main sting position is illustrated in Figure 2-10 for drag measured on an Aerodynamic Force and Moment Model. Located approximately five sting diameters downstream of the model, interference levels are as high $\triangle C_D = .0030$ at low transonic Mach numbers. Figure 2-11 shows interference effects for a Jet Effects Model of the same airplane. In this case the main sting position is approximately eleven sting diameters from the nozzle exit station. Interference levels with the nozzles at a maximum reheat setting, with solid plume simulation, are virtually negligible at $\triangle C_D = .0002$. However, with the nozzles closed to a cruise setting, interference exceeds $\triangle C_D = .0015$ in the low transonic regime. With annular jet plume simulation, there is little difference in interference for the cruise nozzles. But with maximum reheat nozzles inteference is now at a level of $\triangle C_D = .0012$. For all conditions interference remains within thirteen percent of measured afterbody drag.

3. EXHAUST PLUME SIMULATION

As already pointed out, when using a dual-sting support system it is necessary to simulate the exhaust plume with either a solid body or an annular flow about a solid body. For Jet-Effects Models of certain aircraft types it is sometimes even advantageous to use solid plume simulation. This simplifies the model considerably, eliminating the need for a high pressure air supply and the attendant flow handling and measurement devices.

It is difficult, if not impossible, procedure to design a solid plume simulation properly to ensure that it will induce identical influence on the afterbody flowfield as does a full flowing jet. Figure 3-1 is an example where an attempt is made to simulate a fully-expanded flow ($P_S = P_\infty$) with a cylindrical body. In this case, it appears to be an accurate means of simulation with a maximum error of $\triangle C_D = .0006$. However, this is a unique aftend configuration with which a large portion of the exhaust plume is effectively shielded from the external flowfield. Looking at a more conventional twin engine installation as in Figure 3-2, the results are seen to be less favorable with variations of up to $\triangle C_D = .0015$ between afterbody drag with a fully expanded jet and with solid cylindrical plume simulation. It appears that in this instance an underexpanded plume is being simulated by the cylinder.

A second means of exhaust plume simulation which may be used with a dual-sting support system is with annular flow about the sting bodies, as illustrated in Figure 3-3. This allows for maintaining the confluence of internal and external flow and for the simulation of a range of exhaust plume shapes. Figure 3-4 is a comparison of a conventional jet with an annular jet for a typical close-spaced fighter configuration. The nozzle area ratio and nozzle half-angle are identical for the two such that for the

same nozzle pressure ratio (NPR) they have the same static-to-ambient pressure ratio and initial plume angle at the nozzle exit plane. This does not lend itself readily to a correlation between the two nozzles as can be seen in the data. However, if the nozzle pressure ratio for the annular jet is adjusted to give a maximum plume diameter equivalent to that of the conventional jet, the annular jet trend then correlates very well as seen in Figure 3-5, with a maximum error of $\Delta C_D = .0010$ at low transonic Mach numbers and $\Delta C_D = .0015$ at high transonic Mach numbers. A better correlation is obtained with the data in Figure 3-6 where the influence of the main sting support adaptor is accounted for. The maximum error obtained with this correlation is $\Delta C_D = .0005$ for all conditions except at a Mach number of 1.2 where the error is $\Delta C_D = .0011$.

4. INLET FLOW SIMULATION

The use of inlet fairings on Jet Effects Models, as already mentioned, has been a common practice. It is a complicated and costly process to build flow-through capability into a Jet Effects Model. The two problems most difficult to overcome in achieving this are: handling of the inlet flow once inside the model and passage of the flow across metric gaps within the model. Consequently, inlet fairings have been relied upon as a simulation of the inlet flow. The accuracy of this technique, however, is questionable since the inlet stream tube is effectively "spilled" into the model flowfield, creating a disturbance in the afterbody flowfield which is likely to have significant effects on its aerodynamic characteristics. Figure 4-1 gives an example of how sizeable this effect can be on afterbody drag. The results indicate that for a wide-spaced configuration, the effects are in fact negligible. However, for an afterbody with narrow spacing the effect is as much as $\Delta C_D = .0009$ at supersonic Mach numbers which amounts to approximately twenty percent of measured drag.

The sensitivity of the afterbody flowfield to inlet fairing design can also be of importance. Figure 4-2 is a comparison of lift, drag and pitching moment with alternate inlet fairing contours. Differences in all aerodynamic coefficients are negligible for both subsonic and supersonic Mach numbers. This, of course, indicates that design of the fairing contour is less of a problem than it has been thought to be. Figure 4-3, however, shows a similar comparison with an inlet fairing of smooth contour and a blunt inlet fairing. Once again the differences are negligible subsonically, but they become significant at transonic Mach numbers where they are as high as $\Delta C_D = .0008$.

5. CONCLUSIONS

The data indicates that support system interference and blockage effects are most severe for those models which are strut supported. Strut interference is favorable at low subsonic and high supersonic Mach number, but in the important transonic regime they can exceed $\Delta C_D = .0030$. The dual sting support system contributes nothing to the model blockage and has no direct interference with the model flowfield. However, it can have interference effects on afterbody drag that are comparable with those of the strut support if care is not taken in the placement of the main support structure relative to the model. If properly designed, the dual sting support can have interference levels which remain within $\Delta C_D = .0015$, with consideration of the combined effects of the main sting and plume simulation. The wing-tip support system, while it requires some distortion of the wing planform, contributes somewhat less to model blockage than does the strut support. In addition, it has interference effects which remain within $\Delta C_D = .0010$ at transonic Mach numbers.

Simulation of the exhaust plume with a solid body, while it simplifies the model considerably, is not an accurate means of duplicating the effects of a flowing exhaust on afterbody drag. For some unique configurations, levels of accuracy are favorable. However, for conventional twin installations, the error in afterbody drag is as much as $\Delta C_D = .0015$. Annular-jet plume simulation is more attractive since it maintains the confluence of exhaust plume and external flowfield, and allows for the determination of the effects of variation in nozzle pressure ratio. Accuracy with this type of exhaust plume simulation is much more favorable, with general levels not exceeding $\Delta C_D = .0005$.

The effect of the use of inlet fairings in place of flowing inlets appears to be insignificant for afterbody installations with wide spacing. However, for narrow-spaced installations the effect on afterbody drag can be as much as $\Delta C_D = .0009$. While the afterbody is not particularly sensitive to small changes in inlet fairing contour, the use of blunt inlet fairings results in the loss of an additional $\Delta C_D = .0008$ of accuracy at transonic Mach numbers.

REFERENCES

1. Price, Earl A. Jr., "Afterbody Aerodynamic Characteristics and Support System Interference on a Twin-Jet Fighter-Type Aircraft Model at Mach Numbers from 0.6 to 1.5" AEDC-TR-74-13, April 1974.

2. Watson, T.L. and Anderson R.D. "Exhaust System Interaction Program: Analysis of Wind Tunnel Data on a 4.7% Scale F-15 Jet Effects Model in the McDonnell Polysonic Wind Tunnel, PSWT 319" McDonnell Douglas Corporation, A2135, January 1973.

3. Hines, B.G., Marsh, W.H. and Wood, R.A., "Twin Jet Installation and Test Technique Improvement Test", General Electric Company, R74AEG201, January 1974.

4. Galigher, Lawrence L. "Integrated Airframe Nozzle Performance Characteristics of a Generalized Twin-Jet Air Superiority Fighter Aircraft Model at Mach Numbers from 0.6 to 1.6" AEDC-TR-73-125 (AD912073L), July 1973.

5. Glasgow, E.R., Santaran, D.M., Miller, L.D. et al "Integrated Airframe-Nozzle Performance for Designing Twin-Engine Fighters" Lockheed-California Company, AFFDL-TR-73-71, Vol. 1, 30 June 1973.

6. Anderson, R.D., Keller, K.J. and Nieser, D.E., "Exhaust System Interaction Program: Analysis of Wind Tunnel Data on a 5% Scale F-4 Jet Effects Model in the McDonnell Polysonic Wind Tunnel, PSWT Test 295", McDonnell Douglas Corporation, A1   , Vol. I, January 1972.
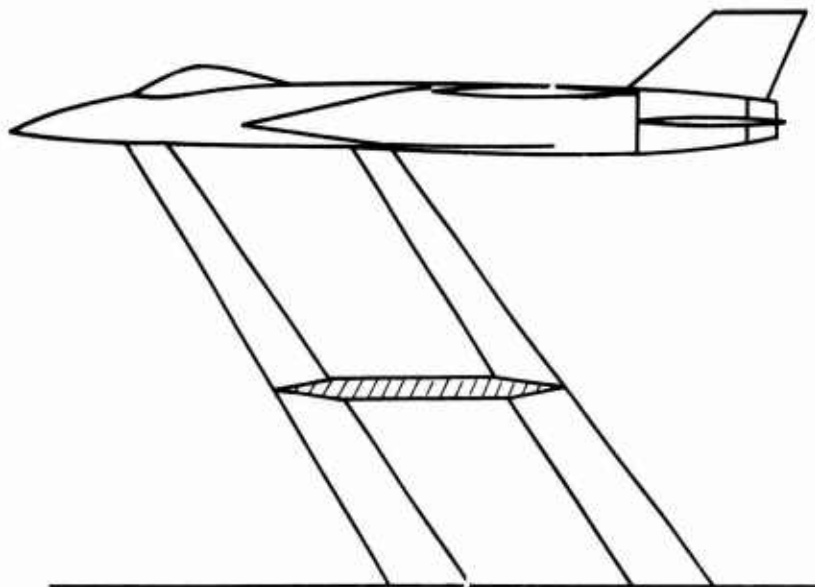
Fig. 2.1 Typical strut support system

$\triangle C_D = C_D$ WITH STRUT $- C_D$ WITHOUT STRUT

EXHAUST SIMULATOR $-$ CI3
- ○ BASE STEP
- □ CYLINDRICAL PLUME
- △ EXPANDED PLUME

◻ CYLINDRICAL PLUME $-$ CD1
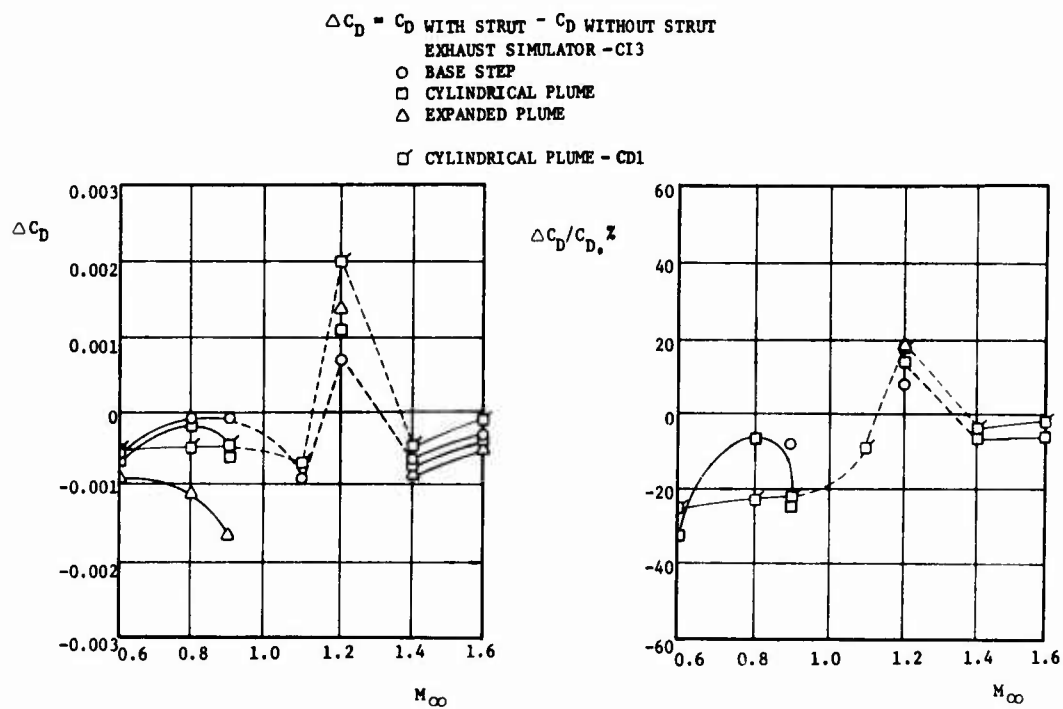
Fig. 2.2 Strut interference effects on afterbody drag.
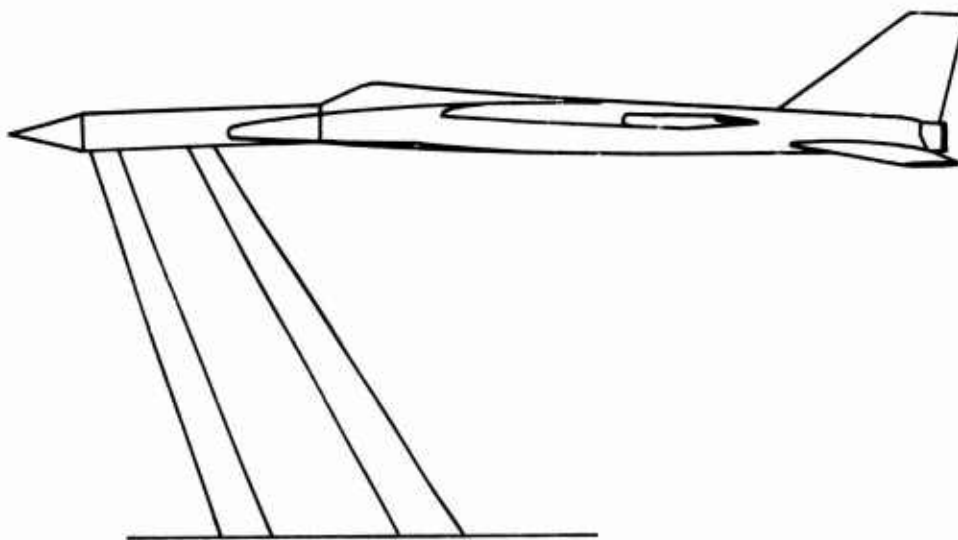
Fig. 2.3   Strut support with extended nose.
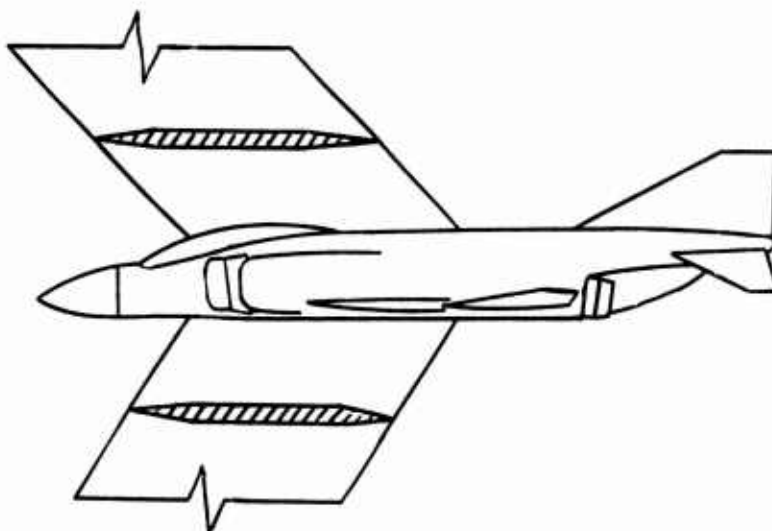
Fig. 2.4   Strut support with forward sweep (over-head or underside).
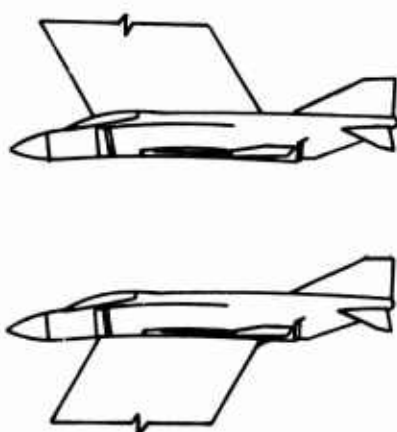
$M_\infty = 0.9$	$M_\infty = 1.2$
AFT-END DRAG, C_D	
0.0059	0.0091
DRAG CORRECTIONS, C_D	
0.0005	0.0024
0.0006	0.0034

Fig. 2.5   Strut interference effects with forward sweep

Fig. 2.6   Wing-tip support system

BOOM NOSE SHAPE
O CONICAL
□ RAMP
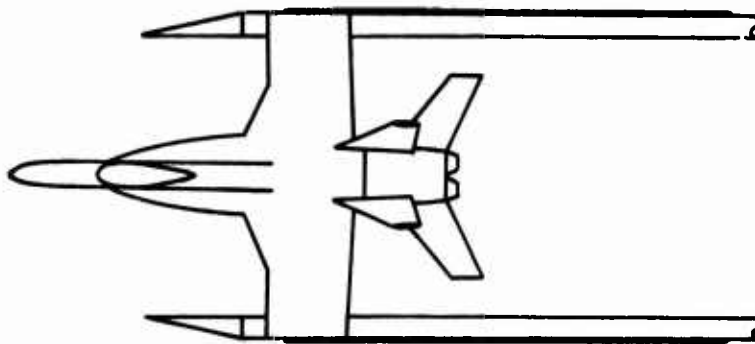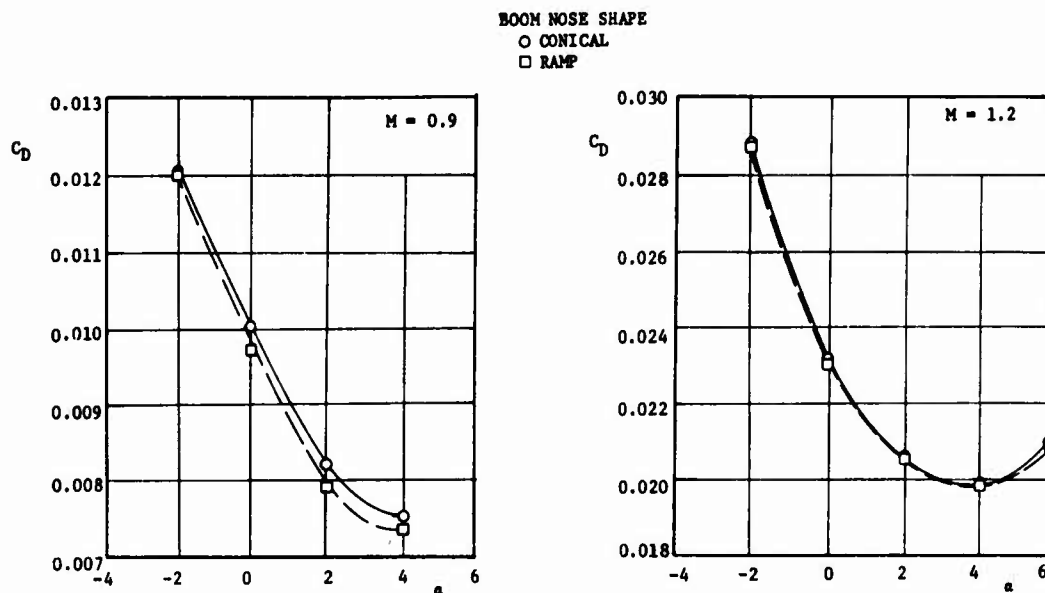
Fig. 2.7   Effect of wing-tip boom leading edge shape on afterbody drag, cruise nozzles.

$$\Delta C_D = C_{D\ BOOMS\ ON} - C_{D\ BOOMS\ OFF}$$

CONFIGURATION
O CRUISE, $\delta_H = 0°$
♂ CRUISE, $\delta_H = -5°$
□ CRUISE, TAILS-OFF
△ REHEAT, $\delta_H = 0°$
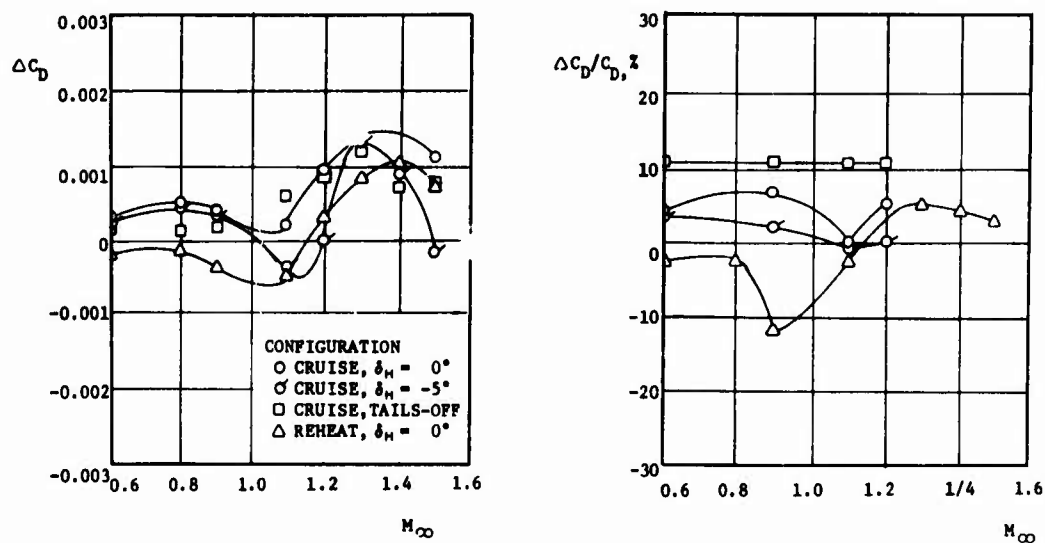
Fig. 2.8   Wing-tip support interference effects on afterbody drag.
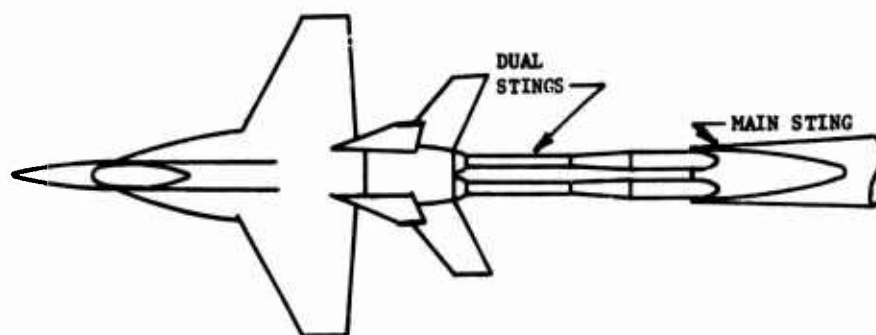
Fig. 2.9 Dual-sting support system.
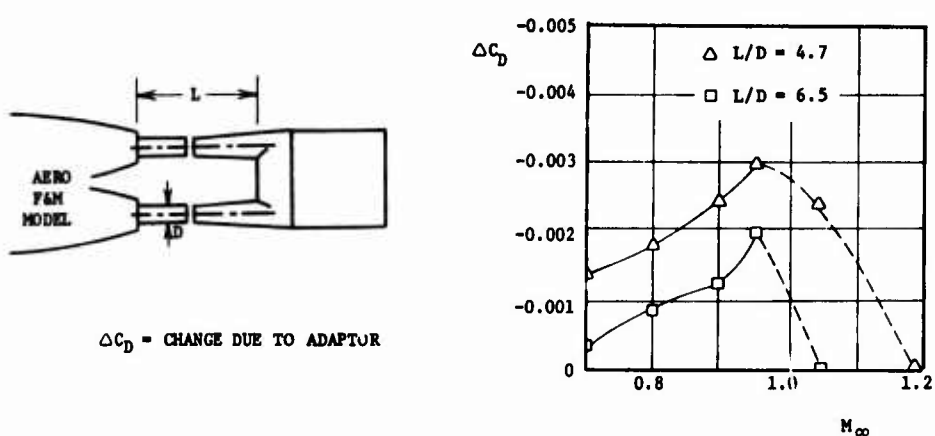
Fig. 2.10 Effect on main sting adaptor position on dual-sting support system interference.
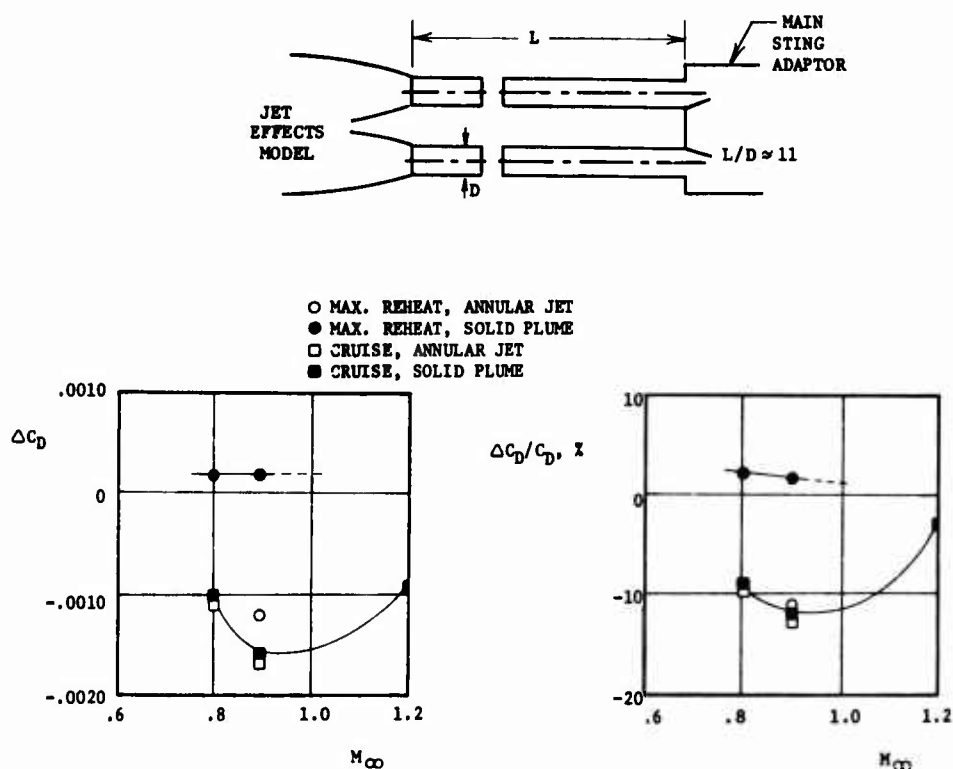
Fig. 2.11 Dual-sting support interference effects on afterbody drag, L/D = 11.
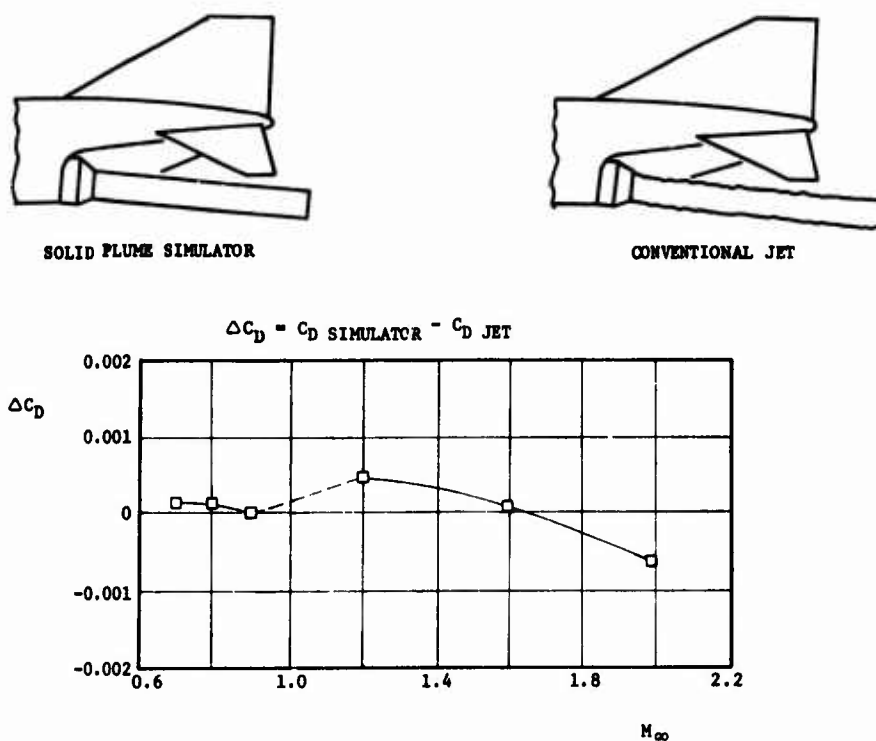
Fig. 3.1   Effect of solid plume simulation on afterbody drag, F−4 afterbody.
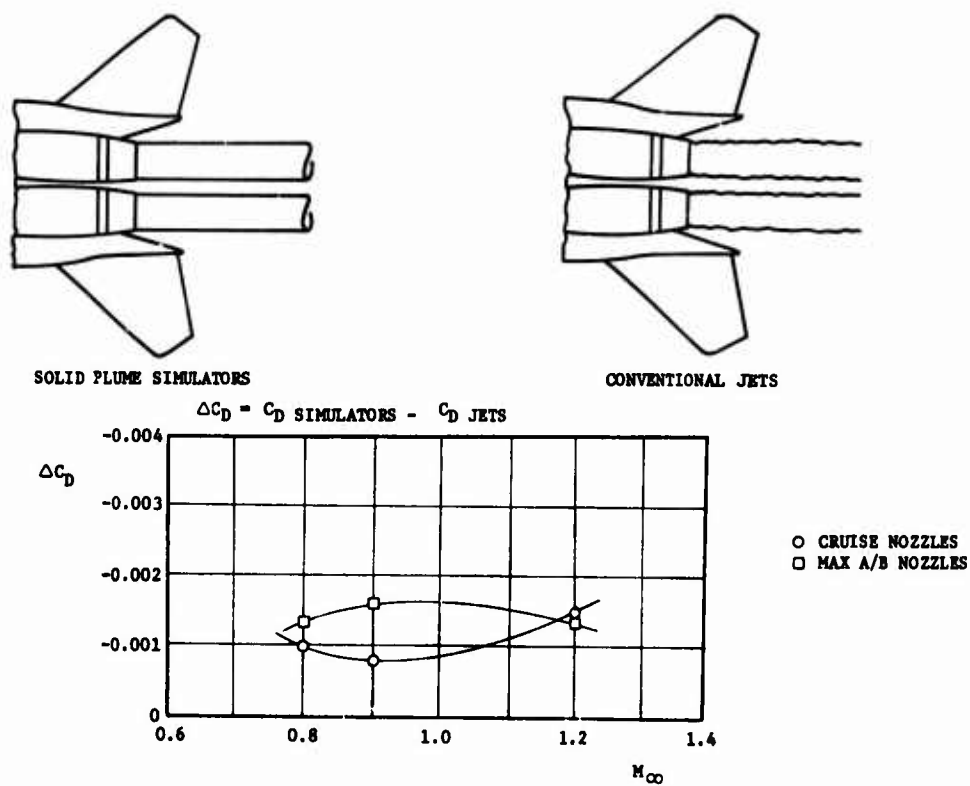
Fig. 3.2   Effect of solid plume simulation on afterbody drag, conventional twin installation.

CONVENTIONAL NOZZLE FLOW

NOZZLE BOATTAIL — CONVENTIONAL JET

INTERNAL NOZZLE

ANNULAR-JET PLUME SIMULATION

ANNULAR JET

STING BODY
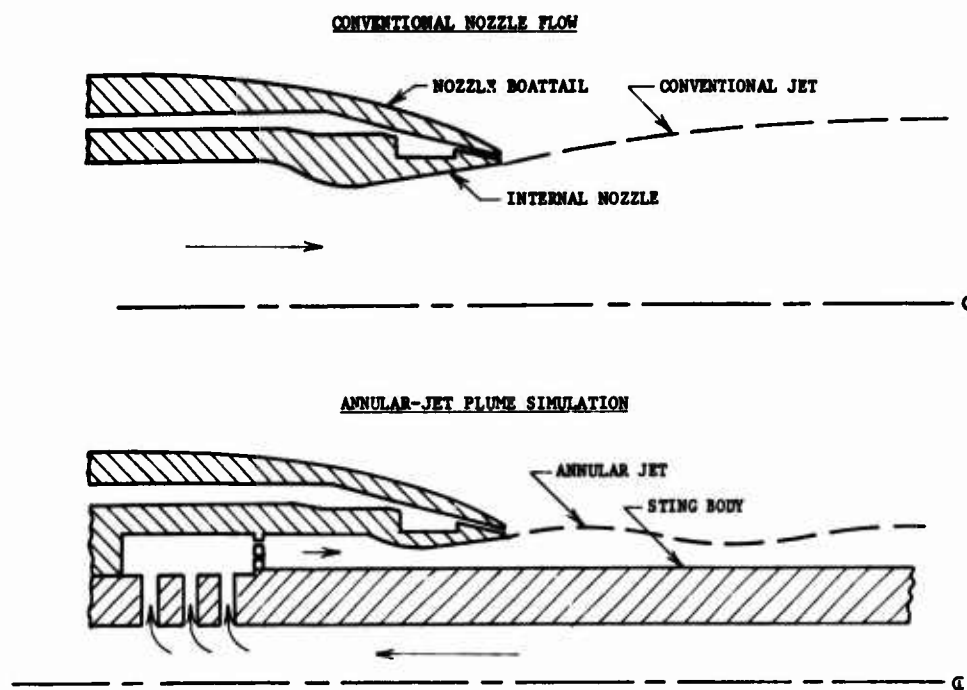
Fig. 3.3   Concept of annular-jet plume simulation with sting support of a jet effects model.

○ CONVENTIONAL JETS
□ ANNULAR JETS

○ CONVENTIONAL JETS
□ ANNULAR JETS
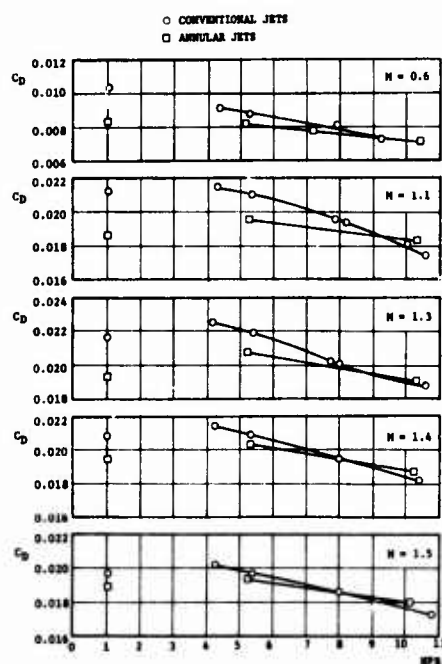
Fig. 3.4   Comparison of afterbody drag with conventional and annular jets for a twin-engine fighter model, reheat nozzles.
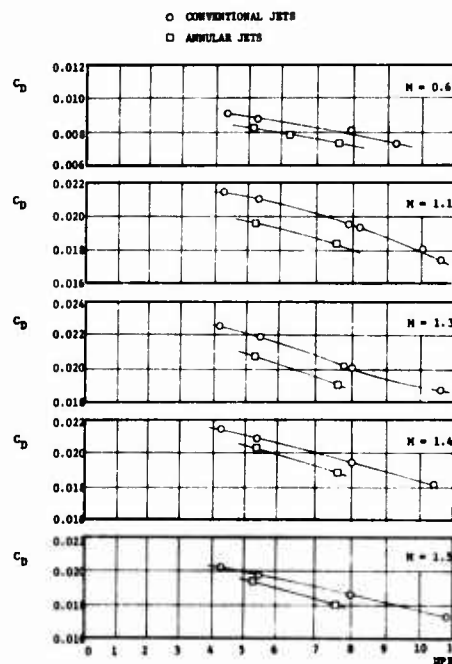
Fig. 3.5   Comparison of afterbody drag with conventional and annular jets, with maximum plume diameter correlation.
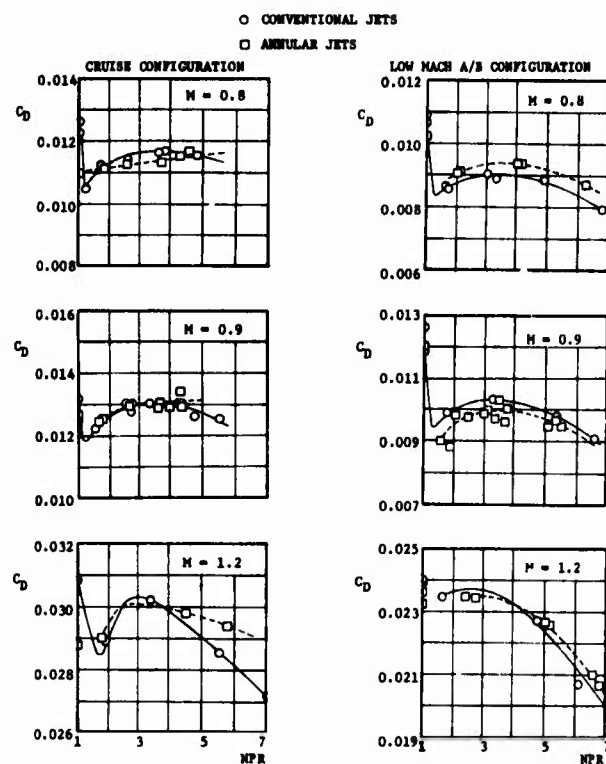
Fig. 3.6   Comparison of afterbody drag with conventional and annular jets for a twin-engine fighter model, with plume correlation and correlation for main sting adaptor effects.
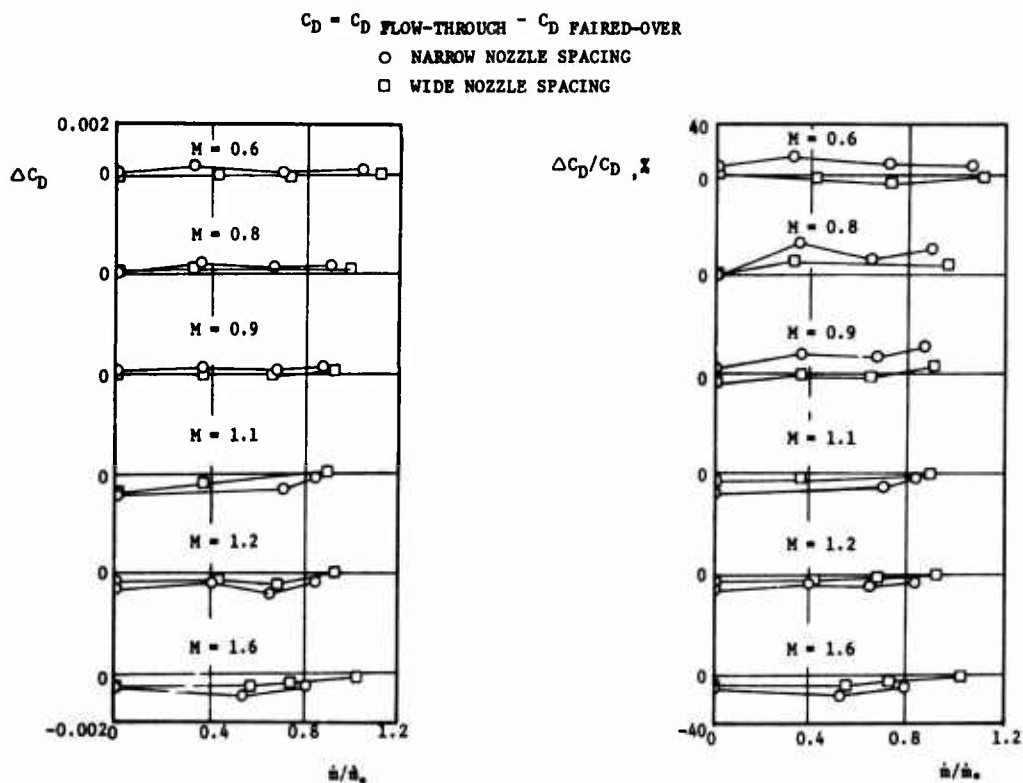
Fig. 4.1   Effects of flow-through inlets on afterbody drag of a twin-engine fighter model, reheat nozzles.
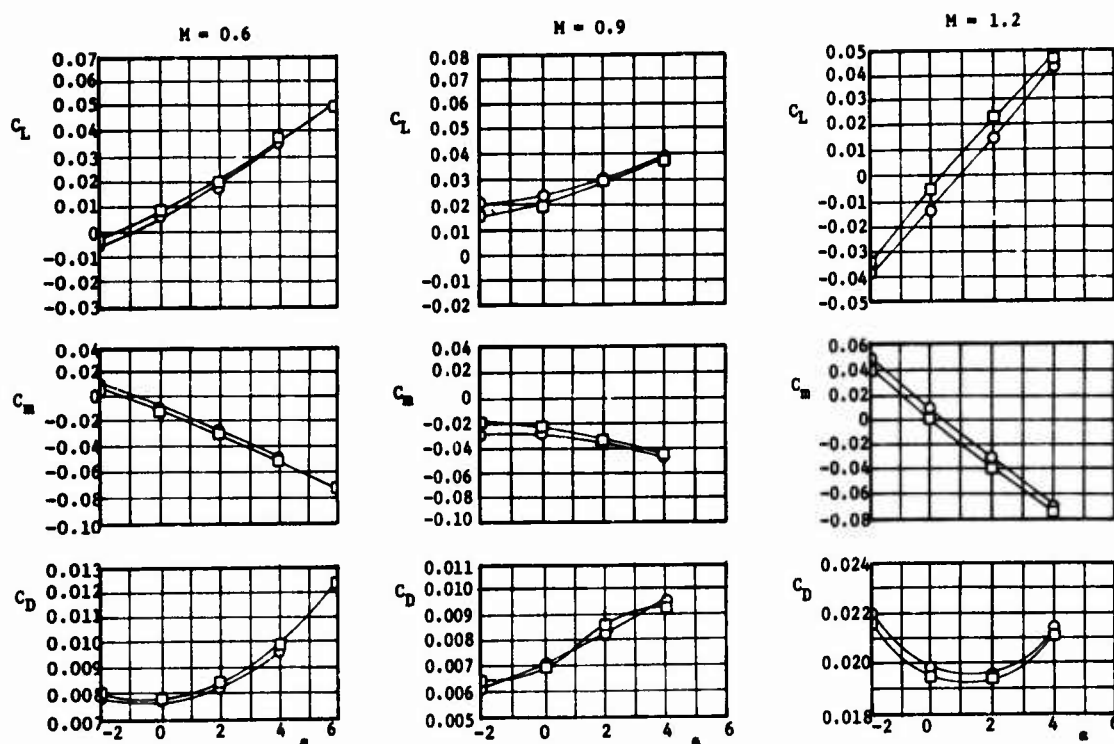
Fig. 4.2   Effects of inlet fairing contour on afterbody aerodynamic characteristics.
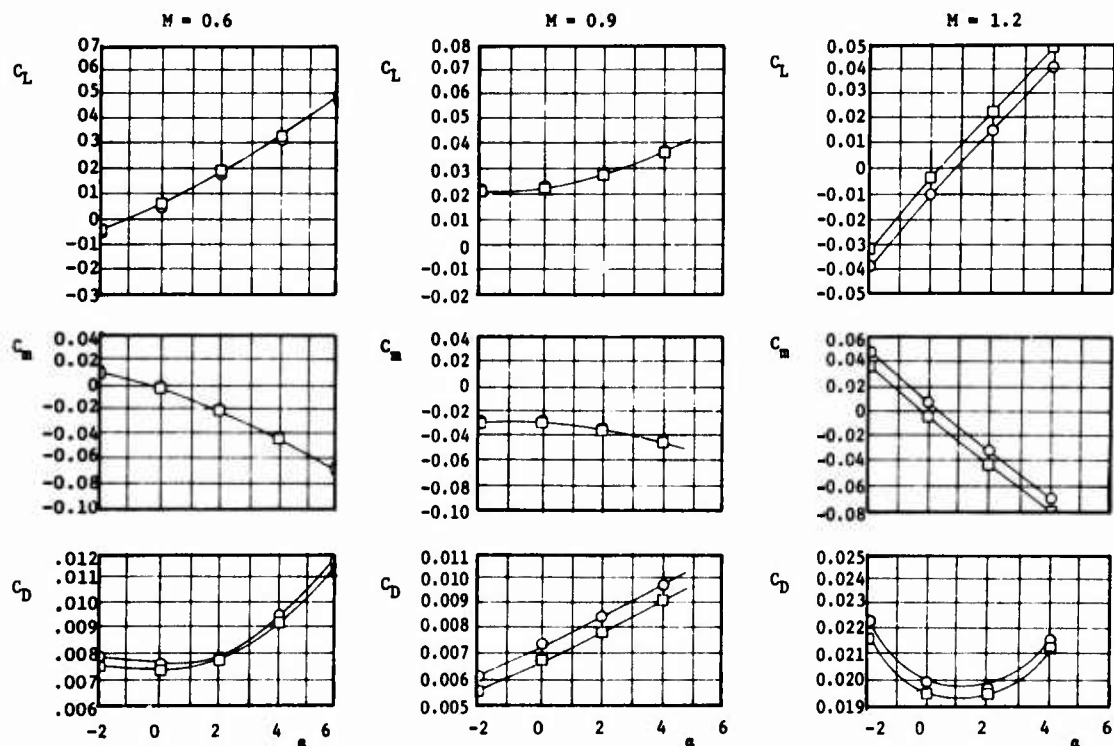
Fig. 4.3   Effects of blunt inlet fairings on afterbody aerodynamic characteristics.

AN EXPERIMENTAL STUDY OF JET EXHAUST SIMULATION

William B. Compton III
Aerospace Technologist
NASA Langley Research Center
Hampton, Virginia 23665, U.S.A.

SUMMARY

Afterbody drag predictions for jet aircraft are usually made experimentally with the jet exhaust flow simulated. The physical gas properties of the fluid used for the model jet exhaust can affect the accuracy of simulation of the airplane's jet exhaust plume. The effect of the accuracy of this simulation on afterbody drag was investigated by making wind-tunnel tests on a single engine model. In addition to unheated air as the exhaust gas, the decomposition products of three different concentrations of hydrogen peroxide were utilized.

The air jet simulation consistently resulted in higher boattail drag than hydrogen peroxide simulation. The differences in drag for the various exhaust gases are attributed to different plume shapes and entrainment properties of the gases. The largest differences in drag due to exhaust gas properties were obtained for the combination of high transonic Mach numbers and high boattail angles. For these conditions, the current data indicate that the use of air to simulate a nonafterburning turbojet exhaust can result in an increase in afterbody drag amounting to 20 percent of the nonafterburning turbojet value.

SYMBOLS

A	Area, meters^2	r_e	Radius of nozzle exit, meters
A_{max}	Maximum cross-sectional area of model, meters^2	T	Temperature, Kelvin
C	Entrainment constant	$V_{j,l}$	Local speed of the jet exhaust, $\frac{meters}{second}$
$C_{D,aft}$	Afterbody pressure-drag coefficient, $\frac{D_{aft}}{q_\infty A_{max}}$	V_∞	Speed of the free stream, $\frac{meters}{second}$
C_p	Pressure coefficient, $\frac{p - p_\infty}{q_\infty}$	w	Axial distance from nozzle exit, aft positive, meters
c_v	Specific heat at constant volume, $\frac{joules}{kilogram\ K}$	x	Axial distance from tangent point of afterbody radius and forward section of model, positive aft (see Fig. 1), meters
		y	Radial distance from model surface, meters
D_{aft}	Afterbody pressure drag, newtons	β	Afterbody boattail angle, angle between axis of symmetry and generatrix of model afterbody (see Fig. 1), degrees
d	Diameter, meters		
d_{max}	Maximum diameter of the model, meters	β_j	$(M_j^2 - 1)^{1/2}$
K	Kelvin		
M	Mach number	β_∞	$(M_\infty^2 - 1)^{1/2}$
MOM	Momentum, $\frac{kilograms\ meters}{second}$	γ	Ratio of specific heats
m_{ent}	Mass of fluid entrained, kilograms	δ_j	Calculated initial inclination angle of the jet exhaust plume, degrees
p	Pressure, $\frac{kilograms}{meter^2}$	$\Delta\nu$	Difference between Prandtl-Meyer turning angles of the jet exhaust just inside the nozzle exit and just downstream of the nozzle exit
q_∞	Free-stream dynamic pressure, $\frac{kilograms}{meter^2}$		
		ρ	Density, $\frac{kilograms}{meter^3}$
R	Gas constant, $\frac{joules}{kilogram\ k}$		
		Subscripts	
RN	Reynolds number		
		aft	Afterbody
r	Radial distance from model center line, meters	b	Base

The investigation was made on single nacelle models in the Langley 16-foot transonic wind tunnel which is a single return, continuous, atmospheric wind tunnel with an octagonal, slotted, test section. Further details of the tunnel are given in Reference 10. Tests were conducted at free-stream Mach numbers from 0.60 to 1.20, at an angle of attack of 0°, and at Reynolds numbers per meter ranging from 10.06×10^6 to 14.05×10^6, depending on the Mach number. The blockage of the model and support system was 0.148 percent of the test section cross-sectional area.

2.2 Model

Two separate models were required to provide an air propellant system and a hydrogen peroxide propellant system. Both models had exactly the same external contours, and were cylindrical nacelles with semi-ogive noses. Various afterbodies were attached to the basic models. The models were supported from the nose by a sting-strut arrangement which positioned the center line of the models on the center line of the tunnel. A sketch of the model and support is shown in Figure 1. The jet total temperatures and pressures were obtained from rake measurements.

The hydrogen peroxide was decomposed by a silver screen catalyst bed in a decomposition chamber producing a gas composed of a mixture of steam and oxygen. The mass ratio of the steam and oxygen, and hence the specific heats, gas constant, and total temperature of the mixture are determined by the concentration of the hydrogen peroxide. Insulation was installed between the inner and outer shells of the hydrogen peroxide model afterbodies to minimize heat transfer and maintain the same external skin temperatures as those of the air model.

Four basic afterbody shapes were tested, the combinations of a 20° boattail, a 10° boattail, and a sonic and Mach 2 jet exit (see Fig. 1). The external contours of all the afterbodies began at model station 144.78 and the base and exit diameters of all the afterbodies did not vary. The rim at the base was kept as small as practical. For the Mach 2 exits, two internal isentropic contours were designed by the method of Reference 11, one for the air nozzles, and one for the hydrogen peroxide nozzles. The internal contours at the exit were essentially parallel to the model axis for all configurations.

CONF.	β	M_e	STA. E
①	20°	1	160.02
②	10°	1	167.64
③	20°	2	160.02
④	10°	2	167.64
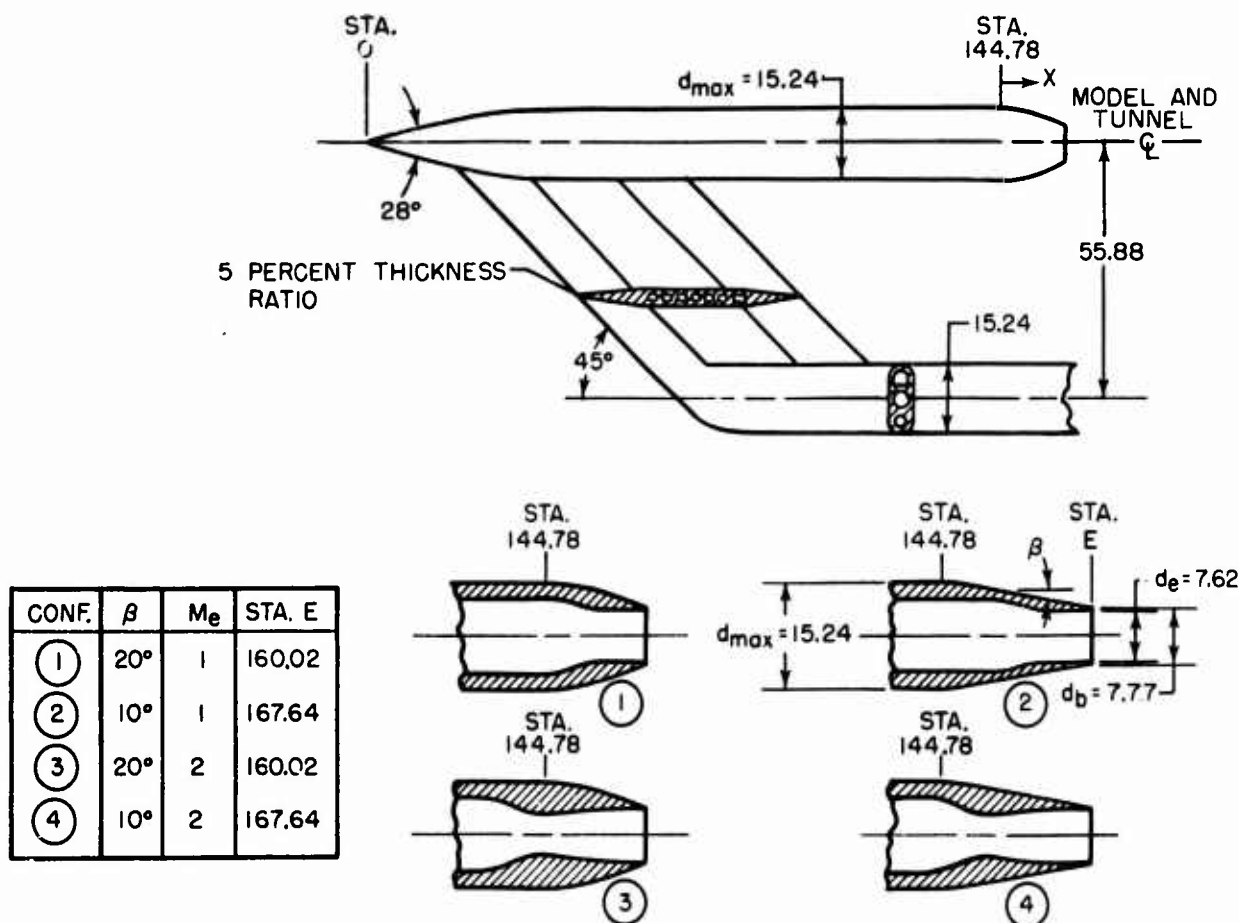
Figure 1. Sketch of model. (All dimensions are in centimeters unless otherwise noted.)

3. ANALYSIS OF EXPERIMENTAL RESULTS

3.1 Factors influencing jet interference

As the jet exhausts from the nozzle exit, it influences the afterbody pressures in two ways: by presenting a body which the external flow must negotiate, plume blockage, and by entraining fluid from the vicinity of the afterbody. These two effects oppose each other, with the plume blockage tending to raise the afterbody pressures, and the entrainment tending to lower them. Both of these effects are strong functions of the gas properties of the jet exhaust. The manner in which the exhaust gas physical properties affect the jet plume shape and entrainment, and hence influence the jet interference on afterbody drag is the subject of this investigation. Figure 2 illustrates plume blockage and entrainment, and includes other flow parameters (free-stream conditions, jet exhaust profiles, and afterbody boundary layers) which can influence the magnitude of the jet interference on the afterbody pressures.

During the investigation, the jet exhaust profiles and afterbody boundary layers were determined for each exhaust gas to insure that these flow conditions were constant. The variation in the free-stream parameters between tunnel runs was small (Fig. 3), and the jet exhaust profiles for each exhaust gas were relatively flat and uniform (Fig. 4). Also, Figure 5 shows that the variation in the model external skin temperatures between the exhaust gases was generally small except very near the nozzle exit. The small skin-temperature variations had no effect on the forward boundary layer, and only a slight, if any, effect on the one at the model trailing edge. Therefore, any differences in jet interference between the four exhaust gases should be due mainly to the effect of the properties of the exhaust gases on plume blockage and entrainment.
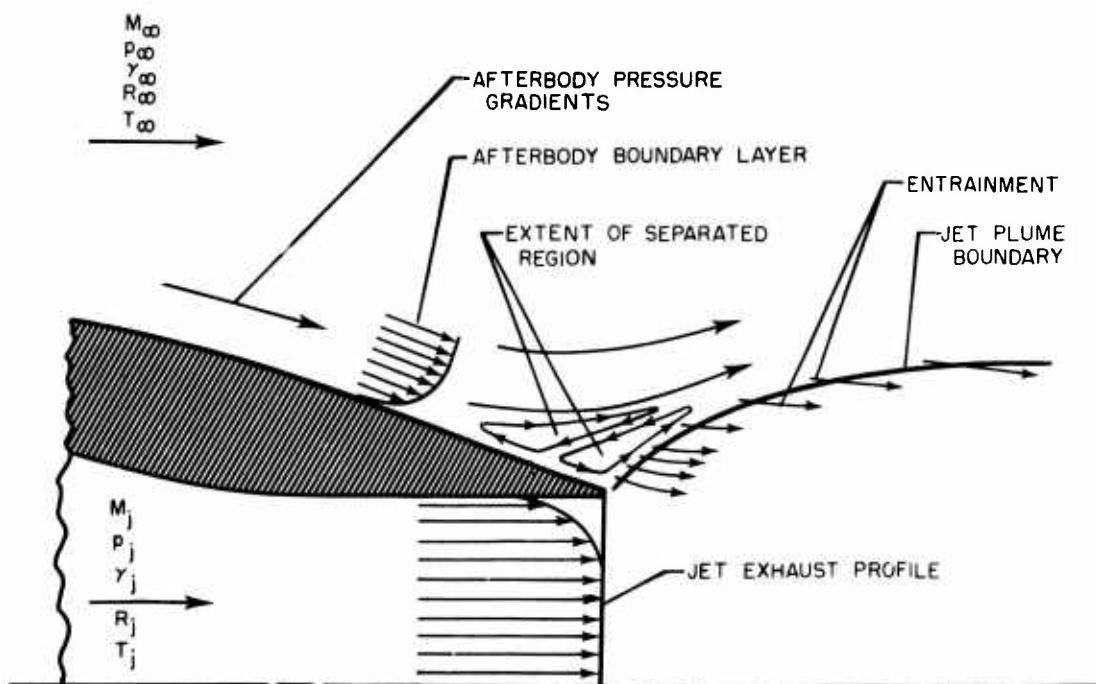
Figure 2. Sketch of factors influencing jet interference.
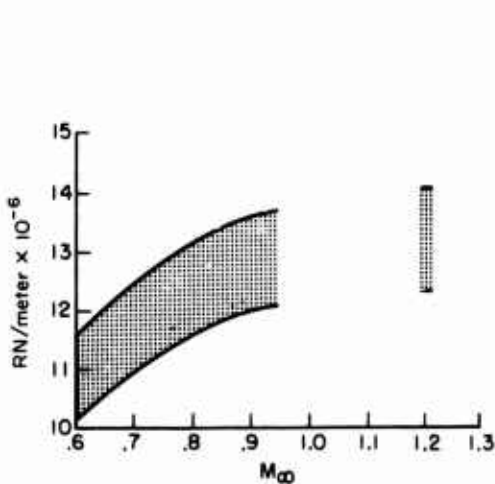
Figure 3. Range of Reynolds numbers per meter encountered during the investigation.
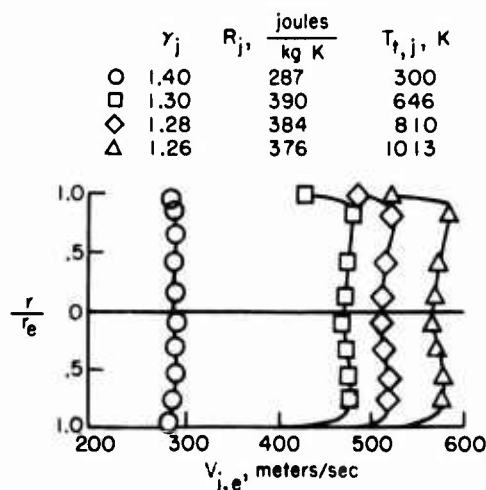
Figure 4. Examples of jet exit velocity profiles for each exhaust gas. $M_e = 1$, $p_{t,j}/p_\infty \approx 4$, $M_\infty = 0$.
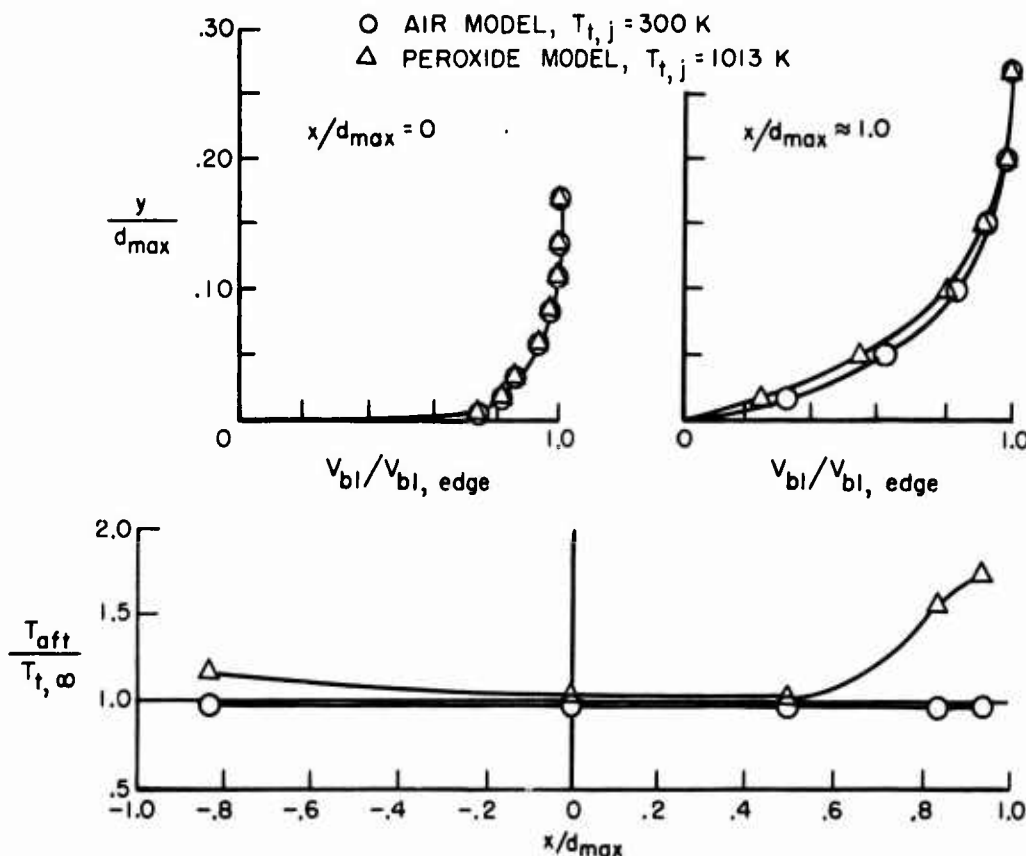
Figure 5. Example of afterbody skin-temperature variations and boundary-layer profiles for the air and hydrogen peroxide models. $M_\infty = 0.80$, $\beta = 20°$, jet off.

3.2 Effect of jet exhaust gas properties on jet interference

Figure 6 illustrates the basic results of the investigation. Substantial differences exist between the afterbody pressure drags for the various exhaust gases. Air, when used as the jet exhaust, consistently results in the least favorable jet interference and therefore the highest drag. The exhaust gases having ratios of specific heats and total temperatures of 1.30 and 646 K, 1.28 and 810 K, and 1.26 and 1013 K generally result in increasingly more favorable jet interference and less drag.

The magnitude of the differences between the afterbody drags for the various exhaust gases depends on the type of external flow conditions encountered. The differences between the afterbody drags for the various exhaust gases are greater for the high subsonic and transonic Mach numbers, $M_\infty = 0.90$ and 0.95, than for the lower Mach numbers. Also, the differences in drag are greater for the afterbody with a boat-tail angle of 20° than for the one with an angle of 10°. The greatest differences between the drags for the various exhaust gases were obtained for the combination of high transonic Mach numbers and a boattail angle of 20°. At these conditions, the strong adverse pressure gradients on the afterbody are probably easily influenced by plume blockage, and the large nonjet-induced separated regions near the exit (Fig. 2) could be easily influenced by entrainment. For the combination of low subsonic Mach numbers and a boattail angle of 10°, the differences between the drags for the various exhaust gases was not very large until high jet pressure ratios were reached. A dry turbojet value, determined by using the $R_j T_{j,\ell}$ ratio in the method described in Section 3.4, is shown on the plot for the high transonic Mach number and high boattail angle. The point illustrates that for operating conditions typical of high nozzle drag (high boattail angles, and transonic speeds and corresponding jet pressure ratios), the use of air to simulate a dry-turbojet exhaust can result in an increase of afterbody drag amounting to as much as 20 percent of the dry turbojet value.

At a Mach number of 1.20, the increments between the drags for the various gases are small when based on the percentage of jet off drag except at the higher jet pressure ratios (Fig. 7). For the configurations with a jet exit Mach number of 2, the jet exit static pressure ratios were not high enough for the jet exhaust to expand very much. The differences between the drags for various exhaust gases for these configurations are similar to the differences for the configurations with Mach 1 exits at the lower jet pressure ratios (Fig. 8). Based on percentage of jet off drag, there are large differences between the jet interference of the various exhaust gases for all configurations and subsonic Mach numbers. Depending on the configuration and free-stream Mach number, the differences between the jet interference of the various exhaust gases generally ranged from 10 to 20 percent of the jet off drag at the low jet pressure ratios, and up to 35 percent of the jet off drag when compared at a jet exit static pressure ratio of 3.

	γ_j	R_j, $\dfrac{\text{joules}}{\text{kg K}}$	$T_{t,j}$, K
O	1.40	287	300
□	1.30	390	646
◇	1.28	384	810
△	1.26	376	1013

$\beta = 20°$, $M_\infty = 0.95$ $\beta = 10°$, $M_\infty = 0.80$
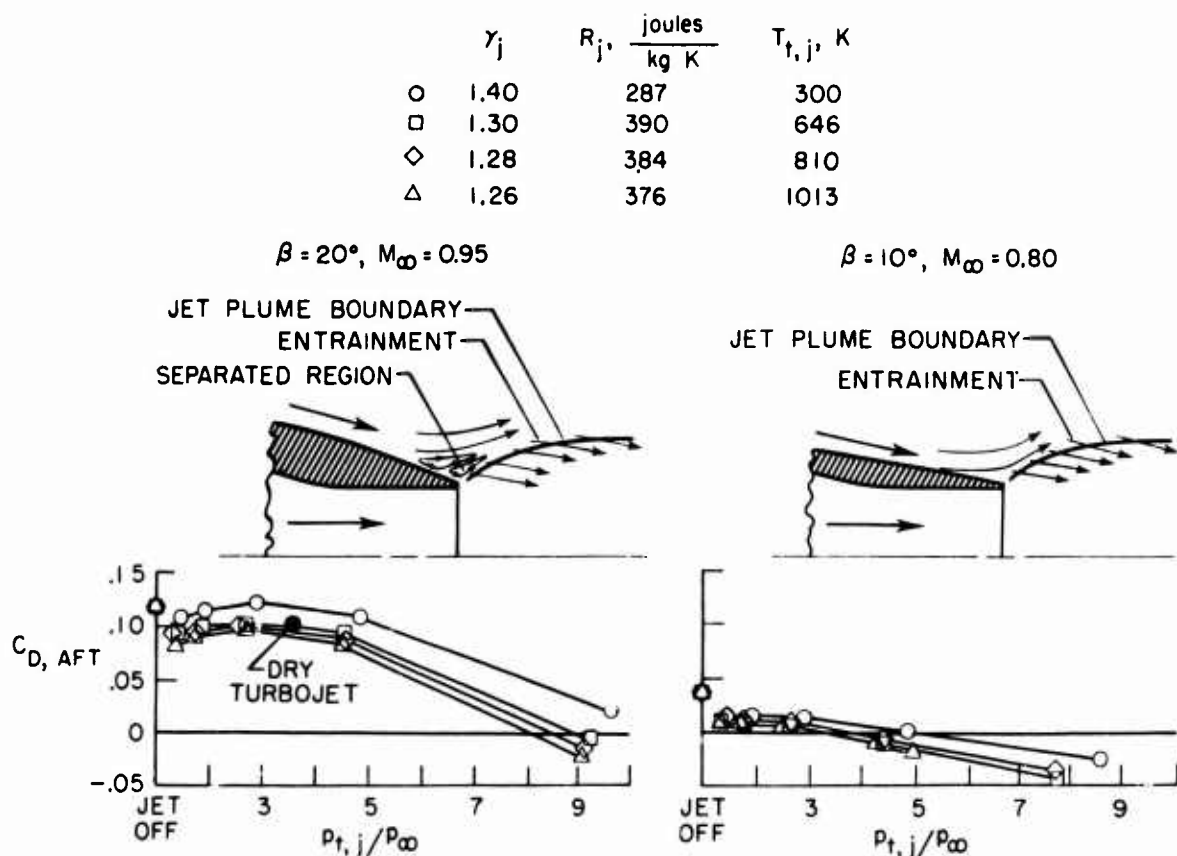
Figure 6. Effect of jet exhaust gas parameters on jet interference.

	γ_j	R_j, $\dfrac{\text{joules}}{\text{kg K}}$	$T_{t,j}$, K
O	1.40	287	300
□	1.30	390	646
◇	1.28	384	810
△	1.26	376	1013

	γ_j	R_j, $\dfrac{\text{joules}}{\text{kg K}}$	$T_{t,j}$, K
O	1.40	287	300
□	1.30	390	646
◇	1.28	384	810
△	1.26	376	1013
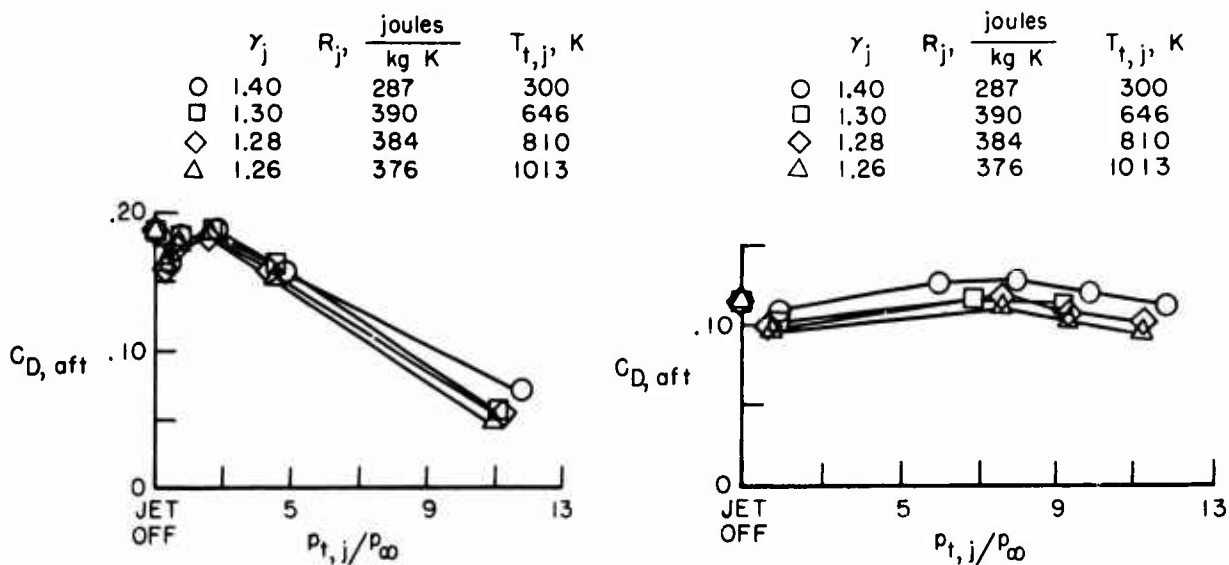
Figure 7. Effect of jet exhaust gas parameters on jet interference. $M_\infty = 1.20$, $\beta = 20°$, $M_e = 1$.

Figure 8. Effect of jet exhaust gas parameters on jet interference. $\beta = 20°$, $M_e = 2$, $M_\infty = 0.95$.

3.3 Correlation of exhaust plume blockage

As explained before, the jet exhaust influences the afterbody pressures by presenting a body which the external flow must negotiate, and by entraining fluid from the vicinity of the afterbody. The plume blockage interference would obviously be a function of the shape of the jet exhaust boundary, and as discussed in Reference 12, the most important factor determining the shape of the jet boundary is its initial inclination angle. That matching this angle does match the initial jet plume shape well in a quiescent atmosphere was verified for several exhaust gases in Reference 13. Therefore, the initial inclination angle of the jet exhaust, δ_j, was calculated and used in an attempt to correlate the effect of jet plume

blockage on afterbody drag (see Sketch (a)). To
calculate δ_j, it was assumed that $p_{aft,te}$ was
the pressure to which the jet exhaust was expand-
ing upon leaving the nozzle. Then, using the
measured values of $p_{aft,te}$, p_e, and the jet total
pressure, δ_j was calculated from the Prandtl-
Meyer relations. The nozzle divergence half
angle was essentially zero for all configurations.
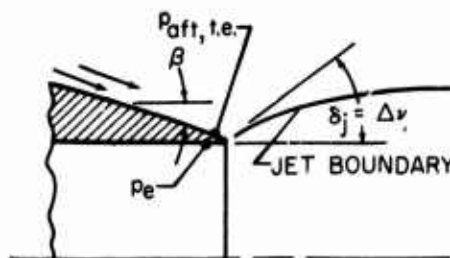
Figure 9 presents an example of the afterbody
pressure drag for each of the exhaust gases as a func-
tion of the jet total pressure ratio, the jet exit
static pressure ratio, and the initial inclination
angle of the jet exhaust plume. As discussed pre-
viously, differences exist between the afterbody
drags for the various exhaust gases. As a function of
jet total pressure ratio, the differences increase
as pressure ratio is increased. When comparing
the drags as a function of the jet exit static

Sketch (a)

pressure ratio, the differences increase at a lower rate. A comparison of the interferences as a function
of the initial inclination angle of the jet exhaust, δ_j, also shows differences between the afterbody
drags for the four exhaust gases. However, at the high pressure ratios and hence high plume angles, the
discrepancy is reduced even more than for the comparison using exit static pressure ratio. Since the
initial plume angle probably gives a good representation of the initial shape of the jet plume in a
moving stream as it does in a quiescent atmosphere (Ref. 13), the discrepancies between the jet inter-
ference of the four jet exhaust gases at a constant value of δ_j should be mainly due to entrainment.
For each free-stream Mach number and configuration these differences seem to be relatively consistant
with δ_j.

The maximum values of exit pressure ratio or initial plume angle for the configurations with Mach 2
jet exits were not large enough to determine if the trends just mentioned were valid for these configura-
tions. However, for these configurations, δ_j seems to be at least as good a parameter as jet pressure
ratio with which to compare the jet interference of the various exhaust gases. Therefore, for under-
expanded jets, the data seem to indicate that the initial inclination angle of the jet exhaust plume is
a more relevant parameter for comparing the jet interference due to plume blockage than either $p_{t,j}/p_\infty$
or p_e/p_∞. The use of δ_j instead of p_e/p_∞ or $p_{t,j}/p_\infty$ would be more helpful when high jet exhaust
plume angles are expected.

In Reference 9, the first term of a series expansion of the ratio of p_l/p_e gives:

$$p_l/p_e = 1 - \frac{\gamma_j M_e^2}{\beta_j} (\Delta \nu) + \ldots \tag{1}$$

where the subscript l denotes the conditions to which the jet is expanding, $\beta_j = (M_e^2 - 1)^{1/2}$, and $\Delta \nu$
is the difference in the Prandtl-Meyer turning angles for the jet exhaust in expanding from M_e to M_l.
For small values of $\Delta \nu$, the following jet boundary simulation parameters, which would provide the same
flow turning angle for the model and full-scale conditions, were suggested.

	γ_j	R_j, $\frac{joules}{kg\ K}$	$T_{t,j}$, K
O	1.40	287	300
□	1.30	390	646
◇	1.28	384	810
△	1.26	376	1013
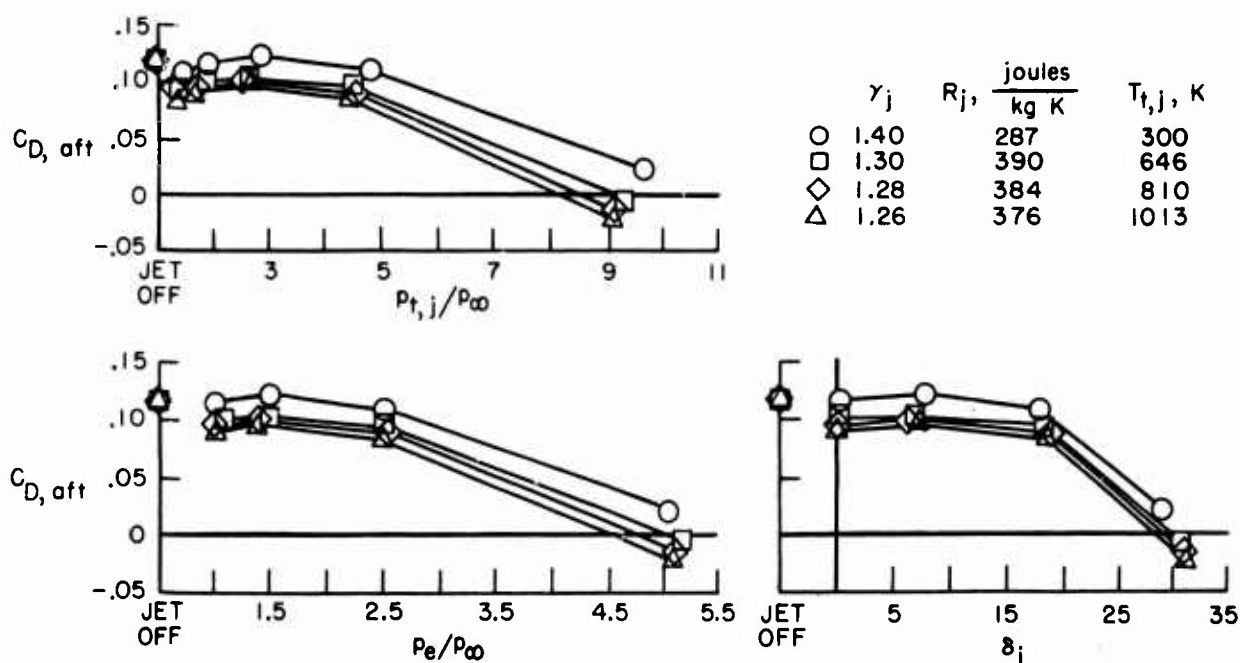
Figure 9. Afterbody drag coefficient as a function of $p_{t,j}/p_\infty$, p_e/p_∞, and δ_j. $\beta = 20°$, sonic
exit, $M_\infty = 0.95$.

$$
\begin{array}{ll}
\text{Jet boundary in a} \\
\text{quiescent medium}
\end{array}
\qquad
\left(1 - \frac{p_\infty}{p_e}\right)\left(\frac{\beta_j}{\gamma_j M_e^2}\right)
$$

$$
\begin{array}{ll}
\text{Jet boundary in} \\
\text{a moving stream}
\end{array}
\qquad
\frac{(p_e - p_l)\, p_\infty\, \beta_j\, \gamma_\infty M_\infty^2}{(p_l - p_\infty)\, p_e\, \beta_\infty\, \gamma_j\, M_e^2}
$$

These parameters were compared to δ_j for the nozzle with a boattail angle of 20° and an exit Mach number of 2. All three parameters seemed to give about equal results in comparing the drag for the various exhaust gases. However, due to the low plume angles obtained for the nozzles with supersonic exits, the results were inconclusive. Since these parameters are approximations for the initial plume angle, and since they can become very large or small for values of M_∞ and M_e near 1, δ_j would be the best of the three with which to compare the jet interference of various gases due to plume blockage.

Reference 13 indicates from quiescent atmosphere studies that excellent plume boundary simulation over a wider range of conditions and to much larger axial distances can be made by duplicating both δ_j and $\frac{M_{j,l}}{\gamma_j}$ instead of just δ_j. It also indicates that a small additional improvement can be made by duplicating the nozzle divergence half angle. This may be important for very large pressure ratios or when surfaces downstream of the nozzle exit present such problems as pressurization or heating of adjacent surfaces. However, Reference 12 indicates that the differences between boundaries for jets having the same jet exit Mach number and nozzle divergence angle are negligibly small when δ_j is duplicated and the difference in ratio of specific heats is not much greater than 0.1. Therefore for most jet airplane configurations and jet pressure ratios, the duplication of M_e, the nozzle divergence angle, and δ_j should give adequate correlation of jet interference on afterbody drag due to plume blockage for various exhaust gases.

3.4 Correlation of entrainment

At supersonic Mach numbers, and low subsonic Mach numbers, exhaust plume blockage usually accounts for nearly all of the jet interference on nozzle boattails. However, at transonic Mach numbers, or when there are bases or large separated regions in the vicinity of the nozzle exit, entrainment of fluid from the region can significantly contribute to jet interference. In these situations, in addition to the proper simulation of the shape of the airplane's exhaust plume, corrections to wind-tunnel values for differences between the entrainment of the real airplane exhaust and the simulation gases used in the wind tunnel become important.

The amount of fluid entrained from the vicinity of the afterbody by the jet exhaust depends on, among other things, the momentums of the jet exhaust and local afterbody flow, and the velocities, energies, and mixing characteristics of the two flows. The momentum of the entraining fluid is generally considered a major factor determining the quantity of fluid entrained. In Reference 14 the following equation is given for the mass of fluid entrained by a jet in a quiescent atmosphere.

$$
\frac{dm_{ent}}{d_w} = C(MOM_{j,l})^{1/2}\, \rho_\infty^{1/2} \tag{2}
$$

In this equation, m_{ent} is the mass of the surrounding fluid entrained, $MOM_{j,l}$ is the momentum flux of the jet exhaust, ρ_∞ is the density of the surrounding fluid, w is the axial distance downstream of the nozzle exit, and C is a constant. Thus the equation predicts that the entrainment varies as the square root of the exhaust momentum.

In addition to the momentum ratio, the following simulation parameters suggested in Reference 9 were considered the ones most likely to correlate the jet interference due to entrainment.

$$
\text{Mass flow} \qquad
\frac{p_j \gamma_j^{1/2} M_j R_\infty^{1/2} T_\infty^{1/2} A_e}{p_\infty \gamma_\infty^{1/2} M_\infty R_j^{1/2} T_j^{1/2} A_\infty}
= \frac{\rho_j A_e V_j}{\rho_\infty A_\infty V_\infty}
$$

$$
\begin{array}{l}
\text{Kinetic energy} \\
\text{per unit mass}
\end{array}
\qquad
\frac{\gamma_j M_j^2 R_j T_j}{\gamma_\infty M_\infty^2 R_\infty T_\infty}
= \frac{V_j^2}{V_\infty^2}
$$

$$
\begin{array}{l}
\text{Internal energy} \\
\text{per unit mass}
\end{array}
\qquad
\frac{(\gamma_\infty - 1)R_j T_j}{(\gamma_j - 1)R_\infty T_\infty}
= \frac{c_{v,j} T_j}{c_{v,\infty} T_\infty}
$$

The maximum cross-sectional area of the model, A_{max}, was substituted for A_∞ in these equations. The ratio:

$$
\frac{R_j T_{j,l}}{R_\infty T_\infty}
$$

was also used to correlate entrainment. Since the jet exhaust interacts with the external flow downstream of the nozzle exit, the correlating parameters were computed for the conditions just behind the nozzle. For these calculations, the local jet static pressure was assumed to be equal to the afterbody trailing-edge pressure. Entrainment in the sense used in this paper refers to the effects of the mixing and aspiration of fluid by the jet exhaust in the region near the nozzle exit, as contrasted to the far downstream mixing region of the exhaust.

These parameters are compared in Figure 10. Afterbody drag coefficient for the 20° boattail is cross-plotted versus the parameters for a constant initial plume angle of 0° and 5°. Therefore, any differences in drag should be mainly due to differences in entrainment. For reference, since entrainment tends to lower the afterbody pressures, the greater the entrainment, the higher the drag. Figure 10 shows that entrainment is not a unique function of any of the parameters presented. For example, the data for the afterbody with the Mach 2 exit do not fall on the same curve as the data for the afterbody with the Mach 1 exit when compared as a function of jet momentum. If entrainment were just a function of jet exhaust momentum, the data for each nozzle would lie on a continuous curve.

For air, the jet exhaust Reynolds numbers based on the exit diameter of the nozzles ranged from 3.71×10^5 to 20.9×10^5 for the sonic nozzle, and from 5.60×10^5 to 25.7×10^5 for the Mach 2 nozzle. Reference 14 reports that for values greater than 3×10^4, the entrainment coefficient, C in Equation (2), is independent of nozzle Reynolds number. Then jet exhaust Reynolds number should not account for the fact that the entrainment of the two exits do not correlate. Therefore, Figure 10 indicates that entrainment is dependent on the jet exhaust Mach number, an observation also suggested in Reference 15.

Although none of the parameters definitely correlated entrainment of the two nozzle exits, for each exit and for each plume angle, the effects of entrainment of the various gases is close to a straight-line function of the parameters, $R_j T_{j,l}/R_\infty T_\infty$, internal energy per unit mass, and the local kinetic energy per unit mass, that is, $V_{j,l}^2/V_\infty^2$. Reference 16 also indicates the dependence of jet interference on the ratio $R_j T_{j,l}/R_\infty T_\infty$. The relatively straight lines of these parameters suggest that they may be used to adjust for entrainment of various gases. Using either parameter, two points on the curve would have to be experimentally established at the proper plume angle for a particular configuration. Then a straight-line interpolation to the value of the parameter for the real jet exhaust gas may give an estimate to the real airplane drag. It should be emphasized though, that since entrainment is dependent on the configuration and external flow conditions, that this is not a prediction method but only an interpolation method for adjusting the wind-tunnel values at the external flow conditions and for the model geometry tested.

4. APPLICATION OF JET SIMULATION PARAMETERS

The preceding discussion has established the importance of simulating the jet plume blockage and entrainment effects. It has been demonstrated that the jet plume blockage effects can be duplicated for various exhaust gases by matching the initial inclination angle of the jet exhaust plume. Corrections to wind-tunnel values for entrainment, however, must be evaluated from results for at least two exhaust simulation gases. Figure 11 shows an example of the procedure for adjusting the experimental value of jet

$M_e = 1$	$M_e = 2$	γ_j	R_j, $\dfrac{\text{joules}}{\text{kg K}}$	$T_{t,j}$, K
●	○	1.40	287	300
■	□	1.30	390	646
◆	◇	1.28	384	810
▲	△	1.26	376	1013

(a) $\delta_j = 0°$.
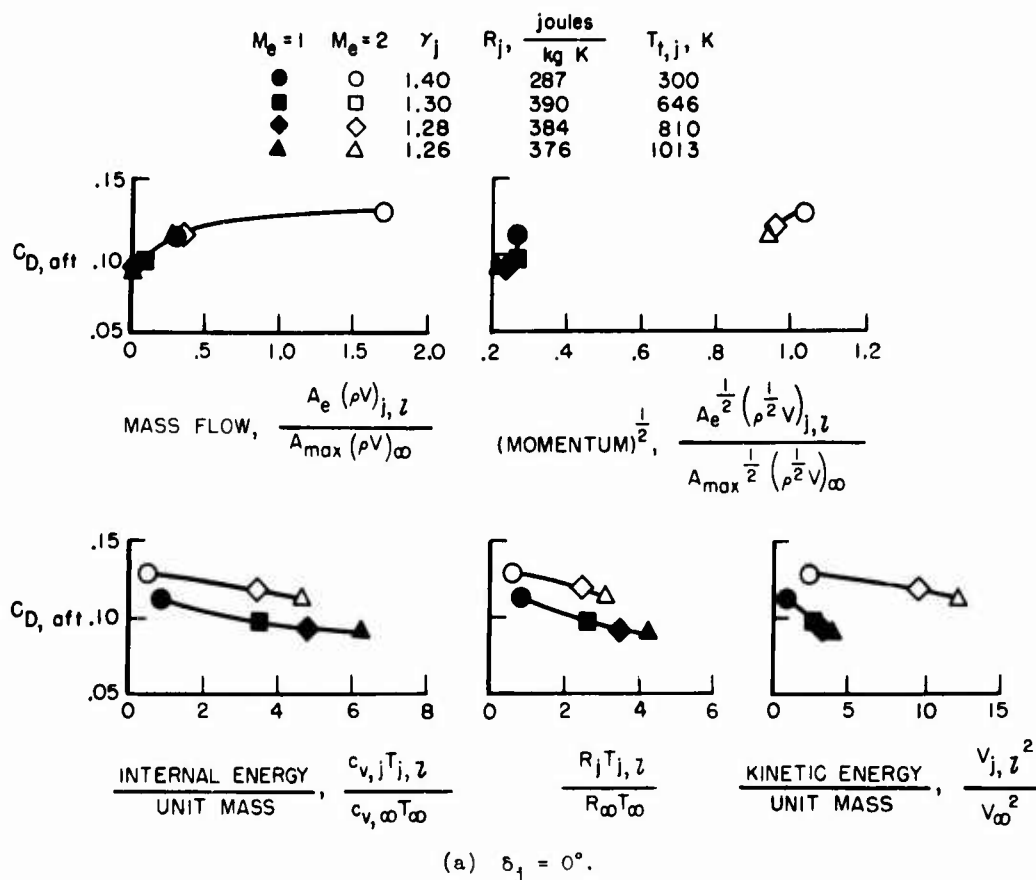
Figure 10. Comparison of entrainment correlation parameters. $\beta = 20°$, $M_\infty = 0.95$.

(b) $\delta_j = 5°$.
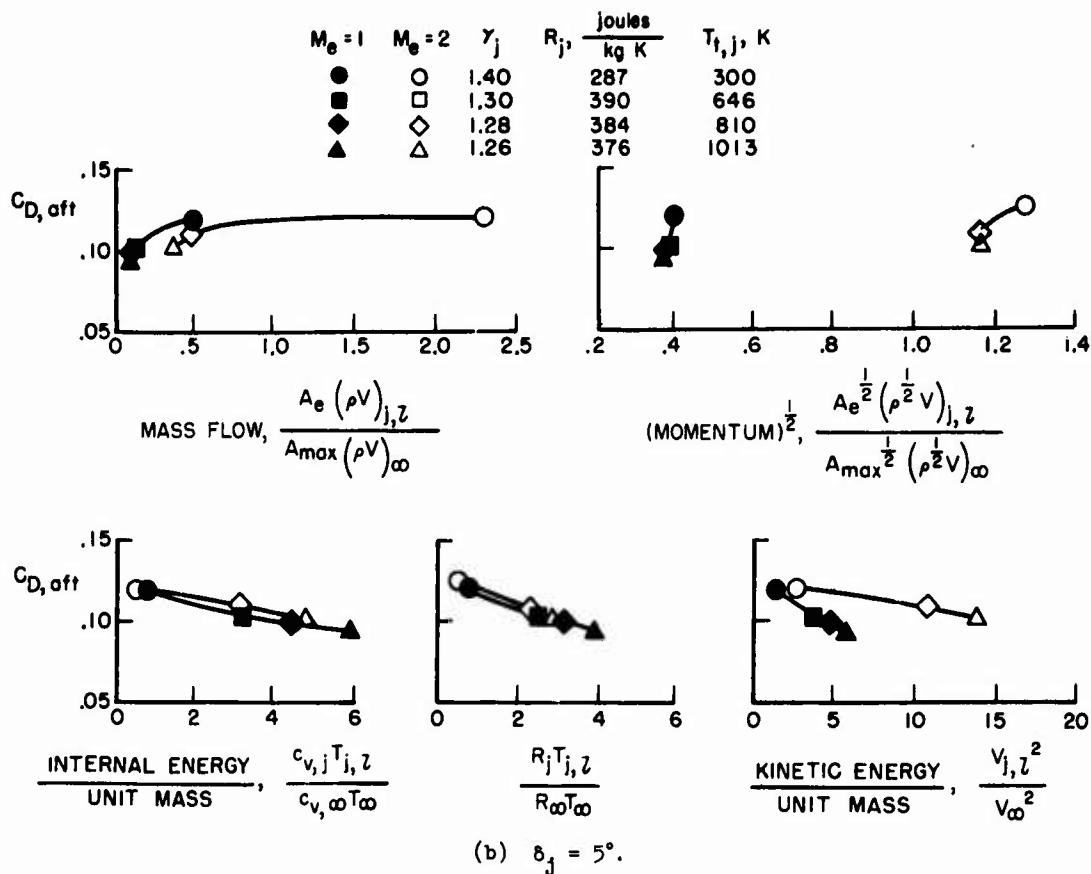
Figure 10. Concluded.

interference to full-scale conditions. First, experimentally determine the variation of afterbody drag with jet pressure ratio for at least two jet exhaust gases. Then, correct for plume shape differences by relating the drag to the initial plume angle of the jet exhaust, and obtain a value of drag at the operating plume angle of the aircraft. Final adjustments to the jet interference for any discrepancies in entrainment could then be made by interpolating with the kinetic energy parameter or the RT ratio as illustrated in Figure 11.

Figure 11. Jet interference comparison parameters.
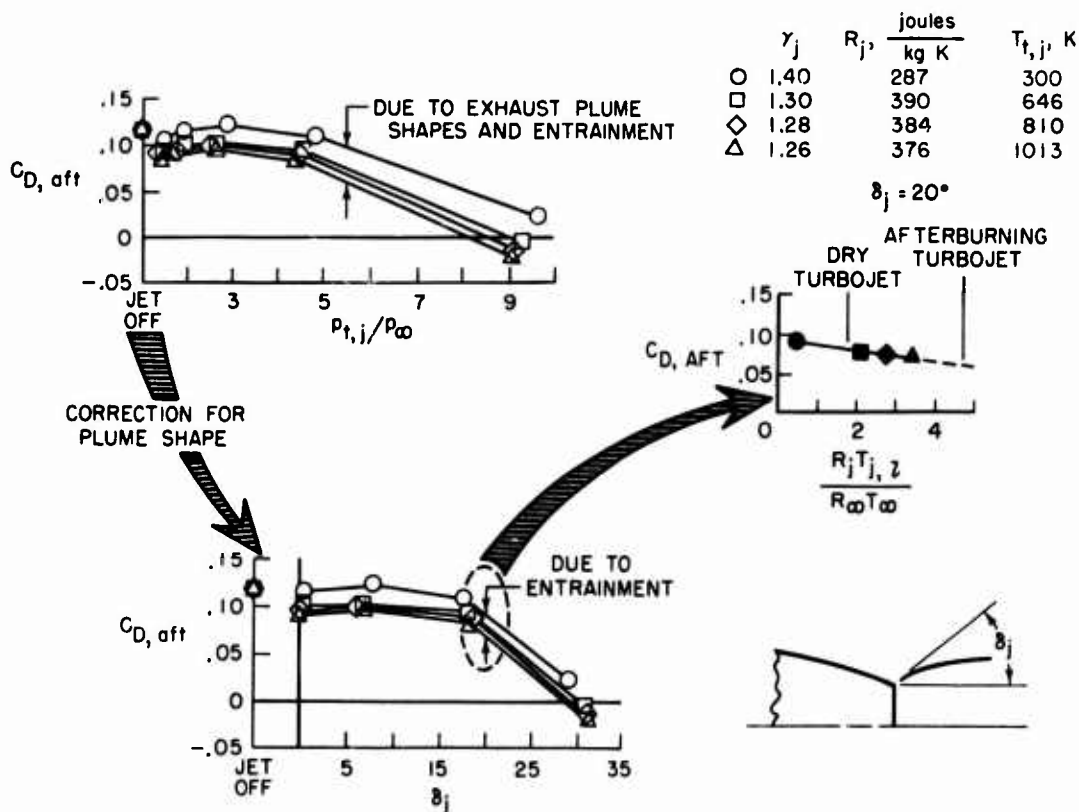
5. CONCLUDING REMARKS

Based on the jet exhaust gases tested and other variables of the investigation, the following effects of the jet exhaust physical gas properties on the influence of the jet exhaust on afterbody drag are indicated.

Substantial differences were obtained between the afterbody drags for the various jet exhaust gases. Air, when used as the jet exhaust, consistently gave the least favorable jet interference and therefore the highest drag. The exhaust gases having ratios of specific heats, gas constants, and total temperatures of: 1.30, 390 joules/kg K, and 646 K; 1.28, 384 joules/kg K, and 810 K; and 1.26, 376 joules/kg K, and 1013 K, generally resulted in increasingly more favorable jet interference and less drag.

The differences between the afterbody drags for the various exhaust gases were greatest for the combination of high boattail angles, 20°, and high subsonic and transonic Mach numbers. For the combination of the lower boattail angles, 10°, and lower Mach numbers, the differences were much less. At a free-stream Mach number of 1.20, the differences in drag were small until large values of jet pressure ratio were obtained. Based on percentage of jet off drag, there were large increments between the afterbody drags for the various jet exhaust gases at all subsonic Mach numbers. Depending on the configuration and free-stream Mach number, the differences generally ranged from 10 to 20 percent of the jet off drag at the low jet pressure ratios, and up to 35 percent of the jet off drag at the jet exit static pressure ratio of 3. For operating conditions typical of high nozzle drag (high boattail angles, and transonic speeds and corresponding pressure ratios) the current data indicate that the use of air to simulate a dry-turbojet exhaust can result in an increase of afterbody drag amounting to as much as 20 percent of the dry-turbojet value.

The differences in jet interference between the various exhaust gases are attributed to different plume shapes and entrainment properties of the gases. Corrections for the plume shape differences can be made by relating the drag to the computed initial inclination angle of the jet plume. Although the entrainment differences are difficult to predict, they seem to be a relatively straight-line function of the product of the jet exhaust gas constant and local temperature, and also of the local jet exhaust kinetic energy per unit mass.

6. REFERENCES

1. Runckel, Jack F.: Interference Between Exhaust System and Afterbody of Twin-Engine Fuselage Configurations. NASA TN D-7525, 1974.

2. Lee, Edwin E., Jr.; and Runckel, Jack F.: Performance of Closely Spaced Twin-Jet Afterbodies With Different Inboard-Outboard Fairings and Nozzle Shapes. NASA TM X-2329, 1971.

3. Cortright, Edgar M., Jr.; and Kochendorfer, Fred D.: Jet Effects on Flow Over Afterbodies in Supersonic Stream. NACA RM E53H25, 1953.

4. Hearth, Donald P.; and Wilcox, Fred A.: Thrust and Drag Characteristics of a Convergent Nozzle With Various Exhaust Jet Temperatures. NACA RM E53L23b, 1954.

5. Henry, Beverly Z., Jr.; and Cahn, Maurice S.: Preliminary Results of an Investigation at Transonic Speeds to Determine the Effects of a Heated Propulsive Jet on the Drag Characteristics of a Related Series of Afterbodies. NACA RM L55A24a, 1955.

6. Baughman, L. Eugene; and Kochendorfer, Fred D.: Jet Effects on Base Pressures of Conical Afterbodies at Mach 1.91 and 3.12. NACA RM E57E06, 1957.

7. Beke, Andrew; and Simon, Paul C.: Thrust and Drag Characteristics of Simulated Variable-Shroud Nozzles With Hot and Cold Primary Flows at Subsonic and Supersonic Speeds. NACA RM E54J26, 1955.

8. Lee, George: An Investigation of Transonic Flow Fields Surrounding Hot and Cold Sonic Jets. NASA TN D-853, 1961.

9. Pindzola, M.: Jet Simulation in Ground Test Facilities. AGARDograph 79, 1963.

10. Corson, Blake W., Jr.; Runckel, Jack F.; and Igoe, William B.: Calibration of the Langley 16-Foot Transonic Tunnel With Test Section Air Removal. NASA TR R-423, 1974.

11. Johnson, Charles B.; Boney, Lillian R.; Ellison, James C.; and Erickson, Wayne D.: Real-Gas Effects on Hypersonic Nozzle Contours With a Method of Calculation. NASA TN D-1622, 1963.

12. Love, Eugene S.; Grigsby, Carl E.; Lee, Louise P.; and Woodling, Mildred J.: Experimental and Theoretical Studies of Axisymmetric Free Jets. NASA TR R-6, 1959.

13. Herron, R. D.: An Investigation of Jet Boundary Simulation Parameters for Underexpanded Jets in a Quiescent Atmosphere. AIAA Third Aerodynamic Testing Conference, AIAA Paper 68-397, 1968.

14. Hill, B. J.: Measurement of Local Entrainment Rate in the Initial Region of Axisymmetric Turbulent Air Jets. Journal of Fluid Mechanics, 1972, Vol. 51, Part 4, pp. 773-779.

15. Berrier, Bobby Lee; and Wood, Frederick H., Jr.: Effect of Jet Velocity and Axial Location of Nozzle Exit on the Performance of a Twin-Jet Afterbody Model at Mach Numbers up to 2.2. NASA TN D-5393, 1969.

16. Jaarsma, F.: Engine Airplane Interference in Transonic Tests. AGARD Advisory Report No. 36, Part II. pp. II-65.

A MODEL TECHNIQUE FOR EXHAUST SYSTEM PERFORMANCE TESTING

by

T.D. Coombes,
Installation Aerodynamics Section Leader,
Rolls-Royce (1971) Limited,
Derby Engine Division,
Derby DE2 8BJ.

SUMMARY

The design of fan cowls and gas generator afterbodies for high bypass ratio engines involves considering the losses occurring from shock waves and boundary layer development in the presence of external flow.

Various aerodynamic techniques are available for synthesising the afterbody shapes, but they do not yet successfully predict the complex boundary layer interactions on asymmetric cowls, effects of curvature of the sonic line at the fan nozzle and installed effects such as those due to the presence of the wing.

The chosen approach was, therefore, to test particular configurations at model scale with the object of initially solving immediate design problems and in the long term developing detailed semi-empirical design rules.

This paper describes an accurate model technique that has been developed by Rolls-Royce (1971) Limited to measure the sum of gross thrust and afterbody drag for nozzle systems with single or two co-axial streams.

The rig uses air at ambient temperature and is designed to operate in the 9ft x 8ft transonic wind tunnel of the Aircraft Research Association Limited at Bedford.

Model test results are also presented in the paper to demonstrate the accuracy and repeatability of the rig and show the considerable progress that has been made at Rolls-Royce in advancing the state of the art on exhaust systems for low specific thrust engines.

NOTATION

M_0	Free stream Mach number
P_F	Fan nozzle total pressure
P_J	Primary nozzle total pressure
p_0	Ambient static pressure
P_F/p_0	Fan nozzle expansion ratio
P_J/p_0	Primary nozzle expansion ratio
m	Mass flow
T	Total temperature
$(m\sqrt{T})_F$	Fan duct mass flow function
$(m\sqrt{T})_{F-ideal}$	Ideal one dimensional mass flow based on P_F/p_0
$(m\sqrt{T})_J$	Primary duct mass flow function
$(m\sqrt{T})_{J-ideal}$	Ideal one dimensional mass flow based on P_J/p_0
X	Thrust
D	Drag
$(X-D)_{measured}$	Corrected force balance measurement
$X_{F-ideal}$	Fan nozzle isentropic thrust
$X_{J-ideal}$	Primary nozzle isentropic thrust
C_T	Exhaust system gross thrust coefficient $= \dfrac{(X-D)\ measured}{X_{F-ideal} + X_{J-ideal}}$
$\triangle C_T$	Thrust coefficient relative to baseline level.

1. INTRODUCTION

The pursuit of better economics for subsonic transport aircraft has led in recent years to the development of high bypass ratio engines of the RB211 type. The specific thrust of these engines is appreciably lower than for a conventional turbojet engine and the ratio of gross thrust to net thrust is higher. Typically for an engine of unity bypass ratio, the ratio of gross to net thrust is about 1.5 under cruise conditions, while for an engine of bypass ratio 5 it is between 2.5 and 3.0.

Since losses in the exhaust system effectively act on the gross thrust level, any inefficiency is magnified by the above ratio. The design of high performance exhaust configurations therefore assumes especial significance.

Various aerodynamic techniques are available for synthesising afterbody shapes but they cannot yet successfully predict the complex boundary layer interactions, effects of sonic line curvature at the fan nozzle and installed effects such as those due to the presence of the wing.

The approach chosen by Rolls-Royce was, therefore, to develop an accurate model technique to measure exhaust system performance with or without external flow. The thrust minus drag rig is designed to operate in the transonic wind tunnel at the Aircraft Research Association Limited, Bedford.

2. MODEL TECHNIQUE

From the start of design it was accepted that the rig should be capable of accepting a wide variety of afterbody arrangements. The original design was, therefore, based on an exhaust system for a high bypass ratio engine with an intermediate length fan cowl. Design schemes for single stream model builds were also prepared.

Model tests to date have been confined to two stream exhaust systems and the general arrangement of the rig for these tests is shown on Figure 1. A photograph of a typical model build installed in the working section of the tunnel is shown on Figure 2.

2.1 Metric (Live) Assembly

Figure 3 illustrates the basic components of the metric assembly.

Test models at a scale of approximately 1/16th of RB211 are mounted on the metric portion of the rig which is supported by three linear bearings. These bearings constrain all but axial loads. Transference of loads from the metric to the non-metric parts is achieved by means of a strain gauged balance.

2.2 Non-Metric (Earthed) Assembly

These components are also illustrated on Figure 3.

The aerofoil support strut forms the main part of this assembly. It is mounted in a vertical plane from the tunnel floor with a sweep angle of 30°.

Airflow supplies at ambient temperature are carried by the strut to provide two independantly controlled co-axial streams through the rig.

Primary mass flow is measured using a calibrated venturi within the rig and the fan duct airflow is determined using a bellmouth situated in a plenum chamber beneath the tunnel floor.

2.3 Complete Assembly

The interface between metric and non-metric sections requires three 0.010ins split lines, two in the fan stream and one in the primary stream. Diaphragm seals are used to prevent flow between the two streams and from the fan stream to the tunnel.

Preliminary tests to examine support strut and forebody interference effects showed that the most suitable location of the fan cowl was 7.4 forebody diameters from the leading edge of the nose fairing.

3. DUCT AIRFLOW DISTORTION

Uniform flow conditions are achieved at the primary duct split line by initially turning the airflow from the strut into the duct by means of a cascade. The distortion of the airflow is then further reduced by the use of two perforated blockage plates located in the duct upstream of the converging section of the primary venturi. Downstream of the venturi, the airflow diffuses rapidly and a package of three gauzes of 64%, 70% and 75% open area is, therefore, used to ensure uniform flow conditions at entry into the test model.

The fan stream emerges from the strut into a short annular duct containing a vertical splitter plate. Proving tests were carried out to devise an effective means of straightening the flow downstream of the splitter. The configuration finally chosen consisted of the following:-

a) A perforated blockage plate designed integrally with the splitter plate.

b) A package of two gauzes of 64% and 75% open area at one inch spacing.

4. **CALIBRATIONS**

A number of calibrations are required to accurately define all the parameters occurring in the calculation of exhaust system thrust and flow coefficients. They are interdependant and carried out in the following order:-

4.1 **Balance Calibration**

The balance is loaded by weights suspended from a harness which passes over pulleys at the front and rear of the rig. Loads are applied in the drag direction only and balance hysteresis loops are defined to cover the full test range and ensure that the balance specification of 0.1% of the full scale load of 600lbs is achieved.

4.2 **Seal Calibrations**

The primary seal constraint is obtained by venting the fan duct to ambient pressure and applying a series of pressure differentials and loads to the seal to cover the full ranges encountered during model tests.

In the case of the fan seal, the above procedure is repeated but with the pressures in the fan and primary ducts equalised.

4.3 **Mass Flow and Inlet Momentum Calibrations**

The primary venturi and fan system bellmouth-plenum chamber combination are calibrated in situ against National Gas Turbine Establishment (NGTE) 'standard nozzles' of known discharge coefficient and thrust efficiency (Reference 1). During the same calibration runs, the metric/non-metric split line stream thrusts are also calculated.

The two airstreams are calibrated separately and a range of nozzles is used with each airstream, the outlet areas being chosen to give adequate coverage over the complete range of mass flow likely to be encountered during model testing. The nozzles are mounted in turn on suitable ducting extending downstream from the model interface plane. In the case of the fan stream calibration, a faired bullet is used to blank off the primary system. An adequate length of ducting is then included to ensure that airflow distortion upstream of the 'standard nozzles' is minimal.

5. **REDUCTION OF RESULTS**

Figure 4 shows the component forces acting on the metric parts of the rig and a typical test model with a pylon represented. The metric split line is located near the nacelle maximum diameter and thrust minus drag aft of this station is measured and incorporated in the thrust coefficient C_T.

Figure 5 shows the magnitude and vector summation of these forces for a high bypass ratio engine exhaust system operating at a typical $M_0 = 0.85$ cruise condition.

A flow chart summarising the main steps in the calculation of thrust and flow coefficients is presented on Figure 6. Duct mean total pressures can be defined either from rakes of pitot tubes provided in both fan and primary ducts or from surface and probe static pressure measurements and a knowledge of the duct mass flows.

Computer programs developed by the Aircraft Research Association Limited are used for the main reduction of test data.

6. **ACCURACY AND REPEATABILITY**

In the following section, the word 'accuracy' is used to refer to the uncertainty of a value due to systematic error. The word 'repeatability' is used to refer to the uncertainty of measurement due to the presence of random errors.

During testing, every effort is made to reduce systematic error to a minimum by careful calibration and the use of a controlled test technique.

The absolute accuracy of the rig cannot be checked by reference to 'standard nozzles' since these are used in the basic calibrations. However, a guide to the validity of the technique is given below by comparing thrust measurements from a quiescent test on a model exhaust system with a theoretical breakdown of losses.

Test Condition: Altitude test facility (ATF) cruise condition $M_0 = 0$: $P_F/p_0 = 2.56$	
Component of Loss	% sfc Loss
Bypass duct and nozzle friction (including pitot rake loss)	0.88
Primary duct and nozzle friction (including pitot rake loss)	0.19
Afterbody friction	1.80
Afterbody wave drag	0.70
Theoretical loss =	3.57
Loss from model test =	3.50

Data point to data point repeatability checks carried out during thrust minus drag measurements on a model of the RB211 exhaust system gave a standard deviation $\sigma = 0.001$. Thus the 95% level of confidence of gross thrust coefficient is $\pm 0.2\%$ for a single test point.

The results of a more rigorous series to series check on the performance of the exhaust system are presented on Figure 7. Although the tests were separated by periods of several months, the maximum scatter about the fitted curve is $\pm 0.2\%$ of C_T.

7. **MODEL TEST RESULTS**

At the time of specifying the original production geometry of the exhaust system for the RB211, extensive model tests were carried out at NGTE and Fluidyne. Twentytwo candidate configurations were considered and the test data indicated that the afterbody profile which most suited the design constraints consisted of a circular arc extending from the maximum diameter set by the turbine to the primary nozzle. The fan nozzle was located near the position of maximum diameter and discharged its airflow almost axially onto the afterbody.

Figure 8 identifies the main features of this exhaust system and presents typical model test results at ATF conditions. Obviously further refinement of the performance of this baseline configuration was possible and this has been the subject of five major test series on the thrust minus drag rig.

Two of the approaches followed are discussed below:-

7.1 Reduction of Losses Through Deletion of Hot Stream Spoiler

When the hot stream spoiler doors and stangs are deleted, the rear afterbody shape can be redesigned with a conical final boattail blending into the existing circular arc profile.

Model builds simulating the baseline RB211 configuration and the exhaust system with the hot stream spoiler deleted are shown on Figure 9 and test results are presented on Figure 10.

The improvement in performance results from elimination of base areas and more efficient turning of the fan nozzle efflux at the primary nozzle plane.

7.2 Reduction of Afterbody Skin Friction Loss

With these exhaust system designs, a considerable reduction in afterbody length has been achieved by turning the fan airflow down the afterbody inside the fan nozzle. By inclining the fan nozzle efflux inwards as shown on Figure 11, adverse pressure gradients on the fan cowl are reduced and the external airflow can be turned through large angles prior to the onset of boundary layer separation.

Model tests were carried out on a series of axisymmetric short afterbody configurations. The main variables considered in designing the exhaust systems are shown on Figure 12. The test results confirmed the anticipated high level of performance and showed that even with the largest boattail angles, the apparent thrust loss due to the steep inclination of the fan nozzle is, in fact, recovered on the afterbody by the gradual turning of the airflow.

When this philosophy is applied to the RB211 engine, the conventional afterbody can be replaced by a simple 15° conical afterbody of approximately half the length. In addition to the reduction of scrubbing drag, an estimated weight saving of some 300lbs - 400lbs is achieved, including deletion of the thrust spoiler.

Model tests on this configuration were sufficiently encouraging to justify proceeding further to establish the performance of full scale hardware. A series of engine tests was, therefore, carried out in the NGTE altitude test facility to compare the performance of the baseline circular arc afterbody with the 15° short afterbody. Results from these tests are shown on Figure 13 compared with performance increments obtained from the earlier model tests at the Aircraft Research Association. The agreement between the two sets of data is good.

8. CONCLUDING REMARKS

The model technique described in this paper has now been used for a number of major test series. Accuracy and repeatability are extremely good and performance increments demonstrated on the rig have been confirmed by actual engine tests.

Particular attention has been given to the design of high performance nozzles and afterbodies for low specific thrust engines and test results are presented to show that:-

o   Base areas must be avoided in the vicinity of the primary nozzle.

o   Afterbody boattail angles of up to 20° are practicable.

LIST OF REFERENCES

1) M.V. Herbert - A convergent nozzle for the standardisation of thrust rig measurements. NGTE Report R293.

ACKNOWLEDGEMENT

THRUST / DRAG
BALANCE HOUSING

SHAFT MOUNT FOR AFTERBODY
GIVES APPROXIMATE REPRESENTATION
OF INTAKE AIRFLOW STREAMTUBE

FIXED PYLON - WING
STRUCTURE
(OPTIONAL)

INSTRUMENTATION COVER

SUPPORT STRUT
SUPPLYING
SEPARATELY METERED
BYPASS AND PRIMARY
DUCT FLOWS

METRIC MODEL PARTS
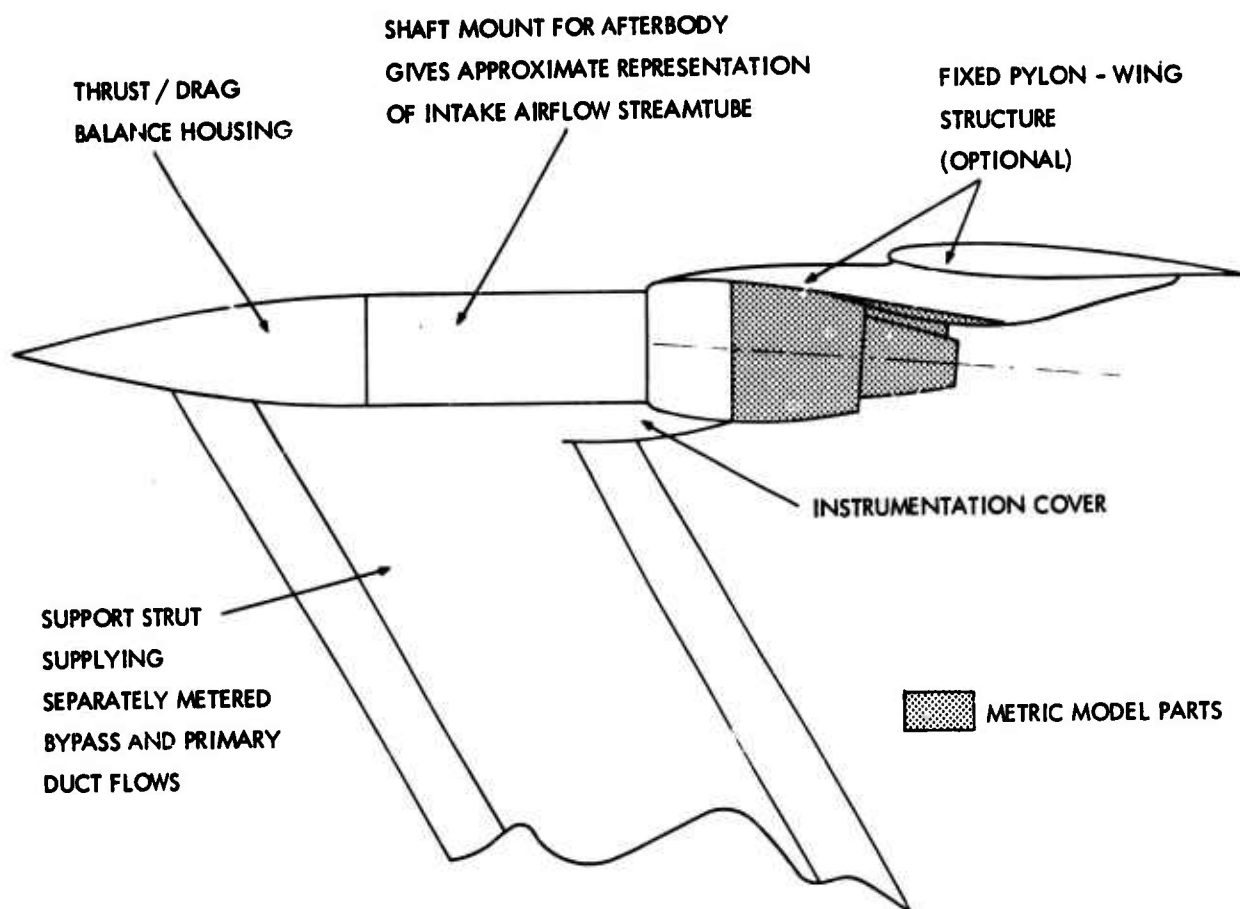
FIG. 1 - TECHNIQUE EXPLANATION
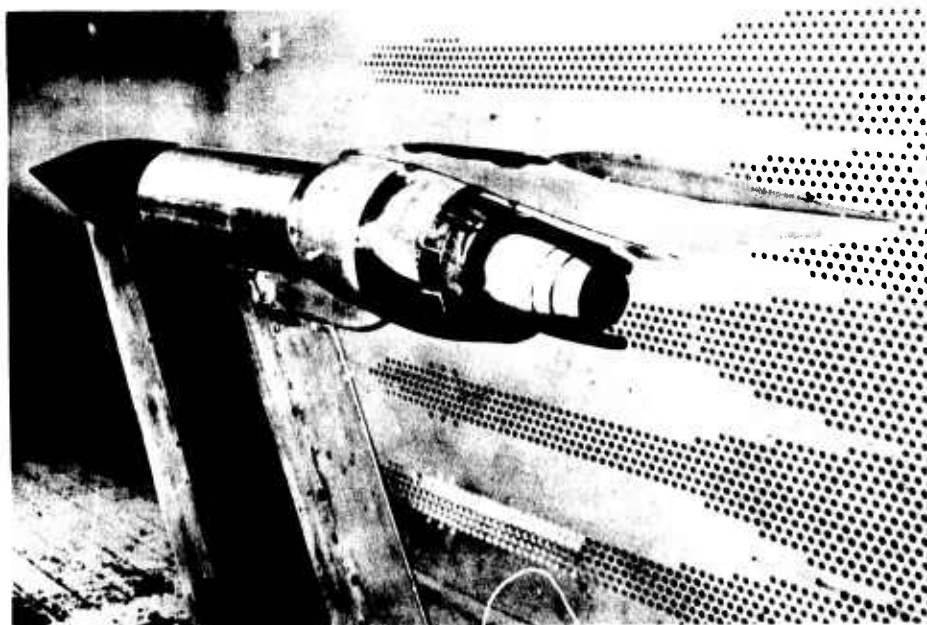
FIG. 2 - TYPICAL MODEL INSTALLED IN TRANSONIC TUNNEL
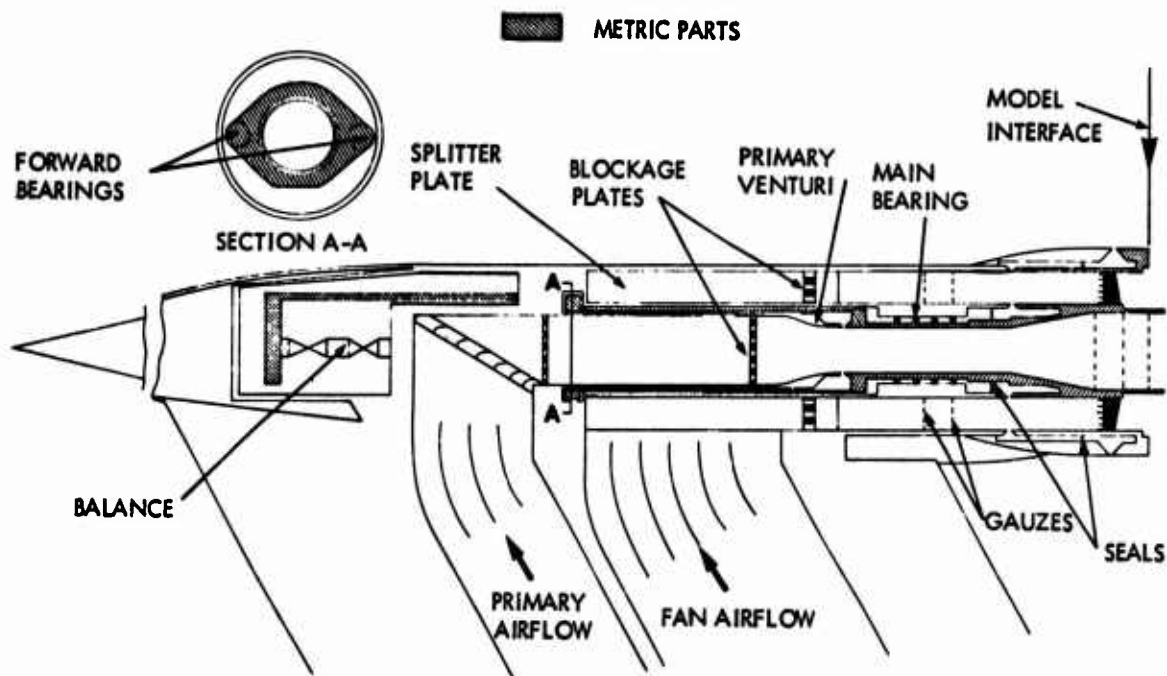
FIG. 3 - BASIC COMPONENTS OF THRUST MINUS DRAG RIG
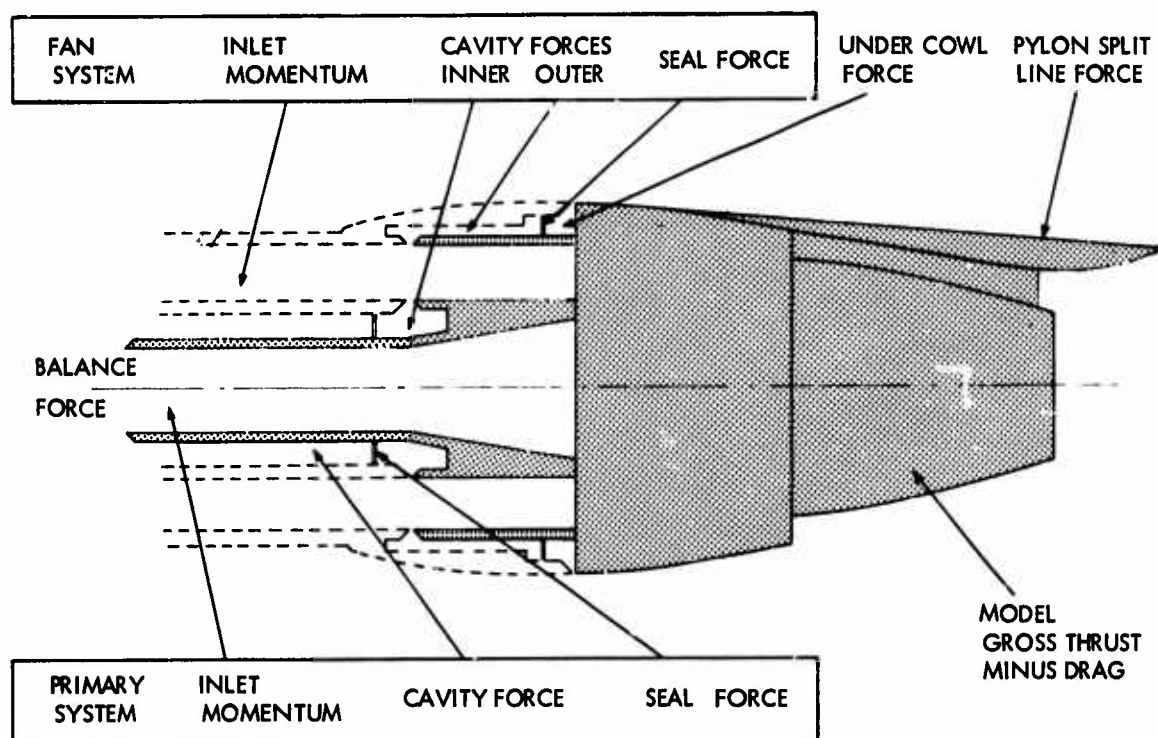
FIG. 4 - COMPONENT FORCES ACTING ON METRIC PARTS

% (X - D) MEASURED

-100   0   +100

BALANCE FORCE	
UNDER COWL FORCE	
PYLON SPLIT LINE FORCE	
INLET MOMENTUM	FAN SYSTEM
CAVITY FORCE - INNER	
CAVITY FORCE - OUTER	
SEAL FORCE	
INLET MOMENTUM	PRIMARY SYSTEM
CAVITY FORCE	
SEAL FORCE	

DRAG ⟷ THRUST
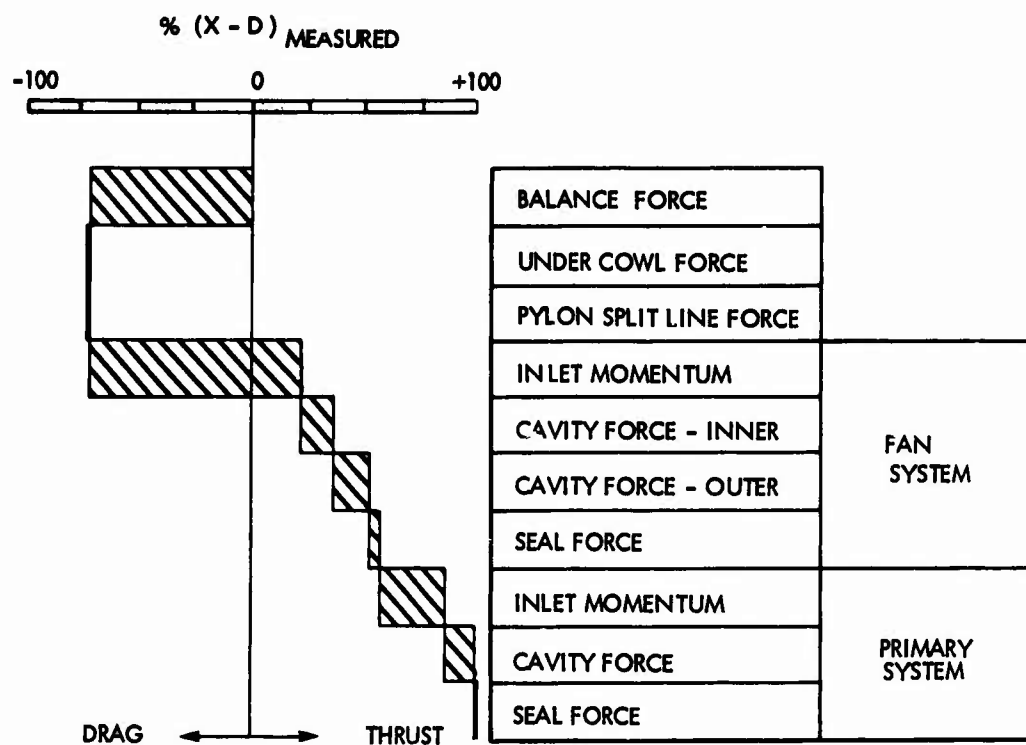
FIG. 5 - VECTOR DIAGRAM OF MODEL FORCES

M_o
P_o

$(m\sqrt{T})_J$ — PRIMARY NOZZLE DISCHARGE COEFFICIENT

P_J — P_J/P_o

$X_{J\ IDEAL}$

$(X - D)_{MEASURED}$ — EXHAUST SYSTEM GROSS THRUST COEFFICIENT

$X_{F\ IDEAL}$

P_F — P_F/P_o

PRIMARY AIRFLOW   FAN AIRFLOW

$(m\sqrt{T})_F$ — FAN NOZZLE DISCHARGE COEFFICIENT

FIG. 6 - CALCULATION OF THRUST AND FLOW COEFFICIENTS

MACH NUMBER $M_o = 0.85$

C_T

1%

SYMBOL	SERIES
+	2
×	3
●	4

2.2 2.3 2.4 2.5 2.6 2.7 2.8 2.9 3.0

FAN NOZZLE EXPANSION RATIO - P_F/P_o
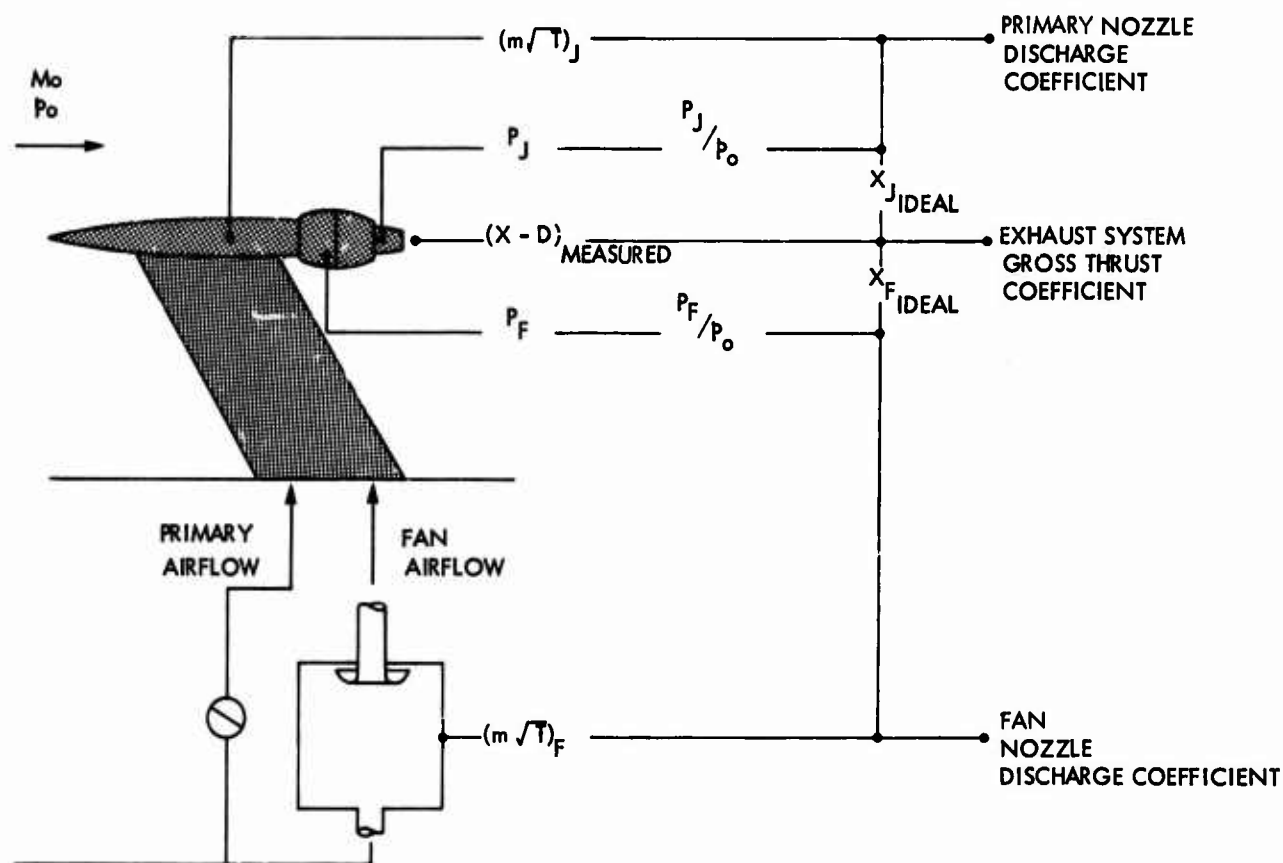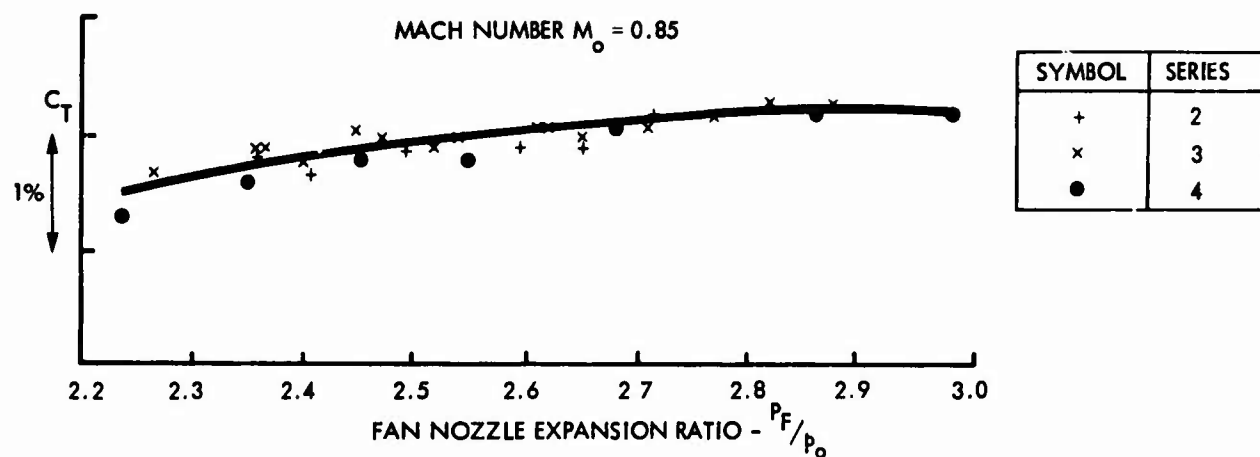
FIG. 7 - SERIES TO SERIES DATA POINT REPEATABILITY

PYLON - SPLITTER

SPOILER DOORS

'ENGINE' $\mathcal{C}_L$
INCLINED TO
FREESTREAM
DIRECTION

SPOILER ACTUATOR
FAIRINGS (STANGS)

AFTERBODY

FAN NOZZLE PLANE

PRIMARY NOZZLE PLANE

1.00

.99

C_T

.98

MODEL TEST DATA

.97

FREE STREAM MACH NUMBER $M_o = 0$

.96

1.4   1.6   1.8   2.0   2.2   2.4   2.6   2.8

FAN NOZZLE EXPANSION RATIO - P_F/P_o
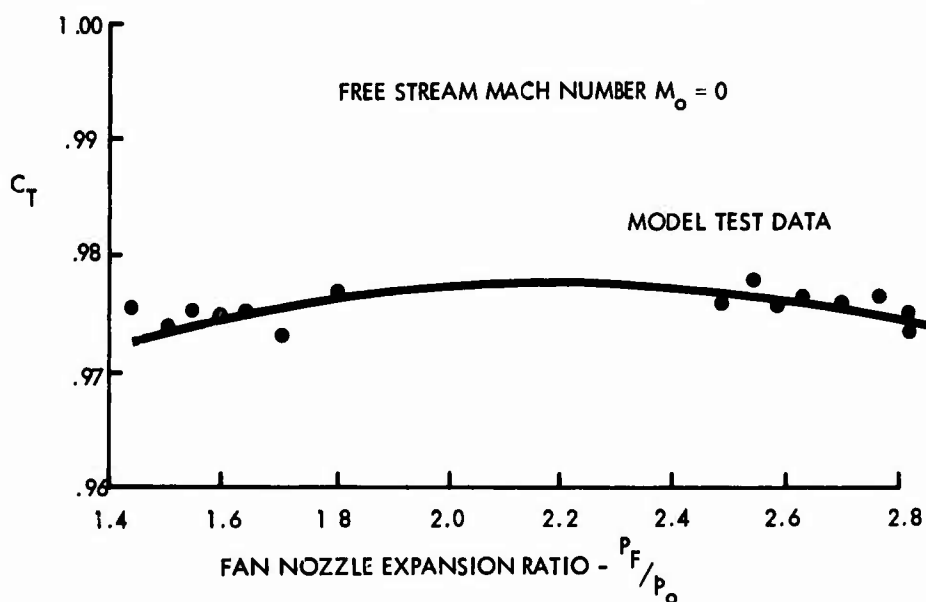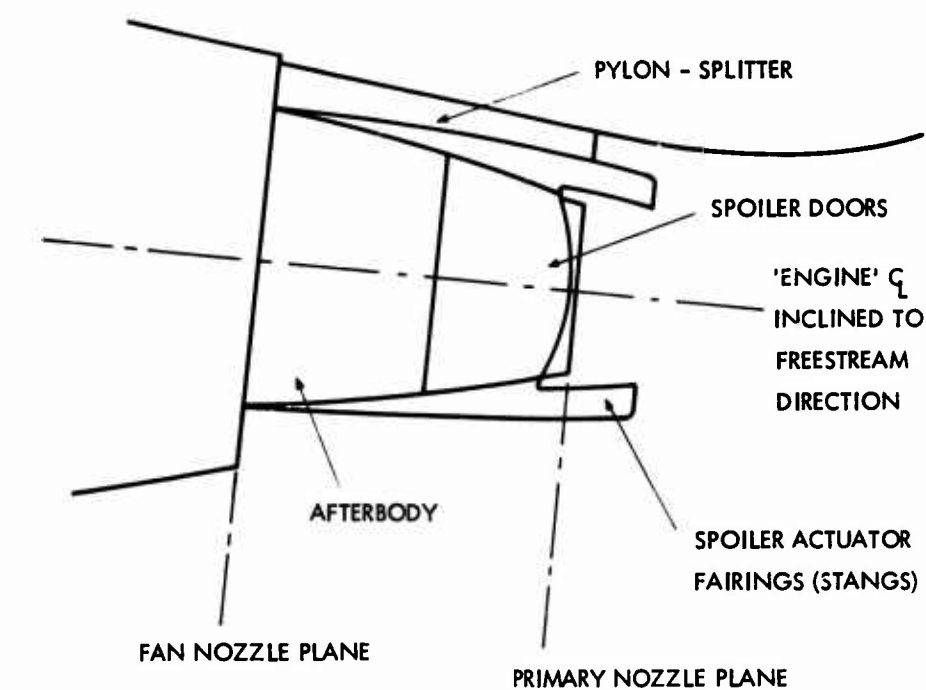
FIG. 8 - RB211 EXHAUST SYSTEM PERFORMANCE
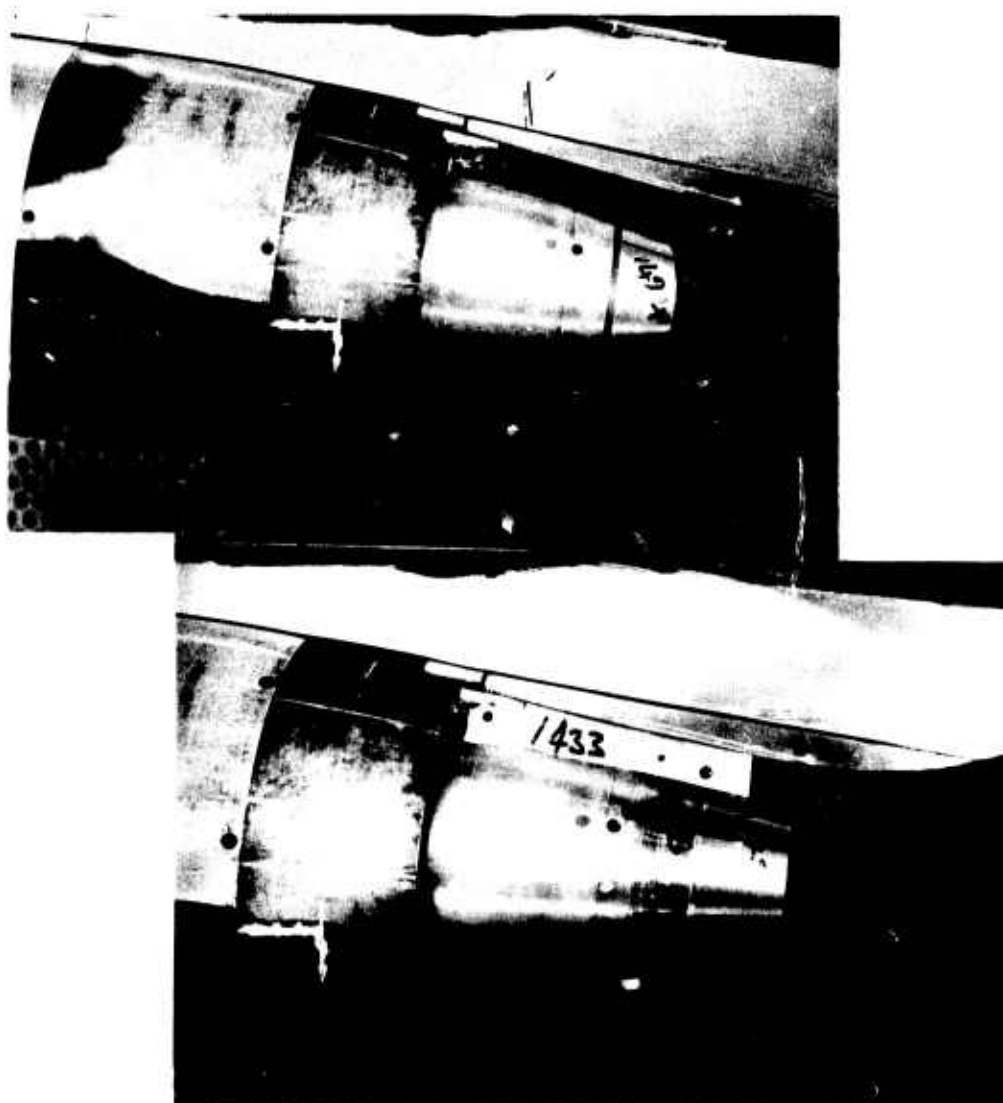
FIG. 9 - MODEL BUILDS TO EXAMINE EFFECT OF SPOILER DELETION
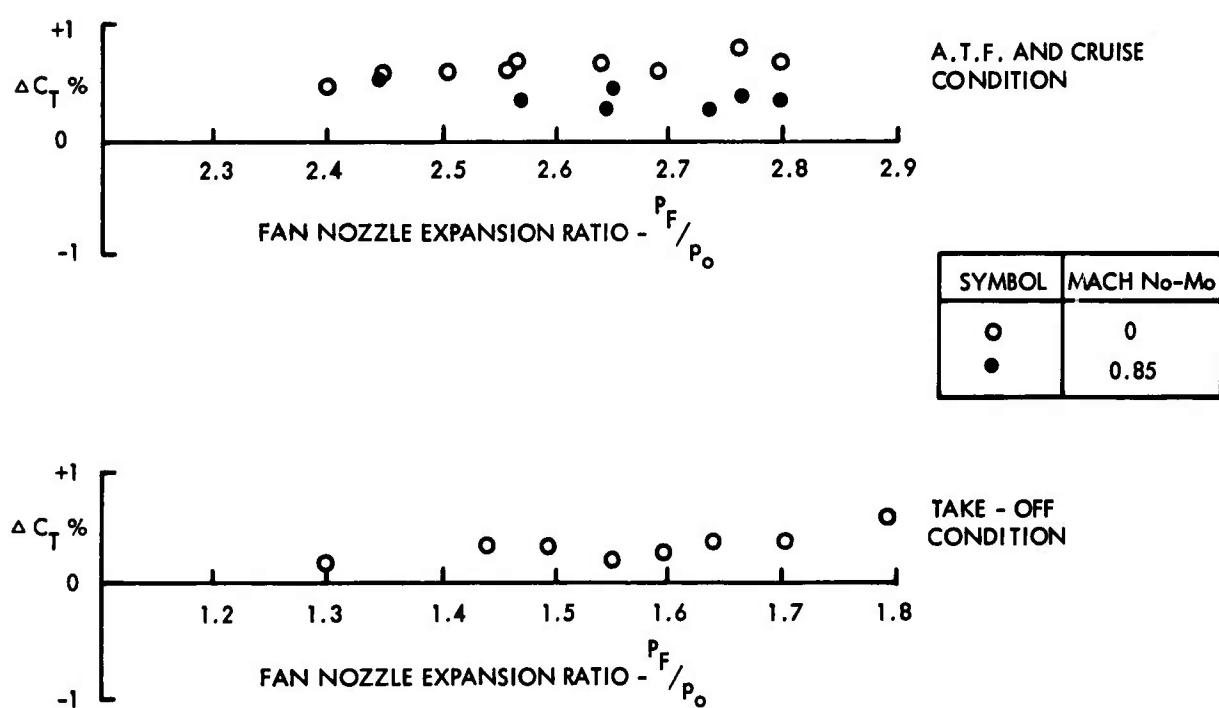
FIG. 10 - PERFORMANCE IMPROVEMENT RELATIVE TO BASELINE CONFIGURATION

FAN FLOW DISCHARGED
AXIALLY ONTO THE
AFTERBODY. FLOW
TURNING ACHIEVED
DOWNSTREAM OF
FAN NOZZLE

CONVENTIONAL
EXHAUST SYSTEM

LONG AFTERBODY REQUIRED
TO TURN FLOW SUPERSONICALLY
DOWN TO PRIMARY NOZZLE

INWARD INCLINATION OF JET
BOUNDARY ALLOWS EXTERNAL
FLOW TO BE TURNED THROUGH
LARGE ANGLES ON FAN COWL

FLOW TURNING
ACHIEVED INSIDE
FAN NOZZLE

EXHAUST SYSTEM
WITH SHORT AFTERBODY

SHORT LIGHTWEIGHT CONICAL
AFTERBODY WITH LOW WETTED
AREA

FIG. 11 - SHORT AFTERBODY DESIGN FOR HIGH BYPASS RATIO ENGINE
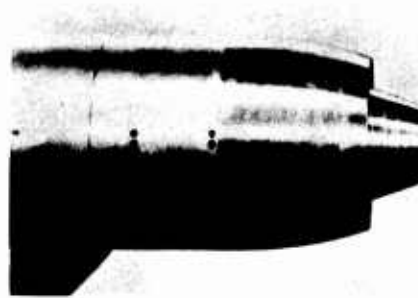
15 ° AND 20° EXTENDED AFTERBODIES (NO PLUGS)
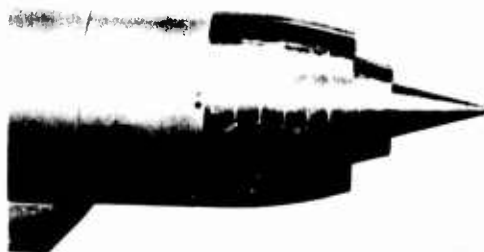
15° FULL PLUG

20° FULL PLUG

15° CUSPED PLUG

20° CUSPED PLUG

FIG. 12 - SHORT AFTERBODY MODEL BUILDS

GROSS THRUST IMPROVEMENT AT A.T.F. CRUISE CONDITION $M_o = 0 : \dfrac{P_F}{P_o} = 2.56$

CONFIGURATION	MODEL TEST AT A.R.A.	RB211 ENGINE TEST AT NGTE (ENGINE 10215)
BASELINE AFTERBODY	DATUM	DATUM
15° SHORT AFTERBODY	0.9 %	0.82 %

FIG. 13 - SHORT AFTERBODY PERFORMANCE COMPARISON

ISOLATING NOZZLE-AFTERBODY INTERACTION PARAMETERS AND SIZE EFFECTS -
A NEW APPROACH

By: S. C. Walker
Vought Systems Division
LTV Aerospace Corporation
P. O. Box 5907
Dallas, Texas   75222

SUMMARY

Isolation of the effects of major parameters, and the determina-
tion of proper correction of wind tunnel model data are major objec-
tives in the Vought Systems Division long range Nozzle-Afterbody
Technology Development program. This isolation is considered
necessary to adequate understanding of the flow and the development
of parameters capable of expressing nozzle-afterbody performance.
This paper reports a flight test of the A-7E airplane, and associated
wind tunnel tests comprising approximately one half of the long range
program. The difficulty of controlling parameters in flight was
overcome by flying into the data point while allowing only slight
variations in ambient pressure.

Wind tunnel tests were made in a 1.2 x 1.2 meter blowdown
tunnel. Models were run with both hot and cold exhaust. One model
was a wingless body of revolution; the second was a geometric repre-
sentation of the airplane.

The flight test demonstrated the practicability of parameter
control testing, and showed applicability of stream thrust parameter
to inflight engine performance evaluation. Wind tunnel data show
trends and general levels comparable to flight, and have verified
some areas in which development of corrections is necessary.

INTRODUCTION

Several current airplanes have not met expectations, or have exhibited surprising changes in drag
with changes in power setting. The cause, in part, has been traced to nozzle-airplane afterbody inte-
gration problems which result in lower thrust and/or higher drag than anticipated. Extensive testing has
been expended to identify the problems and possible solutions. However, the solutions for the most part
were major and came too late in the design-manufacture cycle to be included. Methods (analytical and
experimental) are needed to trade off the various vehicle design parameters early in the design cycle so
major problems can be avoided.

Several approaches to improving technology for design of nozzle-afterbody systems are being pursued
throughout industry and governmental agencies. NASA has conducted studies of a general nature and a few
tests of specific airplane configurations for the Air Force and Navy. References 1 and 2 are representa-
tive of this work. On the other hand, programs such as the Air Force Airframe Propulsion Subsystem
Integration program and the Exhaust System Interaction Program (References 3 and 4) are oriented much
more toward configuration data bank generation. Several analytical performance prediction methods for
the integrated system have been created both on theoretical and empirical bases, of which Reference 5
is a notable example. All of the programs have contributed to improved airplane design, however, all
have fallen short of providing basic understanding of this complex flow.

During development of a method for afterbody drag prediction of single engine airplanes, serious
incompatibilities were shown to exist among various sources of experimental data. These incompatibilities
are most likely due to uncontrolled (or unknown) flow quality, and instrumentation difference. Tests at
two facilities on nearly identical models show variations as large as 25%. Also, neither subscale nor
ground based full scale test data can be consistently related to flight conditions. The problems can be
categorized into those of simulation, flow conditions, and instrumentation. Dimensional tolerances and
small differences in model finish, gaps, steps, mount, and general quality details affect the simulation
and contribute to difficulty in correlating data from other facilities or from flight. Interference of
the mounting structure, flow quality, and blockage are considered the most improtant of the tunnel effects.
Of these, interference of the strut (or sting) is probably the best resolved. The amount of turbulence
and flow angularity in the wind tunnel, model support effects, blockage, the effect of vented walls, and
the use of cold or hot flow or model exhaust all contribute to variation in flow conditions from model to
model and from facility to facility. Although attempts have been made to correct for blockage, and most
wind tunnels have run turbulence and angularity calibration, these effects are generally ignored in the
analysis of data. While the absolute magnitude of the effects may be small for the particular test, they
contribute significantly to the scatter of data when compared to similar tests from other models and
facilities. Differences in instrumentation, particularly in static pressure taps, and in balance concepts
are also critical to data comparisons. The inadequacy of many instrumentation systems to get data to
show complete effects often cause pursuit of analytical approaches that generate misleading conclusions.
In many cases studied at VSD the instrumentation systems of otherwise comparable models, or tests in
different facilities are not complete even though there is little question about the accuracy of the
measurement actually taken. In the case of engine tests in altitude and Mach number facilities the system
is not adequately simulated to avert question between ground and flight data, and usually the same
instrumentation arrangement is not used in both tests. In the case of flight testing, the instrumentation

systems have not been complete enough to adequately relate flight data to ground calibration. Consequently, it seems necessary to carefully control certain items in order to isolate any of the effects to the degree that the results can be applied broadly.

LONG RANGE PROGRAM — A NEW APPROACH

In 1971, VSD initiated a long range plan to isolate major parameters and testing conditions to enhance understanding of inter-test differences and size effects. One of the long range objectives is to establish corrections for sub-scale data. This plan involves testing of a set of models in at least three facilities. The models represent an airplane configuration for which special flight data were obtainable. This test series, and items that can be effectively isolated are illustrated in Figure 1. As shown on the figure, the effects of flow can be isolated among the three test conditions (small wind tunnel, large wind tunnel, and flight); and the effect of size can be isolated among three sizes of test articles (small model, large model, and airplane). Flight test of the production airplane, and wind tunnel tests of the equivalent body of revolution (EBOR) and airplane models have been completed to date. These three tests allow the evaluation of the applicability of the EBOR data to airplane performance, and give an overall comparison of subscale model data to actual flight. This paper describes these completed tests.

The next step of the program will be to run the two existing 0.08 scale models, and a 0.15 scale model of the airplane in a large, continuous flow wind tunnel. The mounting facility used in the previous tests will be used in the large wind tunnel tests. Completion of the test series would involve flying the 0.08 scale airplane model on a pylon of a parent airplane. Dimensions of the pylon would be the same as the wind tunnel mounting strut. Maneuvers flown would be the same as in the flight test of the airplane.

AFTERBODY DRAG FLIGHT TEST

In 1973 a flight test was made on an A-7E airplane to obtain data specifically oriented to Nozzle-Afterbody Technology development. The test was conceived to isolate the effects of four major parameters: (1) jet exit velocity and pressure; (2) altitude (ambient pressure); (3) external (boattail) velocity; and (4) tail flow field. The current U. S. Navy airplane shown in Figure 2, is similar to the U. S. Air Force A-7D. It has a non-afterburning TF-41 turbofan engine with a long, fixed convergent nozzle. A relatively large base area exists between the nozzle exit and the fuselage terminus. Nozzle and fuselage terminus are in the same station plane. Only a small amount of vent flow from the engine compartment exhausts through the base area.

Test Planning - Understanding the effect of each of these parameters is necessary for both the development of performance prediction technology and for synthesizing or improving the integrated design. This understanding has been difficult to obtain in previous flight or wind tunnel test results because several interacting variables change at the same time, thereby making isolation of singular effects difficult or impossible. Planning of this test was concentrated on selectively controlling all but one of the parameters, thus isolating that parameter's effect upon performance. This concept of testing has been named Parameter Control Testing. Parameter control is not difficult to achieve in the wind tunnel, but is quite difficult to achieve under normal flight techniques. For any particular airplane the parameters of interest will have fixed relationships in stabilized flight with variation being effected only by aircraft weight and center of gravity. Consequently, the desired data must be obtained with thrust either excess or deficient to the stabilized requirements, thus creating acceleration of some type. It was determined by analysis during the planning efforts, that a change of ambient pressure (altitude) during the data reading would be the least critical to the results, and also be the easiest to correct. This philosophy was followed throughout the program.

Conditions at approximately the mid point of the flight envelope were chosen as the base, and starting point, so that maximum useful range of data would be obtained. The base point chosen for the A-7E was Mach 0.6, 15,000 feet (4572 meters) pressure altitude, and power to maintain stabilized flight. The effects of external velocity were obtained by establishing a pre-determined power setting above or below 15,000 feet at the predetermined indicated airspeed and recording data as the airplane climbed or descended through 15,000 feet. During this series the maximum rate of climb encountered was 25 feet per second (7.6 meters per second) and the maximum rate of descent was 56 feet per second (17 meters per second). To facilitate recording, the pressures were routed through four Scannivalves which were referenced to the noseboom airspeed system. These were 48 step Scannivalves that completed one revolution in 4.8 seconds. The Scannivalves were synchronized to each other and the patching arrangements were such that the corresponding total and static pressures of individual probes were recorded at the same time. Due to this 4.8 second cycle time there was a 0.09 psi (620 Newton/meter^2) ambient pressure change during the data acquisition. However, ambient pressure was sampled each tenth second and the small change was accounted for by updating the reference pressure for each Scannivalve step. The total pressure change was negligible due to a decrease in indicated airspeed.

Variation of nozzle exit pressure while maintaining constant velocity was performed by setting up at a higher altitude for the low power settings and at a lower altitude for the high power settings and then flying the airplane at the indicated airspeed that will result in a 0.6 MN at 15,000 feet (4572 meters). If the power setting is higher than required for stabilized flight at 0.6 MN but the airspeed maintained, obviously the airplane will climb. Conversely, for lower power settings, if the indicated airspeed is maintained the airplane will descend. As before, the pilot was able to select the correct power setting, climb or glide slope, and indicated airspeed to achieve the correct combination at 15,000 feet (4572 meters) with a 0.6 MN. In this case, the idea was to have the exact velocity and altitude with approximate PTN's to fit above and below the stabilized center point. For this series, the highest rate of change was for the highest power setting. The rate of climb was 95 feet per second or 0.153 psi (1055 Newton/meter^2) increase in static pressure with 0.17 psi (1172 Newton/meter^2) increase in total pressure. These changes were easily accounted for by updating the reference pressure.

During the previous described maneuvers, the Unit Horizontal Tail (UHT) movement covered less than one degree. To determine the effect of UHT variations, velocity was held at 0.6 MN and the PTN held

constant at power required for stabilized flight at 0.6 MN, 15,000 feet and wind-up turns were performed. Velocity and PTN were set up to give the desired combination going through 15,000 feet (4572 meters) as the "g" level was held constant. To increase the UHT spread, gentle pushovers were performed in the same manner; the total spread came to approximately 4 1/2 degrees.

Variation in ambient pressure was obtained by flying the airplane by the same techniques at various altitudes from 2,000 to 25,000 feet (600 to 7600 meters) holding airspeed and nozzle total pressure at the base values.

Since this type of flight testing was new to VSD there was considerable skepticism of the practicality of flying the airplane into the points satisfactorily, and in our ability to resolve non-steady state data. The pilot had little difficulty obtaining the desired flight conditions satisfactorily after a few trial runs in which he developed judgement of engine/airplane control response. This was borne out by the acquisition of all data in five flights instead of seven which were initially planned. Ranges of parameters over which data were obtained are tabulated in Table 1.

TABLE 1

RANGE OF CONTROL PARAMETERS

Exhaust Nozzle Pressure (P_{TN})		10.4 to 25.6 PSIA
Mach Number	(M)	0.4 to 0.8
Ambient Pressure	(P)	13.6 to 5.4 PSIA (2000') (25000')
Horizontal Tail Incidence (δ)		-3.7 to -7.9°

Instrumentation - The airplane had been used in the flight test programs for engine and airplane performance, and consequently, had extensive system instrumentation. Instrumentation which was added for the base drag flight test, illustrated in Figure 3, included afterbody static pressures, boundary layer rakes, base annulus pressures, exhaust nozzle pressure and temperature rakes, and engine core and fan flow pressures and temperatures. The engine manufacturer (Detroit Diesel Allison) provided special internal instrumentation and has cooperated in analysis of data. Instrumentation in the external flow consisted of 12 afterbody static pressures and two boundary layer rakes. The static ports were arranged in three rows along the boattail on the upper left, lower left, and bottom centerline. The boundary layer rakes were 10 inches long and had 8 pitot-static probes. These were located on the upper right and lower right just forward of the fuselage terminus. The plane of the base area had 6 static pressure probes distributed proportionally to the width of the annulus (i.e. two at the top, three on the side, and one at the bottom). Three static probes located 12 inches forward of the nozzle plane averaged engine compartment pressure, and both external and internal taps were located at the top, side, and bottom of the nozzle approximately one fourth inch forward of the nozzle lip.

Four of the nine pressure and temperature probes normally in the production TF-41 engine were replaced by special probes. These probes are located between the turbine discharge and the station at which the fan and core streams are mixed. The production probes average core and fan pressure. The special probes measure the static and total pressures and the temperature of each stream to provide indication of by-pass ratio. The remaining five production probes were used in the normal manner for monitoring and control of the engine. The nozzle rake contained two instrumented legs with ten temperature and total pressure probes, and five static pressure probes on each. Figure 4 shows the nozzle and boundary layer rakes installed on the airplane. Calibration of the engine in the airplane was made on a thrust measuring stand with and without the nozzle rake. This calibration gave base data for use in analysis and also indicated any change of matching within the engine due to the instrumentation. To compensate for the blockage by the rake, a tailpipe with a larger than normal nozzle area was used. Calibrations were made on the engine with a production size nozzle, the larger nozzle without the rake, and the larger nozzle with the rake. This calibration confirmed that engine parametrics with the rake installed were essentially identical to those of the production configuration. To determine the error in the static pressure measurement of the rake probes caused by the relatively thick rake strut, ground runs were made with an unobstructed static probe which could be positioned at various radial locations within the nozzle, and could be translated axially during engine run. Position error derived from this test was applied to rake data. Results of these calibrations appear quite good.

Data System - The airplane was equipped with a fourteen track magnetic tape recorder, a photo observer and a telemetry system. Signal conditioning included PCM and PDM multicoders and continuous FM channels (sub-carrier oscillators).

Data measurements were recorded on magnetic tape through a PCM switch sampled 100 times per second. The Scannivalves were synchronized so that all valves were on position one at the same time and the patching arrangements were such that the corresponding totals and statics of the individual probes were recorded at the same time.

The data reduction was accomplished by the normal scaling of the PCM data to engineering units. Corrections for zero shifts were made by having one position on each Scannivalve measure its reference pressure, and any deviation from zero was corrected. Airspeed, altitude, N1, N2, PT5.1 and free air temperature were obtained from the photo observer and integrated into the PCM data.

Because the test involved quasi-stabilized flight, a lag check was conducted on the noseboom airspeed system and the plumbing associated with the Scannivalves. The lag for the Scannivalve's reference side and the lag for the photo observer were very close to the same: therefore, no lag corrections were made in any of the data.

Engine Performance and Calibration - Calibration of the engine in the airplane was made on a thrust measuring stand with and without the nozzle exit rake. This calibration gave base data for use in analysis and also indicated any change of matching within the engine due to the instrumentation. Initially, a four arm cruciform rake was installed on the production size tailpipe. Since the engine airflow limiter is programmed to the low rotor speed, the reduction in tailpipe effective area caused by the rake resulted in increased high rotor speed and engine pressure ratio to maintain a given engine corrected airflow at a given corrected low rotor speed. A larger tailpipe (4-percent area increase) was installed and the frontal area of the rake reduced by removing two arms and replacing them with a thin brace. The 2-arm rake-large tailpipe combination resulted in engine operating conditions approximately the same as the production tailpipe without a rake.

To determine the error in the static pressure measurement of the rake probes caused by the relatively thick rake strut, ground runs were made with an unobstructed static probe which could be positioned at various radial locations within the nozzle, and could be translated axially during an engine run. Position error derived from this test was applied to rake data. Results of these calibrations appear quite good.

WIND TUNNEL MODEL TESTS

The wind tunnel tests were made in the LTV High Speed Wind Tunnel over essentially the same range of parameters as the flight test. Both wind tunnel models were fitted to the same mounting facility and utilized the same internal parts and internal instrumentation (including exhaust nozzle). The Equivalent Body of Revolution (EBOR, body of revolution model equivalent to the A-7 model fuselage) test was a project of the Vought Systems Divsion Independent Research and Development Program; the airplane model test was sponsored by the U. S. Naval Air Propulsion Test Center.

Wind Tunnel Facility - The tests were run in the LTV High Speed Wind Tunnel on a special Exhaust System Test Facility. The wind tunnel is of blowdown type with a four foot (1.22 meter) square test section. Mach number range is from 0.5 to 5.0. A perforated wall test section is used for transonic testing up to approximately 1.4 Mach. A forty channel analog to digital data system is coupled to an "on-line" IBM 1800 computer.

The Exhaust System Test Facility is a strut mounted metric assembly on which models of specific configuration may be readily attached. The facility was designed to test models up to 48 inches (1.22 meters) in length, with nozzle throat areas up to 5.4 square inches (35 sq. cm) for maximum nozzle pressure ratio of 18. The model may be powered with either cold compressed air or by combustion products of a burner integral to the metric assembly. The combustor uses propane, oxygen, and air, and very closely simulates exhaust gas properties and flows of turbojet and turbofan engines. With the simulator installed, gas flow capability up to 8 pounds/second (3.63 kg/sec) $2000°F$ ($1367°K$) has been demonstrated. This flow will provide nozzle total pressure of approximately 90 psia (6.2×10^5 Newton/meter^2) with a maximum area nozzle. A six component balance in the facility measures net force on the afterbody model (thrust minus drag).

EBOR Test - Most analytic methods for predicting afterbody pressure drag of three-dimensional configurations are based on the assumption that the body can be simulated by an axisymmetric body with the same area distribution. It is well known that this can result in large errors for twin jet configurations but is considered to be an acceptable approach for a single engine configuration such as the A-7 airplane model. The purpose of the EBOR test was to evaluate the accuracy of simulating a three-dimensional, single engine afterbody by a body of revolution.

The EBOR model has fuselage area-length distribution equivalent to the fuselage of the A-7E downstream of facility station 8.0. Upstream, a Sears-Haack nose of the facility is faired into the model lines. Figure 5 is a photograph of the model mounted on the exhaust system test facility in the wind tunnel.

Pressure instrumentation of the external part of the model consisted of a row of static pressure taps running longitudinally at three radial locations: i.e. top, side, and bottom (0°, 90°, and 180°). Figure 6 shows the location of each tap.

Base pressure and nozzle instrumentation are shown in Figure 7.

A-7 Model Test - The A-7 model is approximately 47 inches (119 cm) long and 6 inches thick at the maximum cross-sectional area. The model is 0.08 scale of the flight test airplane. The metric afterbody is approximately 16 inches (40 cm) long. A picture of the model is shown in Figure 8. It should be noted that the model is mounted to the strut in the inverted position. The forebody and wing stubs are non-metric, and the inlet is faired over. The inlet, located on the bottom of the airplane fuselage approximately below the windshield, has been faired into the nose by extending the nose forward and downward. Contours of the model, except for the nose and inlet area are representative of the production A-7E airplane. The outer panels of the wings of the model were left off to reduce the blockage in the tunnel, and to reduce the effects of proximity of the model to the tunnel wall. Geometric blockage of the tunnel was approximately 2.1% at the maximum point which was just aft of the metric break of the model. The horizontal tails were mounted on the metric afterbody at zero angle of attack. Both wings and tails were removable for testing with fuselage only. The vertical tail was non-metric and represented by an insert in the trailing edge of the mounting strut.

Instrumentation of the A-7 model was as similar to that of the flight test airplane as practicable. Differences between the two arrangements were: (1) model nozzle performance was resolved by metered flow and force measurements instead of with internal instrumentation and a nozzle exit rake of the flight vehicle; (2) due to the extremely small size of the scaled probes for exit plane base pressure, and the difficulty of analyzing the data from these probes on the flight test, base pressures were monitored only by taps in the base cavity similar to the compartment pressure probes in the flight test airplane; (3) fuselage static pressures were obtained further forward on the model than on the flight test airplane; (4) because of physical limitations fewer probes on the boundary layer rakes cover greater height (scaled)

than those used in the flight test. The general arrangement of the instrumentation is shown in Figure 9. As noted in the EBOR model description, the internal instrumentation is the same for both models, and is shown in Figure 7.

Data were obtained on the model with and without wings and tails; and with and without the boundary layer rakes. Exhaust gas temperature duplicated that of the flight test, however, data with cold exhaust were obtained at representative conditions. Range of parameters tested was equivalent to the flight test except for Reynolds number, which could not be duplicated.

RESULTS

Nozzle Performance - Parameters used in the wind tunnel tests to simulate the nozzle exhaust conditions of flight were pressure ratio and temperature. To put data from both tests on a common basis, it was necessary to abandon the gas generator method of presenting airplane nozzle performance as a function of ram pressure ratio, and select a method independent of engine and flight condition.

The airplane production turbine out pressure instrumentation samples both the fan and core streams at the nozzle entrance and gives a near average total pressure as shown by the special individual probes at this location. This fact permitted the airplane nozzle stream thrust to be defined as a function of the average pressure regardless of flight condition. Since the model nozzle was calibrated to an average total pressure on a plenum, the stream thrust procedure was a compatible basis for presenting nozzle performance from both types of tests.

The stream thrust function is shown in Figure 10 for all points of the three tests in which the nozzle was choked. Values for the model nozzle were scaled by the ratio of the airplane nozzle geometric area to the model nozzle geometric area. All points are within a +1% band around a straight line from the origin. Data from ground calibration runs on the airplane, static calibration of the model, and all conditions of flight (regardless of altitude or Mach number) were used to establish the line of the curve, and overlap as indicated. The resolution of the stream thrust function in flight from the nozzle exit rake independently from the round calibration confirms the ability to accurately determine in-flight stream thrust from ground calibration of turbine exit total pressure probes.

Parameter Separation - The effects of each of the four parameters that were investigated are summarized in Figure 11. Tail incidence and altitude (ambient pressure) are shown to have almost insignificant effects compared to those of nozzle pressure and external velocity. The curves of Figure 12 show how these major parameters affect base pressure, and compares the effects to data from stabilized flight at 15,000 feet (4572 meters). The variation in boattail pressures from the same range of parameters is shown in Figure 13.

EBOR Applicability - Comparisons of base and average boattail pressures of the EBOR and A-7 models are given in Figures 14 and 15 respectively. Boattail pressures used for the curves are averages of all pressure taps at each fuselage station. The generally more negative pressure on the EBOR base and more positive pressure on the boattail is considered to be the result of the difference in shape of the annulus of the base and the shoulders of the fuselage at the forward part of the afterbody. Flow visualization by oil flow on the A-7 boattail showed severe displacement of the streamlines in the vicinity of the shoulders, and consequently the boundary layer and external flow field of the two models is significantly different near the fuselage terminus.

Comparison of Flight and A-7 Model Data - As stated previously, the primary purpose of this series of tests is to determine wind tunnel and size effects. As yet, data are insufficient for separation of the two. However, the general comparison of the present data is of interest, since in many programs, only superficial corrections are made to wind tunnel data before its use in predicting full scale performance. Comparisons of the flight test and airplane model data are shown in Figure 16 for base pressure, and in Figure 17 for afterbody pressure.

CONCLUSIONS

1. The clarity of the results and the quality of data from this test proves that this innovation in testing techniques is successful, and is necessary to thorough understanding and analysis of nozzle-afterbody interaction and performance.

2. In-flight stream thrust can be verified easily and accurately by ground calibration of engine instrumentation.

3. Body of revolution models are adequate for use in preliminary design of a single engine airplane to obtain trends and comparisons of performance between configurations.

4. Size and/or wind tunnel effects exists ir subscale data of small tunnels which is significant enough to cause unacceptable prediction of full scale performance without the determination and use of corrections.

REFERENCES

1. NASA TM X-1960, Jet Effects on the Boattail Axial Force of Conical Afterbodies at Subsonic and Supersonic Speeds, February 1970, W. B. Compton III and Jack F. Runckel.

2. NASA TM X-2112, Performance of Convergent and Plug Nozzles at Mach Numbers From 0 to 1.97, October 1970, D. E. Harrington.

3. D162-10467-7 Exhaust System Interaction Program Phase I Test Report B005 Contract No. F33615-70-C-1450, 1 September 1972.

4. AFFDL-TR-72-101, Experimental and Analytical Determination of Integrated Airframe Nozzle Performance, October 1972.

5. Journal of Aircraft Vol. 2, No. 3, A correlation of High Subsonic Afterbody Drag in the Presence of a Propulsive Jet or Support Sting, May-June 1965, H. McDonald, and P. F. Hughes.
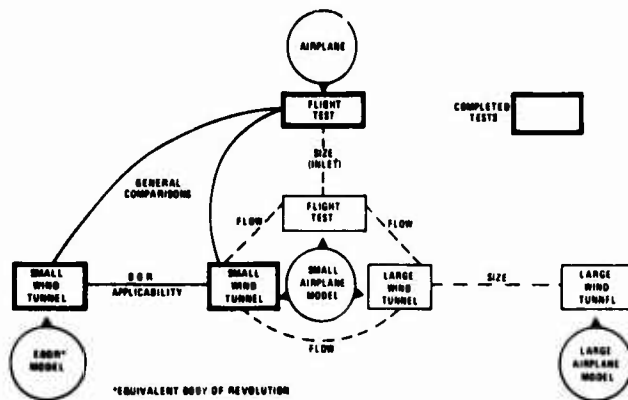
Figure 1.   NOZZLE-AFTERBODY TECHNOLOGY MODEL
DATA QUALITY RESOLUTION

Figure 2.   A-7E AIRPLANE
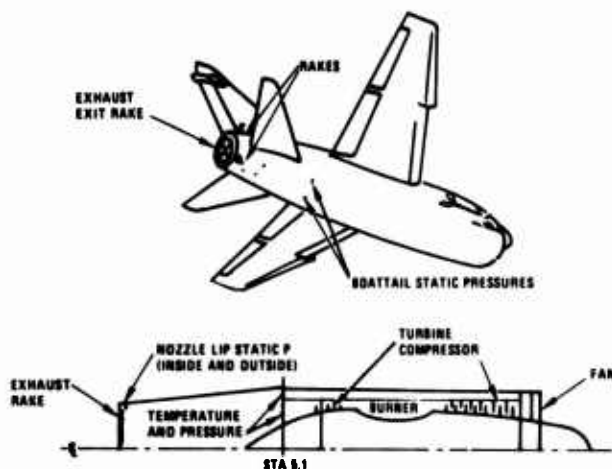
Figure 3.   ENGINE AND AIRPLANE INSTRUMENTATION
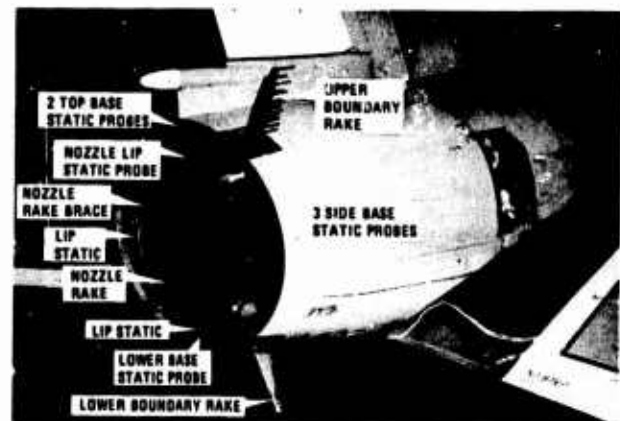
Figure 4.   A-7E AFTERBODY WITH INSTRUMENTATION
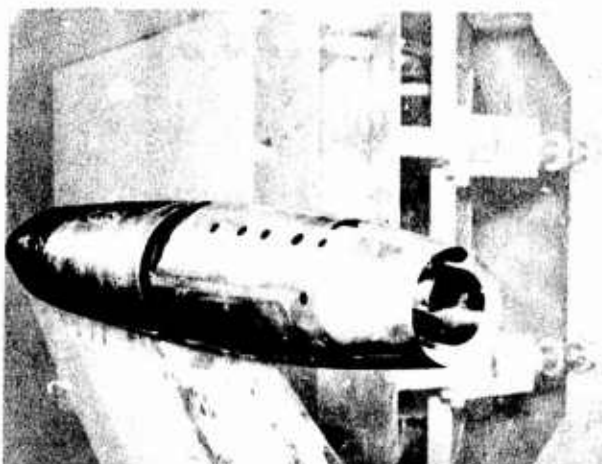
Figure 5.   EQUIVALENT BODY OF REVOLUTION
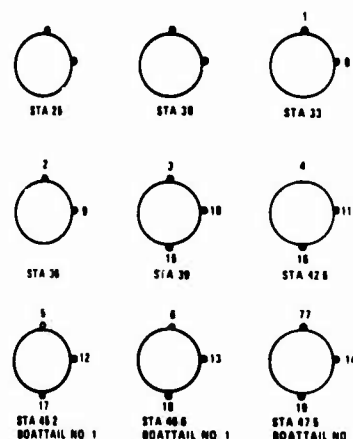
Figure 6.   EBOR EXTERNAL INSTRUMENTATION
(LOOKING FORWARD)
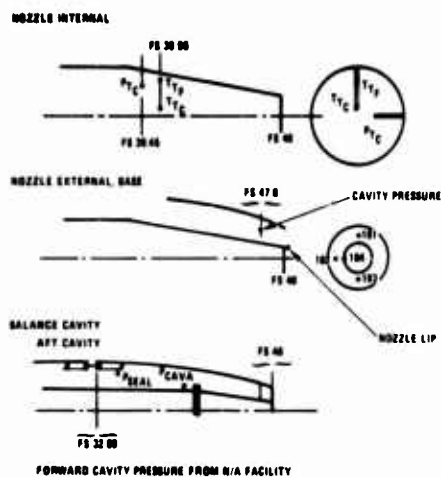
Figure 7. INTERNAL INSTRUMENTATION

Figure 8. A-7 WIND TUNNEL MODEL
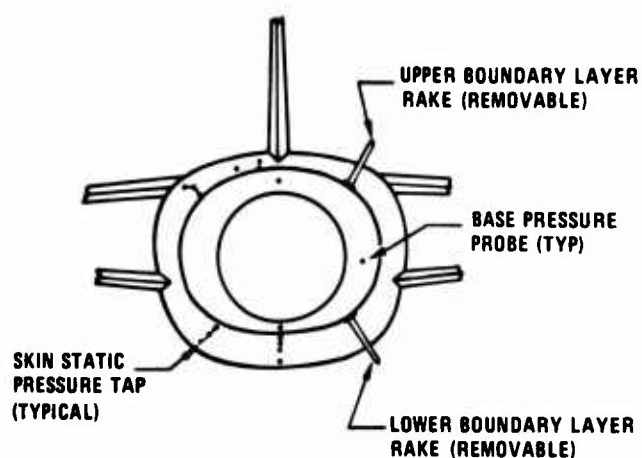
Figure 9. BOATTAIL AND BASE INSTRUMENTATION
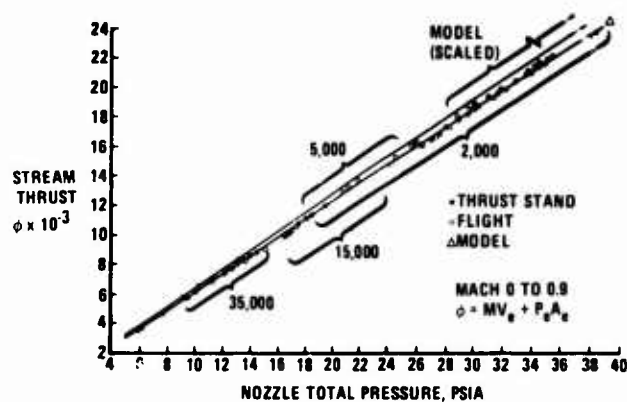
Figure 10. STREAM THRUST FUNCTION
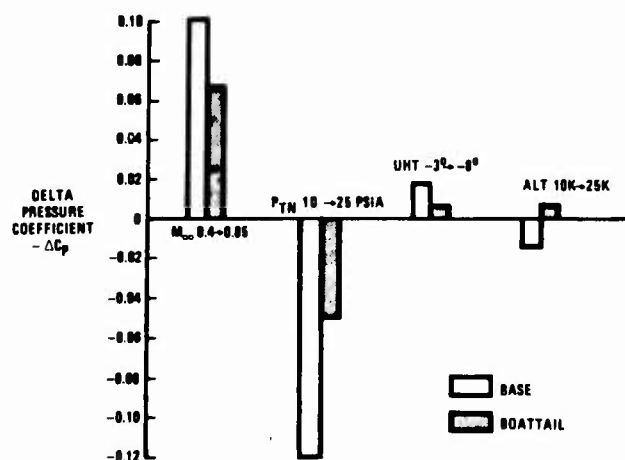
Figure 11. PARAMETER CONTROL DATA SUMMARY
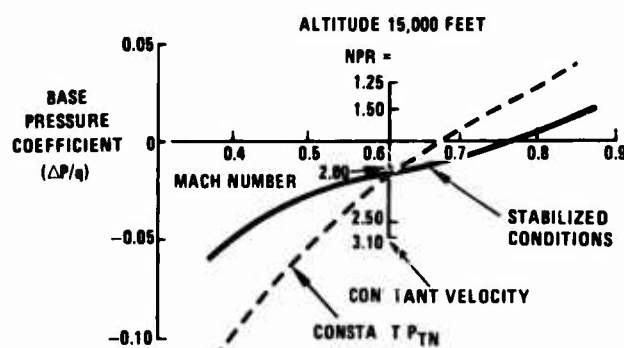
Figure 12. PARAMETER INFLUENCE ON BASE PRESSURE
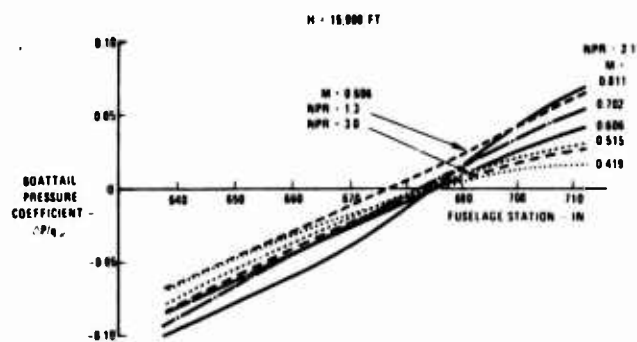
Figure 13. PARAMETER INFLUENCE ON BOATTAIL PRESSURE

Figure 14. BASE PRESSURE VARIATION WITH NOZZLE PRESSURE RATIO
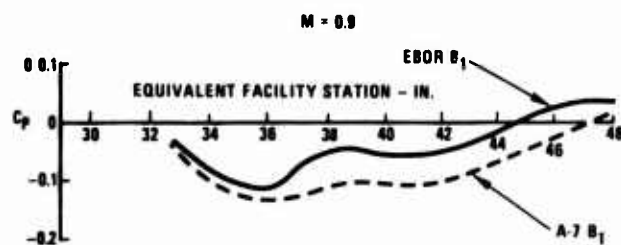
Figure 15. BOATTAIL PRESSURE COMPARISON EBOR/A-7 MODELS
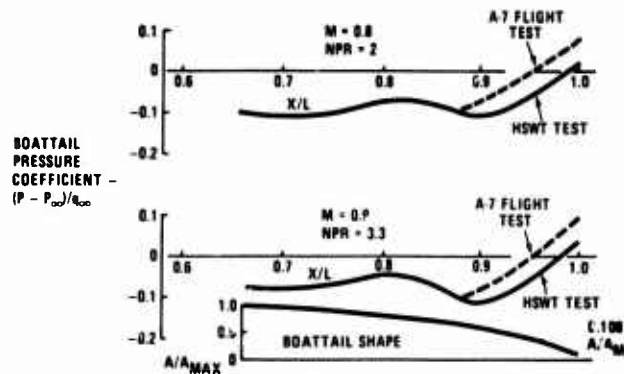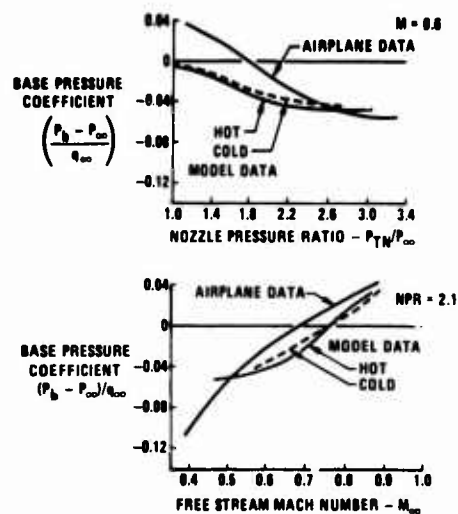
Figure 16. BASE PRESSURE COMPARISON (MODEL TO FLIGHT)

Figure 17. BOATTAIL PRESSURE COMPARISON (MODEL TO FLIGHT)

EXHAUST PLUME TEMPERATURE EFFECTS ON NOZZLE AFTERBODY PERFORMANCE OVER THE TRANSONIC MACH NUMBER RANGE

by

C. E. Robinson
Research Engineer, ARO, Inc.

Dr. M. D. High
Supervisor, ARO, Inc.

E. R. Thompson
Aerospace Engineer, Research and Development Division

Arnold Engineering Development Center
Arnold Air Force Station, TN 37389
USA

SUMMARY

Results of an experimental research investigation on nozzle/afterbody drag are presented. Experimental afterbody (and boattail) drag coefficients and pressure distributions are discussed for an isolated, strut-mounted nozzle/afterbody model for the Mach number range from 0.6 to 1.5. The experimental data were obtained for the basic model with an air-cooled and a water-cooled Ethylene®/air combustor to provide hot-jet duplication as well as cold-jet simulation. The temperature of the nozzle exhaust gas was varied from 530°R (294.4°K) (burner-off) to approximately 2500°R (1388.9°K) for several nozzle pressure ratios from jet-off to those corresponding to a moderately under-expanded exhaust plume. The differences between the cold-jet and hot-jet results are significant, and adjusting the cold-jet pressure ratio to correct for the changes in the jet specific heat ratio with temperature will account for most of the differences observed.

NOMENCLATURE

C_{DAB} Afterbody drag coefficient based on body cross-sectional area

C_{DBT} Boattail drag coefficient based on body cross-sectional area

C_{DT} Total drag coefficient based on body cross-sectional area

C_{DTP} Total pressure drag coefficient based on body cross-sectional area

C_p Pressure coefficient, $(p_i - p_\infty)/q_\infty$

NPR   Nozzle pressure ratio (p_{tj}/p_∞)

p_{E3} Nozzle exit static pressure at 15-deg radial position from top (air-cooled model), psia

p_{E6} Nozzle exit static pressure at 200-deg radial position from top (air-cooled model), psia

p_e Nozzle exit static pressure (water-cooled model), psia

$p_{e_{avg}}$ Nozzle exit static pressure $\left[1/2\left(p_{E3} + p_{E6}\right)\right]$, air-cooled model, psia

p_i Local static pressure on model, psia

p_{tj} Total jet pressure, psia

p_∞ Free-stream static pressure, psia

q_∞ Local dynamic pressure

Re   Reynolds number per foot

STA   Model station from model theoretical nose, in.

T_{GAS} Exhaust gas temperature

W_1 Primary airflow rate, lbm/sec

W_2 Secondary airflow rate, lbm/sec

γ Rates of specific heats, C_p/C_v

INTRODUCTION

A significant amount of testing is involved in developing a new aircraft and power plant. Traditionally, airframe tests have been carried out with careful simulation of the external flow over the airframe but with a rather approximate simulation of the flow issuing from the engine. Similarly, engine tests have been conducted with very careful simulation of the flows internal to the engine but with little or no consideration of the external flow.

In order to properly evaluate afterbody drag, realistic simulation of the internal as well as the external flow is required. The hot-jet exhaust simulation is generally obtained by using a cold fluid (e.g., unheated air) and adjusting the nozzle pressure ratio to match the hot-jet initial inclination angle. Such a procedure then attempts to account for the differences in the plume expansion caused by changes in the jet specific heat ratios with exhaust gas temperature. The plume displacement effects which are simulated in the above manner are inviscid in nature, and although in theory the inviscid plume boundaries are simulated, the effective jet boundaries may differ because of the viscous mixing at the interface of the exhaust flow and the external boattail flow. The nature of the viscous region depends largely on the gradients existing between the internal nozzle flow and the external flow over the afterbody. To investigate this viscous-inviscid interaction, which is particularly strong at transonic speeds, it is necessary to duplicate rather than simulate the engine exhaust gases.

The research reported herein is an experimental effort to determine the effects of the hot jet on the boattail drag and was conducted in two phases, which were differentiated by the combustor design. Phase I was conducted using an Ethylene®/air combustor which had air cooling around the combustor liner. During the Phase I investigation it was observed that the secondary airflow (cooling air) affected the boattail pressure distribution, hence producing drag. This effect opposed the trends resulting from the introduction of the hot jet. Because of the secondary airflow effect, the water-cooled combustor was designed (Phase II) to eliminate secondary airflow and isolate the jet exhaust temperature effect on boattail and afterbody drag. During Phase I, two nozzle configurations representing a typical turbojet nozzle installation and a typical turbofan with low-bypass (1:1) nozzle installation at a military power setting were used. The Phase II investigation utilized the turbojet nozzle installation at a military power setting. Data were obtained for these configurations over the transonic Mach number range. A more detailed report of the results obtained during this investigation is contained in Ref. 1.

APPARATUS

WIND TUNNEL

The AEDC 16-ft (4.88-m) Propulsion Wind Tunnel (16T) is a continuous flow, closed-circuit wind tunnel capable of operation within a Mach number range from 0.20 to 1.60. Tunnel 16T can be operated within a stagnation pressure range from 120 to 4000 psfa (5746 to 191,520 N/m^2), depending on Mach number, with a stagnation temperature variation capability from approximately 80°F (26.7°C) to a maximum of 160°F (71.1°C). Tunnel air is removed and replaced with conditioned makeup air from an atmospheric dryer to facilitate control of vitiation caused by combustion and to control the specific humidity of the tunnel air.

EXPERIMENTAL HARDWARE

The experimental hardware used during the investigation reported herein was the Air Force Flight Dynamics Laboratory (AFFDL)/Lockheed isolated nozzle model previously used for cold-flow nozzle studies reported in Ref. 2. The model, described fully in Ref. 3, was modified to accommodate an Ethylene/air combustor, which was used to provide hot exhaust jet duplication of a typical turbojet operation. The AFFDL/Lockheed isolated nozzle model is an axisymmetric body with an overall length of approximately 153 in. (3.886 m). The model had a 14-deg, half-angle conical nose, which was faired into the primary model diameter of 9.86 in. (25.04 cm). A boundary-layer trip consisting of 0.055-in.(0.13 cm)-diam steel spheres spotwelded to a trip ring at a circumferential spacing of four sphere diameters was located on the conical nose 12 in. (30.48 cm) aft of the cone vertex. The external surfaces of the afterbody and boattail used were the AFFDL/Lockheed configuration CDE1 (Convergent-Divergent Ejector, military power setting) described in Ref. 3. The model was mounted in Tunnel 16T on a strut with an aft sweep angle of 31.8 deg. A sketch showing the basic external model dimensions and the model location in the wind tunnel test section is presented in Fig. 1.

The internal model configurations deviated from the AFFDL/Lockheed CDE1 configuration in order to accommodate the combustor. High-pressure air, which was used to simulate the nozzle exhaust for the cold-flow portion of testing and which was used as an oxidizer in the combustion of Ethylene, was ducted through the strut to a plenum in the forward section of the model.

Combustor (General)

An Ethylene/air combustor based on a National Advisory Committee for Aeronautics (NACA) design (Ref. 4) was used to provide hot exhaust jet duplication. (Ethylene (C_2H_4) is a gaseous hydrocarbon fuel which, when burned in air, produces exhaust products which very closely duplicate the exhaust products of JP-4 burned in air.) Two combustor

configurations were used during the experimental investigation. The overall dimensions of the two configurations were similar, and many components were interchangeable. The first combustor used secondary airflow for cooling the combustor liner and nozzle, whereas the second combustor and nozzle were water cooled.

Air-Cooled Combustor

The air-cooled combustor liner was constructed from stainless steel and had an overall length of 27.45 in. (69.72 cm), an inside diameter of 6.15 in. (15.62 cm), and a wall thickness of 0.125 in. (0.31 cm) (Fig. 2a). The combustor liner terminated in a sonic throat with a contraction ratio of 2.36. Secondary airflow for cooling was ducted to the secondary flow annulus from the primary stream through a variable position sleeve valve. The two air streams, primary and secondary, were mixed at the exit plane of the combustor sonic nozzle and were exited through the common nozzle. Flow conditioners in both the primary and the secondary air streams were used to provide a uniform flow field to the combustor and secondary flow annulus, respectively.

Water-Cooled Combustor

The water-cooled combustor was constructed from copper with an inside diameter of 6.15 in. (15.62 cm) and a wall thickness of 0.125 in. (0.31 cm) (Fig. 2b). The combustor terminated with a convergent-divergent nozzle with a throat diameter of 3.6 in. (9.14 cm). The contraction ratio for this combustor was 2.92. Cooling water was supplied to the combustor through the model strut and flow passages internal to the model. A continuous water flow rate of 70 gal/min (0.0265 m^3/min) was maintained throughout the investigation.

Nozzle Configurations

Two nozzle configurations were used in conjunction with the air-cooled combustor. Each configuration utilized the AFFDL/Lockheed convergent-divergent ejector afterbody and boattail external surfaces (Configuration CDE1) and force balances. The internal military nozzle configuration was constructed from stainless steel and had a throat diameter of 4.8 in. (12.19 cm) and an expansion ratio of 1.0, with a length-to-diameter ratio of 1.25 (Fig. 3a). Since the burner was operated choked, the effective area ratio of the nozzle was 1.44 for this configuration. A secondary air passage sleeve was used to reduce the annulus area around the combustor, thereby restricting the secondary airflow to just the amount required for cooling the combustor liner (approximately 15 percent of primary airflow). The secondary air passage sleeve was removed for the 1:1 bypass nozzle configuration, allowing a secondary airflow rate nearly equal to the primary stream. The 1:1 bypass nozzle configuration was also constructed of stainless steel and had an expansion ratio of 1.06 (Fig. 3b). The nozzle was preceded by a 7.5-in. (19.05-cm) mixing chamber to better simulate the mixing region of the hot core and cold annulus air experienced in turbofan engines.

The internal nozzle configuration used with the water-cooled combustor was a convergent-divergent (CD) military nozzle with a nominal design area ratio of 1.43 and a divergence angle of 6.4 deg. Because of design requirements imposed by water cooling, the base area (4.78 in.^{2}) (30.84 cm^2) of the CD nozzle was significantly larger than the air-cooled military turbojet nozzle (Fig. 3c).

INSTRUMENTATION

The primary instrumentation included external model static pressures, internal model pressures, combustor liner temperatures and mass flow rates of air and ethylene. The external model pressures were integrated to obtain afterbody and boattail pressure drag coefficients. A computed skin friction drag coefficient (Ref. 5) was added to obtain total afterbody and boattail drag coefficients. Mass flow rates were obtained from critical flow venturis.

EXPERIMENTAL RESULTS

GENERAL

The experimental investigation was conducted in two phases. Phase I utilized the air-cooled combustor configuration with both a military turbojet and a 1:1 bypass military turbofan nozzle configuration. Data were obtained using the turbojet nozzle configuration at Mach numbers of 0.6, 0.9, 1.1, 1.2, and 1.5 for a Reynolds number of 2.5 x 10^6/ft (8.20 x 10^6/m). Four nominal temperatures (1000°, 1500°, 2000°, and 2500^oR) (555.6^o, 833.3^o, 1111.1^o, and 1388.9^oK) were investigated at each Mach number. Data were also obtained with the turbojet nozzle using cold exhaust jet simulation for comparison with the hot exhaust jet duplication.

The 1:1 bypass turbofan nozzle configuration was also investigated at Mach numbers of 0.6, 0.9, 1.1, 1.2, and 1.5 at a Reynolds number of 2.5 x 10^6/ft (8.20 x 10^6/m). Two primary stream temperatures of approximately 1000° and 1500^oR (555.6^o and 833.3^oK) were investigated. Cold exhaust jet simulation data for comparison with the hot-jet duplication conditions were also obtained. Cold- and hot-plume data (at the specified exhaust gas temperatures) were also obtained at a Reynolds number of 4.75 x 10^6/ft (15.58 x 10^6/m) and Mach numbers of 0.6, 0.9, and 1.1.

Phase II of the experimental investigation was conducted using the water-cooled combustor configuration. The investigation was conducted at a Reynolds number of 2.5 x 10^6/ft

(8.20 x 10^6/m) over the same Mach number range as Phase I, at four nominal exhaust gas temperatures. The cold exhaust jet simulation conditions were repeated during Phase II for data comparison with the hot exhaust jet duplication. During Phase II, an extensive Reynolds number survey (from 1.0 x 10^6/ft (3.28 x 10^6/m) to 3.0 x 10^6/ft (9.84 x 10^6/m)) was also conducted at Mach numbers of 0.6 and 0.9 over the nominal exhaust gas temperature range.

WATER-COOLED COMBUSTOR CONFIGURATION (PHASE II)

Typical pressure distributions over the boattail obtained from the water-cooled combustor are shown in Figs. 4a through d. The effect that changing the exhaust jet nozzle pressure ratio has on the boattail pressure distribution is shown in Figs. 4a and b for Mach numbers 0.9 and 1.1, respectively. For both Mach numbers, increasing the nozzle pressure ratio caused an increase in the pressure on the boattail. The effect was felt upstream of the boattail on the afterbody at Mach number 0.9 as shown by the pressure difference at the forwardmost station of the boattail. At Mach number 1.1, an imbedded shock occurred on the boattail and restricted the effect of the exhaust plume to the portion of the boattail downstream of the shock. However, the shock tended to move upstream with increasing nozzle pressure ratio. The effect of exhaust plume temperature on pressure distribution at Mach numbers 0.9 and 1.1 is shown in Figs. 4c and d. Increasing exhaust temperature generally causes an increase in pressure on the boattail at Mach number 0.9, with the effect being felt on the afterbody as well. At Mach number 1.1, the imbedded shock isolated the effect of temperature to the segment of the boattail downstream of the shock location.

The component drag coefficients (boattail drag coefficient, C_{DBT}, afterbody drag coefficient, C_{DAB}, and total drag coefficient, C_{DT} – which is the sum of C_{DBT} and C_{DAB}) as a function of nozzle pressure ratio for two of the five Mach numbers investigated at a Reynolds number of 2.5 x 10^6/ft (8.20 x 10^6/m) are shown in Figs. 5a and b. In each case, the cold-plume simulation data are presented with the varying hot-plume duplication for comparison. Above a nozzle pressure ratio of 5.66 (nozzle completely filled), C_{DBT} decreased with increasing pressure ratio. The level of drag coefficient obtained with the hot-exhaust duplication at a given nozzle pressure ratio generally decreased with increasing exhaust temperature. At the subsonic Mach number (0.9), the afterbody drag coefficient, C_{DAB}, decreased slightly with both pressure ratio and exhaust plume temperature increases. At the supersonic Mach number (1.1), however, C_{DAB} was completely insensitive to changes in either of the variables. This insensitivity to pressure ratio and exhaust plume temperature changes is caused by the inability of the pressure ratio and temperature effects to move upstream of the imbedded shock on the boattail (Figs. 4b and d). A complete presentation of the data for the five Mach numbers can be found in Ref. 1.

MATCHING OF THE PLUME INCLINATION ANGLE

If the changes in boattail drag caused by changes in nozzle pressure ratio are primarily inviscid in nature (i.e., are caused by changes in the inviscid plume shape), then corrections to the cold-flow nozzle pressure ratio can be made to simulate the change in plume shape produced by changes in the exhaust gas temperature. The effect of increasing the exhaust gas temperature is to decrease the specific heat ratio (γ) of the exhaust gas with a resulting increase in the exhaust plume initial inclination angle and maximum diameter. Thus, in order to simulate a hot-jet plume ($\gamma < 1.4$) operating at a given pressure ratio using cold air ($\gamma = 1.4$), the nozzle pressure ratio must be increased to offset the effect of γ. The correction for γ effects is to adjust the nozzle pressure ratio at a constant value of drag coefficient to match initial jet inclination angles. The measured performance with the theoretical change in the nozzle pressure ratio predicted from changes in γ at two of the five free-stream Mach numbers investigated are compared in Figs. 6a and b. The correction for γ compensates for a large percentage of the exhaust gas temperature-induced effects. The effect is corrected more accurately at the higher nozzle pressure ratios than at the lower pressure ratios. The effectiveness of the γ correction also appears to be dependent on the free-stream Mach number. The γ correction agrees more closely at Mach number 1.2. At free-stream Mach numbers less than 1.2 the effect of plume temperature is slightly larger than the γ effects predict, while at Mach number 1.5, the γ correction is larger than the measured effects of plume temperature. A complete presentation of the comparison for the five Mach numbers can be found in Ref. 1.

REYNOLDS NUMBER EFFECT

To determine the effect of Reynolds number on boattail drag coefficient, a Reynolds number survey from 1.0 x 10^6 to 3.0 x 10^6/ft (3.28 x 10^6 to 9.84 x 10^6/m) was conducted at Mach numbers of 0.6 and 0.9. Drag data were obtained with cold- and hot-exhaust plumes. The variation of boattail pressure drag with Reynolds number at a constant nozzle pressure ratio and various gas temperatures is shown in Fig. 7. At both Mach numbers 0.6 and 0.9 the effect on C_{DTP} is very small over the range investigated.

AIR-COOLED COMBUSTOR CONFIGURATION (PHASE I)

Phases I and II of the experimental investigation were conducted using the same external afterbody and boattail configuration. The size of the base region was enlarged for the Phase II model because of requirements imposed by water cooling the combustor and nozzle (Fig. 3). This larger base area affected the level of the boattail drag, resulting in greater drag at a given nozzle static pressure ratio than was measured on the Phase I model (Fig. 8). A correction for base area effect for the cold exhaust plume at Mach

number 0.9 was made using the results obtained in Ref. 6 and shown in Fig. 8 to illustrate that the base area was responsible for the Phase II increased drag. The corrected Phase II drag coefficient was comparable to the level measured in Phase I. Sufficient base pressure data to allow correction of C_{DBT} for the remainder of the data were not available; therefore, in reviewing the results of Phase I and comparing them to Phase II, one should remember that the effect of base area was present and that the absolute levels will not be comparable. The trends remain the same, however, for both phases.

Effect of Secondary Airflow on Nozzle Performance (Phase I)

Secondary airflow to provide combustor cooling during hot operation for the air-cooled combustor was introduced into the nozzle as described earlier. During cold-flow operation, the secondary airflow was maintained, and it affected the internal nozzle performance. Figure 9 is a presentation of the boattail drag coefficient (cold-flow) as a function of measured nozzle static pressure ratio for Mach number 1.1. Lines of constant W_2/W_1 are identified. As W_2/W_1 increased, boattail drag coefficient increased at a constant nozzle static pressure ratio. This trend was observed for all of the five Mach numbers investigated, with the exception of Mach number 0.6, as shown in Ref. 1.

Effect of Hot Exhaust on Nozzle Performance (Phase I)

A presentation of the component drag coefficients as a function of nozzle static pressure ratio for two of five Mach numbers investigated is shown in Figs. 10a and b. The drag coefficients were obtained over a wide range of exhaust gas temperatures, using the cold-exhaust plume to establish the relationship between boattail drag coefficient and pressure ratio. An average of the two pressures (p_{E3} and p_{EG}) was used to represent the nozzle static pressure ratio. The boattail drag coefficient for the hot-exhaust plume was then determined at specific values of nozzle static pressure ratio and was compared to the cold-plume drag coefficient on the assumption that the relationship between drag coefficient and pressure ratio remains generally the same even though the exhaust gas temperature is increased. The experimental results of Phase II verified this assumption. The effects of exhaust gas temperature and increasing secondary airflow have opposing trends and tend to cloud the effect of exhaust plume temperature.

CONCLUSIONS

The effect of exhaust plume temperature on afterbody and boattail drag was investigated for two combustor and three internal nozzle configurations installed in an isolated pod. The investigation provided experimental data for the internal and external flow fields. The significant results and conclusions are summarized below. It should be emphasized that the following results and conclusions were obtained for a particular isolated external boattail configuration and may not necessarily be the same for other configurations.

1. For the water-cooled combustor configuration with a turbojet military nozzle, the maximum change in total drag coefficient at a Reynolds number of 2.5×10^6/ft (8.20×10^6/m) was 160 boattail drag counts at Mach 1.1 and 90 counts at Mach 0.9 over an exhaust gas temperature range from 530°R (294.4°K) to approximately 2700°R (1500°K). For each of the Mach numbers investigated, drag coefficient decreased monotonically with increasing exhaust gas temperature at a constant nozzle pressure ratio.

2. From the hot-flow data obtained, it appears that correcting the cold-flow exhaust pressure ratio for changes in specific heat ratio will compensate for a large percentage of the effect of a hot exhaust on afterbody performance. The apparent displacement and entrainment effects produced by differences in viscous mixing between hot and cold exhausts also have to be considered.

3. Exhaust plume temperature affected the afterbody drag coefficient at Mach numbers 0.6 and 0.9. The effect was negligible at Mach numbers 1.1, 1.2, and 1.5.

4. A Reynolds number survey from 1.0×10^6 to 3.0×10^6/ft (3.28×10^6 to 9.84×10^6/m) was conducted at Mach numbers 0.6 and 0.9 for the water-cooled combustor configuration. The effect of Reynolds number variation on total boattail drag coefficient was less than 30 drag counts over the range of the investigation for both Mach numbers 0.6 and 0.9.

5. The boattail drag coefficient obtained with the air-cooled combustor, military nozzle configuration during the cold-exhaust plume investigation showed a strong influence of secondary airflow. When presented as a function of average nozzle static pressure ratio, the boattail drag increased with an increase in percentage of secondary airflow.

6. The boattail drag coefficient obtained with the air-cooled combustor/military nozzle configuration behaved in the same manner as the water-cooled configuration. The maximum change in boattail drag coefficient at a Reynolds number of 2.5×10^6/ft

(8.20 x 10^{6}/m) was 182 drag counts at Mach number 0.9 and 50
drag counts at Mach number 1.5 over an exhaust gas temperature
range from 530°R (294.4°K) to approximately 2900°R (1611.1°K).

REFERENCES

1. Robinson, C. E. and High, M. D. "Exhaust Plume Temperature Effects on Nozzle After-
   body Performance over the Transonic Mach number Range." AEDC-TR-74-9, 1974.

2. Galigher, L. L. "Evaluation of Various Exhaust Nozzles at Free-Stream Mach Numbers
   from 0.6 to 3.0." AEDC-TR-70-256 (AD877896), December 1970.

3. Glasglow, E. R., Santman, D. M., and Miller, L. D. "Experimental and Analytical De-
   termination of Integrated Airframe-Nozzle Performance." AFFDL-TR-72-101, Vol. 1,
   October 1972.

4. Faget, M. A. and Dettwyler, H. R. "Initial Flight Investigation of a Twin-Engine
   Supersonic Ram Jet." NACA RM L50H10, September 1950.

5. Sivells, J. C. and Payne, R. G. "A Method of Calculating Turbulent Boundary-Layer
   Growth at Hypersonic Mach Numbers." AEDC-TR-59-3 (AD208774), February 1959.

6. Aulehla, F. and Latter, K. "Nozzle/Airframe Interference and Integration." AGARD-LS-
   53, May 1972.

ILLUSTRATIONS
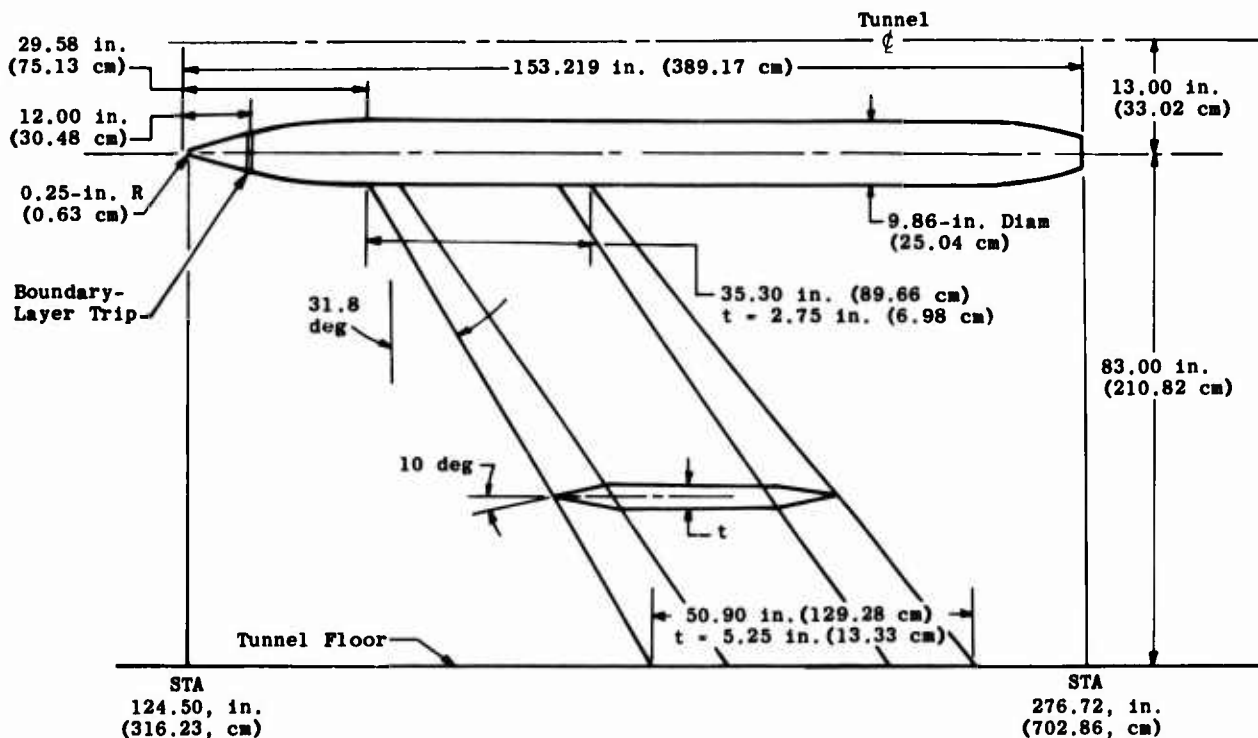
Figure 1. Basic model dimensions and location in test section.
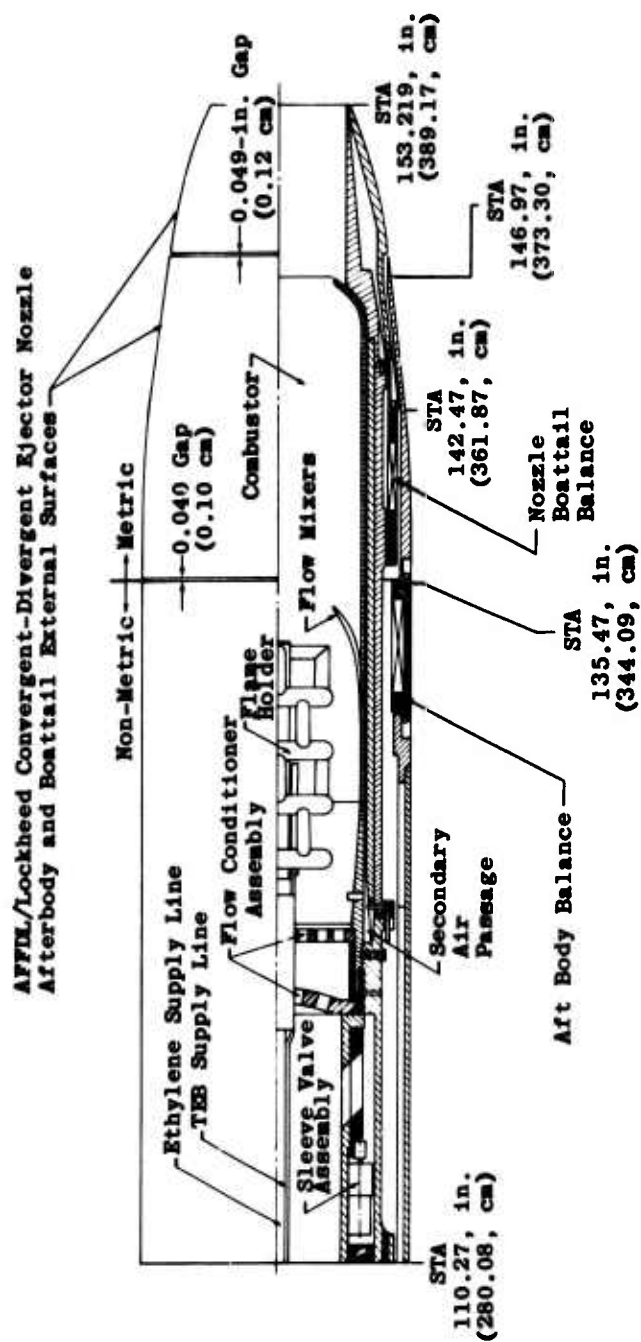
a. Air-cooled combustor

Figure 2. Model internal details.

AFFDL/Lockheed Convergent-Divergent Ejector
Nozzle Afterbody and Boattail External Surfaces

STA 110.27, in. (280.08, cm)

Ethylene Supply Line

TEB Supply Line

Flow Conditioner Assembly

Cooling-Water Supply Passage

Cooling-Water Return Passage

Non-Metric → Metric

0.040-in. Gap (0.10 cm)

Flameholder

Combustor

Flow Mixers

Aft Body Balance

0.049-in. Gap (0.12 cm)

STA 153.219, in. (389.17, cm)

STA 146.97, in. (373.30, cm)

STA 142.47, in. (361.87, cm)

STA 135.47, in. (344.09, cm)

Nozzle Boattail Balance

b. Water-cooled combustor
Figure 2. Concluded.
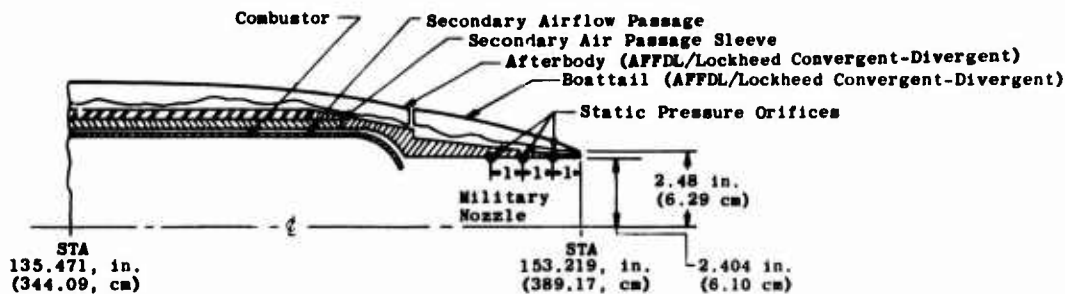
a. Air-cooled combustor, turbojet military nozzle
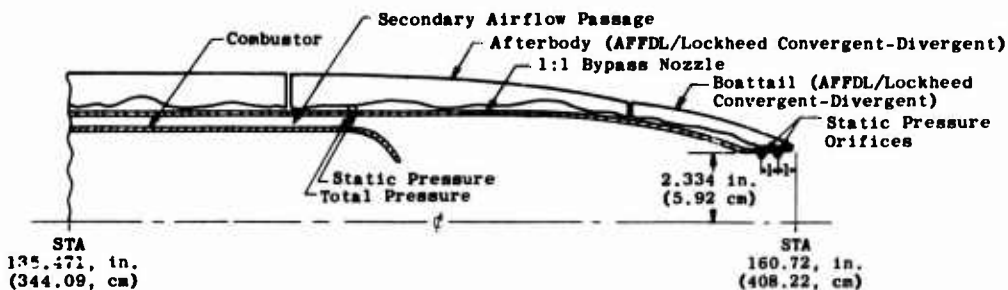
b. Air-cooled combustor, turbofan military nozzle
    (1:1 bypass ratio)
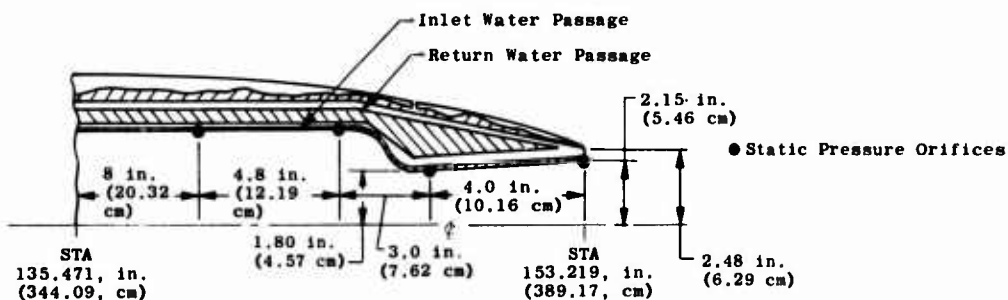
c. Water-cooled combustor, turbojet military nozzle

Figure 3. Schematic of nozzle configurations and nozzle
           pressure instrumentation.
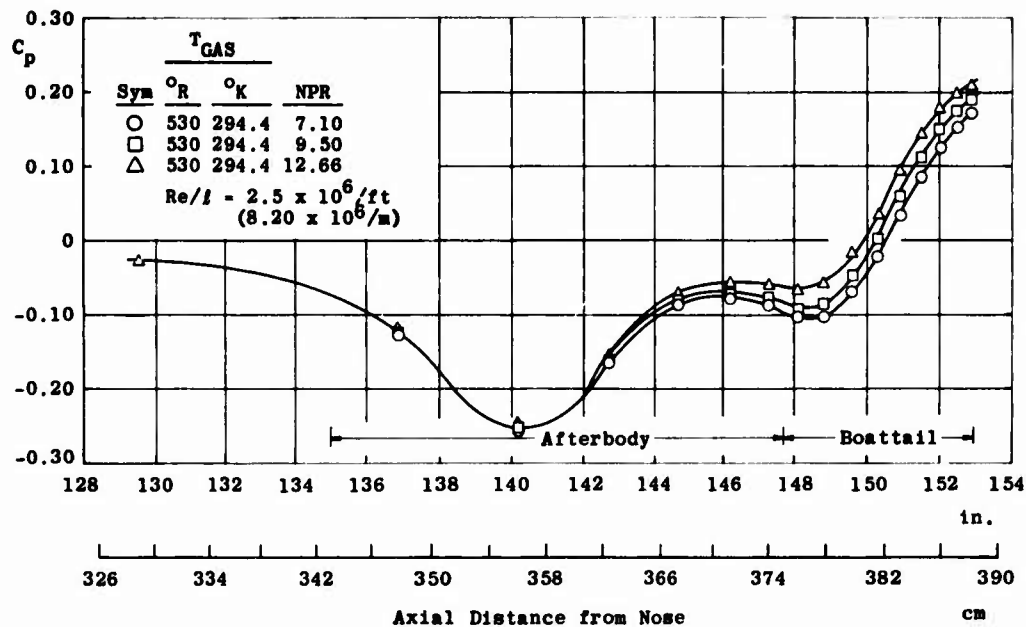
a. Effect of static pressure ratio at $M_\infty = 0.9$
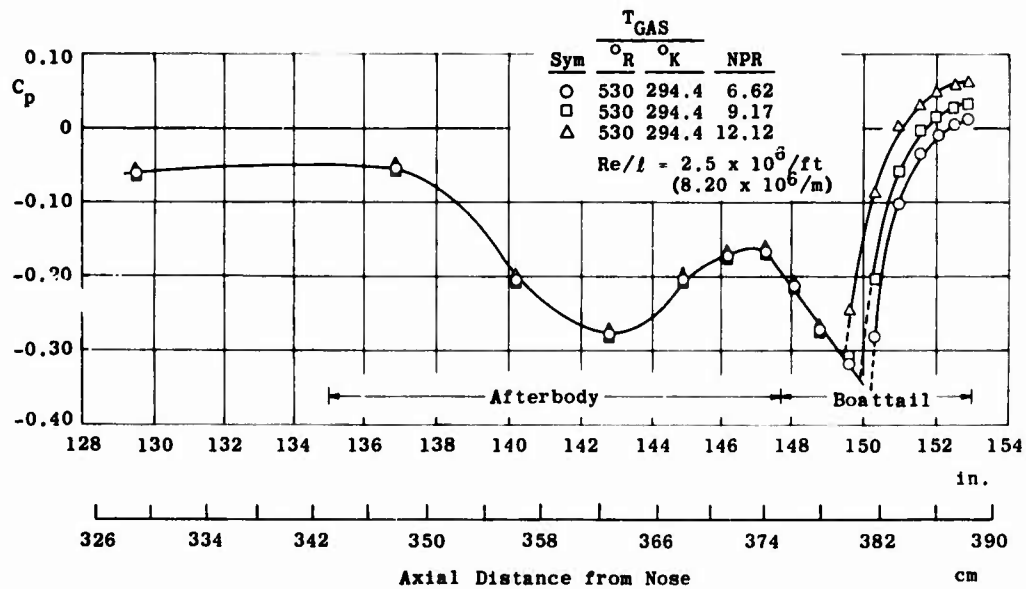
b. Effect of static pressure ratio at $M_\infty = 1.1$

Figure 4. Typical boattail static pressure distributions.
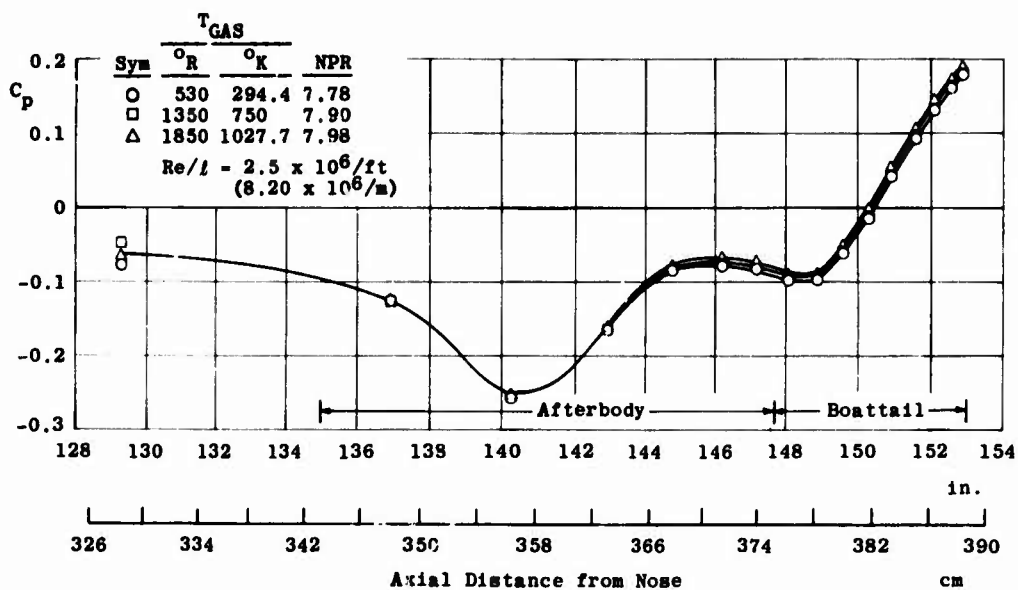
c. Effect of exhaust plume temperature at $M_\infty = 0.9$
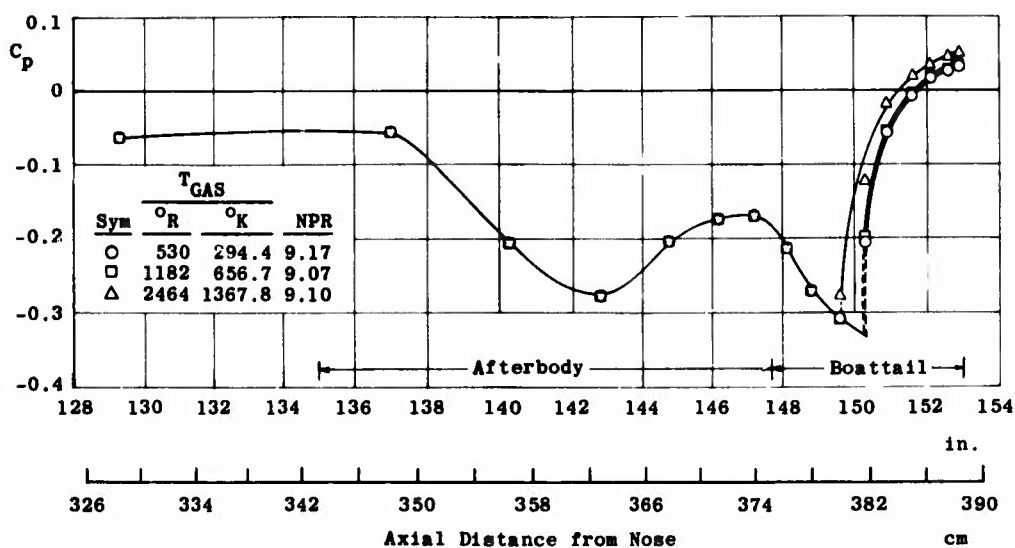
d. Effect of exhaust plume temperature at $M_\infty = 1.1$

Figure 4. Concluded.
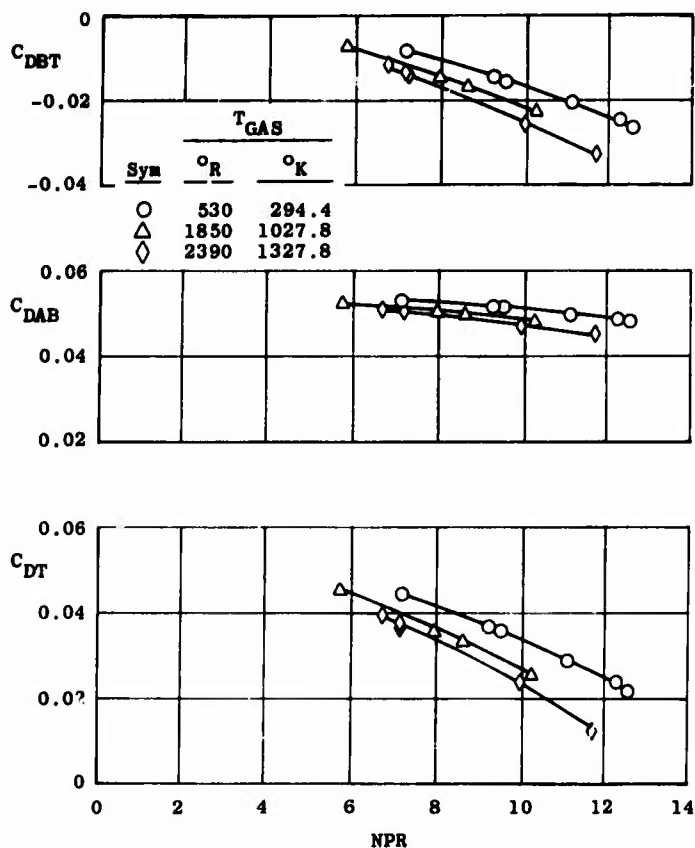
a. $M_\infty = 0.9$
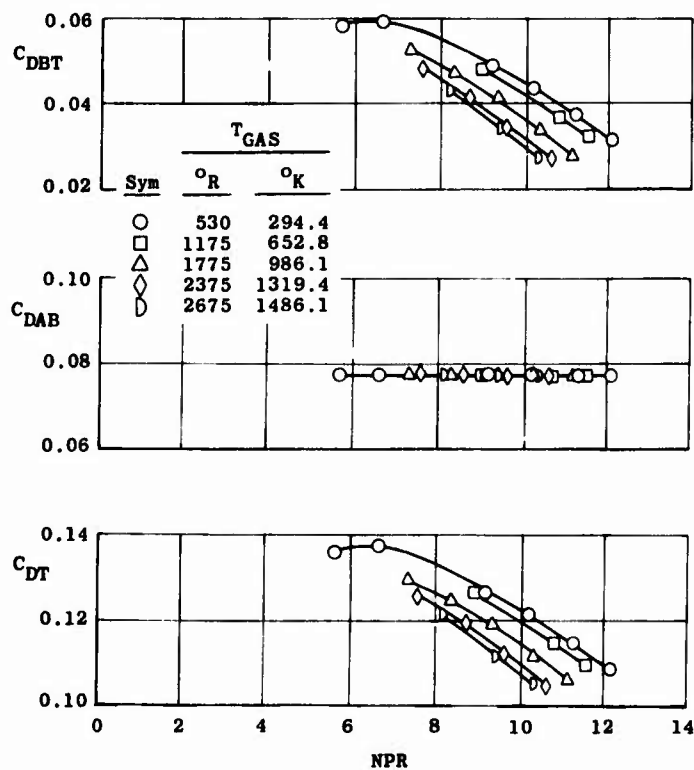
b. $M_\infty = 1.1$

Figure 5. Effect of nozzle pressure ratio on turbojet
nozzle component drag coefficients at various
exhaust jet temperatures using a water-cooled
combustor at Re = 2.5 x 10⁶/ft (8.20 x 10⁶/m).

	γ
———————	1.40
—— · ——	1.37
··········	1.32
—— ——	1.29
—— ·· ——	1.28

Sym	Average γ (Exp.)	T_{GAS} °R	T_{GAS} °K
◯	1.400	530	294.4
△	1.321	1850	1027.8
◇	1.295	2390	1327.8

a. $M_\infty = 0.9$

Sym	Average γ (Exp.)	T_{GAS} °R	T_{GAS} °K
◯	1.400	530	294.4
◻	1.370	1175	652.8
△	1.326	1775	986.1
◇	1.296	2375	1319.4
D	1.286	2675	1486.1

b. $M_\infty = 1.1$

Figure 6. Comparison of the cold-flow data corrected for specific heat ratios to the experimental hot-flow data at Re = 2.5 x 10^6/ft (8.20 x 10^6/m).
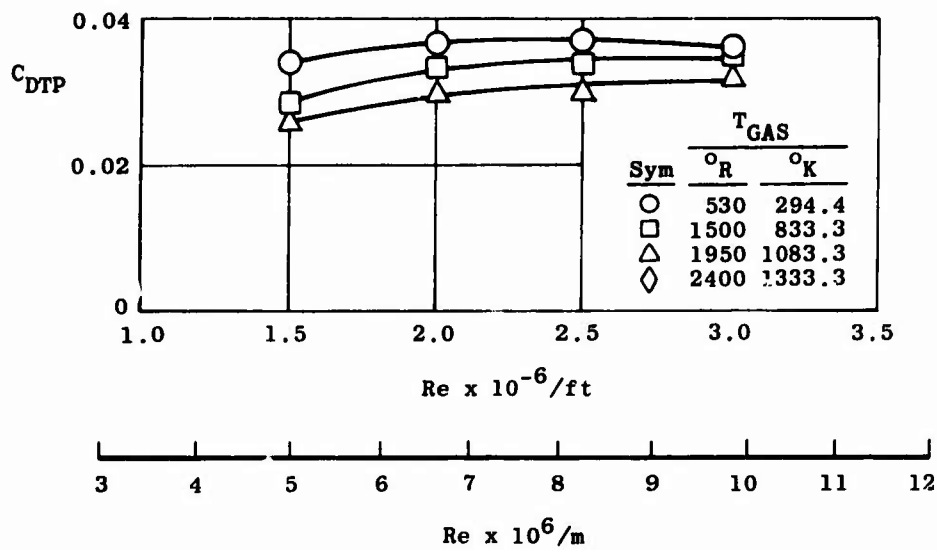
a. $M_\infty = 0.6$
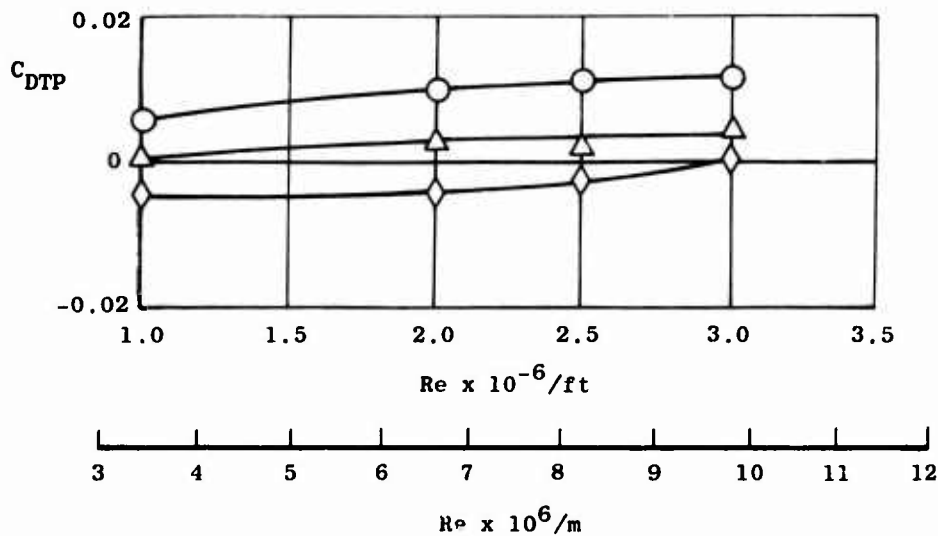
b. $M_\infty = 0.9$

Figure 7. Effect of Reynolds number on total pressure drag coefficient at various exhaust jet temperatures using a water-cooled combustor at a nozzle pressure ratio of 1.5.
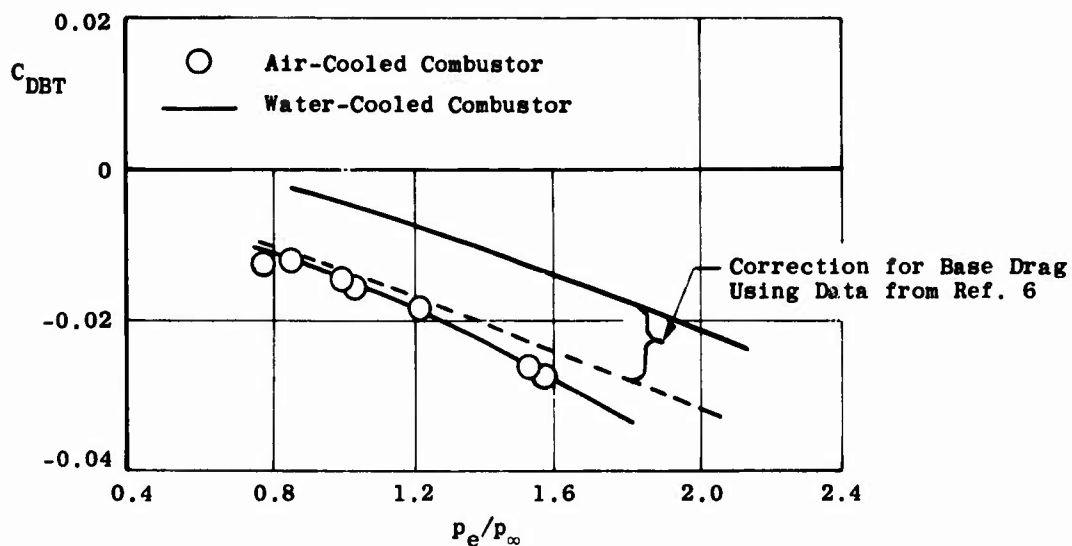
Figure 8. Comparison of boattail drag coefficient levels
using water-cooled and air-cooled combustors at
$M_\infty = 0.9$.
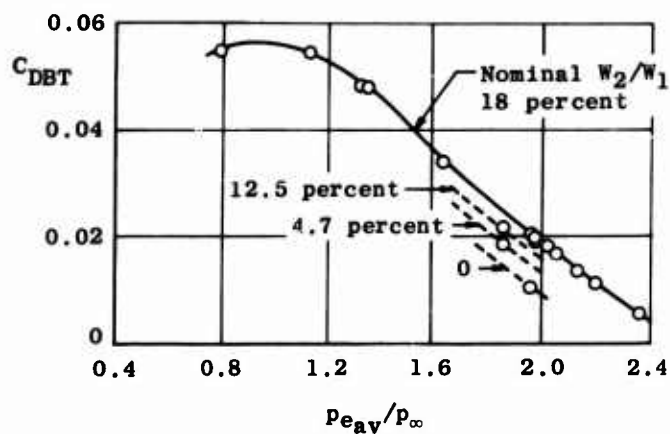
Figure 9. Effect of secondary airflow ratio on turbojet
nozzle component drag coefficients, cold flow,
using an air-cooled combustor at Re $= 2.5$ x
10^6/ft (8.20 x 10^6/m), $M_\infty = 1.1$.

a. $M_\infty = 0.9$

b. $M_\infty = 1.1$

Figure 10. Effect of nozzle pressure ratio on turbojet nozzle component drag coefficients at various exhaust jet temperatures using an air-cooled combustor at $Re = 2.5 \times 10^6/ft$ ($8.20 \times 10^6/m$).

THE INFLUENCE OF NACELLE AFTERBODY SHAPE ON AIRPLANE DRAG

WALTER J. ROHLING
Chief, Aerodynamics Staff
The Boeing Company—Wichita Division
Wichita, Kansas 67210

SUMMARY

A program to design and flight test quiet nacelles suitable for installation on JT3D powered 707 airplanes was conducted by the Wichita Division of The Boeing Company under contract to the Federal Aviation Administration. Design requirements for the quiet nacelle stated that the nacelle shall be flightworthy, flight weight, capable of being certificated to airworthiness standards, and appropriate to the aircraft type. The cruise performance flight tests and the additional performance diagnostic flight tests indicated an unnecessary performance penalty due to the nonoptimum aft translating sleeve and fan nozzle configuration. An unfavorable angle-of-attack-sensitive interplay between the wing and nacelle aft sleeve flow fields was found at all cruise Mach numbers. This penalty was the only significant item discovered during the flight test program which required correction to provide a viable retrofit nacelle configuration.

This paper describes the diagnostic performance flight test, wind tunnel and exhaust system model tests that were conducted to define the required change and to obtain data on the cruise performance benefits that resulted from the change.

LIST OF ABBREVIATIONS AND SYMBOLS

BTU	British Thermal Unit	P	Pressure
C_D	Drag coefficient	PCM	Pulse Coded Modulation
C_{Df}	Fan nozzle discharge coefficient	P_{TF}	Charging station pressure (model analogy to $P_{t2.5}$)
C_{Vf}	Fan nozzle velocity coefficient	P_{am}	Ambient pressure
C_f	Fan gross thrust factor	PSI	Pounds per square inch
C_g	Gross thrust coefficient	$P_{t2.5}$	Fan exit pressure, total
C_{gf}	Fan duct gross thrust coefficient	P_{t7}	Primary nozzle pressure, total
C_p	Pressure coefficient	$P_{t\,rake}$	Total pressure measured by rake
$\bar{\zeta}$	Centerline	$P_{t\,shielded}$	Total pressure measured by shielded probe
D	Drag	P_t	Free stream pressure total
EPNL	Effective perceived noise level	q	Dynamic pressure
FAR	Federal Aviation Regulation	RF	Range factor
FM	Frequency modulation	RF_{BL}	Range factor, baseline nacelle
F_g	Gross thrust	RF_{QN}	Range factor, quiet nacelle
F_n	Engine net thrust	SBID	Small blow-in door
HR	Hour	SFC	Specific fuel consumption
IBM	International Business Machine	TE	Trailing edge
IN	Inch	W	Gross weight
LBID	Large blow-in door	WBL	Wing buttock line
LBS	Pound	α	Angle of attack
M	Mach number	δ	Pressure ratio, P/14.696
NAM	Nautical air miles	δ_{am}	Pressure ratio, P_{am}/14.696
NA 1	Designation for wind tunnel model (Phase 1 quiet nacelle)	Θ_{am}	Temperature ratio, T_{am}/518.688
NA 2	Designation for wind tunnel model (production quiet nacelle)		
NA 5	Designation for wind tunnel model (baseline, i.e., production 707, nacelle)		

INTRODUCTION

To determine the feasibility of, and the net improvement in fuel mileage due to a new engine installation, particular attention must be paid to the placement of the nacelles and pylons on the wing. Wind tunnel and flight experience (References 1, 2, 3 and 4) have shown the sensitivity of airplane drag with respect to placement and local geometry of the pylon, nacelle and wing. The potential interference penalties that can occur are related to the local Mach numbers and pressure coefficients in the channel formed by the wing, pylon, and nacelle and may be manifested as a wave drag and/or as a drag associated with a thickening and possible separation of the boundary layer on the nacelle, pylon or wing. The factors that affect the quiet nacelle geometry are discussed below.

The quiet nacelle program (Reference 1) encompassed two concepts of nacelle acoustic treatment. The Phase I lower goal nacelle utilized an acoustically treated inlet and side cowl; the Phase 2 upper goal nacelle supplemented the noise reduction achieved by the Phase 1 nacelle by including a plug nozzle to suppress jet noise.

In an effort to prevent undue program expenditures, the program was structured to design and fabricate only one configuration side cowl for use on both upper and lower goal configurations. Since the program as initially planned contemplated the flight test of the Phase 2 upper goal configuration, the side cowl was optimized for this configuration. This optimization included the following considerations.

A plug nozzle is somewhat larger in diameter than a conventional nozzle, consequently, the aft translating sleeve for a plug nozzle must be somewhat larger in diameter than a sleeve for a conventional nozzle. The larger diameter sleeve, in turn, establishes the diameter of the aft portion of the side cowl. Since the exit plane of the primary exhaust stream was fixed, the external contours of the lower goal (i.e., conventional nozzle) aft sleeve had to be severely compromised to be compatible with the larger diameter of the side cowl.

Ground testing of the Phase 1 nacelle showed outstanding acoustic performance and static propulsion performance equivalent to, or slightly greater than, the baseline (i.e., production 707) nacelle. Because it was significantly lighter in weight and less complex than the upper goal, Phase 2, nacelle and because of the results obtained from the ground test program, a decision was made to flight test the Phase 1 lower goal quiet nacelle even though it did not represent an optimized configuration.

The Phase 3 flight test revealed cruise performance of the nonoptimized Phase 1 nacelle to be lower than desired. Consequently, a performance improvement program was initiated to identify changes to the nacelle which would improve cruise performance while retaining the demonstrated acoustic performance.

CONFIGURATION

The Phase 1 lower goal quiet nacelle, shown on Figure 1, consists of an acoustically treated inlet, side cowl hydraulically operated fan thrust reversers, 3/4 length side cowls with integral acoustically treated fan ducts, and primary thrust reverser translating sleeve. The primary thrust reverser and exhaust nozzle are unchanged from the production 707 configuration.
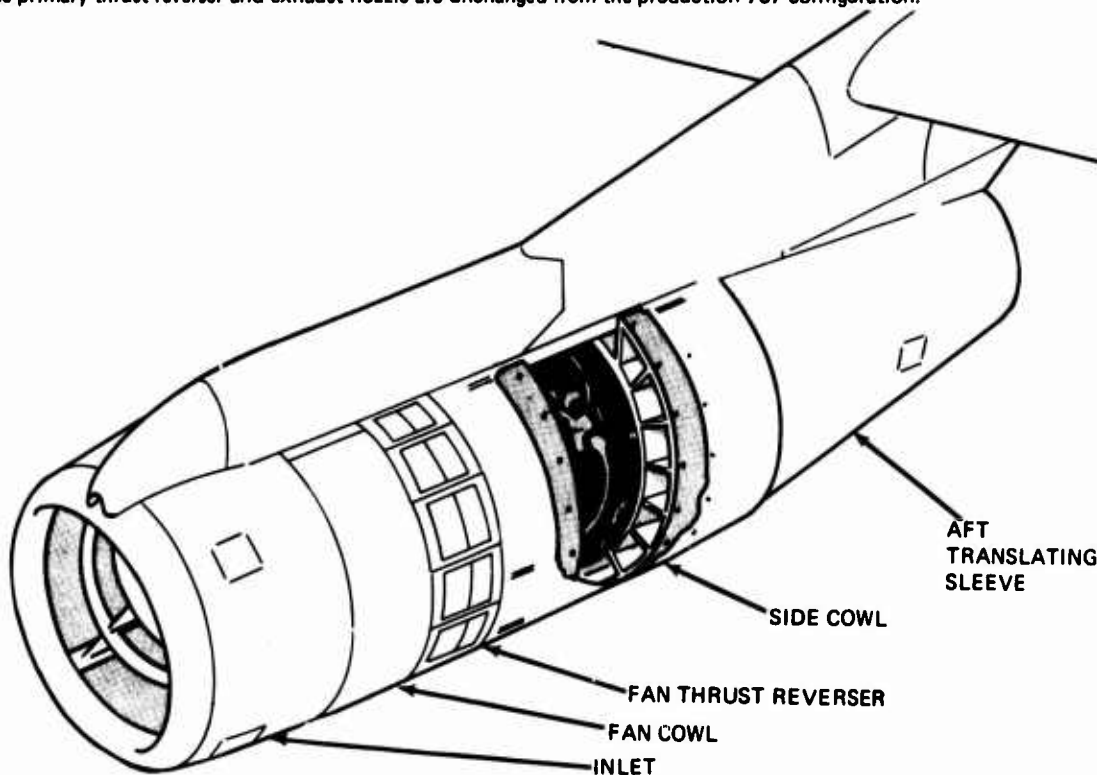
QUIET NACELLE – GENERAL ARRANGEMENT
FIGURE 1

The nacelle inlet includes an acoustically treated nose dome, two acoustically treated concentric rings supported by four struts, and an acoustically treated cowl all with an integral thermal anti-icing system. The fan cowl provides an aerodynamic fairing from the inlet to the fan thrust reverser. The fan air discharge is bifurcated into two streams in the fan thrust reverser section. Reverse fan thrust is accomplished using 14 hydraulically actuated blocker doors and cascades. Each blocker door is mechanically connected to an external door/cascade assembly. After passing through the fan thrust reverser section, fan air enters acoustically treated flow channels in the 3/4 length side cowl. Each side cowl half contains seven flow channels which are separated by six acoustically treated radial splitters. The splitters are formed by two acoustic linings separated by an impermeable septum.

BASELINE TEST PROGRAM

The Phase 1, lower goal, quiet nacelle was subjected to an extensive ground test program. To provide a direct comparison to the current production nacelle, similar tests were also accomplished on a baseline nacelle. Specific areas of investigation included propulsion performance, acoustic performance, systems performance, durability and engine/nacelle compatibility. The results of the propulsion performance testing are discussed in the following paragraphs.

Propulsion Ground Tests

In Phase 1, an extensive series of ground tests were accomplished to define the performance of a JT3D-3B engine installed in a quiet nacelle. Similar tests were accomplished using a production 707 nacelle with a large blow-in door (LBID) and a small blow-in door (SBID) inlet to provide baselines for comparison. Most late production aircraft are equipped with the LBID inlet. The static thrust and specific fuel consumption results of the quiet nacelle and the LBID inlet baseline nacelle are shown on Figure 2. As can be seen from Figure 2, the quiet nacelle takeoff thrust and SFC are slightly improved with respect to the baseline nacelle.
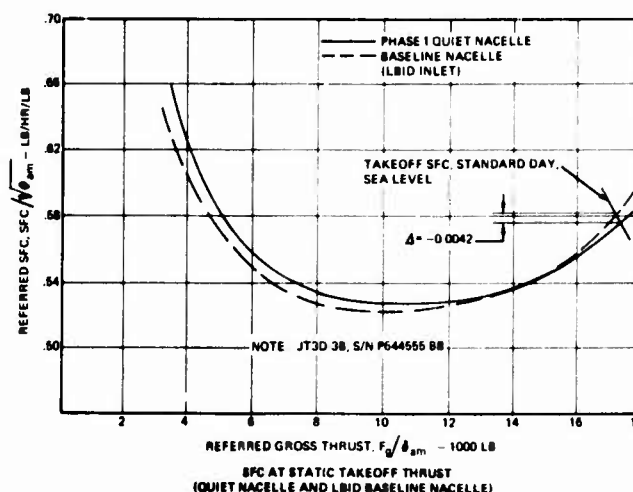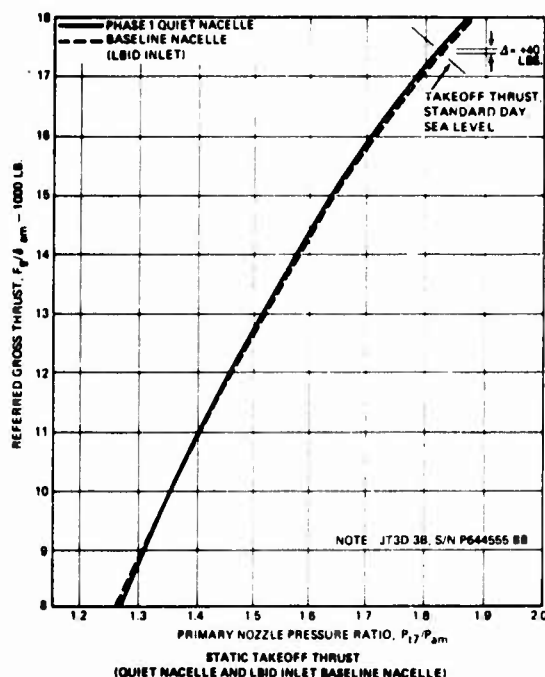
**COMPARISON OF STATIC PERFORMANCE OF PHASE 1
QUIET NACELLE AND LBID INLET BASELINE NACELLE
FIGURE 2**

A series of ground tests were performed to estimate the performance of the quiet nacelle fan ducts. These tests included full-scale and one-fifth scale half model tests of the quiet nacelle and baseline fan ducts. The model tests are required to determine cruise thrust coefficients at cruise nozzle pressure ratios since full scale ground testing is limited to fan nozzle pressure ratios just below the critical pressure ratio. The results of these tests are summarized on Figure 3. These results as well as the results of the other ground tests led to the conclusion that the lower goal configuration should be flight tested in lieu of the upper goal configuration.
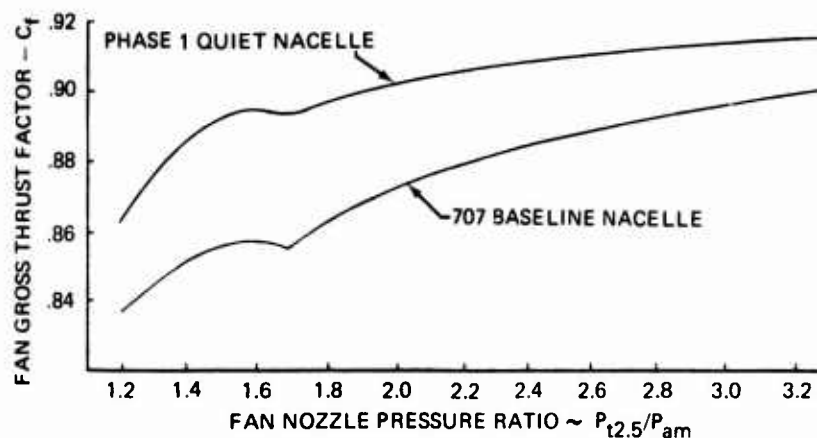
**PHASE 1 QUIET NACELLE AND 707 BASELINE NACELLE
FAN GROSS THRUST FACTORS
FIGURE 3**

Flight Tests

The objectives of the flight test program were to:

- Measure acoustic and aerodynamic performance of an unmodified production 707-300B/C aircraft to establish a baseline.

- Measure acoustic and aerodynamic performance of the baseline aircraft after installation of the Phase 1, lower goal, quiet nacelle.

- Functionally check quiet nacelle mechanical components, systems, and structure under flight operational conditions.

- Analyze acoustic data to determine the effective perceived noise level (EPNL) changes between the baseline aircraft and the quiet nacelle configured aircraft.

- Document FAR Part 36 noise levels for the 707-300B/C airplane with quiet nacelles.

The results of the acoustic testing showed that the airplane could be certified to FAR 36. Functional checks were also

satisfactory. The results of the aerodynamic cruise performance testing are described in the following paragraphs.

Flight tests were accomplished to determine the airplane cruise performance (fuel mileage) for both the quiet nacelle and baseline (i.e., production nacelle) configurations. The cruise test conditions were performed in stabilized level flight at six Mach numbers ranging from 0.70 to 0.86. These conditions were accomplished at airplane gross weight-to-ambient pressure rations (W/δ) of 0.7×10^6, 1.0×10^6, and 1.2×10^6 pounds (nominal). Except for nacelle configuration, the airplane configuration, gross weight, center-of-gravity, and system operations were nearly identical for both the quiet nacelle and baseline configurations.

Airplane and engine performance data were automatically recorded during three to five-minute stabilized conditions with a magnetic tape data acquisition system. The reference static pressure for all conditions was determined from a trailing cone static pressure pickup.

The data were processed using existing IBM 360 computer programs that first established calibrated parameters and then performed calculations using the calibrated parameters.

Installation of the Phase 1 lower goal quiet nacelles on the 707-300B Advanced/C airplane resulted in reduced cruise efficiency at all test Mach numbers and W/δ conditions as shown by Figure 4. The range factor penalty at a Mach number of 0.80 is shown on Figure 5. At a typical W/δ of 1.1×10^6 pounds, the penalty was 3.5 percent. This represents a larger penalty than expected.
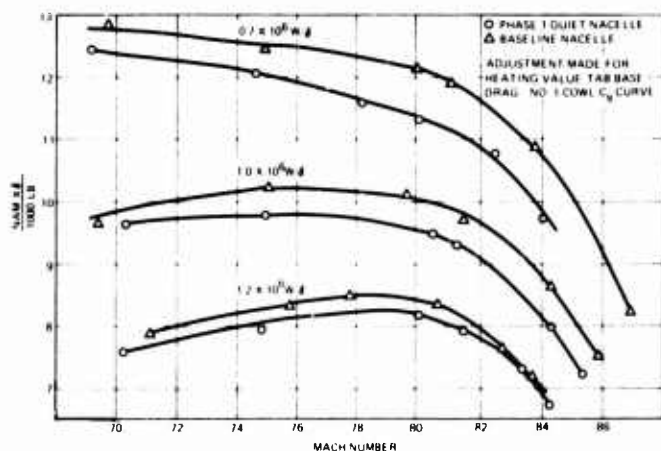
COMPARISON OF FUEL MILEAGE
FIGURE 4
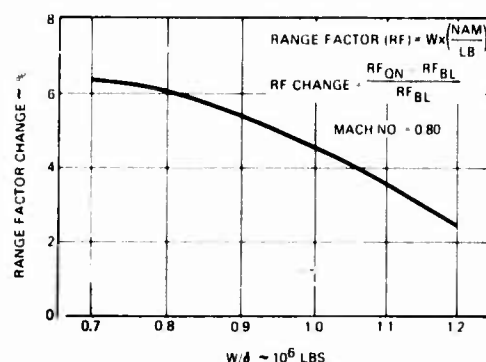
PHASE 1 QUIET NACELLE RANGE PENALTY
FIGURE 5

All data presented on Figure 4 were corrected to standard conditions. In addition, corrections were applied for differences between test W/δ and nominal W/δ, for variations of energy altitude occurring during the test period as well as variations in the heating value of the fuel from a standard 18,400 B.T.U./lb. The drag of the trailing cone was also accounted for in the calculations.

Additional adjustments were made to the quiet nacelle performance data for tab area base drag and for gross thrust deviations on the number one engine. These are explained in more detail below.

The fan nozzle exit area on the Phase 1 nacelles was found to be slightly oversized during ground tests. Tabs were added to reduce the exit area. This created an additional base area of approximately 40 square inches per nacelle that will not be incorporated on a production version. Therefore, this incremental base drag penalty, calculated using base pressures measured in flight, was removed from the quiet nacelle cruise data by adjusting the specific fuel consumption.

An improvement in the design (repositioning the radial splitters in the fan thrust reverser) was made after the fabrication of quiet nacelle unit number one. This design improvement was incorporated in units number two and on. Specific fuel consumption was adjusted to eliminate the bias introduced by the nonstandard configuration of unit number one.

The absolute levels of baseline cruise data are not representative of a new airplane since the test airplane had accumulated approximately 15,900 hours of airline service. Although significant aerodynamic discrepancies were corrected, the airplane did not represent "roll out" conditions during test. Additionally, the absolute level of data was affected by the drag induced by test instrumentation. Since, however, the airplane configuration remained the same for both baseline and quiet nacelle tests, incremental changes in fuel mileage data are valid.

PERFORMANCE IMPROVEMENT PROGRAM

The performance improvement program included a diagnostic flight test program, wind tunnel tests to assess possible nacelle changes, and additional model nozzle tests. The diagnostic flight test program yielded static pressure data on the translating sleeve and wing lower surface, total pressure data in the fan wake and flow visualization by means of tuft photographs. The Mach number and W/δ ranges investigated were the same as those flown in the Phase 3 flight test.

Diagnostic Flight Test

The objectives of the diagnostic flight test program were to identify areas of the nacelle affecting cruise performance and to identify suitable changes to the nacelle to improve cruise performance without impacting the demonstrated acoustic performance.

For those tests, the airplane was configured with quiet nacelles on engines one, two and three. A standard baseline (i.e., production 707) nacelle with a large blow-in door inlet was installed on engine number four.

Prior to the first series of flights, additional static pressure measuring instrumentation was installed on the aft portion of the nacelle side cowl and on the aft translating sleeve. Tufts were installed on the nacelles and struts to permit airflow visualization for inflight evaluation. The first flight was preceded by a static engine ground run on number three engine to acquire surface static pressure and tuft data during ground operation.

The first series of flights were performed to obtain static pressure and flow visualization data at cruise conditions. Data were obtained with number three engine operating at three different thrust levels at each of three Mach numbers. The thrust variations were performed to determine the degree of influence thrust level might have on the nacelle afterbody pressure patterns. The preceding test conditions were accomplished at airplane gross weight-to-pressure altitude ratio factors of 0.7×10^6, 1.0×10^6, and 1.2×10^6 pounds. These data points were representative of flight test conditions during which previous airplane fuel-mileage performance was determined.

During this initial series of flights, movies of the nacelle tufts were taken from a Boeing owned F-86 chase airplane to further support the nacelle airflow and nacelle static pressure data analysis.

After the first series of flights, the airplane was further instrumented with fixed and traversing total pressure rakes on the aft portion of the nacelle and wing static pressure belts.

The second series of flights was accomplished using this additional instrumentation. Again, data were recorded with number three engine set at three different thrust levels at three Mach numbers for W/δ of 1.0×10^6 and 1.2×10^6 pounds and four Mach numbers at W/δ of 0.7×10^6 pounds.

Subsequent to this second series of flights, a static engine ground run was accomplished on engines one and three to check the engine thrust calibration and to acquire total pressure data on the quiet nacelle afterbody area of engine number three.

The airplane instrumentation for the Phase 3 flight test program consisted basically of conventional airplane and engine performance type parameters. Additional instrumentation required for the diagnostic flight test program consisted of the following:

● Static pressures on the aft translating sleeve of engine number three:

12 statics on the 180° radial
16 statics on the 200° radial } Viewed from
23 statics on the 270° radial } rear of engine
16 statics on the 340° radial } looking forward

● Wing static pressure belts on the top and bottom of the wing just inboard of the outboard engine struts

● Three total pressure rakes at 180°, 200° and 270° radial positions at Nacelle Station 270

● A traversing wake rake mounted on the inboard side of engine number three strut with the pitot and static rake located on Nacelle Station 275. The preceding instrumentation is shown on Figure 6.

WING STATIC PRESSURE BELTS   STATIC AND TOTAL PRESSURE RAKES

TRAVERSING TOTAL PRESSURE RAKE

DIAGNOSTIC FLIGHT INSTRUMENTATION
FIGURE 6

These additional static and total pressures were measured using scanner valves to sample the pressures. An aft body trailing cone system was used as the reference static pressure for all static pressures measured. A shielded pitot probe pressure was used as the reference total pressure for all total pressures measured. All scanner valve pressures were recorded on magnetic tape using an FM data system; engine and airplane performance data were recorded on magnetic tape using a PCM type data system.

Performance data were reduced using existing IBM 360 computer programs. Data outputs were tabular listings of both calibrated and calculated parameters and plots of time history data.

Static pressure survey data were reduced using a computer program to compute the pressure coefficient ($\Delta P/q$) for each port measured; the results were plotted versus port location. Total pressure data were also plotted as measured ΔP using two references: (1) Port minus shielded pitot pressure, and (2) port minus fan exit total pressure.

The photographs of the tufts shown on Figure 7 give a visual indication of airflow on the nacelle. Photo (1) shows the inlet and side cowl tufts of the quiet nacelle to be well behaved (steady). Some tuft movement (indicating low momentum airflow) near the turbocompressor fairing is indicated by the blurring near the end of the tufts. Photo (2) shows well behaved tufts at the fan exit but indicates low momentum airflow along the lower portion of the primary aft sleeve over the last 50 percent of sleeve length. The tufts on the sailboat fairing on top of the sleeve are well behaved. Photo (3) indicates that, at increasing W/δ, the low momentum airflow, while still present, acts over a smaller length of the sleeve. Photo (4) depicts flow visualization of the baseline (production short cowl) nacelle at the same condition. The tufts on the sleeve are well behaved. Note, however, the severe tuft movement on the sailboat fairing. These photographs are indicative of tuft behavior during all conditions flown.
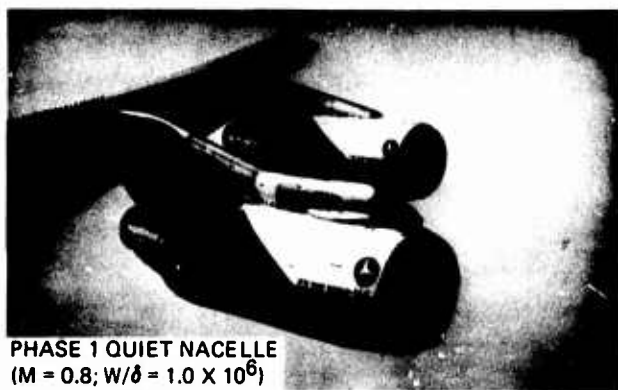
PHASE 1 QUIET NACELLE
(M = 0.8; W/δ = 1.0 X 10^6)
(1)
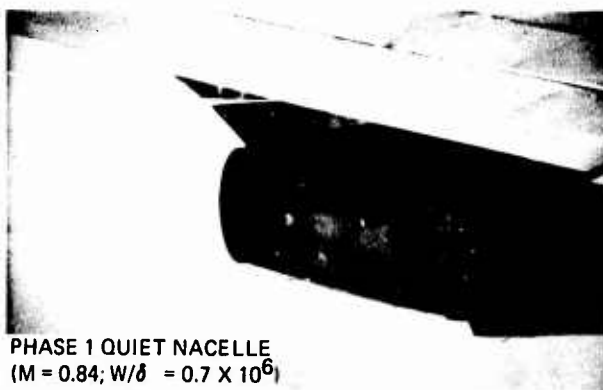
PHASE 1 QUIET NACELLE
(M = 0.84; W/δ = 0.7 X 10^6)
(2)

PHASE 1 QUIET NACELLE
(M = 0.84; W/δ = 1.0 X 10^6)
(3)
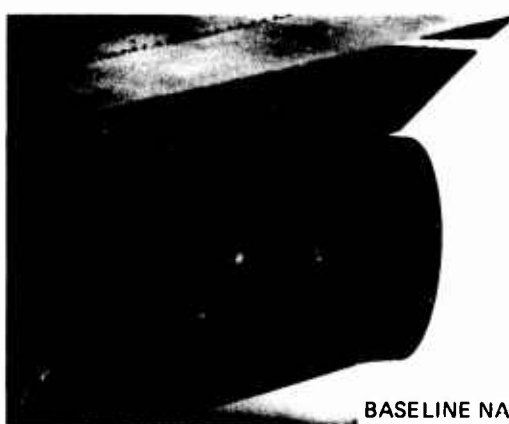
BASELINE NACELLE
(M = 0.84; W/δ = 1.0 X 10^6)
(4)

COMPARATIVE AIRFLOW VISUALIZATION
FIGURE 7

The problem area indicated by the tufts is the aft translating sleeve. The magnitude increases with decreasing W/δ as was found on the fuel mileage tests.

Typical static pressure data at M = 0.8 for W/δ = 0.7 x 10^6 and 1.2 x 10^6 pounds are shown on Figure 8. Data are presented for the 180° radial, 340° radial, and the wing belt. As W/δ decreases, the wing and sleeve negative pressures increased in both magnitude and area of coverage yielding a higher drag component on the sleeve. While positive pressures exist near the leading edge of the wing, there is a very little forward projected area on the side cowl for this pressure gradient to act against.
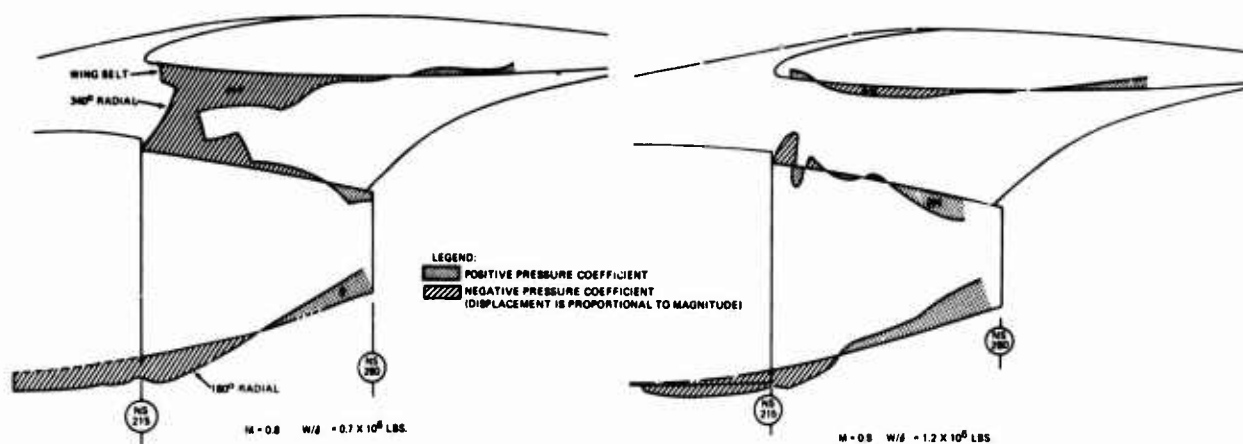
TYPICAL WING-NACELLE-AFTERBODY STATIC PRESSURE DISTRIBUTION
FIGURE 8

Total pressure surveys were conducted using fixed rakes and a translating rake. Data from the translating rake indicates an airflow momentum deficiency near the strut-cowl intersection. A typical condition is presented on Figure 9. A typical pressure survey from the fixed 180° radial rake is shown on Figure 10.
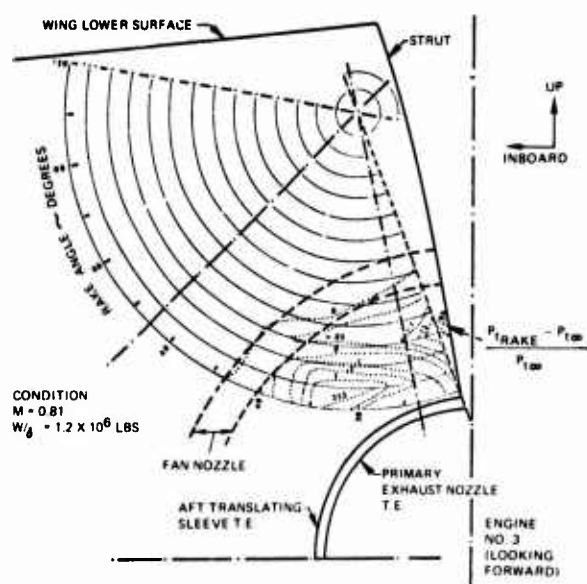
TRANSLATING RAKE TOTAL PRESSURE SURVEY
FIGURE 9
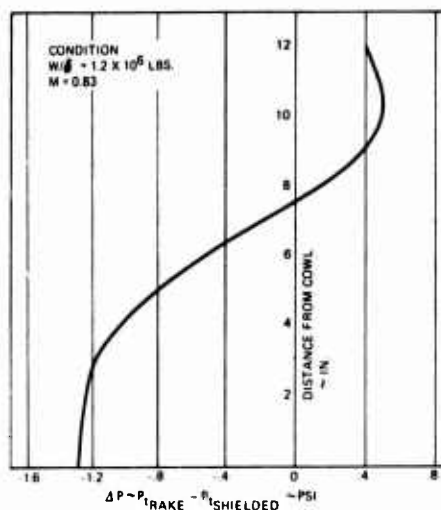
180° RADIAL FIXED RAKE TOTAL PRESSURE SURVEY
FIGURE 10

The major problem area indicated by the pressure data and the tufts is the aft translating sleeve. The static pressures acting on the aft sleeve were integrated to determine the magnitude of the forces as well as to determine the trend of the forces with angle-of-attack. Although this integration of the pressures acting on the aft sleeve does not really define the total pressure drag (because the pressures act on other portions of the nacelle, pylon and wing) the magnitudes and trends of the data did provide direction as to the configurations that should be investigated in the wind tunnel. Also the tuft activity observed indicated that a reduction of the sleeve area would improve the drag.

Additional indications that the aft sleeve was the major problem area were provided by examining the trends of data of Reference 3. Figure 11, taken from Reference 3, shows how the afterbody drag for a 720B fan engine installation (short duct) is affected by wing angle-of-attack and engine fan pressure ratio. As can be seen from Figure 11, the afterbody drag is extremely sensitive to wing angle of attack and relatively insensitive to engine pressure ratio. As noted in Reference 3, the drag change is predominantly due to pressure drag, and is primarily a function of the pressure field around a given wing-nacelle-strut configuration. A predominantly negative pressure field between the wing and nacelle afterbody results in drag forces on the nacelle afterbody and in forward forces on the lower surface of the wing in that area. Therefore, a pressure drag on the nacelle afterbody does not necessarily result in a net drag on the airplane.

M = .80

FAN PRESSURE RATIOS, $\frac{P_{t2.5}}{P_{AM}}$, 2.0, 2.2 AND 2.4

WERE EXTRAPOLATED FOR WING ANGLES, α_W, ABOVE 3.7°
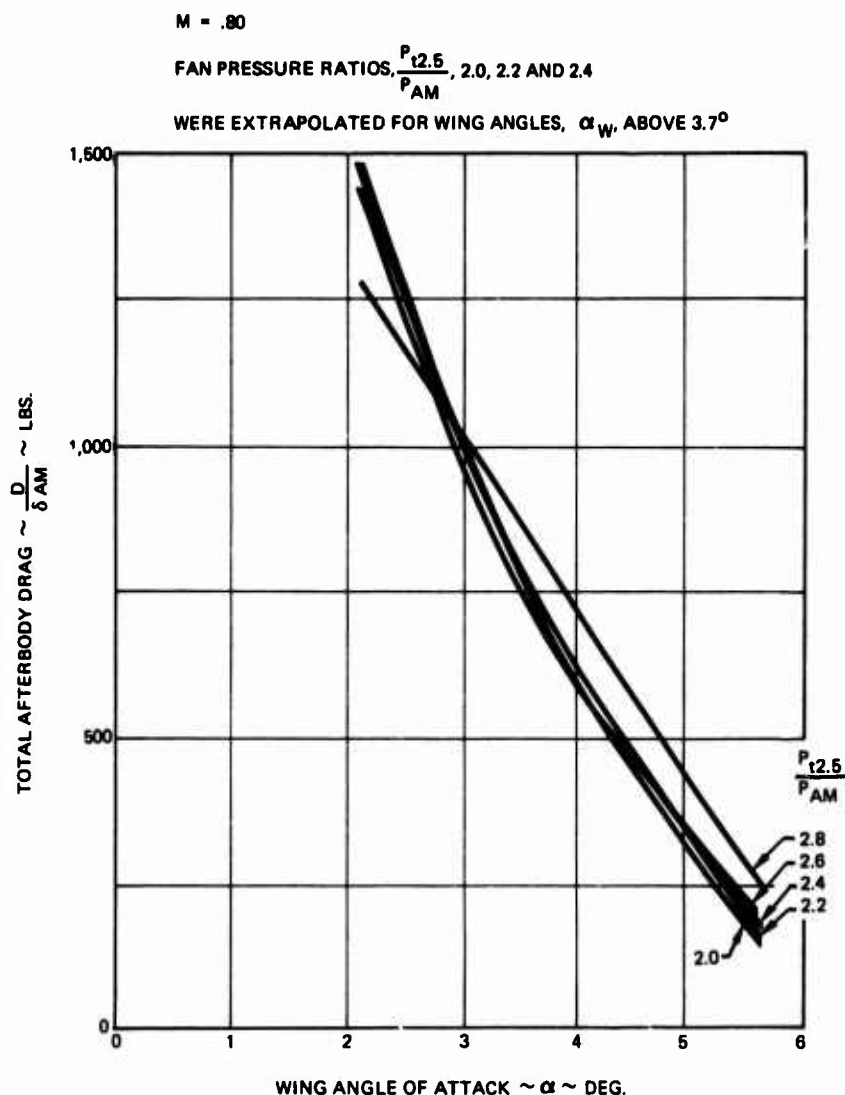
VARIATION OF AFTERBODY DRAG WITH
LOCAL WING ANGLE OF ATTACK
FIGURE 11

Configuration Changes For a Production Quiet Nacelle

Based upon the foregoing considerations the following changes were made to lower goal configuration to define a production quiet nacelle configuration.

- Sleeve projected area reduced to equal that of the baseline (production short cowl) nacelle.

- Fan nozzle exit moved from Nacelle Station 215 to Nacelle Station 212.

- Aft portion of side cowl contoured to provide proper fan nozzle area.

The new sleeve has a more gradual afterbody curvature which reduces wing-nacelle interference and sleeve pressures and provides less projected area for these pressures to act against. By moving the fan nozzle forward and contouring the aft portion of the side cowl, a projected area is generated for the wing leading edge positive pressures to act against and wing-nacelle interference is further reduced. An additional benefit of moving the fan nozzle forward is to further reduce the possibility of impingement of primary exhaust efflux on the fan nozzle during abnormal reverse thrust operation.

To establish the performance improvements resulting from these changes, wind tunnel tests and fan duct model tests were performed as described in the following paragraphs.

Wind Tunnel Test Program

The diagnostic flight test results suggested areas in which drag reduction might be attained by modifying the Phase 1 nacelle design. A Boeing funded wind tunnel test was initiated to confirm these improvements and to define the magnitude of the drag changes.

One-tenth scale models of the baseline (standard 707 short duct) nacelle, the Phase 1 quiet nacelle, and the proposed production quiet nacelle were tested. The models were blowing nacelles which used an external compressed air source to simulate both the fan and primary jet flow. A critical flow venturi was used to determine the mass flow rates. The three nacelle models are illustrated on Figure 12.
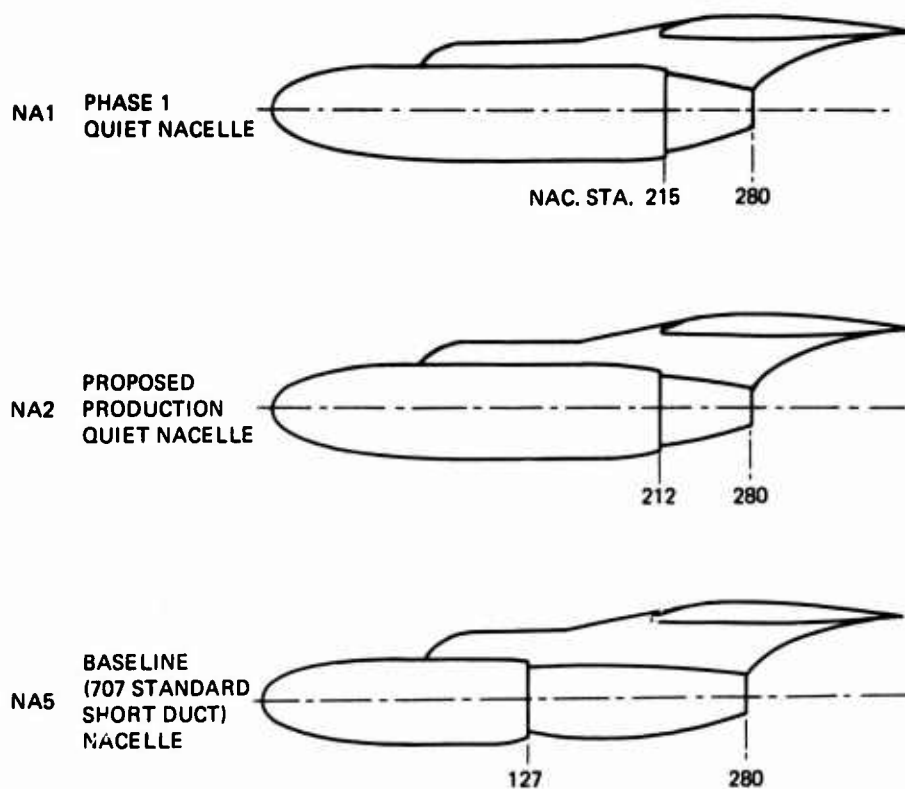
COMPARISON OF WIND TUNNEL NACELLE MODELS
FIGURE 12

The nacelles were mounted on the outboard engine location of a one-tenth scale partial wing of the 707-320B airplane as illustrated on Figure 13. The wing was mounted vertically from the floor of the wind tunnel test section as shown on Figure 14.
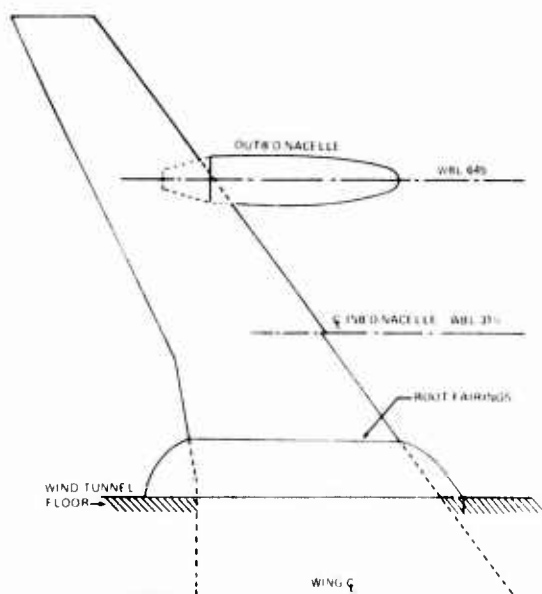
NACELLE INSTALLATION ON WIND TUNNEL MODEL WING
FIGURE 13

FRONT
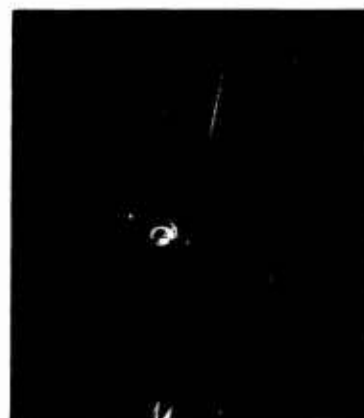
REAR

BLOWN NACELLE MODEL IN WIND TUNNEL
(MODEL NA2)
FIGURE 14

Testing was accomplished in the Boeing Transonic Wind Tunnel located in Seattle, Washington. Test data were force balance measurements, wing and nacelle surface pressure measurements, as well as lamp black flow visualizations. The Mach number range was 0.70 to 0.86 and angles of attack varied between zero and six degrees. The blown airflow was adjusted to obtain fan exit to freestream total pressure ratios from no flow up to 3.0. Ratios of 2.5 and 2.7 received primary emphasis for simulation of cruise conditions.

Surface pressure data obtained on the Phase 1 nacelle model (NA1) correlates very well with similar data obtained in flight as revealed by a comparison of Figure 15 (model data) and Figure 8. The similarity of the pressure coefficient (C_p) trends is obvious. The minor differences in the absolute C_p level are attributed primarily to differences in angle of attack and fan jet velocity.

CONDITIONS:
M = 0.80
$\alpha = 3^0$
$P_t/P_\infty = 2.7$
340^0 COWL POSITION
INBOARD LOWER WING
$W/\delta \approx 0.7 \times 10^6$ LBS.

LEGEND:
▨▨▨ POSITIVE PRESSURE
COEFFICIENT
///// NEGATIVE PRESSURE
COEFFICIENT
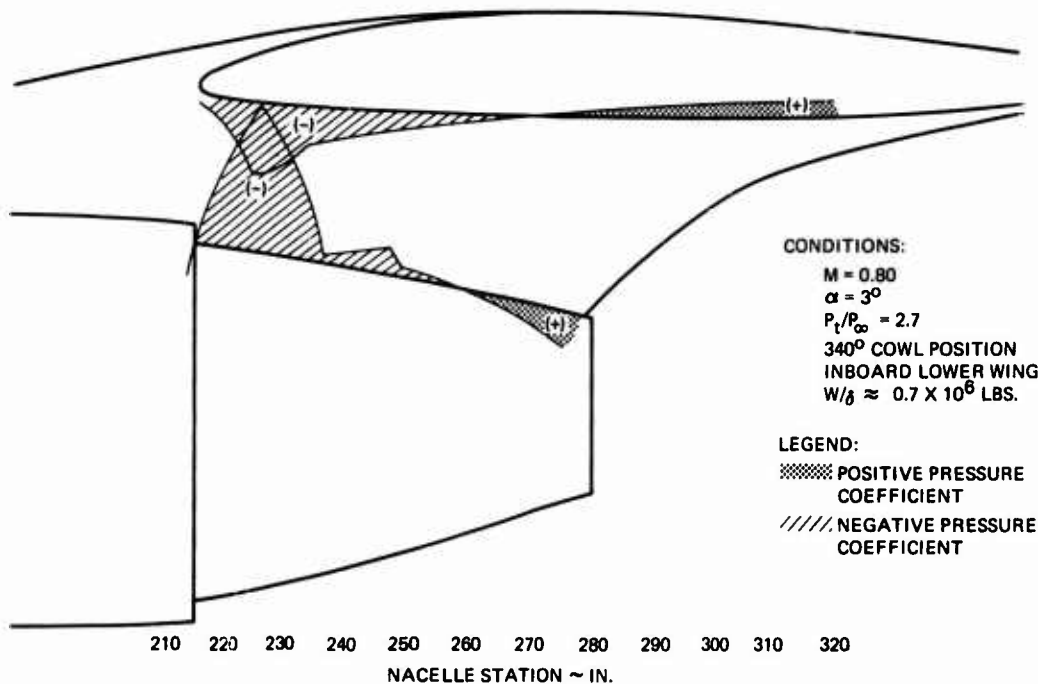
NACELLE STATION ~ IN.

NA1 WIND TUNNEL MODEL WING-NACELLE-AFTERBODY
STATIC PRESSURE DISTRIBUTION
FIGURE 15

Drag increments for the NA1 and production quiet nacelle (NA2) configurations, relative to the baseline (NA5) configuration, are presented as a function of Mach number on Figure 16. Data for W/δ values of 1.2×10^6, 1.0×10^6, and 0.7×10^6 pounds are included.
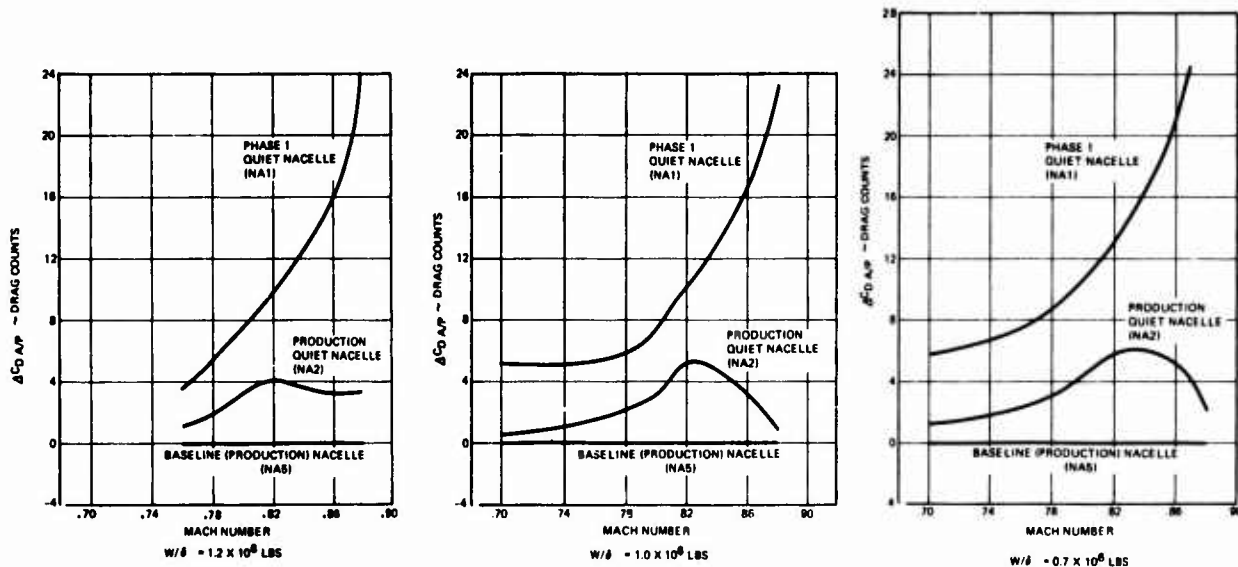
NACELLE DRAG COMPARISONS
FIGURE 16

The Phase 1 quiet nacelle consistently exhibited the highest drag levels for all test conditions. The drag penalty increased with decreasing W/δ and the drag rise characteristics were also more severe.

As expected, the drag increment attributable to the reduced afterbody (i.e., production quiet nacelle) configuration (NA2) was significantly improved with respect to NA1. Like NA1, the drag penalty increased with decreasing W/δ.

The production and the Phase 1 quiet nacelle drag variations as a function of W/δ is presented on Figure 17 for a typical Mach number of 0.8. The drag level of the production quiet nacelle is approximately 1.4 percent higher than the baseline (i.e., current

production 707) nacelle for a typical cruise condition. This is very near the 1.5 percent increase predicted prior to testing and is attributable to the increase in wetted area and interference of the 3/4 length duct over the production airplane short duct.

MACH NO. = 0.80

$$\text{DRAG VARIATION} = \frac{C_{D_{(NA_1) \text{ or } (NA_2)}} - C_{D_{(NA_5)}}}{C_{D_{AIRPLANE}}}$$

PHASE 1 QUIET NACELLE

PRODUCTION QUIET NACELLE

$W/\delta \sim 10^6$ LBS
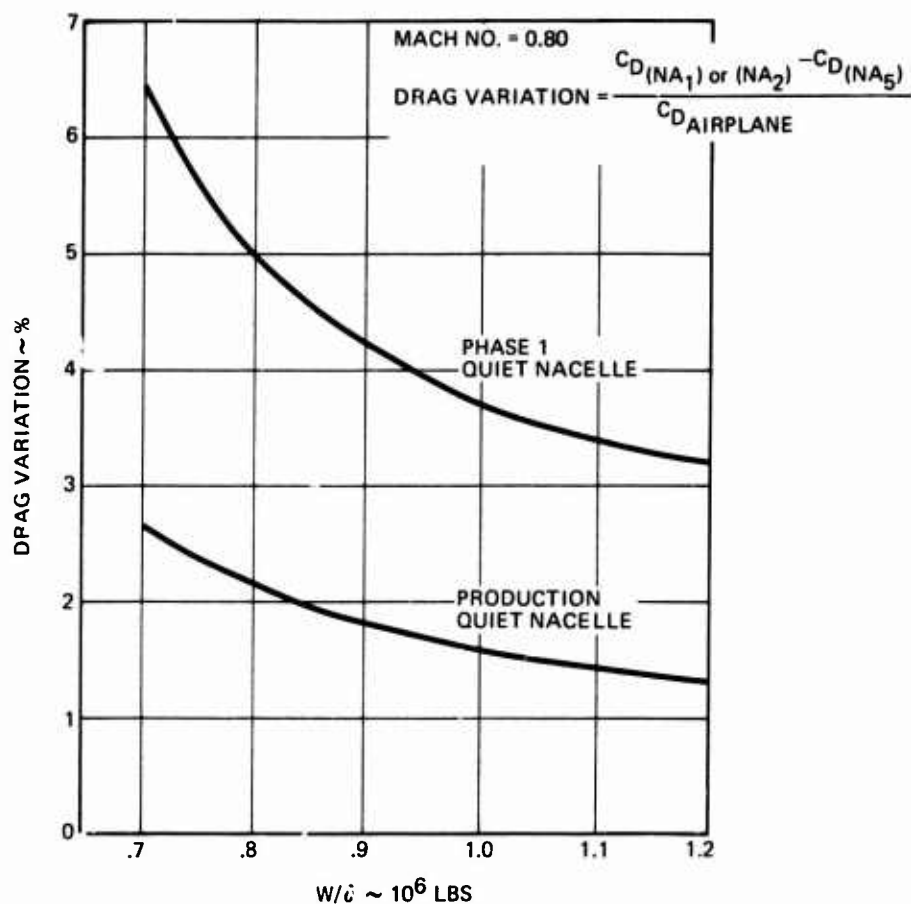
NACELLE DRAG VARIATION
FIGURE 17

The flow visualization pictures support the force balance findings. Figure 18 reveals shocks standing aft of the fan exit on the aft translating sleeve of the NA1 configuration. The reduced afterbody configuration (NA2) has relieved this shock. Additionally, the lamp black that "pooled" on the lower aft portion of the NA1 translating sleeve indicates low momentum or separated airflow in this area. Recontouring of the aft translating sleeve on the production quiet nacelle (NA2) has improved the flow.

PRODUCTION (NA2)   M = .82 ALPHA = 5°   PHASE 1 (NA1)
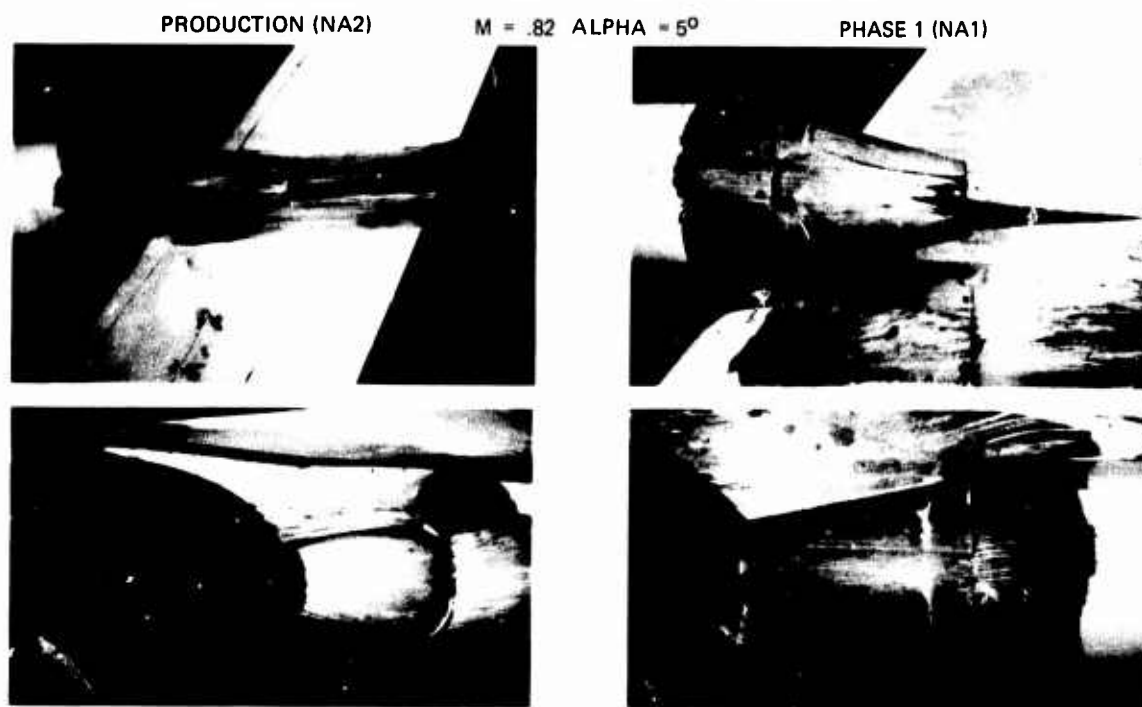
COMPARISON OF PRODUCTION AND PHASE 1 QUIET NACELLE
FLOW VISUALIZATION
FIGURE 18

One-Fifth Scale Model Test.

A one-fifth scale model of the production quiet nacelle fan duct was tested in the nozzle thrust test rig to determine nozzle coefficients. The Phase 1 quiet nacelle one-fifth scale model was retested to check previous test results and to permit "back-to-back" comparisons.

The rig configuration includes a plenum which also serves as a balance beam. The fan duct nozzle and thrust measuring load cell are installed vertically at opposite ends of the plenum equidistant from the fulcrum. Air is supplied to the nozzle from the plenum through torque tubes connected to the plenum at the fulcrum location. A flow straightener is incorporated between the plenum and the nozzle to ensure that a uniform flow profile is supplied to the nozzle.

The estimated full-scale fan duct performance, in terms of velocity coefficient is shown on Figure 19 for the production quiet nacelle, the Phase 1 quiet nacelle, and the baseline nacelle fan ducts.

LEGEND

NOTES:

1 REYNOLDS NUMBER CORRECTIONS
   TO FULL SCALE BASED ON TEST
   TEMPERATURES AND PRESSURES

2 POLYIMIDE FRICTION = 1.5 x SMOOTH
   WALL

CONFIGURATION

.... PRODUCTION QUIET
         NACELLE

- - - PHASE I QUIET
         NACELLE
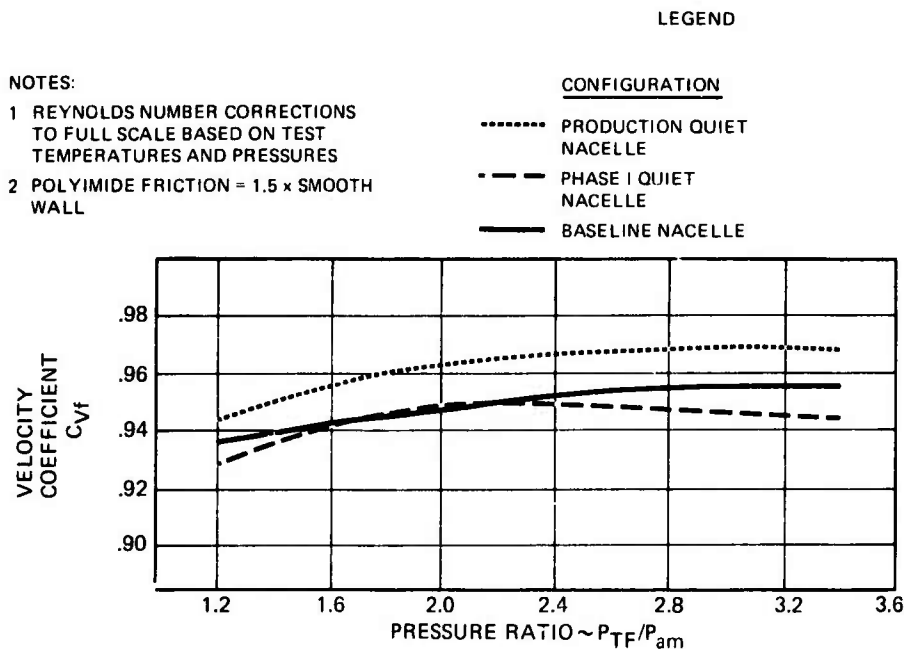
————— BASELINE NACELLE

COMPARISON OF ONE-FIFTH SCALE HALF MODEL FAN DUCT TEST RESULTS
FIGURE 19

The velocity coefficient (C_{V_f} viz., effective velocity divided by ideal velocity) of the production quiet nacelle is greater than either the Phase 1 or baseline configurations. The estimated C_{V_f}'s include afterbody scrubbing effects.

The estimated change in cruise specific fuel consumption is presented in Figure 20 for the production and Phase 1 quiet nacelles compared to the baseline (i.e., production 707) nacelle. As can be seen on Figure 20, the specific fuel consumption of the production configuration is improved with respect to both the demonstrator quiet nacelle and the proposed production quiet nacelle configuration.

NOTES: JT3D-3B ENGINE (INCLUDES TURBO-
COMPRESSOR BLEED)
36,000 FT. ALTITUDE

ESTIMATED SFC CHANGE
FIGURE 20
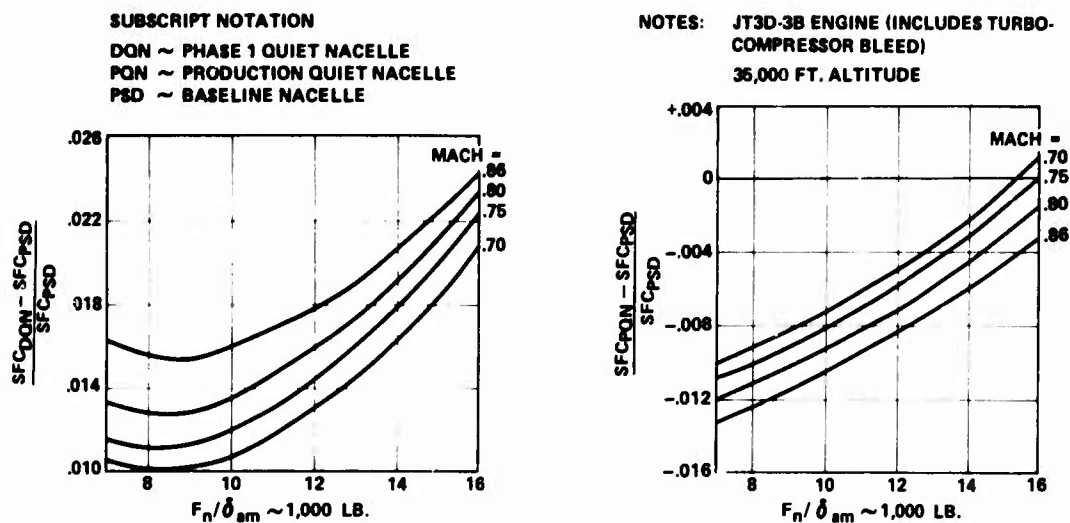
Estimated Cruise Performance

Using the Phase 1 quiet nacelle as a baseline, predicted fuel mileage data were developed for the production quiet nacelle by applying wind tunnel drag increments shown on Figure 16 and SFC increments shown on Figure 20. These data are presented on Figure 21. The flight test data of Figure 4 are also shown for comparison. The performance increment at $W/\delta = 1.0 \times 10^6$ pounds is summarized in Table 1.

TABLE 1
INCREMENTAL PERCENTAGE VARIATIONS WITH RESPECT TO MODEL BASELINE

	Model Data		
	Δ Drag Percent	Δ SFC Percent	Δ Range Factor Percent
Phase 1 Quiet Nacelle (NA1)	+3.72	+1.75	−5.27
Production Quiet Nacelle (NA2)	+1.60	−0.54	−1.05
Net Improvement over Phase 1			+4.22

where: Range Factor = $\dfrac{1}{(\Delta \text{Drag} + 1)\ (\Delta \text{SFC} + 1)} - 1$

The range factor improvement due to the reduced afterbody configuration (NA2) over the Phase 1 quiet nacelle (NA1) is (-1.05) − (-5.27) = +4.22%. From the flight test cruise data, the range factor penalty for the Phase 1 nacelle is 4.79 percent. Applying the wind tunnel model range factor increment to the Phase 1 quiet nacelle flight test data results in a net change of -0.57 percent (viz., (-4.79) + (+4.22) = -0.57%) below the baseline airplane configuration.

A tolerance band is shown on Figure 21 for each W/δ. This tolerance reflects using wind tunnel data and dual nozzle model ground test data and either the baseline flight test data or the Phase 1 quiet nacelle as a baseline. It is believed that the upper and lower values represent extremes with the true value being closer to the upper value. This results from the fact that adjustments to model scale data for scale effects are more nearly the same for the two 3/4 length duct configurations (Phase 1 quiet nacelle to production quiet nacelle) than they would be for a short duct and 3/4 length duct configuration (baseline nacelle to production quiet nacelle).

The data shown on Figure 21 and in Table 1 are a correct representation of the cruise performance data of a production version of the quiet nacelle as configured in February 1974. The data are shown to illustrate the performance improvement that can be obtained through aerodynamic and propulsion performance optimization of a configuration. The production version of the quiet nacelle is undergoing design refinements and additional improvements in cruise fuel mileage are predicted.
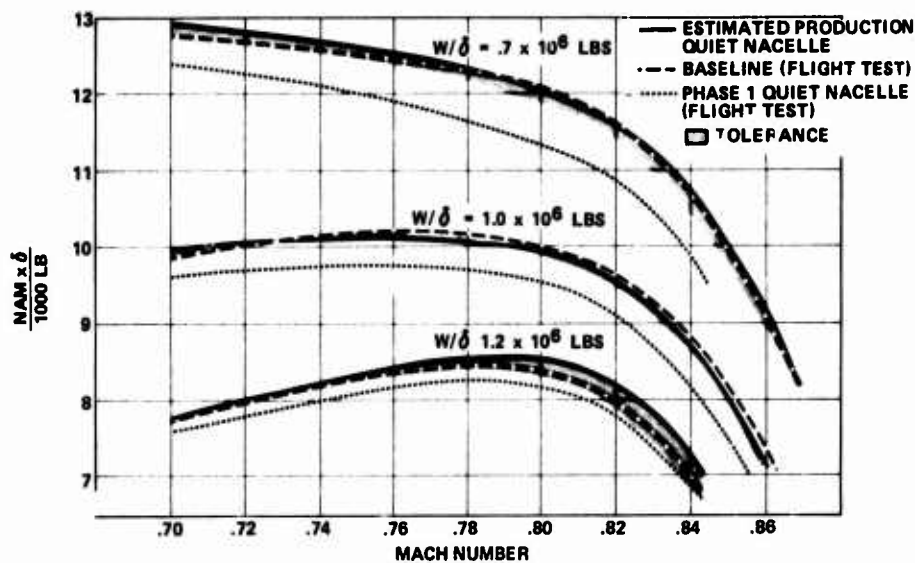
PRODUCTION QUIET NACELLE PREDICTED FUEL MILEAGE
FIGURE 21

CONCLUSIONS

The results of the performance evaluation of the quiet nacelle configuration show that:

- The nacelle afterbody design can significantly affect the airplane performance,

- By optimizing the design a nacelle can be configured that can significantly improve acoustic performance while maintaining good aerodynamic and propulsive performance, and

- A blowing wind tunnel model that duplicates the afterbody geometry and simulates engine mass flow provides good correlation to flight test and thereby proves to be a very valuable design tool.

REFERENCES

1. Mayer, J. E., et al, "FAA JT3D Quiet Nacelle Retrofit Feasibility Program, Volume III, Lower Goal Flight Testing, Economic Analyses, and Summary", D3-9042-4, February 1974, The Boeing Company, Wichita Division, Wichita, Kansas.

2. Callaghan, J. F., Donelson, F. E. and Morelli, J. P., "The Effects on Cruise Drag of Installing Long-Duct Refan-Engine Nacelles on the McDonnell Douglas DC-8 -50 and -61", NASA CR-121218, May 1973, Douglas Aircraft Company, Long Beach, California.

3. McNeill, H. N., Bouwer, D. W., and Copeland, D. D., "Afterbody Drag of the Production JT3D-1, -3, -3B Short Duct Nacelle", D6-10913, December 1965, Boeing Commercial Airplane Company, Renton, Washington.

4. Kutney, John T., and Piszkin, Stanley P., "Reduction of Drag Rise on the Convair 990 Airplane", Journal of Aircraft, Volume 1, January-February 1964.

REYNOLDS NUMBER EFFECTS ON BOATTAIL DRAG OF EXHAUST NOZZLES FROM WIND TUNNEL AND FLIGHT TESTS

Fred A. Wilcox
Head, Flight Systems Section

Roger Chamberlin
Aerospace Engineer

Lewis Research Center
National Aeronautics and Space Administration
Cleveland, Ohio, U.S.A. 44135

SUMMARY

A family of nacelle mounted high angle boattail nozzles was tested to investigate Reynolds number effects on drag. The nozzles were flown on a modified F-106B and mounted on scale models of an F-106 in a wind tunnel. A 19- to 1-range of Reynolds number was covered as a result of the large size differences between models and by flying over a range of altitude. In flight the nozzles were mounted behind J-85 turbojet engines. Jet boundary simulators and a powered turbojet engine simulator were used on the wind tunnel models. Data were taken at Mach numbers of 0.6 and 0.9. Boattail drag was found to be affected by Reynolds number. The effect is a complex relationship dependent upon boundary layer thickness and nozzle boattail shape. As Reynolds number was increased from the lowest values obtained with scale models, boattail drag first increased to a maximum at the lowest flight Reynolds number and then decreased.

SYMBOLS

A_{bt} boattail projected area

A_{max} nacelle cross-sectional area at boattail juncture

C_D boattail pressure drag coefficient, $\dfrac{\int (p - p_o)\, dA_{bt}}{0.7\, p_o\, A_{max}\, M_o^2}$

C_p pressure coefficient, $\dfrac{p - p_o}{0.7\, p_o\, M_o^2}$

D nacelle diameter at boattail juncture

L nozzle length

M_o free-stream Mach number

P total pressure at nozzle throat

p boattail static pressure

p_o free-stream static pressure

Re Reynolds number - based on a characteristic length of 5.18 m for flight and appropriately scaled values for the wind tunnel models

X axial distance from beginning of boattail shoulder

α angle of attack

β boattail terminal angle

INTRODUCTION

Developing a working technique to predict in-flight aerodynamic performance of aircraft components has been a goal of aerodynamicists for many years. To date analytical techniques are not sufficiently developed to handle complex geometries of new aircraft. As a result the best technique available is testing small subscale models in wind tunnels. Wind tunnel testing is limited to small models, especially at transonic Mach numbers where blockage effects are critical. Because of the small size of the models, even variable density wind tunnels cannot achieve flight values of Reynolds number.

It has been found that on certain aircraft components, Reynolds number has an unpredictable effect on the aerodynamic performance. In particular, the aerodynamic drag of boattail nozzles has been found to be thus affected.

Aircraft powered by afterburning turbofan engines require large nozzle exit area variations. In a subsonic cruise condition with the engine in a nonafterburning mode, large projected boattail areas result. In order to keep the nozzle reasonably short, high boattail angles become necessary. The drag of these nozzles can be a significant percentage of total airplane drag. Sensitivity of this drag to Reynolds number introduces a large uncertainty in prediction of aircraft performance.

A family of boattail nozzles was tested, both in flight and in a wind tunnel, over a 19-to-1 range of Reynolds number. The results were previously reported in references 1 through 4. Flight tests were made using an F-106B aircraft modified to carry two underwing research nacelles. These nacelles housed J-85 engines and were 63.5 cm in diameter at the nozzles. Reynolds number was varied by flying at altitudes ranging from 3048 to 13 700 meters at subsonic speeds. The nozzles tested had several boattail geometries that displayed a wide range of sensitivity to Reynolds number. Some of the nozzles were also tested in

the Lewis Research Center 8- by 6-Foot Supersonic Wind Tunnel on 5 and 22 percent scale F-106 models (ref. 2, which provided data at the lower Reynolds numbers.

Initial results from the flight program (refs. 1 and 2), showed a trend of decreasing boattail drag for all the nozzles with increasing Reynolds number. The model data did not follow that trend. At the lower wind tunnel Reynolds numbers boattail drag decreased with decreasing Reynolds number. These drag variations with Reynolds number appeared to be a result of changes in boundary layer thickness and changes in the separated flow on the aft boattail.

A second independent investigation (ref. 5) showed the same trend at the lower Reynolds numbers. In that test, boundary layer over nozzle boattails was artificially thickened by an upstream fence to simulate operation at a lower Reynolds number.

In this paper some of the effects of nozzle boattail shape on drag variation with Reynolds number will be discussed.

APPARATUS AND PROCEDURE

Modifications to Aircraft

An F-106B (two-seat version) has been modified to carry two underwing research nacelles located symmetrically at the 32 percent semi-span position (fig. 1). The elevons were cut out over the nacelles and replaced by a fixed section. The nacelles were mounted to the wing by means of forward and rear links which allowed axial forces to be measured by a load cell (fig. 2). Drag data presented herein, however, were obtained by integration of pressure measurements on the boattail surfaces. Normal shock inlets were used in the flights described. The nacelles were mounted with a negative incidence of $4\frac{1}{2}^{\circ}$ (relative to the wing chord) so that the aft portion of the nacelle was tangent to the wing lower surface. The nacelles housed J-85 afterburning turbojet engines. However, the tests described were restricted to nonafterburning. Secondary air to cool the engine was bled from the inlet through an adjustable valve. The nacelle and exhaust nozzles were 63.5 cm in diameter with a bulged fairing over the engine accessories.

Data were recorded in flight using the digital system described in reference 6. This system used 10 scani valves with a total capability of measuring 480 pressures. Ninety-six other parameters such as flight conditions, voltages, and temperatures could also be recorded. Data system scan time was 11.6 seconds.

Data could be taken simultaneously on left and right nozzles. Each nozzle had 10 rows of area weighted static pressure orifices, 9 in each row, which can be seen in figure 3. Also shown is a window in the tail through which movies of tufts mounted on the nozzles could be taken. A second window was located on the opposite side of the tail permitting photographs to be taken of either the left or right sides.

Flight Procedures

Research flights have been made with the modified aircraft at Mach numbers to 1.3. The flights described herein, however, were made at Mach numbers from 0.6 to 0.9, and altitudes to 13 700 m. In order to vary Reynolds number while holding Mach number and angle of attack constant, most of the data were recorded while in coordinated turns. Flights at the lowest altitudes (3048 m) were made in turns of highest load factor; about 2.5 g. Data at 13 700 m altitude was obtained in level flight. Thus, the high angle of attack required to sustain level flight at high altitude was also obtained at low altitude. The Reynolds number was based on a characteristic length of 5.18 m which takes into consideration the wing chord at the nacelle station (7.32 m) and the nacelle length (3.96 m).

Wind Tunnel Models

Figure 4 shows the 5 percent scale F-106 model that was tested in the Lewis Research Center 8- by 6-Foot Supersonic Wind Tunnel. This model is shown in the photograph with flow through nacelles and solid jet boundary simulators. The data presented were obtained with conical forebodies closing the inlets. Nozzles on this model had 4 rows of 8 area weighted static pressure orifices along the boattails. Data were obtained on this model at Mach numbers of 0.6 and 0.9 at angle of attack up to 15°.

The 22 percent scale half span F-106 model is shown in figure 5 mounted in the 8- by 6-Foot Supersonic Wind Tunnel. It was tested with both a turbojet engine simulator and with a conical forebody closing the inlet and a solid jet boundary simulator on the nozzle. The engine simulator incorporated a 6-stage, axial-flow compressor powered by a 3-stage, axial-flow turbine. High pressure warm air was used to drive the turbine. Details of the turbojet simulator are given in reference 7. The design characteristics of this simulator permitted independent operation over a wide range of both inlet mass flow ratio and nozzle pressure ratio which equaled those in flight.

Reynolds numbers for the models were based on scaled values of the characteristic length used for flight data. Reynolds numbers between 3.5 and 4 million were obtained for the 5 percent model and between 14.5 and 18 million for the 22 percent model.

Boattail Nozzles

Nozzles used in this program were typical of those used on military aircraft having supersonic dash capability and powered by afterburning turbofan engines. They were of three types as shown on figure 6; circular arc, circular arc-conic, and contoured. A numbering system was used to designate the various nozzles. The first two or three digits correspond to the radius ratio multiplied by 100. The last two digits correspond to the terminal boattail angle. The radius ratio is defined as the ratio of the radius of the boattail shoulder to the radius of a complete circular arc boattail with the same projected area and terminal boattail angle. Table I indicates which nozzles were tested on the two models.

All of the nozzles were flight tested. Three of the circular arc-conic boattails had a radius ratio of 0.25, one having a 16° boattail angle and the other two a 24° terminal angle. The second two had identical boattails but one was spaced 25.4 centimeters (0.4 nozzle diameters), further downstream of the wing trailing edge (designation Ex).

There was one 0.65 radius ratio circular arc-conic nozzle with a 24° trailing edge angle; one 24° circular arc nozzle and a contoured nozzle. Dimensions of the contoured nozzle are given in references 3 and 4. It was shaped to have a gradual initial turn followed by a steep turn with a maximum local angle of 31° and a reflex at the trailing edge. Photographs of these nozzles mounted on the aircraft are shown in figure 7. Tufts can be seen on some of the nozzles. The most satisfactory tuft length used is shown in figure 7(g) on the contoured nozzle.

RESULTS AND DISCUSSION

By comparing boattail drag data for the same nozzle at 5 percent, 22 percent, and full-scale, a wide range of Reynolds number could be covered. The 22 percent model was tested with an engine simulator and also with the inlets faired over and solid jet boundary simulators to determine whether data from the 5 percent model could be compared with flight data. The data of figure 8 indicate that nozzle drag is the same for both methods. In addition, the effect of nozzle pressure ratio on boattail drag is relatively small for the range of nozzle pressure ratio investigated.

The 5 percent model was used to determine the sensitivity of boattail drag to angle of attack, since some variation in angle of attack was obtained with the airplane. The effect of angle of attack was found to be small at Mach 0.6 (fig. 9) but became larger at high angles (above approximately 8°), at Mach 0.9. The sensitivity of drag to angle of attack was low at both Mach numbers for the angles obtained in flight.

The trend of boattail drag with Reynolds number is shown in figure 10 for the circular-arc-conic nozzles for both Mach numbers of 0.6 and 0.9. Drag coefficient was maximum at a value near the low end of the flight Reynolds number range and dropped off as Reynolds number was either raised or lowered. Very low values of drag coefficient were obtained with the 5 percent model. Values of drag coefficient for the 22 percent model fell in place between those of the smaller model and those from flight. In the flight range highest drag was obtained with nozzle 2524 Ex which was extended rearward out of the wing flow field. Lowest drag was obtained with the 16° nozzle 2516. The trend with all the nozzles in flight was decreasing drag with increasing Reynolds number.

The observed drag variation with Reynolds number is probably a result of changes in the boundary layer thickness and changes in the separated flow on the aft part of the boattail. Pressure distributions on a typical nozzle boattail are shown schematically in figure 11 for three values of Reynolds number. The solid lines are typical of the observed pressure distributions. The dashed lines represent the pressure distribution for inviscid flow. Drag is low at the very high Reynolds numbers. Due to thin boundary layer, the flow remains attached over all, or a major portion, of the boattail. This results in a large expansion at the boattail shoulder but allows the flow to recompress to relatively high pressures on the aft boattail, which offset the low pressures at the shoulder. As the Reynolds number is decreased the boundary layer becomes thicker. With the thicker boundary layer the flow cannot traverse the adverse pressure gradient as far and will separate sooner. As the separation on the aft boattail increases, the recompression is lost and drag increases. As the Reynolds number is lowered still further the flow at the boattail shoulder begins to change. The boundary layer becomes thicker causing separation to occur closer to the boattail shoulder which decreases the overexpansion. Eventually the beneficial effects of increasing pressure at the shoulder become large enough to offset the adverse effects of increased separation on the back of the boattail. Drag thus reaches a peak and then begins to decrease with further lowering of Reynolds number.

The usefulness of tufts as an indication of flow separation is illustrated in figure 12. Data are shown from four rows of pressure orifices with adjacent rows of tufts on the upper portion of one of the nozzles. An initial examination of the pressure curves shows that they are similar without a clear indication as to whether the flow is attached or separated. However, the last three tufts on the A and B rows indicate separated flow, while all of the tufts on rows C indicate attached flow. A close examination of the pressure curves reveals small differences in the level and shape of the No. 1 and 2 pressure rows which correspond to the separated condition. However, these differences are so small that they could not be used alone to predict separation. Unpublished data taken with dynamic pressure transducers located in a rake near the end of the 2524 boattail verified that the flow was unsteady and thus might be oscillating between attached and separated. Lag in the steady state pressure instrumentation would then produce values intermediate between the two flow conditions, similar to that of rows No. 1 and 2.

The effect of nozzle boattail shape on drag variation with Reynolds number is illustrated in figure 13. Data are shown for one of the circular arc-conic nozzles, the circular arc and the contoured nozzle at a Mach number of 0.9. The 6524 circular arc-conic nozzle was selected since it had the lowest drag at high Reynolds number, at this Mach number, of the high angled nozzles and was similar in length to the contoured nozzle. The circular arc and contoured nozzles had nearly the same low sensitivity to Reynolds number in the flight range. These two nozzles had nearly identical variation of drag with Reynolds number, with two very different boattail flow fields. The circular arc-conic nozzle drag was more sensitive to Reynolds number. Drag for this nozzle was higher than for the other two at intermediate and low Reynolds numbers.

Pressure distributions showing the reasons for these drag variations are given in figure 14 at three Reynolds numbers. Data are presented as a function of percent of boattail projected area to permit a more direct comparison of the various length nozzles. The circular arc-conic and contoured nozzles were nearly the same length and the circular arc nozzle was about 22 percent longer. At the highest flight Reynolds number (fig. 14(a)) the circular arc-conic nozzle had the most overexpansion followed by a rapid recompression and a small amount of separation beginning at about 80 percent of the projected area.

The pressure distributions for the circular arc and contoured nozzles show different types of flow.

With the circular arc nozzle attached flow was maintained over the entire boattail. Because turning is gradual with this nozzle, the expansion at the shoulder was small and the flow had a slow but continuous compression over the remainder of the boattail. The contoured nozzle also had a gradual turn at the shoulder with a relatively small expansion. However, downstream of this point the turning increased rapidly. A rapid recompression ensued followed by separation over about half the boattail projected area. The advantage of this nozzle is the minimum expansion at the shoulder and the fact that the flow compressed to a high value before it separated.

At the lowest Reynolds number obtained in flight (fig. 14(b)) the pressure distribution for the circular arc-conic nozzle showed the greatest change from that at the highest Reynolds number. There was less overexpansion at the shoulder, a less rapid recompression and more flow separation. This accounted for its increase in drag. The circular arc nozzle, because of its gradual turn, maintained an attached flow over most of the boattail and therefore had little change in boattail drag. The contoured nozzle, on the other hand, because of its rapid turning fixes the separation point and the flow remained separated over the same portion of the boattail resulting in little or no change in boattail drag.

At the much lower Reynolds number of the 5 percent scale model (fig. 14(c)), overexpansion at the shoulder was less for all nozzles. Recompression occurred more rapidly and pressures on the aft portion were generally higher than for the higher Reynolds numbers. The result was the low drag for all three nozzles shown in figure 13.

Analytical Prediction

The complex nature of flow over boattail nozzles has thus far precluded the generation of a completely satisfactory analytical model. Presz (ref. 8) has reported success in predicting the point of separation and pressure distribution on boattail nozzles. Variations in boattail pressure distributions reported in this reference are similar to those observed on the F-106 aircraft. More analysis is needed; in particular to include 3-dimensional effects.

CONCLUSIONS

A family of nacelle mounted, high angle boattail nozzles was tested to determine Reynolds number effects on drag. A 19 to 1 range of Reynolds number was covered by using nozzles mounted behind J85 turbojet engines on a modified F-106B in flight and scale models in a wind tunnel. Data were obtained at Mach numbers of 0.6 and 0.9. The following conclusions can be made:

1. Boattail drag can be strongly affected by Reynolds number. The effect is a complex relationship resulting from the effect of boundary layer characteristics on aft boattail separation.

2. As Reynolds number was increased from the lowest values for scale models, boattail drag first increased and then decreased in the range of Reynolds number obtained at full scale in flight. As a result, data from small scale models generally underpredicted full-scale drag.

3. Sensitivity of boattail drag to Reynolds number was dependent on boattail shape.

4. A contoured nozzle having a large region of separated flow had drag as low as a longer circular arc nozzle which had little flow separation. The drag sensitivity to Reynolds number was about the same as for the circular arc nozzle.

REFERENCES

1. R. Chamberlin, "Flight Investigation of 24° Boattail Nozzle Drag at Varying Subsonic Flight Conditions" - NASA TM X-2626, 1972.

2. R. Chamberlin and B. J. Blaha, "Flight and Wind Tunnel Investigation of the Effects of Reynolds Number on Installed Boattail Drag at Subsonic Speeds," AIAA Paper 73-139, AIAA/Aerospace Sciences Meeting, 11th, January 1973.

3. F. A. Wilcox, "Comparison of Ground and Flight Test Results Using a Modified F-106B Aircraft," AIAA Paper 73-1305, AIAA/SAE Propulsion Conference, 9th, November 1973.

4. R. Chamberlin, "Flight Investigation of Reynolds Number Effects on a Contoured Boattail Nozzle at Subsonic Speeds" - NASA TM X-3053, 1974.

5. D. E. Reubush and C. E. Mercer, "Exhaust Nozzle Characteristics for a Twin Jet Variable Wing Sweep Fighter Airplane Model at Mach Numbers to 2.2" - NASA TM X-2947, 1974.

6. H. W. Groth, N. E. Samanich, and P. Z. Blumenthal, "Inflight Thrust Measuring System for Underwing Nacelles Installed on a Modified F-106 Aircraft" - NASA TM X-2356, 1971.

7. F. W. Steffen, E. A. Satmary, M. R. Vanco, and S. M. Nosek, "A Turbojet Simulator for Mach Numbers up to 2.0," ASME Paper 72GT89, ASME/Gas Turbine and Fluids Engineering Conference and Product Show, March 1972.

8. W. M. Presz, Jr. and E. T. Pitkin, "Flow Separation Over Axisymmetric Afterbody Models," AIAA Paper 74-17, AIAA/Aerospace Sciences Meeting, 12th, January-February 1974.

TABLE I. - BOATTAIL NOZZLES TESTED

Type	Designation	Projected area ratio, A_{bt}/A_{max}	Length, L/D	Nozzle tested on		
				F-106	5% model	22% model
Circular arc-conic	2516	0.75	2.20	X	X	X
	2524	0.75	1.43	X	X	X
	2524 Ex	0.75	1.43	X		
	6524	0.75	1.92	X	X	X
Circular arc	10024	0.75	2.35	X	X	
Contoured		0.71	1.94	X	X	
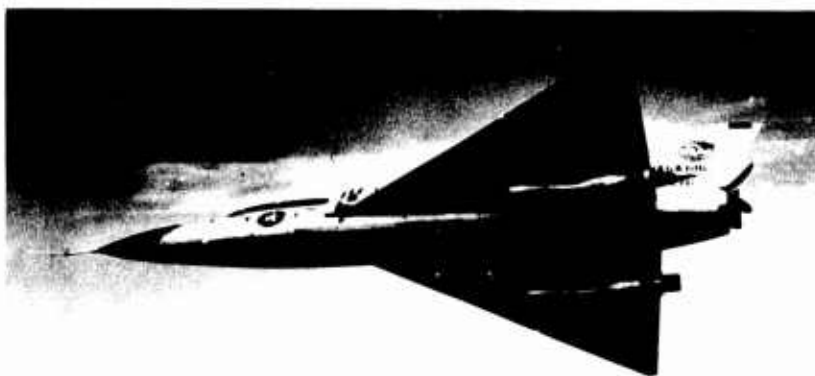
C-69-2871

Figure 1. - Modified F-106B in flight.
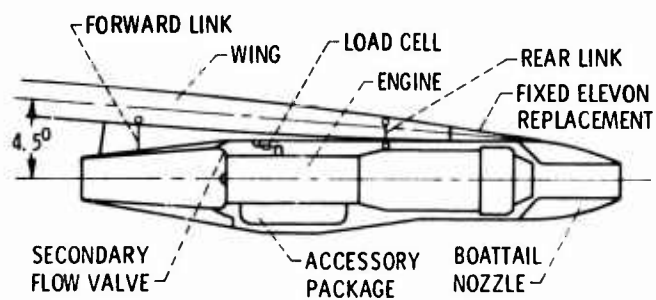
Figure 2. - Nacelle-engine installation.

WINDOW FOR
MOVIE CAMERA

STATIC PRES-
SURE ORIFICES

C-70-2307

Figure 3. – Boattail nozzles installed on F-106B aircraft.

C-67-4332

Figure 4. – 0.05 scale F-106 model in 8x6 tunnel.

CIRCULAR ARC-CONIC

CIRCULAR ARC

CONTOURED
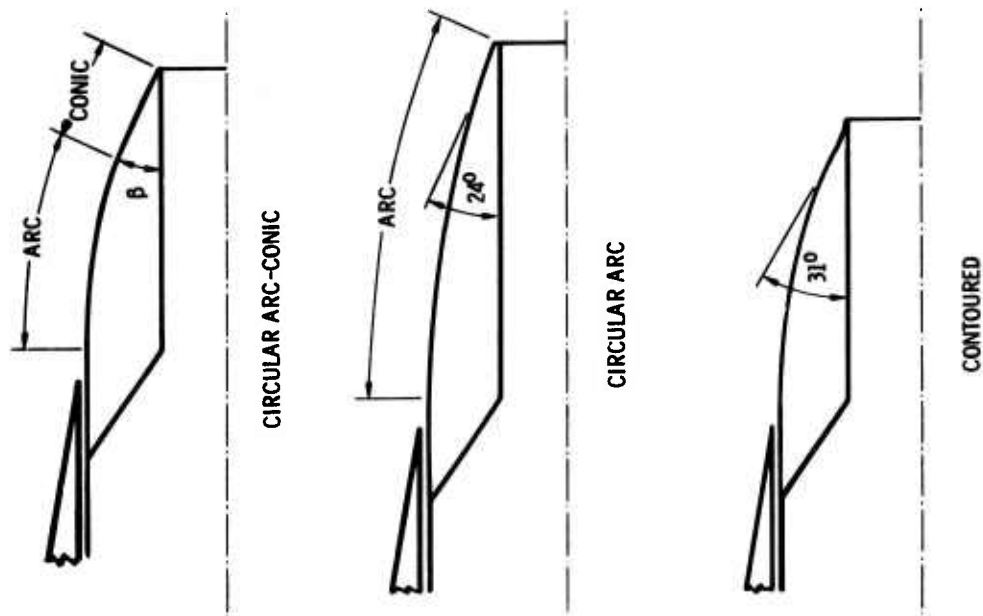
Figure 6. - Schematic of boattail types.

C-72-2068
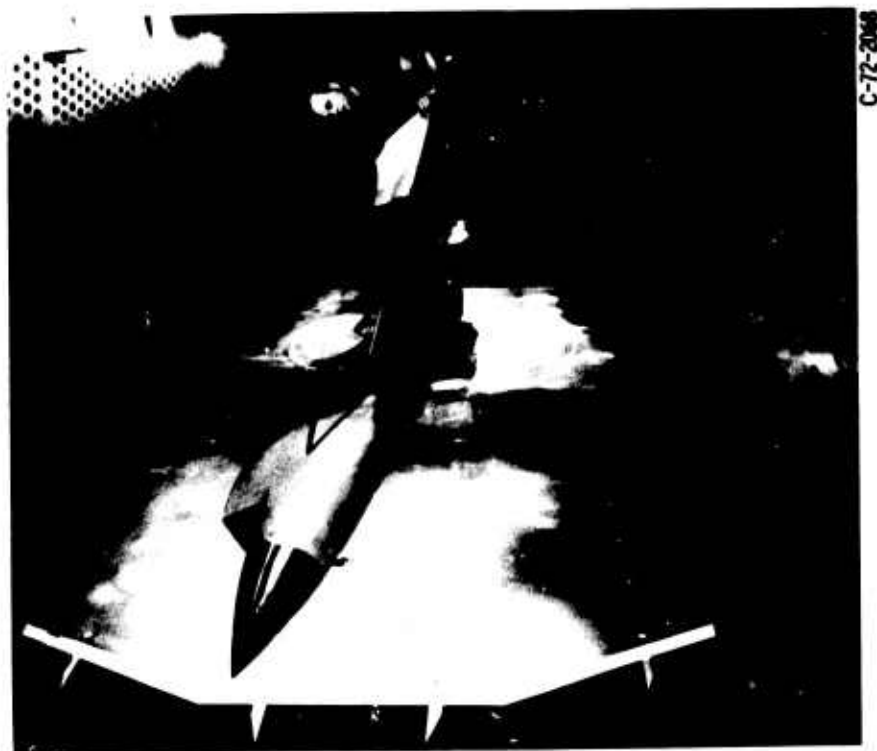
Figure 5. - 0.22 scale F-106 model in 8x6 tunnel.

C-71-4168
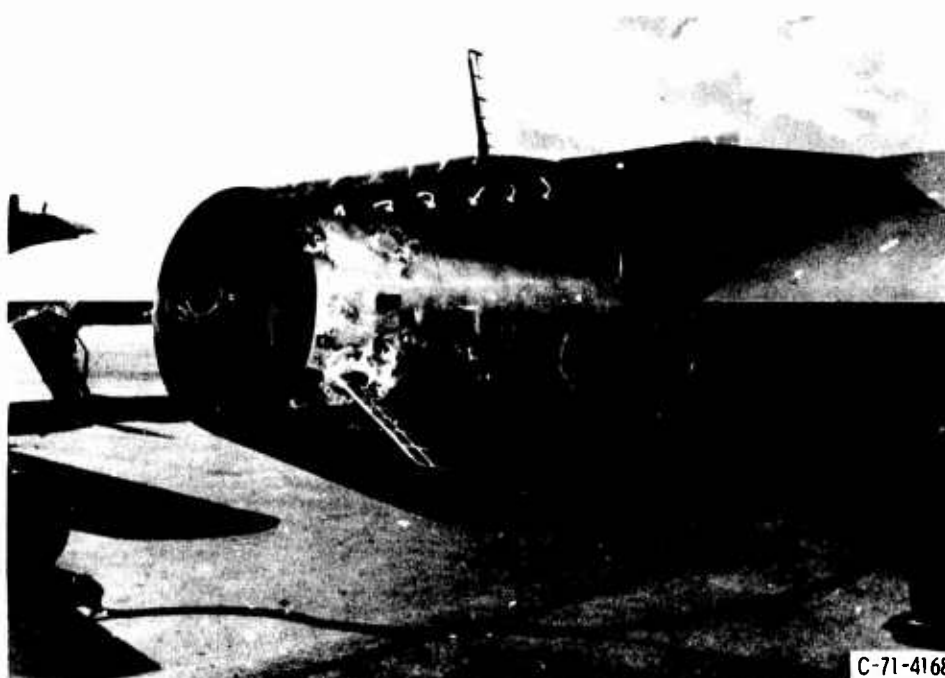
(a) Boattail nozzle 2516, radius ratio 0.25, boattail angle 16°.

Figure 7. - Boattail nozzles.

C-70-2300
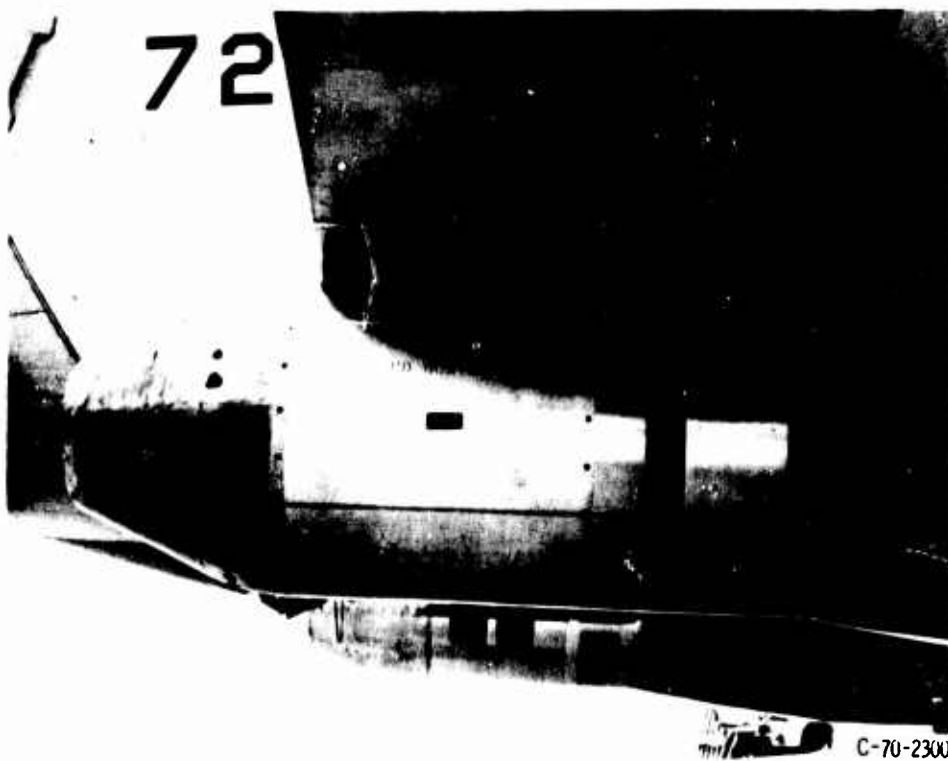
(b) Boattail nozzle 2524, radius ratio 0.25, boattail angle 24°.

Figure 7. - Continued.

C-70-2695

(c) Boattail nozzle 2524 Ex (extended), radius ratio 0.25, boattail angle 24°.

Figure 7. - Continued.

C-70-2299
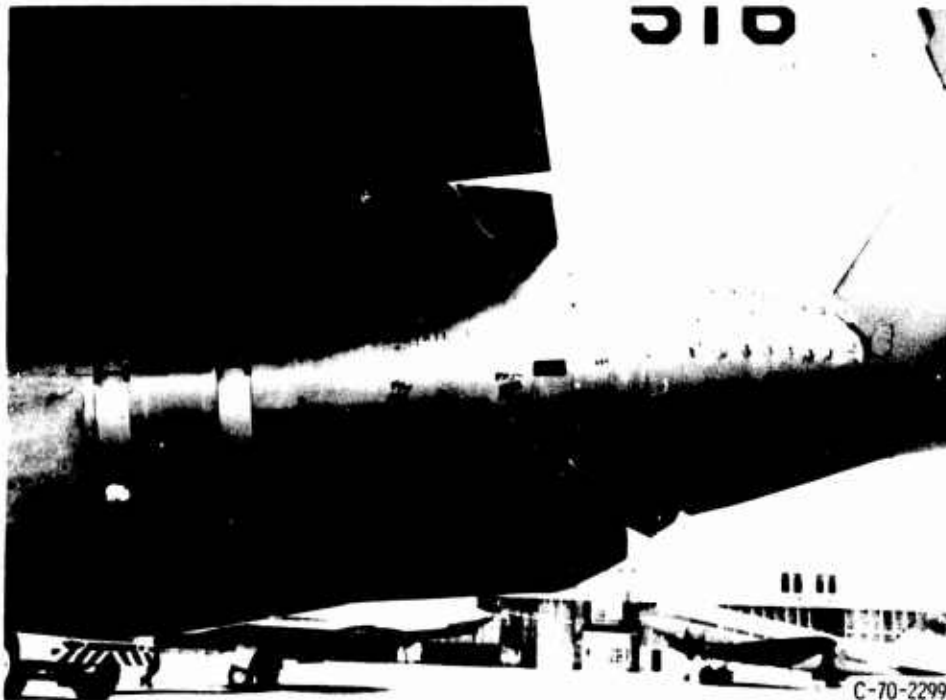
(d) Boattail nozzle 6524, radius ratio 0.65, boattail angle 24°.

Figure 7. - Continued.

C-70-2692

(e) Boattail nozzle 10024, full circular arc, terminal boattail angle 24⁰.

Figure 7. - Continued.

C-73-2035

(f) Contoured boattail.

Figure 7. - Concluded.
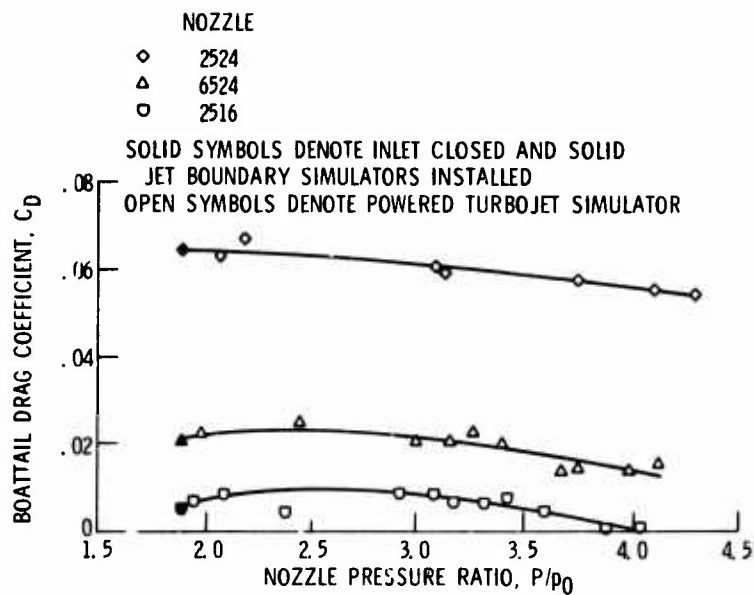
Figure 8. - Effect of pressure ratio on boattail drag on the 0.22 scale model; Mo, 0.9.
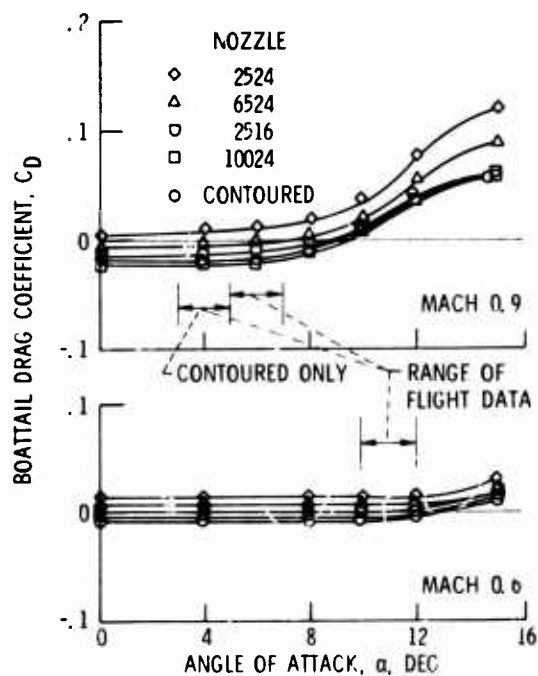
Figure 9. - Effect of angle of attack on boattail drag on the 0.05 scale F-106 model.

(a) MACH NUMBER, 0.6.
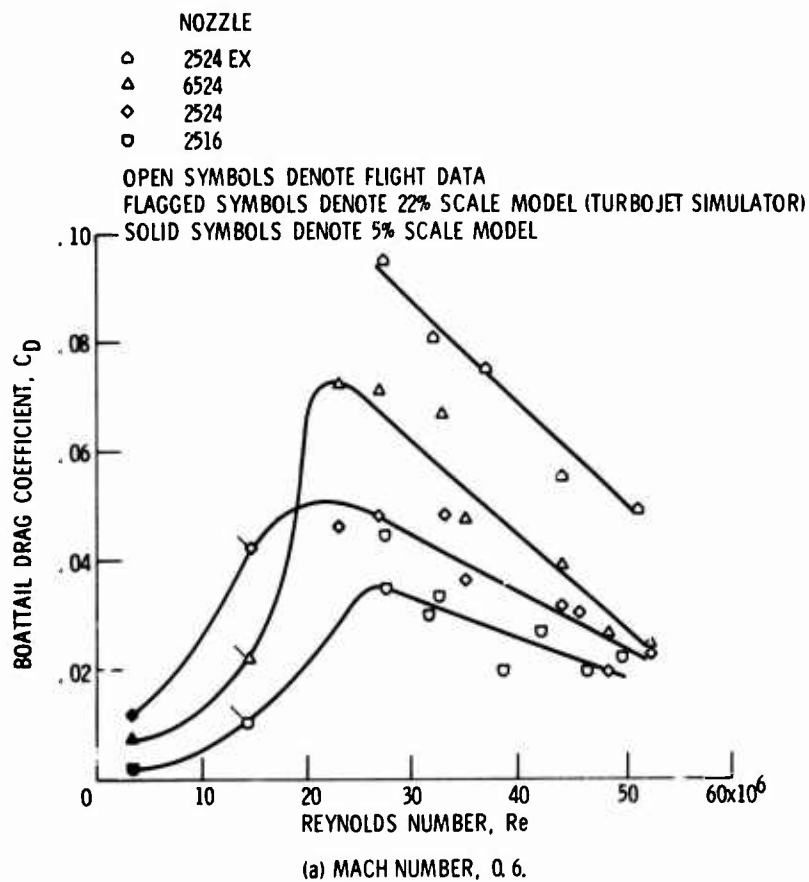
Figure 10. - Reynolds number effect on circular arc-conic boattails.

(b) MACH NUMBER, 0.9.

Figure 10. - Concluded.

(a) TUFT PICTURE.

(b) PRESSURE DISTRIBUTION.
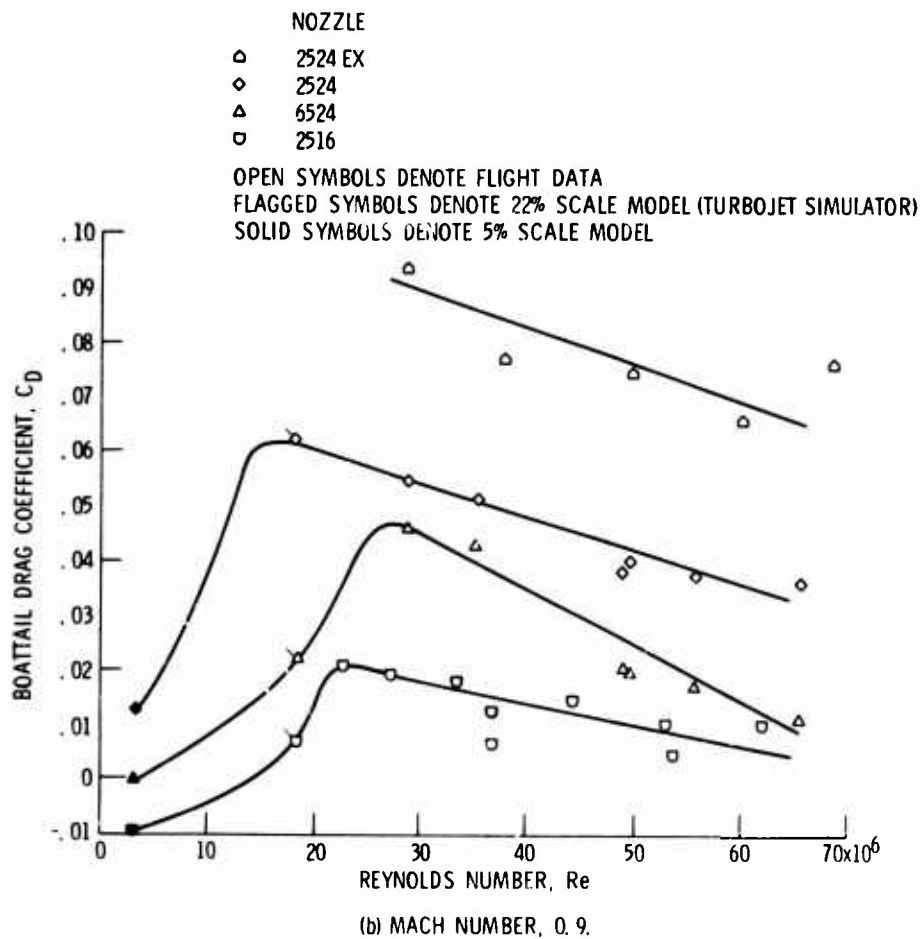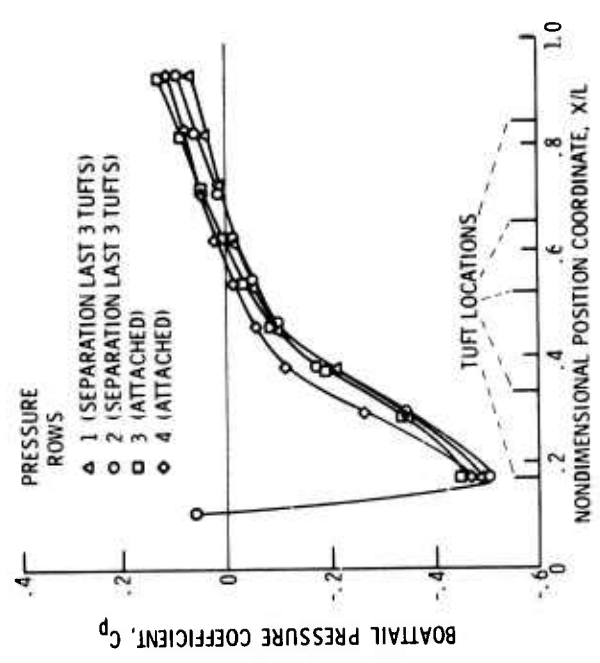
Figure 12. - Determination of separation. Nozzle 2524; M_0, 0.9; Re, 49, 2x10^6.
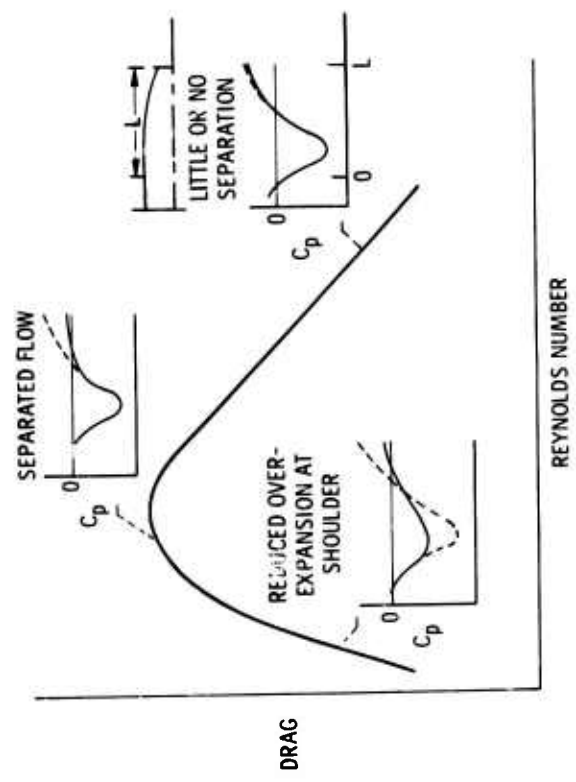
Figure 11. - Reynolds number effects on circular arc-conic boattails.
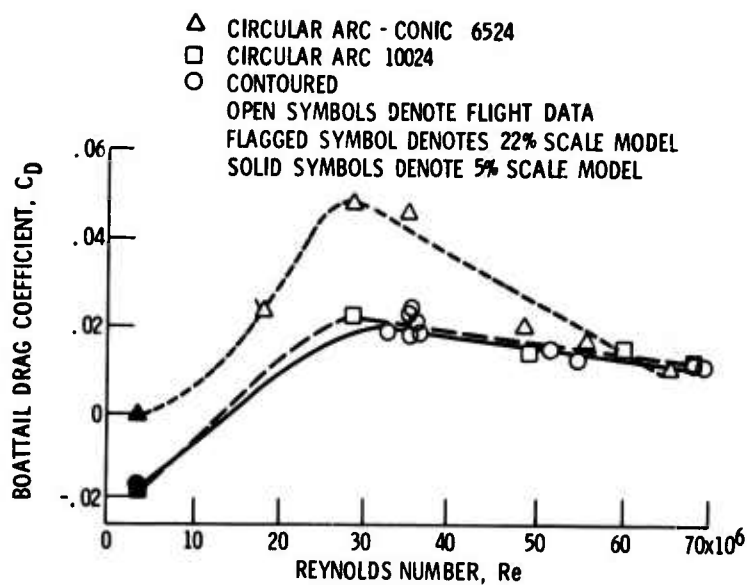
Figure 13. - Reynolds number effect on boattail geometries with attached and separated flows; M_0, 0.9; α, 4°.
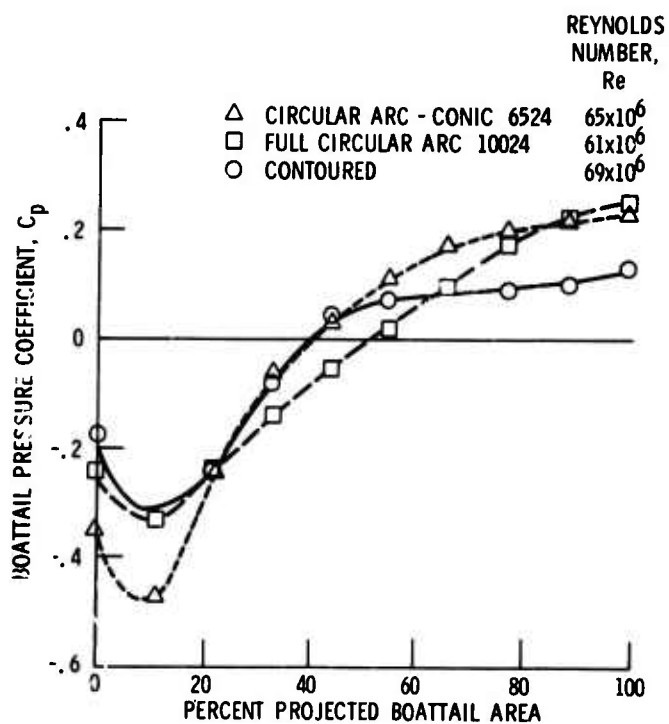
(a) HIGHEST FLIGHT REYNOLDS NUMBER.

Figure 14. - Pressure distributions on boattails with attached and separated flows. M_0, 0.9; 180° meridian angle.
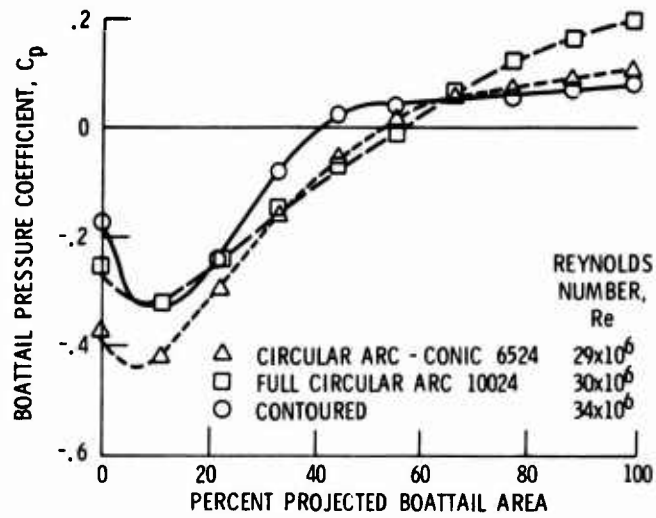
(b) LOWEST FLIGHT REYNOLDS NUMBER.

Figure 14. - Continued.
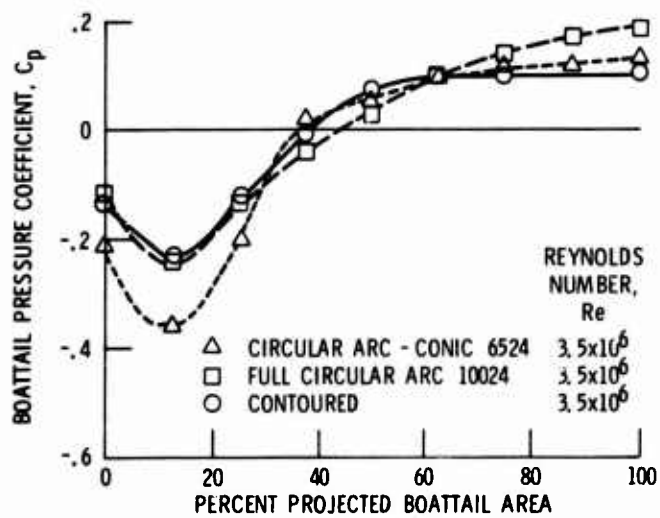
(c) 5 PERCENT SCALE REYNOLDS NUMBER.

Figure 14. - Concluded.

ACCOUNTING OF AERODYNAMIC FORCES ON AIRFRAME/PROPULSION SYSTEMS

by

Michael E. Brazier*
William H. Ball**
The Boeing Aerospace Company
Seattle, Washington 98124

SUMMARY

Proper accounting, prediction, and measurement of propulsion system installation corrections are essential for the successful development of advanced military aircraft. This paper reports the results of recent studies which evaluate the methods used to predict, measure and integrate the aerodynamic and propulsion forces within a force accounting procedure that provides maximum element visibility and accuracy, and is applicable throughout an entire airplane development cycle.

Improved analysis techniques are described which provide more comprehensive and accurate predictions of inlet performance and nozzle/aftbody drag early in the preliminary design process. Inlet analysis techniques make use of standardized data maps for obtaining complete inlet performance characteristics. Nozzle/aftbody drag calculations are performed using a newly-developed truncated Integral Mean Slope technique. Effects of strut interference, blockage, model split-line locations and other factors which introduce uncertainties into airframe/propulsion system data are presented, based on results from recent wind tunnel tests.

NOMENCLATURE AND SYMBOLS

A_c	Inlet capture area	P_{T_2}/P_{T_0}	Total pressure recovery at compressor entrance station
A_0	Freestream tube area	q_0	Freestream dynamic pressure, $q_0 = \frac{1}{2}\rho_0 V_0^2$
A_9	Total nozzle exit area	S/D_{eq}	Non-dimensionalized nozzle spacing
A_{10}	Fuselage maximum cross-sectional area	S_F	Aircraft frontal area
$C_{D_{ADD}}$	Additive drag coefficient, $C_{D_{ADD}} = \dfrac{D_{ADD}}{q_0 A_c}$	$\dfrac{W_2\sqrt{\theta_2}}{\delta_2}$	Corrected airflow
C_{D_P}	Pressure drag coefficient based on projected area $(A_{10}-A_9)$	X	Axial coordinate
$C_{D_{SPILL}}$	Spillage drag coefficient, $C_{D_{SPILL}} = \dfrac{D_{SPILL}}{q_0 A_c}$	δ	Ratio of total pressure to standard pressure
C_p	Pressure coefficient, $C_p = \dfrac{p - p_0}{q_0}$	θ	Ratio of total temperature to standard temperature
ΔC_D	Incremental drag coefficient	**Subscripts**	
D	Drag	0	Freestream station
D_{eq}	Equivalent diameter, $D_{eq} = \sqrt{\dfrac{4 A_{10}}{\pi}}$	1	Inlet throat station
EBOR	Equivalent body of revolution	2	Compressor entrance station
IMS	Integral mean slope parameter	8	Nozzle throat station
IMS_T	Truncated integral mean slope parameter	9	Nozzle exit station
K_{ADD}	Additive drag correction factor	ADD	Additive
M	Mach number	BLC	Boundary layer control
N	Number of shocks in shock system, including normal shock	BP	Bypass
p	Static pressure	LIP	Cowl lip
P_{T_1}/P_{T_0}	Total pressure recovery at inlet throat	SPILL	Spillage
		T/O	Takeoff

1. INTRODUCTION

During recent years much attention has been focused on problems related to the airframe/propulsion system interface of advanced military aircraft. The reason for this attention has been the difficulties experienced during aircraft development programs in integrating engines in aircraft systems to achieve a specified mission requirement. The major problems related to the integration of engine and airframe are the installation corrections due to inlet and nozzle/aftbody internal losses and drag.

---

*Manager, Advanced Military Aircraft Technology

**Senior Specialist/Engineer
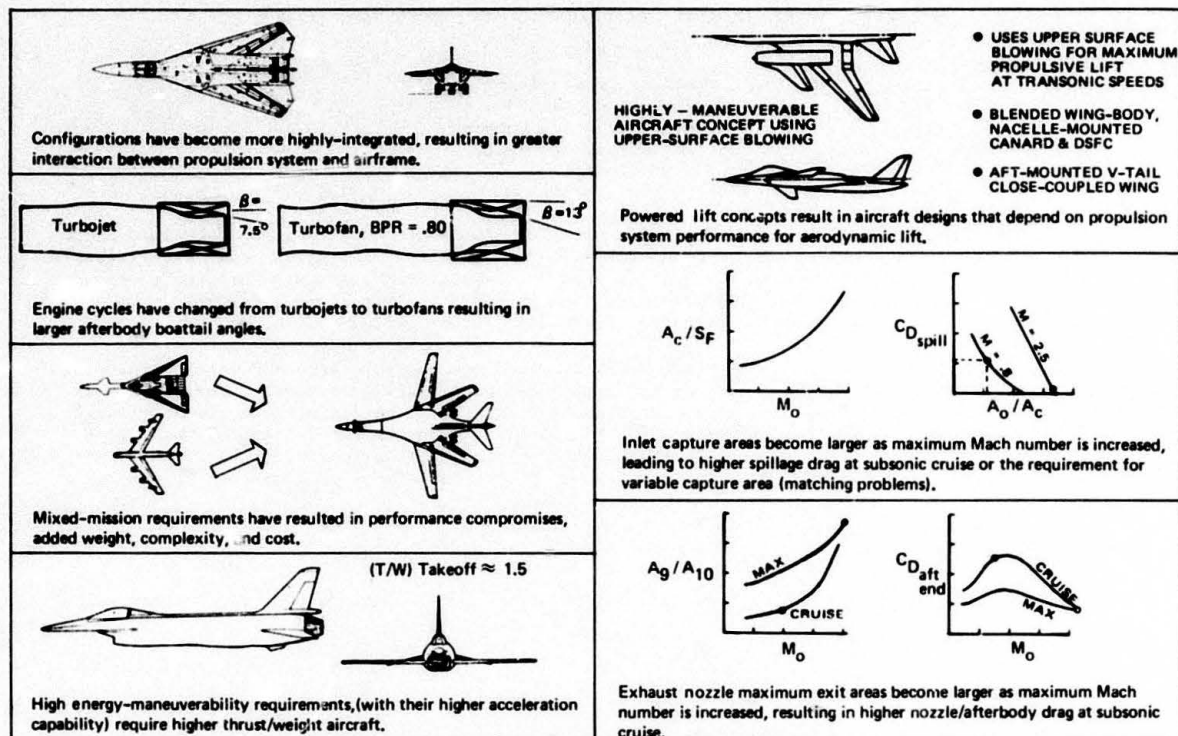
Figure 1 : Summary of Recent Trends in Military Aircraft Design

To understand why these problems have increased in importance, it is helpful to examine the trend of military aircraft design as flight speeds have increased and mission requirements have changed. Figure 1 shows some of the changes that have occurred. The result of these changes in aircraft design requirements is that forces produced by the installed propulsion system, in terms of thrust, drag, and lift, now exert a far greater influence on the design of the aircraft than was true in the past. This has created more complex technical problems in portions of the aircraft design where both aerodynamic and propulsion forces interact. In addition to increased technical complexity, however, the cost of developing aircraft has also increased greatly in recent years. All these factors point to the fact that we must acquire a better understanding, and make more efficient use of all the propulsion-related aircraft forces to have successful aircraft designs. This paper will discuss the important areas of propulsion system force accounting, prediction, and measurement that are related to achieving this objective.

In addition to the information contained in this paper, much recent data dealing with the subjects of airframe/propulsion system integration are contained in two previously published AGARD documents (References 1 and 2).

2.   ACCOUNTING OF AERO/PROPULSION FORCES

Increased interest in making accurate performance predictions for highly-integrated aircraft configurations has resulted in the need for better definition of aerodynamic and propulsion forces. More precise and consistent definitions of these forces will improve all aspects of the aircraft development process from conceptual studies through proposal evaluation, wind tunnel test, and flight test. One of the most important tools in obtaining better predictions of overall aircraft and propulsion forces is the force accounting system used during the aircraft development process. To understand why this is true, this paper will review what force accounting is, what the objectives of accounting are, and examine some of the problems that are associated with not doing the job of accounting well enough. Following this, a review will be made of the advantages and disadvantages of some of the various force accounting methods that have been used. The discussion of force accounting systems is based on results of recently completed studies from industry and military sources.

Force accounting, as applied to the calculation of aero/propulsion forces on aircraft, is the system used to define, relate, and integrate the aerodynamic and propulsion forces acting on the aircraft.

The need for a force (thrust/drag/lift) accounting system arises largely from the inability to determine, in one calculation or test, the total force on the complete airplane system with simultaneous real inlet and exhaust system operation. Furthermore, it is usually desirable or expedient to optimize the inlet and exhaust system components in separate tests which are independent of the general aerodynamic drag testing of the basic airplane configuration. Therefore, a well defined force accounting system is necessary to ensure that the performance predicted for each of the various elements (i.e., inlet, exhaust system airframe, and turbomachinery) is properly integrated to yield an accurate prediction of overall system performance. The accounting procedure must also ensure that appropriate information can be communicated between companies (engine and airframe companies) and to the government in a way that permits an accurate system performance evaluation and thus aids in the development of a successful aircraft design.

Some of the typical problems which show the need for improved force accounting procedures are: lack of standardized nomenclature and data formats, making it difficult to compare the performance of similar configurations obtained from different sources; lack of standardized reference conditions for separating propulsion and aerodynamic forces, causing problems in evaluating subsystem performance; poor element visibility due to improperly selected split planes for component performance; lack of continuity in tracking aircraft performance throughout the aircraft development cycle; lack of communication between airframe and engine company; and failure to include tests at proper reference conditions during all aerodynamic and propulsion wind tunnel tests.

To help avoid these problems, three criteria can be applied to judge the effectiveness of a force accounting system. First, and most important, is the requirement for accuracy in predicting the overall thrust-minus-drag of an airplane system. Second, the accounting system should provide visibility of the individual elements and subsystems of the airplane system. Finally, the accounting system should be applicable with consistent definitions throughout an entire airplane development program.

To satisfy these requirements, individual airframe companies have developed their own methods for defining and integrating aero/propulsion forces. In most cases, these methods are based on experience accumulated during the development of the company product line configurations. Many different types of configurations and wind tunnel test techniques have been developed and some force accounting methods are more suitable for one situation than another. Therefore, it is difficult to develop a general force accounting procedure that is applicable to all configurations and which will be acceptable to all aircraft companies. Despite this difficulty, however, there has been much interest during the last few years in trying to develop a better understanding of force accounting procedures, with the goal of arriving at a common set of standardized definitions and force accounting procedures that can be used by all airframe companies.

Two of the items that most frequently cause confusion and differences of opinion concerning force accounting methods are definition of forces and thrust/drag split. This paper will help clarify the definition of forces by presenting the specific force definitions that have been developed during a recent government contract, and which appear to satisfy the need for a general definition of forces.

To help put the problems related to the thrust/drag split in proper perspective, a discussion is presented which compares the most common ways of separating thrust and drag forces acting on an aircraft, and shows the fundamental differences in the basic approaches.

2.1 Definition of airframe/propulsion forces

The foundation of an adequate thrust/drag accounting system is a consistent definition of aero/propulsion forces within an appropriate reference system and a division of forces into those that are throttle-dependent (installed thrust) and those forces that are not throttle-dependent (to be reflected in the airframe system drag polar).

The throttle-dependent forces include the internal forces and those parts of the external forces (installation loss drags) that are throttle-dependent.

The internal force is defined as the difference between nozzle static gross thrust and engine-streamtube ram drag. In the case of an analytical performance buildup, as well as the case of a jet effects model simulation of real exhaust system operation, the "static gross thrust" is the gross thrust corresponding to the static nozzle thrust coefficient at the operating total pressure ratio and the actual nozzle mass flow rate. In calculating the internal force of the aerodynamic force and moment model, the nozzle gross thrust can correspond to either static or wind-on conditions, as long as the same definition is used when these flow-through nacelle conditions are simulated with the jet effects model as the reference point for external force increments. The "engine streamtube" includes all of the airflow demand at the engine face as well as any secondary airflow captured by the inlet and ducted around the engine to the exhaust system. Any additional airflow captured by the inlet and ducted overboard through bleed or bypass systems is not part of the "engine" streamtube.

The external force is the difference between the total force on the airplane and the internal force defined above. As a consequence, the external force includes: additive drag on engine streamtubes, drag of all inlet surfaces (e.g., a bleed system) wetted by streamtubes other than engine streamtubes, and the change in nozzle thrust forces between static and wind-on conditions.

If all the internal and external forces acting on an aircraft in level flight at a given attitude, Mach number, and altitude are summed, they can be represented by the total force equation of Figure 2. Each of the force components which contribute to F_{TOTAL} is defined in Figure 2 and the force components are grouped into those that are throttle-dependent (included in installed propulsive thrust) and those that are non-throttle-dependent (to be included in the airframe system drag polar).

The engine net thrust $F_{N_{ENG}}$, defined as $F_{G_{STATIC}} - F_{RAM}$, accounts for the effects of inlet internal performance, nozzle internal (static) performance, engine bleed, and power extraction.

The remaining terms in the equation of Figure 2 are keyed to the concepts of operating reference drag polar conditions and aerodynamic (wind tunnel) reference conditions, which will be discussed in Section 2.2.

The terms on the right side of the equation in Figure 2, other than the trim terms, represent the thrust/drag buildup at a reference control surface angle. The procedures outlined here are also directly applicable to lift buildups and, with some modification, to pitching moment buildups. The determination of lift, drag, and pitching moment in this way as a function of control surface angle and angle-of-attack permits the construction of a trimmed drag polar at operating reference conditions. Thus, the term ΔD_{TRIM} is the external force difference associated with changing from the reference control surface angle to the control surface angle required for trim.

$$F_{TOTAL} = F_{N_{ENG}} + \Delta F_{N_{INL}} + \Delta F_{N_{EXH \atop SYS}} + \Delta F_{N_{TRIM}} - D_{REF} - \Delta D_{INL} - \Delta D_{EXH \atop SYS} - \Delta D_{TRIM}$$

$\underbrace{\qquad\qquad}_{\text{Installed Engine Net Thrust}}$

$\underbrace{\qquad\qquad}_{\text{Installed Propulsive Thrust}}$ $\underbrace{\qquad\qquad}_{\substack{\text{Airframe System Drag} \\ \text{(Reflected in the drag polar)}}}$

F_{TOTAL}	=	Total force in the flight direction on an aircraft in level flight at a given attitude, Mach number, and altitude
$F_{N_{ENG}}$	=	Net internal force generated by the engine, accounting for the effects of inlet internal performance, nozzle internal (static) performance, engine bleed, and power extraction
$\Delta F_{N_{INL}}$	=	Throttle-dependent external force increment between operating reference and operating conditions due to inlet
$\Delta F_{N_{EXH} \atop SYS}$	=	Throttle-dependent external force increment between operating reference and any given operating condition due to exhaust system
$\Delta F_{N_{TRIM}}$	=	Changes in trim drag associated with operation at propulsion system conditions other than operating reference
D_{REF}	=	External force (associated with aerodynamic force and moment model) at reference conditions
ΔD_{INL}	=	Non-throttle-dependent external force increment between aerodynamic reference and operating reference inlet conditions
$\Delta D_{EXH} \atop SYS$	=	External force increment due to exhaust system between aerodynamic reference and operating reference conditions
ΔD_{TRIM}	=	External force difference associated with changing from the reference control surface angle to the control surface angle required for trim at operating reference conditions

Figure 2: *Definitions of Installed Thrust and Drag Quantities*

Changes in trim drag increments associated with operation at propulsion system conditions other than operating reference conditions are likely to be very small in most cases. If not, however, they should be included as $\Delta F_{N_{TRIM}}$, which becomes one of the throttle-dependent force increments accounted for in the installed propulsion system performance.

2.2 Reference conditions for airframe/propulsion force accounting

The selection of suitable reference conditions for aero/propulsion force accounting is one of the most controversial subjects involved in airplane system performance prediction. This is true for several reasons: (a) reference conditions are configuration dependent, (b) reference conditions are related to test techniques, (c) reference conditions that are convenient for analytical studies may not be convenient for wind tunnel testing, and (d) the reference conditions required are a strong function of the visibility desired (i.e., element, subsystem, or system).

Despite the difficulties involved, it is always necessary in each aircraft development program to define suitable reference conditions that can be used to split the aerodynamic and propulsion forces acting on the aircraft. Although they may differ in details and nomenclature, the three most common reference systems encountered are those shown in Figure 3. Figures 3a and 3b depict force accounting systems which utilize two references during the process of generating installed airplane system thrust-minus-drag performance data. A more detailed description of the reference conditions of Figure 3a is contained in Figure 4.

The expression "operating reference conditions" is used here specifically to distinguish these conditions from the wind tunnel "aerodynamic reference" conditions which are: (a) used on the aerodynamic force and moment model; and (b) reproduced on the propulsion models to obtain data for propulsion drag increments. The operating reference conditions are those conditions, representative of realistic flight conditions, to which by definition the drag polar corresponds. The definitions apply whether the drag polar results from analytical buildup procedures, wind tunnel tests, or flight test. By use of a separate "operating reference" for the drag polar, the drag polar is not constrained to correspond exactly to aerodynamic force and moment model reference conditions. Therefore, there is considerable freedom in an experimental buildup to tailor the aerodynamic reference conditions to ensure that they can be precisely reproduced on the inlet-drag and jet-effects models, thereby minimizing errors in the overall thrust-minus-drag buildup.

The reference conditions used in the force accounting systems depicted in Figures 3a and 3b are similar except that system 3b uses a reference mass flow ratio for the operating reference that corresponds to the maximum mass flow ratio attained during the inlet drag model tests, while system 3a uses an operating reference mass flow ratio corresponding to a specified engine power setting (usually maximum airflow). The operating reference mass flow used by system 3b, which is obtained from wind tunnel model test, may not correspond to a realistic engine operating condition.

	AERODYNAMIC REFERENCE (AERO MODEL TESTED AT THESE CONDITIONS)				OPERATING REFERENCE (CONDITIONS TO WHICH AIRPLANESYSTEM DRAG POLAR CORRESPONDS)				ADVANTAGES	DISADVANTAGES
	INLET GEOMETRY	INLET AIRFLOW	AFT-END GEOMETRY	NOZZLE PRESSURE RATIO	INLET GEOMETRY	INLET AIRFLOW	AFT-END GEOMETRY	NOZZLE PRESSURE RATIO		
(a)	GENERALLY REALISTIC GEOMETRY, NO BLEED OR BYPASS	MINIMUM SPILLAGE DRAG CONDITION $\left(\frac{A_0}{A_c} = \frac{A_1}{A_c}\right)$	REALISTIC GEOMETRY, BUT MODIFIED WHERE NECESSARY TO AVOID LIKELY REGIONS OF SEPARATED FLOW	RAM PRESSURE RATIO	REALISTIC GEOMETRY, BLEED FLOW, BYPASS FLOW CORRESPONDING TO SPECIFIED AND ACTUAL INLET OPERATING CHARACTERISTIC	REALISTIC MFR CORRESPONDING TO SPECIFIED POWER SETTING (USUALLY MAX) & ACTUAL INLET OPERATING CHARACTERISTIC	REALISTIC GEOMETRY CORRESPONDING TO SPECIFIED POWER SETTING	REALISTIC PRESS. RATIO, (BOTH P_{t_8}/P_0 AND P_9/P_0) CORRESPONDING TO SPECIFIED POWER SETTING	(1) PROVIDES MAXIMUM ELEMENT VISIBILITY AT ALL LEVELS (2) MAKES IT POSSIBLE TO TAILOR WIND TUNNEL MODELS FOR MAXIMUM ACCURACY (3) PROVIDES CONSISTENT TRACKING OF SYSTEM PERFORMANCE THROUGHOUT DEVELOPMENT PROGRAM	(1) REQUIRES USING A DIFFERENT REFERENCE FOR AIRPLANE SYSTEM PERFORMANCE THAN FOR W/T TEST; THEREFORE IT IS A MORE COMPLICATED PROCEDURE
(b)	FLOW-THROUGH NACELLE	MAXIMUM $\left(\frac{A_0}{A_c} \approx 1.0\right)$	WIDE OPEN (FLOW-THROUGH)	RAM PRESSURE RATIO	ACTUAL INLET GEOMETRY	MAXIMUM AIRFLOW ATTAINED ON INLET DRAG MODEL	FLOW-THROUGH WITH STING EFFECTS REMOVED	RAM PRESSURE RATIO	(1) PROCEDURE IS SIMPLE TO USE AND UNDERSTAND	(1) FOR THEORETICAL BUILDUP OF DRAG OR PERFORMANCE BEFORE TESTING IS ACCOMPLISHED, THE INLET REFERENCE AIRFLOW IS UNKNOWN (2) DOES NOT PROVIDE A CONSISTENT REF. FOR TRACKING OF FORCES FROM PREDICTIONS, THROUGH WIND TUNNEL TEST AND FLIGHT TEST. (3) WIND TUNNEL "REFERENCE" MAY NOT CORRESPOND TO A REALISTIC OPERATING CONDITION; THEREFORE, IT CAN MAKE A POOR REFERENCE
(c)	WIDE OPEN INLET (FLOW-THROUGH NACELLE)	MAXIMUM $\left(\frac{A_0}{A_c} \approx 1.0\right)$	WIDE OPEN (FLOW-THROUGH)	RAM PRESSURE RATIO	NO OPERATING REFERENCE (CORRECTIONS ARE APPLIED FROM WIND TUNNEL REFERENCE TO OPERATING CONDITION)				(1) IT IS SIMPLE TO UNDERSTAND AND MAKES GOOD BASIS FOR THEORETICAL PREDICTIONS BEFORE TESTS ARE PERFORMED (2) REFERENCE MASS FLOW IS A CONSTANT	(1) RESULTS IN SOME DRAGS BEING INCLUDED IN PROPULSION SYSTEM PERFORMANCE, THAT ARE NOT THROTTLE-DEPENDENT THEREFORE IT DOES NOT PROVIDE VISIBILITY OF PROPULSION SYSTEM PERFORMANCE (2) REFERENCE MASS FLOW RATIO IS NOT A REALISTIC CONDITION. IT REQUIRES SPECIAL MODELS FOR TESTING. (3) DOES NOT PROVIDE FOR REALISTIC INTERACTIONS BETWEEN INLET SPILLAGE & AIRFRAME (4) REQUIRES EXTENSIVE CORRECTIONS TO W/T DATA

Figure 3: Force Accounting Methods

	Inlet	Exhaust System
Aerodynamic Reference Conditions — Aero model tested at these conditions. Criteria for selection include: 1. Can be reliably reproduced in the separate inlet and nozzle tests. 2. Facilitates accurate measurement of both aero model drag and associated propulsion increments from the separate tests. 3. Represents realistic conditions modified as necessary to satisfy above criteria. Airplane system drag polar need not correspond to these reference conditions	Generally realistic geometry, no bleed or by-pass flow (which are difficult to reproduce at different scales). Mass flow ratio selected to minimize aero model lip separation, which is more accurately simulated on the larger scale inlet spillage drag model. Thus there will be minimal spillage drag at this mass flow ratio.	Realistic geometry, if feasible but modified where necessary to avoid likely regions of separated flow. Any reduced boattail angles would imply extra nozzle base area. Ram pressure ratio (since aero model uses flow-through propulsion simulation).
Operating Reference Conditions — The conditions to which the airplane system drag polar corresponds, by definition. These conditions correspond approximately to a specified engine power setting, usually maximum power, but would not be changed for minor engine variations.	Realistic geometry, bleed flow, bypass flow and inlet mass flow ratio, corresponding to specified engine power setting and actual inlet operating characteristic.	Realistic aft-end geometry and pressure ratio (both P_{T_8}/P_0 and P_9/P_0) corresponding to specified power setting.

Figure 4 : Summary of Aerodynamic and Operating Reference Conditions

The use of realistic operating reference conditions (Figure 3a) corresponding to a specified power setting and the use of a static thrust coefficient in defining nozzle gross thrust offer major benefits in terms of two of the criteria identified for selecting the accounting system. First, performance visibility for airframe system and propulsion system performance is achieved. Thus, the drag polars of competing configurations using the same engines can be meaningfully compared. (The installation loss drag penalties associated with reduced power settings can similarly be directly compared.) Secondly, the thrust/drag definitions can be maintained in a consistent manner throughout an entire airplane development program. The performance evolution with time of the drag polars and installation losses can be tracked from the early mission definition studies, through wind tunnel programs, and into the flight test programs. The reduction in the uncertainty bands associated with improving geometric definition of the configuration and higher level performance evaluation methods can be traced with a common set of thrust/drag accounting definitions.

Figure 3c depicts a method of force accounting wherein all of the force increments between wind tunnel aerodynamic reference conditions and operating conditions are treated as installation losses. Thus, the airframe system drag polar corresponds to the flow-through wind tunnel model without corrections to reflect realistic propulsion system conditions. This sacrifices subsystem visibility (e.g., the ability to compare drag polars of competing systems tested at different aerodynamic reference conditions) and includes in installation losses potentially large force increments which are not throttle-dependent.

An analytical performance buildup using the systems of Figures 3a and 3b could be handled in a manner completely analogous to the experimental buildup, except that wind tunnel reference conditions would not be treated. For example, the aft-end drag already accounted for in a wing-body drag calculation, which is analogous to the aerodynamic reference drag, could become the zero point for aft-end exhaust system drag increments. The drag polar is still corrected to operating reference conditions, and $\Delta F_{N_{EXH\ SYS}}$ still accounts for the effect of operating at real aft-end conditions different from the operating reference condition. Figure 5 illustrates the use of the force accounting procedure with analytical force data.
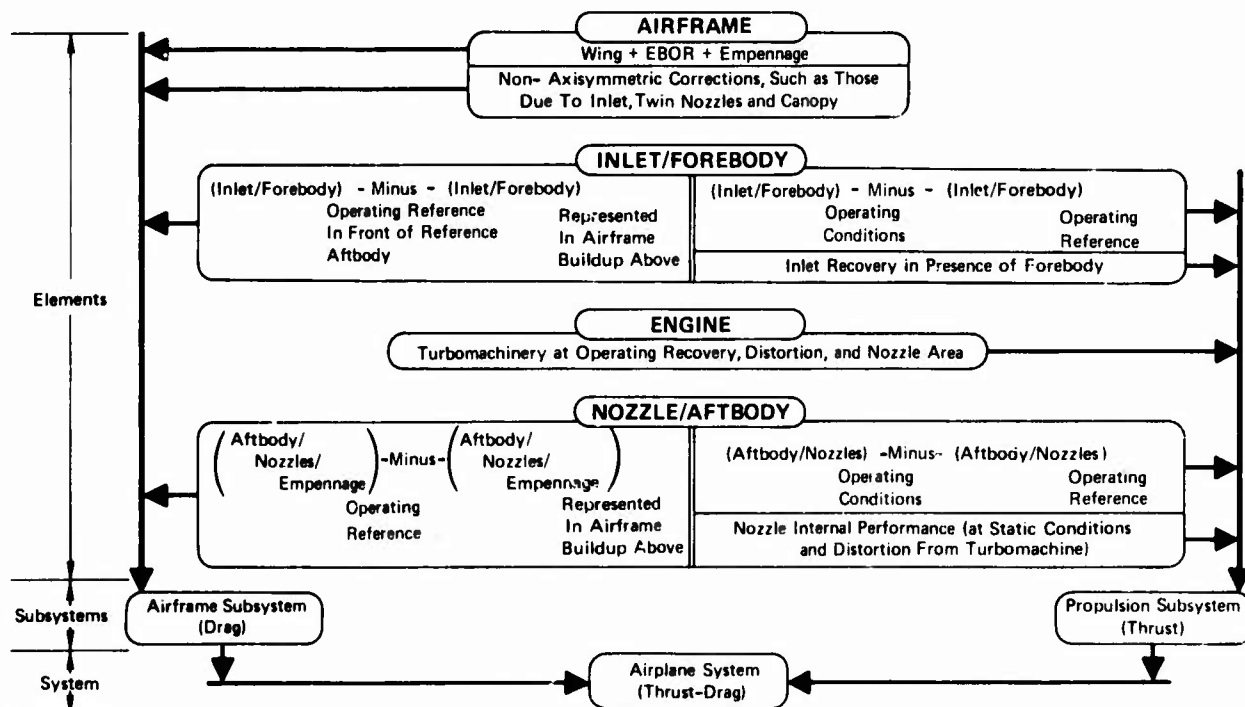
Figure 5: Force Accounting Method Using Analytical Buildup

3. FORCE PREDICTION TECHNIQUES

The force prediction methods most suitable for quantitative analysis of preliminary designs and trade studies are those that can be applied prior to the time scale model wind tunnel testing is conducted. The methods must also allow the use of test data after it is available. Two recently-developed calculation procedures will be discussed and are examples of methods that are easily computerized, require little time to use, and are responsive to prime geometric parameters influenced by engine, structure, payload, and fixed equipment volume requirements and volume distribution.

3.1 Nozzle/aftbody drag prediction method

Correlations of data from a recently-completed parametric wind tunnel investigation of aft-end drag for twin, buried engine configurations have provided the basis for a new drag prediction method. These correlations deal with the pressure drag of the aft fuselage from the maximum cross-sectional area point aft.

The correlation is a modification to the Integral Mean Slope (IMS) approach (Reference 3). The original IMS parameter, calculated analytically from aft-end geometry, is defined as follows:

$$IMS = \frac{\displaystyle\int_{(A_9/A_{10})}^{1.0} \frac{d\ (A/A_{10})}{d\ (X/D_{eq})}\ d\ (A/A_{10})}{1 - (A_9/A_{10})}$$

When aft-body drag data for certain types of afterbodies were plotted as a function of the calculated IMS parameter, it was found that a correlation was obtained which could be useful for drag predictions during preliminary studies.

Analysis of additional test data, however, obtained subsequent to the original correlation, showed that the correlation failed for configurations whose area plots involved regions of steep slopes (Figure 6a), aft of the point where separation occurs. The IMS_T (Integral Mean Slope - Truncated) approach, designed to correct this problem, is based on specifying a maximum slope of the non-dimensional area distribution which can be used in the IMS calculation. This specified maximum slope is substituted for the real slope at each step of the IMS calculation for which the real slope exceeds the maximum. The best data correlations were obtained by making the maximum slope a function of Mach number. The improved correlation is illustrated in Figure 6b. Figure 7 gives data correlations for single and twin vertical configurations with widely varying area plots.
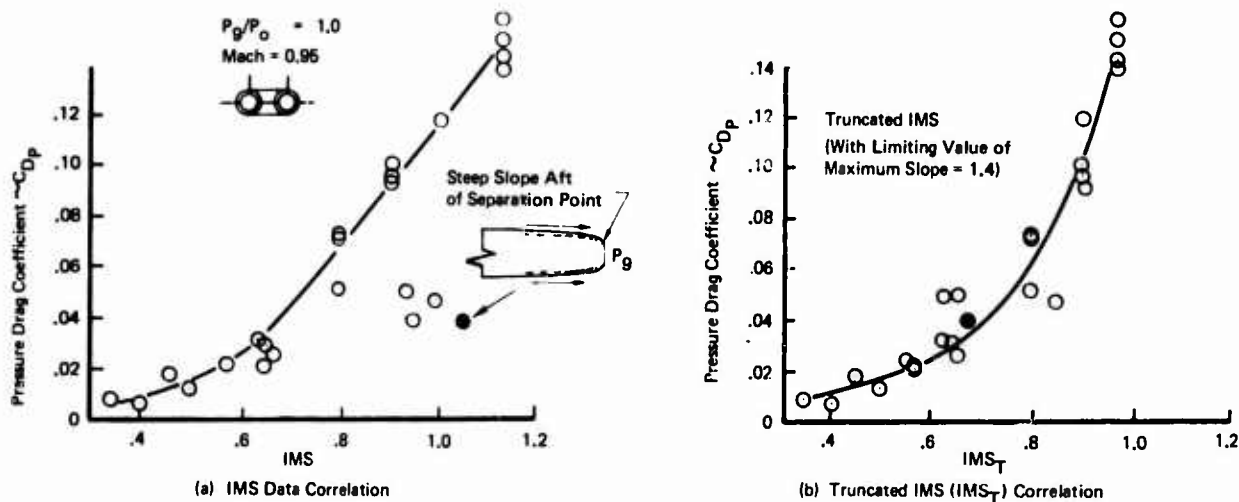
Figure 6 : IMS and IMS_T Data Correlations

Further investigations showed that all the data correlations, when corrected by a ΔC_D for tail type, varied almost exactly as the IMS_T parameter raised to the 2.77 power. Thus, the IMS_T parameter was divided out to obtain a drag parameter,

$$\frac{C_{D_P} + \Delta C_D}{IMS_T^{2.77}}$$

as a function of Mach number only. A summary of the drag prediction procedure is shown in Figure 8. The effectiveness of the correlation method is shown in Figure 9.
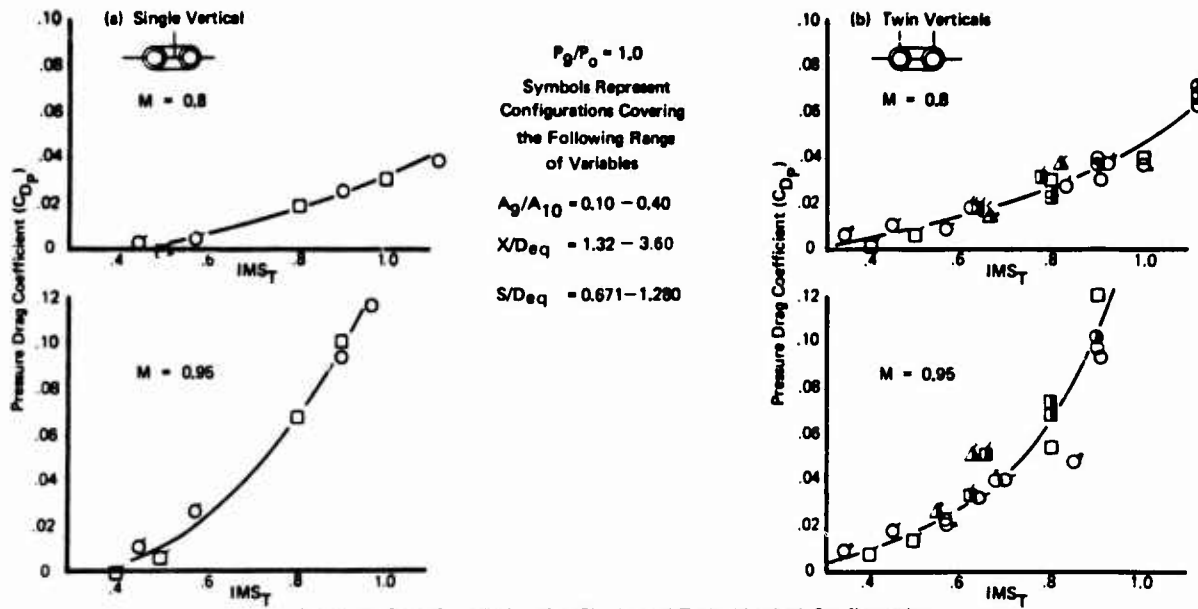
Figure 7: Drag Correlation for Single and Twin Vertical Configuration
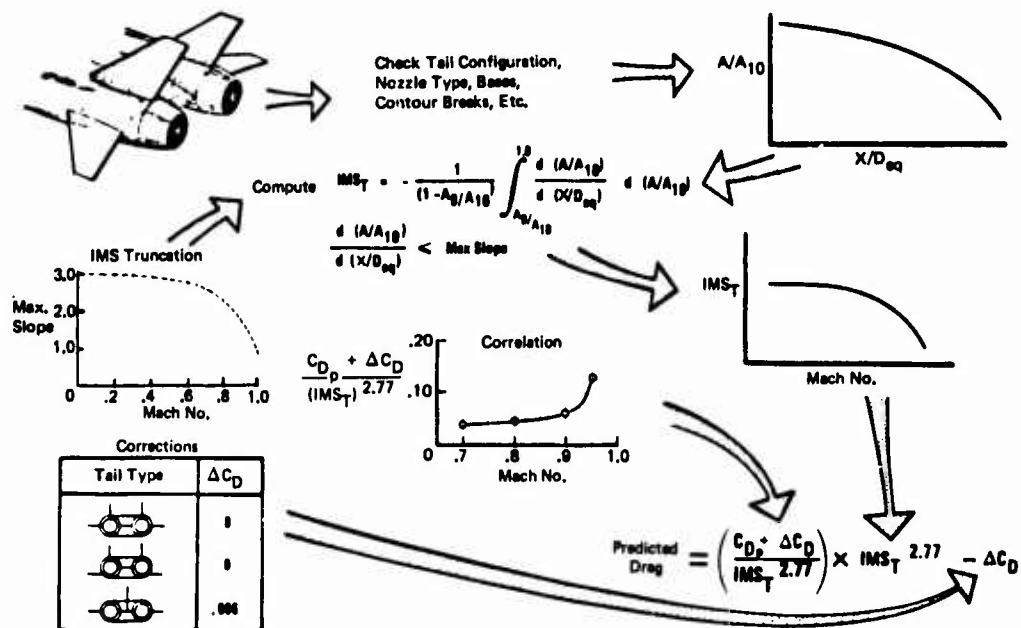
Figure 8: Drag Prediction Procedure
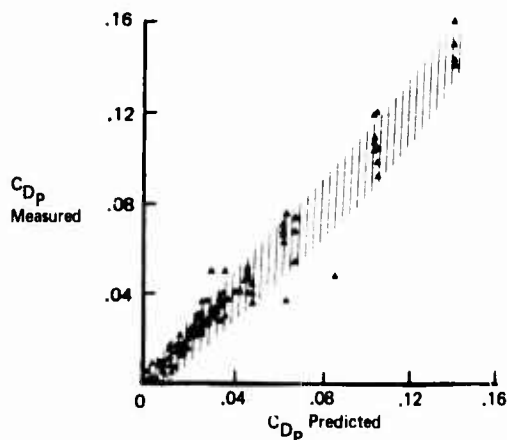
Figure 9: Correlation Method Errors
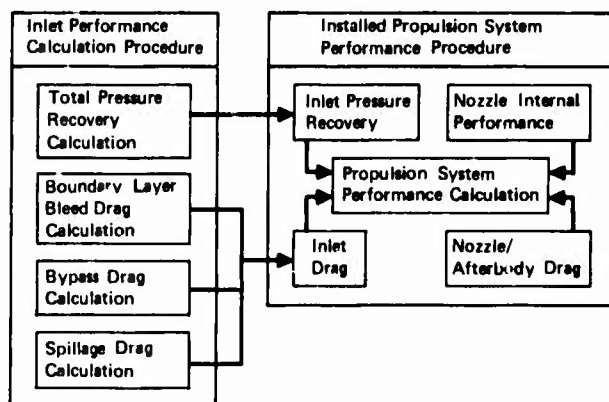
Figure 10: Relationship Between Inlet and Installed Propulsion
System Performance Calculation Procedures
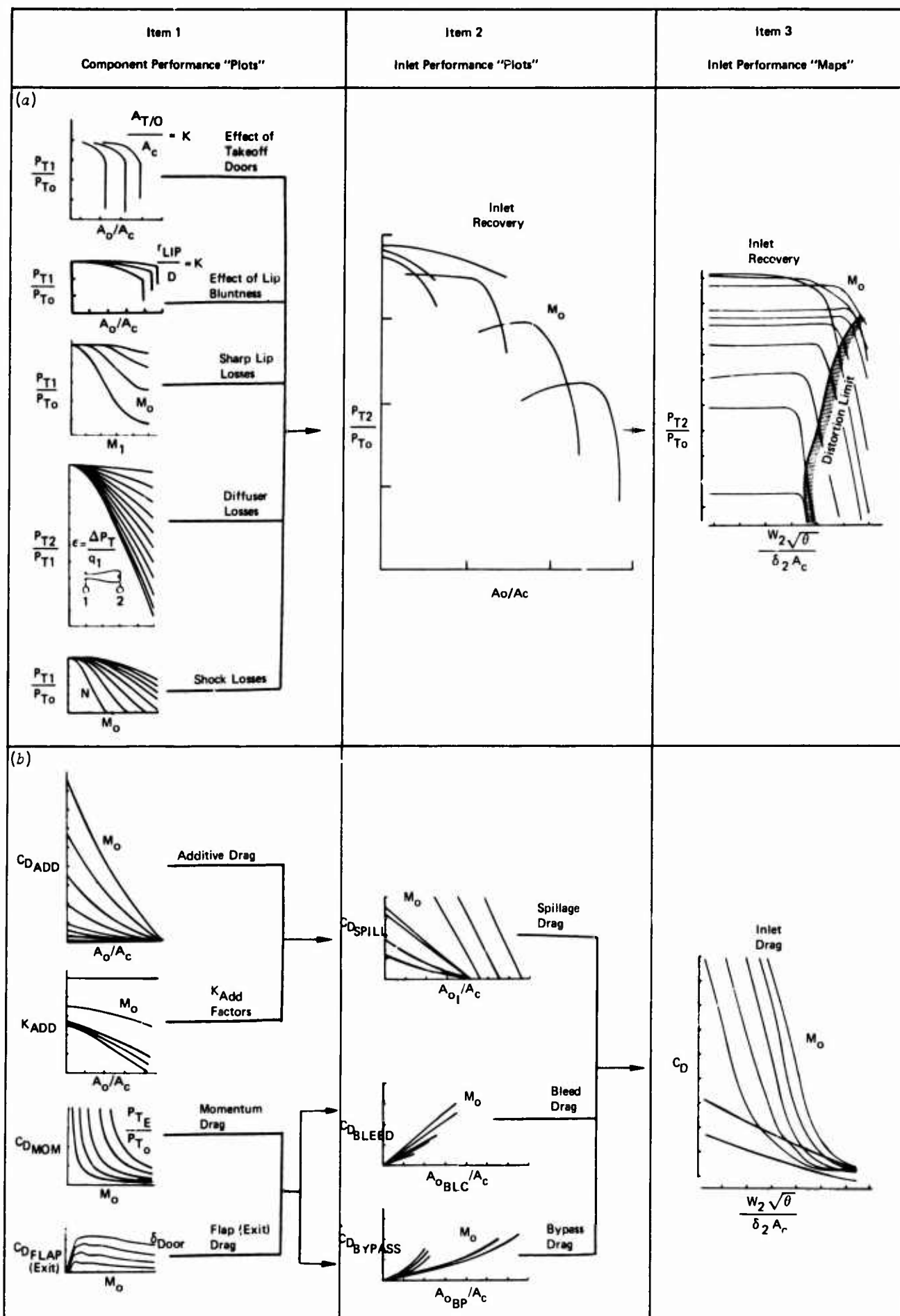
Figure 11 : Inlet Performance Elements

3.2 Inlet recovery and drag prediction method

The inlet recovery and drag prediction method was developed as part of a recent analytical study conducted for the Air Force Flight Dynamics Laboratory. The comprehensive procedure, shown schematically in Figure 10, uses maps of total pressure recovery and inlet drag as a function of engine corrected airflow divided by capture area (Item 3 of Figure 11) to provide a detailed description of the inlet characteristics. These maps directly provide the recovery and drag for installed propulsion system calculations. Corrected airflow is the parameter used to match inlet performance to the engine.

However, most inlet wind tunnel test data are obtained in the form of individual performance plots such as those shown in Item 2 of Figure 11. These performance plots are readily converted into the performance maps by a separate, easily computerized sub-program.

If wind tunnel test data are not available, inlet performance characteristics can be built up by theoretical and semi-empirical procedures, such as those shown as Item 1 of Figure 11, which indicates the major variables that must be considered. The standardized format for performance maps makes it possible to build up a large data bank of maps covering a wide variety of inlet configurations for making rapid calculations of installed propulsion system performance. This provides the capability to quickly evaluate, in detail, a great number of configurations during the conceptual design phase of aircraft development.

To illustrate the application of the inlet performance procedure, Figure 12 presents a comparison of the predicted and measured total pressure recovery for a lightweight fighter study configuration at flight Mach numbers from 0 to 1.60 (Reference 4). Predicted and measured inlet spillage drags are compared in Figure 13 (Reference 5).

(a) Lightweight Fighter Fixed Geometry Inlet
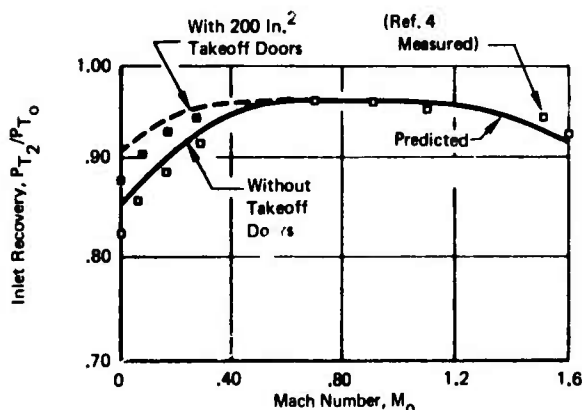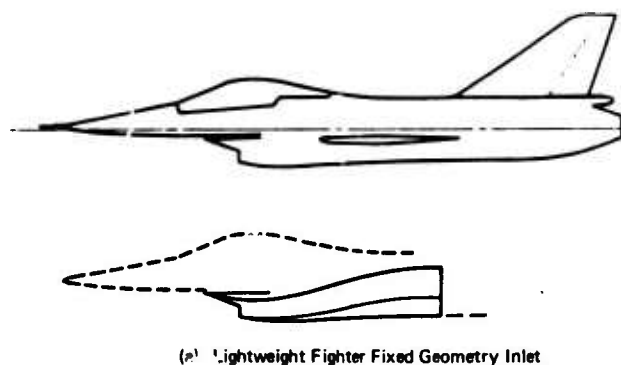
(b) Comparison of Predicted and Measured Total Pressure Recovery Data

Figure 12: Comparison of Predicted and Measured Inlet Recovery
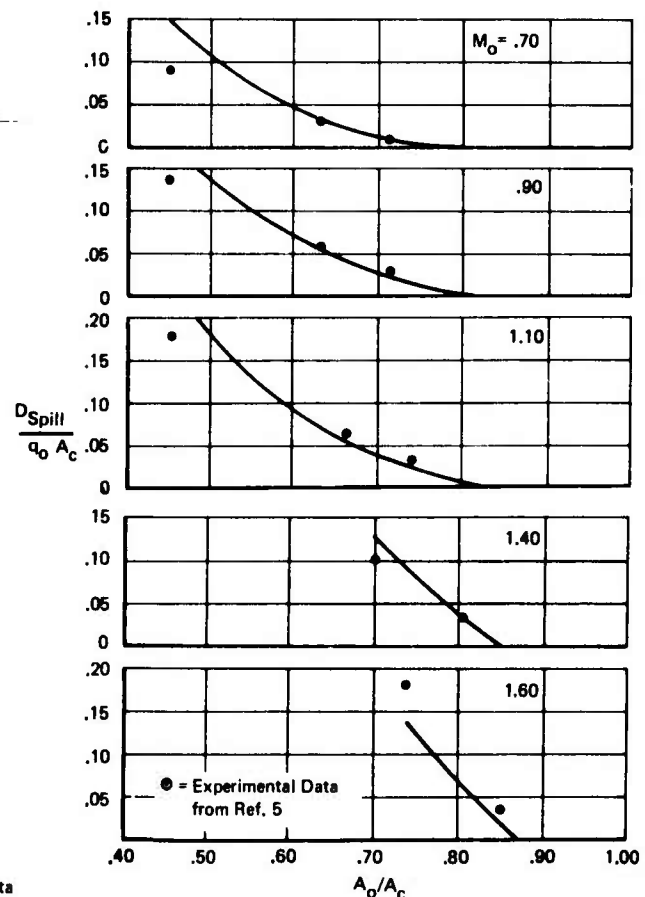
Figure 13: Comparison of Predicted Data and Test Data for LWF Spillage Drag

4. FORCE MEASUREMENT TECHNIQUES

The accurate prediction of aircraft performance depends largely on two factors: (1) proper accounting of all thrust, drag, and lift effects, and (2) the accuracy of the basic data used to predict the performance. Proper accounting of forces has been discussed in a previous section of this paper. This section deals with test techniques for obtaining measurements of forces on airframe/propulsion systems.

A widely used approach to obtaining engine/airframe data involves use of three types of wind tunnel models (Figure 14). The models are typically tested over a range of flight conditions to obtain data that are integrated using the force accounting procedure previously described.

Studies were completed to investigate problems associated with various test techniques. The studies included investigating data uncertainties due to model support systems, metric split-line locations, wind tunnel limitations such as shock reflections and model blockage, scale effects, and model mass flow.
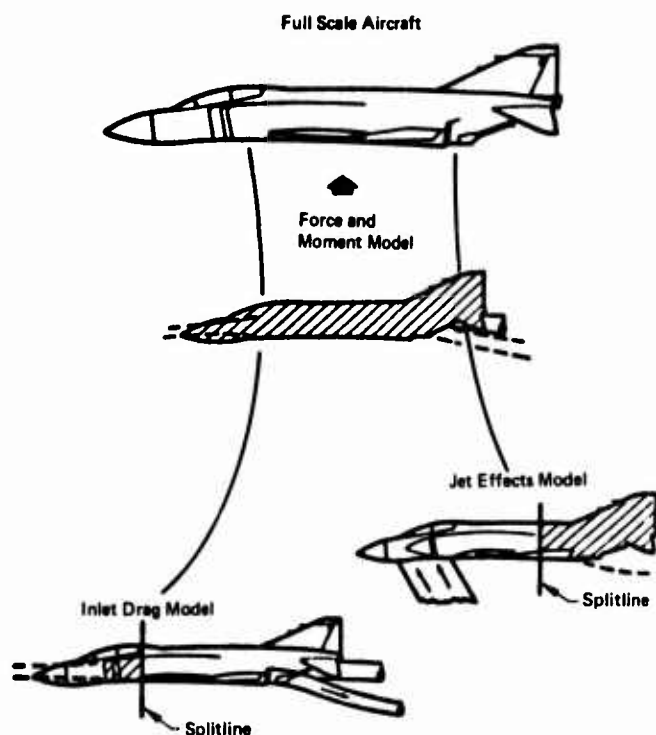
Figure 14: Projection of Full Scale Aircraft Performance
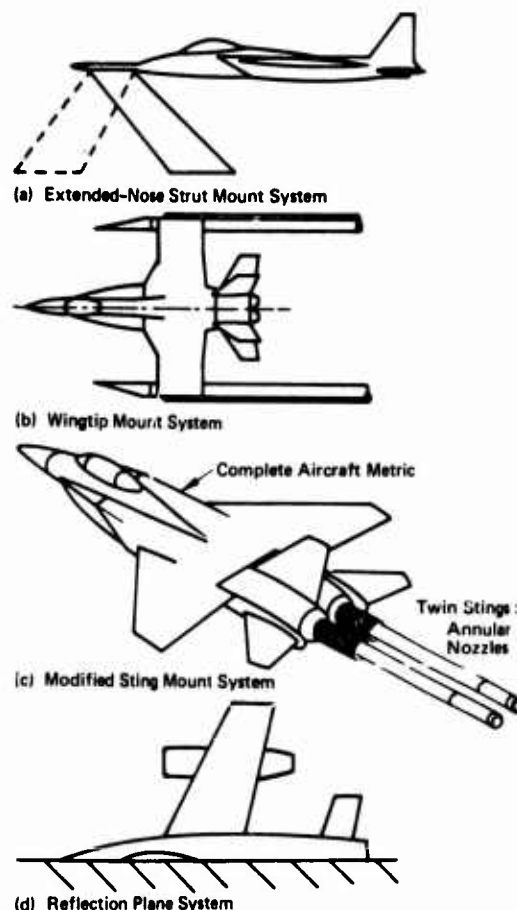
Figure 15: Jet Effects Model Support Systems

4.1 Model support systems

Most model support systems introduce data uncertainties because of flow field interference effects. This problem is most significant for jet effects models because the support strut must be large enough to route the air supply required for jet simulation. Thus, it is mandatory that the interference characteristics be determined for candidate jet effects model support systems. The problems of model support systems summarized below are discussed in detail in Reference 2.

Four possible approaches that have been considered for jet effects model testing are shown in Figure 15. An extended-nose strut mounting system (Figure 15a), has been used, where the nose extends upstream. This type of mount affects fuselage flow fields and boundary layer development. The wing tip mount (Figure 15b), eliminates the strut mount, but the effect of wing distortion required for passage of nozzle high pressure air and mounting pylons must be determined. Also, significant flow field distortion is anticipated at angle-of-attack.

Dual sting mounts entering the exhaust nozzles (Figure 15c) may have potential usefulness for testing where the nozzle configuration has a large enough exit area after sting area is deducted (such as maximum A/B) to allow adequate mass flow through the model for annular jet exhaust simulation. This approach could not be used for plug nozzle configurations but it could be used on aerodynamic force and moment models.

A half model mounted against a reflection plane (Figure 15d) removes all support strut effects and considerably reduces model blockage in the tunnel, but is unsuitable for configurations with close coupled fuselage mounted engines. Tunnel wall boundary layer may also create some problems. Support effects on afterbody pressure drag are shown in Figure 16a. Qualitative data from tests in the AEDC 1-foot tunnel show little evidence of subsonic strut interference with afterbody pressures (Figure 16b).

4.2 Metric split-line locations

The inlet drag and jet effects models (for example, Figure 14) are divided by split-lines, which separate the metric and non-metric sections of the model. Forces on the metric portion are measured with a drag balance. Using a metric break to isolate the smallest acceptable piece of the model on a force balance appears to offer an advantage in accuracy because a more sensitive balance can be used. Care must be taken, however, to be sure metric split-lines are located where they will measure the whole effect. For highly-integrated exhaust systems, pressure disturbances produced by aft-end changes (particularly at subsonic conditions) may be so extensive that a large part of the airplane must be metric to determine accurately the total force increment resulting from the changes. Similarly, during inlet drag testing, mass flow induced disturbances may propagate aft of the split-line and not be accounted for. If metric breaks are used to isolate smaller portions of the force model on balance, it is necessary to first make extensive tests using a pressure model to verify the adequacy of the metric break locations.

Another disadvantage of using metric breaks is that if the metric break involves a significant projected area in the flight direction, internal cavity pressures produce an important tare force which must be subtracted from the balance reading. The limitations in accuracy with which this tare force can be determined can destroy the potential improvement in drag accuracy theoretically possible with the smaller balance.

A common method used to determine afterbody drag is to scale the afterbody, mount it behind a "representative" forebody, and measure the axial force on the afterbody. The location of the split-line for the afterbody drag balance and the shape and length of the "representative" forebody can introduce errors into the measured data. Figure 17 presents the results of a potential flow analysis that was performed to investigate the pressure forces acting on a given afterbody mounted behind two different forebodies. The data illustrate the dangers of using split planes and "representative" forebodies that are different from the actual forebodies. If only the pressure forces on the afterbody are integrated, a significant error in afterbody drag can be introduced by applying the afterbody drag to another forebody of arbitrary shape.
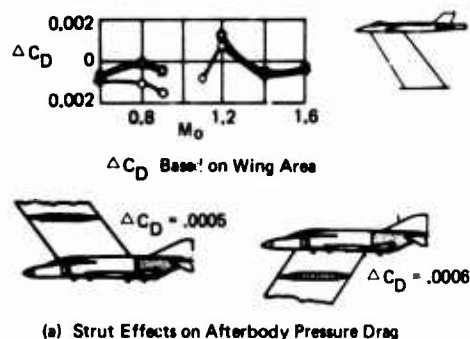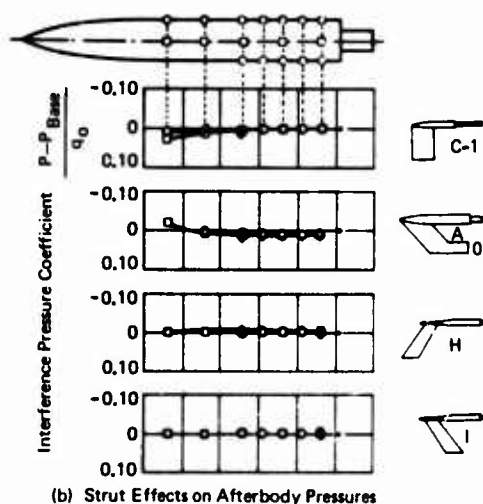
Figure 16 : Strut Interference Effect (Ref. 6)
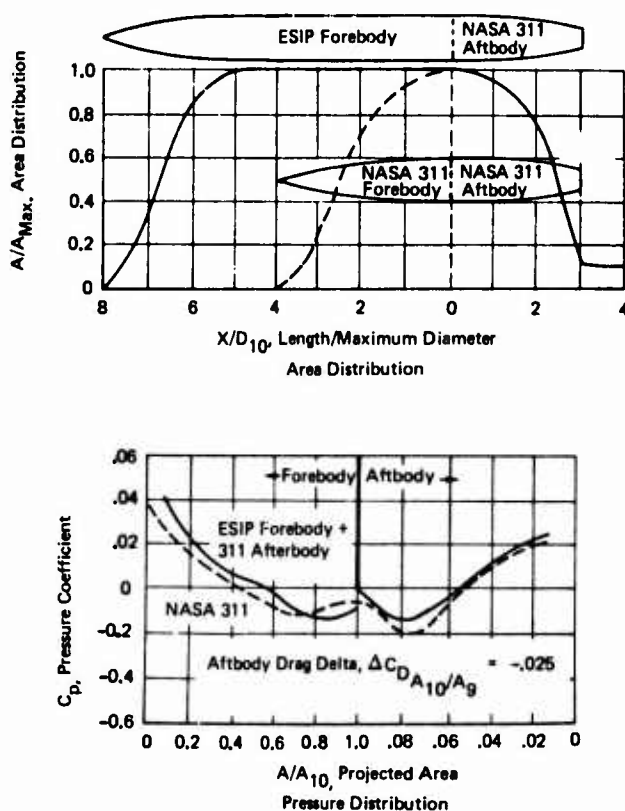
Figure 17: Forebody Effects on Afterbody Drag

It is recommended that inlet and exhaust system force measurements be made with as much of the airplane model on balance as possible, instead of using metric breaks to isolate parts of external surfaces on balance. Drag measurements taken during wind tunnel tests of a Boeing lightweight fighter study configuration have shown that sufficiently accurate drag data can be measured using a full airplane model to detect the effects of even small changes in cowl shape (Figure 18).

4.3   Model mass flow

A number of corrections to aerodynamic force and moment model data are required because of improper mass flow through the model. In fact, the primary purpose of inlet drag and jet effects models is to correct the aerodynamic force and moment model data to the proper airflow conditions. The requirement for using the three models previously described arises from the fact that correct inlet flow conditions and jet effects cannot be simulated at the same time. The propulsion simulator (being studied by the U.S. Air Force) offers a potential solution to this problem by providing simulation of both inlet and nozzle flow conditions simultaneously. Lacking such a simulator, however, jet effects model tests are usually run with faired-over inlets. This introduces uncertainties into the afterbody drag measurements due to lack of the effects of spillage airflow, which could interact with the nozzle/afterbody flow. Effects of inlet spillage or faired-over inlets on afterbody drag are shown in Figure 19. Inlet fairing shape appears to be non-critical. In some cases, afterbody drag is unaffected when the fairing is removed exposing a dead-end inlet (Reference 6).

$$C_{D_{Spill}} = \frac{D_{Spill}}{q_o A_c}$$
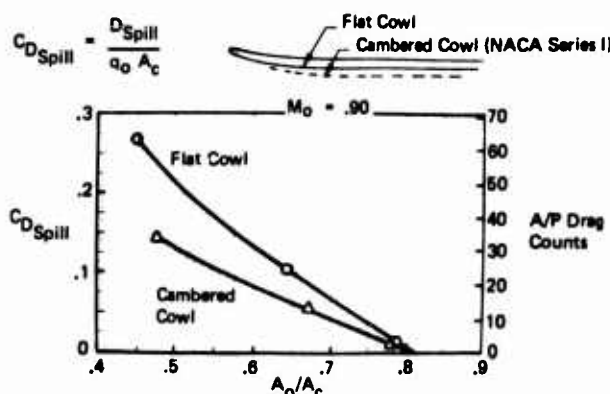
Figure 18: Effect of Cowl Shape on Spillage Drag (Ref. 7)
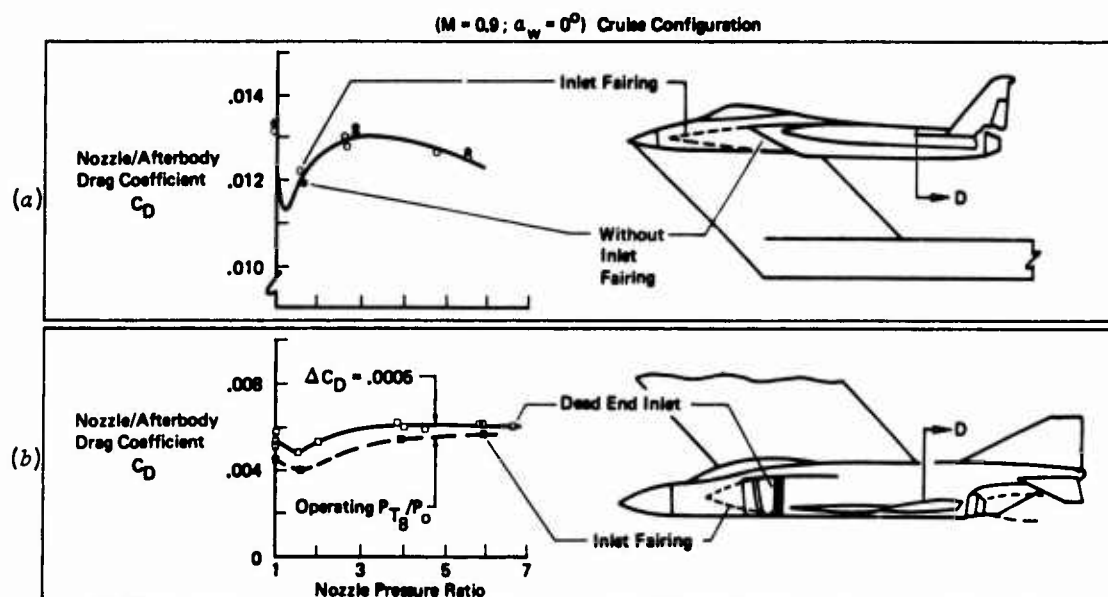
Figure 19: Inlet Fairing Effects on Afterbody Drag (Ref. 6)

4.4 Wind tunnel limitations

Wind tunnel blockage and shock reflections present major sources of testing uncertainties at transonic speeds. Tests were accomplished by Boeing and McDonnell-Douglas to investigate blockage effects and define the range of Mach numbers over which data would be free from, or correctable for, tunnel effects. The Boeing tests were performed in the Boeing 8x12 foot transonic wind tunnel and the McDonnell-Douglas tests were performed in the 16T wind tunnel at AEDC.

The Boeing tests were performed using an axisymmetric model with an area distribution corresponding to the sum of the areas of the forebody and strut and one short afterbody. The results from these tests, shown in Figure 20, indicate that the test data are probably usable up to Mach 0.975.

The McDonnell-Douglas blockage tests were conducted with F-15 equivalent body models of 0.05%, 0.381% and 0.651% blockage (A_{MAX}/A_{TUNNEL}). Each model had a body-of-revolution fuselage and constant thickness wings with scaled F-15 planform (Figure 21).

Subsonic blockage effects were evident with the 0.381% and 0.651% models from Mach 0.60 through 1.20. In the subsonic regime, it was determined that drag, at $\alpha = 0°$, increased linearly as a function of blockage. This trend was independent of Mach number, but varied slightly with angle-of-attack. Subsonic drag rise characteristics were the same for all three models except for the 0.651% model at Mach 0.95. Normal force, at a given angle-of-attack, decreased with increasing wing span ratio in the subsonic regime.

The subsonic blockage effects on drag levels are not understood. It is generally considered that model blockage, of the magnitude used in this test, should have had no effect at low subsonic speeds. These results are evidence that a better understanding of tunnel flow phenomena is required before tests at meaningful Reynolds numbers, which require large scale models, can be accomplished. It is recommended that further analytical and experimental investigations be conducted.

In the transonic regime, pressure disturbances due to blockage effects generally caused lower drag on both the 0.381% and 0.651% scale models, relative to the 0.05% model. There were no blockage effects at Mach 0.40. With the wings off, there were no significant effects above Mach 1.10 and 1.20 for the 0.381% and 0.651% models, respectively. Throughout the transonic regime, normal force data, with wings on, were not affected by span ratios up to 0.35, which corresponds to the 0.381% scale model.
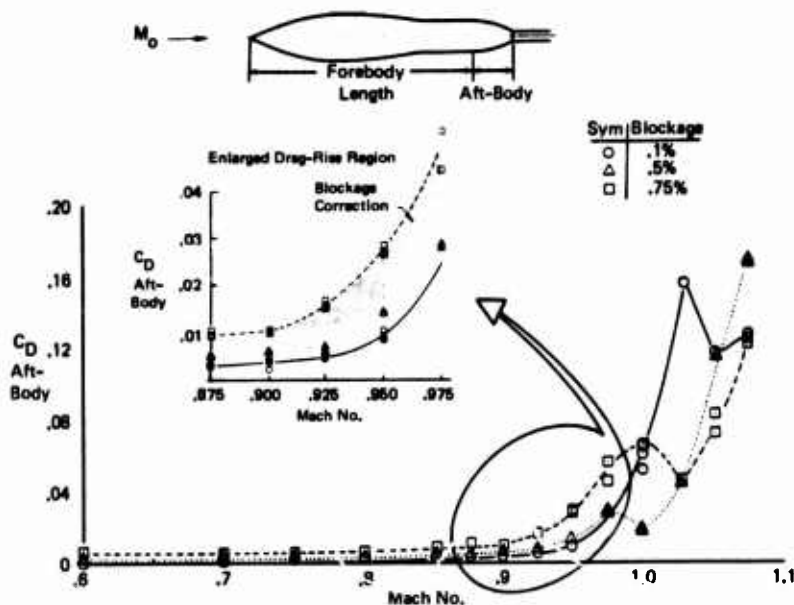
Figure 20: Blockage Effects on Afterbody Drag Characteristics

Figure 21: Blockage Model Characteristics for F-15 Test
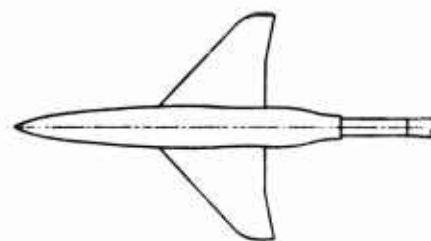
Model Characteristics	4.7%	13%	17%
Scale	4.7%	13%	17%
Length (In.)	35.96	99.45	130.05
Max. Dia. (In.)	4.47	12.36	16.16
Blockage, $\frac{A_{Max}}{A_{Tunnel}}$	0.050%	0.381%	0.651%
Wing Span $\frac{b}{W_t}$, Tunnel Width	0.13	0.35	0.45

During recent Boeing studies, tests were also conducted to evaluate the effectiveness of slotted walls to cancel shock waves which may be present during transonic testing. This investigation was accomplished using the shock reflection model shown in Figure 22. An example of results, showing pressure distributions obtained from the shock reflection test, is presented in Figure 23. Above Mach 0.925, strut influence is strong, but still tends to dissipate upstream of the split plane. The pressure at the split plane, however, gradually increases with Mach number, and reflected disturbances appear at Mach 1.05 and 1.07. These shocks would invalidate data on longer afterbodies. This part of the test confirmed that Mach 0.90 was the limit of interference free testing for the test model sizes used.

Blockage Model

Shock Reflection and Tare Model

Figure 22: Blockage and Shock Reflection Models
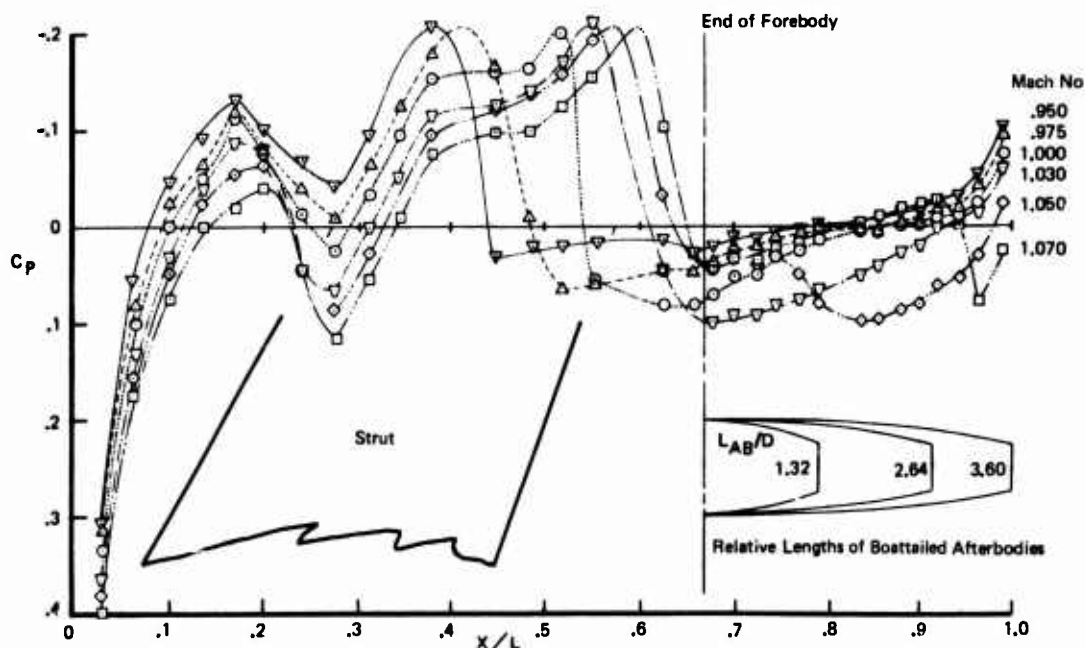
Figure 23: Pressure Distribution Shock Reflection Test, Mach No. > .950

5.   CONCLUSIONS

The force accounting system that is used during an aircraft development cycle can be an important factor in providing element and subsystem visibility. If one is only interested in total airplane system performance, the force accounting system used probably does not matter greatly, assuming that all the data which goes into the system performance calculation is accurate and each piece of data is included once and only once. However, if one is asked to evaluate the performance of the two major subsystems, the propulsion system and the airframe, then it becomes necessary to have a force accounting system that provides visibility of the subsystem performance. Results of the study indicate that an "operating reference" condition should be used which divides the forces into two parts: (a) throttle-dependent forces which are included in installed propulsion system performance, and (b) non-throttle-dependent forces which are accounted for in the drag polar.

Methods for predicting nozzle/aftbody drag for twin, buried engine configurations which are suitable for use during preliminary design studies have been improved by development of a truncated Integral Mean Slope (IMS$_T$) approach, based on correlations of test data.

The communication of inlet total pressure recovery and drag between airframe and engine companies is improved by the use of maps of standardized format which provide the recovery and drag as a function of engine corrected airflow. The maps are built up from individual inlet component performance plots that make it possible to account for all the significant inlet geometric variables at early stages of configuration analysis.

Sources of errors in measuring aero/propulsion forces in the wind tunnel have been shown to be due to model support systems, metric split-line locations, shock reflections and blockage, and non-simulation of model mass flow.

Extreme caution must be used to avoid errors in nozzle/aftbody drag predictions due to applying the aftbody drag results measured behind a "representative" forebody to a forebody of arbitrary shape and length.

In addition to the problems which have been experienced in predicting system performance for conventional aircraft designs, many new concepts for improving performance of vehicles powered by air-breathing propulsion systems are being studied. Examples of some of these concepts are variable cycle engines, two-dimensional nozzles, and powered lift concepts such as jet flaps, augmentor wings and upper surface blowing. Many of these concepts will increase the potential for mutual interference, both desirable and undesirable, between the airframe and propulsion system. Further research is required to establish a firm technology base for force accounting and evaluation of the performance of these concepts.

REFERENCES

1.   *Airframe/Engine Integration*, AGARD Lecture Series No. 53, May 1972, AGARD-LS-53.

2.   *Aerodynamic Drag*, AGARD Conference Proceedings No. 124, October 1973, AGARD-CP-124.

3.   Swavely, C. E. and Soileau, J. F.; *Aircraft Aftbody/Propulsion System Integration for Low Drag*, AIAA Paper No. 72-1101, Presented at the AIAA/SAE 8th Joint Propulsion Specialist Conference, New Orleans, Louisiana, November 29-December 1, 1972.

4.   Ross, P. A. and Ball, W. H.; *Propulsion System Development for Lightweight Fighter*, D180-14475-1TN, The Boeing Company, April 1974.

5.   Gould, D. K. and Eastman, D. W.; *Methods Used to Determine Aerodynamic Drag and Installed Propulsion Thrust for the Boeing Lightweight Fighter*, D199-10003-1, The Boeing Company, November 1972.

6.   Postlewaite, J. E. and Salemann, V; *Prediction and Measurement of Propulsion System Performance*, ASME Paper No. 73-WA/Aero-5, 1973.

7.   Ross, P. A. and Eastman, D. W.; *Propulsion System Development for Lightweight Fighter - Inlet and Exhaust System Drag*, D180-14475-3TN, The Boeing Company, March 1974.

ACKNOWLEDGEMENTS

AIRFRAME/PROPULSION SYSTEM FLOW FIELD INTERFERENCE
AND THE EFFECT ON AIR INTAKE AND EXHAUST NOZZLE PERFORMANCE

By

G. K. Richey
L. E. Surber
J. A. Laughrey

Air Force Flight Dynamics Laboratory
Wright-Patterson Air Force Base, Ohio, U.S.A.

Summary

The interference between the airframe flow field and the internal/external flow in the air intakes and exhaust nozzles of high performance tactical aircraft is shown to have a significant impact on the performance and operating characteristics of these components, and hence on overall aircraft performance.

The internal flow characteristics of an inlet system closely integrated with the airframe are strongly influenced by flow field nonuniformities generated by the airframe forebody and wing, particularly at the higher angles of attack or yaw which modern tactical aircraft are capable of. Comparisons are made of the inlet ambient (capture plane) flow field, and pressure recovery, steady state and dynamic inlet distortion at the simulated engine compressor face for both integrated (side mounted and fuselage or wing-shielded) and isolated inlet systems to quantitatively assess the airframe interference effects.

For the engine exhaust nozzles of closely integrated propulsion system/airframe configurations, the major influence of the airframe flow field is associated with the alteration of the viscous and inviscid external flow in the nozzle region, and its effect on external aftbody/nozzle drag. A detailed discussion, supported by experimental data, shows the effects on airframe aftbody/nozzle pressure distributions and nozzle installed performance with respect to twin jet interference, wing flow, aircraft tail/control surfaces, interfairings and free stream flow conditions.

Introduction

For tactical aircraft which are required to be very maneuverable at high subsonic, transonic and supersonic conditions while giving good cruise efficiency at high subsonic Mach numbers, the integration of the engine inlet and exhaust systems with the airframe is of paramount importance to maintain the desired thrust levels and avoid inlet engine compatibility problems such as compressor stall. The total pressure recovery and flow distortion at the exit of the inlet (engine compressor face plane) for these types of aircraft is dependent on the inlet capture station flow field characteristics which are presented to the inlet as a result of integration with the airframe (i.e. the ambient distortion), and the production of distortion and turbulence in the supersonic and subsonic diffuser sections of the inlet. For practical configurations there are many airframe design variations, then, which can influence the performance and flow distortion of the inlet, particularly at extreme maneuvering conditions. This paper will review the effects of two selected vehicle design parameters, namely the fuselage forebody shape and the inlet installation concept. In the examination of installation concepts the paper first emphasizes the effect of placing the inlet on the side of the fuselage as in several current tactical aircraft. This installation is then compared with inlet systems which are shielded at high angles of attack by the aircraft wing or fuselage. Design parameters such as canopy shape, fuselage camber or nose shaping will not be considered.

For airframe/exhaust nozzle integration, the most important criteria is to have good acceleration characteristics when the nozzles are open during engine afterburner operation, and to have good cruise efficiency (i.e. reduced drag) for subsonic or supersonic cruising. The aftbody/nozzle drag is very sensitive to the pressure field of the aircraft which is impressed upon the basic nozzle flow. This is particularly true for twin jet aircraft where the exhaust nozzles may be placed fairly close to one another for weight and structural considerations, and to improve the overall cross sectional area distribution of the aircraft. At cruise conditions there is considerable data which indicates the type of geometry to use for low drag on an isolated exhaust nozzle. However, when these nozzles are integrated into the aircraft, the results are sometimes disappointing due to adverse interaction effects. Previous AGARD or AIAA papers, for example references 1 and 2, have discussed the overall drag variations with different types of aftbody/nozzle shapes, interfairings and vertical or horizontal tail surfaces. In this paper we will discuss the flow field behavior in the aftbody/nozzle region and how it changes with a typical buildup process from the isolated exhaust nozzle to the integration of these nozzles into a vehicle fuselage/twin jet arrangement. From this baseline twin jet aftbody, we will examine variations with tail, wing, interfairing interference, and nozzle spacing. References 3 and 4 present details on the drag and pressure distribution characteristics of a wide range of nozzle types and aircraft integration designs; however in this paper we will concentrate on a convergent-divergent nozzle system representative of tactical aircraft which are required to perform well at both subsonic and supersonic flight conditions.

Inlet Systems:

As stated above, there are many aircraft design features which directly influence the performance of the inlet system for a closely integrated tactical aircraft. References 5 and 6 have discussed the free stream flow field distortion which can occur with changes in fuselage camber and fuselage cross sectional shape. The upwash and downwash fields associated with large canopies can also affect the inlet performance if the inlet is close enough to be influenced.

In the first section of the inlet discussion of this paper, however, attention will be given exclusively to the detailed effects of fuselage cross-sectional shape on the performance and operational stability of a side-mounted-horizontal ramp two-dimensional inlet system (see Fig 1).

The basic choice for inlet placement may be guided by several operational factors of aircraft utilization such as missile and weapons placement, and foreign object ingestion from unprepared runways. A common design feature of recent tactical aircraft is the placement of the inlet on the side of the fuselage where each inlet is supplying air to one engine. This has advantages of simplicity of design and attempts to position the inlet in a relatively "clean" forebody flow field while at the same time providing sufficient duct length to attenuate distortion of the flow between the inlet throat region and the compressor face. However, in order to provide a good cross-sectional area distribution and to reduce weight installed in the aircraft, it is desirable to position these horizontal ramp inlets fairly close to the fuselage. If the inboard side of the inlet is within roughly one capture height from the side of the fuselage, the flow characteristics associated with the fuselage will be important in determining the performance of the inlet at extreme maneuvering conditions. The effect of the fuselage shape is particularly dependent on the radius of curvature and shape of the lower part of the fuselage since these variables influence the upwash flow field presented to the inlet at high angles of attack and yaw. In the following discussion, then, horizontal ramp two-dimensional side-mounted inlet data will be compared on 3 different types of lower fuselage shoulder contours as shown in Fig 2a: (1) a basic contour which is reasonably well rounded, (2) a more squared off fuselage which could have advantages for missile and weapon placement, and (3) a more nearly circular fuselage cross-section. The effect of these various fuselage shapes is shown first of all in terms of the flow field that the inlet is placed in, secondly in the flow distortion at the throat of the inlet, and finally in the total pressure recovery, time-dependent and time-averaged flow distortion which is measured at the simulated engine compressor face.

As a point of reference for the various effects of fuselage shape and installation type, selected data is compared with the isolated two-dimensional inlet which is completely free of any fuselage or airframe interference effect.
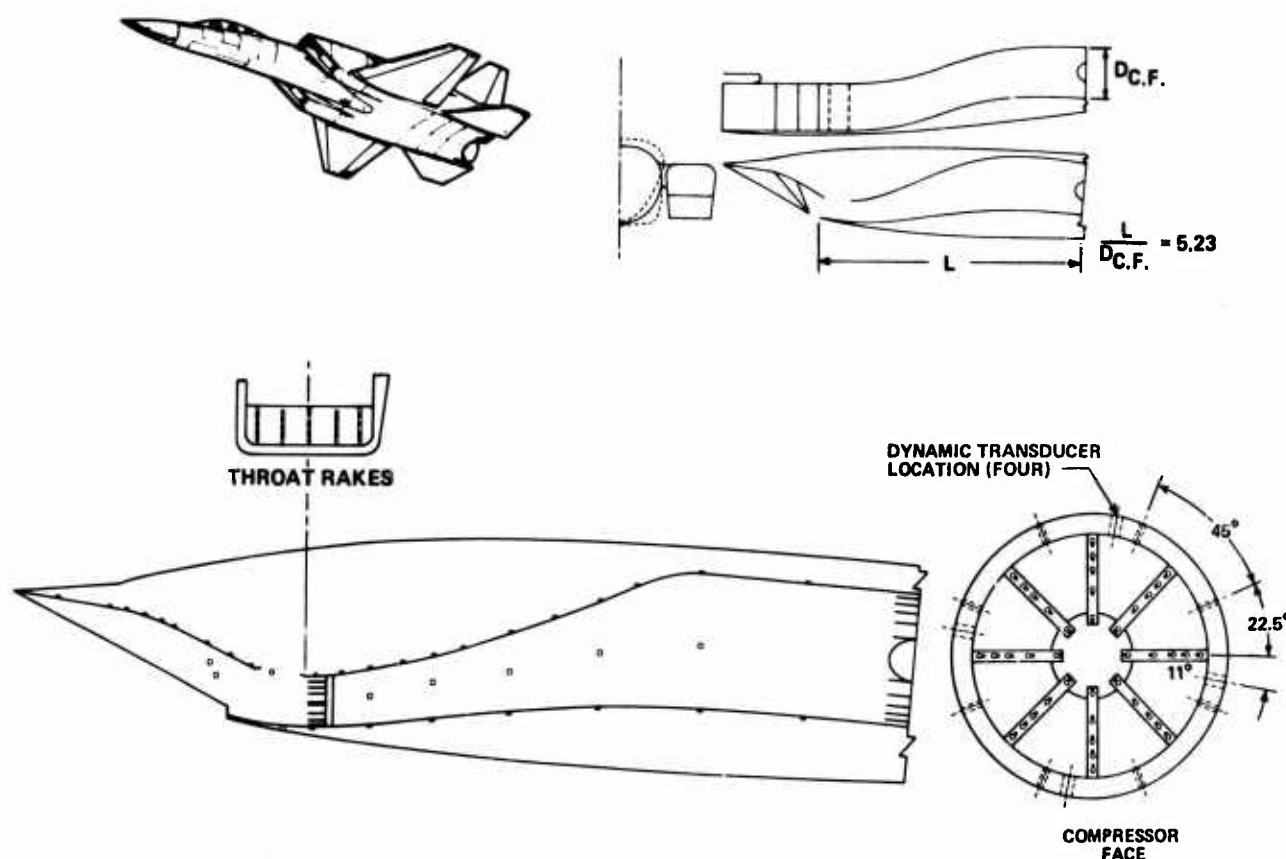
FIGURE 1. SIDE-MOUNTED INLET CONFIGURATION AND INSTRUMENTATION

The data presented in this paper was generated under a United States Air Force sponsored investigation with testing at the Arnold Engineering Development Center Propulsion Wind Tunnels at Tullahoma, Tennessee. The experimental program described in references 7, 8, and 9 explored the effects of many different design considerations on supersonic fighter aircraft inlet and performance compatibility with designs representative of operation with a typical low bypass ratio turbofan engine. The models tested in the program were large (approximately one fourth full scale) and included both two-dimensional and half-axisymmetric inlets. Only the two-dimensional inlet data will be discussed in this paper. The two-dimensional inlet shown in Fig 1 features a variable first ramp as well as variable second and third ramps for efficient compression at supersonic conditions. It is a fairly long inlet system with a rather low diffusion rate subsonic duct ($L/_D$ = 5.23). Boundary layer air control on the ramps is provided by perforated bleed on the compression ramps and on the side plates. Also the gap between the third ramp and aft ramp, shown on Fig 1 provides a combination of flow bypass and boundary layer control at the throat region. Throat bleed flow was measured with flow metering systems, and bleed on the perforated side plates was estimated from plenum and exit static pressure measurements.

Inlet instrumentation was provided at the compressor face to measure total pressure recovery, and both steady state and dynamic inlet flow distortion by use of high response total pressure probes, (40 high response combination steady state and dynamic total pressure). Additional diagnostic instrumentation was provided on the opposite side of the double inlet system, consisting of total pressure rakes and static pressure measurements in the throat of the inlet as noted in Fig 1. Instrumentation for the wing-shielded and fuselage-shielded inlets to be discussed later was similar except that no throat diagnostic instrumentation was used on the fuselage-mounted inlet since this was a single inlet/single engine configuration and the throat total pressure instrumentation could not be put in without disturbing the flow at the compressore face. Test conditions in the program were over a range of Mach number from 0.9 to 2.5, angles of attack (α_0) from -5 to +25°, and angles of sideslip (β_0) from -8° to +8°. In the following discussion, "positive sideslip" is interpreted as being on the leeward side of the fuselage and therefore is the condition where the fuselage is partly blocking the flow.

Two-Dimensional Side Mounted External Compression Inlet-Fuselage Lower Shoulder Effects

Figure 2a shows the cross-section of the three fuselage shapes tested with the two-dimensional inlet. They are labeled simply the round shape, basic, and square; the basic shape being an intermediate rounding between the other two. A separate test established the airframe flow field in the vicinity of the inlet (reference 8). Figure 2a shows the flow field local angularities at a Mach number of 2.2, 15° angle of attack, 0° sideslip from these test results. With the three fuselage cross-sections, the basic character of the flow fields is the same but with variations in degree. The angle of attack condition at 15° also introduces fairly significant sideslip, particularly into the lower inboard portion of the flow field. It is in this portion of the flow field where we see the primary effect of the fuselage shape. For a more complete range of test conditions with the various forebodies, Fig 2b shows the flow field average variations with angle of attack at various Mach numbers. Note that these data are for zero model sideslip. There is very little difference in local average Mach number values with the variance from the free stream Mach number the greatest at Mach 1.6 and high free stream angle of attack. The three fuselages show very similar effects on .verage local angle of attack; generally the local average angle of attack runs somewhat higher than free stream angle of attack indicating an upwash flow field induced by the fuselage, especially at the lower free stream Mach numbers. The square and the basic fuselage shapes indicate average induced sideslip values which are greater than that associated with the round shape but in all cases the local induced sideslip values grow larger with increasing free stream angle of attack.

FIGURE 2a. EFFECT OF FUSELAGE SHAPE ON FLOW APPROACHING INLET:
SAMPLE FLOWFIELD ANGULARITY MAPS,
$M_o = 2.2$, $\alpha_o = 15°$, $\beta_o = 0°$

FIGURE 2b. EFFECT OF FUSE' AGE SHAPE ON FLOW APPROACHING INLET:
FLOWFIELD AVERAGE TRENDS, $\beta_o = 0°$

Next we consider the effect of the different fuselage shapes on the inlet throat flow. Fig 3 shows the inlet throat total pressure recovery and the total pressure distortion at the inlet throat station which is defined as the difference between maximum total pressure and the average of the four lowest total pressures at the throat divided by average throat total pressure. For Mach 1.6, we can see by comparing the rounded, basic, and squared fuselage shape results with the isolated inlet data that the forebody effect is to generally lower throat total pressure recovery up to free stream angles of attack of about 20°. At the extreme maneuver points, that is, angle of attack of 15° or sideslip of 8° it appears that rounding the fuselage lower shoulder can be of significant benefit by reducing the unfavorable upwash or acceleration around the body in yaw. That is, the rounded fuselage tends to bring the throat total pressure recovery much closer to the value associated with the isolated inlet and the throat distortions closer to this value. Figure 4 shows the inlet throat pressure recovery and distortion conditions at a Mach number of 2.2 over a range of angle of attack from -5° to 25° (zero yaw). Here the benefit of at least some fuselage lower shoulder rounding is seen in that both the basic and the rounded lower fuselage shoulder shapes tend to approach the values of the isolated inlet recovery and distortion much more closely than do values for the squared lower shoulder shapes.
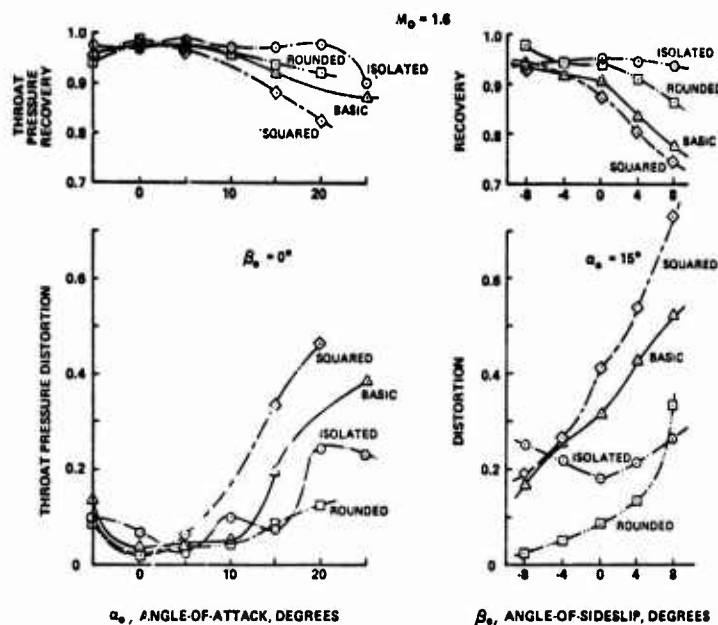
FIGURE 3. INLET THROAT PERFORMANCE: COMPARISON OF FUSELAGE SHAPES, $M_0 = 1.6$
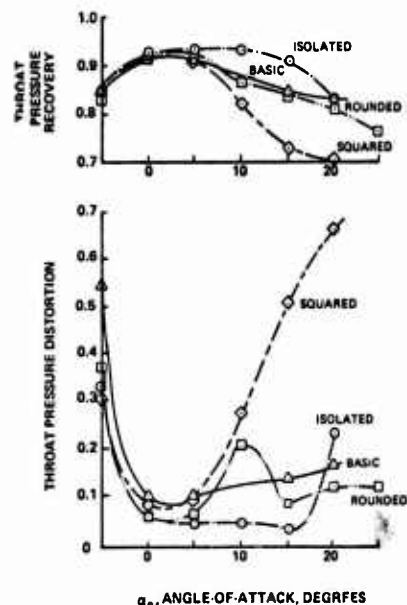
FIGURE 4. INLET THROAT PERFORMANCE: COMPARISON OF FUSELAGE SHAPES, $M_0 = 2.2$, $\beta_0 = 0°$

These trends can be understood more fully by examining the detailed data from the inlet throat rakes with the various forebody shapes. Figure 5 shows a particular case of Mach number 1.6, angle of attack of 15° and angle of sideslip of 8°. These throat total pressure maps indicate that the separated flow spilling into the lower inboard side of the isolated inlet from the crossflow on the sideplate is greatly increased by the fuselage presence and it is further magnified by the squared lower fuselage shoulder.
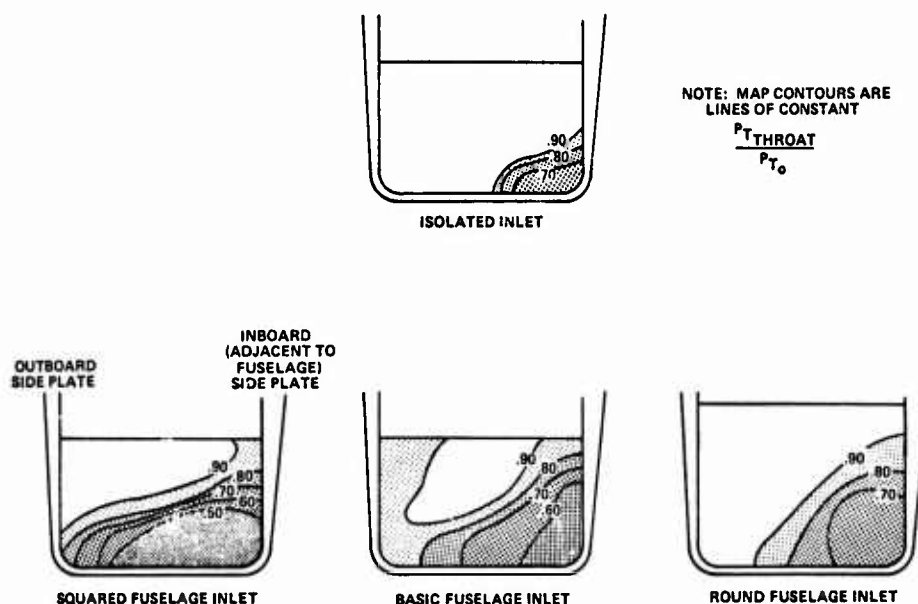
FIGURE 5. INLET THROAT TOTAL PRESSURE MAPS FOR VARIOUS SIDE-MOUNTED INLET FUSELAGE SHAPES, $M_0 = 1.6$, $\alpha_0 = 15°$, $\beta_0 = 8°$

Similar results are shown in Fig 6 which gives the throat total pressure profiles for the condition of Mach 2.2, angle of attack of 15° and zero sideslip. Again, data in this figure indicates that the fuselage upwash and inlet capture plane flow distortion has an adverse effect on pressure recovery and flow distortion at the throat, primarily because it amplifies the massive flow separation in the lower inboard corner of the inlet. The adverse interaction is particularly prevalent for the squared lower fuselage shoulder shape, with the rounded fuselage providing the least amount of adverse interaction.
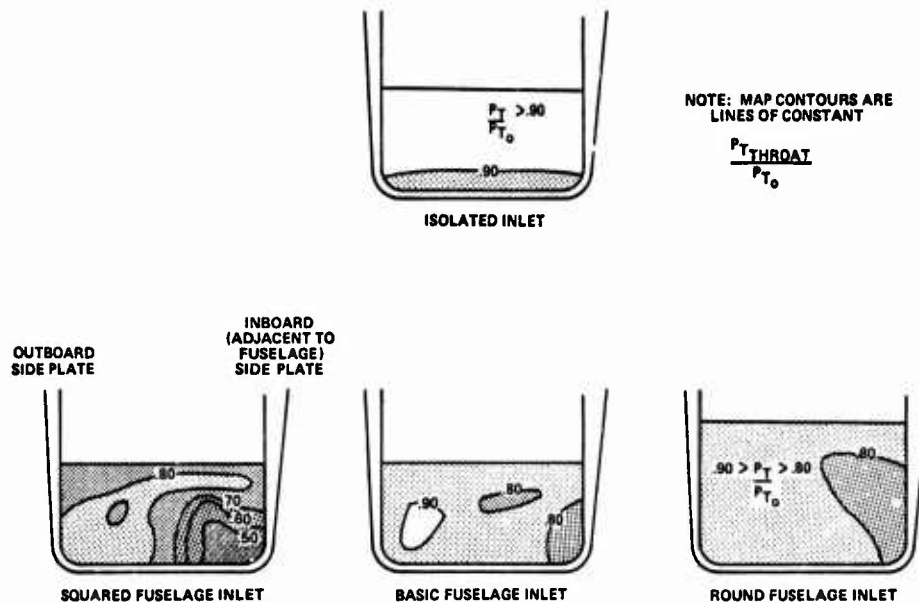
FIGURE 6. INLET THROAT TOTAL PRESSURE MAPS FOR VARIOUS SIDE-MOUNTED INLET FUSELAGE SHAPES, $M_0 = 2.2$, $\alpha_0 = 15°$, $\beta_0 = 0°$

Having traced the airframe/inlet interactions for the three fuselage shapes from the free stream through the inlet throat, we now consider their effect on compressor face total pressure recovery and flow distortion.

Figure 7 gives the variations of total pressure recovery (average steady state total pressure from all 40 probes divided by free stream total pressure) and "RMS Turbulence", which is defined as the average (40 probe) root mean square of the total pressure fluctuations at the compressor face divided by the average steady state total pressure at the compressor face. In Fig 7a, the data is for Mach 1.6 (zero sideslip) and compares the compressor face conditions for the isolated two-dimensional inlet, and the three fuselage cross-section shapes (basic, round, and square). Figure 7b is for 15° angle of attack and with sideslip variations from -8° to +8°. Negative sideslip (windward side) is favorable to the inlet and positive sideslip (leeward side) is adverse. All compressor face pressure recovery and distortion data is for a matched airflow condition with a low bypass ratio turbo-fan engine. Generally, there is adequate mass flow ratio margin so that the inlets are not close to subcritical flow instabilities (inlet "buzz"). With increasing angles of attack the various fuselage shapes give about the same compressor face characteristics at moderate maneuvering conditions, that is up to approximately 10° angle of attack, but more extreme flow angularities show the same basic effect as seen at the throat. The basic fuselage shape, which is somewhat rounded, facilitates higher pressure recovery and lower RMS turbulence at high angle of attack than does the squared fuselage shape. The rounded fuselage-two-dimensional inlet configuration has the lowest RMS turbulence level above 5° angle of attack. This is felt to be due to the better flow distribution at the inlet face for this configuration relative to the basic or squared lower shoulder configurations which in turn improves the flow quality at the inlet throat and compressor face. At positive sideslip, both the basic and squared lower shoulder fuselage shapes give a severe adverse interaction with the inlet, resulting in low pressure recovery and a high RMS turbulence level. The rounded fuselage appears to give a better flow distribution to the inlet at +β, and this is reflected in the data at the compressor face. At negative sideslip the round fuselage helps to turn the flow into the inlet, relative to the isolated case, and improves its performance.

Several references, e.g. 10 and 11 have shown that most engines are sensitive to a dynamic distortion at the compressor face which is related to the time that the compressor blades spend in a distorted flow area as they pass through it. The dynamic distortion is found by calculating the instantaneous circumferential and radial distortion from the output of the 40 high response probes at the compressor face (Fig 1) which have been recorded on analog tape. To get the correct dwell time for the blades passing through the distorted region, the probe data is filtered at a frequency corresponding to about one rotor revolution of the engine. The instantaneous distortion data shown in this paper was computed using a general purpose distortion analysis system called DYNADEC (Dynamic Data Editing and Computing) which is further described in reference 12.
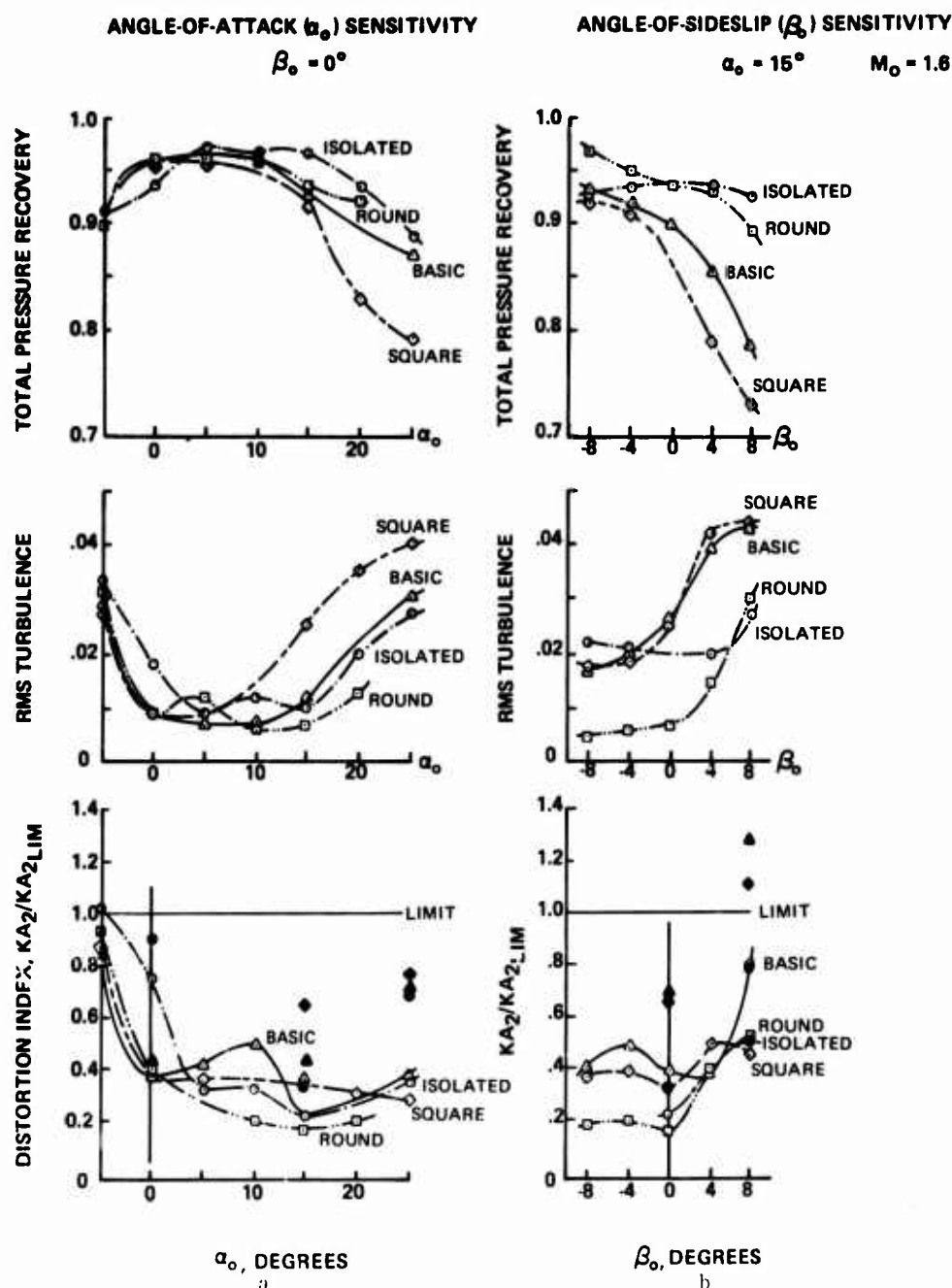
FIGURE 7. INLET PERFORMANCE AND FLOW DISTORTION: COMPARISON OF FUSELAGE SHAPE EFFECTS, $M_o = 1.6$

In general, it has been found that there is a relationship between the maximum instantaneous distortion (i.e. the one most likely to cause compressor stall) and the steady state (time averaged) distortion through correlations based on the level of RMS turbulence. The higher the RMS turbulence, the greater the difference between steady state and instantaneous distortion. In other words, when the inlet is "noisy" as it is at high angle of attack or yaw with the squared lower shoulder fuselage (Fig 7) there should be a large discrepancy between the steady state distortion factor K_{A_2} and the maximum instantaneous K_{A_2} determined from the detailed analysis of all 40 high response probes. The distortion index K_{A_2} is described in Appendix I.

Figure 7, which shows the variation of the circumferential/radial distortion factor K_{A_2} (divided by its expected limit value for the particular engine being used), verifies that the instantaneous distortions are much greater than the steady state at conditions where the RMS turbulence is above 0.02. Steady state distortion as seen in this figure would indicate compatible operation at almost all points, whereas the dynamic distortion points shown by the filled symbols reveal potential inlet-engine problems at some of the high sideslip maneuver points, specifically at an angle of attack of 15° and sideslip of 8°. At this condition, the data indicates that both the basic and squared fuselage shapes result in inlets flows being incompatible with the distortion limits for the particular engine being used in the analysis.

Figure 8 shows pressure recovery, turbulence and distortion at Mach 2.2 for variations in angle of attack. The data also indicates that the primary problems in this case actually occur at the lower angles of attack, e.g. zero and -5°, as well as at the higher angles of attack. The low angle of attack compatibility problem is felt to be associated more with inlet design than fuselage design. At high angles of attack, the squared fuselage shape has an adverse effect on turbulence and distortion, and the inlet performance in terms of total pressure recovery is quite severely affected. Rounding of the fuselage lower shoulder is observed to result in substantially higher pressure recovery and lower turbulence/flow distortion at the compressor face than can be obtained with a squared shape.

Comparing fuselage designs at all Mach numbers, the point to be made from this data is that there is a significant advantage associated with the rounded fuselage shape due to the fact that such a design reduces flow angularity approaching the lower inboard region of the inlet sideplate for a wide range of flight maneuvers. Reduced flow separation at this point results in higher pressure recovery and lower flow turbulence at the duct exit.
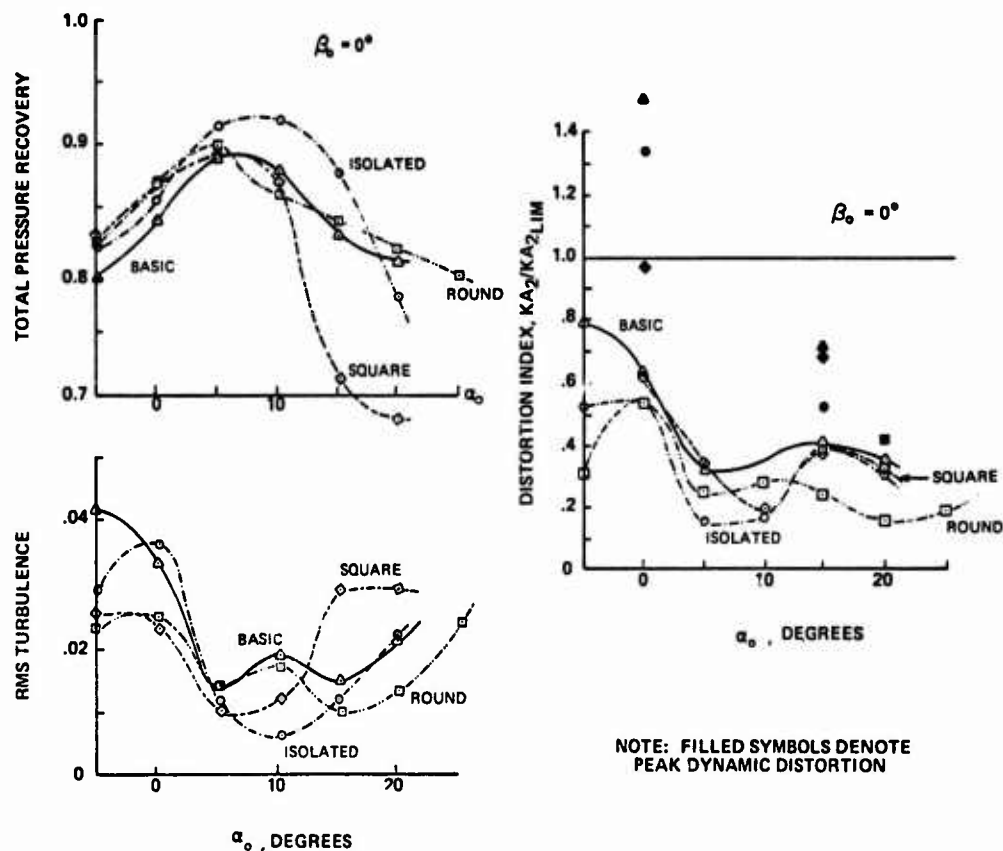
FIGURE 8. INLET PERFORMANCE AND FLOW DISTORTION: COMPARISON OF FUSELAGE SHAPE EFFECTS, $M_o = 2.2$, $\beta_o = 0$

Airframe/Inlet-Installation Effects For Vehicle Integrated Concepts

From this point we will consider only the basic fuselage shape with its side-mounted two-dimensional inlet system as one type of installation and compare it with two other installation types as shown in Fig 9. Both of the alternate installation types employ two-dimensional inlets in "shielded" positions: one is shielded by the wing, the other by the fuselage. By shielding it is meant that the wing or fuselage drastically alters the flow field seen by the inlet and is designed to reduce the inlet capture face flow angularity and decelerate the flow approaching the inlet. Figure 9a shows samples of the inlet face flow fields at Mach number 2.2, angle of attack of 15° and zero sideslip. In this case there are fundamental differences between the flow fields of the shielded inlets and that of the side-mounted inlet. While the local angle of attack seen by the side-mounted inlet ranges from 12° to 24° indicating upwash around the fuselage, the wing-shielded and fuselage-shielded local average angle of attack is quite low and in the case of the wing-shielded inlet, the angle of attack only ranges from -1° to 4° over the entire inlet face region. The range of induced flow field local sideslip is approximately the same for the three configurations (going from zero to about 8 degrees). The data indicates that the high sideslip condition for the side-mounted inlet is in the lower inboard portion of the inlet (near the side plate and cowl), while for both of the shielded inlet arrangements the high values of the local induced sideslip are found in the upper outboard portion of the inlet where the flow has washed outboard along the fuselage centerline or along the bottom of the wing toward the low pressure regions on the aircraft.
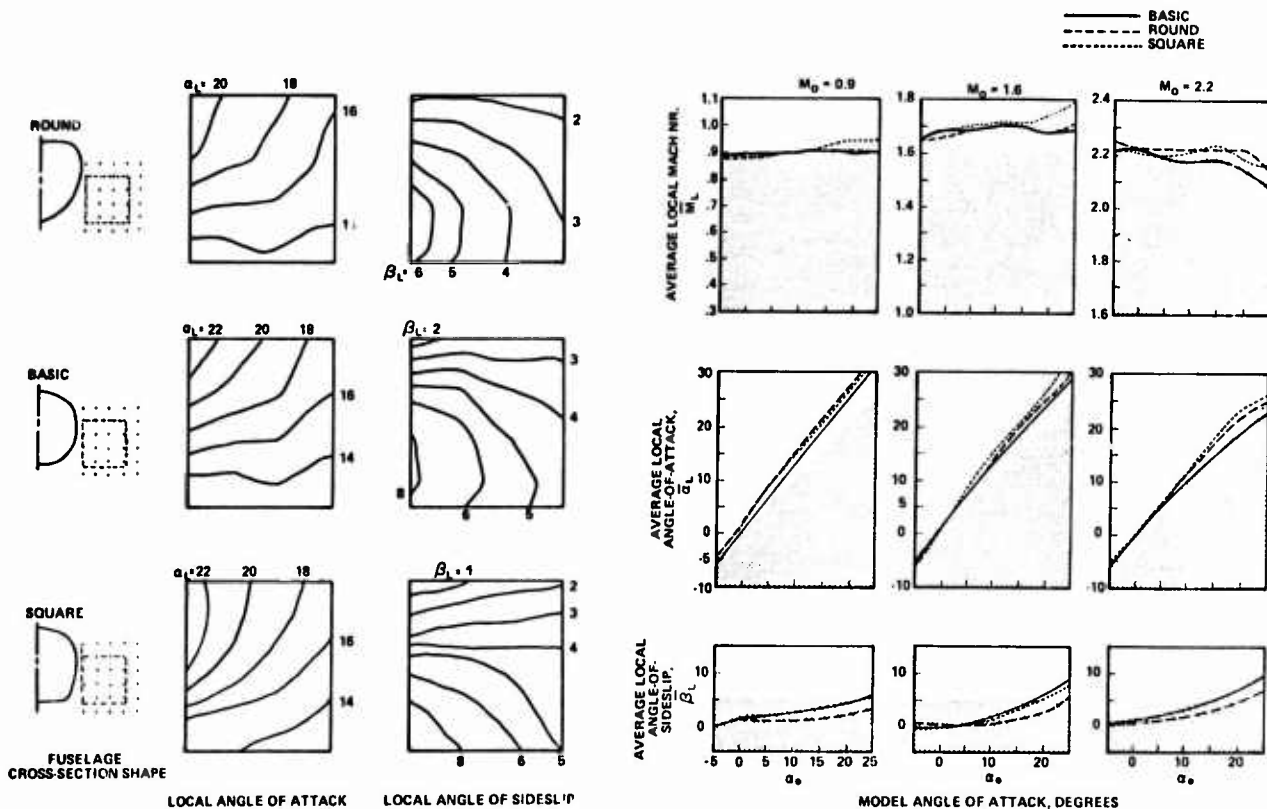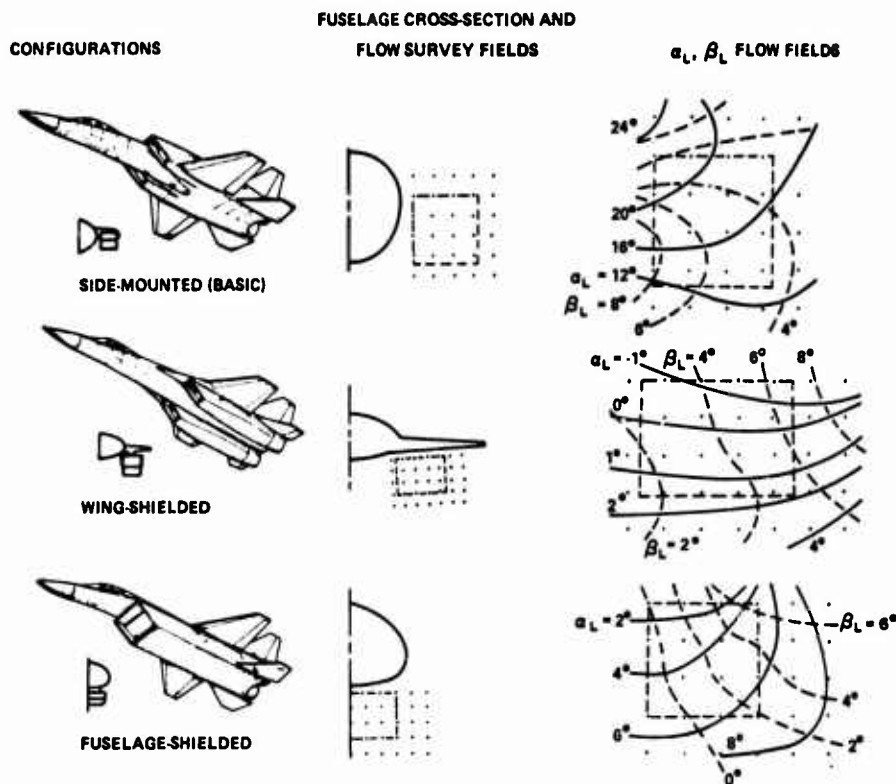
FIGURE 9a. EFFECT OF CONFIGURATION TYPE ON FLOW APPROACHING INLET: SAMPLE FLOWFIELD ANGULARITY MAPS AT $M_0 = 2.2$, $\alpha_0 = 15°$, $\beta_0 = 0°$

Figure 9b shows the effect of the inlet installation type on the average flow conditions at the inlet face region for Mach 0.9, 1.6 and 2.2, for aircraft angles of attack to 25 degrees (all zero model sideslip). Comparing side-mounted and shielded concepts, the difference in the ambient flow field in which the inlet will operate is dramatic. The local Mach number and angle of attack are substantially reduced by shielding the inlet at the high free stream angles of attack with wing-shielding being somewhat more effective than fuselage-shielding.
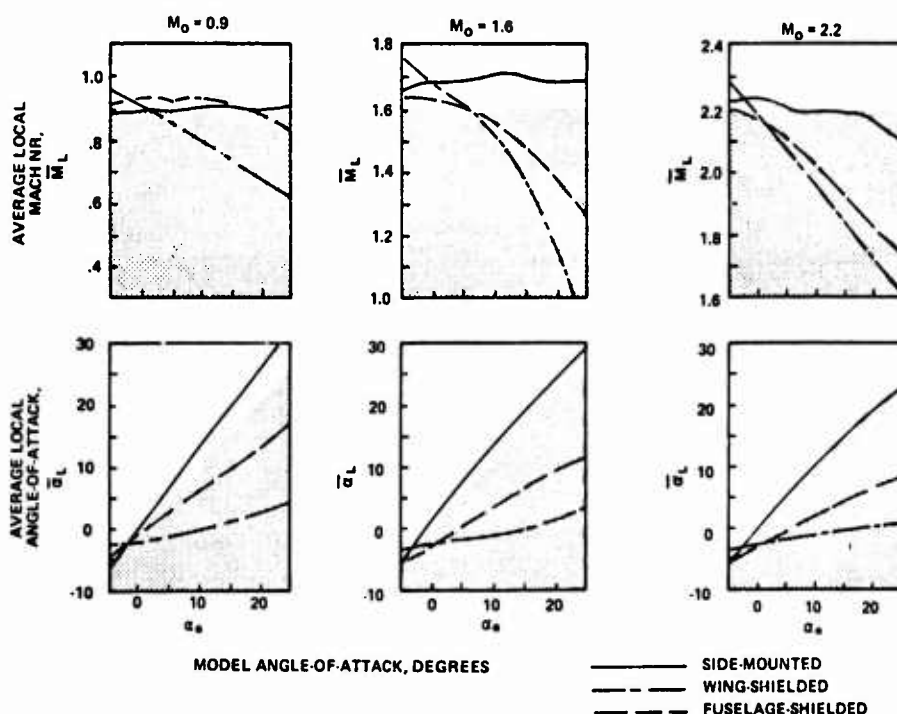
FIGURE 9b. EFFECT OF INLET INSTALLATION TYPE ON FLOW APPROACHING INLET: FLOWFIELD AVERAGE TRENDS, $\beta_0 = 0$

Before considering throat flow conditions and the differences between the three installation types, we should consider some fundamental differences in the inlet designs. The wing-shielded inlet system shown in Fig 10 has a somewhat greater aspect ratio and a much shorter subsonic duct with a higher diffusion rate ($L/_D$ = 2.92). The instrumentation in both cases is essentially the same, and provisions for boundary layer control bleed flow and its measurement are essentially identical. Figure 10 also shows the design features of the inlet used in the fuselage-shielded configuration. It is much simpler, having one fixed and one variable compression ramp, a low diffusion rate subsonic diffuser ($L/_D$ = 4.88) and a smaller amount of boundary layer control bleed at the inlet throat. The compressor face instrumentation is identical to the other configurations, with the same 40 combination steady state and dynamic probes being used. In this particular inlet there was no throat instrumentation (since it is a single engine arrangement) so the comparisons of throat flows will be between the side-mounted, wing-shielded inlets, and the isolated two-dimensional inlet.
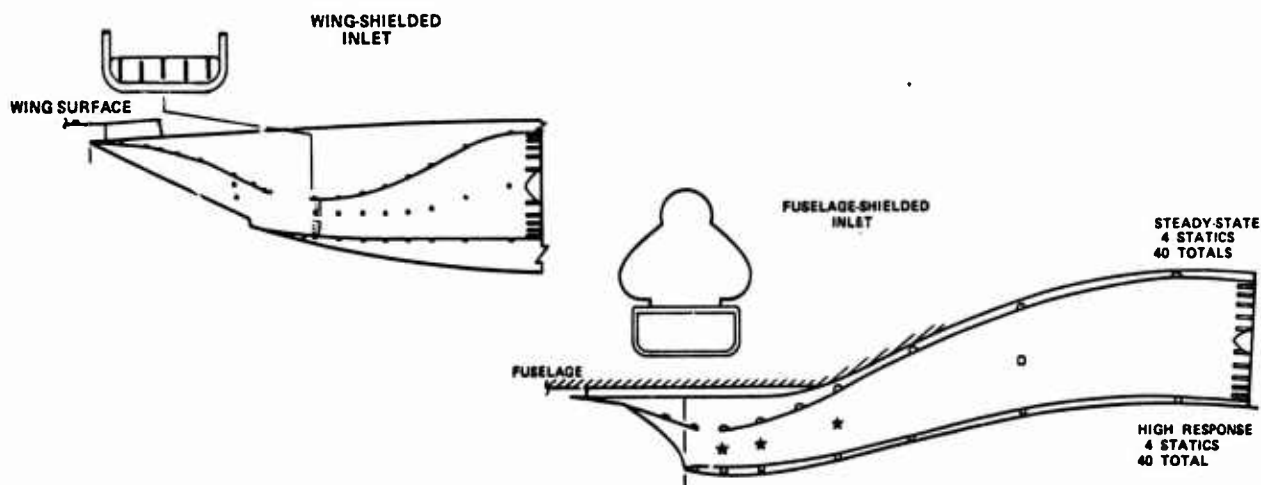
FIGURE 10. SHIELDED INLET CONFIGURATIONS AND INSTRUMENTATION

The effect of inlet installation type on inlet throat flow in terms of throat pressure recovery and throat pressure distortion is shown in Fig 11. For Mach 1.6 we see that the basic side-mounted inlet installation has slightly lower throat pressure recovery and considerably higher throat distortion than the wing-shielded inlet for angles of attack over 20°. Figure 11 gives the throat flow properties for 15° angles of attack for a range of sideslip. For an extreme maneuver point at Mach 1.6, that is at angle of attack of 15° and positive sideslip of 8°, the isolated inlet is superior in both recovery and distortion to the two types of installed inlets but there is still a definite benefit associated with the wing-shielded configuration relative to the side-mounted configuration. Profiles
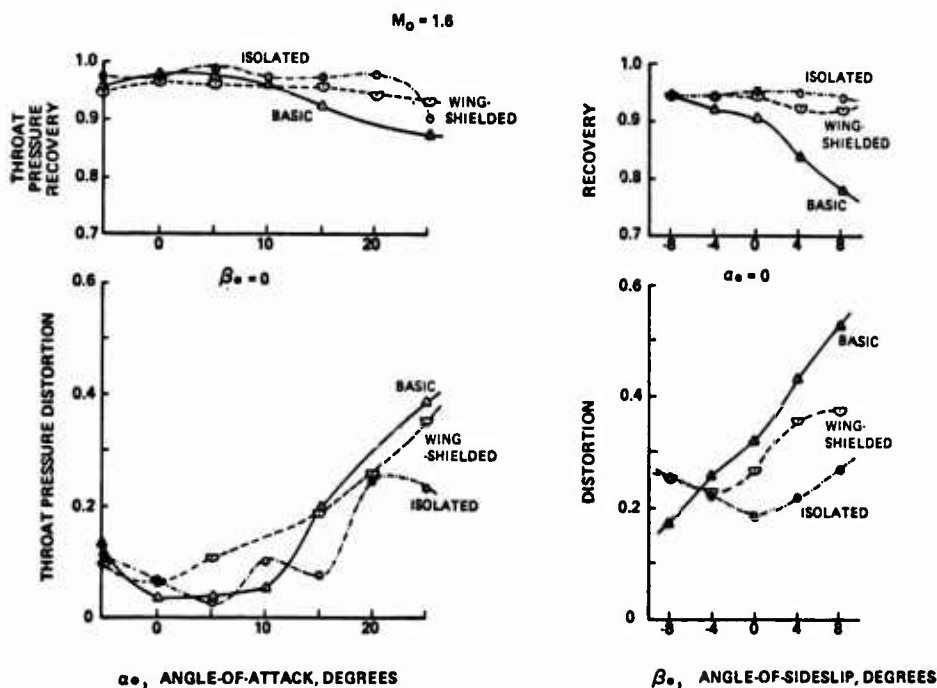
FIGURE 11. INLET THROAT PERFORMANCE: COMPARISON OF
INSTALLATION TYPES, M_o = 1.6

of total pressure at the inlet throat at this condition are given in Fig 12 at Mach number of 1.6, angle of attack 25°, and zero degree sideslip. At this extreme angle of attack condition, the deterioration of the isolated inlet flow and the advantage of the wing-shielded inlet are seen more clearly. There is a much smaller region of separation near the inboard lower sideplate for the wing-shielded configuration. The profiles in Fig 13 for an angle of attack of 15° and an angle of sideslip of 8° at Mach 1.6, compare the wing-shielded inlet with the basic side-mounted inlet and the isolated two-dimensional inlet. The wing-shielded inlet flow is clearly much better than the basic fuselage side-mounted inlet flow in the lower inboard region. Total pressure of the isolated inlet is higher than the other two in the upper inboard region and about the same as the wing-shielded inlet in the lower inboard corner of the inlet. From these data it is apparent that the two-dimensional inlet is being influenced considerably by the high outwash (induced sideslip flow) beneath the wing. There is some improvement over the side-mounted inlet, but not as much as desired.
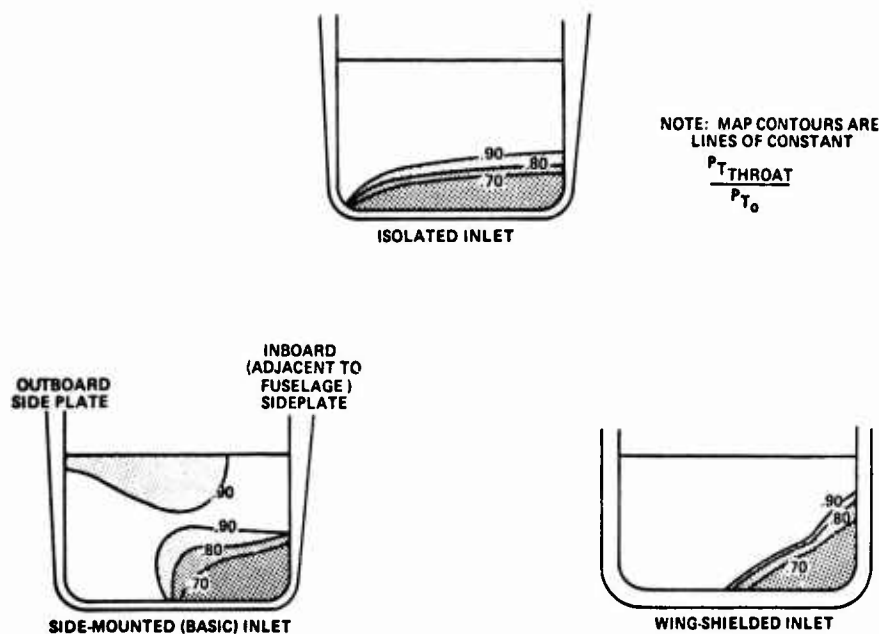
FIGURE 12. INLET THROAT TOTAL PRESSURE MAPS FOR DIFFERENT INLET INSTALLATION TYPES, $M_0 = 1.6$, $\alpha_0 = 25°$, $\beta_0 = 0°$
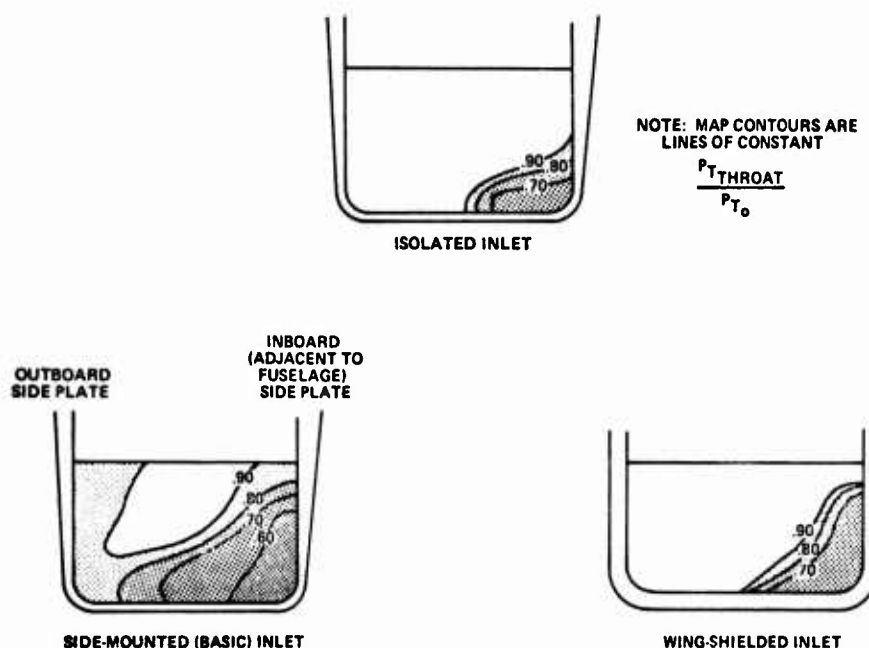
FIGURE 13. INLET THROAT TOTAL PRESSURE MAPS FOR DIFFERENT INLET INSTALLATION TYPES, $M_0 = 1.6$, $\alpha_0 = 15°$, $\beta_0 = 8°$

Similar results are shown at Mach 2.2 (Fig 14). At the higher angles of attack with zero sideslip the wing-shielding provides considerable advantages in terms of both total pressure recovery and a very low level of flow distortion at the throat. Above 10° angle of attack, the throat pressure recovery is about 10% higher for the wing-shielded configuration because of the reduction in local Mach number at the inlet face. This provides more engine thrust during maneuvers.
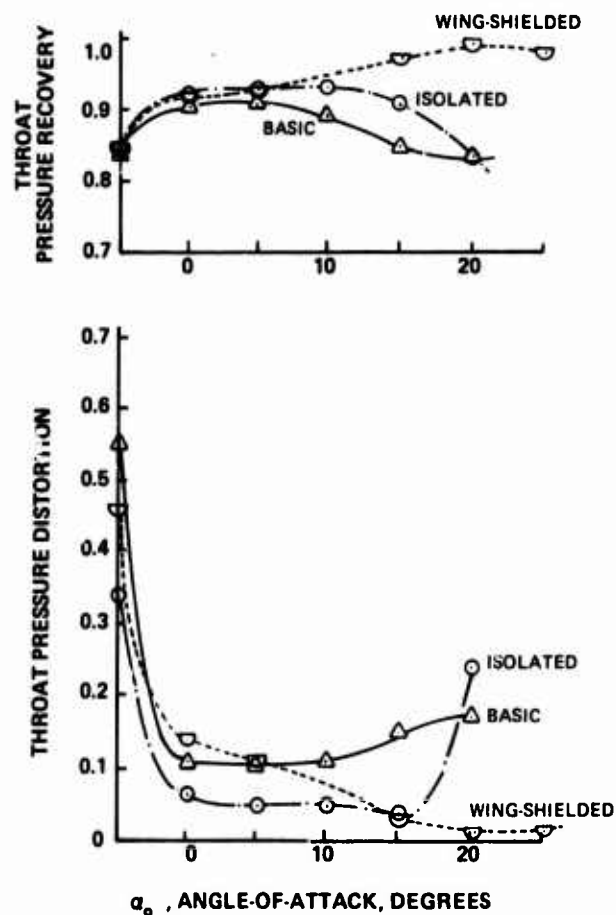
FIGURE 14. INLET THROAT PERFORMANCE: COMPARISON OF INSTALLATION TYPES, M_o = 2.2, β_o = 0°

Figure 15 shows the contours of throat total pressure recovery for 15° angle of attack at zero sideslip. The wing-shielded profile is much more uniform than the side-mounted inlet, and higher in its level of recovery than the isolated inlet, due to the fact that the inlet face Mach number is reduced. However, when four degrees of sideslip is introduced, as for the data in Fig 16, the wing-shielded inlet throat flow shows a serious depression on the inboard lower sideplate, indicating lip separation associated with the outwash along the wing lower surface.

Although there are no throat total pressure profiles for the fuselage-mounted configuration, it is expected that this configuration should have some benefit of shielding from the fuselage in reduced Mach number and flow angularity at high angles of attack, and perform similarly to the isolated inlet in sideslip since there should be little amplification of the basic sideslip due to outwash or flow separation.

The analysis of the flow at the inlet face and in the inlet throat is useful in understanding the behavior of the flow at the compressor face plane for the shielded configurations, and comparisons with the side-mounted inlet (basic fuselage) and the isolated two-dimensional inlet. The compressor face parameters being calculated from the data are defined the same as for Figures 7 and 8.
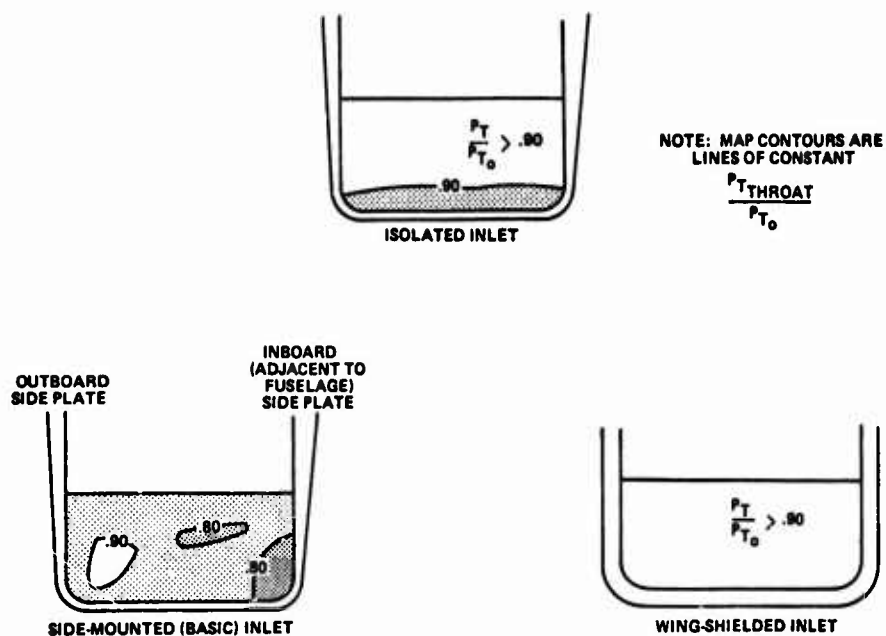
FIGURE 15. INLET TOTAL PRESSURE MAPS FOR DIFFERENT
INLET INSTALLATION TYPES,
$M_0 = 2.2$, $\alpha_0 = 15°$, $\beta_0 = 0°$
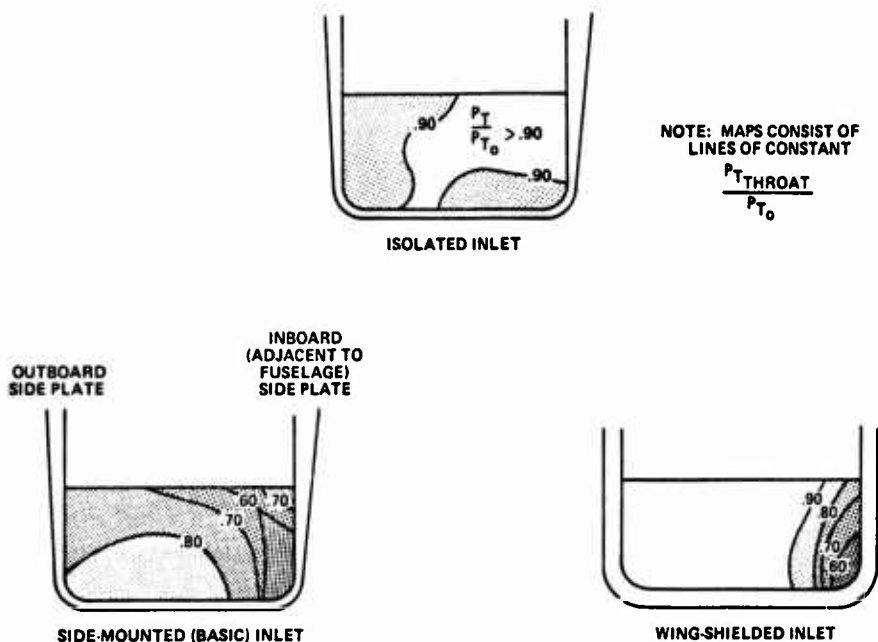
FIGURE 16. INLET TOTAL PRESSURE MAPS FOR DIFFERENT
INLET INSTALLATION TYPES,
$M_0 = 2.2$, $\alpha_0 = 15°$, $\beta_0 = 4°$

At transonic maneuvering conditions, Fig 17 summarizes the compressor face total pressure recovery and "RMS Turbulence" for the three types of inlet installations for a range of angle of attack to 25° (zero model sideslip) and for a range of sideslip at 15° angle of attack. These conditions are typical of highly maneuverable tactical aircraft where the inlet must have good performance while maintaining acceptable distortion to avoid inlet-engine compatibility problems.

At Mach number 0.9 the data of Fig 17 indicates that the compressor face flow is very similar for the side-mounted and wing-shielded inlets at all angles of attack and sideslip. The fuselage-shielded inlet has considerably higher pressure recovery and lower turbulence than the other two configurations. This difference is particularly prevalent at higher angles of attack and with positive sideslip. The relative behavior of the three inlet types is verified by the data of Fig 17 which shows the distortion index K_{A_2} divided by its limit value for the particular engine being considered. The fuselage-shielded inlet configuration has very little increase in distortion over the complete range of angle of attack and yaw at Mach number 0.9.
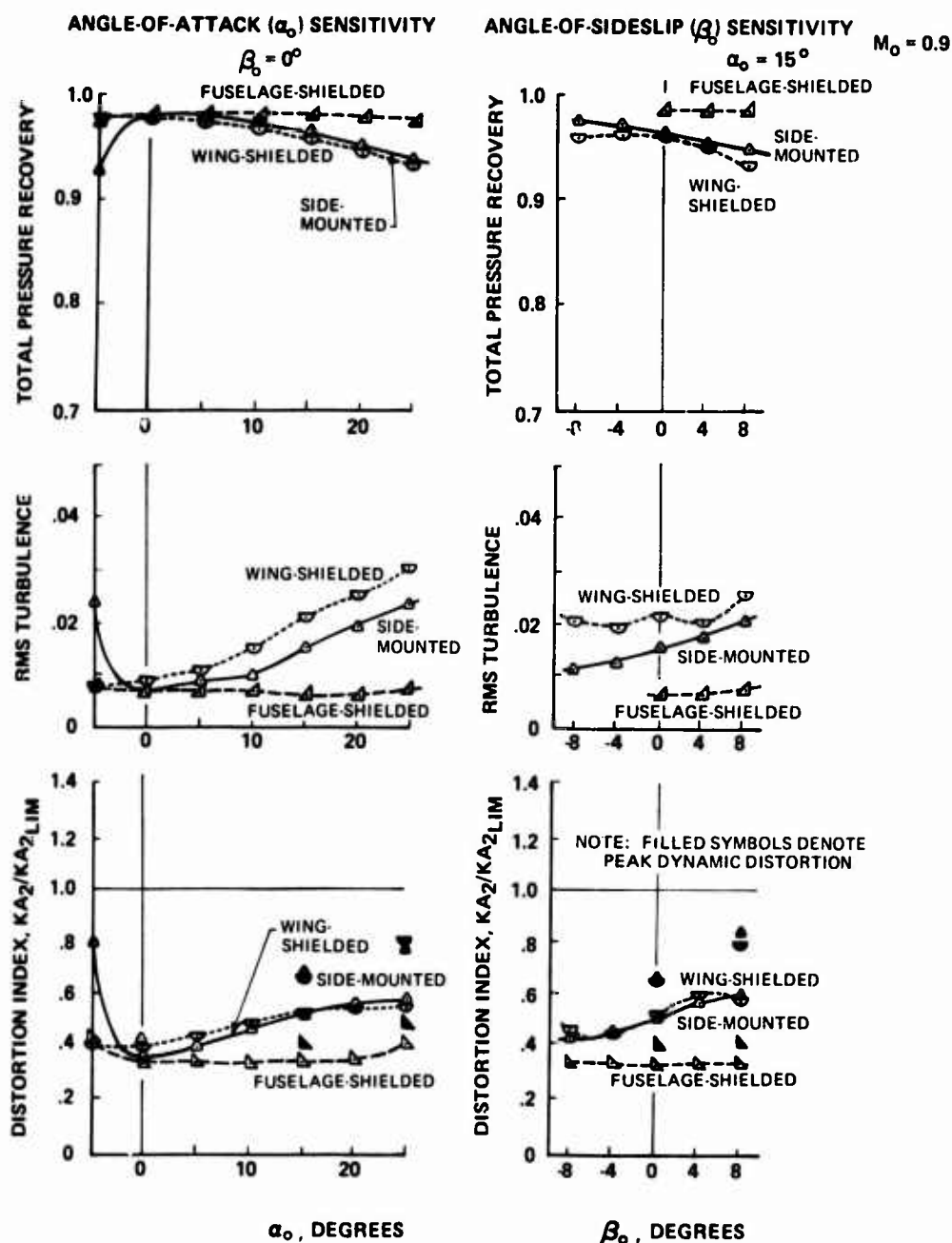
FIGURE 17. INLET PERFORMANCE AND FLOW DISTORTION:
COMPARISON OF INLET INSTALLATION TYPE,
$M_0 = 0.9$

At Mach number of 1.6, the data of Fig 18 shows a distinction in the characteristics of the shielded configurations and the side-mounted two-dimensional inlet. Both the wing-shielded and fuselage-shielded inlets maintain a high pressure recovery as angle of attack is increased to 25°, however the wing-shielded configuration shows an increase in RMS turbulence level at the higher angles of attack. This increased turbulence and distortion is consistent with the flow patterns observed at the throat and is related to the high level of outwash beneath the wing for the wing-shielded configuration. At increased angles of sideslip for angle of attack of 15°, both the wing-shielded and side-mounted inlet configurations show a drop in pressure recovery and increase in turbulence level above 4° of positive sideslip. However the fuselage-shielded inlet does not drop off in pressure recovery and maintains a low level of RMS turbulence even out to 8° positive sideslip. The distortion index values shown in Fig 18 indicate that the maximum instantaneous distortion for the wing-shielded and side-mounted two-dimensional inlet configurations approaches or exceeds the limit value as the angle of attack or angle of sideslip increases to extreme values. However, the distortion index for the fuselage-shielded inlet does not increase with either angle of attack or angle of sideslip and it is also noted that the steady state and maximum instantaneous distortion levels are very nearly the same, consistent with a low level of RMS turbulence.
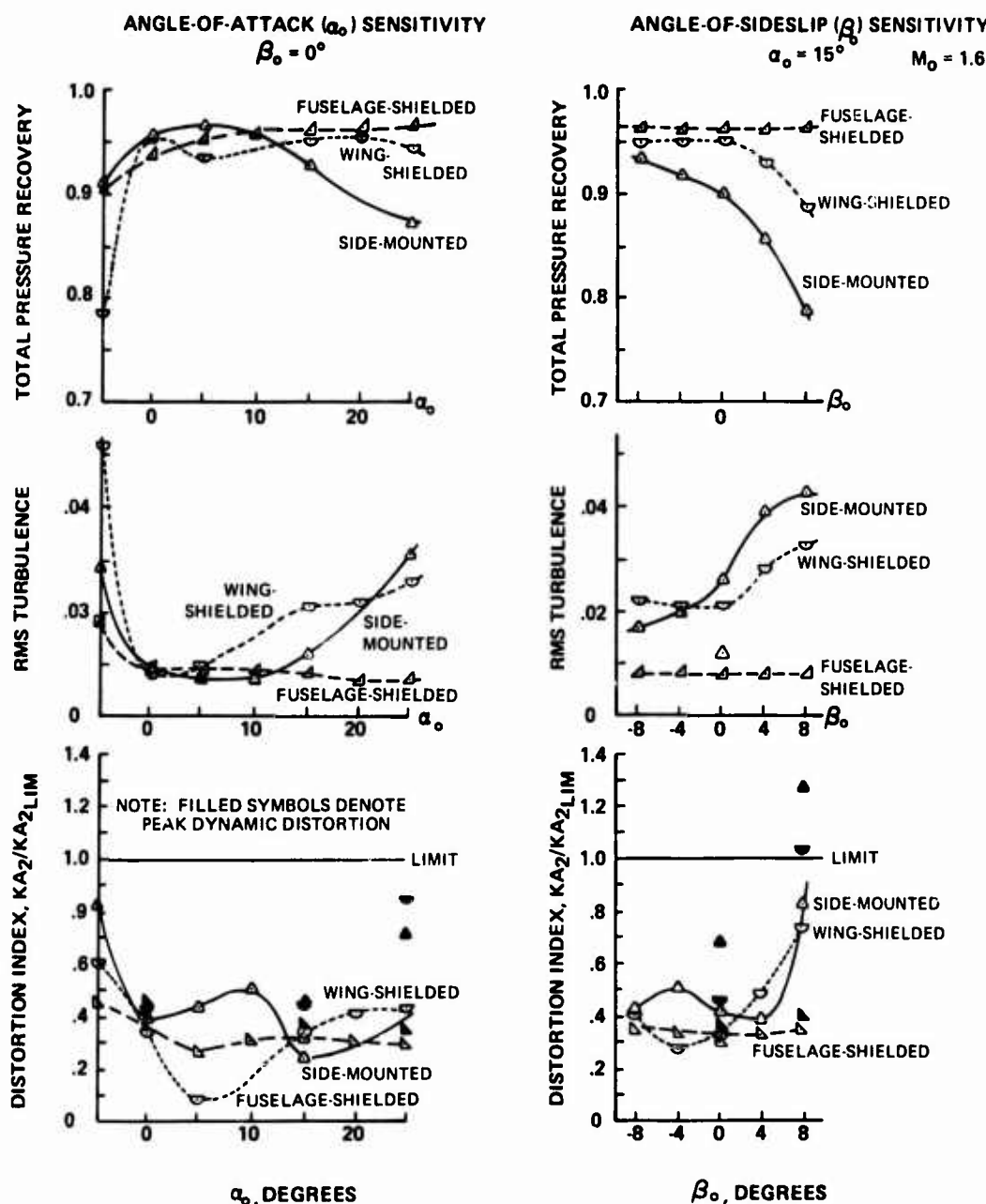
FIGURE 18. INLET PERFORMANCE AND FLOW DISTORTION:
COMPARISON OF INLET INSTALLATION TYPES,
M_o = 1.6

Figures 19 to 21 compare the compressor face total pressure maps (lines of constant total pressure) for the steady state or time average conditions and the maximum instantaneous value of K_{A_2} as shown in Fig 18. The conditions chosen for this comparison are Mach 1.6, angle of attack of 15° and angle of sideslip of +8°. At a condition where the RMS turbulence is high there is a large difference between the steady state and maximum instantaneous dynamic pattern, for example see Figures 19 and 20 for the fuselage-shielded and wing-shielded inlet. Where there is a low level of turbulence in the inlet at the compressor face, the steady state and maximum instantaneous compressor face maps are very similar as, for example, in Figure 21 for the fuselage-shielded inlet.

STEADY-STATE
TOTAL PRESSURE CONTOURS

PEAK DYNAMIC DISTORTION
TOTAL PRESSURE CONTOURS

M_0 = 1.6

α_0 = 15°, β_0 = 8°
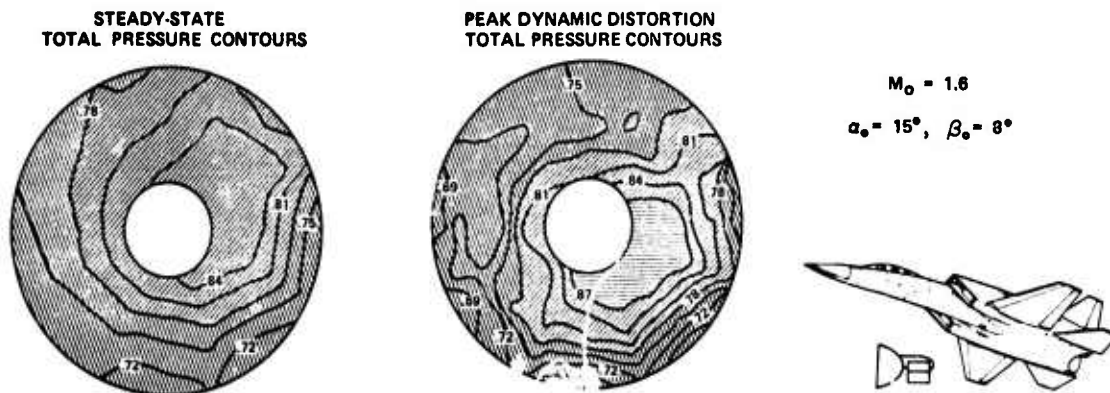
FIGURE 19. COMPRESSOR FACE TOTAL PRESSURE CONTOURS:
SIDE-MOUNTED CONFIGURATION,
M_0 = 1.6, α_0 = 15°, β_0 = 8°

STEADY-STATE
TOTAL PRESSURE CONTOURS

PEAK DYNAMIC DISTORTION
TOTAL PRESSURE CONTOURS

M_0 = 1.6

α_0 = 15°, β_0 = 8°
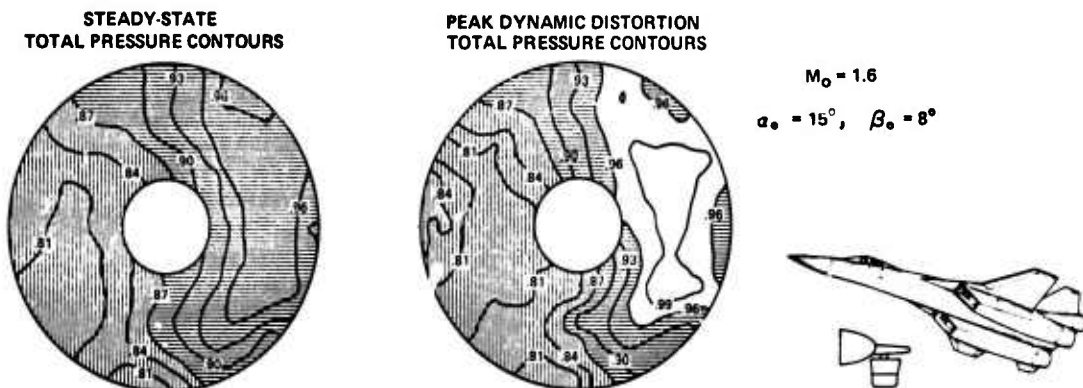
FIGURE 20. COMPRESSOR FACE TOTAL PRESSURE CONTOURS:
WING-SHIELDED CONFIGURATION,
M_0 = 1.6, α_0 = 15°, β_0 = 8°

STEADY-STATE TOTAL
PRESSURE CONTOURS

PEAK DYNAMIC DISTORTION
TOTAL PRESSURE CONTOURS

M_0 = 1.6

α_0 = 15°, β_0 = 8°
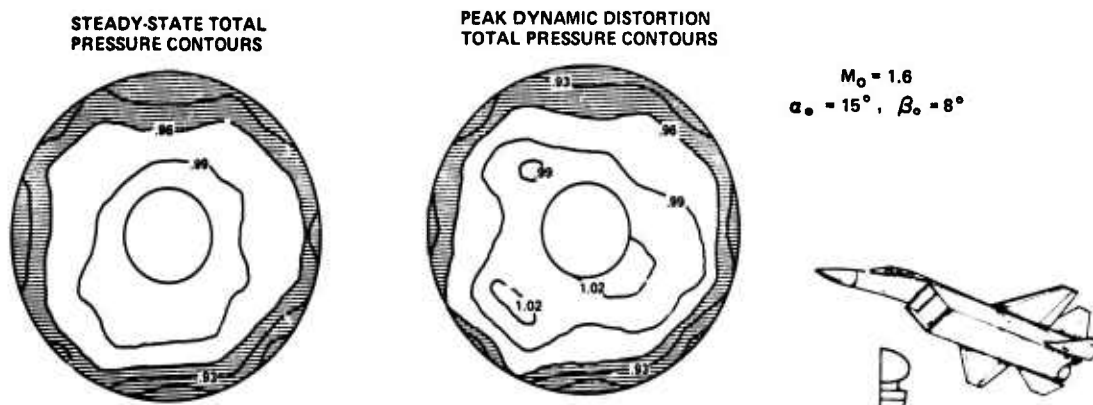
FIGURE 21. COMPRESSOR FACE TOTAL PRESSURE CONTOURS:
FUSELAGE-SHIELDED CONFIGURATION,
M_0 = 1.6, α_0 = 15°, β_0 = 8°

At Mach 2.2, the data of Fig 22 indicates that the side-mounted two-dimensional inlet and isolated two-dimensional inlet have a severe loss in pressure recovery and moderate increase in turbulence level above 10° angle of attack. The favorable flow field created by the wing or fuselage in terms of reducing local Mach number and flow angularity results in a higher level of pressure recovery for the wing-shielded and fuselage-shielded inlet configurations at angle of attack. The primary difference between the wing-shielded and fuselage-shielded inlets is in their performance at angles of sideslip as shown in Fig 22 where alpha = 15°. With a positive sideslip of 4° there is a very large drop-off in pressure recovery and increase in turbulence level with the wing-shielded configuration, whereas the fuselage-shielded configuration maintains a turbulence level of approximately 1% and a very high pressure recovery. The large increase in distortion with a small amount of positive sideslip for the wing-shielded configuration is felt to be related to an increase in the lower inboard sideplate flow separation (Fig 16) caused partly by the amplification of the outwash along the bottom of the wing at sideslip angles. Even though the throat flow distortion for the wing-shielded inlet at this condition was lower than the basic side-mounted inlet (Fig 16), the distortion at the compressor face is much higher. It is felt that this result is due to the fact that the wing-shielded inlet has a much shorter duct and the throat distortion may be amplified rather than attenuated as it is with the long duct. The trends in the pressure recovery and turbulence level are verified by the variations of distortion index as shown in Fig 22. Again, for simple angle of attack maneuvers with no sideslip, the wing-shielded and fuselage-shielded configurations both have a low level of steady state and time dependent distortion. For slight sideslip angles (for example 4°) there is a significant difference in the distortion level of the fuselage-shielded and wing-shielded configurations, with the fuselage-shielded inlet being much superior.
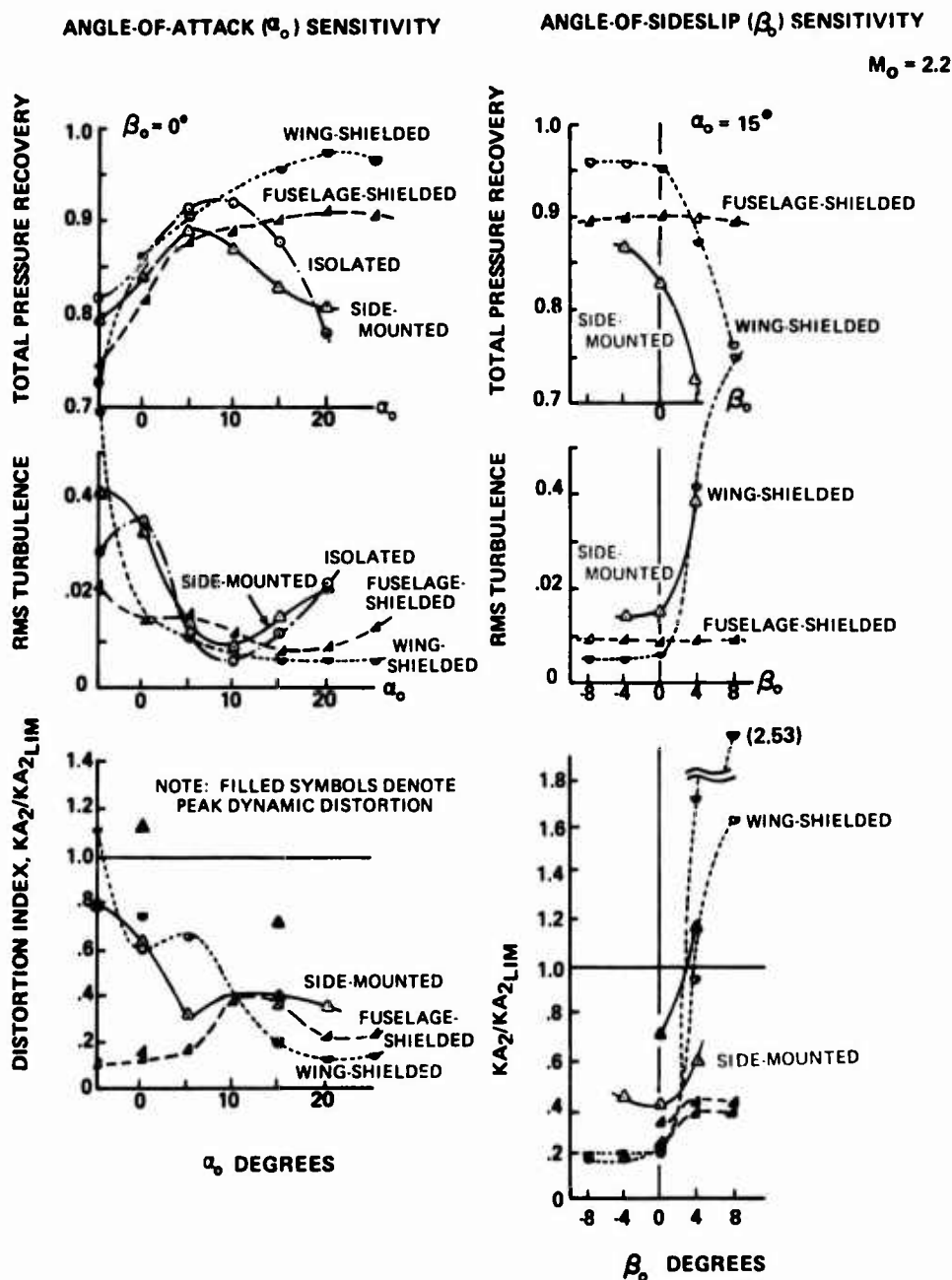
FIGURE 22. INLET PERFORMANCE AND FLOW DISTORTION:
COMPARISON OF INLET INSTALLATION TYPES,
$M_O = 2.2$

It should be recalled when comparing the various installation types as we have done in this paper, that there are significant differences in inlet design and the applications of these designs for the side-mounted, wing-shielded and fuselage-shielded configurations. However it is felt that the results of the comparisons show that there are advantages associated with shielding of an inlet during supersonic maneuvering flight. The fuselage-shielded configuration appears to have the benefits of reduced Mach number and angularity at the inlet face while not suffering from adverse effects in sideslip. The data also points to the possibility of employing a vertical ramp wing-shielded inlet as a possible alternative to the horizontal ramp wing-shielded configuration. In this case use would be made of the ability of the two-dimensional inlet to turn the flow into the compression ramps and avoid some of the cross-flow on the sideplates, since the outwash flow would then appear to the vertical ramp inlet as a local angle of attack.

Aftbody/Nozzle Systems:

As mentioned previously, one of the more important problems of aircraft propulsion systems integration is associated with the airframe-nozzle interface. The interaction between the external airframe generated flow field and the exhaust nozzle flow frequently results in higher drag than anticipated. Widely different nozzle area ratios are required for peak operating efficiency at subsonic, transonic, and supersonic flight conditions. The combined effect of compromised fuselage lines, proximity of large control surfaces, and interfairings in the case of dual nozzles, is to produce a non-uniform external flow field in the aftbody/nozzle region. The interaction of this non-uniform flow and the exhaust plume may produce separation or significantly alter the pressure distribution and drag of the aft end. The internal and external performance characteristics of axisymmetric nozzles are reasonably well understood for isolated nozzle systems not influenced by variations in the aircraft flow fields. However, the proper integration of the exhaust nozzle with the aircraft to reduce installation penalties and minimize aftbody drag is severely limited with present capability. A twin exhaust nozzle arrangement is especially subject to airframe nozzle interaction effects because of the difficulty of providing a suitable aft end geometry that reduces base drag and flow separation.

In order to better understand this problem area, an experimental and analytical program was initiated in 1969 for the development of design criteria, guidelines and predictive techniques for improved nozzle installations. This program included both isolated nozzle aftbody configurations and twin-nozzle airframe installations. The purpose of the isolated nozzle investigation was to determine the gross thrust, external drag, and internal and external pressure distributions for large scale exhaust nozzles installed in a single isolated pod. The purpose of the twin nozzle aftbody investigation was to determine similar parameters for a generalized twin jet tactical aircraft model. Test data were obtained over the 0.6 to 2.5 Mach number range with configuration variables as follows: nozzle type, power setting, lateral spacing, axial position, aftbody contour, horizontal stabilizer area and deflection,vertical stabilizer type and longitudinal position, and rudder deflection. The type, length and position, of interfairings between the nozzles were also investigated. Analytical methods for predicting twin nozzle aftbody performance were evaluated and improved using the twin jet test results.

The isolated nozzle test rig and strut arrangement is shown in Fig 23. The pod has a conical nose which faired into the cylindrical body. Nozzle thrust coefficient and pod aftbody and nozzle boattail drag coefficients were obtained from force balance data during the test and from area integrated pressure drags plus calculated skin friction drags. The pod internal arrangement included the air supply, ducting and force balances to measure thrust, aftbody plus boattail, and nozzle boattail drag. The nozzle boattail balance was attached to the flow tube which was supported by the thrust balance so that the thrust balance senses nozzle thrust and boattail drag directly.

Selected nozzles designed for the isolated nozzle investigations were also used in the twin nozzle aftbody investigation. The model scale chosen was approximately 18 percent and was based on considerations of full scale Reynolds number simulation, model airflow limitations, model and support strut blockage, and full model wing-span limitations. The strut supported twin jet fighter aircraft model used during the investigation is shown in Fig 24. The model is approximately 3.66 meters in length and has a wing-span of 2.41 meters. Six force balances plus approximately 250 static pressure taps were installed in the model to obtain the thrust and drag values. Further details of the experimental program and the data may be found in references 3 and 4.

Some of the pressure and drag coefficient data obtained from the isolated nozzle and twin jet test will be used in this paper to describe in detail how the external flow field over the aftbody and nozzle changes when the isolated nozzle is installed in the twin-jet aircraft model. References 2 and 3 contain data for several nozzle types. In this paper, only the data obtained for a convergent-divergent nozzle will be discussed and is thought to be typical of tactical aircraft exhaust nozzle designs.

Results will be presented for a convergent-divergent nozzle in cruise mode during subsonic operation and in maximum afterburner for a Mach number greater than 1. The geometry of these nozzles is shown in Fig 25. All of the nozzle data considered in this paper is at an operating nozzle pressure ratio (jet total pressure divided by free stream static), NPR, compatible with the Mach number being investigated.
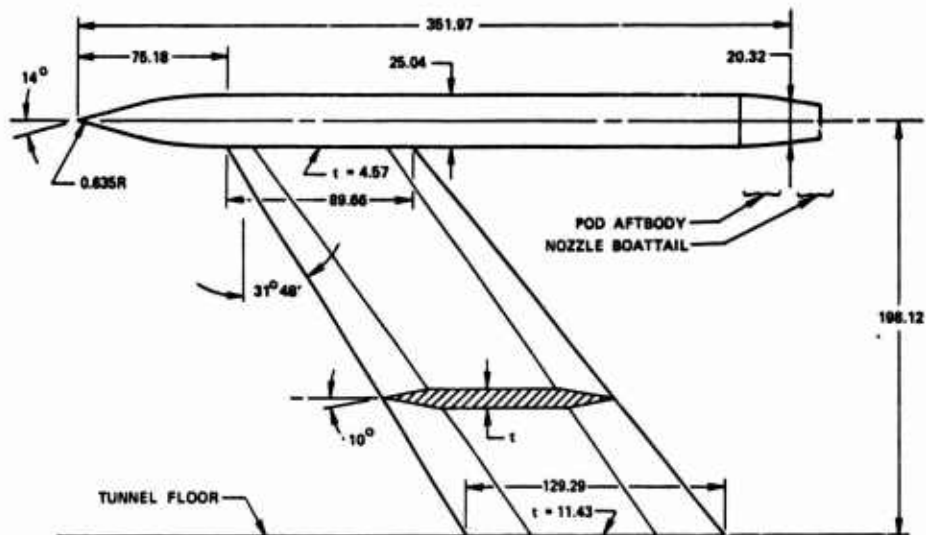
DIMENSIONS IN CENTIMETERS

FIGURE 23. SCHEMATIC OF ISOLATED MODEL AND SUPPORT STRUT
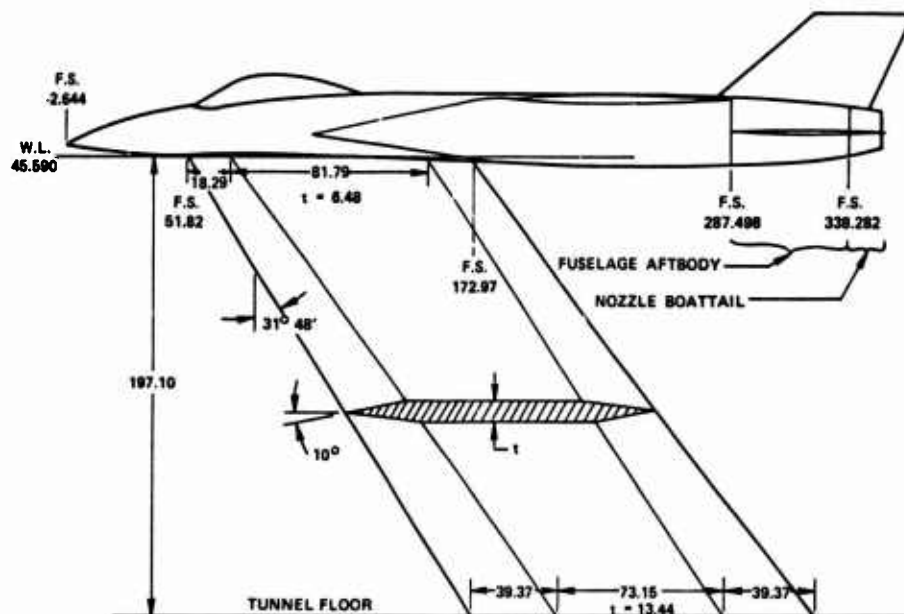
DIMENSIONS IN CENTIMETERS

FIGURE 24. SCHEMATIC OF TWIN JET MODEL AND SUPPORT STRUT
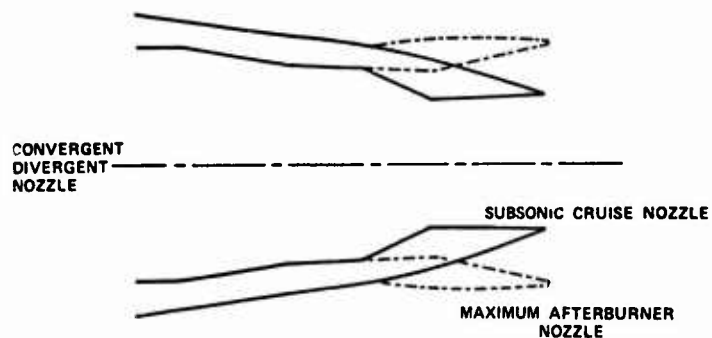
FIGURE 25. CONVERGENT-DIVERGENT NOZZLE GEOMETRY

In discussing the effects of installing the nozzle in the aircraft the approach will be to first present the isolated nozzle static pressure and drag data and compare it with similar data for the nozzle installed on the twin jet aircraft model without the horizontal and vertical tails. Both partial and full span horizontal and vertical tail surfaces were used on the model (Fig 26). Most of the twin jet tests were conducted with the partial span model to reduce the structural loads on the model. The results indicate a very small change in aftbody nozzle drag when going from partial to full span tail surfaces. It should be noted that the drag values discussed here are for the aftbody and/or nozzles excluding the horizontal and vertical tails, but including their influence. That is, the forces on the tail surfaces were not measured by the force balances. Although data was obtained for a Mach number range of 0.6 to 2.5 (reference 3), the Mach numbers to be discussed in this paper will be 0.6, 0.9, 1.2 and 1.6. All of the data on exhaust nozzle interference in this paper is for a unit Reynolds number of 2.5 X 10^6 per foot, except at M = 1.6 where the Reynolds number is 2.1 X 10^6 per foot.

DIMENSIONS IN CENTIMETERS
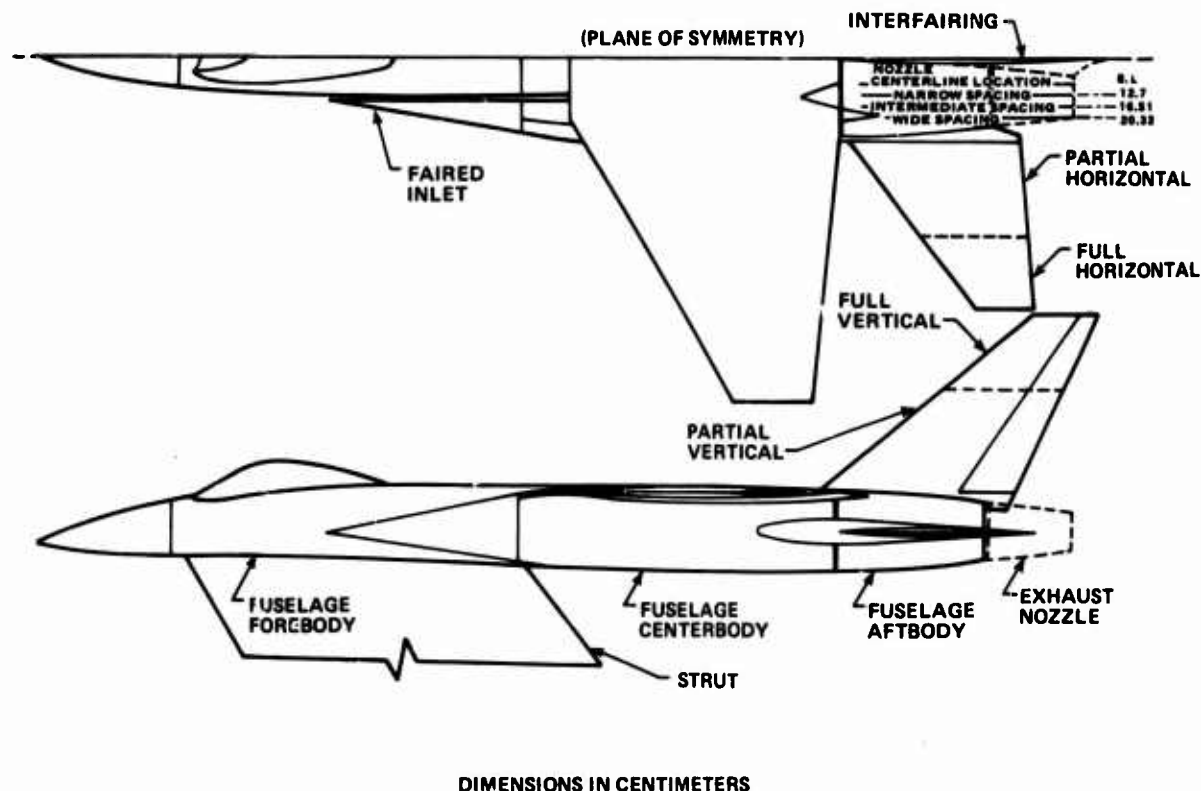
FIGURE 26. DIAGRAM OF TWIN JET AIRCRAFT MODEL

The various steps in the configuration buildup are shown in Fig 27. Configuration A, the isolated nozzle, is the initial configuration. This nozzle is then installed to give configuration B, a narrow spaced twin jet afterbody with no tails. Partial span tails are then added, configuration D.

With partial tails installed on the model, the interfairings and tail location are changed to investigate the effect on pressure distribution and drag. First the high, short horizontal wedge interfairing on configurations B and D is extended to the nozzle exit, giving configuration G in Fig 27. Configuration H has a vertical interfairing ending at the nozzle exit, and configuration I has a longer vertical interfairing.

The aftbody nozzle pressure coefficient distributions and drag coefficients are then presented for two other configurations where the distance between the nozzles is increased. These are indicated as configurations J and K in Fig 27. The interfairing on these configurations is similar to the high short horizontal wedge interfairing of configurations B and D. Table 1 gives a more complete description of the nozzle and aftbody/nozzle configurations.
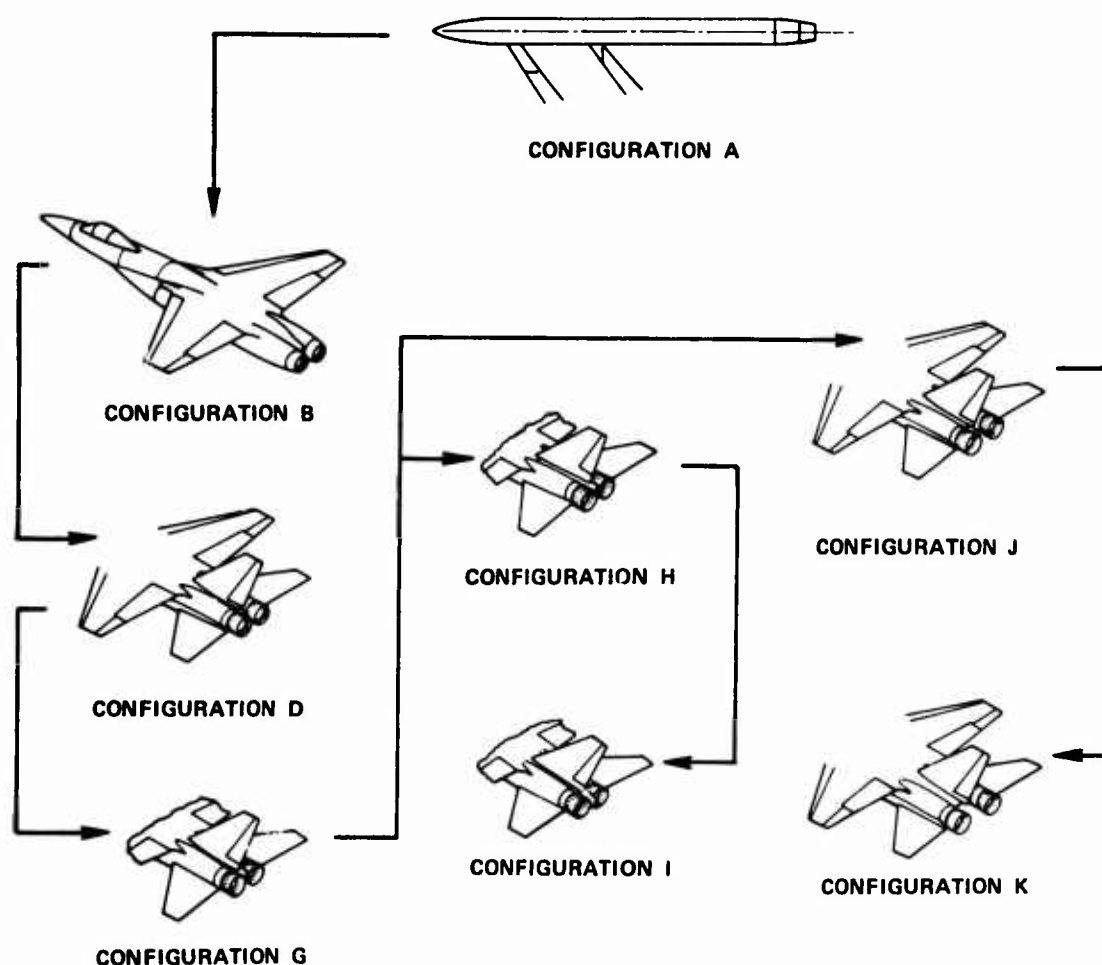
FIGURE 27. AFTBODY NOZZLE CONFIGURATION BUILDUP

Table 1.   Description of Nozzle and Aftbody/Nozzle Configurations

Configuration

A1   Isolated Subsonic Cruise Nozzle

A2   Isolated Maximum Afterburner Nozzle

B1   Twin Jet Without Tails - $S/_D$=1.25
Short Horizontal Interfairing
Subsonic Cruise Nozzle

B2   Same as B1 except
Maximum Afterburner Nozzle

D1   Twin Jet With Partial Span Tails - $S/_D$=1.25
Short Horizontal Interfairing
Subsonic Cruise Nozzle

D2   Same as D1 except
Maximum Afterburner Nozzle

G1   Twin Jet With Partial Span Tails - $S/_D$=1.25
Long Horizontal Interfairing
Subsonic Cruise Nozzle

H1   Twin Jet With Partial Span Tails - $S/_D$=1.25
Long Vertical Interfairing
Subsonic Cruise Nozzle

Configuration

I1   Twin Jet With Partial Span Tails - $S/_D$=1.25
Extra Long Vertical Interfairing
Subsonic Cruise Nozzle

J1   Twin Jet With Partial Span Tails - $S/_D$=1.625
Short Horizontal Interfairing
Subsonic Cruise Nozzle

J2   Same as J1 except
Maximum Afterburner Nozzle

K1   Twin Jet With Partial Span Tails - $S/_D$=2.0
Short Horizontal Interfairing
Subsonic Cruise Nozzle

K2   Same as K1 except
Maximum Afterburner Nozzle

The models were quite well instrumented, as shown on Fig 28. Data was measured on the top ($\theta = 0^{\circ}$) and bottom ($\theta = 180^{\circ}$) of the aftbody and nozzle, top and bottom of the interfairing and on the inboard side ($\theta = 135^{\circ}$) of the nozzle. All pressure coefficient distributions are plotted such that the exit of the nozzle is at a value of $\frac{X}{D}$ equal to zero.
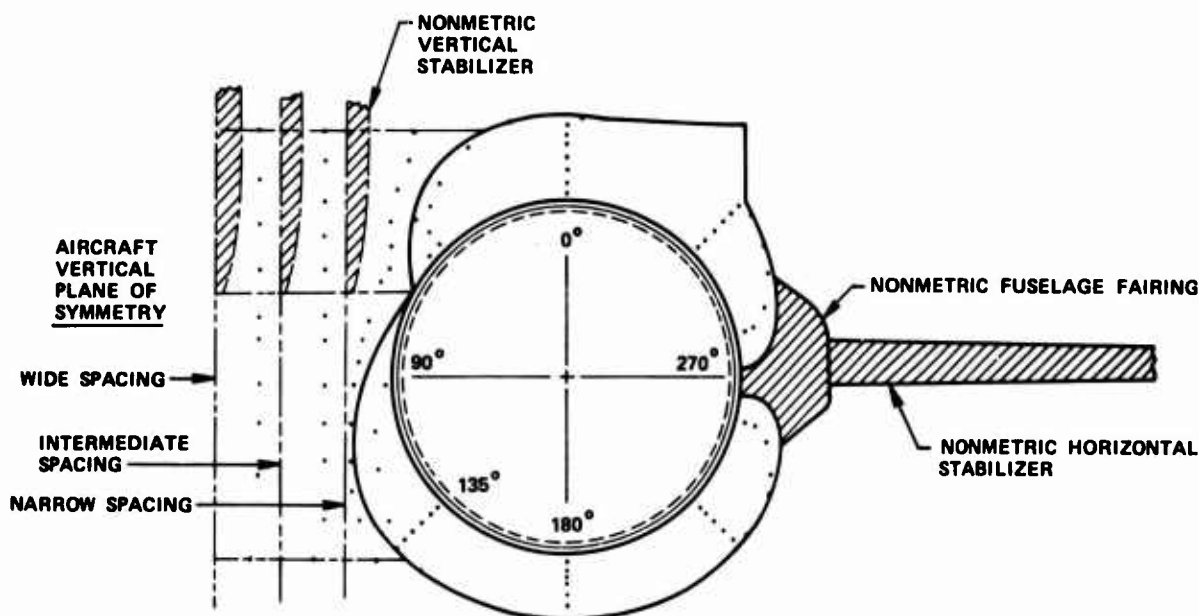
FIGURE 28. PRESSURE TAP LOCATIONS

Figure 29 shows the change in pressure coefficient distributions and drag coefficients on the aftbody/nozzle and interfairing when the subsonic cruise nozzle is installed on the twin jet model without the tails installed and then with the tails on at 0.6 Mach number and nozzle pressure ratio (NPR) of 3.0. Pressure distributions at the 0°, 135°, and 180° radial positions on the aftbody/nozzle combination (see Sig 28 for instrumentation layout) are given in Figures 29e and 29f for the isolated and installed configurations, respectively. The pressure distributions on Figures 29a and 29b indicate a significant change in the magnitude of the static pressures on the aftbody/nozzle when the nozzle is installed on the twin jet model (configurations A1 to B1) and again when the partial tails are installed (configurations B1 to D1). The change in pressures from isolated (A1) to installed (B1) appears to be favorable (toward lower drag) since the pressure coefficients become more positive on the nozzle and less negative on the aftbody (particularly at $\theta = 0^{\circ}$). However, when the tails are installed the pressure levels become more negative again on the aftbody and remain about the same on the nozzle. The change in pressure levels on the interfairing when the vertical and horizontal tails are installed is shown on Figures 29b and 29d, and indicate that the pressure levels on this surface also become more negative when the tails are installed. There is a significant decrease in pressure on the top of the interfairing with a smaller change on the bottom. The pressure decrease on the upper aftbody and interfairing surface is undoubtedly due to the influence of the vertical tail.

The drag coefficients listed are based cn the projected area of the surface on which the drag force acts. This choice of reference area was selected so that the isolated and installed drag coefficients can be compared even when the spacing ratio is changed for the installed configuration. The projected areas of the nozzles (boattail) remain the same from the isolated to the installed. The projected areas of the aftbodies increase from the isolated to the installed, so the projected area of the aftbody/nozzle combinations increases. The increase in drag should be directly proportional to the increase in projected area, which would tend to keep the drag coefficient constant if the pressure distributions are similar when going from one configuration to another. This is not exactly true in the case of the aftbody and the aftbody/nozzle combinations because the increase in wetted surface area may be greater in proportion to the increase in projected area and the drag change would be influenced more by the change in friction drag. The drag coefficients for the aftbody, nozzle and the aftbody/nozzle combination are designated as CD_A, CD_N and $CD_{A/N}$, respectively. The drag coefficients tabulated on Figure 29 reflect the changes in pressure distribution discussed above. There is a significant decrease in the nozzle drag coefficient CD_N (actually an increase in nozzle thrust) going from the isolated configuration (A1) to the tailless installed configuration (B1). This is felt to be due to the fact that the flow field ahead of the nozzle section did not expand as greatly on the installed configuration as it did on the isolated model, which in turn allowed the flow to recompress to higher pressure on the nozzle and create a lower drag (higher thrust). The aftbody and aftbody/nozzle drag coefficients both indicate an increase in drag when tails are added (B1 to D1).

FIGURE 29. INSTALLATION EFFECTS ON AFTBODY/NOZZLE PRESSURES AND DRAG;
S/$_D$ = 1.25, SUBSONIC CRUISE NOZZLE, M = 0.6, NPR = 3
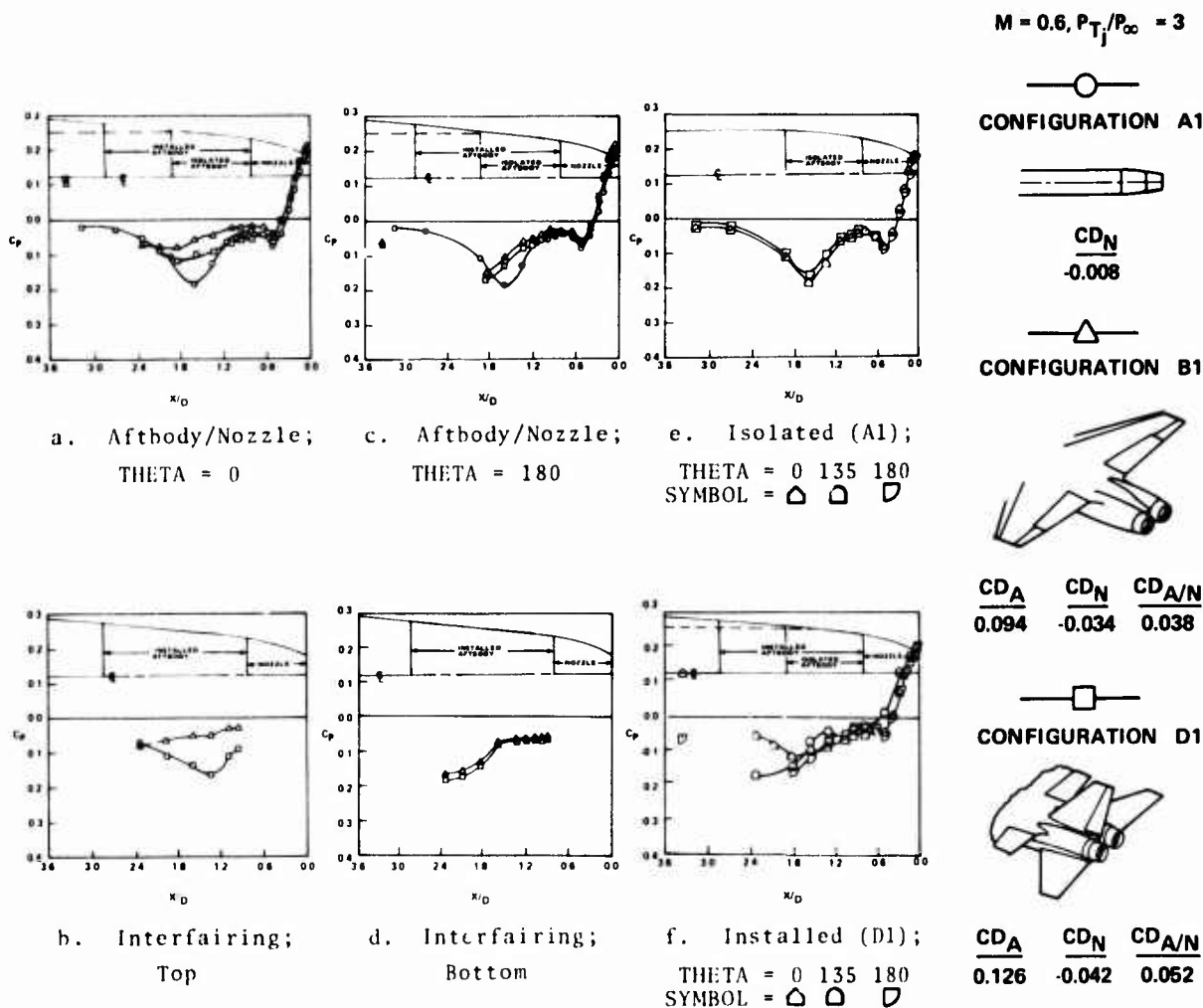
At 0.9 Mach number, similar changes in pressure distributions and drag coefficient behavior on the cruise nozzle are observed. Figure 30 indicates that the difference in pressure distribution from isolated to installed aftbody/nozzle without tail surfaces is significantly greater at M = 0.9 than at M = 0.6, resulting in a larger decrease in drag. The same is true in an opposite sense (larger increase in drag) when partial tails are installed on the model. These changes in the nozzle and aftbody/nozzle pressure drags are verified by the measured drag coefficients tabulated in Figure 30. The nozzle (boattail) drag decreases when the nozzle is installed on the twin jet model, with a further decrease when the tails are installed, while the aftbody drag increases with the installation of the tails. This gives a net increase in total aftbody/nozzle drag when the tails are added. The total aftbody/nozzle drag with the tails is about the same at M = 0.9 as it was at M = 0.6 (0.048 vs 0.052 respectively). As was true at 0.6 Mach number, installing the nozzle on the twin jet model apparently places the nozzle boattail in a more favorable flow field which decreases the drag.

a. Aftbody/Nozzle; THETA = 0

c. Aftbody/Nozzle; THETA = 180

e. Isolated (A1); THETA = 0 135 180 SYMBOL = △ ◻ ▽

b. Interfairing; Top

d. Interfairing; Bottom

f. Installed (D1); THETA = 0 135 180 SYMBOL = △ ◻ ▽

$M = 0.9, P_{T_j}/P_\infty = 3$

CONFIGURATION A1

$$\frac{CD_N}{-0.040}$$

CONFIGURATION B1

CD_A	CD_N	$CD_{A/N}$
0.085	-0.062	0.020

CONFIGURATION D1

CD_A	CD_N	$CD_{A/N}$
0.135	-0.065	0.048

FIGURE 30. INSTALLATION EFFECTS ON AFTBODY/NOZZLE PRESSURES AND DRAG; $S/_D = 1.25$, SUBSONIC CRUISE NOZZLE, M=0.9, NPR=3

The above pressure and drag data are for an aircraft operating in the subsonic flight regime with a nozzle installed that has a very small internal expansion ratio and a fairly steep boattail angle. When operating in the supersonic flight regime, possibly using afterburner, a nozzle with a much larger expansion ratio is needed to obtain the required thrust. The external geometry will also differ greatly from that of the subsonic cruise nozzle, generally having much lower boattail angles. The nozzle contours shown next are representative of the external geometry of a nozzle which has a cusp or inflection in the contour upstream of the nozzle exit. With the nozzles in the maximum afterburner position, the aft-facing projected area used as the drag coefficient reference area is very small. Therefore, the magnitude of drag coefficients for this configuration may be somewhat deceiving. The pressure coefficient distributions and drag coefficients presented on Figures 31 and 32 are for Mach numbers of 1.2 and 1.6, respectively. In general the pressure levels on the nozzle boattail decrease (i.e. the pressure coefficients become more negative) when the isolated nozzle is installed on the twin jet model and then decrease further when the tails are added. This would be expected to indicate an increasing drag when the nozzle is installed on the twin jet configuration and a further increase when the tails are installed. However, the nozzle drag coefficients tabulated on Figures 31 and 32 show a nozzle drag decrease when the nozzles are put on the twin jet model (A2 to B2) but a drag increase when the tails are added (B2 to D2). An explanation of this anomaly can be attributed to the rather unique geometry of this nozzle. For the isolated nozzle configuration, the higher pressures on the recompression region ($C_p > 0.0$) are mainly acting on the forward facing surface area (producing drag) of the nozzle just aft of the cusp. When this nozzle is installed on the twin jet model, these pressures in the recompression region (forward facing surface) decrease somewhat at M = 1.2, and significantly at M = 1.6. Also, the rearward facing surface area near the exit had mostly positive pressures acting on it (thrust component). There is very little change in these pressures when the isolated nozzle is installed on the twin jet model. The net effect, considering the surface slopes, indicated by these pressure changes is a drag reduction which is substantiated by the nozzle drag coefficients (CD_N) for configurations A2 and B2. When the tails are added (configuration D2) the pressure coefficients along the entire nozzle boattail become more negative relative to configuration B2, and the

drag increases. As indicated by the tabulated drag coefficients, the drag of the aftbody decreased when the tails were added. However, the total drag changed only slightly due to the drag increase on the nozzles.
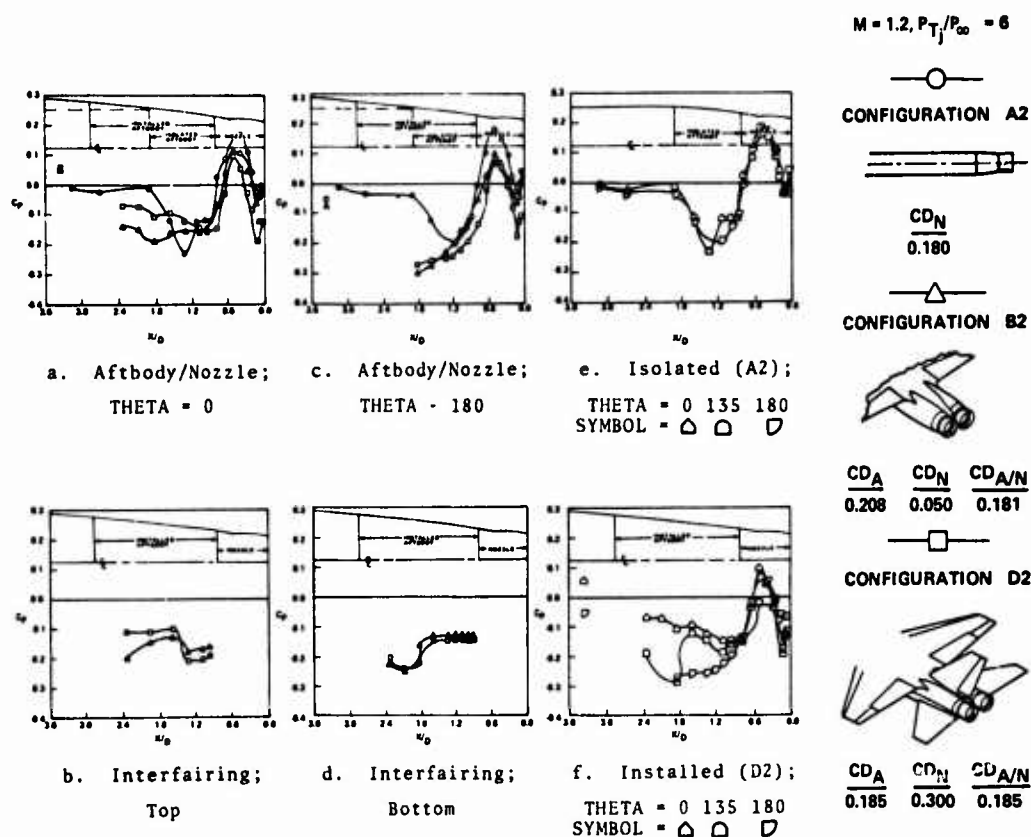
FIGURE 31. INSTALLATION EFFECTS ON AFTBODY/NOZZLE PRESSURES AND DRAG; S/D = 1.25, MAXIMUM AFTERBURNER NOZZLE, M = 1.2, NPR = 6
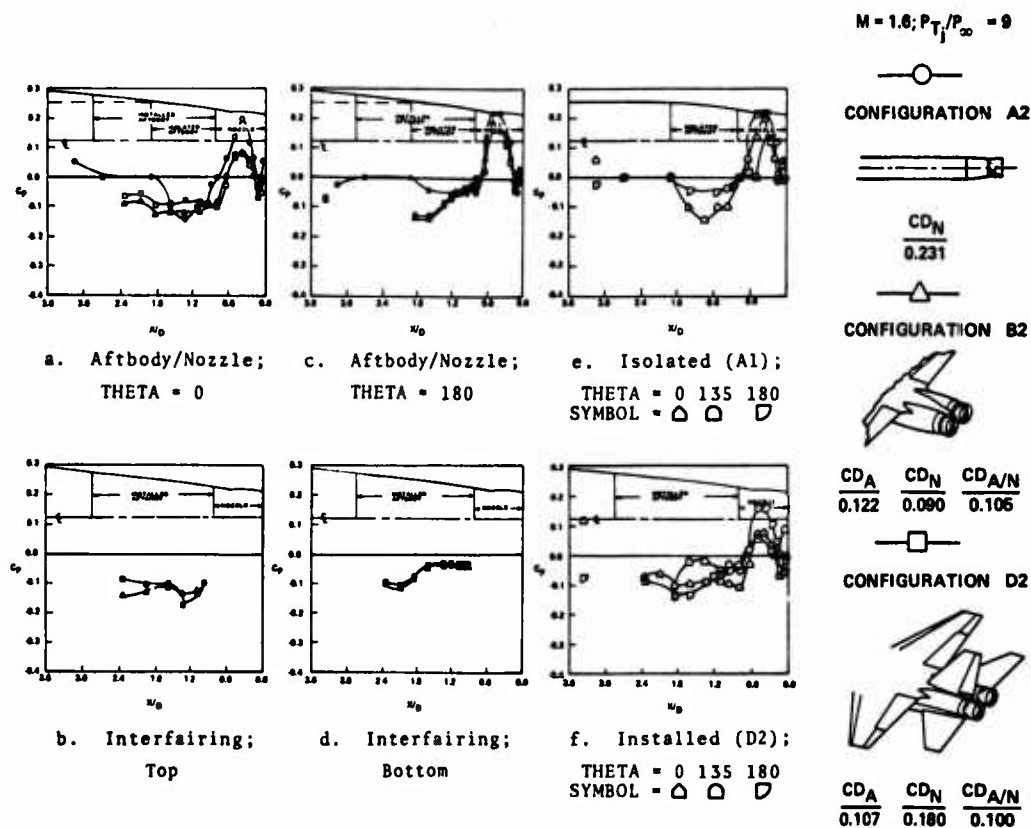
FIGURE 32. INSTALLATION EFFECTS ON AFTBODY/NOZZLE PRESSURES AND DRAG; S/D = 1.25, MAXIMUM AFTERBURNER NOZZLE, M = 1.6, NPR = 9

Nozzle Interfairing and Nozzle Spacing Effects

Geometrical changes other than the nozzle must be considered when designing twin jet aftbody/ nozzle systems to obtain the best performance. Sometimes changes in interfairing geometry can improve (i.e. decrease drag) the performance of particular configurations. In Figures 33 and 34 the short horizontal wedge interfairing, which is on all the twin jet configurations discussed above, is extended from the beginning of the nozzle boattail to the nozzle exit. The vertical tail is also moved rearward for better control characteristics when the interfairing is lengthened. Data for Mach numbers 0.6 and 0.9 are shown on Figure 33. At a Mach number of 0.6, the level of static pressure increases on the aftbody and interfairing and decreases on the nozzle when the horizontal interfairing is extended and the vertical tail moved rearward. The change in pressure levels correlate with the indicated changes in drag. That is, the drag decreased on the aftbody and increased on the nozzle. The total drag ($CD_{A/N}$) increased, indicating that the change in nozzle drag had the greater influence. Similar results on the aftbody and nozzle are observed at M = 0.9, except the total aftbody/nozzle drag decreased slightly, indicating that the change on the aftbody was the dominate factor. As shown on Figure 34, the levels of the static pressures increase along the aftbody/nozzle and the interfairing at both Mach numbers (1.2 and 1.6) for the longer horizontal wedge interfairing. This trend is reflected in the drag coefficients which indicate a decrease in drag. Most of the change in drag is on the aftbody (CD_A) as the maximum afterburner nozzle boattail has a relatively small projected area. The aft movement of the vertical tail is likely as important as the change in interfairing, since the tail interference is moved further aft on the aftbody/nozzle.

Pressure and drag data given in Figure 35 compares a horizontal interfairing (configuration G1) to a vertical wedge interfairing of the same length. Both terminate at the nozzle exit. The vertical interfairing is then extended beyond the exit of the nozzle giving configuration I1. Change from the horizontal to the vertical interfairing has very little effect on the aftbody drag, but a significant increase in nozzle drag for the subsonic cruise nozzle (M = 0.6 and M = 0.9). Extending the vertical interfairing beyond the nozzle exit (configuration I1) has very little effect on the nozzle and aftbody pressure distributions and drags.

M	CD_N
0.6	-0.008
0.9	-0.040

CONFIGURATION A1
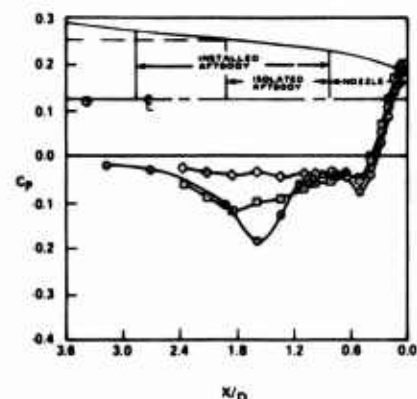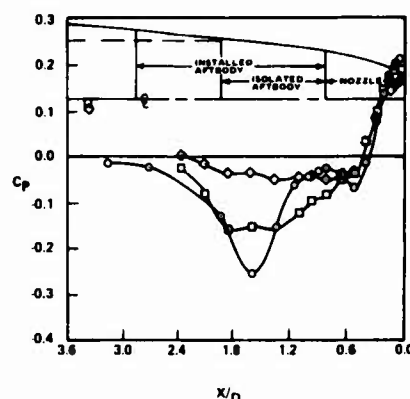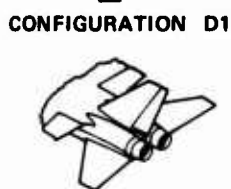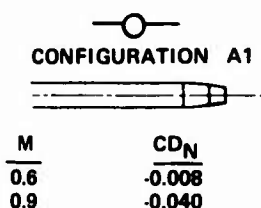
M	CD_A	CD_N	$CD_{A/N}$
0.6	0.126	-0.047	0.052
0.9	0.135	-0.065	0.048
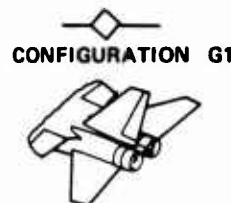
CONFIGURATION D1

M	CD_A	CD_N	$CD_{A/N}$
0.6	0.115	-0.015	0.057
0.9	0.115	-0.040	0.045

CONFIGURATION G1

a. Aftbody/Nozzle; THETA = 0, M = 0.6, NPR = 3

b. Interfairing; Top

c. Aftbody/Nozzle; THETA = 0, M = 0.9, NPR = 3
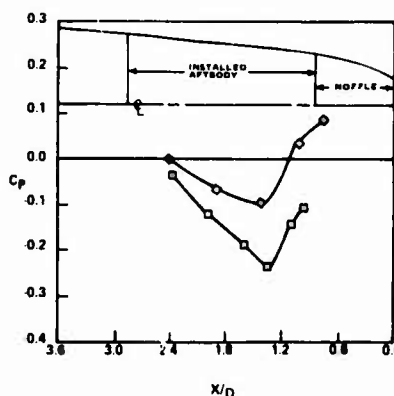
d. Interfairing; Top

FIGURE 33. INTERFAIRING CHANGE EFFECTS ON AFTBODY/NOZZLE PRESSURES AND DRAG; S/D = 1.25, SUBSONIC CRUISE NOZZLE, HORIZONTAL INTERFAIRING

a. Aftbody/Nozzle; THETA = 0
   M = 1.2, NPR = 6

CONFIGURATION A2

M	CD_N
1.2	0.180
1.6	0.231

c. Aftbody/Nozzle; THETA = 0,
   M = 1.6, NPR = 9

CONFIGURATION D2

M	CD_A	CD_N	CD_A/N
1.2	0.185	0.300	0.185
1.6	0.107	0.180	0.100

CONFIGURATION G2

M	CD_A	CD_N	CD_A/N
1.2	0.181	0.205	0.184
1.6	0.092	0.140	0.086

b. Interfairing; Top

d. Interfairing; Top

FIGURE 34. INTERFAIRING CHANGE EFFECTS ON AFTBODY/NOZZLE PRESSURES AND DRAG;
S/D = 1.25, MAXIMUM AFTERBURNER NOZZLE, HORIZONTAL INTERFAIRING

CONFIGURATION A1

M	CD_N
0.6	-0.006
0.9	-0.040

CONFIGURATION G1

M	CD_A	CD_N	CD_A/N
0.6	0.115	-0.015	0.057
0.9	0.115	-0.040	0.045

a. Aftbody/Nozzle; THETA = 0,
   M = 0.6, NPR = 3

c. Aftbody/Nozzle; THETA = 0,
   M = 0.9, NPR = 3

CONFIGURATION H1

M	CD_A	CD_N	CD_A/N
0.6	0.117	0.017	0.072
0.9	0.110	-0.005	0.069

CONFIGURATION I1

M	CD_A	CD_N	CD_A/N
0.6	0.107	0.015	0.065
0.9	0.100	-0.010	0.053

b. Interfairing; Top

d. Interfairing, Top
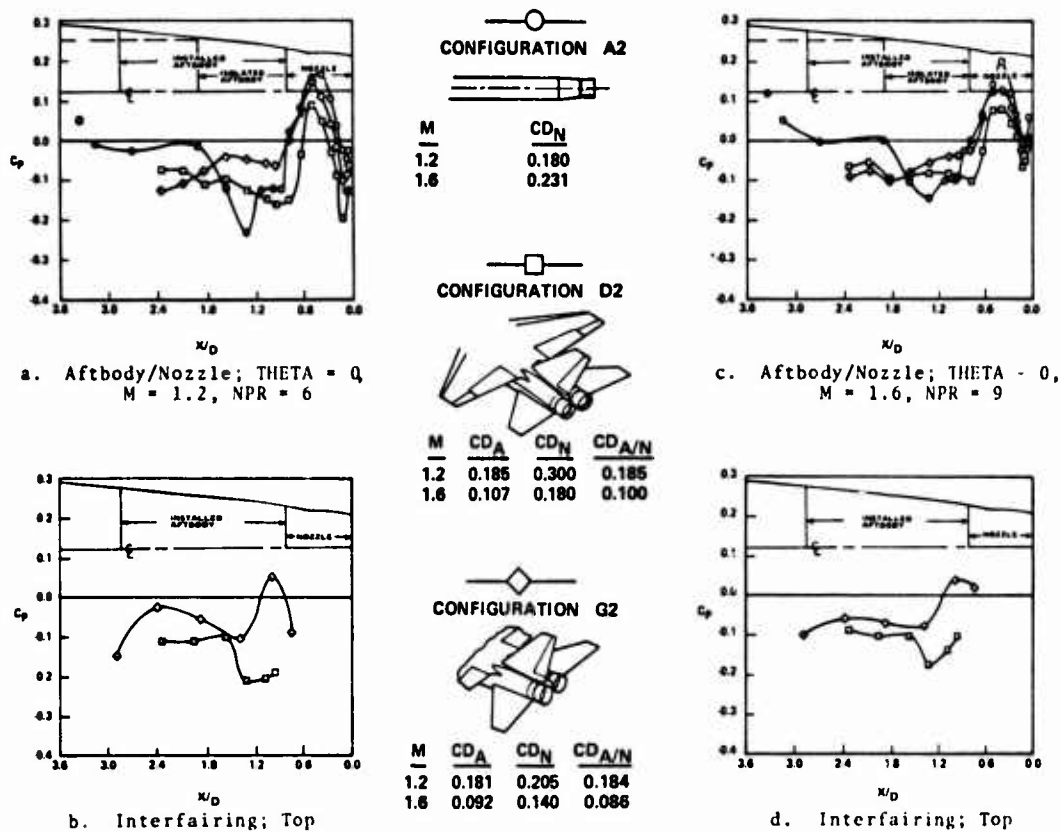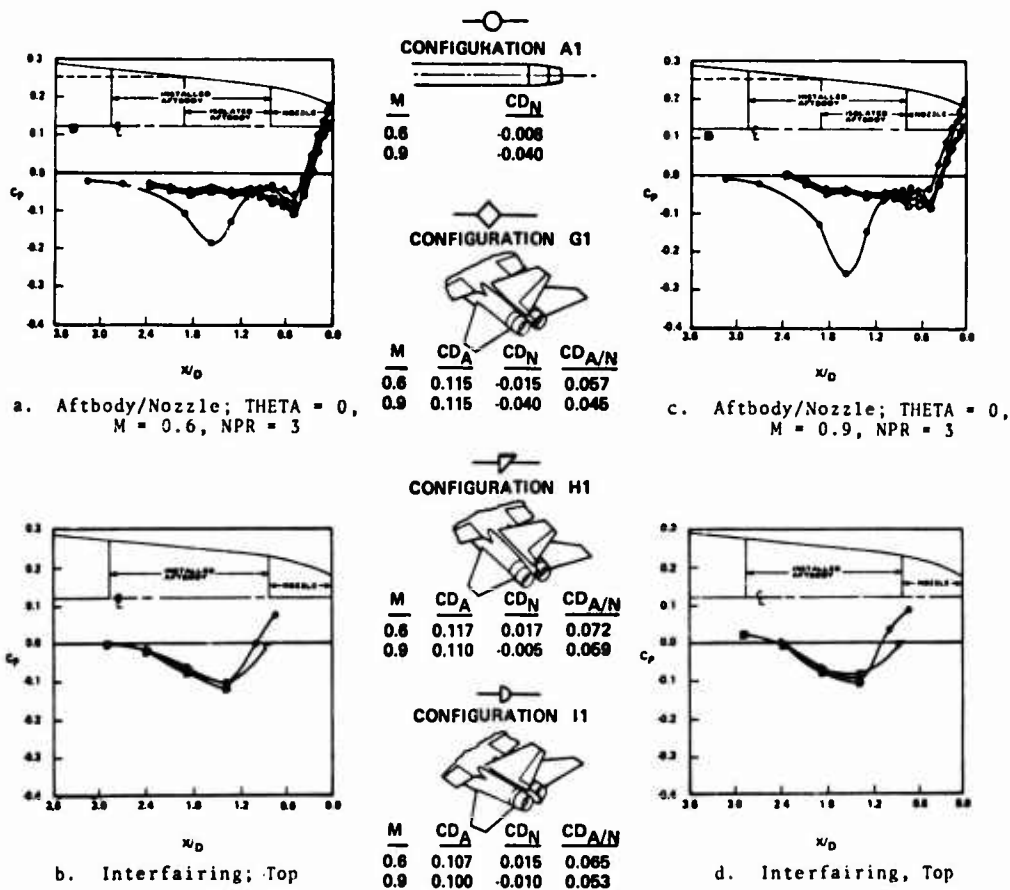
FIGURE 35. INTERFAIRING CHANGE EFFECTS ON AFTBODY/NOZZLE PRESSURES AND DRAG;
S/D = 1.25, SUBSONIC CRUISE NOZZLE, HORIZONTAL AND VERTICAL INTERFAIRINGS

Another major design choice in airframe/exhaust nozzle integration for a twin jet tactical aircraft is the distance between the nozzles. Representative data showing the spacing effects on aftbody/nozzle pressures and drags are given in Figures 36 and 37. The data on Figure 36 is for the subsonic cruise nozzle installed on the narrow (S/$_D$ = 1.25), intermediate (S/$_D$ = 1.625) and wide (S/$_D$ = 2.0) nozzle spacing. For subsonic Mach numbers the pressure levels on the aftbody, nozzle, and interfairing increase as spacing between the nozzles is increased. This indicates a decreasing drag on all components which is substantiated by the tabulated drag coefficients given on Figure 36. Results obtained in the supersonic flight regime, Figure 37, show a significant increase in aftbody and total aftbody/nozzle drag when changing to the intermediate spacing ratio. This is reflected in the more negative pressure ratio on the aftbody, indicative of higher wave drag. Comparing the wide spacing to the intermediate, there is a further increase in drag and decrease in pressure but not as great. In fact, the nozzle boattail drag coefficients indicate a slight decrease. However, for this configuration (maximum afterburner nozzle) the aftbody drag has a much greater influence on the total aftbody/nozzle drag because of the aftbody's larger projected area.

CONFIGURATION A1			
M	CD$_N$		
0.6	-0.008		
0.9	-0.040		

CONFIGURATION D1			
M	CD$_A$	CD$_N$	CD$_{A/N}$
0.6	0.126	-0.042	0.052
0.9	0.135	-0.065	0.048

CONFIGURATION J1			
M	CD$_A$	CD$_N$	CD$_{A/N}$
0.6	0.116	-0.055	0.051
0.9	0.135	-0.105	0.045

CONFIGURATION K1			
M	CD$_A$	CD$_N$	CD$_{A/N}$
0.6	0.095	-0.080	0.038
0.9	0.110	-0.115	0.037

a. Aftbody/Nozzle; THETA = 0, M = 0.6, NPR = 3

c. Aftbody/Nozzle; THETA = 0, M = 0.9, NPR = 3

b. Interfairing; Top
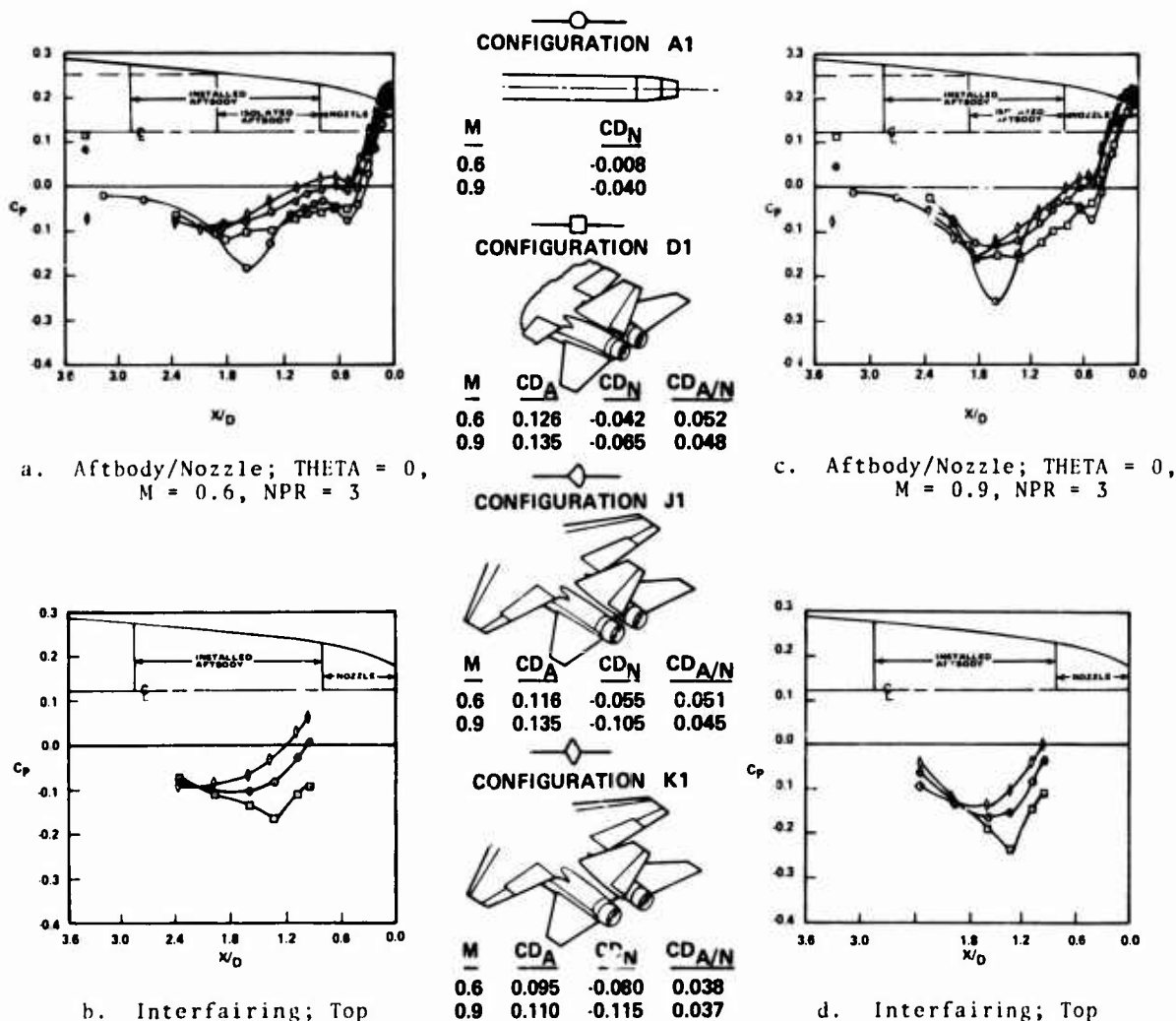
d. Interfairing; Top

FIGURE 36. NOZZLE SPACING CHANGE EFFECTS ON AFTBODY/NOZZLE PRESSURES AND DRAG; SUBSONIC CRUISE NOZZLE, HORIZONTAL INTERFAIRING

CONFIGURATION A2

M	CD_N
1.2	0.180
1.6	0.231

CONFIGURATION D2

M	CD_A	CD_N	$CD_{A/N}$
1.2	0.185	0.300	0.185
1.6	0.107	0.180	0.100

a. Aftbody/Nozzle; THETA = 0, M = 1.2, NPR = 6

c. Aftbody/Nozzle; THETA = 0, M = 1.6, NPR = 9

CONFIGURATION J2

M	CD_A	CD_N	$CD_{A/N}$
1.2	0.225	0.520	0.233
1.6	0.137	0.360	0.140

CONFIGURATION K2

M	CD_A	CD_N	$CD_{A/N}$
1.2	0.257	0.300	0.250
1.6	0.150	0.290	0.149

b. Interfairing; Top
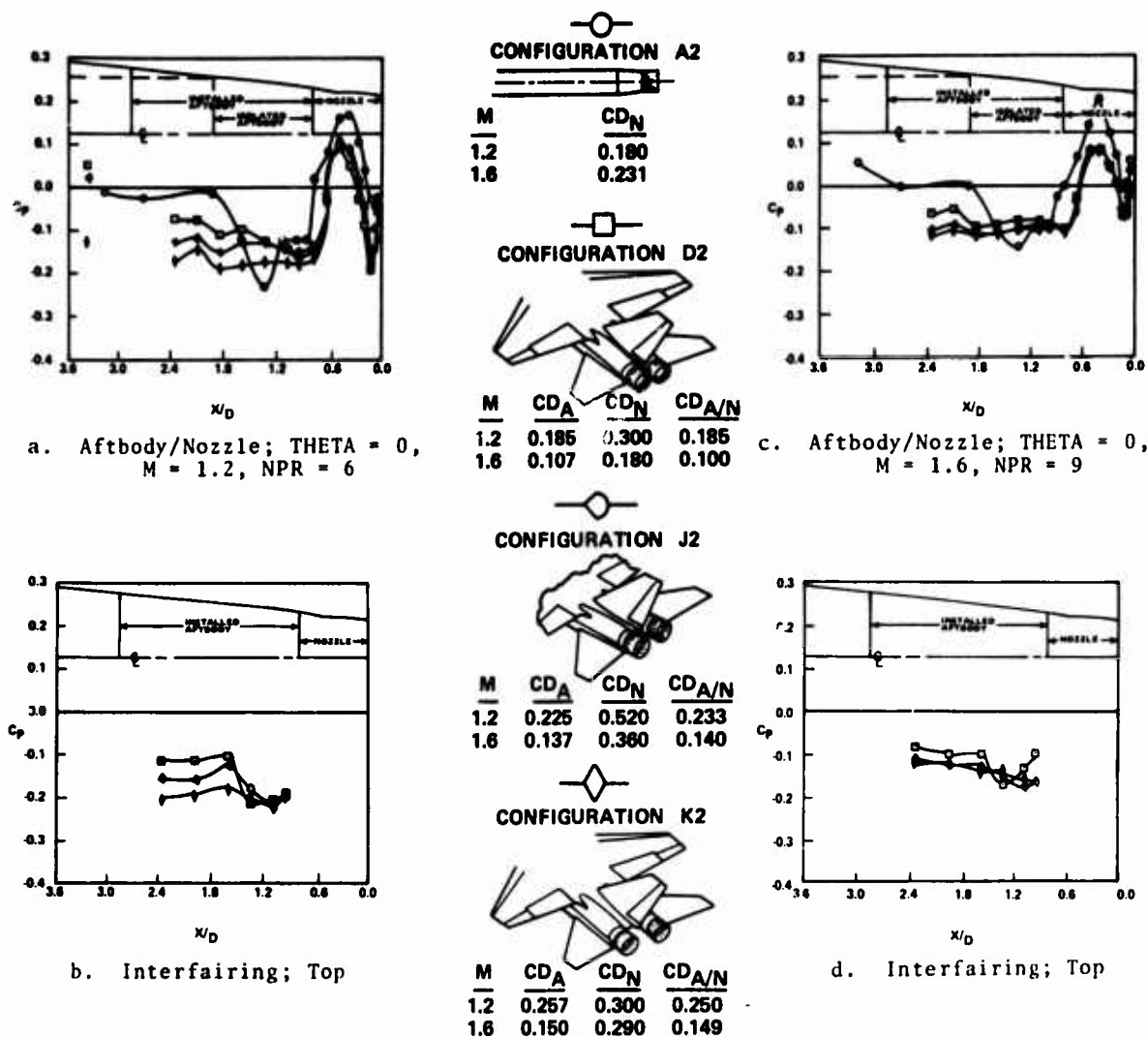
d. Interfairing; Top

FIGURE 37. NOZZLE SPACING CHANGE EFFECTS ON AFTBODY/NOZZLE PRESSURES AND DRAG; MAXIMUM AFTERBURNER NOZZLE, HORIZONTAL INTERFAIRING

CONCLUSIONS

Inlet/Airframe Interference Results:

The stream flow approaching a two-dimensional side-mounted inlet is substantially distorted by the presence of the fuselage, especially in maneuvering flight. This flow distortion has a generally adverse effect on inlet total pressure recovery and inlet-engine compatibility. Careful rounding of the fuselage lower shoulder, however, can result in significant improvement in both areas of performance over a fuselage incorporating a squared lower shoulder.

An examination of three inlet installation types for two-dimensional, horizontal ramp inlets revealed dramatic advantages of inlet shielding in supersonic high angle-of-attack flight. However, of the two shielding techniques tested, only the fuselage-shielded installation retains this benefit when angle-of-sideslip is added to produce a more realistic maneuver condition. Examination of the wing-shielded inlet data suggests that its maneuvering performance could be improved considerably by introducing a combination of vertical compression ramp orientation to reduce the adverse effect of flow outwash under the wing, and increased subsonic diffuser length to attenuate distortion generated at the inlet throat.

Actual peak compressor face flow distortion to which a turbine engine may respond must be measured by dynamic pressure instrumentation giving accurate resolution of pressure fluctuations in the range of the engine blade passing frequency ($\sim$ 150 H_z full scale). The flow distortion thus measured can be very much greater than time-averaged distortion measurements would indicate. A rough estimate of the magnitude of this difference can be inferred from the average level of compressor face RMS turbulence, i.e., high turbulence is generally associated with large increases in dynamic distortion measurements over time-averaged measurements.

Aftbody/Nozzle Results:

Detailed pressure and drag information clearly shows the result of alterations in the external flow over a nozzle and aftbody/nozzle as a result of various geometry changes, including the installation of the nozzle in the aircraft. During subsonic operation, installing the nozzle on the twin jet appears to place the nozzle itself in 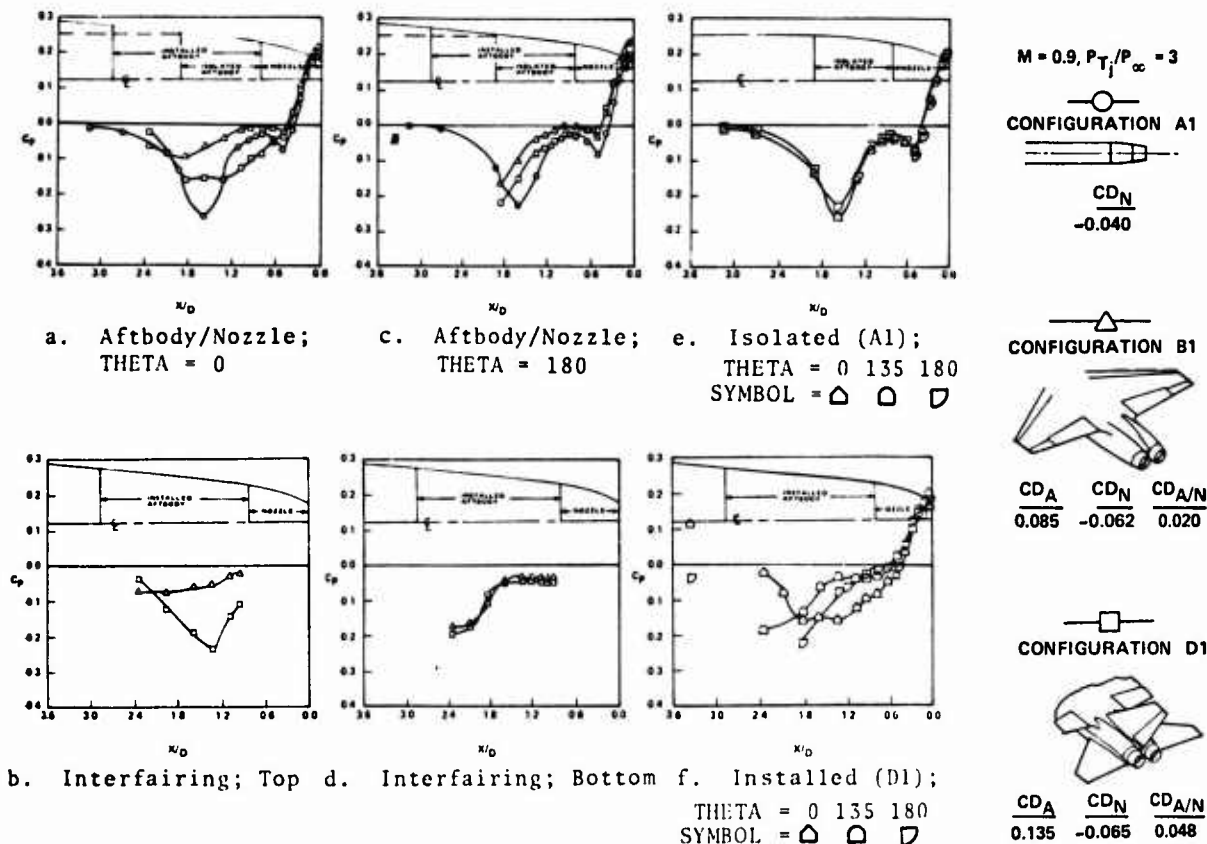a more favorable flow field which decreases the nozzle drag. However, the total aftbody/nozzle drag, in general, increases when the tails are installed. Supersonically, the nozzle drag decreases when installed, but increases when the horizontal and vertical tails are added. An opposite trend in drag is observed on the aftbody when the tails are installed and the total aftbody/nozzle drag changes very little.

Refinement in twin jet aftbody/nozzle design is sometimes accomplished by changing the interfairing geometry or the distance between the nozzles. The data presented here indicates that the interfairing design and vertical tail location can have a noticeable effect on aftbody and nozzle drags. Extending the horizontal wedge interfairing and moving the tail aft decreased the aftbody drag and increased the nozzle drag at the subsonic flight speeds. The total aftbody/nozzle drag increased at M = 0.6 and decreased slightly at M = 0.9. Changing from a horizontal to a vertical interfairing at Mach numbers 0.6 and 0.9 increased both the nozzle and total aftbody/nozzle drag. Increasing the spacing ratio between the nozzles decreased the drags at subsonic speeds and increased the aftbody and total drags significantly at supersonic speeds.

<div align="center">

Appendix I   -   Distortion Index K_{A_2}

</div>

The distortion factor K_{A_2} (reference 13) is equal to the sum of the circumferential and weighted radial distortion,

$$K_{A_2} = K_\theta + bK_{R_{A_2}}$$

K_θ represents the circumferential distortion and is equal to the following expression,

$$K_\theta = \frac{\displaystyle\sum_{R=1}^{J}\left[\left(\frac{A_n}{N^2}\right)_{MAX}\right]_{RING} \times \frac{1}{D_{RING}}}{\left(Q/P_{T_2}\right)_{REF} \times \displaystyle\sum_{R=1}^{J}\frac{1}{D_{RING}}}$$

A_n is the polar magnitude of the largest nth harmonic coefficient of a Fourier series curve fit of the pressure distribution around a ring at the engine compressor face. $\left(Q/P_{T_2}\right)_{REF}$ is the reference value of engine face dynamic pressure head which is a function of engine face Mach number.

The radial distortion factor is defined as,

$$K_{R_{A_2}} = \frac{\displaystyle\sum_{R=1}^{J}\left(\frac{\Delta P_{T_2}}{\overline{P}_{T_2}}\right)_{RING} \times \frac{1}{x}D_{RING}}{\left(Q/P_{T_2}\right)_{REF} \times \displaystyle\sum_{R=1}^{J}\frac{1}{x}D_{RING}}$$

$\left(\Delta P_{T_2}/P_{T_2}\right)$ represents the change or deviation of the ring averaged recovery from a reference radial profile reflecting inlet guide vane schedule, fan speed, and fan design. The exponent, x, is a weighting factor for the ring components of radial distortion from hub to tip and is a function of engine design. The b factor is the radial distortion weighting factor and is a function of engine design and engine face Mach number.

REFERENCES

1. Antonatos, P. P., Surber, L. E., Laughrey, J. A., and Stava, D. J.: "Assessment of the Influence of Inlet and Aftbody/Nozzle Performance on Total Aircraft Drag", AGARD CP 124, Aerodynamic Drag, April 1973.

2. Glasgow, E. R.: "Integrated Airframe-Nozzle Performance for Designing Twin-Engine Fighters", AIAA Paper 73-1303, November 1973.

3. Glasgow, E. R., Santman, D. M., and Miller, L. D., et al: "Experimental and Analytical Determination of Integrated Airframe Nozzle Performance", AFFDL TR-72-101, Vols. I & II, October 1972.

4. Glasgow, E. R., Santman, D. M., and Miller, L. D., et al: "Integrated Airframe Nozzle Performance for Designing Twin Engine Fighters", AFFDL TR-73-71, June 1973.

5. Surber, L. E., and Stava, D. J.: "Supersonic Inlet Performance and Distortion During Maneuvering Flight", AGARD CP 91-71, Inlets and Nozzles for Aerospace Engines, December 1971.

6. Antonatos, P. P., Surber, L. E., and Stava, D. J.: "Inlet/Airplane Interference and Integration", AGARD Lecture Series No. 53, May 1972, AGARD-LS-53.

7. Cawthon, J. A., Truax, P. P., and Savage, T. M.: "Advanced Inlet Study (Tailor-Mate II)", AFFDL TR-73-72, June 1973.

8. Cawthon, J. A., Truax, P. P., et al: "Supersonic Inlet Design and Airframe-Inlet Integration Program", AFFDL TR-71-124, Vols. I, II, & III.

9. Sanders, M. A., and Christenson, R. J.: "Inlet Performance Characteristics of Generalized 1/4 Scale and 1/2.83 - Scale Tactical Aircraft Models at Transonic and Supersonic Speeds", AEDC TR-72-188, December 1972.

10. Plourde, G. S., and Brimelow, B.: "Pressure Fluctuations Cause Compressor Instability", Proceedings of the Air Force Airframe-Propulsion Compatibility Symposium, 24-26 June 1969, AFAPL TR-69-103.

11. Burcham, F. W., and Hughes, D. L.: "Analysis of In-Flight Pressure Fluctuations Leading to Engine Compressor Surge in an F-111A Airplane for Mach Numbers to 2.17", AIAA Paper 70-624, June 1970.

12. Marous, J. J., and Sedlock, D.: "Dynamic Data Editing and Computing System (DYNADEC)", Proceedings of the AFSC Schence and Engineering Symposium, October 1973, Kirtland AFB, New Mexico.

13. Farr, A. P., "Evaluation of F15 Inlet Dynamic Distortion", MCAIR 73-011, presented at 5th Aircraft Design, Flight and Operations Meeting, AIAA, August 1973.

DETAILED EXPERIMENTAL AND THEORETICAL ANALYSIS OF THE AERODYNAMIC
INTERFERENCE BETWEEN LIFTING JETS AND THE FUSELAGE AND WING

by

G. SCHULZ & G. VIEHWEGER

Deutsche Forschungs- und Versuchsanstalt
für Luft- und Raumfahrt E.V.

505 Porz-Wahn, (German Federal Republic)

Summary

The aerodynamic interference between lifting jets blown across their axis and the fuselage and wing respectively is an important problem of the V/STOL aircraft. The parameters which influence it are rather numerous: The diameter and velocity of the jet (or jets), the flight velocity, the angle between the latter and the jet axis, the geometry of the fuselage/wing combination and the relative location of the jets with respect to them and to each other.

The experimental approaches done in favour of this subject are mostly of two very different characters:

a) Pressure distribution measurements on jets emerging from an infinite plane or simular simplified shapes.

b) Force measurements on real prototype aircraft models.

It is considered to be useful to combine these methods. In the present investigation, an aircraft model of simple shape for pressure distribution measurements is used, which allows the variation of all main geometrical parameters mentioned above. The jets reach Mach number 1. Measurements of the velocity directional flow field are added.

The pressure distributions as well as the flow directional field allow the physical interpretation of the several aerodynamic effects. By integration of the pressure field, the forces and moments caused by the jets are obtained. The integration of the directional field leads to the stream lines of the complicated field of cross blown jets.

Theoretical momentum considerations enable the calculation of the jet path and lead to transcalculation rules for flow directional fields (downwash) from one dynamic pressure ratio to another.

Notation

D	fuselage diameter	$= 0,15$ m
d	nozzle exit diameter	$= 30/37,5/45$ mm
F_j	cross section of jet	$= \frac{\pi}{4} \cdot d_j^2$
L_j	distance between the jet axes	$= 1,5/2/3/4 \cdot D$
L	length of the cylindrical fuselage part	
L_s	length of the fuselage front part	
x, y, z	cartesian coordinates	$\left(x^{\ast} = x + L_s\right)$
φ	angular coordinate of the fuselage	
h	distance between fuselage and ground	
v_∞	free-stream velocity	
ρ_∞	free-stream density	
q_∞	free-stream dynamic pressure	$= \frac{\rho_\infty}{2} \cdot v_\infty^2$
v_j	jet initial velocity	
ρ_j	jet initial density	
q_j	jet initial dynamic pressure	$= \frac{\rho_j}{2} \cdot v_j^2$
ϕ	dynamic pressure ratio	$= q_j/q_\infty$
M_j	jet Mach number	
P_∞	free-stream static pressure	
P_n	static pressure on the fuselage surface	
$\dfrac{P_n - P_\infty}{q_\infty}$	static pressure coefficient on the fuselage	$= \dfrac{\Delta p}{q_\infty}$
$c_{p\infty}$	normal force coefficient of a fuselage length element dx	$= \displaystyle\int_0^{2\pi} \frac{P_n - P_\infty}{q_\infty} \cdot \frac{\cos\varphi}{2\pi} \cdot d\varphi$
$c_{N\infty}$	normal force coefficient of the fuselage cylindrical part	$= \displaystyle\int_0^{1}\int_0^{2\pi} \frac{P_n - P_\infty}{q_\infty} \cdot \frac{\cos\varphi}{2\pi} \cdot d\varphi \cdot \frac{dx}{L}$
$c_{M\infty}$	pitching moment coefficient of the fuselage cylindrical part	$= \displaystyle\int_0^{1}\int_0^{2\pi} \frac{P_n - P_\infty}{q_\infty} \cdot \frac{x^{\ast}}{L} \cdot \frac{\cos\varphi}{2\pi} \cdot d\varphi \cdot \frac{dx}{L}$
$\alpha \ [^o]$	angle of attack	

Indices

j	=	jet
∞	=	free-stream

Further notations are defined within the text.

<center>Detailed Experimental and Theoretical Analysis of the Aerodynamic

Interference between Lifting Jets and the Fuselage and Wing</center>

1. Introduction

The aerodynamic interference between lifting jets blown across their axis and the fuselage and wing respectively is an important problem of the V/STOL aircraft:
Numerous parameters influence this problem: The diameter and velocity of the jet (or jets respectively), the flight velocity, the angle between the latter and the jet axis, and the geometry of the fuselage/wing-combination as well as the relative location of the jets with respect to them and to each other.

Moreover even the initial turbulence and homogenity of the jets exhausting from the nacelle influences the interference feelably, as will be shown in this reference.

The experimental approaches done in favour of this subject are in most cases of the following very different character:
They concern partly jets emerging from an infinite plane or other simple shapes and on the other hand force measurements on real prototype aircraft models [2, 3]. Both kinds of investigation are useful, but they are unable to bring the knowledge of the interference problem of aircraft to a satisfactory understanding of the physical nature of the technical free jet behaviour. This reference tries to reach this aim without going to far from the technical situation cf practical aircraft. The experimental investigation comprehends two sections:

      (a) The near-field interference
      (b) The far-field interference.

The above experimental results are supported by theoretical considerations.

2. The model and the programme of measurements

In section (a) a fuselage model is used, which allows the following variations (Fig. 1):
The fuselage central region has a cylindrical shape and constant cross section. It contains two jet nozzles one behind the other, blowing downward. The diameter of the nozzles can be varied as well as their distance from each other. The model is composed by a number of interchangeable annular sections of different lengths, thus allowing numerous variations of fuselage configurations. The whole fuselage surface is covered by pressure measurement holes leading to an inside scanivalve arrangement for some hundred holes (Fig. 2).

The angle of attack has been varied between -6° and $+15^{\circ}$ degrees. The angle of yaw was zero. The value of ϕ has been varied in the range of 16 to 290. The engine jets are simulated by compressed cold air up to Mach numbers of 1. The pressure holes are distributed over the whole surface of the central fuselage part, but concentrate preferentially in the vicinity of the nozzles exits. The pressure distribution measurements of these configurations are presented by a considerable number of isobar-diagrams, showing the cylindrical fuselage surface unwrapped into a plane. These diagrams show in detail how the pressure round the nozzles is influenced by the jet. The influence comes from the following reasons:

      a) the air entrainment effect (ejector effect)
      b) the displacement and wake effect
      c) the interaction between two jets.

The pressure distribution fields of the fuselage show very much details, which allow a physical explanation of the several effects and their mutual interference.

In order to come to informations about the forces and moments acting on the fuselage, we integrate the pressure fields in the circumferential direction and get the pressure coefficient $c_p = f(x/L)$. A second integration in the axial direction leads to the normal forces and pitching moments on the fuselage central part, where the jet interference takes place (c_N, c_M). In section b) the far-field interference is treated: The flow field is measured within a wide volume range around the nozzle exit. The direction and amount of the local velocity is found by a probe measurement (with 5 holes). The results are presenced by isocline-diagrams, showing lines of equal flow direction respectively. By integration of these directional flow fields, diagrams with stream lines are obtained. Both isocline diagrams and stream line diagrams show, in spite of their complexity, typical similar forms in configurations of highly variable pressure ratio ϕ.

3. Influence of the main parameters

In the AGARD-CPP 135 (lecture 12), reference [1] and in reference [5], several of the main configurations of the near field programme have been already presented: The influence of the nozzle diameter d_j, the distance L_j between two jets, and the influence of the dynamic pressure ratio ϕ. We confine therefore the presentation in the near field range on the following problems:

      a) Influence of the wing forward position in presence of jets.
      b) Influence of the ground in presence of jets.

In the far field range, the influence of the geometry of the aircraft drops by and by as the distance from the nozzle exit is increased. Within practical distances, their efficacy cannot be neglected fully. But in order to facilitate the analysis, we restrict for this purpose the investigation to the following configuration: A single lifting jet exhausting from the cylindrical fuselage (at $\alpha = 0^{\circ}$, without wing) perpendiculary into the parallel stream. The Mach number varies between 0,68 and 1,0. Its influence is not very important, but feelable. The most important parameter in the far field is apart from the coordinates of the local point considered, undoubtedly the dynamic pressure ratio ϕ.

With the aid of a momentum theory, combining ejector effect and jet path, an attempt is made to calculate the path of cross blown jets and to derive similarity rules for flow fields with different values of ϕ.

3.1 Influence of wing forward position in presence of jets (Fig. 3 to 7)

The wing forward or rearward position with respect to the jet nozzles is an important parameter for the construction of aircraft. With regard to the aerodynamic jet interference too, this parameter turns out to be effective. Three wing positions are chosen (Fig. 3):

      a) Wing exactly above the front jet nozzle: $x_F/D = -1,5$
      b) Wing exactly between the two jet nozzles: $x_F/D = 0$
      c) Wing exactly above the rear jet nozzle: $x_F/D = +1,5$

(x_F is counted from the center of L_j, rearward positive). The vertical position of the wing was held constant at the level of the fuselage axis.

The diagrams 4a to 4d show the pressure distribution on the cylindrical fuselage middle part by isobare chards, in which (as mentioned above) the fuselage surface has been unwrapped into a plane. Fig. 4a shows the pressure distribution without wing. This is the well known pattern of the pressure distribution in the vicinity of the nozzle exit of a cross blown free jet [1, 2, 4, 5]. The following details may be repeated:
On both sides of each jet, regions of low pressure arise, partly because of the jet displacement, partly because of the ejector effect, which accelerates the flow strongly into the direction of the jet axis, especially in the next environs of it. In front of the jets, a region of higher pressure is found, caused by the ram pressure region of the displacement flow around the jet. But at this place the overpressure can be reduced considerably or even disappear, depending on the value of ϕ. Behind the jets a wake is formed. All these effects are found to be weaker at the rear jet, because its cross flow is shielded by the front jet. When the wing is added, the aerodynamic effect consists above all in that the secondary air flow into the jets is hindered in a quite different manner, depending on the wing position.

The big underpressure within the whole region of the jet exhausting below the wing respectively is especially obvious at the forward and at the rearward position. (Fig. 4b and 4d). Here the wing blocks up the secondary air flow from the upper fuselage part. Consequently the jets have to exhaust this air from their next vicinity, this means from the lower part of the fuselage and wing and from the external region in front of the wing.

The stagnation-point of the wing lies, according to fig. 4a, b, c, for all the three wing positions on the upper wing surface, in spite of an angle of attack of 0°, because of the jet induced downwash. For the fuselage part ahead of the wing, this means as well a feelably more negative effective local angle of attack. Above the wing, its diplacement effect causes a weak underpressure region on the upper fuselage part.

In fig. 5 the normal force distribution coefficient c_p is presented for the three wing positions and the configuration "without wing" for comparison. This kind of diagram known from [1] and [5] shows still the typical concentration of the interference effect on the next vicinity of the nozzle exits, but highly distorted by the wing influence.

In fig. 6 the configuration "without wing" has been subtracted from the others in order to show the additional influence of the wing. Its efficacy is mainly restricted to a fuselage longitudinal section of the size of the wing chord. The main effect is done by the leading edge of the wing. The rearward wing position is most effective. As mentioned above the jets produce an underpressure region below the wing, and this causes (at $\alpha = 0^\circ$) a depressive force, i.e. a negative normal force. At positive angles of attack of the fuselage and the wing, the underpressure region in question below the wing diminishes remarkably, because a secondary air flow enters from below.

The normal force coefficients are presented in fig. 7. At angles of attack $\alpha < 3^\circ$, the depression is sustained by the underpressure below the wing. At higher angles this region is filled up, until at $\alpha = 15^\circ$ even positive normal forces are produced.

3.2 Influence of the ground in presence of jets (Fig. 8 to 10)

The interference of the ground is tested with a single and with a double jet configuration. The dimensionless distance from the ground was varied within the range of $0,5 < h/D < 3,8$. The jet velocity ($M_j = 1$) and the angle of attack ($\alpha = 0^\circ$) were held constant.

In the single jet configuration (fig. 8) the depression in the fuselage region in front of the jet increases steadily when the ground distance decreases, because the influx of secondary air is blocked more and more. By this the influx velocities increase and the pressure on the lower fuselage is dropped. Behind the jet the ground interference is small and practically negligible. In the configuration with double jet (fig. 9) the influence of the ground on the normal force distribution is very different at the location of the two jets:
By addition of the rear jet the underpressure field caused by the front jet is but altered insignificantly, even in this configuration with its small value of L_j/D. The comparison with the single jet shows that here also the typical fan-shaped c_p-distribution is produced. The shape of the c_p-pattern at the rear jet fuselage region is quite another one. It is nearly symmetrical to the rear jet axis. At ground distances below $h/D = 1,8$ the c_p-values drop much more severely when the distance decreases. The fuselage tail experiences a heavy additional downward load. The reason for the behaviour is the blockage of the secondary air influx by the front jet.

At the measured ground distance of $h/D = 0,8$, the well know fountain flow pattern arises at $x/L = 0,5$ between the jets and is demonstrated by the overpressure at this point of the fuselage.

The results are shown in fig. 10 in the integrated form $c_{N\infty} = f(h/D)$. A remarkable increase of the depression is not obvious above ground distance of $h/D > 1,5$. In the configuration with double jet the decrease of the normal force coefficient is caused mainly by the rear jet.

The variation of the angle of attack demonstrates that the latter plays a subordinate part in some cases of near field interference. This is because the jets leave the fuselage initially as body-fixed volumes, which follow the α-turn, especially at high values of φ. This phenomenon is confirmed by force measurements on jet-equipped aircraft models [3].

4. Momentum theory of cross blown jets

In order to understand better the events going on in a cross blown free jet, a simple theory is developped. It will not be able to describe the complicated mixing process of the jet and the cross flow in detail, but it will give a connection between the ejector effect and the path of the jet axis. Besides it will enable to transcalculate the path of the jet and moreover the whole directional flow field from one value of φ to the other.

In general, the jet does not have the same density, temperature, and pressure as the medium into which it is blown. We restrict for simplicity the considerations to the case where the pressure, the density and the temperature at the nozzle exit are equal. An extension of the theory with respect to compressibility effects should not be too difficult. We limit further the theory within this paper to jets blown exactly perpendicular to its initial axis, because our experiments are restricted to this case.

We consider a jet volume element of the length $dz/d_j = d\zeta$ (fig. 11). From above the mass m enters this volume. On the lower side the mass m+dm leaves the volume element. The increase dm comes from the mixing of the parallel stream with the jet. The mixing causes the vertical jet velocity component to be dropped, and the horizontal component to be increased. It has to be remarked that a rather big mass of the cross flow meets the jet, but only a share of it is mixed or entrained into it. The rest flows around the jet, not unlike a displacement flow round a solid body. [4][8].

The momentum in the x-direction as well as that in the z-direction remains unaltered while the mixing process is going on. This leads to the following equations:
Momentum in the z-direction:

$$(4/1) \quad mv_z - (m + dm) \cdot (v_z + dv_z) = 0 \; ; \quad mdv_z + v_z \cdot dm = 0 \; ; \quad \frac{dm}{m} = -\frac{dv_z}{v_z} \quad \ln\frac{m}{m_o} = -\ln\frac{v_z}{v_j}$$

$$(4/2) \quad \frac{m}{m_o} = \frac{v_j}{v_z}$$

Momentum in the x-direction:

$$(4/3) \quad v_\infty dm - (m + dm) \cdot dv_x = 0 \; ; \quad \frac{dm}{m} = \frac{dv_x}{v_\infty} \; ; \quad d\ln m = \frac{dv_x}{v_\infty} \; ; \quad \ln\frac{m}{m_o} = \frac{v_x}{v_\infty}$$

$$(4/4) \quad \frac{m}{m_o} = e^{v_x/v_\infty}$$

In the equations (4/2 and 4/4) no information is yet given how m increases along the path of the jet. In spite of this a fundamental information can already be given about the shape of the path of the axis: The local inclination of the path $dx/dz = d\xi/d\zeta$ equals the ratio of the two velocity components:

$$(4/5) \quad \tan\theta = \frac{d\xi}{d\zeta} = \frac{v_x}{v_z} \quad .$$

By combination of the equations (4/2) and (4/4) follows:

$$(4/6) \quad \frac{d\xi}{d\zeta} = \frac{v_\infty}{v_j} \cdot \frac{m}{m_o} \cdot \ln\left(\frac{m}{m_o}\right)$$

or if $\phi = q_j/q_\infty \approx \left(\frac{v_j}{v_\infty}\right)^2$ is introduced:

$$(4/7) \quad \frac{d\xi}{d\zeta} = \frac{1}{\sqrt{\phi}} \cdot \frac{m}{m_o} \cdot \ln\left(\frac{m}{m_o}\right) \quad .$$

In order to integrate this differential equation, the functional dependance between m/m_o and the coordinates ξ and ζ (the so-called ejector effect) must be known.

For jets blown into still air or parallel to their axis numerous measurements are made to give an idea how this function is built. It is a pity that several parameters influence it: The Mach number, the jet turbulence and not least the size and shape of the environment. This means: The influx conditions for the secondary air flow. In a special research about this problem, GRAEFE [7] has made measurements on lifting jets of high subsonic Mach numbers flowing out of an aircraft fuselage model. Fig. 12 shows the ejector effect of two jets, one with a high, the other with a low initial turbulence. Turbulence increases mixing and thereby the ejector effect. Fig. 13 shows the ejector effect of a jet (of low turbulence) at several Mach numbers. It is obvious that the effect can be represented approximately by a straight line:

$$(4/8) \quad \frac{dm}{m_o} = k \cdot d\zeta \quad \text{or by integration:} \quad \frac{m}{m_o} = 1 + k \cdot \zeta$$

where k is a function of the turbulence, the Mach number and other parameters. The curves mostly tend to grow a bit steeper than linear, especially when the turbulence is high. When equation (4/8) is introduced into equation (4/7), we obtain:

$$(4/9) \quad \frac{d\xi}{d\zeta} = \frac{1}{\sqrt{\phi}} \cdot (1+k\zeta)\ln(1+k\zeta) \quad .$$

The integration leads to the jet path:

$$(4/10) \qquad \xi = \frac{1}{k\sqrt{\phi}} \cdot \left[\frac{(1+k\zeta)^2}{2} \cdot \ln(1+k\zeta) - \frac{(1+k\zeta)^2}{4} + \frac{1}{4} \right] .$$

This gives an idea of the path for big values of ϕ. For lower values, the representation of the measurements by this equation is poor. This is quite natural because the above relation (4/8) was taken from jets without cross flow.

We use from now the "reduced" coordinate $\zeta^{x} = \zeta/\sqrt{\phi}$ and try the relation:

$$(4/11) \qquad \frac{m}{m_0} = 1 + k_1 \cdot \zeta^{x} + k_2 \zeta^{x2} .$$

The analysis of the measurements allows the solution for our arrangement: $k_1 = 1,40$; $k_2 = 1$. This will represent all the measurements within the big range of ϕ (fig. 14). Obviously the curves of fig. 14 are of similar shape. We draw them in the form $\xi = f(\zeta^{x})$ in fig. 15 and find the result, that all curves fall into one single curve.

We add to these measured path points the theoretical curve:

$$(4/12) \qquad \xi = \int_0^{\zeta^{x}} (1 + 1,4\zeta^{x} + \zeta^{x2}) \cdot \ln(1 + 1,4\zeta^{x} + \zeta^{x2}) d\zeta^{x} .$$

by integration of the combined equ.(4/7) and (4/11). The integration was but carried out numerically.

The theoretical curve is a very good approximation and a universal relation for the whole range of ϕ (fig. 15). The relation (4/11) states that the ejector effect of a cross blown jet is much bigger than that of a jet without cross flow. It is no longer linear because of the high turbulence which is generated while the jet is bent into the curved path.

5. The far-range field of a cross blown free jet

The most striking result of section 4 is that the jet paths of jets with very different values of ϕ can be represented by one single curve. This leads to the supposition that the whole flow field around a cross blown jet can be transculculated from one value of ϕ to another one by the following rules:

a) Transform all ζ-lengths by multiplying them with $\sqrt{\phi_2/\phi_1}$.
b) Transform all flow inclinations in xz-planes and in yz-planes by multiplying them by $\sqrt{\phi_2/\phi_1}$.
c) All other lengths and inclinations remain unaltered.

We refer now to the numerous far field measurements done by GRAEFE [6]. From this research program we show only the figures 16 to 19. This program comprehends measurements of the flow direction within the whole volume around the jet up to values of ξ and ζ of 15 and $\eta = y/d_j$ up to 4,5. We confine here to the plane of symmetry ($\eta = 0$), but examine the whole range $16<\phi<290$. The figures 16 and 17 show the field of flow directions in the manner of isocline lines. In front of the jet we find an upwash region, behind and below the jet downwash regions of very inhomogeneous character, especially close behind the jet. The stream line pictures fig. 18 and 19, corresponding to the above mentioned isocline fields, show also the plane of symmetry. Among the stream lines we find the jet axis path, already treated in figures 14 and 15.

We take now the values of the flow direction θ along ζ at a constant value of $\xi = x/d_j$ respectively and plot $\tan \theta$ against ζ (fig. 20). The curves for different values of ϕ are very different in size. Now we follow the similarity rules given above and plot $\tan\theta/\sqrt{\phi}$ against $\zeta/\sqrt{\phi}$ (fig. 21a). The curves are threaded up to one curve, except close to the nozzle exit. The figures 21b and 21c show the same pattern, taken at smaller values of $x/d_j = 11$ and 8. The similarity rule holds still down to values of 4. At still smaller ξ, it becomes invalid because of the jet wake and the nearness of the fuselage, the contours of which are, of course, not included in the similarity rule for ϕ.

The similarity rule for the cross blown jet holds also for places out of the plane of symmetry and even for the upwash region in front of the jet (fig. 16 and 17). These results will be published later on.
The shape of the $\tan\theta$-curves in fig. 21a, b, c resembles the GAUSS distribution, known from the velocity distribution in a free jet without cross flow. Its maximum is found always at a value ζ^{x} which is 70 % of that of the corresponding ζ^{x} of the jet axis.

It is supposed that problems of the far field, especially downwash problems, can be treated in practice and research much more effective with the aid of the similarity rule.

6. Concluding remarks

Some recent results of an extensive research program of the DFVLR on VTOL-jet-nacelle interference are referred: The wing position influence and the ground influence in presence of lifting jets, measured by pressure distribution on the fuselage surface.

The connection between the ejector effect and the path of a cross blown jet is derived theoretically and compared with measurements.

The directional flow field of a lifting cross blown jet is determined and analysed with the aid of a similarity rule derived herein. This rule makes it convenient to convert the results at a given dynamic pressure ratio to another one.

7. References

[1] VIEHWEGER, G.

Aerodynamic Interference between Fuselage and lifting
Jets emerging from its lower part.

AGARD-CPP 135, p. 12-1 to 12-13 (Sept. 73)
(Further literature cited there)

[2] KEFFER, J.F. &
BAINES, W.D.

The round turbulent Jet in a Cross Wind.

J. Fluid, Mech. 15, p. 481-496 (1963)

[3] SCHULZ, G.   &
VIEHWEGER, G.

Sekundärkräfte an einem Senkrechtstarter beim Schwebe-
und Transitionsflug mit Berücksichtigung des Bodeneffekts.

WGL-Jahrbuch 1967, p. 152-161

[4] SCHULZ, G.

Berechnung der Druckverteilung auf einem Flugzeugrumpf
mit austretenden Hubstrahlen mittels Singularitäten.

DLR-Mitteilung 70-28 (April 1971)
(Lecture on the DGLR-Sympos. Düsseldorf, Dez. 1970)

[5] VIEHWEGER, G.

Interferenz von Triebwerksstrahlen untereinander sowie
mit dem Rumpf, dem Flügel und dem Erdboden.

DLR-Mitteilung 74-18, p. 7-1 to 7-43 (1974)
(Lecture on the DGLR-Sympos.at Porz-Wahn, 6.12.73)

[6] GRAEFE, H.J.

Vermessung des Außenfeldes quer angeblasener Strahlen.
(Darstellung des Richtungsfeldes durch Isoklinen.)

DLR-Mitteilung 74-18, p. 2-1 to 2-30 (1974)
(Lecture on the DGLR-Sympos. at Porz-Wahn, 6.12.73)

[7] GRAEFE, H.J.

Injektoreffekt bei Freistrahlen mit hoher Austritts-
machzahl.

DLR-Mitteilung 74-18, p. 5-1 to 5-16 (1974)
(Lecture on the DGLR-Sympos. at Porz-Wahn, 6.12.73)

[8] SNEL, H.

A Method for the Calculation of the Flow Field induced
by a Jet exhausting perpendicularly into a cross flow.

AGARD-CPP-143 "V/STOL Aerodynamics", lecture 18
Delft, April 1974

Exchangeable intermediate sections

Fig. 1: Scheme of fuselage model
with two lifting jet nozzles and pressure
distribution measuring device
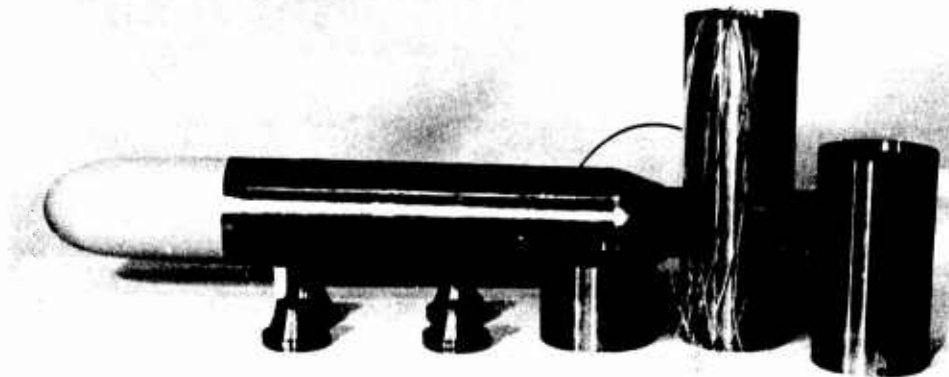
Fig. 2: Model of Fig. 1 with interchangeable nozzles
and fuselage sections
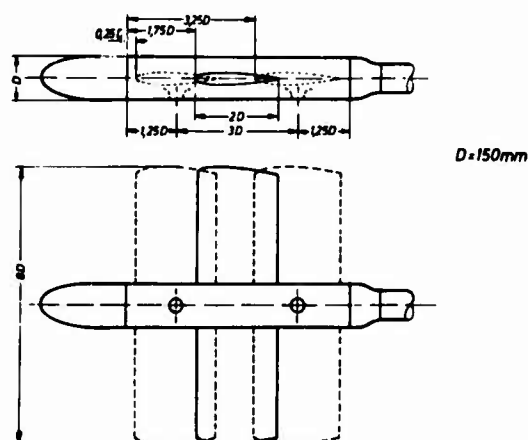
D=150mm

Fig. 3: Model configurations with wing in forward,
middle and rearward position and with two
jet nozzles . Fuselage diameter D = 150 mm
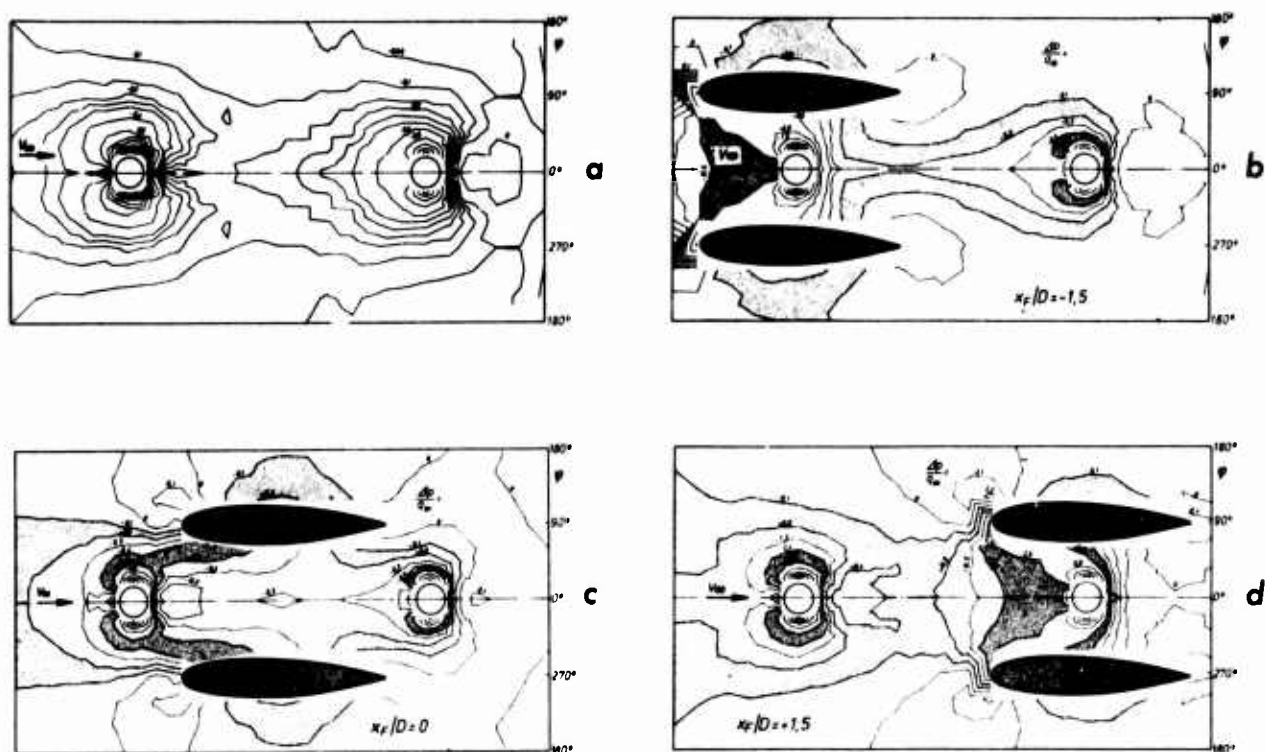
Fig. 4: Isobare-diagrams of the fuselage cylindrical
part unwrapped into a plane. (See Fig. 3)
a) without wing   c) middle wing position
b) forward wing position   d) rearward wing position
$\alpha = 0^o$; $\phi = 290$; $M_j = 1$; $L_j/D = 3$; $d_j/D = 0,3$
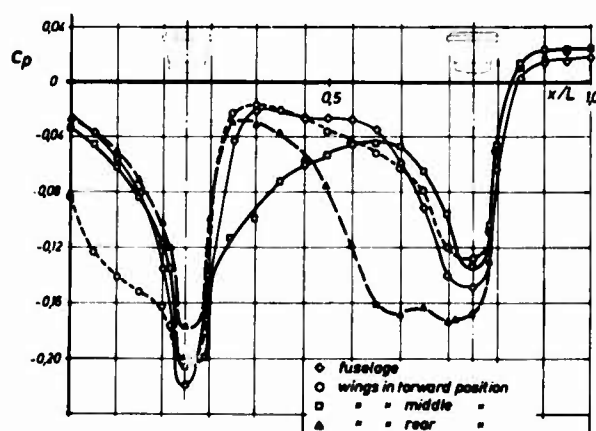
Fig. 5: Normal force distribution over the fuselage
length with three wing positions: $c_p = f(x/L)$

$\alpha = 0^o$, $M_j = 1$, $\phi = 290$, $L_j/D = 3$, $d_j/D = 0,3$
(See Fig. 3)
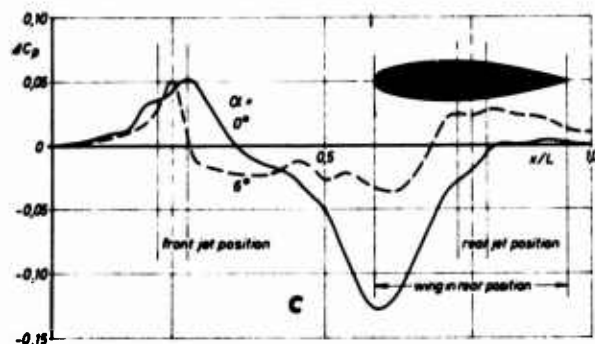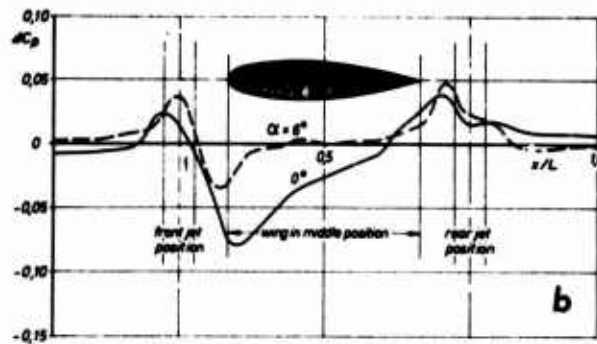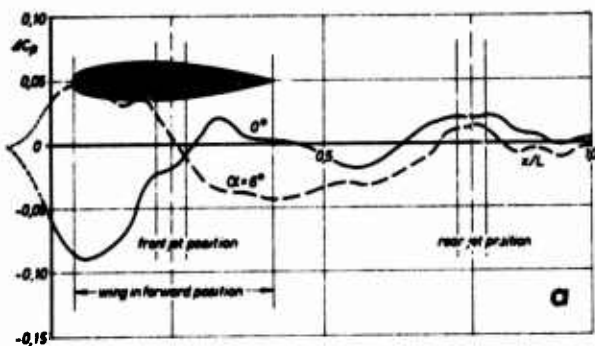
Fig. 6:

The Influence of the wing on the normal force
distribution over fuselage length

$\Delta c_p = f(x/L) = c_p(\text{with wing}) - c_p(\text{without wing})$

$M_j = 1$, $\phi = 290$, $L_j/D = 3$, $d_j/D = 0,3$

Fig. 8:

Normal force distribution over the fuselage length
Variation of fuselage distance from the ground.
One nozzle blowing. $\alpha = 0^0$, $M_j = 1$, $\phi = 290$, $d_j/D = 0,3$

Fig. 7: Normal force coefficient of the fuselage for three
wing positions as a function of the angle of attack
(Integration of fig. 5 and corresponding configurations)
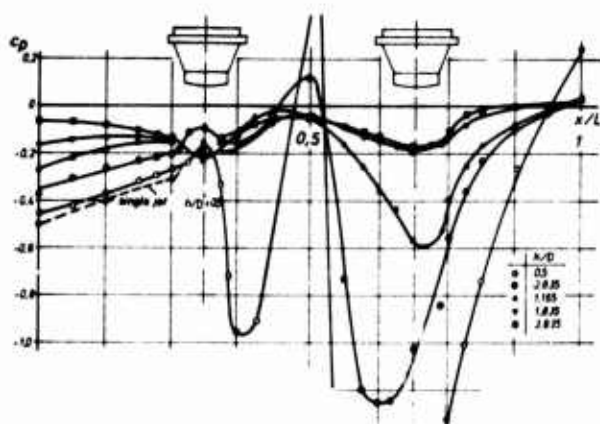
Fig. 9: Normal force distribution over the fuselage length.
Variation of fuselage distance from the ground.
Both nozzles blowing.

$\alpha = 0^o$, $M_j = 1$, $L_j/D = 1,5$, $\phi = 290$, $d_j/D = 0,3$
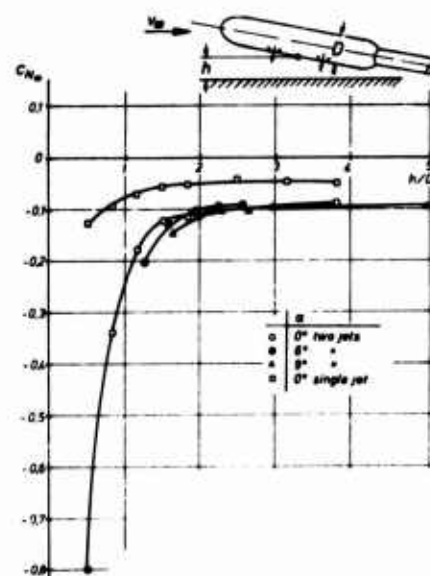
Fig. 10: Normal force coefficient ot the fuselage at variable
distance from the ground, and several angles of attack

$M_j = 1$, $\phi = 290$, $L_j/D = 1,5$, $d_j/D = 0,3$

Fig. 12: Ejector effect of two free jets with different initial
turbulence. No cross flow. $M_j = 1$.
Nozzle contraction factor: $k = 2,78$

Fig. 11: Free jet in a cross flow.
Definitions for the momentum theory.
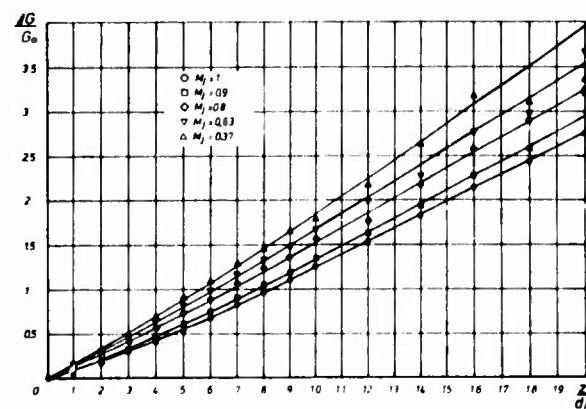
Fig. 13: Ejector effect of a free jet at different initial
Mach numbers.   No cross flow.
Nozzle contraction factor: $k = 6,5$
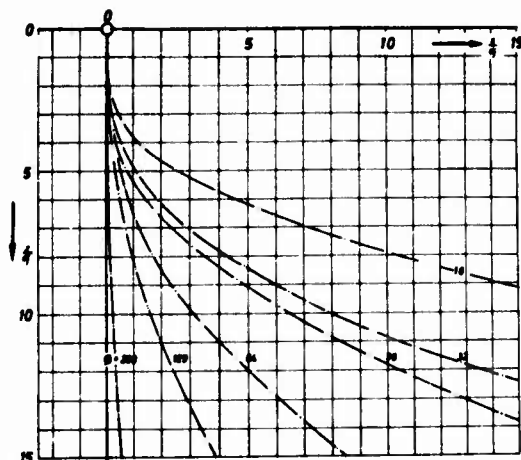
Fig. 14:

Paths of cross blown free jets with different
dynamic pressure ratio φ
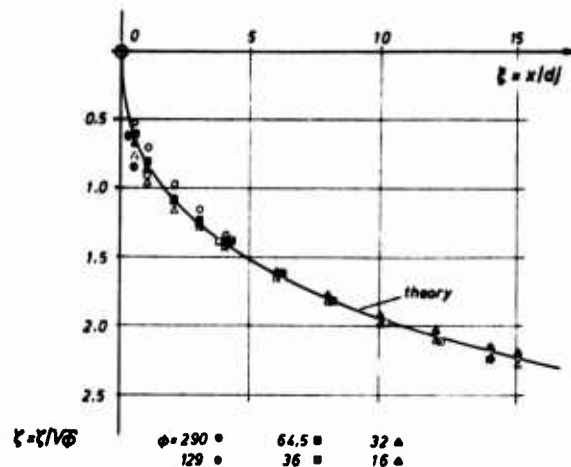
Fig. 15:

The path of cross blown jets in dimensionless
standardized coordinates:

$$x/d_j = f\left(\frac{z}{d_j} \cdot \frac{1}{\sqrt{\phi}}\right)$$

Measured paths of different pressure ratio φ
(see fig. 14) compared with theoretical result
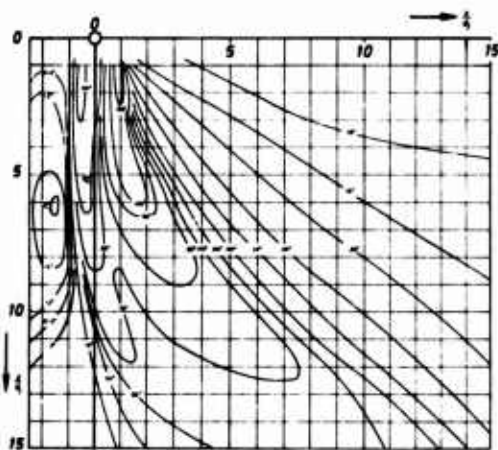
Fig. 16:
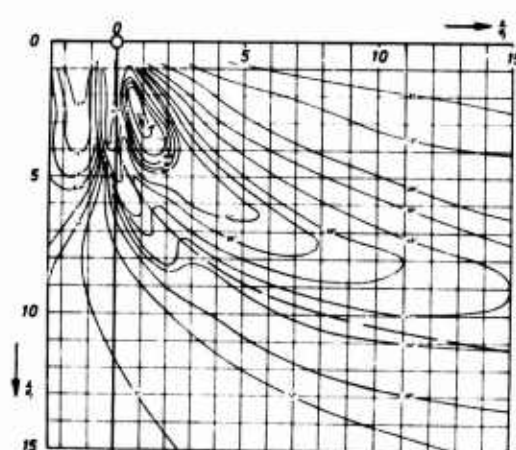
φ = 129 ; M_j = 0,68

Fig. 17:

Flow field of a cross blown free jet exhausting from a fuselage
Isocline lines in the vertical plane of symmetry
φ = 36,3 ; M_j = 1

Stream lines in the flow field of a cross blown jet
φ = 36,3 ; M_j = 1 ; d_j/D = 0,3
Calculated according to the directional field of Fig. 17
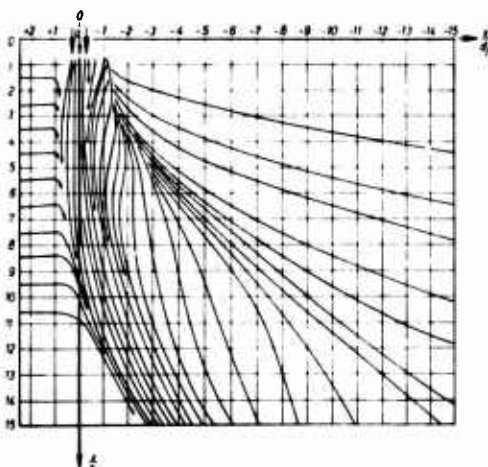
Fig. 18:

Stream lines in the flow field of a cross blown jet
φ = 129 ; M_j = 0,68 ; d_j/D = 0,3
Calculated according to the directional field of fig. 16

Fig. 19:
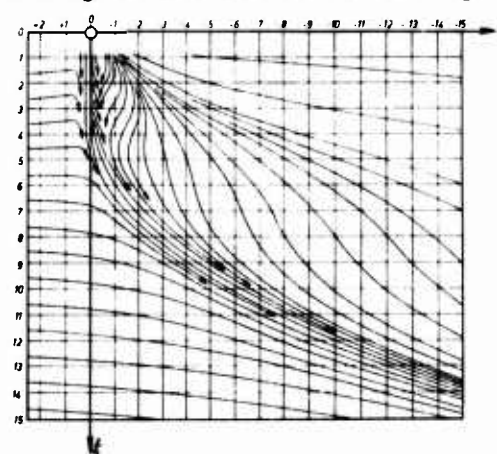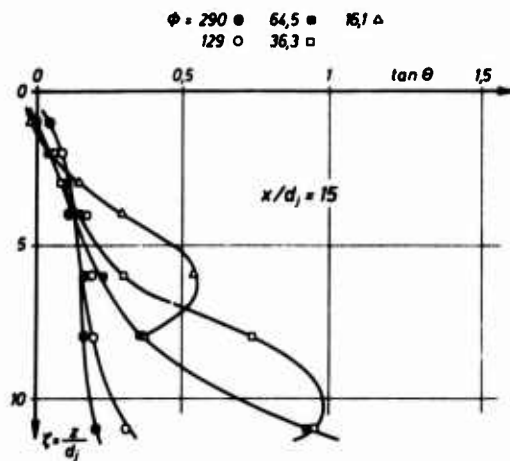
Fig. 20: Free jet in a cross flow (see fig. 16 and 17)
Flow inclination in the plane of symmetry at various
values of φ
θ = angle of inclination towards the horizontal
direction, downward +.

Fig. 21: Free jet in a cross flow (see fig. 16 and 17)
Standardized flow inclination as a function of
standardized downward coordinate
tan θ/√φ̄ = f(ζ/√φ̄)

PREDICTION OF THE OPTIMUM LOCATION OF A NACELLE SHAPED BODY ON THE WING
OF A WING-BODY CONFIGURATION BY INVISCID FLOW ANALYSIS

S.R. Ahmed[*]

SUMMARY

Some results of a basic study are presented which aims at the prediction of optimum location of a pylon-mounted engine nacelle on the wing of a wing-body configuration with the help of inviscid flow analysis. The options considered are the underwing and overwing positions of the nacelle. Varied parameters are its spanwise and chordwise location along the wing.

The criterion for the choice of the optimum location is the minimum possible induced drag of the wing-body-pylon-nacelle configuration. The theoretical calculation of the inviscid flow is done by the so-called 'panel method'. Feasibility of these predictions for subcritical flow is checked on the basis of extensive pressure and force measurements in a wind tunnel.

In the presented results, the engine nacelle is simulated by an ellipsoidal solid body neglecting the effect of intake and exhaust streams. These effects are to be considered in a subsequent investigation to be undertaken later on.

NOTATION

AR	wing aspect ratio	v	velocity component in y-direction
b	wing span	V_∞	free-stream velocity
c	wing chord	x	distance measured along chord from wing leading edge
C_p	static-pressure coefficient		
C_ℓ	section lift coefficient	x_B	distance measured along fuselage centre line from nose
C_L	lift coefficient	x_N	distance measured along nacelle centre line from nose
C_D	drag coefficient	x_P	distance measured along pylon chord from pylon leading edge
C_{DO}	drag coefficient at zero lift		
$C_{Di} = C_D - C_{DO}$	induced drag coefficient	y	distance measured along span from fuselage centre line
e_N	horizontal distance between wing leading edge and nacelle nose	z	distance measured along normal to x-y plane
$K = \dfrac{C_{Di}}{C_L^2/(\pi AR)}$	induced drag factor	y_N, z_N	lateral and vertical distance of nacelle axis from fuselage centre line
K_{wb}	induced drag factor for clean wing-body configuration	α	angle of attack
		v	kinematic viscosity
ℓ_B, ℓ_N, ℓ_P	fuselage length, nacelle length and pylon chord		

1. INTRODUCTION

The developments in the field of propulsion have enhanced greatly the variety of ways in which the jet engines can be installed on an aircraft. The wide range covered extends from completely external nacelles to the totally airframe integrated propulsion systems. In the case of externally mounted engines, there is a fair amount of freedom available as to the placement of the engine. The external drag of partly or wholly airframe integrated engines is generally small compared to that of nacelled engines attached externally to the wing or body. In the latter case additional drag results from the interference between the nacelle and wing-body.

With the size of high bypass ratio engines used for modern transport type aircraft becoming large, their relative size to other aircraft components is considerable, so that their drag as a whole and the interference drag created can have significant effect on the performance of the aircraft. In addition to the drag, the lift and stability depend strongly upon the location of the engine.

The increase in the induced drag of an aircraft is caused by the accentuated vortex formations in the combined flow field under mutual interference effects of the wing, body and nacelles changing the pressure distributions on the individual components which would otherwise exist in the absence of the engine nacelles.

This mutual superimposition of pressure fields can cause local changes in angles of attack, changes in the direction and distribution of lift and drag and creation of side forces on the engine installation. Also shedding of vorticity from trailing edges of the engine installation components such as pylon can add to the induced drag.

The change of pressure field has a corresponding influence on the development of the boundary layer, often enhancing the adverse effects leading to its separation.

Because of the complexity of the problem an analytical approach to the viscous flow field calculation around the complete configuration seems as yet out of reach. However, the use of digital computers to calculate the inviscid irrotational subcritical flow around complicated configurations has enabled accurate prediction of the flow field, so long viscous effects do not dominate in the flow situation considered. If attention is restricted to low angle of attack flight conditions such as exist a cruise, these inviscid calculations can form the basis for a parametric study to evaluate the induced drag of a wing-body-pylon-nacelle configuration.

[*] Dr.-Ing., Research Scientist, Institut für Aerodynamik der DFVLR, Braunschweig, Germany.

Most of the work done till now in this area has been experimental in nature (Refs. 1, 2, 3, 4, 5 and 6). A theoretical treatment of the interference between the wing-pylon-nacelle configuration for a transport aircraft is reported by Spangler et al. (Ref. 7). Swan and Sigalla (Ref. 8) deal at length with the problem of installing a high bypass engine on a twin jet transport aircraft, reporting extensive experimental data and some theoretical results. Some results of the calculation of pressure distribution on the wing and stores of a wing-pylon-store configuration are presented by Loeve and Slooff (Ref. 9).

2. OBJECTIVE OF THE STUDY

This paper presents some theoretical and experimental results with an aim to predict the optimum location of a pylon-mounted engine nacelle on the wing of a wing-body configuration with the help of subcritical inviscid flow analysis.

The options considered are the overwing and underwing arrangement of the nacelle; the varied parameters being its wing spanwise and chordwise location.

Although finding the best location for the engine nacelle means a compromise among many engineering disciplines, from the aerodynamic view point the important criterion for the decision can be the induced drag of the complete configuration.

Attention is restricted to the low angle of attack flight regime prevalent at cruise. The feasibility of these predictions is verified on the basis of extensive low speed pressure and force measurements.

The presented results constitute the first part of the investigation; the engine nacelle is simulated hereby as an ellipsoidal solid body and the effect of intake and exhaust streams is neglected. These effects would be considered in the second part of this study to be undertaken later on.

3. INVISCID FLOW ANALYSIS

The analytical concept of the incompressible inviscid flow around an arbitrarily shaped body consists of a linear superposition of an uniform translatory flow and a perturbation flow. The perturbation flow is required to be irrotational, so that together with the continuity equation, one obtains the Laplace equation for the determination of the perturbation potential. Boundary conditions to be imposed on the solution of the Laplace equation are the disappearance of perturbation velocity at infinite distance from the body and the flow tangency condition on the body surface.

The principle behind the solution for the Laplace equation is the well-known approach of summing sources, sinks and dipoles on the body and wake surface and employing Green's theorem to form an integral equation describing the perturbation potential. The procedure has been developed by Hess and Smith (Ref.10) and extended to the case of lifting bodies by Rubbert and Saaris (Ref. 11).

Difficulties arise in the case of lifting bodies due to two reasons. Firstly, the shape of the wake which has to be accounted for in the flow model is unknown in advance so that the problem becomes nonlinear. Secondly, in the case of arbitrarily shaped bodies, the line of origin of the wake and its subsequent shape are difficult to predict. For practical purposes recourse is taken to arbitrary prescription of the wake shape and origin.

Once these assumptions are made, the body and wake surface is approximated by quadrilateral plane panels, each carrying a constant singularity distribution. The solid surface panels carry source or sink distribution for the non-lifting case and in addition dipole or vortices distribution on the wing camber surface for the lifting case. For the wake surface panels a dipole distribution is used which is subsequently replaced by an equivalent multi-horseshoe vortex network for reasons of numerical simplicity.

The integral equation obtained for the perturbation potential as mentioned above is converted after this surface approximation to a sum of integrals each corresponding to a panel. Each of these integrals is essentially composed of the unknown singularity strength on the panel and its known geometry. Satisfying the flow tangency condition on the body or wake surface results in a linear equation connecting the unknown singularity strengths and the known body and wake geometry. In this manner, the solution to the integral equation for the perturbation potential leads to the solution of a large system of linear equations for the panel singularity strengths. Detailed description of the formulation, assumptions and experience with numerical calculations of this method are given in Refs. 12, 13 and 14. The present version of the programme accomodates just over 2000 equations on a Siemens 4004 computer. An example of this type of numerical flow model of a wing-body-pylon-nacelle configuration with an overwing nacelle as used in the present calculations is shown in Fig. 1. Wake representation has been provided for the wing and fuselage only.

The theoretical calculations comprise of the determination of pressure distributions on wing, body, nacelle and pylon, lift distributions, cross flow velocities on wing and the total lift and drag forces for various nacelle locations above and below the wing. The calculations were carried out for two wing-body combinations, namely for an unswept wing and for a swept wing. Details of the arrangement of the wing, body and nacelles are described in the next section dealing with the experimental investigations.

4. WIND TUNNEL MODELS AND TESTING PROCEDURE

The wing-body-pylon-nacelle models selected for a comparison of theory and experiment were tested in the 1.3 m dia. low speed wind tunnel of the Technical University Braunschweig. A drawing of the models giving pertinent dimensions is shown in Fig. 2. Both wings, the rectangular and the swept back were untapered and had an aspect ratio of 6, the angle of sweep for the latter being 45°. The wings had a constant, symmetrical 9 % thick RAE 101 section profile.

Both wings were alternately combined to a fuselage in the mid-wing position, the wing chord being aligned with the body axis. The fuselage of fineness ratio 0.125 had a circular cylindrical middle section with identical ellipsoidal nose and afterbody. Unswept pylons with blunt elliptical leading and trailing edge were fixed vertically on the wing and aligned with the inflow direction. No chordwise displacement or variation of pylon height could be undertaken with the present models.

Solid nacelle type bodies of fineness ratio 0.2 with a circular cylindrical middle section and blunt ellipsoidal nose and aft portions were used for the engine simulation. These could be displaced chordwise relative to the pylon.

Holes were drilled at five identical spanwise locations in both the wings for the alternative over-wing and underwing pylon-nacelle attachment.

Closely spaced static pressure orifices were arranged on the wing, body, pylon and nacelle surface. Same models were used for the pressure and force measurements. Pressure measurements were made with the model mounted on a sting-sickle fixture in the tunnel. For force measurements, the model was hung on a wire suspension from the overhead balance.

All test data were obtained for a wind speed of 40 m/s, corresponding to a Reynolds number of about $3.3 \cdot 10^5$ based on wing chord. Calibration tests indicated the probable limit of accuracy for the pressure data of $C_p = \pm 0.003$, for the lift $C_L = \pm 0.0005$ and for the drag $C_D = \pm 0.0002$. Maximum manufacturing inaccuracies in the model wing section profile amounted to about 2 % of the profile thickness. A fuller report of the experimental results is given in Ref. 15.

5. RESULTS

5.1 Surface Pressure Distribution

Fig. 3 and Fig. 4 show a representative comparison of the computed pressure distributions with experimental data on the wing and nacelle of the rectangular wing-body-pylon-nacelle configuration, as well as on the wing, pylon and body of the swept wing configuration. The case chosen is that of the innermost spanwise location of the nacelle under the wing and an angle of attack $\alpha = 6°$. It was anticipated that the interference and viscous effects for this configuration would be quite evident.

Inspite of the rather simple representation of the wing-body wake and absence of wake representation for the pylon and nacelle in the theoretical model used, the agreement between the measured and calculated surface pressures is good. The acceleration of flow below the wing in sections 1 and 2 and flow decelera-tion in nacelle sections 5 and 6 in front of the pylon nose, is predicted very well. Discrepancies occur near wing leading edge where the strong curvature changes of the profile are alleviated in the real flow by boundary layer development, and at the aft end of nacelle and pylon where the flow is affected by the thickening of boundary layer and tends to separate.

5.2 Spanwise Lift Distribution

A comparison of the measured and calculated spanwise lift distribution for the rectangular and swept wing-body configurations is given in Fig. 5 and Fig. 6. Two underwing nacelle locations on the wing span are considered, for the outer location in addition the results of the overwing arrangement are shown. It should be noted that the theoretical value of lift C_L is obtained by summation of the lift of all source panels describing the configuration. The corresponding C_L value for experimental data is obtained from force measurements. Agreement between experiment and theory is good and the distortion of spanwise lift distribution due to presence of nacelle and pylon is depicted correctly. In general due to viscous effects the experimental values of section lift lie below the theoretical values by as much as 10 %. The lift distribution for the overwing and underwing nacelle position lies almost symmetrical to the distribution for clean wing configurations.

5.3 Variation of Lift with Angle of Attack

Lift results for both configurations are presented in Fig. 7 and Fig. 8. Two spanwise locations of the nacelle with overwing and underwing attachment are investigated. Also shown in these figures are the cor-responding experimental results. The lift curves show excellent agreement up to an angle of attack of about 7° for both configurations. The lift variation in the real flow becomes non-linear above this inci-dence, as the effects of nacelle and fuselage lift, separation of flow at the trailing edge, and formation of vortices at wing-fuselage and wing-pylon-nacelle juncture become increasingly significant. These pheno-mena were confirmed by oil flow patterns observed on the model surface (see Ref. 15).

5.4 Drag Polars for Wing-Body-Pylon-Nacelle Configurations

Analytical results for the induced drag of the rectangular wing and swept wing configurations are shown in Figs. 9 and 10.

Considered options are the overwing and underwing nacelle arrangement, the parameter varied being span-wise location of the nacelle on the wing. The position of nacelle nose was kept constant at a distance of $e_N/c = 0.5$ from wing leading edge. The theoretical induced drag values are obtained by summing the pressure force components in direction of flow for all source panels comprising the configurations. To this is added the mean profile drag from wind tunnel force measurements. Taken together, Figs. 9 and 10 are proof that the drag polars can be predicted reasonably well for the low lift regime, with C_L-values ranging up to 0.3.

For the rectangular wing-body configuration, there appears to be little difference in the behaviour of overwing and underwing nacelle positions along the wing. The curves diverge somewhat for mid-span location, indicating a more favourable behaviour of the conventional underwing installation. A similar but more pro-nounced effect can be seen in Fig. 10 for the swept wing-body configuration, whereby a clear superiority of underwing installations can be observed.

Theoretical and experimental results for clean wing-body configurations are also shown in these figures. To facilitate the comparison between theory and test data, the measured zero lift drag is added to the computed values of induced drag.

The results of Figs. 9 and 10 indicate that the wing sweep, and with it the cross-flow velocity on the wing surface could be responsible for the significant difference between the rectangular wing and swept wing-body drag polars. To investigate this further, the calculated cross-flow velocity on the wing surface at three spanwise stations for both clean wing-body configurations is plotted in Fig. 11. Except in wing tip vicinity the magnitude of cross flow velocity on the upper and lower surface of the rectangular wing is much smaller than for the swept wing. The placement of a nacelle and pylon on the wing, which in effect acts as a fence to the cross-flow, has then an appreciable effect only in the case of the swept wing.

The change in induced drag can be attributed to the local distortion of wing load at nacelle location and to the change in wing tip vorticity strength. Fig. 12 illustrates the reduction of cross-flow velocity in wing-tip vicinity of the swept wing caused by an underwing nacelle at mid span compared to the conditions

for the clean wing. On the major part of the wing lower surface, a reduction of about 13 % and on the upper surface a reduction of 4 % in the cross flow velocities is noticeable. Apparently the change in wing tip vorticity strength plays a secondary role in causing the difference in behaviour of overwing and underwing nacelle placement.

In Fig. 13 the cross flow velocities on the wing sections inboard and outboard of nacelle location are presented. These are compared for the overwing and underwing nacelle placement with the conditions prevalent for the clean wing configuration. The relative change of cross flow velocity on the lower surface with the nacelle placed underwing is much higher than vice versa. At the same time, the deviation in cross flow velocity on the wing upper surface with nacelle placed underwing is less than the deviation caused on the wing lower surface. Specially the curves for the outboard station $y/(b/2) = 0.6$ demonstrate this. Although the pylon extends from the wing leading edge downstream up to about mid chord, the change in cross flow velocity is felt over the whole wing chord.

5.5 Effect of Nacelle Spanwise and Chordwise Location on Induced Drag

The final set of results presented in Figs. 14 and 15 illustrate the variation of induced drag with nacelle spanwise location. In Fig. 16 the effect of nacelle chordwise location on induced drag of the swept wing body configuration is investigated. Both, overwing and underwing nacelle positions are considered and theoretical results compared with the wind tunnel force measurements data. The induced drag factor K is referred to the factor for the clean wing-body configuration.

Although the induced drag is underestimated by the potential flow analysis the trend of its variation is predicted very well. The advantage of an underwing nacelle position is apparent for both the rectangular and swept wing-body configurations, the induced drag difference between overwing and underwing nacelle placement being very significant for the low lift regime. For higher C_L-values this difference narrows down, as seen in Figs. 14 and 15.

As noted in section 5.4, the similarity in behaviour of overwing and underwing nacelle placement on the rectangular wing-body configuration is visible in Fig. 14. The swept wing-body results in Fig. 15 show in contrast the markedly different induced drag variation for the overwing and underwing nacelle positions, whereby for the overwing position the induced drag variation with spanwise location is relatively small.

The induced drag values show a minimum for spanwise locations $y_N/(b/2)$ between 0.5 and 0.6 in Figs. 14 and 15, except for the overwing nacelle position in Fig. 15. For this case the highest induced drag values result at these spanwise locations.

Moving the underwing nacelle outboard up to mid-span position sizably reduces the induced drag of the swept wing-body configuration, whereafter the drag values again rise, this rise, however, being less steep than the preceding fall.

The placement of pylon and nacelle on the wing has a favourable influence on the induced drag, compared to the values of a clean wing-body configuration. This is obvious from the results of Figs. 14 and 15, except of course for the overwing nacelle placement on the swept wing body where the induced drag values are much higher than that for the clean wing-body configuration. Such a reduction of induced drag has been predicted theoretically by Mangler (Ref. 16). Limited wind tunnel test data was available for a chordwise location of the nacelle other than till now considered. Induced drag results for the swept wing-body configuration for two nacelle locations along wing chord are compared with theoretical results in Fig. 16. Due to the relatively high value of $C_L = 0.4$, the difference in overwing and underwing curves is small, as can be anticipated from previous results of Figs. 14 and 15. Nevertheless the basic results are the same.

6. CONCLUSIONS

The feasibility of subcritical inviscid flow analysis to predict the induced drag of wing-body-pylon-nacelle configurations has been demonstrated by comparing the results with wind tunnel test data for two models.

Attention was restricted to the low lift regime which is of interest during cruise. The agreement between calculated and measured pressure distribution, lift and drag coefficients is good.

Using the induced drag value as the criterion, the wing spanwise and chordwise location of the nacelle was varied to determine the optimum location resulting in minimum induced drag. Although the induced drag is underestimated by the theory, the theoretical results predict the variation shown by experimental results very well. Minimum drag values are obtained for about mid-span locations.

Both overwing and underwing nacelle positions were considered. The underwing positions show a more favourable induced drag behaviour for both the rectangular wing and swept wing-body configurations. This superiority is very pronounced for the swept wing-body configuration.

REFERENCES

1   Patterson, J.C., Jr.   A wind-tunnel investigation of jet-wake effect of a high-bypass
                                   engine on wing-nacelle interference drag of a subsonic transport.
                                   NASA TN D-4693, (1968).

2   Patterson, J.C., Jr. and   Jet-wake effect of a high-bypass engine on wing-nacelle interference
    Flechner, S.G.   drag of a subsonic transport airplane.
                                   NASA TN D-6067, (1970).

3   Aldridge, S.E. and   Experimental results of high bypass ratio turbofan and wing aero-
    Nye, J.L.   dynamic interference.
                                   AGARD-CP-71-71, (1971), 23, 1-9.

4   Kutney, J.T.   Airframe/propulsion system integration analysis using the propulsion
                                   simulator technique.
                                   AGARD-CP-71-71, (1971), 16, 1-19.

5   Bagley, J.A.   Some experiments on an engine installation above the wing of a swept-
                                   winged aircraft.
                                   RAE Techn. Memorandum Aero 1271, (1970).

6   Kettle, D.J.;   Exploratory tests on a forward-mounted overwing engine installation.
    Kurn, A.G. and
    Bagley, J.A.   ARC C.P. No. 1207, (1972).

7   Spangler, S.B.;   Theoretical investigation of ducted fan interference for transport-
    Mendenhall, M.R. and   type aircraft.
    Dillenius, M.F.E.   NASA SP-228, (1970), 703-716.

8   Swan, W.C. and   The problem of installing a modern high bypass engine on a twin jet
    Sigalla, A.   transport aircraft.
                                   AGARD-CP-124, (1973), 17, 1-12.

9   Loeve, W. and   On the use of 'panel methods' for predicting subsonic flow about
    Slooff, J.W.   aerofoils and aircraft configurations.
                                   NLR MP 71018 U, (1971).

10 Hess, J.L. and   Calculation of non-lifting potential flow about arbitrary three-
    Smith, A.M.O.   dimensional bodies.
                                   Douglas Aircraft Report Nr. E.S. 40622, (1962).

11 Rubbert, P.E. and   A general three-dimensional potential-flow method applied to V/STOL
    Saaris, C.R.   aerodynamics.
                                   SAE Air Transportation Meeting, New York, (1968).

12 Kraus, W.   Das MBB-Unterschall-Panel-Verfahren.
                                   Teil II: Das auftriebsbehaftete Verdrängungsproblem in kompressibler
                                   Strömung.
                                   Messerschmitt-Bölkow-Blohm GmbH
                                   MBB-Bericht Nr. UFE 633-70, (1970).

13 Labrujere, Th.E.;   An approximate method for the calculation of the pressure distribution
    Loeve, W. and   on wing-body combinations at subcritical speeds.
    Slooff, J.W.   AGARD-CP-71-71, (1971), 11, 1-15.

14 Ahmed, S.R.   Berechnung des reibungslosen Strömungsfeldes von dreidimensionalen
                                   auftriebsbehafteten Tragflügeln, Rümpfen und Flügel-Rumpf-Kombina-
                                   tionen nach dem Panel-Verfahren.
                                   DLR-FB 73-102, (1973).

15 Ahmed, S.R.   Druckverteilungs- und Kraftmessungen an zwei Flügel-Rumpf-Anordnungen
                                   mit Außenlasten und Flügelendbehältern.
                                   DFVLR-IB 151-74/8, (1974).

16 Mangler, W.   Die Auftriebsverteilung am Tragflügel mit Endscheiben.
                                   Luftfahrtforschung, (1937), 14, 564-569.

Surface source - panel arrangement
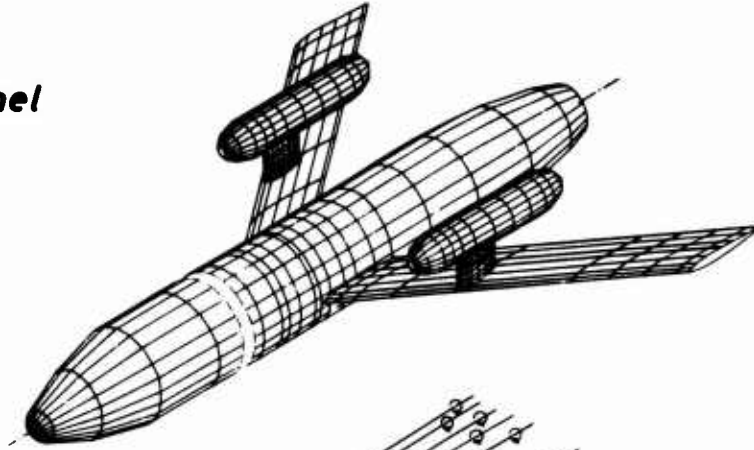
Internal multi - horseshoe vortex arrangement
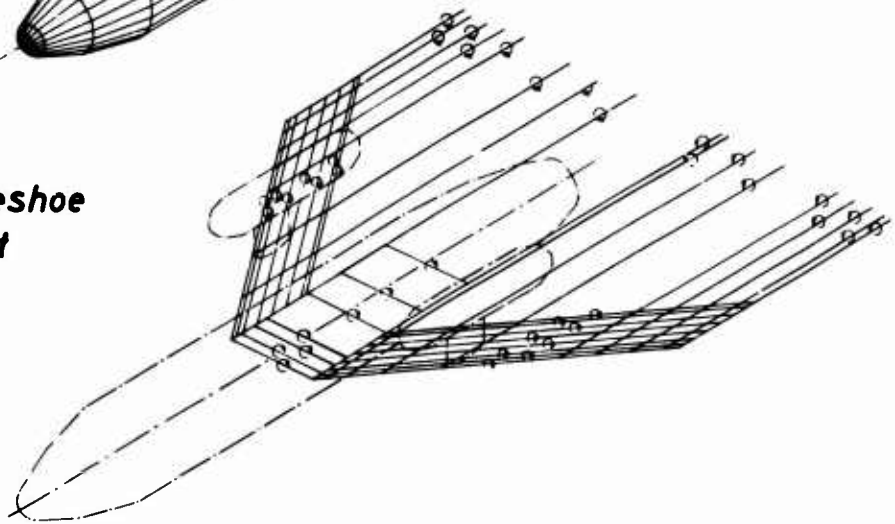
Fig. 1 : Numerical model of wing - body configuration with overwing nacelle

Rectangular wing - body

416·25

⌀125

250   500   210

125

Swept wing - body

Ellipse (axis ratio 1:4)

45°

416·25

125

375
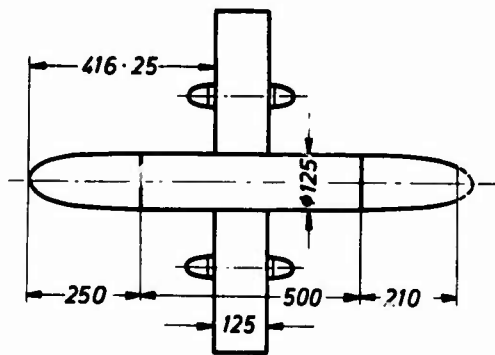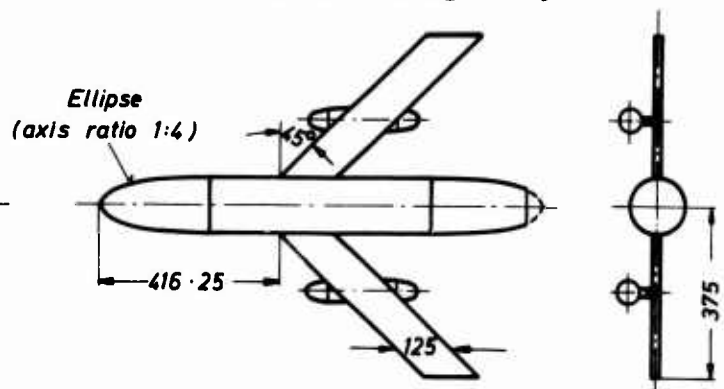
Pylon cross - section

Ellipse (axis ratio 1:4)

20   20

60

10
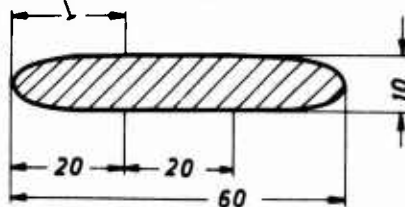
Nacelle - Pylon mounting on wing

Ellipse (axis ratio 1:2)

60

50

50   150

250

60

All dimensions in millimeters
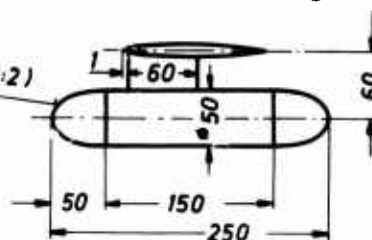
Fig. 2 : Modell configurations

Fig.4 Surface pressure distribution on swept wing – body configuration
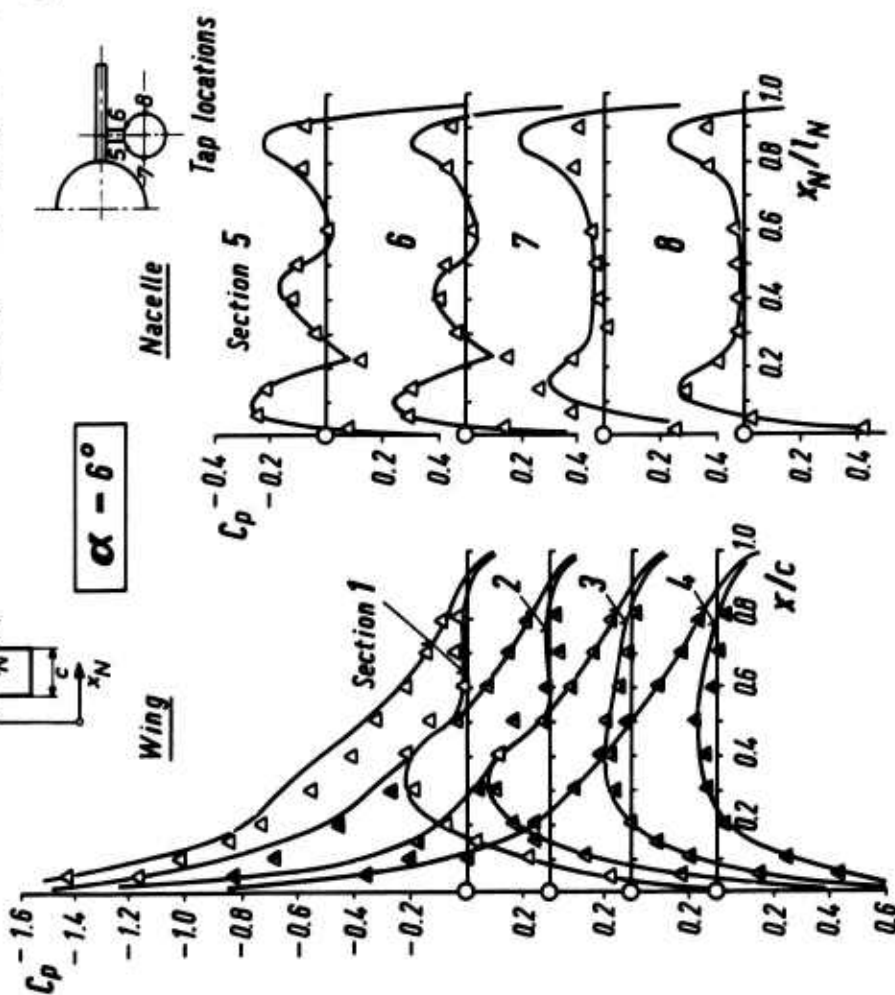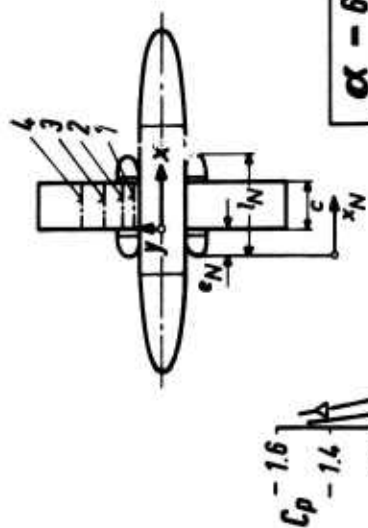
Fig. 3 Surface pressure distribution on rectangular wing – body configuration
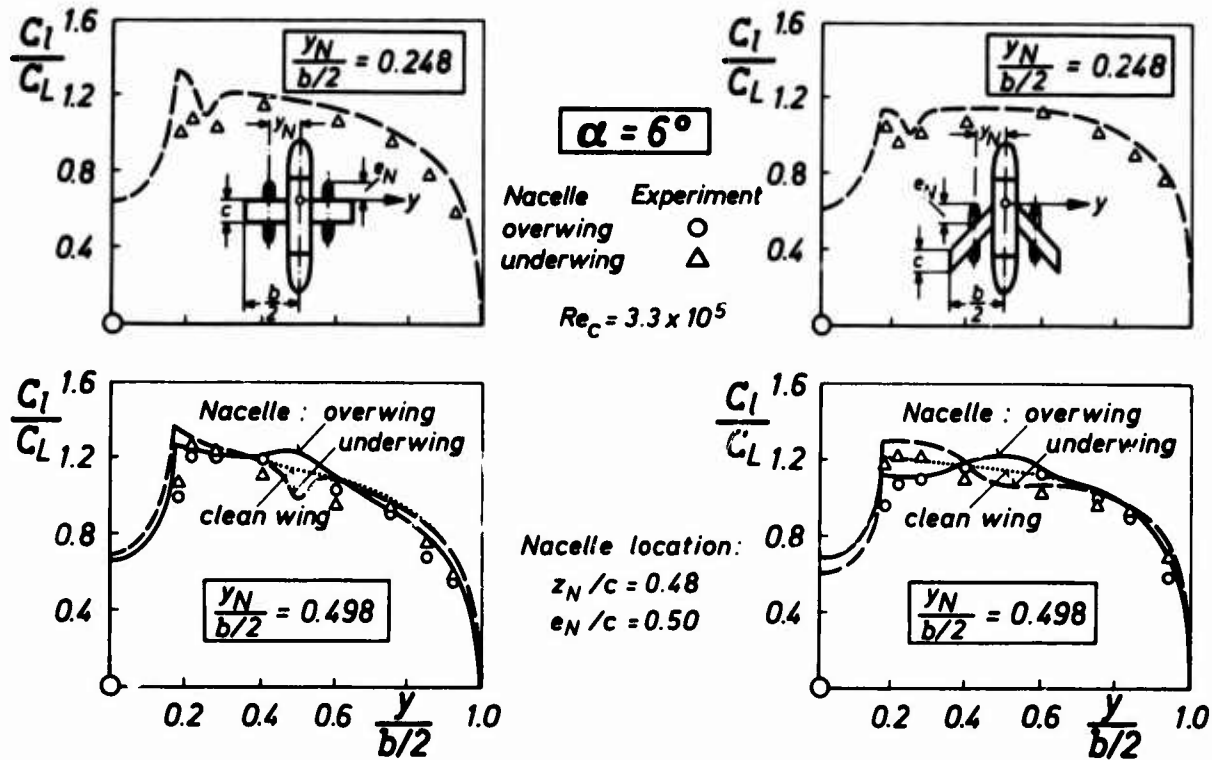
Fig. 5 : Spanwise lift distribution for rectangular wing-body configuration

Fig. 6 : Spanwise lift distribution for swept wing-body configuration

$\alpha = 6°$

Nacelle   Experiment
overwing   O
underwing   △

$Re_c = 3.3 \times 10^5$

Nacelle location:
$z_N/c = 0.48$
$e_N/c = 0.50$
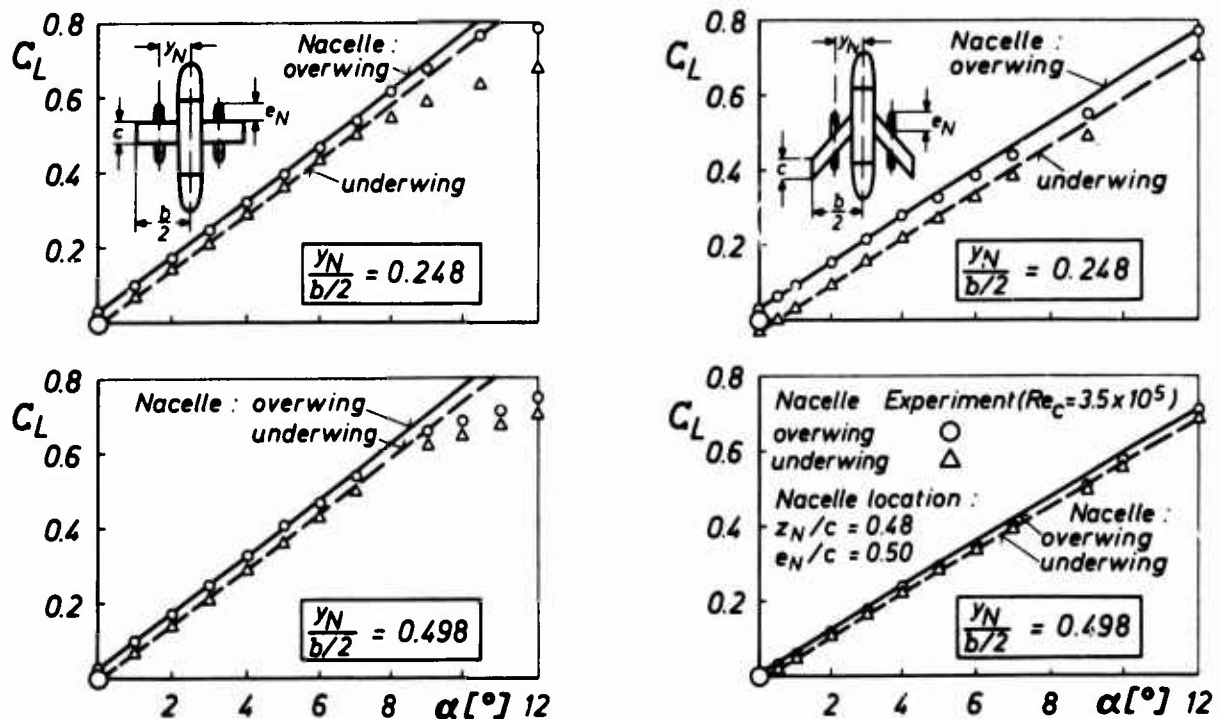
Fig. 7 : Variation of lift with angle of attack (rectangular wing-body configuration)

Fig. 8 : Variation of lift with angle of attack (swept wing-body configuration)
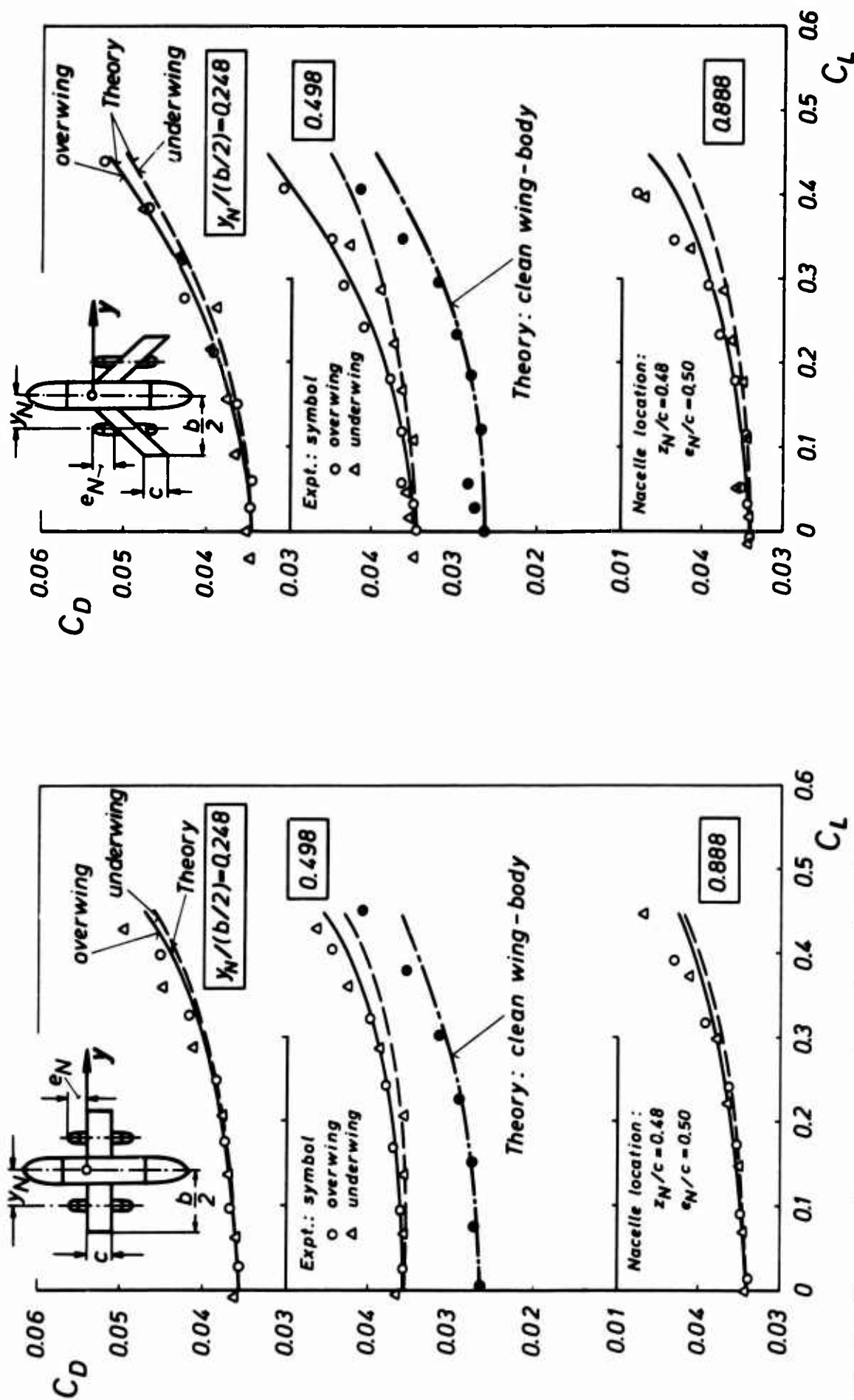
Fig.9 Drag polars for rectangular wing-body configuration with nacelles
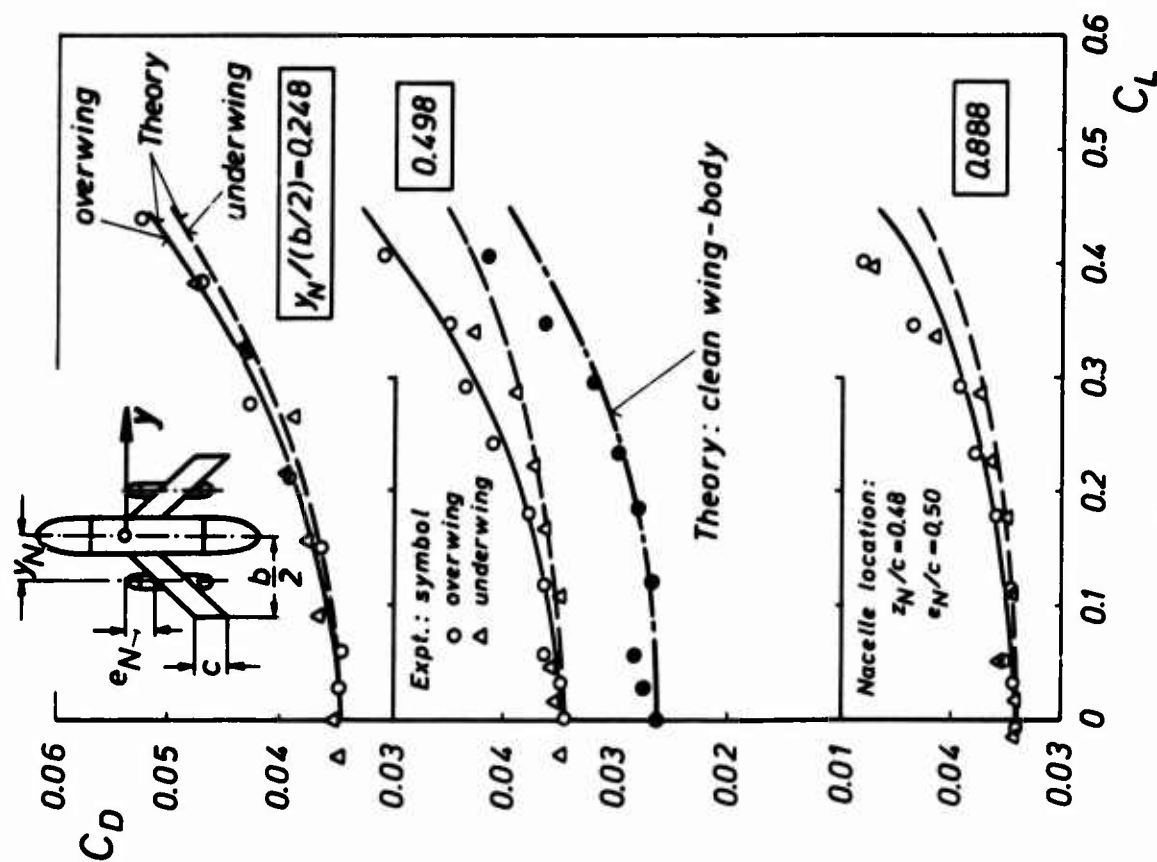
Fig.10 Drag polars for swept wing-body configuration with nacelles
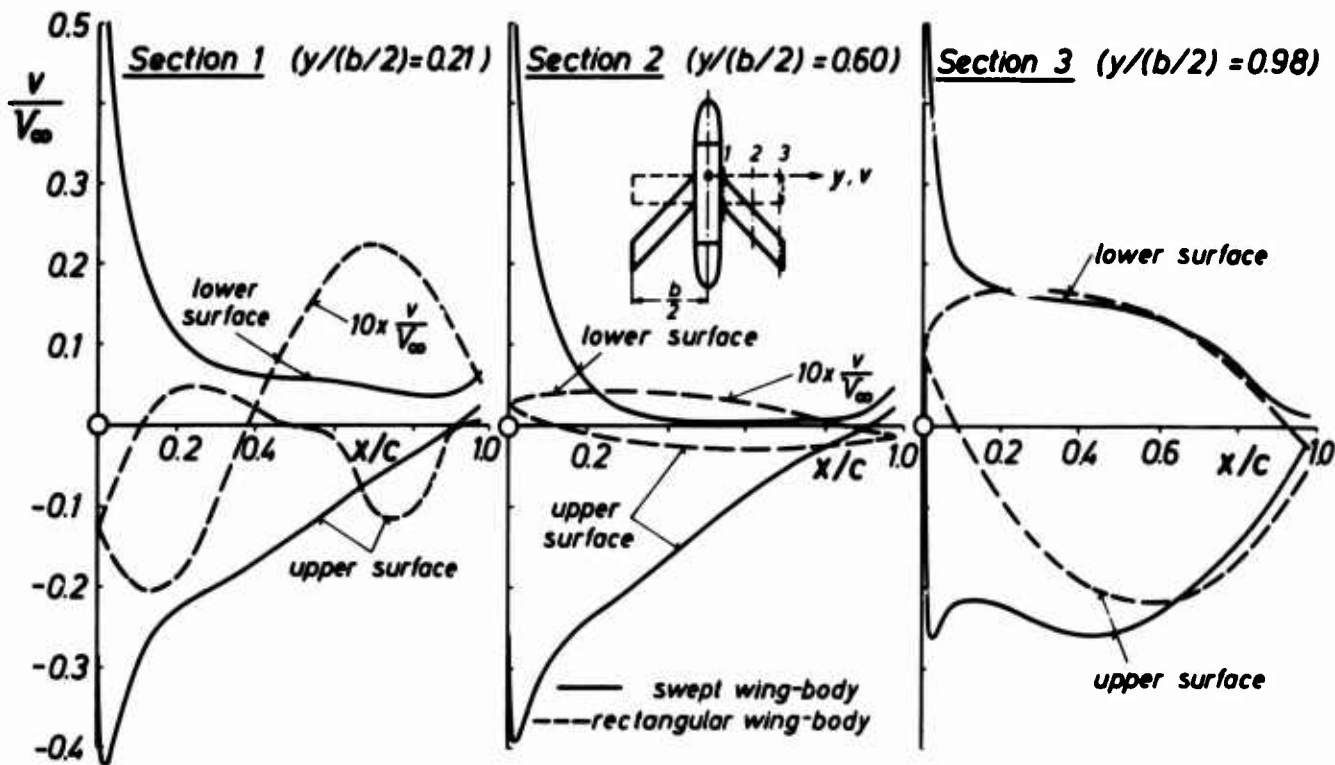
Fig. 11: Cross-flow velocity on wing surface for clean rectangular wing and swept wing-body configurations
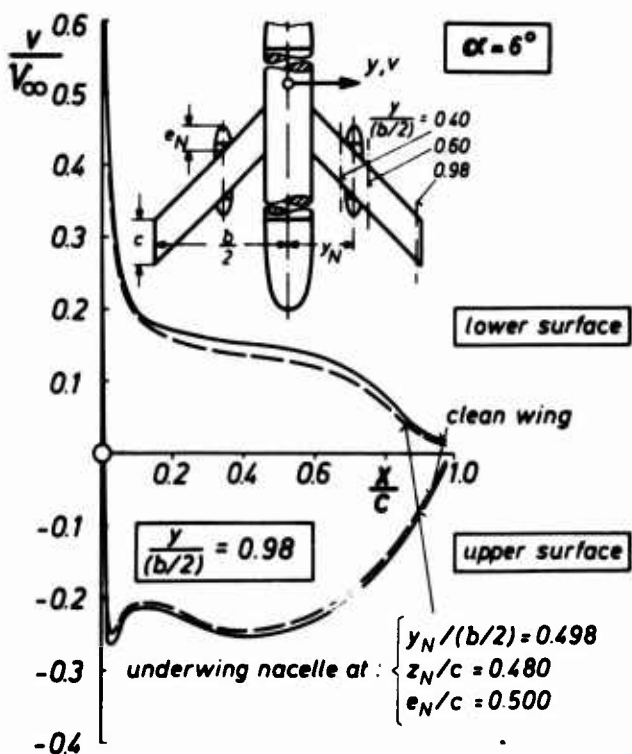
Fig. 12: Effect of underwing nacelle on cross-flow velocity in wing-tip vicinity
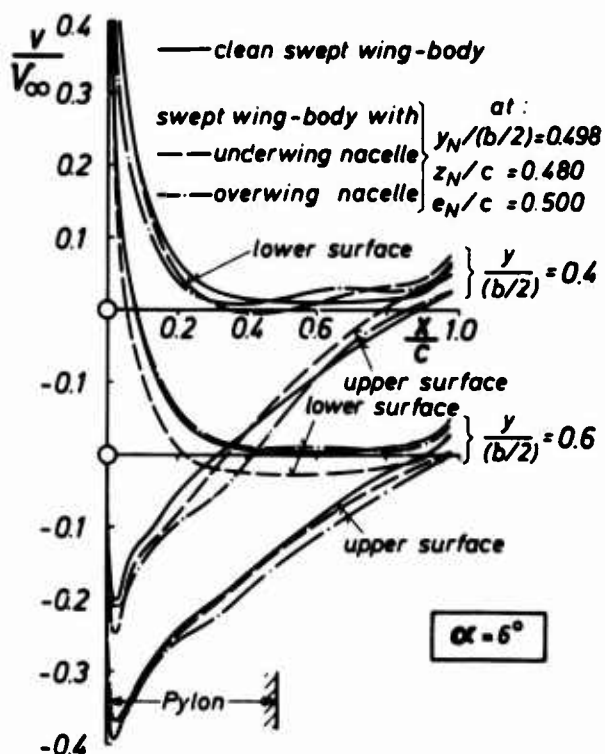
Fig. 13: Cross-flow velocity on wing sections inboard and outboard of nacelle location
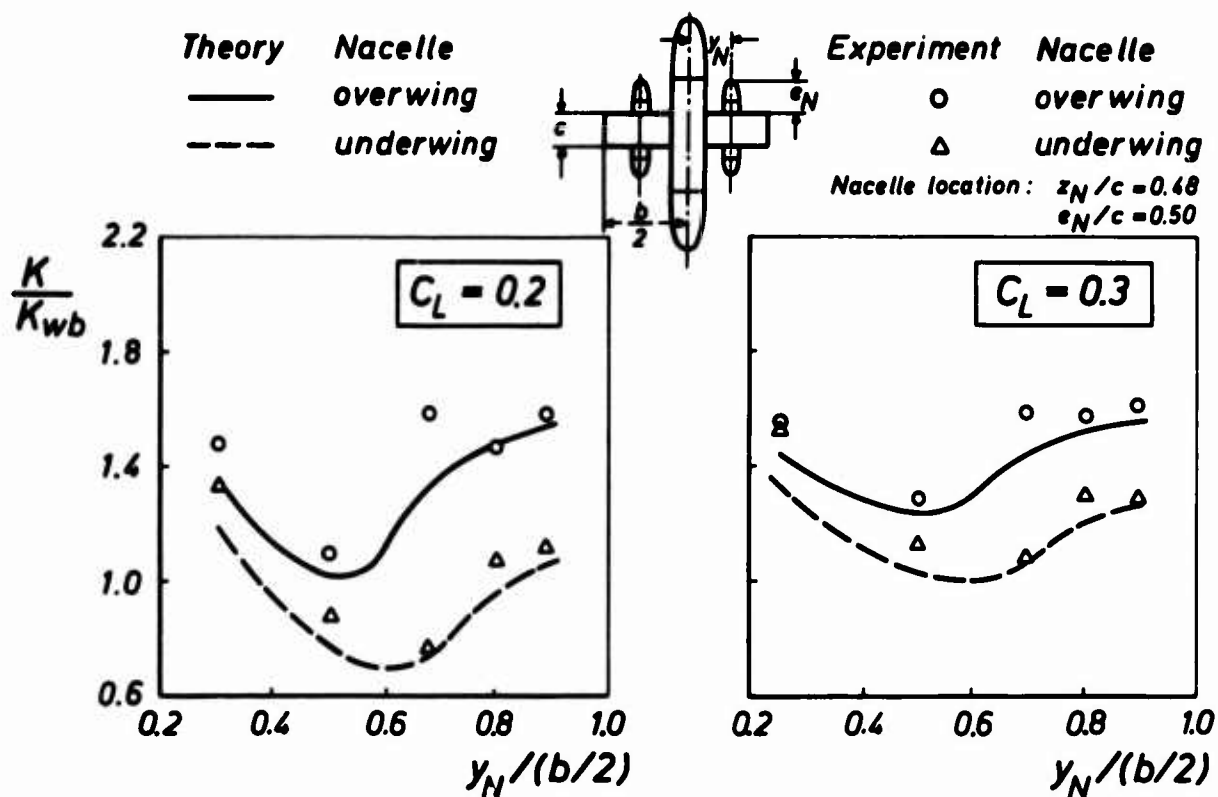
Fig.14 Effect of nacelle spanwise location on induced drag
(rectangular wing-body configuration)
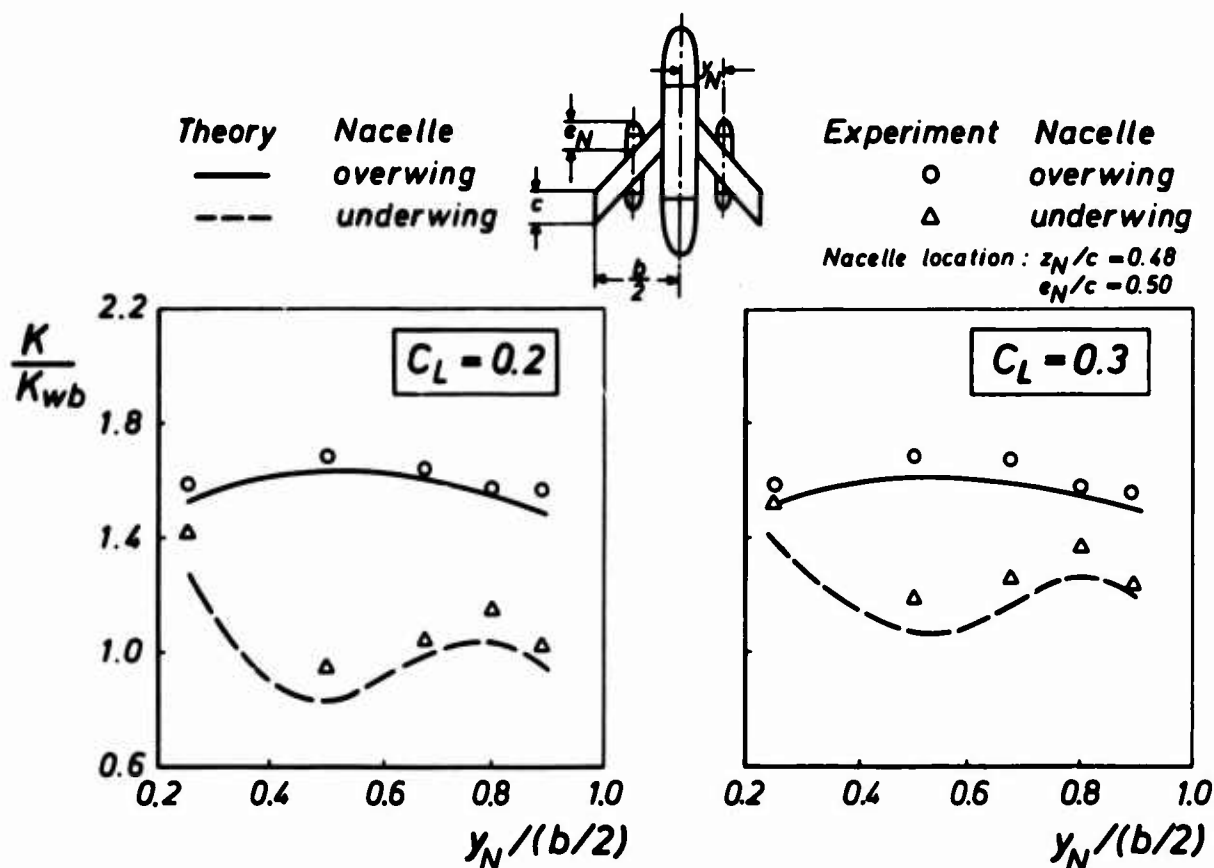
Fig.15 Effect of Nacelle spanwise location on induced drag
(swept wing-body configuration)
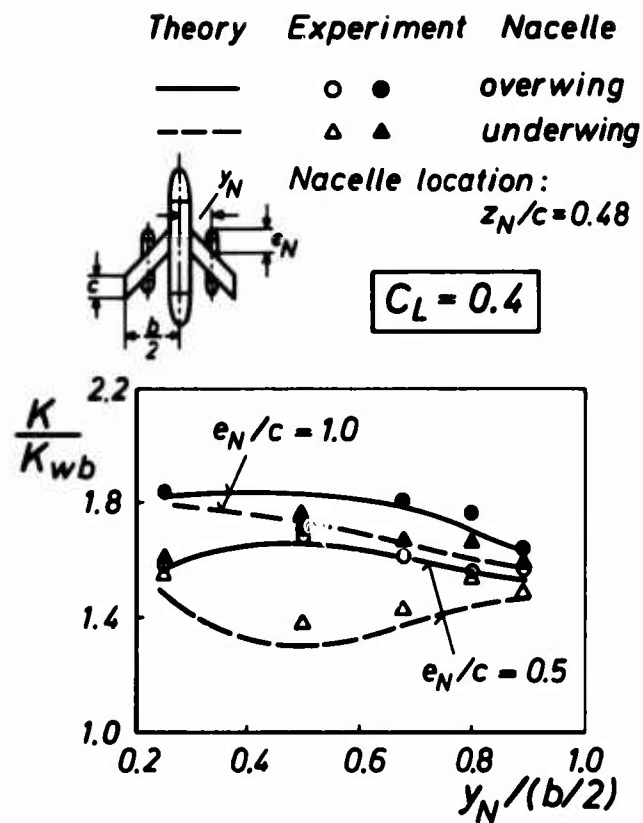
Fig.16 Effect of nacelle chordwise location on induced drag

AIRFRAME – ENGINE INTERACTION FOR ENGINE CONFIGURATIONS MOUNTED ABOVE THE WING
PART I: INTERFERENCE BETWEEN WING AND INTAKE/JET

by

G. Krenz *

Vereinigte Flugtechnische Werke-Fokker GmbH
2800 Bremen 1, Hünefeldstraße 1-5, Germany

SUMMARY

Advanced technology of airframe-propulsion-integration confirm the feasibility for over-the-wing engine installation of transport aircraft. In this paper basic areas of interaction between wing and engine flows are described together with specific investigations associated with fore and aft engine locations.

For the aft location, W/T results are presented with flight test data including stall and high speed flight characteristics. Further, low speed tunnel investigations of aircraft configurations with engine intakes well in front of wing L.E., result in increasing lift as well as improving the lift/drag ratio during T/O and landing.

A theoretical approach was conducted, using the well established panel method, and comparison of theoretical and experimental pressure distributions proved well for spacing of one nozzle diameter between the wing and nozzle-jet sheet.

1. INTRODUCTION

The development of high bypass-ratio engines for Transport-Aircraft has produced some new problems, both for the aircraft designer and the engine manufacturer, because of the interference of airframe and engine aerodynamics.

The main features are the interaction between wing and engine flow and the influence of ground proximity on the engine intakes.

During the last years VFW-Fokker has performed research and flight testing work on new aircraft configurations aiming to improve performance as well as reduce noise levels. This was done by evaluating and comparing under wing with above the wing mounted configurations.

This paper deals with propulsion-wing interference for engines mounted above the wing, as a problem area both for high and low speed performance and characteristics for future transport aircraft.

2. BASIC AREAS OF INTERACTION

Fig. 1 summarises the specific problem areas of a whole field of configurations with engines above the wing. Advanced technological development (in fig. 1 from left to right) represented by exemplary aircraft, is classified according to following engine locations:

- o intake nearby wing TE
- o engine located above rear-wing surface
- o intake well in front of wing LE

W/T tests have been carried out at VFW-Fokker for the right hand configuration, but no aircraft project is known to exist at the present moment.

The specific interaction problems (refer fig. 1 left hand side) are:

- o engine reaction on wing flow separation during stall and due to sideslip resulting from intake pressure distortions
- o influence of engine flow on stall propagation and on high speed flight characteristics, caused by throttling effects.

In addition to the above there arises for the second configuration type (fig. 1 center) interference effects caused by:

- o engine-pylon-displacement and pylon-fence effects on wing flow pattern during the stall as well as in the high speed flight regime

Concerning the forward engine location instead of intake interference, consideration has to be made for:

- o jet influence and pod-displacement on wing aerodynamics
- o change of nozzle pressure and engine flow characteristics caused by wing flow, especially for wing mounted engines

Considering that the specific interaction problems of the first configurations to be included in

---

* Dipl.-Ing.
Head of Project Aerodynamics

the second (see fig. 1), this paper outlines two categories of interactions:

       o wing-<u>intake</u> - pod displacement - pylon fence interference
          for layout with the intake behind wing leading edge
       o wing-<u>jet</u>-pod displacement and jet suction interference for
          arrangements with intake well in front of wing leading edge.

The engine located on wing upper surface was excluded in this treatment, being considered by other authors and published in [1] . VFW-Fokker W/T-results on this engine location are summarised in [2] .

3. WINDTUNNEL MODEL TESTS

A detailed description of windtunnel work, including engine simulation technique etc, will be presented by Mr. Ewald in the second part of this paper.

Therefore only some basic information on that matter will be given at this stage.

3.1 LOW SPEED TESTS

Fig. 2 shows two specific models in the test section, where on the left side a through-flow-model with grids for simulating the influence of power setting and pod-pylon-displacement, and on the right hand side a model with engine jet simulation can be seen. The models, which represent the mentioned categories of wing-propulsion interaction in the VFW-Fokker low speed tunnel at Bremen, were tested at about 2 Million Re-Number and up to about 1,7 pressure at engine nozzle exit. In addition to 3-component tests in longitudinal motion, pressure measurements on the wing upper and lower surface were conducted, to clarify single components of interference, such as pod-displacement, jet suction, intake flow throttling etc. Engine height and depth positioning to wing as well as jet performance were tested for flapped and unflapped wings.

3.2 HIGH SPEED TESTS

Through-flow-models, shown on the left side of fig. 2, were also used for high speed W/T-tests at ARA-Bedford and NLR-Amsterdam, covering the influence of engine-pylon-displacement and power setting on wing pressure distribution, lift, drag, pitching and rolling moments, including extreme conditions such as both engine throttled or one engine out. The model geometry for all tests, both at high speeds and low speeds, was the VFW-Fokker 614 in an earlier stage of development as published in [3].

4. REARWARD ENGINE LOCATIONS

4.1 WINDTUNNEL RESULTS

Basic results refering to the above mentioned main topics of the more rearward engine location are presented in the next two pictures. Fig. 3 contains the engine intake flow as influenced by the wing flow, when the angle of attack is increased beyond that for maximum lift. Intake distortion factor DC_{60} - as used by RR and defined in [4] - is plotted against angle of incidence for a free flying engine compared with the engine mounted above the wing. The picture is qualitatively correct for pressure losses in the intake plane, marked by the dotted line.

It can be seen, that the presence of the wing eliminates the strong influence of velocity ratio on free flying pod, showing that for this configuration with hardly any distortion at wing stall,there is a rapid increase and we may conclude, thereafter for the complete velocity range between take off/landing and cruise. It is obvious, that the progress of DC_{60} during the stall depends on stall propagation on the wing, leading edge separation resulting in higher distortion gradients compared to trailing edge separation.

Fig. 4 shows engine influence on wing aerodynamics. The pressure coefficient cp_u on the upper wing surface beneath the pod is plotted for two rearward engine locations.

Additional tests with pylon show that the general tendency in the curves remain, becoming more pronounced in the rear wing area caused by pylon displacement. For the given value of pod diameter and distance, velocity ratio and lift coefficient, representing a high speed case, the pressure decreases in front of the pod and increases on the rear wing part. This change in pressure distribution does not affect the aerodynamic derivatives sensitively as long as compressiblity can be neglected.

Section lift coefficients remain unchanged and thereby spanwise lift distribution as well as induced drag.

Contrary to expectations, there was no measured increase in zero lift drag caused by additional suction forces on rear wing. The only noticable change was higher nose down pitching moments, being rather sensitively influenced by compressibility effects. Thus for higher Mach numbers we touch the problem of speed instability caused by tuck under effects, to be described in flight test results in chapter 4.2.

Concerning the low speed features of engine influence on wing aerodynamics we found that wing pressure distribution being more insensitive than shown in fig. 4, mainly due to velocity ratio, which is $1 \lesssim v^i/v_\infty \lesssim 2$ for take-off and landing.

Thus from about 3/4 pod diameter distance between wing and engine surface any pressure change in front of the engine arising from intake suction effects on the wing surface, can be neglected, whilst underneath the engine the flow is accelerated due to pod/pylon displacement.

From these results we can derive that main low speed characteristics such as stall propagation, maximum lift and lift/drag ratio remain unchanged by engine interference.

This is no longer true, however, for configurations with close to the wing engine locations described in chapter 5.

4.2 FLIGHT TEST RESULTS

The experimental data, described in the last figures, were used as basic information during the development of the VFW 614. They were encouraging for this new aircraft design with engines mounted above the upper wing surface leaving some questions unanswered for flight testing. Besides the more general aerodynamic problems of Re- and Mach-number correction, other aereas of uncertainty were:

- o high speed test technique of propulsion simulation, coupling true intake flow conditions but wrong jet efflux
- o reaction of new developedengines on intake distortions in heavy cross winds with stall induced wing flow separation.

The aircraft - shown in fig. 5 - is the world's first jet liner with engines mounted on the upper side of the wing. Among the aspects in low and high speed particulary connected with that engine position, are:

- o wing stall aerodynamics in correlation with intake flow distortion and the resulting engine reaction
- o high speed characteristics in longitudinal and lateral motion due to engine throttl or single engine out, respectively

4.2.1 WING STALL AERODYNAMICS

The expected advantages of engine position were verified (fig. 3), the most important open question of engine response on unsteady wing or intake lip separation effects remained. Nevertheless the original VFW 614 wing design philosophy at stalling speeds had to be considered for determining uncertain engine reaction so that,

- o the steady distortion factor given by the engine manufacturer may not be exceeded during stall
- o a time limitation for tolerated overstepping angles of attack beyond maximum lift
- o the intake flow should not influence the stall flow pattern to avoid power setting interference

Combining the above with classical characteristics and performance requirements such as

- o high C_{Lmax} at take-off and landing
- o low drag for take-off flap settings
- o increased nose down pitching moments at maximum lift
  and
- o no roll-off tendency and full lateral control

led to a wing design with separation starting at the trailing edge of the inner wing panel, extending forward and sideward but excluding the wing leading edge part in front of the engine.

In fig. 6 a sketch of the recommended flow pattern is compared with 1:5 scale model test results at $2,5 \cdot 10^6$ Reynolds number. The agreement between both patterns was satisfactory enough to start aircraft flight testing without expecting severe engine trouble.

During the stall tests, in addition to the normal test equipment tuft studies were recorded by a video system as well as by a tail camera. The evaluation of all information sources indicated, that

- o the flow separation started as predicted
- o the separation boundary however spreaded more intensive in spanwise rather than in chordwise direction, thus
- o giving reduced longitudinal stability and
- o increased rolling moments due to both flow break down and reduced aileron effectiveness

In addition power-on and power-off stalls demonstrated, that

- o the engines were less sensitive to unsteady wing separation effects, even at combination of angles of attack well beyond maximum lift with side slip angles in the order of 30°

This encouraging engine experience could be used to improve the stall propagation considerably by a modification of the outboard wing's leading edge together with a 6" stall promotor in the wing-body fairing. These short-time, low-cost changes resulted in favorable stall characteristics and high maximum lift for all flap settings.

In fig. 7 a typical stall history is illustrated.
From on-line-data of the flight:

        o angle of attack
        o indicated airspeed
        o elevator control forces
        o aileron control forces

were plotted against flight time T (sec) on the right hand side of the figure. At three time steps, marked by the dotted lines, wing flow development is taken by tuft photos, shown on the left side of the figure.

The propagation of flow break down can be followed above to below. At flight time 2871 separation starts near the fuselage at an indicated angle of incidence of about 14 degrees. Some 0,5 degree later the separation spread over the wing panel between fuselage and engine position, further at an angle of 18° the wing is stalled up to about 0,4 semispan at the leading edge and 0,6 at the trailing edge. The complete stall was enforced by continuously increasing elevator pull force, and during the whole manoeuvre the bank angle was kept in limits of $\pm$ 5° by about 15 kp aileron force at maximum.

To reach an overall understanding of the wing stall behaviour fig. 8 gives the propagation of flow break down for cruise, take-off and landing configuration, which were plotted from tuft photos during flight test. For all flap settings a rather similar flow developement was achieved, resulting in favorable performances and stall characteristics. This can be checked from the lift data on the right hand side, obtained from flight performance test evulation for 3 flap settings and 1-g-stall. Applying FAA-stall procedure about six percent of minimum speed are saved thus gaining more than ten percent of C_{Lmax} in comparision to the plotted C_L- values.

4.2.2 HIGH SPEED FLIGHT CHARACTERISTICS

Engine simulation technique, representing the true intake flow only, proved inadequate to predict the aircraft characteristics accurately. However, acceptable high speed flight characteristics could be derived from these W/T-results, even in the most critical cases of both engines throttled back in longitudinal motion and one engine cut for lateral characteristics.

Adding the jet effects by theoretical estimations, we found this further decreased the engine influence, however no values were stated, because of lack of the method's accuracy.

A Mach trim compensator was developed as stand-by during the flight test period, to overcome any unforseen trouble during the 614 development, but proved to be unnecessary after high speed flight evaluation.

To judge the power influence on pitching and rolling moments, elevator and aileron deflection after engine throttling was considered, which were needed to keep the aircraft in straight and wings level flight.

Fig. 9 shows the result of flight tests in comparison with windtunnel data. On the left side elevator angle is shown to push the aircraft to higher Mach-number. The curves are derived from W/T-tests for engine power on and engine in idle.

These two curves show that throttling the engines would increase nose down pitching moments which can be compensated by additional elevator deflection. This nose down pitching moment increases with Mach-number effects, thus leading to speed instability at about 0,6 Mach-number for the idle case.

During flight testing the pilots did not find any engine influence on longitudinal motion, and the symbols-representing flight test results from power on and idle operation-confirm this. On the right hand side aileron deflection is given to keep wings level in the case of one engine cut. Again flight test evaluation produced much less engine interaction as should be expected from W/T-results. The pilots noticed no influence of one engine shut down on the lateral characteristics.

Thus we concluded that W/T-tests overestimated engine influence on high speed flight characteristics due to false jet simulation using the technique of through flow models.

5.   FOREWARD ENGINE LOCATION

5.1   WINDTUNNEL RESULTS

To extend the aerodynamic information of reward engine positions, a windtunnel program committed to foreward engine location was conducted. As influence of intake flow is small, only the jets and the engine body were simulated. Jet pressure was varied within the limits of $1 \lesssim Pt/P\infty \lesssim 1,7$ based on CFM 56 values for take-off and landing. With nozzle center as reference, the engine wing position was $0,1 \leq x/c \leq 0,4$ behind the leading edge in wing chord direction and $1,1 \lesssim Z/Dj \lesssim 1,85$ in height above the wing reference chord at 0,35 semispan position.

The choice of these engine locations were to:

      o increase lift and lift/drag ratio by jet interference with the wing upper surface flow

      o avoid skin buffeting and high level noise arising from jets acting immediately on the structure

      o decrease interference drag for high speed flight, compared to on wing engine location

Fig. 10 shows the influence of propulsion on lift and drag for an upper and lower engine position. The latter was tested at rather the same chord and height distances to the wing as the upper was to:

      o establish comparisons on equivalent low and high engine locations
        and

      o enable low wing aircraft with a short gear to facilitate a closer wing-engine mounting, providing for step by step increases in engine diameter.

Fig. 10 shows remarkable improvements in lift and drag can be achieved with the upper engine position compared to the lower one. Lift is increased for zero incidence as well as for maximum angle of attack, zero lift drag is lowered as well as lift/drag ratio is improved.

Corresponding data for 40 deg. flap setting are presented in the next fig. 11, where again improvements in lift and drag - rather of the same size as with flaps up - can be observed. The values are true for 7,5 velocity ratio v_j/v_∞, and for an engine position $x/c = 0,1$ and $z/D_j = \pm 1,2$ respectively, which is a rather close to the wing engine location.

From fig. 12, however, we can derive, that increasing x/c and z/D_j produce smaller gains in lift. The same is true for drag, though not shown in the picture. Fig. 12 furthermore shows, that improvement in lift is also reduced with increasing velocity ratio. Thus the questions arise, what may really be saved in aircraft performance for instance at take-off and landing, corresponding to improvements in lift and lift/drag ratio. Considering modern by-pass-engines, such as CFM 56, with aircraft of rather conservative aerodynamic performance of wing and flap system, one can gain about 10% in maximum lift for take-off and landing, and about 20% in lift/drag ratio for take-off flap settings. This profit - based on configurations without propulsion interference - is about 5% and 10% in lift and lift/drag respectively even in the case of one engine out take-off performance of a twin engine aircraft.

Pressure distributions over the wing surface are shown in fig. 13, clarifying the differences in lift and drag for upper and lower wing engine positions. The results are valid for the wing section just underneath the engine at 8 deg. of model incidence and velocity ratio $v_j/v_\infty = 7,5$. For clearer illustration of the dominant effects at 8 deg. angle of attack, a rather high velocity ratio with a close to the wing positions was chosen, showing:

      o jet induced suction forces at the upper or lower wing surface, corresponding to engine position producing increased or reduced lift, respectively and

      o the suction forces are concentrated either in the wing nose for upper engine location, or in the rear part of the wing for the lower position - thereby decreasing or increasing drag.

The next two pictures fig. 14 and fig. 15 show the influence of velocity ratio in the range of $1 \leq v_j/v_\infty \leq 7,5$ for the lower and upper engine position respectively. Suction effects diminish with velocity ratios to values below the clean wing case; this could result from wake effects behind the pod for $v_j = v_\infty$, the jet efflux velocity being lower than increased acceleration between wing and jet for 8 deg. incidence case.

5.2 THEORETICAL APPROACH

The experimental results were approached theoretically by using the well established panel method [5]. In addition to the wing fuselage flow, the pod- and jet- part of the engine were represented by surface distributions of singularities. In a first step, jet suction effects were approximated as shown in fig. 16 for incompressible stationary jet flow emerging into still air [6]. Jet spreading as well as jet massflow and entrainment velocity normal to the jet boundary are presented. Jet surface was introduced into the program, beginning at the jet exit and cutting at two wing chord lengths behind the wing trailing edge. Sink strength at panels equidistant from the exit was taken constant and of normal velocity value as shown in fig. 16. In total there were used 260 panels for the wing, 160 for the fuselage and 80 for the pod displacement, whereas the jet was represented by 180 panels.

Calculations were performed for the whole range of measured engine distances and velocity ratios, whereby one example is shown in fig. 17. There is good agreement between calculation and measurement in this case of rather far engine distance and this calculation method proved well for other wing sections at this engine position, with the exception of close to the wing engine location, obviously due to the simple theoretical model introduced, which did not include wing interaction on the jets, resulting in jet boundary deformation as well as modified jet suction effects. It was concluded, that these effects of interference are to be taken into account for distances less than one nozzle diameter between wing and body-jet-surface, by comparison of theoretical and experimental pressure distributions.

6. CONCLUSION

Some aerodynamic results, concerning the interaction of wing-propulsion-flow were presented. Comparisions of windtunnel and flight test data for rearward engine locations have shown, that:

  o specific interference problems for the airframe which can be simulated in the wind-tunnel by rather simple test technique, for example by through flow models, must be finally solved during flight tests
  o engine intake distortions in extreme flight conditions, such as stall, can be measured rather accurately, but engine reaction on it is normally unknown until flight testing, mainly in the case of fluctuating intake pressure on high bypass ratio engines
  o engine shielding by the wing allows good aerodynamic performance and characteristics both at low and high speeds, but cruise Mach-number is limited by increasing interference of engine with wing suction side.

Engine locations with the intake well in front of the wings leading edge were measured in a low speed tunnel, the dominant results being:

  o maximum lift as well as lift/drag ratio are increased by jet interaction with the wing flow for rather close to the wing engine locations
  o intake-wing-interference is of secundary order for these locations

Theoretical estimations show good agreement with experimental pressure distributions, using a quite simpel theoretical model embracing jet boundary as well as to jet suction effects for configurations with one nozzle diameter between wing and engine surface. Close to the wing engine positions need improved theory both concerning jet boundary and jet suction effects.

REFERENCES

[1] Walter C. Swan   The problem of installing a modern high bypass engine on a twin jet
     Armand Sigalla   transport aircraft.
                           AGARD-CP-124

[2]   Gegenseitige Beeinflussung von Zellen- und Triebwerkströmung.
                           VFW-Fokker Ex 1-473

[3] Stüssel, R.   Jet bus VFW 614, Flugrevue Heft 5/6 1968

[4] Göthert, R.   Inlet measurements on a V/TOL aircraft model.
                           AGARD-CP No. 22

[5] J.L. Hess   Calculation of non-lifting potential flow about arbitary three dimensional
     A.M.O. Smith   bodies.
                           Douglas Aircraft Corp. Rep. E.S. 40622 (1962)

[6]   Zur Abschätzung strahlinduzierter Kräfte und Momente.
                           VFW-Fokker Ex 1-467

Advanced Airframe - Propulsion Development →

Turbojet	High Bypass	Turbojet	Bypass	High Bypass	High Bypass
Hr B 320	Europlane	not investigated	VFW 614	Boeing 7x7	VFW-Fokker W/T Study

Interaction:
Wing ⟶ Intake distortion
         Stall
         Sideslip
Intake ⟶ Wing
         Stallcharacter.
         H/S Character.

dto as left

Pod/Pylon ⟶ Wing
         Stall
         H/S Character.

Interaction:
Jet/Pod ⟶ Wing
         Stallcharacter.
         H/S Characte.
         Performance
Wing ⟶ Engine
         Nozzle Pressure
         Characteristics

VFW-FOKKER — **WING ENGINE INTERACTION** — Fig.1 EF.60/74

CONTINUOUS FLOW MODEL   JET SIMULATION MODEL

VFW-FOKKER — SPECIFIC W/T-MODELS — Fig. 2 EF. 61/74

26-8

Legend:
— · — Free flying Engine
——— Engine above Wing ($\delta_f = 0°$)
– – – Engine above Wing ($\delta_f = 40°$)

Graph axes: $-D_{c_{60}}$ (vertical, 0 to 0,5), α [°] (horizontal, 0 to 20), $\alpha_{max.}$, V_∞/V_i, v_i, P_{t_i}

VFW-FOKKER | INTAKE FLOW DISTORTION | Fig. 3 EF. 62/74

$X_i/C = 0,5$

$X_i/C = 0,75$

C_{Pu} axes from -1,2 to 0; X/C axis 0 to 1,0

Geometry : $h/C \approx 0,4$
            $D/C \approx 0,4$

Jet : $V_i/V_\infty \approx 0,4$
       $V_j/V_\infty \approx 1,2$
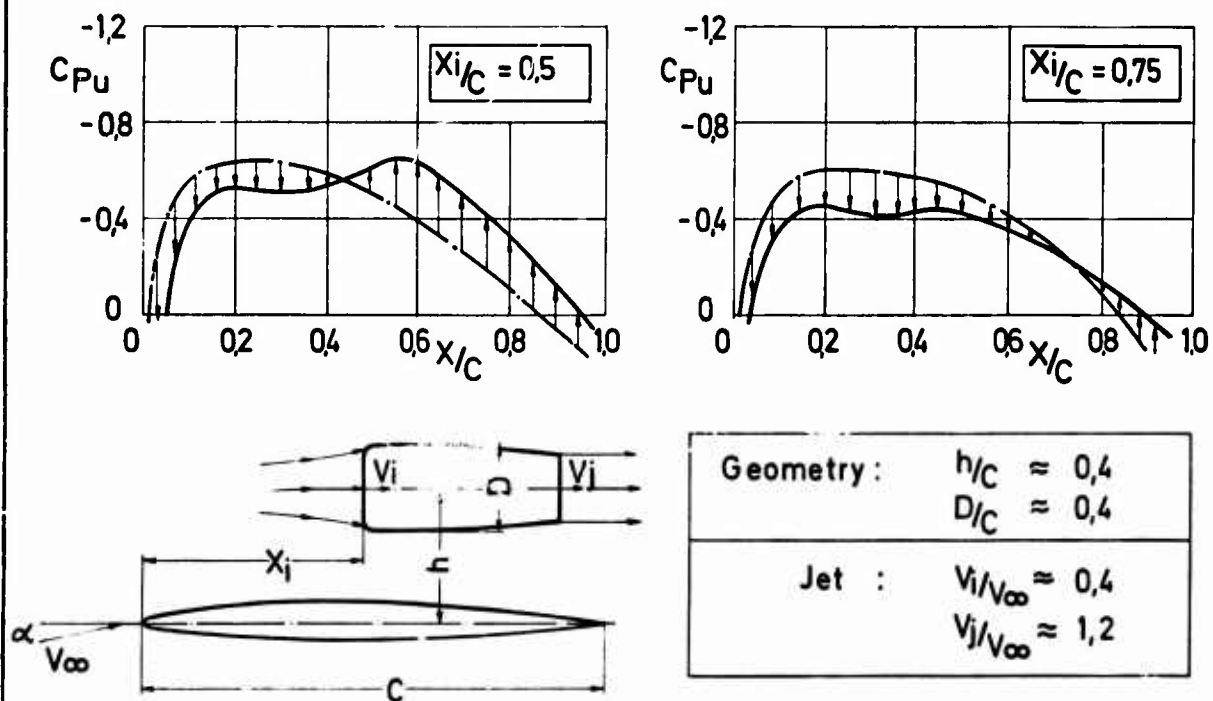
VFW-FOKKER | PRESSURE DISTRIBUTION ON WING UPPER SURFACE | Fig. 4 EF.63/74

VFW-FOKKER | **VFW-614 LANDING** | **Fig. 5** / **EF 64/74**

DESIGN GOAL

W/T TEST 2.5·10^6 RE
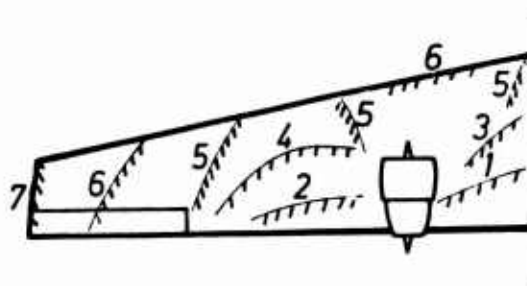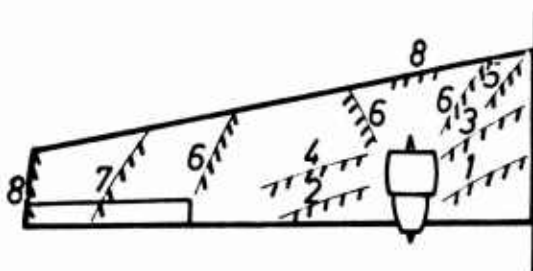
α− RANGE	1	3	5	6	7	8
	0°-12°	13°-14°	15°-16°	17°-18°	18°-20°	>20°

VFW-FOKKER | STALL PROPAGATION DESIGN / MODEL TEST | FIG. 6 / EF 65/74

TITLE: **STALL - TEST**

OP.NO.: *2154*	ITEM-NO.	TEST-NO.
WEIGHT: *17800* KP	C.G.: *26.0* %MAC	FLAPS: *16 DEG*
GEAR: *EXT*	ALTITUDE: *15000* FT	SPEED: KTS(M) IAS

REMARKS: STALL NR 3
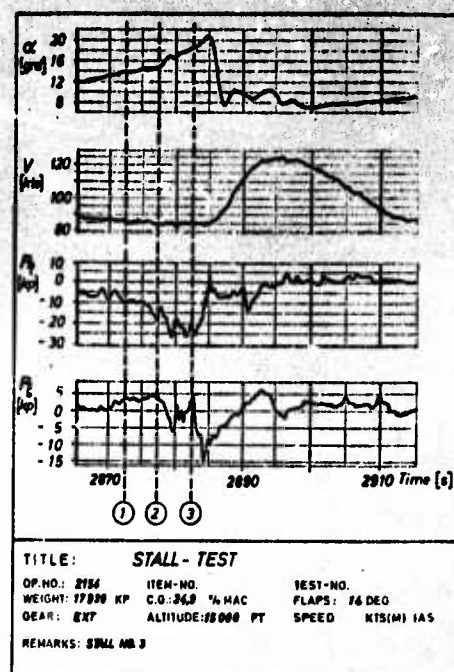
VFW-FOKKER

STALL PROPAGATION FLIGHT TEST

FIG. 7

EF 66/74

FLIGHT TEST OP. NR 2154

PERFORMANCE TEST

Cruise, $\delta_f = 0°$

Take-off, $\delta_f = 14°$

Landing, $\delta_f = 40°$

$\delta_f = 40°$

GUARANTEED VALUES

$14°$

$0°$

OP. NR 2203 ×
2209 □
2211 ○
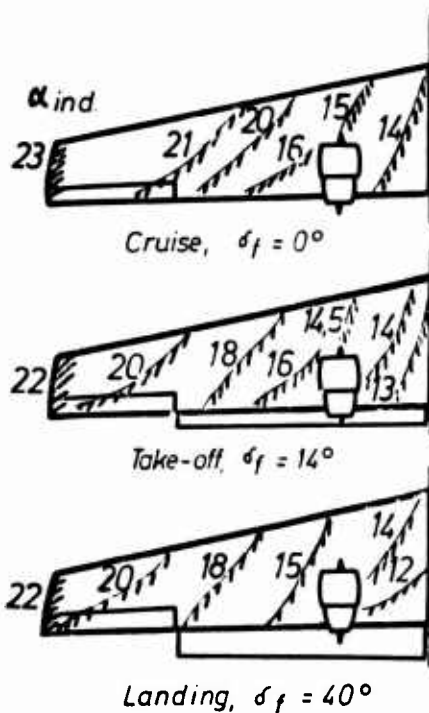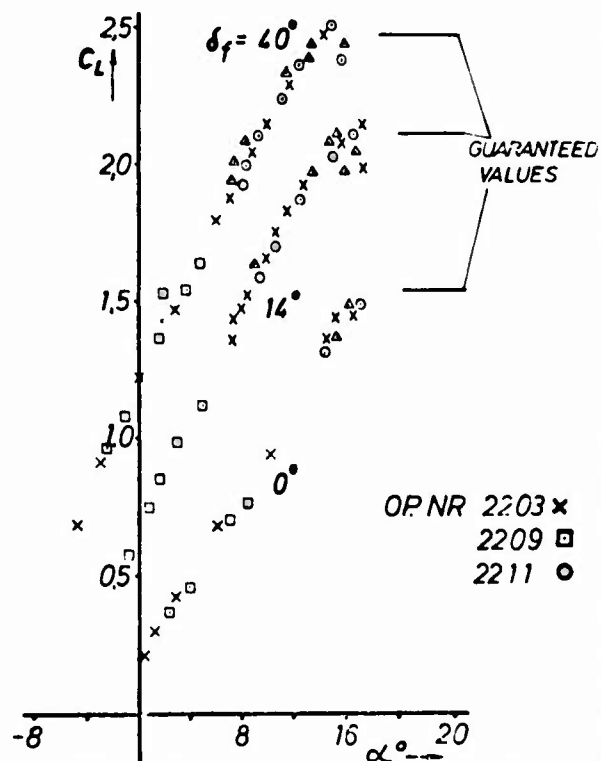
VFW-FOKKER

STALL PROPAGATION/ LIFT

FIG. 8

EF 67/74

W/T-TEST	Flight Test
—— Power on	⊙OP-No 2216
--- I d l e	×OP-No 2208

One Engine
shut down

$\delta_e°$

CRUISE

$\delta_a°$

W/T-Test

Flight-Test

CRUISE
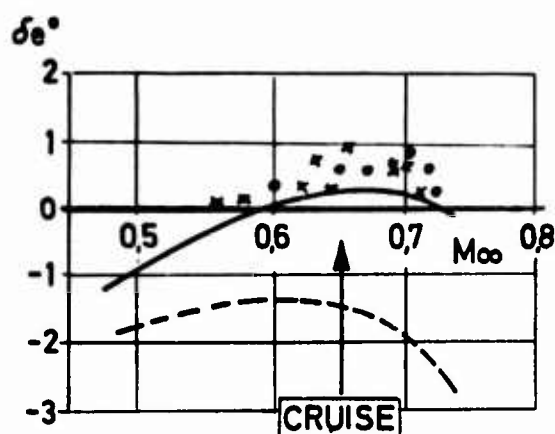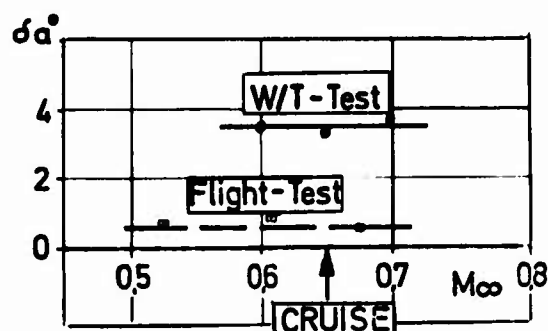
| **VFW-FOKKER** | ELEVATOR AND AILERON DEFLECTION WITH ENGINE INFLUENCE | Fig. 9 E.F.68/74 |

C_L

C_L

A

B

C

A

B

C

$\alpha°$

C_D

(A)

(B)

(C)

$X/C = 0,1$
$Z/D_j = ±1,2$
$V_j/V_∞ = 7,5$
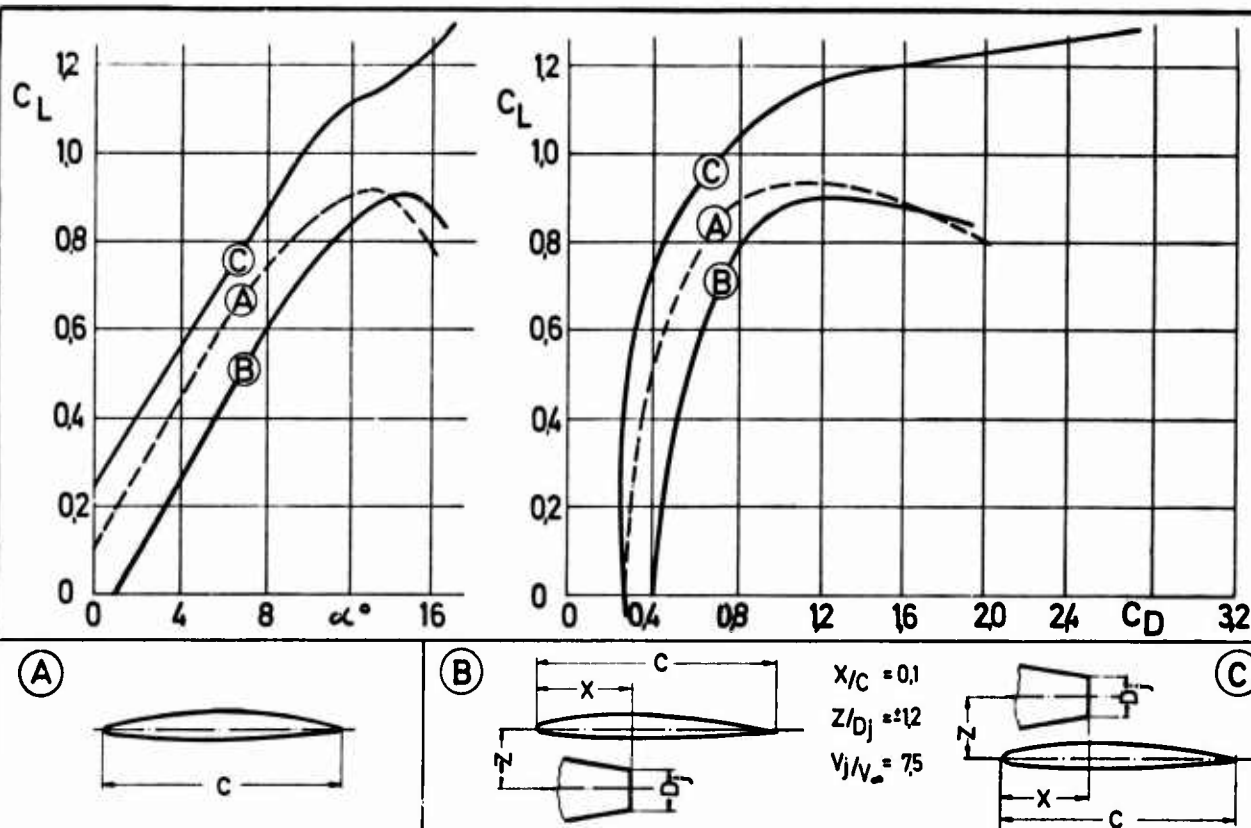
| **VFW-FOKKER** | JET INFLUENCE ON LIFT AND DRAG | Fig. 10 E.F.69/74 |

JET INFLUENCE ON LIFT AND DRAG

Fig. 11
EF. 70/74

$$\Delta C_L / C_L = \left[C_L(V_j) - C_L(V_j = V_\infty) \right] / C_{L\,\text{A}} \quad \text{for } \alpha = 0$$

JET INFLUENCE ON LIFT

Fig. 12
EF. 71/74

Fig. 13
EF. 72/74
WING PRESSURE AT ENGINE POSITION

Fig .14
EF. 73/74
WING PRESSURE AT ENGINE POSITION

Fig. 15 — WING PRESSURE AT ENGINE POSITION

SPANWISE ENGINE STATION $\eta_E = 0.35$

V_j/V_∞ = 7.5, 4.4, 1.0

$Z/D_j = 1.2$
$X/C = 0.1$
$\alpha = 8°$

VFW-FOKKER — Fig. 15 EF. 74/74

Fig. 16 — JET ENTRAINMENT

SUCKED AIR

STATIONARY INCOMPRESSIBLE $V_\infty \to 0$

INITIAL REGION | TRANS REGION | MAIN REGION

$$\dot{m}_j = \pi \varrho \cdot v_j \cdot R_j^2$$

$$\dot{m}(x) = 2\pi\varrho \int_0^R v(x)\, r\, dr$$

$$\frac{v_n}{v_j} \approx -\frac{1}{2}\frac{R_j}{R}\frac{d(\dot{m}/\dot{m}_j)}{d(x/R_j)}$$

INITIAL REGION $\quad \frac{v_n}{v_j} \approx 0.027 - 0.0043\frac{R_k}{R}$

MAIN REGION $\quad \frac{v_n}{v_j} \approx 0.076\frac{R_i}{R}$

VFW-FOKKER — Fig. 16 EF. 75/74
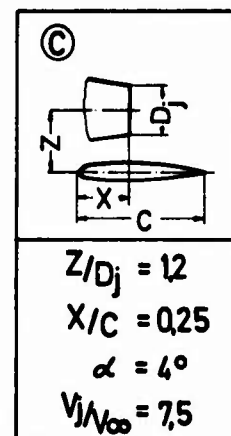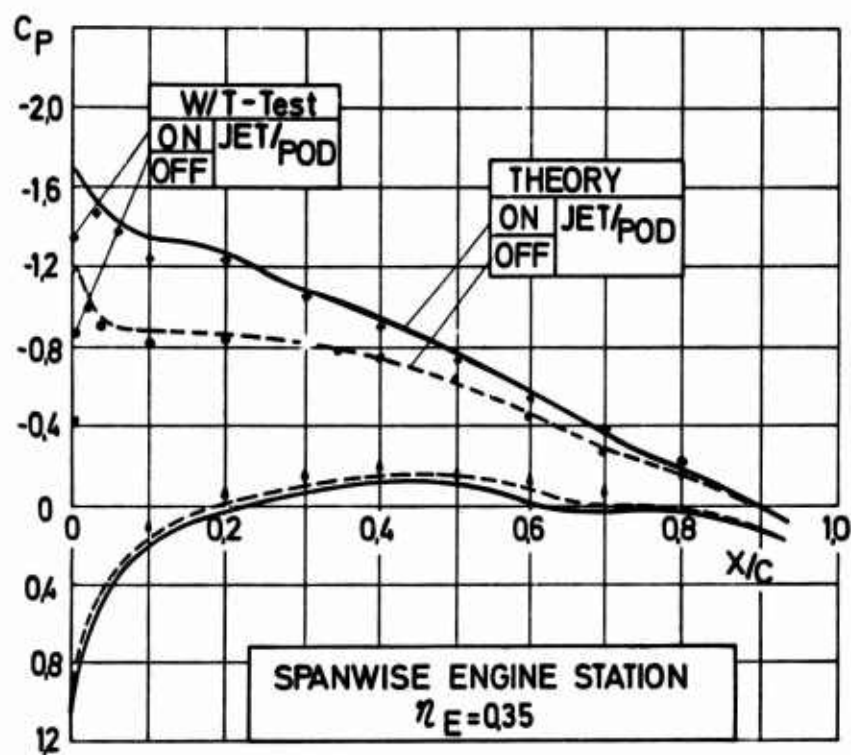
WING PRESSURE AT ENGINE POSITION

Fig. 17
EF. 76/74

AIRFRAME – ENGINE INTERACTION FOR ENGINE CONFIGURATIONS MOUNTED ABOVE THE WING

PART II: ENGINE JET SIMULATION PROBLEMS IN WIND TUNNEL TESTS

by

B. Ewald *

Vereinigte Flugtechnische Werke-Fokker GmbH
2800 Bremen 1, Hünefeldstraße 1-5, Germany

SUMMARY

The advanced technology of airframe propulsion system integration for transport aircraft has made engine simulation an important test parameter in wind tunnel tests on such aircraft.

In contrary to conventional force and pressure distribution measurements engine simulation has not jet become a standard test technique. A wide variety of methods has been used; the high massflow and the relatively short length of modern high bypass ratio engines makes things even more difficult.

In this paper a critical survey is given on the methods used so far.

A test technique developed for the VFW-Fokker Low Speed Wind Tunnel is presented. In this technique the airframe model is mounted to the external mechanical balance (wire suspension). The engine pod is mounted separately on a tail sting suspension system. Due to the design of this tail sting system its angle of attack axis of rotation coincides with the corresponding axis of the external balance. So separate mounting of airframe and engine with very small gaps is possible.

The air is fed to the engine pod with high pressure (up to 20 atmospheres). This pressure is decreased to the required nozzle exit pressure ratio by perforated plates very close to the nozzle exit. Calibration results of this nozzle arrangement are given.

Typical test results (force measurements, wing pressure distribution) are presented for several engine locations (Over-Wing, On-Wing, Under-Wing).

Further evaluation of the results and theoretical considerations on this subject are given in the paper of Mr. Krenz, VFW-Fokker, at this meeting.

1.   INTRODUCTION

One of the most complicated problems in the design of modern jet aircraft is the choice of the engine location. In addition well known problems of engine location noise shielding of the fan and the jet as well has become a major design parameter.

The efforts towards optimum noise shielding lead project aerodynamicists to engine locations (e.g. the on-wing position), which gives rise to serious propulsion-airframe interference problems, especially in the case of a supercritical wing design.

The problems facing the project aerodynamicist in this field have been described in more detail in the paper of Mr. Krenz at this meeting.

Since these problems cannot be solved simply by theoretical approach, sophisticated wind tunnel tests are necessary.

2.   ENGINE SIMULATION IN WIND TUNNEL TESTS

The true simulation of the propulsion system has been a most embarassing problem in wind tunnel technique ever since propulsion systems became important for the aerodynamic behaviour of airplanes. It is not possible to build real "model engines" in the models scale, which offer similarity in terms of jet momentum, power density and mass flow. So the wind tunnel engineer is dependant on a more or less realistic simulation of the engines influence on the airframe.

A wide variety of techniques has been developed and used for engine simulation; the most important are shown in figure 1.

For the simulation of fan- and jet engines with moderate to high bypass ratios the simple use of cold compressed air for jet simulation prooved quite successful. Things become much more difficult, when simulation of the hot jet is required. In this case the use of Hydrogen Peroxide is the most promising technique. The high specific volume of hot compresses air causes problems with big supply tubes. On the other hand the use of burning chambers inside the model engine nacelle is not fully developed up to now.

---

* Dipl.-Ing.
  Head of Experimental Aerodynamics

If simultaneous simulation of intake and jet is required, the use of suction and pressure plants outside of the model is not longer possible because of the necessary space for the supply tubing (especially for the intake air). So one must look for a simulation of the real engine.

The use of a fan driven by an electric motor is simple and reliable, but the performance of this technique is rather poor because of the limited energy concentration even of high speed a/c motors.

If a mismatching of intake and jet flow up to 25 % is tolerable and if a certain length of the nacelle is available, the injector scheme offers a well proven and relatively simple solution.

In the case of the modern high bypass ratio fan engines with their extremely short length the tip or hub turbine driven fan is the most promising solution. The power of these model engines does not jet reach real engine performance but a lot of further development can be done in this field.

A summary of the advantages and disadvantages of the different techniques is given in figure 2.

3. Mounting Problems

The most practical mounting of the model and the engine nacelle depends on the proposed measurements. If only pressure distribution measurements are required, mounting of model and model engine in the wind tunnel creates no problem at all.

If three or six component force measurements are necessary, a mounting scheme must be found which eliminates the jet momentum from the force measurements. Normally it is not possible to get a jet calibration which is accurate enough for a successful evaluation of a jet momentum plus aerodynamic force measurement.

The figures 3, 4 and 5 show the possible mounting schemes in principle (for the example of jet simulation by cold compressed air).

The integral mounting of model and powered nacelle is shown in figure 3. Force measurements can be achieved by a force free air supply linkage but the results contain the jets momentum and evaluation is difficult.

Figure 4 shows the principle of pick-a-back mounting. The primary mounting stings are connected to the powered nacelles; the stings are serving as air supply too. For measurement of the total force the stings may be connected to an external balance. The model is connected to the nacelle by a strain gage balance; this balance gives the aerodynamic forces on the model.

In figure 5 the principle of separate mounting is shown. The model is mounted on a normal sting suspension with internal or external balance. The nacelle is mounted to another sting. Between nacelle and model is a small gap; the nacelle does not touch the model.

This principle of separate mounting allows very accurate measurement of the aerodynamic forces. Basic requirement is the availability of two separte mounting systems in the wind tunnels test section, which are synchronised in the angle of attack motion.

4. JET INFLUENCE TEST INSTALLATION AT THE VFW-FOKKER LOW SPEED TUNNEL

As an example for the separate mounting system with jet simulation by cold compressed air a test arrangement for jet transport configurations in the VFW-Fokker Low Speed Wind Tunnel will be described.

Figure 6 gives an impression of the test task. For three different engine positions pressure distribution and 3-component force results were required.

The VFW-Fokker Low Speed Tunnel is of the open return type in a closed building. The tunnel has closed test section of 2,1 x 2,1 m² size. Maximum speed is 70 m/s.

Figure 7 gives a view into the tunnels tests section. The tunnel is equipped with an overhead external six component balance. The models are mounted to this balance by sting or wire suspension. In addition to the external balance the tunnel is equipped with a tail sting mounting system. A heavy steel circular arc is mounted at the end of the test section. The sting is carried by a sled which is moved on the steel arc by a chain drive.

The center of revolution of this arrangement is identical with the pitch axis of the external balance. Since the angle of attack drive systems of the overhead balance and the tail sting are synchronised by electronic connection, both systems can be used for the separated mounting scheme shown in figure 5.

The tail sting mounting system is equipped with a compressed air supply which is shown in figure 8. A maximum of 3 lbs/sec of cold air at a maximum pressure of 20 atmospheres is available at the tail sting.

Figure 9 shows the complete test arrangement. The model is mounted to the overhead balance by a wire suspension. The nacelles are mounted by their air supply tubes to the tail sting sled. The engine pylon is not simulated for the over-wing and the under-wing engine position because its existence does not affect the low speed jet influence characteristics in principle. For the on-wing engine position with a D-shaped nozzle the system allowed a minimum gap between wing and nacelle of 3 mm without contact through the whole range of angle of attack and nozzle pressure ratio.

To minimise the disturbance of the flow field, the air supply tubes should be very small. In the VFW-Fokker test arrangement the air was fed to the nacelles at a pressure of up to 10 atmospheres; so we could use very small pipes.

Figure 10 shows the design principle of the nacelle. The high supply pressure is throttled down to the required nozzle pressure ratio by a plate with a great number of very small holes. The small high pressure jets emerging from the plate with a supersonic free expansion mix up to a uniform subsonic flow over a very short distance. So with only a small contraction ratio one gets a jet with a useful nozzle exit profile.

Figure 11 shows the perforated plate used for the tests and the calibration results. A plate with 241 holes of 1,3 mm diameter was used.

The maximum required exit Mach Number of 0.82 was reached at a supply pressure of slightly below 8 atü with a satisfying exit velocity profile.

At higher pressures resp. exit velocities the jet flow became unstable with very bad exit profiles. A possible reason for this unstable condition may be an interaction of the free expansion cells of the individual small primary jets. It was found, that the unstable condition could be avoided resp. moved to higher exit Mach Numbers by the use of two perforated plates with bigger holes in tandem arrangement.

5. TEST RESULTS

The influence of the jet on the wing with and without flap deflection is shown on figure 12 and 13 for different engine positions. The velocity ratio is constant $v_j/v_\infty = 7,5$ through these figures and refers to the take off case.

The figures show a significant increase in zero incidence lift and maximum lift for the engine positions on-wing and over-wing and a loss in zero incidence lift for the under-wing position.

Drag is decreased for the over-wing position especially at high lift and is increased by a more or less constant value for the under-wing case. In case of the on-wing position the decreased-drag tendency of the over-wing position is overcome by scrubbing and turning drag; in addition to this it should be noted, that the wing-nacelle junction was not optimised for this case and that the necessary gap may have bad effects on drag.

The figures 14 to 19 show the force measurement results for different exit velocity ratios. The test run with $v_j/v_\infty = 1,0$ gives the pure nacelle displacement effect.

Obviously the jet effects are not simply proportional to the jet exit velocity ratio. The effects at $v_j/v_\infty = 7,5$ are much more significant than at $v_j/v_\infty = 4,4$, so jet effects are more or less restricted on the take off case.

The pressure distribution at the wing station below the engine resp. above the engine is shown on figure 20. The most significant information of this figure is the nearly perfect concentration of the engine influence on one side of the wing, the upper side for the over-wing position and the lower side for the under-wing position.

The drag increase of the under-wing case results from a heavy suction peak on the rear part of the lower wing side and a reduction in nose suction. An increase in nose suction is the main reason for the drag decrease of the over-wing case.

The figures 21 and 22 show the tendencies of the pressure distribution with increasing jet exit velocity ratio.

6. CONCLUSION

To investigate the engines jet influence on a transport configuration for different engine positions, a wind tunnel test arrangement was constructed for the VFW-Fokker Low Speed Tunnel which is based on the separate mounting of model and engine nacelle and the use of cold compressed air for jet simulation.
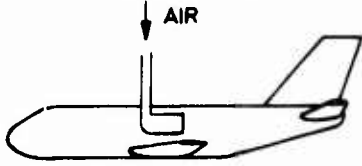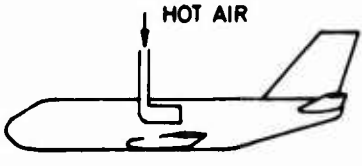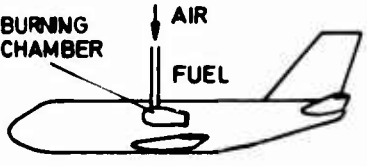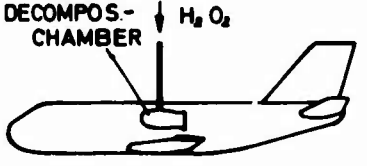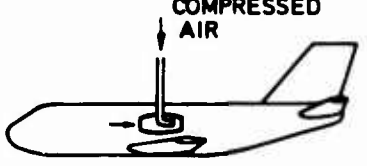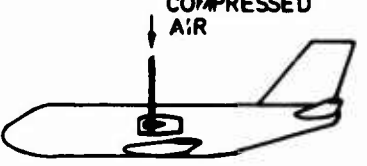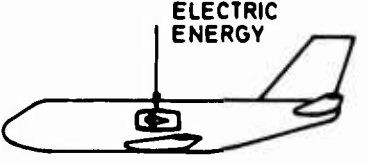
The test arrangement gave satisfactory results and allowed simultaneous 3-component force and pressure distribution measurements.

The results gave information on the principle differences of jet interference for the over-wing and the under-wing engine position. The over-wing position proved favourable due to a significant

lift increase and drag decrease. The jet influence on the wing pressure distribution was nearly restricted on the wing side adjacent to the engine.

REFERENCES

[1]   VFW-Fokker Low Speed Wind Tunnel
       User's Manual

[2]   Unpublished VFW-Fokker Development Reports

SIMULATION OF COLD JET	COMPRESSED AIR	AIR
SIMULATION OF HOT JET	HOT COMPRESSED AIR	HOT AIR
	COMPRESSED AIR+ BURNING	BURNING CHAMBER / AIR / FUEL
	HYDROGEN PEROXYDE	DECOMPOS.-CHAMBER / H₂O₂
SIMULATION OF JET+INTAKE	INJECTOR	COMPRESSED AIR
	TIP TURBINE DRIVEN FAN	COMPRESSED AIR
	ELECTRIC MOTOR DRIVEN FAN	ELECTRIC ENERGY

VFW-FOKKER — PRINCIPLES OF JET ENGINE SIMULATION IN WIND TUNNELS — Fig.1 EF 77/74

Simulation Requirement	Recommended Technique	Disadvantages Of Other Techniques
Cold Jet	Compressed Air	—
Hot Jet	Hydrogen Peroxyde	<u>Hot compressed Air</u>: Large specific volume of hot air — big supply tubes. Heat expansion problems. <u>Compressed Air + Burning</u> : Extremely small and short burning chamber needs extensive development.
Simultaneous Simulation of Jet and intake	Exact mass flow ratio intake - jet required : Tip-Turbine driven Fan not required : Injector	<u>Electric motor driven fan</u> : Power per unit volume too small

VFW-FOKKER	Recommended Simulation Technique	Fig. 2 EF-78/74

Force free Air Supply Linkage

Sting mounting to external balance

Compressed Air
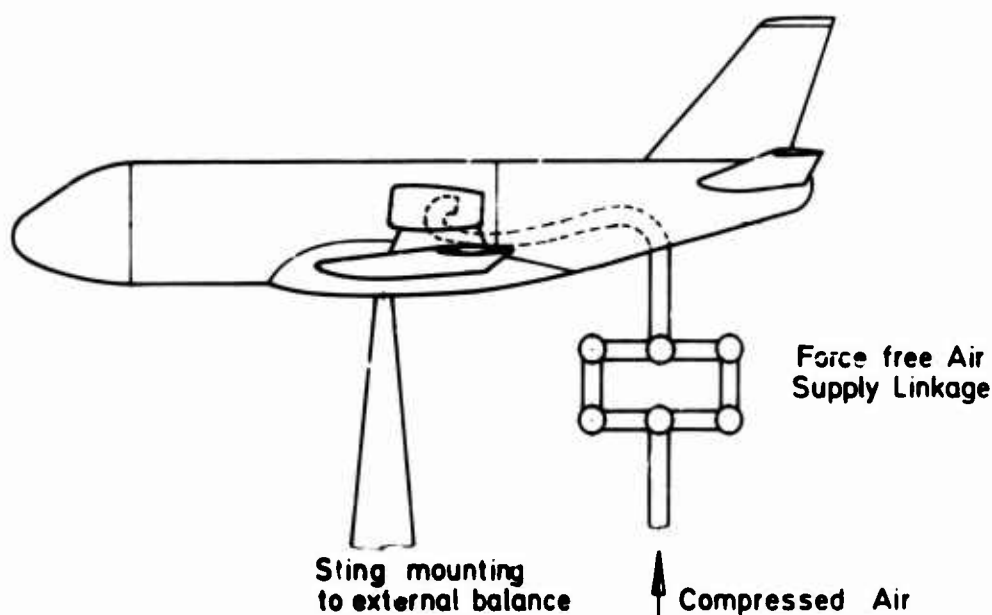
VFW-FOKKER	ENGINE JET SIMULATION WITH INTEGRAL MOUNTING	Fig. 3 EF 79/74

Compressed Air Supply

Mounting sting
to nacelle

(eventually to
external balance)

Model mounted to
nacelle by

Six-Component
Strain Gauge Balance
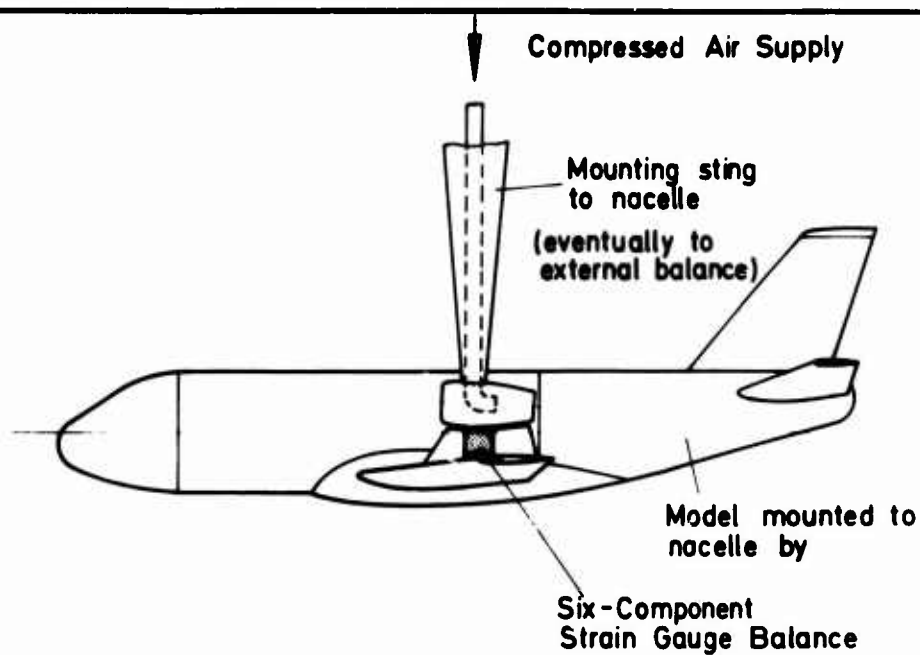
VFW-FOKKER	ENGINE JET SIMULATION WITH PICK-A-BACK MOUNTING	Fig. 4 EF 80/74

Compressed Air Supply

Mounting Sting
to nacelle

Free gap between nacelle
and model

Model Sting Mounting
to external balance
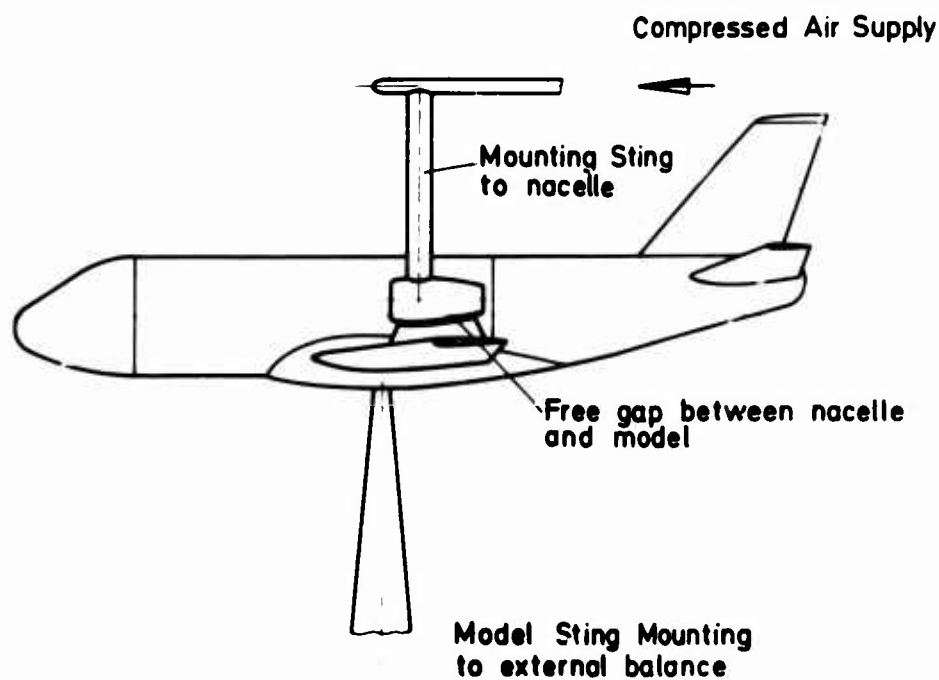
VFW-FOKKER	ENGINE JET SIMULATION WITH SEPERATE MOUNTING	Fig. 5 EF 81/74

On Wing Position   Over Wing Position

Under Wing Position
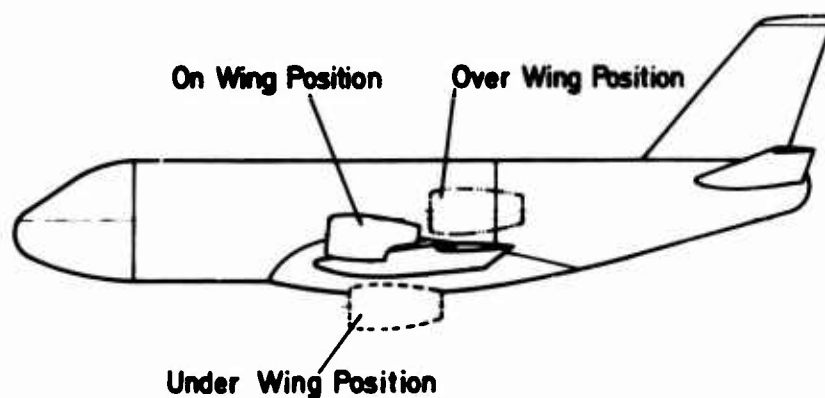
Test Tasks: 3-Component Force-Test
Pressure Distribution

VFW-FOKKER	**PROPOSED WIND TUNNEL TEST** **JET INFLUENCE FOR DIFFERENT ENGINE LOCATIONS**	**Fig. 6** **EF 82/74**

VFW-FOKKER	**VFW-FOKKER Eiffel Wind Tunnel** **Rear Sting Mounting**	**Fig. 7** **EF -83/74**
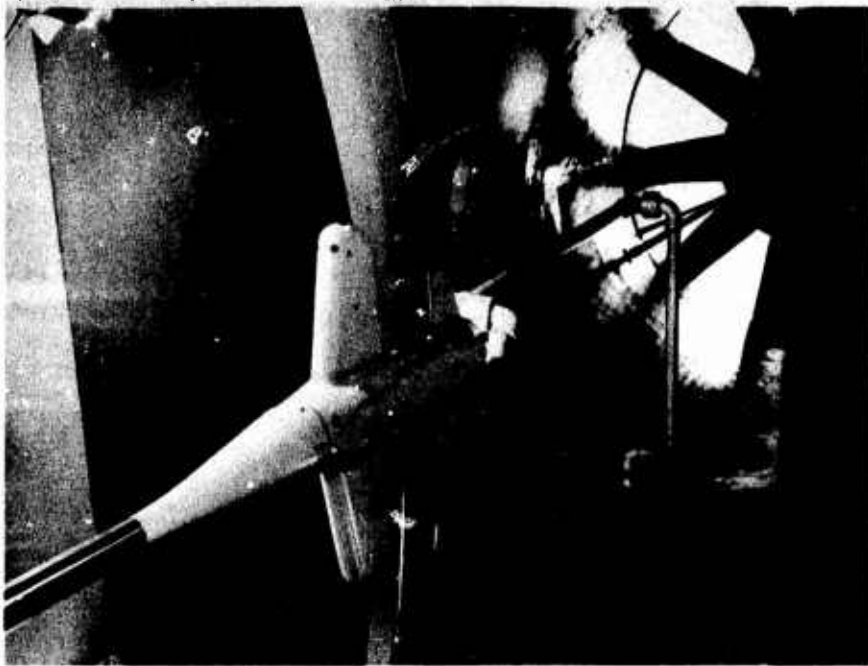
VFW-FOKKER

VFW-FOKKER Eiffel Wind Tunnel
Rear Sting Compressed Air Supply

Fig. 8
EF 84/74
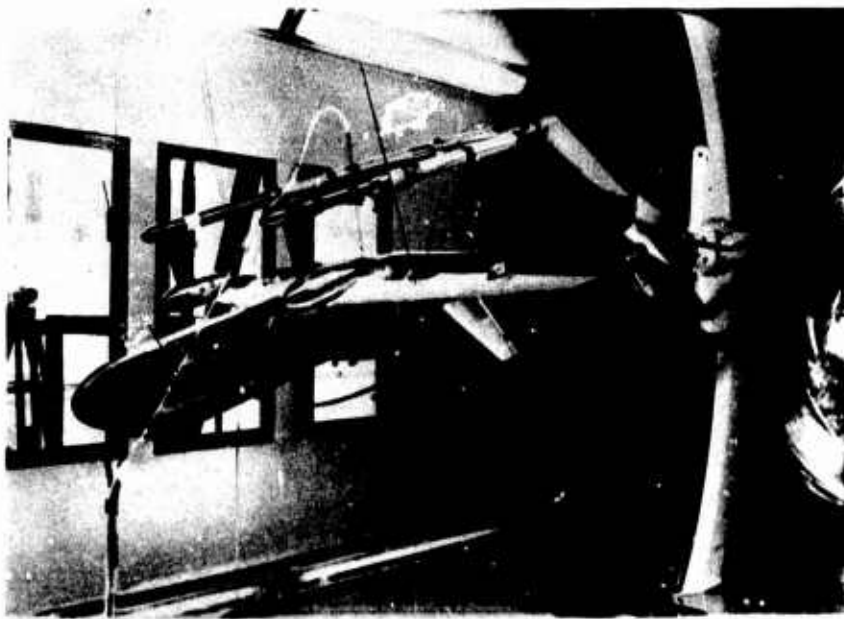
VFW-FOKKER

Jet Influence Test Arrangement
Seperate Mounting of Model and Nacelle

Fig. 9
EF - 85/74
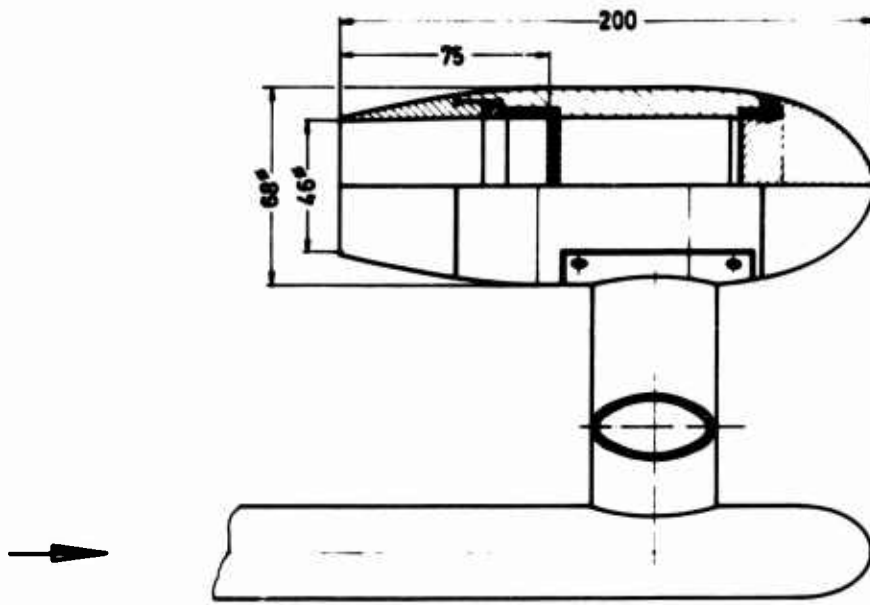
VFW-FOKKER | DESIGN OF MODEL ENGINE NACELLE | Fig. 10 EF 86/74

Design of
perforated plate:

n = 241 Löcher
d_L = 1,3 mm ⌀
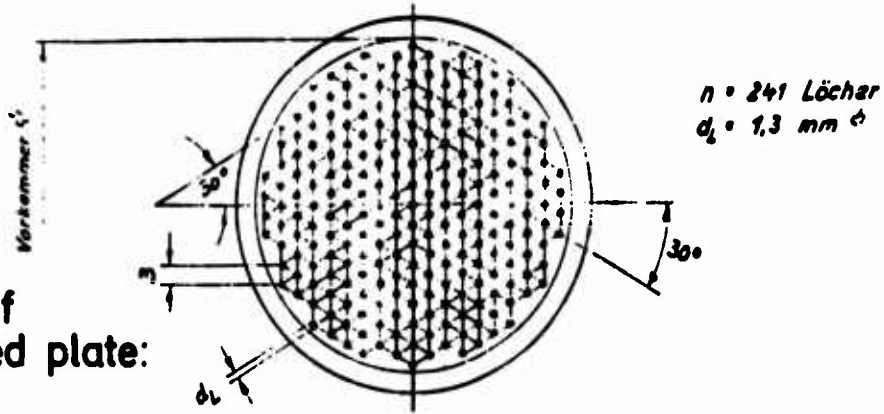
Total Pressure Distribution at Nozzle Exit:

Chamber pressure: 8,03 ata

y [mm]

20

0

-20

ΔPt mm Ws

1000   2000   3000   4000

Nacelle Calibration

Chamber Pressure

ΔP_Ch

atm.

10

8

6

4

2

0   0,1   0,2   0,3   0,4   0,5   0,6   0,7   0,8   M̄_E   1,0

Mean Nozzle
Mach Number
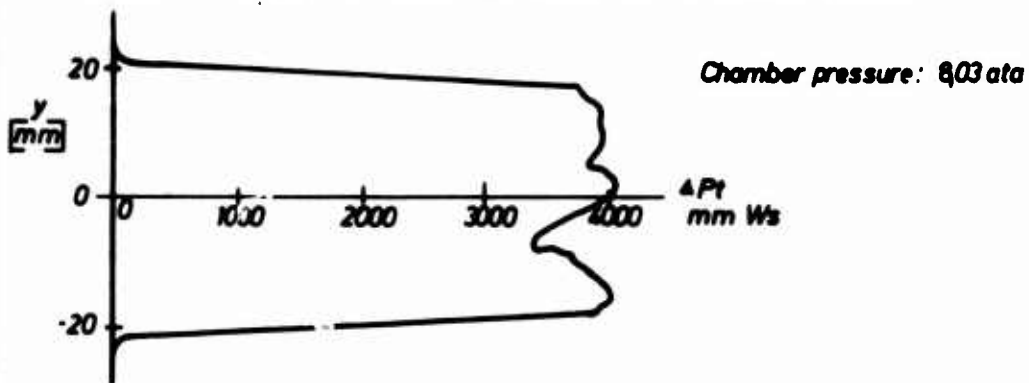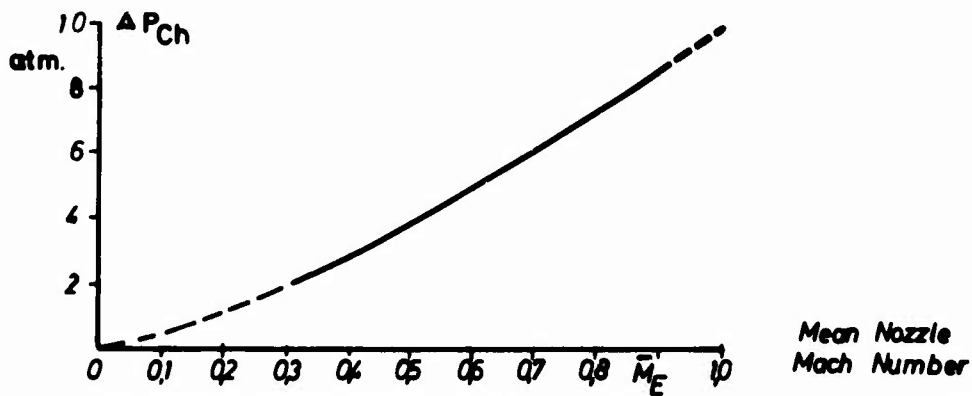
| **VFW-FOKKER** | PERFORATED PLATE ENGINE NACELLE CALIBRATION RESULTS | Fig. 11 EF 87/74 |

Figure 12:

ENGINE POSITION	Clean (A)	Under Wing (B)	Over Wing (C)	On Wing (D)
Nozzle Position $\begin{cases} z_A/D_A \\ x_A/D_A \end{cases}$	—	$-1,19$	$1,12$	$s/\sqrt{4/\pi \cdot F_A} = 0,1$
	—	$0,1$	$0,1$	$0,1$
Velocity Ratio V_j/V_∞	—	$7,5$	$7,5$	$7,5$

VFW-FOKKER

JET-WING INTERFERENCE

ENGINE POSITION FORCE MEASUREMENTS

Fig. 12

EF 88/74

Figure 13:

ENGINE POSITION	Clean (A)	Under Wing (B)	Over Wing (C)	On Wing (D)
Nozzle Position $\begin{cases} z_A/D_A \\ x_A/D_A \end{cases}$	—	$-1,19$	$1,12$	$s/\sqrt{F_A \, 4/\pi} = 0,1$
	—	$0,1$	$0,1$	$0,1$
Velocity Ratio V_j/V_∞	—	$7,5$	$7,5$	$7,5$

VFW-FOKKER

JET WING INTERFERENCE

ENGINE POSITION FORCE MEASUREMENTS

Fig. 13

EF 89/74

JET-WING INTERFERENCE
VELOCITY RATIO   FORCE MEASUREMENTS
Fig. 14
EF 90/74

JET-WING INTERFERENCE
VELOCITY RATIO   FORCE MEASUREMENTS
Fig. 15
EF 91/74

Fig. 16 — JET-WING INTERFERENCE — VELOCITY RATIO — FORCE MEASUREMENTS — EF 92/74

Fig. 17 — JET-WING INTERFERENCE — VELOCITY RATIO — FORCE MEASUREMENTS — EF 93/74

JET WING INTERFERENCE — VELOCITY RATIO — FORCE MEASUREMENTS

VFW-FOKKER

Fig. 18

EF 94/74

JET-WING INTERFERENCE — VELOCITY RATIO — FORCE MEASUREMENTS

VFW-FOKKER

Fig. 19

EF 95/74

Velocity Ratio	$V_j / V_\infty = 7,5$
Wing Section	$\eta = \eta_E = 0,35$
Angle of Attack	$\alpha = 8°$

Engine Position		Nozzle Position	
		z_A/D_A	x_A/l
Clean	Ⓐ		
		-	-
Under Wing	Ⓑ	-1,19	0,1
Over Wing	Ⓒ	1,12	0,1

JET-WING INTERFERENCE

ENGINE POSITION   PRESSURE DISTRIBUTION

VFW-FOKKER

Fig. 20

EF 96/74

Under Wing	Ⓑ

Engine Position		
Nozzle Position	z_A/D_A	-1,19
	x_A/l	0,1
Wing Section	$\eta = \eta_E$	0,35
Angle of Attack	α	8°

JET-WING INTERFERENCE

VELOCITY RATIO, PRESSURE DISTRIBUTION MEASUREMENT

VFW-FOKKER

Fig. 21

EF 97/74

JET-WING INTERFERENCE

VELOCITY RATIO , PRESSURE DISTRIBUTION MEASUREMENT

Fig. 22

EF 98/74

AERODYNAMIC ASPECTS AND OPTIMISATION OF THRUST REVERSER SYSTEMS

Kurt Lotter and Wolfgang Kurz

Messerschmitt-Bölkow-Blohm GmbH
Unternehmensbereich Flugzeuge
D 8 München 80
Postfach 801160
Germany

SUMMARY

The present generation of commercial aircraft and future advanced military aircraft require thrust reversal for reduction of landing distances, especially for wet or icy runways. The various design and integration features for jet deflection are summarized and the requirements and problem areas discussed under special consideration of a target type reverser system. The paper deals with the important engine/airframe interference problems and aerodynamic aspects associated with thrust reversal. Parametric investigation of thrust reverser geometry on efficiency, reingestion structure heating and longitudinal stability during ground roll is presented. Results are based on an intensive wind tunnel test program using various types of scale models with cold and hot jet, intake suction and fixed and moving ground simulation. Emphasis is given to the overall optimisation of often conflicting requirements from parameters like for example thrust reverser performance and reingestion. The essential influence of appropriate thrust reverser operation and landing techniques at or shortly before touch-down on landing distance is shown.

LIST OF SYMBOLS

a	engine spacing	$\Delta \overline{T}$	mean intake total temperature above ambient temperature
b	bucket height		
c	bucket excentricity	v_R	reingestion speed or reverser cut-off speed
Δc_D	incremental drag coefficient	$v_{Touch-Down}$	airplane touch-down speed
Δc_L	incremental lift coefficient	v_∞	free stream velocity
Δc_M	incremental pitching moment	x	lip height
c_{D_o}	aircraft zero lift drag	γ	bucket sweep angle
d	end plate distance	ς	bucket turn angle
D_j	jet diameter	ε	bucket tilt angle
h	end plate height	η	thrust reverser efficiency $= \dfrac{F_{reverse}}{F_{forward}}$
P_{oj}/P_∞	jet pressure ratio	φ_L	circumferential jet deflection angle of lower jet
s	axial spacing between nozzle exit and bucket	φ_U	circumferential jet deflection angle of upper jet
t	time	Θ_L	effective jet deflection angle of lower jet (Fig. 5)
T_{oi}	intake total temperature		
T_L	local temperature	Θ_U	effective jet deflection angle of upper jet (Fig. 5)
$T_{o\,max}$	maximum intake total temperature	ζ	rudder deflection angle
T_{oj}	jet total temperature		
T_∞	ambient temperature		
ΔT_i	$T_{oi} - T_\infty$		
ΔT_{max}	$T_{o\,max} - T_\infty$		

1. INTRODUCTION

Most of the commercial aircraft today use thrust reversal as additional braking device to reduce landing ground roll distance. Recent developments of high performance fighters with STOL characteristics have also generated requirements for thrust reversal, since a drag parachute will not contribute very much to decelerate the aircraft at low touch-down speeds. A thrust reverser further increases safety during an aborted take-off. Future development is now directed towards in-flight reverser operation to improve manoeuvring capabilities.

The potential benefit of thrust reverser operation during aircraft deceleration on the ground is illustrated in Fig. 1. Especially for wet and icy runways the use of thrust reversal is superior to wheel braking. But even on a dry runway the landing ground roll distance is considerably reduced with reverse thrust applied.

From the various thrust reverser designs which have evolved in the past some of the most commonly used solutions are shown in Fig. 2. The integrated thrust reverser incorporates mechanical blockage doors with turning vanes to deflect the exhaust gases into the desired direction. Another successful design is the target type thrust reverser: two buckets are deployed into the exhaust jet to produce reverse thrust. In the retracted position the buckets form a part of the boattail structure. This type of reverser, moreover, is suitable for integration into a blow-in-door ejector nozzle.

A great many of the general effects described in this paper hold true for any type of thrust reverser. For most applications, however, specific tailoring is required so as to find a reverser design which produces minimum interference with the overall aircraft. This paper deals with the development of a target type thrust reverser for a high performance fighter airplane with two engines mounted close together in the rear end of the fuselage. Emphasis is given to the aerodynamic problems which raise special difficulties for such a type of configuration during reverser operation.

2. REQUIREMENTS AND PROBLEM AREAS

There are a number of requirements during the preliminary design phase of a thrust reverser system for a new airplane (Fig. 3). The primary design objective of a thrust reverser is to substantially reduce the ground roll distance. Other requirements like suitable integration into the airplane and/or engine structure, minimum operational limitations, simple reverser selection procedure and fail safe philosphy must be met.

In Fig. 3, three major areas of problems are shown which need consideration during the thrust reverser development: structural design, aero-/gasdynamic problems and control. Detailed description of the structural design would be beyond the scope of this paper. These aspects will be only briefly mentioned here. The extensive experimental investigation and optimisation of the aero-/gasdynamic aspects will be thoroughly dealt with; the considerable influence of the mode of reverser control will be discussed in detail, too, since it affects the overall performance of the total system.

2.1. Structural Design

Depending on the type of installation of the engine(s) and on the selected nozzle configuration, the mechanical design of the thrust reverser will influence the degree of impact on the structure. For isolated engine installations as is the case for pod-mounted nacelles the installation of a thrust reverser generally causes little problems. The more the engines are integrated into the aircraft, however, the more the reverser system will compromise the overall airplane design. Other factors to be considered are structure weight, actuation means, ground clearance, maintainability, reliability, complexity, etc. These items will not be treated any further in this context.

2.2. Thrust Reverser and Engine Control

Thrust reverser actuation time, engine response, mode of thrust reverser selection and operation strongly influence the landing ground roll distance. The development of the control system itself is not described here but the importance of the above stated parameters for the overall system optimisation emphasized chapter 8.3.

2.3. Aerodynamic and Gasdynamic Problems

During thrust reversal the deflected jets can produce considerable interference effects. High deflection angles are desirable in order to obtain maximum reverser performance. This, however, gives rise to potential hot gas reingestion and stability problems. Other factors like structure heating, debris ingestion, ground erosion, buffeting, noise etc. can call for additional operational limitations. The more important of the above items and their effects on the overall reverser system will be treated in this paper.

Due to the complex flow field of the deflected jets, theory can only be applied to establish general trends. Reverser development must be supplemented by experiment for nearly every individual design. Fig. 4 depicts a typical experimental program incorporating scale model tests and full scale tests to investigate the most important aerodynamic problems associated with thrust reversal.

Thrust reverser performance is measured on static thrust test rigs with cold compressed air applied to the scale model and by full scale simulation behind the real engine. Bucket loads, effective jet deflection angles and general parametric investigations of bucket geometry are also tested on these rigs.

Hot gas reingestion, debris ingestion and structure heating usually are studied using a wind tunnel model with hot jet simulation, intake suction and simulated fixed or moving ground. Results from these model tests are later confirmed and supplemented by taxi trials with the prototype aircraft.

A complete aircraft model with an internal six-component balance supplies information on longitudinal and lateral stability. In order to measure only the induced aerodynamic effects with a high degree of accuracy, the thrust of the simulated jets is not measured by the balance: a separate non-metric air supply system delivers compressed air from the rear to the exhaust system. Again, taxi trials are required for final confirmation of the previously measured directional stability.

3. THRUST REVERSER PERFORMANCE

3.1. Design Parameters

Thrust reverser efficiency η is dependent on both the effective turning angle of the deflected jets and the turning losses. Ideally, with a bucket designed to accomplish a nearly 180° turning of flow, the efficiency can be as high as 80 %. In practice, however, there are limitations to the design of a bucket. When the thrust reverser is not in operation, the buckets must be stowed within the aircraft contour. The space available in that position usually does not allow the design of a bucket with a sufficiently large wrap angle. Other restrictions like weight, linkages, load vector, etc. are also to be considered during the design. Yet there are a number of geometric design parameters to influence the degree of jet deflection.

The principal geometry of a target type thrust reverser bucket is shown in Fig. 5. The effective jet deflection angle Θ can be considerably varied by changes in bucket height b, bucket sweep angle γ and lip height x. Lateral deflection of the reversed jets is required for some airplane configurations in order to avoid strong jet interference problems especially if the engines are installed at close distance. This lateral deflection can be accomplished by circumferential rotation of the buckets or by incorporation of turning vanes within the buckets (circumferential deflection angle φ). Side spillage of the exhaust gas is reduced by end plates, whose width d is determined by the jet diameter D_j. The height h of these end plates is limited by the available space in the stowed position.

Parameters like bucket excentricity c, bucket turn angle ς and bucket tilt angle ε are other design aids in achieving the desired angles of jet deflection. Due to the then required asymmetric linkages, these parameters will bring about complications with respect to design.

The axial spacing s of the bucket to the nozzle exit must be chosen larger than a critical value in order to avoid back-pressure to the engine during reverser operation. Too large spacing on the other hand requires long linkages resulting in high weight.

3.2. Efficiency

The efficiency η of a target type thrust reverser has been measured on a static thrust test rig at systematic variation of most of the parameters described in the preceding section. Typical results covering the effects of bucket sweep angle, axial spacing and lip height are presented in Fig. 6 and 7. The measured efficiency of a practical bucket geometry generally lies between 40 and 60 %.

From Fig. 6 it can be seen that the optimum sweep angle is about $\gamma = 130^{\circ}$ to 140° for the two considered bucket spacings. Higher sweep angles reduce the degree of flow turning (decreasing Θ), lower sweep angles cause the flow to spill over the side in the corner formed by the two buckets. The bucket sweep angle can be increased only up to a certain limit if the buckets are required to move out of the propulsive jet in case of actuation failure.

Increasing lip height increases the degree of flow turning and thereby efficiency, too (Fig. 7). When the lip height of $x/D_j = 0.12$ up to 0.14 was exceeded for the considered configuration no improvement in efficiency was measured, since too high lips again cause the exhaust gas to spill over the side. For the smaller spacing ratio of $s/D_j = 0.7$ throttling of the exhaust gas was noticed with a subsequent reduction in efficiency. Too large spacings will also reduce the efficiency since the effective flow turning is again decreasing. Optimum spacing ratios were between $s/D_j = 0.8$ to 1.2, depending on overall bucket geometry.

Increasing jet pressure ratio improves efficiency as being demonstrated by Fig. 8 for two basic bucket geometries with $\varphi = 0^{\circ}$ and $\varphi = 30^{\circ}$. Optimum efficiencies were measured for jet pressure ratios of about 2.4.

The two deflected jets issued from a pair of buckets can be made asymmetric to each other with respect to deflection angles and mass flow by variation of parameters like excentricity c, bucket tilt angle ε and different lip heights for both buckets. This may be applied in cases where different mass flow rates and turning for both jets are desired for reasons like improved reingestion or compensation of a jet-induced pitching moment. Detailed measurements for different bucket geometries are discussed in [1].

4. REINGESTION

4.1. Hot Gas Reingestion

During reverser operation reingestion of hot gases into the engine intakes raises a potential problem. Reingested gases cause pressure and temperature distortions at the compressor face of the engine. Thrust losses or in worse cases engine surges are encountered. During landing ground roll the initially forward directed reverser efflux is more or less deflected backward, depending on rolling speed. The reverser can only be used down to rolling speeds at which the exhaust gases are just ingested into the engine inlet. At this rolling speed the reverser operation must be cancelled or the engine is to be continuously throttled down as the rolling speed diminishes. For a target type reverser with jets deflected up and downward, reingestion is mainly determined by the flow field of the lower jet, which impinges on the ground and develops into a forward spreading wall jet. The upper deflected jet will only be reingested if extreme high flow turning should occur.

4.1.1. Wind Tunnel Model

The complex flow field of the reverser efflux in a cross flow can hardly be covered by theory. Tests are required with scale models to investigate the flow field and to determine the forward speeds of the airplane at which the reversed jets are ingested into the engine intakes.

Fig. 9 shows a wind tunnel model specifically designed for experimental investigation of the reingestion problem. Hot gases are supplied to the model through a pipe entering the nose and then issued through the exhaust nozzle. Exactly duplicated thrust reverser buckets deflect the jet into forward direction. Engine intake flow is simulated by sucking air through the wing and pipes mounted to the wing tips. Water-cooling of the high temperature air pipes is provided. The ground is simulated by a fixed plate which can be yawed to measure cross wind effects. At times this plate was replaced by a moving ground belt to simulate the movement of the airplane relative to ground.

The model is instrumented with mass flow measurement devices for the exhaust- and the intake airflow. Fast response thermocouples in the intake indicate the event of reingestion of hot gases. Interference of the jet efflux with the airplane structure is measured by thermocouples at critical locations on the surface of the model.

The flow pattern as measured in the wind tunnel at various forward speeds with jets deflected up and down is drawn in Fig. 10. The efflux was made visible by injecting water into the exhaust gas. All pictures clearly show how the lower jet extends more forward than the upper one. This is due to the ground being close to the bottom of the fuselage. The cut-off speed caused by reingestion therefore is determined by the speed at which the lower jet is ingested into the intake ($V_\infty/V_{T.D.} = 0.5$ for an early design of the reverser).

Fig. 11 discloses how the cut-off speed was determined from model tests. A sudden rise in intake temperature was measured when the forward airspeed in the tunnel was gradually lowered from touch-down velocity to a critical value. At this velocity the efflux of the lower jet separates from the ground underneath the intake and is sucked into the model. Since at this velocity the efflux is drawn into the intake at the shortest way the intake temperature reaches a maximum for that case. Further reduction of the rolling speed allows the lower jet to extend upstream i.e. ahead of the intake. Due to increased mixing with the surrounding air the intake temperature continuously decreases with reduction in forward speed.

In practice, operation of the reverser is possible only above the critical velocity at which the sudden temperature rise occurs. The cut-off speed or "reingestion speed" v_R was derived from the model tests as that forward speed at which a mean temperature rise in the intake of $\Delta T = 5^{\circ}C$ was measured by the 9 temperature probes.

4.1.2. Effect of Bucket Geometry

Since the lower jet is more critical to reingestion, wind tunnel investigations with that model were concentrated on variation of the lower jet efflux. Some results are selected here from the comprehensive test program performed. Fig. 12 shows the effect of the circumferential or side deflection angle φ_L on reingestion speed v_R. As the lower jet is deflected to the side, the reingestion speed is at first only slightly reduced. Once a critical angle φ_L^* has been reached, a sudden reduction in reingestion speed will be obtained. This becomes evident when the separation line at the ground is considered. With deflection angles $\varphi_L < \varphi_L^*$, the separation line reaches far upstream along the ground

underneath the aircraft centreline due to mutual interference of the deflected lower jets. If $\varphi_L > \varphi_L^*$, the separation point underneath the fuselage centre line is moving backward. There are now two foremost points located outside of the intakes in the plan view projection. At this condition, the exhaust gases can only be ingested by intakes at rather low rolling speeds.

An alternative solution to deflect the jets outward is to turn the buckets around a vertical axis by an angle ζ or to incorporate a combination of circumferential deflection angle φ and bucket turn angle ζ. Fig. 13 shows the required combination of φ and ζ for two given reingestion speed ratios $v_R/v_{T.D.} = 0.2$ and 0.3. If symmetric bucket linkages are mandatory, a circumferential deflection φ_L of about 45 degrees is necessary to meet reasonable low reingestion speeds.

Hot gas reingestion from the upper jet was only measured for extreme high deflection angles of Θ_U greater than 60° for the considered configuration (Fig. 14). At those deflection angles a sudden attachment of the flow to the upper surface of the fuselage occurs due to the induced pressure reduction along the surface (Coanda-effect). It can be seen from Fig. 14 that the reingestion speed is drastically increased in the case of upper jet reingestion.

4.1.3. Thrust Reverser Operation Boundary Due to Reingestion

In practice, thrust reverser cancellation speed is chosen somewhat higher than established from reingestion tests to maintain a sufficient safety margin. To take, however, full advantage of thrust reversal the engine can be continuously throttled down as the rolling speed is decreased. In Fig. 15 the measured mean intake temperatures for various engine power settings are shown. In the model tests, the various engine settings were simulated by simultaneously reducing nozzle pressure ratio, jet total temperature and degree of intake suction.

It will be seen from Fig. 15 how reingestion speed and maximum mean intake temperature decrease with reduction of engine power setting. The boundary line of the thrust reverser operation at engine throttling can be established from these tests. In Fig. 16 this boundary is shown for a thrust reverser configuration with jet angles as defined in the diagram. It is evident that thrust reversal can ideally be applied until very low rolling speeds, provided that the jet pressure ratio is reduced accordingly. At the very low engine power settings, however, contribution of thrust reversal to overall retarding force becomes insignificant.

The more representative ground simulation with a moving belt reduces the measured reverser cut-off speeds by about 15 % (Fig. 16) when compared with results from the fixed ground simulation. The speed of the moving ground belt was adjusted here to be identical with the tunnel velocity.

4.2. Debris Ingestion

Debris ingestion becomes an important problem if the aircraft is designed to operate from semi- or unprepared runways. Model-scale and full-scale tests with salt and chalk chip simulations already carried out for other aircraft projects indicate, that reverser cancellation speeds are higher and, therefore, more arduous for debris avoidance than for hot-gas ingestion avoidance: due to inertia the ground debris, put into motion by the forward deflected lower jets, follow a path further upstream towards the aircraft nose than the exhaust gas particles. Consequently, thrust reverser cancellation procedures cater for debris ingestion avoidance resulting in a sufficient safety margin with respect to hot gas reingestion.

5. STRUCTURE HEATING

Consideration should be given to the possibility of overheating the airplane or nacelle structure by impingement of exhaust gases. For configurations with the jet plume(s) in close proximity to aerodynamic surfaces, heat-resistant materials may be required in certain critical areas.

For an airplane design with two engines mounted close together in the rear end of the fuselage, air temperatures were measured close to the surface using the reingestion model described in section 4.1.1. Results are presented in Fig. 17 for temperature probes located at relevant stations of fuselage, fin, rudder, taileron and wheel. Data shows that the reversed stream temperature rapidly drops after a relatively short distance from the bucket exit.

The highest temperatures were measured at the rear end of the fuselage (nozzle) which anyway is designed to withstand high thermal loads. Temperatures in other regions generally were acceptable except at some locations on the fin and at the rudder when deflected. Therefore, heat resistant materials are required for those spots of the structure. The sudden rise of the temperature at the main wheel indicates the rolling speed at which the forward front of the lower jet is just reaching as far upstream as the location of the main landing gear.

6. STABILITY

During thrust reversal aerodynamic interference of the reverser efflux with fin, tail and wing can raise serious stability problems. Changes in lift, drag and pitching moment are introduced, varying with rolling speed. Results from model tests are shown in Fig. 18. The change in lift, drag and pitching moment with rolling speed was found to be entirely different for high and low jet pressure ratios. For high pressure ratios even a change in sign was measured for lift and pitching moment, if the rolling speed was reduced. These changes, however, occur at velocities low enough that the actual forces or moments involved do not noticeable impair overall longitudinal stability. The measured changes in stability at high rolling speeds were sufficiently small and did not cause severe problems.

The degree in which the upper jets are laterally deflected (φ_U) must be carefully investigated, since the lateral stability is largely affected by that angle. Especially for aircraft with more than one engine in or at the rear end of the fuselage the reversed upper jets shall be directed sufficiently away from the fin and rudder in order to encounter minimum aerodynamic interference. On the other hand large side deflections cause losses in efficiency and create an additional yawing moment due to the lateral thrust vector in case of the other engine failing. Reasonable balancing of the degree of jet deflection is, therefore, required.

7. AIRPLANE DRAG

Another aspect of thrust reverser/airframe interference which becomes very important during cruise is the additional drag caused by the installation of the reverser system. While design is aimed at providing clean external lines for the reverser in the stowed position the presence of unavoidable gaps, steps and linkage fairings produces parasitic drag (Fig. 19). These effects were investigated by wind tunnel tests with a special afterbody drag test rig. For a target type reverser with faired linkage arms on either side of the nozzle, drag increased typically between 2 to 4 % of total airplane zero lift drag. The drag increment is especially high if the reverser is combined with an aerodynamically clean nozzle (Iris nozzle; lower half of the picture).

8. REVERSER SYSTEM OPTIMISATION

In the preceding sections the important considerations involved in thrust reverser design have been discussed. Parametric investigations in the first instance have led to design rules which yield maximum efficiency, low reingestion, good stability etc. Thorough optimisation however is now required to obtain minimum landing ground roll distance together with safe airplane operation during thrust reversal by searching for a best compromise of often conflicting parameters.

8.1. Involved Parameters

A great number of parameters is to be considered and balanced against each other to obtain a solution compatible with the various design- and operational requirements. The most important of those parameters to be taken into account in the optimisation process are shown in Fig. 20.

Low reingestion is not compatible with large effective jet deflection angles Θ. High reverser performane, however, requires large angles Θ. A reasonable compromise with respect to Θ is therefore a major task during the optimisation. The same opposite requirements appear with respect to the circumferential deflection angle φ. Low deflection angles φ_U and φ_L for the upper and lower jets respectively are desired to achieve high performance, but from the reingestion point of view a large angle φ_L is benefitial. Sufficient large lateral stability again can only be maintained when the upper jet is deflected sufficiently off the fin (large φ_U).

Another essential field to be covered during reverser system optimisation is the mode of reverser operation. The way how and the moment at which the reverser is initiated largely influence the landing ground roll distance. The time required for full deployment of the buckets (actuation time), the engine response time and the engine power setting at the moment of reverser selection are also playing an important role.

8.2. Aerodynamic Optimisation

Typical results of a parametric ground roll distance computation are presented in Fig. 21 with wheel braking applied as additional braking device. This graph is valid only for a given aircraft weight and aerodynamic layout. For the considered configuration a 10 per cent reduction in landing ground roll distance can for example be achieved by either improving the reverser performance η by about 12 per cent or reducing the reverser cut-off speed by about 32 % ($\Delta V_R/V_{T.D.}$ =0, 16 at η =0. 5).

As described in detail in section 3 and 4, reverser performance and cut-off speed can directly be altered with variation of the jet deflection angles. A trade-off study must be performed to decide on the optimum deflection angles with respect to reverser performance and reingestion. The extensive information obtained from the various model tests produces the basis for this trade-off. The

optimisation with respect to reverser performance and reingestion for an airplane configuration with engines mounted at close distance in the rear end and jets deflected up and down resulted in reversed efflux angles for the lower jet of about $\varphi_L = 45^\circ$ and $\Theta_L = 40$ to 45°.

Similarly the upper efflux angles are to be optimised with respect to lateral stability and reverser performance.

It shall be emphasized, that it is mainly the hot gas reingestion which causes severe problems during the development of a reverser system for closely spaced engines due to the mutual interference of the reversed jets underneath the fuselage. A thrust reverser configuration however was developed by extensive model testing which allows reasonable low reverser cut-off speeds while simultaneously maintaining acceptable performance, stability, loads and safe operation.

8.3. Thrust Reverser Operation Technique

To obtain full advantage of a thrust reverser system, aerodynamic optimisation alone is not sufficient. Landing ground roll distance can be considerably reduced by fast engine response times and by special thrust reverser operation techniques. It is essential that full reverse thrust is at once available after touch-down because at high rolling speeds wheel braking alone is less effective due to the remaining lift component. The covered distances would become large if full reverse thrust will not be available during that phase.

The landing ground roll distance can essentially be improved by initiation of thrust reversal immediately at or even shortly prior to touch-down and by short reverser actuation times. In Fig. 22 the retarding force of the thrust reverser is shown versus ground roll velocity. If thrust reversal and engine acceleration from idling is initiated at touch-down (see curve ①) in Fig. 22) an increasing forward thrust is present at first until the buckets have been deployed into the exhaust jet. When the buckets are fully deployed, the engine is further accelerating to full thrust level. Early availability of the full retarding force is desired and obtained by fast response engines. This becomes evident from Fig. 22 which shows a reduced response time when proceding from curve ①c to ①a.

Full reverse thrust will be available at much earlier time (curve ②) if a higher thrust level at touch-down is feasible. The thrust reverser can thus be operated at full thrust level over a much longer period. A similar improvement consists in initiating thrust reversal already shortly prior to touch-down (curve ③).

Having reached maximum retarding force after full engine acceleration, the thrust reverser can be operated at this condition until the reingestion speed is reached. The throttle lever must then be set to idle (curve ④) or the engine be throttled down along the reingestion boundary (curve ⑤) as experimentally established by scale model and prototype testing.

If thrust reversal would be operated as shown by curve ①c and ④ it will be questionable if the overall design of an aircraft will benefit at all from installation of a reverser system. Development aim of the reverser system must be to provide full reverse thrust at the earliest possible time after touch-down by a suitable operation technique and to move the reingestion boundary to low rolling speeds.

The order of magnitude of thrust reverser contribution to overall braking energy is depicted in Fig. 23 for a selected case. The result is largely dependent on a number of further parameters like aircraft weight, aerodynamics, runway condition etc. In Fig. 23 the retarding forces from the various braking devices contributing to aircraft deceleration are plotted versus ground run distance. The integral of the thick solid curve constitutes the total braking energy, identical to the kinetic energy of the aircraft at touch-down. For the nose wheel only rolling friction has been considered. Conventional braking using the main wheels absorbs a major part of the overall energy for the considered case. Full main wheel retarding force can be applied only after touch-down of the nose wheel. Aircraft drag also contributes to aircraft deceleration but reduces rapidly with diminishing rolling speed.

The thrust reverser retarding force in this diagram corresponds to an operation technique with a slow engine acceleration as shown by case ①c in Fig. 22 and a high reingestion speed (case ⑤a in Fig. 22). The contribution of the thrust reverser to overall braking energy is considerable for that type of operation. Shorter response times and lower reingestion speeds will further improve the contribution of the thrust reverser to overall braking energy.

The presentation of braking energy by corresponding areas (Fig. 23) will be a substantial aid during the optimisation process: it has been found for example during the study that improvements of the thrust reverser operation technique during the acceleration phase of the engine are more advantageous than reducing the reverser cut-off speed to extreme low rolling speeds.

9. CONCLUDING REMARKS

An attempt has been made to summarise the highlights of an extensive test program with various wind tunnel and static models carried out during the development of a target type thrust reverser system by teams from different engineering groups.

Data from the model tests have supplied sufficient background for the aerodynamic optimisation of a thrust reverser to be installed in a high performance twin-engine fighter to reduce landing ground roll distance. The initial reverser configurations investigated produced extreme deterioration in longitudinal and directional stability and also required early reverser cancellation due to reingestion. As a result of careful analysis and design development it was, however, possible to achieve a thrust reverser configuration which is highly effective and at the same time quite acceptable from stability point of view.

Considerable improvements were also obtained by suitable thrust reverser operation techniques which will immediately provide high retarding forces at touch-down or at least very shortly afterwards.

10. REFERENCES

[1] W.J.Lewis, H.Prechter   Aerodynamics of Thrust Reverser Design
AGARD CP 91-71, Paper No. 10

Unpublished model test reports from static and wind tunnel tests carried out during the period from 1970 to 1973
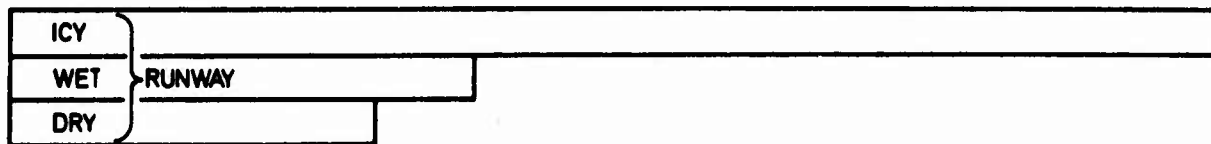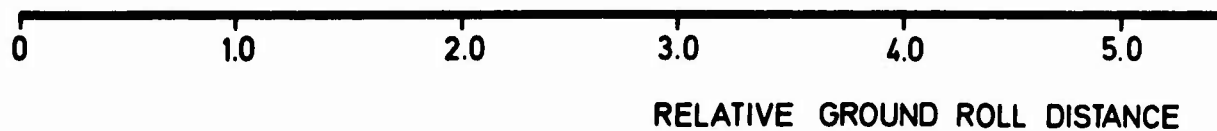
BRAKES ALONE

BRAKES + THRUST REVERSAL

RELATIVE GROUND ROLL DISTANCE

Fig. 1   Effect of thrust reversal on landing ground roll distance

INTEGRATED THRUST REVERSER WITH IRIS NOZZLE

TARGET-TYPE THRUST REVERSER WITH IRIS NOZZLE

TARGET-TYPE THRUST REVERSER, INTEGRATED IN
BLOW-IN-DOOR-EJECTOR

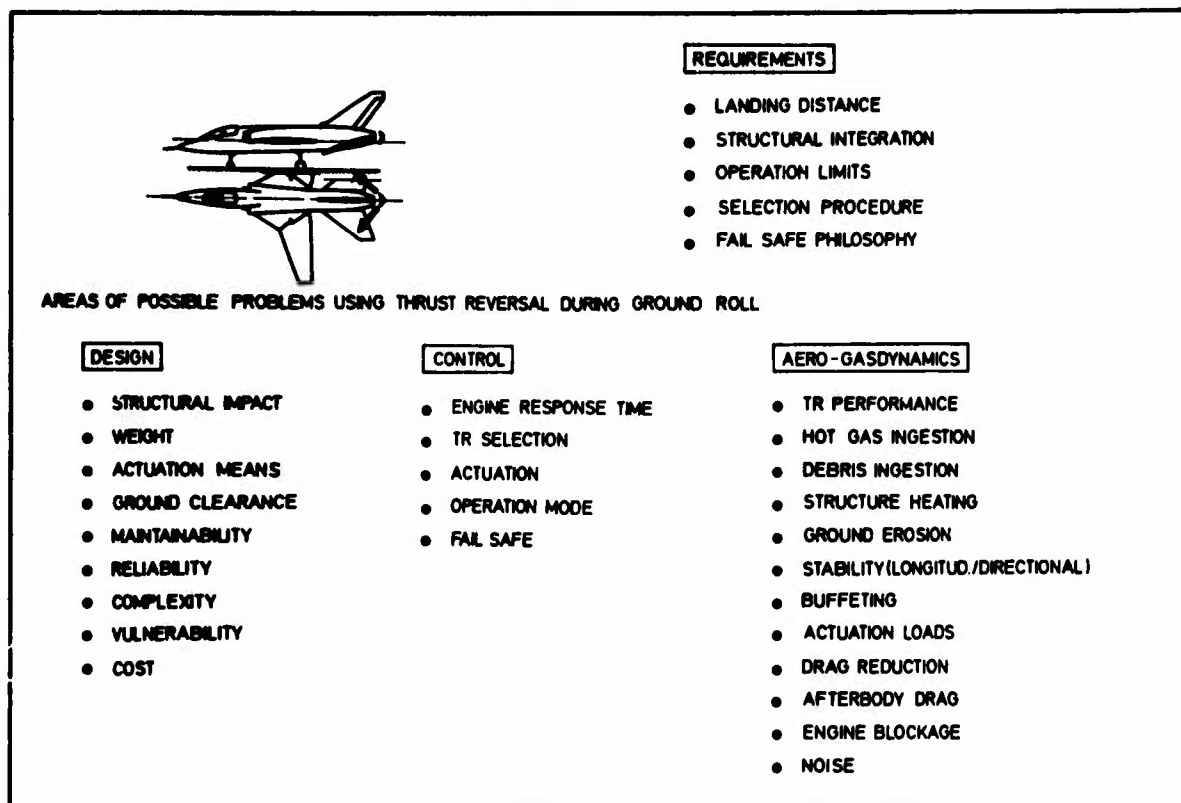Fig. 2   Thrust reverser/airframe integration

Fig. 3 Requirements and problem areas during thrust reverser development

PROBLEM	MODEL TESTS	FULL SCALE TESTS
THRUST REVERSER PERFORMANCE & STRUCTURAL IMPLICATIONS	STATIC THRUST RIG • REVERSE THRUST • BUCKET LOADS • JET DEFLECTION ANGLES • PARAMETRIC INVESTIGATIONS OF WRAP ANGLE END PLATE HEIGHT SPACING RATIO LIP HEIGHT ETC.	STATIC ENGINE TEST RIG • REVERSE THRUST • BUCKET LOADS • JET DEFLECTION ANGLES • DEPLOYMENT AND RESTOWAGE TESTS
HOT GAS REINGESTION	REINGESTION MODEL WITH HOT JET SIMULATION AND INTAKE SUCTION • LARGE LOW SPEED WIND TUNNEL • VELOCITIES UP TO TOUCH-DOWN SPEED • FLOW VISUALIZATION • FIXED AND MOVING GROUND	PROTOTYPE AIRCRAFT • TAXI TRIALS AT VARIOUS ROLLING SPEEDS AND ENGINE RPM
DEBRIS INGESTION	REINGESTION MODEL • TESTS DESIRABLE, BUT SCALING LAWS QUESTIONABLE	PROTOTYPE AIRCRAFT • TAXI TRIALS WITH CHALK CHIP TECHNIQUE
STRUCTURE HEATING	REINGESTION MODEL • TEMPERATURE SENSORS AT VARIOUS LOCATIONS OVER A/C-SURFACE	PROTOTYPE AIRCRAFT • TEMPERATURE SENSORS AT RELEVANT LOCATIONS
STABILITY	STABILITY MODEL • WIND TUNNEL MODEL WITH INTERNAL 6-COMP. BALANCE • COLD JET SIMULATION WITH BUCKETS FIXED TO EARTH • FIN BALANCE	PROTOTYPE AIRCRAFT • TAXI TRIALS WITH INVESTIGATION OF DIRECTIONAL STABILITY

Fig. 4 Experimental investigations for target-type thrust reverser development

SIDE VIEW

REAR VIEW

PLAN VIEW

s   AXIAL SPACING
b   BUCKET HEIGHT
D_j JET DIAMETER
d   END PLATE DISTANCE
h   END PLATE HEIGHT
x   LIP HEIGHT
c   BUCKET EXCENTRICITY
γ BUCKET SWEEP ANGLE
δ BUCKET TURN ANGLE
ϵ BUCKET TILT ANGLE
ψ CIRCUMFERENTIAL
      DEFLECTION ANGLE
θ EFFECTIVE JET
      DEFLECTION ANGLE
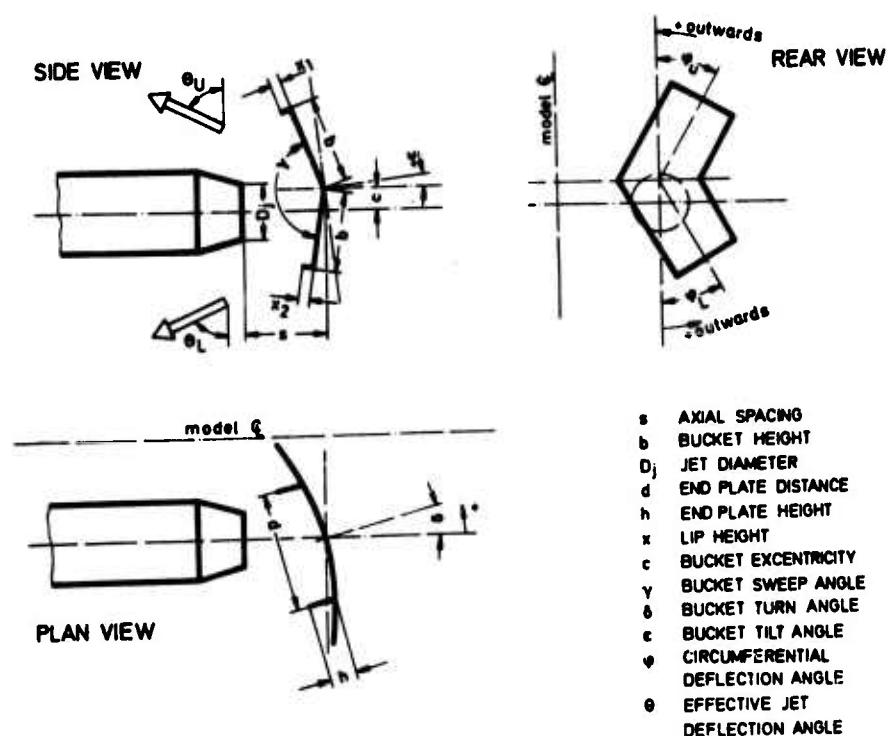
Fig. 5   Definition of geometric bucket parameters
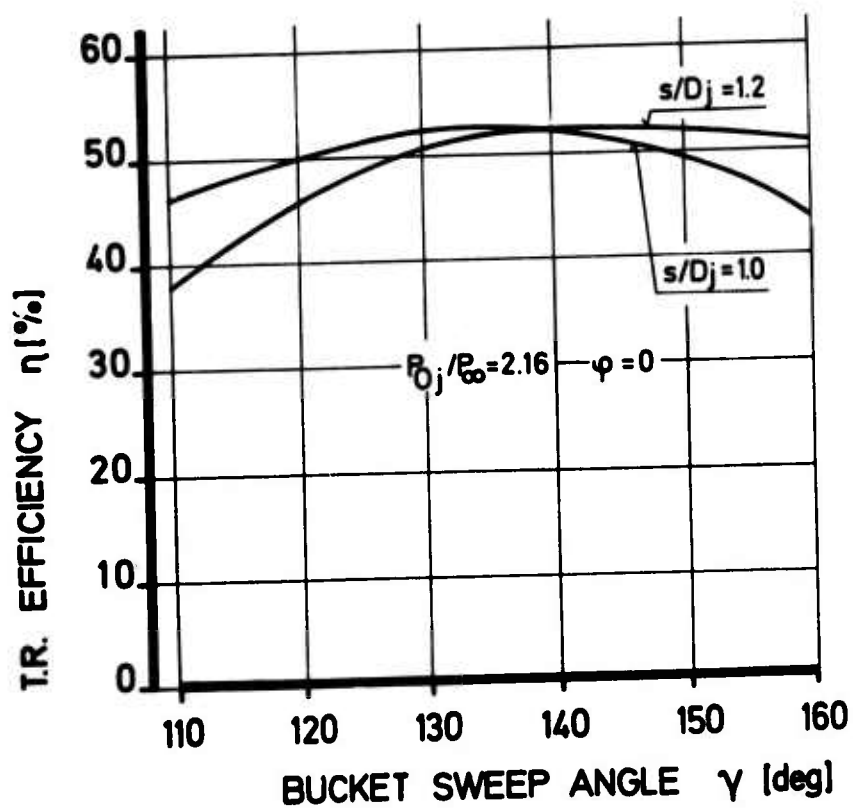
Fig. 6   Effect of bucket sweep angle and spacing on thrust reverser efficiency
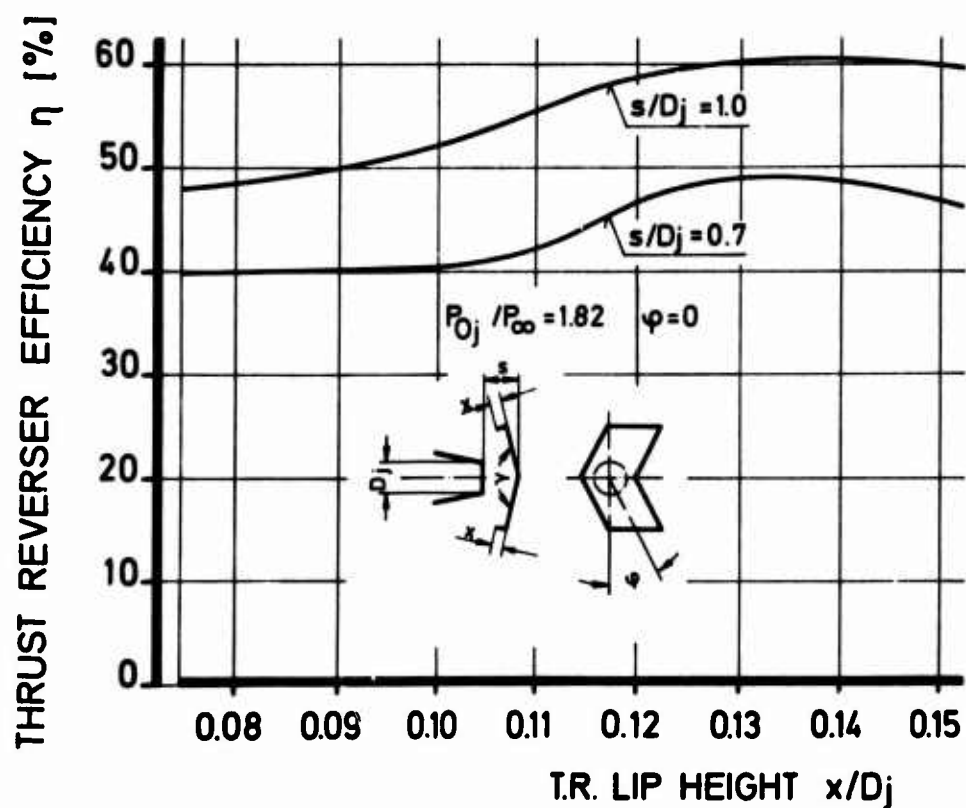
Fig. 7   Effect of lip height on thrust reverser efficiency
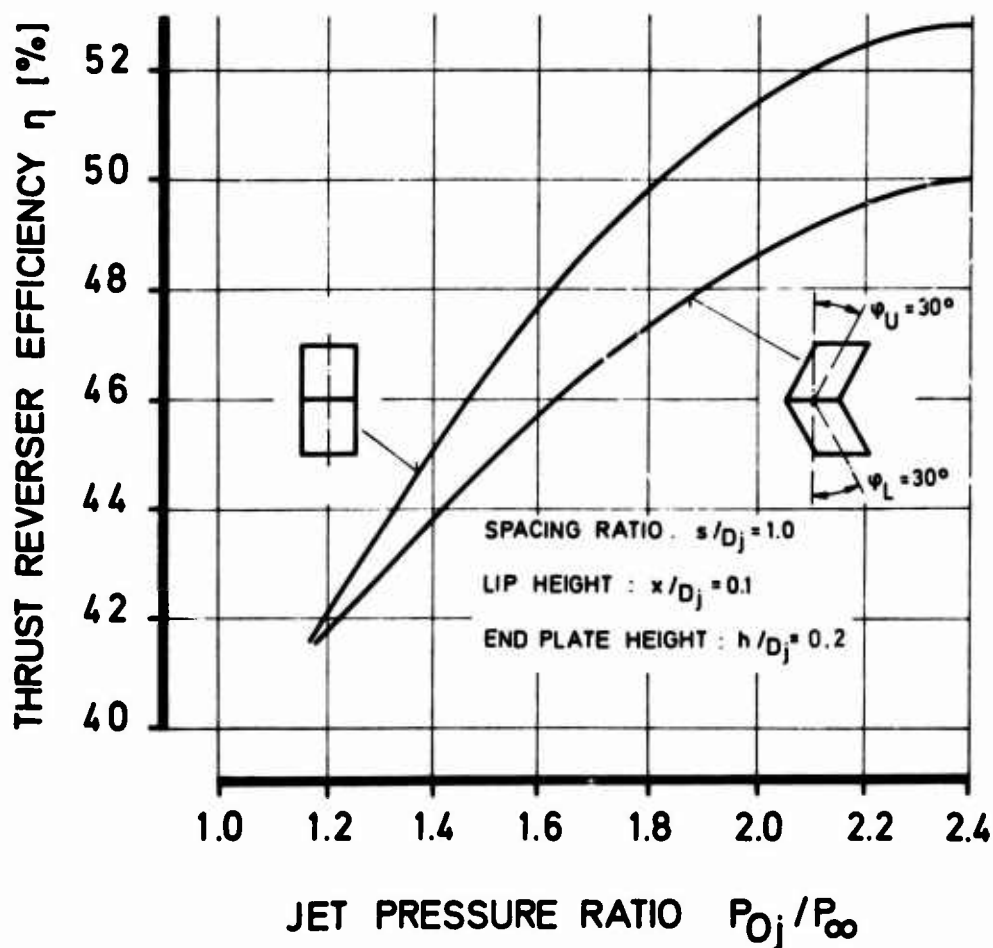
Fig. 8   Effect of jet pressure ratio on thrust reverser efficiency

Fig. 9   Reingestion model

1

$V_\infty / V_{TOUCH\ DOWN} = 0.5$

2

$V_\infty / V_{TOUCH\ DOWN} = 0.4$

3

$V_\infty / V_{TOUCH\ DOWN} = 0.3$

4

$V_\infty / V_{TOUCH\ DOWN} = 0.2$

5

$V_\infty / V_{TOUCH\ DOWN} = 0.1$

$V_\infty / V_{TOUCH\ DOWN} = 0$
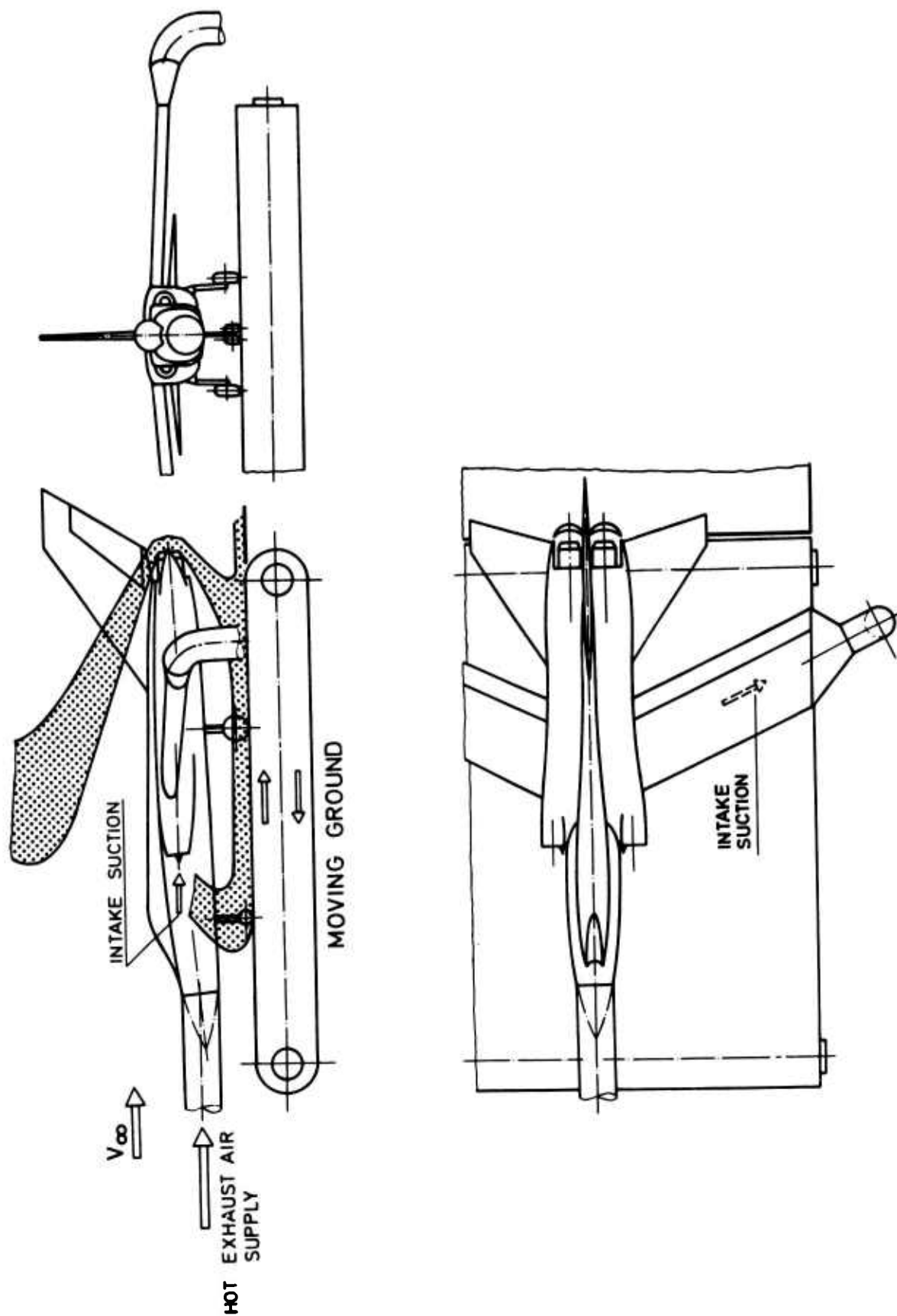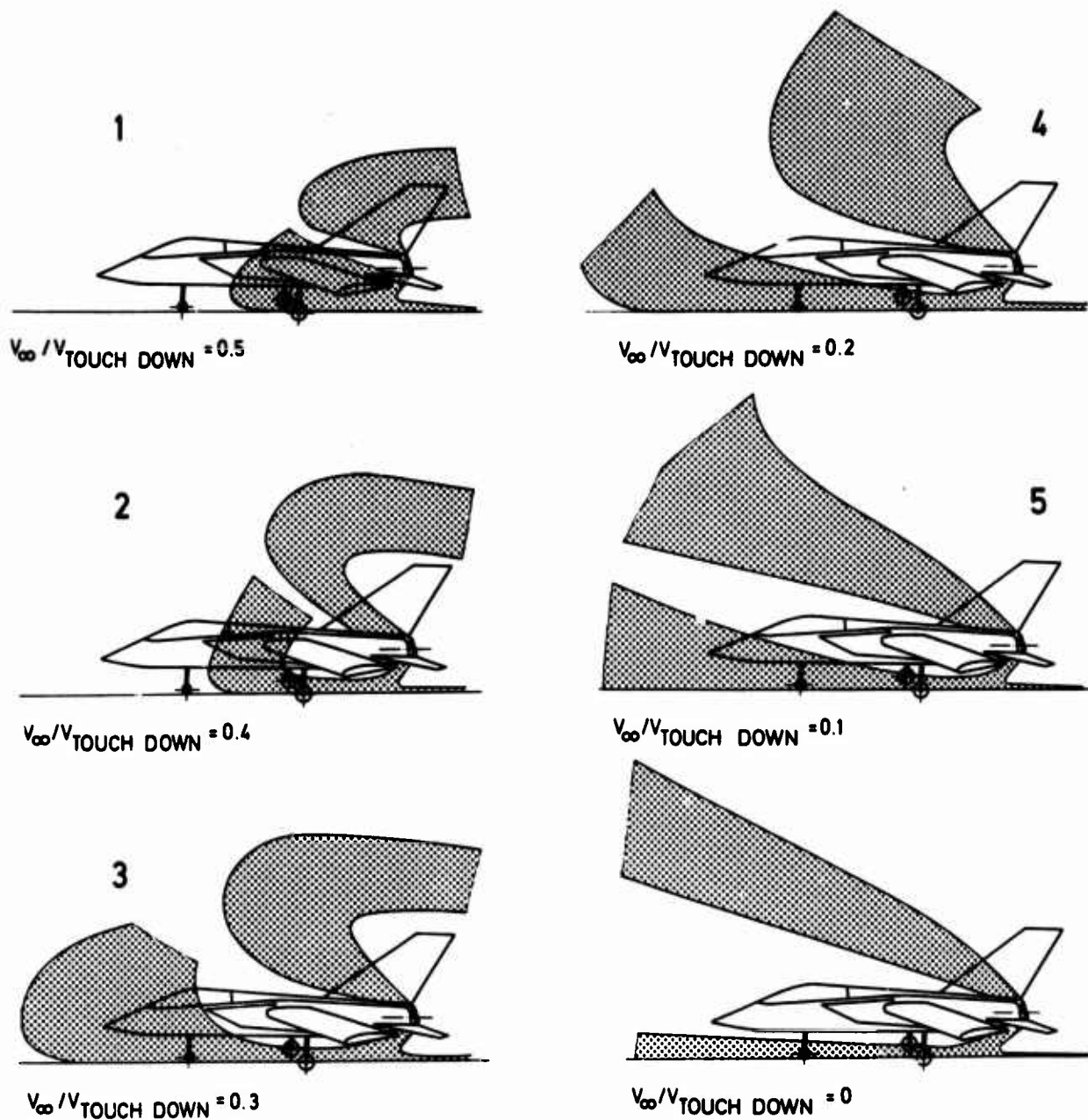
Fig. 10   Flow pattern at various forward speeds

INTAKE TEMP. RISE ΔT_i

$\Delta T_i = T_{0i} - T_\infty$

$\Delta T_{max.}$

$\overline{\Delta T}$

5°C

①

ROLLING SPEED

① REINGESTION
SPEED OR THRUST
REVERSER
CUT-OFF SPEED V_R

T_{0i}

T_∞

$\Delta T_{max.}$

$\overline{\Delta T}$

$\longrightarrow t$ [sec]

Fig. 11   Definition of thrust reverser cut-off speed
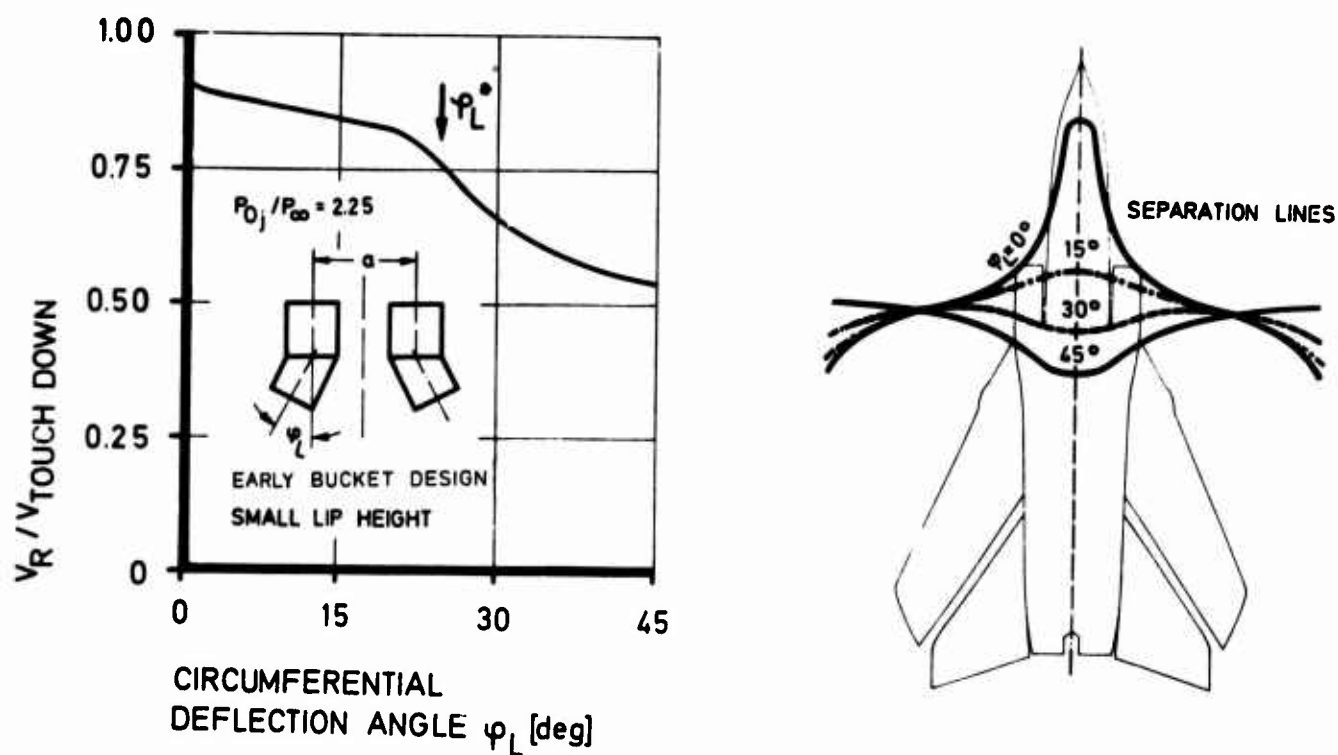
Fig. 12   Variation of thrust reverser cut-off speed with circumferential jet deflection
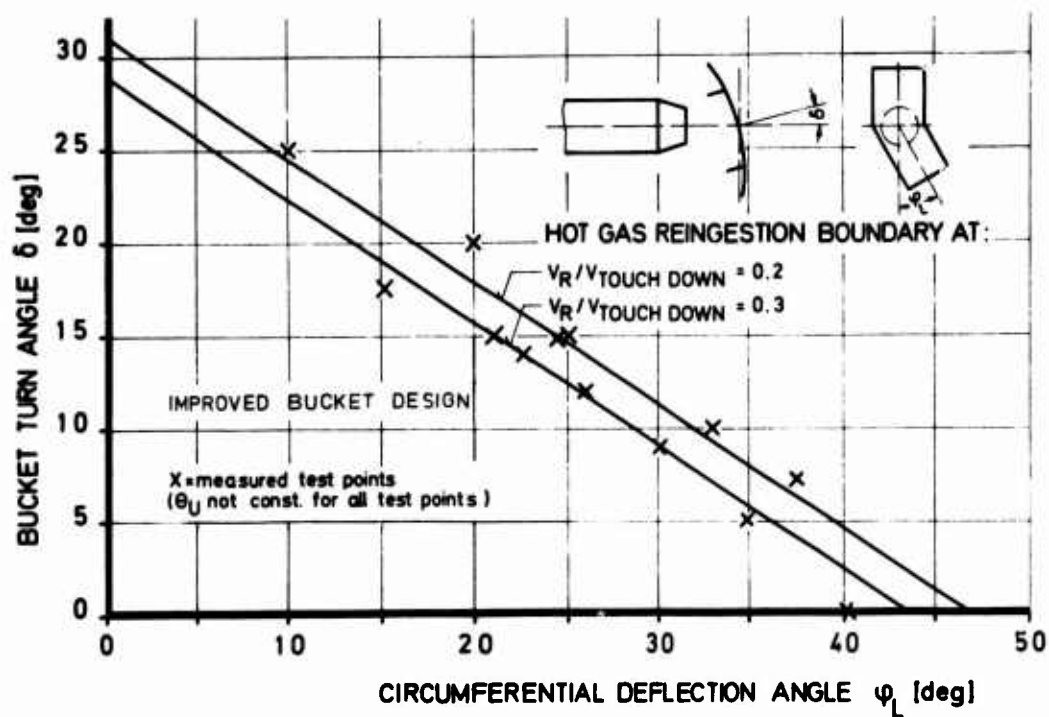
Fig. 13   Required deflection for given reingestion speed
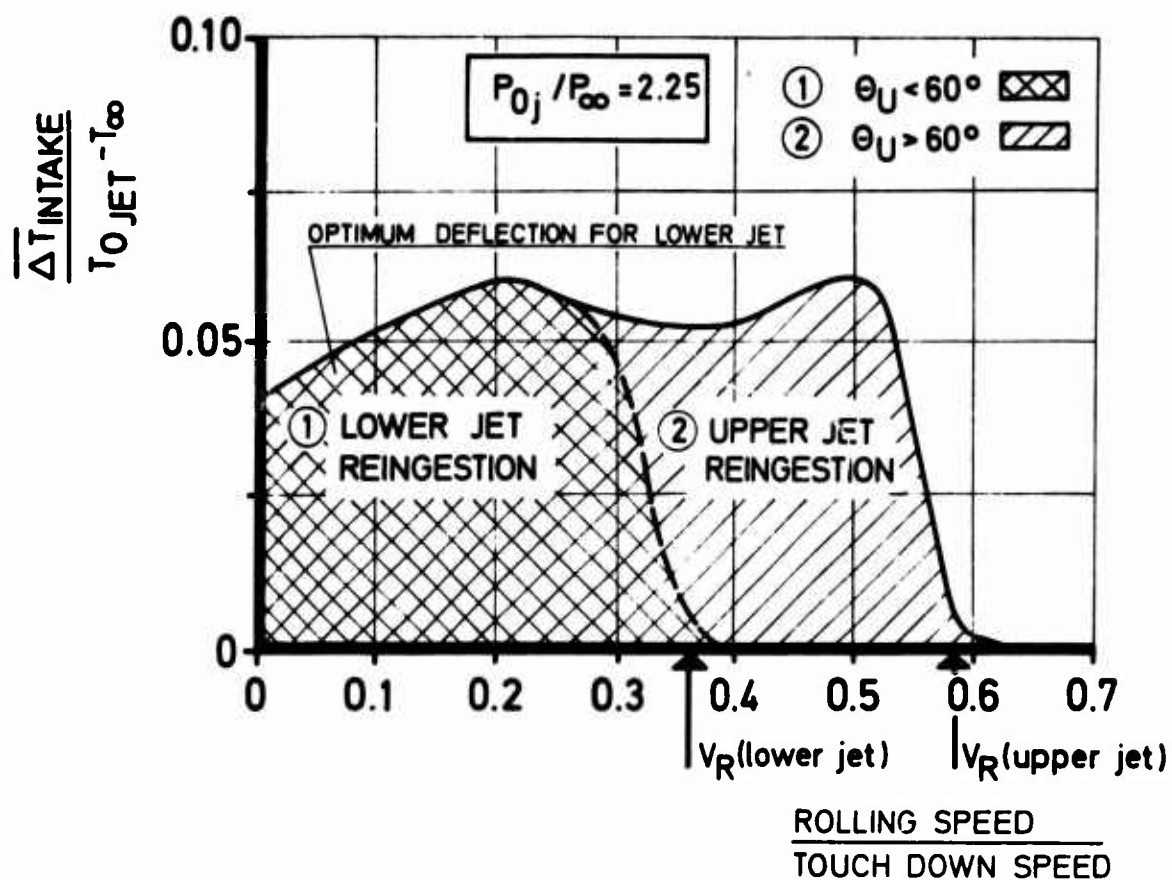
Fig. 14   Limiting upper jet deflection angle
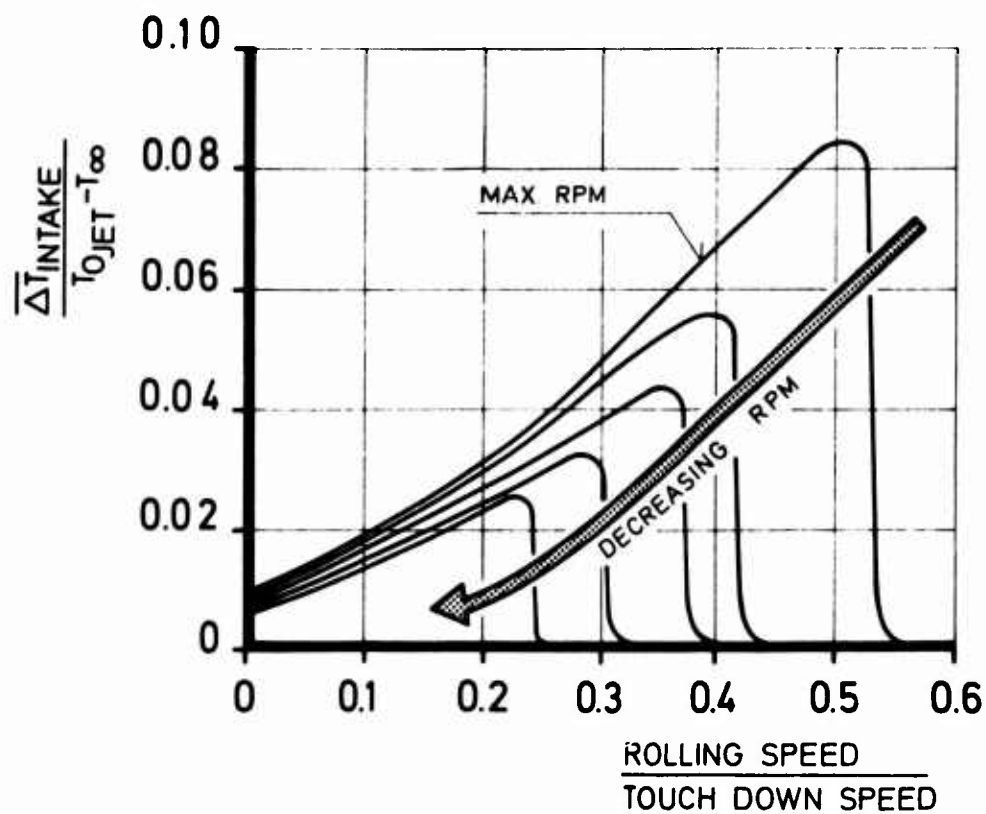
Fig. 15   Variation of thrust reverser cut-off speed and intake temperature rise
with engine power setting
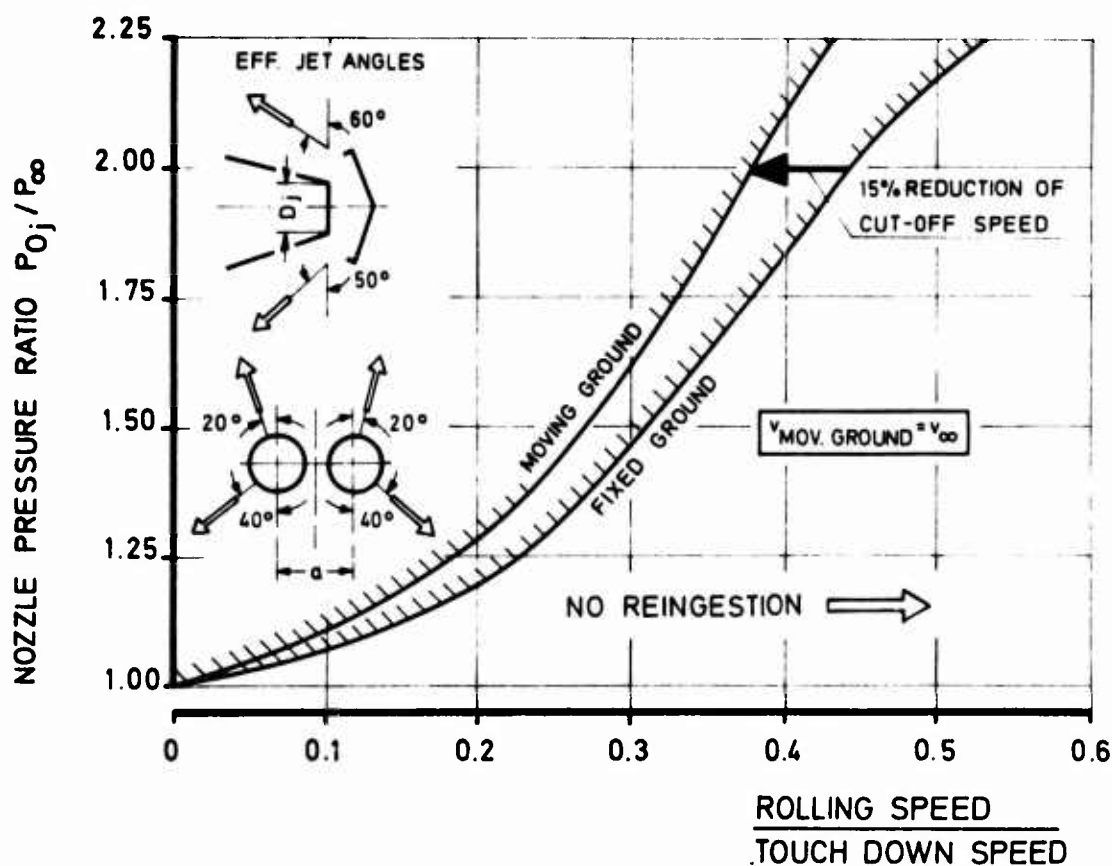
Fig. 16 Thrust reverser operation boundary due to reingestion for fixed and moving ground
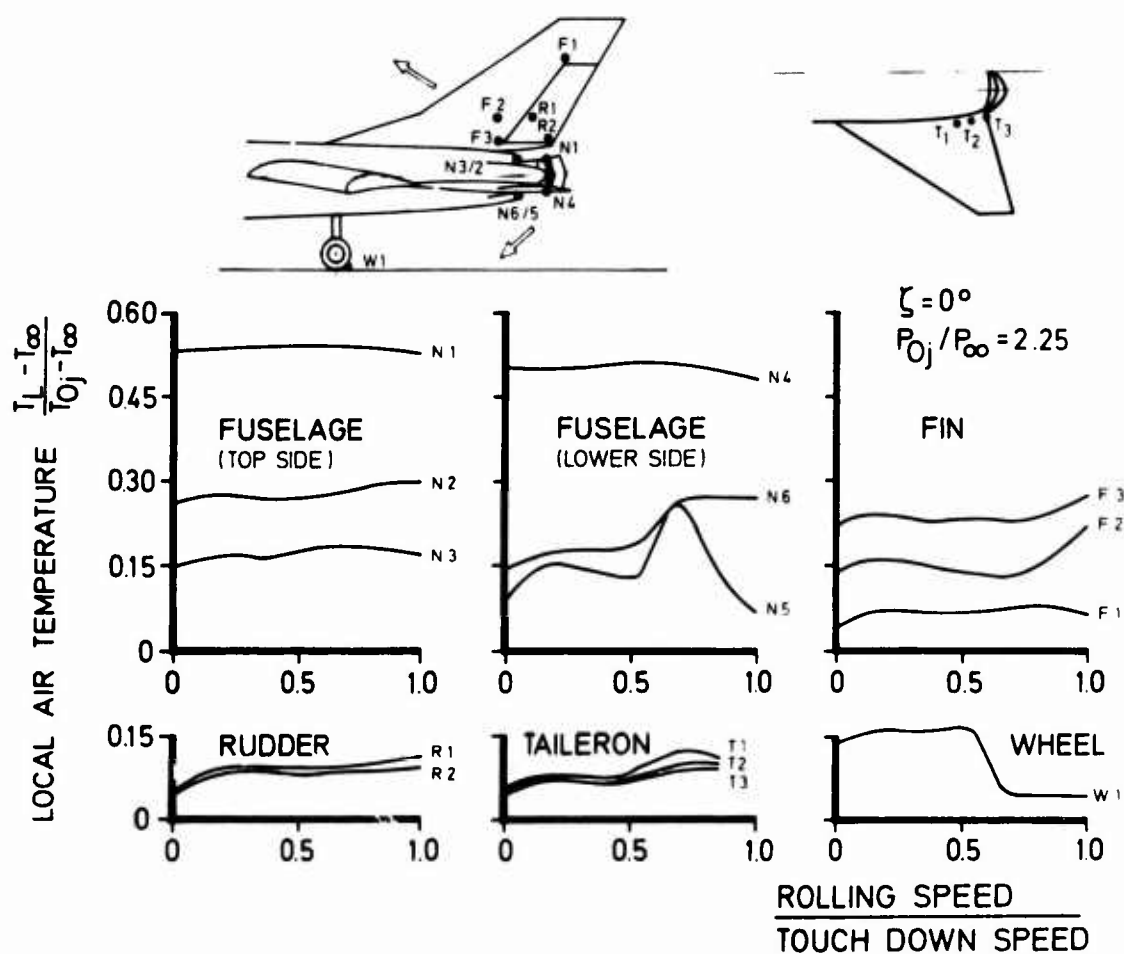
Fig. 17 Structure heating during thrust reverser operation
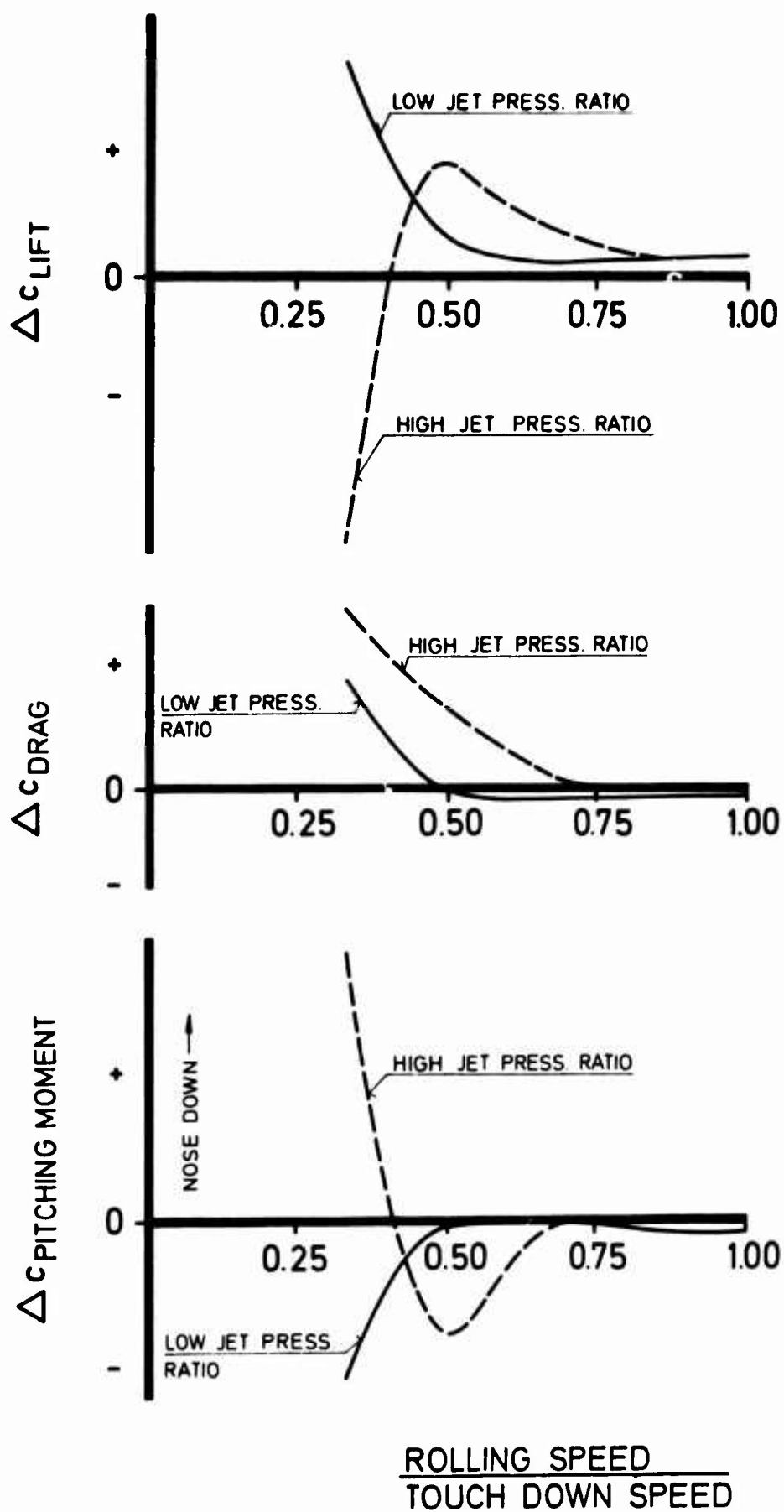
Fig. 18   Induced effect of reversed jet on lift, drag and pitching moment

SHORT CONVERGENT NOZZLE
WITH TARGET-TYPE THRUST REV.

IRIS NOZZLE
WITH TARGET-TYPE THRUST REV.
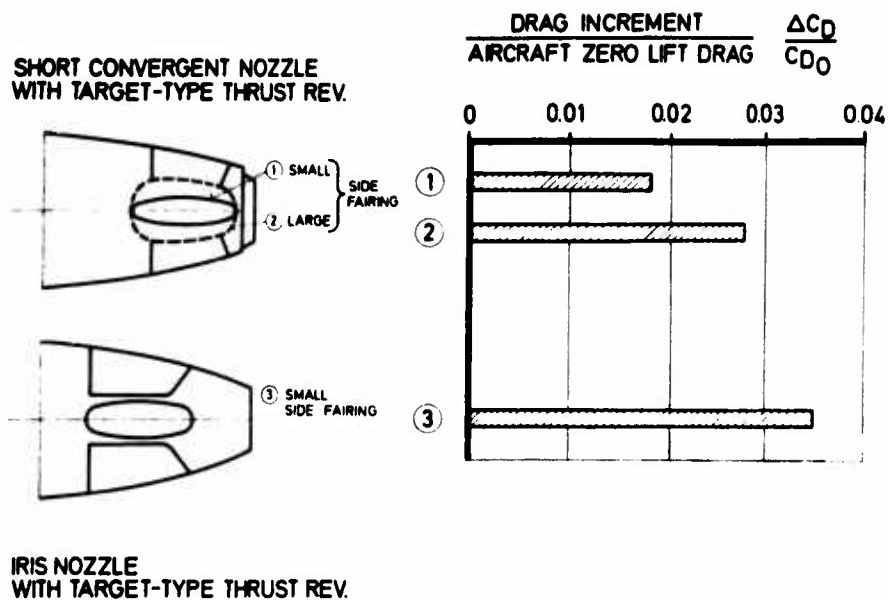
Fig. 19   Drag increment due to thrust reverser installation

1. Reingestion

2. Performance

3. Stability

4. Thrust Reverser Operation
    - Reverser initiation (prior to or at touch-down)
    - Reverser actuation time
    - Engine response time
    - Engine power setting at thrust reverser selection

Reingestion improved by: low Θ_U
Performance improved by: high Θ_U
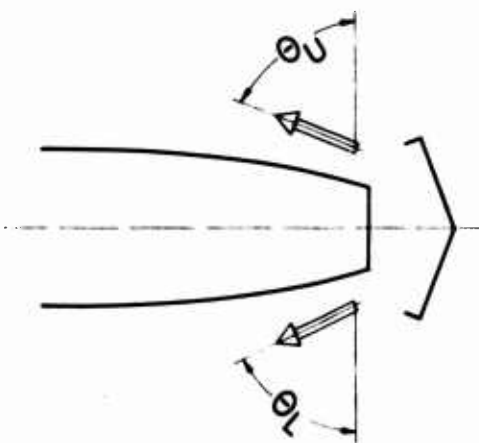
Lateral stability improved by: high φ_U
Performance improved by: low φ_U (small side spillage)

Reingestion improved by: low Θ_L
Performance improved by: high Θ_L
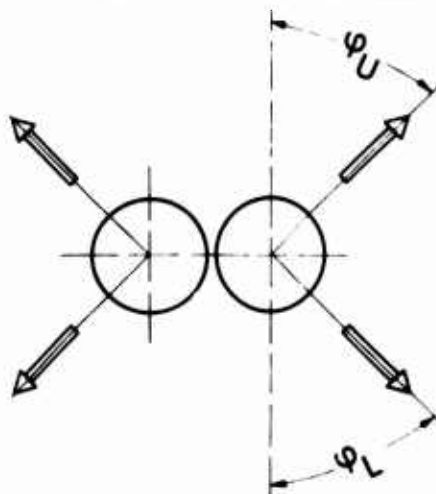
Reingestion improved by: high φ_L
Performance improved by: low φ_L (small side spillage)

Fig. 20   Parameters involved in thrust reverser optimisation
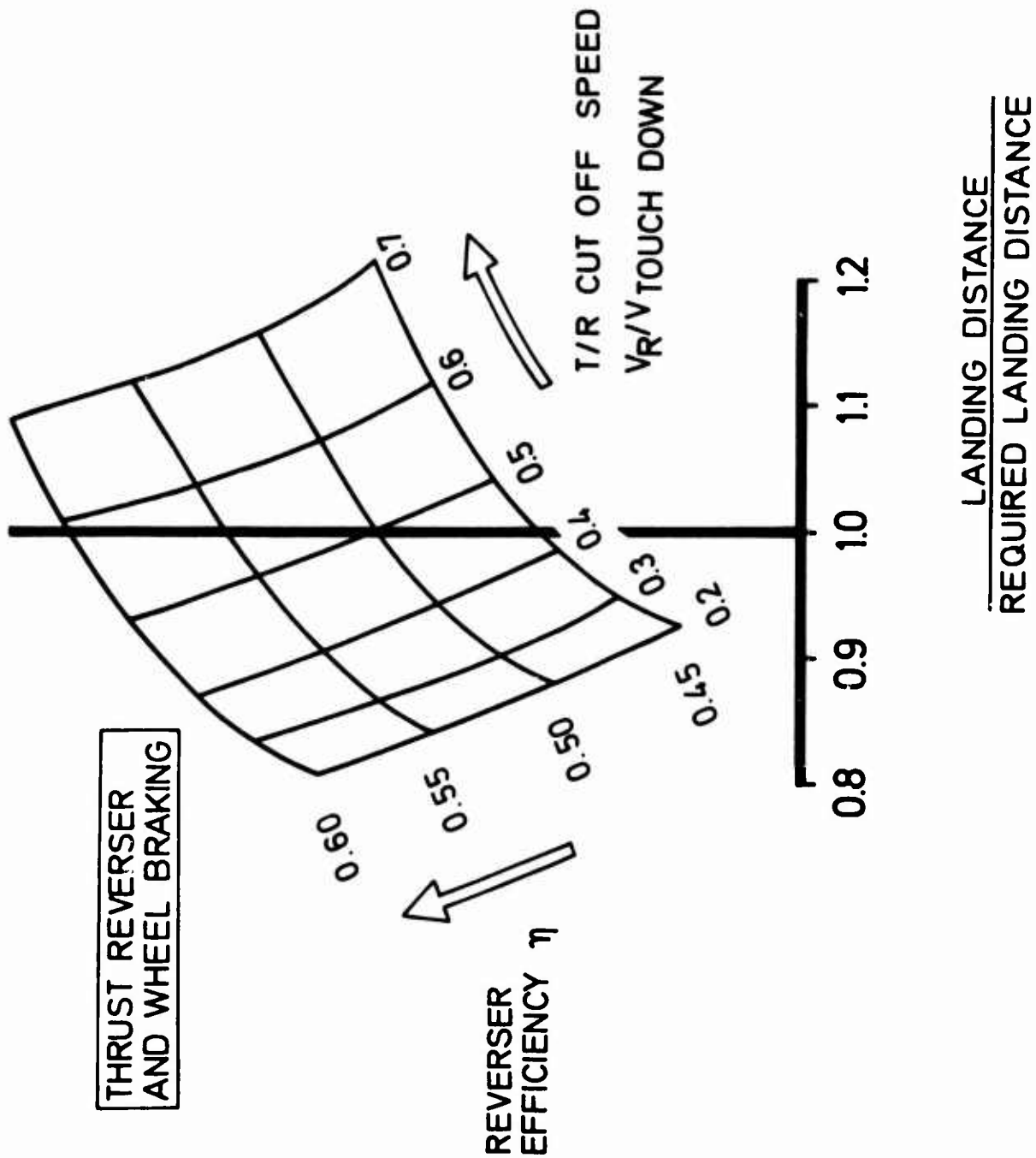
Fig. 21   Variation of landing distance with thrust reverser efficiency and cut-off speed
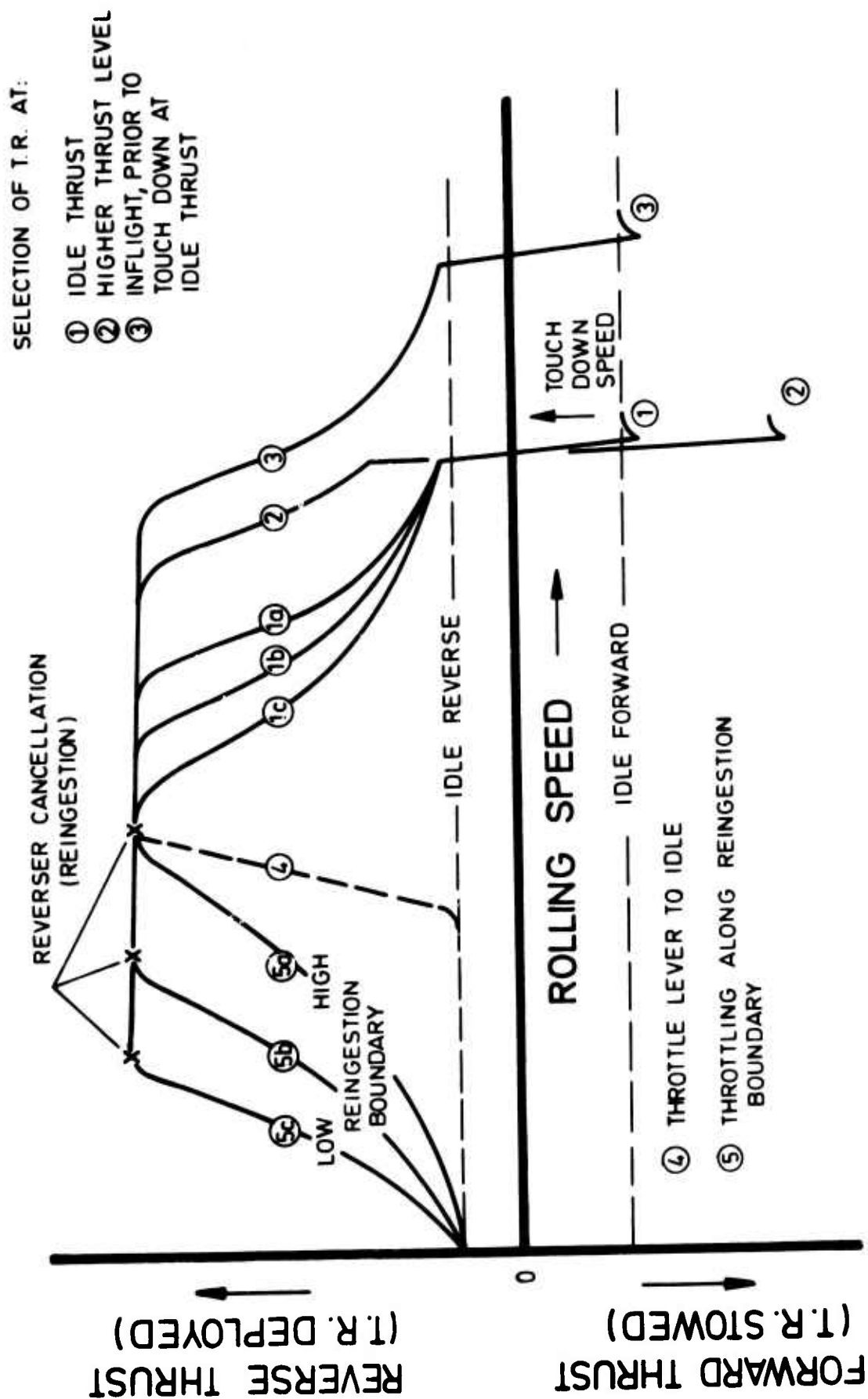
Fig. 22   Gross thrust during thrust reverser operation
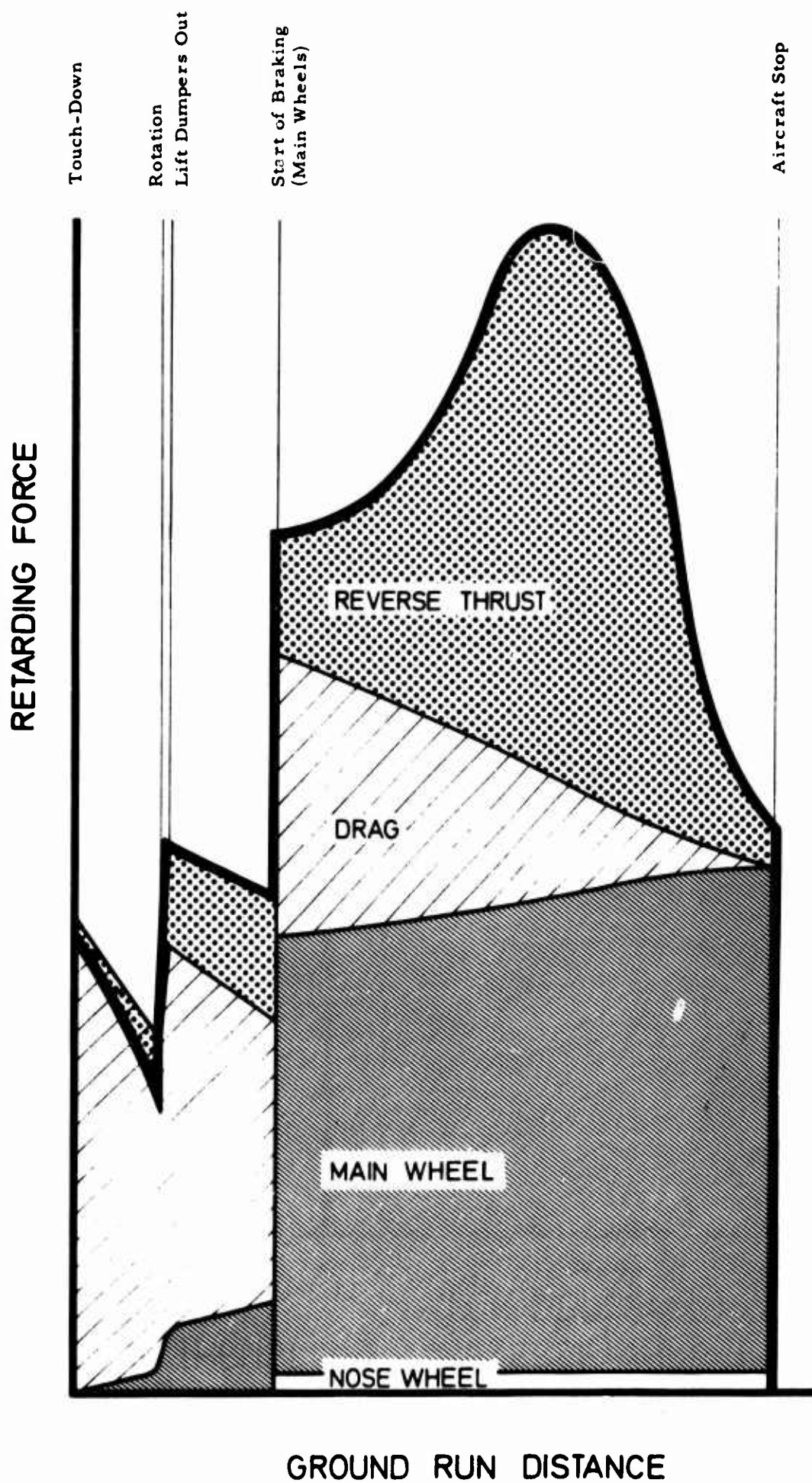
Fig. 23   Contribution of thrust reverser to overall braking energy

A P P E N D I X

ROUND TABLE DISCUSSION AT
CONCLUSION OF SYMPOSIUM

Mr P.P.ANTONATOS (Chairman) :   Flight-Mechanics Div.
Wright-Patterson AFB,
USA

Mr M.P.CARRIERE   ONERA
Châtillon
France

Professor A.FERRI   New York University
Long Island, New York
USA

Mr E.C.CARTEP.   Aircraft Research Association
Bedford
U.K.

Professor J.BARCHE   FVW-Fokker GmBH
Germany

Mr F.JAARSMA   NLR
Amsterdam
Netherlands

ROUND TABLE DISCUSSION

Mr Antonatos: I would like to introduce the participants in the Round Table Discussion. First, on my left, your right, is M. Carrière of ONERA, France. Next to him is Dr Ferri, from the U.S. Next is Mr Ted Carter of ARA, UK. Then, on my right, your left; first is Dr Barche, VFW-Fokker, Germany, and finally Mr Jaarsma of NLR, Netherlands. I think in the last few days we have seen a very interesting collection of papers on the two subjects that are very critical to understanding the total airframe propulsion system integration phenomena. It would be a little presumptuous on my part to try to summarize all the various conclusions or part conclusions that have been reached, but it was interesting to note that in the first session on air intakes there was an emphasis, of course, on buzz phenomena. I am sorry that we did not have more papers and more discussion on the inlet and inlet performance, since I personally consider this a very critical area in the design of an aircraft. The stability phenomena that can occur, especially at off-design points, can cause a major deficiency, not only in the performance, but in the manoeuvring capability of the aircraft. I feel that the phenomena that have been discussed, require much closer attention than we probably have given them in the past, and the details of this should be expanded, so that we can assure ourselves of a more accurate definition of the flow phenomena that cause these instabilities. In addition, of course, from the pure performance viewpoint, the bleed flow requirements, the spillage drag, all play a very important part in the specific importance of any particular aircraft. In the nozzles and afterbody sessions, including the wind tunnel testing and flight correlation, we did discover quite a number of interesting facts, that is, data that are applicable to the design of afterbodies and nozzle installations. It was apparent that, at this point in time, there can be no final conclusions from the results that we have seen because the testing techniques play a very important role. Although at certain Mach Numbers the data showed somewhat inadequate correlation, at the higher transonic speeds it became obvious that the correlations still lack an adequate understanding of the phenomena that are occurring. Probably, as Dr Ferri pointed out, there are other parameters that should be investigated a lot more closely than has been done in the past, before we can reach a very definite position on understanding the complete nozzle flow conditions and be able to establish drag values that would be highly accurate and applicable to the performance of aircraft. It was also very interesting to sit through the discussions on the PEP/Fluid Dynamics Panel Ad Hoc group, again highlighting very specifically some of the discussions that took place in the earlier sessions.

In the halls, occasionally I was asked the significance of some of these parameters with respect to total flight vehicle capability. I have taken this opportunity to ask for your indulgence to look at a few viewgraphs that we prepared back at the Flight Dynamics Laboratory to give some indication of the importance of the losses that we have been discussing.

SOURCES OF INSTALLATION LOSS AT PART POWER SUBSONIC CRUISE OPERATION
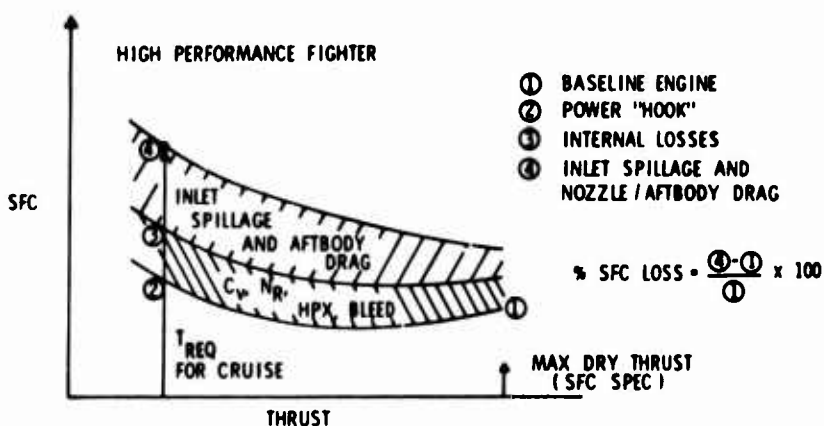
Figure 1

On the first viewgraph you can see a plot of the sources of installation losses for 3 classes, for part power subsonic cruise operation. The plot is specific fuel consumption versus thrust. The arrow on the right is an indication of the maximum dry thrust of the bare engine. Way on the left, is the thrust required for a cruise condition. The items 1 through 4 are shown as: 1 the baseline engine, 2 the curve of the power hook, and from 2 to 3 the internal losses that can occur on an aircraft, including bleed, horsepower extraction, off-design on the inlet pressure recovery

and also the nozzle coefficient. Added to that would be inlet spillage drag and afterbody drag. All these tend to severely increase the specific fuel consumption of an aircraft.

INSTALLATION PENALTIES AT SUBSONIC CRUISE
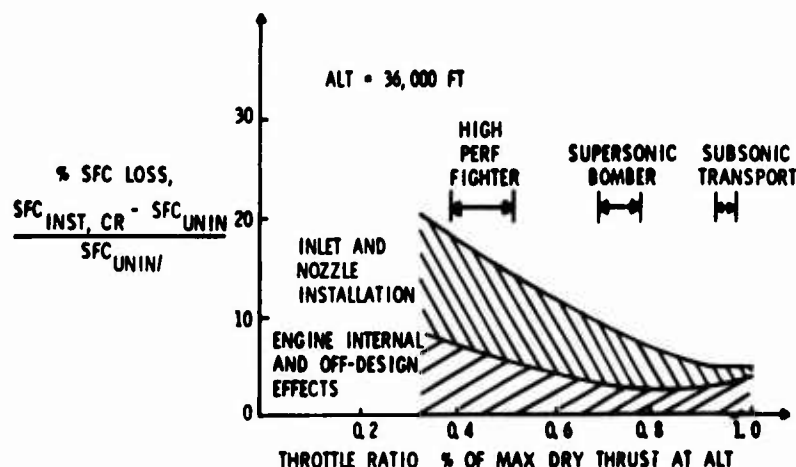
Figure 2

On the next figure is shown the percentage of SFC loss plotted for percent throttle ratio as against max dry thrust at altitude. Here again, we see the delineation of the various losses that can occur and specifically outlined or bordered by three types of aircraft; the high performance fighter, the supersonic bomber and a subsonic transport. You can see that losses of SFC as high as 20% can occur for a fighter in a cruise condition, whereas the losses in a subsonic transport can be much less than 10%. Of course, in a transport design, it is a specific point design aircraft, and therefore, the losses can be completely minimized as compared to what can be done in a military aircraft. In the

EFFECT OF PROPULSION INSTALLATION ON SUBSONIC CRUISE EFFICIENCY
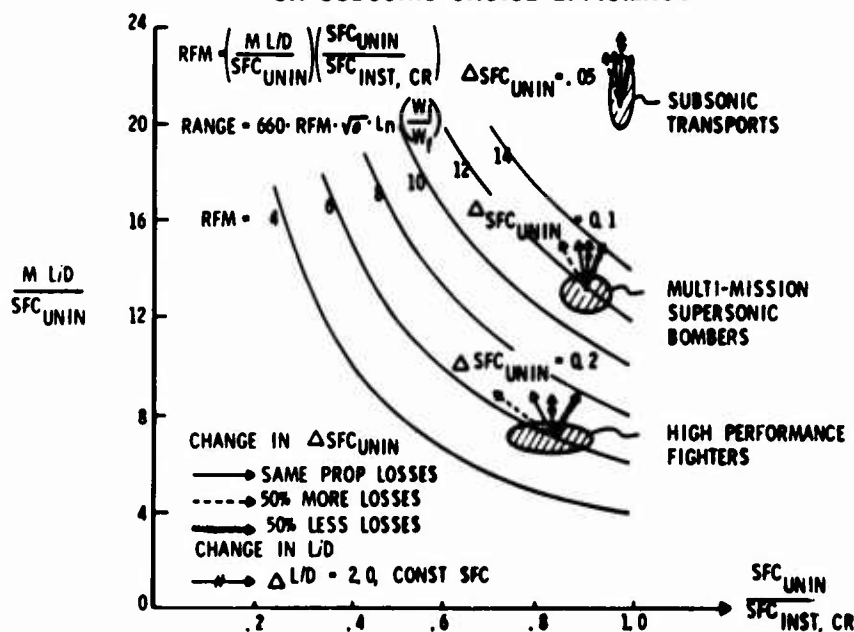
Figure 3

next viewgraph is a plot of the range parameter versus the ratio of uninstalled specific fuel consumption to the installed SFC for equal, constant range factors. Here again, in the little circles are the areas for the specific type of aircraft; the lowest one being again on the high performance fighters, the middle one on supersonic bombers and the upper one, of course, on the subsonic transports. The vectors here show what can be the result of increasing or reducing for example the losses in the installation and, at the same time, what the effect of L/D improvement can be in relation to the losses. As you can see, the vectors can either follow a constant range factor line, or be normal to

it and show a decided increase either in range factor or in equivalent range factor, due to the accuracy of estimating the losses which can occur. With these three viewgraphs, I have tried to indicate what the importance can be of understanding the specific problems and the application of these problems to the design of aircraft. With this initial comment, I would like to ask the members of the Round Table to carry on with the discussion. Hopefully, we can engender more comments from the floor. We will be willing to answer any questions that you will pose. First I would like to have M. Carrière.

M. Carrière: Mon commentaire portera sur la première partie de notre réunion. C'est-à-dire, le problème des prises d'air et de leur interaction avec le reste de la cellule. Ce problème a été, à mon avis, convenablement couvert par les différents papiers qui ont été presentés. Les points de vue essentiels concernent l'évaluation des performances, les problèmes de stabilité, et l'influence que la prise d'air peut avoir sur l'écoulement externe autour de l'arrière-corps. Ces points de vue sont nuancés suivant qu'il s'agit d'un avion commercial ou d'un avion militaire. Enfin, un troisième aspect de nos travaux concerne les apports que la théorie ou l'expérience peut actuellement fournir à ces recherches. Je parlerais de trois points principaux. D'abord, le problème des performances. Je crois que ce problème a été particulièrement bien traité par la conférence d'entrée de M. Leynaert, en ce qui concerne spécialement un avion commercial tel que le Concorde. M. Leynaert a montré que les connaissances actuelles théoriques et expérimentales, ainsi que les données empiriques déjà acquises permettent, dans chaque cas particulier, de découvrir une solution satisfaisante et de la vérifier expérimentalement avec une excellent précision. Les méthodes spécialement expérimentales ont été discutés plus en detail dans des papiers de M. Thornley et M. Carter, M. Callahan, et un aperçu général a été également donné par M. Brazier et M. Ball.

Le deuxième point concerne, comme vient de la souligner le Dr Antonatos, le problème de la stabilité de l'écoulement. C'est un problème trés important, spécialement pour l'avion militaire. Il ne servirait à rien, en effet, de réaliser des performances sensationnelles en configuration de croisière, si la moindre manoeuvre déclenchait le buzz. L'interaction de la prise d'air et de l'écoulement autour de la cellule joue, de ce point de vue, un rôle qui peut-être déterminant et qui a été analysé par plusieurs auteurs. Le Dr Hall, en particulier, nous a montré l'intérêt d'un critère simple qui permet de caractériser les risques de buzz pour une entrée d'air en fonction du champ d'écoulement devant l'entrée de la prise d'air. Les exposés de Callahan et Richey ont également montré l'influence du positionnement de la prise d'air par rapport au fuselage en ce qui concerne la stabilité et la performance. Dans ces problèmes, la théorie peut donner quelques indications sur la structure de l'écoulement incident devant la prise d'air. Je pense par exemple à la théorie de Moretti. Mais il semble, en tout cas, indispensable de recourir à l'expérience pour une telle caractérisation, notamment dans le cas des forts angles d'incidence et de dérapage. La mesure des spectres spatiaux temporels de la turbulence dans l'écoulement interne, c'est-à-dire, à la sortie de la prise d'air, commence à être practiquée couramment avec la finesse nécessaire pour préciser le problème d'interface avec le moteur.

Enfin, le troisième point que je mentionnerai concerne l'influence de la forme du bord d'attaque de la prise d'air sur les performances d'arrière corps spécialement dans les régimes subcritiques. Ce que nous savons maintenant sur les profils d'ailes transsoniques permet d'affirmer que la forme locale du profil de lèvres de la prise d'air et le nombre de Reynold peuvent modifier considérablement, par exemple, la transition de l'écoulement sur l'arrière-corps et, par conséquent, les conditions intiales du calcul de couche limite turbulente sur le carénage. A cet égard, dans les essais à petit échelle, il ne suffit pas, comme on le fait souvent, de représenter seulement l'épaisseur relative du profil. La forme detaillée du profil est également très importante. Ce point ne doit pas être perdu de vue, spécialement dans les essais de configuration complète en soufflerie. Dans ces essais, en effet, l'échelle rend difficile de respecter la similitude géométrique et elle impose également des nombres de Reynolds beaucoup trop faibles. Dans ces conditions, non seulement la performance, mais aussi les conditions d'apparition d'instabilités pourraient être fortement faussées. Dans l'ensemble, à titre de conclusion, je pense que les progrès réalisés d'une façon constante depuis quelques années, aussi bien en théorie, que du point de vue expérimental, permettent de penser que nous disposons actuellement des éléments suffisants pour mener correctement au sol une étude de prise d'air.

Mr Antonatos: Thank you M. Carrière. I would now like to ask Dr Barche if he has any comments to make.

Dr Barche: My comments are concentrated on Session 4, Integration, Design and Accounting Procedures. In order to summarize Session 4 work, we have to answer two questions. "What was presented here", and "what can be concluded from the papers presented?" First, what was presented? Please remember that we had 6 papers on the table. Only one paper was on accounting procedures, but 5 were on intake/exhaust flow, or displacement effects in cruise/ manoeuvre VTOL flight, or for landing using thrust reversers. Generally speaking, the papers were based more or less on highly sophisticated modern flight test techniques, and the theoretical approaches are mainly applications of panel methods. What can be concluded from the presentations? First, on accounting procedures, we all know that accounting or bookkeeping procedures are of the highest interest in aircraft design. The existing company or institute-built systems have generally similar components, but no standardization exists up to now. Therefore, I would strongly recommend that the FDP should establish a specialist group to define a generally acceptable bookkeeping system, and I believe that a powerful basis has been presented during this meeting. Another point is on intake flow, and in addition to M. Carrière's comments, I would like to point out once again that we still have the problem of matching complicated airframe and intake configurations with rather sensitive engines over a rather broad flight regime. We

should not, in my opinion hope, that in the near future, the problems can be treated more analytically, since our knowledge in predicting the distortion factors in engines is still very, very small, and I believe that we should continue and extend model and flight testing as the main approach to solve that special kind of intake problem. As the third point, in Session 4 we had some very interesting comments and papers on afterbody interactions. I believe that we should leave this out here, because most probably the interaction problems will be thoroughly discussed by Dr Ferri. We should discuss however the jet flow problems which have been attacked here. It has been demonstrated in Session 4 that jet interactions are quite nicely simulated using panel methods, but there are still some main problems, and the main problem is the proper definition of the boundary conditions on a jet, especially for jets exhausting close to solid surfaces or which are in strong cross flows. We may hope that the experimental work as well as the theoretical work will continue, and in the near future we could have a better prediction technique for jet engine simulation theoretically. We had another paper on thrust reversers. I feel that thrust reverser problems are obviously interference problems which can only be treated by extensive model and full-scale testing techniques. Since the optimization is an expensive task, guidelines as they have been presented here should be welcomed and hopefully extended from other specialists in future meetings. To conclude my conclusion, I feel that the papers presented here helped us to understand complicated flow phenomena. They gave us some pretty good tools to attack those problems, but there is still a lot left to do for future meetings on that problem.

Mr Antonatos: Thank you Dr Barche. Can we now hear from Dr Jaarsma.

Mr Jaarsma: I would first like to express my appreciation to be here in this Fluid Dynamics Panel meeting, and I am talking now for the Propulsion and Energetics Panel. I really appreciate the good cooperation between both panels. In particular, in this effort we have had very good coordination, as we have also in the past; but, if we discuss such a topic, the main difference is that the Fluid Dynamics Panel calls such an effort airframe-propulsion interference, whereas the PE Panel would call it propulsion-airframe interference. This situation actually brings me to the point I would like to discuss now shortly. In this meeting the majority of the papers dealt with the influence of the engine aerodynamics on the airframe aerodynamics and how the adverse effects can be minimized, for example, by proper afterbody shaping, etc. The influence of the external aerodynamics on the engine or, being more precise, on the inlet flow field, has been considered in a few papers. However, very little mention has been made of the external flow effects on the nozzle flow field. In almost all cases in the past, the nozzle flow field was choked, at least at cruise conditions and many times at takeoff conditions as well. However, with the introduction of the new high-bypass ratio engines, (I am talking now of the civil branch of aviation) the situation becomes more complex. At the cruise condition the nozzle flow field might be supercritical, though in many instances it will not be choked. This means that owing to the external flow field and the installation effect the nozzle flow will change, yielding a different position of the sonic line and hence an altered nozzle discharge coefficient as we have seen this morning. This means that owing to installing a fan engine into an airframe, the engine will run at a different operating point with respect to static engine tests. Hence, the efficiency might alter and also the ram drag might change. This effect will increase with increase in bypass ratio. As was mentioned by Mr Groothoff this morning, there is a strong effect of external flow on the nozzle discharge coefficient. Therefore, in order to predict what will happen, it is necessary to have more knowledge of the nozzle flow field. This flow field is rather complex, for convergent nozzles which will be used in the future. Because the flow field in such a nozzle has a curved sonic line, the branch line which originates from the point where the sonic line and the streamline are perpendicular hits the slipstream line very far downstream of the nozzle lip. At this point, you will find the maximum inflection of the external flow, due to jet pluming.

In the past in computing external flow fields people assumed that this maximum inflection occurred at the nozzle lip. This is completely wrong. Therefore, we need better methods of computing the nozzle flow field in order to obtain the interaction of the external flow field and the internal nozzle flow field and then to compute the engine performance. I heard from Mr Hardy of SNECMA, that in France, hodograph methods have been developed recently treating such a problem, and I certainly encourage such an effort. To my belief, hodograph methods are the only means of better predicting such a nozzle flow field.

Mr Carter: One consolation of being somewhere near the end of the discussion is that one's prepared remarks gradually get crossed out and one sort-of asymptotically arrives at a state of having nothing left to say. Many valuable points have been raised throughout this meeting as I have learned from my diligent attendance — due to the fact that I have to write a critique of the meeting. Consequently I have a fairly overall view of the papers even if I am rather saturated.

In terms of general comments, my feeling is that having been involved in the Lecture Series 53 on the same subject 2 years ago, this meeting has shown quite considerable progress in this field of work. I think there has been a sensible recognition of the problems and the papers have not been purely statements of techniques and results. There has not been just a mass of data and there has been a serious attempt by all authors to look critically at the work they have been presenting. In some areas there is obviously a very long way to go, but there has been a serious attempt to discuss all subjects.

None of the previous panel speakers has mentioned the afterbody Reynolds Number effects. There have been

some strong views expressed and this discussion may well provide the opportunity for the audience to "have a go" this afternoon. Briefly, thinking of the points that have been made on this subject, we had the only fairly extreme view, that the current Reynolds Number trends which we are seeing, are a function of tunnel wall characteristics and the use of part-body methods. The second view was quite to the contrary, that the Reynolds Number trends that were shown were quite well validated by experimental pressure distributions, oil flows and tufts. A third view was that another parameter, other than Reynolds number, as expressed by Mr Walker could be important in the sluggish boundary layer flow on afterbodies. I have talked to Mr Walker since the meeting discussions and whilst still not being completely clear I can understand his point that there may be parameters other than Reynolds Number which, a long way back on an aircraft, could well be of strong influence. A final view was that of John Reid of RAE, who showed that use of a pressure plotted cylindrical afterbody on the back of a test rig to obtain forebody and strut interference fields was not valid for the interference correction of the base pressure answers. So we are left with many conflicting views to the effect that we can measure afterbody forces but do not believe the answers, or that we can do the job accurately but may not be using the right scaling parameters or that the correction technique may invalidate the results. So I have no doubt that the floor will talk at some length on the subject.

I am sure that this meeting has brought home to everybody that you just cannot go sticking afterbodies in wind tunnels, supporting them in multifarious ways and expecting your results to correlate with other peoples. We are at present only getting to the stage of trying to correlate with each other and cannot sift in absolute terms the right from the wrong.

Considering now the four sections of the meeting as they were presented, I would like to comment on things that I might have expected to see or hear about, and did not. Most of the papers have been related to transonic problems and I would have liked to have had some views on how far we are prepared to compromise the supersonic part of the flight mission to improve transonic operation. There is obviously a long way to go in the improvement of transonic interference performance with thickened lips and internal matching – is the supersonic penalty very significant? I would also have liked to have heard some comment on the benefits of a moveable inlet to better match the interference flow-fields. It is not beyond the wit of the designer to effect this if the benefits are significant. M. Leynaert made an excellent review of the intake problem in general. I would have liked to have seen some comment from him on the work of Nangia of BAC, who shows that our simple two-dimensional analyses of rectangular intakes are so very far from the truth that it is really surprising that we get anywhere near the right performance estimates. In the third section I would have like to have seen a little more comment on wing/pod installations. We really still do not know how to take a complete aircraft model and put it in a tunnel with fully representative inlet and exhaust flows (even cold) and devise techniques to measure and believe the drag results to the nearest 2 or 3 drag counts, which is needed.

Referring to the afterbody papers in the various sections, the thrust reverser problem seems to have been well tackled. One wonders whether, because this is a new subject, the size of the initial problems that everyone is looking at, is so large that the experimental exercise appears to be comparatively easy. I wonder whether there are other problems that are going to loom in 2 or 3 year's time where the thrust reverser may throw up problems as difficult as the current afterbodies. In particular, I expected some comments on the use of in-flight thrust reversers and their representation and interference.

In lighter vein – and I am now jumping back to the afterbody/Reynolds number flight tests – I am sure we all agree that a flight experiment over the low Reynolds Number range is needed. I now understand that Mr Wilcox is looking for a large parachute and a willing pilot!

The last item I would like to mention is Mike Brazier's paper. I do not think many of us have had sufficient time to digest a lot of what he has put there. It seems to me that he has built up an accounting procedure which most of us probably agree with in principle. He has liberally distributed a lot of correction deltas all the way along his path. This of course is where the whole performance accounting system stands or falls, can you define your delta corrections to the accuracy he needs? When somebody has read Brazier's paper in detail and picked out all his interference terms, I would like to see him write a paper to go in parallel with Brazier's, defining the experimental techniques needed to obtain these deltas, and the accuracy and methods whereby one might do this.

Dr Ferri: Everybody has been very polite, and I don't think I should be less polite, but now I will try to fulfill my duty. In this problem of engine airplane interference we are doing a tremendous amount of testing without doing a parallel amount of thinking. We are trying to use the wind tunnel to obtain absolute information. Really, you cannot get absolute information. The wind tunnel is some kind of analog machine, that, like a digital machine, helps you to determine what is a good solution for what you are trying to do. So, one main point that I have tried stressing for the last two years is that we should be sure we do not fool ourselves. This can be done, if we start to question everything that we do from the beginning. I will try to explain what I have in mind with an example, related to twin engine airplane testing. If we try to figure out how we should design the back part of the airplanes, first, we should be sure that we know what are the limitations of our testing procedure. In windtunnel testing we introduce a very large number of simplifications, which are necessary, because we cannot test a model of the airplane at the right condition without the right support, without walls. However we should be very careful to analyze the effects of our

testing simplifications. Let me give an example. We have done a very large amount of testing of twin engine nozzles. The model is supported by a big sting. The model is in a wind tunnel that has some kind of interference. The front part of the flow has not been represented, because the inlet has been faired in, and there is no flow inside. In the final report that I read, I did not see one single number which could tell me the blocking effect, due to the fact that the inlet is not represented. I know that if the flow does not go inside the engine, but goes around, this is equivalent to changing the geometry of the airplane. It seems to me that if we really do not want to fool ourselves, we should look at this effect as an important one. Secondly we have a big sting, which is necessary, because we need to bring air to the jet, but we should analyze the effect and determine that this sting does not change the flow field too much. It is possible that what is happening in the nozzle is partly due to the geometry of the nozzle, and partly to the interference. This part of the investigation is difficult, but it is possible. It requires a lot of testing, before you start to investigate the actual geometry, but it is testing which is necessary; it cannot be avoided.

The last session of the meeting has shown clearly that we do not even know how to test a single axially symmetric nozzle so that we can believe in the results. The investigation shows that around 0.8 to 0.9, we find a lot of discrepancy among different windtunnels. Two sets of tests made with the same sets of parameters do not give the same results.

In addition we should make a major effort not only to analyze better what we do, but also to improve on what we do. For example, I am convinced that the drag of the airplane, especially in twin engines could be reduced substantially, if we had the courage to look at different configurations. A simple experiment that we did at New York University (which was not taken very seriously), showed that if you inject dead air near the separation region you can move the separation region of the transonic flow a very large amount, with a very small amount of air injection. In any air intakes we have a big problem of taking care of the boundary-layer. In fact, we remove the boundary-layer with a scoop. This is dead air that we want to dispose of. In the wing we have a very large amount of boundary-layer, that such flow could be used for injection in the separation region. I did not see one single paper in all this meeting try to invent a new way of designing the nozzle. All the nozzles are axi-symmetric, everything is traditional. I feel, and I am a little old to start to be prejudiced, that we get too much involved in accounting and too little involved in new thinking. My comment to this meeting is that I would like to see more new ideas, even wrong ones, in place of analyzing to death what we have done 20 years ago.

Mr Antonatos: Thank you Dr Ferri. I would like to use one more viewgraph to show that there are some developments going on in nozzles that are not axi-symmetrical. There are some interesting concepts coming along which have unique problems of their own, but they are very helpful in the design/design performance of aircraft, from the last two speakers. I would like to show you a two-dimensional nozzle which is used from the thrusting viewpoint, but which also has a capability of changing the induced flow fields around the wing.

ADVANCED NOZZLE CONCEPT
COANDA/HIGH AR SINGLE RAMP/VECTORING
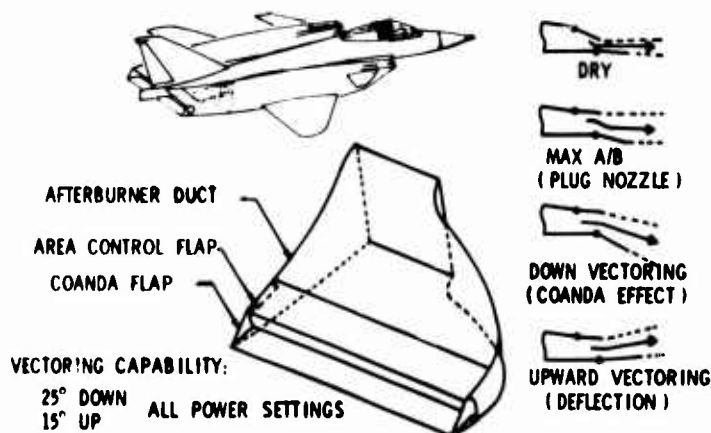
Figure 4

Therefore, through the application of a two-dimensional effect, the vectoring capability of the aft flaps, it is possible to achieve an improved thrusting condition, an improved manoeuvring condition and an improved lifting condition of the aircraft, because of induced flows through super-circulation. Programs like that, in which we change the whole concept of the aft-end of the aircraft are now being envisaged. This, of course, is not a big breakthrough of any type, but it requires a more complicated analysis than we have had on the particular axisymmetric nozzles, because it involves the total flow field about the wing, the empanage and any canard surfaces that would be used.

Mr Aulehla: In order to demonstrate the large discrepancies between the measured and expected Reynolds number effects on fore- and aftbody pressure drag, I would like to show the last slide (fig. 32) of our second paper [+].
In this diagram the forebody pressure drag coefficient $C_{DP\ FB}$ for an ellipsoid of revolution with a relative thickness of 12,5 % was computed using a simplified, hypothetical boundary layer concept which is also described in our second paper.

The simplification was considered acceptable since the main objective of this computation was to check the order of magnitude rather than to produce exact values for the Reynolds number influence on forebody pressure drag. Nevertheless, the hypothetical flow model is able to show that $C_{DP\ FB}$ is small and changes little when Reynolds number is lowered from infinity (exact value of $C_{DP\ FB}$) to practical Reynolds numbers. This is simply because at these Reynolds numbers the boundary layer displacement thickness is very small and changes little when Reynolds number is varied.

For the example of the Göttingen measurements, in which the Reynolds number was increased from 5 to 15 million, fig. 32 gives a change in computed forebody pressure drag coefficient of approximately $2 \cdot 10^{-4}$, which is about hundred times smaller than the measured decrease of $1,5 \cdot 10^{-2}$. Therefore, the change in displacement thickness can by no means explain the changes in forebody pressure drag measured in the Göttingen tunnel even when taking into account that bodies No.1 and 3 were not ellipsoids.
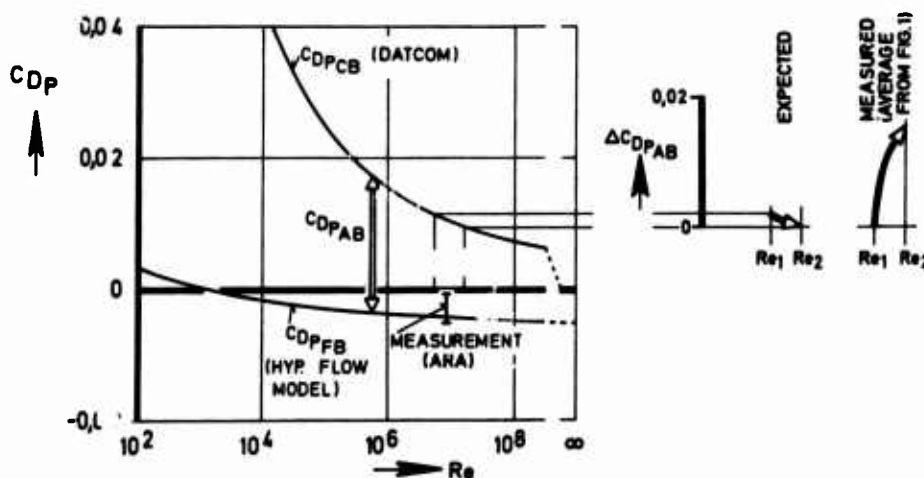

Fig.32 Decrease of pressure drag with Reynolds number

The only explanation for this fundamental discrepancy we can think of for the time being is an undetected deviation in the level of the free stream static pressure when Reynolds number was varied. This supposition is supported by the fact that

(1) the surface pressures along the whole length of the model were shifted by the same amount as the wind tunnel wall pressures when Reynolds number was varied (Fig.21).

(2) the calibration of the wind tunnel test section established for the intermediate Reynolds number, i.e. for a tunnel total pressure of one atmosphere, was used also for all other Reynolds numbers in our Göttingen measurements.

If the above supposition is correct, then the pressure drag changes on the aftbody must be of equal amount and of opposite sign to those on the forebody, which, indeed, was found in our tests (Fig.16).

The aftbody drags measured by others in different wind tunnels (Fig.1) showed a similar increase of roughly $\Delta\ C_{DP\ AB} = 0,015$ over the Reynolds number range tested. This increase is also much bigger than the expected amount. This is illustrated in the right half of Fig.32. The upper curve in the left half of this figure represents the pressure drag of the complete body computed according to the DATCOM -method. Even if this curve should not be quite exact, the figure does suggest that the aftbody pressure drag can increase or decrease only by small amounts, since the pressure drag of the forebody is virtually constant in the practical Reynolds number range.

In the same diagram the forebody pressure drag of a sting mounted ellipsoid of revolution measured in the ARA transonic tunnel is also shown for comparison. The relative thickness of this model was also 12,5 %. Within the accuracy of the test, biased by model surface imperfections, the measured forebody pressure drag agrees with the computed curve.

In conclusion it follows that part-model testing is much more sensitive to deviations in free stream static pressure than complete models. One therefore should take into account the corresponding, compensating effects on the fore-

[+]   Reynolds Number Effects on Fore- and Aftbody Pressure Drag, II (Extended and revised version of paper No.12 in AGARD CPP No.150; also to appear as MBB report No. UFE 1130.)

body, either by testing complete models or by applying appropriate static pressure corrections to the part-model. In addition, for practical aircraft design, I doubt the usefulness of testing an isolated aftbody with a cylindrical forebody since fore- and aftbody flowfields are interrelated and therefore render aircraft drag synthesis under such conditions very difficult, maybe even impossible. Perhaps somebody from the audience can comment.

Mr Antonatos: The meeting is now open for any further questions or comments from the floor.

Dr Ferri: You're assuming that this goes to zero is correct, if you do not have any shock. If you have a shock, it does not go to zero, so all this argument does not apply.

Dr Zonars: I don't think that we from the U.S. are ready to admit, one way or the other, that the Reynolds Number effects on the aft-body will drive it either up or down. We have seen it go both ways. If you are a nation that has facilities that operate at low Reynolds Numbers and have a capability to vary the Reynolds Number, you will see it go up. If you are a nation that has a high Reynolds Number capability, you may see it go down. I do not think that we are in a position to fix this, until we have some appropriate flight data, and can find out eventually what it does at the very high flight Reynolds Numbers.

Mr Aulehla: Certainly, flight tests are the ultimate proof of our wind tunnel results. However, for our particular problem and remembering the Reynolds number trends Mr Wilcox showed us today, I suggest to aim not so much for the high flight Reynolds numbers but for the very low ones in order to have some overlap with our wind tunnel data. From a discussion with Mr Wilcox I understand that such an extension of the F-106 flight envelope may be rather difficult.

Dr Zonars: Again the argument that Mr Aulehla used, relative to the pressures in the fore-body, the center body and finally to the afterbody, is a pretty good argument, but it may be representative of only a short configuration. I don't think that this is an example of the properties that exist with a long aircraft such as the Concorde. I do not know if this exists. I know that in the fighter configurations that we see we always look for the pressure distribution before the expansion in the nozzle region. There, just as we saw in the pressure distribution right before the flow goes into the expansion region of the nozzle, (and if you saw the U.S. data, you saw this in all cases), the data was the same whether the Reynolds Number varied or not, and it did come back to the free-stream conditions. So we have no apprehensions as to what occurred there versus what you have shown on a shorter body.

Mr Aulehla: I am not sure I understood you quite correctly. If you refer to the data you showed today i.e. to your contribution to the AGARD Study[+]), then you mean isolated aftbodies attached to long cylindrical centre bodies. For this case, the interrelation between fore- and aftbody flow fields should be less pronounced, however, the deviations in free stream static pressure, i.e. the "pseudo" Reynolds number effects should be clearly detachable. Or do your statements apply to other papers and to more practical e.g. fighter type configurations with their relatively short fuselages?

Dr Zonars: I don't think fighters have relatively short fuselages. To me they are long. I do not see on practical configurations, where we get the phenomena that you showed on a relatively short body.

Mr Antonatos: Keither Richey from the U.S. just ran some tests rather recently which backs up the comments that Dr Zonars was saying with respect to the long fuselage types. Do you have any comments to make?

Dr Zonars: My comments are from hundreds of experiments in the transonic speed regime.

Prof Ferri: No one talks of the real problem, the airplane. In the airplane it is all three-dimensional, so all these philosophical considerations do not apply. Mr Aulehla is talking about an axi-symmetric body, which is really an idealized problem.

Dr Zonars: That is right, he is talking about the idealized problem, I try to relate to the real circumstances. I agree with the comments you made, and they are further compounded when you must realistically put a horizontal tail, a vertical tail in there, and you manoeuvre other than at zero degrees angle of attack. It becomes a very difficult problem.

Prof Ferri: You measure only one part of the drag, so at this stage, you cannot even see if this is good or bad, and that is really what we want to find out.

Dr Zonars: My experience on the practical configuration, for a fighter which has sufficient length compared to its effective hydraulic diameter, if I may put it that way, normally does not show the characteristics displayed by Mr Aulehla in a shorter body version.

Mr Richey: I think that the question is related to the length of the body, and on a short body like that tested by Mr Aulehla, you can see the communication between the front and rear portions. On the longer AGARD nozzle aft-body configurations we did have enough cylindrical length so that we did not see the influence. I might also mention that when we retest the AGARD nozzles, we are going to measure the forebody pressures, completely along the length of the forebody, so perhaps we will be able to shed some light on this. In twin-jet fighter type aircraft configurations, we have seen for a typical length of nacelle that we can change things quite a bit in the inlet area and not change things back in the nozzle, both on the pressure distribution and the drag. However, this is very configuration dependent. If you look at Figure 19 in Mike Brazier's paper, he has one configuration where there is no difference in the afterbody drag coefficient with a faired over inlet versus the flow through inlet. He has another configuration where there is a very considerable difference on the aftbody drag, whether the inlet is faired over or not. Since it appears to be pretty highly configuration dependent, our approach has been to pressure instrument a model before deciding on a split line location.

Mr Aulehla: As to the length of our models, they have a relative thickness of 15%, which corresponds to fuselages of combat aircraft we are interested in. Besides, some of the US fighters are not so vastly different.

Also, I am not quite convinced, Dr Zonars, by your statement about the free stream conditions. In spite of the greater cylindrical centre body of the AGARD models, none of your data you presented, neither from experiment nor from theory, showed that you actually had come back to free stream conditions upstream of the nozzle: in some cases your surface pressures came close to, but just not quite to the free stream static pressure. In this context we should remember that overall pressure changes of about $\Delta C_p = 0,01$ suffice to account for typical neglected upstream influences and might also well explain some of the unexpected drag tends measured in wind tunnels.

As to your mention that varying Reynolds number did in none of all cases alter those crucial pressures on the cylinder, at least some of your data seem to disagree: your Fig.5 for example shows in fact an almost constant drop in C_p of about 0,015 over the pressure plotted cylindrical portion when Reynolds is increased by a factor of 5.

This drop in C_p versus Reynolds number corresponds almost exactly to the curve shown in our Fig.21. Thus your AEDC data for the 15° boattail at $M_\infty = 0,8$ seem to confirm our hypothesis about an overall deviation in free stream static pressure. Furthermore, if you correct for this deviation, your pressure drag coefficients change from an increasing to the expected decreasing trend versus Reynolds number.

As recommended previously, to achieve a proper drag synthesis, aftbody testing should not be limited to measurements of the aftbody alone, but should take into account the forebody as well. The planned forebody pressure measurements mentioned by Mr Richey will, therefore, be a useful contribution to our problem.

Prof Küchemann: Mr Chairman, if I may I would like to bring up another question. One of the points that were made at this meeting concerned a rather unusual installation of engine nacelles over the wing and, contrary to what most people have thought before, this turned out to be quite attractive. It had several advantages which were pointed out in the papers we have heard. One that was not mentioned was that the noise generated by the engine may be partly shielded by the wing. I do not think that was mentioned, and I would have thought it was a definite advantage of such an installation. On the other hand, the advantages may be offset by rather large drag forces, and they must come from interference with the wing and the strut. I think there may be another effect, which has been observed in some tests at the RAE, which comes in when the nozzle is not circular. On a non-circular nozzle, the flow direction on the outside of the rim of the nozzle is usually not the same as the velocity vector in the jet itself, so a shear layer is produced at the nozzle exit which has vorticity components along the stream, like trailing vortices. Tests show that such vortices do exist and that they roll up like trailing vortices. An oval exit may even have four vortex cores in the end. All these must produce some drag. What I am really getting onto is the question, would people say – perhaps Professor Barche – that there is scope for improvement; that one could shape the wing and the struts and possibly the nozzle and the relative positions, in order to reduce the drag so that this nacelle installation would in the end prove more attractive than it is even now?

Dr Barche: That is a very good question, Professor Küchemann. Indeed the shaping of the wing, and especially the shaping of the strut was one of the main jobs we had to do in designing the VFW 614. I feel that we got a good solution even at lower transonic speeds. Indeed from some tests that we did in the ARA tunnel, together with Mr

Carter, we found out that, because of the presence of the rather thick pylon, the drag at Mach numbers between 0.6 and 0.7 was reduced. This is some kind of an area-ruling displacement effect, or 2 - D "Küchemann carrots effect", which is really working there, and that we could use designing the aircraft. We believe therefore, that engine configuration, – apart from the noise shielding which is actually true, and felt on the aircraft, – is a rather attractive solution. On the other hand, and not mentioned in our paper, we had some troubles in the beginning of the design work on gust exited vibrations due to that engine fixation, mainly because the maximum thickness of the strut is somewhat behind the main wing box, and a lot of structural work had to be done to get that engine configuration working. Indeed, we must say that some aerodynamic advantages have to be paid for by our structural people. Another problem on overwing designs is that the Mach number range, where we can use overwing engines, is somewhat limited. I believe that we could have transport airplanes with overwing installations similar to the 614 design up to Mach numbers 0.8. Further increases in Mach number seem to be a very expensive approach, and I am not sure that we should have overwing installations for real transonic Mach numbers. Does that answer your question?

Mr Compton: NASA's Langley Research Center has made a preliminary investigation of Reynolds Number effects on afterbody drag. The work was done in their pilot tunnel for the proposed cryogenic high Reynolds Number wind-tunnel at Langley. I have a viewgraph summarizing the results.

PRELIMINARY RESULTS FROM AN INVESTIGATION OF THE EFFECT OF REYNOLDS NUMBER ON BOATTAIL DRAG

M = 0.6
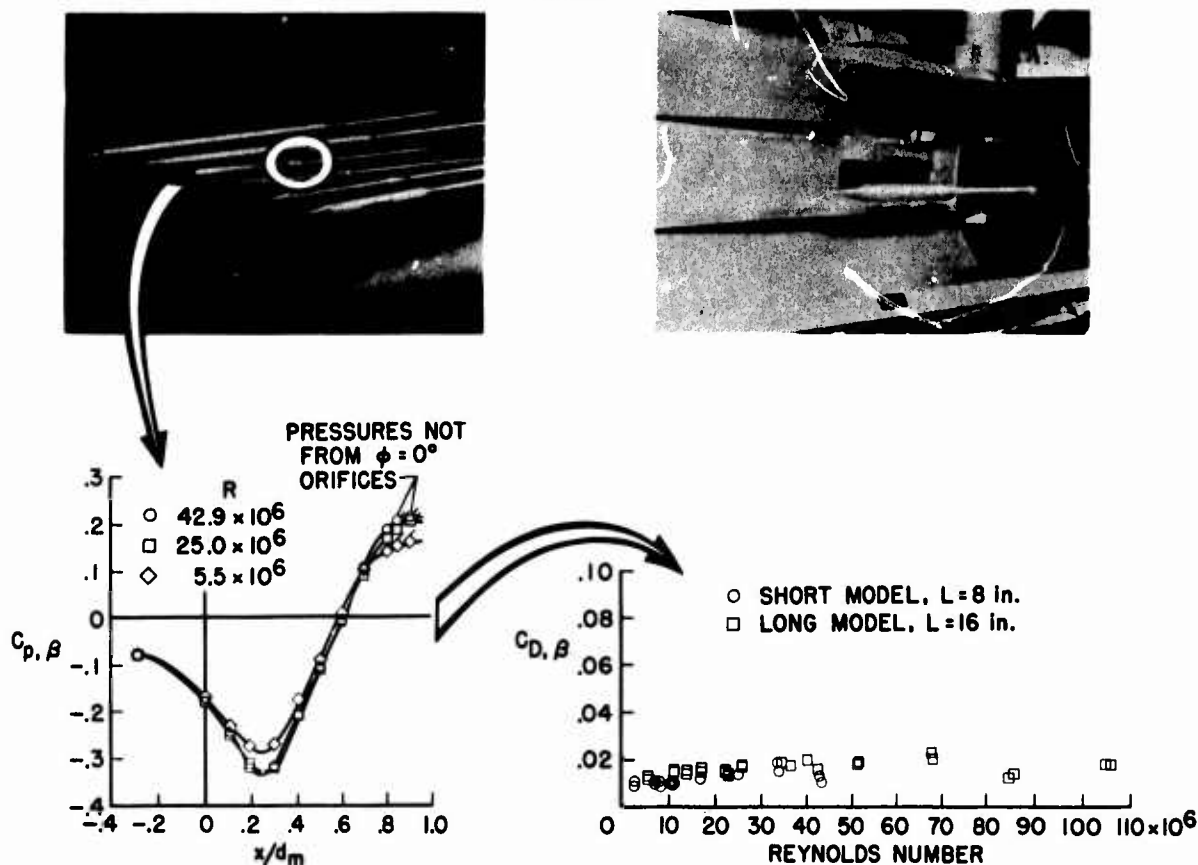
Figure 1

Two cylindrical nacelle models with fineness ratios of 8 and 16 were tested with several afterbodies installed on each model. The models were supported from the rear by a sting. This figure shows the pressure coefficient distribution for a circular-arc-conical afterbody with a fineness ratio of 0.96. The three Reynolds Numbers shown are 5.5 million, 25.0 million, and 42.9 million. The data is for a free stream Mach Number of 0.6, and is typical of the data at subsonic speeds.

Basically, the higher Reynolds Numbers resulted in an increased expansion at the negative pressure peak, and a higher recompression at the aft end, the positive pressure peak. The right side of the figure presents the boattail drag coefficient as a function of Reynolds Number for both the long and short models. The effect of Reynolds Number on the absolute value of isolated boattail pressure drag coefficient is small.

Mr Jaarsma: This still concerns the question that Mr Aulehla and Prof Ferri brought up on this influence of the fore-body on the afterbody. I would like to refer to Mr Munniksma's paper. He did the test on Airbus models. He had first a flow through model and then completely faired the inlet. Surprisingly, after about one engine diameter down-stream, he did not see any effect of closing or fairing over the inlet. He could not observe any effect on the fan cowl, on the engine cowl, nor on the pylon or wing. My belief is that at M = 0.8 you can very well fair over an inlet and get very reliable data in such a configuration. It is configuration dependent; you must be very careful on it. With this particular configuration which is quite popular for civil transport, you really can do it.

Prof Ferri: The answer to this is, if you are a very good experimental man, you can make an experiment to prove anything you like. If you want to prove that there is no effect, you can do it, but that does not mean that it is right. We spend half a day to discuss the effect of Reynolds Number, that means boundary layer thickness. Now, we have a very highly three-dimensional body, we put an arbitrary fairing that moves the three-dimensional boundary layer around, and we claim that it does not make any difference. At this stage we should stop working, because nothing makes any difference. It can be right for one configuration but it does not mean it is a good technique, unless you prove that you are right every time.

Mr Jaarsma: For that particular configuration, which is a very usual one, you can do it. Of course, here the boattail angle is very small compared with the boattail angles we discussed this morning.

Prof Ferri: Yes, for that particular configuration.

Mr Jaarsma: You have to check for angle of incidence, etc. Also for very low Mach Numbers it has been proven to give reliable results.

M. Antonatos: I have to agree that it is configuration sensitive, because we have seen results that do not give us a firm conclusion, and we have seen some specific results where you get some very unusual changes in pitching moments, by using a faired or flow-through nacelle.

Mr Jaarsma: We also measured pitching moment. The results agreed very well.

Prof Ferri: I did a very rough analysis to try to analyze the flow field of the support in some of these tests with respect to the flow field of the body. I find that the support produces a local flow field as big as the body. So I believe that the shape of the body is not the fundamental parameter. I am talking of M = 0.93 to 0.95. The point I am trying to make is that you should prove what you say before you accept it. You must do an experiment. Once you prove it, there is no question.

Dr Das: During this symposium quite a number of papers have been presented aiming to correlate or compare the results of drag and pressure distributions of afterbodies. What is often missing, in these investigations, is the unique definition of the oncoming flow and detailed analysis of the flow field about the body especially in the three sub-regions, forebody, midbody and afterbody. Also a clear definition of the flow in the jet has often been lacking.

When one defines the oncoming flow on the basis of Reynolds Number without mentioning the turbulence level, the flow is then not completely defined. The turbulence level in the tunnel or the turbulence that is created through the model mountings, as Prof Ferri mentioned, can have a large effect on the flows about the afterbodies which are investigated.

In many of the comparisons or correlations little attempt was made to analyse the flow field. A typical example which Prof Ferri also pointed out was that the inviscid flow pressure drag of bodies need not always be zero, as was assumed in some cases, because embedded shocks may be present in the flow. So one should definitely resort to detailed flow analysis before making global correlations or comparisons. One further example is the variation of the jet pressure ratio whereby it is assumed that the jet thrust is kept constant. In many of the experimental results no mention was made of how constant the jet thrust was and whether the velocity distribution in the jet was similar for all the comparisons.

Reviewing the experience we have gained here it is very necessary to concentrate efforts on three points, namely, complete details of the oncoming flow with the upstream disturbances created, flow analysis in the field around the body, complete definition of the flow parameters in the jets used. Comparisons and correlations will be more mean-ingful if the flow conditions under which they are done are fully defined.

Mr Antonatos: I believe there was some discussion this morning concerning the effect of the internal flow, the distortion of the internal flow, that type of parameter, to ensure that you are getting the right conditions to be able to determine what your nozzle/nozzle-afterbody effects would be.

Mr Walker: I would like to comment on Dr Ferri's comment a while ago. In looking over nozzle afterbody work for the last 7 years and trying to make it work practically, I find that the analytical, so-called theoretical treatment of flow is far worse when one is trying to correlate something than a very bad wind tunnel. The noise in the analytical treatment is at least as bad as a noisy wind tunnel. Although we are dealing with a completely new science or art, I have heard only one mention in this whole meeting of something that is new that applies to this art. I think that we are trying to bend the old aerodynamics and the old parameters around to fit something new and something that they do not fit. The one mention of something that was new, and directly applicable to nozzle afterbody, is the IMS value, which describes the geometry of the afterbody. I would like to challenge this panel to look for something more applicable to our part-body aerodynamics.

Prof Ferri: You assume that I claim that you can calculate better than you can measure. I was just stating, that if you make an analysis, and you find that your support influences the flow field as much as the model you tested, then without necessarily believing all the analysis I would question the test results. This is the extent of the use of the analysis. The point I tried to get across, really there are two. The experiments are very difficult to perform. I am not criticizing the experiments because they are difficult to do. You need to support the model, you need to have a wind tunnel that has small dimensions; usually you cannot get the right Reynolds Number, so you must trip the boundary-layer. The only comments I would make are that we should spend more time in understanding the limitations of our experiments and spend less time making lots of experiments we do not understand. My comments were not a criticism, just a suggestion.

M. Laynaert: Je dois d'abord m'excuser de ne pas avoir cité M. Nancia, dont je connais bien le travail.* Effectivement, le problème des limites de fonctionnement d'une entrée d'air supersonique en dérapage est fortement lié au fait que les chocs de la compression supersonique pénètrent localement sous la carène de l'entrée d'air, du fait du dérapage. Le travail de M. Nangia comportait l'étude d'une dièdre placé sur une plaque plane en incidence. L'écoulement ainsi obtenu se rapproche beaucoup de ce qui se passe sur le côté d'une entrée d'air, qui comporte un premier dièdre et dont le flan latéral représente la plaque plane en incidence. Toutefois, seul le cas d'une flanc lateral sans flèche a fait jusqu'ici l'objet d'une étude analytique, l'étude de M. Nangia sur un flanc avec flèche étant essentiellement experimentale. Mais il est certain que c'est une étude très interessante, et que c'est en travaillant dans cette direction là, qu'on fera des progrès dans le prédétermination, par exemple, des découpes de carènes, pour ameliorer le fonctionnement d'une prise d'air en dérapage.

J'avais une autre remarque, sur le problème de l'arrière-corps et des nombres de Reynolds. Je ne suis peut-être pas aussi pessimiste que le Professeur Ferri. J'ai remarqué, quand même, que l'une des principaux résultats du travail de l'AGARD a été de démontrer qu'on avait à peu près le même effet quand on augmente le nombre de Reynolds que lorsqu'on reduit la couche limite par un soufflage pariétal. Ceci semble bien indiquer que l'effet principal du nombre de Reynolds est de réduire la couche limite, et que, cet effet, on le reproduit correctement en soufflerie à faible nombre de Reynolds en ajustant la couche limite, par exemple, par un soufflage. Je pense que cette orientation nouvelle va certainement se généraliser et que, pour des études d'arrière-corps sur des montages par dard amont on verra de plus en plus des dispositifs permettant de faire varier la couche limite pour étudier avec une chance raisonnable de succès l'influence du nombre de Reynolds, sous une forme artificielle, puisque on ne peut pas obtenir de très grands nombres de Reynolds en soufflerie.

Mr Antonatos: He was referring really at the end there to adjusting the boundary layer when you have a low Reynolds Number in a complicated configuration, where you have to understand the boundary layer before you have any results, so that you know that you are matching properly.

Prof Ferri: First let me answer M. Leynaert's suggestion. We have done some work that is along the same line, changing the boundary layer characteristics in transonic flow by injection and suction. By two controls you can change the velocity profile, the temperature profile, density profile, and you can simulate time-independent quantities, for example, the velocity profile, fairly well. However, we found that the time-dependent characteristics: for example the spectrum of turbulence changes substantially with respect to a natural boundary layer. Now in order to use this kind of approach, we should convince ourselves that the time-dependent characteristics of the boundary layer are not important for local flow separation. I am not convinced at all that this is so. The other point that has been raised here is that if we look at the practical problem, in the practical problem the boundary layer is three-dimensional. You have a local separation in some regions, and you have a different separation in others. When you talked about three-dimensional boundary layer, we know so little that we cannot really try to simulate it. This is my main worry,

---

* R. K. NANGIA. Three-dimensional wave interactions in supersonic wakes. 2nd I.S.A.B.E. March 1974, Sheffield.

for example, in twin jet testing, because we do not really know how the boundary layer behaves and what produces a local separation in three-dimensions; therefore I am not sure that this approach could be generalized for a practical configuration.

Mr Antonatos: The reason I brought it up is that in Mike Brazier's paper he talked about having exact geometric simulation in the wind tunnel. It seems to me that the geometric simulation is not compatible with the complete flight test results because of the boundary-layer conditions, the viscous effects would be completely different in a low Reynolds Number tunnel as compared to a high Reynolds Number flight test. For example, locating a splitter: where would you put the splitter plate to ensure that you are getting the proper duplicative results?

Prof Ferri: Also, for the nozzle you have two Reynolds numbers, i.e., the Reynolds number of two boundary layers, the inside and outside, and you must simulate both in order to really have the right mixing downstream. Until now we never simulated everything in the windtunnel, and we never will be able to simulate everything in the windtunnel. We try to make a really high Reynolds Number windtunnel, with the illusion that this will solve our problems. Still you will have a support, still you will have some non-uniformity, so you need to be more intelligent and not to have a bigger tool. This is the point that we really many times overlook. You need to be able to understand much more with respect to the limitations of your special experiment. I never will be convinced that you can make a windtunnel experiment that represents flight conditions, and never make a flight test that represents windtunnel conditions. I think we should understand more of the physics of the phenomena and be sure that the important parameters are represented. This requires that you be much more careful when you make an experiment. You must measure a lot more things, control a lot more things, and do a lot more analysis. This we are not doing.

Prof Murthy: Is there some serious difficulty in providing us some more measurements other than just model wall pressure measurements? Is it difficult, for example, to trace one more stream line in the flow?

Without such additional data, I think the flow field is rather incomplete for any kind of analysis.

Mr Antonatos: It is difficult in the sense that we have done some work in measuring another parameter at the wall which is the local angle near the wall.

Well, I do not think it is that difficult, it is just another time-consuming part of the experiment. That is what it boils down to. In developing some of these better approaches, for example, in looking at the wall corrections a little better than we have in the past, it requires much more sensitive equipment than we have used in the past. Some of the flow inclination equipment that we have had to use has to measure things in the order of a minute of deflection, and this is rather difficult.

Prof Ferri: We are going in the opposite direction. We try to convince ourselves that we need much bigger and much more expensive facilities. Now, when we have one of these facilities, you can do much less measurements because you have a tremendous cost and so you cannot run long tests. I believe that we must convince ourselves to use a lot of small facilities in which you can do a lot of good experiments and make a few experiments in the large facility. So, I would like, when you build a big huge windtunnel, I would like you to build three or four small wind tunnels so that people can play around and become more intelligent in what they measure in the big wind tunnel.

Mr Antonatos: I would like to point out here that there is a MiniLaWs Group here that is going to look at some of these testing techniques and be able to report on them at some future date.

I would like to conclude this afternoons Round Table. I think along with the conclusions we received from the sessions up to this morning, we have probably achieved some further conclusions which still indicate the inconclusiveness of the work that we are doing and the data that we are obtaining. However, I would like to thank the members of the Round Table and the members who participated from the various countries as coordinators, for getting these papers for presentation today. I would like to thank the authors and the session chairmen for a wonderful job in giving us a lot of room for thought. I hope we renew some portions of this discussion at some future date.

At this time I would like to turn the meeting over to Dr Küchemann, the Chairman of the Fluid Dynamics Panel.

Prof Küchemann: Ladies and Gentlemen, we are coming to the end of our Symposium, and I would like to say that it did confirm some of the things that I said at the beginning. I would like to point out that apart from Mr Antonatos, M. Carrière, M. Auriol and myself — the only ones who still have a jacket and a tie on — we seem to be a company of workers, and that we have really worked hard. If I look around I can see the workers. If we had been Managers or Ministry Officials, we might have repaired long ago to a bar or a swimming pool and would not be here any more.

The fact that we have all stuck it out all these long four days means that we really are interested and that what was going on was interesting. The second thing that has been confirmed to me is that the aerodynamics of propulsion is really a fascinating subject, and I am convinced that this will be so for a very long time. AGARD can be sure to be occupied with these problems for many years to come.

At this meeting, we have had some people who said that they could compute the interference between an engine nacelle, a wing, a fuselage, and struts; and that it would all work out fine. We have had other people who could not even sort out what happens on a simple body of revolution. That means to me that there is a lot more to be done. I do not quite agree with Professor Ferri, that we do not need new facilities. I think that if we really want to sort out what is going on at higher Reynolds Number we had better build some new facilities. But I do agree with him that it is no use having a facility, and the same goes for a computer, unless we understand the physics. We obviously must feed into the computer what the physics of the problem are. The computer will not sort it out for us, nor will the windtunnel. Only intelligent experiments will help us further. I do hope that progress will be made on both fronts, on the theoretical and on the experimental side, and that some day we shall have answers to the many questions, which we obviously cannot answer now. Some of the problems are related to the phenomenon of flow separation. It has come up occasionally during this meeting. As you know, the Fluid Dynamics Panel is going to have a Symposium next spring on the subject of flow separation, and I hope to see some of you there to discuss these problems, which are obviously so very important.

Now, it remains to thank all the many people who have helped to make this meeting so successful. I did thank our Italian hosts last night. Today, I would like to add the thanks of all of us to Mr Antonatos and his Program Committee, to the authors, the members of the Round Table Discussion, and all those who contributed to the discussion. I would like to mention our Executive, and his secretary, who have done so much to help here. Speaking of AGARD, I think that we have demonstrated very convincingly how well various Panels of AGARD work together. For example, we have the Chairman of the Propulsion and Energetics Panel, Mr Jaarsma, helping us on our Round Table Discussion, and our Executive was supported by the Executive of the Propulsion and Energetics Panel. We do help one another out to the benefit of everybody. Lastly, I think that we should thank the interpreters, who stuck it out in a little box all these four days. One thing I noticed was the considerable variations you can have in the English language and in the speed with which it is delivered. One man, I know, who was London born and should really know it, probably spoke slowest of all, whereas other people who certainly were not born in London and who had to learn this tongue, spoke very fast, so fast that the poor interpreters could not keep up with them. What that means for the future of the English language, I really do not know. Maybe the Englishmen have to speed up or the others slow down.

I think this brings us to the end of our meeting and thank you very much for taking part. I hope you will find it worthwhile.